Handbook on the Physics and Chemistry of Rare Earths, volume 19

Lanthanides/Actinides: Physics II

Elsevier, 1994

Edited by: Karl A. Gschneidner, Jr., LeRoy Eyring, G.H. Lander and G.R. Choppin
ISBN: 978-0-444-82015-0

PREFACE

Karl A. GSCHNEIDNER, Jr., LeRoy EYRING, Gerry H. LANDER and Gregory R. CHOPPIN

These elements perplex us in our rearches [sic], *baffle us in our speculations, and haunt us in our very dreams. They stretch like an unknown sea before us – mocking, mystifying, and murmuring strange revelations and possibilities.*

Sir William Crookes (February 16, 1887)

This volume of the Handbook is the third of a three-volume set of reviews devoted to the interrelationships, similarities, differences and contrasts of the lanthanide and actinide series of elements. The idea of these volumes grew out of a conversation between one of the editors, KAG, and a member of the editorial board, Stefan Hüfner, in early June 1986. This idea was enthusiastically received by the other editor (LE) and editorial board members, and also the publishers. Numerous topics and authors were suggested and soon it was apparent that this special subject was too large to be covered in one or possibly two volumes, and that the editors (KAG and LE) of this series would need help from two leading scientists who had considerable experience and knowledge of both series of elements. Thus, Gerry H. Lander and Gregory R. Choppin were invited to be guest editors for this special set of volumes on the lanthanides/actinides. After they accepted, the four editors carefully and critically chose the various topics, and top experts in the various areas were invited to write reviews keeping in mind that the emphasis was to be on the interrelationships of the lanthanides and actinides. Now, more than seven years after Stephen Hüfner's initial suggestion, the first volume, which is devoted to the physical aspects, and the second volume, which emphasizes chemical comparisons, are in print. In this volume additional physical topics are covered.

The observations and comments of Sir William Crookes (as noted above) over 107 years ago about the lanthanides are even more appropriate to these lanthanide/actinide volumes. This is especially noteworthy because only two of the actinide series of elements were then known (Th and U), and the concept of such a series was not to develop for about 50 years. But we hope that the material presented in these three lanthanide/actinide volumes will shed light on some of the mysteries of yesterday, but as surely as we begin

to understand them, new ones will arise to continue to haunt us as we move forward and ever onward.

This volume comprises five chapters on the comparative physics and thermodynamics of the lanthanide and actinide materials. The first two chapters are concerned with neutron scattering studies, while the next two are concerned with physical property studies involving electronic, thermal and magnetic behaviors, and the final chapter covers the thermodynamic properties of metallic systems.

The lead-off chapter (130) by Holland-Moritz and Lander compares the neutron inelastic scattering behaviors of the lanthanides and actinides. Neutron inelastic scattering is useful in probing dynamical processes which occur in solids, especially low energy elementary excitations. The authors have narrowed their coverage to the anomalous lanthanides (cerium, samarium, europium, thulium and ytterbium) and primarily uranium of actinide series elements. The systems covered include: those in which the crystal-field interaction dominates; systems that magnetically order, but in which the f–d hybridization is significant; mixed (or intermediate) valent materials which do not exhibit sharp excitations; and strongly interacting systems such as heavy fermions.

Chapter 131 by Aeppli and Broholm builds on the first chapter in this volume and concentrates on neutron scattering by heavy fermion single crystal materials. These compounds include metallic materials with a paramagnetic ground state, superconductors, metallic and semiconducting antiferromagnets, and nearly insulating paramagnets. The most important contribution of these single crystal neutron scattering studies has been the demonstration of strong antiferromagnetic (AFM) correlations in heavy fermion systems. These strong AFM correlations distinguish the concentrated heavy fermion materials from their dilute Kondo relatives, and possibly account for the observed metamagnetic and unconventional superconductivity phenomena.

The chapter by Wachter (132), which is one of the most extensive and comprehensive ones in the entire Handbook series, reviews intermediate valence and heavy fermions in a wide variety of lanthanide and actinide compounds, ranging from metallic to insulating materials. The behaviors of these materials are discussed from the basic idea that a gap exists between two narrow f-like subbands, i.e. the hybridization gap model, which can account for the observed physical and electronic properties. As pointed out by Wachter, heavy fermions are intermediate valence materials by virtue of the fact that they have non-integral f occupation values. The main difference between normal intermediate valence materials is that their Fermi energies are in the hybridization gap, while for the heavy fermion materials the Fermi energy is *not* in the gap.

In chapter 133 Thompson and Lawrence have focused on two issues on the high pressure behaviors of anomalous cerium, ytterbium and uranium compounds. The first is concerned with the degree to which the pressure response of the electrical resistivity, magnetic susceptibility and heat capacity is similar in the given class of materials, and how this pressure dependence is related to the Grüneisen constant obtained from ambient pressure measurements. The second issue deals with how well this comparison holds in both anomalous lanthanide and actinide materials. They have shown that although there is some consistency in their high pressure behaviors to a level of ± 10–20%, there are still many issues, e.g. validity of scaling laws, equality of electronic and

magnetic Grüneisen parameters, which are not well established, and this leaves substantial work for the future.

The last chapter (134) in this volume is an extensive review by Colinet and Pasturel of the thermodynamic properties of lanthanide and actinide metallic systems. In addition to compiling useful thermodynamic data, such as enthalpies, entropies, and free energies of formation and of mixing, the authors have made an extensive comparative analysis of the thermodynamic behavior of the rare earths and actinides when alloyed with metallic elements. They note that when alloyed with non-transition metals, the enthalpies of formation of uranium alloys are *less* negative than those of the rare earths while those of thorium and plutonium are about the same as the latter. For transition metal alloys the formation enthalpies of thorium and uranium are *more* negative than those of the rare earths and plutonium (the latter two are about the same). The anomalous behaviors of cerium, europium and ytterbium in various compounds and alloys are also discussed along with the effect of valence state changes found in uranium and plutonium alloys.

Dedicated to

GLENN T. SEABORG

Among the many noteworthy scientific achievements of the 20th century, there are only a very few that can match the discovery of the actinide elements in its impact on science and society. The addition of an entire new family of largely man-made elements to the Periodic Table, and the formulation of the actinide concept have had a profound influence on the way physicists and chemists think about the electronic structures of the elements. The new insights arising from studies on the chemistry and physics of the heaviest elements has had an especially important influence on the way we think about the more familiar elements of the Periodic Table, in particular, the rare earths. In the saga of the actinide elements, Glenn Seaborg has been the pivotal figure. The dedication to Glenn Seaborg of these volumes of *the Handbook on the Physics and Chemistry of Rare Earths,* which deal with the relationships of the lanthanide and actinide elements, is thus a fitting recognition of the exceptionally important contribution that his actinide element studies have made to many branches of science.

Glenn Seaborg's scientific career began in the 1930's as a research associate of G.N. Lewis at the University of California. He early became convinced that the science of nuclear chemistry, then in its infancy, provided challenging opportunities for scientific discovery. In the Lawrence Radiation Laboratory, in the course of a few years, he validated his intuition by the discovery of a host of isotopes, many of which have become important in research and medicine. Among these are cobalt-60, iodine-131, technetium-99m, cesium-137, and, of course, the plutonium isotopes. In 1944, he formulated the actinide concept of heavy-element electronic structure that accurately predicted the existence of a family of rare earth-like elements at the end of the Periodic Table as it was generally presented at that time. The actinide concept was the guide to the discovery of the remaining members of the actinide elements. In addition to the fissile plutonium isotopes, he and his co-workers over the years discovered no less than nine additional members of the new rare earth-like family of elements. These discoveries have been of great relevance not only to purely scientific matters but also to such global problems as nuclear energy and the control of nuclear weapons.

In addition to his life as an active scientist, Glenn Seaborg has had a distinguished career in academic and public life. He served at various times as Chancellor of the University of California at Berkeley, Chairman of the Atomic Energy Commission for a period of ten years, and Chairman of the Lawrence Hall of Science, to name only a few of his extra-scientific activities. He was the recipient of a Nobel Prize (1951) for his

discoveries in the chemistry of the transuranium elements, and has received encomiums from most of the scientific societies of the world.

In spite of worldly distractions, Glenn Seaborg has never wavered in his life-long commitment to science. He continues his research into the chemistry and nuclear systematics of the actinide elements. Recently, he has focused his attention on the possible existence of still another family of superheavy elements at the end of the Periodic Table, and the development of new methods for the synthesis of superheavy elements. The dedication of these volumes to Glenn Seaborg is not only a testimonial to his scientific achievements, it is also an appreciation of the example that he continues to set.

J.J. Katz
December 5, 1991

CONTENTS

CONTENTS OF VOLUMES 1–18

VOLUME 4: Non-metallic compounds – II

1979, 1st repr. 1984; ISBN 0-444-85216-6

VOLUME 5

1982, 1st repr. 1984; ISBN 0-444-86375-3

VOLUME 6

1984; ISBN 0-444-86592-6

VOLUME 7

1984; ISBN 0-444-86851-8

VOLUME 8

1986; ISBN 0-444-86971-9

VOLUME 9

1987; ISBN 0-444-87045-8

VOLUME 10: High energy spectroscopy

1988; ISBN 0-444-87063-6

VOLUME 11: Two-hundred-year impact of rare earths on science

1988; ISBN 0-444-87080-6

VOLUME 12

1989; ISBN 0-444-87105-5

VOLUME 13

1990; ISBN 0-444-88547-1

VOLUME 14

1991; ISBN 0-444-88743-1

VOLUME 15

1991; ISBN 0-444-88966-3

MASTER INDEX, Vols. 1–15
1993; ISBN 0-444-89965-0

VOLUME 16
1993; ISBN 0-444-89782-8

VOLUME 17: Lanthanides/actinides: Physics – I
1993; ISBN 0-444-81502-3

VOLUME 18: Lanthanides/actinides: Chemistry
1994; ISBN 0-444-81724-7

Handbook on the Physics and Chemistry of Rare Earths
Vol. 19 – Lanthanides/Actinides: Physics – II
edited by K.A. Gschneidner, Jr., L. Eyring, G.H. Lander and G.R. Choppin

Chapter 130

NEUTRON INELASTIC SCATTERING FROM ACTINIDES AND ANOMALOUS LANTHANIDES*

E. HOLLAND-MORITZ
II. Physikalisches Institut, University of Cologne, 50937 Cologne, Federal Republic of Germany

G.H. LANDER
European Commission, Joint Research Centre, Institute for Transuranium Elements, Postfach 2340, 76125 Karlsruhe, Federal Republic of Germany

Contents

* We dedicate this chapter to the memory of Dieter Wohlleben and Jean Rossat-Mignod, who did so much to stimulate the physics of unstable f systems.

Symbols and abbreviations

barn	unit of cross section ($=10^{-24}$ cm^2), denoted also by b
CF	crystal field
C_2	coefficient of $\langle j_0 \rangle$ in the magnetic form factor
D	stiffness constant in the dispersion relationship
E_A	anisotropy gap in excitation spectrum
E_F	Fermi level
E_i or E_0	incident neutron energy in experiments
E_f	final neutron energy
FWHM	full width at half maximum (usually $=\Gamma$)
$f(\boldsymbol{Q})$	magnetic form factor
g_J	Landé g-factor
g_N	gyromagnetic ratio of the neutron ($=1.91$)
HET	high-energy transfer spectrometer at ISIS (Rutherford Laboratory, UK)
HF	heavy fermions
HWHM	half-width at half maximum (usually $=\Gamma/2$)
ILL	Institute Laue-Langevin, Grenoble, France
INE	inelastic contribution to the scattering response
IN4	time-of-flight spectrometer using thermal neutrons at ILL
IN6	time-of-flight spectrometer using cold neutrons at ILL
IMT	intermultiplet transitions
ISIS	spallation neutron source at Rutherford-Appleton Laboratory (RAL), Chilton, UK
IV	intermediate valence
J_{ex}	exchange integral
$\boldsymbol{k}$	wavevector of magnetic structure
k_B	Boltzmann's constant
$\boldsymbol{k}_i$ or $\boldsymbol{k}_0$	initial neutron wavevector
$\boldsymbol{k}_f$ or $\boldsymbol{k}_1$	final neutron wavevector
N_f	degeneracy of the magnetic ground state
n_f	fractional occupation number of the magnetic ground state
$N(E_F)$	density of electron states at the Fermi level
$P(\boldsymbol{Q}, \omega, T)$	spectral function defined in eqs. (6, 10)
$\boldsymbol{Q}$	momentum transfer or scattering vector
$\boldsymbol{q}$	reduced wavevector in the first Brilloiun zone
QE	quasielastic contribution to the scattering response
r_e	classical electron radius
rlu	reciprocal lattice units
$S(\boldsymbol{Q}, \omega, T)$	scattering function (see eq. 1 et seq.)
T	temperature
T_C	Curie temperature (ferromagnetic ordering)
T_K	Kondo temperature
T_N	Néel temperature (antiferromagnetic ordering)
T_{VF}	valence fluctuation temperature
t	time
$U_f^2(r)$	single-electron density distribution
Z	sum over all the states
α	ratio n_f/N_f in Kuramoto–Müller-Hartmann theory
β	$1/(k_B T)$
$\chi_{bulk}(T)$	bulk susceptibility, see eq. (12) $[=\chi'(0, 0, T)]$

$\chi^{st}(Q, T)$	local static susceptibility, see eq. (5) [$=\chi'(Q, 0, T)$]	γ	Sommerfeld coefficient of electronic specific heat, in mJ mol^{-1} K^{-2}
$\chi^{st}_{n,m}$	contribution of individual levels to the static susceptibility (eqs. 5, 7)	η	Korringa constant in eqs. (15, 16)
$\chi'(Q, \omega, T)$	real part of the magnetic susceptibility, see eq. (5)	μ	magnetic moment, in Bohr magnetons (μ_B)
$\chi''(Q, \omega, T)$	imaginary or dynamic part of the magnetic susceptibility, eq. (3)	μ_B	Bohr magneton
Δ	position in energy of inelastic line	μ_L	orbital component of magnetic moment
Δ_{nm}	energy differences between states n and m	μ_S	spin component of magnetic moment
ε_f	characteristic energy	ν	used to denote valence of the material
ϕ	scattering angle (also θ)	θ	scattering angle (also ϕ)
Γ	full width at half maximum (FWHM) of quasielastic response function, see eq. (10)	σ_a	absorption cross section
Γ_0	full width at half maximum at $T = 0$ K	σ_{mag}	total magnetic cross section, eq. (8)
		τ	time constant of decay to 1/e of relaxation process, eq. (11)
		$(1 - e^{-\beta\omega})^{-1}$	detailed balance factor (see eq. 3 et seq.)

1. Introduction

1.1. *General remarks*

Neutron inelastic scattering is a particularly appropriate probe for studying the dynamical processes in solids. In this chapter we shall be covering the dynamical processes involving the unpaired f (and possibly d and s) electrons in actinide (5f) and anomalous lanthanide (4f) systems. The properties of neutron scattering that we make use of are: (a) the neutron has a magnetic moment that interacts with the unpaired electrons in the solid, and (b) the energy of thermal (25 meV $\approx$ 295 K) neutrons is small; in contrast, photons of the same wavelength have an energy of 6.8 keV. Since this energy of the neutrons is comparable to that of elementary excitations in solids, the *change* in the neutron energy after an interaction with an elementary excitation is usually large, and easily measurable. Furthermore, the finite mass of the neutron means that momentum is involved in any scattering process so neutron experiments probe both energy and wavevector space *simultaneously*. In this aspect they are unique.

This chapter will be concerned primarily with neutron inelastic *magnetic* scattering. The lanthanides have their 4f wavefunctions well shielded from their nearest neighbors so that the electronic structure and magnetism of most lanthanide systems are rather well understood in terms of localized 4f moments (Jensen and Mackintosh 1991). However, in some cases, notably most compounds of Ce and some of Sm, Eu, Tm, and Yb, they form a more complex ground state (Wohlleben and Coles 1973). In the case of the four last elements this complex ground state is a consequence of the two 4f configurations being close in energy, e.g., Sm^{2+} ($4f^6$) and Sm^{3+} ($4f^5$), so that some combination of them, or fluctuation between them (intermediate valence, IV), is possible. The physics

of Ce compounds is often different to that of the other anomalous rare-earths, although it is not possible to make a complete separation. The single 4f electron around the nucleus in the Ce^{3+}: $4f^1$ configuration has a spatial character much more extended than the other lanthanides. In this respect it is similar to the actinides, where the 5f electrons are considerably extended spatially (Desclaux and Freeman 1984). As a result, in Ce and actinide compounds (where we limit our discussion of actinides to U, Np, and Pu) the f-electron wavefunction may interact not only with the conduction d and s states, but also with electron wavefunctions from neighboring ions.

Our discussion will be centered on these anomalous lanthanides and the actinides. For completeness we shall also discuss certain actinide systems, such as the oxides, which do not at first glance fit into the above category. However, important work has been done since the last review (Buyers and Holden 1985) so that this coverage is justified. There is, as yet, no direct analogy in the actinides of the intermediate-valent systems as proved by neutron scattering, and other measurements, in the lanthanides. PuTe may be just such a system, but no inelastic experiments have been reported; we cover this aspect of lanthanides to show the general progression from localized moment systems to the strong Kondo regime. In the case of heavy fermions (Stewart 1984) the valence is almost integral, but there is an interaction between f and conduction-electron states to form a so-called quasi-particle, and then there are strong interactions between the quasi-particles. It is no coincidence that heavy fermions are found *only* in Ce, U, and Np compounds. A separate chapter (Aeppli and Broholm 1994) on neutron scattering from single crystals of heavy fermions follows this chapter.

After a brief review of the neutron formalism, we shall give examples of systems in which the crystal-field interaction dominates (sections 2, 3), then turn to systems that order, but in which the f–d hybridization is significant (sect. 4), then cover materials with intermediate valence (sect. 5), which do not exhibit sharp excitations, and conclude with strongly interacting systems, such as heavy fermions (sect. 6). The conclusions are given in sect. 7. Except for the heavy fermions, the rationale for this order is that it corresponds to increasing hybridization between the 5f and other electron states. We have placed heavy fermions at the end because they are the most complex materials we will discuss, and, in addition, the chapter by Aeppli and Broholm (1994) covers them.

1.2. *Neutron scattering formalism*

Here only those basic neutron scattering facts will be explained that are important for the later discussion of the experimental data. A more detailed description of the neutron scattering technique will be found in the books by Bacon (1975), Marshall and Lovesey (1971), Squires (1978), and Lovesey (1984). A good theoretical overview on the magnetic relaxation in solids is given by White (1970, second edition 1983).

The interactions between neutrons and the magnetic electrons in materials are rather small. Cross sections are typically few barns (10^{-24}cm^2). This, together with the relatively low flux of neutrons available from present day sources, requires the use of large (>5 g) samples for inelastic scattering investigations on polycrystalline samples. The advantage

of neutron studies is that they are a microscopic probe, giving exact information on quantities that can be calculated from first principles.

In addition to the large quantities required, which immediately precludes any inelastic studies of transplutonium materials, we should mention another disadvantage that is often serious in 4f and 5f elements: the problem of absorption resonances. These occur for particular energies and isotopes and the neutron is then strongly absorbed to create an excited state that (usually) decays to give a γ-ray. The most abundant isotopes of Eu, Sm, Gd, Np, and Pu all suffer from high absorption in the energy range of interest in inelastic studies (1–1000 meV). In some cases other isotopes may be used, but this is often expensive, and in the case of Np, for example, none exist. In this sense, therefore, inelastic scattering of f systems is often more complicated than for d based materials, in which the offending resonances occur in the keV rather than eV range.

The two principal neutron interactions are:

(1) *Nuclear interactions* between the neutron and the nucleus giving most of the elastic scattering and the inelastic scattering from the phonon contributions. The phonon contribution will consists of a number of terms: the normal one-phonon, two-phonon (multiphonon) contribution from the coherent part of the cross section, and the density-of-states of the total phonon spectrum as seen by the incoherent cross section. Naturally, the ratio of these two contributions will depend on the relative coherent and incoherent cross sections.

(2) *Magnetic interactions* between the magnetic moment of the neutron and the unpaired electrons of the system under investigation. The magnetic response function, which we discuss below in detail, can also contain many contributions. If the material orders and there are spin waves then scattering from a polycrystalline material will contain contributions similar to the contributions from phonons mentioned above. Other contributions can arise from (single-ion) crystal-field or spin–orbit interactions and relaxation processes are observed by broadening effects in a generalized $S(\boldsymbol{Q},\omega)$. There is no analogy to the nuclear incoherent cross section in magnetic scattering, as we assume that the moments are *equal* on each magnetic ion (recall that the incoherent nuclear cross section arises from the random distribution of nuclei of different isotopes and thus different scattering amplitude).

The presence of two major contributions to the scattered intensities immediately poses the question of how to separate them, particularly as the magnetic contribution, which is the one we want to study, is usually the weaker of the two. The only unambiguous method is polarization analysis (Moon et al. 1969), but in practice this technique has two flaws, namely, the intensity is decreased and the resolution is worse. A few examples of using this technique will be presented in this chapter; however, for the most part other methods of separating the nuclear and magnetic parts are used. The reader should be aware that aspects of some of these methods are controversial.

Whereas in the chapter by Lander (1993) only the spatial component of the magnetic cross section was discussed, we must now include the dynamics, i.e., the cross section must be extended to the full double differential cross section. The full information is

given by the scattering function $S(\boldsymbol{Q},\omega,T)$,

$$\frac{\mathrm{d}^2\sigma}{\mathrm{d}\omega\,\mathrm{d}\Omega} = \frac{k_\mathrm{f}}{k_\mathrm{i}} S(\boldsymbol{Q}, \omega, T), \tag{1}$$

where k_i and k_f are the magnitude of the incident and scattered wavevectors, respectively, and the momentum transfer $\boldsymbol{Q} = \boldsymbol{k}_\mathrm{i} - \boldsymbol{k}_\mathrm{f}$. We use $h/2\pi = 1$ for convenience in the formulae. There are three different styles of presenting the scattering law. First, starting from Fermi's golden rule and using the well known magnetic interaction potential one can write the scattering law in terms of a correlation function (see e.g., White 1970, 1983):

$$S(\boldsymbol{Q}, \omega, T) = \frac{1}{2}\left(\frac{g_\mathrm{N} r_\mathrm{e}}{\mu_\mathrm{B}}\right)^2 \frac{1}{2\pi} \int_{-\infty}^{\infty} \langle\{M(\boldsymbol{Q}, 0)\, M(-\boldsymbol{Q}, t)\}\rangle_\mathrm{T}\, \mathrm{e}^{\mathrm{i}\omega t}\mathrm{d}t. \tag{2}$$

Here $g_\mathrm{N} = -1.91$ is the gyromagnetic ratio of the neutron, $r_\mathrm{e} = 2.82 \times 10^{-13}$cm the classical electron radius, and μ_B is the Bohr magneton. The factor $(1/2)(g_\mathrm{N} r_\mathrm{e})^2$ is 0.145 barn, and gives the relationship between the magnetic moment and the magnetic cross section. In this form the scattering is given by the Fourier transform of the temporal correlation function $\langle\{M(\boldsymbol{Q}, 0)\, M(-\boldsymbol{Q}, t)\}\rangle_\mathrm{T}$, which includes an averaging over the temperature of the sample. Thus eq. (2) has meaning in a conceptual sense.

The second, more practical, expression is in terms of the dynamic magnetic susceptibility $\chi''(\boldsymbol{Q}, \omega, T)$. Its connection to the correlation function described by eq. (2) is given via the fluctuation dissipation theorem,

$$\int_{-\infty}^{\infty} \langle\{M(\boldsymbol{Q}, 0)\, M(-\boldsymbol{Q}, t)\}\rangle_\mathrm{T}\, \mathrm{e}^{\mathrm{i}\omega t}\, \mathrm{d}t = \frac{2}{1 - \mathrm{e}^{-\beta\omega}} \chi''(\boldsymbol{Q}, \omega, T), \tag{3}$$

where $\beta = (k_\mathrm{B} T)^{-1}$ and the term $(1 - \mathrm{e}^{-\beta\omega})^{-1}$ is the so-called detailed balance factor which is related to the number of possible states occupied at a certain temperature. Then eq. (2) can be written as

$$S(\boldsymbol{Q}, \omega, T) = \frac{1}{2}\left(\frac{g_\mathrm{N} r_\mathrm{e}}{\mu_\mathrm{B}}\right)^2 \frac{1}{\pi} \frac{1}{1 - \mathrm{e}^{-\beta\omega}} \chi''(\boldsymbol{Q}, \omega, T). \tag{4}$$

By using the Kramers–Kronig relation ($\omega' = 0$) that connects the real χ' and imaginary parts χ'' of the susceptibility, we find

$$\chi''(\boldsymbol{Q}, \omega, T) = \pi\omega \sum_{n,m} \chi'_{n,m}(\boldsymbol{Q}, \omega' = 0, T)\, P_{n,m}(\boldsymbol{Q}, \omega, T). \tag{5}$$

Here

$$\sum_{n,m} \chi'_{n,m}(\boldsymbol{Q}, \omega' = 0, T) = \sum_{n,m} \chi^{\mathrm{st}}_{n,m} = \chi^{\mathrm{st}}(\boldsymbol{Q}, T)$$

is the local susceptibility, where the Curie terms are represented by $n = m$ (quasielastic in nature) and the van Vleck terms by $n \neq m$. $P(\boldsymbol{Q}, \omega, T)$ is any spectral function such that

$$\int_{-\infty}^{+\infty} P(\boldsymbol{Q}, \omega, T)\, \mathrm{d}\omega = 1. \tag{6}$$

Using eq. (5) the above eq. (4) can be rewritten as

$$S(\boldsymbol{Q}, \omega, T) = \frac{1}{2}\left(\frac{g_N r_e}{\mu_B}\right)^2 \frac{\omega}{1 - \mathrm{e}^{-\beta\omega}} \sum_{n,m} \chi^{\mathrm{st}}_{n,m}(\boldsymbol{Q}, T)\, P_{n,m}(\boldsymbol{Q}, \omega, T). \tag{7}$$

The strength of the inelastic magnetic response is directly proportional to the static susceptibility, but only in special cases is it proportional to the localized magnetic moment (Holland-Moritz 1985). The latter can be extracted only by a complete integration over the double differential cross section

$$\sigma_{\mathrm{mag}} = 4\pi \int_{-\infty}^{\infty} S(\boldsymbol{Q}, \omega, T)\, \mathrm{d}\omega. \tag{8}$$

The static susceptibility can be written from eqs. (7) and (8) as

$$\chi^{\mathrm{st}}_{nm}(T) = \frac{\sigma_{nm}(T)\mu_B^2/1.82}{\int_{-\infty}^{\infty} \frac{\omega}{1-e^{-\beta\omega}} P_{nm}(\boldsymbol{Q}, \omega, T)\, \mathrm{d}\omega}, \tag{9}$$

where $2\pi(g_N r_e)^2 = 1.82$. Due to the effects of detailed balance, such an integration can be performed easily only in the limit of sharp magnetic lines. Assuming $\delta(\omega - \Delta_{nm})$ for the spectral function, the integration results in the Curie ($n = m$) and the van Vleck ($n \neq m$) terms for the static susceptibility with effective moments proportional to the magnetic cross sections. Here Δ_{nm} is the transition energy from the nth to the mth level and $\Delta_{nm} = 0$ for $n = m$. For broad lines, especially those quasielastic in nature, the integration must be performed numerically. The resulting cross section usually has a rather large uncertainty as the shape of the scattering response is unknown for high-energy transfers. The Lorentzian ansatz is commonly used for the cross section and fits to most data, at least for low energies,

$$P(\boldsymbol{Q}, \omega, T) = \frac{1}{\pi} \frac{\Gamma/2}{(\Gamma/2)^2 + \omega^2}. \tag{10}$$

Note that the *full* width at half maximum (FWHM) of this function is Γ. We shall retain this nomenclature throughout. However, the reader should be aware that the use of FWHM $= 2\Gamma$ also occurs in the literature. The assumption of this form for $P(\boldsymbol{Q},\omega,T)$ implies an exponential form for the decay of the temporal correlations

$$\langle\{M(\boldsymbol{Q}, 0)M(-\boldsymbol{Q}, t)\}\rangle_T \propto \exp(-|t|/\tau), \tag{11}$$

where τ is the time constant describing the temporal relaxation. This function has a cusp at $t=0$, i.e., a discontinuity in the first derivative, and this implies an unphysical behavior at small t. Therefore, the Lorentzian ansatz is invalid for high-energy transfers, and leads to the unfortunate property that the integral for the total magnetic cross section diverges. A more realistic assumption is a Gaussian function at small t. However, the change from a Lorentzian at low energies (long t) to a Gaussian at high energies (short t) is still unclear, both theoretically and experimentally. One reasonable assumption is that it is connected experimentally with the bandwidth of the f electrons. Thus a cut-off energy of ~1.5 eV for 4f electrons may be reasonable (Holland-Moritz 1985).

Moreover the local static susceptibility can be factorized into the bulk susceptibility, $\chi_{\text{bulk}}(T) = \chi^{\text{st}}(\boldsymbol{Q}=0, T)$, and the magnetic form factor $f^2(\boldsymbol{Q})$:

$$\chi^{\text{st}}(\boldsymbol{Q}, T) = \chi_{\text{bulk}}(T) f^2(\boldsymbol{Q}). \tag{12}$$

We assume in this separation that the spatial and temporal aspects of the fluctuations are independent. The term $f^2(\boldsymbol{Q})$ is the magnetic form factor and is related to the spatial extent of unpaired electrons. The form factor can be approximated as $f(\boldsymbol{Q}) = \langle j_0 \rangle + C_2 \langle j_2 \rangle$, where $\langle j_i \rangle$ are Bessel transforms of the single-electron density, $U_f^2(r)$, and C_2 is a coefficient normally between 0 (for spin only systems) and ~2. In most cases the form factor is a monotonically falling function with $\boldsymbol{Q}$, although there are some important exceptions. For a fuller discussion and complete references, see Lander (1993). Due to the finite mass of the neutron, investigations at $\boldsymbol{Q}=0$ are impossible. If we consider the electrons contributing to the dynamical susceptibility, which describes the temporal and spatial behavior of the magnetic response of a solid, $\chi''(\boldsymbol{Q}, \omega, T)$, then we frequently think of two types of electron wavefunctions. The first are the "localized" states, or those with their wavefunction energies near the bottom of the band, e.g., 3d states in Fe and Ni, 4f in Gd, 5f in U, and the second are the conduction electrons, s-like in the transition metals, and s–d like in f systems. The conduction electrons are almost plane-wave in nature so that their Fourier transform is a delta function in $\boldsymbol{Q}$-space. A delta function at $\boldsymbol{Q}=0$ is *not* observable in conventional neutron scattering. The "localized" states, on the other hand, have a form factor $f(\boldsymbol{Q})$ that decreases with $\boldsymbol{Q}$ so that it can be observed in scattering experiments. In a *real* system, of course, these two types of contribution interact (indeed this interaction is the basis for much physics in this and other chapters), but it is still safe to say that the neutrons measure predominantly the localized response function. In contrast, the de Haas–van Alphen technique measures *only* the free electron part of the response function. A further discussion of this point is given by Liu (1989).

The third way to present the scattering law is more applicable when crystal field (CF) and intermultiplet transitions (IMT) excitations dominate the scattering. It is then necessary to divide the static susceptibility into Curie-like and van Vleck-like terms, contributing to the quasielastic and inelastic lines, respectively. The intensities are given by the matrix elements $|\langle n | J_z | m \rangle|^2$ following the diagonalization of the CF Hamiltonian

(e.g., Hutchings 1964, Birgeneau 1972). This leads to

$$S(\boldsymbol{Q}, \omega, T) = \tfrac{1}{2}(g_N r_e)^2 \frac{\omega}{1 - e^{-\beta\omega}} [g_J f(\boldsymbol{Q})]^2 \times \sum_{nm} \rho_m |\langle n | J_z | m \rangle|^2 \frac{1 - \exp(-\beta \Delta_{nm})}{\Delta_{nm}} P(\boldsymbol{Q}, \omega - \Delta_{nm}, T). \tag{13}$$

Δ_{nm} is again the transition energy from the nth to the mth level and $\rho_m = Z^{-1}\exp(-\beta\Delta_{1m})$, where Z is the sum over all the states, describes the occupation of the mth level at a temperature T. Birgeneau (1972) has given the scattering law for the crystal-field case in the limit of δ-functions

$$S(\boldsymbol{Q}, \omega, T) = \frac{1}{2}(g_N r_e)^2 [g_J f(\boldsymbol{Q})]^2 \sum_{nm} \rho_m |\langle n | J_z | m \rangle|^2 \delta(\boldsymbol{Q}, \omega - \Delta_{nm}, T). \tag{14}$$

The connection of this formula to eqs. (7) and (13) is described in detail by Holland-Moritz et al. (1982). Note that $|\langle n | J_z | m \rangle|^2 = \frac{1}{2} |\langle n | J_\perp | m \rangle|^2$, where $J_\perp$ is the perpendicular moment operator used, for example, by Lovesey (1984).

We end with a discussion of the difficult problem of the cross section of unstable f systems. The observed spectral function is no longer quasielastic at low temperatures for unstable 4f moments. There are two analytic functions in the literature; one given by Kuramoto and Müller-Hartmann (1985) and the other by Zwicknagl et al. (1990). We shall discuss the first in more detail as it has been used frequently for analyzing low-temperature neutron spectra. This function has inelastic character and is shown in fig. 1a (solid lines). The shape is given by two parameters. Firstly, the characteristic temperature T_K, the Kondo temperature, determines both the inelastic peak position and the width on the high-energy side. Secondly, a factor α influences the low-energy side of the spectral function ($\omega < k_B T_K$) being responsible for the increasing asymmetry of the spectral function with decreasing α. This factor is given by the fraction $\alpha = n_f/N_f$. Here, N_f is the degeneracy of the magnetic ground state and n_f is the fractional occupation number of the magnetic ground state (e.g., of Ce^{3+}, Eu^{2+}, Sm^{3+}, Yb^{3+} or of a corresponding CF ground state). As the minimum degeneracy of a magnetic state is 2 and as $n_f < 1$, it follows that $0 < \alpha < 0.5$. For $\alpha > 0.25$ this analytical spectral function can be well approximated by an inelastic (INE) and a quasielastic (QE) contribution (dotted and dashed lines in fig. 1a, respectively). Applying the argument of Shiba (1975) to this case, the Fermi liquid theory gives an *exact* value of χ'' for $\omega = 0$, which turns out to be about 20% larger than that of the analytical function (Kuramoto and Müller-Hartmann 1985), i.e., the QE component is underestimated by the analytical function. Thus, the exact solution for $\alpha = 0.5$ (doublet ground state) will be compatible with a QE contribution in agreement with other theories. A recent extension of the NCA theory yields a magnetic response being also inelastic in nature for a doublet ground state (Anders 1995). For $\alpha < 0.15$ (high degeneracy) a description by Lorentzian functions is no longer sufficient at the low-energy side because of the strong asymmetry of the analytic function. Therefore, a fit with a

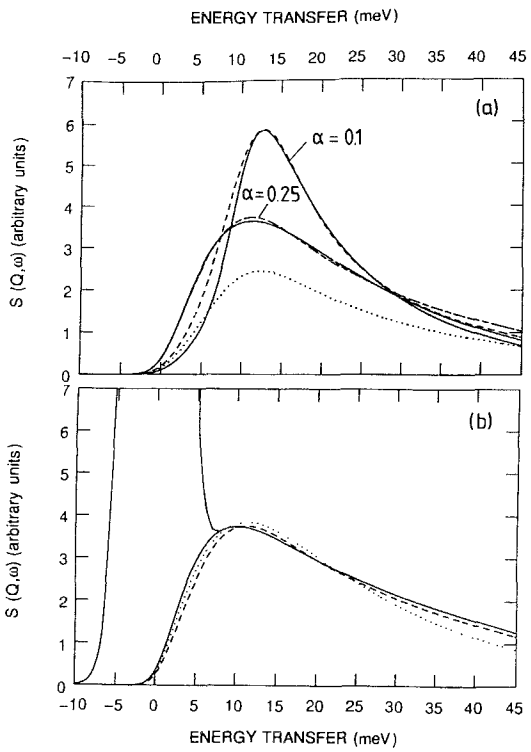

Fig. 1. The magnetic scattering law is plotted for different spectral functions in the limit of $T \rightarrow 0$ K by assuming an incident neutron energy $E_i = 50$ meV and an energy resolution with respect to IN4 at ILL. (a) the full lines represent the analytic function given by the theory of Kuramoto. Approximations to the theoretical function are given by the dashed lines. For $\alpha = 0.1$ the approximation contains only an INE component ($\Delta = 10.8$ meV and $\Gamma/2 = 6.9$ meV), while for a larger α (0.25 corresponding to a quartet) the approximation is done by a QE ($\Gamma/2 = 7.6$ meV) and INE component ($\Delta = 7.8$ meV and $\Gamma/2 = 9.5$ meV). The dotted line indicates the INE component. (b) three different spectral functions, in addition to the elastic incoherent peak: a QE line with $\Gamma/2 = 10$ meV (full line), an inelastic line at $\Delta = 5$ meV and $\Gamma/2 = 10$ meV (dashed line) and the analytic function with $kT_K = 10$ meV and $\alpha = 0.5$ (dotted line).

pure inelastic Lorentzian is definitively poorer (dashed line). Moreover, with increasing energy transfers this analytic function decreases generally faster than a Lorentzian. In fact, this is a desirable property of this function, because the integral over $S(\boldsymbol{Q},\omega,T)$, which gives an estimation of the local magnetic moment (see above), converges using this analytic function, whereas it diverges for a Lorentzian. For more details see Holland-Moritz et al. (1982) and Holland-Moritz (1985).

If the width of the spectral function becomes larger than the thermal energy, it is almost impossible to distinguish between different shapes of the spectral function. Figure 1b shows three examples of spectral functions in the limit $T \rightarrow 0$: a QE line, an INE line and the analytical function with $\alpha = 0.5$. The width of the QE as well as that of the INE line are 10 meV. The same value was chosen for $k_B T_K$ in the analytic function. The position of the INE line is 5 meV and hence just half of its width. The intensities are slightly different, so that all three different spectral functions display roughly the same energy dependence at low temperatures. In practice, the always present incoherent elastic scattering with a width given by the instrumental resolution will smear out the remaining small differences at low energy transfers. Thus, in the energy window $\omega < \Gamma$ the determination of the true spectral function is impossible. Even at high-energy transfers the difference between the Lorentzian and the analytical function will be very small. The above example may be an

extreme case, but it shows that generally a broad INE line with a position $\Delta < \Gamma/2$ cannot be distinguished from a QE line with a slightly larger width. The more Δ is increased with respect to $\Gamma/2$ the more the differences are distinct. As shown in fig. 1a the degeneracy of the magnetic ground state determines the shape of the analytic function. The higher the degeneracy, i.e., the smaller α, the larger is the asymmetry of the peak and the sharper becomes the inelastic peak. Therefore, if the degeneracy is sufficiently high, the analytic function will strongly differ from both a QE and an INE line shape.

The static susceptibility $\chi'(\boldsymbol{Q},0,T)$ derived from neutron scattering data may be in disagreement with the direct measurement of the static bulk susceptibility, which, by definition, corresponds to the $Q=0$ value, i.e., $\chi'(0,0,T)$. Because of the form factor discussed earlier, part of the electron wavefunctions (the free-electron part) will contribute to the bulk susceptibility, but not to the neutron signal at finite Q (see Liu 1989 for a discussion of this point). In addition, there may be correlations between the localized part of the response function which cause oscillations in $\chi'(\boldsymbol{Q},0,T)$ as a function of $\boldsymbol{Q}$. We shall give examples of this kind of phenomenon. However, if the bulk susceptibility coincides with the local susceptibility extracted from neutron scattering data by assuming just a local free-ion form factor (Stassis et al. 1977), one may conclude that the system under investigation does not show any important spatial magnetic correlations.

A final word should be said about technique related to the point that we can follow spatial correlations by their $\boldsymbol{Q}$ dependence. Many of the experiments described in this chapter have been performed with time-of-flight spectrometers on polycrystalline samples. The experimental parameters in such an experiment are the scattering angle (noted as either θ or ϕ) and t, the time-of-flight, of the neutron. It is trivial to convert t to energy (ω) knowing the parameters of the instrument, but a constant-$|\boldsymbol{Q}|$ plot (recognizing that only the modulus of $\boldsymbol{Q}$, not its direction, can be determined with a polycrystalline sample) requires interpolation of the data since the scattering angle is not simply related to Q. Only in a few cases, in which extensive angular coverage of the scattered signal has been measured, have constant-Q plots been made. The situation is simpler for a triple-axis spectrometer, which operates in a constant-Q mode. However, such an instrument is inefficient when studying polycrystalline samples, because of its single detector. With single crystals the full power of the 3-axis instrument comes into play; the only disadvantage being the preventive amount of experimental time required if anything like a complete coverage of both $\boldsymbol{Q}$ and ω space is required. The reader should be aware of the pros and cons of both types of instruments when consulting this chapter and the following chapter by Aeppli and Broholm (1994).

2. Stable f electron systems

2.1. *General remarks*

The crystal field (CF) potential arises from the electrostatic interaction of charges on neighboring ions with the wavefunction of the unpaired electrons. Thus, the energy

intervals between CF levels should become larger, as the wave functions of the unpaired electrons are more spatially extended. The observation with neutrons of CF transitions in polycrystalline material was reported on CeAs by Rainford et al. (1968) and then on the Pr pnictides and chalcogenides in 1970 by Turberfield et al. (1970, 1971). These studies led to the development of the useful formalism given by Birgeneau (1972) and noted here as eq. (13). Since that time a truly enormous number of CF schemes in stable metallic lanthanide materials have been determined with neutron spectroscopy. Stable signifying here integral valence, localized, and no, or relatively small, interaction with the conduction-electron states. CF neutron spectroscopy is established as an important tool in the study of magnetic materials. The CF interaction often determines whether or not a material orders magnetically and almost always is an important contributor to any magnetic anisotropy. The establishment of the CF level structure, and hence the nature of the ground-state wavefunction, is important for magnetic and thermodynamic properties. More complete references and further discussion will be found in the article by Fulde and Loewenhaupt (1986) and the excellent recent book by Jensen and Mackintosh (1991). Among the most interesting recent work related to stable 4f materials has been that on lanthanide 1:2:3 systems (derived from the famous $YBa_2Cu_3O_7$ high-T_c superconductor) and observations on the change in the *widths* and positions of the peaks as the material becomes superconducting (e.g., Walter et al. 1988, Osborn and Goremychkin 1991, Allenspach et al. 1992, Mesot et al. 1992, and references therein).

However, our object in this chapter is to cover *unstable* f-electron systems so that our discussion of the above subjects is brief and, at least in 4f materials, we select one or two examples only. For actinides the situation is more complex, as we shall see below.

2.2. *Intermetallic lanthanides*

Figure 2 shows some spectra of the intermetallic $\mathbf{R}_x\mathbf{Y}_{1-x}\mathbf{Pd}_3$ system (Walter and Holland-Moritz 1981). These spectra taken at $T = 20\,\mathrm{K}$ show distinct CF excitations. The widths of these CF transition lines are small, but are somewhat broadened if the concentration is increased. The temperature dependence of the quasielastic linewidth increases linearly with temperature as shown in fig. 3 for the example of Dy, and can be described by

$$\Gamma(T) = \Gamma_0 + \eta k_B T \tag{15}$$

with

$$\eta = 4\pi(g_J - 1)^2 J(J+1)(N(E_F)J_{ex})^2. \tag{16}$$

Here $N(E_F)$ is the density of electron states at the Fermi level and J_{ex} is the exchange integral. The linear term in T is in accordance with the Korringa (1950) law, which was deduced for NMR relaxation processes, but can be applied generally to relaxation processes governed by temperature. The residual linewidth Γ_0 is due to the spatial interaction of the electron system. One component, but not necessarily the only one, that

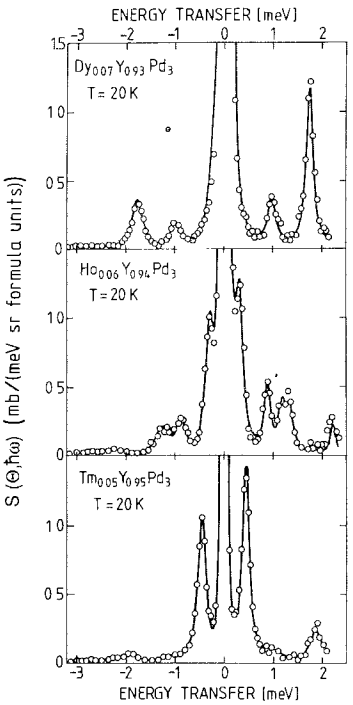

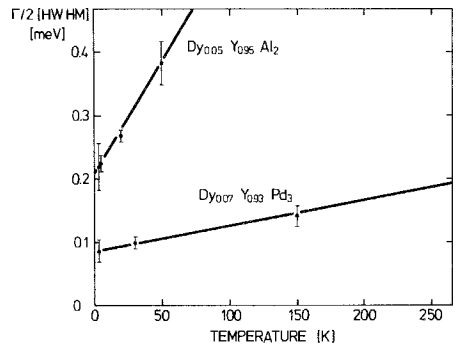

Fig. 3. The temperature dependence of the quasielastic line in $Dy_{0.05}Y_{0.95}Pd_3$ and $Dy_{0.07}Y_{0.93}Al_2$. (From Walter and Holland-Moritz 1981.)

Fig. 2. Magnetic excitation spectra of $R_xY_{1-x}Pd_3$ in the dilute limit: $S(\Theta, \omega)$ signifies spectra taken at constant scattering angle Θ. (From Walter and Holland-Moritz 1981.)

influences Γ_0 is again the factor $N(E_F).J_{ex}$. Therefore Γ_0 increases with η as demonstrated in fig. 3. Usually, the influence of $N(E_F)$ and J_{ex} cannot be separated. The data shown in fig. 2 can be analyzed completely in terms of a CF splitting using the nomenclature of Lea, Leask and Wolf (1962). A detailed analysis of most R in $R_xY_{1-x}Pd_3$ is given by Walter and Holland-Moritz (1981). In some cases application of the theory by Becker, Fulde and Keller (1977) (BFK-theory) yields better results. This theory takes into account exchange interactions between the 4f wave function and the conduction electrons, which result in a small shift of the CF excitations.

2.3. *Intermetallic actinides*

Because the 5f electrons are more spatially extended and less shielded than the 4f electrons in the lanthanides, we should expect the CF effects in actinides to be larger than in the lanthanides. Spectroscopic experiments on dilute lanthanide and actinide ions in ionic hosts (Carnall and Wybourne 1964, Carnall and Crosswhite 1986) show this to be the case with the actinide potentials being ~5 times stronger than in the equivalent f configuration in the lanthanides. These optical experiments, despite their high resolution (< 1 meV) and enormous energy range (up to at least 2 eV) suffer from the

problem that they are easy to interpret only when the ions are dilute, and they are difficult to perform on metals (Blumenröder et al. 1988). Neutron experiments are therefore of considerable value in this field, as they have been in the "normal" 4f systems (see Fulde and Loewenhaupt 1986 for a review). One difficulty with the larger CF splittings anticipated in the actinides (perhaps as great as ~500 meV) is that at reactor sources the present limitations of energy transfer are ~100 meV. Spallation neutron sources provide an answer to this problem in that they have a copious supply of epithermal neutrons, and the building of time-of-flight spectrometers has meant that large energy transfers can be obtained at small values of Q (Windsor 1981, Carpenter et al. 1984, Osborn et al. 1991). Although many efforts have been, and still are being, made to find CF splittings in actinide intermetallic materials, this has proved a difficult endeavor. Extensive discussion of these efforts will appear in sections 4–6. We now know that these problems are not because of inadequacies in neutron technology, but because of the physics, mainly strong hybridization effects between the localized 5f and 6d-7s conduction electron states smearing out the CF states.

2.3.1. *Crystal-field levels in UPd_3*

We shall discuss in some detail in sections 4–6 the unsuccessful search for CF levels in a large number of actinide compounds. There is one exception to this difficulty – **UPd_3**. An extensive discussion of the properties may be found elsewhere (Buyers and Holden 1985, pp. 289–296, which also contains much material that is not published elsewhere). In brief, UPd_3 exhibits sharp CF excitations, consistent with a $J=4$, $5f^2:{}^3H_4$ configuration for the U^{4+} ion. The crystal structure is hexagonal and analogous to the double-hexagonal close-packed (DHCP) structure of the rare-earth metals with two sites for the U atom, one of hexagonal and one of cubic symmetry. Buyers and Holden reported experiments on single crystals, which allowed the higher energy excitation at ~14 meV to be identified as a transition between the singlet and doublet states at the hexagonal sites. The lower energy excitation (~1.6 meV) was associated with the cubic sites. Buyers and Holden (1985) also reported that a lattice distortion takes place below 6.5 K with wavevector $[\frac{1}{2},0,0]$ and discussed various aspects of the quadrupolar susceptibility, which could give rise to such distortions.

That UPd_3 is a *localized* system is beyond doubt, not only because of the observation of CF levels, but also because the photoemission experiments of Baer et al. (1980) reveal that the 5f peak is ~1 eV below E_F. Since these experiments discussed by Buyers and Holden, a number of other studies have been performed. Johansson et al. (1986) and Eriksson et al. (1988) performed theoretical studies showing that the localized nature of UPd_3 can be understood by the lack of hybridization that occurs. By chance, the spin-up 5f states lie mainly in the hybridization gap between the 4d and 6d states so there is little overlap between the 4d and 5f states, and the latter are relatively well localized. For the alloy systems UPd_3–URh_3 and UPd_3–UPt_3 the bonding orbital moves up in energy and the hybridization between the 4d and 5f states increases steadily.

Using polycrystalline material McEwen et al. (1988) examined the CF transitions as a function of Pt doping into UPd_3. The experiment focussed on the 15 meV excitation, which by $U(Pd_{0.75}Pt_{0.25})_3$ shifts to lower energy (~9 meV) and becomes significantly broader. McEwen et al. (1990) then went on to acquire single crystals of $U(Pd_{1-x}Pt_x)_3$ with $x=0$, 0.25, and 0.5, and gave a preliminary report of the changes in the excitation spectra. The high-energy branch does indeed shift downward in energy with increased Pt alloying, and the damping becomes more important. In the low-energy spectra (between 2 and 4 meV) there is a substantial increase in the dispersion of the mode with substituting 25% Pt. Evidence was presented also for another excitation in the 30 to 32 meV range.

The same authors have recently focussed their attention on the phase transitions that occur at low temperature in the parent compound ($x=0$) UPd_3. These transitions were first reported by Buyers and Holden (1985), and, like these earlier authors, Steigenberger et al. (1992) report that the transitions are particularly complex. Using polarization analysis Steigenberger et al. (1992) show that the transition at T_1 (~7 K) has a structural character, whereas the transition at T_2 (~5 K) has both structural and magnetic components. The picture emerging for UPd_3 is of a quadrupolar phase transition resulting in a modulated lattice distortion with a wavevector of $[\frac{1}{2},0,0]$ at T_1, and at T_2 an additional distortion sets in when the small magnetic moments on the cubic sites order. The existence of a magnetic character to the T_2 phase transition is reflected in the temperature dependence of the CF excitations at low energy (1–2 meV).

Clearly, much remains to be done in the UPd_3 and mixed systems. One complication is the presence of *two* uranium sublattices. The appearance of quadrupolar distortions (McEwen et al. 1993, Zochowski and McEwen 1994) emphasizes their importance in actinide systems; similar effects occur in the oxides.

2.4. *Oxides*

The first observation with neutrons of a CF splitting in an f-electron oxide was that by Kern et al. (1984) on **PrO_2**. This is a $4f^1:{}^2F_{5/2}$ configuration with only two levels, a doublet Γ_7 and a ground-state quartet Γ_8. The Γ_7–Γ_8 separation was found to be 130(5) meV. The material orders at $T_N=14$ K with a low moment of $0.6(1)\,\mu_B$. The degeneracy of the ground-state Γ_8 is lifted, probably by a quadrupolar interaction, and this has been seen directly in a low-energy experiment (Kern et al. 1990a). The V_4 potential to the CF was found to be −57(3) meV.

Attention was then turned to **UO_2**. The CF level structure was, in fact, estimated for UO_2 in a classic paper by Rahman and Runciman (1966) and with $V_4=-409$ meV, the first excited state (a Γ_3 doublet) was predicted at ~170 meV above the Γ_5 triplet ground state with the second excited state at 624 meV. The first experiments showing two energy levels in the region of 140 to 170 meV were performed at the Intense Pulsed Neutron Source at Argonne National Laboratory and reported by Kern et al. (1985). The higher intensity and better resolution at the ISIS source (Rutherford-Appleton Laboratory, UK) allowed a more detailed study by Amoretti et al. (1989), and we present their data and

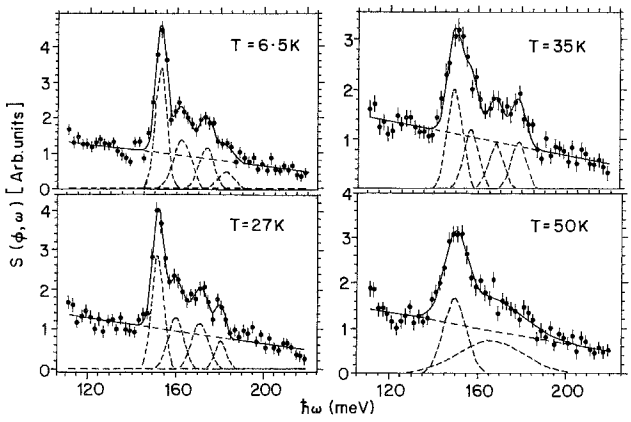

Fig. 4. Neutron spectra of UO_2 measured at the ISIS spallation source with $E_i = 290$ meV for different temperatures. The Néel temperature of UO_2 is 30.8 K. The smooth line is the fit to four Gaussian line shapes and a sloping background. These five components are shown by the dashed lines. (From Amoretti et al. 1989.)

fits in fig. 4. From this and other spectra the values of V_4 and V_6 were deduced as -125 and +25 meV, respectively. These are only ~30% of the values predicted by Rahman and Runciman (1966) and about twice the values found for PrO_2. Despite the larger extent of the 5f radial wavefunctions, and thus a larger value for the effective electron radius $\langle r \rangle$, the screening of the effective charges at the oxygen site is more substantial than first-principles calculations estimate.

What was not expected in these studies was the extremely well resolved "hyperfine splitting" of the $\Gamma_5 \rightarrow \Gamma_4$ and $\Gamma_5 \rightarrow \Gamma_3$ transitions and seen in fig. 4. It was known from diffraction work (Faber and Lander 1976) that below T_N (30.8 K) in UO_2 the oxygen atoms are displaced from their equilibrium positions and the highly resolved inelastic lines reflect the destruction of the cubic symmetry around the uranium ions. To understand the origin of these small energy differences additional terms reflecting the distortion of the nearest-neighbor oxygen configuration around the uranium atom have to be introduced into the CF Hamiltonian. These terms must, of course, be consistent with the underlying symmetry of the magnetic structure, as the material is antiferromagnetic below 30 K (Siemann and Cooper 1979). However, there was some ambiguity over whether the magnetic structure of UO_2 was a single- or triple-$\boldsymbol{k}$ one (see Rossat-Mignod et al. 1984 and the chapter by Lander 1993 for a general discussion of these multi-$\boldsymbol{k}$ structures). Burlet et al. (1986) claimed to have shown that the 3$\boldsymbol{k}$ structure was correct. These experiments were based on the observation of a null effect when a single crystal was cooled in a 80 kOe magnetic field. In such a situation one can always argue that the critical field is above that used, so the claim is always somewhat tenuous. In these circumstances, the fitting of the inelastic spectra was better with the symmetry deduced from the 3$\boldsymbol{k}$ arrangement, so confirmed that the magnetic structure of UO_2 is 3$\boldsymbol{k}$.

The situation in **NpO_2** is not yet completely clear despite a number of inelastic scattering experiments (Kern et al. 1988, Fournier et al. 1991, Amoretti et al. 1992).

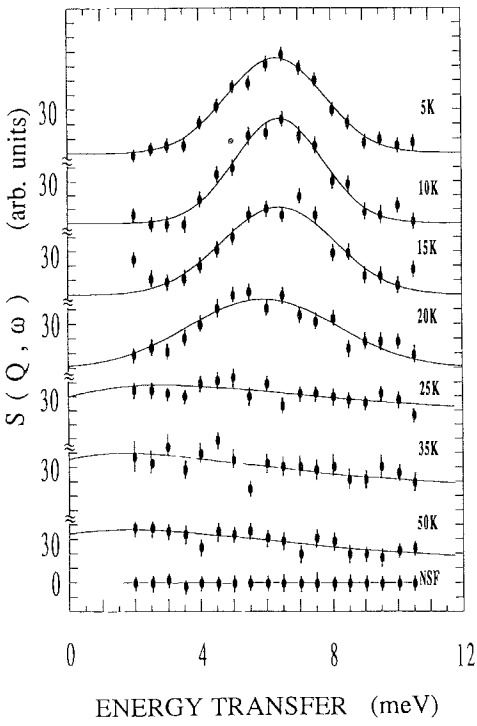

Fig. 5. Polarization analysis spectrum measured from polycrystalline NpO_2 at the IN20 three-axis spectrometer (ILL) as a function of temperature. The magnetic contribution is identified as the spin–flip cross-section. The non-spin–flip (NSF) is independent of temperature. The solid lines are best fits to the data. The transition temperature in NpO_2 is 25 K. (From Amoretti et al. 1992.)

The ground state is a Γ_8 quartet, which is separated from the next nearest state (also a Γ_8) by ~55 meV. The matrix elements for this transition are large, so a clear sharp transition should be seen, but this is not the case. Probably an interaction occurs with an optic phonon involving motions of the oxygen atoms and this gives rise to a $\boldsymbol{q}$ dependence, where $\boldsymbol{q}$ is a vector in the first Brillouin zone of the CF transition. Since with a polycrystalline sample we measure the density-of-states across the Brillouin zone, $\boldsymbol{q}$-dependent effects give rise to a broad peak. The recent inelastic experiments (Amoretti et al. 1992) have been able to shed further light on a very old riddle of what exactly happens at the "25 K transition" in NpO_2. Magnetic and Mössbauer experiments (Friedt et al. 1985) showed that the material does not order magnetically, and yet a sharp peak is seen in the specific heat. At low energy (see fig. 5) the use of polarization analysis has shown that the Γ_8 ground state is split into two doublets at 25 K with an energy gap of 7 meV. This is very similar to what happens to the Γ_8 ground state in PrO_2 (Kern et al. 1990a). This splitting is a manifestation of the ordering of the magnetic quadrupoles, an effect which occurs also in UO_2. In the case of NpO_2, due to the special values of V_4 and V_6, the dipole ordered moment in the quantization direction is essentially zero. Such an unusual situation was actually predicted for NpO_2 by Erdos et al. (1980) and Solt and Erdos (1980).

The experiments on **PuO_2** have required the use of the special ^{242}Pu isotope, which was kindly supplied for the Argonne experiments (Kern et al. 1990b) by Los Alamos National Laboratory. The initial experiments discovered a broad CF peak at 110 meV, but the sample also contained some impurity with an OH radical which gave a peak at 90 meV. In PuO_2 the ground state is a nonmagnetic Γ_1 singlet, with the first excited state being a Γ_4 triplet. Although quadrupole ordering cannot effect the Γ_1 singlet, it lifts the degeneracy of the Γ_4 triplet and hence can split the Γ_1–Γ_4 transition. Because of the singlet nature of the ground state in PuO_2, and hence the temperature-independence of the susceptibility (Raphael and Lallement 1968), one can also compare the absolute value of χ with that predicted by the CF parameters. In the case of materials with strong antiferromagnetic correlations in the ground state such as UO_2 and NpO_2, this comparison is more difficult. For PuO_2, the value of χ calculated with the V_4 and V_6 parameters consistent with the neutron spectroscopy of all the actinide oxides is almost twice the observed value. These estimates are, of course based on the assumption of non-interacting ions (free-ion theory) and clearly this is inappropriate. How exactly to modify the theory remains a matter of current debate.

To summarize the work on the oxides, two things are clear. First, the values of V_4 and V_6 are consistent for all three materials (Caciuffo et al. 1992), and smaller by a factor of about three than predicted by Rahman and Runciman (1966). This gives us confidence in using the Russell–Saunders LS coupling scheme as a good first approximation, although some caveats need to be attached to this statement – see Kern et al. (1990b) on PuO_2. It is known from the lanthanide series that the CF potentials are larger for ionic-like materials (e.g., the oxides) than for those containing conduction electrons, because the latter contribute to the screening. Thus, for conducting actinide systems, where the CF parameters remain something of an enigma (see below), we know at least from the oxides the upper limits of V_4 and V_6. Second, in all three oxide materials there is clear evidence for important effects involving the ordering (either statically or dynamically) of the magnetic quadrupoles. It is certainly not coincidental that quadrupole effects are observed in those actinide systems such as UPd_3 (see sect. 2.3.1 above) and the oxides, in which crystal fields are observed and the 5f electrons may be regarded as localized. The extended and anisotropic nature of the 5f electron wavefunctions is responsible for these effects, and, along with similar effects seen in some cerium compounds, will require a more extensive theoretical treatment.

Early experimental work on UO_2 showed anomalies in the elastic constants at temperatures far above T_N (Brandt and Walker 1968) and this was followed by a theoretical paper by Sasaki and Obota (1970). Further theoretical efforts seem warranted now that considerably more experimental information is available. Of course, the quadrupole ordering effects that occur in the oxides are, strictly speaking, cooperative effects. We should therefore expect to see dispersion in the energy levels; this, however, is not the case in UO_2 where the levels are extremely sharp in a polycrystalline sample (fig. 4).

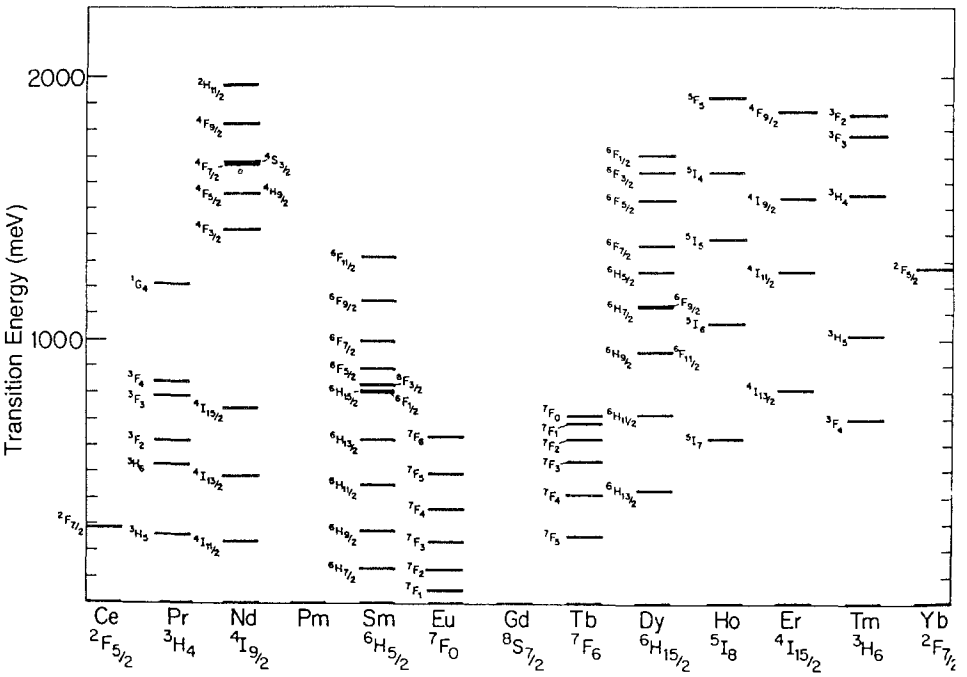

Fig. 6. Energies of intermultiplet transitions in trivalent lanthanides doped into LaF_3. The transitions are labelled by the final state of the transitions from the ground-state level specified at the bottom of each column. (From Carnall et al. 1989, modified by Osborn et al. 1991.)

3. Intermultiplet transitions

3.1. *Introduction*

In conventional neutron spectroscopy of CF levels (Fulde and Loewenhaupt 1986) we are dealing with transitions *within* the ground-state J multiplet, so-called *intramultiplet* transitions. As is well known, J multiplets exist at energies above that of the ground-state J-multiplet. The value of performing *intermultiplet* spectroscopy has been demonstrated by optical results on ionic systems. Well-defined atomic spectra from inter-4f transitions have been measured up to 6 eV in all trivalent lanthanides, except promethium, and these are illustrated up to 2 eV in fig. 6. A complete review of both the experiments (up to ~1990) and theory has recently been given by Osborn et al. (1991) and the reader is referred to this for more details. In this section we shall summarize the salient points needed to interpret the experiments.

In *both* lanthanides and actinides the levels may be characterized by the notation $^{2S+1}L_J$. *Spin–orbit* transitions are those between levels with the same value of L and S but different values of J. Since the neutron couples directly to the J quantum number, dipole transitions correspond to $\Delta J = \pm 1$. The cross section is finite at $Q = 0$, but for increasing Q falls as $(\langle j_0 \rangle - \langle j_2 \rangle)^2$ in intensity, where the $\langle j_0 \rangle$ and $\langle j_2 \rangle$ functions are Bessel transforms

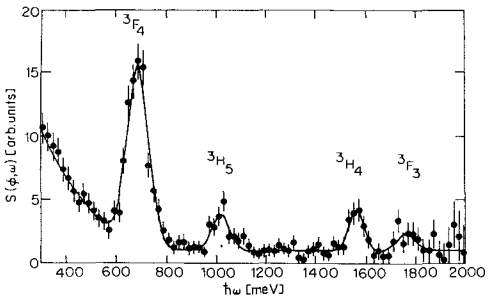

Fig. 7. Neutron scattering cross-section of intermultiplet transitions from the $^3H_6$ ground level in thulium metal at 20 K, measured at an angle of 5° with an incident neutron energy of 2140 meV at the ISIS spallation source. The instrumental resolution varies from 56 to 27 meV as the energy transfer increases from 500 to 1800 meV. The data have been fitted by four Gaussians and a tail of low-energy scattering. The peaks are labelled by the final state of the transition. (From Osborn et al. 1991.)

of the single-electron density $U_f^2(r)$. [Note that this form factor, or Q dependence, is quite different from that of intramultiplet transitions – see the discussion in connection with eq. (12), and Lander (1993).] These spin–orbit transitions are the most intense of the intermultiplet transitions, but are still an order of magnitude smaller than most intramultiplet cross sections. The second type within the general frame of intermultiplet transitions are *Coulomb* transitions. In these $\Delta L \neq 0$, i.e., transitions between levels derived from different Russell–Saunders $^{2S+1}L_J$ terms. Their energies, which are large as shown in fig. 6, depend on the Coulomb repulsion between the electrons in the f shell and are thus more sensitive to changes in the local environment than the spin–orbit transitions. The Coulomb transitions are non-dipolar, so that they have zero or very small cross section at $Q = 0$, but at finite Q the cross section can often be greater than spin–orbit transitions, although still substantially below those of intramultiplet transitions.

We have seen in the above discussion the considerable information that can be obtained by measuring intermultiplet energies; information that cannot be obtained either reliably or routinely in metallic systems by optical techniques (Güntherodt et al. 1981, Schoenes 1984, Blumenröder et al. 1988). Not surprisingly, the experimental neutron data are limited. There is a straightforward reason for this: the energies of these transitions are far greater than those normally observed (< 100 meV) in neutron inelastic scattering. Thus, except in the case of Sm and Eu (fig. 6), the experiments have required the high epithermal flux of spallation sources. All experiments so far, with the exception of a few early experiments at Argonne National Laboratory (Stirling et al. 1986), have been performed at ISIS, the world's premier spallation neutron source at Rutherford–Appleton Laboratory, UK. The experimental methods, their difficulties and limitations, are discussed by Osborn et al. (1991). In some cases the successes have been spectacular. We show in fig. 7 the inelastic scattering from a 100 g sample of thulium metal (Osborn et al. 1990). Tm has a $^3H_6$ ground state; thus we expect two spin–orbit transitions to $^3H_5$ and $^3H_4$ states and two Coulomb transitions to $^3F_4$ and $^3F_3$ states. An analysis of these results shows that neither the spin–orbit nor the Slater integral parameters, which are used to describe the Coulomb interaction, are much changed from dilute Tm in LaF_3. This is to be expected as the f electrons in Tm are well localized. In contrast, results on Pr metal (Taylor et al. 1988) did show an appreciable change, particularly in the Slater integrals.

These changes for Pr may be understood as a consequence of increased hybridization of the f states in the lighter lanthanides.

3.2. *Application to anomalous lanthanides*

With respect to the intermultiplet transitions, samarium and europium have particular interest among the intermediate-valent lanthanide ions. That is because the energy for the $^7F_0$ to $^7F_1$ transition within the electronically isostructural Sm^{2+} and Eu^{3+} configuration is rather low, 36.4 meV and 46.5 meV, respectively (Martin et al. 1978, Ofelt 1963 and fig. 6). This may be the origin for the temperature-driven valence change in most of the Sm and Eu intermediate-valent systems. Unfortunately, the experimental neutron scattering data on Eu and Sm systems are limited, because the absorption cross section of both natural samarium and europium are very large. Thus the use of the more suitable, but expensive, ^{154}Sm and ^{153}Eu isotopes is necessary. The magnetic cross section of the dipolar $^7F_0 \rightarrow ^7F_1$ transition is 7.2 barn, and is suitably large for inelastic scattering experiments. In this section we will discuss only the intermultiplet excitations, while we refer to sect. 5 for the discussion of the quasielastic magnetic scattering. We shall discuss these in the order Sm, Eu, and Ce that corresponds to the increasing energy of the intermultiplet transition.

3.2.1. *Samarium systems*

Of particular interest is **SmS** because of its first-order metal–insulator phase transition at about 6 kbar (Maple and Wohlleben 1971). This phase transition is consistent with a collapse in the size of the Sm ion, i.e., with a change in the Sm valence. Shapiro et al. (1975) found a sharp excitation in neutron scattering experiments on a SmS single crystal at atmospheric pressure. The excitation shows dispersion, i.e., the energy depends on $\boldsymbol{q}$. At the zone boundary the energy is about 36.5 meV, and it is somewhat lower at the Γ-point. This Γ-point energy is decreasing from 33.8 meV at room temperature to 31 meV at liquid nitrogen temperature. At the zone boundary the excitation energy was found to be almost temperature independent. When applying pressure of about 0.6 GPa the intermultiplet transition is no longer observable (McWhan et al. 1978), although from the valence $v \approx 2.6$ (Shaburov et al. 1974, Coey et al. 1976, Röhler 1987) a magnetic cross section of about 2.8 barn would be expected.

The same valence phase transition can be induced by lattice pressure, e.g., in the system $\mathbf{Sm_xY_{1-x}S}$. For a Sm concentration of $x \approx 0.75$ the valence increases with temperature by about 0.13 as measured by L_{III} X-ray absorption. The absolute value seems to depend on the sample (or on sample preparation for the X-ray absorption experiment), whereas the relative valence change is constant. Martin et al. (1980) gave a room temperature value of 2.53, Lossau et al. (1988) a value of 2.56 and Ravet and Krill (unpublished) found only 2.44. Surprisingly, in a polycrystalline sample of $Sm_xY_{1-x}S$ the $^7F_0 \rightarrow ^7F_1$ transition could be detected at about 30 meV in the whole temperature range from 15 K to 300 K (Mook et al. 1978a). They give an upper bound of about 15 meV for the intrinsic width, which seems to be temperature independent. Due to the temperature dependence of

the valence the intensity decreases with increasing temperature. However, when plotting the peak intensity this decrease is stronger than expected from the valence change. As the room temperature valence of Sm in the collapsed phase of SmS is surely larger than in $Sm_xY_{1-x}S$, the observed rapid decrease in the peak intensity is in agreement with the fact that this dipolar intermultiplet transition was not observed in the collapsed phase of SmS.

A more recent experiment, with better energy resolution, by Holland-Moritz et al. (1988) shows that the behavior of this dipolar intermultiplet transition is more complicated. The excitation is split into four lines, each of which depends on the momentum transfer $\boldsymbol{Q}$. As the sample was polycrystalline, only an analysis with respect to the absolute value of $\boldsymbol{Q}$ was possible. The width of each line was found to be about 2 meV between 5 K and 200 K, but above 200 K the width seems to increase. The absolute Sm valence in this sample was fixed at room and liquid nitrogen temperature (2.44 and 2.31, respectively) by L_{III} edge measurement (Ravet and Krill, unpublished). Using the temperature dependence measured by Lossau et al. (1988), intensities for the dipolar intermultiplet transition were calculated. Comparing these intensities with the observed integral intensities, i.e., taking the width into account, the relative changes as a function of temperature are in good agreement. However, the absolute experimental value of 3.15 barn at $T = 5$ K is less than the value of 5.1 barn calculated from a valence of 2.3. There are two possible origins for this deviation. The first is the experimental uncertainty in the absorption correction. The second is based on a more complicated physical behavior of the intermultiplet transition. The splitting was interpreted as resonant electron–phonon coupling between optical phonons and a magnetic excitation consisting of the dipolar multiplet transition modulated by magnetic intersite coupling. The corresponding matrix elements $\langle 1 | J_\perp | 0 \rangle$ describing the probability for transitions to the excited $J = 1$ multiplet are unknown, and may be smaller than in the undisturbed case.

SmB_6 has also been studied by inelastic neutron scattering. Here the Sm ion has a valence of about 2.53 and 2.6 at liquid helium and room temperature, respectively (Tarascon et al. 1980). Neutron scattering on this system is extremely difficult, because the absorption is rather high, even when using the ^{11}B and ^{154}Sm isotopes. In a first experiment at $T = 5$ K on a polycrystalline sample no intermultiplet transition could be detected around 30 meV (Holland-Moritz and Kasaya 1986). Alekseev et al. (1993a) have recently reported experiments and suggest that IMT's from both Sm^{2+} and Sm^{3+} are present, but are broad. These studies, especially the comparison to LaB_6, show that the existence of optical phonons between 30 and 50 meV, and also at high energies up to 140 meV, makes it difficult to identify the IMT's unambiguously. The behavior of the low-energy response will be discussed in sect. 5.

An interesting study has been reported on **$SmFe_{11}Ti$** by Moze et al. (1990). This material has a high Curie temperature of 584 K and the Sm ion experiences a strong exchange field from the Fe sublattice. Such an exchange field mixes the ground and excited multiplets, which for the case of trivalent Sm^{3+} would be separated by 129 meV (fig. 6). The resulting J mixing must be taken into account to understand the magnetization processes, so it is of considerable importance to have direct spectroscopic

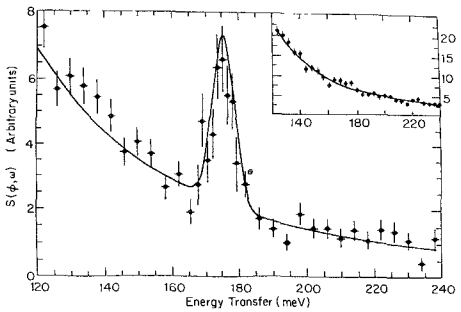

Fig. 8. Inelastic neutron-scattering cross section of $SmFe_{11}Ti$ at 20 K, measured with an incident-beam energy of 400 meV at an angle of 5°. The spectrometer energy transfer resolution at 176 meV is about 8 meV. The smooth line is the fit to a Gaussian line shape, a sloping background, and a Gaussian multiple scattering contribution. The inset shows the data obtained in the same configuration for $YFe_{11}Ti$. (From Moze et al. 1990.)

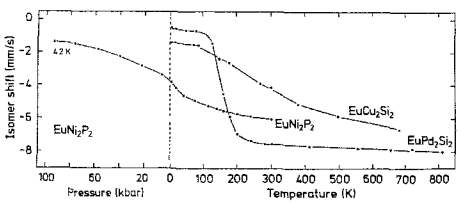

Fig. 9. The isomer shift of Eu as a function of temperature for several Eu compounds and as function of pressure for $EuNi_2P_2$ (adapted from Perscheid et al. 1985). The valence may be related to the isomer shift so that in $EuPd_2Si_2$ the valence changes from $v=2.2$ to ~2.85 as T is decreased from 200 to 4 K.

evidence for the change in intermultiplet splitting that is predicted by the J mixing. In fig. 8 we show the data taken on the time-of-flight spectrometer HET at ISIS using a sample of 72 g containing natural Sm. The peak at ~175 meV can be understood by a complete diagonalization of the Hamiltonian including the strong exchange field. Other transitions are predicted at 31 and 207 meV. The former is obscured by phonon effects and the latter is predicted to be some 20 times weaker than the peak in fig. 8. The observations are important for understanding the exchange effects in lanthanide intermetallic compounds, and we can anticipate more studies of this sort.

3.2.2. *Europium systems*

Inelastic neutron scattering data on intermediate-valent Eu are available only for two systems: **$EuPd_2Si_2$** (Holland-Moritz et al. 1987a) and **$EuNi_2P_2$** (Holland-Moritz et al. 1989a). Even the best suited Eu isotope, ^{153}Eu, has a rather large neutron absorption so that only small samples (few grams) can be investigated by inelastic neutron scattering. From lattice parameter (Sampathkumaran et al. 1981), L_{III}-edge (Kemly et al. 1985) and Mössbauer (Perscheid et al. 1985 and references therein) measurements it is well known that the Eu valence is changing with temperature. Most of the Eu IV systems are close to divalent at room temperature. With decreasing temperature they shift to trivalent. Figure 9 shows isomer shift data as function of temperature and pressure at $T=4$ K as measured by the Mössbauer technique. The isomer shift, in principle, can be related directly to the valence. $EuPd_2Si_2$ shows almost the full valence transition from $v \approx 2.2$ above $T=200$ K to $v \approx 2.85$ at $T=4$ K. The Eu valence in $EuNi_2P_2$ reaches only 2.5 at $T=4$ K and at zero pressure. The full valence transition can be observed only by applying pressure on the system at $T=4$ K shown in the left part of fig. 9.

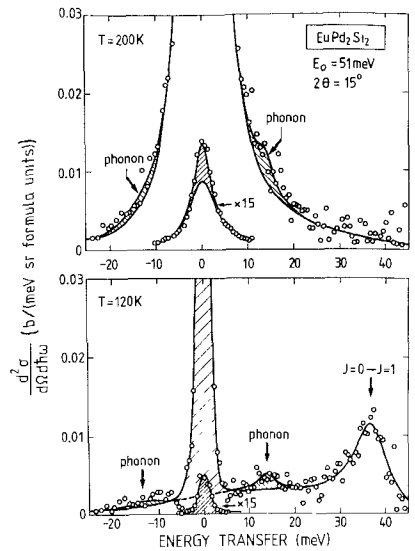

Fig. 10. Background corrected spectra of $EuPd_2Si_2$ at $T = 120\,K$ and $T = 200\,K$ showing the vanishing of the $^7F_0 \rightarrow {}^7F_1$ transition with increasing temperature. The hatched areas around zero energy transfer represent the elastic nuclear scattering with experimental energy resolution, and the hatched areas around 14 meV represent the phonon contribution to the scattering response. (From Holland-Moritz et al. 1987a.)

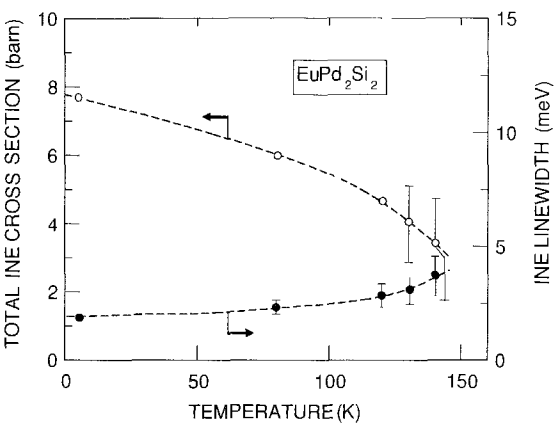

Fig. 11. Linewidth (HWHM) and intensity of the $^7F_0 \rightarrow {}^7F_1$ transition in $EuPd_2Si_2$ as a function of temperature (adapted from Holland-Moritz et al. 1987a).

From the above valence data it is obvious that $EuPd_2Si_2$ is the best candidate for studying the dipolar $^7F_0 \rightarrow {}^7F_1$ intermultiplet transition as a function of the valence via its temperature dependence. Whereas for $T > 150\,K$ no such intermultiplet transition was found, a peak of magnetic origin was observed at ~38 meV at low temperatures, as shown in fig. 10. The width of this peak increases with increasing temperature, as shown in fig. 11. The increase of the width turns out to accelerate, when the valence decreases for $T > 120\,K$. Already at $T = 150\,K$, i.e., when the valence has reached a value of 2.5, the width seems to be so large that the intermultiplet transition is no longer readily observable. This is in agreement with the results on $EuNi_2P_2$. On cooling the Eu valence reaches only a value of 2.5, and thus even at $T = 5\,K$ a comparable intermultiplet transition could not

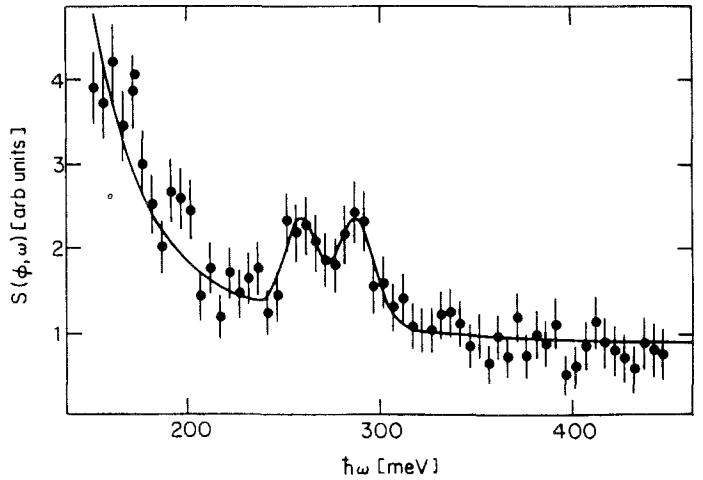

Fig. 12. Neutron inelastic scattering from $CeAl_3$ at 20 K, measured at an angle of 5° with an incident neutron energy of 600 meV on a time-of-flight spectrometer at the Rutherford Laboratory spallation source, ISIS. The data have been fitted by two Gaussian and a tail of low-energy scattering. (From Osborn et al. 1990.)

be detected in $EuNi_2P_2$. This is consistent also with the findings in Sm systems. The farther the valence is from integral, the broader is the corresponding IMT, and thus the more difficult to observe.

3.2.3. *Cerium systems*

Recalling the results for Eu and Sm compounds, it may be understood why no intermultiplet transition was found for a strong intermediate-valent Ce system like **$CePd_3$** (Osborn, unpublished). On the other hand, the $^2F_{5/2} \rightarrow ^2F_{7/2}$ intermultiplet transition could be detected in the heavy-fermion system **$CeAl_3$** (Osborn et al. 1990) with its almost integral Ce valency (fig. 12). The excitation is clearly split into two lines separated by about 30 meV. This is a surprising result, because CF splitting energies within a J multiplet are expected to be in the range of 10 meV for intermetallic systems. The peaks are also some 4 times broader than the experimental resolution of ~12 meV. The origin of this large splitting is still unclear, but one can speculate that the same enhanced hybridization between $4\underline{f}$ and conduction electrons, which is responsible for the Fermi liquid behavior, could cause the anomalous CF potential. For more theoretical details see, e.g., Wills and Cooper (1987), Levy and Zhang (1989) and Schrieffer and Wolff (1966). Recently, Goremychkin and Osborn (1993a) have shown that the intermultiplet transition decreases in intensity on doping with Y.

3.2.4. *Conclusion*

There is strong evidence that the observation of intermultiplet transitions is related to the hybridization strength of the corresponding $4\underline{f}^n$ configuration. In the case of Ce (Yb) this can be qualitatively described by the Kondo temperature T_K or by the valence fluctuating temperature T_{VF}. More care is necessary for Eu and Sm. If the valence is close to the $4\underline{f}^6$

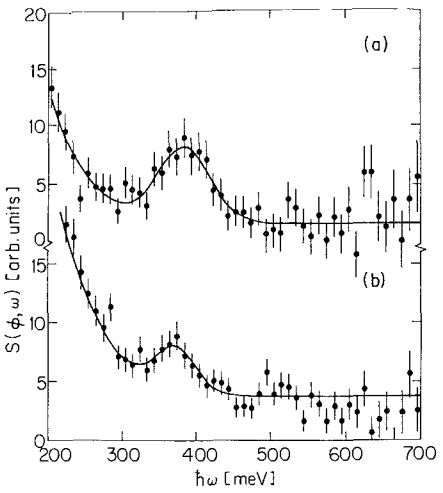

Fig. 13. Neutron inelastic scattering from (a) UPd_3 and (b) UPt_3 at 20 K, measured at an angle of 5° with an incident energy of 800 meV. The data have been fitted to a Gaussian and a tail of low-energy scattering. (From Osborn et al. 1990.)

configuration (Sm^{2+} or Eu^{3+}), the Hund's rule ground state $^7F_0$ is rather stable, and thus the intermultiplet transition to the $^7F_1$ state is clearly observable. On the other hand, when the 4f count is close to the $4f^5$ (Sm^{3+}) or to the $4f^7$ configuration (Eu^{2+}) the $^7F_0$ ground state of the $4f^6$configuration is broadened and the $^7F_0 \rightarrow ^7F_1$ intermultiplet transition is no longer observable. In the latter case one should expect that the $^6H_{5/2}$ to $^6H_{7/2}$ transition within the $4f^5$ configuration (Sm^{3+}) should be detectable at $\Delta < 130$ meV. See, for example, the discussion with respect to $SmFe_{11}Ti$ above and fig. 8. A comparable transition within the $4f^7$ configuration (Eu^{2+}) does not exist because $L = 0$.

Whereas for $CeAl_3$ the observed spin–orbit splitting is in agreement with the free-ion calculations, the observed energies for the IV Sm and Eu systems are significantly smaller than the free-ion values. Interestingly, the spin–orbit coupling constant is smaller for Sm^{3+} than for Sm^{2+}: 191 meV and 216 meV, respectively. The $^7F_0 \rightarrow ^7F_1$ transition energy calculated from the lower value is in rather good agreement with the experimentally found excitation energies in $Sm_xY_{1-x}S$ and SmS ($P = 0$). However, such an analogy does not exist for europium: spin–orbit coupling is absent for the Eu^{2+} configuration because $L = 0$.

3.3. *Application to actinides*

The energy level splittings in actinides are greater than those in the lanthanides (Carnall and Wybourne 1964, Carnall and Crosswhite 1986) by a factor of between 2 and 5. Moreover, the stronger spin–orbit and CF interactions gives rise to a partial break down in the Russell–Saunders coupling scheme that we have assumed is valid for the lanthanides in this section. Levels with a given J value will now be composed of more than one L and S value; this is usually referred to as intermediate coupling. When the CF interaction is also large, even J is not conserved and J-mixing appears. Fortunately, despite early predictions that J-mixing would be important (Chan and Lam 1974), this has not turned

out to be the case, mainly because of substantial screening effects which reduce the size of the CF potential. Intermultiplet transitions will still be present in actinides and no doubt more will be found in the future. For the moment, however, such transitions have been seen only in **UPd_3** and **UPt_3** (Osborn et al. 1990). Figure 13 shows the results for these materials. According to spectroscopy of dilute ions in solution, the first transition in a U^{4+}: $5\underline{f}^2$ state is the $^3H_4 \rightarrow {}^3F_2$ transition (non-dipolar) at ~450 meV (Osborn et al. 1990). The first dipolar transition $^3H_4 \rightarrow {}^3H_5$ is at 690 meV. For a U^{3+}: $5\underline{f}^3$ state it is the dipolar $^4I_{9/2} \rightarrow {}^4I_{11/2}$ at ~500 meV. UPd_3 is a localized system with the U ion in a $5\underline{f}^2$ state. However, the Slater parameters must be reduced by ~20% to explain the downward shift from 450 to the observed 385 meV in UPd_3. Given the greater spatial extent of the $5\underline{f}$ wavefunctions this is reasonable. The suggestion that the ground state in UPt_3 is predominantly $5\underline{f}^2$ in character also receives support from theory (Johansson et al. 1986). The observation of a intermultiplet transition $^3H_4 \rightarrow {}^3F_2$ in UPt_3, albeit broader and weaker than in the well-localized system UPd_3, shows that the Coulomb repulsion is consistent with a predominantly $5\underline{f}^2$ configuration. Intermultiplet transitions were also observed in the heavy-fermion $CeAl_3$ (Osborn et al. 1990). In this case, *intra*-multiplet transitions are also observed, so that this shows directly that the hybridization is greater in the actinides than in a similar (i.e., heavy-fermion with a large γ value) lanthanide, but not sufficient in UPt_3 to completely broaden the intermultiplet transition.

The large samples (excess of 60 g in all the experiments so far) excludes any transuranium materials. Furthermore, the large multiphonon background present if any light atom is used (e.g., oxygen in UO_2, chlorine in UCl_4, nitrogen in UN, fluorine in UF_4), severely limits the number of samples in which one can anticipate detecting the weak signals from intermultiplet transitions. The case of Tm (fig. 7) is thus truly exceptional (!); a large pure sample readily available, no light atoms to contribute a multiphonon background, sharp levels (i.e., no broadening of levels as, for example, is seen in both UPd_3 and UPt_3) and relatively large cross sections.

To illustrate the difficulties, we follow the work by Jones et al. (1992) in trying (unsuccessfully) to find a transition in a $5\underline{f}^3$ system, viz. USb. The sample size was 62 g. The first transition $^4I_{9/2} \rightarrow {}^4I_{11/2}$ is anticipated at ~500 meV, and the second $^4I_{9/2} \rightarrow {}^4H_{3/2}$ at ~870 meV. Incident energies of 800 and 1000 meV were used in an attempt to find the first transition, but no measurable signal was seen for Q values between ~6 and 9 Å^{-1}. Jones et al. (1992) pointed out the increased difficulties anticipated in a $5\underline{f}^3$ system with respect to seeing transitions as compared to either actinide $5\underline{f}^2$ or lanthanide $4\underline{f}^3$ systems. These comparisons are illustrated in fig. 14. (a) shows that at $Q \approx 8$ Å^{-1} the $5\underline{f}^3$ transition is weaker by almost an factor of two than that in $5\underline{f}^2$. Similarly, as shown in fig. 14b, the maximum (for $Q > 0$) in the scattering cross section for the $4\underline{f}^3$ analogue Nd^{3+} is at a higher Q value than that for U^{3+}; this is because the $4\underline{f}$ wavefunctions are more localized than their $5\underline{f}$ counterparts. Recall that experimentally the difficulty is always to get to *small* Q because of the so-called kinematic restrictions (Loewenhaupt 1985, Osborn et al. 1991), so that the experiments on lanthanides are always easier than those on actinides.

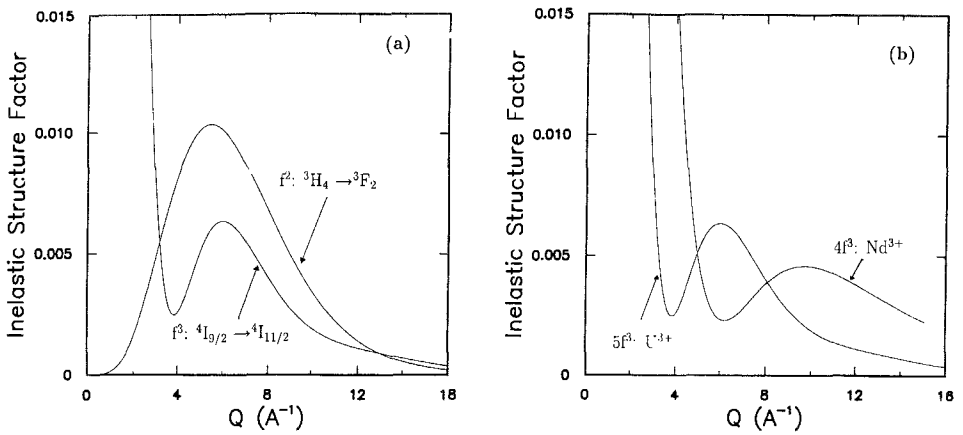

Fig. 14. The calculated inelastic neutron cross section versus momentum transfer Q for a number of f-electron intermultiplet transitions: (a) IMT for $5\underline{f}^2$: $^3H_4 \rightarrow {}^3F_2$ and for $5\underline{f}^3$: $^4I_{9/2} \rightarrow {}^4I_{11/2}$; (b) a comparison of the first intermultiplet ($^4I_{9/2} \rightarrow {}^4I_{11/2}$) cross sections for $5\underline{f}^3$ (500 meV) and $4\underline{f}^3$ (230 meV). (From Jones et al. 1992.)

3.4. *Conclusions*

Although the observations of intermultiplet transitions in some systems, e.g. Tm (fig. 7), have been an experimental tour de force, the *new* scientific content has not been overwhelming. Part of the difficulty lies in the fact that only a relatively few systems have been studied so that we lack systematic information on, for example, the changes in the Slater integrals for the 4f series. The experimental difficulties of absorption (particularly for Eu and Sm) and the kinematic restrictions on studies above 100 meV will always remain, so this field is not one that will develop rapidly. Nevertheless the potential information available from studying systems such as $CeAl_3$ and even Ce metal would seem worth the necessary effort. Further perspectives can be found in Osborn et al. (1991).

For the actinides we point out the promise, so far unfulfilled, of important information on the interactions between 5f electrons on the same atom. Further efforts at ISIS will hopefully provide progress, but it appears that we may need a new generation of spallation sources to make major advances. The kinematical constraints (i.e., having to keep Q small, while transferring a large energy) are more restrictive in the actinides than in the lanthanides. There is also the possibility that resonant magnetic X-ray scattering, which is particularly strong from actinides at the M edges (McWhan et al. 1990), will make contributions in the region of inelastic scattering above ~500 meV (Lander and Stirling 1992).

4. Ordered magnetic systems with large moments

4.1. *General remarks*

We concentrate in this section on materials that order magnetically; the magnetic response from paramagnets will be discussed in sect. 5. We distinguish between systems that have reasonably large moments (e.g., USb with $2.8\,\mu_B$) and heavy-fermion type materials (sect. 6) that have moments usually much less than $1\,\mu_B$. Most of the experiments described in this section involve single crystals. We shall discuss a series of compounds whose magnetic properties often resemble those of localized f-electron systems, such as UO_2, for example. However, on closer examination, especially of the density of states (by photoemission), or of the neutron inelastic response function, it becomes clear that a localized-type f-electron model will not explain the experimental results. In general, as we shall see, the results are more inconsistent for the actinides than for the lanthanides.

4.2. *Lanthanide compounds with the NaCl crystal structure*

These materials have been of interest for many years because of their unusual properties. In the last decade reasonably large crystals have become available by using the "mineralization technique" (Spirlet and Vogt 1984), so that many different neutron inelastic experiments have been performed. Although TmSe orders with a moment of about $2\,\mu_B$ (Bjerrum-Møller et al. 1977), we shall discuss the Tm compounds with the NaCl-type structure in sect. 5 in connection with effects of intermediate valence (IV).

The magnetic structures of these compounds are often complex (Rossat-Mignod et al. 1984, Lander 1993). Although the magnetic structure defines the position of the lowest energy in the excitation spectrum, the shape of the magnon dispersion curves are not usually sensitive to the exact magnetic structure.

4.2.1. *Cerium systems*

Interestingly, **CeAs** and **CeSb** were two of the first 4f materials to be examined (in polycrystalline form) by neutron inelastic scattering, by Rainford et al. (1968). Soon after, Birgeneau et al. (1973) showed that the crystal-field (CF) splittings within the $4f_{5/2}$ manifold for the Ce monopnictides are much less than expected from extrapolation from other lanthanide monopnictides. For cubic materials the sixfold degenerate $^2F_{5/2}$ multiplet is split into a Γ_8 quartet and a Γ_7 doublet. In all the Ce monopnictides the Γ_7 is the ground state but the Γ_8 state lies between 1 and 10 meV above in energy, whereas an extrapolation from other lanthanides would expect this energy difference to be between 20 and 30 meV. This reduction in the CF splitting has been explained theoretically both by Takahashi and Kasuya (1985) and by Wills and Cooper (1987). In the first case the authors place more emphasis on the coupling between the f and pnictogen p states, whereas the latter emphasize the hybridization between the f and band states.

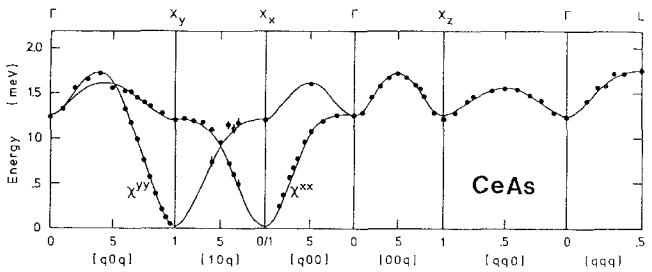

Fig. 15. Dispersion curves of magnetic excitations of CeAs as deconvoluted to give the spectra for a single AF-I z domain. The solid lines represent the theoretical dispersion curves. (From Hälg and Furrer 1986.)

The excitation spectra, measured on single crystals, of CeAs, CeSb, and CeBi have all been reported. All order with single $\boldsymbol{k}$ magnetic structures with either the type I (CeAs) or type IA (CeSb, CeBi) being stable at low temperature. The ordering temperatures are below 30 K so that the exchange effects are small, and the total dispersion is less than 2 meV.

The data for CeAs (Hälg et al. 1983, Hälg and Furrer 1986) are shown in fig. 15. The anisotropy gap is small (< 0.03 meV). The polarization of all the observed excitations is transverse, as expected for a conventional spin-wave excitation. The dispersion is seen to be almost quadratic; whereas in a normal antiferromagnet one anticipates a linear dispersion as a function of $\boldsymbol{q}$. Hälg and Furrer (1986) have shown that this quadratic behavior is a consequence of the anisotropic exchange interactions. In fact the solid lines in fig. 15 are the result of a calculation including these anisotropic exchange interactions. We noted in connection with the magnetic critical scattering (Lander 1993, sect. 5) that the J^{zz} component of the exchange for z-domain i.e., (001) planes coupled ferromagnetically and with the magnetic moment parallel to [001] was much greater than J^{xx} or J^{yy}, and the interpretation of the inelastic spectrum is also consistent with the dominance of the J^{zz} component. The small anisotropy gap in CeAs suggests that it is an almost ideal $S = 1/2$ antiferromagnet.

The excitation behavior of CeSb has been measured by Rossat-Mignod et al. (1985a,b) and Hälg et al. (1985, 1987) and Hälg and Furrer (1986). CeBi has been investigated by Rossat-Mignod et al. (1983, 1985b). We show the spectra for CeSb and CeBi in fig. 16. The spectra as shown come from the three different domains, but for a single-domain state, e.g., $K_z(\boldsymbol{k} = [001])$, only a single mode is observed, which corresponds to a transverse excitation, and no other mode has been detected up to 25 meV energy transfer. Excitations of wavevectors perpendicular to the ferromagnetic planes are dispersionless, whereas for a wavevector within the (001) ferromagnetic planes a dispersion exists with a minimum at the zone boundary X-point. Both systems would, in fact, like to order with a simple type I magnetic structure consisting of a plane stacking +−+−, but higher-order interactions favor more complex magnetic structures.

Although Hälg and Furrer (1986) have succeeded in "fitting" the data with a model Hamiltonian including bilinear and higher-order anisotropic interactions, these

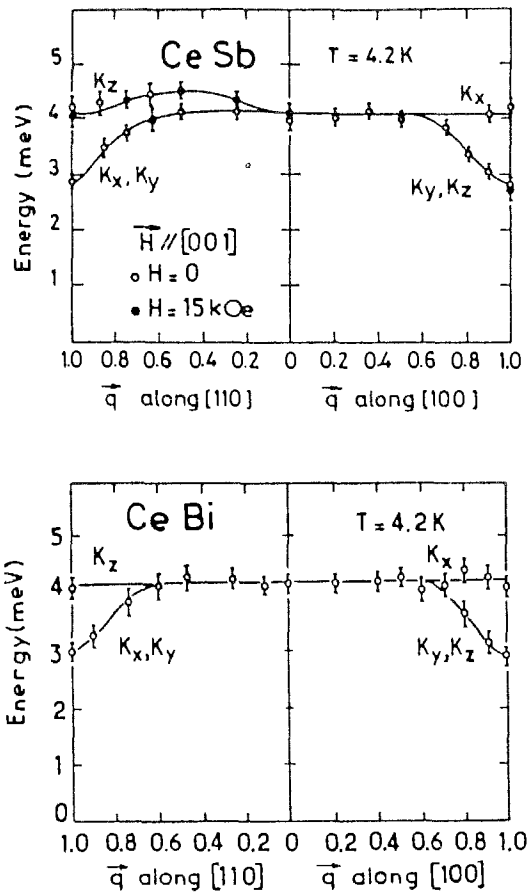

Fig. 16. Dispersion curves of magnetic excitations in CeSb and CeBi measured along the [100] and [110] directions. K_x, K_y, and K_z label the dispersion curves in the magnetic domains associated with the wavevectors $\mathbf{k} = [k00]$, $[0k0]$ and $[00k]$, respectively. Open symbols correspond to measurements in a multidomain state in zero field with the type-IA (CeSb) or the type-I (CeBi) structure. Solid symbols correspond to measurements with an applied field of 15 kOe, and yielding a single K_z domain. (From Rossat-Mignod et al. 1985b.)

parameter "fits" must be regarded as phenomenological, as the authors themselves admit. A basic difficulty is that the magnetic interactions appear to have planar rather than the cubic symmetry of the crystal structure. This is *exactly* the problem that arises in explaining the magnetic critical effects, so that there is a close relationship between these two phenomena, as we would expect. This planar symmetry is a signature of the hybridization process, as discussed by Wills and Cooper (1987), and we shall find it even stronger in the uranium compounds.

Neutron inelastic experiments have also been reported by Rossat-Mignod et al. (1985b) on $\mathbf{CeSb_{1-x}Te_x}$ solid solutions. The CF splitting between the Γ_7 ground state and Γ_8 excited state initially rises for small x, reaches a maximum (of ~8 meV) at $x = 0.5$ and then decreases to ~3 meV for CeTe. However, the small CF splitting in Te makes it difficult to explain the susceptibility and resistivity as measured at low temperature in CeTe (and other Ce chalcogenides). For these materials, which have small moments

and low-ordering temperatures, Kondo-like fluctuations have been proposed. It is unclear how these will affect the excitation spectra.

Recently, some inelastic scattering experiments have been reported on CeSe by Dönni et al. (1992a, 1993). CeSe orders with a type II structure with $\boldsymbol{k} = \langle \frac{1}{2}, \frac{1}{2}, \frac{1}{2} \rangle$ and a very small moment of ~0.2 μ_B. The result of an analysis similar to that performed by Hälg and Furrer (1986) is that the strength of the longitudinal nearest-neighbor coupling for a spin configuration parallel to the bond axis is at least one order of magnitude larger than the transverse coupling. This is similar to what is found in the Ce monopnictides. The excitation spectrum shows a gap of ~0.3 meV at L($\frac{1}{2}$, $\frac{1}{2}$, $\frac{1}{2}$), but there is also a minimum of almost the same magnitude at the X(1,1,0) point. This shows the effect of competing interactions.

4.2.2. *Ytterbium systems*

The Yb monopnictides YbX (X = N, P, As, and Sb), which have the NaCl crystal structure, have only recently been synthesized in single crystal form (Dönni et al. 1990a). It is found that the Yb ions have a 3+ valence. the CF interaction produces a Γ_6 doublet as the ground state, an excited Γ_8 quartet above (by at least 13 meV in practice) and a further Γ_7 doublet at even higher energy. The Γ_6 ground state should support a moment of 1.33 μ_B, but the moment in all the Yb monopnictides is considerably lower than this value, ranging from 0.4 to 1 μ_B. There have been a number of CF investigations (Dönni et al. 1990b, Kohgi et al. 1990a, Ohoyama et al. 1992) and some evidence was presented for a possible interaction between the CF levels and the phonons; this would especially involve the Γ_8 quartet, which is susceptible to such effects. Recent single-crystal experiments (Dönni et al. 1992b) on **YbAs** are too complex to interpret unambiguously because of the many domains present (the ordering wavevector is $\boldsymbol{k} = [1,0,\frac{1}{2}]$), but suggest that the dispersion of the excitation as determined by bilinear exchange interactions is larger than that arising from the molecular field. The authors then conclude that due to Kondo hybridization in YbAs the onset of long-range magnetic ordering is suppressed. Experimentally, T_N for YbAs is found to be ~0.6 mK, and all the other monopnictides also order below 1 K, which is not expected on the basis of exchange interactions extrapolated from neighboring lanthanides. YbAs was also examined by Oyamada et al. (1990), who found a type-III ordering with the moments perpendicular to the propagation direction. In the studies of Oyamada et al. (1990) and Dönni et al. (1992b) there is evidence for an unusual type of ordering in which the AF order coexists over ~0.2 K with paramagnetic behavior. One would normally associate such effects with inhomogeneities in the sample, but Dönni et al. (1992b) point out that the effects are reproducible on a number of samples. Further work is clearly required.

Yb, which has a doublet ground state, as found in Ce, is also anomalous. However, the exact nature of the hybridization (or Kondo mechanism) is not yet clear, and because of the low-ordering temperature and complex magnetic structure, we are unlikely to see clear excitation spectra in the near future.

4.3. *Actinide compounds with the NaCl crystal structure*

The review by Buyers and Holden (1985) discusses at length the neutron inelastic experiments performed on UN, UAs, USb, US, and UTe. We shall recapitulate and then review the work that has been done since the chapter by Buyers and Holden. Table 1 gives details of the actinide NaCl structure compounds that have been examined in single crystal form with inelastic neutron scattering. More details of the magnetic structure, etc., may be found in the literature (Rossat-Mignod et al. 1984, Burlet et al. 1986, 1988, Lander 1993).

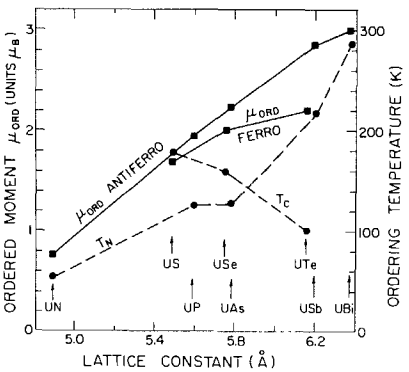

Fig. 17. Ordered magnetic moments and ordering temperatures of uranium monopnictides and monochalcogenides as a function of the lattice constant a_0. The U–U separation is simply $a_0/\sqrt{2}$. The ordering temperatures are indicated by the right-hand scale and marked as solid circles. The values of the ordered moments are indicated by the left-hand scale and marked with solid squares. (From Buyers and Holden 1985.) Note that this figure appeared also in many earlier works.

Figure 17 is used to illustrate one aspect of the interesting physics of these systems. The main point of this figure is that at small U–U separation both the moment and the ordering temperature are small. In the case of the U compounds the figure shows that the moment scales almost linearly with the U–U distance. This trend is also present in Np compounds with the NaCl structure, but not so clear for Pu compounds. Many efforts have been made to understand the dependence of the ordered moment on the U–U separation. The accepted view of the electronic structure at this time is to start with a $5f^3$ configuration for *both* the monopnictides and monochalcogenides, add a crystal-field interaction to give a Γ_8 quartet as the ground state, and then switch on hybridization effects. It is the role of the latter that is still difficult to quantify. The results of neutron inelastic scattering have been central to the development of the hybridization model. However, the role of the crystal field is less clear. Wedgwood (1974) was the first to search for CF energy splittings with neutron spectroscopy using polycrystalline samples. He found no evidence for crystal-field excitations. Indirect evidence for a Γ_8 CF ground state was found in the form-factor measurements on USb by Lander et al. (1976). A more recent neutron inelastic scattering experiment by Osborn et al. (1988) at the ISIS spallation source (Rutherford Laboratory, UK) on both USb and UTe has provided no evidence for CF transitions up to 200 meV. Thus, although there is little doubt that CF interactions exist, and are even quite strong (indirect evidence suggests the multiplet splittings are between 30 and 70 meV), they are strongly damped and are not readily visible as is the case in 4f and insulating 5f compounds. This would seem to eliminate explanations based on sharp CF levels, such as

Table 1
Properties of single crystals of the rocksalt structure that have been examined by neutron inelastic scattering

Compound	a_0 (300 K)	T_N (K)	T_C (K)	k	ordering	μ_B ($T = 0$)	E_A (meV) [a]	Comment[b]	Ref.
UN	4.89	53		$\langle 001 \rangle$	1k type I	0.75	~16	broad	1,2
UAs	5.779	124		$\langle 001 \rangle$	1k type I	1.7			
		62		$\langle 00\frac{1}{2} \rangle$	2k type IA	2.25	~0?	broad	3,4
USb	6.191	212		$\langle 001 \rangle$	3k type I	2.85	6.5(2)	sharp	5–7
US	5.489		170	0	ferro	1.70	~40	broad	2
USe	5.750		160	0	ferro	2.0	~38	broad	2,8
UTe	6.155		104	0	ferro	2.25	14.8(3)	sharp, but ...	2,9
$USb_{0.8}Te_{0.2}$	6.180	204.5		$\langle 00{\sim}0.4 \rangle$	3k type (inc)			unknown	
			155	0	ferro	2.8	30(2)	sharp	10
NpSb	6.254	202		$\langle 001 \rangle$	3k type I	2.5	–	unknown	11
PuSb	6.240	85		$\langle 000.13 \rangle$	1k, Inc.				
			70	0	ferro	0.74	18.5(3)	sharp	12

[a] E_A is the anisotropy gap.
[b] Comments refer to whether the excitations are broad or sharp, see text.

References
(1) Holden et al. (1984)
(2) Buyers and Holden (1985)
(3) Stirling et al. (1980, 1983)
(4) Loewenhaupt et al. (1982)
(5) Lander and Stirling (1980)
(6) Hälg and Furrer (1986)
(7) Hagen et al. (1988)
(8) Holden et al. (1986)
(9) Lander et al. (1991b)
(10) Langridge et al. (1992)
(11) Stirling et al. (unpublished)
(12) Lander et al. (1986)

proposed by Holden et al. (1987) and Hälg and Furrer (1986). The difficulty at this time is that the "hybridization models", at least for the actinides, are rather qualitative in nature, although steady progress is being made, see Hu et al. (1989) and Hu and Cooper (1990).

We mentioned earlier the central importance of the excitation spectra in developing this hybridization model. In fact the single most important fact to emerge from the inelastic studies of the U compounds is that *at small U–U separation no well-defined magnetic excitations are seen.*

Thus, referring to fig. 17, the excitation spectra are broad in UN, UAs, US, and USe, whereas they become well defined in USb and UTe, which have the larger U–U distance. These results are reviewed by Buyers and Holden (1985) but are not yet quantitatively understood. Unquestionably they are the most interesting in the study of these NaCl structure materials. It is, of course, normal in a *paramagnetic* system to have a wide (in energy) relaxation spectrum, but quite unusual in a material that orders with a well-defined magnetic moment. Moreover, consistent with the large anisotropy of these actinide compounds, we find a large *anisotropy* gap in the excitation spectrum. Qualitatively, at least for the ferromagnets, the value of this anisotropy gap (E_A) is consistent with bulk anisotropy measured by other techniques (see Lander et al. 1991a for a review).

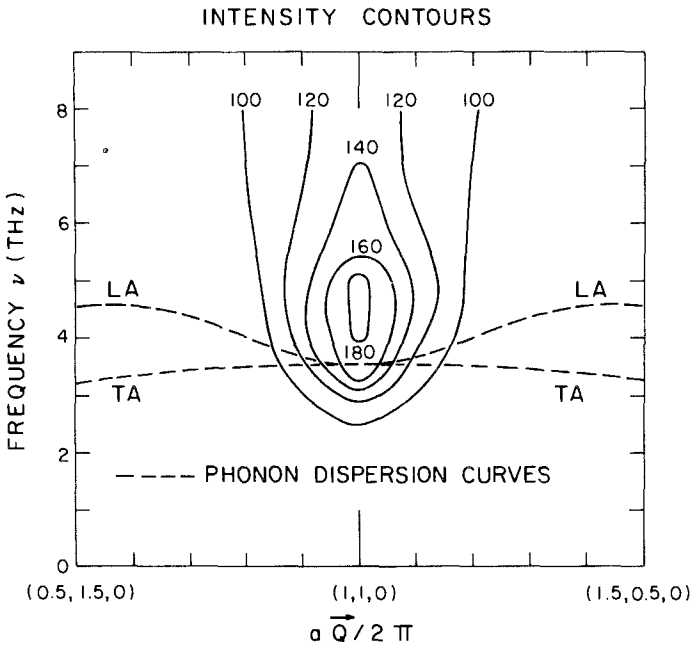

Fig. 18. Contours of constant magnetic neutron scattering intensity in UN at 4.2 K. (From Holden et al. 1982.) (1 THz = 4.12 meV)

4.3.1. *Uranium antiferromagnets*

The first detailed experiments were performed on single crystals of UN (Holden et al. 1982, 1984). The anisotropy gap is ~16 meV at [1,1,0], the magnetic ordering wavevector. This coincides with the frequency of the phonons at the X point [1,1,0] although no interaction between the two has yet been found. No sharp excitations are seen. Contours of constant magnetic neutron intensity are shown in fig. 18.

Studies of both polycrystalline (Loewenhaupt et al. 1982), and single crystals (Stirling et al. 1980, 1983) have been performed on UAs. No sharp excitations have been seen. The absence of an anisotropy gap in UAs is most unusual. Buyers and Holden (1985) have pointed out that because the magnetic structure is a 2***k***-type IA at low temperature a number of domains are possible and the resulting spectra may be more complicated than if a single domain could be examined. The work on polycrystalline samples (Loewenhaupt et al. 1982) also shows a broad distribution of magnetic scattering centered about $E = 0$ (i.e., $E_A \approx 0$) and extending to ~40 meV. Above T_N the fitted Lorentzian spectral function had a half-width of $\Gamma/2 = 17.3$ meV, and this gradually decreased to ~8 meV at low temperature. Experiments on large single crystals of UAs would still be of interest.

Because some of the best crystals can be produced, and it has a large magnetic moment and type I ordering, USb has been a favorite for inelastic studies. The early

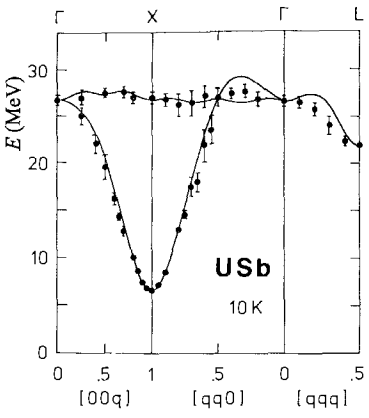

Fig. 19. Experimentally observed dispersion curves for USb in the 3**k** type-I structure at 10 K. The solid lines correspond to a model proposed by Hälg and Furrer (1986). (From Hälg and Furrer 1986.)

work (Lander et al. 1979, Lander and Stirling 1980) showed that *sharp* excitations did exist in USb, but reported that they were predominantly longitudinal in nature. However, Jensen and Bak (1981) pointed out that if the structure was 3***k***, as suggested by uniaxial stress measurements (Rossat-Mignod et al. 1980) and the absence of a measurable lattice distortion (Knott et al. 1980), then the observed polarization of the excitations could be understood as transverse excitations in a 3***k*** structure, in which the moments are along ⟨111⟩ directions. (A more complete discussion of the static aspects of multi-***k*** structures is given by Lander 1993.) Hälg and Furrer (1986), using a much better crystal, produced the complete excitation spectrum at 10 K and this is shown in fig. 19. The excitation spectrum is similar to that of CeAs (fig. 15) in that it is split into two modes at the X point, but the anisotropy gap (E_A) is much larger in USb and the dispersion is also greater. The latter, of course, is a reflection of the stronger exchange and ordering temperature in USb ($T_N = 213$ K) as compared to CeAs ($T_N = 8$ K). Hälg and Furrer (1986) have fit the USb excitation spectrum with a model including strong higher-order magnetic interactions. Whereas this model is useful at low temperatures, it is difficult to see how it can explain some of the temperature dependent effects even in USb (see below) or the broad featureless spectrum found in UN or UAs.

More recently, USb has been re-examined by Hagen et al. (1988) with particular emphasis on the temperature dependence effects and the critical regime. It was known from the earlier work that the energy of the magnetic excitation at the X point corresponded to that of the acoustic phonon, a situation similar to that found in UN, and that the dispersion appeared to increase with temperature. Both of these are unusual effects. Although the magnon and phonon frequencies at the X point are apparently the same, no evidence has yet been found for any interaction (to obtain such evidence probably requires using polarized neutrons and polarization analysis). However, the T dependence does show some unusual effects, and the spin-wave peak frequency and damping parameter as measured by Hagen et al. (1988) are shown in fig. 20. The initial rise of the frequency and the dispersion are evident for temperatures up

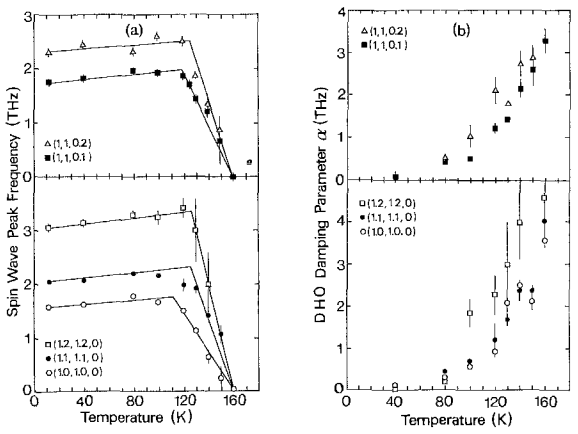

Fig. 20. Measurements of (a) the spin-wave peak frequency and (b) the damping parameter as a function of temperature in USb. Recall that $T_N = 212$ K and 1 THz = 4.12 meV. (From Hagen et al. 1988.)

to ~100 K. Above 100 K the excitation rapidly broadens and softens. One would have expected $T_N \approx 160$ K (fig. 20a), but in fact the ordered (elastic) signal disappears unambiguously at 212 K, so that the "transition" at ~160 K is at $T \approx 0.75\, T_N$. There has been some indication from muon spectroscopy (Asch et al. 1990) that some "transition" occurs in USb around 150 K, but the exact nature is still elusive.

Single crystals of **UP** or **UBi** of sufficient size for neutron inelastic scattering have not been grown.

4.3.2. *Uranium ferromagnets*

Single crystals of the monochalcogenides US, USe and UTe were all examined by the group at Chalk River National Laboratory in Canada, and much of this is reviewed by Buyers and Holden (1985). Since that time, it was realized that more information could be obtained if the crystal was a *single domain.* Experiments on single-domain ferromagnets, in which all the magnetic moments are parallel, have been performed on UTe, $USb_{0.8}Te_{0.2}$ and PuSb, at the Institut Laue-Langevin in Grenoble.

For **US** and **USe** no sharp excitations have been found. A number of experimental scans were presented by Buyers and Holden (1985), but are all somewhat similar to those shown in fig. 21. The peak in the USe spectra at 6 THz (= 25 meV) is the optic phonon. There is a further broad peak at [220], which is assumed to be magnetic. On going from [220] to [440] the square of the magnetic form factor drops from ~0.51 to ~0.07, thus rendering the magnetic scattering invisible at [440]. The excitation is very broad in USe, and a similar situation exists in US. In this latter material the excitation is so broad (see lower panel of fig. 21) that it is even difficult to define E_A.

UTe was also examined at Chalk River (Buyers et al. 1983, Buyers and Holden 1985), and relatively sharp excitations were found at the zone center (Γ point) with E_A = 14.4 meV. Away from this point the situation was unclear. Some of these ambiguities were resolved by Lander et al. (1991b) by working on a single-domain sample. This latter state is produced simply by cooling in a modest ($1 < H < 4$ kOe) magnetic field;

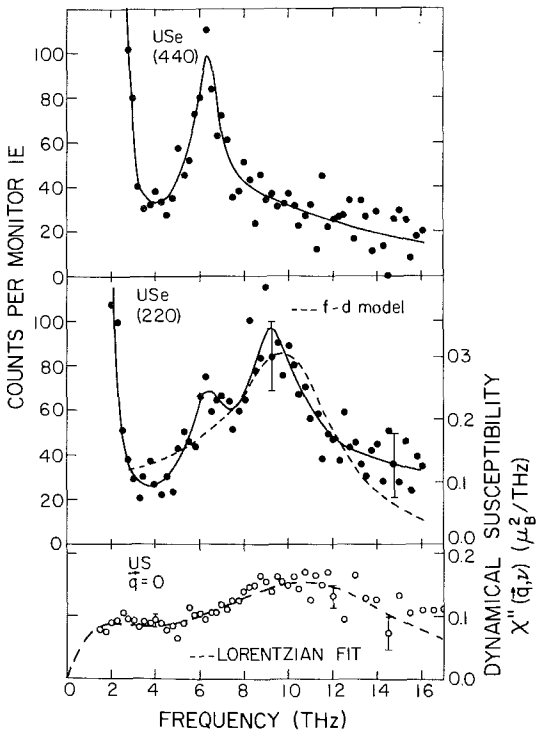

Fig. 21. Neutron scattering measurements at the wavevectors [220] and [440], corresponding to $q=0$, for USe. The left-hand scale gives the observed counts, the right-hand scale gives the susceptibility in μ_B^2/THz. 1 THz = 4.12 meV. Solid lines are guides to the eye. The dashed line in the middle panel represents a fit to a model. The lower panel gives the derived dynamical susceptibility for US at $q=0$, and the dashed line is a fit to the sum of two Lorentzians. (From Holden et al. 1986.)

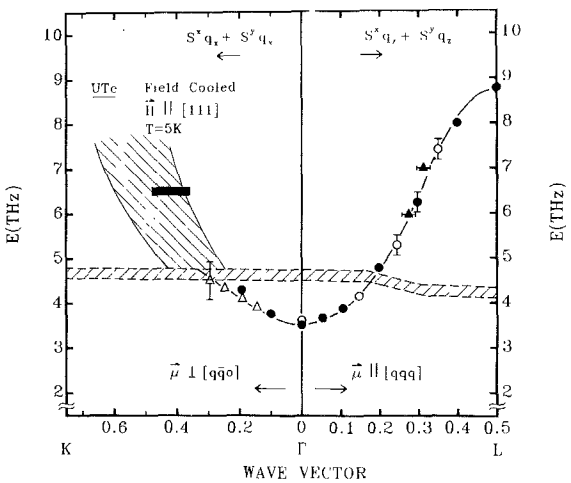

Fig. 22. Dispersion curve for UTe along the q_z (parallel to the moment) and q_x (perpendicular to the moment) directions at 5 K. The narrow hatched area shows the optic-phonon frequency. The different symbols correspond to different spectrometer conditions. The wide hatched area on the left-hand side corresponds to the region where the specific peak positions are uncertain. (From Lander et al. 1991b.)

the field may then be removed and, provided the sample is not warmed above T_C, it stays in a single-domain state. The resulting dispersion curve is shown in fig. 22. The

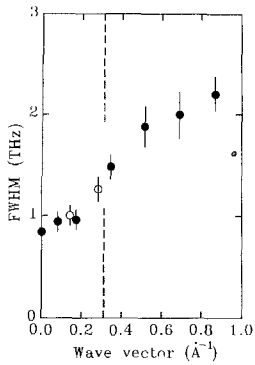

Fig. 23. FWHM of Lorentzian damping function at 5 K for excitation peaks in UTe as a function of wavevector. Solid points correspond to q_z, open points to q_x. The dashed vertical line indicates the wavevector at which the magnetic and optic-phonon excitation intersect. (From Lander et al. 1991b.)

anisotropy gap E_A (= 14.8 meV) is in excellent agreement with earlier work. However, $S(\boldsymbol{q},\omega)$ is anisotropic; parallel to the moment direction from Γ to L in the Brillouin zone the excitation is well defined with a relationship

$$E = E_A + Dq^2,$$

with $E_A = 14.8(3)$ meV and $D = 40(4)$ meV Å^2, whereas in the perpendicular direction for $q > 0.3$ reciprocal lattice units (rlu) the excitation becomes difficult to observe. This is a most unusual phenomenon, and has not previously been observed in cubic ferromagnets. Hu et al. (1989) claim that this is direct evidence for anisotropic hybridization of the same sort that establishes the anisotropy in the critical scattering from antiferromagnets (Lander 1993). The anisotropy in the excitation spectrum depending on whether $\boldsymbol{q} \parallel \boldsymbol{\mu}$ or $\boldsymbol{q} \perp \boldsymbol{\mu}$ explains the difficulty the earlier workers had with multidomain samples, where there is no single direction parallel to $\boldsymbol{\mu}$. Such problems do not, of course, affect the measurement of E_A, so this quantity was measured correctly.

UTe is thus a most interesting material in that it lies on the border line between the broad inelastic features found in UN, UAs, US and USe, and the resolution-limited (at least at low T) excitations of USb. This point was further amplified when the line widths were examined at low temperature and found to be considerably wider than the resolution (= 3.9 meV or equivalently 0.94 THz). The additional width at 5 K is plotted as a function of wavevector in fig. 23. This should be contrasted with fig. 20 for USb, in which, at low temperature, the excitation width is resolution limited. The additional width in UTe is assumed to arise from interactions between almost localized 5f and band states.

UTe is also known to have phonon anomalies connected with a negative Poisson ratio, see Buyers and Holden (1985). Schoenes et al. (1984) proposed on the basis of transport measurements that UTe was a Kondo system with a large value of the Kondo temperature. Similarly, the photoemission experiments of Reihl et al. (1981) were interpreted as showing a strong resonance occurring between the 5f and 6d band states. It is perhaps not surprising then that the neutron inelastic scattering gives such unusual results.

Recently, some experiments have been reported by Langridge et al. (1992) on a single crystal of $USb_{0.8}Te_{0.2}$, which becomes AF at $T_N \approx 190$ K and then becomes ferromagnetic at $T_C \approx 155$ K. Preliminary measurements in the ferromagnetic regime at 5 K show a dispersion curve (at small q values) similar to UTe but with E_A much increased to ~30 meV. Intuitively, one might anticipate this lying between those of USb and UTe, but this is not the case; it is larger than both the end members of the solid solution.

4.3.3. *Transuranium materials*

Crystals for neutron inelastic scattering must be at least 100 to 300 mm^3, so that the production of such crystals for work on transuranium compounds represents a formidable task. Indeed, except for the actinide oxides (sect. 2) *no* such experiments even on polycrystalline samples have been performed. On the other hand, we know that concentrating on uranium will give us only a part of the total picture. A good example of the need for systematic studies in the actinides is provided by the neutron form factor work determining the ratio of the orbital to spin magnetic moments, see sect. 3 of Lander (1993). Although the biggest reduction of μ_L/μ_S from the free-ion value is found in uranium compounds, we would be unable to draw any definitive conclusion without a study including Np, Pu and Am compounds. So, although we anticipate the vast majority of neutron studies to be performed on U compounds, it is important that at least a few be attempted on transuranium compounds. At the Institute for Transuranium Elements in Karlsruhe special equipment exists to grow such crystals, especially of the rocksalt structure (Spirlet and Vogt 1984).

Reasonably large crystals have been grown of **NpSb**. Experiments were performed to measure the critical magnetic scattering (Jones et al. 1991), but attempts to find the inelastic excitation spectrum were unsuccessful. This could be due to the high absorption (162 b at thermal energies of 25 meV) of the only available isotope ^{237}Np. New attempts are scheduled on "plate-like" crystals of NpTe and NpBi.

A successful effort was, however, mounted on a plutonium compound, **PuSb** (Lander et al. 1986). Because the most common isotope ^{239}Pu has an enormous capture (and fission) cross section (total ~1000 b) for thermal neutrons, it is useful only for small crystals used in diffraction experiments. A crystal was therefore made at Karlsruhe of the rare ^{242}Pu (thermal absorption 18.5 b) isotope, which was kindly loaned by the US Department of Energy.

The ground state of PuSb is known to be a Γ_8 quartet from the polarized-neutron measurements (Lander et al. 1984) so that the principal excitation is expected to be transverse $|5/2\rangle$ to $|3/2\rangle$ within the Γ_8 ground state. PuSb is a ferromagnet at low temperature (Burlet et al. 1984), so that, as with the experiments on UTe, it proved possible to obtain a single-domain crystal. The geometry of the experiment is shown in fig. 24 (left-hand side). The scattering function is written as $S^{\alpha\beta}(\boldsymbol{Q},\omega)$, where we can conveniently break down the directional aspect into components along the three cubic directions. We neglect non-diagonal terms. Recalling that the neutrons are sensitive only to components perpendicular to the momentum transfer $\boldsymbol{Q}$, we can readily understand

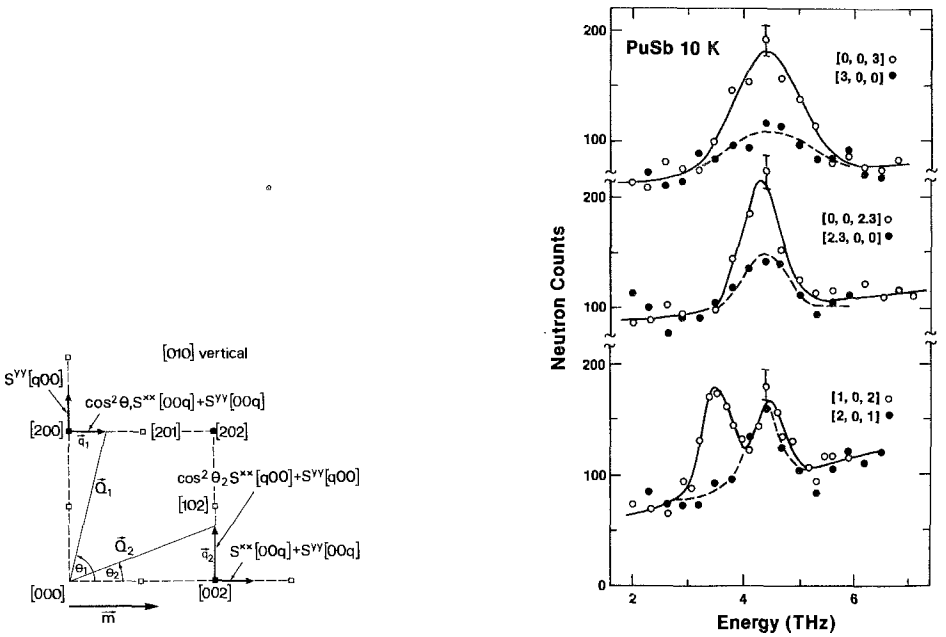

Fig. 24. (left) Geometry of the scattering experiment on PuSb. Scattering vectors are $\boldsymbol{Q}$, with $\boldsymbol{q}$ the reduced wavevector from a zone center. The components of $S(\boldsymbol{q},\omega)$ that are measured along $\boldsymbol{q}$ direction are marked on the diagram; (right) experimental scans with Cu(220) monochromator and pyrolytic graphite (002) analyzer and $k_f = 4.0\,\text{Å}^{-1}$. Lines are Gaussian fits to the data. (From Lander et al. 1986.)

the significance of the scans shown at right in fig. 24. Restricting our consideration to transverse components, i.e., longitudinal components such as $S^{zz}(\boldsymbol{q}) \approx 0$, is an assumption verified by the observed intensities. For $\boldsymbol{Q}=[0,0,2+q]$ we will observe transverse components $S^{xx}[0,0,q]+S^{yy}[0,0,q]$, which must be equivalent by symmetry, whereas for $\boldsymbol{Q}=[2+q,0,0]$ we observe only $S^{yy}[q,0,0]$. The frequencies of these two components are the same as shown in fig. 24(right), and the change in intensity by a factor of two confirms that we have produced a single domain. (It is only for a single-domain state that the intensity difference is a factor of two.) However, for $\boldsymbol{Q}=[q,0,2]$ we observe both $S^{xx}[q,0,0]$ and $S^{yy}[q,0,0]$. The new mode at 14.4 meV (at the X point) in fig. 24(right) corresponds to transverse fluctuations of a mode that is propagating along the moment direction. At the Γ-point $E_A = 18.5(3)$ meV, but the presence of an excitation at lower frequency at the X point shows that PuSb would prefer to form a simple +−+− type I *antiferromagnetic* structure.

The dispersion curves are illustrated in fig. 25. Banerjea and Cooper (1986) have made considerable progress in understanding this excitation spectrum in terms of their hybridization model. There are still some discrepancies, e.g., the observed dispersion is less than expected for a ferromagnet ordering at 86 K, and the dispersion in the theoretical fits is bound to reflect that fact. Nor does the theory convincingly reproduce the low-lying mode at the X point.

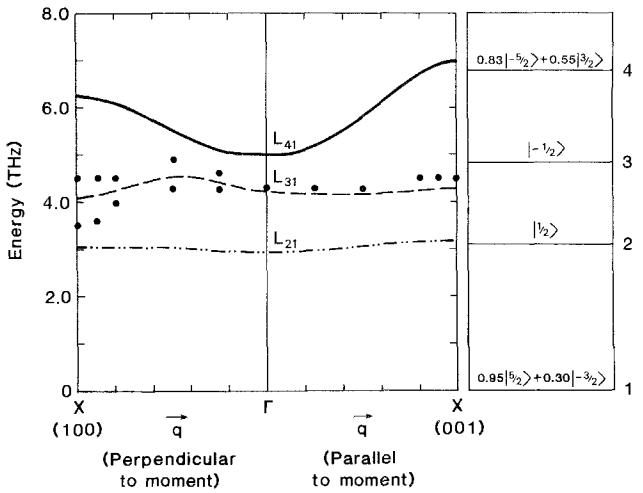

Fig. 25. Dispersion curves for PuSb (solid vertical bars and open points) as taken from Lander et al. (1986), together with the theoretical results derived by Banerjea and Cooper (1986). Molecular-field states are shown to the right taking the [100] axis of quantization. Both theory and experiment are at low temperature ($T = 10$ K). (From Banerjea and Cooper 1986.) [1 THz = 4.14 meV]

Note the superficial similarities between the excitation spectra of CeSb, CeBi (fig. 16) and PuSb (fig. 25). On closer examination, however, it must be remembered that the Ce compounds are antiferromagnets so that a minimum at the X point ($\boldsymbol{q} = 1$) is anticipated. Furthermore, it is the mode that is transverse to the moment direction that has the minimum at X. E_A is smaller by a factor of ~6 for the Ce compounds compared with PuSb, but the dispersion is similar, despite a factor of ~4 in the ordering temperatures. Clearly, more experiments and theory are required before the complex polarization dependence of the excitations in such systems as UTe and PuSb are understood.

4.3.4. *Remarks on damping of excitations*

As indicated earlier, perhaps the major puzzle in the actinide rocksalt compounds, all of which have well-defined *static* magnetic properties, is the fact that in most compounds the excitations are broad and well-defined spin waves do not exist. Moreover, in the few materials in which sharp excitations are seen (USb, UTe and PuSb), there are unusual "broadening effects" that appear when the temperature is raised. Buyers and Holden (1985) have considered possible damping from a number of sources. First, they consider mechanisms arising from phonons. Although such interactions undoubtedly play a role in the actinide oxides, it seems unlikely that their contribution is of major importance for the compounds discussed in this section. Apart from the oxides (sect. 2.3), there are no examples of strong magnon–phonon coupling as found, for example, in $CeAl_2$ (Loewenhaupt et al. 1979a, 1987), and treated theoretically by Thalmeier and

Fulde (1982). Second, they consider electronic damping between localized 5f states and d band states. Their model assumes isotropic interactions, whereas we know that the mechanism is anisotropic. It thus seems more appropriate to follow the approach of Cooper and his colleagues (Cooper et al. 1985, Hu et al. 1989, Cooper et al. 1992). Another interesting idea is due to Edwards (1984) and has been presented in a slightly different form by Brooks (unpublished). This is due to the inapplicability of the Wigner–Eckart theorem when orbital moments exist in itinerant systems. The orbital part of the magnetic moment operator does not commute with the one-electron Hamiltonian. For strong spin–orbit coupling the spins are hindered as they rotate. In this picture there are single-particle transitions between several one-electron bands. The addition of exchange enhancement to this picture then gives the broadened excitation spectra seen in neutron scattering.

At this time most of these ideas cannot be tested because they have not been carried through to make quantitative comparison with experiment. The work of Cooper and his colleagues is an exception. It is now generally accepted that the damping is a signature of the strong interaction between almost localized 5f electrons and the s–d band states. This has no close analogy in the 4f series. As soon as such an interaction occurs in cerium compounds, for example, the magnetic ordering is almost always destroyed. It is the stronger exchange interaction that give these actinide compounds the ability to order magnetically, even at high temperature, and sustain the strong 5f–band electron interactions. The fact that these effects have been found so far only in the rocksalt-type compounds is, in our view, simply due to the fact that large crystals of other systems have not been available for neutron experiments. Thus, we regard this field as a promising one for future work.

4.4. *Compounds with other crystal structures*

Recalling that this section is devoted to systems that order with large (or relatively large) moments, and excludes heavy-fermion materials, there are very few experiments on actinide materials apart from the oxides and NaCl-structure compounds. There are good reasons for this. The normally high ordering temperatures of U and Np compounds imply a large exchange interaction; this, in turn, implies considerable dispersion in the excitation spectrum. (It is interesting to note in passing that the experiments on PuSb discussed in the previous paragraph do not follow this assumption!) Under these conditions, neutron inelastic experiments on polycrystalline samples would be expected to give little information. Single crystals are required and they have simply not been produced except in the NaCl-structure compounds and a selection of heavy fermions.

It is worth making a cautionary remark at this stage. Early neutron experimenters were, of course, expecting that metallic actinide compounds would exhibit crystal-field splittings when viewed with neutron scattering. This attitude comes from a simple extrapolation of the situation found in lanthanides, where this technique has been such a considerable success (Fulde and Loewenhaupt 1986). Indeed, the first experiments on actinide rocksalt materials by Wedgwood (1974), in which he claimed to see nothing

but broad magnetic scattering in UN, US etc. were initially treated with scepticism. Claims of CF transitions were made in a number of materials, but closer examination with better instrumentation has shown that these "peaks" in the inelastic spectrum almost always come from phonons. A good example is **UPb_3**, where Murasik and Zolnierek (1980) claimed an inelastic CF transition at ~12 meV, corresponding to the transition between Γ_5 and Γ_3 states in the U^{4+}: $^3H_4$ multiplet. However, a recent study (all on polycrystalline samples, no single crystals have yet been reported) by Marshall et al. (1992a) using time-of-flight techniques with a much more extensive Q coverage than in the earlier studies has shown that no sharp excitations exist below ~60 meV. UPb_3 orders at $T_N = 32$ K with a moment of 1.7 μ_B. The magnetic scattering may be fit to a quasielastic Lorentzian but the half-width $\Gamma/2$ varies across the zone from about 8 meV at small Q to a maximum of almost 20 meV at the Q corresponding to the first Bragg peak. One may note, as the authors themselves do, that single crystals are needed to extend this work, but the absence of peaks due to dispersionless CF interactions is established.

Recently, CF transitions have been reported in the antiferromagnetic tetragonal system **UPt_2Si_2** by Steeman et al. (1988). It remains to be seen whether these CF transitions stand up to the test of time, and this material is completely localized as in the case of UPd_3 (see sect. 2.2.2), or if they are later assigned to phonons. We do not believe that one experiment with a triple-axis spectrometer and a polycrystalline sample is sufficiently definite. The Q dependence of phonons with such a technique is by no means straightforward, especially at small Q.

A discussion of a few other Ce and Yb compounds that fall into the category covered in this section can be found in the recent work by Loewenhaupt and Fischer (1993), and will not be repeated here.

With respect to the systems of the CeM_2X_2 type (X = Ge or Si), discussed in sections 5 and 6, and to the intermediate-valent compound $YbAgCu_4$ presented in sect. 5, we mention the studies of the temperature dependence of the quasielastic linewidth of systems with the same structure, but which order magnetically. For the Ce compounds these are $CeRh_2Si_2$, $CeAu_2Si_2$, $CeAg_2Si_2$, $CeRu_2Ge_2$, $CeAu_2Ge_2$ and $CeAg_2Ge_2$, and for the Yb systems $YbAuCu_4$ and $YbPdCu_4$. More data on these systems are listed in table 3 in sect. 6. The temperature dependence of the quasielastic linewidth for $CeAu_2Si_2$ is added to fig. 57, and that for the Yb compounds to fig. 37. Although the temperature dependence of the QE line linewidth of $CeAg_2Ge_2$ behaves anomalously (non-linear with T), we include it here instead of in sect. 6. This is because the full ordered moment of 1.85 μ_B is developed (with respect to the CF ground state), and the QE linewidth is small (0.5 meV at 150 K) as determined by Loidl et al. (1992).

Comparisons between these lanthanide and actinide compounds are clearly difficult. For materials that order below 10 K the exchange interactions are weak. The Kondo temperatures, which reflect the strength of the antiferromagnetic interaction developing between the f states and the band states, are normally of the same magnitude, so that it is the interplay between these two that normally determines the physics. On the other hand, exchange interactions are much greater (by at least an order of magnitude for U

and Np compounds) and the hybridization effects are also greater and more complex; in part because more than one electron (or one hole in the case of Yb) are present.

5. Paramagnetic systems without sharp CF-excitations

In this section we will discuss systems that do not show distinct CF-excitations. This group of 4f materials are called intermediate-valent (IV) systems, and are discussed in detail by Loewenhaupt and Fischer (1993). Here we will give a survey and cover recent work. The most important data are summarized in table 2. Concerning the 5f materials, studies have been performed only on compounds containing uranium. Sharp CF levels are reported for UPd_3 (sect. 2.3.1). None of the systems discussed in this section order magnetically, with the exception of TmSe. Ordering in this compound probably occurs because both valence states, divalent and trivalent, are magnetic. Such a situation is also true for Pr_6O_{11}, in which no magnetic order has been reported to our knowledge. We discuss TmSe here because it is characterized by a wide structureless response in the neutron inelastic scattering. This latter feature is common to IV compounds.

5.1. *Lanthanide systems*

Systems that exhibit intermediate valency behave in a completely different way to stable lanthanides (sect. 2). In materials that exhibit intermediate valency the Coulomb exchange interaction is more than an order of magnitude larger than the direct magnetic dipole interactions. One has to distinguish the following classes:

(1) Lanthanides fluctuating between a nonmagnetic ($J=0$) and a magnetic ($J>0$) Hund's rule ground state, where the magnetic component can be classified: (a) $L=0$: Eu^{2+}(pure spin state) (b) $L\neq 0$: Ce^{3+}, Sm^{3+}, Yb^{3+}.

(2) Lanthanides fluctuating between two magnetic Hund's rule ground states: Pr and Tm.

With respect to these different types of fluctuating 4f states we will discuss the compounds below in this (at first sight somewhat confusing) order, viz. Eu, Ce, Sm, Yb, Pr, Tm. Usually IV systems do not change their valence drastically as a function of temperature, i.e., the hybridization strength of IV systems is usually independent of temperature, in contrast to Kondo and heavy-fermion systems, but there are a few exceptions. One group consists of the Sm and Eu systems, where the valence change is probably forced by the rather close-lying (in energy) first excited multiplet level (see sects. 3.2.1 and 3.2.2). The other prominent example is Ce metal.

The static magnetic susceptibility of intermediate-valent systems is not Curie-like. Below a certain temperature the susceptibility is essentially independent of temperature, and has a low value for $T\rightarrow 0$, as shown for $CePd_3$ in fig. 26. A consequence of this electronic state is a broad excitation in the neutron inelastic scattering. Following eq. (9) the integration over the quasielastic line of ~20 meV width (dashed line in fig. 26) gives a result in rough agreement with the bulk susceptibility. For many systems the static

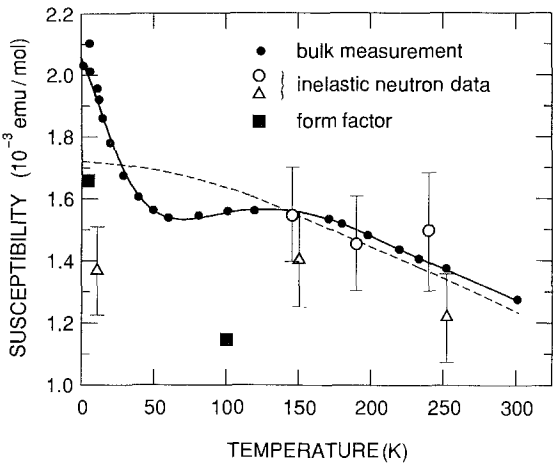

Fig. 26. Static susceptibility of $CePd_3$: the bulk measurement (solid circles) was performed on a sample used by Holland-Moritz et al. (1977, 1982), the local susceptibility obtained from neutron scattering are taken from Holland-Moritz et al. (1982) (open circles) and from Galera et al. (1987) (triangles). Susceptibility values obtained from form factor measurements by Stassis et al. (1982) are added (solid squares). The dashed line represents the model calculation using eq. (9) with a cut-off energy of 1.5 eV, a temperature-independent quasielastic linewidth of 20 meV, and a linear change of the valence for cerium from 3.23 at room temperature to 3.29 as $T \rightarrow 0$ K.

susceptibility shows even a maximum at a certain temperature T_{max}, as can be seen, for example, at $T \approx 150$ K in $CePd_3$ (fig. 26). This maximum, in most cases, reflects the change of a broad quasielastic magnetic response at temperatures larger than T_{max} into a broad inelastic response at low temperatures. The larger the absolute decrease of the static susceptibility below T_{max}, the lower is the magnetic intensity at low-energy transfer at low temperatures. A sharp decrease in the low-energy response may be caused also by the appearance of a "gap" in the energy spectrum, as was proposed for $YbAl_3$ (Murani 1985), for $Ce_3Bi_4Pt_3$ (Severing et al. 1991), and for CeNiSn (Mason et al. 1992). The position of the inelastic excitation is usually larger than the QE width at high temperatures. This behavior is discussed by many theoretical and experimental studies. For theory see e.g., Fedro and Sinha (1981), Mazzaferro et al. (1981), Schlottmann (1982, 1984a,b), Gunnarsson and Schönhammer (1985), Bickers et al. (1987), Kojima et al. (1984), Kuramoto and Kojima (1984), Kuramoto and Müller-Hartmann (1985), Kuramoto (1986); for experiments see tables 2 and 6, and for a review Holland-Moritz (1993). This inelastic response can be demonstrated unambiguously if no CF splitting is expected, i.e., on predominantly divalent Eu systems.

5.1.1. *Europium systems*

As already mentioned in sect. 3, natural Eu has a large neutron absorption cross section, which makes the use of ^{153}Eu isotopes necessary for inelastic neutron scattering investigations with cold or even thermal neutrons. Therefore, inelastic neutron scattering data are only available for two systems: **$EuPd_2Si_2$** (Holland-Moritz et al. 1987a) and **$EuNi_2P_2$** (Holland-Moritz et al. 1989a). Even the isotopically enriched samples have a rather large neutron absorption, so that only small samples (few grams) can be investigated by neutron inelastic scattering. The advantage of Eu compared to Sm (see below) is the large magnetic cross section of the Eu^{2+} configuration (≈ 20 barn). Moreover, Eu has

Table 2

Relaxation data as determined by neutron scattering for strongly unstable 4f systems. The Sommerfeld coefficient for the electronic contribution to the specific heat and some magnetic data are also given[a]

System	Bulk data					Neutron data						
	Specific heat		Susceptibility			High temperature			Low temperature			
	γ ($\frac{mJ}{mol\,K^2}$)	Ref.	$\chi_{bulk,T=0}$ ($\frac{10^{-3}emu}{mol}$)	T_{max} (K)	Ref.	T (K)	$\Gamma_{QE}/2$ (meV)	Ref.	T (K)	Δ (meV)	$\Gamma_{INE}/2$ (meV)	Ref.
γ-Ce						300	16.5	I				
α-Ce	12.8	2	0.51[b]		2				8	230.0	50.0	3
$Ce_{0.74}Th_{0.26}$	17.4[c]	4	0.54	VT	5	200	16.0	6	10	139.0	87.0	6
$CeBe_{13}$	115	7	2.17	140	8	300	17.0	9				
$CePd_3$ (p.cry.)	39	10,11	1.45[b]	130	12	300	19.0	9	5	55.0	24.0	12
(s.cry.)									10	–	3.0	13
									10	10.0	15.0	13
$CePd_{2.85}Ag_{0.15}$	100	14	2.8		14				5	35.0	~15.0	15
$CePd_2Ag$									5	25.0	~5.0	15
$CePd_3B_x$[d]	230	16	2.4		17	250	3.5	18	70	–	2.3	18
						250	1.0	18	10	–	0.1	18
$CeSn_3$	53–68	7,19	1.85[b]	130	20	300	23.0	9	5	40.0	14.0	20
$CeSn_{2.5}In_{0.5}$			3.3	60	21,22				5	18.0		23
$CeSn_{2.25}In_{0.75}$	190	19	5.4	38	21,22				5	13.0		23
$CeSn_2In$			8.0	25	21,22				5	9.0		23
$Ce_3Bi_4Pt_3$	3.3	24	2.0[b]	80	25	150	~20.0	25	2	20.0	asym.	25
CeNiSn (s.cry.)	200	26	5.0	12[e]	27				1.4	2.1	0.5	28
$CeNi_2Ge_2$	300	29				200	6.0	29	5	–	3.8	29
$CePt_2Si_2$	86	30	3.55	55	30	100	10.0	31	5	–	15.0	31
$Sm_{0.75}Y_{0.25}$			10.0[f]	VT	32	250	7.5	33				
SmB_6			3.2[b]	50	34				5	15.0	<2.0	35
									5	21.0	Q-dep.	35
$EuPd_2Si_2$			30.0[b]	VT	36	250	2.5	36	5	?[g]	~30.0	36
$EuNi_2P_2$			45.0[b]	30	37	270	6.0	38	5	9.2	1.8	38
TmSe						300	7.2	39	5	–	0.5	39
									5	10.0	2.0	39,40
$TmSe_{0.85}Te_{0.15}$						250	5.8	39	5	–	0.5	39
									5	7.8	1.8	39
$TmY_{0.05}Se_{0.95}$						150	8.2	39	15	–	3.0	39
									15	11.5	3.0	39
$TmLa_{0.05}Se_{0.95}$						220	4.4	39	5	–	0.5	39
									5	2.6	1.0	39
TmTe (28 kbar)						300	10.5	41				
$YbAl_2$	16.8	42	0.41	850	43				20	180.0	95	44

continued on next page

Table 2, *continued*

System	Bulk data					Neutron data					
	Specific heat		Susceptibility			High temperature			Low temperature		
	γ ($\frac{mJ}{mol\,K^2}$)	Ref.	$\chi_{bulk,T=0}$ ($\frac{10^{-3}emu}{mol}$)	T_{max} (K)	Ref.	T (K)	$\Gamma_{QE}/2$ (meV)	Ref.	T (K)	Δ (meV)	$\Gamma_{INE}/2$ (meV)	Ref.
$YbAl_3$	45	45	4.65	125	43				6	32.0	0.5	46
										46.0	40.0	46
YbCuAl	260	47	25.0	28	43	250	9.6	48	5	10.0	36	48
$YbCu_2Si_2$ (CF)	135	49	15.7	45[h]	51,52	300	5.3	9	5	–	3.5	9
(here[i])					50,51	300	20.0		5	3.5	3.0	
									5	~22.0	~10.0	
(17 kbar,CF)						300	3.1	41				
$YbPd_2Si_2$	203	52	18.2	30	53	250	13.0	54	5	21.0	12.0	54
									5	4.7	3.8	54
$YbAgCu_4$	245	55	25.0	30	55	250	7.6	56	15	3.9	6.1	56
$YbInCu_4$	50	57	9.1	VT	58				5	40.0	18.0	58

continued on next page

the important property of exhibiting no CF splittings, because the Eu^{2+} configuration with $J=S=\frac{7}{2}$, is a pure spin state, and the Eu^{3+} configuration is nonmagnetic because of $J=0$. We have already discussed the intermultiplet transition $J=0\rightarrow J=1$ observed below $T=150\,K$. Here we will concentrate on the consequences of this valence change on the behavior of the Hund's rule ground state.

The neutron scattering results of $EuPd_2Si_2$ are summarized in fig. 27. Above 200 K the quasielastic linewidth is about 2.5 meV and nearly temperature independent. As the valence increases below $T=140\,K$ the quasielastic magnetic linewidth increases rapidly. Both the increase of the valence (decrease of local magnetic moment) and the increase of the linewidth result in a magnetic scattering intensity at 5 K being hard to detect; only rough estimates can be given for the width of the magnetic line. No information on the shape (quasielastic or inelastic?) can be extracted from these data.

For studying the low-temperature response of an intermediate-valent rare-earth ion with no orbital moment, $EuNi_2P_2$ is more suitable than $EuPd_2Si_2$, because in the latter the valence transition is not completed when decreasing the temperature to $T\rightarrow 0\,K$; $v=2.5$ for $T\rightarrow 0$ (see fig. 9). The temperature dependence of the quasielastic magnetic linewidth extracted from neutron inelastic scattering measurements is also shown in fig. 27. It is almost temperature independent above $T=100\,K$ and decreases below that temperature to a value of about 2 meV at $T=5\,K$. This decrease of the QE linewidth is connected with the appearance of an inelastic excitation line. Figure 28 shows some constant-Q spectra of $EuNi_2P_2$ as a function of temperature. The position of the excitation line is shifted from $\Delta=9.2$ meV at $T=5\,K$ to $\Delta=8.4$ meV at $T=30\,K$ and $\Delta=7.5$ meV at $T=50\,K$. This excitation is no longer visible for $T\geqslant 100\,K$ and completely merged with the QE component in one broad QE line. The intensity of the inelastic excitation is increasing,

Table 2, notes

[a] Unless specifically stated, the parameters are all based on experiments with polycrystalline samples. VT means that a maximum in the static susceptibility cannot be observed because of a temperature-driven valence transition. In some cases the low-temperature magnetic response was fitted only by a quasielastic Lorentzian – this is then given in the column $\Gamma_{INE}/2$.

[b] Extrapolated value without tail.

[c] Value for $Ce_{0.8}Th_{0.2}$.

[d] $x=0.35$ for γ and χ_0, $x=0.32$ for neutron data. Note that in this material the authors state that two quasielastic lines are present.

[e] T_{max} is found only for $H \parallel a$.

[f] Value for $Sm_{0.77}Y_{0.23}S$.

[g] ?: no decision can be made about QE or INE.

[h] T_{max} is found only for $H \perp c$ (Currat et al. 1989).

[i] (here): In addition to the published values for $YbCu_2Si_2$, obtained from a CF analysis (CF), we give values from an analysis similar to that performed on $YbPd_2Si_2$ (see text).

References

(1) Rainford et al. (1977)
(2) Koskimaki and Gschneidner (1975)
(3) Fillion et al. (1985)
(4) Elbenaas et al. (1979)
(5) Shapiro et al. (1977)
(6) Loong et al. (1987)
(7) Cooper et al. (1971)
(8) Kappler and Meyer (1979)
(9) Holland-Moritz et al. (1982)
(10) Hutchins et al. (1972)
(11) Besnus et al. (1983)
(12) Galera et al. (1987)
(13) Shapiro et al. (1989)
(14) Mihalisin et al. (1981)
(15) Severing and Murani (1990)
(16) Sereni et al. (1986)
(17) Kappler et al. (1985)
(18) Culverhouse et al. (1992)
(19) Elbenaas et al. (1980)
(20) Murani (1983b)
(21) Lawrence (1979)
(22) Dijkman et al. (1980)
(23) Murani (1987a)
(24) Hundley et al. (1990)
(25) Severing et al. (1991)
(26) Aliev et al. (1988)
(27) Takabatake et al. (1990)
(28) Mason et al. (1992)
(29) Knopp et al. (1988)
(30) Ayache et al. (1987)
(31) Grier et al. (1988)
(32) Tao and Holtzberg (1975)
(33) Weber et al. (1989a)
(34) Menth et al. (1969)
(35) Holland-Moritz and Kasaya (1986)
(36) Holland-Moritz et al. (1987a)
(37) Sampathkumaran et al. (1982)
(38) Holland-Moritz et al. (1989a)
(39) Holland-Moritz (1983)
(40) Shapiro and Grier (1982)
(41) Walter et al. (1992)
(42) Gossard et al. (1964)
(43) Klaasse et al. (1977)
(44) Murani et al. (1992)
(45) Havinga et al. (1973)
(46) Murani (1985)
(47) Mattens et al. (1977)
(48) Murani et al. (1985)
(49) Pott (1982)
(50) Sales and Wohlleben (1975)
(51) Currat et al. (1989)
(52) Dhar et al. (1987a)
(53) Sampathkumaran et al. (1984)
(54) Weber et al. (1989b)
(55) Rossel et al. (1987)
(56) Severing et al. (1990a)
(57) Pillmayr et al. (1992)
(58) Severing et al. (1990b)

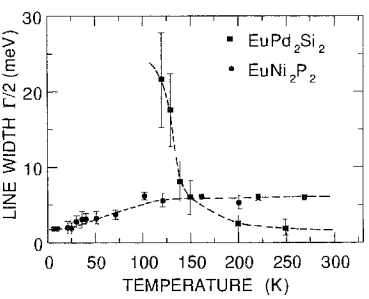

Fig. 27. The *QE* linewidth of Eu IV compounds as function of temperature (from Holland-Moritz et al. 1987a, 1989a).

at the expense of the quasielastic line, with decreasing temperature. As mentioned above, Eu cannot exhibit any CF splitting. Therefore, this observation is direct proof

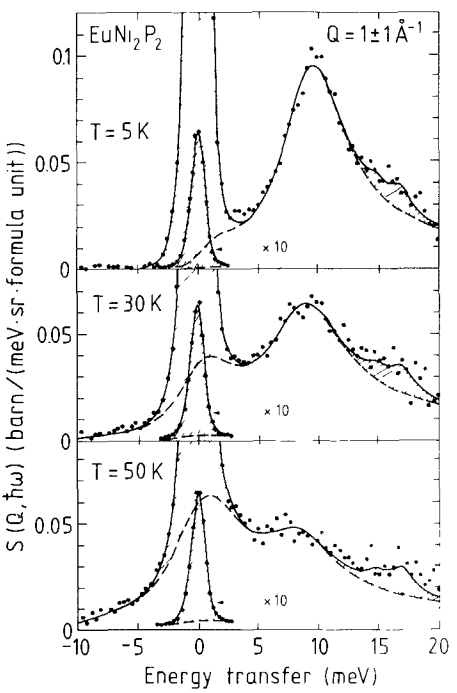

Fig. 28. Background corrected constant-Q spectra of $EuNi_2P_2$ as function of temperature ($E_i \approx 30$ meV). The hatched area is due to the nuclear incoherent elastic scattering and the inelastic phonon scattering. (From Holland-Moritz et al. 1989a.)

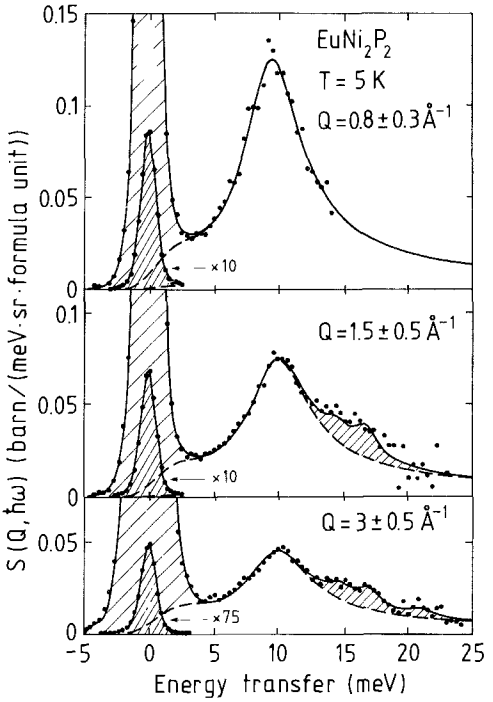

Fig. 29. The low-temperature spectrum of $EuNi_2P_2$ as function of momentum transfer ($E_i \approx 30$ meV). The hatched area is due to the nuclear incoherent elastic scattering and inelastic phonon scattering. (From Holland-Moritz et al. 1989a.)

that the magnetic scattering response of an intermediate-valent ion becomes an inelastic contribution at low temperatures, as was predicted by theories (Fedro and Sinha 1981, Mazzaferro et al. 1981, Schlottmann 1982, 1984a,b, Gunnarsson and Schönhammer 1985, Bickers et al. 1987, Kojima et al. 1984, Kuramoto and Kojima 1984, Kuramoto and Müller-Hartmann 1985, Kuramoto 1986).

The low-temperature response is presented in fig. 29 as a function of Q. The intensity of the inelastic excitation decreases with increasing Q much faster than the free-ion form factor of the Eu^{2+} configuration. The analytic formula given by Kuramoto and Müller-Hartmann (1985) was applied to the low-temperature spectra of $EuNi_2P_2$. At high Q the fit is reasonably good except at low frequencies, which can be understood by the underestimation of $\chi''(\omega = 0)$ mentioned above, compared to the exact solution. However, at low Q the fits with the analytic function are unacceptable. This is probably due to the calculations being restricted to single-ion behavior and neglecting spatial correlations. The full lines shown in figs. 28 and 29 are simple descriptions of the magnetic response by quasielastic (QE) and inclastic (INE) Lorentzians. Nevertheless, this description should not be understood as a two level system, but only as an approximation to the real spectral

function for a hybridizated ground state at low temperatures. This spectral function should be similar to that given by Kuramoto and Müller-Hartmann (1985), which is adequate at high Q, but the modified spectral function should also describe the Q dependence of the magnetic scattering. In this connection experiments on single crystals (when available) to measure the real Q dependence will be important.

5.1.2. *Cerium systems*

The properties of cerium differ from that of the other IV 4f ions, because the 4f wave function has just changed from delocalized character in Ba to localized in Ln (Göppert-Mayer 1941). Thus the localized electron state of the $4f^1$ configuration is unstable due to a double well potential as suggested by Bauchspiess et al. (1981). These authors used this model to explain the difference in the behavior of a series of Ce and Yb systems. Whereas Yb compounds have valences close to both extreme integral valences (e.g., $Yb^{3+}Pd_3$ and $Yb^{2+}Se$), CeO_2 and CeF_4, in which the Ce ion is expected to be tetravalent, show a distinct double structure in the L_{III} X-ray absorption spectra, see also Röhler (1987).

This has to be remembered in context with *cerium metal*, the only Ln metal that undergoes a first-order phase transition with a remarkable change of atomic volume. Despite a considerable effort, there is still not complete agreement on the exact nature of this phase transition in cerium. Some have argued that it represents a change of valence, whereas an alternative explanation is that it is a Mott transition in which the 4f electron changes its nature from localized (in the γ-phase) to itinerant (in the α-phase). A more complete survey of the theoretical situation is given by Johansson and Brooks (1993). By lowering the temperature at atmospheric pressure the transition of the γ-phase to the collapsed α-phase is possible only by passing through the β-phase. This complication by the β-phase can be avoided by applying external pressure or introducing lattice pressure by alloying with thorium. Shapiro et al. (1977) performed inelastic scattering experiments with thermal neutrons on $\mathbf{Ce}_x\mathbf{Th}_{1-x}$ alloys. They found that at low temperatures Ce in $Ce_{0.74}Th_{0.26}$ behaves like α-Ce, i.e., a small magnetic cross section spread over a large energy range. The full excitation spectrum could not be observed at that time due to limitations of the incident energy. Using epithermal neutrons from Argonne's spallation source, Loong et al. (1987) were able to confirm the early results and to detect the complete magnetic response at low temperatures on the same material. Figure 30 shows spectra between 100 and 300 K observed with $E_i = 300$ meV and the spectrum at 10 K taken with $E_i = 1200$ meV. The data at 10 K could be fitted best by an inelastic Lorentzian centered at 139 meV, with a width of 87 meV. CF effects are negligible. Even at high temperatures, i.e., for γ-Ce, CF excitations cannot be observed because the magnetic response is strongly broadened due to thermally driven interactions. The quasielastic width at 200 K is given as about 16 meV, which is in agreement with measurements by Stassis et al. (1979a) on elementary γ-Ce at room temperature.

The $\gamma \rightarrow \alpha$ collapse can be shifted to lower temperatures by additional substitution of Ce by La, e.g., $\mathbf{Ce}_{0.9-y}\mathbf{La}_y\mathbf{Th}_{0.1}$. This system does not show a sharp $\gamma \rightarrow \alpha$ transition,

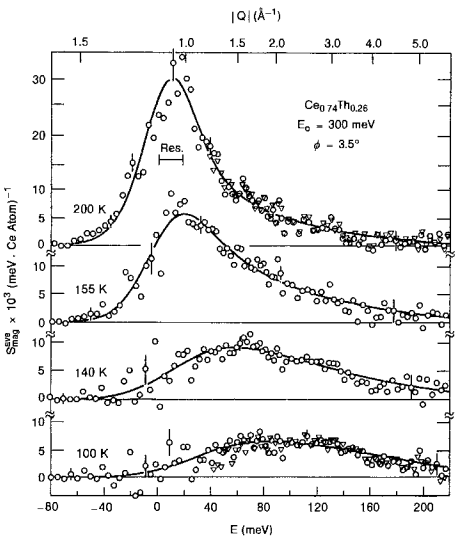

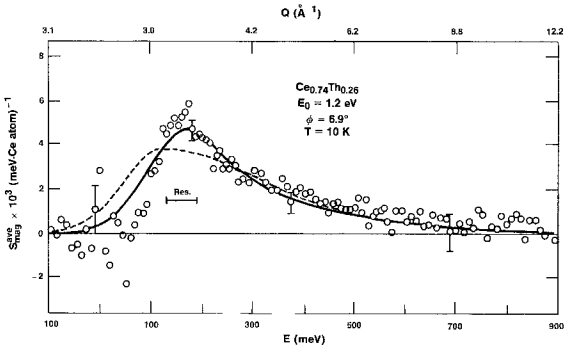

Fig. 30. Background corrected spectra of $Ce_{0.74}Th_{0.26}$ as function of temperature: upper panel has $E_i = 300$ meV and lower panel at $T = 10$ K has $E_i = 1200$ meV. The solid lines in the upper panel are fits with quasielastic lines, whereas in the lower panel the solid is an inelastic line and the dashed is quasielastic. (From Loong et al. 1987.)

however, with decreasing temperature an increase of the valence occurs at about 50 K. Therefore, whereas a distinct CF excitation is still visible at $T = 35$ K, it is smeared out by hybridization effects at 5.2 K (Grier et al. 1980, 1981). Moreover, the peak position is shifted to higher energies when the temperature is lowered. This behavior may be understood by considering the two extremes; the intermediate-valent Ce (α-Ce) at low temperatures described in this section, and the almost stable Ce (γ-Ce) at high temperatures.

There are only a few inelastic experiments done as function of pressure. This is due to two disadvantages: only small samples can be used in a pressure cell, which will decrease the sample signal, and, in addition, the large mass of the pressure cell gives additional background scattering. One of these difficult experiments was performed by Rainford et al. (1977) on *cerium metal* at room temperature. They found magnetic scattering for γ-Ce at atmospheric pressure which could be described by just one QE line of 10 meV

width. This value is somewhat less than found by Stassis et al. (1979a). At 8 kbar, i.e., for α-Ce, the magnetic response is decreased due to an increase of the width to 14 meV. The analysis of Rainford et al. (1977) may be questioned because of uncertainties in the phonon correction.

Fillion et al. (1985) investigated the α-phase of cerium at low temperature. To avoid the problems with the β-phase they applied pressure on the sample, cooled it down in liquid nitrogen, released the pressure, and removed the sample from the pressure cell keeping it at liquid nitrogen temperature. The sample was then cooled to 8 K. At this temperature the experiment was performed with polarized neutrons. Almost no magnetic scattering is detected up to an energy transfer of about 200 meV, but the authors claim that there is an inelastic response centered on ~230 meV. In addition, their fit contains a weak and broad quasielastic line.

All experiments on Ce show that the cross section at low temperature is small and spread over a large energy width. Unfortunately, this does not help decide whether the $\gamma \rightarrow \alpha$ transition involves a valence change, or a delocalization of the 4f electron. The experimental results are consistent with either interpretation in the first approximation. What is needed is more complete calculations so that they can be compared to the neutron results.

There are also two experiments dealing with *liquid cerium*. The first performed by Millhouse and Furrer (1975) at a triple-axis machine and at a fixed $\boldsymbol{Q} = 2.5\,\text{Å}^{-1}$ shows two excitations at ~3 and 7 meV, which were suggested to arise from the crystal field. However, this structure could not be confirmed by an experiment on a time-of-flight spectrometer by Rainford and Nguyen (1979). The latter present angles only up to 25°, i.e., this corresponds to an upper limit of $\boldsymbol{Q} = 1.3\,\text{Å}^{-1}$ at an energy transfer of 8 meV. This value of $\boldsymbol{Q}$ is below the position of the first maximum in $S(\boldsymbol{Q})$ of liquid cerium, and the scattering should be dominated by magnetic contributions. The earlier work of Millhouse and Furrer (1975) probably corresponds to phonon scattering.

$CePd_3$ is the most appropriate compound to demonstrate the principal behavior of the inelastic magnetic response by an intermediate-valent lanthanide ion. It has been studied extensively by several experimental methods (Gardner et al. 1972, Aarts et al. 1985 and references therein). The specific heat γ-value is about $40\,\text{mJ mol}^{-1}\,\text{K}^{-2}$ (Hutchins et al. 1972, Besnus et al. 1983). The neutron inelastic-scattering response at $T = 145\,\text{K}$ is shown in fig. 31 (Holland-Moritz et al. 1977, 1982). The magnetic spectrum does not contain any sharp peaks, which could be attributed to CF excitations, but the magnetic signal is spread over a wide energy range. The magnetic character of this scattering was proven by two findings. First, the phonon scattering contribution is rather small as demonstrated by the comparison to the diamagnetic reference compound YPd_3 in fig. 31 (lower part). Second, the $\boldsymbol{Q}$ dependence of the scattering intensity in the energy window between −1 and −6 meV (Holland-Moritz et al. 1982) is consistent with a magnetic free-ion form factor of Ce^{3+} (Stassis et al. 1977).

The energy dependence of the quasielastic scattering may best be analyzed in terms of a single Lorentzian. The temperature dependence of this linewidth is shown in fig. 32 (solid circles). The lower solid line represents qualitatively the Korringa behavior of a stable

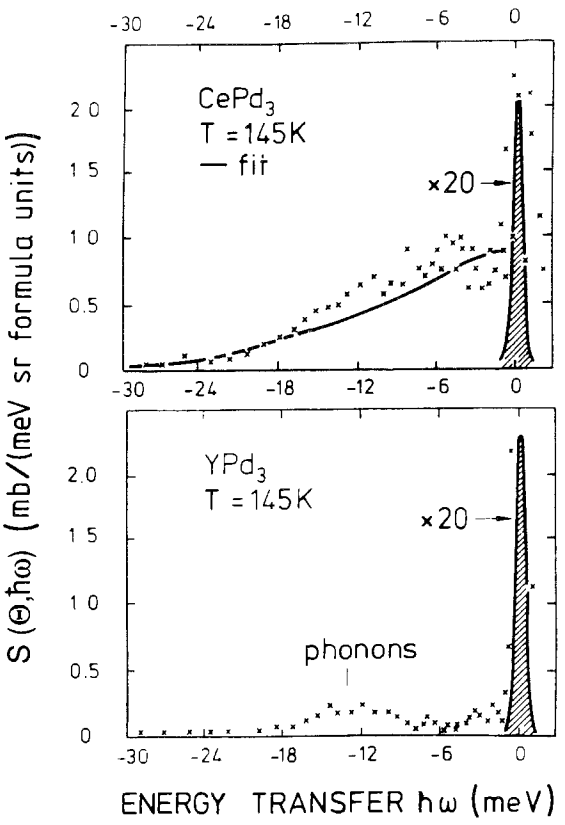

Fig. 31. Background corrected neutron inelastic scattering spectrum of $CePd_3$ and its diamagnetic reference compound YPd_3 at $T = 145$ K. The hatched area is due to the nuclear incoherent elastic scattering. (From Holland-Moritz et al. 1982.)

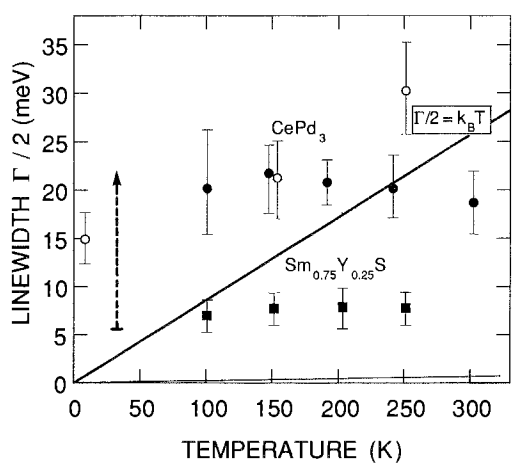

Fig. 32. The quasielastic linewidth of $CePd_3$ and $Sm_{0.75}Y_{0.25}S$ as function of temperature. Data taken from Holland-Moritz et al. (1982) (solid circles), Galera et al. (1987) (open circles), and Weber et al. (1989a) (solid squares). The dashed arrow at $T = 30$ K represents a lower limit of $\Gamma/2$ expected from the cold neutron scattering experiment. The thick solid line represents $\Gamma/2 = k_B T$ and the solid line at the bottom the Korringa behavior.

lanthanide ion shown in detail in fig. 3. In contrast, the quasielastic linewidth of $CePd_3$ is almost temperature independent and larger by a factor of at least 20 ($T = 300$ K). This implies that below a certain characteristic temperature the width becomes larger than the thermal energy $k_B T$, indicated in fig. 32 by the crossing point of $\Gamma_{QE}(T)/2$ with the bold line representing $\Gamma(T)/2 = k_B T$. If CF transitions are hidden underneath this broad magnetic response, the energy must be smaller than 15 meV, yielding a lower limit of the *QE* linewidth of about 13 meV (Holland-Moritz et al. 1982). The intensity obtained from a single *QE* line is in good agreement with the static bulk susceptibility (see fig. 26). The values by Galera et al. (1987) are somewhat smaller than those by Holland-Moritz et al. This is probably due to slightly different samples, because the bulk measurement performed on the sample used by Galera et al. (1987) is again in excellent agreement with their neutron data. In fig. 26 two susceptibility values extracted from form factor measurements by Stassis et al. (1982) are added. They do not coincide exactly with the bulk and inelastic neutron measurement, but they demonstrate that the low-temperature upturn in the bulk susceptibility is an intrinsic feature of $CePd_3$ (compare also $CeSn_3$: Murani 1983a,b, Stassis et al. 1979b,c). This upturn in the susceptibility is interpreted as due to an admixture of a 5d component to the local 4f form factor (see also Lander 1993). The total integrated magnetic cross section extracted from eqs. (7) and (8) with a cut-off energy of 2 eV (Holland-Moritz et al. 1982) yields a valence which is in rather good agreement with the L_{III}-edge results (Bauchspiess et al. 1981).

Due to the use of cold neutrons, $E_0 \approx 3.5$ meV, the above experiments cannot give information about the linewidth at low temperatures. They only provide lower limits of the linewidth if one quasielastic line is assumed. This information is indicated by the dashed arrow in fig. 32. Using thermal neutrons Galera et al. (1985, 1987) were successful in obtaining more detailed information. Both experiments with polarized and unpolarized neutrons show clearly the existence of a broad inelastic excitation. Their results, presented in fig. 33, show that the magnetic response changes its shape from a pure quasielastic one at $T = 280$ K to a dominant inelastic feature centered around 60 meV at $T = 5.5$ K. It is a quite general property (see table 2, above) that the position of the inelastic line at low temperature is at a greater energy than the width of the quasielastic line at high temperature. A residual weak quasielastic component seems to exist as well. The quasielastic linewidths of Galera et al. (1985, 1987) are added to fig. 32 (open circles).

Later, additional experiments were performed on the alloy $\mathbf{CePd_{3-x}Ag_x}$ by Severing and Murani (1990). These confirmed the earlier results on $CePd_3$. With increasing Ag concentration the high-energy peak becomes narrow and shifts to lower energies ($\Delta = 25$ meV for $CePd_2Ag$). Moreover, a second inelastic feature at ~10 meV and a quasielastic line with $\Gamma \approx 2$ meV become apparent. The authors interpret the low-energy peak as a CF transition $\Gamma_8 \rightarrow \Gamma_7$, which is related to an Ag-rich neighborhood of Ce, whereas the high-energy peak arises from the Pd-rich neighborhood. An analysis within the model of Jaccarino and Walker (1965) suggests that only 1–2 neighboring Ag atoms are sufficient to drive Ce into a trivalent state (Severing, private communication). This CF splitting of ~10 meV is consistent with the fact that an unresolvable CF transition may be hidden in the spectra of $CePd_3$ at $T > 120$ K (see above). The magnitude of the CF splitting also

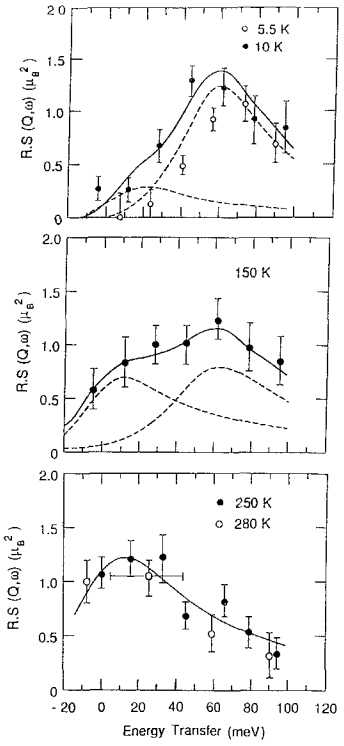

Fig. 33. Energy dependence of the magnetic response in $CePd_3$ by using polarized neutron scattering technique. The function plotted is the usual scattering law as defined in eq. (2) or (7) transformed to units of μ_B; i.e. $S(\boldsymbol{Q}, \omega)$ multiplied by $(4\pi\Delta)/(r_e g_N)$, where Δ is the energy resolution at the corresponding energy. The solid lines are fits to the magnetic cross section including a convolution with the resolution function. (Adapted from Galera et al. 1985, 1987.)

agrees well with the systematics of the RPd_3 series (Walter and Holland-Moritz 1981). The high-energy excitation at low temperatures, which shifts from 60 meV in $CePd_3$ to 25 meV in $CePd_2Ag$, cannot be understood in terms of a CF excitation. A similar change from the structureless response in $CePd_3$ to a crystal-field excitation spectrum was observed by Culverhouse et al. (1992) by alloying $CePd_3$ with boron.

An experiment on single-crystal $CePd_3$ has also been conducted by Shapiro et al. (1989). One of their spectra, obtained with a $\boldsymbol{Q}$ vector close to the almost forbidden Bragg point [011] at $T = 10$ K is shown in fig. 34. This exhibits a clear low-energy structure that is compatible with a rather narrow quasielastic line of ~3 meV width. This increases to an approximately constant value of ~6 meV for temperatures above 70 K. It is immediately clear that these results are in disagreement with the results reported earlier by using polycrystalline materials. Moreover, there is a further significant intensity above the phonon peak in the spectrum at 10 K, which has been interpreted by Shapiro et al. (1989) as an *inelastic* line with $\Gamma/2 \approx 15$ meV and centered at ~12 meV. Whereas the width is almost independent of temperature, the position changes to ~16 meV above 40 K. The discrepancy at low energy between the experiments on a single crystal and on polycrystalline material are not easy to reconcile. As the experiments on polycrystalline material are an average across the complete Brillouin zone, the only explanation seems

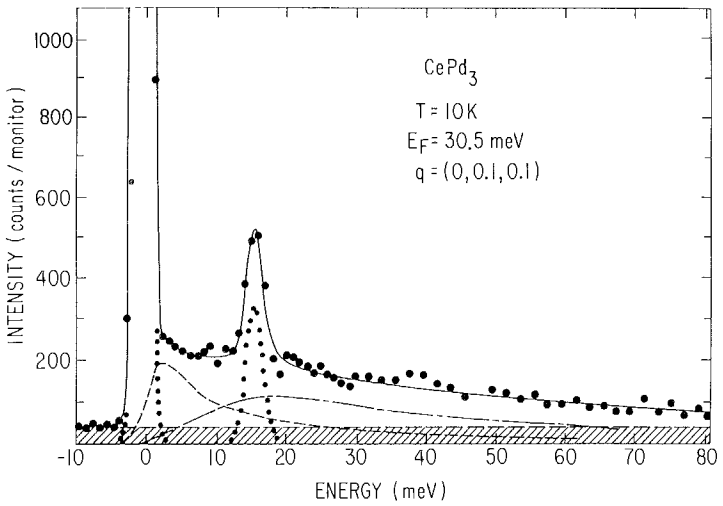

Fig. 34. Inelastic spectrum measured at 10 K from a single crystal of $CePd_3$. The peak at ~15 meV arises from phonons. The magnetic scattering was analyzed as consisting of a narrow ($\Gamma/2 \approx 3$ meV) quasielastic Lorentzian, and a relatively wide ($\Gamma/2 \approx 15$ meV) inelastic one centered at ~12 meV. (From Shapiro et al. 1989.)

to be that the *QE* response seen by Shapiro et al. (1989) is limited to a small part of the Brillouin zone. Clearly, it will be important to resolve this discrepancy in one of the most studied IV systems, and it does emphasize, again, the importance in many cases of trying also to perform experiments with both techniques, provided large single crystals are available.

Another compound that has been studied extensively with unpolarized neutrons (Holland-Moritz et al. 1982, Murani 1983a,b) and with polarized neutrons (Capellmann et al. 1985) is **$CeSn_3$**, in which γ is ~60 mJ mol^{-1}K^{-2}, and in which an inelastic response at ~40 meV is found. On alloying with indium to give the compositions $CeSn_{3-x}In_x$, Murani (1987a) showed that the peak scaled with the T_{max}, the maximum in the susceptibility. Doping with In also increases γ to a value of ~300 mJ mol^{-1}K^{-2} by $x = 1.1$ and Murani points out that the form of the observed spectra can be reasonably well accounted for by the analytic formula proposed by Kuramoto and Müller-Hartmann (1985).

Two other CeM_2X_2 compounds are worth mentioning here, because they behave from the point of view of neutron inelastic scattering like unstable 4f systems; **$CePt_2Si_2$** (Grier et al. 1988) and **$CeNi_2Ge_2$** (Knopp et al. 1988). This is particularly surprising for $CePt_2Si_2$ because a valence of 3.0 is reported for cerium (Röhler 1987). Grier et al. (1988) have fitted their spectra with a quasielastic line of width ~10 meV at 100 K, increasing to 15 meV at 5 K. This increase may again be an indication for an inelastic feature appearing in the magnetic low-temperature response. On the other hand, for $CeNi_2Ge_2$ a valence of 3.07 is reported (Röhler 1987). The spectra obtained with $E_i = 3.1$ and 12.5 meV are fitted with a quasielastic line, giving a linewidth of ~4 meV at low

temperatures, increasing slightly to ~6 meV at 200 K. This is quite similar to that found in $YbCu_2Si_2$ (see below). However, the experiments on $CeNi_2Ge_2$ by Knopp et al. (1988) do not give information on whether a high-energy excitation exists, as is the case for $YbCu_2Si_2$ and $YbPd_2Si_2$ discussed below. $CeNi_2Si_2$ may also behave in a similar fashion as L_{III}-edge measurements give a valence of ~3.15, but no neutron inelastic experiments have been reported.

An important problem in all this work on unstable f systems is the exact shape of the magnetic frequency response at low energy and at low temperature. We have already discussed this in sect. 1.2, and it becomes of much interest if the possibility of a "gap" in the spectrum occurs. This means, of course, that the response is zero up to some finite frequency, and then is positive definite. In most systems a clear decision about the existence of a gap in the magnetic excitation spectrum is difficult. However, recent inelastic neutron scattering by Severing et al. (1991) on cubic **$Ce_3Bi_4Pt_3$**, which is a semiconductor at low temperatures, clearly shows such a gap-like behavior. Up to an energy transfer of 12 meV no magnetic scattering could be detected. This is especially demonstrated by the data taken with $E_i = 17$ meV (fig. 35). Above 12 meV a rapid increase of the magnetic contribution is observed, which reaches its maximum value at about 20 meV. The decrease of the scattering at higher energies is much more gradual, resulting in a strongly asymmetric structure. For $T > 150$ K the magnetic response is again compatible with a single broad quasielastic line with a linewidth of ~20 meV.

Mason et al. (1992) have found a similar situation in orthorhombic **CeNiSn**, which is also a semiconductor at 5 K. They used a single crystal in their neutron studies and found that a gap occurs in the magnetic excitation spectrum only close to the (0,0,1) reciprocal lattice point (top frame of fig. 36). Since this corresponds to a position forbidden by the crystal symmetry, it suggests that the correlations are predominantly antiferromagnetic. Away from this point, e.g. (1.2,0,0), only weak, essentially isotropic, quasielastic scattering was found (lower frame of fig. 36). As observed in $Ce_3Bi_4Pt_3$ the gap character vanishes quickly with increasing temperature in CeNiSn. Work has been reported on polycrystalline samples of CeNiSn by Kohgi et al. (1992, 1993), who presented spectra up to an energy transfer of 60 meV. At about 20 K the magnetic response is broad and quasielastic, in agreement with the work of Mason et al. (1992). At 3 K their spectrum differs from that observed at certain reciprocal lattice points with a single crystal, but even in a polycrystalline sample an inelastic excitation was observed with an energy of about 4 meV instead of the 2.5 meV found by Mason et al. (1992). No CF transitions were seen at higher energy.

Semiconducting behavior seems to be a requirement for the direct observation of a hybridization gap in the magnetic excitation spectrum. If this f–d hybridization gap is responsible for the semiconducting nature, then the Fermi level must fall into the gap. In this situation no low-lying empty states of f character exist so that quasielastic magnetic scattering is forbidden. A hybridization "gap" is therefore observed. An indication for such a gap will also be found, of course, in the magnetic susceptibility. For $Ce_3Bi_4Pt_3$ the susceptibility drops by a factor of two below ~80 K, indicating a drastic decrease in

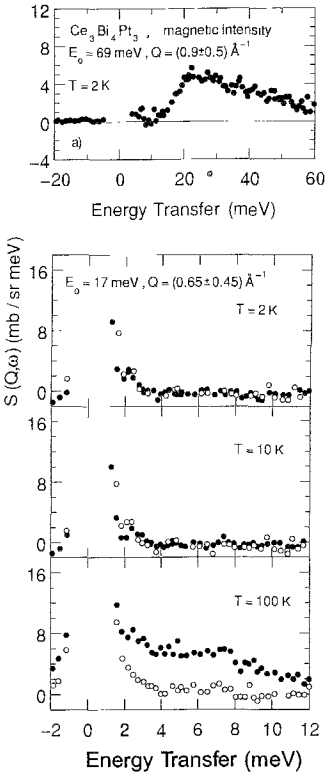

Fig. 35. Spectra of $Ce_3Bi_4Pt_3$ obtained with two different incident energies, $E_i \approx 69$ meV and 17 meV. (From Severing et al. 1991.) In the lower three panels the open points are from $La_3Bi_4Pt_3$ and the solid ones from $Ce_3Bi_4Pt_3$. The difference can be taken as a measure of the magnetic scattering.

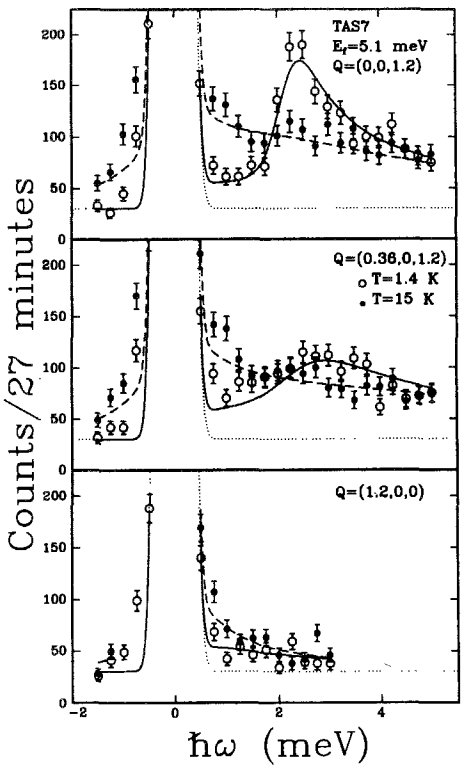

Fig. 36. Constant Q spectra obtained at $T = 1.4$ K (open circles) and at $T = 15$ K (solid circles) from CeNiSn. The dotted curve represents the flat background and the elastic nuclear peak. The dashed curve is a fit to the high-temperature data using a quasielastic Lorentzian, and the solid line is a fit to the low-temperature data using a spectral function that is a combination of a Lorentzian and a step-like function. (From Mason et al. 1992; for more details see this reference.)

population of the magnetic states at low energy. Such a decrease is consistent with the observations in fig. 35.

5.1.3. *Samarium systems*

SmS is particularly interesting because of its first-order metal–insulator phase transition at about 6 kbar (Maple and Wohlleben 1971), and the fact that it was the first f material to be identified as having a valence transition. This phase transition may be understood as a sudden change in the size of the Sm ion, i.e., with a change in the Sm valence. By alloying with Y the lattice pressure in (Sm,Y)S can be arranged so that this change in valence

can be observed also by varying the temperature. In contrast to Ce, this drastic valence change is probably caused by the rather low energy of the first excited Hund's rule state. Nevertheless, there are only few neutron scattering experiments on Sm IV systems. One reason for the lack of neutron data is the low magnetic cross section of the $J = 5/2$ Hund's rule ground state (Sm^{3+}). Because of the g_J factor (2/7 for Sm^{3+}) this cross section is just a ninth of that of Ce^{3+} ($g_J = 6/7$). Moreover, the neutron absorption cross section of natural Sm is very high. Therefore, all neutron scattering experiments must be performed on samples with enriched ^{154}Sm isotopes, and only small samples can be used due to the unavoidable contamination by strongly absorbing isotopes. The only successful measurement of the QE linewidth was performed on $\mathbf{Sm_{0.75}Y_{0.25}S}$ (Weber et al. 1989a) using the time-of-flight spectrometer IN6 at the high-flux-reactor in Grenoble (ILL). The result is comparable to that of $CePd_3$ and is included in fig. 32. The width is smaller by a factor of about 3 compared to $CePd_3$, which facilitated the detection for this very low cross section of only 0.2 barn (in contrast $\sigma_{mag} \approx 2.7$ barn for $CePd_3$). As the neutron flux on sample, at a thermal beam (such as IN4), is smaller by at least one order of magnitude compared to that available from a cold-beam spectrometer (such as IN6), low-temperature data with thermal neutrons ($E_0 \geqslant 12$ meV) are of rather poor quality. Our knowledge of the magnetic response at low temperatures is therefore relatively uncertain. There is no sharp magnetic excitation, which should be expected for a simple CF splitting, but there are again indications that the magnetic response becomes inelastic, as happens in $CePd_3$. CF effects do not appear to play an important role in Sm IV systems. The behavior of the intermultiplet transition is discussed in sect. 3.

Due to the large absorption of $\mathbf{SmB_6}$ (to reduce absorption, isotopes of both species, ^{154}Sm and ^{11}B, must be used) inelastic scattering measurements with cold neutrons, as done on $Sm_{0.75}Y_{0.25}S$, were impossible. The data taken with thermal neutrons do not contain information about quasielastic magnetic scattering, but show unusual inelastic magnetic excitations at low temperatures which vanish rapidly with increasing Q (Holland-Moritz and Kasaya 1986). Alekseev (1993), and Alekseev et al. (1992, 1993a,b) have performed experiments on single crystals and polycrystalline material. They confirmed the unusual Q-dependence, and suggested that the magnetic excitation may be influenced by interactions with acoustic phonons.

5.1.4. *Ytterbium systems*

We will start our discussion of the Yb systems with the cubic system $\mathbf{YbAgCu_4}$. This IV system was studied within the series $YbMCu_4$ with M = Pd, Au and Ag (Severing et al. 1990a) and In (Severing et al. 1990b). Whereas the two former compounds show distinct CF excitations, the magnetic scattering of $YbAgCu_4$ appears over a large energy range, and no sharp CF excitations are visible. The QE width is about 8 meV at $T = 250$ K, a factor of 4 larger than in the isostructural compounds with M = Pd, Au (see fig. 37). It decreases with decreasing temperature, but there is a cross-over point at about $T = 75$ K. When the spectra at temperatures $T < 75$ K are fitted with a single QE line the fits get worse (see dashed line in fig. 38) and the widths derived from the best fit are increasing

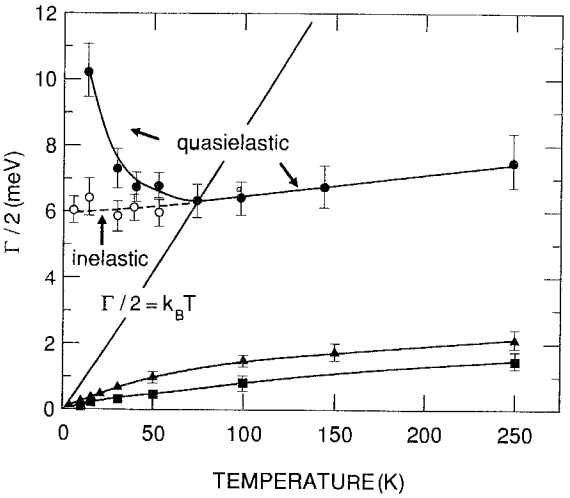

Fig. 37. The QE linewidth of $YbMCu_4$ systems as function of temperature. The solid circles for $YbAgCu_4$ correspond to an analysis with a quasielastic line only, whereas the open circles give the width assuming an inelastic contribution (see text). The triangles and squares represent the isostructural systems with M = Au and Pd, respectively. (From Severing et al. 1990a.)

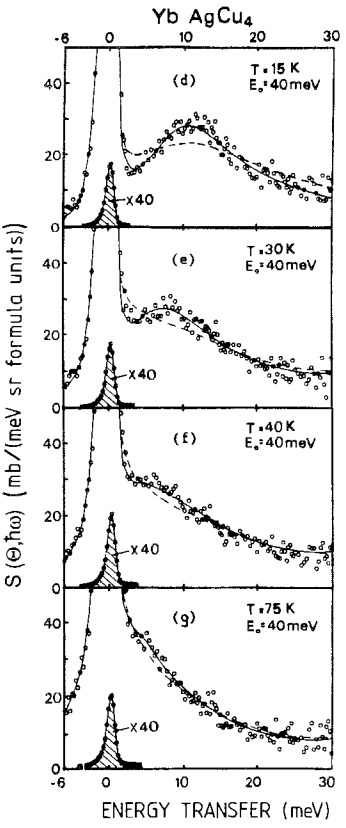

Fig. 38. Background corrected inelastic neutron scattering spectra of $YbAgCu_4$. The full line represents the best fit using an inelastic Lorentzian, whereas the dashed line represents a fit with a quasielastic Lorentzian line only. The hatched area is the nuclear incoherent elastic scattering. (From Severing et al. 1990a.)

with decreasing temperature. The spectra below $T = 75$ K are much better described with a single inelastic line (solid line in fig. 38) and the temperature dependence of this inelastic linewidth (open circles in fig. 37) fits better to the high-temperature behavior of the *QE* linewidth. This finding is compatible with that described for Ce systems and its behavior is intermediate between that of $CePd_3$ (fig. 32) and $CeRu_2Si_2$ (see sect. 6).

As visible from fig. 38 the total magnetic intensity does not change significantly with temperature and is close to the full moment of Yb^{3+}. From this one can exclude a further inelastic line at energies larger than 30 meV which could have been missed using $E_i = 40$ meV. The authors state that a CF explanation for the inelastic excitation at low temperatures cannot be ruled out completely. However, a CF analysis yielded three unusual properties. First, the *QE* linewidth is of the same magnitude as the inelastic one; second, the resulting CF parameter W is about 2.5 times larger than in the isostructural systems assuming the same x parameter; and, third, the CF splitting energy shifts towards lower energies with increasing temperature, i.e., it is no longer temperature independent

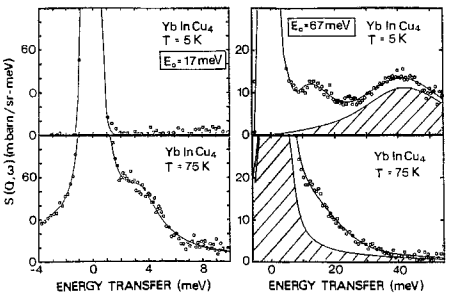

Fig. 39. Background corrected spectra of $YbInCu_4$ showing the different magnetic relaxation behavior above and below the valence phase transition which occurs at ~45 K. The hatched area on the right-hand side represents the magnetic contribution. (From Severing et al. 1990b.)

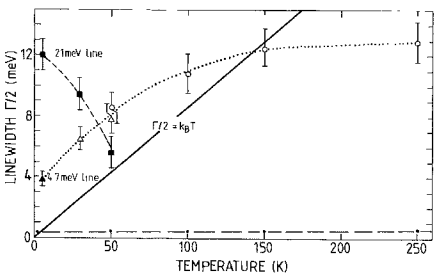

Fig. 40. The linewidth as function of temperature for $YbPd_2Si_2$. Open (solid) symbols represent the quasielastic (inelastic) linewidths. The circles correspond to analysis of spectra taken with $E_i = 3.1$ meV, the triangles to 12.5 meV, and the squares to 50 meV. The different lines through the points are simply guides to the eye. The lower dashed line is the quasielastic width associated with the impurity phase. (From Weber et al. 1989b.)

as in stable 4f systems (compare sect. 2). The last point, the change with temperature, may be due to effects such as those discussed by Becker et al. (1977).

Another interesting compound of the $YbMCu_4$ type has M = In. To date this is the only known Yb system in which a valence phase transition occurs as a function of temperature. Above 45 K Yb is trivalent, i.e., similar to M = Au and Pd, whereas below 45 K the valence starts to decrease into an intermediate valent state. Inelastic neutron scattering data by Severing et al. (1990b) are compatible with CF excitations for $T > 45$ K. Below 45 K these CF transitions vanish and a broad inelastic excitation appears around 40 meV, see fig. 39. The intensity above 45 K is in good agreement with the full Yb^{3+} moment, whereas the intensity of the magnetic spectrum at low temperatures has not yet been reliably estimated. Experiments with higher incident energies are required to characterize the total response function.

Many intermediate-valent Yb systems studied by inelastic magnetic neutron scattering are of lower crystal symmetry than cubic (e.g., $YbPd_2Si_2$, YbCuAl). This anisotropy complicates the situation, and might result in a wrong interpretation of the data when polycrystalline samples are used. We start our discussion with **$YbPd_2Si_2$**. This system was investigated intensively by Weber et al. (1989b) with three different incident energies: $E_i = 3.1$ meV for temperatures larger than 50 K, and $E_i = 12.5$ and 50 meV for low temperature. The comparison to the nonmagnetic reference compound $LaPd_2Si_2$ shows clearly the existence of a broad magnetic feature at high temperatures, which could be well described by just one quasielastic line of 12 meV width. This QE width decreases with decreasing temperature to a value of about 8 meV at $T = 50$ K (fig. 40), as proven by using

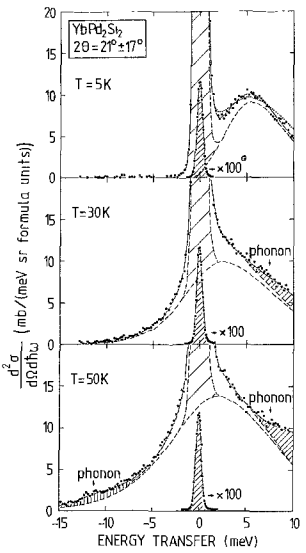

Fig. 41. Response of $YbPd_2Si_2$ as measured with $E_i = 12.5$ meV. This illustrates how the quasielastic response at higher temperatures changes to an inelastic response (top panel) at $T = 5$ K. The hatched areas are due to both nuclear incoherent scattering and to phonons. The area that is not hatched between the full and dashed lines represents the scattering from the impurity phase. (From Weber et al. 1989b.)

two different incident energies, 3.1 meV and 12.5 meV. Whereas at $T = 30$ K the magnetic response as measured with $E_i = 12.5$ meV appears to be purely quasielastic in character, it has changed its character to an inelastic excitation at about 4.7 meV at $T = 5$ K. This may be seen more clearly by the low-energy spectra shown in fig. 41. An additional very small quasielastic line with an almost temperature independent width is associated with an impurity phase, and seen only when low-energy incident neutrons are used as shown in fig. 41. Although this behavior looks qualitatively quite similar to that of $YbAgCu_4$, there are some significant differences. First, the decrease of the linewidth when lowering the temperature is stronger in $YbPd_2Si_2$ than in $YbAgCu_4$. Moreover, the temperature dependence of the linewidth in $YbPd_2Si_2$ is not linear, but is more compatible with a square-root dependence, which is used to describe the lanthanide behavior in Kondo or heavy-fermion systems (see sect. 6). The most obvious difference, however, is the existence of a second broad inelastic excitation line at about 21 meV. This was readily observable in the spectra taken with $E_i = 50$ meV and at $T \leqslant 50$ K (fig. 42). All linewidth data are summarized in fig. 40.

The authors state that simple single-ion CF theory cannot explain the observed temperature dependence of the excitation spectra. They suggest a dependence of the dynamic spin behavior on the crystallographic direction, for example, a higher fluctuation rate in the ***a–b*** plane than in the ***c*** direction. That such a behavior is realistic is shown by the anisotropy in the static magnetic susceptibility found by using single crystals of several materials, e.g., $YbCu_2Si_2$ or URu_2Si_2 (see below). Unfortunately such data do not exist for $YbPd_2Si_2$. Comparing the sum of magnetic neutron scattering intensities (local static susceptibility), excluding the impurity phase, with the static bulk susceptibility ($\boldsymbol{Q} = 0$) as measured by Sampathkumaran et al. (1984) the agreement is

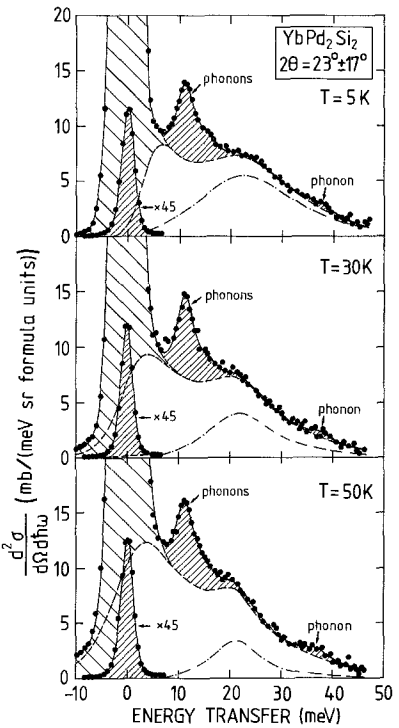

Fig. 42. Spectra of $YbPd_2Si_2$ as a function of temperature obtained with $E_i = 50$ meV. This shows the progressive enhancement of the scattering at higher-energy transfer due to the development of an inelastic line at ~22 meV (dashed–dotted line). The fit to the total scattering is drawn as a solid line. The hatched areas represent scattering from nuclear incoherent (elastic) and phonon (inelastic) scattering. The total magnetic scattering (quasielastic + inelastic) cross section is shown as a dashed line. (From Weber et al. 1989b.)

excellent (Weber et al. 1989b). The total magnetic cross section, which cannot be extracted exactly due to the uncertainties in the cut-off energy (see sect. 1), is in rough agreement with a valence of $v \approx 2.9$.

There were two early experiments on two similar Yb systems using $E_i \approx 3.5$ meV and $E_i \approx 12.5$ meV neutrons: hexagonal YbCuAl (Mattens et al. 1980) and tetragonal $YbCu_2Si_2$ (Holland-Moritz et al. 1978). Both systems show broad magnetic scattering even at low temperatures. At this early stage of investigations it was thought that the magnetic response of IV systems was purely quasielastic at low temperatures so that in both these works the data were analyzed in this way. Later, both groups performed additional experiments using $E_i = 50$ meV, which resulted in additional information.

In fig. 43 the width found for **YbCuAl** by an analysis with just one quasielastic line is plotted as a function of temperature (circles) together with the relaxation rates extracted from NMR data (open circles, MacLaughlin et al. 1982). Whereas the NMR rate shows a strong increase below $T = 40$ K, this increase is much smaller for the relaxation rates extracted from the neutron scattering data. With new experiments, and an improved analysis, Murani et al. (1985) showed the existence of at least two inelastic magnetic excitations in YbCuAl. They added to fig. 43 the quantity $\chi\omega_n/\chi''(\omega_n)$, where χ is the static bulk susceptibility, represented by $\chi'(\boldsymbol{Q}, \omega' = 0, T)$ in eq. (5), ω_n is the peak

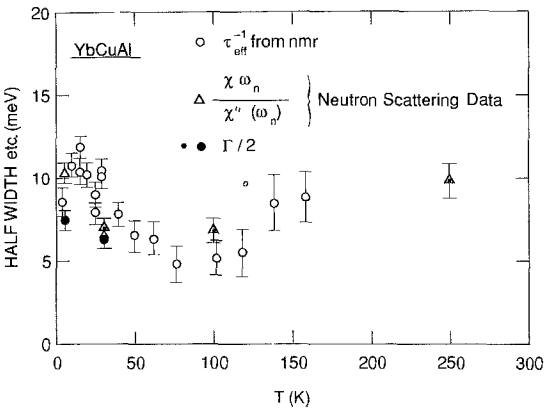

Fig. 43. Relaxation behavior of YbCuAl as function of temperature. The open circles represent the NMR data. The solid circles represent the linewidth obtained from the magnetic neutron scattering response assuming just a QE Lorentzian spectral function, and the triangles give the quantity $\chi\omega_n/\chi''(\omega_n)$. The last quantity is equivalent to an inelastic linewidth, assuming a Lorentzian shape. (From Murani et al. 1985.)

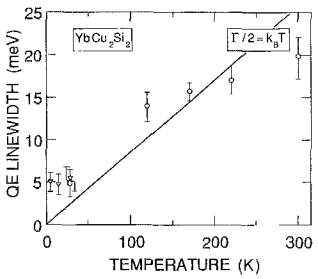

Fig. 44. Temperature dependence of the linewidth (HWFM) in $YbCu_2Si_2$. At high temperature ($T > 120$ K) the whole magnetic spectrum can be fit with a *QE* line; at low temperature only the low-energy part of the spectrum is used to extract a *QE* linewidth. The circles and triangles represent data taken with $E_i = 3.65$ and 12.5 meV, respectively. (Adapted from Holland-Moritz et al. 1982.)

position in the neutron spectra and $\chi''(\omega_n)$ is the value of the dynamic susceptibility at the peak position. Assuming a Lorentzian shape, and a free-ion Yb^{3+} form factor, this quantity should be identical with the linewidth extracted from eqs. (5) and (10). As shown for $CeRu_2Si_2$ and $YbAgCu_4$, the interpretation in terms of an inelastic line in general yields widths somewhat smaller than the quasielastic one. However, in this case $\chi\omega_n/\chi''(\omega_n)$ is even larger than the *QE* linewidth, but coincides quite well with the NMR relaxation rate. This indicates that either the line is no longer of Lorentzian shape or that spatial correlations may be present at low temperatures.

Holland-Moritz et al. (1982) reported a crystal-field analysis of their data on **$YbCu_2Si_2$**. They performed this analysis because the simple picture of just one quasielastic line in the whole temperature range led to contradictions, especially at low temperature. Although the data analysis was consistent, questions on the derived CF scheme have been raised by Tomala et al. (1990), after a Mössbauer study. The temperature dependence of the Yb quadrupole moment could not be explained by the set of CF parameters given by Holland-Moritz et al. (1982). Instead, another CF scheme based on theoretical treatments of Zevin et al. (1988), is favored. However, with the interpretation of the $YbPd_2Si_2$ spectra in mind, an analogous interpretation of the $YbCu_2Si_2$ might be possible. This would lead to a quasielastic width of about 20 meV at room temperature, decreasing to a value of about 5 meV at $T = 5$ K. The full temperature dependence is shown in fig. 44. As in $YbPd_2Si_2$, a strong inelastic magnetic excitation exists at about 23 meV with a width of about 10 meV, which covers all CF excitations of the earlier interpretation. Whether

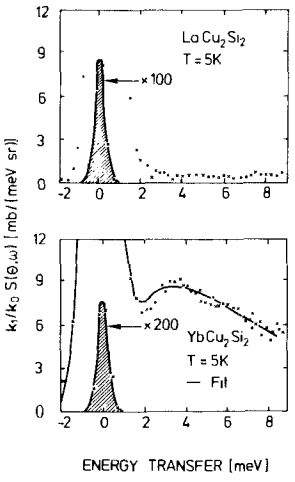

Fig. 45. Background-corrected spectra of $YbCu_2Si_2$ (lower frame) and the reference system $LaCu_2Si_2$ (upper frame) showing the broad magnetic response in the Yb system. The solid line is a fit assuming a quasielastic Lorentzian, and demonstrates that this assumption is probably inadequate. (Adapted from Holland-Moritz et al. 1978.)

the low-energy response, which is characterized in fig. 45 by just one quasielastic width, is really of quasielastic or of inelastic nature, cannot be decided easily. There is also the possibility of strong $\boldsymbol{Q}$ dependent effects in $YbCu_2Si_2$, which are not easy to address with polycrystalline samples. In $YbCu_2Si_2$ such a behavior is suggested by the anisotropy in the static susceptibility measured on a single crystal. The susceptibility is smaller for $\boldsymbol{H} \perp \boldsymbol{c}$ than for $\boldsymbol{H} \parallel \boldsymbol{c}$ (Shimizu et al. 1985, Currat et al. 1989). From these observations we can propose that the low-energy response is associated with the susceptibility parallel to the $\boldsymbol{c}$ axis, and the high-energy response to that in the basal plane.

To test these ideas, Currat et al. (1989) performed neutron inelastic scattering experiments on a single crystal of $YbCu_2Si_2$ using the triple axis spectrometer IN8 at the ILL. This is one of the few inelastic neutron scattering experiments on a single crystal of a strongly interacting 4f system with a crystal symmetry lower than cubic. Unfortunately, the resolution was insufficient to draw conclusions about any possible low-energy response around 4 meV (~1 THz). At low energies there are only small differences between the spectra taken at different $\boldsymbol{Q}$, in disagreement with the strong dependence proposed by Zwicknagl et al. (1990). Qualitatively the two peaks at about 16 meV (~4 THz) and 32 meV (~8 THz) are consistent with the work done on polycrystalline samples.

Attempts were made by Walter et al. (1992) to study $YbCu_2Si_2$ under pressure. There is some indication that at $P = 17$ kbar more scattering is seen at ~15 meV, which would be consistent with the earlier CF interpretation, but these experiments are difficult because of the large amount of scattering from the pressure cell.

The interpretation of the low-temperature response obtained on Yb samples is clearly still complex. In low-symmetry structures the dependence on crystallographic direction implies that the crystal-field interactions must be important, although bearing in mind the physics of cerium and uranium systems discussed in sect. 4, the effects of hybridization will have to be incorporated into any comparison between theory and the neutron results.

It will be nccessary also to characterize the low-energy response of the single crystal of $YbCu_2Si_2$, for example with a cold-source triple-axis spectrometer, as has been done for a number of heavy-fermion systems (see sect. 6).

Whereas the former Yb systems show a rather strong temperature dependence in the static susceptibility with a maximum at about 40 K, i.e., a Curie-like behavior for temperatures $\gtrsim 60$ K, **$YbAl_3$** shows a rather flat behavior (Klaasse et al. 1977) with a less pronounced maximum at about 150 K. As this behavior is quite similar to that of $CePd_3$, one would expect for this cubic Yb compound a broad quasielastic response at high temperatures and a structureless broad inelastic excitation for $T \to 0$ K. Surprisingly, a complicated magnetic response with many details was reported. Murani (1985) used incident energies of $E_i = 50$ meV and 115 meV and states that there is a low level of magnetic scattering below 30 meV, and then a sharp increase in magnetic scattering, peaking at ~32 meV. Using cold neutrons ($E_i = 3.1$ meV), Walter et al. (1991) found a fourth inelastic excitation line at about 12 meV, and at a temperature of 50 K. A recent work by Murani (1994) includes also data with $E_i = 3.1$ meV using the IN6 spectrometer with the same experimental set-up as done by Walter et al. (1991). Surprisingly, the spectra, especially those of $LuAl_3$, look very different. As commented by Holland-Moritz and Walter (1994), the origin for this lies in the shape of the sample: Murani (1994) used a powdered sample, while Walter et al. (1991) used a bulk polycrystalline $LuAl_3$ sample yielding drastically different nuclear cross sections for both elastic and inelastic scattering (last partly due to enhanced double scattering). The error in the analysis by Walter et al. (1991) was to estimate the inelastic nuclear scattering for a *powdered* $YbAl_3$ sample by comparison with the inelastic nuclear scattering of a *bulk* $LuAl_3$ sample. Both groups agree now in the picture of only *one* quasielastic line for $T \gtrsim 120$ K, which changes below this temperature continuously to a striking gap-like inelastic feature at liquid helium temperature. This inelastic response is strongly asymmetric, increasing rapidly between 30 and 32 meV and decreasing slowly to higher energies. There is also a fine structure in the magnetic response above 32 meV. For more details see Murani (1994).

Many intermediate-valent Yb systems exist showing an even smaller susceptibility than $YbAl_3$, e.g., $YbAl_2$, $YbCu_2$, $YbZn_2$ or $YbGa_2$ (Klaasse et al. 1977). All these systems have valences significantly smaller than 2.8 and susceptibilities smaller than 0.5×10^{-3} emu/mol for low temperature. As the temperature increases, so does the susceptibility, attaining a maximum at high temperatures, which frequently required experiments up to 1000 K. **$YbAl_2$** shows a maximum at 900 K. In the magnetic response one would, therefore, expect a broad inelastic excitation at high energies. This was estimated to be outside the range of spectrometers at reactors; however, a recent experiment at the ISIS spallation source by Murani et al. (1992) was successful. Figure 46 shows a low-temperature spectrum of $YbAl_2$ with a broad inelastic excitation centered at ~180 meV and with a width of ~90 meV. This spectrum was then analyzed in terms of the expression given by Kuramoto and Müller-Hartmann (1985) and gave a characteristic energy $\varepsilon_f \approx 155$ meV $\approx T_K$ and a degeneracy of the ground state $N_f \approx 9$. From this, using the literature value for the electronic specific coefficient, γ, together with the Fermi-liquid

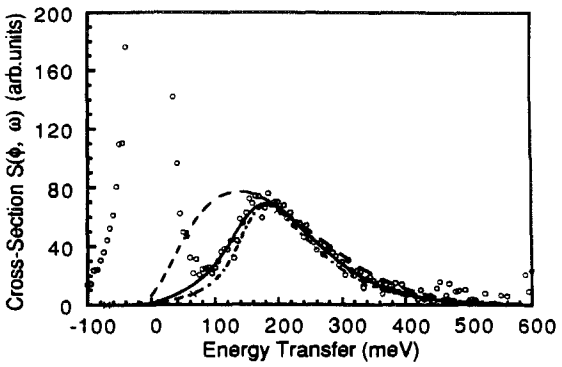

Fig. 46. Spectrum of $YbAl_2$ obtained with $E_i = 600$ meV at $T = 20$ K for a mean scattering angle of 7°. The solid curve is the best fit to the analytical spectral function of Kuramoto and Müller-Hartmann (1985), which gives $\varepsilon_f(T_K) \approx 155$ meV and $N_f \approx 9$. The calculated spectral forms for the same ε_f but with $N_f = 2$ and $N_f = 14$ are given by the dashed and dashed–dotted curves, respectively. (From Murani et al. 1992.)

relation linking γ and ε_f (see sect. 7) the authors find that the Yb ion in $YbAl_2$ is close to trivalent. However, the Fermi-liquid relation between $\chi(0)$ and ε_f suggests a valence closer to 2.4, as extracted from the L_{III} measurements by Bauchspiess et al. (1981), and Röhler (1987). One reason for this discrepancy is linked to the fact (Newns and Hewson 1980) that the Wilson ratio, $\chi(0)/\gamma$, is unusually low for $YbAl_2$. This is discussed further in sect. 7.

5.1.5. *Thulium systems*

There are only two intermediate-valent Tm systems in the literature. First, **TmSe** which orders antiferromagnetically below 3.5 K with an ordered moment of ~2.5 μ_B (Bjerrum-Møller et al. 1977), but is strongly intermediate valent at atmospheric pressure ($v \approx 2.58$, Launois et al. 1980). Second, **TmTe** which is almost divalent at atmospheric pressure, but is driven into an intermediate valent state by applying external pressure (Wohlleben et al. 1972). The first compound was investigated intensively by various techniques. Neutron inelastic scattering measurements were performed as a function of temperature on both TmSe and TmTe. TmTe was also investigated at $P \approx 20$ kbar and room temperature (Walter et al. 1992). In addition to the compound TmSe, the two diluted systems $Tm_{0.05}Y_{0.95}Se$ and $Tm_{0.05}La_{0.95}Se$, as well as the alloy $TmSe_{0.85}Te_{0.15}$, have been investigated (Holland-Moritz 1983). Qualitatively, all these systems with intermediate-valent Tm behave similarly. Therefore, we will concentrate just on the compound TmSe (Loewenhaupt and Holland-Moritz 1978, 1979, Holland-Moritz and Loewenhaupt 1979, Shapiro and Grier 1982, Holland-Moritz 1983). The results are summarized in fig. 47. The quasielastic linewidths is almost temperature independent between 300 K and 120 K but decreases rapidly below $T = 120$ K. At $T = 5$ K the linewidth is about 0.4 meV; the material orders at $T_N \approx 3.5$ K. Associated with the decrease of the QE linewidth, an inelastic response appears, whose position shifts from 6.5 meV at $T = 75$ K to 10 meV at 2 K shown by the squares in fig. 47. The data in fig. 47 are obtained from measurements on polycrystalline material (Loewenhaupt and Holland-Moritz 1978, 1979). Comparing the quasielastic width and the inelastic excitation energy with those of the other

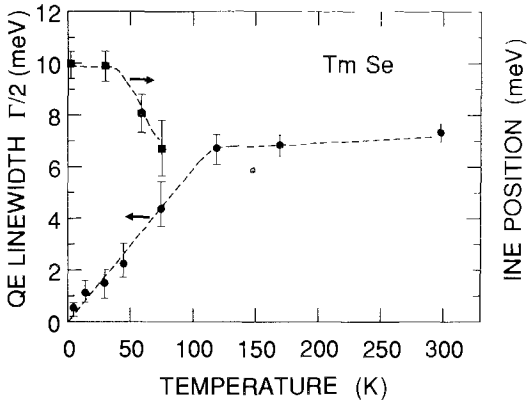

Fig. 47. QE linewidth (solid circles) and inelastic excitation energy (solid squares) observed in TmSe as function of temperature. (Adapted from Holland-Moritz 1983.)

Tm systems they depend monotonously on the lattice parameter, i.e., with increasing volume available for the valence-fluctuating Tm ion both the quasielastic width and the inelastic excitation energy decrease (Holland-Moritz 1983).

The existence of the inelastic excitation was also confirmed by Shapiro and Grier (1982) by an experiment on a single crystal. This work shows elegantly that the existence of this inelastic excitation depends strongly on the stoichiometry. A sample with a room-temperature lattice constant of about 5.71 Å is thought to be stoichiometric (e.g., Köbler et al. 1981). In fig. 48 spectra of two samples with different lattice constants are compared. The upper spectrum is from a sample with a room-temperature lattice parameter of 5.714 Å close to stoichiometry and shows the inelastic excitation at 10 meV, whereas the lower spectrum is from a sample with a lattice constant of 5.69 Å at room temperature, and the inelastic structure is almost vanished. This gives an explanation why Furrer et al. (1981) could not confirm the existence of the inelastic excitation by measuring on a single crystal.

TmSe was for a long time the only IV system for which such an inelastic excitation was found at low temperatures. Thus the existence of that excitation was thought to be a special property of Tm, because both mixing Tm valences states are magnetic. Several models were developed to understand this. Fedro and Sinha (1981) suggested an excitation across a hybridization gap. This was experimentally supported by the strong Q-dependence of the intensity found for the inelastic excitation by Shapiro and Grier (1982). The existence of this excitation for diluted Tm systems (Holland-Moritz and Prager 1983, Holland-Moritz 1983) seems to favor single-ion models such as that of Mazzaferro et al. (1981) or Schlottmann (1984b). However, provided the excitation involves only a 4f electron and a conduction-band state, it is not necessary that the ion be concentrated for dispersion to arise. The latter may simply be a consequence of the q dependence of the conduction band. The presence of this excitation in dilute systems does rule out cooperative effects involving more than one 4f site, but does not necessarily exclude the presence of a hybridization gap. More recently, similar excitations were detected in several systems (see above), in which one of the mixing Hund's rule ground states is nonmagnetic. The

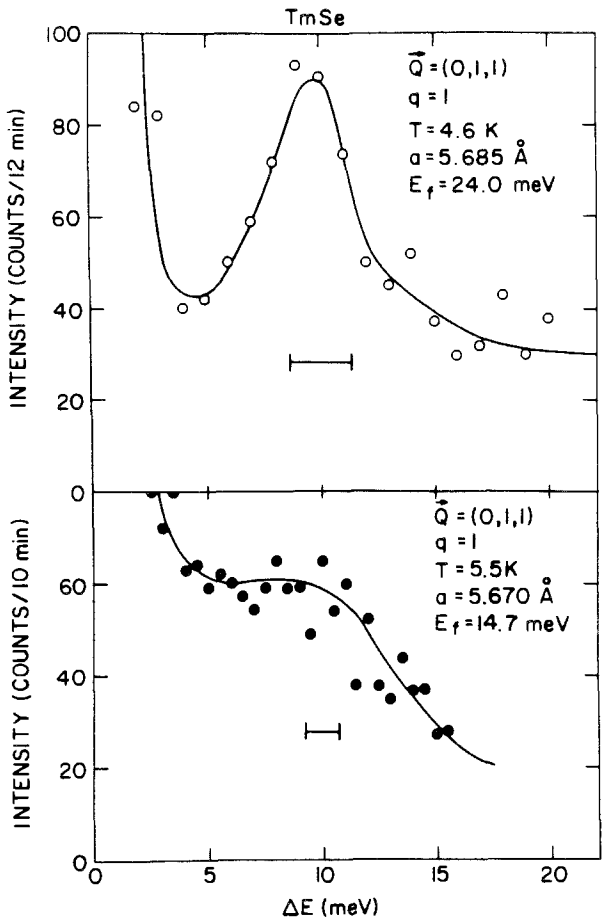

Fig. 48. Energy spectra of $Tm_{1.0}Se$ (upper panel) and $Tm_{0.99}Se$ (lower panel). Note that the lattice parameters given in the figure are low-temperature values. (From Shapiro and Grier 1982.)

only distinct difference between Tm and the other strongly intermediate-valent lanthanides seems to be the much smaller QE and INE linewidth at low temperatures observed in Tm systems. Therefore, the narrowing effect may be just a consequence of both the valence states, which are involved in the mixing process, being magnetic.

This 10 meV excitation remains almost unaffected by the magnetic order below T_N = 3.2 K (Holland-Moritz and Loewenhaupt 1979, Shapiro and Grier 1982). However, the quasielastic scattering vanishes below the Néel temperature and an inelastic magnon-like excitation at about 1 meV is observed (Loewenhaupt and Holland-Moritz 1978). An investigation as a function of magnetic field by Loewenhaupt and Bjerrum-Møller (1981) shows a strong field dependence of this magnon-like excitation, from which a doublet ground state was deduced for the paramagnetic regime (see also the work by Loewenhaupt and Fischer 1993).

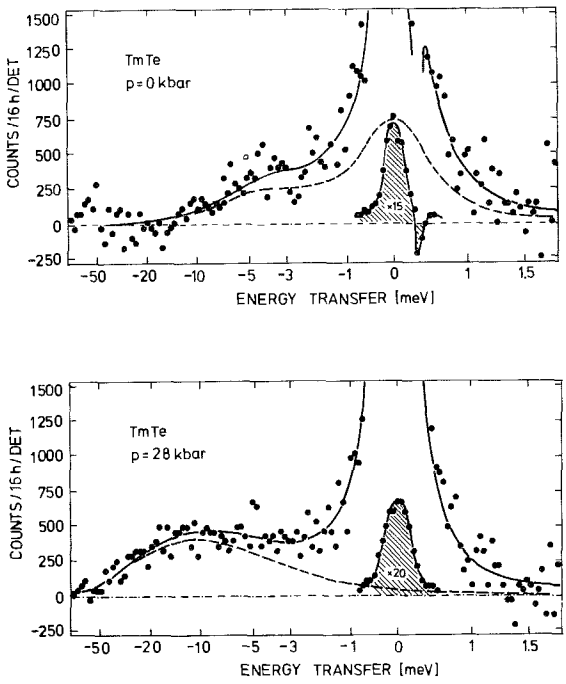

Fig. 49. Background-corrected spectra of TmTe at 300 K obtained with $E_i = 3.65$ meV as a function of energy, but presented in a scale linear in time-of-flight. The upper frame shows the spectra at ambient pressure in the pressure cell, and the lower frame the one at 28 kbar. The solid line represents the best fit, the dashed line is the magnetic component, whereas the hatched area is due to nuclear elastic scattering. (From Walter et al. 1992.)

TmTe was investigated at room temperature and at ambient and 28 kbar pressure (Walter et al. 1992). This is one of the few inelastic neutron scattering experiments involving pressure. The results are shown in fig. 49. The comparison of the ambient pressure (upper frame) spectrum with that at 28 kbar (lower frame) shows an increase of the quasielastic linewidth with increasing pressure. The ambient pressure spectrum was analyzed in terms of a CF splitting, in agreement with the interpretation of measurements on a larger sample without the pressure cell. The *QE* linewidth is $\Gamma/2 = 0.8$ meV. The spectrum at 28 kbar is quite similar to that found for TmSe, and was therefore analyzed with a single broad *QE* line, yielding a width of 10.5 meV, which can be compared to the ~7 meV found for TmSe. This pressure dependence, as well as that of $YbCu_2Si_2$, can be understood with the theory of Kuramoto and Müller-Hartmann (1981), which is valid only in the high-temperature limit.

5.1.6. *Praseodymium systems*

Attempts have been made to force praseodymium, which follows cerium in the lanthanide series, into an intermediate valent state. Since all intermetallic systems have a Pr ion with a valence close to three, pressure was applied to some of these systems, but all efforts have failed. Enhanced hybridization, however, was found in insulating Pr systems containing oxygen. Within the $RBa_2Cu_3O_{7-\delta}$ series, which usually exhibit high-temperature superconductivity, the suppression of superconductivity in $PrBa_2CuO_7$

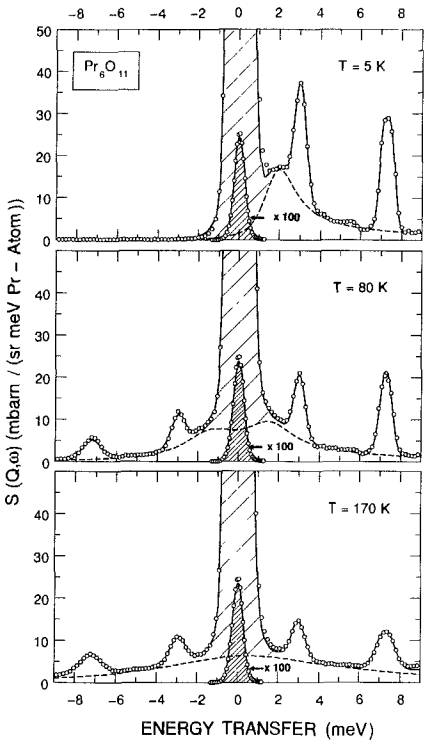

Fig. 50. Background corrected inelastic neutron scattering spectra obtained for Pr_6O_{11} with $E_i = 12.5$ meV. The nuclear incoherent elastic scattering is marked by the hatched area, and the dashed line represents the broad magnetic component. (From Holland-Moritz 1992.)

(a semiconductor) is probably caused by such enhanced hybridization effects (Walter et al. 1988, Skanthakumar et al. 1990, Soderholm et al. 1990, Jostarndt et al. 1992). The only other unstable Pr moments were found in the oxides. For PrO_2 a valence of about 3.4 is reported by Dexpert et al. (1987) from L_{III} edge measurements. Pr_6O_{11} has the same cubic crystal structure (CaF_2 type) as PrO_2. In spite of the empty oxygen sites in Pr_6O_{11}, the lattice constant ($a \approx 5.465$ Å) is about 1.3% larger compared with stoichiometric PrO_2 ($a = 5.3938$ Å). This indicates that the Pr valence is shifted towards trivalency. Indeed Bauchspiess (1982) reports a valence of 3.17 for Pr_6O_{11}. These valence states have been determined by measurements of the position of the L_{III} edge (compare Röhler 1987). An alternative method is from electron spectroscopy, but caution is required in interpreting the results from this latter method (Baer and Schneider 1987).

Neutron inelastic scattering on PrO_2 (sect. 2.2.1) were performed by Kern et al. (1984, 1990a). They report a CF splitting of 130 meV and magnetic ordering, but do not mention any broad magnetic component as would be expected for a Pr ion with a valence of 3.4. They interpret their data in terms of CF splitting of a tetravalent Pr ion, a $4f^1$ configuration. Recently published neutron scattering spectra on the naturally formed Pr_6O_{11} are shown in fig. 50 (Holland-Moritz 1992). The spectra exhibit two quite different magnetic responses, very narrow inelastic excitations and a rather broad

weak feature. The narrow component was interpreted as CF excitations due to trivalent Pr ions surrounded by only seven oxygen atoms. The broad component behaves like a response of a valence fluctuating ion. This response is quasielastic in character at high temperatures but becomes inelastic at low temperatures, as discussed above for many other intermediate-valent systems. Thus the magnetic scattering response of Pr_6O_{11} is interpreted as a static mixture of two valence states, one of which is fluctuating in valence. The valence-fluctuating Pr ion sits on a site with a fully occupied eightfold oxygen coordination, i.e., comparable to PrO_2 itself, but with a slightly larger Pr–O distance. An approximate valence of 3.66 was extracted for these ions from the neutron intensities, which is slightly greater than the valence of 3.4 given by Dexpert et al. (1987) for stoichiometric PrO_2. The new experiments (Holland-Moritz 1992) have not been extended in energy to search for any excitation at 130 meV in Pr_6O_{11}, as was found by Kern et al. (1984) in PrO_2. However, the Jahn–Teller splitting of the Γ_8 ground-state quartet as found at ~5 meV by Kern et al. (1990a) in PrO_2 is clearly *not* seen in the Pr_6O_{11} spectra (fig. 50). The excitations in this figure have a small temperature dependence only, whereas the excitation in PrO_2 at 5 meV has essentially disappeared by 80 K. The difference between PrO_2 and Pr_6O_{11} is quite remarkable, and shows the sensitivity to stoichiometry.

5.2. *Actinide systems*

As already indicated in the previous sections, we anticipate that the actinides should show a larger f–d hybridization than the lanthanides. Surprisingly, therefore, for the few U compounds which fit into this class of material, showing no structure in the magnetic response function, the susceptibility is more temperature dependent than found, for instance, in $CePd_3$.

Only two U compounds have been examined in detail in this category: UAl_2 and USn_3. The first studies of these were published some years ago (Horn et al. 1978, Loewenhaupt et al. 1979b). More recently, both have been re-examined. These new experiments confirm the existence of a broad quasielastic response in both systems. For **UAl_2** (Loong et al. 1986) fig. 51 shows the quasielastic linewidth as a function of temperature. At low temperature the new and old results coincide, whereas at room temperature the old data give a linewidth that is too large, probably due to the uncertainties in the correction for phonons.

Figure 52 shows some spectra from **USn_3** (Loewenhaupt and Loong 1990) as a function of Q at low temperature. Data taken with thermal neutrons ($E_i = 12.5$ meV) and cold neutrons (3.1 meV) are plotted on one graph in the upper three frames. The spectrum at the bottom ($E_i = 50$ meV) demonstrates the increase in the phonon contribution in the inelastic spectrum with increasing incident energy. This increase is due to additional multiple scattering processes as observed generally when using higher incident energies. There are two parts to the inelastic magnetic response; one is very broad and indicated by a solid line, the other is at much lower energies and indicated by the cross hatching. This last contribution is *inelastic* at low temperature, but rapidly merges into a quasielastic

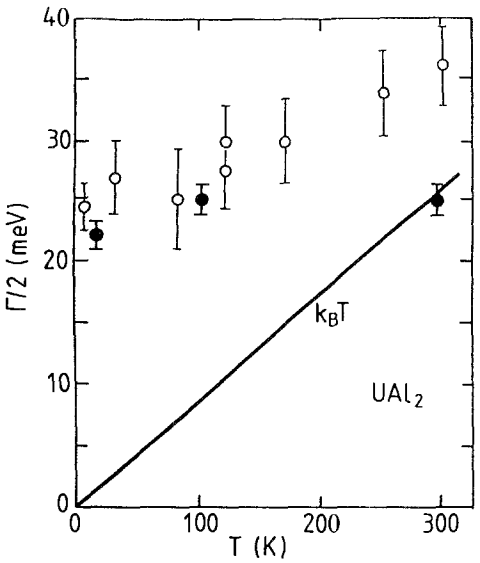

Fig. 51. QE linewidth for UAl_2 as a function of temperature. The open circles are from earlier work, and the solid circles from the more recent. The solid line represents $\Gamma/2 = k_B T$. (From Loong et al. 1986.)

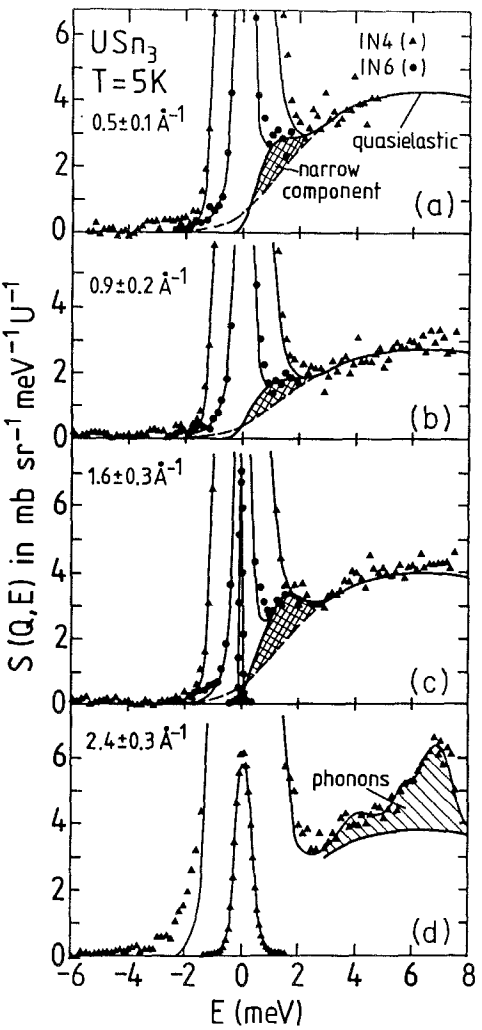

Fig. 52. Background corrected neutron spectra for USn_3 as a function of temperature obtained with $E_i = 12.5$ meV and with $E_i = 3.1$ meV (upper three frames). The full line represents the results of a fit and the cross-hatched area, the low-energy magnetic response. The spectrum in the lower frame is taken with $E_i = 50$ meV. The hatched area represents phonon and multiple inelastic scattering. (From Loewenhaupt and Loong 1990.)

line with increasing temperature. Its origin is still unclear. The linewidth of the broad quasielastic part is plotted versus temperature in fig. 53. The values extracted with an even higher incident energy are shown as the squares; the use of three different instruments in this study gives considerable confidence in the results.

The intensity, i.e., the static single-site (local) susceptibility varies with Q. In fig. 54 Loewenhaupt and Loong (1990) compare the local susceptibility as deduced from different Q values with the values obtained in the bulk. For all Q the local (neutrons)

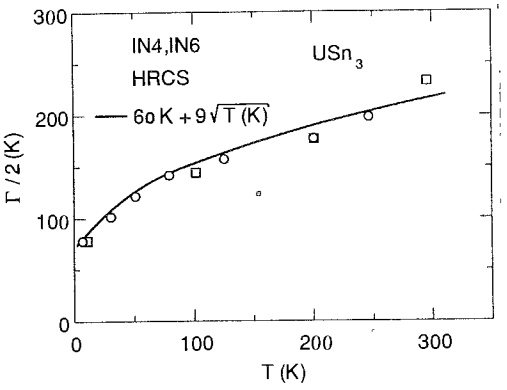

Fig. 53. QE linewidth observed for USn_3 as a function of temperature. (From Loewenhaupt and Loong 1990.)

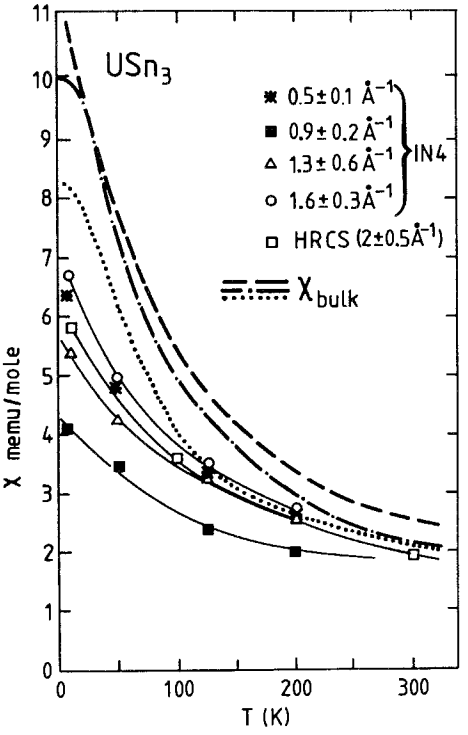

Fig. 54. Comparison of the local static susceptibility (as derived from neutron measurements) with the bulk susceptibility. Samples used: Loewenhaupt and Loong (1990) (dashed curve), Lin et al. (1985) (dotted curve), Buschow and van Daal (1972) (dashed–dotted curve). The solid curves passing through the neutron data are a guide to the eye. The estimated absolute uncertainty for the neutron data is ~10%, whereas the relative uncertainty between data at a given temperature is ~5%. (From Loewenhaupt and Loong 1990.)

value is smaller than the bulk value. This suggests that ferromagnetic correlations occur in USn_3, and it is these that cause $\chi^{st}(Q = 0, T) = \chi_{bulk}$ to be greater than the susceptibility at finite Q as measured by the neutrons. Further Q-dependent effects have been reported by Marshall et al. (1992b) in a study of the solid solutions $\mathbf{USn_{3-x}In_x}$. The Q-averaged linewidths of these authors are more than a factor of 2 greater than those reported by Loewenhaupt and Loong (1990). There is some concern over the corrections for phonons in this more recent work as only one incident energy, and a high one of 67 meV, was used. The Q-dependence of the scattered intensity suggested in this work of Marshall et al. is interesting, but it is unclear to what extent the data have been analyzed as constant-$|Q|$, or constant angle. Unfortunately, they do not reference the earlier paper by Loewenhaupt and Loong (1990), so presumably were unaware that there was such a large discrepancy. It is, however, clear that more experiments, particularly if good single crystals could be obtained, would be worthwhile on USn_3.

5.3. *Phonon anomalies in unstable or hybridized f electron systems*

Our discussion of the total electronic response of these materials would not be complete without a short note on the observation of electron–phonon effects in unstable f electron systems. Soon after the discovery of valence fluctuations it was realized that due to

the large difference between the ionic radii in the two valence states and because the appropriate time scale is $\sim 10^{-12}$ s, which corresponds to a quasielastic linewidth of ~4 meV, there should be a "breathing" of the lanthanide ion with a frequency compatible with typical phonon frequencies. Some effects in the phonon spectra have been found, as we shall describe below, but phonon anomalies appear to be the exception rather than the rule, so the precise nature of the coupling between the electronic and vibronic states in unstable f electron systems remains obscure.

Such anomalies appear to be clearly present in the NaCl-structure compounds: SmS under pressure (Mook et al. 1982), $Sm_{0.75}Y_{0.25}S$ (Mook et al. 1978b), TmSe (Mook and Holtzberg 1981) and $Tm_{0.05}Y_{0.95}Se$ (Holland-Moritz and Severing 1986). The anomaly is observed in the phonon spectra in the [1,1,1] direction. The longitudinal modes, both acoustic and optic, lie lower in frequency than the transverse modes, whereas it is usually the reverse. The theories of Bilz et al. (1979), Bennemann and Avignon (1979), and Entel et al. (1979) have shown that these effects can be understood on the basis of both size differences between Sm^{2+}/Tm^{2+} and Sm^{3+}/Tm^{3+} and f–d interactions.

Anomalies in the phonon spectra of UTe have also been found (Buyers and Holden 1985) and attempts were made by the authors to use the same theories described above, which essentially relate to an intermediate-valence picture. Unfortunately, as Buyers and Holden describe (see their p. 304) this does not lead to a convincing conclusion. There is, of course, no direct electronic evidence (e.g., from photoemission) that materials such as UTe exhibit valence fluctuations. We must conclude that the electron–phonon interaction is different in detail between the 4f intermediate-valence materials and the actinide compounds. In both cases, however, the result is a negative Poisson ratio (which is directly related to the elastic constant C_{12}).

A careful study of the phonons was also undertaken in both $CeSn_3$ and $CePd_3$, both of which have the cubic $AuCu_3$ structure. After some controversy surrounding the effects in $CeSn_3$, a joint publication of the two groups confirmed that the effects were small (Pintschovius et al. 1983). Severing et al. (1988) and Loong et al. (1988) reported further work on $CePd_3$, but their interpretations, some of which depended on the models used, were different. The effects in the compounds with the $AuCu_3$ structure are not as marked as in the compounds with the NaCl structure that were discussed above.

The temperature dependence of the phonons has also been measured in SmB_6 by Alekseev (1993) and by Alekseev et al. (1993b). They reported an unusual increase of the longitudinal acoustic branches, but a softening of the longitudinal optic branches with decreasing temperature. In addition, they found an unexpected peak at ~20 meV at high temperatures, and this was interpreted as a "resonant gap" mode. This mode apparently disappears at low temperature.

Phonon anomalies have been found only in a few systems, so there is a tendency to regard them as not particularly relevant in understanding the electronic effects. We should remember, however, that searching for such anomalies is difficult and time consuming. To measure the complete phonon spectrum requires single crystals of sufficient size for triple-axis spectroscopy, and the phonon spectrum consists of many branches, all of which must be mapped out in the absence of theoretical predictions. This is a time consuming

(and neutron-consuming!) effort. In addition, many of the materials discussed in this and the following section are not cubic and have many atoms per unit cell. In such a situation it is clear that phonon anomalies will be found only when more systematic theoretical predictions are available.

6. Strongly interacting f-electron systems

Many of the systems discussed in this section are "real" heavy-fermion systems, i.e., following the arbitrary definition by Stewart (1984) they exhibit a specific heat γ larger than $400\,\mathrm{mJ\,mol^{-1}K^{-2}}$. However, we include also the so-called medium heavy-fermion systems, which usually order magnetically with a moment smaller than $1\,\mu_B$. All the lanthanide systems discussed in this section differ from those in sect. 5 by having a strong temperature dependence of the magnetic relaxation rate. We have classified these systems in tables 3 and 4: those ordering magnetically in table 3, those with large γ values in table 4. Such a classification is not possible for the actinides, because the U based heavy-fermion compounds exhibit also a rather structureless broad magnetic spectrum as described in the section below. The U systems are summarized in table 5 (sect. 6.2). Reviews of the physical properties of the heavy-fermion compounds have been given by Stewart (1984), Steglich et al. (1985) and Ott and Fisk (1987).

6.1. *Lanthanide systems*

There is a large variety of compounds among the lanthanide systems showing a strong temperature dependence in the quasielastic linewidth. At low temperature the linewidth is of the same order of magnitude as the thermal energy. It increases rapidly with temperature (see fig. 55 for Ce systems). Often the absolute values of the *QE* linewidth at room temperature are of the same order of magnitude as in unstable 4f systems. As the width is comparable with the thermal energy at low temperatures, the interactions of the 4f electrons are enhanced compared to stable lanthanides (see sect. 2). However, at low temperatures the hybridization between the 4f and conduction electrons is usually small enough that CF excitations are clearly observable and magnetic order possible. The CF transition lines broaden with increasing temperature due to the increase of the interactions.

6.1.1. *Cerium systems*

Following Loewenhaupt and Fischer (1993) the most suitable method of classification of the Ce systems is with the type of magnetic ordering. There is a group of *ferromagnetically* ordering systems (CeAg, $CeNi_xPt_{1-x}$ and $CeSi_x$ with $1.6 \leqslant x \leqslant 1.83$), a large group of *antiferromagnetically* ordering systems ($CeAl_2$, CeB_6, $CeCu_2$, $CePb_3$ and most of the CeM_2X_2 systems with M for transition metal and X for Si, Ge), and finally the group of the *nonordering* Ce systems $CeAl_3$ ($\gamma \approx 1600$), $CeCu_6$ ($\gamma \approx 1600$), $CeCu_2Si_2$ ($\gamma \approx 1100$), CePtSi ($\gamma \approx 800$) and $CeRu_2Si_2$ ($\gamma \approx 350$), where γ, the electronic

Table 3

Relaxation data as determined by neutron inelastic scattering for materials that order magnetically with unstable 4f electrons. Ordering temperatures and, in some cases, ordered moments are given. All values are based on experiments with polycrystalline samples

System	Magnetic ordering			Neutron data						
				High temperature			Low temperature			
	T_N (K)	μ_{ord} (μB)	Ref.	T (K)	$\Gamma_{QE}/2$ (meV)	Ref.	T (K)	$\Gamma_{QE}^{Lor}/2$ (meV)	$\Gamma_{QE}^{Gau}/2$ (meV)	Ref.
$CePb_3$	1.2	0.55	1,2	128	1.5	2	1.5	0.28		3
$CeAl_2$	3.8	0.7	4,5	300	5.0	6	1.5	0.52		6
				80	1.4	6				
$Ce_{0.6}Sc_{0.4}Al_2$				80	3.8	6	1.5	0.85		6
$Ce_{0.4}La_{0.6}Al_2$				60	0.87	6	1.5	0.21		6
$CeCu_2$	3.5		7	200	1.4	8	5	0.4	0.8	8
CeB_6	2.3	0.28	9	280	2.0	10	5	0.4		10
$CeRh_2Si_2$ [b]	37	2.39	11	150	3.6	12	40	2.8		10
$CeAu_2Si_2$ [b]	10	1.29	11	150	0.64	12	10	0.13	0.58	10
$CeAg_2Si_2$ [b]	10	0.83 [a]	11	200	1.2	11,13	10	0.42	0.83	11,13
$CePd_2Si_2$ [b]	10	0.62	11	200	2.13	12	10	0.87		12
$CeAu_2Ge_2$ [b]	16	1.88	13	200	0.64	13	10	0.09		13
$CeAg_2Ge_2$ [b]	6.3	1.85	13	150	0.51	13	5	0.19	0.8	13
$CeRu_2Ge_1Si_1$ [b]	10.2	1.53	14	250	2.3	15	15	0.3		15
$CeRu_2Ge_{0.5}Si_{1.5}$ [b]	10.2	1.20	14	250	3.5	15	15	0.5		15
$YbBe_{13}$	1.3		16	300	1.2	17	10	0.09	0.23	17
YbPd	1.9		18	300	1.5	19	5	0.15	0.6	19
				200	>10.0	19				
Yb_3Pd_4	3		20	300	3.2	19	5	0.15	0.4	19
				300	1.43	19				
$YbAuCu_4$ [b]	0.6		21	250	2.2	22	1.5	1.0	3.4	22
$YbPdCu_4$ [b]	0.8		21	300	1.6	22	1.5	1.2	2.3	22
	T_c									
$CeRu_2Ge_2$	8.7	1.98	14	200	0.79	13,15	5	0.09		13,15
CePt	5.7		23	200	1.48	23	10	0.39		23
$CeNi_{0.5}Pt_{0.5}$	8.5		23	200	1.48	23	10	0.33		23
$CeNi_{0.8}Pt_{0.2}$	8.3		23	200	1.2	23	10	0.2		23
$CeSi_{1.7}$	~10.0	0.3	24	180	5.0	25				
CeAg	5.3	0.8	26,27	300	1.7	28	10	0.56		28

continued on next page

specific heat or Sommerfeld coefficient, is in $mJ\,mol^{-1}\,K^{-2}$. All the nonmagnetic compounds exhibit $\gamma > 250\,mJ\,mol^{-1}\,K^{-2}$, except $CeSi_{1.95}$ (see table 4). This classification on the basis of magnetic ordering agrees with that of tables 3 and 4, except $CeCu_2Ge_2$,

Table 3, notes

[a] Indicates the average of a sine and a square wave.
[b] Systems are discussed in sect. 3.

References

(1) Cooper et al. (1971)
(2) Vettier et al. (1986)
(3) Balakrishnan et al. (1989)
(4) Barbara et al. (1977, 1979)
(5) Forgan et al. (1990)
(6) Horn et al. (1981b)
(7) Trump (1991)
(8) Loewenhaupt et al. (1990)
(9) Effantin et al. (1985)
(10) Horn et al. (1981c)
(11) Grier et al. (1984)
(12) Severing et al. (1989a)
(13) Loidl et al. (1992)
(14) Dakin et al. (1992)
(15) Rainford et al. (1992)
(16) Heinrich et al. (1979)
(17) Walter et al. (1985)
(18) Pott et al. (1985)
(19) Walter and Wohlleben (1987)
(20) Politt et al. (1985)
(21) Rossel et al. (1987)
(22) Severing et al. (1990a)
(23) Blanco et al. (1992)
(24) Yashima et al. (1982a,b)
(25) Kohgi et al. (1990b)
(26) Tacke et al. (1981)
(27) Schmitt et al. (1978)
(28) Frick et al. (1983)

which orders magnetically, but is listed in table 4 because of its large Sommerfeld constant $\gamma \approx 1400\,\mathrm{mJ\,mol^{-1}\,K^{-2}}$. Furthermore, $CeCu_2Si_2$ is an exception among the nonmagnetic compounds because of its superconductivity.

In fig. 55 the temperature dependence of the quasielastic linewidth is plotted versus temperature for one member of each class given above. For the nonmagnetic heavy-fermion $CeCu_2Si_2$ (Horn et al. 1981a,b) and antiferromagnctic Kondo-lattice $CeAl_2$ (Horn et al. 1981b) the slope $(\Delta\Gamma/\Delta T)$ decreases with increasing temperature. For $CeCu_2Si_2$ the temperature dependence of the *QE* linewidth can be described by a square-root dependence, $\Gamma(T) = \Gamma_0 + c\sqrt{T}$, where c is a constant, and is shown by the solid lines in fig. 55. Such a relationship is unsatisfactory for $CeAl_2$. In contrast, the width of **CeAg** (Frick et al. 1983) varies almost linearly between room temperature and 150 K, and extrapolates to $\Gamma_0 = 0$ for $T \to 0$ K. Below 100 K the linewidth deviates significantly from this linear behavior so that for $T \to 0$ K a residual linewidth of ~0.55 meV was found.

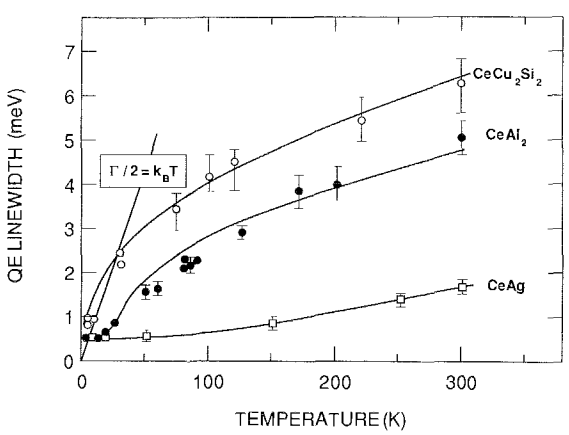

Fig. 55. The QE linewidth of some Kondo-lattice and heavy-fermion systems as a function of temperature. ($CeCu_2Si_2$ and $CeAl_2$ adapted from Horn et al. 1981b and CeAg adapted from Frick et al. 1983.)

Table 4

Relaxation data as in the previous table for 4f heavy-fermion systems. The Sommerfeld coefficient and, in some cases, ordering data are also given. All values are based on experiments with polycrystalline samples

System	Bulk data					Neutron data						
	Specific heat		Magnetic ordering			High temperature			Low temperature			
	γ ($\frac{mJ}{mol\,K^2}$)	Ref.	T_N (K)	μ_{ord} (μ_B)	Ref.	T (K)	$\Gamma_{QE}/2$ (meV)	Ref.	T (K)	$\Gamma_{QE}^{Lor}/2$ (meV)	$\Gamma_{QE}^{Gau}/2$ (meV)	Ref.
$CeAl_3$	1620	1				125	3.1	2	2	0.66		2
$CeCu_6$	1600	3				150	3.4	4	1.5	0.5		4
$CeCu_2Ge_2$	1400	5	4.1	0.74	6	150	1.6	6	10	0.6	0.74	6
$CeCu_2Si_2$	1100	7	s.c.[a]		8	300	6.1	9,10	5	0.75		9,10
CePtSi	800	11				150	2.9	12	5	1.4		12
$CeSi_{1.95}$	104	13,14				135	11.0	15	5	4.0		15
$CeSi_{1.85}$	270	16							5	2.0		15
			$\chi_{bulk,T=0}$ ($\frac{10^{-3}emu}{mol}$)							Δ (meV)	$\Gamma_{INE}/2$ (meV)	
$CeRu_2Si_2$	350	17–19	~16		20	250	9.0	21	1.5	1.3	1.0	21

[a] s.c.: this material becomes superconducting.

References

(1) Andres et al. (1975)
(2) Murani et al. (1980)
(3) Stewart et al. (1984a)
(4) Walter et al. (1986a)
(5) Knopp et al. (1989)
(6) Loidl et al. (1992)
(7) Stewart (1984)
(8) Steglich et al. (1979)
(9) Horn et al. (1981a)
(10) Holland-Moritz et al. (1989c)
(11) Lee and Shelton (1987)
(12) Krimmel et al. (1992)
(13) Dijkman et al. (1982)
(14) Yashima et al. (1982a)
(15) Galera et al. (1989)
(16) Dhar et al. (1987b)
(17) Thompson et al. (1985)
(18) Besnus et al. (1985)
(19) Steglich et al. (1985)
(20) Grier et al. (1988)
(21) Severing et al. (1989a)

Such a linear behavior was found also for the ferromagnetically ordering systems **$CeNi_xPt_{1-x}$** (Blanco et al. 1992) and **$CeRu_2Ge_2$** (Rainford et al. 1992). For **$CeSi_x$** this linearity is not clear with the present data. However, the data on $CeSi_{1.85}$ by Galera et al. (1989) show a linearity of the quasielastic linewidth for this nonmagnetic system, whereas the linewidth data for $CeSi_{1.95}$ seem to be more compatible with a square-root dependence as shown in fig. 56. We add to this figure the data of Kohgi et al. (1990b) on $CeSi_{1.7}$ and this shows that the data might also be compatible with a linear dependence, although two data points are no proof. As no magnetic order is reported for $CeSi_{1.85}$ we include it in table 4. Additional neutron work on $CeSi_x$ has been reported by Kohgi et al. (1991) and for a discussion of the bulk properties of $CeSi_x$ alloys see Dhar et al. (1987b).

Next we discuss antiferromagnetic systems. As many features are discussed in the chapter by Loewenhaupt and Fischer (1993), we will concentrate here on the most important points. **$CeAl_2$** has the cubic structure of Laves-type (C15), exhibits $\gamma \approx 130\,mJ\,mol^{-1}K^{-2}$, and orders antiferromagnetically at $T_N = 3.8\,K$ with a moment of $\sim 0.7\,\mu_B$ (Barbara

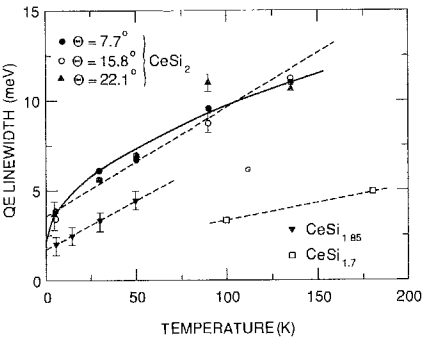

Fig. 56. The quasielastic linewidth of $CeSi_x$ for several x values (taken from Galera et al. 1989, $x=2$, 1.85 and taken from Kohgi et al. 1990b, $x=1.7$). Note that according to Dhar et al. (1987b) $x=2$ does not exist as a single phase; this should probably be $x=1.95$.

et al. 1977, 1979, Forgan et al. 1990). We draw attention to an anomalous splitting of the $\Gamma_7 \rightarrow \Gamma_8$ transition observed by Loewenhaupt et al. (1979a, 1987), which was treated theoretically by Thalmeier and Fulde (1982), and in more detail by Thalmeier and Lüthi (1991) in terms of electron–phonon interactions, i.e., a similar mechanism as discussed above for the splitting of the intermultiplet transition in $Sm_{0.75}Y_{0.25}S$. The temperature dependence of the quasielastic linewidth of $CeAl_2$ is shown in fig. 55; the propagating excitations in the antiferromagnetic state, first observed by Loewenhaupt and Steglich (1977a,b), have been investigated in more detail by Osborn et al. (1987). The fact that the single crystal was multidomain in nature made it difficult to make unambiguous assignments of these low-energy excitations (<2 meV). The acoustic magnon branch is centered at 0.7 meV, and the optical branch at 1.2 meV, but both are broader than instrumental resolution. Very little dispersion was observed.

Another interesting compound is **$CePb_3$** with the cubic $AuCu_3$ structure. This has a reasonably high γ value of 225 mJ mol^{-1}K^{-2} (Cooper et al. 1971) but orders antiferromagnetically at 1.16(5) K according to neutron experiments by Vettier et al. (1986). The magnetic ordering is complex being incommensurate in two components, thus $\boldsymbol{k}=[q_x, q_y, \frac{1}{2}]$ with $q_x=0.135(1)$ and $q_y=0.058(1)$ at 30 mK. q_x appears independent of temperature (perhaps because it is commensurate with $2/15=0.1333$), whereas q_y changes rapidly. The moments are 0.55 (10) μ_B at the lowest temperature and are parallel to the [001] direction. No evidence for a higher-order modulation, indicating a partial squaring, was found. This is a particularly unusual magnetic structure and the authors claim that it represents one possible ground state of a Kondo system. In this there is an interplay between the localized 4f electrons and the conduction electrons, resulting in different moments on different sites. From magnetization measurements the CF ground state of $CePb_3$ was deduced as Γ_7.

The CF splitting was confirmed and investigated more quantitatively with neutron inelastic scattering on polycrystalline material by three groups. The spectra given by Vettier et al. (1986) for 200 mK and Renker et al. (1987) for 4 K are similar and were taken with a triple-axis spectrometer with $E_f=14.7$ meV and 13.8 meV, respectively. A clear CF peak exists at ~6 meV. Renker et al. (1987) performed a detailed analysis, and deduced a quasielastic component, suggesting a Γ_7 ground state. Finally, Balakrishnan et al. (1989)

performed experiments with the cold source time-of-flight spectrometer IN6 ($E_i = 3.1$ and 2.3 meV) with much better resolution at low energy. They agree with the earlier interpretations on the CF peak at ~6 meV, but concentrate on the QE component. They found a $T^{1/2}$ dependence of $\Gamma/2$ with T. At low temperatures $\Gamma/2 = 0.3$ meV, but this rises to ~1.5 meV by 130 K. Such a temperature dependence fits well with our understanding of Kondo systems. Since Γ (the quasielastic linewidth) is often, at least for Ce-based systems, inversely proportional to the electronic specific heat coefficient γ, the narrow low-temperature Γ of $CePb_3$ suggests γ should be comparable to that found in $CeAl_3$, i.e., more than 1000 mJ mol^{-1}K^{-2} rather than the ~200 mJ mol^{-1}K^{-2} extrapolated from measurements above the antiferromagnetic ordering temperature. $CePb_3$ would then be a "real" heavy-fermion system.

Vettier et al. (1986) also point out that all the trivalent Ce compounds $CeAl_3$, $CeCu_6$ and $CeCu_2Si_2$ have reduced symmetry. They speculate that the anisotropy enhances electronic correlations and reduces magnetic couplings. These arguments, although interesting, are somewhat weakened by the observation of antiferromagnetic order in the Kondo system **$CePd_2Si_2$** (same tetragonal structure as $CeCu_2Si_2$), $T_N = 10$ K, by Hippert et al. (1992). They used a (small) single crystal and determined the ordered moment to be ~0.6 μ_B. Sharp excitations were *not* seen in the ordered state, instead two rather broad modes, almost independent of $\boldsymbol{q}$, were found, centered at ~0.7 and ~2 meV. The total intensity can also be fairly well reproduced by a quasielastic Lorentzian of $\Gamma/2 \approx 1$ meV as found earlier in experiment on polycrystalline samples (Grier et al. 1988, Severing et al. 1989a).

CeB_6 has a rather large γ of 260 mJ mol^{-1} K^{-2} (Bredl 1987). The temperature dependence of the quasielastic linewidth was reported first by Horn et al. (1981b), and later by Neuhaus (1987) with a better energy resolution, see also Loewenhaupt and Fischer (1993). In contrast to the old, the new data do not follow a square-root law, but exhibit a change of the slope at 30 K. A large crystal-field splitting of 47 meV was found (Zirngiebl et al. 1984, Loewenhaupt et al. 1985). A further splitting of the Γ_8 quartet ground state by about 2.5 meV (~30 K), as suggested by Zirngiebl et al. (1984), could not be confirmed by neutron-scattering experiments on either polycrystals or single crystals (Regnault et al. 1988a). Only the observed change of the slope in the temperature dependence of the quasielastic linewidth indicates some anomalous behavior at low temperatures.

For orthorhombic **$CeCu_2$** Loewenhaupt et al. (1988, 1990) report a crystal field of two excited-state doublets separated by 9 and 23 meV from the ground state. The quasielastic linewidth increases linearly with temperature, although the material orders in a simple antiferromagnetic structure at $T_N = 3.5$ K (Lebech et al. 1987). The Lorentzian quasielastic linewidth at 200 K is only 1.3 meV. Thus, the small ordered magnetic moment is probably a consequence of the CF ground state rather than signifying a Kondo lattice. Furthermore, this explains why the temperature dependence of the linewidth behaves Korringa-like instead of the square-root dependence observed in the compounds with strongly interacting electrons. Intensive investigations of the excitations have been performed by Trump (1991).

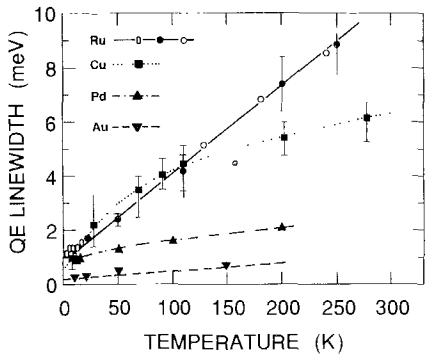

Fig. 57. The QE linewidth of CeM_2Si_2 systems as function of temperature [(M = Au, Pd, Cu, Ru (from Severing et al. 1989a) and Cu (from Horn et al. 1981a)].

Finally, we discuss the properties of the **CeM_2X_2** series (X = Si or Ge), which show the whole spectrum from a stable 4f moment to the strongly unstable moment of an intermediate-valent Ce ion. $CeAu_2Si_2$, $CeAg_2Si_2$ and $CeRh_2Si_2$ order magnetically with a moment larger than 1 μ_B, and therefore belong to sect. 4, but their data are included in table 3 for completeness. The temperature dependences of the linewidth of two of these systems are included in fig. 57. The linewidth of $CeAg_2Si_2$ (Loidl et al. (1989), Culverhouse and Rainford, unpublished), behaves like that of $CeAu_2Si_2$. Both are even smaller than found in $CeCu_2$ (see above) and behave almost Korringa-like, although some weak curvature cannot be excluded. This is compatible with a well-defined magnetic moment. In contrast, the linewidth in $CeRh_2Si_2$ is quite large, although the ordering temperature ($T_N = 37$ K) and the ordered magnetic moment (2.39 μ_B) are larger than for $CeAu_2Si_2$. This is still a puzzle, and it is assumed that the 4d electrons on Rh play an active role. At the other end of the spectrum is the intermediate-valent system $CeNi_2Si_2$ with $v \approx 3.18$ (Röhler 1987), about which no reliable inelastic neutron scattering data exist. The data obtained on the related system $CeNi_2Ge_2$ (Knopp et al. 1988) with $v \approx 3.07$ (Röhler 1987) have been given in sect. 5. A good survey of the results of the Mainz/Darmstadt group on these systems, especially CeM_2Ge_2, was given recently by Loidl et al. (1992). Some of the results are summarized in table 3, above. As for the Si group, M = Au is the most stable. Heavy-fermion behavior is found for M = Cu (see below). The M = Ag system is unusual. On the one hand, it has as small a linewidth as M = Au at $T = 150$ K, but, on the other, the T-dependence of the linewidth is non-linear, which is unexpected for an otherwise stable Ce ion.

Representative spectra of CeM_2Si_2 (Severing et al. 1989b) are shown in fig. 58. Due to the stable 4f moment, CF excitations are sharp in **$CeAg_2Si_2$**. Crystal-field excitations are also observable in **$CePd_2Si_2$**. Its level scheme is shown in comparison with other members of this group in fig. 59. Experiments by Steeman et al. (1990) on a single crystal are qualitatively in agreement, but show some quantitative differences in the CF parameters and corresponding wave functions. In agreement with the increased linewidth in $CePd_2Si_2$, the ordered magnetic moment is suppressed. The spin dynamics of the ground state were investigated as a function of temperature by Grier et al. (1988) and

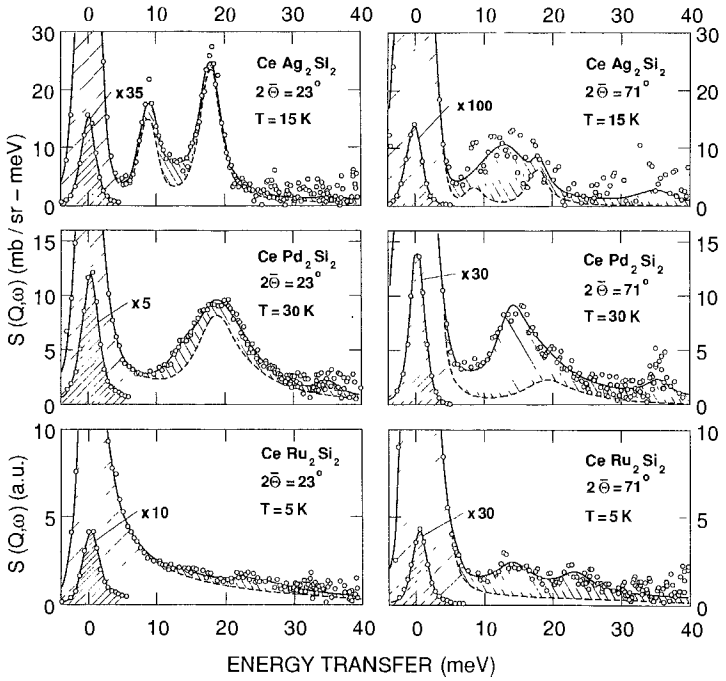

Fig. 58. Background corrected inelastic neutron scattering spectra of CeM_2Si_2. The hatched area is due to nuclear incoherent elastic and inelastic phonon scattering. (From Severing et al. 1989b.)

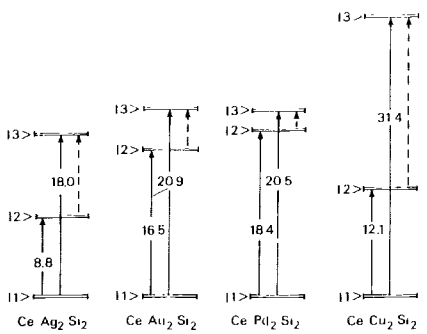

Fig. 59. CF schemes of the CeM_2Si_2 series. The energy is given in units of meV. Note that recent experiments by Goremychkin and Osborn (1993b) dispute the CF level at 12 meV in $CeCu_2Si_2$. (Adapted from Severing et al. 1989b.)

Severing et al. (1989a). Both are in agreement and report on a magnon-like structure below $T_N = 10$ K. As in $CeAu_2Si_2$, the linewidth increases linearly with temperature above the Néel temperature.

$CeCu_2Si_2$ is the well known, and first-discovered, heavy-fermion compound within this isostructural group. The crystal-field levels are broadened in energy even at $T = 5$ K (Horn et al. 1981a). There is still controversy over the crystal-field splitting. In addition to this controversy, there is confusion over the values of the crystal-field parameters used by

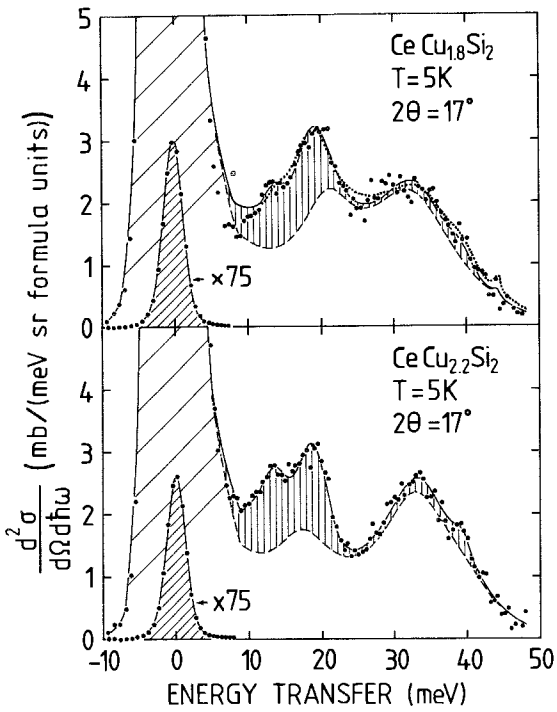

Fig. 60. Background corrected inelastic neutron scattering spectra of $CeCu_{2\pm0.2}Si_2$. The solid line in the upper frame is the best fit with a ground state of mainly $|5/2\rangle$ character. For comparison the dotted curve shows a fit with a ground state of mainly $|3/2\rangle$ character, which is significantly worse. The hatched area is due to nuclear incoherent elastic and inelastic phonon scattering. (From Holland-Moritz et al. 1989c.)

various authors in fitting their spectra. The value of B_{44} given by Horn et al. (1981a) is wrong: the correct value is ± 6.25 K. Holland-Moritz et al. (1989c) and Severing et al. (1989b) give the wrong sign for the B_{40} parameter: the correct value is -0.034 meV. Horn et al. (1981a) report in their early work two inelastic excitations, one distinct line at about 30 meV and a weaker one at about 12 meV. The fact that a significant phonon contribution is present just around 15 meV casts doubt on the existence of the line at 12 meV, which was then the subject of several later investigations. There are two studies with polarized neutrons. Stassis et al. (1986) claim to have seen magnetic scattering around 12 meV and that their data are consistent with Horn et al. (1981a), but due to their poor energy resolution this is not a clear proof of the existence of the second CF level at about 12 meV. Johnson et al. (1985) report only one inelastic line, but their energy resolution was even worse than that of Stassis et al. (1986), so that the asymmetry of their peak may be an indication for a second unresolvable magnetic level.

Holland-Moritz et al. (1989c) performed additional experiments on copper-excess and copper-deficient material, $CeCu_{2\pm0.2}Si_2$. The two resulting spectra obtained at $T = 5$ K are shown in fig. 60. Their careful analysis of the phonon distribution based on high-angle spectra reveals that the phonon spectrum is almost the same in both the copper-excess and the copper-deficient systems. Therefore, the differences at low angles are thought to be due to magnetic scattering as indicated by the dashed line in fig. 60.

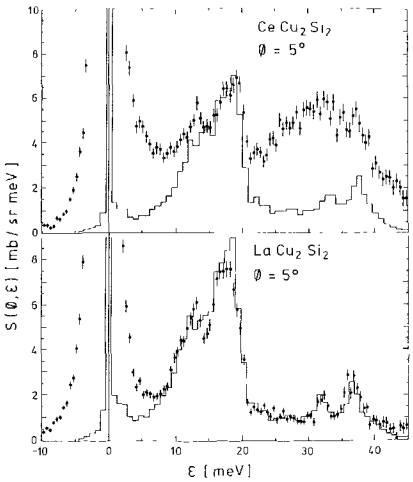

Fig. 61. Neutron energy spectra from (a) $CeCu_2Si_2$ and (b) $LaCu_2Si_2$ measured at the Rutherford spallation source at a scattering angle of 5° (filled circles) with an incident neutron energy of 60 meV. The histograms are the total phonon scattering determined by Monte Carlo simulation and are derived from the high-angle data, in which the magnetic scattering is absent. Note that the simulation has not been convoluted with the experimental resolution function so that the elastic scattering is confined to one channel. (From Goremychkin and Osborn 1993b.)

Whereas the spectrum of $CeCu_{1.8}Si_2$ could be interpreted by single-ion CF theory, this analysis failed for $CeCu_{2.2}Si_2$, because the high-energy excitation at ~33 meV has an enhanced intensity. Holland-Moritz et al. (1989c) suggest that one possible explanation could involve a static mixture of almost trivalent (γ-Ce) and an amount of about 20% intermediate-valent Ce ions (α-Ce). The latter will yield a broad inelastic excitation at low temperatures (in analogy to intermediate-valent 4f moments in sect. 5), which may be the reason for the enhanced intensity around 35 meV. This unusual behavior may be a consequence of the slightly smaller unit cell volume of $CeCu_{2.2}Si_2$. Of course other explanations may be possible, especially those admitting that single-ion CF theory does not apply to this strongly hybridized 4f moment (enhanced 4f instability). It should be pointed out that the total CF splitting of 31 meV in $CeCu_2Si_2$ is about 50% larger than that in other CeM_2Si_2 systems (fig. 59). This experiment shows clearly that the inelastic magnetic response depends on the Cu content and that the 30 meV peak becomes stronger with increasing Cu.

A recent experiment by Goremychkin and Osborn (1993b) again raises doubts on the 12 meV line. We show the comparison between their data on $CeCu_2Si_2$ and $LaCu_2Si_2$ in fig. 61. The upper frame (i.e., spectra of $CeCu_2Si_2$) look nearly the same as shown in fig. 60. A direct phonon subtraction is unsuitable because of the different scattering lengths of La and Ce. Whereas Holland-Moritz et al. (1989c) scaled the phonon density of states from high to low angles, Goremychkin and Osborn (1993b) used a new method that involves Monte Carlo calculations, which also simulate higher-order processes. This method is still in its testing phase, although it has promise for wider use in this difficult problem of establishing the non-magnetic scattering. Excellent agreement was found for the high-angle spectra (not shown) of both $LaCu_2Si_2$ and $CeCu_2Si_2$; however, the application to the low-angle data is still not perfect, as the lack of complete agreement for the histogram for $LaCu_2Si_2$ in fig. 61b shows. Thus, we believe that the analysis

cannot exclude the possibility of a weak CF transition at ~12 meV. Goremychkin and Osborn (1993b) suggest a CF scheme which accounts for the magnetic susceptibility and the specific heat. Their CF scheme is a doublet ground state, and a quasi-quartet (actually two doublets) at ~30 meV, and thus different from that shown in fig. 59. They deduce the CF parameters and show that there is probably considerable hybridization between the cerium 4f and silicon p electron states. This is demonstrated by work of Goremychkin et al. (1992) on $NdCu_2Si_2$ which compares the CF parameters for these two isostructural compounds. The temperature dependence of the quasielastic line (see fig. 57) in $CeCu_2Si_2$ can be well described by a square-root law. Within the experimental error the width extracted from the polarized data are in agreement with those of the unpolarized neutron scattering experiments.

Difficulties in establishing the true magnetic response in stoichiometric $CeCu_2Si_2$ clearly would benefit from enhanced capabilities of separating the magnetic from the nuclear scattering with polarization analysis, a point we discussed in sect. 1. Despite the demonstration of the power of this technique as long ago as 1969 (Moon et al. 1969), the present intensities are too low and the energy resolution too poor for the studies to be definitive, as the work on $CeCu_2Si_2$ of both Johnson et al. (1985) at the ILL and Stassis et al. (1986) at BNL aptly demonstrates.

Within the CeM_2Si_2 series, **$CeRu_2Si_2$** is a compound on the border between heavy-fermion and intermediate-valent behavior, but close to trivalent. Although the low-temperature magnetic response does not show any sharp structures, and no magnetic ordering was observed, we will discuss this compound here. It has a rather large specific heat γ of about 350 mJ mol^{-1}K^{-2} (Thompson et al. 1985, Besnus et al. 1985, Steglich et al. 1985), but the value is smaller than that for $CeCu_2Si_2$. Distinct CF excitation as found for the systems discussed above are not detectable, see lower panel of fig. 58. As in the case of $CeRh_2Si_2$, this is due to an enhanced linewidth. However, whereas in $CeRh_2Si_2$ this was related to magnetic ordering, ordering has not been found so far in $CeRu_2Si_2$. Thus, instead of rather sharp magnon-like excitations, a broad excitation spectrum was detected at low temperatures. At $T \approx 20$ K the spectrum exhibits a quasielastic linewidth of 2 meV and the magnetic response starts to change its character, an inelastic excitation at about 1.6 meV is found at lower temperatures. The intensity of this low-energy response coincides well with the static susceptibility, but the total magnetic cross section is about a factor of 3 lower than expected for a trivalent Ce ion (3.92 barn). A second broad magnetic excitation, assumed at energies between 20 and 35 meV and carrying the rest of the full Ce^{3+} cross section, may therefore exist. Due to its width this response cannot be separated easily from the phonon background. If such a broad excitation line does exist, a decision whether it should be interpreted as a CF field splitting or as a second inelastic hybridization line due to the tetragonal symmetry (see $YbPd_2Si_2$ in sect. 5) will be difficult.

The quasielastic Lorentzian linewidth of $CeRu_2Si_2$ increases linearly with temperature above 20 K. The results given by Severing et al. (1989a) are in good agreement with those by Grier et al. (1988). This linear dependence is also in agreement with the results of Rainford et al. (1992), who found a quite analogous behavior for

the complete $CeRu_2Si_{2-x}Ge_x$ series. On the one hand, this unusual linear behavior in $CeRu_2Si_2$ may be related to some surviving ferromagnetic correlations, which are evident when Ge is substituted for Si. But, on the other hand, the comparison of the local susceptibility with the bulk value indicates antiferromagnetic correlations (Severing et al. 1989a). Important work on the compound $CeRu_2Si_2$ has also been performed on single crystals by Regnault et al. (1988c, 1990), Rossat-Mignod et al. (1988) and Jacoud et al. (1989). These will be discussed in more detail by Aeppli and Broholm (1994) in chapter 131. In fact, $CeRu_2Si_2$ is an excellent example of the complementarity of the techniques using polycrystalline samples with the time-of-flight neutron method and those on single crystals with the triple-axis spectrometer. The broad structureless quasielastic response seen in the former experiments is difficult to quantify with a triple-axis spectrometer, whereas the anisotropic correlations seen by the latter are too weak to be measured on polycrystals, in which the average is over a large volume of reciprocal space. An important point established by the experiments on single crystals is that magnetic fluctuations occur only along the easy c-axis of the tetragonal structure and that, in addition to the uniform (nearly $\boldsymbol{Q}$-independent) response probed by experiments on polycrystals, there are incommensurate antiferromagnetic correlations with a smaller energy scale (~1 meV). The latter are quenched by higher magnetic fields ($H > 80$ kOe), when the material is a meta-magnet. Regnault et al. (1988c, and references therein) report that substitution of 13% La on the Ce site leads to magnetic order with an incommensurate structure at approximately the same $\boldsymbol{q}$ vector at which the maximum correlations are found with the pure compound. Replacing Ru with Rh leads to a commensurate AF order.

Before turning to some heavy-fermion systems with a γ value larger than for $CeCu_2Si_2$ we will mention a work on the heavy-fermion system **CePtSi** [$\gamma \approx 800\,\mathrm{mJ\,mol^{-1}K^{-2}}$] by Krimmel et al. (1992). The temperature dependence of the quasielastic linewidth behaves again consistent with a square-root dependence, but no magnetic order or superconductivity is reported up to now.

$CeCu_2Ge_2$ [$\gamma \approx 1400\,\mathrm{mJ\,mol^{-1}K^{-2}}$] is a heavy-fermion system with a larger γ value than $CeCu_2Si_2$; however, instead of superconductivity it shows antiferromagnetic order below $T_N = 4.1$ K with an ordered moment of $0.74\,\mu_B$. Thus, an inelastic magnon-like excitation was observed below the Néel temperature and a Gaussian quasielastic component below $T \approx 60$ K (see fig. 62) according to Knopp et al. (1989). The quasielastic linewidth versus temperature again follows a square-root law.

Next is **$CeAl_3$** with $\gamma \approx 1620\,\mathrm{mJ\,mol^{-1}K^{-2}}$ (Andres et al. 1975). Because of the hexagonal crystal symmetry the crystal-field states are the pure $|\pm 1/2\rangle$, $|\pm 3/2\rangle$ and $|\pm 5/2\rangle$ states, with only two allowed transitions. Murani et al. (1977) reported two inelastic broad excitations at ~5.2 meV and ~7.6 meV in the low-temperature spectra, and assumed a $|\pm 3/2\rangle$ wavefunction as the ground state. Due to an intrinsic width of the CF levels, the excitations could not be well resolved, even by a later experiment with better experimental resolution, (Murani 1987b). From this later experiment Murani concluded that the excitation energies were 6 and 8 meV. The square-root law behavior of the temperature dependence of the quasielastic linewidth is shown by Murani et al. (1980). From these earlier experiments Murani et al. (1980) also extracted a narrow quasielastic

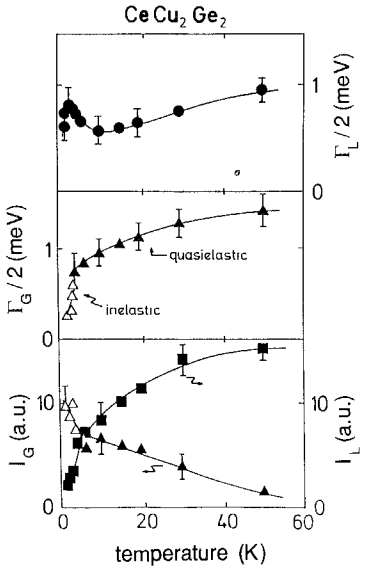

Fig. 62. The temperature dependence of the quasielastic Lorentzian (upper frame), of the quasielastic and inelastic Gaussian linewidth (middle frame) and of their intensities (lower frame) for $CeCu_2Ge_2$. (From Knopp et al. 1989.)

linewidth of ~1 meV. Such a narrow width is consistent with the scaling such that $\Gamma \propto \gamma^{-1}$, where γ is the electronic specific heat or Sommerfeld coefficient, and Γ is the quasielastic linewidth, that is generally apparent when considering Ce compounds, see sect. 7 for a further discussion. However, Goremychkin et al. (1987) and Goremychkin and Osborn (1993a) claim that a much broader ($\Gamma/2 \approx 8$ meV) response is present as well. The integrated neutron intensity is in good accord with the susceptibility if the data is extrapolated to high energy transfer. Their recent data as a function of temperature are shown in fig. 63. It appears from this data that *three* components are present in the scattering from $CeAl_3$. Two, the narrow quasielastic and the inelastic component at 6.4 meV, are from the usual CF levels, and the third is a broad feature that was analyzed by the authors as a second quasielastic line with a width of ~7.5 meV. The total scattering is in good agreement with that anticipated on the basis of the bulk susceptibility. With fig. 1 and the relevant discussion in mind it is clear that we cannot decide whether this broad feature is quasi- or inelastic in nature. The presence of two energy scales in $CeAl_3$ is a feature also found also in $YbPd_2Si_2$, USn_3 (sect. 5), URu_2Si_2, UPt_3 and UBe_{13} (see below).

Finally, there is **$CeCu_6$** with $\gamma \approx 1600\,\mathrm{mJ\,mol^{-1}K^{-2}}$. There are detailed single-crystal studies as a function of temperature and magnetic field by Aeppli et al. (1986), Regnault et al. (1987, 1988b), which will be covered by Aeppli and Broholm (1994) in chapter 131. As with $CeRu_2Si_2$ discussed above, the single-crystal experiments show the presence of $\boldsymbol{Q}$ dependent effects signifying intersite correlations. The experiments on polycrystalline samples give information primarily on the single-site correlations of the 4f electrons with the conduction band, and only when strong $\boldsymbol{Q}$-dependent effects can be extracted do they address the correlations between neighboring 4f sites. We will

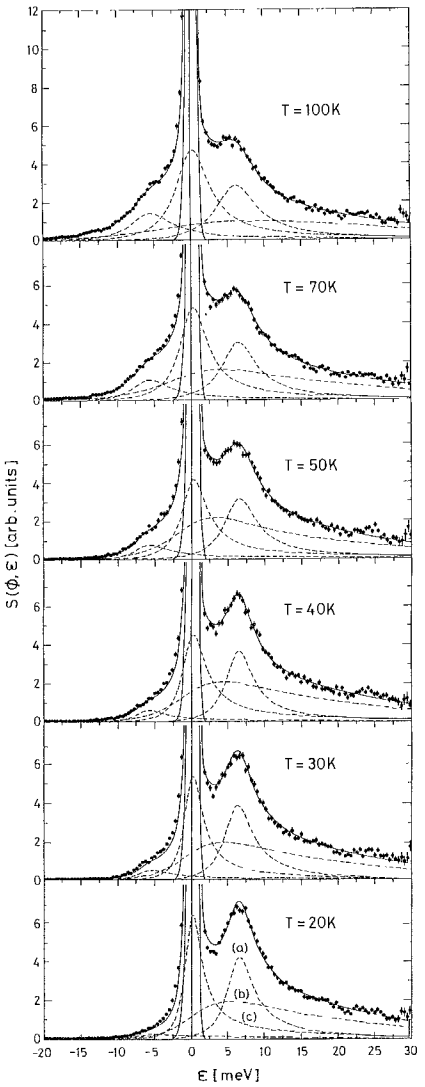

Fig. 63. Neutron inelastic spectra of $CeAl_3$ at different temperatures taken with $E_i = 35$ meV. The solid line is a fit to three Lorentzian lineshapes (dashed lines): (a) an inelastic CF transition at 6.4 meV; (b) a broad QE response; (c) a narrow QE response. (From Goremychkin and Osborn 1993a.)

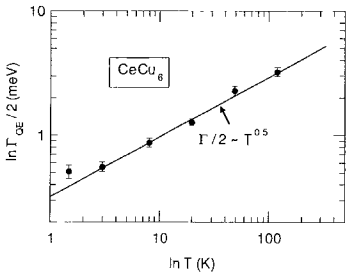

Fig. 64. The QE linewidth of $CeCu_6$ plotted on a log-log plot. The solid line gives a square-root dependence above $T = 3$ K. (Adapted from Walter et al. 1986a.)

give here the results of the two experiments on polycrystalline samples. The first was done by Walter et al. (1986a). They found a square-root dependence for the quasielastic linewidths versus temperature (see fig. 64) down to 3 K; below that temperature the width seems to saturate at a value of 0.5 meV. Walter et al. (1986a) suggest a crystal-field level scheme of doublets at 5.5 and 11 meV from the ground-state doublet. As they used cold neutrons, the deduction of the crystal-field scheme was done from spectra at $T > 50$ K. Recent experiments with thermal neutrons by Goremychkin and Osborn (1993c) at lower

temperatures yield a smaller intrinsic linewidth and a better experimental resolution (energy loss side), and result in a slightly modified level scheme of the excited doublets at 7 and 13.8 meV.

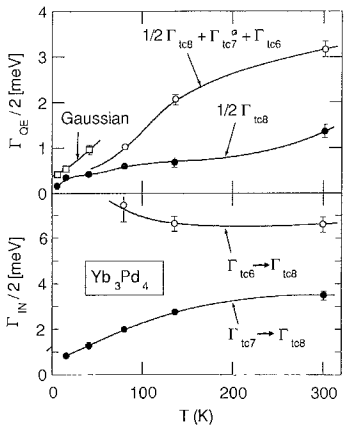

Fig. 65. The temperature dependence of the quasielastic (upper panel) and inelastic (lower panel) linewidths for Yb_3Pd_4. For the quasielastic linewidths the filled circles correspond to the linewidth of only one Kramers doublet of the Γ_{tc8} quartet, the open circles to the linewidth of the Gaussian critical spin fluctuations. The index "ten" used to classify the CF levels indicates that Yb_3Pd_4 behaves "cubic-like", and that the analysis was performed with the CF Hamiltonian of cubic symmetry, although the real crystallographic structure is triclinic. The CF level is identified by the integer n. (From Walter and Wohlleben 1987.)

6.1.2. *Ytterbium systems*

There are two Yb systems for which intermediate valency is reported, but which show a strong temperature dependence of the quasielastic linewidth and hence will be discussed here: **YbPd** and **Yb_3Pd_4**. The valence change of Yb in YbPd is given as 2.80–2.83 from 10 to 300 K (Pott et al. 1985) and that in Yb_3Pd_4 as 2.81–2.95 (Politt et al. 1985). In spite of this rather strong intermediate valency, the quasielastic linewidth decreases with decreasing temperatures, resulting finally in magnetic order of the Yb moments (Walter and Wohlleben 1987). We discuss here one unusual feature found in both systems. Figure 65 shows the quasielastic linewidths as a function of temperature for Yb_3Pd_4. Surprisingly, there exist, in addition to the Lorentzian and Gaussian lines at low temperatures, two Lorentzian lines at $T \geqslant 80$ K, one with a rather narrow component and a second broader one. The intensity of the narrow quasielastic line is rather precisely determined. Whereas for $T \leqslant 30$ K the quasielastic intensity is compatible with a Γ_8 ground state, the intensity of the narrow quasielastic Lorentzian at $T > 120$ K is compatible only with just half this value, i.e., with a doublet. Walter and Wohlleben (1987) therefore interpreted the high-temperature spectra by two quasielastic lines of which the narrow one represents one doublet of the Γ_8 ground state, whereas the other doublet, as well as the higher Γ_6 and the Γ_7 states, are represented by the broader quasielastic components. Whether this anomaly is also connected with an energy splitting of the Γ_8 state at higher temperatures cannot be decided from the data because of the enhanced width of the crystal-field levels. A similar effect was found for YbPd (Walter and Wohlleben 1987). Finally, fig. 66 gives an instructive example of how magnetic ordering can be detected even on polycrystals by neutron inelastic scattering experiments. The spectrum at 3.12 K (lower right), i.e., just above the Néel temperature (= 3 K), shows a

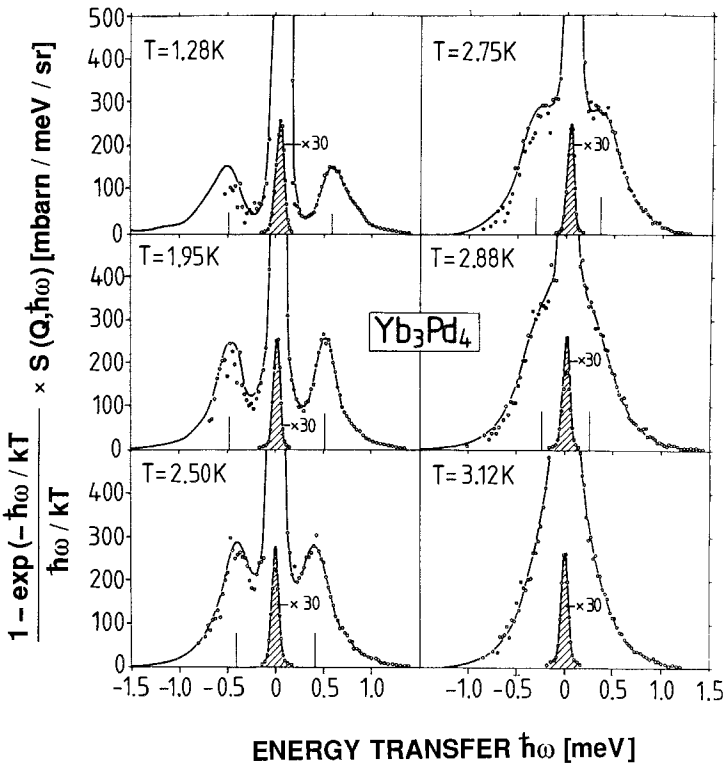

Fig. 66. Background corrected inelastic neutron scattering spectra of Yb_3Pd_4 showing the formation of magnon lines when decreasing the temperature below $T_N = 3$ K. The hatched area is due to the nuclear incoherent elastic scattering. (From Walter and Wohlleben 1987.)

single Gaussian quasielastic contribution. With decreasing temperature (below T_N) this splits slowly into two inelastic Gaussians, due to spin-wave excitations.

6.2. *Actinide systems*

In the actinides one expects a larger f–d hybridization than in the lanthanides. In fact, the static bulk susceptibility of most U-systems is strongly reduced compared to the Curie behavior. This yields a negative Curie–Weiss temperature Θ, which is due mostly to the enhanced f–d hybridization and only partly due to antiferromagnetic correlations. Ordering of the 5f moments occurs if the static bulk susceptibility exhibits a maximum. Although this maximum is clearly related to magnetic correlations, often long-range ordering sets in at a lower temperature as indicated by a further discontinuity in the slope of the susceptibility, e.g., URu_2Si_2 (Palstra et al. 1985) or U_2Zn_{17} (Ott et al. 1984). The lower the ordered magnetic moment, the less pronounced is the change in the static susceptibility. Among the heavy-fermion U systems there are three, UPt_3, UBe_{13}, and

Table 5
Data as in previous tables for uranium-based systems. All data are from experiments on polycrystalline samples, except where noted.

System	Bulk data					Neutron data						
	Specific heat		Magnetic ordering			High temperature			Low temperature			
	γ ($\frac{mJ}{molK^2}$)	Ref.	T_N (K)	μ_{ord} (μ_B)	Ref.	T (K)	$\Gamma_{QE}/2$ (meV)	Ref.	T (K)	$\Gamma_{QE}^{Lor}/2$ (meV)	$\Gamma_{QE}^{Gau}/2$ (meV)	Ref.
Materials discussed in section 3												
UAs			124	1.7	1	300	16.4	2	5	7.5		2
			62	2.25	1							
UPb_3			32	~1.6	3	300	5.5	4,5	40	19.5		4,5
Materials discussed in section 4												
USn_3	170	6				300	20.0	7	5	6.6		7
UAl_2	133	8				300	25.0	9	10	22.0		9
Materials discussed in section 5												
UBe_{13} (SC)	1100	10							10	10.0		11
									1.5	~1.5		12
U_2Zn_{17}	535	13	9.7	0.8	14	50	14.1	15	10	8.9	0.75	15
UPt_3 (SC)	450	16	5	0.02	17				1.3	~9.0		18
									0.5	~0.2		18
UCu_5	250	19	15	0.9	20	50	8.2	15	10	9.8	2.2	15
										Δ (meV)	$\Gamma_{INE}/2$ (meV)	
URu_2Si_2 (SC)	180	21	17.5	0.04	22	120	6.7	23	5	6.3	1.7	24
single crystal						80	14.4[a]	25				

[a] Data taken from the [100] direction and the analysis by Broholm et al. (1991).

References

(1) Stirling et al. (1980, 1983)
(2) Loewenhaupt et al. (1982)
(3) Leciejewicz and Misiuk (1972)
(4) Marshall et al. (1992a)
(5) Murasik et al. (1980)
(6) van Maaren et al. (1974)
(7) Loewenhaupt and Loong (1990)
(8) Trainor et al. (1975)
(9) Loong et al. (1986)
(10) Ott et al. (1983)
(11) Goldman et al. (1986)
(12) Lander et al. (1992)
(13) Ott et al. (1984)
(14) Cox et al. (1986)
(15) Walter et al. (1987)
(16) Stewart et al. (1984b)
(17) Aeppli et al. (1988)
(18) Aeppli et al. (1985)
(19) Fisk et al. (1985)
(20) Murasik et al. (1974)
(21) Palstra et al. (1985)
(22) Broholm et al. (1987a)
(23) Walter et al. (1986b)
(24) Holland-Moritz et al. (1987b)
(25) Broholm et al. (1991)

URu_2Si_2, that become superconducting. [Note added in proof: These have now been joined by UPd_2Al_3 and UNi_2Al_3 but the latter two are not discussed in this review.]

We start our discussion with a system that does not fit into any possible classification of U systems: **URu_2Si_2**. It orders antiferromagnetically with a very low magnetic moment of 0.04 μ_B at $T_N = 17.5$ K (Broholm et al. 1987a) and becomes superconducting below 1 K (Palstra et al. 1985, Schlabitz et al. 1986, Maple et al. 1986). This compound has a γ value of only 180 mJ mol^{-1}K^{-2} (Palstra et al. 1985, Schlabitz et al. 1986, Maple et al. 1986)

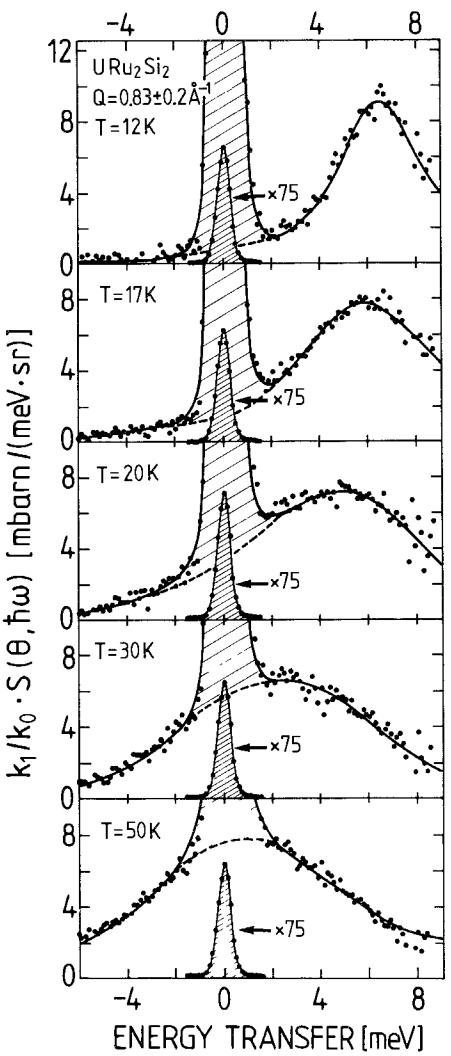

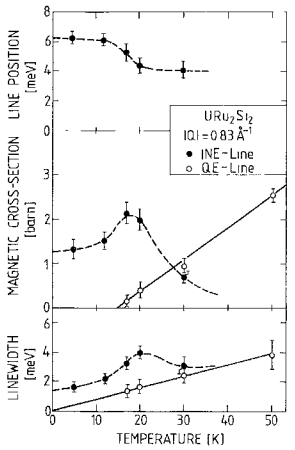

Fig. 68. Position, intensity and linewidth as function of temperature for the quasielastic and inelastic line in URu_2Si_2. (From Holland-Moritz et al. 1987b.)

Fig. 67. Background corrected inelastic neutron scattering spectra of URu_2Si_2 as function of temperature obtained with $E_i \approx 12.5$ meV. The hatched area is due to the nuclear incoherent elastic scattering. (From Holland-Moritz et al. 1987b.)

and does not show distinct CF excitations. We will discuss the experiments done on polycrystals in this section. There are also intensive investigations on single crystals which are recently reviewed by Broholm et al. (1991), and will be covered in chapter 131 (Aeppli and Broholm 1994). We stress that measurements on polycrystals give information about averaged Q behavior only, and much detailed information is missed. On the other hand, such experiments can give important hints for more detailed investigations on single crystals. Measurements with single crystals may also miss some important details if only a part of the Brillouin zone is examined.

There is some analogy to the behavior of intermediate-valent lanthanide systems discussed below. As URu_2Si_2 has a tetragonal crystallographic structure, a comparison to the intermediate-valent $YbPd_2Si_2$ (see sect. 5) and to the heavy-fermion compound $CeRu_2Si_2$ is probably most suitable. The first investigations by Walter et al. (1986b) with $E_i = 50$ meV reported a clear change from a quasielastic feature above $T = 50$ K to an asymmetric gap-like excitation at about 8 meV. A complete "gap" could not be confirmed by further experiments with $E_i = 12.5$ meV by Holland-Moritz et al. (1987b); however, the change in the shape of the magnetic response as a function of temperature is confirmed and shown in fig. 67. Although these data are averaged over Q, anomalies are observable at the Néel temperature for almost all the parameters as shown in fig. 68. The quasielastic line vanishes close to the Néel temperature, above which its width increases linearly with temperature. The linewidths of 5.6 and 6.7 meV given from experiments with $E_i = 3.1$ meV by Walter et al. (1986b) at 50 and 120 K, respectively, are in rough agreement with the new results. The effect of the magnetic order on the dynamic susceptibility (neutron inelastic response) is, of course, better visible in experiments on single crystals (Broholm et al. 1991), but there is no disagreement between the results on polycrystalline and single-crystal samples.

Holland-Moritz et al. (1989b) also performed a constant-$|\boldsymbol{Q}|$ (magnitude of $\boldsymbol{Q}$) analysis by rearrangement of the constant-angle spectra into constant-$|\boldsymbol{Q}|$ spectra. One remarkable result is shown in fig. 69. For $|\boldsymbol{Q}|$ values corresponding to the first Brillouin zone, the intensity as a function of Q still contains significant structure that could be related to certain points in the Brillouin zone. They found that the N-point (1/2,0,1/2) seems to be the most important concerning magnetic correlations. In the magnetic ordered phase ($T = 5$ K) the absolute maximum in the intensity was found at $|\boldsymbol{Q}| \approx 0.85$ Å corresponding to the N-point (fig. 69a). Describing the $|\boldsymbol{Q}|$ dependence in the paramagnetic phase by a damped mode, the periodicity is described by the lattice vector $2 \cdot G_N$ where $[G_N = 0.5 \cdot G_{(1,0,1)}]$ (fig. 69b,c). Unfortunately, to date no results are reported for single crystals around the lattice point (1/2,0,1/2). Other less pronounced features found in the polycrystalline studies by Holland-Moritz et al. (1989b) are in agreement with the single-crystal study of Broholm et al. (1987a, 1991).

As usual, a comparison of the bulk susceptibility with the local susceptibility derived from the neutron inelastic scattering is useful, especially as for URu_2Si_2 bulk measurements on single crystals exist. This is shown in fig. 70; the neutron data on polycrystalline material correspond to an average value of the susceptibility, i.e., to the dashed line in fig. 69. Whereas the susceptibility measured in a field parallel to the ***a*** axis is low and nearly temperature independent, the one in a field parallel to the ***c*** axis is much larger, and exhibits a well-defined maximum at ~50 K. Below this temperature the inelastic structure occurs in the neutron data. Thus, as has been shown for the intermediate-valent lanthanides in sect. 5, the maximum in the static bulk susceptibility and the appearance of an inelastic response occur at roughly the same temperature. By adding the quasielastic and inelastic contributions the local susceptibility looks qualitatively like the ***c*** axis value of the bulk susceptibility. The magnetic response, as obtained by neutrons on a polycrystalline material, appears compatible with fluctuations in

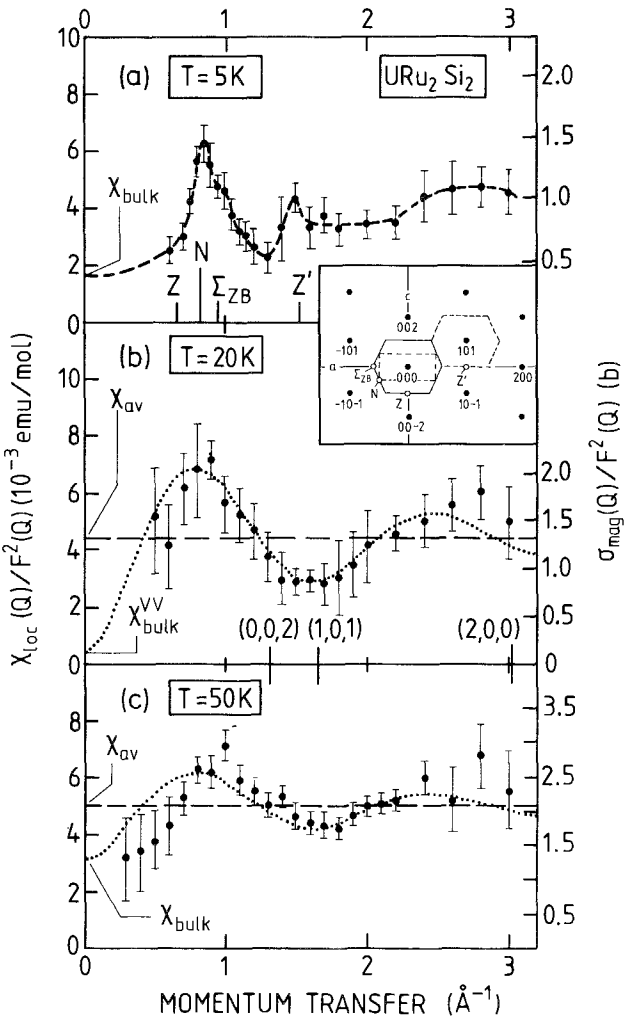

Fig. 69. The $|Q|$-dependent intensity of the main magnetic signal measured from a polycrystalline sample of URu_2Si_2 for three temperatures. The total cross section was obtained by integrating the spectra up to a cut-off energy of ~1.5 eV (see section 1.2). The inset gives the reciprocal lattice for the a–c plane and defines the Brillouin zone. The values of the bulk and neutron average susceptibility are marked on the ordinate axis. (From Holland-Moritz 1989b.)

the c direction. Assuming the fluctuations in the a–b plane are spread over a much larger energy scale, the experiments on polycrystals will be sensitive to only the c components of the fluctuations, so to make a comparison with the susceptibility we multiply the

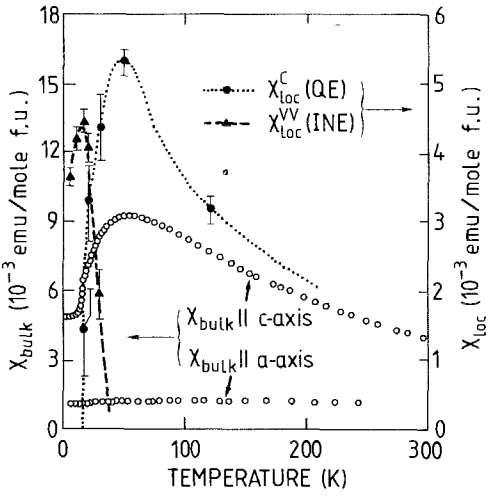

Fig. 70. Comparison of static susceptibility values obtained by neutron inelastic scattering with static bulk measurements in a field parallel to the *c* axis for URu_2Si. Assuming that the neutron data from a polycrystalline sample reflect just $\chi \| c$ the scale (right hand side) is multiplied by a factor of three. Moreover, the neutron data correspond to an average value, i.e., to the dashed line in Fig. 69. Due to antiferromagnetic correlations the susceptibility derived from the neutron experiments is greater than that derived from the bulk susceptibility. (From Holland-Moritz et al. 1989b.)

right-hand scale of fig. 70 by three. We see then that the local neutron susceptibility is somewhat larger than the bulk, which is in good accord with the idea of antiferromagnetic fluctuations as suggested in fig. 69. A magnetic signal related to the bulk susceptibility measured in a field parallel to the *a* axis cannot be detected unambiguously in the neutron experiments. However, the asymmetry reported by Walter et al. (1986b) may be an indication for a very broad inelastic magnetic response which is related to the temperature independent part of the bulk susceptibility in the *a–b* plane.

The inelastic line at about 6 meV cannot be explained by single-ion crystal field theory. From fig. 68 (extrapolation of dashed line in the middle part) we see that, in contrast to the single-ion crystal-field picture, the intensity of this inelastic excitation vanishes above 50 K, i.e., at temperatures above the maximum in the static susceptibility. Although the temperature where this maximum occurs is not in all cases identical with the ordering temperature, such a maximum is only observed in U systems that order magnetically. Therefore, an interpretation of the inelastic excitation as paramagnons (short-range ordering above the Néel point) is more likely than the crystal-field interpretation. In fact, the strong dispersion effects observed by single-crystal investigations (see chapter 131) would fit into this picture. More recent papers addressing the CF states (Santini and Amoretti 1994) and the possibility of quadrupolar (or other) types of ordering (Walker et al. 1993) show that the essential physics of this material at low temperature is still open.

Small amounts of Re substituted for Ru into URu_2Si_2 rapidly suppress superconductivity and induce ferromagnetic interactions. Neutron studies by Torikachvili et al. (1992) on polycrystalline material were able to show ferromagnetic order in $U(Ru_{1.2}Re_{0.8})Si_2$ of $\sim 0.5\,\mu_B$, but could not draw any conclusions about the inelastic magnetic response.

Another U compound that shows superconductivity and magnetic order is **UPt_3**. Although with $\gamma = 450\,\mathrm{mJ\,mol^{-1}\,K^{-2}}$ it belongs to the "real" heavy-fermion systems, it is comparable to URu_2Si_2 in many of its physical properties. The static bulk susceptibility

exhibits a maximum at $T = 18$ K, but the U moments order only at the significantly lower temperature of 5 K. The ordered magnetic moment is ~$0.02\,\mu_B$ (Aeppli et al. 1988), comparable to that in URu_2Si_2. The bulk susceptibility depends strongly on the crystal direction (Frings et al. 1983). In contrast to URu_2Si_2, the susceptibility in the $\boldsymbol{a}$–$\boldsymbol{b}$ plane of this hexagonal system is the greatest and shows a maximum at ~20 K, whereas it is almost featureless and small for $\boldsymbol{H} \parallel \boldsymbol{c}$.

Inelastic scattering experiments with polarized neutrons were reported on polycrystals by Aeppli et al. (1985). In contrast to URu_2Si_2, they did not find any indications for a distinct inclastic excitation at low temperatures. They could explain their data with a single quasielastic Lorentzian line of 9 ± 2 meV width. The structureless magnetic response was confirmed by single-crystal measurements; however, the quasielastic width extracted from these data was only 5 ± 0.2 meV (Aeppli et al. 1987, Goldman et al. 1987). Moreover, the single-crystal data, which will be discussed in detail in chapter 131 (Aeppli and Broholm 1994), show distinct Q-dependent effects in the intensity. From that, and the comparison to the static bulk susceptibility, the authors explain the maximum in the susceptibility as an onset of antiferromagnetic correlations, which is quite analogous to URu_2Si_2. As the maximum in the susceptibility of UPt_3 is not as pronounced as in URu_2Si_2, no distinct inelastic excitation was observed in UPt_3. It is also worthwhile to note another feature that emerges from the single-crystal experiment. This is the observation of a low-energy response at the reciprocal lattice point $(\frac{1}{2},0,1)$. The measurements above and below the critical superconducting temperature do not show significant differences. The magnetic response represents a magnetic fluctuation energy of about 0.2 meV, which is not far from the pair breaking energy associated with superconductivity in UPt_3. Similar diffuse magnetic scattering was found also in the alloy $U(Pt_{0.95}Pd_{0.05})_3$ by Frings et al. (1987).

Next we will discuss **UCu_5** and **U_2Zn_{17}**, which exhibit specific heat γ values of 250 (Fisk et al. 1985) and 535 mJ/(mol U K^{-2}) (Ott et al. 1984), respectively. There is some controversy of the interpretation of the low-temperature specific heat data, from which the γ value is extracted. Gschneidner et al. (1990) claim that the value for U_2Zn_{17} may be as low as 50 mJ/(mol U K^2). Whatever the values of γ, the other properties of both systems are similar. The susceptibilities are low and show a maximum at about 17 K (Brodsky and Bridger 1973, Ott et al. 1984). UCu_5 as well as U_2Zn_{17} order magnetically at 15 and 9.7 K with rather small ordered moments of 0.9 (Murasik et al. 1974) and $0.8\,\mu_B$ (Cox et al. 1986), respectively. Thus, it is not surprising that in the only neutron inelastic scattering work on polycrystalline materials of these compounds a single broad quasielastic line is reported by Walter et al. (1987).

Figure 71 shows representative spectra of UCu_5 and U_2Zn_{17}. By comparing with high-angle data (high Q) Walter et al. (1987) extracted a broad quasielastic magnetic line for both compounds. For UCu_5 the width of this broad Lorentzian increases slightly from $\Gamma/2 = 8.2$ meV at $T = 50$ K to $\Gamma/2 = 9.8$ meV at $T = 10$ K, whereas for the same temperature range a decrease was found from 14.1 meV to 8.9 meV in U_2Zn_{17}. The derived magnetic scattering intensities are smaller by a factor of about three in UCu_5 than in U_2Zn_{17}, and they are in rather good agreement with the static bulk susceptibilities. A sharp magnetic excitation at low temperatures, similar to that of URu_2Si_2, can be

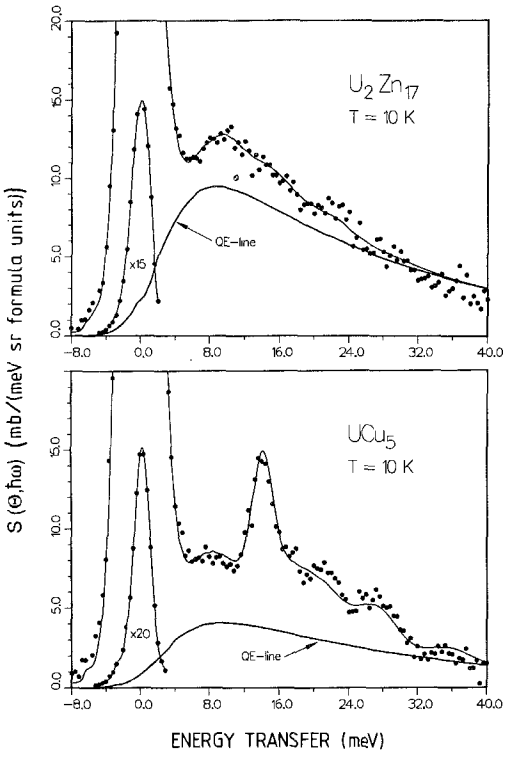

Fig. 71. Background corrected neutron inelastic scattering spectra of UCu_5 and U_2Zn_{17} measured with $E_i = 60$ meV. The sharp features arise from the phonons. (From Walter et al. 1987.)

excluded. However, a more detailed structure of the magnetic response, i.e., an additional broad inelastic excitation, cannot be excluded from the analysis of these polycrystalline data. Especially in UCu_5 the increase of the quasielastic linewidth may be an indication for inelastic character, as observed in 4f intermediate-valent materials (compare sect. 5). Moreover, in UCu_5, because of the large nuclear cross section of Cu, the phonon contribution dominates the magnetic scattering and may therefore conceal details in the energy structure of the magnetic response.

There is another interesting feature in the magnetic response of these polycrystalline samples, a low-energy quasielastic response of Gaussian character. This was found by experiments with cold neutrons, which have the best resolution. In fig. 72 we show the spectra of UCu_5, because the intensity of the Gaussian is larger than in U_2Zn_{17}. It has a maximum cross section of 0.3 barn at about 20 K, i.e., ~40% of the intensity of the broad Lorentzian. The maximum in the static bulk susceptibility also appears at this temperature. One cannot conclude from the present data whether the decrease in the intensity of the Gaussian line below 20 K is compensated by intensity centered at some finite energy. Unfortunately, there is no experiment with an incident neutron energy of about 12 meV, as is the case for URu_2Si_2, for example. The intensity of the Gaussian shows a strong dispersive behavior as shown in fig. 73. From the maximum at a $\boldsymbol{Q}$ value

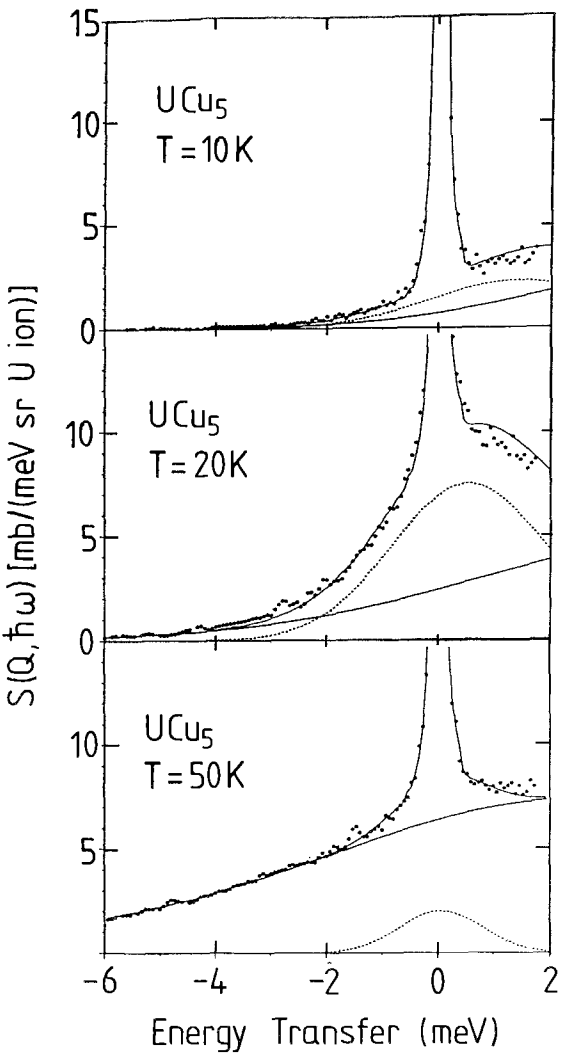

Fig. 72. Background corrected neutron inelastic scattering spectra of UCu_5 as function of temperature obtained with $E_i = 3.1$ meV. The dotted curves represent the Gaussian component of the magnetic scattering. (From Walter et al. 1987.)

corresponding to $(\frac{1}{2},\frac{1}{2},\frac{1}{2})$ Walter et al. (1987) suggest that antiferromagnetic correlations exist between the U moments along the [1,1,1] direction.

We also want to refer to the experiments on single crystals by Broholm et al. (1987b) on U_2Zn_{17}, which will be discussed in more detail in chapter 131 (Aeppli and Broholm 1994). Energy scans at the (1,0,2) point were analyzed as a function of temperature by a single quasielastic line. The linewidth (~10 meV) found at 25 K is in reasonable agreement with that given by Walter et al. (1987) on a polycrystalline sample. However, in contrast to the polycrystalline data, the width of the quasielastic line increases with decreasing temperature following the analysis of the single-crystal data by Broholm

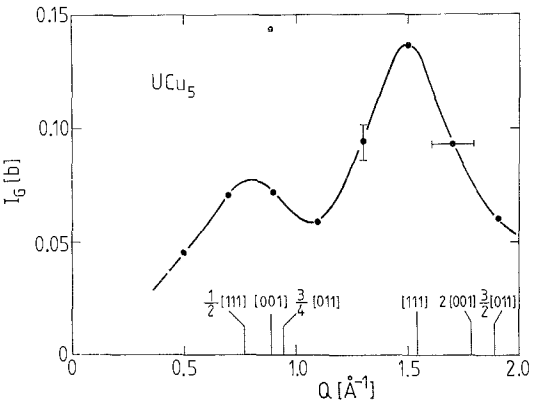

Fig. 73. The intensity of the Gaussian quasielastic line in UCu_5 as a function of momentum transfer. The Brillouin-zone boundaries along the main crystal axes of the fcc lattice are given in square brackets. (From Walter et al. 1987.)

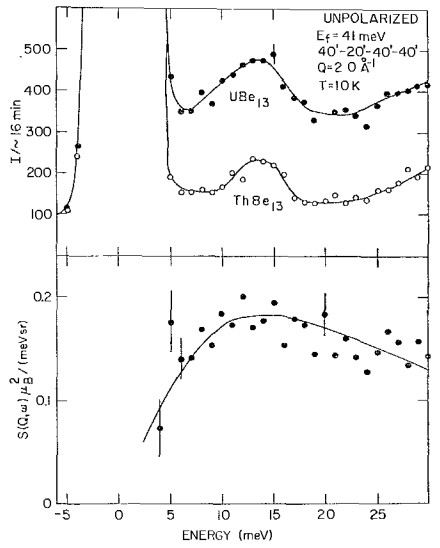

Fig. 74. Inelastic neutron scattering spectra of UBe_{13} and its reference compound $ThBe_{13}$ (upper frame). The lower frame shows the difference spectrum, i.e., the magnetic scattering response. (From Goldman et al. 1986.)

et al. (1987b). Especially below the Néel temperature the width increases to a value of about 24 meV and the intensity decreases sharply. However, it is also possible from the data presented by Broholm et al. (1987b) to propose that the response becomes partially inelastic ($\omega \approx 2$ meV) at $T = 2$ K. At low temperature it is always difficult to differentiate between a quasielastic and inelastic response because of the detailed-balance factor. These experiments do show, however, that there are important $\boldsymbol{Q}$-dependent effects in U_2Zn_{17}.

At the end of this section we describe the experiments on **UBe_{13}**. This compound has $\gamma \approx 1100\,\mathrm{mJ\,mol^{-1}K^{-2}}$, which implies approximately the same effective electron mass as in $CeCu_2Si_2$. It becomes superconducting at 0.9 K, but the U moments do not order, in contrast to the U systems discussed above. This is analogous to $CeCu_2Si_2$. There are two inelastic neutron scattering experiments on polycrystalline samples. One experiment is performed with unpolarized thermal neutrons by Goldman et al. (1986) and the other by Lander et al. (1992) with cold neutrons on a time-of-flight spectrometer with good energy resolution. Spectra obtained with thermal unpolarized neutrons at $T = 10$ K are shown for UBe_{13} and the reference compound $ThBe_{13}$ in the upper frame of fig. 74. The difference spectrum shown in the lower frame yields a quasielastic linewidth of 13 ± 2 meV. (The results of experiments performed with polarized neutrons are consistent with this interpretation of the unpolarized thermal neutron results, but the resolution and intensity were too poor to extract any additional information.) The scattered intensity gives only 0.7 ± 0.2 of the value expected from the static bulk susceptibility.

Because of the high γ value it has always been assumed that a low-energy response should exist also in UBe_{13} (for Ce compounds there is a rough proportionality between Γ and γ^{-1}). Goldman et al. (1986) were unable to find such a response, but this was found by Lander et al. (1992) using cold neutrons. The quasielastic linewidth $\Gamma/2 \approx 1.5$ meV and the intensity gave 0.6 ± 0.1 of the expected total magnetic scattering. Surprisingly, over the temperature range 0.5 K (i.e., $T < T_c$) to ~40 K, the width of this low-energy response appears independent of temperature, but its intensity scales with the bulk susceptibility. No detailed experiments have yet been reported on single crystals of UBe_{13}.

6.3. *Conclusions*

The lanthanide systems discussed in this section show a much stronger increase of the quasielastic linewidth with temperature than the usual Korringa-like behavior found in compounds with stable lanthanides. To date, all the Ce systems that show a strong linear increase order ferromagnetically except $CeRu_2Si_2$. The majority of Ce systems show a dependence of the linewidth on temperature which resembles a power law $\sim T^{1/2}$. Nonlinearity in $\Gamma(T)$ is always associated with the observation of crystal-field excitations. Such CF levels were assumed, but not yet detected, in $CeRu_2Si_2$ with its rather large electron mass. The general temperature dependence of the linewidth in Ce compounds is probably related more to the population of excited crystal field levels than to any heavy-fermion character, although there is insufficient evidence to make a clear decision at this stage. All uranium systems discussed show larger linewidths at low temperatures than the lanthanide systems; however, the larger hybridization of 5f electrons does not necessarily suppress magnetic ordering.

7. Final remarks

The study of unstable f electron systems naturally consists of two separate categories. The first addresses the dynamics of the *local* moments. As these phenomena usually involve little dispersion (i.e., there is little dependence on the reduced wavevector $\boldsymbol{q}$ in the Brillouin zone), polycrystalline samples can be used. Sample masses range from about 20 to 60 g, even more being required for experiments on intermultiplet transitions as discussed in sect. 3. The second category addresses *collective* (or cooperative) phenomena such as phonons and magnons. Although some aspects of collective phenomena may be observed with experiments on polycrystalline samples (e.g., URu_2Si_2), unambiguous characterization requires the use of single crystals. For inelastic scattering with present-day neutron fluxes, crystal volumes must approach 1 cm^3 – a most severe requirement for some of the complex materials discussed in the present article. A complete understanding of the magnetic response function requires the characterization of both the local and cooperative effects, and it is not surprising that few studies are complete in this respect. Nevertheless, it is worth emphasizing the uniqueness of this information from neutron

scattering. No other technique can simultaneously probe the energy and wavevector dependence of the elementary excitations.

In addition to the stringent requirements of large samples, we have mentioned the experimental limitations, and it is worth repeating them here before continuing our summary. The local moment behavior is best investigated with polycrystalline samples. Time-of-flight spectrometers then allow a good averaging over q and the experiments are sensitive to small effects, provided adequate separation of the vibronic and magnetic effects can be made. Methods for the separation of phonons and magnetic scattering are frequently controversial. The only unique method is with polarization analysis. However, the penalty paid in intensity (and resolution) is considerable. We have given examples in $CeCu_2Si_2$, $CePd_3$ and UBe_{13} where polarization experiments have been undertaken. In all these cases, in which attempts were made to characterize broad featureless magnetic responses, the experiments with polarization analysis have not added appreciably to our knowledge. On the other hand, in systems such as $CeAl_2$ and NpO_2, in which reasonably sharp excitations are present, the polarization analysis technique has unambiguously answered the questions raised by the use of unpolarized neutrons. A new generation of polarizers and/or analyzers, or a considerable increase in available neutron flux, will be needed before this situation changes.

Certainly the clearest conclusion from the examples of this chapter is the total absence of sharp features in the inelastic response function of anomalous lanthanide and metallic actinide materials. This contrasts strongly with the sharp dispersionless crystal-field excitations observed in most lanthanide compounds, in which the exchange interactions are weak (fig. 2), and with the sharp spin-wave excitations found in systems with strong exchange interactions. In many of the early studies with neutron inelastic scattering, for example of the heavy lanthanides or transition metals and their compounds, the width of the excitations was never an issue. It was almost always limited by the instrumental resolution, although it should be stressed that this resolution is relatively poor compared to that obtained by optical techniques. However, the situation is completely different in the materials discussed in this chapter. Now the dominant factor is often the width; indeed in some materials the width of the over-damped response function is almost the only remaining parameter with which to characterize the response.

The physical reason for this importance of the width is the interaction between the f and conduction-electron states. Ideal single-ion magnetic behavior can be observed only in stable lanthanides, whereas the compounds with unstable 4f moments and the actinides show strong interactions between the f and conduction-electron states. Whether this leads to dispersion in the Brillouin zone depends on the nature of the interaction. If it is stochastic, as it is in most valence-fluctuating systems (sect. 5) then little dispersion is expected, and experiments on polycrystalline samples are adequate. However, as correlations develop in systems such as heavy fermions (sect. 6) dispersion can be anticipated in any of the three parameters: position, intensity, and linewidth. In these circumstances the averaging process attempting to use a single-ion picture is a relatively poor approximation, and experiments on single crystals, as well as a complete study of

the dispersive nature of the response function becomes essential for an understanding of the physics.

In sect. 2 we have discussed some localized 5f electron systems, particularly the oxides UO_2, NpO_2 and PuO_2. Considerable progress has been made in the last decade by using the epithermal neutrons from spallation sources. The crystal-field potentials V_4 and V_6 have been established and shown to be ~50% of the predictions based on point-charge estimates. This shows that even in the insulating oxides the screening of the effective charges of the surrounding oxygens is important. One of the most interesting aspects of the oxides is the presence of subtle lattice distortions caused by the quadrupole interactions. In UO_2 the history of these effects goes back to early work by Allen (1968) and the neutron inelastic scattering experiments by Cowley and Dolling (1968), followed by the direct observation of the internal lattice distortion by Faber and Lander (1976). The neutron experiments on NpO_2 by Amoretti et al. (1992) have, finally, shown some evidence for the breaking of the symmetry of the Γ_8 ground state, but the nature of the microscopic distortion in NpO_2 still remains a mystery. These quadrupole effects may well be present in many other f electron systems. For example, there has been speculation that they drive the magnetic ordering in the heavy-fermion systems, and recently a clearer picture of the quadrupole distortions in the localized system UPd_3 has emerged from neutron experiments of McEwen et al. (1993). In UPd_3 a moment of $< 0.1\,\mu_B$ is induced by the quadrupole effects. This has nothing to do with heavy-fermion behavior, and, as remarked by McEwen et al., one must be careful in associating the presence of small magnetic moments with a heavy-fermion ground state.

In sect. 3 we have discussed the observation of intermultiplet transitions (IMT). Once again this is an area to which spallation neutron sources, and the ISIS source in the UK in particular, have made major contributions. The first measurements were made on SmS (Shapiro et al. 1975) at a reactor source. The transitions $J=0$ to $J=1$ are at ~30 meV, so are relatively easy to observe. As discussed at length by Osborn et al. (1991) the measurements of both spin–orbit and Coulomb transitions within the general framework of the IMT's can give a complete picture of the Slater integrals and Coulomb parameters in the solid, so that the potential for much new information is certainly present in the IMT's. That this new field has been relatively slow to develop is in part due to the fact that the instruments at the ISIS source are the only ones capable of doing this work (none of the other spallation sources in the world have sufficient intensity), and in part due to lack of theoretical models for hybridized systems. Thus, the transitions in integral valence systems seem to be relatively narrow, but it is difficult to observe them in systems with intermediate valence. Initial attempts led to the conclusion that none could be observed in SmB_6, for example, but recently Alekseev and collaborators (Alekseev et al. 1993a) have been able to identify a wide transition in this material. The situation with uranium systems is equally fluid at this time. It is clear that the U^{4+} (f^2) state is relatively easy to identify, viz. the measurements in UPd_3, UPb_3 (McEwen 1992, private communication), and possibly UPt_3. We say "possibly" UPt_3, because the IMT data appear to indicate a U^{4+} state, and yet no intramultiplet crystal-field levels are observed at low energy. Attempts

to observe the IMT for the U^{3+} state in USb failed, but will presumably succeed in the future as the intensity of ISIS improves and we obtain more experience at working at these high values of energy transfer (> 500 meV in this case). It is unfortunate that the high multiphonon background generated by light elements makes it experimentally impractical to examine materials such as UO_2, UCl_4 and UCl_3, in which the $\underline{f}$ occupation is beyond doubt.

In sect. 4 we have discussed materials that order magnetically and yet are of the anomalous kind. The section focuses almost exclusively on materials with the simple NaCl cubic fcc crystal structure. In the lanthanides this includes compounds with Ce and Yb; in the actinides it includes compounds with U and one example of a heavier element – PuSb. The underlying theme of these materials is the strength of the hybridization between the $\underline{f}$ and conduction electrons. This is the smallest in the lanthanide pnictides, and in these the excitations are well defined. The interaction is stronger in the uranium pnictides, but the stronger exchange in the actinides as compared to the lanthanides ensures that the excitations are well defined so long as the hybridization does not dominate. The hybridization strength dominates in materials such as UN with a small U–U spacing, and in which no well-defined excitations exist. It is this interplay that is at the base of the so-called "Hill criterion", in which ordering occurs in actinide materials only when the actinide atoms are well separated. Major progress has been made since the review of this subject by Buyers and Holden (1985) in showing that the hybridization is *anisotropic* and that this anisotropy is similar in form to that observed in the critical fluctuations of the magnetization near the ordering temperatures. Progress in understanding this in terms of the hybridization between the $\underline{f}$ and conduction electrons has been made by Cooper and his colleagues (Cooper et al. 1985, 1992, Hu et al. 1989). The hybridization is stronger in the chalcogenides than in the pnictides in both the lanthanide and actinide compounds. Inelastic scattering experiments have only just been reported on Ce chalcogenides (Dönni et al. 1992a,b, 1993) and the multidomain nature of the antiferromagnetic structures makes conclusions difficult to draw. The experiments on single crystals of ^{242}PuSb represent a tour de force and show the importance of extending the work to a few transuranium systems. The hybridization decreases as we move across the actinide period, but the nearly half-filled shell of the $Pu^{3+}(5\underline{f}^5)$ configuration brings some additional complications. The Pu chalcogenides are a most interesting series, in which intermediate valence (Wachter et al. 1991) may be present, and we can hope that by the time of the next review (!) some neutron inelastic scattering experiments will be performed on them.

In sect. 5 we discuss a large number of paramagnetic systems that exhibit no sharp crystal-field excitations. For the most part the materials are of intermediate valence (IV). Most of the experiments have been performed on polycrystalline materials. As discussed above, for the most part the interactions that lead to intermediate behavior are stochastic in nature so that little dispersion is anticipated – see also below. A good test for this is whether there is agreement between the neutron magnetic intensities (local susceptibility) and the bulk susceptibility. There is now considerable evidence that the magnetic response of these systems is inelastic at low temperatures. The energy of the peak position is

larger than the width of the quasielastic line observed at high temperatures, but the linewidth is still considerable. The appearance of the inelastic response is clearly related to the maximum in the static magnetic susceptibility at T_{max}. Well above T_{max} the susceptibility is suppressed, but *almost* Curie-like, and the magnetic response consists of a broad quasielastic line. Around and below T_{max} the bulk susceptibility deviates strongly from a Curie-like behavior, and the magnetic response becomes inelastic (i.e., it is no longer centered at $\omega = 0$). The position of the peak scales roughly with T_{max}. In many systems the response may have both an inelastic and a quasielastic part. Since both are broad, it is almost impossible to make a complete separation. Examples are $CePd_3$, $EuNi_2P_2$ and $YbAgCu_4$. However, the example of $EuNi_2P_2$, in which Eu has a $L = 0$ ground state so that no crystal fields are present, shows that the crystal field has much less influence on the low-temperature magnetic response than the f-conduction electron hybridization. In the actinides, for example USn_3 and UAl_2, such an inelastic response has not yet been reported, although in USn_3 there is some evidence for a low-energy inelastic response from the work of Loewenhaupt and Loong (1990). More complete neutron experiments, especially at low-energy transfer in UAl_2, would seem to be worthwhile. UAl_2 has a plateau in the susceptibility, or a $T_{max} \approx 50$ K, so one would expect an inelastic contribution in analogy with the lanthanide systems.

Dispersive effects indicating collective correlations have been difficult to find in intermediate-valence materials. TmSe, which is one of the few systems to order magnetically, does exhibit some dispersion, and there has been speculation that the excitation represents interband transitions. A strong increase in the response as $\boldsymbol{Q} \rightarrow 0$ was also observed in $EuNi_2P_2$. In this respect we note the controversial situation with respect to $CePd_3$. Since this is a canonical IV system, we would like to encourage the resolution of the experimental differences between those working on poly- and single-crystalline samples.

Many features of the data may be conveniently discussed in terms of theoretical descriptions based on the Fermi-liquid model. We shall start by considering the shape of the low-temperature response, for which the analytic function given by Kuramoto and Müller-Hartmann (1985) is useful. This is followed by a discussion of some more general aspects arising from a consideration of the Wilson ratio (Wilson 1975, Lustfeld and Bringer 1978).

As pointed out in sect. 2 the analytic function includes two parameters, the characteristic temperature T_K and the parameter α. The appearance of an inelastic feature at low temperature is associated with the "Kondo resonance" in the energy spectrum of the material, so that the characteristic temperature T_K is often called the Kondo temperature, even in the extreme case of intermediate valency. In principle, this temperature has the same meaning as the fluctuation temperature introduced by Maple and Wohlleben (1971), and is given by $T_K \equiv T_f \approx \Delta/k_B$, where Δ is the position of the inelastic line given in table 2. The parameter α is related to the valence and the degeneracy of the magnetic ground state. If a valence is determined from other measurements, e.g., the position of the L_{III} edge, then a degeneracy can be assigned from the value of α. Assuming a value of n_f, the fractional occupancy of the magnetic valence state, the results for N_f (the

Table 6
Values for the degeneracy of the ground state, N_f, and Kondo temperature, T_K, for several materials as obtained by fitting the low-temperature response to the analytic function of Kuramoto and Müller-Hartmann, and using a fractional occupation n_f determined from other measurements

Material	n_f	N_f	T_K	Reference
$EuNi_2P_2$	0.5	8(3)	85(10)	Holland-Moritz et al. (1989a)
$YbPd_2Si_2$	0.82	5(1)	56(5)	Weber et al. (1989b)
$YbAgCu_4$	1.0	7(1)	96(8)	Severing et al. (1990a)
$YbAl_2$	0.9	9(1)	1800(60)	Murani et al. (1992)
	0.4	4(1)		Bauchspiess et al. (1981) [valence]
$CeSn_{2.5}In_{0.5}$	1.0	~5	16(1)	Murani (1987a)
$CeSn_{2.25}In_{0.75}$	1.0	~5	12(1)	Murani (1987a)
$CeSn_2In$	1.0	~5	9(1)	Murani (1987a)
$CeRu_2Si_2$	1.0	4(1)	17(2)	Severing et al. (1989a)
$CeCu_2Si_2$	1.0	~6	8(1)	Holland-Moritz et al. (1989c)

ground-state degeneracy) and T_K (Kondo temperature) obtained from fitting the low-temperature neutron response to the analytic form are given in table 6 for a series of compounds. In particular, N_f has a large uncertainty because the experimentally observed low-temperature response is not well described by the analytic expression. For example, the fits for $EuNi_2P_2$ are unsatisfactory at low Q, so the value of N_f is uncertain. The expected value of 8 for the $J=7/2$ Hund's rule ground state is as good as any other, but degeneracies of less than 4 can be excluded. $CeSn_{3-x}In_x$ shows the full degeneracy of 6 so that crystal-field effects would appear to be negligible. This result is in agreement with the form factor measurements on $CeSn_3$ by Stassis et al. (1979c) and on $CeSn_2In$ by Benoit et al. (1985), which, in contrast to the results for $CeIn_3$ by Boucherle et al. (1983), do not show any anisotropy arising from crystal-field effects. Note that an assumption of a valence of 2.9 for $YbAl_2$ by Murani et al. (1992) is in contradiction to the value of 2.4 found by Bauchspiess et al. (1981). At the other extreme are systems such as $YbPd_2Si_2$ and $CeRu_2Si_2$, in which N_f deviates strongly from the full degeneracy. In both systems CF effects cannot be excluded from playing a major role in the inelastic magnetic response. In $CeCu_2Si_2$, an inelastic response appears below 1 K (Holland-Moritz et al. 1989c) but these features are poorly defined, so that the value of N_f is uncertain.

The analytic function cannot be applied to Tm because both ground states are magnetic. Although the model of Kuramoto (1986) does not predict an inelastic line for Tm compounds, such a signal is predicted by other single-ion model calculations, e.g., Mazzaferro et al. (1981) or Schlottmann (1982, 1984a,b). The model of Fedro and Sinha (1981), which is based on intersite correlations rather than single-ion effects, was developed specifically for the case of Tm compounds, especially TmSe (Shapiro and Grier 1982) and predicts a gap in the excitation spectrum arising from the intersite correlations at low temperature. On the other hand, the finding of a similar gap in the

dilute Tm systems (Holland-Moritz 1983) implies that cooperative effects cannot be solely responsible for such an excitation.

It is useful at this stage to discuss the relation between an observed "gap" in the excitation spectrum and the analytic form. The latter becomes more asymmetric the larger N_f becomes, i.e., the closer α is to zero. This means that the function has more of an apparent "gap" with increasing degeneracy of the ground state. Nevertheless, a significant amount of intensity remains at zero energy transfer – there is no real "gap" in terms of the theory. This is supported by experimental results on $EuNi_2P_2$ (Holland-Moritz et al. 1989a), as a quasielastic component remains as T tends to 0 K (see fig. 28). Following the theoretical single-ion picture, the intensity at $E=0$ decreases approximately as $1/T_K$, so that the amount of quasielastic scattering should decrease for systems with larger T_K's. Thus, $YbAl_2$ with $T_K \approx 1800$ K clearly should have little quasielastic scattering at $E=0$. A smooth transition occurs between the two extremes, a single-ion Kondo resonance and a gap-like band behavior, and this is probably responsible for some of the controversy in the literature. For example, $CeSn_3$ has been interpreted both with (Murani 1983b) and without (Capellman et al. 1985) a quasielastic response at low temperature. The cleanest "gap" behavior is found for $Ce_3Bi_4Pt_3$ by Severing et al. (1991) and CeNiSn by Mason et al. (1992). However, these systems are semiconductors and are not immediately comparable to the intermetallics discussed above.

In concluding the discussion about the low-temperature magnetic response, we note that the analytic function of Kuramoto and Müller-Hartmann is the first one derived theoretically for unstable-valence materials in which there is a strong interaction between the f and conduction electrons. Although this function describes many of the important features, it still has some inadequacies. In particular, because it is based on a single-ion picture, it cannot describe the Q dependence (apart from the local form factor) so neglects intersite correlations. These are clearly important in many cases, for example TmSe, $EuNi_2P_2$ and $CeRu_2Si_2$ (Regnault et al. 1988c). Moreover, the meaning of "degeneracy" as derived for the ground state in the analytical function is not well understood. A single-ion picture is necessary, but not sufficient, to describe all the features, and we hope that efforts will be made to include cooperative effects in the theory.

Turning to the evaluation of the so-called Wilson ratio, Fermi-liquid theory can be used to calculate the Sommerfeld constant γ and the low-temperature magnetic susceptibility $\chi^{st}(Q=0, T=0)$ (see eqs. 5, 12) as shown by Ramakrishnan and Sur (1982) and Newns et al. (1982):

$$\gamma = \frac{\pi^2 k_B^2}{3T_K} n_f, \qquad \chi^{st}(0) = \frac{\mu_{eff}^2}{3T_K} n_f.$$

Here $\mu_{eff} = [J(J+1)]^{1/2} g_J \mu_B$ is the effective moment of the magnetic ion. It follows from the above that the Wilson ratio is defined as

$$\left(\frac{\pi k_B}{\mu_{eff}}\right)^2 \frac{\chi^{st}(0)}{\gamma} = 1.$$

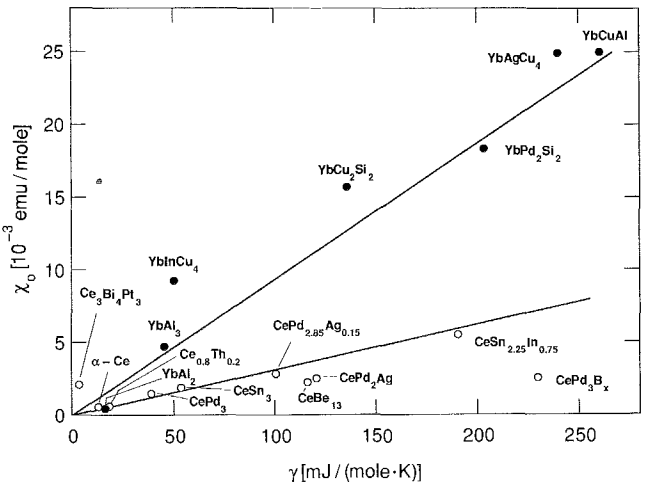

Fig. 75. The Sommerfeld constant γ vs. the static bulk susceptibility $\chi(T=0)$. The solid and open circles represent Yb and Ce compounds, respectively (values from tables 2 and 4).

Other derivations yield a correction term roughly equal to the inverse degeneracy $1/N_f$ so that the right hand side is $1 + 1/N_f$, which would mean that the Wilson ratio should always be equal to or larger than unity. We will now consider the behavior of intermediate-valent systems with respect to this ratio. Furthermore, we will show a relationship between the excitation energy Δ and the values of γ and $\chi^{st}(0)$. Using the values given in tables 2 and 4, $\chi^{st}(0)$ is plotted versus γ in fig. 75. The two straight lines are defined by the Wilson ratio equal to unity for Ce^{3+} and Yb^{3+}, respectively. There is a reasonable agreement, except that the data lie both below and above the line, which is not expected on the basis of the possible theoretical corrections to the Wilson ratio described above. Materials with large Wilson ratios are $Ce_3Bi_4Pt_3$ and $YbInCu_4$. Both behave exceptionally in other senses as well; the Ce system is semiconducting with a gap in the excitation spectrum, and the Yb compound is the only known intermetallic Yb compound that exhibits a valence transition as a function of temperature.

Further systematics are shown in fig. 76. In the upper frame $\mu_{eff}/\chi^{st}(0)$ and in the lower frame $1/\gamma$ are plotted as a function of the low-temperature excitation energy Δ. For the upper frame the tendency of a linear increase is observable, but there is considerable scatter in the data, with the largest deviations for α-Ce and $YbAl_2$. On the other hand, the lower frame shows a good correlation, except for $Ce_3Bi_4Pt_3$ ($1/\gamma \approx 303$, see arrow). In this case, the material is a semiconductor so that the Sommerfeld constant γ is naturally a different average over the electronic properties than those in intermetallic intermediate-valence compounds. Examination of fig. 76 shows that the position of the low-temperature peak correlates better with γ than with the low-temperature magnetic susceptibility. Note that the highest excitation energy given in table 2 was used for $YbAl_3$, $YbPd_2Si_2$ and $YbCu_2Si_2$. In the inset of fig. 76 we show, for comparison, the relationship between the quasielastic linewidth and the inverse of the Sommerfeld coefficient for the cerium

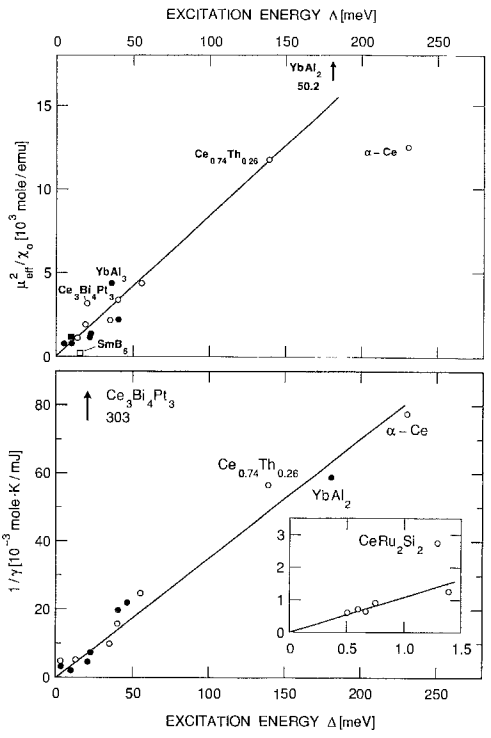

Fig. 76. The upper frame shows $\mu_{\rm eff}/\chi(T=0)$ versus the excitation energy Δ observed in the magnetic response at low temperatures (values from table 2). The lower frame presents the same dependence for $1/\gamma$.

heavy-fermion systems. All Ce samples, except $CeRu_2Si_2$, follow a good linear behavior, however the slope is about three times greater than for the IV compounds shown in the main part of fig. 76. In analogy with $YbCu_2Si_2$ and $YbPd_2Si_2$, there may also be a response in $CeRu_2Si_2$ at even higher energy that is, as yet, undetected. In the uranium heavy-fermion systems there is increasing evidence that two components exist, see Aeppli et al. (1988), Holland-Moritz et al. (1989b), Lander et al. (1992), and Aeppli and Broholm (1994, this volume), so that no simple relationship between a single quasielastic linewidth and γ is found.

We have ended this review with heavy-fermion systems. In fact, in terms of their hybridization, they lie intermediate between the materials discussed in sect. 4, and those discussed in sect. 5. What is extraordinary about the heavy-fermion compounds, and has been responsible for the great interest in them, has been the formation of a correlated state at low temperature. That the superconductivity appearing in some of these systems is intimately connected, if not driven by, the magnetic interactions is beyond doubt, although a complete theory is still lacking. The heavy-fermion state involves *both* the localized-like f electrons and the conduction-electron states. For example, extremely large masses are seen in the de Haas–van Alphen experiments (Reinders et al. 1986, Taillefer and Lonzarich 1988), but these do not account for all the susceptibility; a large

component giving rise to antiferromagnetic corrclations is also present in most systems and can be observed directly with neutron inelastic scattering. Thus, collective effects are important in heavy fermions and have been observed in $CeRu_2Si_2$, $CeCu_6$, URu_2Si_2 and UPt_3. These are discussed in more detail in ch. 131 (Aeppli and Broholm 1994). Although the quasielastic linewidth strongly decreases with decreasing temperature, an inelastic magnetic response was found at low temperature in some systems, e.g., $CeRu_2Si_2$ below 20 K. This is again in agreement with the idea that an inelastic feature develops when the susceptibility has a maximum, which in $CeCu_2Si_2$ occurs at about 10 K. We may remark here that the presence of broad crystal-field excitations in Ce heavy-fermion systems, e.g. $CeCu_2Si_2$, shows that the hybridization in this system is evidently *just* enough to form the heavy-fermion state at low temperature. In retrospect it is perhaps surprising that this was indeed the first such system discovered! It is clear from this section that neutron inelastic scattering continues to play an important role in the characterization of the heavy-fermion state, and that single crystals are important so that the full $\boldsymbol{q}$-dependence of the magnetic response can be established.

We end this summary, as we began, with a reminder of the limitations of the technique of neutron inelastic scattering because of the large samples required. By the standards of most techniques in solid-state research *enormous* samples, often of single-crystal form, are required. The fact that so much progress has been made is a testament to the unique information obtained from the technique – but think of the opportunities with new more powerful sources and polarization devices. That remains a challenge for the future!

Acknowledgments

We have benefited greatly from fruitful collaborations with many colleagues over the years. In particular, we thank Karl Gschneidner, Michael Loewenhaupt, Chun Loong, Amir Murani, Ray Osborn, Andrea Severing, Steve Shapiro and Ulrich Walter for helpful comments on the manuscript. The responsibility for errors of interpretation rests, of course, with the authors. GHL thanks the Physics Dept., Brookhaven National Laboratory, for a guest appointment, during which some of this was written. The help of Erika Lander in typing the manuscript is appreciated.

References

Aarts, J., F.R. de Boer, P.F. de Châtel and A. Menovsky, 1985, Solid State Commun. **56**, 623.

Aeppli, G., and C. Broholm, 1994, ch. 131, this volume.

Aeppli, G., E. Bucher and G. Shirane, 1985, Phys. Rev. B **32**, 7579.

Aeppli, G., H. Yoshizawa, Y. Endoh, E. Bucher, J. Hufnagl, Y. Onuki and T. Komatsubara, 1986, Phys. Rev. Lett. **57**, 122.

Aeppli, G., A.I. Goldman, G. Shirane, E. Bucher and M.-Ch. Lux-Steiner, 1987, Phys. Rev. Lett. **58**, 808.

Aeppli, G., E. Bucher, C. Broholm, J.K. Kjems, J. Baumann and J. Hufnagl, 1988, Phys. Rev. Lett. **60**, 615.

Alekseev, P.A., 1993, Physica B **186–188**, 365.

Alekseev, P.A., A.S. Ivanov, V.N. Iazukov, I.P. Sadikov and A. Severing, 1992, Physica B **180–181**, 281.

Alekseev, P.A., V.N. Lazukov, O. Osborn, B.D. Rainford, I.P. Sadikov, E.S. Konovalova and Y.B. Paderno, 1993a, Europhys. Lett. **23**, 347.

Alekseev, P.A., J.M. Mignot, J. Rossat-Mignod, V.N. Lazukov and I.P. Sadikov, 1993b, Physica B **186–188**, 384.

Aliev, F.G., N.B. Brandt, V.V. Moshchalkov, M.K. Zalyalyutdinov, R.V. Skolozdra, O.E. Koretskaya and G.I. Pik, 1988, JETP Lett. **48**, 536.

Allen, S.J., 1968, Phys. Rev. **166**, 530; **167**, 492.

Allenspach, P., J. Mesot, U. Staub, A. Furrer, H. Blank, H. Mutka, R. Osborn, A. Taylor, H. Maletta, M.J. Kramer, S.I. Yoo, E. Kaldis, J. Karpinski and S. Rusiecki, 1992, Physica B **180–181**, 389.

Amoretti, G., A. Blaise, R. Caciuffo, J.M. Fournier, M.T. Hutchings, R. Osborn and A. Taylor, 1989, Phys. Rev. B **40**, 1856.

Amoretti, G., A. Blaise, R. Caciuffo, D. Di Cola, J.M. Fournier, M.T. Hutchings, G.H. Lander, R. Osborn, A. Severing and A. Taylor, 1992, J. Phys.: Condens. Matter **4**, 3459.

Anders, F.B., 1995, in: Proc. Conf. on Strongly Correlated Electron Systems, Amsterdam, 1994, Physica B, to be published.

Andres, K., J.E. Graebner and H.R. Ott, 1975, Phys. Rev. Lett. **35**, 1779.

Asch, L., G.M. Kalvius, A. Kratzer, F.J. Litterst, F.N. Gygax, A. Schenk, K. Mattenberger and O. Vogt, 1990, Hyperfine Int. **64**, 453.

Ayache, C., J. Beille, E. Bonjour, R. Calemczuk, G. Creuzet, D. Gignoux, A. Najib, D. Schmitt, J. Voiron and M. Zerguine, 1987, J. Magn. & Magn. Mater. **63–64**, 329.

Bacon, G.E., 1975, Neutron Diffraction (Clarendon Press, Oxford).

Baer, Y., and W.D. Schneider, 1987, in: Handbook on the Physics and Chemistry of Rare Earths, Vol. 10, eds K.A. Gschneidner Jr and L. Eyring (North-Holland, Amsterdam) ch. 62, pp. 53–56.

Baer, Y., H.R. Ott and K. Andres, 1980, Solid State Commun. **36**, 387.

Balakrishnan, G., D.McK. Paul and N.R. Bernhoeft, 1989, Physica B **156–157**, 815.

Banerjea, A., and B.R. Cooper, 1986, Phys. Rev. B **34**, 1607.

Barbara, B., J.X. Boucherle, J.L. Buevoz, M.F. Rossignol and J. Schweizer, 1977, Solid State Commun. **24**, 481.

Barbara, B., M.F. Rossignol, J.X. Boucherle, J. Schweizer and J.L. Bouevoz, 1979, J. Appl. Phys. **50**, 2300.

Bauchspiess, K.R., 1982, Diplom thesis (University Cologne).

Bauchspiess, K.R., W. Boksch, E. Holland-Moritz, H. Launois, R. Pott and D. Wohlleben, 1981, in: Valence Fluctuations in Solids, eds L.M. Falicov, W. Hanke and M.B. Maple (North-Holland, New York) p. 417.

Becker, K.W., P. Fulde and J. Keller, 1977, Z. Phys. B **28**, 9.

Bennemann, K.H., and M. Avignon, 1979, Solid State Commun. **31**, 645.

Benoit, A., J.X. Boucherle, J. Flouquet, J. Sakurai and J. Schweizer, 1985, J. Magn. & Magn. Mater. **47–48**, 149.

Besnus, M.J., J.P. Kappler and A. Meyer, 1983, J. Phys. C **13**, 597.

Besnus, M.J., J.P. Kappler, P. Lehmann and A. Meyer, 1985, Solid State Commun. **55**, 779.

Bickers, N.E., D.L. Cox and J.W. Wilkins, 1987, Phys. Rev. B **36**, 2036.

Bilz, H., G. Güntherodt, W. Kleppmann and W. Kress, 1979, Phys. Rev. Lett. **43**, 1998.

Birgeneau, R.J., 1972, J. Phys. Chem. Solids **33**, 59.

Birgeneau, R.J., E. Bucher, J.P. Maita, L. Passell and K.C. Turberfield, 1973, Phys. Rev. B **8**, 5345.

Bjerrum-Møller, H., S.M. Shapiro and R.J. Birgeneau, 1977, Phys. Rev. Lett. **39**, 1021.

Blanco, J.A., J.C. Gomez Sal, J. Fernandez Rodrigez, J. Sandonis and J.M. Barandiaran, 1992, Physica B **180–181**, 217.

Blumenröder, S., H. Brenten, E. Zirngiebl, R. Mock, G. Güntherodt, J.D. Thompson, Z. Fisk and J. Naegele, 1988, J. Magn. & Magn. Mater. **76–77**, 331.

Boucherle, J.X., J. Flouquet, Y. Lassailly, J. Palleau and J. Schweizer, 1983, J. Magn. & Magn. Mater. **31–34**, 409.

Brandt, O.G., and C.T. Walker, 1968, Phys. Rev. **170**, 528.

Bredl, C.D., 1987, J. Magn. & Magn. Mater. **63–64**, 355.

Brodsky, M.B., and N.J. Bridger, 1973, AIP Conf. Proc. **18**, 357.

Broholm, C., J.K. Kjems, W.J.L. Buyers, P.T. Matthews, T.T.M. Palstra, A.A. Menovsky and J.A. Mydosh, 1987a, Phys. Rev. Lett. **58**, 1467.

Broholm, C., J.K. Kjems, G. Aeppli, Z. Fisk, J.L. Smith and H.R. Ott, 1987b, Phys. Rev. Lett. **58**, 917.

Broholm, C., H. Lin, P.T. Matthews, T.E. Mason, W.J.L. Buyers, M.F. Collins, A.A. Menovsky, J.A.

Mydosh and J.K. Kjems, 1991, Phys. Rev. B **43**, 12809.

Burlet, P., S. Quezel, J. Rossat-Mignod, J.C. Spirlet, J. Rebizant, W. Mueller and O. Vogt, 1984, Phys. Rev. B **30**, 6660.

Burlet, P., J. Rossat-Mignod, S. Quezel, O. Vogt, J.C. Spirlet and J. Rebizant, 1986, J. Less-Common Met. **121**, 121.

Burlet, P., J.M. Fournier, E. Pleska, S. Quezel, J. Rossat-Mignod, J.C. Spirlet, J. Rebizant and O. Vogt, 1988, J. Phys. **49**, C8–469.

Buschow, K.H.J., and H.J. van Daal, 1972, AIP Conf. Proc. **5**, 1464.

Buyers, W.J.L., and T.M. Holden, 1985, in: Handbook on the Physics and Chemistry of the Actinides, Vol. 2, eds A.J. Freeman and G.H. Lander (North-Holland, Amsterdam) pp. 239–328.

Buyers, W.J.L., T.M. Holden, J.A. Jackman, A.F. Murray, P. de V. du Plessis and O. Vogt, 1983, J. Magn. & Magn. Mater. **31–34**, 229.

Caciuffo, R., G. Amoretti, A. Blaise, J.M. Fournier, M.T. Hutchings, G.H. Lander, R. Osborn, A. Severing and A.D. Taylor, 1992, Physica B **180–181**, 149.

Capellman, H., P.J. Brown, S.M. Johnson, K.R.A. Ziebeck and J.G. Booth, 1985, J. Magn. & Magn. Mater. **49**, 137.

Carnall, W.T., and H.M. Crosswhite, 1986, in: The Chemistry of the Actinide Elements, Vol. 2, eds J.J. Katz, G.T. Seaborg and L.R. Morss (Chapman and Hall, London) p. 1235.

Carnall, W.T., and B.G. Wybourne, 1964, J. Chem. Phys. **40**, 3428.

Carnall, W.T., G.L. Goodman, K. Rajnak and R.S. Rana, 1989, J. Chem. Phys. **90**, 3443.

Carpenter, J.M., G.H. Lander and C.G. Windsor, 1984, Rev. Sci. Instrum. **55**, 1019.

Chan, S.K., and D.J. Lam, 1974, in: Actinides Properties and Electronic Structure, Vol. 1, eds A.J. Freeman and J.B. Darby (Academic Press, New York) p. 1.

Coey, J.M.D., S.K. Ghatak, M. Avignon and F. Holtzberg, 1976, Phys. Rev. B **14**, 3744.

Cooper, B.R., R. Siemann, D. Yang, P. Thayamballi and A. Banerjea, 1985, in: Handbook on the Physics and Chemistry of the Actinides, Vol. 2, eds A.J. Freeman and G.H. Lander (North-Holland, Amsterdam) p. 435.

Cooper, B.R., Q.G. Sheng, S.P. Lim, C. Sanchez-Castro, N. Kioussis and J.M. Wills, 1992, J. Magn. & Magn. Mater. **108**, 10.

Cooper, J.R., C. Rizzuto and G.L. Olcese, 1971, J. Phys. (Paris) Colloq. **32**, C1-1136.

Cowley, R.A., and G. Dolling, 1968, Phys. Rev **167**, 464.

Cox, D.E., S.M. Shirane, G. Aeppli, G. Fisk, J.L. Smith, J. Kjems and H.R. Ott, 1986, Phys. Rev. B **33**, 3614.

Culverhouse, S., B.D. Rainford and D.McK. Paul, 1992, J. Magn. & Magn. Mater. **108**, 121.

Currat, R., R.G. Lloyd, P.W. Mitchell, A.P. Murani and J.W. Ross, 1989, Physica B **156–157**, 812.

Dakin, S., G. Rapson and B.D. Rainford, 1992, J. Magn. & Magn. Mater. **108**, 117.

Desclaux, J.P., and A.J. Freeman, 1984, in: Handbook on the Physics and Chemistry of the Actinides, Vol. 1, eds A.J. Freeman and G.H. Lander (North-Holland, Amsterdam) p. 1.

Dexpert, H., T.R.C. Karnatak, J.-M. Esteva, J.P. Connerade, M. Gasgnier, P.E. Caro and L. Albert, 1987, Phys. Rev. B **36**, 1750.

Dhar, S.K., E.V. Sampathkumaran, R. Vijayaraghavan and R. Kuentzler, 1987a, Solid State Commun. **61**, 479.

Dhar, S.K., K.A. Gschneidner Jr, W.H. Lee, P. Klavins and R.N. Shelton, 1987b, Phys. Rev. B **36**, 341.

Dijkman, W.H., F.R. de Boer, P.F. de Châtel and J. Aarts, 1980, J. Magn. & Magn. Mater **15–18**, 970.

Dijkman, W.H., A.C. Moleman, E. Kesselere, F.R. de Boer and P.F. de Châtel, 1982, in: Valence Instabilities, eds P. Wachter and H. Boppart (North-Holland, Amsterdam) p. 515.

Dönni, A., P. Fisher, A. Furrer, P. Bonville, F. Hulliger and H.R. Ott, 1990a, Z. Phys. B **81**, 83.

Dönni, A., P. Fischer, A. Furrer, W. Bacsa and P. Wachter, 1990b, Z. Phys. B **80**, 269.

Dönni, A., A. Furrer, P. Fischer, F. Hulliger and S.M. Hayden, 1992a, J. Magn. & Magn. Mater. **104–107**, 1204.

Dönni, A., A. Furrer, P. Fischer, F. Hulliger and S.M. Hayden, 1992b, J. Phys. CM **4**, 4283.

Dönni, A., A. Furrer, P. Fischer, S.M. Hayden, F. Hulliger and T. Suzuki, 1993, J. Phys. CM **5**, 1119.

Edwards, D.M., 1984, in: Moment Formation in Solids, ed. W.J.L. Buyers (Plenum Press, New York) p. 105.

Effantin, J.M., J. Rossat-Mignod, P. Burlet, H. Bartholin and T. Kasuya, 1985, J. Magn. & Magn. Mater. **47–48**, 145.

Elbenaas, R.A., C.J. Schinkel and E. Swakman, 1979, J. Phys. F **9**, 1261.

Elbenaas, R.A., C.J. Schinkel and C.J.M. van Deudekom, 1980, J. Magn. & Magn. Mater **15–18**, 979.

Entel, P.N., N. Grewe, M. Sietz and K. Kowalski, 1979, Phys. Rev. Lett. **43**, 2002.

Erdos, P., G. Solt, Z. Zolnierek, A. Blaise and J.M. Fournier, 1980, Physica B **102**, 164.

Eriksson, O., B. Johansson, M.S.S. Brooks and H.L. Skriver, 1988, Phys. Rev. B **38**, 12858.

Faber, J., and G.H. Lander, 1976, Phys. Rev. B **14**, 1151.

Fedro, A.J., and S.K. Sinha, 1981, in: Valence Fluctuations in Solids, eds L.M. Falicov, W. Hanke and M.B. Maple (North-Holland, New York) p. 329.

Fillion, G., R.M. Galera, D. Givord, J. Pierre, J. Schweizer and C. Vettier, 1985, J. Appl. Phys. **57**, 3179.

Fisk, Z., J.L. Smith, H.R. Ott and B. Batlogg, 1985, J. Magn. & Magn. Mater. **52**, 79.

Forgan, E.M., B.D. Rainford, S.L. Lee, J.S. Abell and Y. Bi, 1990, J. Phys. C **2**, 10211.

Fournier, J.M., A. Blaise, G. Amoretti, R. Caciuffo, J. Larroque, M.T. Hutchings, R. Osborn and A. Taylor, 1991, Phys. Rev. B **43**, 1142.

Frick, B., M. Loewenhaupt, D. Debray and W. Just, 1983, Z. Phys. B **52**, 223.

Friedt, J.M., F.J. Litterst and J. Rebizant, 1985, Phys. Rev. B **32**, 257.

Frings, P.H., J.J.M. Franse, F.R. de Boer and A.A. Menovsky, 1983, J. Magn. & Magn. Mater. **31–34**, 240.

Frings, P.H., B. Renker and C. Vettier, 1987, J. Magn. & Magn. Mater. **63–64**, 202.

Fulde, P., and M. Loewenhaupt, 1986, Adv. Phys. **34**, 589.

Furrer, A., W. Bührer and P. Wachter, 1981, Solid State Commun. **40**, 1011.

Galera, R.M., D. Givord, J. Pierre, A.P. Murani, C. Vettier and K.R.A. Ziebeck, 1985, J. Magn. & Magn. Mater. **47–48**, 139.

Galera, R.M., A.P. Murani, J. Pierre and K.R.A. Ziebeck, 1987, J. Magn. & Magn. Mater. **63–64**, 594.

Galera, R.M., A.P. Murani and J. Pierre, 1989, Physica B **156–157**, 801.

Gardner, W.E., J. Penfold, T.F. Smith and I.R. Harris, 1972, J. Phys. F **2**, 133.

Goldman, A.I., S.M. Shapiro, G. Shirane, J.L. Smith and Z. Fisk, 1986, Phys. Rev. B **33**, 1627.

Goldman, A.I., G. Shirane, G. Aeppli, E. Bucher and J. Hufnagl, 1987, Phys. Rev. B **36**, 8523.

Göppert-Mayer, M., 1941, Phys. Rev. **60**, 184.

Goremychkin, E.A., and R. Osborn, 1993a, RAL Report 1992.

Goremychkin, E.A., and R. Osborn, 1993b, Phys. Rev. B **47**, 14280.

Goremychkin, E.A., and R. Osborn, 1993c, Phys. Rev. B **47**, 14580.

Goremychkin, E.A., I. Natkaniec and E. Mühle, 1987, Solid State Commun. **64**, 553.

Goremychkin, E.A., A. Muzychka and R. Osborn, 1992, Physica B **179**, 184.

Gossard, A.C., V. Jaccarino and J.H. Wernick, 1964, Phys. Rev. **133**, A881.

Grier, B.H., S.M. Shapiro, C.F. Majkrzak and R.D. Parks, 1980, Phys. Rev. Lett. **45**, 666.

Grier, B.H., R.D. Parks, S.M. Shapiro and C.F. Majkrzak, 1981, Phys. Rev. B **24**, 6242.

Grier, B.H., J.M. Lawrence, V. Murgai and R.D. Parks, 1984, Phys. Rev. B **29**, 2664.

Grier, B.H., J.M. Lawrence, S. Horn and J.D. Thompson, 1988, J. Phys. C **21**, 1099.

Gschneidner Jr, K.A., J. Tang, S.K. Dhar and A. Goldman, 1990, Physica B **163**, 507.

Gunnarsson, O., and K. Schönhammer, 1985, J. Magn. & Magn. Mater. **52**, 227.

Güntherodt, G., A. Jayaraman, E. Anastassakis, E. Bucher and H. Bach, 1981, Phys. Rev. Lett. **46**, 855.

Hagen, M., W.G. Stirling and G.H. Lander, 1988, Phys. Rev. B **37**, 1846.

Hälg, B., and A. Furrer, 1986, Phys. Rev. B **34**, 6258.

Hälg, B., A. Furrer, J.K. Kjems and O. Vogt, 1983, Phys. Rev. Lett. **50**, 1085.

Hälg, B., A. Furrer and O. Vogt, 1985, Phys. Rev. Lett. **54**, 1388.

Hälg, B., A. Furrer and O. Vogt, 1987, J. Magn. & Magn. Mater. **63–64**, 55.

Havinga, E.E., K.H.J. Buschow and H.J. van Daal, 1973, Solid State Commun. **13**, 621.

Heinrich, G., J.P. Kappler and A. Meyer, 1979, Phys. Lett. A **74**, 121.

Hippert, F., B. Hennion, J.-M. Mignot and P. Lejay, 1992, J. Magn. & Magn. Mater. **108**, 177.

Holden, T.M., W.J.L. Buyers, E.C. Svensson and G.H. Lander, 1982, Phys. Rev. B **26**, 6227.

Holden, T.M., W.J.L. Buyers, E.C. Svensson and G.H. Lander, 1984, Phys. Rev. B **30**, 114.

Holden, T.M., W.J.L. Buyers, P. de V. du Plessis, K.M. Hughes and M.F. Collins, 1986, J. Magn. & Magn. Mater. **54–57**, 1175.

Holden, T.M., J.A. Jackman, W.J.L. Buyers, K.M. Hughes, M.F. Collins, P. de V. du Plessis and O. Vogt, 1987, J. Magn. & Magn. Mater. **63–64**, 155.

Holland-Moritz, E., 1983, J. Magn. & Magn. Mater. **38**, 253.

Holland-Moritz, E., 1985, J. Magn. & Magn. Mater. **47–48**, 127.

Holland-Moritz, E., 1992, Z. Phys. **89**, 285.

Holland-Moritz, E., 1993, in: Selected Topics in Magnetism, eds L.C. Gupta and M.S. Multani, Vol. 2 of Frontiers in Solid State Science (World Scientific, Singapore) p. 199.

Holland-Moritz, E., and M. Kasaya, 1986, Physcia B **136**, 424.

Holland-Moritz, E., and M. Loewenhaupt, 1979, J. Phys. (Paris) Colloq. **40**, C5-359.

Holland-Moritz, E., and M. Prager, 1983, J. Magn. & Magn. Mater. **31–34**, 395.

Holland-Moritz, E., and A. Severing, 1986, Z. Phys. B **63**, 313.

Holland-Moritz, E., and U. Walter, 1994, unpublished.

Holland-Moritz, E., M. Loewenhaupt, W. Schmatz and D. Wohlleben, 1977, Phys. Rev. Lett. **38**, 983.

Holland-Moritz, E., D. Wohlleben and M. Loewenhaupt, 1978, J. Phys. (Paris) Colloq. **39**, C6-835.

Holland-Moritz, E., D. Wohlleben and M. Loewenhaupt, 1982, Phys. Rev. B **25**, 7482.

Holland-Moritz, E., E. Braun, B. Roden, B. Perscheid, E.V. Sampathkumaran and W. Langel, 1987a, Phys. Rev. B **35**, 3122.

Holland-Moritz, E., W. Schlabitz, W. Loewenhaupt, U. Walter and C.-K. Loong, 1987b, J. Magn. & Magn. Mater. **63–64**, 187.

Holland-Moritz, E., E. Zirngiebl and S. Blumenröder, 1988, Z. Phys. B **70**, 395.

Holland-Moritz, E., W. Weber, Ch. Sauer and A. Mewis, 1989a, Z. Physik B **77**, 105.

Holland-Moritz, E., W. Schlabitz, M. Loewenhaupt and U. Walter, 1989b, Phys. Rev. B **39**, 551.

Holland-Moritz, E., W. Weber, A. Severing, E. Zirngiebl, H. Spille, W. Baus, S. Horn, A.P. Murani and F. Douchin, 1989c, Phys. Rev. B **39**, 6409.

Horn, S., M. Loewenhaupt, F. Steglich and W. Just, 1978, J. Magn. & Magn. Mater. **9**, 54.

Horn, S., E. Holland-Moritz, M. Loewenhaupt, F. Steglich, H. Scheuer, A. Benoit and J. Flouquet, 1981a, Phys. Rev. B **23**, 3171.

Horn, S., F. Steglich, M. Loewenhaupt and E. Holland-Moritz, 1981b, Physica B **107**, 103.

Horn, S., F. Steglich, M. Loewenhaupt, H. Schcuer, W. Felsch and K. Winzer, 1981c, Z. Phys. B **42**, 125.

Hu, G.J., and B.R. Cooper, 1990, Physica B **163**, 483.

Hu, G.J., B.R. Cooper and G.H. Lander, 1989, Physica B **156–157**, 822.

Hundley, M.F., P.C. Canfield, J.D. Thompson, Z. Fisk and J.M. Lawrence, 1990, Phys. Rev. B **42**, 6842.

Hutchings, M.T., 1964, in: Solid State Physics, Vol. 16, eds F. Seitz and D. Turnbull (Academic, NY) p. 227.

Hutchins, R.D., V.V.S. Rao, J.E. Greedan and R.S. Craig, 1972, J. Phys. Soc. Jpn. **32**, 451.

Jaccarino, V., and L.R. Walker, 1965, Phys. Rev. Lett. **15**, 258.

Jacoud, J.L., L.P. Regnault, J. Rossat-Mignod, C. Vettier, P. Lejay and J. Flouquet, 1989, Physica B **156–157**, 812.

Jensen, J., and P. Bak, 1981, Phys. Rev. B **23**, 6180.

Jensen, J., and A.R. Mackintosh, 1991, Rare Earth Magnetism (Clarendon Press, Oxford).

Johansson, B., and M.S.S. Brooks, 1993, in: Handbook on the Physics and Chemistry of Rare Earths, Vol. 17, eds K.A. Gschneidner Jr, L. Eyring, G.H. Lander and G.R. Choppin (North-Holland, Amsterdam) ch. 112.

Johansson, B., O. Eriksson, M.S.S. Brooks and H.L. Skriver, 1986, Physica Scripta T **13**, 65.

Johnson, S.M., J.A.C. Bland, P.J. Brown, A. Benoit, H. Capellmann, J. Flouquet, H. Spille, F. Steglich and K.R.A. Ziebeck, 1985, Z. Phys. B **59**, 401.

Jones, D.L., W.G. Stirling, G.H. Lander, J. Rebizant, J.C. Spirlet, M. Alba and O. Vogt, 1991, J. Phys. CM **3**, 3551.

Jones, D.L., W.G. Stirling, G.H. Lander, O. Osborn, A.D. Taylor, K. Mattenberger and O. Vogt, 1992, Physica B **180–181**, 199.

Jostarndt, H.-D., U. Walter, J. Harnischmacher, J. Kalenborn, A. Severing and E. Holland-Moritz, 1992, Phys. Rev. B **46**, 14872.

Kappler, J.P., and A. Meyer, 1979, J. Phys. F **9**, 143.

Kappler, J.P., M.J. Besnus, E. Beaurepaire, A. Meyer, J. Sereni and G. Nieva, 1985, J. Magn. & Magn. Mater **47–48**, 111.

Kemly, E., M. Croft, V. Murgai, L.C. Gupta, C. Godart, R.D. Parks and C.U. Segre, 1985, J. Magn. & Magn. Mater. **47–48**, 403.

Kern, S., C.K. Loong, J. Faber and G.H. Lander, 1984, Solid State Commun. **49**, 295.

Kern, S., C.K. Loong and G.H. Lander, 1985, Phys. Rev. B **32**, 3051.

Kern, S., J. Morris, C.K. Loong, G. Goodman, G.H. Lander and B. Cort, 1988, J. Appl. Phys. **63**, 3598.

Kern, S., F. Trouw, C.K. Loong and G.H. Lander, 1990a, J. Appl. Physics 67, 4830.

Kern, S., C.K. Loong, G.L. Goodman, B. Cort and G.H. Lander, 1990b, J. Phys.: Condens. Matter **2**, 1933.

Klaasse, J.C.P., W.C.M. Mattens, F.R. de Boer and P.F. de Châtel, 1977, Physica B **86–88**, 234.

Knopp, G., A. Loidl, R. Caspary, U. Gottwick, C.D. Bredl, H. Spille, F. Steglich and A.P. Murani, 1988, J. Magn. & Magn. Mater. **74**, 341.

Knopp, G., A. Loidl, K. Knorr, L. Pawlak, M. Duczmal, R. Caspary, U. Gottwick, H. Spille, F. Steglich and A.P. Murani, 1989, Z. Phys. B 77, 95.

Knott, H.W., G.H. Lander, M.H. Mueller and O. Vogt, 1980, Phys. Rev. B **21**, 4159.

Köbler, U., K. Fischer, K. Bickmann and H. Lustfeld, 1981, J. Magn. & Magn. Mater. **24**, 34.

Kohgi, M., K. Ohoyama, A. Oyamada, T. Suzuki and M. Arai, 1990a, Physica B **163**, 625.

Kohgi, M., T. Satoh, K. Ohoyama, M. Arai and R. Osborn, 1990b, Physica B **163**, 137.

Kohgi, M., T. Satoh, K. Ohoyama and M. Arai, 1991, Physica B **169**, 501.

Kohgi, M., K. Ohoyama, T. Osakabe and M. Kasaya, 1992, J. Magn. & Magn. Mater. **108**, 187.

Kohgi, M., K. Ohoyama, T. Osakabe, M. Kasaya, T. Takabatake and H. Fujii, 1993, Physica B **186–188**, 409.

Kojima, H., Y. Kuramoto and M. Taschiki, 1984, Z. Phys. B **54**, 293.

Korringa, J., 1950, Physica **16**, 601.

Koskimaki, D.C., and K.A. Gschneidner Jr, 1975, Phys. Rev. B **11**, 4463.

Krimmel, A., A. Severing, A. Murani, A. Grauel and S. Horn, 1992, Physica B **180–181**, 191.

Kuramoto, Y., 1986, Z. Phys. B **65**, 29.

Kuramoto, Y., and H. Kojima, 1984, Z. Phys. B **57**, 95.

Kuramoto, Y., and E. Müller-Hartmann, 1981, in: Valence Fluctuations in Solids, eds L.M. Falicov, W. Hanke and M.B. Maple (North-Holland, New York), p. 139.

Kuramoto, Y., and E. Müller-Hartmann, 1985, J. Magn. & Magn. Mater. **52**, 122.

Lander, G.H., 1993, in: Handbook on the Physics and Chemistry of Rare Earths, Vol. 17, eds K.A. Gschneidner Jr and G.H. Lander (North Holland, Amsterdam) ch. 117.

Lander, G.H., and W.G. Stirling, 1980, Phys. Rev. B **21**, 436.

Lander, G.H., and W.G. Stirling, 1992, Physica Scripta T **45**, 15.

Lander, G.H., M.H. Mueller, D.M. Sparlin and O. Vogt, 1976, Phys. Rev. B **14**, 5035.

Lander, G.H., W.G. Stirling and O. Vogt, 1979, Phys. Rev. Lett. **42**, 260.

Lander, G.H., A. Delapalme, P.J. Brown, J.C. Spirlet, J. Rebizant and O. Vogt, 1984, Phys. Rev. Lett. **53**, 2262.

Lander, G.H., W.G. Stirling, J. Rossat-Mignod, J.C. Spirlet, J. Rebizant and O. Vogt, 1986, Physica B **136**, 409.

Lander, G.H., M.S.S. Brooks, B. Lebech, P.J. Brown, O. Vogt and K. Mattenberger, 1991a, J. Appl. Phys. **69**, 4803.

Lander, G.H., W.G. Stirling, J. Rossat-Mignod, M. Hagen and O. Vogt, 1991b, Phys. Rev. B **41**, 6899.

Lander, G.H., S.M. Shapiro, C. Vettier and A.J. Dianoux, 1992, Phys. Rev. B **46**, 5387.

Langridge, S., W.G. Stirling, G.H. Lander and O. Vogt, 1992, Physica B **180–181**, 194.

Launois, H., M. Rawiso, E. Holland-Moritz, R. Pott and D. Wohlleben, 1980, Phys. Rev. Lett. **44**, 1271.

Lawrence, J.M., 1979, Phys. Rev. B **20**, 3770.

Lea, K.R., M.J.M. Leask and W. Wolf, 1962, J. Phys. Chem. Solids **23**, 1381.

Lebech, B., Z. Smetana and V. Sima, 1987, J. Magn. & Magn. Mater. **70**, 97.

Leciejewicz, J., and A. Misiuk, 1972, Phys. Status Solidi A **13**, K79.

Lee, W.H., and R.N. Shelton, 1987, Phys. Rev. B **35**, 5369.

Levy, P.M., and S. Zhang, 1989, Phys. Rev. Lett. **62**, 78.

Lin, G.L., L.W. Zhou, J.E. Crow and R.P. Guertin, 1985, J. Appl. Phys. **57**, 3146.

Liu, S.H., 1989, Phys. Rev. B **39**, 7381.

Loewenhaupt, M., 1985, Physica B **130**, 347.

Loewenhaupt, M., and H. Bjerrum-Møller, 1981, Physica **108**, 1349.

Loewenhaupt, M., and K.H. Fischer, 1993, in: Handbook on the Physics and Chemistry of Rare Earths, Vol. 16, eds K.A. Gschneidner Jr and L. Eyring (North-Holland, Amsterdam) p. 1.

Loewenhaupt, M., and E. Holland-Moritz, 1978, J. Magn. & Magn. Mater. **9**, 50.

Loewenhaupt, M., and E. Holland-Moritz, 1979, J. Appl. Phys. **50**, 7456.

Loewenhaupt, M., and C.-K. Loong, 1990, Phys. Rev. B **41**, 9294.

Loewenhaupt, M., and F. Steglich, 1977a, in: Crystal Field Effects in Metals and Alloys, ed. A. Furrer (Plenum Press, New York) p. 198.

Loewenhaupt, M., and F. Steglich, 1977b, Physica B **86–88**, 187.

Loewenhaupt, M., B.D. Rainford and F. Steglich, 1979a, Phys. Rev. Lett. **42**, 1709.

Loewenhaupt, M., S. Horn, F. Steglich, E. Holland-Moritz and G.H. Lander, 1979b, J. Phys. (Paris) Colloq. **39**, C4-142.

Loewenhaupt, M., J.M. Carpenter and C.-K. Loong, 1985, J. Magn. & Magn. Mater. **52**, 245.

Loewenhaupt, M., W. Reichardt, R. Pynn and E. Lindley, 1987, J. Magn. & Magn. Mater. **63–64**, 73.

Loewenhaupt, M., M. Prager, E. Gratz and B. Frick, 1988, J. Magn. & Magn. Mater. **76–77**, 413.

Loewenhaupt, M., E. Gratz, N. Pillmayr and H. Müller, 1990, Physica B **163**, 427.

Loewenhaupt, M.L., G.H. Lander, A.P. Murani and A. Murasik, 1982, J. Phys. C **15**, 6199.

Loidl, A., G. Knopp, H. Spille, F. Steglich and A.P. Murani, 1989, Physica B **156–157**, 794.

Loidl, A., K. Knorr, G. Knopp, A. Krimmel, R. Caspary, A. Böhm, G. Sparn, C. Geibel, F. Steglich and A.P. Murani, 1992, Phys. Rev. B **46**, 9341.

Loong, C.-K., M. Loewenhaupt and M.L. Vrtis, 1986, Physica B **136**, 413.

Loong, C.-K., B.H. Grier, S.M. Shapiro, J.M. Lawrence, R.D. Parks and S.K. Sinha, 1987, Phys. Rev. B **35**, 3092.

Loong, C.-K., J. Zarestky, C. Stassis, O.D. McMasters and R.M. Nicklow, 1988, Phys. Rev. B **38**, 7365.

Lossau, N., G. Neumann, W. Schlabitz and D. Wohlleben, 1988, Phys. Scr. **37**, 809.

Lovesey, S.W., 1984, Theory of Neutron Scattering from Condensed Matter (Oxford University Press).

Lustfeld, H., and A. Bringer, 1978, Solid State Commun. **28**, 119.

MacLaughlin, D.E., F.R. de Boer, J. Bijvoet, P.F. de Châtel and W.C.M. Mattens, 1982, J. Appl. Phys. **53**, 7890.

Maple, M.B., and D. Wohlleben, 1971, Phys. Rev. Lett. **27**, 511.

Maple, M.B., J.W. Chen, Y. Dalichaouch, T. Kohara, C. Rossel, M.S. Torikachvili, M.W. McElfresh and J.P. Thompson, 1986, Phys. Rev. Lett. **56**, 185.

Marshall, W., and S.W. Lovesey, 1971, Theory of Thermal Neutron Scattering (Clarendon Press, Oxford).

Marshall, W.G., K.A. McEwen and D. Fort, 1992a, Physica B **180–181**, 256.

Marshall, W.G., A.P. Murani and K.A. McEwen, 1992b, J. Magn. & Magn. Mater. **104–107**, 67.

Martin, R.M., J.B. Boyce, J.W. Allen and F. Holtzberg, 1980, Phys. Rev. Lett. **44**, 1275.

Martin, W.C., R. Zalubas and L. Hagan, 1978, Atomic Energy Levels - The Rare-Earth Elements, National Bureau of Standards NSRDS-NBS (U.S. Dept. of Commerce, Washington, DC).

Mason, T.E., G. Aeppli, A.P. Ramirez, K.N. Clausen, C. Broholm, N. Stücheli, E. Bucher and T.T.M. Palstra, 1992, Phys. Rev. Lett. **69**, 490.

Mattens, W.C.M., R.A. Elbenaas and F.R. de Boer, 1977, Commun. Phys. **2**, 147.

Mattens, W.C.M., F.R. de Boer, A.P. Murani and G.H. Lander, 1980, J. Magn. & Magn. Mater. **15–18**, 973.

Mazzaferro, J., C.A. Balseiro and B. Alascio, 1981, Phys. Rev. Lett. **47**, 274.

McEwen, K.A., W.G. Stirling, C.K. Loong, G.H. Lander and D. Fort, 1988, J. Magn. & Magn. Mater. **76–77**, 426.

McEwen, K.A., U. Steigenberger, J.L. Martinez and J.S. Abell, 1990, Physica B **163**, 371.

McEwen, K.A., U. Steigenberger and J.L. Martinez, 1993, Physica B **186–188**, 670.

McWhan, D.B., S.M. Shapiro, J. Eckert, H.A. Mook and R.J. Birgeneau, 1978, Phys. Rev. B **18**, 3623.

McWhan, D.B., C. Vettier, E.D. Isaacs, G.E. Ice, P. Siddons, J.B. Hastings, C. Peters and O. Vogt, 1990, Phys. Rev. B **42**, 6007.

Menth, A., E. Buehler and T.H. Geballe, 1969, Phys. Rev. Lett. **22**, 295.

Mesot, J., P. Allenspach, U. Staub, A. Furrer, H. Mutka, R. Osborn and S. Bennington, 1992, Physica B **180–181**, 405.

Mihalisin, T., P. Scorboria and J.A. Ward, 1981, in: Valence Fluctuations in Solids, eds L.M. Falicov, W. Hanke and M.B. Maple (North-Holland Amsterdam) p. 61.

Millhouse, A.H., and A. Furrer, 1975, Phys. Rev. Lett. **35**, 1231.

Mook, H.A., and F. Holtzberg, 1981, in: Valence Fluctuations in Solids, eds L.M. Falicov, W. Hanke and M.B. Maple (North-Holland) p. 113.

Mook, H.A., T. Penney, F. Holtzberg and M.W. Shafer, 1978a, J. Phys. C **6**, 837.

Mook, H.A., R.M. Nicklow, T. Penney, F. Holtzberg and M.W. Shafer, 1978b, Phys. Rev. B **18**, 2925.

Mook, H.A., D.B. McWhan and F. Holtzberg, 1982, Phys. Rev. B **25**, 4321.

Moon, R.M., T. Riste and W.C. Koehler, 1969, Phys. Rev. **181** 920.

Moze, O., R. Caciuffo, H.S. Li, B.P. Hu, J.M.D. Coey, R. Osborn and A.D. Taylor, 1990, Phys. Rev. B **42**, 1940.

Murani, A., A.D. Taylor, R. Osborn and Z.A. Bowden, 1992, Philos. Mag. **65**, 1333.

Murani, A.P., 1983a, J. Phys. C **33**, 6359.

Murani, A.P., 1983b, Phys. Rev. B **28**, 2308.

Murani, A.P., 1985, Phys. Rev. Lett. **54**, 1444.

Murani, A.P., 1987a, Phys. Rev. B **36**, 5705.

Murani, A.P., 1987b, in: Theoretical and Experimental Aspects of Valence Fluctuations and Heavy Fermions, eds L.C. Gupta and S.K. Malik (Plenum Press, New York and London) p. 287.

Murani, A.P., 1994, Phys. Rev., in press.

Murani, A.P., K. Knorr and K.H.J. Buschow, 1977, in: Crystal Field Effects in Metals and Alloys, ed. A. Furrer (Plenum Press, New York) p. 268.

Murani, A.P., K. Knorr, K.H.J. Buschow, A. Benoit and J. Flouquet, 1980, Solid State Commun. **36**, 523.

Murani, A.P., W.C.M. Mattens, F.R. de Boer and G.H. Lander, 1985, Phys. Rev. B **31**, 52.

Murasik, A., and Z. Zolnierek, 1980, Physica B **98**, 306.

Murasik, A., S. Ligenza and A. Zygmunt, 1974, Phys. Status Solidi a **23**, K163.

Murasik, A., P. Fischer and Z. Zolnierek, 1980, Physica B **102**, 188.

Neuhaus, W., 1987, KFA report, Jülich, JÜ-2165.

Newns, D.M., and A.C. Hewson, 1980, J. Phys. F **10**, 2429.

Newns, D.M., A.C. Hewson, W.J. Rasul and N. Read, 1982, J. Appl. Phys. **53**, 7877.

Ofelt, G.S., 1963, J. Chem. Phys. **38**, 2171.

Ohoyama, K., M. Kohgi, T. Nakane, M. Arai, A.D. Taylor, A. Oyamada and T. Suzuki, 1992, Physica B **180–181**, 250.

Osborn, R., and E.A. Goremychkin, 1991, Physica C **185–189**, 1179.

Osborn, R., M. Loewenhaupt, B.D. Rainford and W.G. Stirling, 1987, J. Magn. & Magn. Mater. **63–64**, 70.

Osborn, R., M. Hagen, D.L. Jones, W.G. Stirling, G.H. Lander, K. Mattenberger and O. Vogt, 1988, J. Magn. & Magn. Mater. **76–77**, 429.

Osborn, R., K.A. McEwen, E.A. Goremychkin and A.D. Taylor, 1990, Physica B **163**, 37.

Osborn, R., S.W. Lovesey, A.D. Taylor and E. Balcar, 1991, Intermultiplet transitions using neutron spectroscopy, in: Handbook on the Physics and Chemistry of Rare Earths, Vol. 14, eds K.A. Gschneidner Jr and L. Eyring (North-Holland, Amsterdam) ch. 93.

Ott, H.R., and Z. Fisk, 1987, in: Handbook on the Physics and Chemistry of the Actinides, Vol. 5, eds A.J. Freeman and G.H. Lander (North-Holland, Amsterdam) p. 85.

Ott, H.R., H. Rudigier, Z. Fisk and J.L. Smith, 1983, Phys. Rev. Lett. **50**, 1595.

Ott, H.R., H. Rudigier, P. Delsing and Z. Fisk, 1984, Phys. Rev. Lett. **52**, 1551.

Oyamada, A., P. Burlet, L.P. Regnault, A. Bouvet, R. Calemczuk, J. Rossat-Mignod, T. Suzuki and T. Kasuya, 1990, J. Mag. & Magn. Mater. **90–91**, 441.

Palstra, T.T.M., A.A. Menovsky, J. van den Berg, A.J. Dirkmaat, P.H. Kes, G.J. Nieuwenhuys and J.A. Mydosh, 1985, Phys. Rev. Lett. **55**, 2727.

Perscheid, B., E.V. Sampathkumaran and G. Kaindl, 1985, J. Magn. & Magn. Mater. **47–48**, 410.

Pillmayr, N., E. Bauer and K. Yoshimura, 1992, J. Magn. & Magn. Mater. **104–107**, 639.

Pintschovius, L., E. Holland-Moritz, D. Wohlleben, S. Stähr, J. Liebertz, W. Assmus, C. Stassis, C.K. Loong, J. Zaretsky and R.M. Nicklow, 1983, Solid State Commun. **47**, 663.

Politt, B., D. Dürkop and P. Weidner, 1985, J. Magn. & Magn. Mater. **47–48**, 583.

Pott, R., 1982, Dissertation (University of Cologne).

Pott, R., W. Boksch, G. Leson, B. Politt, H. Schmidt, A. Freimuth, K. Keulertz, J. Langen, G. Neumann, F. Oster, J. Röhler, U. Walter, P. Weidner and D. Wohlleben, 1985, Phys. Rev. Lett. **54**, 481.

Rahman, H.U., and W.A. Runciman, 1966, J. Phys. Chem. Solids **27**, 1833.

Rainford, B.D., and V.T. Nguyen, 1979, J. Phys. (Paris) Colloq. **40**, C5-262.

Rainford, B.D., K.C. Turberfield, G. Busch and O. Vogt, 1968, J. Phys. C **1**, 679.

Rainford, B.D., B. Buras and B. Lebech, 1977, Physica B **86–88**, 41.

Rainford, B.D., S. Dakin and A. Severing, 1992, J. Magn. & Magn. Mater. **108**, 119.

Ramakrishnan, T.V., and K. Sur, 1982, Phys. Rev. B **26**, 1798.

Raphael, G., and R. Lallement, 1968, Solid State Commun. **6**, 383.

Regnault, L.P., W.A.C. Erkelens, J. Rossat-Mignod, J. Flouquet, E. Walker, D. Jaccard, A. Amato and B. Hennion, 1987, J. Magn. & Magn. Mater. **63–64**, 289.

Regnault, L.P., W.A.C. Erkelens, J. Rossat-Mignod, C. Vettier, S. Kunii and T. Kasuya, 1988a, J. Magn. & Magn. Mater. **76–77**, 413.

Regnault, L.P., W.A.C. Erkelens, J. Rossat-Mignod, J.L. Jacoud, J.M. Mignot, E. Walker, D. Jaccard, A. Amato and C. Vettier, 1988b, J. Phys. (Paris) Colloq. **40**, C8-773.

Regnault, L.P., W.A.C. Erkelens, J. Rossat-Mignod, P. Lejay and J. Flouquet, 1988c, Phys. Rev. B **38**, 4481.

Regnault, L.P., J.L. Jacoud, J.M. Mignot, J. Rossat-Mignod, C. Vettier, P. Lejay and J. Flouquet, 1990, Physica B **163**, 606.

Reihl, B., N. Martensson, P. Heimann, D.E. Eastman and O. Vogt, 1981, Phys. Rev. Lett. **46**, 1480.

Reinders, P.H.P., M. Springford, P.T. Coleridge, R. Boulet and D. Ravot, 1986, Phys. Rev. Lett. **57**, 1631.

Renker, B., E. Gehring, F. Gompf, H. Schmidt and H. Rietschel, 1987, J. Magn. & Magn. Mater. **63–64**, 31.

Röhler, J., 1987, in: Handbook on the Physics and Chemistry of Rare Earths, Vol. 10, eds K.A. Gschneidner Jr, L. Eyring and S. Hüfner (North-Holland, Amsterdam) p. 506.

Rossat-Mignod, J., P. Burlet, S. Quezel and O. Vogt, 1980, Physica B **102**, 237.

Rossat-Mignod, J., D. Delacote, J.M. Effantin, C. Vettier and O. Vogt, 1983, Physica B **120**, 163.

Rossat-Mignod, J., G.H. Lander and P. Burlet, 1984, in: Handbook on the Physics and Chemistry of the Actinides, Vol. 1, eds A.J. Freeman and G.H. Lander (North-Holland, Amsterdam) p. 415.

Rossat-Mignod, J., J.M. Effantin, C. Vettier and O. Vogt, 1985a, Physica B **130**, 555.

Rossat-Mignod, J., J.M. Effantin, P. Burlet, T. Chattopadhyay, L.P. Regnault, H. Bartholin, C. Vettier, O. Vogt, D. Ravot and J.C. Achard, 1985b, J. Magn. & Magn. Mater. **52**, 111.

Rossat-Mignod, J., L.P. Regnault, J.L. Jacoud, C. Vettier, P. Lejay, J. Flouquet, E. Walker, D. Jaccard and A. Amato, 1988, J. Magn. & Magn Mater. **76–77**, 376.

Rossel, C., K.N. Yang, M.B. Maple, Z. Fisk, E. Zirngiebl and J.D. Thompson, 1987, Phys. Rev. B **35**, 1914.

Sales, B.C., and D. Wohlleben, 1975, Phys. Rev. Lett. **35**, 1240.

Sampathkumaran, E.V., R. Vijarayhavan, K.V. Gopalakrishnan, R.G. Pilay, H.G. Devare, L.C. Gupta, B. Post and R.D. Parks, 1981, in: Valence Fluctuations in Solids, eds L.M. Falicov, W. Hanke and M.B. Maple (North-Holland, Amsterdam) p. 193.

Sampathkumaran, E.V., L.C. Gupta and R. Vijayaraghavan, 1982, Phys. Lett. A **88**, 180.

Sampathkumaran, E.V., K.H. Frank, G. Kalkowski, G. Kaindl, M. Domke and G. Wortmann, 1984, Phys. Rev. B **29**, 5702.

Santini, P., and G. Amoretti, 1994, Phys. Rev. Lett. **73**, 1027.

Sasaki, K., and Y. Obota, 1970, J. Phys. Soc. Japan **28**, 1157.

Schlabitz, W., J. Baumann, B. Politt, U. Rauchschwalbe, H.M. Mayer, U. Alheim and C.D. Bredl, 1986, Z. Phys. B **62**, 171.

Schlottmann, P., 1982, Phys. Rev. B **25**, 2371.

Schlottmann, P., 1984a, Phys. Rev. B **29**, 630.

Schlottmann, P., 1984b, Phys. Rev. B **29**, 4468.

Schmitt, D., P. Morin and J. Pierre, 1978, J. Magn. & Magn. Mater. **8**, 249.

Schoenes, J., 1984, in: Handbook on the Physics and Chemistry of the Actinides, Vol. 1, eds A.J. Freeman and G.H. Lander (Amsterdam, North-Holland) p. 341.

Schoenes, J., B. Frick and O. Vogt, 1984, Phys. Rev. B **30**, 6578.

Schrieffer, J.R., and P.A. Wolff, 1966, Phys. Rev. **149**, 491.

Sereni, J., G. Nieva, J.P. Kappler, M.J. Besnus and A. Meyer, 1986, J. Phys. F **16**, 435.

Severing, A., and A.P. Murani, 1990, Physica B **163**, 699.

Severing, A., W. Reichardt, E. Holland-Moritz, D. Wohlleben and W. Assmus, 1988, Phys. Rev. B **38**, 1773.

Severing, A., E. Holland-Moritz and B. Frick, 1989a, Phys. Rev. B **39**, 4164.

Severing, A., E. Holland-Moritz, B.D. Rainford, S.R. Culverhouse and B. Frick, 1989b, Phys. Rev. B **39**, 2557.

Severing, A., A.P. Murani, J.D. Thompson, Z. Fisk and C.-K. Loong, 1990a, Phys. Rev. B **41**, 1739.

Severing, A., E. Gratz, B.D. Rainford and K. Yoshimura, 1990b, Physica B **163**, 409.

Severing, A., J.D. Thompson, P.C. Canfield, Z. Fisk and R. Riseborough, 1991, Phys. Rev. B **44**, 6832.

Shaburov, V.A., A.E. Sovestnov and O.I. Sumbaev, 1974, Phys. Lett. A **49**, 83.

Shapiro, S.M., and B.H. Grier, 1982, Phys. Rev. B **25**, 1457.

Shapiro, S.M., R.J. Birgeneau and E. Bucher, 1975, Phys. Rev. Lett. **34**, 470.

Shapiro, S.M., J.D. Axe, R.J. Birgeneau, J.M. Lawrence and R.P. Parks, 1977, Phys. Rev. B **16**, 2225.

Shapiro, S.M., C. Stassis and G. Aeppli, 1989, Phys. Rev. Lett. **62**, 94.

Shiba, H., 1975, Prog. Theor. Phys. **54**, 967.

Shimizu, T., H. Yasuoka, Z. Fisk and J.L. Smith, 1985, J. Phys. Soc. Jpn. **56**, 4113.

Siemann, R., and B.R. Cooper, 1979, Phys. Rev. B **20**, 2869.

Skanthakumar, S., W.H. Li, J.W. Lynn, A. Kebede, J.E. Crow and T. Mihalisin, 1990, Physica B **163**, 239.

Soderholm, L., G.L. Goodman and C.K. Loong, 1990, J. Appl. Phys. **67**, 5067.

Solt, G., and P. Erdos, 1980, Phys. Rev. B **22**, 4718.

Spirlet, J.C., and O. Vogt, 1984, in: Handbook on the Physics and Chemistry of the Actinides, Vol. 1, eds A.J. Freeman and G.H. Lander (North-Holland, Amsterdam) pp. 79–151.

Squires, G.L., 1978, Thermal Neutron Scattering (Cambridge Univ. Press, London).

Stassis, C., H.W. Deckmann, B.N. Harmon, J.P. Desclaux and A.J. Freeman, 1977, Phys. Rev. B **15**, 369.

Stassis, C., T. Gould, O.D. McMasters, K.A. Gschneidner Jr and R.M. Nicklow, 1979a, Phys. Rev. B **19**, 5746.

Stassis, C., C.-K. Loong, O.D. McMasters and R.M. Moon, 1979b, J. Appl. Phys. **50**, 2091.

Stassis, C., C.-K. Loong, B.N. Harmon, S.H. Liu and R.M. Moon, 1979c, J. Appl. Phys. **50**, 7567.

Stassis, C., C.-K. Loong, J. Zarestky, O.D. McMasters, R.M. Moon and J.R. Thompson, 1982, J. Appl. Phys. **53**, 7890.

Stassis, C., D. Batlogg, J.P. Remeika, J.D. Axe, G. Shirane and Y.J. Uemura, 1986, Phys. Rev. B **33**, 1680.

Steeman, R.A., E. Frikkee, C. van Dijk, G.J. Nieuwenhuys and A.A. Menovsky, 1988, J. Magn. & Magn. Mater. **76–77**, 435.

Steeman, R.A., T.E. Mason, H. Lin, W.J.L. Buyers, A.A. Menovsky, M. Collins, E. Frikkee, G.J. Nieuwenhuys and J.A. Mydosh, 1990, J. Appl. Phys. **67**, 5203.

Steglich, F., J. Aarts, C.D. Bredl, W. Lieke, D. Meschede, W. Franz and H. Schäffer, 1979, Phys. Rev. Lett. **43**, 1892.

Steglich, F., U. Rauchschwalbe, U. Gottwick, H.M. Mayer, G. Sporn, N. Grewe, U. Poppe and J.J.M. Franse, 1985, J. Appl. Phys. **57**, 3054.

Steigenberger, U., K.A. McEwen, J.L. Martinez and D. Fort, 1992, J. Magn. & Magn. Mater. **108**, 163.

Stewart, G.R., 1984, Rev. Mod. Phys. **56**, 755.

Stewart, G.R., Z. Fisk and M.S. Wire, 1984a, Phys. Rev. B **30**, 482.

Stewart, G.R., Z. Fisk, J.O. Willis and J.L. Smith, 1984b, Phys. Rev. Lett. **52**, 679.

Stirling, W.G., G.H. Lander and O. Vogt, 1980, Physica B **102**, 249.

Stirling, W.G., G.H. Lander and O. Vogt, 1983, J. Phys. C **16**, 4093.

Stirling, W.G., K.A. McEwen and C.K. Loong, 1986, Physica B **136**, 420.

Tacke, R., N. Dolezal, W. Assmus and B. Lüthi, 1981, J. Magn. & Magn. Mater. **23**, 247.

Taillefer, L., and G. Lonzarich, 1988, Phys. Rev. Lett. **60**, 1570.

Takabatake, T., F. Teshima, H. Fujii, S. Nishigori, T. Suzuki, T. Fujita, Y. Yamaguchi, J. Sakurai and D. Jaccard, 1990, Phys. Rev. B **41**, 9607.

Takahashi, H., and T. Kasuya, 1985, J. Phys. C **18**, 2697.

Tao, L.J., and F. Holtzberg, 1975, Phys. Rev. B **11**, 3842.

Tarascon, J.M., Y. Ishikawa, B. Chevalier, J. Etourneau, P. Hagenmuller and M. Kasaya, 1980, J. Phys. (Paris) **41**, 1141.

Taylor, A.D., R. Osborn, K.A. McEwen, W.G. Stirling, Z.A. Bowden, W.G. Williams, E. Balcar and S.W. Lovesey, 1988, Phys. Rev. Lett. **61**, 1309.

Thalmeier, P., and P. Fulde, 1982, Phys. Rev. Lett. **49**, 1588.

Thalmeier, P., and B. Lüthi, 1991, in: Handbook on the Physics and Chemistry of Rare Earths, Vol. 14, eds K.A. Gschneidner Jr and L. Eyring (North-Holland, Amsterdam) p. 225.

Thompson, J.D., J.O. Willis, C. Godart, D.E. MacLaughlin and L.C. Gupta, 1985, J. Magn. & Magn. Mater. **47–48**, 281.

Tomala, K., D. Weschenfelder, G. Czjzek and E. Holland-Moritz, 1990, J. Magn. & Magn. Mater. **89**, 143.

Torikachvili, M.S., L. Rebelsky, K. Motoya, S.M. Shapiro, Y. Dalichaouch and M.B. Maple, 1992, Phys. Rev. B **45**, 2262.

Trainor, R.J., M.B. Brodsky and H.V. Culbert, 1975, Phys. Rev. Lett. **34**, 1019.

Trump, R., 1991, Dissertation (University of Cologne) unpublished.

Turberfield, K.C., L. Passell, R.J. Birgeneau and E. Bucher, 1970, Phys. Rev. Lett. **25**, 752.

Turberfield, K.C., L. Passell, R.J. Birgeneau and E. Bucher, 1971, J. Appl. Phys. **42**, 1746.

van Maaren, M.H., H.J. van Daal, K.H.J. Buschow and C.J. Schinkel, 1974, Solid State Commun. **14**, 145.

Vettier, C., P. Morin and J. Flouquet, 1986, Phys. Rev. Lett. **56**, 1980.

Wachter, P., F. Marabelli and B. Bucher, 1991, Phys. Rev. B **43**, 11136.

Walker, M.B., W.J.L. Buyers, Z. Tun, W. Que, A.A. Menovsky and J.D. Garrett, 1993, Phys. Rev. Lett. **71**, 2630.

Walter, U., and E. Holland-Moritz, 1981, Z. Phys. B **45**, 107.

Walter, U., and D. Wohlleben, 1987, Phys. Rev. B **35**, 3576.

Walter, U., Z. Fisk and E. Holland-Moritz, 1985, J. Magn. & Magn. Mater. **47–48**, 159.

Walter, U., D. Wohlleben and Z. Fisk, 1986a, Z. Phys. B **62**, 325.

Walter, U., M. Loewenhaupt, W. Schlabitz and C.-K. Loong, 1986b, Phys. Rev. B **33**, 7875.

Walter, U., M. Loewenhaupt, E. Holland-Moritz and W. Schlabitz, 1987, Phys. Rev. B **36**, 1981.

Walter, U., E. Holland-Moritz, A. Severing, A. Erle, H. Schmidt and E. Zirngiebl, 1988, Physica C **153–155**, 170.

Walter, U., E. Holland-Moritz and Z. Fisk, 1991, Phys. Rev. B **43**, 320.

Walter, U., E. Holland-Moritz and U. Steigenberger, 1992, Z. Phys. B **89**, 169.

Weber, W., E. Holland-Moritz and K. Fischer, 1989a, Europhys. Lett. **8**, 257.

Weber, W., E. Holland-Moritz and A.P. Murani, 1989b, Z. Physik B **76**, 229.

Wedgwood, F.A., 1974, J. Phys. C 7, 3203.

White, R.M., 1970, Quantum Theory of Magnetism (McGraw Hill, New York). 2nd Ed.: 1983 (Springer, Berlin).

Wills, J.M., and B.R. Cooper, 1987, Phys. Rev. B **36**, 3809.

Wilson, K.G., 1975, Rev. Mod. Phys. **47**, 773.

Windsor, C.G., 1981, Pulsed Neutron Scattering (Taylor and Francis, London).

Wohlleben, D., and B.R. Coles, 1973, in: Magnetism, Vol. V., eds G. Rado and H. Suhl (Academic Press, New York) p. 3.

Wohlleben, D., J.G. Huber and M.B. Maple, 1972, AIP Conf. Proc. **5**, 1478.

Yashima, H., H. Mori, T. Satoh and K. Kohn, 1982a, Solid State Commun. **43**, 193.

Yashima, H., T. Satoh, H. Mori, D. Watanabe and T. Ohtsuka, 1982b, Solid State Commun. **41**, 1.

Zevin, V., G. Zwicknagl and P. Fulde, 1988, J. Magn. & Magn. Mater. **76–77**, 475.

Zirngiebl, E., B. Hillebrands, S. Blumenröder, G. Güntherodt, M. Loewenhaupt, J.M. Carpenter, K. Winzer and Z. Fisk, 1984, Phys. Rev. B **30**, 4052.

Zochowski, S., and K.A. McEwen, 1994, Physica B **199–200**, 416.

Zwicknagl, G., V. Zevin and P. Fulde, 1990, Physica B **163**, 577.

Handbook on the Physics and Chemistry of Rare Earths
Vol. 19 – Lanthanides/Actinides: Physics – II
edited by K.A. Gschneidner, Jr., L. Eyring, G.H. Lander and G.R. Choppin

Chapter 131

MAGNETIC CORRELATIONS IN HEAVY-FERMION SYSTEMS:
Neutron Scattering from Single Crystals

Gabriel AEPPLI
AT&T Bell Laboratories, Murray Hill, NJ 07974, USA

Collin BROHOLM
The Johns Hopkins University, Baltimore, MD 21218, USA

Contents

List of symbols and abbreviations

Å	ångstrøm (10^{-10} m)
AFM	antiferromagnet or antiferromagnetic
$\boldsymbol{a}$, $\boldsymbol{b}$, $\boldsymbol{c}$	real space Bravais lattice vectors
$\boldsymbol{a}^*$, $\boldsymbol{b}^*$, $\boldsymbol{c}^*$	reciprocal lattice vectors
c	velocity of light (3×10^8 m/s) or lattice parameter of non-cubic crystal structure
FCC	Face Centered Cubic Bravais lattice
g	Landé g-factor
GPa	unit of pressure, 1 GPa = 9.86923 kbar
$\boldsymbol{H}$	magnetic field vector
H_{c1}	lower critical field of type II superconductor
H_{c2}	upper critical field of type II superconductor
H_{10}	magnetic scattering length associated with the (10) reflection of a vortex lattice in a type II superconductor
$\hbar\omega$	energy transfer in inelastic scattering process
HFBR	High Flux Beam Reactor at Brookhaven National Laboratory
Im	imaginary part of a complex number
J	total spin and orbital angular momentum quantum number
J_{nn}, J_{nnn}	nearest neighbor and next nearest neighbor exchange interaction
J_Q	Fourier-transformed exchange interaction: $J_Q = \sum_d J_d \exp(i\boldsymbol{Q}\cdot\boldsymbol{d})$
J_{RKKY}	exchange constant for Ruderman–Kittel–Kasuya–Yosida conduction electron mediated exchange interaction
K	Kelvin, unit for temperature
k_B	Boltzmann's constant, 0.08617 meV/Kelvin
$\boldsymbol{k}_f$	final neutron wavevector
$\boldsymbol{k}_i$	incident neutron wavevector
kbar	unit of pressure: 1 kbar = 0.101325 GPa
m_q	staggered magnetization in antiferromagnet
meV	10^{-3} electronvolt (= 1.602×10^{-22} J)
$n(\omega)$	thermal population of a Bosonic excited state: $[\exp(\beta\hbar\omega)-1]^{-1}$
p_F	Fermi vector of a Fermi liquid
$\boldsymbol{Q}$	wavevector transfer $\boldsymbol{Q} = \boldsymbol{k}_i - \boldsymbol{k}_f$
r_0	prefactor in magnetic scattering cross-section: $r_0 = 0.54\times10^{-12}$ cm
Risø	Risø National Laboratory in Denmark; houses the DR3 thermal and cold neutron scattering facility
RKKY	Ruderman–Kittel–Kasuya–Yosida conduction electron mediated exchange interaction
$S(\boldsymbol{Q},\omega)$	dynamic magnetic structure factor or scattering law (Lovesey 1984)
T	tesla, unit of magnetic field
T	temperature
T_c	critical temperature of superconductor
T_F	Fermi temperature of metal
T_K	Kondo temperature
T_N	critical temperature for antiferromagnet
THz	unit of frequency or energy: 1 THz = 10^{15} s^{-1}. $2\pi\hbar\times1$ THz = 4.138 meV
β	$1/k_BT$, the inverse thermal energy
Γ	local magnetic relaxation rate
$\Gamma(\boldsymbol{Q})$	wavevector-dependent collective magnetic relaxation rate
γ	Sommerfeld coefficient (in mJ/mol K^2) of the linear term in the electronic specific heat
Δ	gap in magnetic excitation spectrum or separation in energy between two crystal-field levels
Θ_{CW}	Curie–Weiss temperature in high-temperature bulk susceptibility of the form $\chi = g\mu_{eff}^2/[3k_B(T-\Theta_{CW})]$
Θ_D	Debye temperature
λ	magnetic penetration depth in superconductor or neutron wavelength

μ_B	Bohr magneton unit of dipole moment: 9.2741×10^{-24} joule/tesla	$\chi''(\boldsymbol{Q}, \omega)$	imaginary part of the generalized complex dynamic susceptibility (Lovesey 1984)
ξ	real space magnetic correlation length or superconducting coherence length	$\chi'(\boldsymbol{Q})$	wavevector-dependent static $\omega = 0$ susceptibility
$\frac{d^2\sigma}{d\Omega\, dE}$	partial differential neutron scattering cross-section (Lovesey 1984)	$\chi_{a^*}, \chi_{c^*}, \chi_b$	shorthand notation for the diagonal components of the generalized dynamic susceptibility tensor along specific crystalline directions
χ, χ_{bulk}	bulk susceptibility	ω_p	plasma frequency of a metal
χ_0	non-interacting single-site $\omega = 0$ susceptibility	$\omega(\boldsymbol{Q})$	$\hbar\omega(\boldsymbol{Q})$ is the energy of an excitation with associated wavevector $\boldsymbol{Q}$
$\chi(\boldsymbol{Q}, \omega)$	generalized complex dynamic susceptibility (Lovesey 1984)		

1. Introduction

1.1. *General*

Heavy electron systems represent a remarkable opportunity to study solid state physics with the Fermi temperature T_F well below the Debye temperature Θ_D. As described in other chapters of this Handbook series (Vol. 10, chs. 63 and 70, Vol. 14, chs. 94, 96 and 97, Vol. 15, ch. 98, Vol. 16, chs. 105 and 106, Vol. 17, chs. 110 and 111; and this volume, chs. 130, 132 and 133) having $T_F \ll \Theta_D$ makes it possible to examine many fundamental phenomena, for example band formation, using the techniques of conventional low-temperature physics. In addition, it permits a thorough investigation of electronic correlations using thermal and cold neutron scattering, which today are much more established than the hot neutron spectroscopies required for the study of similar phenomena, if even accessible before the samples melt or decompose, in broader bandwidth materials such as transition metals. Such experiments are the subject of this chapter as well as that by Holland-Moritz and Lander, see previous chapter (130). The reader unfamiliar with neutron scattering is directed to the latter chapter for a thorough introduction to the technique and cross-section, as well as its application to powders.

The present chapter is devoted exclusively to single-crystal studies which are unique in their ability to reveal intersite correlations. Because making powders is much simpler than making the ~1 cm^3 crystals required for inelastic scattering experiments at current neutron sources, far more compounds have been studied as powders than as crystals. Indeed, to the best of our knowledge, only ten compounds have been subject to scrutiny by single-crystal neutron scattering. Table 1 lists some of the important bulk properties of the compounds. The organization of this chapter is quite simple: we discuss in successive sections experiments on the metallic Ce-based compounds $CeCu_6$, $CeRu_2Si_2$, $CeInCu_2$ and $CeInSn_2$, superconducting UPt_3 and its doped derivatives, the metallic antiferromagnet U_2Zn_{17}, the superconducting small moment antiferromagnet URu_2Si_2, the insulating antiferromagnet TmSe and the nearly insulating paramagnet CeNiSn. Holland-Moritz and Lander review the experiment of Vettier et al. (1986) on single

Table 1
Some key properties of the single crystalline heavy-fermion systems which are covered in this chapter. Numbers separated by a slash in a single column correspond to measurements along the ***a*/*b*/*c*** axis in non-cubic systems

Compound	γ (mJ/mol K^2)	$\chi(T=0)$ (10^{-3} emu/mol)	Θ_{CW} (K)	μ_{ord} (μ_B)	T_N (K)	T_c (K)
$CeCu_6$	1600[a]	15/10/100[b]	−54/−70/−8[b]	–	–	–
$CeRu_2Si_2$	385[c]	2.6/35[d]	–	–	–	–
$CeInCu_2$	1200[e]	25[f]	−30[g]	0.4[h]	2[h]	–
UPt_3	450[i]	8.55/4.46[j]	−39/−151[j]	0.02[k]	5[k]	0.43, 0.49[i]
$U(Pt_{0.95}Pd_{0.05})_3$	500[l]	14/5.9[l]	−44/−190[l]	0.6[m]	6[l]	–
$U_{0.95}Th_{0.05}Pt_3$	430[n]	13.5[n]	–	0.65[o]	7[o]	–
U_2Zn_{17}	535[p]	9[p]	−95/−130[q]	0.81[r]	9.7[r]	–
URu_2Si_2	180[s]	1.2/4.9[s]	–/−65[s]	0.04[t]	17.5[s]	0.8–1.3[s]
TmSe	350[v]	–	−133[w]	1.7[x]	3.2[x]	–
CeNiSn	200[y]	7.7/4.3/3.0[z]	–	–	–	–
$CeInSn_2$	270[aa]	8.0[ab]	−59[ab]	–	–	–

References

(a) Stewart et al. (1984a)
(b) Onuki et al. (1985)
(c) Thompson et al. (1985), Besnus et al. (1985)
(d) Flouquet et al. (1986)
(e) Najib et al. (1988a), Onuki et al. 1987, Takagi et al. (1988)
(f) Takayanagi et al. (1988)
(g) Lahiouel et al. (1987b)
(h) Kadowaki et al. (1989), Pierre et al. (1990)
(i) Stewart et al. (1984b), Hasselbach et al. (1989)
(j) Frings et al. (1983), Frings (1984)
(k) Aeppli et al. (1988a)
(l) van Sprang et al. (1987)
(m) Frings et al. (1987)
(n) Ramirez et al. (1986)
(o) Goldman et al. (1986)
(p) Ott et al. (1984)
(q) Ott and Fisk (1987)
(r) Cox et al. (1986)
(s) Palstra et al. (1985)
(t) Broholm et al. (1987b)
(u) Ramirez et al. (1991)
(v) Bucher et al. (1975), Berton et al. (1981)
(w) Batlogg et al. (1979) [high-temperature extrapolation]
(x) Bjerrum-Møller et al. (1977)
(y) Mason et al. (1992a,b)
(z) Takabatake et al. (1990)
(aa) Elenbaas et al. (1980)
(ab) Lawrence (1979)

crystals of the tenth material, $CePb_3$. The last section includes a summary of the key achievements of single-crystal neutron scattering in heavy-fermion science.

We have quite arbitrarily set a lower limit of 180 mJ/mol K^2 on the Sommerfeld constant as a criterion for inclusion of a compound for review in this article. Even so, there are other materials, most notably UN (Buyers and Holden 1985), and certain transition metal compounds (Lonzarich 1986, Moriya 1985) as well as the classic model system, liquid ^{3}He (for a review see Glyde and Svensson 1987) which show substantial, but smaller mass enhancements due to strong interactions between fermions. Not surprisingly, neutron scattering data for some of these systems bear similarities to what is found for heavy-fermion compounds. Because excellent reviews of such data have appeared elsewhere, we will not describe them here. However, for the reader's convenience and as a basis for discussion and comparison below, we reproduce in fig. 1 the dynamical structure factor $S(\boldsymbol{Q}, \omega)$, directly proportional to the magnetic scattering cross-section, for a Fermi liquid with a spherical Fermi surface of radius p_F (Pines and Nozières 1966). Figure 2 shows

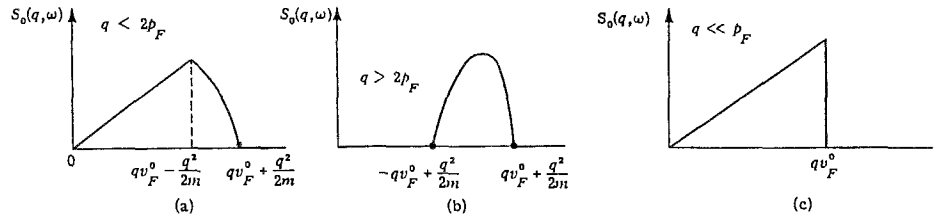

Fig. 1. Dynamical structure factor $S(\boldsymbol{Q}, \omega)$ for non-interacting Fermi liquid. (From Pines and Nozières 1966.)

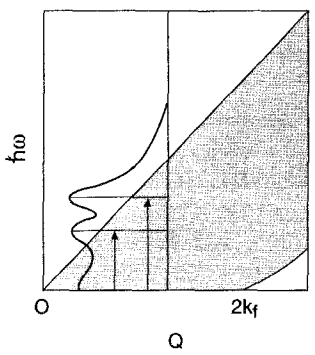

Fig. 2. Electron–hole pair continuum for Fermi liquid with crystal-field levels for local moments superposed. When the Kondo coupling is strong, there will be considerable admixture of the crystal-field and electron–hole pair excitations, resulting in a broadening or even elimination of sharp features in the local moment density of states.

the region in $\boldsymbol{Q}$–ω space where $S(\boldsymbol{Q}, \omega) \neq 0$. Especially noteworthy is the absence of scattering when $Q \to 0$, and for small ω when $Q > 2p_F$. The heavy-fermion problem arises when such an electron–hole pair continuum is made to overlap with the excitations of a lattice of local moments, whose crystal-field levels are indicated schematically by the horizontal lines drawn across the figure.

1.2. *Related experiments and theory*

In this chapter we do not describe the theory potentially applicable to single-crystal neutron data because it is the subject of Handbook chapters by Norman and Koelling and by Liu (Vol. 17, chs. 110 and 111, respectively). Scattering overlaps with and complements two other techniques sensitive to microscopic magnetic correlations. The techniques are nuclear resonance (NMR) and muon spin relaxation (μ^+SR) spectroscopies whose applications to heavy-fermion materials are reviewed by Nakamura et al. (1988) (NMR) and Barth et al. (1988) and Schenck (1992) (μ^+SR). Finally, there have by now been nearly countless general reviews of experiments and theory on heavy-fermion systems, many of which have appeared in this Handbook series (Vol. 10, chs. 63 and 70, Vol. 14, chs. 94, 96 and 97, Vol. 15, ch. 98, Vol. 16, chs. 105 and 106, Vol. 17, chs. 110 and 111; and this volume, chs. 130, 132 and 133). For a recent pedagogical introduction, the reader can consult the book by Hewson (1993).

2. Metallic and mainly paramagnetic Ce compounds

2.1. *Introduction and $CeCu_6$*

Superficially, $CeCu_6$ and $CeRu_2Si_2$ are quite different. The former has a complicated monoclinic crystal structure and one of the highest Sommerfeld coefficients ($\gamma = 1600\,\mathrm{mJ/mol\,K^2}$ (Stewart et al. 1984a) ever reported, while the latter crystallizes in the same tetragonal and relatively simple structure as $CeCu_2Si_2$ and URu_2Si_2 (space group I4/mmm) and has relatively modest $\gamma = 385\,\mathrm{mJ/mol\,K^2}$ (Thompson et al. 1985, Besnus et al. 1985).

In spite of these differences, both systems are Ising-like, with the magnetic response largest along the $\boldsymbol{c}$-axis, and the characteristic temperatures and magnetic fields deduced from bulk measurements appear to scale with γ. For example the T^2 behavior of the resistivity, commonly associated with the Fermi liquid regime, sets in below 0.25 K and 1 K in $CeCu_6$ and $CeRu_2Si_2$, respectively (Onuki et al. 1984, Haen et al. 1987, Sumiyama et al. 1985, Penney et al. 1986). Beyond basic energy scales different by a factor of four, the properties of $CeCu_6$ and $CeRu_2Si_2$ are the same, a result remarkable in view of the very different structures of the two materials.

An important feature which these materials share not only with each other but essentially all ordered (stoichiometric) heavy-fermion materials is that bulk measurements yield characteristic temperatures and fields low compared to the Fermi temperatures one would associate with the Sommerfeld constants. In other words, different measurements yield different energy scales. The first inelastic neutron scattering experiments (Aeppli et al. 1986) to be performed on single-crystal $CeCu_6$ (and indeed on any single-crystal heavy-fermion material not ultimately magnetic) immediately showed why this is the case: the magnetic response is very $\boldsymbol{Q}$-dependent. Given that different bulk properties represent different averages over reciprocal space, they will have different field and temperature dependences in as much as $\chi''(\boldsymbol{Q}, \omega)$ depends differently on field and temperature at different values of $\boldsymbol{Q}$. Figure 3 reproduces the original data, collected as constant-$\boldsymbol{Q}$ scans for two different values of $\boldsymbol{Q}$ along the $\boldsymbol{a}^*$ direction. In addition to the resolution-limited nuclear incoherent scattering at $\hbar\omega = 0$, there is inelastic continuum scattering which increases with decreasing energy transfer and also is largest for $\boldsymbol{Q}$ near (1, 0, 0). A field of $H = 6.4\,\mathrm{T}$ along the $\boldsymbol{c}$-axis greatly reduces the magnetic scattering, but does not yield resonances of the type one might associate with Zeeman-split bands or local moment doublets ($g\mu_B H = 0.74\,\mathrm{meV}$ for $g = 2$). The single (imaginary)-pole approximation to the dynamical susceptibility,

$$\chi(\boldsymbol{Q}, \omega) = \chi'(\boldsymbol{Q}) \frac{\Gamma(\boldsymbol{Q})}{\Gamma(\boldsymbol{Q}) - \mathrm{i}\omega}, \tag{2.1}$$

together with the cross-section,

$$\frac{\mathrm{d}^2\sigma}{\mathrm{d}\Omega\,\mathrm{d}E} = \frac{r_0^2}{\pi} \frac{k_f}{k_i} \frac{1}{1 - \mathrm{e}^{-\beta\hbar\omega}} \chi''(\boldsymbol{Q}, \omega), \tag{2.2}$$

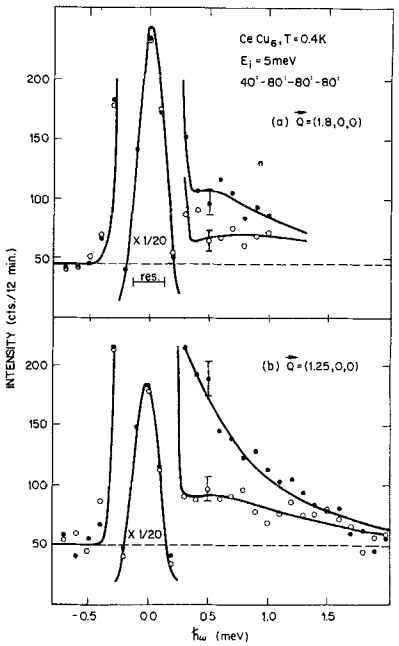

Fig. 3. Constant-$\boldsymbol{Q}$ energy spectra for $CeCu_6$ at $T = 0.4$ K in zero (solid circles) and 6.4 T (open circles) applied fields. Orthorhombic notation is used to label points in reciprocal space. (From Aeppli et al. 1986.)

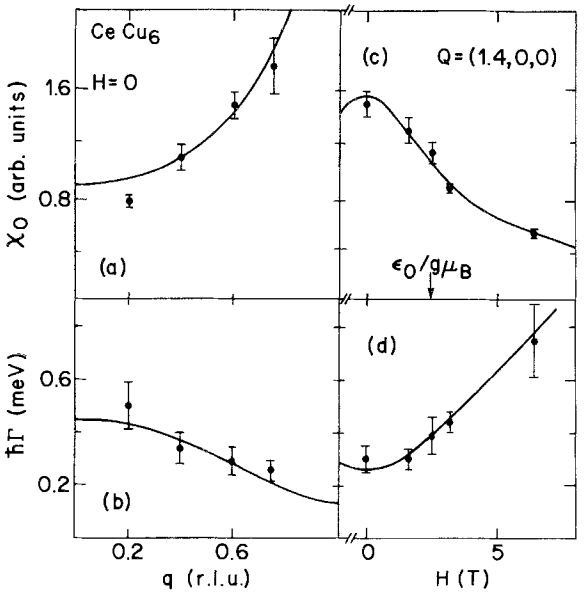

Fig. 4. Dependence of $\hbar\Gamma(\boldsymbol{Q})$ and $\chi'(\boldsymbol{Q})$ ($\equiv\chi_0$ in figure) for $CeCu_6$ on reduced momentum $\boldsymbol{Q} = (2-q, 0, 0)$, for $T = 0.4$ K and $H = 0$ (a, b) and on H for $T = 0.4$ K and $\boldsymbol{Q} = (1.4, 0, 0)$. (From Aeppli et al. 1986.)

corrected for resolution effects, gives an excellent description of all of the data, both for different momentum transfers $\boldsymbol{Q}$ and different fields H. Equation (2.1) corresponds to choosing a Lorentzian spectral weight function with half width at half maximum $\Gamma(\boldsymbol{Q})$. The solid lines in fig. 3 and the parameter values $\chi'(\boldsymbol{Q})$ and $\Gamma(\boldsymbol{Q})$ shown in fig. 4 correspond to the best fits of eqs. (2.1) and (2.2) to various constant-$\boldsymbol{Q}$ scans.

In agreement with direct inspection of the data, $\chi'(\boldsymbol{Q})$ is largest for $\boldsymbol{Q}$ near $(1, 0, 0)$ and $H = 0$, while the converse obtains for the energy scale $\hbar\Gamma(\boldsymbol{Q})$. Furthermore, $\hbar\Gamma(\boldsymbol{Q})$ and $\chi'(\boldsymbol{Q})$ vary in such a way that the product $\chi'(\boldsymbol{Q})\Gamma(\boldsymbol{Q})$ is roughly $\boldsymbol{Q}$- and H-independent. Given that eq. (2.1) describes the magnetic response, this result is equivalent to finding that $\chi''(\boldsymbol{Q}, \omega)$ is $\boldsymbol{Q}$- and H-independent at sufficiently large ω, which is also consistent with the raw data, but in complete disagreement with what is expected for a single-component Fermi liquid (see figs. 1, 2). Thus, in addition to giving a natural explanation for the many anomalous bulk properties of $CeCu_6$ in terms of the onset of antiferromagnetic correlations, the original single-crystal neutron data showed that a simple Fermi liquid response could not account for the magnetic susceptibility of $CeCu_6$. Thus the coherent quasiparticles responsible for the de Haas van Alpen oscillations found by Springford and Reinders (1988) yield a very small fraction of χ. At the same time, a

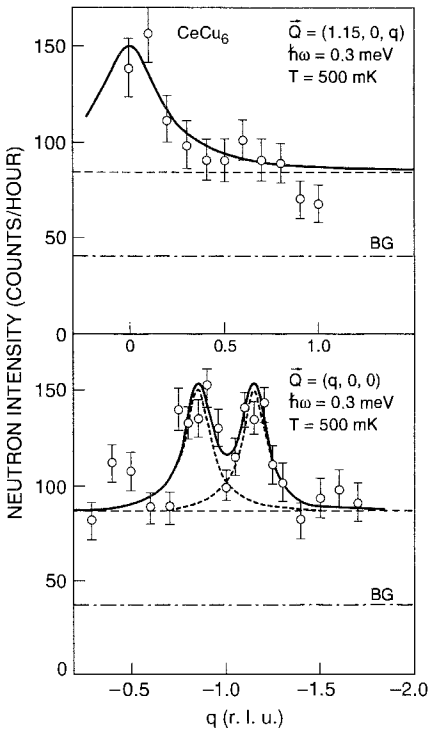

Fig. 5. Constant $\hbar\omega = 0.3$ meV scans along (0 0 l) and (1 0 0) for $CeCu_6$. Monoclinic notation is used to label points in reciprocal space. (From Rossat-Mignod et al. 1988.)

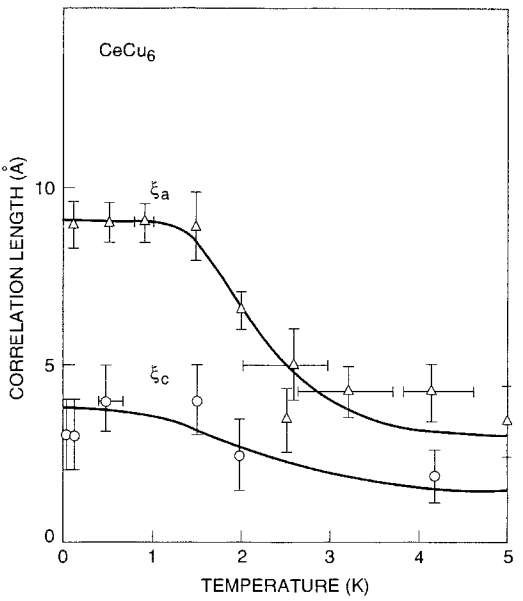

Fig. 6. Temperature dependence of magnetic correlation lengths along *a* and *c* in $CeCu_6$. (From Rossat-Mignod et al. 1988.)

local moment picture which would give rise to well-defined excitons in a zero-temperature paramagnet and Zeeman split levels in an external field is also inapplicable.

Subsequent experiments on $CeCu_6$ by Regnault et al. (1987), Regnault et al. (1988b) and Rossat-Mignod et al. (1988) verified these conclusions, most notably the commensurate peak at $(1,0,0)$, and provided much greater detail on the nature of the antiferromagnetic correlations. Unlike Aeppli et al. (1986) who use orthorhombic notation, Regnault et al. and Rossat-Mignod et al. use monoclinic notation to label points in reciprocal space. Figure 5 shows their most interesting finding, namely a second set of peaks in the $\boldsymbol{Q}$-dependent magnetic fluctuations. They occur at the incommensurate orthorhombic $(0, \pm 1 \pm 0.15, 0)$ points. Because the peak is sharper in the monoclinic $(q_x, 0, 0)$ [=orthorhombic $(0, q_x, 0)$] than in the $(1.15, 0, q_z)$ [=orthorhombic $(q_z, 1.15, 0)$] scan, the magnetic correlations are quite anisotropic, extending approximately twice as far along (monoclinic) $\boldsymbol{a}$ as along $\boldsymbol{c}$. Figure 6 demonstrates the pronounced evolution in the correlation length along $\boldsymbol{a}$ for $1.5 < T < 3$ K.

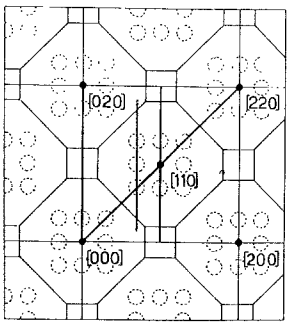

Fig. 7. The $(h, k, 0)$ zone for $CeRu_2Si_2$. Magnetic scattering is peaked in the dashed circles, whose radii correspond to the half-width-at-half-maxima of the peaks. Regnault et al. 1988a investigated the magnetic scattering along the solid lines. (From Regnault et al. 1988a.)

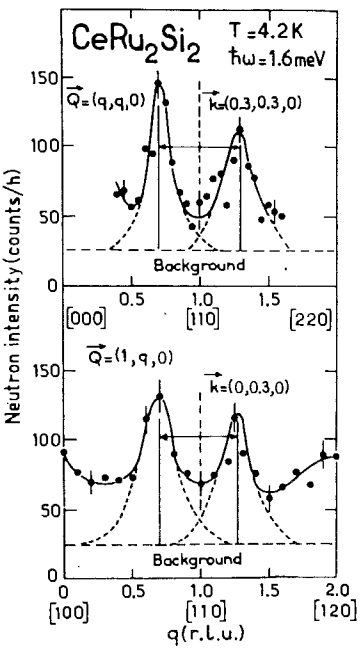

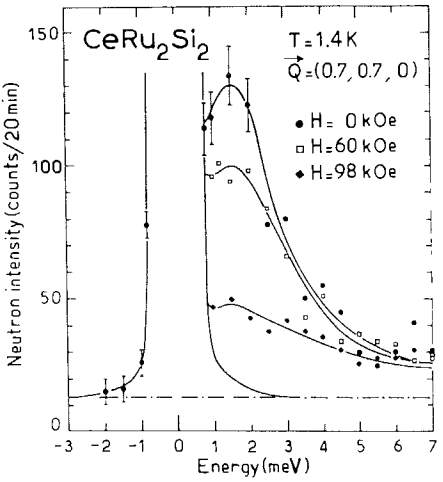

Fig. 9. Constant $\boldsymbol{Q} = (0.7, 0.7, 0)$ scans for several magnetic fields applied along (0 0 1) in $CeRu_2Si_2$. (From Rossat-Mignod et al. 1988.)

Fig. 8. Constant $\hbar\omega = 1.6$ meV scans for $CeRu_2Si_2$ (From Regnault et al. 1988a.)

2.2. *$CeRu_2Si_2$*

Experiments on $CeRu_2Si_2$ (Regnault et al. 1988a, Rossat-Mignod et al. 1988) yield very similar results. Figure 7 gives the locations in the $\boldsymbol{a}^*$–$\boldsymbol{b}^*$ plane of peaks in the inelastic scattering, while fig. 8 shows representative constant-$\hbar\omega$ scans revealing the peaks, which turn out to have roughly the same width as those in $CeCu_6$. In analogy with fig. 3, fig. 9 presents a series of constant-$\boldsymbol{Q}$ scans for different applied fields. Again, there is a suppression of the low frequency response, while at high ω the scattering is essentially field-independent. However, there is one small but nonetheless noticeable difference between the data for $CeCu_6$ and $CeRu_2Si_2$. This has to do with the adequacy of the simple

form (2.1) as a representation of the data. In particular, eq. (2.1) implies that the position of the maximum and high frequency half-width of $\chi''(\boldsymbol{Q}, \omega) = \omega\Gamma(\boldsymbol{Q})/[\omega^2 + \Gamma^2(\boldsymbol{Q})]$ $[\approx \mathrm{d}^2\sigma/(\mathrm{d}\Omega\,\mathrm{d}E)]$ for the measured temperatures and frequencies in figs. 3 and 9 scale together. While consistent with the data for $CeCu_6$, where a flat $\chi''(\boldsymbol{Q}, \omega)$ emerges at ~0.5 meV for $H = 6.4$ T, such scaling is not found for $CeRu_2Si_2$, where the position of the flat portion of $\chi''(\boldsymbol{Q}, \omega)$ remains fixed at ~2 meV, even though the signal has broadened considerably on the high ω side of the maximum. Unfortunately, due to the incoherent scattering it is impossible to determine $\chi''(\boldsymbol{Q}, \omega)$ in the region below its flat maximum. Thus, it is not known whether there is a gap ($\chi''(\boldsymbol{Q}, \omega) = 0$ for $\hbar\omega < \Delta$) or even a frequency-independent response for $\hbar\omega < 1$ meV. We emphasize, however, that given that we are dealing with a metal, it is unlikely that $\chi''(\boldsymbol{Q}, \omega)$ should be zero for any non-zero ω. The best one has done so far is to introduce an additional parameter and generalize eq. (2.1) to

$$\chi(\boldsymbol{Q}, \omega) = \chi'(\boldsymbol{Q})\frac{1}{2}\left\{\frac{\Gamma(\boldsymbol{Q}) - \mathrm{i}\omega(\boldsymbol{Q})}{\Gamma(\boldsymbol{Q}) - \mathrm{i}(\omega + \omega(\boldsymbol{Q}))} + \frac{\Gamma(\boldsymbol{Q}) + \mathrm{i}\omega(\boldsymbol{Q})}{\Gamma(\boldsymbol{Q}) - \mathrm{i}[\omega - \omega(\boldsymbol{Q})]}\right\}, \tag{2.3}$$

a form suitable for a damped excitation at energy $\hbar\omega(\boldsymbol{Q})$. The result (Regnault et al. 1988a) of fitting eq. (2.3) to the data is that $\hbar\omega(\boldsymbol{Q}) = 1.2 \pm 0.2$ meV and $\hbar\Gamma(\boldsymbol{Q}) = 1.2 \pm 0.2$ meV for $\boldsymbol{Q}$=(0.7, 0.7, 0), i.e., the mode is critically damped.

2.3. *Magnetic order in (Ce, La)Ru_2(Si, Ge)$_2$, Ce(Cu, Au)$_6$ and $NpRu_2Si_2$*

The inelastic scattering measurements on $CeCu_6$ and $CeRu_2Si_2$ clearly demonstrate that both of these compounds are close to antiferromagnetic instabilities. This suggests that alloying studies, where long-range magnetic order could appear at compositions beyond a critical value, might be fruitful. Neutron scattering studies (Quezel et al. 1988, Regnault et al. 1990a, Mignot et al. 1990, Mignot et al. 1991) of single crystals of $(Ce, La)Ru_2(Si, Ge)_2$ have indeed identified such order. Figure 10 shows the magnetic phase diagram for $Ce_{1-x}La_xRu_2Si_2$, as well as the x-dependent ordered moment (Quezel et al. 1988). The magnetic structure is incommensurate, with wavevectors of the type $\boldsymbol{q} = (k, 0, 0)$, which with k fixed at 0.309 ± 0.002, is independent of x. Also, as can be seen from fig. 7, the incommensurate fluctuations in pure paramagnetic $CeRu_2Si_2$ peak at the same wavevectors. These fluctuations also peak at wavevectors of the type $(k,k,0)$, which are not the locations of magnetic Bragg peaks in the doped samples for zero applied field. However, they can be induced by an external field.

One might imagine that disturbing the Ce and ligand sublattices might yield different magnetic behaviors. Experiments on $CeRu_2Ge_xSi_{2-x}$ show this not to be the case (Mignot et al. 1991). Exactly the same magnetic structure is found, as well as an elaborate field–temperature phase diagram. From comparison of the La and Ge dilution series, it appears that the variable controlling the presence of order is the lattice constant and not the type of impurity.

In addition to the many papers on elastic diffraction from alloys based on $CeRu_2Si_2$, there are also reports (Regnault et al. 1990a, Regnault et al. 1990b, Jacoud et al. 1992) on

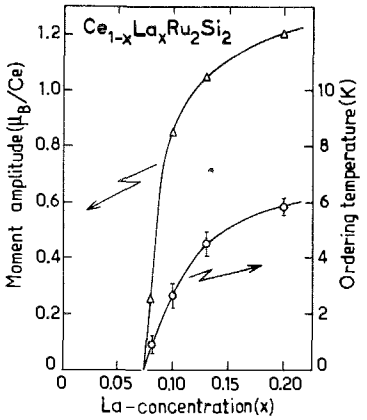

Fig. 10. Néel temperature and ordered moment versus x in $Ce_{1-x}La_xRu_2Si_2$ at atmospheric pressure. (From Quezel et al. 1988.)

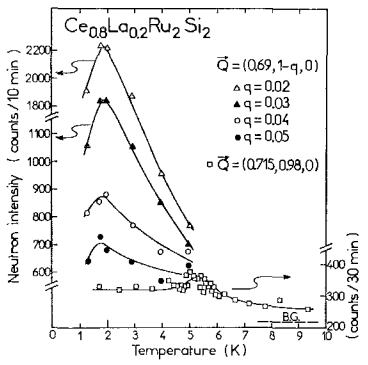

Fig. 11. Quasielastic neutron scattering intensities at wavevectors offset to varying degrees from the ordering vector (0.695, 1, 0) for $Ce_{0.8}La_{0.2}Ru_2Si_2$. (From Regnault et al. 1990b.)

magnetic fluctuations. The fluctuations, observed by quasielastic scattering (see fig. 11) where the energy transfer is nominally zero and $\boldsymbol{Q}$ is offset slightly from a magnetic Bragg peak, persist below T_N and have profiles which become narrower as $T \to 0$ rather than becoming infinitely narrow at T_N. The extent to which they are intrinsic to disordered antiferromagnets, derived from domain wall scattering (their correlation length becomes large only as the spin density wave acquires higher harmonics and "squares up"), or due to compositional inhomogeneities is unknown.

Much less effort has been devoted to derivatives of $CeCu_6$ than to those of $CeRu_2Si_2$. However, the one single-crystal experiment performed so far indicates that $CeCu_6$ is a more complicated system. Specifically, Schröder et al. 1994 have found an ordering vector $\boldsymbol{Q} = (\pm 0.59, 0, 0)$ (orthorhombic notation where $a = 8.16$ Å, $b = 5.067$ Å, $c = 10.24$ Å) and temperature $T_N = 1$ K for one single crystal of $CeCu_{5.5}Au_{0.5}$. This vector is not obviously related to the (orthorhombic) vectors $\boldsymbol{Q} = (0, 0.15, 0)$ and $(1, 0, 0)$ at which the $\hbar\omega = 0.3$ meV scattering peaks in pure $CeCu_6$.

We conclude this section by noting that a single-crystal diffraction experiment (Bonnisseau et al. 1988) on $NpRu_2Si_2$, isostructural with $CeRu_2Si_2$ and URu_2Si_2, displayed incommensurate magnetic order with a Néel temperature of 25.2 K. The ordered moment at $T = 1.3$ K is $1.6\mu_B$/Np and the ordering vector changes continuously from $(0, 0, 0.76)$ to $(0, 0, 0.865)$ on cooling from T_N to 1.3 K.

2.4. *$CeInCu_2$*

Apart from being extremely heavy ($\gamma = 1200$ mJ/mol K^2, Najib et al. 1988a, Onuki et al. 1987, Takagi et al. 1988), $CeInCu_2$ with the Fm3m Heusler structure deserves attention because of potential magnetic frustration in the face centered cubic cerium

lattice. Strong hybridization between 4f and conduction electrons is already apparent from the anomalously small room temperature unit cell ($a = 6.784$Å compared to $a = 6.849$Å for $LaInCu_2$). In addition, the non-phonon resistivity shows classical heavy-fermion behavior increasing upon cooling from room temperature to a maximum at $T_{max} = 10$ K before settling into low temperature T^2 behavior (Najib et al. 1988b). Simple one-parameter Kondo behavior is not obtained even in dilute alloys because of the varying degeneracy resulting from the 98 K splitting between a Γ_7 doublet and a Γ_8 excited crystal-field level (Najib et al. 1988a). Nevertheless Najib et al. quote a Kondo temperature $T_K = 3$–6 K deduced, for example, from the width of the quasielastic magnetic neutron scattering in polycrystalline samples. In contrast to $CeCu_6$ and $CeRu_2Si_2$, where a cross-over to positive magnetoresistance for $T < T_K/5$ marks the development of a coherent heavy-fermion ground state, the magnetoresistance of $CeInCu_2$ remains negative as for a local moment paramagnet to the lowest temperatures. However, the application of pressure increases T_K and induces a cross-over to positive magnetoresistance at around 1 GPa for $T = 4.2$ K (Kagayama et al. 1991, Kagayama et al. 1992).

As for all other heavy-fermion systems, $CeInCu_2$ is close to an antiferromagnetic instability. This was discovered in studies of the dilution series $CeInAg_{2-x}Cu_x$ (Lahiouel et al. 1987b). The end compound, $CeInAg_2$, is a type I FCC antiferromagnet ($T_N = 2.7$ K) in which ferromagnetic $(1,0,0)$ planes with spins oriented along the $(1,0,0)$ direction are stacked antiferromagnetically along $(1,0,0)$. The volume of the unit cell is substantially larger for $CeInAg_2$ than for $CeInCu_2$ ($a(CeInAg_2) = 7.108$Å compared to $a(CeInCu_2) = 6.784$Å). This, as well as the smaller absolute value of the Curie–Weiss temperature ($\Theta_{CW}(CeInAg_2) = -9$ K, $\Theta_{CW}(CeInCu_2) = -30$ K) and the much smaller Γ_7–Γ_8 crystal-field splitting ($\Delta(CeInAg_2) = 18$ K, $\Delta(CeInCu_2) = 98$ K), indicates that the 4f states in $CeInAg_2$ are less hybridized with the conduction electrons than those in $CeInCu_2$. As x is increased and the solid solution approaches the $CeInCu_2$ heavy-fermion limit there is a monotonic rise in $|\Theta_{CW}|$. Initially T_N also rises but it goes through a maximum at $x = 1.5$ followed by a decrease as $x \to 2$. Anomalies in resistance and susceptibility become less pronounced in this limit and it appears from such measurements that $CeInCu_2$ does not order. However, specific heat does show a broad peak at 2.3 K (Najib et al. 1988a, Onuki et al. 1987, Takagi et al. 1988), and copper and indium Nuclear Magnetic Resonance (Takagi et al. 1988, Nakamura et al. 1988) reveal that static internal magnetization develops in that temperature range. Magnetic neutron scattering from single crystals subsequently showed that short-range order similar to the type I long-range order of $CeInAg_2$ develops for $T < 2$ K (Kadowaki et al. 1989). In this experiment, the incident neutron energy was 13.7 meV and there was no energy analysis of the outgoing neutrons (see also Pierre et al. 1990). The corresponding staggered magnetization is $0.40 \pm 0.07 \mu_B$, about half of the full moment of the Γ_7 doublet ($0.71 \mu_B$). The correlation length is anisotropic with respect to the $(1,0,0)$ direction in which the magnetization density is modulated: $\xi_{\parallel} = 48 \pm 3$Å $= 7.1a$ and $\xi_{\perp} = 13.4 \pm 0.7$Å $= 2.0a$. Both the magnetic correlation length and the moment may be strongly dependent on the degree of random cerium–indium site mixing, leading also to large residual resistivity, typically 50 μΩ cm (Lahiouel et al. 1987b). Even so, the type of short-range order

indicates strong antiferromagnetic nearest-neighbor exchange coupling. It is thus likely that frustration in the face centered cubic latticc plays a role in suppressing ordinary antiferromagnetic order.

2.5. *$CeInSn_2$*

$CeIn_{3-x}Sn_x$ is an isostructural Cu_3Au type alloy series extending from the mixed-valent paramagnet $CeSn_3$ to the reduced moment antiferromagnet $CeIn_3$. For the latter, the ordered moment is $0.5\mu_B$/Ce, the propagation vector is of the (0.5, 0.5, 0.5) variety, and the Néel temperature is 10 K (Benoit et al. 1980, Lawrence and Shapiro 1980). On increasing x beyond 0.4, the magnetic order is lost, and the compound becomes a moderately "heavy" paramagnet, achieving a maximum Sommerfeld constant of 270 mJ/mol K^2 for $x \approx 2$ ($CeInSn_2$), which is substantially larger than the value of 50 mJ/mol K^2 for $CeSn_3$ (Elenbaas et al. 1980, Murani 1987). Murani and coworkers (1990) have used triple-axis inelastic neutron scattering spectroscopy to examine a single crystal of $CeInSn_2$. They find magnetic scattering describable using eq. (2.1) with $\hbar\Gamma(\boldsymbol{Q}) = 8 \pm 1$ meV for $\boldsymbol{Q} = (1.5, 0, 0)$ and $(0, 1.1, 1.1)$. In addition, constant-E scans at 25 meV, which is substantially larger than 8 meV, reveal that the magnetic response is $\boldsymbol{Q}$-dependent with possible maxima at $(1.5, 0, 0)$ and $(1.25, 1.25, 0)$.

3. Superconducting UPt_3 and its derivatives $(U, Th)(Pt, Pd)_3$

3.1. *Preliminaries*

UPt_3 ($\gamma = 450$ mJ/mol K^2) is the most studied heavy-fermion system, both because of the availability of large single crystals and its unusual superconductivity, with an onset at $T_c \approx 0.5$ K. The most important properties of this compound are

(1) The ^{3}He-like normal state specific heat (Stewart et al. 1984b).
(2) De Haas–van Alphen oscillations corresponding to heavy mass quasiparticles with long mean free paths (Taillefer and Lonzarich 1988).
(3) Magnetic susceptibility and other thermodynamic data indicating a relatively sharp cross-over between low-temperature, low-field and high-temperature, high-field regimes of undefined character (Frings and Franse 1985).
(4) The rapid suppression of superconductivity and appearance of a well-defined transition at $T \approx 6$–7 K on substitution of Pt by Pd or U by Th at the few percent level (Ramirez et al. 1986, de Visser et al. 1986, Stewart et al. 1986).
(5) Multiple superconducting phases, as evidenced by ultrasound, torsional oscillator, and specific heat data (Kleiman et al. 1989, Müller et al. 1987, Schenstrom et al. 1989, Fisher et al. 1989, Hasselbach et al. 1989).
(6) Experiments showing that two quantities, namely ultrasonic attenuation (Shivaram et al. 1986, Schmitt-Rink et al. 1986) and magnetic penetration lengths (Broholm et al. 1990), display anisotropic temperature dependences below T_c. Fevcrish

activity (Goss-Levi 1993) on the high-T_c cuprates notwithstanding, UPt_3 remains the one superconductor for which such anisotropies have been seen. Remarkably, only these experiments, among the many bulk measurements performed on UPt_3, have addressed the anisotropy of the superconducting state. More recently, the microscopic techniques of electron tunneling (Goll et al. 1993) and small angle neutron diffraction (Kleiman et al. 1992) (to be described below) have revealed an anisotropic superconducting state of the type deduced from the magnetic penetration depth and ultrasonic attenuation data.

Magnetic neutron scattering has played an important role both in uncovering new phenomena in UPt_3 as well as accounting for many of the unusual properties found in other experiments. Indeed, for each of the above properties (1)–(6), neutron scattering data have provided essential complementary information, if not an explanation. In addition, and most significantly, neutron scattering revealed the strong antiferromagnetic fluctuations most favored as the origin of the unusual superconductivity in UPt_3 (Miyake et al. 1986, Scalapino et al. 1986, Béal-Monod et al. 1986, Hirsch 1985, Norman and Koelling 1993).

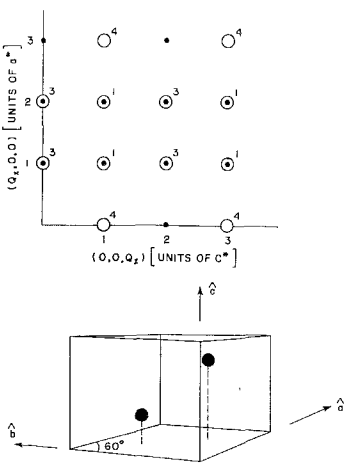

Fig. 12. The (h 0 l) zone (upper frame) and real space unit cell (lower frame) for UPt_3. Nuclear Bragg peaks are located at the solid vertices, while open circles and numbers represent positions and relative intensities expected for magnetic order of the type shown in fig. 15a. (From Goldman et al. 1987.)

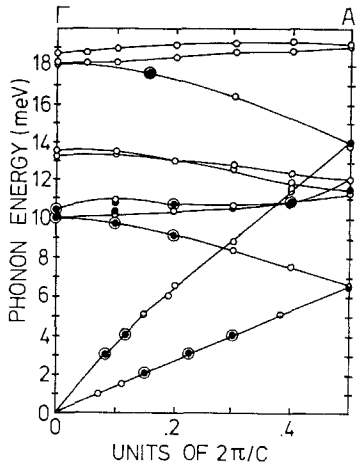

Fig. 13. Dispersion along c^* for selected phonons in UPt_3 at 300 K (open circles) and 10 K (closed circles). (From Renker et al. 1987.)

3.2. *Structure and phonons*

UPt_3 has the double hexagonal close packed structure (space group $P6_3/mmc$) with two uranium atoms per unit cell, at the positions $(\frac{1}{3}, \frac{2}{3}, \frac{1}{4})$ and $(\frac{2}{3}, \frac{1}{3}, \frac{3}{4})$. The lattice constants

are $a = 5.752$ Å and $c = 4.889$ Å, which implies that each U atom is surrounded by a triangle of nearest neighbors (at a distance of 4.124 Å) in each of the two adjacent hexagonal basal planes (Heal and Williams 1955). Figure 12 gives the locations of the U atoms in the real lattice of UPt_3, and also shows the $(h, 0, l)$ plane of reciprocal space. Throughout this chapter, the wavevectors $\boldsymbol{Q} = (Q_x, Q_y, Q_z)$ are written in hexagonal coordinates, with Q_x and Q_y in units of $a^* = b^* = 4\pi/(a\sqrt{3}) = 1.261$ Å^{-1} and Q_z in units of $c^* = 2\pi/c = 1.285$ Å^{-1}. Renker et al. (1987) have reported the phonon dispersion curves shown in fig. 13. The frequencies of the measured phonons do not change on cooling from 300 to 10 K. However, it is possible (Loidl et al. 1988) that cooling below 20 K may slightly decrease the lifetimes of transverse acoustic phonons propagating along $\boldsymbol{c}^*$. Based on the published scans, this interesting result depends on the choice of background, and therefore deserves further investigation.

3.3. *Medium energy fluctuations*

Figure 14 shows some constant $\hbar\omega = 8$ meV scans taken at 1.2 K using unpolarized thermal three-axis instruments at the Brookhaven High Flux Beam Reactor (HFBR) (Goldman et al. 1987). The key conclusions are that the magnetic continuum scattering seen here (the phonons yield sharp peaks marked by dashed lines) has maxima at the points $(0,0,1)$, $(0,0,3)$, and $(\pm 1, 0, 2)$, and an obvious minimum at $(0,0,2)$. Thus, on the 5×10^{-13} second time scale corresponding to 8 meV, each U moment is correlated antiferromagnetically with its six nearest neighbors, as illustrated in fig. 15a.

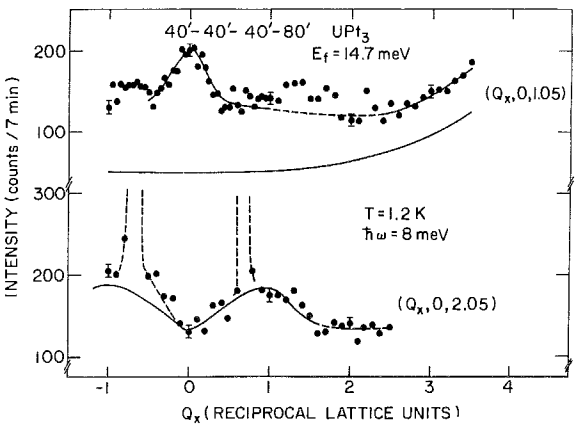

Fig. 14. Constant $\hbar\omega = 8$ meV scans for UPt_3 at $T = 1.2$ K. Solid lines through data are guides to the eye; the solid line below the data in (a) represents estimated multiphonon scattering. Dashed lines departing in the vertical direction in (b) correspond to phonons. (From Goldman et al. 1987.)

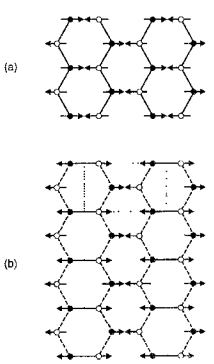

Fig. 15. Schematics of (a) magnetic short-range order accounting for high-frequency ($\hbar\omega \approx 8$ meV), and (b) intermediate-range (~200 Å) static order in nominally pure UPt_3, as well as conventional long-range order in $(U_{1-x}Th_x)(Pt, Pd)_3$. (Adapted from Goldman et al. 1986.)

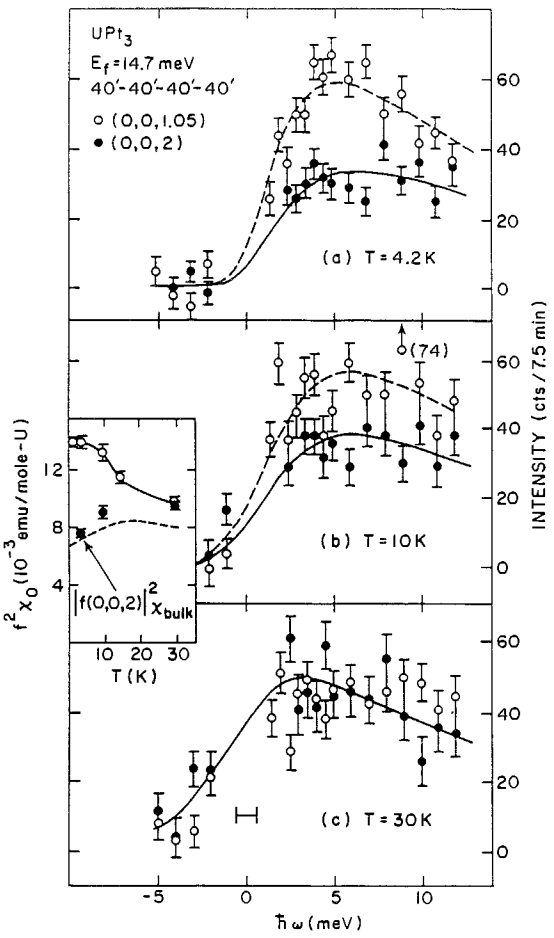

Fig. 16. Constant-$\boldsymbol{Q}$ scans near zone centers, with [$\boldsymbol{Q}$ = (0 0 2)] and without [$\boldsymbol{Q}$ = (0 0 1)] allowed nuclear Bragg spots. Solid lines correspond to eq. (2.1) with parameters chosen for best fit to data. The inset shows how the real $\omega = 0$ susceptibility, as deduced from scattering data, varies with temperature for the two momentum transfers probed; the dashed line represents bulk ($\boldsymbol{Q} = 0$) susceptibility. (From Aeppli et al. 1987.)

Energy scans (see fig. 16) near the wavevectors (0, 0, 2) and (0, 0, 1.05) where $\chi''(\boldsymbol{Q}, \omega)$ reaches its minimum and maximum, respectively, also contain important information (Aeppli et al. 1987). Firstly, they demonstrate the continuum nature of $\chi''(\boldsymbol{Q}, \omega)$. The quasielastic form, eq. (2.1), corrected for resolution effects, gives a good description of the data. At low T and $\boldsymbol{Q}$ = (0, 0, 1.05) one has $\hbar\Gamma(\boldsymbol{Q}) = 5$ meV, which is twenty times larger than the corresponding rate for $CeCu_6$, with its five times larger Sommerfeld constant. Another interesting result is that at $\boldsymbol{Q}$ = (0, 0, 2) the magnetic response does not vanish below some well-defined pseudogap associated with the interband transitions of typical mean field treatments of the heavy-fermion problem. Such a gap should be especially obvious at the zone center, (0, 0, 2), where intraband Fermi liquid contributions to $S(\boldsymbol{Q}, \omega)$ should disappear. One might question whether at frequencies lower than those reached at the (0, 0, 2) Bragg point, there might be a cross-over to the gapped spectrum given by the

mean field theories. We find this possible, but improbable, given that the Kramers–Kronig transform of our data yields a value for the zero frequency real susceptibility, $\chi'(\boldsymbol{Q} = 0)$ in eq. (2.1), very close to the bulk result, χ_{bulk}, thus implying that an inelastic continuum and not the heavy band seen in the de Haas–van Alphen measurements (Taillefer and Lonzarich 1988) accounts in large measure for the enhanced low-temperature limit of χ_{bulk} in UPt_3. The conclusion is that as for $CeCu_6$, a simple Fermi liquid description, even with corrections for interband transitions, has serious difficulties. The most obvious explanation for this involves the novel physics of the two-impurity Kondo effect (see, e.g., Jones and Varma 1987, Abrahams and Varma 1987, and Sire et al. 1993). Even so, there are claims that a more conventional understanding is also possible. One approach treats the correlations in a $1/N$ approximation and assumes a simple cubic tight-binding model for the band structure (Auerbach et al. 1987, 1988). The second is to simply calculate $\chi(\boldsymbol{Q}, \omega)$ using conventional band theory for UPt_3 (Norman and Koelling 1993). Given the assumptions, neither approach yields an outcome which can be compared in detail to experiments, and so it is not surprising that neither accounts for the data.

Figure 16 also shows how the spectra at $(0, 0, 1.05)$ and $(0, 0, 2)$ evolve with rising temperature. The inset gives the temperature dependences of the corresponding real susceptibilities at $\omega = 0$, obtained from eq. (2.1) and a phonon-based absolute unit conversion; the dashed line represents χ_{bulk} (Frings and Franse 1985) multiplied by the square of the ionic form factor at $\boldsymbol{Q} = (0, 0, 2)$. From these results, it is very clear that the bulk susceptibility maximum at $T_{\max} = 18\,\text{K}$ coincides with the almost order parameter-like onset of short-range antiferromagnetic correlations, thus providing a microscopic understanding not only of the maximum, but also of the entire "metamagnetic" line (Frings and Franse 1985) in the H–T plane, terminating at $H = 0$ and $T_{\max} = 18\,\text{K}$. Another interesting aspect of the data is that on warming from 4.2 to 30 K, the substantial difference between the spectra vanishes to energies considerably larger than $2.6\,\text{meV} \equiv 30\,\text{K}$. Therefore, the onset of the antiferromagnetic fluctuations is a strong coupling phenomena where the coherent ground state wave function has a structure, reflected in the matrix elements connected to high lying states, quite different from the low-lying ($E < k_B T$) excited states which dominate the behavior in the incoherent regime above $T_{\max}$.

3.4. *Magnetic order in (U, Th)(Pd, Pt)$_3$*

3.4.1. *Deliberately doped UPt_3*

The inevitable alloy dilution studies (Ramirez et al. 1986, de Visser et al. 1986, Stewart et al. 1986) which followed the discovery that UPt_3 is an interesting material revealed clear phase transitions at $T \approx 6$–$7\,\text{K}$ in $U_{1-x}Th_xPt_3$ and $U(Pt_{1-x}Pd_x)_3$ for $x > 0.03$. Neutron diffraction experiments (Goldman et al. 1986, Frings et al. 1987) on single crystals of both Pt- and Th-doped samples showed that these transitions are magnetic. The associated Bragg vectors have half-integer in-plane components, which is surprising given that we expected to find magnetic reflections at the points, such as $(0, 0, 1)$ and $(2, 0, \pm 1)$, where the medium energy scattering peaked in *pure* UPt_3. Thus, the more

complicated and somewhat frustrated unit cell doubling of fig. 15b, rather than the simple structure of a nearest neighbor coupled antiferromagnet (fig. 15a), characterize the order in doped UPt_3. The ordered moment, $0.65\pm0.1\,\mu_B$/U, is considerably below the effective moment ($3\mu_B$/U) derived from the high-temperature susceptibility, but is indistinguishable from that of U_2Zn_{17} (Cox et al. 1986) and UN (Buyers and Holden 1985). Also, as in UN and U_2Zn_{17}, the magnetic order grows conventionally below T_N (see fig. 17). The associated Bragg peaks are resolution-limited (Hayden et al. 1994), implying a magnetic correlation length in excess of 2400 Å in this disordered alloy with a relatively high residual resistivity.

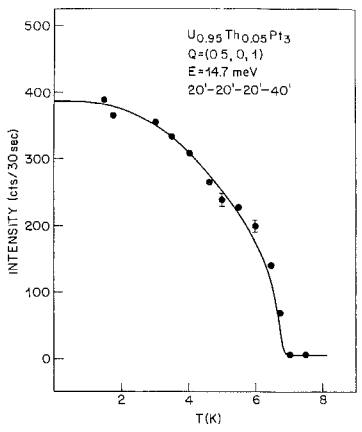

Fig. 17. Temperature dependence of $(\frac{1}{2},0,1)$ magnetic Bragg intensity in $U_{0.95}Th_{0.05}Pt_3$. (From Goldman et al. 1986.)

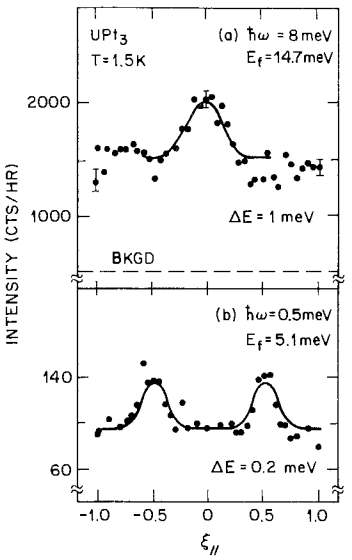

Fig. 18. Scans along $\boldsymbol{Q} = (\xi_{\|}, 0, 1)$ in high-frequency ($\hbar\omega$ = 8 meV) and low-frequency ($\hbar\omega$ = 0.5 meV) regimes for UPt_3. (From Goldman et al. 1987 and Aeppli et al. 1988a,b.)

3.4.2. *Pure UPt_3*

Knowledge of the magnetic ordering vectors in doped UPt_3 prompted a closer examination (Aeppli et al. 1988a,b) of the magnetic scattering near these vectors in nominally pure UPt_3. Figure 18 shows two constant-$\hbar\omega$ scans along $(\xi_{\|},0,1)$, a line in reciprocal space which contains the $(0,0,1)$ and $(\pm\frac{1}{2},0,1)$ points associated with simple nearest neighbor antiferromagnetism and the order in doped UPt_3, respectively. For the lower $\hbar\omega$, the magnetic fluctuations peak at the Bragg points for *doped* UPt_3, indicating that the magnetic susceptibility of our pure UPt_3 crystals presages the order induced by doping. Unexpectedly, though, we also found *elastic* ($\hbar\omega = 0$) peaks, associated with the very small ordered moment of $0.02\pm0.01\,\mu_B$/U-atom at $(\pm\frac{1}{2},0,1)$. The peaks are energy-resolution limited, indicating that the order is static on time scales exceeding

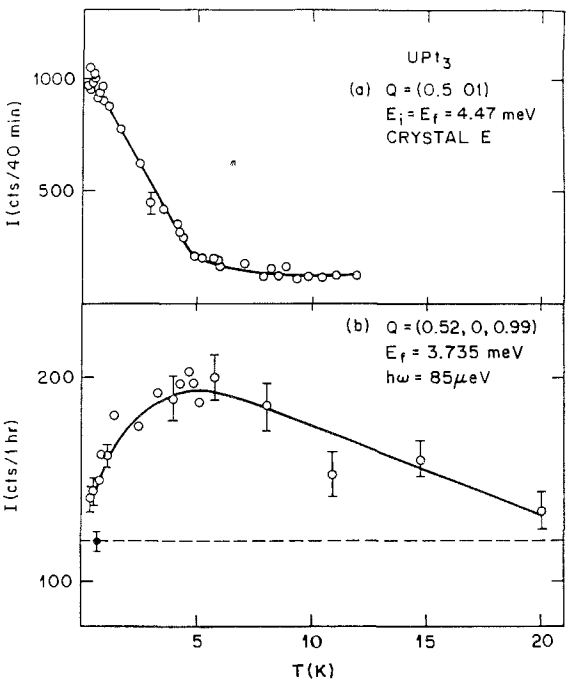

Fig. 19. Temperature dependence of (a) elastic and (b) critical magnetic scattering in nominally pure UPt_3. (From Aeppli et al. 1988a.)

5×10^{-10} s and can therefore account for the previously discovered muon depolarization characteristic of pure UPt_3 at low temperatures (Heffner et al. 1989, Heffner 1987). At the same time, and in contrast to what is found for $U_{0.95}Th_{0.05}Pt_3$, they are not momentum-resolution limited. The corresponding coherence length for the antiferromagnetism in an annealed sample is 500±130 Å along the $\boldsymbol{c}$-axis and 280±50 Å along the $\boldsymbol{a}^*$-axis (Hayden 1994). For comparison, the superconducting coherence length of UPt_3 is 111±2 Å (Kleiman 1992). Another anomaly is the temperature dependence of the order below the Néel temperature of 5 K (sec fig. 19). Instead of the classical curve with steadily increasing slope as $T \rightarrow T_N$, which is seen for $U_{0.95}Th_{0.05}Pt_3$ (fig. 17), the Bragg intensity rises linearly with temperature from T_N down to the superconducting transition temperature $T_c \approx 0.5$ K. The unconventional evolution of the Bragg intensity is matched by the unusually smooth evolution of $S(\boldsymbol{Q}_0, \omega)$, and more importantly, $\chi''(\boldsymbol{Q}_0, \omega) \approx S(\boldsymbol{Q}_0, \omega)(n(\omega)+1)^{-1}$ for $\boldsymbol{Q}_0 = (\frac{1}{2}, 0, 1)$ and the lowest frequency, $\hbar\omega = 85\,\mu$eV, reached in our inelastic measurements. The many pathological features of the magnetic order in UPt_3 are reminiscent of central peak phenomena near structural phase transitions (Axe et al. 1974) as well as in various deliberately disordered magnets (Youngblood et al. 1982, Aeppli et al. 1984). Consequently, efforts were directed towards finding chemical impurities and structural defects (Demcsyk et al. 1992, Midgley et al. 1993) in nominally pure UPt_3. The conclusion is that the crystals are chemically clean, while they do contain structural defects which vary from sample to sample. The

most dramatic is the modulated structure found by transmission electron microscopy (Midgley et al. 1993) in thin (1000 Å) slivers from annealed, but not from unannealed, crystals of UPt_3. In spite of substantial work, no clear correlation between a particular defect and magnetic order has been identified. Of special interest is that the range of the magnetic order seems unrelated to whether the superconducting transition is resolvably split, as well as unrelated to the residual resistivity (Hayden et al. 1994).

3.5. *Coupling between magnetic and superconducting order parameters*

3.5.1. *Effect of superconductivity on Bragg intensity*

Its small size and other peculiarities notwithstanding, the magnetic order in pure UPt_3 has received considerable attention, most notably as a potential source for the split superconducting transition. Most papers (Joynt 1988, Machida et al. 1989, Hess et al. 1989) on this subject are theoretical, with the fundamental idea that for a tensor superconducting order parameter, the magnetic order acts as a symmetry-reducing field. Thus, the magnetic order parameter has a direct influence on the superconducting order parameter via the lowest-order, symmetry-allowed phenomenological coupling term in a Landau–Ginzburg expansion of the free energy. The corollary of this idea, namely that the same coupling also guarantees the influence of superconductivity on the magnetic order, motivated the most direct experiment (Aeppli et al. 1989) to demonstrate the coupling of the two order parameters in a heavy-fermion superconductor. In this neutron diffraction experiment (see fig. 20), the magnetic $(1, \frac{1}{2}, 0)$ intensity actually decreased with $T < T_c$. Application of a modest field parallel to $\boldsymbol{c}$ eliminated this reduction. Because $\boldsymbol{c}$ is the hard axis for this planar magnet (Frings and Franse 1985), as also demonstrated by the field-independent magnetic intensity in the normal state, the only explanation for the reduced intensity at $T = 0$ and $H = 0$ can be the coupling between magnetic and superconducting order parameters, the last of which does couple to modest H applied parallel to $\boldsymbol{c}$. A curiosity is that the region (fig. 21) in the H–T plane where the antiferromagnetic order is H-and T-dependent lies discernibly below the $H_{c2}(T)$ line determined from *in-situ* magnetic susceptibility measurements, also shown in fig. 20. Instead, this region seems bounded by the lines of anomalies found in ultrasonic and torsional oscillator data within the superconducting state (Kleiman et al. 1989, Müller et al. 1987, Schenstrom et al. 1989, Fisher et al. 1989, Hasselbach et al. 1989).

The lower frame of fig. 22 shows the fractional increase of the magnetic peak profile as a function of the momentum transfer $\boldsymbol{Q}$, on going from the superconducting to the normal state. These data establish that superconductivity affects the Bragg intensity but not the correlation length for the small moment ordering in UPt_3. Thus, we can exclude models where the magnetism penetrates from simple point nuclei over a distance determined by the electronic state (e.g. superconducting or not) of the unperturbed material. However, because only the $(1, \frac{1}{2}, 0)$ Bragg peak was studied in detail, the first experiments did not determine whether the intensity reduction was due to a rotation of the ordered moments in the basal plane or to a decrease in the total moment amplitude. This ambiguity was resolved in a recent experiment by Isaacs et al. (1994) which established that the intensity

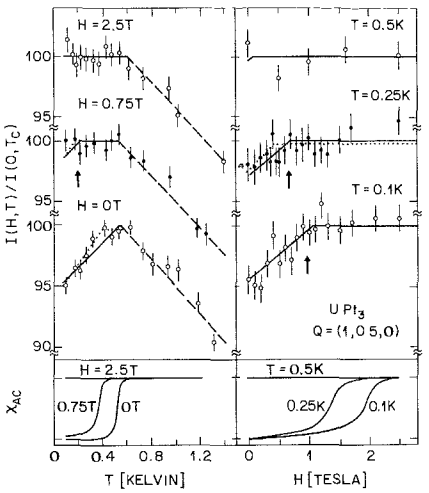

Fig. 20. Temperature and field dependence of a.c. susceptibility and $(1, \frac{1}{2}, 0)$ magnetic Bragg intensity in superconducting UPt_3. (From Aeppli et al. 1989.)

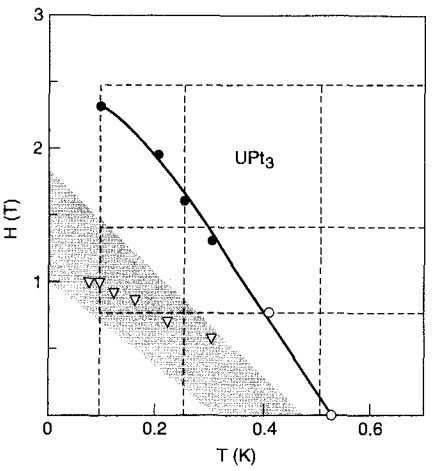

Fig. 21. Phase diagram for superconducting UPt_3 with external field H along $\hat{c}$. Open and solid circles are from a.c. susceptibility data, while triangles are locations of torsional oscillator anomalies (Kleiman et al. 1989). The shaded area represents the boundary between states where antiferromagnetic intensity varies with field and temperature and where it is H and T independent. The dashed lines are trajectories followed to accumulate diffraction data. (From Aeppli et al. 1989.)

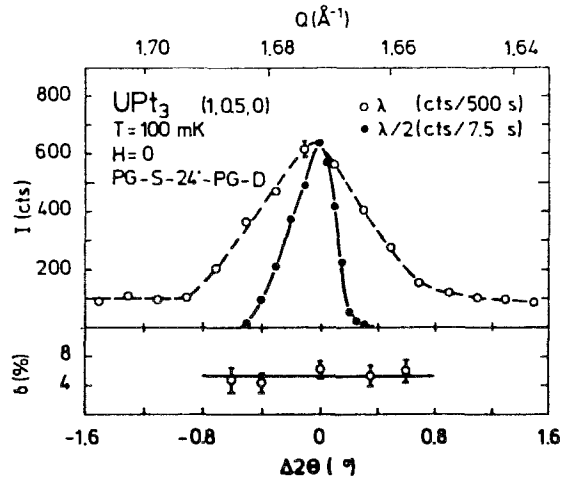

Fig. 22. Upper frame: longitudinal $(\Theta-2\Theta)$ scan through magnetic $(1, \frac{1}{2}, 0)$ and nuclear $(2, 1, 0)$ reflections observed with first- and second-order neutrons, respectively. $\Delta 2\Theta = 0$ at the Bragg points. Lower frame: Q dependence of the fractional increase of the magnetic intensity on going from the superconducting ($T = 100$ mK, $H = 0$) to the normal ($T = 540$ mK, $H = 0$) state. (From Aeppli et al. 1989.)

reduction occurs as a consequence of a reduction in the staggered magnetization which leaves the symmetry of the antiferromagnetic order parameter unchanged.

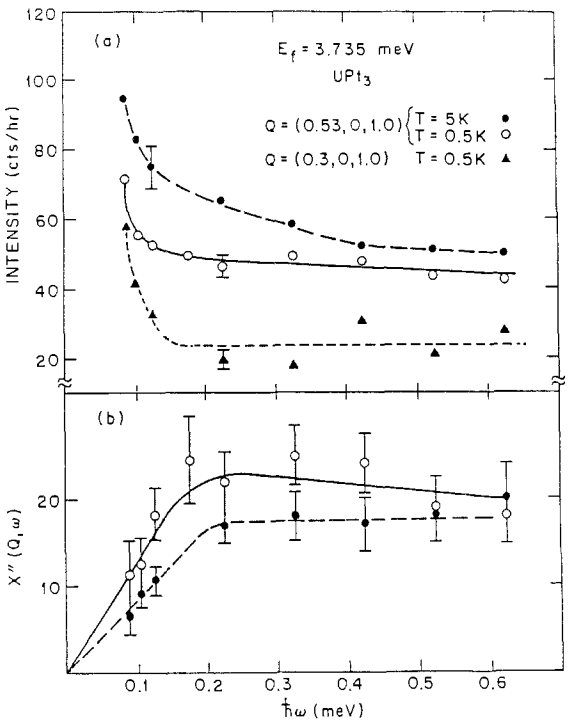

Fig. 23. Low-frequency magnetic fluctuations in UPt_3 near $(\frac{1}{2}, 0, 1)$ ordering vector: (a) raw constant-$\boldsymbol{Q}$ scans; (b) $\chi''(\boldsymbol{Q}, \omega)$ deduced from data in (a). (From Aeppli et al. 1988a.)

3.5.2. *Low frequency magnetic fluctuations*

Magnetic spectroscopy at energies close to the pairing energy of a superconductor (Aeppli et al. 1994) is interesting because it reveals both processes which may compete with superconductivity (Millis et al. 1988) and the size (Feile et al. 1981) and nature (Mason et al. 1993, Joynt et al. 1990) of the superconducting gap function. Figure 23 shows the only data available on the magnetic fluctuations of UPt_3 in the range of frequencies where $\hbar\omega \approx 3.5kT_c = 0.15$ meV. The wavevectors $\boldsymbol{Q}$ probed are close to $(\pm\frac{1}{2}, 0, 1)$, where the weak magnetic order is found. There are two important results: the first is that the characteristic energy $\hbar\Gamma$ for the fluctuations, defined as the energy where $\chi''(\boldsymbol{Q}, \omega)$ crosses over from linear to flat behavior, is at 0.2 meV, which is remarkably close to $3.5kT_c$. The second is that $\chi''(\boldsymbol{Q}, \omega)$ changes relatively little on warming from 0.5 to 5 K, even though $\hbar\Gamma$ is substantially smaller than 5 K. No neutron experiment to date has directly revealed changes in $\chi''(\boldsymbol{Q}, \omega)$ on lowering T through T_c in UPt_3. In this respect, neutron scattering from UPt_3 is less mature than neutron scattering from the high-T_c oxides, whose magnetic response functions undergo obvious changes at T_c for readily accessible energy

transfers (see e.g. Mason et al. 1992a,b, Aeppli et al. 1994, Mook et al. 1993 and Rossat-Mignod et al. 1991).

3.5.3. *Pressure effects*

Specific heat measurements indicate that hydrostatic pressure or uniaxial stress applied along c (but not a) can cause the splitting of the superconducting transition to vanish (Jin et al. 1992, Trappman et al. 1991). Thus motivated, Hayden et al. (1992) performed a neutron diffraction experiment to determine the effect of hydrostatic pressure on the weak antiferromagnetism of pure UPt_3. Figure 24 shows the outcome, namely that modest pressure does indeed suppress the magnetic Bragg peaks in UPt_3. Also, the pressure beyond which the peaks are not observed coincides with the critical (hydrostatic) pressure for the double superconducting transition. Given this result, it is tempting to ascribe the double transition to magnetic order. The difficulty is that the weak antiferromagnetism (Aeppli et al. 1988a) has also been shown to exist in material with a single broad transition at $P = 1$ atm. Furthermore, in a study (Hayden et al. 1994) of crystals fabricated by E. Bucher and collaborators, the antiferromagnetic coherence length did not increase substantially after an annealing protocol which did yield a resolved double transition in the specific heat and a reduced normal state resistivity. As pointed out by Fisk and Aeppli (1993) it is not easy to imagine how magnetism characterized by a correlation length of 280–500 Å can split the superconducting transition in a material whose $T = 0$ superconducting coherence length is 111 Å (see below). To the best of our knowledge, among all theories of superconductivity in UPt_3, only one, associated with Mineev and described, for example, by Joynt et al. (1990), can be seen as attempting to deal with this issue.

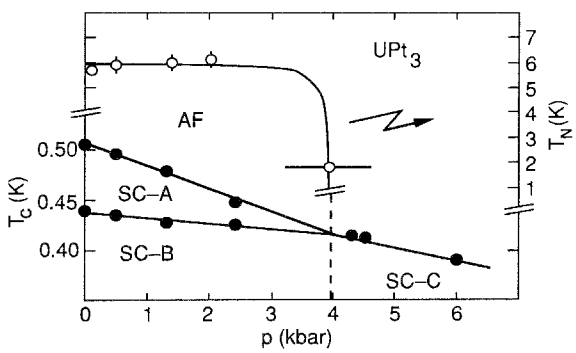

Fig. 24. Antiferromagnetic (AF) and superconducting (SC) phase boundaries of UPt_3 from neutron scattering data (open circles) and specific heat data (closed circles). (From Hayden et al. 1992.)

3.6. *The vortex lattice in superconducting UPt_3*

Neutron scattering is an excellent probe (Cribier et al. 1964) of flux lattices in superconductors because the dipole moment of the neutron couples to the magnetic field inhomogeneities associated with such lattices. Of course, the length scales for the

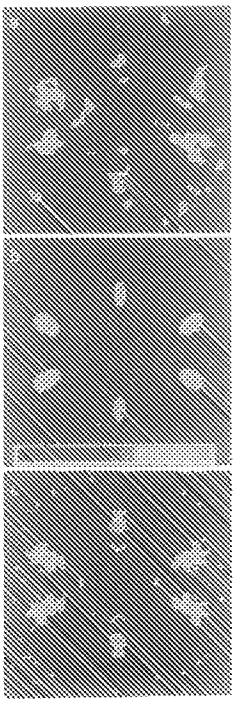

Fig. 25. Diffraction pattern for flux lattice in superconducting UPt_3 at $T = 50\,\text{mK}$ and a magnetic field $H = 0.425\,\text{T}$ applied along $\boldsymbol{a}^*$, perpendicular to the region of the $(h, 0, l)$ zone shown. The corners of the region are at $(\pm 0.016\,\text{Å}^{-1}, 0, \pm 0.016\,\text{Å}^{-1})$. (a) Background-corrected data; (b) calculated response of instrument to flux lattice with infinite-range order; (c) the data of (a) symmetrized to reduce the statistical errors in the peak intensities. (Adapted from Kleiman et al. 1992.)

inhomogeneities are simply λ and ξ, the bulk magnetic penetration depth and pair coherence length, respectively, for the superconductor. Thus, beyond allowing determinations of the vortex lattice structure, neutron diffraction yields values for λ and ξ.

In view of speculation (Volovik 1988, Tokuyasu et al. 1990) that transitions between different vortex lattices are responsible for the many anomalies found in bulk measurements below the $H_{c2}(T)$ line of UPt_3, Kleiman et al. (1992) carried out a neutron diffraction study of the vortex lattice. They used the small angle neutron scattering instrument in the Risø cold neutron guide hall to obtain patterns such as that shown in fig. 25. An immediate conclusion from the pattern is that the vortex lattice, formed in the $\boldsymbol{a}$–$\boldsymbol{c}^*$ plane, is highly anisotropic hexagonal, with conventional quantization. The anisotropy is substantially larger than what one expects for a conventional superconductor with the quite isotropic normal state transport properties of UPt_3. However, it is consistent with these properties if the superconducting gap function has the nodal structure implied by ultrasound (Shivaram et al. 1986, Schmitt-Rink et al. 1986) and μSR measurements (Broholm et al. 1990) as well as subsequent electron tunneling experiments (Goll et al. 1993).

Figure 26 shows how the parameters describing the vortex lattice change with external field $H \parallel \boldsymbol{a}^*$ at 50 mk. Torsional oscillator and ultrasound anomalies (Kleiman et al. 1989, Müller et al. 1987, Schenstrom et al. 1989, Fisher et al. 1989, Hasselbach et al. 1989) had been found at $H \approx 0.6\,\text{T}$. Figure 26a demonstrates that the vortex

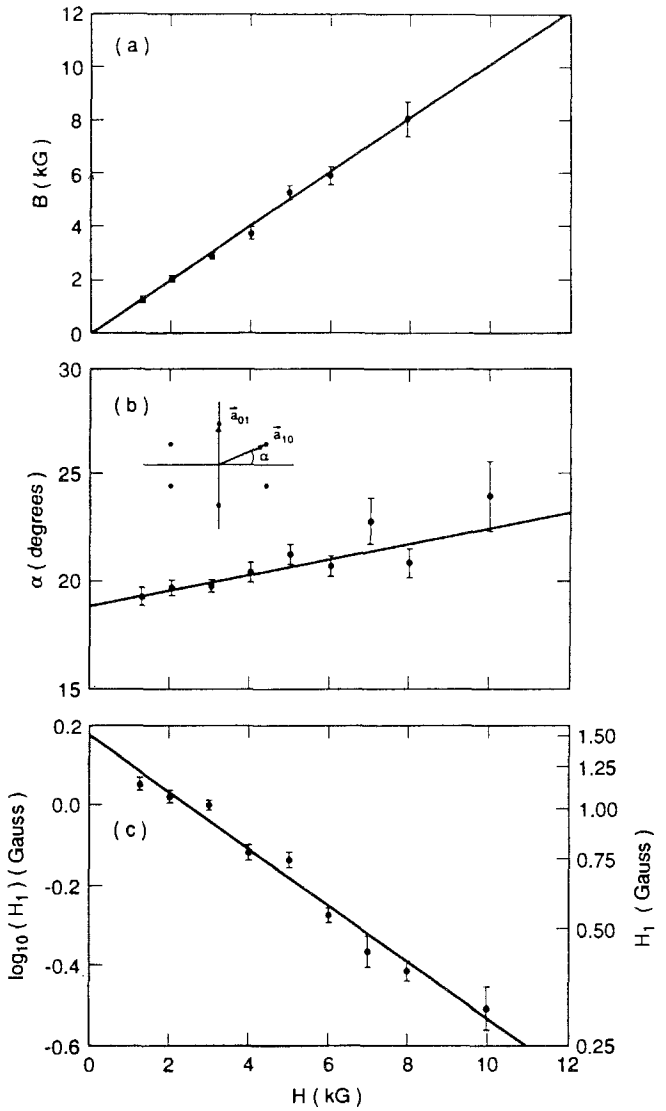

Fig. 26. Parameters describing diffraction from vortex lattice in superconducting UPt_3 as a function of field H applied along a^*. (a) Internal field deduced from the unit cell size. The line with slope unity is expected for singly quantized vortices. (b) Crystallographic angle α defined in the inset. For a conventional hexagonal lattice, $\alpha = 30°$. (c) Scattering length, in magnetic field units, for the (1, 0) Bragg reflection from the vortex lattice. (From Kleiman et al. 1992.)

quantization remains conventional over the entire field range probed. Furthermore, within experimental error, the angle α, representing the obliqueness of the vortex lattice, and

the scattering length H_{10} evolve smoothly. Thus, at present, one cannot explain the field-dependent anomalies seen at low temperatures in superconducting UPt_3 in terms of exotic phase transitions undergone by the vortex lattice.

The slope and intercept of the logarithm of the field-dependent scattering length H_{10} (fig. 26c) determine ξ and λ respectively. The principle is that varying the external field varies the flux lattice constant, thus allowing the individual vortex structure factor to be measured as a function of wavevector $\boldsymbol{Q}$. In contrast to the discrete nature of the structure factors measured by diffraction from conventional crystals, $\boldsymbol{Q}$ for vortex lattices is a continuous variable because of the continuity of H. The structure factor analysis of Kleiman et al. (1992) yields $\lambda_\perp = 5190 \pm 70$ Å, $\lambda_\parallel = 7150 \pm 15$ Å, $\xi_\perp = 121 \pm 2$ Å and $\xi_\parallel = 93 \pm 3$ Å, where the subscripts denote directions parallel and perpendicular to $\boldsymbol{c}$. The large values for the magnetic penetration depth show that the mere observation of the vortex lattice in UPt_3 is itself quite remarkable – the $\boldsymbol{Q} \rightarrow 0$ scattering cross-section is proportional to λ^{-4} implying that the UPt_3 signal is at least 5000 times weaker than that for $YBa_2Cu_3O_7$, the previously studied superconductor with the longest λ (~1400 Å) and hence smallest cross-section (Forgan et al. 1990). Finally, the SANS values of ξ, which are the most directly determined pair coherence lengths for UPt_3, are consistent with the upper critical field $H_{c2}(T \rightarrow 0)$. They are also sufficiently large to account for the disappearance of vortex lattice signals at high fields in μSR measurements (Broholm et al. 1990). The muon spin relaxation rate is directly proportional to H_{10} which, as fig. 26c shows, becomes small for the several kG fields employed in μSR determinations of λ (for a review see Aeppli 1992) for most materials. In their μSR measurements on UPt_3, Broholm et al. (1990) used substantially smaller fields (~175 G, still much larger than $H_{c1} \approx 15$ G and the ambient, time-varying fields at a typical μSR facility) and obtained clean limit values, $\lambda_\parallel = 6920 \pm 40$ Å and $\lambda_\perp = 7200 \pm 100$ Å, not far from those given by the SANS experiment of Kleiman et al. (1992). Thus, SANS and low-field μSR both yield magnetic penetration depths in good agreement with c/ω_p, where $\omega_p = 4.8 \times 10^{14}\ s^{-1}$ is the normal state plasma frequency deduced from infrared reflectivity data (Sulewski et al. 1988). Contrary to Luke et al. (1993), we conclude that microscopic, flux-lattice-based measures of λ are more reliable than those based on the notoriously difficult technique of low field bulk magnetometry.

4. Antiferromagnetic heavy-fermion systems

4.1. U_2Zn_{17}

Because the 4f and 5f moments in heavy-fermion systems are largely quenched by Kondo screening, conventional Néel ordering at low temperatures is less likely than for ordinary rare-earth–actinide compounds. Indeed, U_2Zn_{17}, UCd_{11} UPd_2Al_3 (Krimmel et al. 1992) and UCu_5 (Murasik et al. 1974, Schenck et al. 1990) are the only known stoichiometric heavy-fermion systems which develop long-range antiferromagnetic order with staggered magnetization in excess of $0.1\mu_B$. Of these, U_2Zn_{17} has received the most attention

because it is the only material of which large single crystals amenable for inelastic neutron scattering experiments are available.

U_2Zn_{17} has the rhombohedral (space group $R\bar{3}m$) Th_2Zn_{17} structure (Iandelli and Palenzona 1967). Single crystals grown from melts consist of twins related to each other by reflection in a plane perpendicular to the 3-fold axis. In addition, some crystals contain a hexagonal modification with $c' = \frac{2}{3}c(U_2Zn_{17})$. In the following, wavevector transfer is indexed using the hexagonal reciprocal lattice with $a^* = 4\pi/(a\sqrt{3}) = 0.811\,\text{Å}^{-1}$ and $c^* = 2\pi/c = 0.479\,\text{Å}^{-1}$.

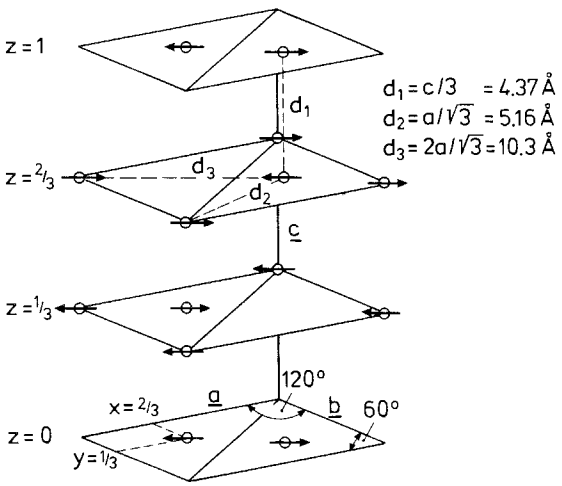

Fig. 27. Antiferromagnetic structure of U_2Zn_{17}. The ordered moment is $0.8\mu_B$. Only one of three magnetic domains related to each other by a 120° rotation around the c-axis is shown. (From Broholm 1988.)

4.1.1. *Long-range antiferromagnetic order*

High-temperature susceptibility measurements in U_2Zn_{17} indicate an effective moment of $2–3\mu_B$ and strong 5f-conduction electron hybridization ($\Theta_{cw} = -95/-130\,\text{K}$, Ott and Fisk 1987). However, antiferromagnetic ordering occurs only at low temperatures ($T_N = 9.7\,\text{K}$) and with an ordered moment of just $0.80\mu_B$. Figure 27 shows the magnetically ordered structure (Cox et al. 1986). The magnetic order is commensurate, corresponding to simple antiparallel arrangement of the two spins in a unit cell along one of the three lines separating nearest in-plane neighbors (the $\boldsymbol{a}^*$ directions). The antiferromagnetic correlation length exceeds 500 Å.

Figure 28 shows that the antiferromagnetic phase transition proceeds as for conventional three-dimensional antiferromagnets: the critical exponent $\beta = 0.36 \pm 0.02$ ($I_{\text{Bragg}} = I_0(T - T_N)^{2\beta}$), which is indistinguishable from the critical exponent for the three-dimensional Heisenberg ($\beta = 0.367$) and XY ($\beta = 0.345$) magnets (Collins 1989). In addition fig. 28 shows that critical magnetic fluctuations give rise to a peak in the low-energy quasielastic scattering at T_N. It is interesting that contrary to the resistivity of URu_2Si_2, which increases at T_N due to the opening of a gap on the Fermi surface,

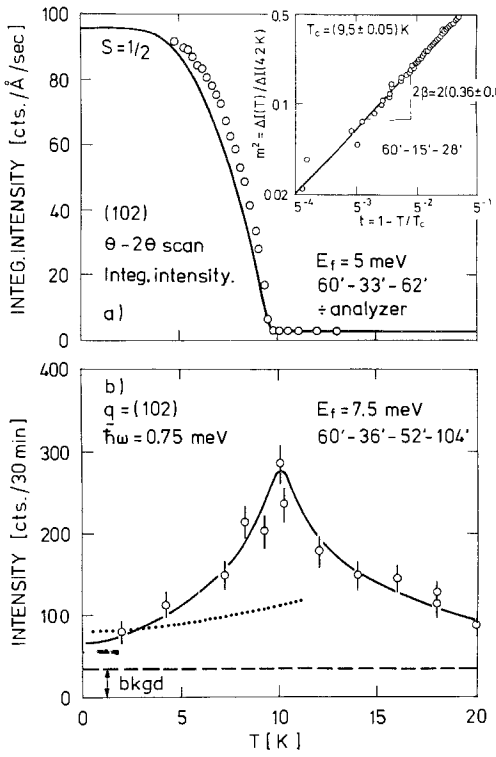

Fig. 28. Elastic and inelastic data characterizing the antiferromagnetic phase transition in U_2Zn_{17} at $T_N = 9.7$ K. The top frame shows the development of the order parameter at $(1,0,2)$ compared to an $S = \frac{1}{2}$ mean-field model. The inset shows a double logarithmic plot of the reduced squared staggered magnetization versus reduced temperature in the critical regime. The bottom frame shows the temperature dependence of the quasielastic magnetic neutron scattering at an energy transfer of $\hbar\omega = 0.75$ meV. (From Broholm 1988.)

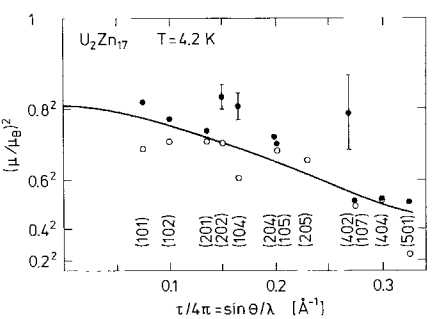

Fig. 29. Form factor of the antiferromagnetically ordered moment in U_2Zn_{17} derived from the difference in integrated intensities of antiferromagnetic Bragg peaks at $T = 1.4\,K < T_N$ and $T = 20\,K > T_N$. In this figure τ denotes wavevector transfer. The solid and open symbols correspond to data from each of two structural twins present in our sample. The solid line is a suitably scaled interpolation of the form factor for UO_2 (Frazer et al. 1965). (From Broholm 1988.)

the resistivity of U_2Zn_{17} decreases precipitously at T_N, as in conventional rare-earth magnets (Andersen and Smith 1979). Thus, simple Born-type scattering of conduction electrons from paramagnetic fluctuations must contribute substantially to the resistivity (Ott et al. 1984).

Figure 29 shows the squared form factor of the ordered moment in U_2Zn_{17} derived from the intensities of magnetic Bragg peaks. As discussed more thoroughly in chapter 130 (Holland-Moritz and Lander 1994), the form factor is a measure of the spatial

extent of the spin density. The similarity between the data for U_2Zn_{17} and the solid line, which is a scaled interpolation of the form factor for insulating UO_2, shows that despite hybridization, the spin density associated with the static antiferromagnetic correlations remains as localized about the U atoms as for atomic 5f electrons.

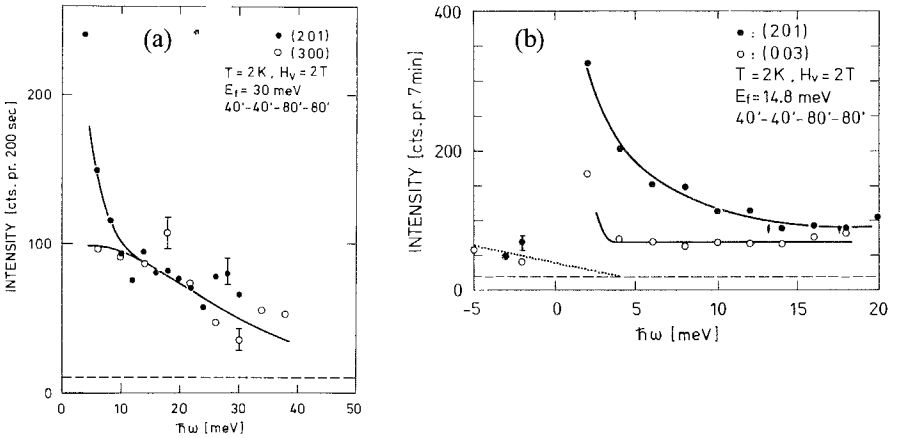

Fig. 30. High-energy inelastic magnetic scattering probing antiferromagnetic [$\boldsymbol{Q}$ = (2, 0, 1)] and ferromagnetic [$\boldsymbol{Q}$ = (3, 0, 0) and $\boldsymbol{Q}$ = (0, 0, 3)] spin fluctuations in U_2Zn_{17} in its single-domain antiferromagnetically ordered state: $T = 2\,\mathrm{K}$, $|\boldsymbol{H}| = 2\,\mathrm{T}$ and $\boldsymbol{H} \parallel \boldsymbol{b}$. Broken lines indicate the analyzer-turned background, solid lines are guides to the eye. The dotted line in (b) is the contribution to the count rate from inelastic scattering of $\lambda/2$ neutrons from the unfiltered incident beam. The data in (b) have not been corrected for the $\lambda/2$ contribution to the monitor count rate. (From Broholm 1988.)

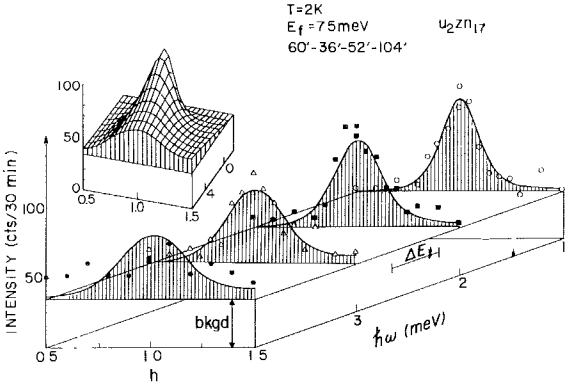

Fig. 31. Constant-energy scans along $\boldsymbol{Q} = (h, 0, 3-h)$ in the ordered phase of U_2Zn_{17} at $T = 2\,\mathrm{K}$. The solid lines result from the three-parameter fit described in the text. The inset shows the corresponding model scattering function in a perspective view. (From Broholm et al. 1987a.)

4.1.2. *Magnetic fluctuations in the ordered state*

The total moment sum-rule implies that the part of the 5f-moment which is not statically ordered accounts for the $T \rightarrow 0$ spin fluctuations. Figures 30 and 31 show inelastic magnetic neutron scattering probing such magnetic fluctuations in different ranges of energy transfer $\hbar\omega$ in the ordered state of U_2Zn_{17} (Broholm et al. 1987,

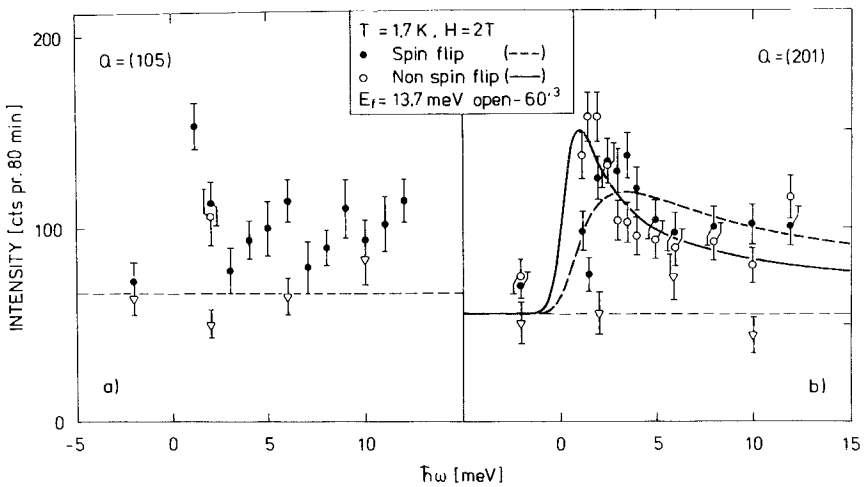

Fig. 32. Vertical field polarization-resolved constant-$\boldsymbol{Q}$ scans in the single-domain antiferromagnetically ordered state of U_2Zn_{17}: $T = 2$ K, $H = 2$ T: (a) is for $\boldsymbol{Q} = (1, 0, 5)$ and shows only neutron spin flip scattering; (b) is for $\boldsymbol{Q} = (2, 0, 1)$ and shows spin-flip and non-spin-flip scattering. In both figures the triangles and thin dashed lines indicate the analyzer-turned background. The thick lines in (b) are single-pole relaxation responses (eq. 2.1) appropriately corrected for finite energy resolution and the varying contribution of neutrons at the desired wavelength to the monitor count rate. (From Broholm 1988.)

Broholm 1988). Figure 30a demonstrates that the overall bandwidth for magnetic fluctuations is around 30meV, comparable to $|\Theta_{CW}| \equiv T_K$ but exceeding $k_B T_N$ by far. At high energies, the scattering with wavevector transfer $\boldsymbol{Q} = (2, 0, 1)$, which is associated with spin fluctuations with the same antiferromagnetic modulation as the ordered moment, is indistinguishable from the scattering at $\boldsymbol{Q} = (3, 0, 0)$, which probes ferromagnetic spin fluctuations. In the high energy limit, the spin fluctuations are therefore uncorrelated, localized excitations. For $\hbar\omega < 10$ meV fig. 30b shows that inelastic scattering is strongest for wavevector transfer in the vicinity of the antiferromagnetic zone center, $(2, 0, 1)$. Figure 31 details this low-energy part of the response as a function of energy and wavevector transfer $\boldsymbol{Q} = (h, 0, 3-h)$. The data are *not* resolution limited. Therefore, well-defined spin waves, which would give rise to two ridges emanating from the antiferromagnetic Bragg point, do not exist for $\hbar\omega > 1$ meV $\approx k_B T_N$. Instead, $S(\boldsymbol{Q}, \omega)$ consists of a single ridge extending along $\hbar\omega$ and centered at the antiferromagnetic zone center $\boldsymbol{Q} = (1, 0, 2)$. Obviously the experiment does not exclude conventional spin-waves for $\hbar\omega < k_B T_N$ where no measurements were performed. Even so, given the strong spin fluctuation continuum for $\hbar\omega > 1$ meV, conventional spin waves are not the dominant excitations in U_2Zn_{17}.

The data of figs. 30 and 31 do not distinguish fluctuations of different polarization relative to the staggered magnetization. Figure 32 shows polarized neutron scattering from a single-domain antiferromagnetic state with moments maintained $\|\boldsymbol{a}^*$ by a 2 T field normal to the $(h01)$ scattering plane. As a result of the selection rules for polarized neutron

Table 2
Magnetic form factor for uranium (Frazer et al. (1965) and the contribution to spin-flip and non-spin-flip scattering for $\boldsymbol{Q}$ in the $\boldsymbol{a}^*$–$\boldsymbol{c}^*$-plane and $\boldsymbol{H} \parallel \boldsymbol{b}$ from each component of the generalized susceptibility tensor[a]

(hkl)	$\boldsymbol{Q}$ (Å^{-1})	$\lvert F_m(\boldsymbol{Q})\rvert^2$	spin-flip	non-spin-flip
(1 0 2)	1.26	0.95	Im $\{0.58\chi_{a^*} + 0.42\chi_{c^*}\}$	Im$\{\chi_b\}$
(2 0 1)	1.69	0.86	Im $\{0.08\chi_{a^*} + 0.92\chi_{c^*}\}$	Im$\{\chi_b\}$
(1 0 5)	2.53	0.71	Im $\{0.90\chi_{a^*} + 0.10\chi_{c^*}\}$	Im$\{\chi_b\}$

[a] Recall that by the definition of the reciprocal lattice $\boldsymbol{b}$ is normal to the $\boldsymbol{a}^*$–$\boldsymbol{c}^*$-plane.

scattering, longitudinal ($\mu \parallel \boldsymbol{a}^*$), out-of-plane transverse ($\mu \parallel \boldsymbol{c}$) and in-plane transverse ($\mu \parallel \boldsymbol{b}$) fluctuations contribute with the varying amounts listed in table 2 to spin flip and non-spin flip scattering for different magnetic Bragg points. The data of fig. 32 illustrate the distinct nature of the fluctuations polarized parallel to the staggered magnetization. Though clearly above background, the longitudinal spin flip scattering at $\boldsymbol{Q} = (1, 0, 5)$ (solid symbols in fig. 32a) is, to within the statistical accuracy of the data, independent of energy for $2 \leqslant \hbar\omega < 15$ meV. The enhanced low-energy antiferromagnetic fluctuations for wavevectors in the vicinity of the antiferromagnetic zone center thus have polarization transverse to the staggered magnetization. Figure 32b shows polarized neutron spectra at $\boldsymbol{Q} = (2, 0, 1)$ which probe out-of-plane transverse magnetic fluctuations in the neutron spin flip channel and in-plane transverse magnetic fluctuations in the non-spin-flip channel. The energy associated with out-of-plane transverse spin fluctuations is somewhat larger than that associated with in-plane transverse spin fluctuations, indicating the presence of planar anisotropy in antiferromagnetically ordered U_2Zn_{17}.

4.1.3. *Magnetic fluctuations above* T_N

Not surprisingly given the large energy scale for magnetic fluctuations, short-range antiferromagnetic correlations persist well into the paramagnetic state of U_2Zn_{17}. Since there is no distinction between transverse and longitudinal fluctuations for $T > T_N$, a simple para-magnon theory may be used to parametrize the data. Within the random phase approximation (RPA), the generalized susceptibility of interacting local moments is

$$\chi^{-1}(\boldsymbol{Q}, \omega) = \chi_0^{-1}(\omega) - J_{\boldsymbol{Q}}, \tag{4.1}$$

where $\chi_0(\omega)$ represents the generalized susceptibility of a single uranium atom and $J_{\boldsymbol{Q}}$ the Fourier-transformed RKKY interaction between sites. The non-resonant magnetic fluctuation spectra suggest choosing $\chi_0(\omega) = \chi_0\Gamma/(\Gamma - i\omega)$, a form that accounts well for the excitation spectra in mixed-valence and Kondo systems (see chapter 130, Holland-Moritz and Lander 1994, this volume). For simplicity and because in- and out-of-plane fluctuations are not resolved in the unpolarized experiments to establish the T dependence of $S(\boldsymbol{Q}, \omega)$ for U_2Zn_{17} (Broholm et al. 1987), $\chi_0(\omega)$ was chosen to be isotropic, thus representing an average of the anisotropic response function which would be required to account for the crystalline anisotropy uncovered by polarized neutron scattering

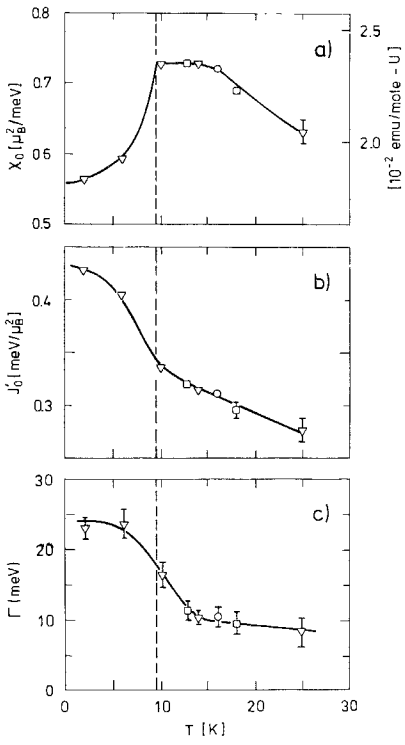

Fig. 33. Temperature dependence of the parameters in a para-magnon model described in the text, obtained from fits to inelastic magnetic neutron scattering and bulk susceptibility data in U_2Zn_{17}. The solid lines are guides to the eye. (From Broholm et al. 1987a.)

for $T = 2\,\mathrm{K} < T_N$. For computing J_Q, all but the nearest neighbor exchange, J_0', are neglected. The resulting interacting susceptibility in eq. (4.1) then becomes

$$\chi(\boldsymbol{Q}, \omega) = \frac{\chi_0 \Gamma}{\Gamma(\boldsymbol{Q}) - i\omega} \equiv \chi'(\boldsymbol{Q}) \frac{\Gamma(\boldsymbol{Q})}{\Gamma(\boldsymbol{Q}) - i\omega}, \tag{4.2}$$

where $\Gamma(\boldsymbol{Q}) = \Gamma(1 - \chi_0 J_Q)$, and $\chi'(\boldsymbol{Q}) = \chi_0 \Gamma / \Gamma(\boldsymbol{Q})$ is the $\boldsymbol{Q}$-dependent static ($\omega = 0$) susceptibility. Figure 33 shows the temperature dependence of the parameters derived from this analysis. These account both for the temperature dependence of the inelastic magnetic scattering and the bulk susceptibility, $\chi'(\boldsymbol{Q}=0)$ (Ott et al. 1984). As in RPA theories of conventional crystal-field dominated rare-earth magnets with resonant single-site response functions, the collective susceptibility diverges when $\chi_0 J_{Q_0} \to 1$, thus defining T_N and the ordering wavevector, $\boldsymbol{Q}_0$. In the case of rare-earth magnets the increase in $\chi_0 J_{Q_0}$ results from the low-temperature enhancement of the single-ion susceptibility, χ_0, whereas the RKKY interaction is temperature independent. For the heavy-fermion antiferromagnet U_2Zn_{17}, fig. 33 shows that the phase transition is driven by an increase in $J_{Q_0} \propto J_0'$ rather than χ_0 which depends only weakly on T immediately above T_N. Such renormalization of RKKY interactions has indeed been predicted for two Kondo impurities coupled to the same conduction electron sea (Jones and Varma 1987,

Abrahams and Varma 1987, Sire et al. 1993). Figure 33 also shows that the development of static antiferromagnetic spin correlations is accompanied by an increase in the local energy scale, Γ which correlates well with the two and one-half-fold decrease in the Sommerfeld constant at T_N (Ott et al. 1984).

4.2. *URu_2Si_2*

URu_2Si_2 belongs to the large group of ternary intermetallics RT_2Si_2 with R a rare earth or actinide and T a 3d, 4d or 5d transition metal (Palstra 1986, Palstra et al. 1986a,b). All these compounds crystallize in one of two allotropic modifications of the tetragonal $BaAl_4$ structure: $CaBe_2Ge_2$ or $ThCr_2Si_2$. Compounds with R = Ce or U display varied metallic behavior ranging from Pauli paramagnetism for earlier members in a transition-metal series through heavy-fermion behavior (see, e.g., the section on $CeRu_2Si_2$) involving superconductivity in the cases of URu_2Si_2 and $CeCu_2Si_2$, to antiferromagnetism for later members of a series.

Moderately heavy URu_2Si_2 ($\gamma = 50\text{mJ/mol K}^2$ for $T \to 0$; $\gamma = 180\text{mJ/mol K}^2$ for $T > T_N$) gained much interest as the first heavy-fermion system in which coexistence of antiferromagnetism ($T_N = 17.5\,\text{K}$) and superconductivity ($T_c = 1.2\,\text{K}$) was established (Palstra et al. 1985, Maple et al. 1986, Schlabitz et al. 1986, Broholm et al. 1987b). The magnetic susceptibility (Palstra et al. 1985, Maple et al. 1986, Schlabitz et al. 1986) and resistivity (Palstra et al. 1985, 1986a,b) display pronounced uniaxial anisotropy, which is common for magnetic RT_2Si_2 intermetallics. What is uncommon, of course, is superconductivity, which displays a similar anisotropy in its properties such as the upper critical field (Palstra et al. 1985).

4.2.1. *Antiferromagnetic order*

An unusual property of URu_2Si_2 is the weak antiferromagnetism which appears below $T_N = 17.5\,\text{K}$. Figure 34 depicts the corresponding simple type-I order. The ordered moment is oriented along the *c*-axis and its magnitude is just $0.04\mu_B$, apparently independent of sample quality. The correlation length is sample dependent, ranging from 102(4) Å (Broholm et al. 1991) to 450 Å (Isaacs et al. 1990) along the *c*-axis whereas the correlation length in the basal plane does not exceed 200 Å in the best samples available (Isaacs et al. 1990, Mason et al. 1990a).

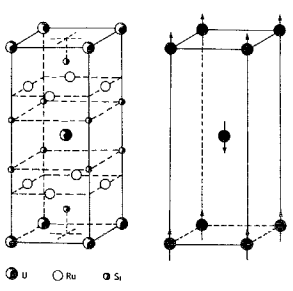

Fig. 34. Left panel: crystal structure of URu_2Si_2; right panel: antiferromagnetic order which appears below $T_N = 17.5\,\text{K}$. (From Broholm et al. 1991.)

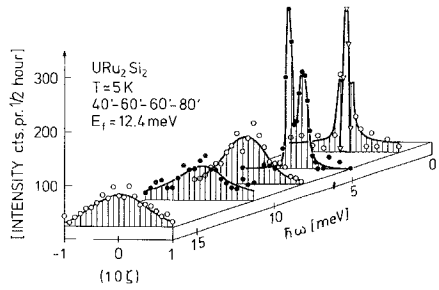

Fig. 35. Perspective view of the scattered neutron intensity versus energy transfer and momentum transfer along $(1,0,\zeta)$ in URu_2Si_2. The data were taken in the ordered phase at $T = 5$ K. The asymmetry in the double peak structure is due to instrumental resolution. The solid lines are guides to the eye. Solid and open symbols are used for clarity of presentation. At $\hbar\omega = 2.1$ meV the data plotted as triangles, which define the hatched region, have been divided by 10. (From Broholm et al. 1991.)

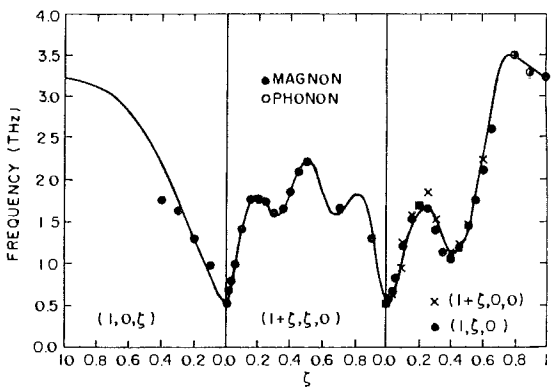

Fig. 36. Measured dispersion relation for low-energy magnetic excitations in URu_2Si_2 along the $(1,0,\zeta)$, $(1+\zeta,\zeta,0)$ and $(1,\zeta,0)$ directions in reciprocal space. Note that $2\pi\hbar \times 1$ THz $= 4.138$ meV. The lines result from a fit to a simple theory of exchange-coupled crystal-field excitations. (From Broholm et al. 1991.)

4.2.2. *Magnetic excitations*

Susceptibility and resistivity measurements show that URu_2Si_2 is very anisotropic, with the c-axis being the easy magnetic axis and normal to the plane with highest resistivity (Palstra et al. 1985, 1986a,b). Magnetic excitations found to date in URu_2Si_2 are exclusively polarized along this axis and hence are longitudinal with respect to the small ordered moment.

Figure 35 shows inelastic magnetic neutron scattering data as a function of energy and wavevector transfer in the vicinity of the antiferromagnetic zone center $\boldsymbol{Q} = (1, 0, 0)$. At high energies the dynamic correlation function $S(\boldsymbol{Q}, \omega)$ depends weakly on $\boldsymbol{Q}$ and ω; it resembles, apart from its strict polarization along the c-axis, that found in many other heavy-fermion systems. The simple sinusoidal $\boldsymbol{Q}$ dependence indicates that the antiferromagnetic correlations associated with these high-energy magnetic fluctuations do not extend far beyond a single tetragonal unit cell.

At lower energies there is a gradual cross-over to resonant excitations in which scattering only occurs when $\boldsymbol{Q}$ and ω lie on a dispersion relation as in crystal-field dominated rare-earth metals (Jensen and Mackintosh 1991). The corresponding dispersion relation is shown in fig. 36. The rapid oscillations over the course of a single Brillouin zone indicate the presence of relatively long-ranged exchange interactions between local moments. Indeed, the dispersion relation was fit to an RPA theory of exchange-coupled crystal-field excitations (Buyers et al. 1975, see also Buyers and Holden 1985) yielding

finite values for coupling constants between atoms separated by up to 10 Å (Broholm et al. 1991). Lacking in this model is of course any account of the high-energy overdamped magnetic fluctuations. It is therefore not surprising that the simplest singlet–singlet model cannot explain fully the strongly $\boldsymbol{Q}$-dependent integrated intensity of the resonant mode (Broholm et al. 1991).

4.2.3. *Temperature dependence of magnetic excitations*

Since resonant and overdamped excitations exist in different energy ranges, one might expect that each has a characteristic temperature scale associated with it. To determine the evolution with temperature of the overdamped magnetic fluctuations, Broholm et al. (1991) measured (see fig. 37) the temperature dependence of inelastic magnetic scattering at $\hbar\omega = 8$ meV for wavevectors $\boldsymbol{Q} = (1, 0, 0)$ and $(1, 0, 1)$, corresponding to antiferromagnetic and ferromagnetic fluctuations respectively. Antiferromagnetic correlation of the overdamped magnetic fluctuations, signaled by the difference in inelastic scattering intensities at these two wavevectors, develops for $T < 150$ K. Interestingly, around 150 K the resistivity of URu_2Si_2 decreases smoothly by over an order of magnitude (Schlabitz et al. 1986), suggesting that the development of short-range antiferromagnetic correlations results in a dramatic reduction in spin-disorder scattering of conduction electrons.

Contrary to the crystal-field excitations in conventional rare-earth metallic magnets the resonant excitations in URu_2Si_2 are strictly a low-temperature phenomenon: they do not develop until $T < T_N = 17.5$ K, the temperature associated with the magnetic phase transition.

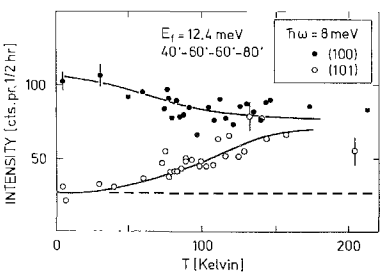

Fig. 37. Scattered neutron intensity in URu_2Si_2 versus temperature at an energy transfer of 8 meV and scattering vectors (1 0 0) and (1 0 1). The broken line is the analyzer-turned background. The solid lines are guides to the eye. (From Broholm et al. 1991.)

4.2.4. *The magnetic phase transition*

Figure 38 shows the precipitous manner in which the low-energy resonant band develops from the otherwise overdamped magnetic excitations at $\boldsymbol{Q} = (1, 0.4, 0)$. In light of this dramatic change in the dynamics, it is not surprising that there is a λ-like anomaly in the specific heat at 17.5 K with an associated change in entropy of order $R \ln 2$ (Palstra et al. 1985). An important question is whether this modification of the dynamics is simply a result of a phase transition involving well-defined J-multiplets or whether a simultaneous modification in the hybridization of f-electrons with conduction electrons takes place.

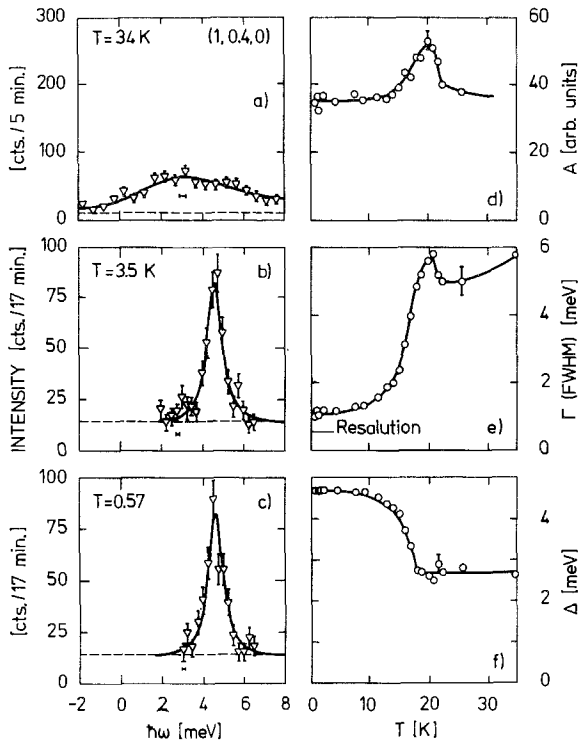

Fig. 38. Constant-$\boldsymbol{Q}$ scans at $(1, 0.4, 0)$ in: (a) the paramagnetic, (b) the antiferromagnetic and (c) the superconducting phase. The solid lines in (a)–(c) are fits to a resolution- and background-corrected Lorentzian response function (eq. 2.3), and (d)–(f) show the temperature dependence of the three parameters A $[\equiv \chi'(\boldsymbol{Q})]$, Γ $[\equiv \Gamma(\boldsymbol{Q})]$ and Δ $[\equiv \hbar\omega(\boldsymbol{Q})]$ obtained from these fits. The lines through these points are guides to the eye. (From Broholm et al. 1991.)

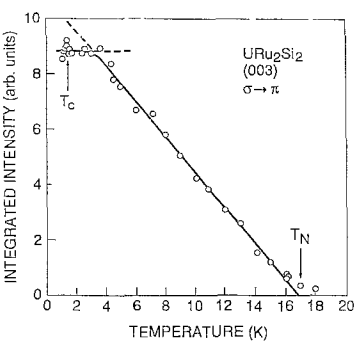

Fig. 39. Integrated intensity versus temperature for the $(0, 0, 3)$ magnetic Bragg peak in URu_2Si_2 as determined by resonant magnetic X-ray scattering. The solid line is a guide to the eye. Saturation corresponds to 8 counts/s at the Bragg peak. (From Isaacs et al. 1990.)

The drastic alterations in the magnetic excitation spectrum overshadows the gradual development of the squared staggered magnetization, m_q^2, shown in fig. 39. There is an anomalously large temperature regime in which m_q^2 rises linearly with decreasing temperature, followed eventually by saturation for $T < 2.5$ K (Isaacs et al. 1990). As is the case for the static magnetic correlation length, the variation of the staggered magnetization with T depends strongly on sample purity. In samples with stacking faults and possibly silicon off-stoichiometry, significant temperature-dependent elastic scattering persists for

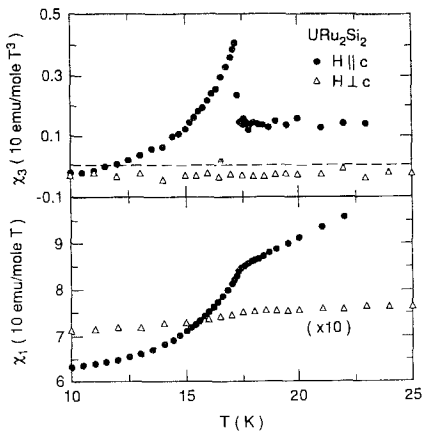

Fig. 40. Nonlinear susceptibility χ_3 and linear susceptibility χ_1 for URu_2Si_2 parallel and perpendicular to the tetragonal c-axis. (From Ramirez et al. 1992.)

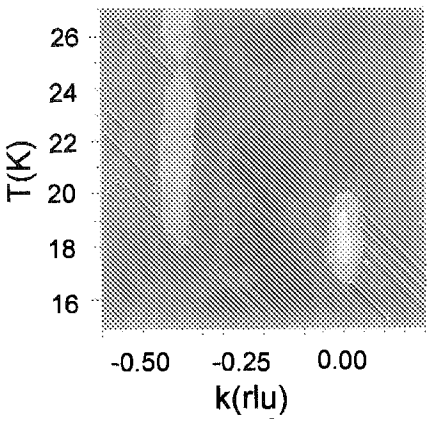

Fig. 41. Contour map of critical scattering in URu_2Si_2 at energy transfer $\hbar\omega = 0.4$ meV as a function of temperature and wavevector transfer along the $(1,k,0)$ direction. (From Buyers et al. 1994.)

$T > 20$ K and this despite the sharpness of the phase transition as monitored by specific heat or inelastic neutron scattering measurements in the same material. These and other observations have led to speculations that the weak antiferromagnetic order is not the primary order parameter of the transition (Broholm et al. 1991, Gorkov 1991, Ramirez et al. 1992, Barzykin and Gorkov 1993).

Gorkov (1991) suggested that the primary order parameter could be a triple spin correlator and Barzykin and Gorkov (1993) predicted that in that case, a magnetic field would enhance the staggered magnetization. A recent neutron scattering experiment (Mason et al. 1993b) however showed that magnetic Bragg scattering in URu_2Si_2 actually decreases with field so the theory may be inapplicable to this material.

To probe higher-order spin correlations, Ramirez et al. (1992) measured the nonlinear magnetic susceptibility, χ_3, shown in the upper frame of fig. 40. A λ-like anomaly similar to that found in the thermal expansion (de Visser et al. 1986b) marks the phase transition. Both of these anomalies suggest that although Walker et al. (1993) confirmed a staggered dipole moment with $\boldsymbol{q} = (1, 0, 0)$ by polarized neutron diffraction, the principal order parameter may be some form of staggered quadrupolar order with a different characteristic wavevector. Ramirez et al. (1992) suggested an interesting non-local quadrupolar order parameter, but it is also possible that conventional ordering of the quadrupolar moment of each uranium atom known for example from UPd_3 (Buyers and Holden 1985) has escaped discovery in URu_2Si_2 (Broholm et al. 1991).

Frustration caused by competing exchange interactions may also play a role in this anomalous phase transition. Indeed, competing exchange is common to many RT_2Si_2 intermetallics where R = Ce, Np (see sect. 2.3) or U (for work on UNi_2Si_2, see Lin

et al. 1991 and Rebelsky et al. 1992). Figure 41 shows the evolution with temperature of low-energy critical scattering at $\hbar\omega = 0.4$ meV and for wavevector transfer along the $(1k0)$ direction (Buyers et al. 1994). For $T > 20$ K, low-energy magnetic fluctuations peak at the incommensurate wavevector $\boldsymbol{q}_m \approx (1, 0.4, 0)$. Interestingly, this wavevector is close to that associated with the incommensurate antiferromagnetic order in doped isostructural $CeRu_2Si_2$ (see sect. 2.3). Low-energy magnetic fluctuations with the wavevector of the antiferromagnetic order in URu_2Si_2 appear only very close to T_N and simultaneously with the development of a pronounced gap in the spectrum for $\boldsymbol{Q} = (1, 0.4, 0)$ (see figs. 36, 38). Perhaps the combination of frustration and a local singlet ground state leads to the unusual antiferromagnetic phase.

It may also be impossible to account for the phase transition within the framework of crystal-field theory. Specifically, sharp crystal-field levels do not exist in the paramagnetic state but emerge from paramagnetic continuum scattering at T_N. To understand why URu_2Si_2 fails to develop stronger static spin correlations (Mason and Buyers 1990), one might then have to consider the modification of hybridization as an integral part of the phase transition.

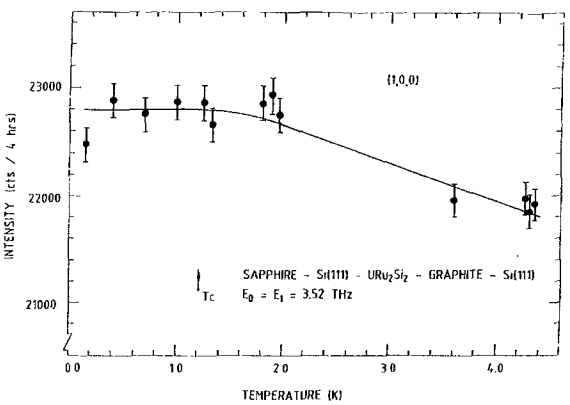

Fig. 42. Temperature dependence of the (1,0,0) magnetic Bragg peak intensity in URu_2Si_2 through its superconducting transition. The line is a guide to the eye. (From Mason et al. 1990.)

4.2.5. *The superconducting phase transition*

The superconductivity below $T_c = 1.1$ K affects neither the static nor the dynamic spin correlations in URu_2Si_2 (Broholm et al. 1991, Mason et al. 1990b). Figure 42 shows the squared staggered magnetization as a function of temperature in the vicinity of T_c. Any anomaly at T_c must be a less than 1% effect, which was taken as evidence against isotropic singlet pairing (Mason et al. 1990b). The field dependence of the staggered magnetization, m_q, for $\boldsymbol{H} \parallel \boldsymbol{c}$ however appears to be different depending on whether the material is superconducting or not. In the normal state there is a linear decrease in the sublattice magnetization with field corresponding to $d \ln m_q / dH = -7.1 \times 10^{-3} T^{-1}$ whereas preliminary data indicate that in the superconducting state obtained after cooling in zero field, m_q is field independent until $H \approx 2$ T (Mason et al. 1990b). Curiously,

though, field cooling does not yield the same result. Further experiments are needed to both confirm and extend these measurements.

5. Strongly correlated insulators

5.1. *Antiferromagnetic TmSe*

Many of the classic intermediate-valence materials discovered in the late seventies (Parks 1977, Falicov et al. 1981) have strongly renormalized metallic ground states with some similarities to the heavy-fermion compounds. The distinction between these related classes of materials is that intermediate-valence systems have real charge fluctuations between two 4f valence states (e.g. $4f^n$ and $4f^{n-1}$) whereas the generic heavy-fermion system has near-integral valence, making magnetic fluctuations the dominant low-energy excitations. When considering the properties of real compounds the distinction appears artificial and we have therefore chosen to include neutron scattering experiments from one of the traditional intermediate-valence compounds in our review.

The characteristic spin fluctuation spectrum of intermediate-valence compounds is not confined to a dispersion relation, but is instead broad and only weakly dependent on temperature. In addition, many intermediate-valence systems remain paramagnetic to the lowest temperatures. This is not the case, however, for the rare-earth chalcogenide TmSe. Among intermediate-valence compounds TmSe is special in that the two 4f electron configurations [$4f^{12}, J=6$ (Tm^{3+}) and $4f^{13}, J=\frac{7}{2}$ (Tm^{2+})] are both magnetic. This leads to magnetic properties which are very different from those for intermediate-valence compounds in which one valence is nonmagnetic ($J=0$). The most notable is a magnetic phase transition at 3.2 K.

The case for intermediate valence in TmSe is as follows: (i) The Curie constant derived from high-temperature susceptibility measurements in apparently single-phase homogeneous material lies between the values expected for $J=6$ ($4f^{12}$) and $J=\frac{7}{2}$ ($4f^{13}$) (Batlogg et al. 1979). (ii) L_{II} and L_{III} X-ray absorption shows multiple edges corresponding to coexistence of Tm^{2+} and Tm^{3+} in stoichiometric samples (Launois et al. 1980). (iii) Magnetic X-ray scattering experiments show that both the Tm^{2+} and Tm^{3+} L_{III} edges contribute in approximately equal proportions to the resonant enhancement of resolution-limited antiferromagnetic Bragg scattering (McWhan et al. 1993).

With intermediate valence come special concerns and opportunities in solid state chemistry: In particular, Tm_xSe exists as a single-phase material for $0.9 < x < 1.04$ (Batlogg et al. 1979). The physical properties vary dramatically over this composition range because of varying cation valence. For $x \approx 0.9$ the valence state of thulium appears close to 3+. As x increases, the average valence decreases but remains between 2+ and 3+ even for the most thulium-rich samples (Batlogg et al. 1979). These changes of valence with composition are reflected in large variations in the room-temperature lattice parameter of the rocksalt structure, from $a = 5.628(5)$ Å for $x = 0.87$ to $a = 5.715(5)$ Å for $x = 1.05$ (Batlogg et al. 1979).

The electronic specific heat of the paramagnetic zero-field state of stoichiometric TmSe (Bucher et al. 1975, Berton et al. 1981) may be interpreted as the superposition of a large linear term, γT with $\gamma = 350\,\mathrm{mJ/mol\,K^2}$, and the tail of a Schottky anomaly with $\Delta \approx 80\,\mathrm{K}$ (Berton et al. 1981). Below the magnetic phase transition, which we shall discuss below, $\gamma \leqslant 50\,\mathrm{mJ/mol\,K^2}$.

5.1.1. *Antiferromagnetic order and phase diagram*

Figure 43b shows the magnetic phase diagram of TmSe [$a(300\,\mathrm{K}) = 5.71\,\text{Å}$] as derived mainly from single-crystal neutron diffraction (Bjerrum-Møller et al. 1977). Boundary I represents a second-order phase boundary between a paramagnet and a type-I FCC antiferromagnet. Figure 43a depicts the antiferromagnetic order which doubles the unit cell along a (0, 0, 1) direction while maintaining the spins in the (0, 0, 1) plane. The ordered moment is $1.7\mu_B$, strongly reduced from the saturation moment of $4\mu_B$ achieved in an applied field of 15 T (Chouteau et al. 1977). Resistivity (Haen et al. 1979) and specific heat measurements (Berton et al. 1981) suggest that the antiferromagnetic phase may be a small band-gap semiconductor, whereas the high-field induced ferromagnetic phase above the first-order phase boundary III is metallic. Indeed, in thulium-rich samples Batlogg et al. (1979) report a hundred-fold reduction in resistivity at 2 K upon the application of a 2 T field, consistent with the presence of a field-induced $T = 0$ metal–insulator transition. Phase boundary II is where a zero-field cooled sample as a function of increasing magnetic field passes from a multi-domain to a single-domain state. Phase boundary IV indicates the locus of points where measurements of bulk properties such as susceptibility (Ott 1977), specific heat and magneto-transport (Lapierre et al. 1981) show anomalies. It is not clear, however, whether this line represents a true phase transition.

From the $H = 0$ critical temperature, the $T = 0$ critical field, and the spin-canting angle α at the critical field, Bjerrum-Møller et al. (1977) derived estimates for the nearest- and next-nearest neighbor exchange constants, $J_{nn} = -3 \times 10^{-3}\,\mathrm{meV}$ and $J_{nnn} = 1.3 \times 10^{-1}\,\mathrm{meV}$, and the cubic crystal-field parameter $B_4 = 4 \times 10^{-4}\,\mathrm{meV}$.

The phase diagram is strongly dependent on the sample stoichiometry: thulium-deficient samples in which thulium is believed to be close to a valence of 3+ have FCC type-II antiferromagnetic order below $T_N \approx 4.6\,\mathrm{K}$, though with a correlation length limited to 100 Å (Shapiro et al. 1978). It is interesting to note that in mean field theory the stability of this phase in a localized spin model implies that both J_{nn} and J_{nnn} are antiferromagnetic (<0) and that $|J_{nn}| < 2|J_{nnn}|$. Therefore, the ferromagnetic next-nearest-neighbor exchange coupling observed for stoichiometric and thulium-rich samples is an oddity of the intermediate-valence state of Tm. Varma and Schlüter (1981) suggested that the constraints on spin correlations imposed by charge fluctuations lead to a double exchange mechanism for ferromagnetic couplings in the intermediate valence limit. Indeed, following Varma's prediction, $TmSe_{0.83}Te_{0.17}$, in which Tm^{2+} is more favored than in stoichiometric TmSe (thulium has valence 2+ in TmTe at ambient pressure), was found to have ferromagnetic order.

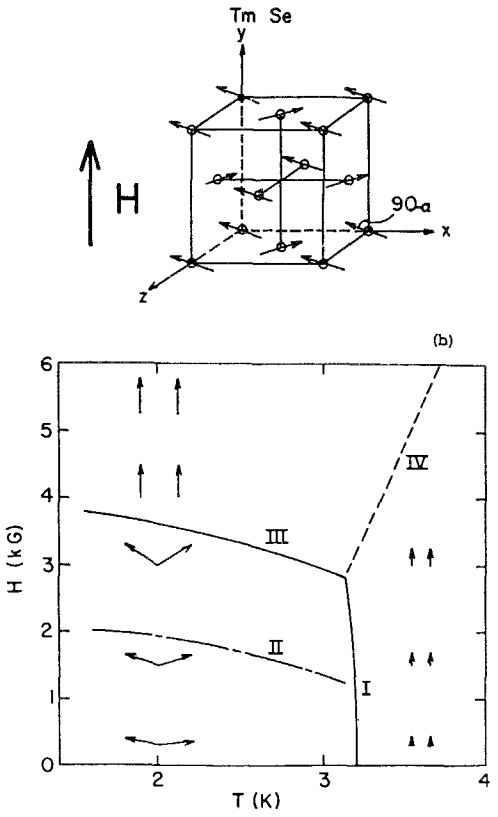

Fig. 43. (a) One domain of the antiferromagnetic structure of TmSe in an applied field along the (0, 1, 0) direction. Here as in zero-field the spins are perpendicular to the high-symmetry tetragonal z-axis of the antiferromagnetic phase. The applied field tilts the spins by an angle α out of their zero-field positions along the (1, 0, 0) axis. (b) Magnetic phase diagram of TmSe with magnetic field applied in a (0, 1, 0) direction. Line II represents a spin-flop transition, line IV represents the location of maxima in the bulk susceptibility. (From Bjerrum-Møller et al. 1977.)

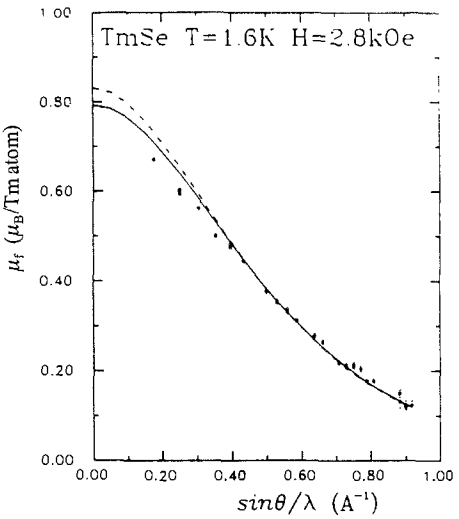

Fig. 44. Magnetic form factor of TmSe in the antiferromagnetic insulating phase. The solid line is the form factor for Tm^{3+}, the dashed line that for Tm^{2+}. (From Bonnet et al. 1986.)

Pressure increases the d–f hybridization and thus tends to stabilize the Tm^{3+} valence and reduce the ferromagnetic next-nearest-neighbor exchange. As a function of pressure there is a maximum in the transition temperature to the antiferromagnetic insulating phase at 1.5 GPa (Ribault et al. 1980) resulting from competition between type-I and type-II antiferromagnetic order. Neutron diffraction experiments as a function of pressure by Debray et al. (1981) have shown that the type-I phase is stable up to 1.5 GPa whereas the type-II phase is stable for pressures beyond 3 GPa, where TmSe remains metallic to $T = 0$

(Ribault et al. 1980). For 1.5 GPa $< P <$ 3 GPa there appears to be a sample-dependent coexistence regime.

Figure 44 shows the magnetic form factor associated with the magnetization induced by a small external field in the antiferromagnetic insulating phase derived from polarized neutron diffraction measurements (Bonnet et al. 1986). Contrary to the high-field induced ferromagnetic phase, the 4f form factor for neither of the two valence states accounts for the results. Bonnet et al. (1986) interpreted their data as indicating the presence of 5d spin density opposed to the induced 4f magnetization density in the insulating phase.

5.1.2. *Low-temperature magnetic excitations in TmSe*

Two energy scales separated by an order of magnitude are important in the low-temperature magnetic excitation spectrum of TmSe. Figure 45 shows the spectrum in the 2–20 meV range (Shapiro and Grier 1982). There is a peak centered around 10 meV which broadens and decreases in intensity as wavevector transfer is varied from the position of the antiferromagnetic Bragg peak (1,0,0) to the position of the nuclear Bragg peak (2,0,0). This energy is close to the characteristic energy of the high-temperature Schottky-like anomaly found in specific heat measurements (Berton et al. 1981). For energies below 2 meV, single-crystal inelastic experiments do not exist. Figure 46 shows data obtained from a stoichiometric TmSe powder sample as a function of applied magnetic field below and immediately above T_N = 3.2 K. At T = 1.9 K in zero field it is apparent that 1 meV represents another characteristic energy for this system. The width of the peak is not due to resolution. Because of the spherical averaging inherent to powder scattering, the experiment leaves open whether the broadening results from the finite lifetime of a collective excitation or the dispersion of a resonant mode.

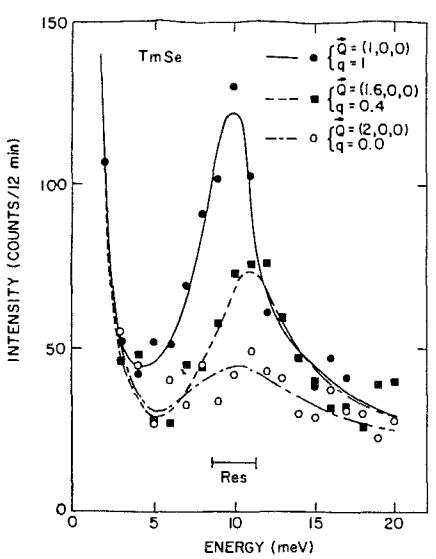

Fig. 45. Inelastic magnetic neutron scattering from single-crystal TmSe at T = 4.6 K. Data for three values of wavevector transfer along the (1,0,0) direction are shown. (From Shapiro and Grier 1982.)

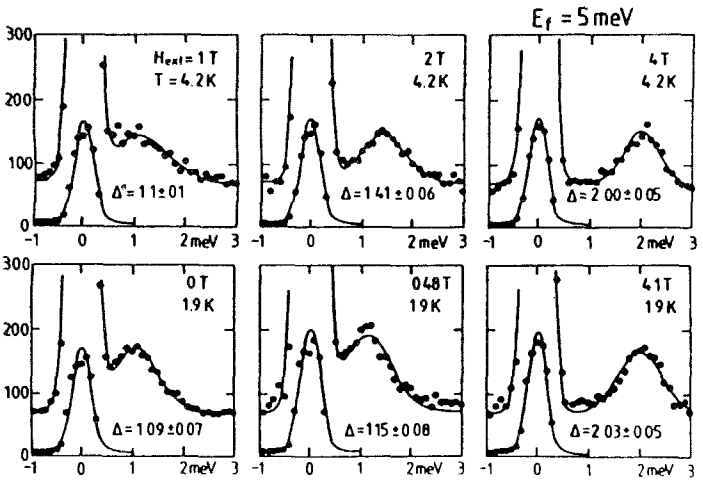

Fig. 46. Inelastic magnetic neutron scattering from polycrystalline TmSe at $T = 4.2\,\mathrm{K} > T_N$ (top row) and $T = 1.9\,\mathrm{K} < T_N$ (bottom row) as a function of applied magnetic field (columns). (From Loewenhaupt and Bjerrum-Møller 1981.)

The 10 meV excitation may be distinguished from a conventional crystal-field excitation by its finite width in energy and its strong dependence on sample stoichiometry (Shapiro and Grier 1982, Holland-Moritz 1983). Furthermore, 10 meV is higher than expected for a crystal-field excitation, exceeding the Γ_1–Γ_4 splitting observed in isostructural TmAs by a factor of 4. A compelling interpretation is that the peak is associated with the excitation of an f–d quasiparticle across a 10 meV hybridization gap (Shapiro and Grier 1982. This interpretation was promoted by Fedro and Sinha (1982) who reproduced some qualitative features of the data when calculating the dynamical correlation function for the f–d hybridized quasiparticles associated with a band containing a single f electron (contrary to the case for thulium) crossing a free electron band. This interpretation was however brought into question by experiments which showed a similar inelastic excitation in diluted polycrystalline Tm(La, Y)Se alloys (Holland-Moritz 1983, Holland-Moritz and Lander 1994).

5.2. *Paramagnetic CeNiSn*

With the discovery of the semiconducting behavior of CeNiSn (Takabatake et al. 1990, Aliev et al. 1988) and $Ce_3Bi_4Pt_3$ (Hundley et al. 1990, Severing et al. 1991) one could legitimately assert that heavy-fermion compounds display the entire gamut of electronic ground states one associates with conventional, three-dimensional solids. While experience with materials such as FeSi (Foëx 1938, Shirane et al. 1987, Tajima et al. 1988), SmB_6 (Nickerson et al. 1971) and TmSe (Shapiro and Grier 1982, see above) long presaged these discoveries, the existence of Ce-based heavy-mass semiconductors greatly simplified systematic investigation of strongly correlated insulators (Aeppli and

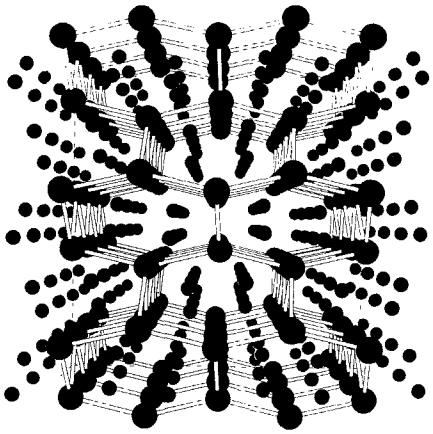

Fig. 47. Structure of CeNiSn, looking along the *b* direction. The *a* and *c* directions are vertical and horizontal, respectively. Large spheres are Ce atoms, small spheres are Ni and Sn atoms. (Drawing kindly provided by T.E. Mason.)

Fisk 1992). Especially important is the ease with which large crystals (volume $\geqslant 1\,\mathrm{cm}^3$) of CeNiSn could be fabricated, thus making neutron scattering experiments possible.

CeNiSn belongs to the orthorhombic ε-TiNiSn family (see fig. 47) with room-temperature lattice parameters $a = 7.523$ Å, $b = 4.592$ Å, $c = 7.561$ Å (Skolozdra et al. 1984). Single-crystal investigations (Aeppli et al. 1992, Mason et al. 1992a,b) published thus far have been limited to the $(h, 0, l)$ zone. Figures 48 and 49 show the main results of these investigations in the form of a survey, with coarse energy resolution, of the $\boldsymbol{Q}$ dependence of the scattering and constant-$\boldsymbol{Q}$ scans at a variety of momentum transfers. The first conclusion is that as in metallic heavy-fermion paramagnets, cooling leads to the development of pronounced antiferromagnetic correlations, peaked in this zone at (0, 0, 1). At the same time and in contrast to what occurs in the metallic systems, it also yields a cross-over from the quasielastic continuum scattering characteristic of Kondo systems to a clearly gapped signal at particular values of $\boldsymbol{Q}$, for example, those near (0, 0, 1) (see upper frame of fig. 49). Of course, we expect (Riseborough 1992, Millis 1992, Fedro and Sinha 1982) such behavior for a semiconductor which emerges from a dirty metal at low temperature in the same way that we eventually expect to see Fermi liquid behavior in a strongly interacting metal like UPt_3. However, just as the latter has been difficult to find in the metals, the mean field (Lindhard) approach has severe qualitative difficulties in the case of nearly insulating CeNiSn.

The middle frame of fig. 49 shows the most obvious problem, namely that at $\boldsymbol{Q} = (0.36, 0, 1.2)$ there are substantial low-frequency magnetic fluctuations remaining in the "insulating" regime. Thus, in contrast to an ordinary semiconductor, CeNiSn displays a gap which is well-defined only at particular wavevectors. Another curious result is that while $\chi''(\boldsymbol{Q}, \omega)$ is obviously a strong function of $\boldsymbol{Q}$, the zero-frequency real part of $\chi(\boldsymbol{Q}, \omega)$, defined by the Kramers-Kronig relation,

$$\chi'(\boldsymbol{Q}, 0) = \frac{1}{\pi} \int \frac{1}{\omega} \chi''(\boldsymbol{Q}, \omega)\, \mathrm{d}\omega, \tag{5.1}$$

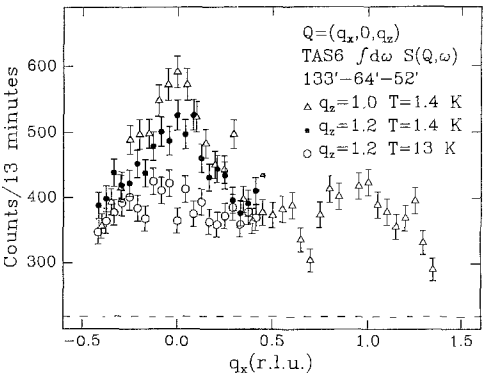

Fig. 48. $\boldsymbol{Q}$ dependence of energy-integrated scattering from CeNiSn. The dashed–dotted line represents $\boldsymbol{Q}$-independent scattering (including nonmagnetic background) established for $\boldsymbol{Q} \parallel \boldsymbol{a}^*$. (From Mason et al. 1992a,b.)

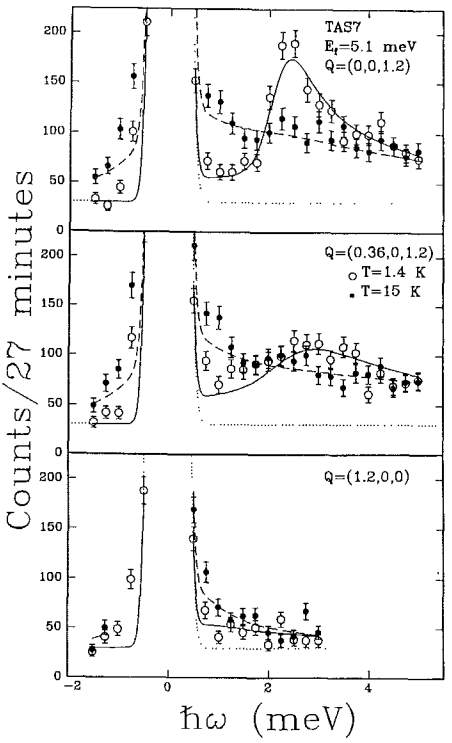

Fig. 49. Constant-$\boldsymbol{Q}$ scans collected for CeNiSn at temperatures above (15 K) and below (1.4 K) the cross-over to "insulating" behavior. (From Mason et al. 1992a,b.)

is not a strong function of $\boldsymbol{Q}$. When we recall that $\chi'(\boldsymbol{Q}, 0)$ can be used to define an effective coupling $J(\boldsymbol{Q})$ via the RPA expression $\chi'(\boldsymbol{Q}, 0) = \chi_0/[1 - \chi_0 J(\boldsymbol{Q})]$, this means that, in the limit $\omega \to 0$, the moments in this dense rare-earth compound effectively do not interact, even though they manifestly do so at $\omega \neq 0$. The last result is entirely contrary to experience with the metallic heavy-fermion systems, as well as with essentially all rare-earth and actinide materials. The only compound for which a similar phenomenon has been reported for the thermally activated excitations below the gap is FeSi (Foëx 1938, Shirane et al. 1987, Tajima et al. 1988). Because of neutron energy limitations which do not apply to CeNiSn, magnetic excitations across the 60 meV gap of FeSi have yet to be observed (Schlesinger et al. 1993).

6. Form factor measurements

Using polarizeddiffraction, it is possible to examine the field-induced contribution to zone-center reflections and thereby deduce the form factors for the electrons yielding the magnetic response. Such investigations have been very productive when applied to both mixed-valence compounds and conventional superconductors. For example Shull

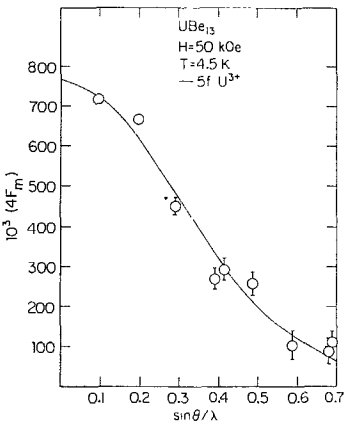

Fig. 50. Induced moment form factor of UBe_{13}. (From Stassis et al. 1986.)

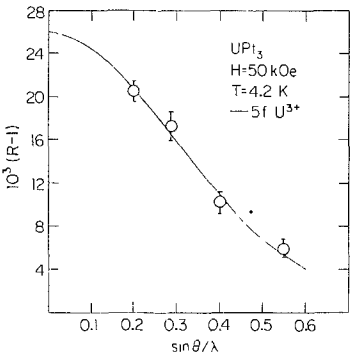

Fig. 51. Induced moment form factor of UPt_3. (From Stassis et al. 1986.)

and Wedgewood (1966) were able to demonstrate that in V_3Si the Cooper pairs are formed between d-electrons. Also, they showed that superconductivity does not affect the orbital susceptibility. Motivated by the success of Shull and Wedgewood (1966), Stassis et al. (1986) performed similar measurements on single crystals of three heavy-fermion superconductors, namely UPt_3, UBe_{13}, and $CeCu_2Si_2$. Their findings were (1) that the magnetic form factors contain discernible contributions only from 4f (Ce) or 5f (U) electrons (see figs. 50, 51) and (2) that to within the 10–20% uncertainty of the measurements, superconductivity does not affect field-induced moments. Result (1) was also obtained by Benoit et al. (1985) for the induced moment form factor of the non-superconducting paramagnet $CeInSn_2$ (see sect. 2.5). The simplest interpretation of both of these result is that (f shell) orbital terms dominate the magnetic susceptibility, a result also consistent with the difficulty of finding an intraband Fermi-liquid contribution to the inelastic neutron scattering data. The small Kondo temperatures of the heavy-fermion materials correspond to greatly enhanced f-electron susceptibilities at low temperatures, thus obscuring s and d contributions found in mixed-valent compounds such as $CeSn_3$ (Stassis et al. 1979), $CePd_3$ (Stassis et al. 1982), and TmSe (see sect. 5.1.1).

7. Summary and conclusions

The most important contribution of single-crystal neutron scattering experiments to our knowledge of heavy-fermion systems has been to demonstrate the strong antiferromagnetic (AFM) correlations in these unusual compounds. The AFM correlations distinguish the concentrated heavy-fermion systems from their dilute Kondo relatives, and are responsible for phenomena ranging from 'metamagnetism' to unconventional superconductivity. The neutron measurements show that a single effective-band theory cannot account for all of the correlations, thus proving that combining single-impurity

physics with Bloch's theorem constitutes at best a partial description of even the low-T behavior of heavy-fermion materials. The fundamental reason for the failure of such a mean-field description is perhaps most obvious for U_2Zn_{17}, where a temperature-dependent effective RKKY coupling J_{RKKY} rather than a rising single-ion susceptibility drives the antiferromagnetic transition.

Numerous diffraction studies revealing long-range antiferromagnetic order upon doping almost all heavy-fermion compounds also demonstrate that a nearly critical J_{RKKY} is a defining feature of such compounds. That J_{RKKY} can be renormalized downwards as well as upwards with decreasing T and ω follows from the neutron measurements on low carrier density CeNiSn.

Beyond the very basic result that multi-site correlations are not a simple outgrowth of single-impurity physics, single-crystal neutron experiments have made several other key contributions to heavy-fermion science:

(1) An explicit demonstration of the coupling between magnetic and superconducting order parameters in UPt_3.
(2) Discovery of a highly anisotropic vortex lattice, with conventional quantization in UPt_3, a compound whose normal state properties are quite isotropic.
(3) Observation and characterization of the spin gap which appears upon the onset of semiconducting behavior in the Kondo insulator CeNiSn.

Acknowledgements

We are very grateful to our generous collaborators and correspondents whose names appear in the references but who are far too numerous to list here. Without them the work reported here would not have been possible. However, we single out G.H. Lander for special thanks, on account of his advice, encouragement, and infinite patience during the long gestation of this manuscript.

References

Abrahams, E., and C.M. Varma, 1987, unpublished.

Aeppli, G., 1992, in: Phenomenology and Applications of High-Temperature Superconductors, eds K.S. Bedell, M. Inui, D. Meltzer, J.R. Schrieffer and S. Doniach (Addison-Wesley, Reading, MA) p. 335 (for a brief introduction to μSR technique applied to vortex lattices).

Aeppli, G., and Z. Fisk, 1992, Comm. Condens. Matter Phys. **16**, 155.

Aeppli, G., S.M. Shapiro, R.J. Birgeneau and H.S. Chen, 1984, Phys. Rev. B **29**, 2589.

Aeppli, G., H. Yoshizawa, Y. Endoh, E. Bucher, J. Hufnagl, Y. Onuki and T. Komatsubara, 1986, Phys. Rev. Lett. **57**, 122.

Aeppli, G., A.I. Goldman, G. Shirane, E. Bucher and M.-Ch. Lux-Steiner, 1987, Phys. Rev. Lett. **58**, 808.

Aeppli, G., E. Bucher, C. Broholm, J.K. Kjems, J. Baumann and J. Hufnagl, 1988a, Phys. Rev. Lett. **60**, 615.

Aeppli, G., E. Bucher, A.I. Goldman, G. Shirane, C. Broholm and J.K. Kjems, 1988b, J. Magn. & Magn. Mater. **76–77**, 385.

Aeppli, G., D. Bishop, C. Broholm, E. Bucher, K. Siemensmeyer, M. Steiner and N. Stüsser, 1989, Phys. Rev. Lett. **63**, 676.

Aeppli, G., E. Bucher and T.E. Mason, 1992, in: Physical Phenomena at High Magnetic Fields, eds E. Manousakis, P. Schlottmann, P. Kumar,

K. Bedell and F.M. Mueller (Addison-Wesley, Redwood City).

Aeppli, G., H.A. Mook, T.E. Mason, S.M. Hayden, A.D. Taylor, T.G. Perring, K.N. Clausen, P. Littlewood, S.-W. Cheong and Z. Fisk, 1994, in: Perspectives in Many Particle Physics, Proc. Int. School of Physics "Enrico Fermi", 1992, Varenna, Italy (North-Holland, Amsterdam).

Aliev, F.G., N.B. Brandt, V.V. Moshchalkov, V.A. Kozyr'kov, M.K. Zalalutdinov and R.V. Skolozdra, 1988, JETP Lett. **48**, 581.

Andersen, N.H., and H. Smith, 1979, Phys. Rev. B **19**, 384.

Asayama, K., Y. Kitaoka and Y. Kohori, 1988, J. Magn. & Magn. Mater. **76–77**, 449.

Auerbach, A., J.H. Kim and K. Levin, 1987, Physica B **148**, 50.

Auerbach, A., J.H. Kim, K. Levin and M.R. Norman, 1988, Phys. Rev. Lett. **60**, 623.

Axe, J.D., S.M. Shapiro, G. Shirane and T. Riste, 1974, in: Proc. NATO Advanced Study Institute on Anharmonic Lattices, Structural Phase Transitions, and Melting, Geilo, Norway, 1973, ed. T. Riste (Noordhoff, Leiden).

Barth, S., H.R. Ott, F.N. Gygax, B. Hitti, E. Lippelt and A. Schenck, 1988, J. Magn. & Magn. Mater. **76–77**, 455.

Barzykin, V., and L.P. Gorkov, 1993, Phys. Rev. Lett. **70**, 2479.

Batlogg, B., H.R. Ott, E. Kaldis, W. Thöni and P. Wachter, 1979, Phys. Rev. B **19**, 247.

Béal-Monod, M.T., C. Bourbormais and V.J. Emery, 1986, Phys. Rev. B **34**, 7716.

Benoit, A., J.X. Boucherle, P. Conukt, J. Flouquet, J. Palleau and J. Schweizer, 1980, Solid State Commun. **34**, 293.

Benoit, A., J.X. Boucherle, J. Flouquet, J. Sakurai and J. Schweizer, 1985, J. Magn. & Magn. Mater. **47–48**, 149.

Berton, A., J. Chaussy, B. Cornut, J. Flouquet, J. Odin, J. Peyrard and F. Holtzberg, 1981, Phys. Rev. B **23**, 3504.

Besnus, M.J., J.P. Kappler, P. Lehmann and A. Mayer, 1985, Solid State Commun. **55**, 779.

Bjerrum-Møller, H., S.M. Shapiro and R.J. Birgeneau, 1977, Phys. Rev. Lett. **39**, 1021.

Blount, E.I., C.M. Varma and G. Aeppli, 1990, Phys. Rev. Lett. **64**, 3074.

Bonnet, M., J.X. Boucherle, J. Flouquet, F. Holtzberg, D. Jaccard, J. Schweizer and A. Stunault, 1986, Physica B **136**, 428.

Bonnisseau, D., P. Burlet, M. Bogé, S. Quezel, J. Rossat-Mignod, J.C. Spirlet and J. Rebizant, 1988, J. Phys. **49**, C8-491.

Broholm, C., 1988, in: Magnetic Fluctuations in Heavy Fermion Systems, Risø-M-2731. Available on request from the Library of Risø National Laboratory, Box 49, 4000 Roskilde, Denmark.

Broholm, C., J.K. Kjems, G. Aeppli, Z. Fisk, J.L. Smith, S.M. Shapiro, G. Shirane and H.R. Ott, 1987a, Phys. Rev. Lett. **58**, 917.

Broholm, C., J.K. Kjems, W.J.L. Buyers, P. Matthews, T.T.M. Palstra, A.A. Menovsky and J.A. Mydosh, 1987b, Phys. Rev. Lett. **58**, 1467.

Broholm, C., G. Aeppli, R.N. Kleiman, D.R. Harshman, D.J. Bishop, E. Bucher, D.L. Williams, E.J. Ansaldo and R.H. Heffner, 1990, Phys. Rev. Lett. **65**, 2062.

Broholm, C., H. Lin, P.T. Matthews, T.E. Mason, W.J.L. Buyers, M.F. Collins, A.A. Menovsky, J.A. Mydosh and J.K. Kjems, 1991, Phys. Rev. B **43**, 12809.

Bucher, E., K. Andres, F.J. di Salvo, J.P. Maita, A.C. Gossard, A.S. Cooper and G.W. Hull Jr, 1975, Phys. Rev. B **11**, 500.

Buyers, W.J.L., and T.M. Holden, 1985, in: Handbook on the Physics and Chemistry of the Actinides, Vol. 2, eds A.J. Freeman and G.H. Lander (North-Holland, Amsterdam).

Buyers, W.J.L., T.M. Holden and A. Perreault, 1975, Phys. Rev. B **11**, 266.

Buyers, W.J.L., Z. Tun, T. Petersen, T.E. Mason, J.-G. Lussier, B.D. Gaulin and A.A. Menovsky, 1994, in: Proc. Int. Conf. on Strongly Correlated Electron Systems, San Diego, CA, August 1993, Physica B **199–200**, 95.

Chelmicki, L., J. Lcciejewicz and A. Zygmunt, 1985, J. Phys. Chem. Solids **46**, 529.

Chouteau, G., F. Holtzberg, J.M. Mignot, O. Pena and R. Tournier, 1977, in: Valence Instabilities and Related Narrow Band Phenomena, ed. R.D. Park (Plenum Press, New York).

Collins, M.F., 1989, Magnetic Critical Scattering (Oxford University Press, Oxford).

Cox, D.E., G. Shirane, S.M. Shapiro, G. Aeppli, Z. Fisk, J.L. Smith, J.K. Kjems and H.R. Ott, 1986, Phys. Rev. B **33**, 3614.

Cribier, D., B. Jacrot, L.M. Rao and B. Farmoux, 1964, Phys. Lett. **9**, 106.

de Visser, A., S.C.P. Klaase, M. van Sprang, J.J.M. Franse, A. Menovsky and T.T.M. Palstra, 1986a, J. Magn. & Magn. Mater. **54–57**, 375.

de Visser, A., F.E. Kayzel, A.A. Menovsky, J.J.M. Franse, J. van den Berg and G.J. Nieuwenhuys, 1986b, Phys. Rev. B **34**, 8168.

Debray, D., R. Kahn, D.L. Decker, A. Werner, M. Loewenhaupt, E. Holland-Moritz and D.K. Ray, 1981, in: Valence Fluctuations in Solids, eds L.M. Falicov, W. Hanke and M.B. Maple (North-Holland, New York).

Demcsyk, B.G., M. Aronson and B. Coles, 1992, preprint.

Elenbaas, R.A., C.J. Schinkel and C.J.M. van Deudekom, 1980, J. Magn. & Magn. Mater. **15–18**, 979.

Ellman, B., J. Yang, T.F. Rosenbaum and E. Bucher, 1990, Phys. Rev. Lett. **64**, 1569.

Falicov, L.M., W. Hanke and M.B. Maple, 1981, Valence Fluctuations in Solids (North-Holland, New York).

Fedro, A.J., and S.K. Sinha, 1982, in: Valence Fluctuations in Solids, eds L.M. Falicov, W. Hanke and M.B. Maple (North-Holland, New York).

Feile, R., M. Loewenhaupt and J.K. Kjems, 1981, Phys. Rev. Lett. **47**, 610.

Fisher, R.A., S. Kim, B.F. Woodfield, N.E. Phillips, L. Taillefer, K. Hasselbach, J. Flouquet, A.L. Giorgi and J.L. Smith, 1989, Phys. Rev. Lett. **62**, 1411.

Fisk, Z., and G. Aeppli, 1993, Science **260**, 38.

Flouquet, J., P. Haen, F. Lapierre, D. Jaccard and G. Remenyi, 1986, J. Magn. & Magn. Mater. **54–57**, 322.

Foëx, S., 1938, J. Phys. Radium **9**, 37.

Forgan, E.M., et al., 1990, Nature (London) **343**, 735.

Frazer, B.C., G. Shirane, D.E. Cox and C.E. Olsen, 1965, Phys. Rev. 140, A1448.

Frings, P.H., 1984, Thesis (University of Amsterdam) unpublished.

Frings, P.H., and J.J.M. Franse, 1985, Phys. Rev. **31**, 4355.

Frings, P.H., J.J.M. Franse, F.R. de Boer and A.A. Menovsky, 1983, J. Magn. & Magn. Mater. **31–34**, 240.

Frings, P.H., B. Renker and C. Vettier, 1987, J. Magn. & Magn. Mater. **63–64**, 202.

Glyde, H.R., and E.C. Svensson, 1987, in: Methods of Experimental Physics, Vol. 23B, eds D.L. Price and K. Skold (Academic Press, New York) pp. 303–403.

Goldman, A.I., G. Shirane, G. Aeppli, B. Batlogg and E. Bucher, 1986, Phys. Rev. B **34**, 6564.

Goldman, A.I., G. Shirane, G. Aeppli, E. Bucher and J. Hufnagl, 1987, Phys. Rev. B **36**, 8523.

Goll, G., H. v. Löhneysen, I.K. Yanson and L. Taillefer, 1993, Phys. Rev. Lett. **70**, 2008.

Gorkov, L.P., 1991, Europhys. Lett. **16**, 301.

Goss-Levi, B., 1993, Phys. Today **46**, 9.

Haen, P., F. Lapierre, J.M. Mignot and R. Tournier, 1979, Phys. Rev. Lett. **43**, 304.

Haen, P., J. Flouquet, F. Lapierre, P. Lejay and G. Remenyi, 1987, J. Low Temp. Phys. **67**, 391.

Hasselbach, K., L. Taillefer and J. Flouquet, 1989, Phys. Rev. Lett. **63**, 93.

Hayden, S.M., L. Taillefer, C. Vettier and J. Flouquet, 1992, Phys. Rev. B **46**, 8675.

Hayden, S.M., C. Broholm, L. Taillefer, G. Aeppli, A. Ramirez, E. Bucher and N. Stücheli, 1994, unpublished.

Heal, T.J., and G.I. Williams, 1955, Acta. Crystallogr. **8**, 494.

Heffner, R.H., 1987, in: Proc. 5th Int. Conf. on Valence Fluctuations, Bangalore, India, eds S. Malik and K. Gupta (Plenum Press, New York).

Heffner, R.H., D.W. Cooke, A.L. Giorgi, R.L. Hutson, M.E. Schillaci, H.D. Rempp, J.L. Smith, J.O. Willis, D.E. MacLaughlin, C. Boekema, R.L. Lichti, J. Oostens and A.B. Denison, 1989, Phys. Rev. B **39**, 11345.

Hess, D.W., T.A. Tokuyasu and J.A. Sauls, 1989, J. Phys. Condens. Matt. **1**, 8135.

Hewson, A.C., 1993, The Kondo Problem to Heavy Fermions (Cambridge University Press, Cambridge).

Hirsch, J.E., 1985, Phys. Rev. Lett. **54**, 1317.

Holland-Moritz, E., 1983, J. Magn. & Magn. Mater. **38**, 253.

Holland-Moritz, E., and G.H. Lander, 1994, ch. 130, this volume.

Hundley, M.F., P.C. Canfield, J.D. Thompson, Z. Fisk and J.M. Lawrence, 1990, Phys. Rev. B **42**, 6842.

Iandelli, A., and A. Palenzona, 1967, J. Less-Common Met. **12**, 1333.

Isaacs, E.D., D.B. McWhan, R.N. Kleiman, D.J. Bishop, G.E. Ice, P. Zschack, B.D. Gaulin, T.E. Mason, J.D. Garrett and W.J.L. Buyers, 1990, Phys. Rev. Lett. **65**, 3185.

Isaacs, E.D., P. Zschack, C. Broholm, C. Burns, G. Aeppli, A.P. Ramirez, R.W. Erwin, C.S. Oglesby, N. Stücheli and E. Bucher, 1994, unpublished.

Jaccarino, V., G.K. Wertheim, H.H. Wernick, L.R. Walker and S. Arajs, 1967, Phys. Rev. **160**, 476.

Jacoud, J.L., L.P. Regnault, J.M. Mignot, J. Rossat-Mignod, J. Flouquet and P. Lejay, 1992, J. Magn. & Magn. Mater. **108**, 131.

Jensen, J., and A.R. Mackintosh, 1991, Rare Earth Magnetism (Oxford University Press, Oxford).

Jin, D.S., S.A. Carter, B. Ellman, T.F. Rosenbaum and D.G. Hinks, 1992, Phys. Rev. Lett. **68**, 1597.

Jones, B., and C.M. Varma, 1987, Phys. Rev. Lett. **58**, 843.

Joynt, R., 1988, Supercond. Sci. Tech. **1**, 210.

Joynt, R., and T.M. Rice, 1988, Phys. Rev. B **38**, 2345.

Joynt, R., V.P. Mineev, G.E. Volovik and M.E. Zhitomirsky, 1990, Phys. Rev. B **42**, 2014.

Kadowaki, K., S. Mitsuda, H. Yoshizawa, L. Rebelsky, S.M. Shapiro, A. Kobori, Y. Onuki and T. Komatsubara, 1989, J. Phys. Soc. Jpn. **58**, 4292.

Kagayama, T., G. Oomi, H. Takahashi, N. Mori, Y. Onuki and T. Komatsubara, 1991, Phys. Rev. B **44**, 7690.

Kagayama, T., G. Oomi, R. Yagi, Y. Iye, Y. Onuki and T. Komatsubara, 1992, J. Phys. Soc. Jpn. **61**, 2632.

Kleiman, R.N., P.L. Gammel, E. Buchcr and D.J. Bishop, 1989, Phys. Rev. Lett. **62**, 328.

Kleiman, R.N., C. Broholm, G. Aeppli, E. Bucher, N. Stücheli, D.J. Bishop, K.N. Clausen, K. Mortensen, J.S. Pedersen and B. Howard, 1992, Phys. Rev. Lett. **69**, 3120.

Krimmel, A., P. Fischer, B. Roessli, H. Maletta, C. Geibel, C. Schank, A. Grauel, A. Loidl and F. Steglich, 1992, Z. Phys. B **86**, 161.

Lahiouel, R., J. Pierre, E. Siaud and A.P. Murani, 1987a, J. Magn. & Magn. Mater. **63–64**, 104.

Lahiouel, R., J. Pierre, E. Siaud, R.M. Galera, M.J. Besnus, J.P. Kappler and A.P. Murani, 1987b, Z. Phys. B **67**, 185.

Lapierre, F., M. Mignot, J. Flouquet, P. Haen, M. Ribault and F. Holtzberg, 1981, in: Valence Fluctuations in Solids, eds L.M. Falicov, W. Hanke and M.B. Maple (North-Holland, New York).

Launois, H., M. Rawiso, E. Holland-Moritz, R. Pott and D. Wohlleben, 1980, Phys. Rev. Lett. **44**, 1271.

Lawrence, J.M., 1979, Phys. Rev. B **20**, 3770.

Lawrence, J.M., and S.M. Shapiro, 1980, Phys. Rev. B **22**, 4379.

Lin, H., L. Rebelsky, M.F. Collins, J.D. Garrett and W.J.L. Buyers, 1991, Phys. Rev. B **43**, 13232.

Liu, S.H., 1993, in: Handbook on the Physics and Chemistry of Rare Earths, Vol. 17, eds K.A. Gschneidner Jr and L. Eyring (North-Holland, Amsterdam) ch. 111.

Loewenhaupt, M., and H. Bjerrum-Møller, 1981, Physica B **108**, 1349.

Loidl, A., B. Renker, H. Rietschel, P. Frings, E. Bucher and M.-Ch. Lux-Steiner, 1988, J. Magn. & Magn. Mater. 76–77, 441.

Lonzarich, G.G., 1986, J. Magn. & Magn. Mater. **54–57**, 612.

Lovesey, S.W., 1984, Theory of Neutron Scattering From Condensed Matter, Vols. 1, 2 (Clarendon Press, Oxford).

Lu, J.P., 1992, Phys. Rev. Lett. **68**, 125.

Luke, G.M., A. Keren, L.P. Le, W.D. Wu, Y.J. Uemura, D.A. Bonn, L. Taillefer and J.D. Garrett, 1993, Phys. Rev. Lett. **71**, 1466.

Machida, K., M. Ozaki and T. Ohmi, 1989, J. Phys. Soc. Jpn. **58**, 4116.

Maple, M.B., J.W. Chen, Y. Dalichaouch, T. Kohara, C. Rossel, M.S. Torikachvili, M.W. McElfresh and J.D. Thompson, 1986, Phys. Rev. Lett. **56**, 185.

Mason, T.E., and W.J.L. Buyers, 1990, Phys. Rev. B **43**, 11471.

Mason, T.E., B.D. Gaulin, J.D. Garrett, Z. Tun, W.J.L. Buyers and E.D. Isaacs, 1990a, Phys. Rev. Lett **65**, 3189.

Mason, T.E., H. Lin, M.F. Collins, W.J.L. Buyers, A.A. Menovsky and J.A. Mydosh, 1990b, Physica B **163**, 45.

Mason, T.E., G. Aeppli and H.A. Mook, 1992a, Phys. Rev. Lett. **68**, 1414.

Mason, T.E., G. Aeppli, A.P. Ramirez, K.N. Clausen, C. Broholm, N. Stücheli, E. Bucher and T.T.M. Palstra, 1992b, Phys. Rev. Lett. **69**, 490.

Mason, T.E., G. Aeppli, S.M. Hayden, A.P. Ramirez and H. Mook, 1993a, Phys. Rev. Lett. **71**, 919.

Mason, T.E., W.J.L. Buyers, T. Petersen, A.A. Menovsky and J.D. Garrett, 1993b, Phys. Rev. B, submitted.

McWhan, D.B., E.D. Isaacs, P. Paolo Carra, S.M. Shapiro, B.T. Thole and S. Hoshino, 1993, Phys. Rev. B **47**, 8630.

Midgley, P.A., S.M. Hayden and L. Taillefer, 1993, Phys. Rev. Lett. **70**, 678.

Mignot, J.M., J.L. Jacoud, L.P. Regnault, J. Rossat-Mignod, P. Haen, P. Lejay, Ph. Boutroville, B. Hennion and D. Petitgrand, 1990, Physica B **163**, 611.

Mignot, J.M., P.H. Boutrouille, L.P. Regnault, P. Haen and P. LeJay, 1991, Solid State Commun. **77**, 317.

Millis, A., 1992, in: Physical Phenomena at High Magnetic Fields, eds E. Manousakis, P. Schlottmann, P. Kumar, K. Bedell and F.M. Mueller (Addison-Wesley, Redwood City).

Millis, A., S. Sachdev and C.M. Varma, 1988, Phys. Rev. B **37**, 4975.

Miyake, K., S. Schmitt-Rink and C.M. Varma, 1986, Phys. Rev. B **34**, 6554.

Mook, H.A., M. Yethiraj, G. Aeppli and T.E. Mason, 1993, Phys. Rev. Lett. **70**, 3490.

Moriya, T., 1985, Spin Fluctuations in Itinerant Electron Magnetism (Springer, Berlin).

Müller, V., Ch. Roth, D. Maurer, E.W. Scheidt and K. Lüders, 1987, Phys. Rev. Lett. **58**, 1224.

Murani, A.P., 1987, Phys. Rev. B **36**, 5705.

Murani, A.P., R. Currat, A. Severing and R. Raphel, 1990, Physica B **163**, 717.

Murasik, A., S. Ligenza and A. Zygmunt, 1974, Phys. Status Solidi a 23, K163.

Najib, A., J. Pierre, M.J. Besnus, P. Haen, A.P. Murani and E. Siaud, 1988a, Z. Phys. B **73**, 49.

Najib, A., J. Pierre, M.J. Besnus, P. Haen, A.P. Murani and E. Siaud, 1988b, J. Magn. & Magn. Mater. **76–77**, 135.

Nakamura, H., Y. Kitaoka, K. Asayama, Y. Onuki and T. Komatsubara, 1988, J. Phys. Soc. Jpn. **57**, 2276.

Nickerson, J.C., R.M. White, K.N. Lee, R. Bachmann, T.H. Geballe and G.W. Hull Jr, 1971, Phys. Rev. B **3**, 2030.

Ning, Y.B., J.D. Garrett and W.R. Datars, 1990, Phys. Rev. B **42**, 8780.

Ning, Y.B., V.V. Gridin, C.V. Stager, W.R. Datars, L.R. Dawson and D.H. Ryan, 1991, J. Phys. Condens. Matter **3**, 4399.

Norman, M.R., and D.D. Koelling, 1993, in: Handbook on the Physics and Chemistry of Rare Earths, Vol. 17, eds K.A. Gschneidner Jr, L. Eyring, G.H. Lander and G.R. Choppin (North-Holland, Amsterdam) ch. 110, p. 1.

Onuki, Y., Y. Shimizu and T. Komatsubara, 1984, J. Phys. Soc. Jpn. **53**, 1210.

Onuki, Y., Y. Shimizu and T. Komatsubara, 1985, J. Phys. Soc. Jpn. **54**, 304.

Onuki, Y., T. Yamazaki, A. Kobori, T. Omi, S. Komatsubara, S. Takayanagi, H. Kato and N. Wada, 1987, J. Phys. Soc. Jpn. **56**, 4251.

Ott, H.R., 1977, in: Valence Instabilities and Related Narrow Band Phenomena, ed. R.D. Park (Plenum Press, New York).

Ott, H.R., and Z. Fisk, 1987, in: Handbook on the Chemistry and Physics of the Actinides, eds A.J. Freeman and G.H. Lander (North-Holland, Amsterdam).

Ott, H.R., H. Rudiger, P. Delsing and Z. Fisk, 1984, Phys. Rev. Lett. **52**, 1551.

Palstra, T.T.M., 1986, in: Magnetism, Superconductivity and their Interplay, Thesis (University of Leiden).

Palstra, T.T.M., A.A. Menovsky, J. van den Berg, A.J. Dirkmaat, P.H. Kes, G.J. Nieuwenhuys and J.A. Mydosh, 1985, Phys. Rev. Lett. **55**, 2727.

Palstra, T.T.M., A.A. Menovsky and J.A. Mydosh, 1986a, Phys. Rev. B **33**, 6527.

Palstra, T.T.M., A.A. Menovsky, G.J. Nieuwenhuys and J.A. Mydosh, 1986b, J. Magn. & Magn. Mater. **54–57**, 435.

Parks, R.D., 1977, ed: Valence Instabilities and Related Narrow Band Phenomena (Plenum Press, New York).

Penney, T., J. Stankiewicz, S. von Molnar, Z. Fisk, J.L. Smith and H.R. Ott, 1986, J. Magn. & Magn. Mater. **54–57**, 370.

Pierre, J., P. Haen, C. Vettier and S. Pujol, 1990, Physica B **163**, 463.

Pines, D., and P. Nozières, 1966, Quantum Liquids (Benjamin, New York).

Quezel, S., P. Burlet, J.L. Jacoud, L.P. Regnault, J. Rossat-Mignod, C. Vettier, P. LeJay and J. Flouquet, 1988, J. Magn. & Magn. Mater. **76–77**, 403.

Ramirez, A.P., B. Batlogg, A.S. Cooper and E. Bucher, 1986, Phys. Rev. Let. **57**, 1072.

Ramirez, A.P., T. Siegrist, T.T.M. Palstra, J.D. Garrett, E. Bruck, A.A. Menovsky and J.A. Mydosh, 1991, Phys. Rev. B **44**, 5392.

Ramirez, A.P., P. Coleman, P. Chandra, E. Bruck, A.A. Menovsky, Z. Fisk and E. Bucher, 1992, Phys. Rev. Lett. **68**, 2680.

Rebelsky, L., H. Lin, M.W. McElfresh, M.F. Collins, J.D. Garrett, W.J.L. Buyers and M.S. Torikachvili, 1992, Physica B **180–181**, 43.

Regnault, L.P., W.A.C. Erkelens, J. Rossat-Mignod, J. Flouquet, E. Walker, D. Jaccard, A. Amato and B. Hennion, 1987, J. Magn. & Magn. Mater. **63–64**, 289.

Regnault, L.P., W.A.C. Erkelens, J. Rossat-Mignod, P. LeJay and J. Flouquet, 1988a, Phys. Rev. B **38**, 4481.

Regnault, L.P., W.A.C. Erkelens, J. Rossat-Mignod, J.L. Jacoud, J. Flouquet, J.M. Mignot, E. Walker, D. Jaccard, A. Amato and C. Vettier, 1988b, J. Phys. **49**, C8-773.

Regnault, L.P., J.L. Jacoud, J.M. Mignot, J. Rossat-Mignod, C. Vettier, P. LeJay and J. Flouquet, 1990a, Physica B **163**, 606.

Regnault, L.P., J.L. Jacoud, J.M. Mignot, J. Rossat-Mignod, C. Vettier, P. LeJay and J. Flouquet, 1990b, J. Magn. & Magn. Mater. **90–91**, 398.

Renker, B., F. Gompf, E. Gering, P. Frings, H. Rietschel, R. Feltin, F. Steglich and G. Weber, 1987, Physica B **41–44**, 148.

Ribault, M., J. Flouquet, P. Haen, F. Lapierre, J.M. Mignot and F. Holtzberg, 1980, Phys. Rev. Lett. **45**, 1295.

Riseborough, P.S., 1992, Phys. Rev. B **45**, 13984.

Rossat-Mignod, J., L.P. Regnault, J.L. Jacoud, C. Vettier, P. Lejay, J. Flouquet, E. Walker, D. Jaccard and A. Amato, 1988, J. Magn. & Magn. Mater. **76–77**, 376.

Rossat-Mignod, J., L.P. Regnault, C. Vettier, P. Bourges, P. Burlet, J. Bossy, J.Y. Henry and G. Lapertot, 1991, Physica C **185–189**, 86.

Scalapino, D.J., E. Loh Jr and J.E. Hirsch, 1986, Phys. Rev. B **34**, 8190.

Schenck, A., 1992, in: Selected Topics in Magnetism, eds L.C. Gupta and M.S. Multani (World Scientific, Singapore) p. 269.

Schenck, A., P. Birrer, F.N. Gygax, B. Hitti, E. Lippelt, M. Weber, P. Böni, P. Fischer, H.R. Ott and Z. Fisk, 1990, Phys. Rev. Lett. **65**, 2454.

Schenstrom, A., M.-F. Xu, Y. Hong, D. Bein, M. Levy and B.K. Sarma, 1989, Phys. Rev. Lett. **62**, 332.

Schlabitz, W., J. Baumann, B. Pollit, U. Rauchschwalbe, H.M. Mayer, U. Ahlheim and C.D. Bredl, 1986, Z. Phys. B **62**, 171.

Schlesinger, Z., Z. Fisk, H.T. Zhang, M.B. Maple, J.F. Ditusa and G. Aeppli, 1993, Phys. Rev. Lett. **71**, 1748.

Schmitt-Rink, S., K. Miyake and C.M. Varma, 1986, Phys. Rev. Lett. **57**, 2575.

Schröder, A., J.W. Lynn, R.W. Erwin, M. Loewenhaupt and H. v. Löhneysen, 1994, in: Proc. Int. Conf. on Strongly Correlated Electron Systems, San Diego, CA, August 1993, Physica B **199–200**, 47.

Severing, A., J.D. Thompson, P.C. Canfield, Z. Fisk and R. Riseborough, 1991, Phys. Rev. B **44**, 6832.

Shapiro, S.M., and B.H. Grier, 1982, Phys. Rev. B **25**, 1457.

Shapiro, S.M., H. Bjerrum-Møller, J.D. Axe, R.J. Birgeneau and E. Bucher, 1978, J. Appl. Phys. **49**, 2101.

Shirane, G., J.E. Fischer, Y. Endoh and K. Tajima, 1987, Phys. Rev. Lett. **59**, 351.

Shivaram, B.S., T.F. Rosenbaum and D.G. Hinks, 1986, Phys. Rev. Lett. **56**, 1078.

Shull, C.G., and F.A. Wedgewood, 1966, Phys. Rev. Lett. **16**, 513.

Sire, C., C.M. Varma and H.R. Krishnamurthy, 1993, Phys. Rev. B, to be published.

Skolozdra, R.V., O.F. Koretshraya and Yu.K. Gorolenko, 1984, Inorg. Mater. **20**, 604.

Springford, M., and P.H.P. Reinders, 1988, J. Magn. & Magn. Mater. **76–77**, 11.

Stassis, C., C.K. Loong, B.N. Harmon, S.H. Liu and R.M. Moon, 1979, J. Appl. Phys. **50**, 7567.

Stassis, C., C.-K. Loong, J. Zaretsky, O.D. McMasters and R.M. Moon, 1982, J. Appl. Phys. **53**, 7890.

Stassis, C., J. Arthur, C.F. Majkrzak, J.D. Axe, B. Batlogg, J. Remeikor, Z. Fisk, J.L. Smith and A.S. Edelstein, 1986, Phys. Rev. B **34**, 4382.

Stewart, G.R., Z. Fisk and M.S. Wire, 1984a, Phys. Rev. B **30**, 482.

Stewart, G.R., Z. Fisk, J.O. Willis and J.L. Smith, 1984b, Phys. Rev. Lett. **52**, 679.

Stewart, G.R., A.L. Giorgi, J.O. Willis and J. O'Rourke, 1986, Phys. Rev. B **34**, 4629.

Sulewski, P.A., A.J. Sievers, M.B. Maple, M.S. Torikachvili, J.L. Smith and Z. Fisk, 1988, Phys. Rev. B **38**, 5338.

Sumiyama, A., Y. Oda, H. Nagano, Y. Onuki and T. Komatsubara, 1985, J. Phys. Soc. Jpn. **54**, 877.

Taillefer, L., and G. Lonzarich, 1988, Phys. Rev. Lett. **60**, 1570.

Tajima, K., Y. Endoh, J.E. Fischer and G. Shirane, 1988, Phys. Rev. B **38**, 6954.

Takabatake, T., F. Teshima, H. Fujii, S. Nishigori, T. Suzuki, T. Fujita, Y. Yamaguchi, J. Sakurai and D. Jaccard, 1990, Phys. Rev. B 41, 9607, and references therein.

Takagi, S., T. Kimura, N. Sato, T. Satoh and T. Kasuya, 1988, J. Phys. Soc. Jpn. **57**, 1562.

Takayanagi, S., S.B. Woods, N. Wada, T. Watanabe, Y. Onuki, A. Kobori, T. Komatsubara, M. Imai and H. Asuno, 1988, J. Magn. & Magn. Mater. **76–77**, 281.

Thompson, J.D., J.O. Willis, C. Godard, D.E. McLaughlin and L.C. Gupta, 1985, Solid State Commun. **56**, 169.

Tokuyasu, T.A., D.W. Hess and J.A. Sauls, 1990, Phys. Rev. B **41**, 8891.

Trappman, T., H. v. Löhneysen and L. Taillefer, 1991, Phys. Rev. B **43**, 13714.

van Sprang, M., A. de Visser, J.J.M. Franse, A.A. Menovsky and A.J. Dirkmaat, 1987, J. Magn. & Magn. Mater. **63–64**, 393.

Varma, C.M., and M. Schlüter, 1981, in: Valence Fluctuations in Solids, eds L.M. Falicov, W. Hanke and M.B. Maple (North-Holland, New York) p. 37, and references therein.

Vettier, C., P. Morin and J. Flouquet, 1986, Phys. Rev. Lett. **56**, 1980.

Volovik, G.E., 1988, J. Phys. C **21**, L215, L221.

Walker, M.B., W.J.L. Buyers, Z. Tun, W. Que, A.A. Menovsky and J.D. Garrett, 1993, Phys. Rev. Lett. **71**, 2630.

Youngblood, R.W., G. Aeppli, J.D. Axe and J.A. Griffin, 1982, Phys. Rev. Lett. **49**, 1724.

Zha, Y., K. Levin and Q. Si, 1993, Phys. Rev. B **47**, 9124.

Handbook on the Physics and Chemistry of Rare Earths
Vol. 19 – Lanthanides/Actinides: Physics – II
edited by K.A. Gschneidner, Jr., L. Eyring, G.H. Lander and G.R. Choppin

Chapter 132

INTERMEDIATE VALENCE AND HEAVY FERMIONS*

P. WACHTER
Laboratorium für Festkörperphysik, Eidgenössische Technische Hochschule (ETH) Zürich, 8093 Zürich, Switzerland

Contents

* *To Sonja.*

List of symbols

a	interatomic separation
a_0	lattice constant
B	bulk modulus
B_0	bulk modulus at zero pressure
B_0';	derivative of the bulk modulus at zero pressure
B_S	adiabatic bulk modulus
B_T	isothermal bulk modulus
BW	bandwidth
c	constant
c_{ij}	elastic moduli
C	specific heat at constant pressure
C_2	coefficient of the magnetic form factor
C_v	specific heat at constant volume
C_M	molar Curie constant
d	degeneracy
Dq	unit of crystal field strength
e	electrical charge of an electron
E	energy
E_B	binding energy of exciton
E_{cv}	energy difference between conduction and valence band
E_{ex}	optical excitation energy into exciton state
E_f	energy of the f level
E_F	Fermi energy
E_k	dispersion of E vs. k
E_{so}	spin–orbit splitting
f	oscillator strength
f_F	Fermi distribution function
FIR	far infrared spectroscopy
g	Landé factor
h	Planck's constant
$\hbar$	Planck's constant divided by 2π
H	Hamiltonian
H	magnetic field
I	current
J	magnetic exchange (k=0)
J	total angular momentum
J_{ij}	interatomic magnetic exchange
J_{cv}	joint density of states
k	wavevector
k_B	Boltzmann constant
k_F	Fermi wavevector
k_i	absorption index
K	absorption coefficient
l	orbital momentum of one conduction electron
L	mean distance between impurities
L	angular momentum
m	mass of the electron
m^*	effective mass
m_l	magnetic quantum number
M	magnetization
M_{sat}	saturation magnetization
$M_{1,2}$	masses of atoms
n	occupation number

n_i	refractive index
N	carrier concentration
N_a	atomic concentration
N_c^{exc}	electron concentration thermally excited across the gap
N_e	electron concentration
N_c^c	electron concentration in the conduction band
N_{eff}	effective electron concentration taking part in an optical transition
N_f	f-electron concentration
N_h	hole concentration
p	pressure
p_c	critical pressure
p_{cv}	momentum operator
p_{eff}	effective magnetic moment
P	photoconductivity
Q	quantum efficiency
R	resistivity
R	reflectivity
R_H	Hall constant
s_{ij}	compliance
S	surface in k space
S	spin momentum
SMT	semiconductor–metal transition
T	absolute temperature
T_c	critical temperature
T_C	Curie temperature
T_K	Kondo temperature
T_N	Néel temperature
T^*	Fermi temperature
U	voltage
U_C	Coulomb correlation energy
U_i	inner energy
U_{tot}	total energy
v	velocity
v_L	sound velocity of longitudinal acoustic phonons
v_{RSW}	velocity of the Raleigh Surface Wave
v_T	sound velocity of transverse acoustic phonons
V	hybridization energy
V_c	critical volume
V_k	hybridization matrix element
x	molar ratio
α	reduced Slater parameter
α_0	proportionality constant of the momentum operator
α_T	thermal coefficient of volume expansion
β	critical exponent for magnetization
γ	electronic contribution to the specific heat C at constant pressure
γ_G	Grüneisen constant
Γ	damping constant
δ	critical exponent for volume
Δ	self energy in the Kondo expression
Δ_{SO}	spin–orbit splitting
Δ_{CF}	crystal-field splitting
ΔE	energy gap, hybridization gap
ΔE_{red}	"red shift" of the energy gap
ΔE_μ	mobility gap
ΔL	length change
ΔV	volume change
Δv	velocity change
Δx	length change in x direction
Δy	length change in y direction
ε_1	real part of the dielectric constant
ε_{1b}	ε_1 due to bound electrons
ε_{1D}	ε_1 due to free electrons
ε_2	imaginary part of the dielectric constant
ε_{2b}	ε_2 due to bound electrons
ε_{2D}	ε_2 due to free electrons
ε_{opt}	optical dielectric constant
ε_{stat}	statical dielectric constant
η	anisotropy ratio
Θ_p	paramagnetic Curie temperature
Θ_K	Kerr rotation
κ	compressibility
λ	mean free path
μ	mobility
μ_0	magnetic moment
μ_B	Bohr magneton
μ_H	Hall mobility
ρ	electrical resistivity
ρ_d	density of material
ρ_D	density of states
ρ_s	resistivity for $\Delta E \to 0$
σ	electrical conductivity
σ_1	real part of the optical conductivity
σ_{dc}	dc conductivity
σ_D	Drude part of optical conductivity
τ	relaxation time or life time

Φ_k	conduction band wavefunction	ω	circular frequency
Φ_f	f wave functions	ω_i	resonance frequency of ith oscillator
χ	magnetic susceptibility	ω_p	plasma resonance frequency
χ_R	response function	ω_p^*	screened plasma resonance frequency

1. Introduction

The two phenomena, intermediate valence and heavy fermions, are inherently connected inasmuch as every heavy fermion is simultaneously intermediate valent, however, not every intermediate-valent material is a heavy fermion. In fact, the term heavy fermion came into use only about ten years after the phenomenon had been described in many examples on intermediate-valent metallic systems like YbCuAl, e.g. by Cooper et al. (1971) and Pott et al. (1981). In these genuine intermediate-valent systems the γ value of the specific heat is ten to thousand times the value of a normal metal, which implies a large density of states at the Fermi level and, for narrow bands, a correspondingly large effective mass. Also, the system $CeCu_2Si_2$ for which the term heavy fermion has been used for the first time by Steglich et al. (1979) consists of cerium with a valency between 3 and 4, similarly as in $CeAl_3$ (Andres et al. 1975), which, however, has been classified as intermediate valent by, e.g., Campagna et al. (1975) in early publications. There is even a classical statement by Wohlleben (1981) that all Ce-based compounds or alloys are intermediate valent. In its generality the statement is not correct, but possibly all Ce-based *alloys* are intermediate valent in spite of the fact that most of them are nowadays termed heavy fermions. It is thus obvious that the two phenomena are intrinsically connected and must be treated by the same type of theory.

We also have to clarify the terminology *intermediate valence*, since many different but less precise names have been given to the field. In the last 15 years 6 international conferences have been devoted to this topic, the first and the third using "valence instabilities" in the title, the others using "valence fluctuations". However, the latter expression insinuates a dynamic process and is derived from the early assumption that there exist "fast" and "slow" measurements relative to an intrinsic charge fluctuation between the two valences in question. In fact, the quantum-mechanical ground state of an intermediate-valence system at $T=0$ is by definition static. Since typical measurements like X-ray photoemission spectra (XPS) or Mössbauer effect are considered fast and slow, respectively, but are largely temperature independent, they would all yield the same results for these materials at $T=0$, thus invalidating the fluctuation picture. More about this will be said below.

We have to consider that beside the intermediate-valent systems which we consider as a quantum-mechanical hybridization where each cation has the same but non-integer valence, there exists also a classical mixture of different but integer valences. These materials have been known for a long time, and probably the first mixed-valence material on which some science has been executed was magnetite, Fe_3O_4, when Genghis Khan used it as a compass while crossing the Mongolian desert. Only in these materials is there

a real and temperature dependent charge fluctuation and here one can scan the fluctuation rate over a fixed time scale of an experiment like the Mössbauer effect.

About 15 years ago a classification scheme of mixed-valence compounds had been proposed by Batlogg et al. (1976a). For cations at equivalent lattice sites with quasi-localized f states and broad bands degenerate at the Fermi level the term "homogeneously mixed" or "interconfiguration fluctuation" has been used. This group of materials we would now better baptize "intermediate valence". For the "inhomogeneously" mixed materials with no quasi-localized states at the Fermi level we must distinguish between cations at equivalent and inequivalent lattice sites. To the former group belong Fe_3O_4, Sm_3S_4, Eu_3S_4 and many others with a temperature-dependent charge fluctuation and into the latter group belong $CaFe_2O_4$ or Eu_3O_4 with no charge dynamics at all. In conclusion the term "mixed valence" can be used for homogeneously or inhomogeneously mixed systems, while the term "intermediate valence" is best used for the quantum mechanically hybridized systems, formerly homogeneously mixed or interconfiguration fluctuation. In this article we will treat only intermediate valence and heavy fermions.

Since intermediate valence apparently is a very "hot topic", we also have to comment in this article on some materials which have been claimed to be intermediate valent but in reality do not belong to this category. Here we are dealing with large-gap insulators like CeO_2, CeF_4, NiO or UO_2 in which a strong p–f hybridization occurs (Allen 1985), an effect which in earlier days has been named covalency. However, covalency is not intermediate valence and in fact the relevant cations are integer-valent as shown by Marabelli and Wachter (1987a) and Marabelli et al. (1992a). In other cases the γ value of the specific heat has been used without criticism to deduce a heavy-fermion or intermediate-valent material in spite of the fact that some materials show magnetic order, or at least a very unusual type of magnetism. It is then extremely difficult to subtract the magnetic contribution to the specific heat and a plot of C/T versus T^2 only seems to reveal an anomalously large γ value as believed by Ott et al. (1985a) in the case of the Yb-pnictides (Degiorgi et al. 1990). These and other possibilities of "false heavy-fermion" behavior have been discussed by Gschneidner et al. (1990).

An interesting topic in itself is the question why only 4f materials exhibit intermediate valence. Some of the actinides, in fact, are well-known heavy fermions, like UPt_3 (Frings et al. 1983) or UBe_{13} (Stewart 1984). As we have stated above they are also intermediate valent although the apparent valency of uranium in UPt_3 is nearly integer (Marabelli et al. 1986a). A problem still rests with the uranium chalcogenides, especially USe and UTe which exhibit negative Poisson ratios as shown by Neuenschwander et al. (1986), in general an excellent indication of intermediate valence; however, they also show ferromagnetic order, which generally is not typical for intermediate valence. Thus it is very interesting that it has recently been shown by Wachter et al. (1991) that the plutonium chalcogenides are indeed intermediate valent and simultaneously "light-weight" heavy fermions. However, in the whole large field of 3d materials nobody has claimed intermediate valence or heavy fermions. We think that the new high-T_c compounds of the type $YBa_2Cu_3O_7$ not only are mixed-valent regarding Cu^{3+} and Cu^{2+} ions but are also intermediate valent. Definite experimental evidence, however, is still missing.

2. The hybridization gap model

Generally speaking lanthanide metals or alloys can be subdivided into "normal" ones in which the 4f level (E_f) lies several eV below the Fermi level E_F and "anomalous" ones (containing Ce, Sm, Eu, Tm and Yb) where the 4f level is close to or even degenerate with E_F, which may exhibit the phenomenon of intermediate valence. The normal materials show well ordered magnetic moments and the Ruderman–Kittel–Kasuya–Yoshida (RKKY) interaction is mainly responsible for the magnetic order. When the 4f state is close to the Fermi energy, the Kondo energy $\Delta \exp(-E_f/\Delta)$, where Δ is a self energy, can be larger than the RKKY energy and then there is no magnetic order, each magnetic moment is performing independent spin flips. This material is usually called a Kondo metal. Its resistivity is zero at $T=0$ for a perfect crystal, then rises with temperature to a maximum at T_K where $k_B T_K \propto \Delta \exp(-E_f/\Delta)$ and then decreases. This decrease is caused by a steadily diminishing amount of electrons proportional to T_K/T which can scatter into the high-density region of 4f states below E_F. When the scatterers are lanthanide impurities one has the normal Kondo effect; when one has a lanthanide lattice one speaks of the Kondo lattice or a dense Kondo system (Frings et al. 1983, Stewart 1984). There is of course a hybridization, i.e., mixing of wavefunctions of 4f and conduction band and in this sense also a Kondo metal has some intermediate valence because a fraction $\exp(-E_f/\Delta)$ of the lanthanide ions will have a valence different by one from the rest. The interesting case occurs when $E_f \rightarrow E_F$ i.e., the 4f states are at E_F and then all lanthanide ions become intermediate valent. The reason is that hybridization will mix into the originally localized 4f states also conduction band states (usually of a 5d band) thus the 4f states acquire a width and a dispersion, albeit very narrow. This narrow, only partially filled, band at E_F with its enormous density of states will act like a sink for other conduction electrons so that the crystal as a whole can minimize its energy. The originally localized 4f state which was filled with an integer number of electrons is now filled, in the narrow band case, with a non-integer number of electrons per lanthanide ion and in this sense each lanthanide ion has the same, non-integer valence.

When the 4f states are still below, but close to E_F the intermediate valence state can sometimes be reached experimentally by applying pressure. In the free lanthanide atom the energy separation 4f–5d, 6s can be taken from atomic tables (e.g. Freeman et al. 1966). In the solid the 5d and 6s states form bands around the atomic energy states and the 5d band will be subject to the strong crystal field which splits the band according to the crystal symmetry. This splitting occurs in such a way that the center of gravity of the 5d band, the atomic level, will remain at the same energy relative to the atomic 4f state. Applying pressure will enhance the crystal-field splitting and increase the bandwidth. In the case of a lanthanide metal where the conduction bands are already partially filled with electrons, the conduction band and thus the Fermi level will be lowered with respect to the 4f state until $E_f \rightarrow E_F$ and intermediate valence sets in. This is the case for the γ–α transition in Ce (which has sometimes been described as the 4f level pushing upwards versus the Fermi level with application of pressure, as, e.g., by Coqblin et al. (1977). In a semiconductor like SmS with the 4f state and the Fermi level below the conduction band, pressure will

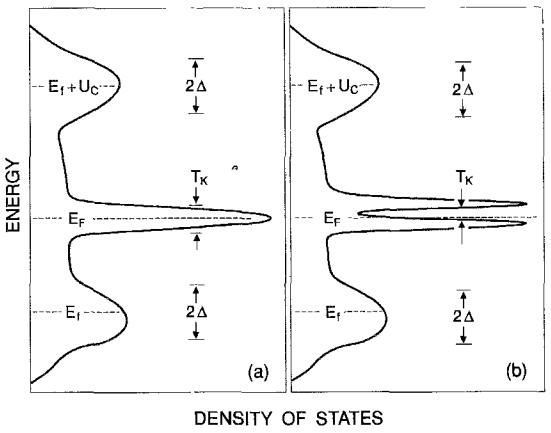

Fig. 1. Schematic spectrum of the density of states of (a) the impurity Kondo case and (b) the Kondo lattice, including split-off bands at E_f and $E_f + U$ and the many-body resonance of width T_K. The scale T_K is expanded for clarity. (After Martin 1982.)

increase the 5d crystal-field splitting until the bottom of the 5d band crosses the 4f state and 4f electrons from the now hybridized 4f band will spill into the conduction band until again the energy of the crystal is minimized (Batlogg et al. 1976b).

Theoretically there has been a continuous development from the simplest Hamiltonian containing the essence of the Kondo and intermediate-valence problem to the inclusion of periodicity in the Kondo lattice problem or the heavy-fermion case. A simple Hamiltonian could look like

$$H = \sum_{k,\sigma} E(k)\, d^{\dagger}_{k\sigma}\, d_{k\sigma} + \sum_{i,\sigma} \left\{ E_f f^{\dagger}_{i\sigma} f_{i\sigma} + \tfrac{1}{2} U_C\, n^{f}_{\sigma}\, \underline{n}^{f}_{\sigma} + V(f^{\dagger}_{i\sigma}\, d_{i\sigma} + d^{\dagger}_{i\sigma} f_{i\sigma}) \right\}, \quad (1)$$

where d stands for a simple band (in reality it should be a d band, but theory treats it as a s type band with only spin degeneracy) with dispersion $E(k)$ and bandwidth BW, f stands for a localized state with again only spin degeneracy, having a Coulomb correlation energy U_C, n^f_σ being the occupation number and V being the mixing or hybridization energy, assumed to be site diagonal (see Martin 1982, Grewe 1984, Anderson 1961, Coqblin and Blandin 1968, Martin and Allen 1979, Lawrence et al. 1981, Martin and Allen 1981, Lustfeld and Bringer 1980, Jullien et al. 1981, Brandow 1979). When the f state is only at site i, eq. (1) is the impurity Anderson Hamiltonian (Anderson 1961).

In fig. 1a we present a schematic picture of the density of states $\rho_D(E)$ for the impurity Kondo case following from this Hamiltonian. For large U_C the f spectral weight is split into two parts at E_f and $E_f + U_C$, having a width $\Delta \approx V^2/\mathrm{BW}$. When E_f and $E_f + U_C$ are well separated from E_F, eq. (1) describes the Kondo case for a nonperiodic array of f states. When $E_f \to E_F$ one enters the intermediate-valent state with nonintegral f occupation. At E_F a many-body resonance occurs caused by the lifting of the degeneracy due to the crossing of the $E(k)$ relations of the d and f states at E_F (Martin 1982). With large U_C and small hybridization energy V and E_f well removed from E_F there is only a small amount of spectral weight in the density of states peak

at E_F, but in the intermediate-valent case with $E_f \rightarrow E_F$ a large spectral weight is restored with $\rho_D(E_F)$. The width of this peak is about $k_B T_K \approx \Delta$ (Martin 1982).

One of the problems associated with such a simple model has been phrased by Anderson (Anderson 1981), namely that the spin degeneracy of the conduction band is taken to be 2 and the spin degeneracy of the f state is also assumed to be only 2, whereas in reality, for instance in a $4f^5$ state, the spin degeneracy is 6, so the conduction band wavefunctions Φ_k can hybridize with only one Φ_f, namely the one with $m_l = 0$, leaving the other 5 Φ_f unhybridized. Thus Anderson concluded that e.g. hybridization gaps are unrealistic. The problem can be reduced by using more complex (but realistic) conduction bands, such as d bands, but this does not solve the problem principally. Mott (1982a), however, argues that all 4f states will hybridize and behave in the same way: into whichever 4f band a quasiparticle will be excited, it can move *via* the conduction band. If n is the number of f electrons per atom and d its degeneracy then each f band will be filled only to n/d states. The $E(k)$ plots for each of the f bands will then be identical. The very existence and the experimental proof of hybridization gaps left Anderson's argumentation too critical.

Another problem which has to be solved experimentally will be the magnitude of U_C and V. Whereas there is no doubt that V is of the order 0.1–0.01 eV (Varma 1976) U_C is theoretically taken to be between 0 and ∞. In ordinary lanthanide compounds $U_C \approx 6$ eV as also determined by, e.g., XPS results (Campagna et al. 1975) or optical spectroscopy (Batlogg et al. 1975), but in the hybridized, intermediate-valent case hybridization gaps appear (see below) and optical transitions across them, so dielectric constants of up to 3×10^4 can be measured (Marabelli et al. 1986a, Travaglini and Wachter 1984a,b). It is not at all clear whether these large dielectric constants screen the Coulomb interaction drastically, resulting in dramatically reduced effective U_C values.

Whereas up to about 1981 only impurity models using eq. (1) existed, progress was achieved when a *periodic* solution of eq. (1) was tried. In the periodic version a gap of order T_K appears in the many-body resonance at E_F as depicted in fig. 1b (Martin and Allen 1979, Martin 1982, Grewe 1984, Iglesias and Mors 1985, Brandow 1986). In the periodic Kondo problem or the Kondo lattice E_f is still below E_F and, in fact, one obtains now a 4-peak structure as seen in fig. 1b with most of the spectral weight at E_f and $E_f + U_C$, but as E_f approaches E_F and one enters the intermediate-valence regime, spectral weight is in fact restored to the density of states peaks at E_F. If the d–f hybridization is non-zero throughout the Brillouin zone the quasiparticle spectrum will always exhibit a gap with prominent density of states peaks on each side of the gap (Brandow 1986, 1988, Nolting 1982). Thus especially from the results of a variational theory applied to the quasiparticle spectrum it has been shown that the best low-temperature description is a periodic Fermi liquid also using the Luttinger effective band structure aspect (Brandow 1986, 1988). A simplified dispersion and density of states diagram is shown in figs. 2a–d.

For the $U_C = 0$ case, i.e., already in ordinary band theory, a gap has been predicted by Coqblin and Blandin (1968) and by Mott (1960) and an insulator is obtained. For the $U_C \neq 0$ case the only question remaining is: where is the Fermi energy, in the gap –

resulting in an insulating ground state – or in one of the density of states peaks – resulting in metallic behavior.

Here Martin and Allen (1979) have shown that for an even count of f and d electrons, and with no other electrons in the conduction band, the application of the Luttinger theorem (Luttinger 1960) leads to E_F being in the gap of an intermediate-valent system. For an odd electron count the Fermi level lies in one of the density of states peaks resulting in intermediate-valent and heavy-fermion behavior (Martin 1982). This theory has been greatly stimulated by the establishment of an insulating behavior of SmB_6 at low temperatures, which has taken 12 years of research (Nickerson et al. 1971) and 3 conferences on intermediate valence (1977, 1981, 1982).

In fact Sm and Yb compounds are the only ones obeying the Luttinger criterion for E_F in the gap. The condition is that the lanthanide ions can exist in a divalent state $4f^6$ and $4f^{14}$ for Sm and Yb, respectively, with even number of electrons. In the intermediate-valent state due to hybridization, part of the 4f electrons obtain 5d character, but the sum of f and d electrons remains even. For other divalent lanthanide ions such as Eu or Tm with $4f^7$ or $4f^{13}$ states, respectively, the 4f count is odd. For Tm, however, an additional condition, namely antiferromagnetic order has been found, which doubles the chemical unit cell and one arrives nevertheless at an even f and d electron count (more about this below, section 4.3).

Thus up to now only SmB_6, the high-pressure phases of SmS, SmSe and SmTe, YbB_{12}, TmSe and some alloys with TmTe, the high-pressure phase of TmTe and the Pu chalcogenides are known to have the Fermi level in the gap and being intermediate valent. In the light of what has been said in the introduction they are not heavy fermions, although the effective mass of the carriers in the high density of states region around the gap can reach up to $1000m$ (Brandow 1986). The new, relatively recent experimental progress lies in the evidence that also for the metallic lanthanide or actinide systems hybridization gaps exist across which thermal and optical excitations are possible.

As a summary of this chapter it can be said that any periodic solution of the Hamiltonian of eq. (1) will result, independently of the size of U_C, in a hybridization gap. For an even count of f and d electrons (and no other electrons in the conduction band) the Fermi level will be in this gap and the materials will be intermediate-valent insulators at $T \to 0$. For an odd electron count the Fermi level will be in one of the density of states peaks above or below the gap, and the materials are intermediate-valent and heavy-fermion metals at $T \to 0$. In fig. 2 a simplified dispersion and density of states diagram is shown with most of the spectral weight in the f-like states. In fig. 2d the f–d hybridization extends over the whole Brillouin zone. The true experimental evidence of gaps in intermediate-valent insulators is about 12 years old (Batlogg et al. 1981), the experimental proof of gaps in heavy fermions is only 6 years old (Marabelli et al. 1986a).

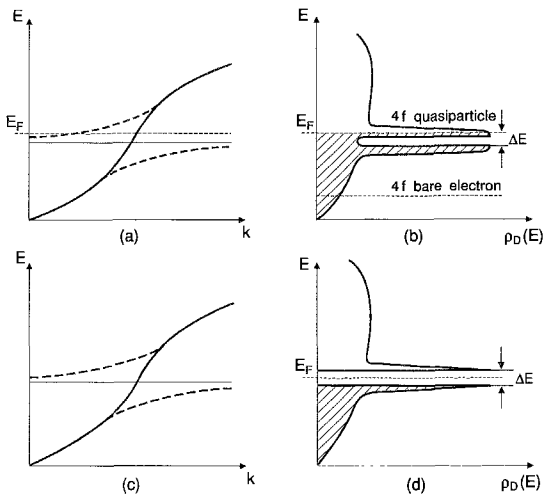

Fig. 2. Dispersion and density of states of quasiparticle bands. (a,b) non-integer f–d count or additional other electrons, (c,d) integer f–d count, no additional other electrons.

3. "Soft" and "hard" spectroscopies for narrow band materials

Soon after the first description of an intermediate-valent material, SmB_6 (Nickerson et al. 1971) 20 years ago, high-energy investigations of the XPS type have been performed (Campagna et al. 1975). In these measurements an Al or Mg K_α X-ray radiation is directed onto the sample and the emitted electron beam is analyzed for its energy loss. With non-monochromatic radiation an energy resolution of 0.5 eV is possible, with monochromatic X-ray radiation 0.3 eV has been obtained. In f-type materials it is essential to use high-energy radiation $\gg 40$ eV because the matrix element for f electrons increases with energy as shown by Eastman and Kutznietz (1971) and Wertheim et al. (1971). The spectra of the 4f photoemission have to be understood in terms of the hole left behind in the 4f shell after the electron has been emitted or the $n-1$ electron state. The hole state can occupy various spin–orbit coupled multiplet states under the condition that spin is conserved. The probabilities of occupying the different states is governed by the square of the coefficient of fractional parentage (Racah 1949). The simplest spectrum can be obtained from integer divalent Eu or trivalent Gd compounds or alloys which are both in the $4f^7\ ^8S_{7/2}$ state. The $n-1$ electron state is a ^7F_J multiplet and the intensity distribution due to the coefficient of fractional parentage results in a simple peak (Campagna et al. 1975, 1979).

For intermediate-valent compounds the spectra can be interpreted as if the initial state would consist of a mixture of divalent and trivalent ions because the final hole state or the n-1 electron state, due to their fingerprint like multiplets, can be associated with two valence states. In the case of chemically collapsed intermediate-valent $Sm_{0.85}Th_{0.15}S$ or $Sm_{0.82}Gd_{0.18}S$ the XPS spectra are shown in fig. 3 (Campagna et al. 1975). Sm^{2+} has the configuration $4f^6\ ^7F_0$, the $n-1$ state $4f^5$ has the multiplets ^6H_J, ^6F_J and ^6P_J. Sm^{3+} has the configuration $4f^5\ ^6H_{5/2}$, the $n-1$ state $4f^4$ has the multiplets ^5I_J, ^5F_J, ^5G_J and ^5D_J. Their coefficients of fractional parentage can be calculated and their relative energy

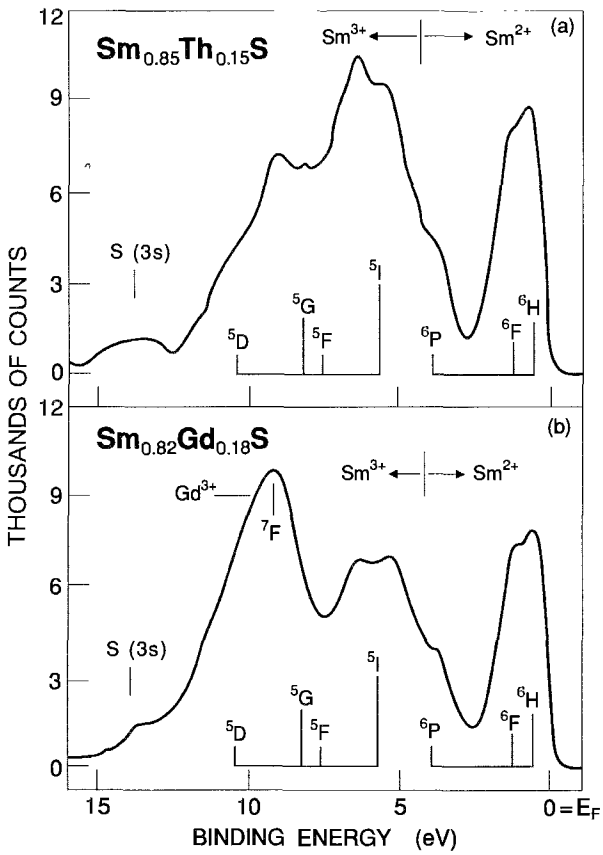

Fig. 3. Coexistence of divalent and trivalent Sm ions in chemically collapsed phases of SmS, as detected by XPS. (After Campagna et al. 1975.)

and intensity is shown in the ladder-like structure in fig. 3. The Fermi level is in the low binding energy edge, indicating metallic behavior at room temperature, and the two $n-1$ spectra (taking e.g. the energy difference between ^{6}H and ^{5}I) are shifted by about 5 eV, the Coulomb correlation energy U_C.

Above we have argued that each cation of an intermediate-valent material has the same non-integer valence independent of temperature. How can this be reconciled with fig. 3 indicating practically a mixture of integer valent, e.g. Sm^{2+} and Sm^{3+} ions? The interpretation used so far is based on the "inter-configuration-fluctuation model" proposed by Hirst (1971, 1974) where it is assumed that the valence is fluctuating with a certain frequency. The XPS measurement is taken to be "fast" ($\approx 10^{-15}$–10^{-18} s) with respect to this intrinsic charge fluctuation so that the incoming X-ray beam makes a momentary picture of e.g. the Sm^{2+} or the Sm^{3+} configuration. The integrated

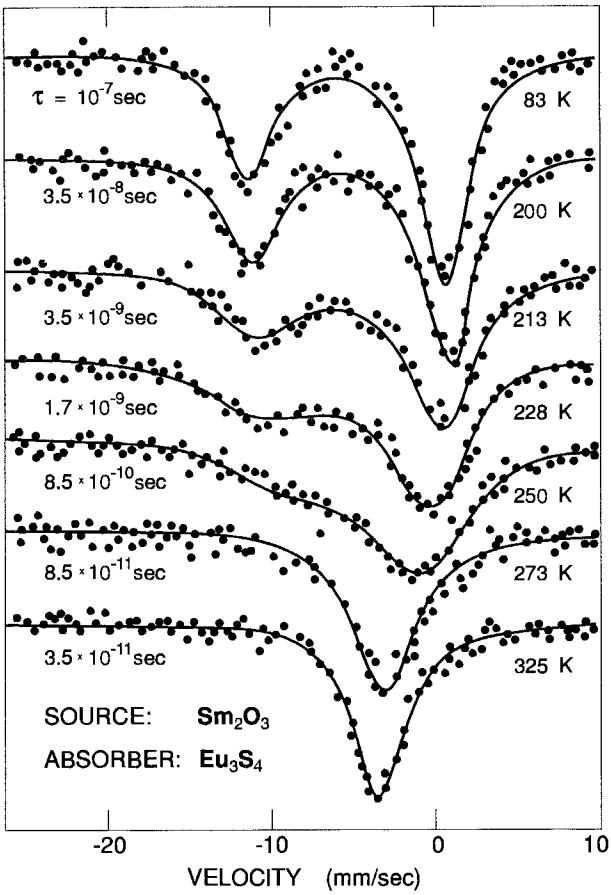

Fig. 4. Mössbauer spectra of Eu_3S_4. Dots indicate experimental results and the solid lines are the calculated spectra for different relaxation times τ, using the formula of Wickman et al. (1966). (After Berkooz et al. 1968).

intensity under the two multiplets can be used to estimate the degree of valence mixing: if a and b are the intensities corresponding to the trivalent or divalent configuration, respectively, $2+a/(a+b)\approx 2.6$ is the degree of valence mixing in the Sm compounds of fig. 3 (Campagna et al. 1975). Of course contributions from other than 4f electrons must be suitably subtracted by calibrating with a non 4f reference compound, such as LaS in the above example.

On the other hand the isomer shift in a Mössbauer experiment on an intermediate-valent system is considered to be "slow" relative to the intrinsic time scale of the valence fluctuations. The hyperfine interaction of the nucleus with mainly the 5s character electronic charge at the nucleus is an electric monopole interaction (only s electrons can interact with the nucleus, but the 5s electrons being outside the 4f shell are quite sensitive to the occupation of the 4f shell because of different screening of the nuclear

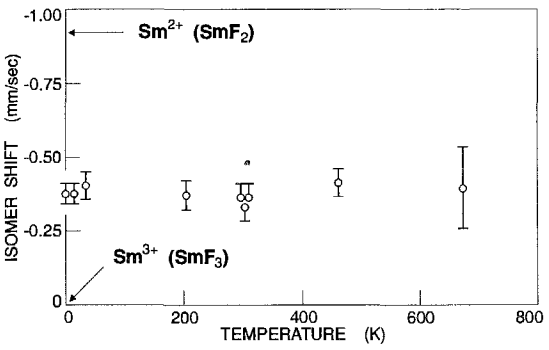

Fig. 5. Isomer shift vs. temperature for SmB_6. Typical values measured for ionic Sm^{2+} and Sm^{3+} compounds are also shown. (After Cohen et al. 1970.)

charge). Since the nuclear radius is different in the ground and excited states the resonance absorption of a γ-ray occurs at a slightly different energy between emitter and absorber if the electronic configurations of source and absorber differ, e.g. by a 4f electron. Whereas the energy of the γ-ray is about 10^4–10^5 eV the difference in resonance lines between absorber and emitter is only about 10^{-7} eV or 10^{-8}–10^{-10} s. The shift of the resonance lines is measured via the Doppler effect when source and emitter are moved relative to each other with a velocity v. However, the isomer shift corresponding to a change of one in the 4f occupation is measurable with some accuracy only in ^{149}Sm or ^{153}Eu where it is maximal -1.64 and -14.6 mm/s, respectively. In other lanthanides either the isomer shift between different valent ions is too small or the half-width of the peaks is too large (Coey and Massenet 1977). In fig. 4 we reproduce the beautiful experiment of Berkooz et al. (1968) on Eu_3S_4, an inhomogeneously mixed valence compound with equivalent lattice sites for di- and trivalent Eu, where the isomer shift has been measured in function of temperature and this time the temperature dependent fluctuation time (electron hopping time (Wachter 1977) has been scanned over the time scale of the isomer shift, being about 1.3×10^{-7} s for ^{151}Eu. At high temperatures with a fluctuation time faster than 10^{-7} s a single peak appears at the time averaged isomer shift between the positions of Eu^{3+} (0 mm/s) and Eu^{2+} (-12 mm/s), whereas at low temperatures with slow fluctuations each individual configuration lives long enough to be sampled by the isomer shift as a separate line. The intensities of these lines have a ratio of 1:2 as demanded by the ratio of Eu^{2+}/Eu^{3+} equal to 1:2. In fig. 5 we show the isomer shift of intermediate-valent SmB_6 as a function of temperature with respect to divalent (SmF_2) and trivalent (SmF_3) integer valent reference compounds. Indeed, over 700 K and down to 4.2 K the degree of valence mixing is constant (Cohen et al. 1970).

How can the XPS and the Mössbauer results be reconciled with the more modern model of f–d hybridization and hybridization gaps? The key words are no longer "fast" and "slow" but "hard" and "soft". Thus we are switching from a time scale to an energy scale $E=h/\tau$. No longer do we need a critical fluctuation rate (which for $T\rightarrow0$ is questionable anyhow because of the static quantum mechanical ground state) but a critical energy. This, of course, is not the energy with which we perform the experiment (e.g. the

γ-ray energy of the Mössbauer effect) but the energy transferred to the hybridized electron system in relation to the hybridization energy V, which can be considered as the binding energy of the hybridized state with a magnitude in the meV range. It is thus that XPS (or any other high-energy transfer) breaks up the hybridization at the site of the absorption of the X-ray quantum and one observes only the integer valent constituents out of which the hybridized state was formed (this effect is quite general: when one transfers to a molecule an energy larger than its binding energy it dissociates into atoms). As a consequence only low-energy or "soft" methods really sample the hybridized state and the Mössbauer effect with its energy transfer of about 10^{-7} eV is ideally suited for these experiments. Unfortunately it is practically limited to Eu and Sm systems (Coey and Massenet 1977). To great advantage one uses also spectroscopical methods where the energy transfer can be scanned over the hybridization energy like optical absorption between eV and meV, Raman, Brillouin scattering and point contact spectroscopy. Even room temperature is already too large an excitation energy, so all these experiments must be done at low temperatures. Indeed, Mock et al. (1986) show that when the phonon frequency is larger than the fluctuation frequency, which again we would now call the hybridization energy, the phonons probe a static mixture of the $4f^n$ and the $4f^{n-1}$ configuration. This means that the phonon energy is intermediate between the corresponding energies of the stable valent reference compounds. On the other hand for the phonon energy less than the hybridization energy the phonon energy softens with respect to both reference compounds. X-ray scattering to determine the lattice parameters is of course an elastic experiment with little or no energy transfer, just as low-temperature thermodynamic methods such as specific heat, electrical resistivity and not too high magnetic fields.

Whereas the above discussion yields textbook examples of hard and soft spectroscopies and what one can get out of it, the methods cannot be used uncritically. Thus XPS cannot distinguish between an inhomogeneously mixed or a homogeneously mixed or intermediate-valent compound, in other words whether, e.g., Sm^{2+} and Sm^{3+} ions are integer valent and statically mixed or the charge between them just fluctuates slower (to use the old terminology) then the time resolution of XPS, cannot be decided. Examples of such inhomogeneously mixed compounds are Fe_3O_4, Eu_3S_4, Eu_3Se_4, Eu_3Te_4, Sm_3S_4, Sm_3Se_4, Sm_3Te_4, Sm_4As_3, Sm_4Sb_3, etc. Whereas the first three Sm examples are narrow gap semiconductors crystallizing in the Th_3P_4 structure, the latter two examples are semimetals which crystallize in the anti-Th_3P_4 structure. In fig. 6 we give an example of XPS on intermediate-valent $Sm_{0.85}Th_{0.15}S$ (6a) (Campagna et al. 1975), inhomogeneously mixed Sm_3S_4 (6b) (Wachter 1989a) and the refraction and absorption index, derived from a Kramers–Kronig analysis of an optical reflectivity spectrum of Sm_3S_4 (6c) (Batlogg et al. 1976a). In all cases the ladder-like multiplet spectrum of the final state $n-1$ is shown (in fig. 6c the ladder-like multiplets appear twice for each configuration, because the final state is a crystal-field split Δ_{CF} 5d conduction band, and not a (single) vacuum level as in XPS). In fact the XPS information is the same for $Sm_{0.85}Th_{0.15}S$ and Sm_3S_4, but the materials are vastly different in their physical properties regarding valence. Sm_3S_4, though a semiconductor, has the $4f^6$ state only 0.14 eV below the conduction band or E_F (Batlogg et al. 1976a), much less than the energy resolution of XPS with 0.5 eV.

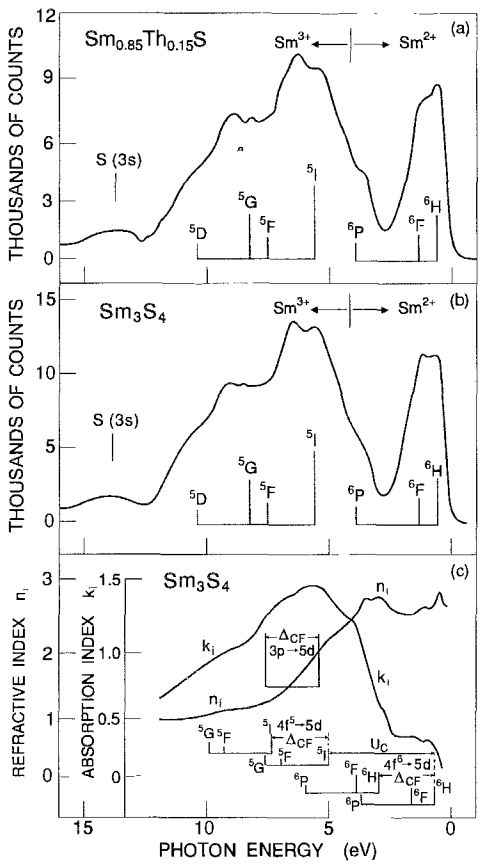

Fig. 6. (a) XPS spectrum of chemically collapsed (intermediate-valent) $Sm_{0.85}Th_{0.15}S$ (same as in fig. 3a) (after Campagna et al. 1975). (b) XPS spectrum of inhomogeneously mixed (integral-valent) Sm_3S_4 (after Wachter 1989a). (c) Optical constants of Sm_3S_4 with 5d crystal-field splitting Δ_{CF} and Coulomb correlation energy U_C (after Batlogg et al. 1976a).

Another serious problem arises when performing XPS on Ce compounds or alloys. Ce^{3+} is $4f^1$ and the $n-1$ final state spectrum is $4f^0$ so no multiplet structure can be assigned to it. Even worse, when one has an intermediate-valent Ce compound the valency is expected to be between 3 and 4, i.e., a configurational mixing between $4f^1$ and $4f^0$ initial states or only a partial filling of the $4f^1$ state. The high energy of the XPS experiment breaks up the hybridization and one only measures the position of the final state. For all Ce compounds this unhybridized, uncoupled, undressed or bare electron state is found about 2–3 eV below E_F by comparison with, e.g., isoelectronic La compounds (Campagna et al. 1979, Patthey et al. 1986), even when the hybridized state is at E_F as in $CeCu_6$ (Patthey et al. 1986). It must be said clearly that this final bare electron state is a result of the electron emission, it does not exist before the X-ray absorption. Sometimes this state has been taken as the initial $4f^1$ state. An apparent solution to the problem has been to perform core level spectroscopy where an inner 2p or 3d electron is ejected. However, the presence of a core hole is a dramatic disturbance of all the outer electron

shells since the charge of the nucleus is now less screened. All the energies of the outer electrons are renormalized. In all cases one now measures f^0, f^1 and f^2 uncoupled final state amplitudes, from which one attempts to calculate the hybridized initial state with the Gunnarsson–Schönhammer (1983) mechanism. However, this mechanism uses the single impurity Anderson Hamiltonian (Anderson 1961) and not the Anderson lattice, thus no hybridization gap will appear and the distribution of electrons over the two-peak density of states structure at E_F will be reproduced incorrectly.

Also the isomer shift of the Mössbauer effect is not free from pitfalls. The isomer shift, being dependent on the s electron density at the nucleus, has a large chemical shift which is rarely taken into account. Thus in the example of fig. 5 the reference compounds for integer valent Sm^{2+} and Sm^{3+} were SmF_2 and SmF_3, respectively, with isomer shifts of -0.9 and 0 mm/s, respectively. If, for instance, instead of the fluorides one had taken the iodides, the interpolated degree of intermediate valence of SmB_6 would have been different. This is exemplified on divalent and trivalent Eu systems with different chemical surroundings and thus different covalency by Gerth et al. (1968). The divalent Eu compounds range from -11.9 to -14.6 mm/s, the trivalent Eu compounds from $+0.22$ to -0.7 mm/s. The difference between EuF_2 and EuF_3 amounts to -13.5, between EuJ_2 and EuJ_3 to -14.0 mm/s. Thus, statements regarding the precision of the absolute value of the degree of valence mixing should be accepted only within about 10 to 20%, especially since in pressure experiments the degree of covalency is changing (Coey et al. 1975).

4. Materials exhibiting intermediate valence and having the Fermi energy in the hybridization gap

4.1. *Lanthanide borides*

4.1.1. *Electronic properties*

4.1.1.1. *Transport properties and specific heat.* Borides of the transition metal elements and the lanthanides are among the boron compounds which have found the most important practical applications. Diborides are stable refractory compounds. Among the hexaborides LaB_6 has a good chemical stability, high electrical conductivity and with a melting point of 2500°C has become the best material for high electron density thermionic cathodes. Dodecaborides, and also other boron rich borides are among the solids which exhibit the highest hardness and stiffness known so far.

The lanthanide tetraborides seem to have a stable 3+ oxidation state except YbB_4, for which intermediate valence is assumed by Berrada et al. (1976) and Bonville et al. (1978) on the basis of absence of magnetic order above 4.2 K and the isomer shift of the Mössbauer effect being between metallic Yb^{2+} and Yb^{3+} reference compounds. In the light of what has been said above (section 3) the isomer shift of Yb requires careful calibration because the line width is large and the shift between the two valences is small.

The lanthanide hexaboride series also includes divalent compounds such as EuB_6 being a ferromagnet and YbB_6. However, SmB_6 is intermediate valent and the first material

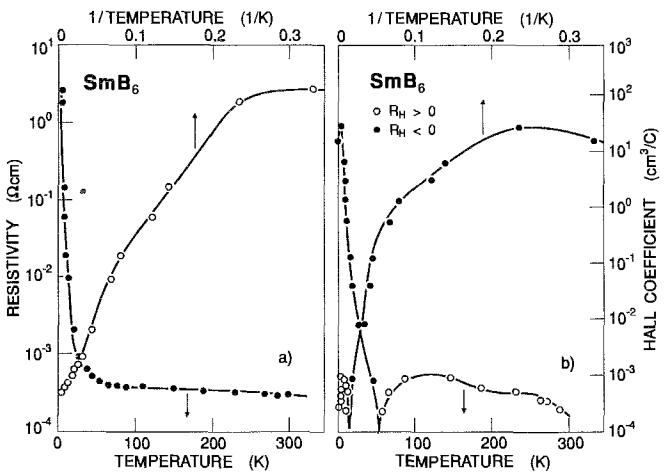

Fig. 7. (a) Resistivity vs. temperature (upper scale vs. reciprocal temperature) of SmB_6 single crystals. (b) Hall constant vs. temperature (upper scale vs. reciprocal temperature) of SmB_6 single crystals. (After Allen et al. 1979.)

being recognized as such (Nickerson et al. 1971). In the series of the dodecaborides TmB_{12} (Bonville et al. 1978) is proposed as intermediate valent again only on the basis of the isomer shift (with the problems discussed above in section 3) and the absence of magnetic order down to 1.35 K. Its intermediate valency remains questionable (Kasaya et al. 1983a). However, YbB_{12} has been found to be intermediate valent on the basis of various measurements to be discussed below (Bonville et al. 1978, Kasaya et al. 1983a). Thus only 3 established intermediate-valent compounds exist amongst the borides which all have an even f–d electron count and thus, according to the Luttinger theorem discussed above, can have the Fermi level in a hybridization gap. Since little is known about YbB_4 (Berrada et al. 1976, Bonville et al. 1978) we will concentrate on SmB_6 and YbB_{12} in this section.

The simplest means to determine the degree of intermediate valence is to measure the lattice constant of, e.g., a lanthanide boride series, which usually has trivalent oxidation state (note that X-ray diffraction is an elastic process with no energy transferred to the hybridized electronic states). Strong deviations from the average trend will be observed for divalent and tetravalent oxidation states. The degree of intermediate valence can then be linearly interpolated since the 4f occupation and thus the valency is directly connected with the ionic radius (for a difference in the 4f occupation of one the radius may change up to 10%). Although this linear interpolation scheme is questioned for intermediate-valent alloys (Weidner et al. 1985), it is nevertheless so that for ionic compounds Vegard's law holds, especially when the lattice constant can be calculated from the ionic radii using the hard sphere model. In this way SmB_6 has a valency of 2.6 (Nickerson et al. 1971) and YbB_{12} of nearly 3 (Bonville et al. 1978, Kasaya et al. 1983a).

The first hint that a gap might be present in SmB_6 has come from resistivity versus temperature measurements (Nickerson et al. 1971) where resistivity increases with decreasing temperature. The gap, however, was not associated with a hybridization gap, but rather with a semiconducting gap involving narrow 5d bands. In those days the sample quality was not yet so good and the resistivity increase was only about 2 orders of magnitude. Improved sample quality and the use of single crystals later led to an increase of resistivity between 300 K and 2 K of more than 4 orders of magnitude (Allen et al. 1979, Kasuya et al. 1983) depicted in fig. 7a. It is surprising that independent of sample quality over the years a saturation of the resistivity–temperature behavior is observed for the lowest 2–3 degrees (Nickerson et al. 1971, Allen et al. 1979, Kasuya et al. 1983) and down to 15 mK (Kasuya et al. 1979). Mott (1982b) suggests that this impurity limited maximal resistivity or minimal conductivity is $\sigma_{\min} \approx ce^2/\hbar L$ with L the mean distance between impurities and c a constant. Mott also suggests that long range fluctuations in composition do exist leading to percolation channels.

Now since a resistivity increase with decreasing temperature and a resistivity saturation at the lowest temperatures is not sufficient to establish a gap, Hall effect measurements have been performed (Nickerson et al. 1971, Allen et al. 1979). In fig. 7b we show the temperature dependence of the Hall effect of the same sample as in fig. 7a. From room temperature down to about 50 K the sign of the Hall effect is positive and the magnitude is largely temperature independent, indicating metallic behavior. Below 50 K the sign is negative and down to 2 K the Hall effect increases by 6 orders of magnitude. In the temperature range 4–13 K the plots of $\log_{10}|R_H|$ and $\log_{10}\rho$ vs. $1/T$ are roughly linear, implying activation energies of 1.8 and 2.7 meV, respectively, and in the same order of magnitude as obtained from resistivity plots by Nickerson et al. (1971). The formula used in all these cases is proportional to $\exp(-\Delta E/k_B T)$. Now ΔE counts from the position of the Fermi energy, which for the hybridization model, should be in the middle of the gap. A better formula to obtain the gap thus would be proportional to $\exp(-\Delta E/2k_B T)$ and the gap ΔE would amount to 3.6 and 5.2 meV, respectively. It is then established that one has an extremely small gap which, above about 50 K, is no longer observable as such since the Fermi edge has already become so much washed out that metallic conductivity prevails (at 50 K the Fermi function drops from 90% to 10% within 18 meV). A word of caution: the use of Arrhenius plots is only permitted when Fermi statistics can be replaced by Boltzmann statistics which holds when the Fermi energy in the gap is separated from the band edges by an energy which is large compared to $k_B T$. With a gap in the order of meV the use of an Arrhenius plot is restricted to temperatures less than about 20 K and it is exactly at this energy where the gaps are determined. Usually intrinsic activation energies are determined at high temperatures, whereas at low temperatures impurity activation energies are measured. That the above meV gaps are nevertheless intrinsic will be confirmed by spectroscopic methods discussed below (section 4.1.1.2).

We now follow an analysis by Allen et al. (1979) to show the fallacy of a possible scattering model as explanation of the low-temperature resistivity increase. Then for a metallic number of carriers k_F is approximately π/a with a the interatomic separation which is equivalent to L (the mean distance between scatterers) $\gg a$. One simple estimate

of minimum conductivity is to put L equal to a, thus $\sigma_{\min} \approx e^2/3\hbar a$. This "unitarian limit" results in $\rho_{\max}$ about $5\times10^{-4}\,\Omega\,\mathrm{cm}$ compared to the measured $2.6\,\Omega\,\mathrm{cm}$ at low temperatures, which is about 5000 times larger than $\rho_{\max}$. It is then obvious that the low-temperature resistivity increase cannot be due to scattering when starting from a metallic carrier concentration, which for SmB_6 with a valency of 2.6 and in the absence of a gap would amount to $8.5\times10^{21}\,\mathrm{cm}^{-3}$. Exactly such a hopping model has been considered by Kasuya (1976) and Kasuya et al. (1979, 1983), assuming undoped SmB_6 to be a metal in which disorder due to off stoichiometry causes Anderson localization. The measured activation energy was associated with excitation of carriers to delocalized states. This model is inconsistent with the experimental fact, as described above, that the maximum resistivity increases with decreasing number of defects, and the resistivity does not approach zero for $T \to 0$ but saturates at $2.6\,\Omega\,\mathrm{cm}$ even down to 15 mK (Kasuya et al. 1979). Assuming that this behavior extends down to $T = 0$ it must be concluded that hopping transport does not occur even at the lowest temperatures and that nonlocalized states are above and below the Fermi energy.

The analysis of the Hall data should serve to estimate the carrier concentration at low temperatures. Since the Hall effect is changing sign with temperature it is obvious that a two band model involving electrons and holes must be used. In this model the electron and hole concentration as well as the electron and hole mobility are involved, and thus there are too many parameters to be obtained from the two experimental entities, the resistivity and Hall effect. However, it has been shown by Allen et al. (1979) that the one band model $(-1/R_{\mathrm{H}}e)$ is an *upper bound* on N_{e} and that $N_{\mathrm{h}} \leqslant 2.5 N_{\mathrm{e}}$. At 4 K the expression $-1/R_{\mathrm{H}}e = N_{\mathrm{e}}$ amounts to $2.08\times10^{17}\,\mathrm{cm}^{-3}$ and $N_{\mathrm{h}} \leqslant 5.2\times10^{17}\,\mathrm{cm}^{-3}$. This analysis implies mobilities in the range 1 to $40\,\mathrm{cm}^2/\mathrm{V\,s}$, where the lower limit certainly is typical for extremely narrow bands when magnetic scattering can be excluded. This analysis has also been carried to room temperature where SmB_6 behaves as a poor metal with a carrier concentration of about $9\times10^{21}\,\mathrm{cm}^{-3}$, the carriers being strongly scattered with a mobility of about $1.7\,\mathrm{cm}^2/\mathrm{V\,s}$. In conclusion then it can be said that the carrier concentration drops from about $9\times10^{21}\,\mathrm{cm}^{-3}$ at room temperature by more than 4 orders of magnitude to about $5\times10^{17}\,\mathrm{cm}^{-3}$ caused by a narrow gap of about 4 meV in the density of states.

For YbB_{12} the data are not as detailed, but the problems and questions are similar. After the discovery of YbB_{12} as intermediate valent by Bonville et al. (1978), in the first paper on transport properties of YbB_{12} by Kasaya et al. (1983a) the resistivity increase with decreasing temperature (between 1.7 and 300 K) was only 2 orders of magnitude, in the second paper (Kasaya et al. 1985) it was already 5 orders of magnitude indicating the progress in sample preparation. Other authors like Moser et al. (1985) found between 4.2 and 300 K a more than 4 orders of magnitude increase in resistivity. There is consequently appreciable scattering in the activation energy, reported to be 3 meV (Kasaya et al. 1983a), 6 meV (Kasaya et al. 1985) and 5.2 meV (Moser et al. 1985). Again, when the Fermi level is assumed to be in the middle of the gap, as was done by Kasaya et al. (1985), the gap values would have to be doubled, residing between 10 and 11 meV. The resistivity of YbB_{12} is shown in fig. 8. The Hall effect is negative in the whole investigated temperature

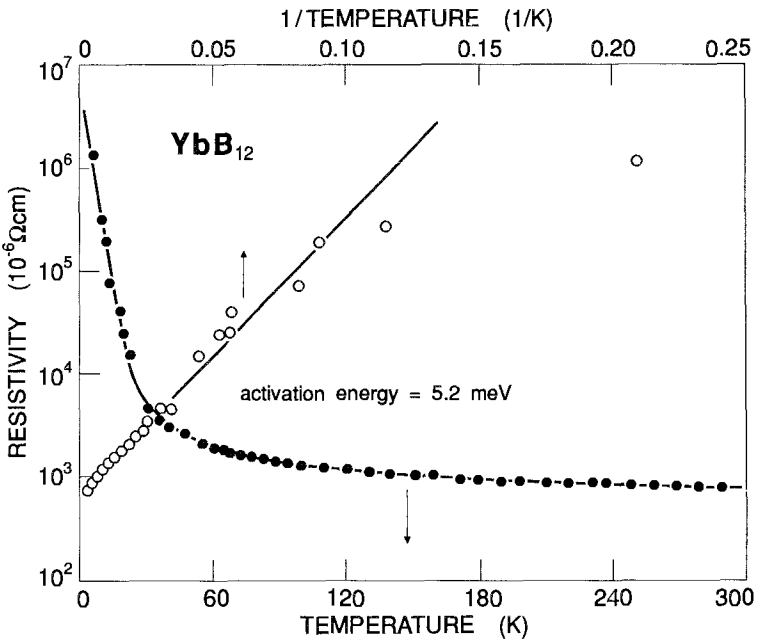

Fig. 8. Resistivity vs. temperature (upper scale vs. reciprocal temperature) of YbB_{12}. (After Moser et al. 1985.)

range below 300 K. An activation energy of 8 meV can be extracted at low temperatures. As we have shown extensively above the one band electron density represents an upper bound for the carrier concentration even in a two band model, and in this sense the carrier concentration at room temperature is reported to be 0.93 per formula unit by Kasaya et al. (1985) which agrees with the earlier statement that the valency in YbB_{12} is nearly 3+. This carrier concentration decreases to 7.4×10^{-6} per formula unit at 1.7 K, compared with the room temperature value by a factor of 1.2×10^{5}. Again it is obvious that one has a gap in the density of states with the Fermi level being right in the middle for $T\rightarrow 0$. Kasaya et al. (1985) express their surprise that the trivalent Yb ion, being similar to the Ce ion in the sense of electron–hole symmetry, shows substantial differences in the same type of compounds, for instance CeB_6 on the one side and SmB_6 and YbB_{12} on the other. They argue that in the latter compounds a Wigner crystal is formed, and in the former no such crystal is formed due to different d–f mixing. According to Kasaya et al. (1985) this excludes the hybridization model. We, however, have shown above that in fact, the different behavior of Ce and Yb/Sm compounds results from the Luttinger theorem as a consequence of the hybridization model, inasmuch as in Yb and Sm compounds the Fermi level is in the hybridization gap, as experimentally verified by the measurements above, whereas in Ce compounds the Fermi level is not in the gap, but we will show below that Ce compounds or alloys nevertheless have a hybridization gap.

The γ value of the specific heat is another entity which brought confusion into the models. When the Fermi level is in a gap the γ value should be zero, if it is a pseudo

gap it should at least be small. However, in the first measurement on SmB_6 a γ value of 90 mJ/mol K^2 has been found by Nickerson et al. (1971), too large to be compatible with the Fermi level in a gap. Later, values of 6 mJ/mol K^2 have been reported by Kasuya et al. (1979) with the proposal that this value is caused by defects, again later, and with still better samples, a γ value of 2.1 mJ/mol K^2 has been found by von Molnar et al. (1982) together with the statement, that there is probably not even a linear term. For YbB_{12} the specific heat has not been analyzed to extract a linear term because of the conviction that the Fermi level lies in a gap (Kasaya et al. 1985).

The specific heat gives a further indication of a gap in the density of states. After subtracting a suitable lattice term in the specific heat of SmB_6 by comparing with LaB_6 (von Molnar et al. 1982) and of YbB_{12} by comparing with LuB_{12} (Kasaya et al. 1985) a peak remains near 30 K for SmB_6 and near 50 K for YbB_{12} strongly representing a Schottky anomaly (Wachter 1987). Regarding fig. 2d we realize that the hybridized ground state near E_F resembles in principle a two level system where thermally induced electronic transitions contributing to the specific heat are possible. The standard formula for the analysis of a Schottky anomaly is $0.41\,\Delta E = k_B T_{max}$, which holds for equal degeneracy of the two states, which is not so unreasonable since the two-peaked density of states (DOS) originated from a single 4f multi-electron level. The gap values determined from these Schottky anomalies are 6 and 10 meV for SmB_6 and YbB_{12}, respectively, in good agreement with the gap values determined from the transport properties.

4.1.1.2. *Spectroscopies.* Valence band XPS spectroscopy has been performed on SmB_6 and the interpretation is straightforward along the same lines as for the chemically collapsed SmS systems (fig. 3) (Campagna et al. 1975). The two hole states (or $n-1$ electron states) are represented by the ladder-like structures in fig. 9 (Campagna et al. 1979) with Coulomb correlation energy of 6.5 eV and valence ratio of about 2.6 in agreement with other methods. In addition the L_{III} edge ($2p^6 4f^6 \rightarrow 2p^5 4f^6 5d$ and $2p^6 4f^5 \rightarrow 2p^5 4f^5 5d$) and the XANES (X-ray absorption near edge structure) has been measured for SmB_6 and a double structure, interpreted as a valence mixing of 2.6, has been found (Beaurepaire et al. 1986).

The results of the Mössbauer spectroscopy on SmB_6 have been shown in fig. 5 from which a valence ratio of 2.6 and the important conclusion of the temperature independence for $T \rightarrow 0$ has been inferred (Cohen et al. 1970). Later it will be shown that a small temperature dependence of the valency in the order of 3% exists.

For YbB_{12} the L_{III} edge has been used as high-energy method (Kasaya et al. 1983a) and been compared with divalent YbB_6 and trivalent Yb_2O_3. The valency is nearly 3+. About the same valency has been obtained in Mössbauer spectroscopy (Bonville et al. 1978) which is completed by the statement that the valency remains the same at 4.2 K.

However, the above spectroscopies do not yield information about the hybridized ground state or the existence of a hybridization gap. Thus in the following we will discuss optical spectroscopies and tunneling or point contact spectroscopies. The first attempts to approach experimentally the meV region on an intermediate-valent compound have been by Allen (1977) on SmB_6 and by Batlogg and Wachter (1977) and by Allen et al. (1978)

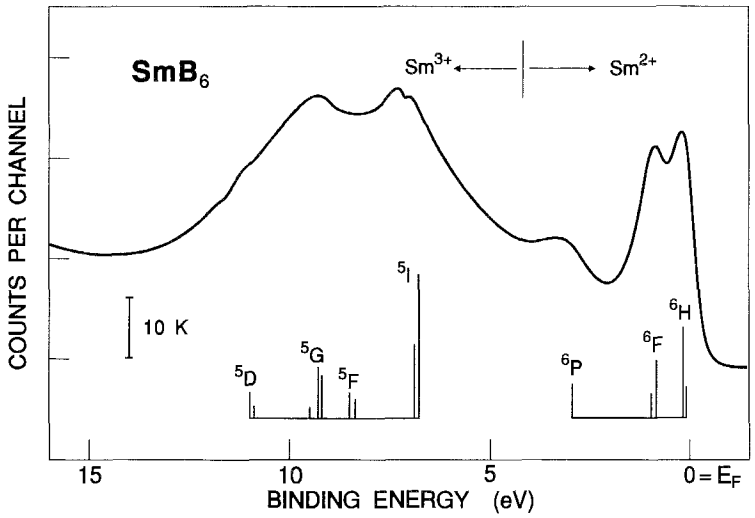

Fig. 9. XPS spectrum of intermediate-valent SmB_6. Also shown is the ladder like structure of the $4f^{n-1}$ final state. The Coulomb correlation energy UC can be taken to be about 7 eV. (After Campagna et al. 1979.)

on the high-pressure phase of SmS. However, the spectral range ended at the lower limit at 35 meV and 30 meV, respectively, which left too much ambiguity in the extrapolation towards zero energy. The next successful attempt has been optical absorption on thin films of SmB_6 in the meV range where between 300 and 4.2 K in the meV range a drop of one order of magnitude has been observed (Batlogg et al. 1981). The first optical transmission spectrum on a SmB_6 single crystal in the meV range and at 4.2 K has been performed by von Molnar et al. (1982). From the sharp increase of optical transmission at about 3.5 meV a gap of about the same size has been inferred. The latest transmission spectrum on a single crystal of SmB_6 at 1.5 K between about 2 and 15 meV is by Ohta et al. (1991) and reports about two absorption edges, one at about 3.5 meV and one at about 10 meV.

The most complete reflectivity measurements on a single crystal of SmB_6 over more than three decades of photon energy and also at low temperatures have been performed by Travaglini and Wachter (1984a). This large photon range (1.5 meV–8 eV) permits the use of a Kramers–Kronig analysis of the data from which the optical constants can be obtained with great precision. The spectrum has been extended at room temperature towards 40 eV by Faberovich et al. (1982). Quite recently the far-infrared–low-temperature reflectivity measurements have been repeated by Nanba et al. (1993) and the experimental data agree excellently with the earlier data. The results of Travaglini and Wachter (1984a) are shown in fig. 10. Above about 2×10^{-2} eV the reflectivity is nearly the same for room and low temperature. The increase of the reflectivity towards 1 for $\omega \to 0$ at room temperature indicates metallic behavior with a plasma edge due to free carriers at 1.75 eV. Here we have to think in terms of the hybridization model again. Room temperature is an energy much larger than the binding energy of the hybridized state thus a hybridization gap is not

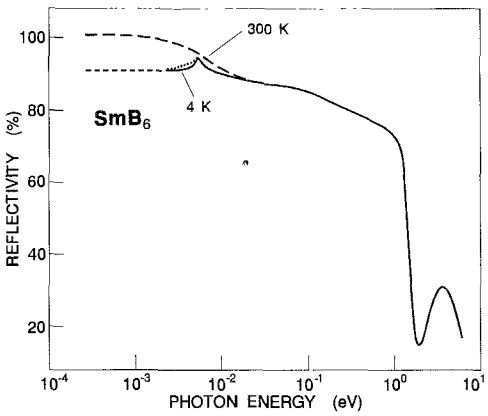

Fig. 10. Optical reflectivity of a SmB_6 single crystal at 4 K and 300 K. The small dashed lines are the extrapolations of $\omega \rightarrow 0$. The solid and the dotted lines are the lower and upper limit of error of the far infrared measurements. (After Travaglini and Wachter 1984a.)

manifest and all electrons in the hatched region of fig. 2d will take part in the collective plasma resonance. We can discern an interband transition at 4 eV, probably boron p to Sm 5d. For photon energies larger than about 10 meV, the estimated hybridization energy, we should observe the ladder-like structure as in XPS spectra (fig. 9), which, however, is completely covered by the plasma resonance of the free carriers. As mentioned above, the power of optical spectroscopy lies in the fact that it can scan the excitation energy over the hybridization energy, and in fact, as can be seen in fig. 10 at low temperatures a maximum in the reflectivity at 5.5 meV is observed, which lies below possible optical phonon energies (Mörke et al. 1981, Alekseev et al. 1989). The reflectivity stays at a constant value of 90% for $\omega \rightarrow 10^{-3}$ eV. Below 10^{-4} eV and towards $\omega \rightarrow 0$ the reflectivity has been extrapolated towards 1 to take into account the finite and measured conductivity at 4.2 K (Allen et al. 1979, von Molnar et al. 1982), using the Hagens–Rubens relation. It is remarkable that already at 10 K and above the reflectivity turns into the room temperature spectrum, i.e., a possible hybridization gap is completely smeared out already by the width of the Fermi distribution, even assuming a rigid and temperature independent f density of states. The 4 K curve of fig. 10 now resembles a semiconductor with a small gap, less than 5 meV, and the high reflectivity values are caused not so much by high absorption but by large dispersion constants, as will be shown below. However, before going into the analysis of the spectra it can already be said from the raw data of fig. 10 that a gap value of 10 meV as mentioned by Ohta et al. (1991) appears impossible because one has a reflectivity peak, caused by an absorption process at 5.5 meV, so an absorption edge must be at lower energy. A peak in the reflectivity is always caused by an intrinsic process with a relatively strong oscillator strength. It appears highly probable that in the transmission measurement on a single crystal by Ohta et al. (1991) light was leaking in, in contrast to the same type of measurements performed 10 years earlier by von Molnar et al. (1982).

The Kramers–Kronig analysis performed by Travaglini and Wachter (1984a) on fig. 10, reveals that the real part of the optical conductivity, i.e., the absorptive part, exhibits a

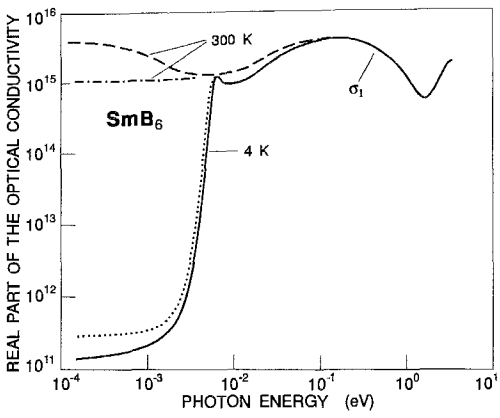

Fig. 11. Real part σ_1 of the optical conductivity of SmB_6. Note the large difference between the dc value at 4 K and 300 K. The dashed and dashed–dotted lines at 300 K bracket the possible error in the extrapolation of $\omega \rightarrow 0$ in the reflectivity curve of fig. 10. The same holds for the dotted and solid lines at 4 K. (After Travaglini and Wachter 1984a.)

metallic behavior at room temperature with the conductivity extrapolating to the measured dc value (fig. 11). At 4 K, however, for lower photon energies than the peak at about 5 meV, a drop of the conductivity by about 4 orders of magnitude is observed within one or two meV, definitely indicating an absorption edge. Without a detailed analysis of the edge shape (we assume an Urbach tail) it is difficult to determine a gap value, but it is evident that the value is between 3 and 4.7 meV and it is thus in agreement with all other gap values determined by other methods (electrical conductivity, Hall effect, optical transmission, tunneling, point contact spectroscopy (with one exception to be discussed below)). It is evident that we interpret this experimental gap as the hybridization gap.

In fig. 12 we show the real and imaginary part of the dielectric functions at room and at low temperature. It is obvious that such a small gap causes an enormous dielectric constant and the dc extrapolation (taking into account experimental errors) amounts to between 1500 and 1700 at 4 K, yielding a refractive index of about 40. It is these high values which may cause a screening of the Coulomb correlation energy U_C at low temperatures and in the hybridized state into the meV range. (Of course this value cannot be taken from a high-energy XPS measurement at room temperature!). The imaginary part of the dielectric constant ε_2 shows the well known absorption edge near 4 meV, a large and narrow peak at 5.5 meV and a second weaker peak at 0.1 eV, having a 100 times larger width. (The peak in ε_2 at about 4 eV is, with a magnitude of about 3, not visible in the scale of fig. 12.)

To understand quantitatively these two electronic transitions in the near and far infrared we have fitted ε_2 with two oscillators:

$$\varepsilon_2 = \frac{4\pi e^2 N}{m} \sum_{i=1}^{2} f_i \frac{\omega \Gamma_i}{(\omega_i^2 - \omega^2)^2 + \Gamma_i^2 \omega^2}, \tag{2}$$

where f_i is the oscillator strength, Γ_i is the damping constant and ω_i is the resonance frequency for the ith oscillator. Although we might expect from fig. 2c an indirect

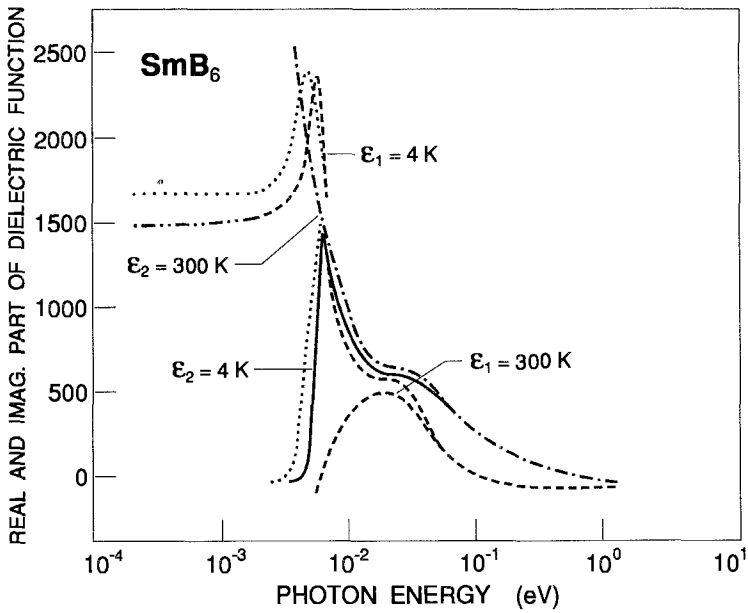

Fig. 12. Real (ε_1) and imaginary (ε_2) parts of the dielectric functions of SmB_6. Double-dotted and double-dotted dashed extrapolations $\omega \rightarrow 0$ following from fig. 10. Dashed curves ε_1 at 4 K and 300 K. Solid curve ε_2 at 4 K. Dotted–dashed curve ε_2 at 300 K. Dotted curves $\varepsilon_{1,2}$ at 4 K within the error limits of fig. 10. (After Travaglini and Wachter 1984a.)

Table 1
Input parameters of the ε_2 fit of SmB_6 (after Travaglini and Wachter 1984a)

	$\hbar\omega$ (eV)	$\hbar\Gamma$ (eV)	f
Oscillator 1	0.0055	0.0016	0.00033
Oscillator 2	0.1	0.5	0.3

transition between the two f-like density of states peaks, we assume in a first approximation direct transitions thus avoiding phonon matrix elements. With two oscillators centered at 5.5 meV and 0.1 eV and with input parameters given in table 1 we obtain a very good fit of ε_2 of fig. 12 shown in fig. 13. The oscillator strength in table 1 gives further hints on the interpretation of the results. For the low-energy oscillator the oscillator strength is only 0.00033, which implies that the transition is nearly forbidden. This fact corroborates the mainly f–f character of the first transition. However, if the transition would be f–f atomic-like, the oscillator strength would only be 10^{-6}. Our oscillator strength, which is 100 times larger, indicates a strong d admixture exactly in the spirit of the hybridization model. For the higher energy oscillator the transition probability is 0.3, a typical value for a f–d or d–f transition. The width of this transition extends over at least 2–3 eV and agrees with the estimated d bandwidth.

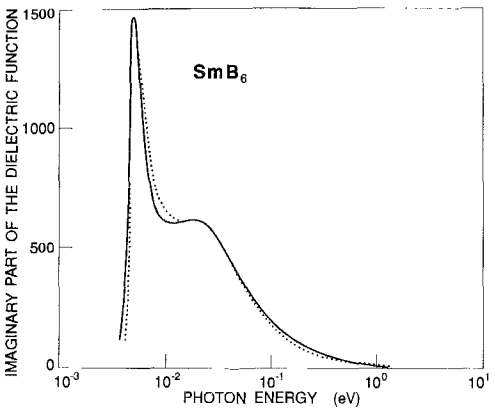

Fig. 13. The ε_2 fit: the dotted line is ε_2 at 4 K from fig. 12 and the solid line is the fit result. (After Travaglini and Wachter 1984a.)

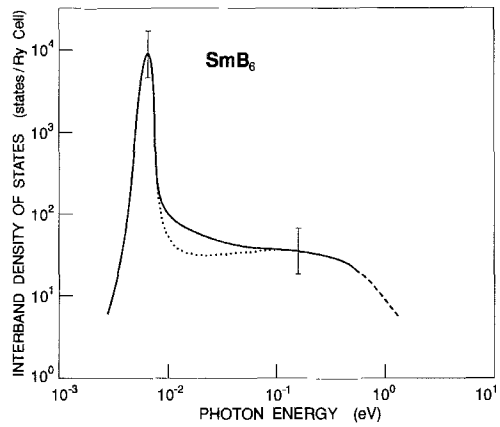

Fig. 14. Interband density of states (IDS) of SmB_6 at 4 K calculated with the use of the resulting fit oscillator strength in the constant matrix element approximation: the dotted line gives the uncertainty between the peak with f character and the one with d character. (After Travaglini and Wachter 1984a.)

We can also estimate in a first approximation the joint density of states J_{cv} assuming constant matrix elements within an f–f or d–f transition, respectively. We can describe the imaginary part of the dielectric function in terms of an integration over a surface in the reciprocal space k. For direct optical transitions one finds

$$\varepsilon_{2_i}(\omega) = \frac{e^2}{\pi m^2 \omega^2} \int |\alpha_0 p_{cv}|_i^2 \frac{dS}{|\nabla_k E_{cv}(k)|_i} = 8 \left(\frac{\pi e}{m\omega}\right)^2 |\alpha_0 p_{cv}|_i^2 J_{cv_i}, \tag{3}$$

where dS is a simple surface element in k space such that $E_{cv}(k) = \hbar\omega$ and p_{cv} is the momentum operator. The oscillator strength is coupled to p_{cv} with a relation

$$f_i = 2 \frac{|\alpha_0 p_{cv}|_i^2}{\hbar\omega m}. \tag{4}$$

We can now calculate from ε_2 the joint density of states J_{cv} or interband density of states (IDS) which is $2J_{cv}$. The IDS is shown in fig. 14: there exists a giant peak

of about 10900 states per Rydberg per cell located at 6.3 meV and a shoulder of about 50 states per Rydberg per cell at 0.1 eV (Wachter and Travaglini 1985). If we had explicitly taken an indirect f–f transition into account the matrix elements would have become smaller and thus J_{cv} would have become even larger. The numbers shown in fig. 14 thus only represent a lower limit. By comparing figs. 13 and 14 we must note that, although apparently similar, fig. 14 is a logarithmic scale and thus the density of f states is about 3 orders of magnitude larger than the one of the d states. The optical density of states with f character has a maximum at 6.3 meV. This energy is the difference between the maxima of the density of states of f states shown in fig. 2d and it is thus larger than the gap value of 3–4.7 meV. We assign the shoulder at 0.1 eV to the band with d character having 50 states per Rydberg per cell. The half-width of the IDS at the low-energy transition is 5 meV which would correspond to the bandwidth of the f-like bands which are thus nearly atomic-like. The f bandwidth is in any case much smaller than the 40 meV assumed by Takigawa et al. (1983). It is intriguing to tilt fig. 14 by 90°, it then resembles nearly quantitatively the density of occupied states sketched in fig. 2d.

The analysis of the spectra also yields interesting results at temperatures above 10 K and up to room temperature. As seen in fig. 12 ε_2 diverges positively and ε_1 diverges negatively for $\omega \to 0$, but these functions exhibit a shoulder and a peak, respectively, at about 0.1 eV. Clearly at 300 K gaps are no longer detectable because most electrons are thermally excited above the gap and the materials behave like metals, but hybridization is still present as evidenced by the intermediate values of the lattice constant and the isomer shift of the Mössbauer effect. We thus expect at the Fermi level electrons with f and with d character, having heavy and normal effective masses, respectively.

A collective oscillation of carriers with a plasma resonance is obtained whenever $\varepsilon_1 = 0$ and $(d\varepsilon_1/d\omega)_{\varepsilon_1=0} > 0$. We notice that at 300 K ε_1 in fig. 12 has three zero crossings, where those at 1.75 and 0.0053 eV fulfill the conditions for a longitudinal oscillation of free carriers. The transition at about 0.1 eV with $(d\varepsilon_1/d\omega)_{\varepsilon_1=0} < 0$ indicates a transverse excitation and is due to the d–f interband transition.

The two plasma resonances correspond to normal (d) and heavy (f) electrons, which generally must be assumed to give rise to coupled oscillations. However, since the resonances are so far apart, the coupled system has its eigenfrequencies practically at the resonance frequencies of the uncoupled resonators. In this case we can compute the independent plasma frequencies which are screened by ε_{opt} of higher energy interband transitions. For the resonance at 1.75 eV we use $\varepsilon_{opt} \approx 2.7$ due to p–d interband transitions located around 4 eV (see fig. 10) and from $\omega_{pd}^2 = (4\pi N_d)/(m_d^* \varepsilon_{opt})$ we obtain $(N_d m)/m_d^* = 0.42$ electrons per Sm ion. For the resonance at 0.0053 eV we use $\varepsilon_{opt} \approx 400$ due to d–f interband transitions located at 0.1 eV (fig. 13) and from $\omega_{pf}^2 = (4\pi N_f)/m_f^* \varepsilon_{opt})$ obtain $(N_f m)/m_f^* = 5.7 \times 10^{-4}$ electrons per Sm ion.

The valence determination of Sm in SmB_6 by means of the isomer shift (Cohen et al. 1970) or the lattice parameter (Nickerson et al. 1971) has given a nearly temperature-independent valence of 2.6. We thus expect $N_f \approx 0.4$ and $N_f + N_d = 1$. Using these numbers we obtain $m_d^* \approx 1.4m$ (± 0.1) and $m_f^* \approx 1000m$ (± 500). Optical effective

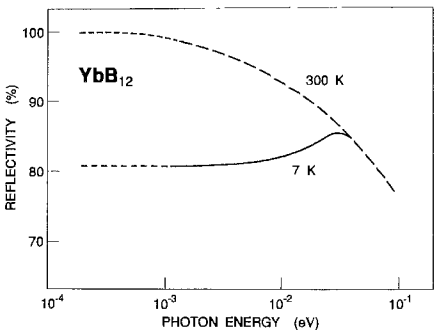

Fig. 15. Far infrared reflectivity of YbB_{12}. (After Travaglini and Wachter 1985.)

masses m_d^* of this magnitude have been observed before by Beckenbaugh et al. (1975) for 5d electrons in the La and Gd chalcogenides. However, an optical effective mass m_f^* of about $1000m$ has never been determined experimentally so far. It is remarkable that only optical methods have revealed the high density of states at E_F and the enormous masses connected with this. γ values of the specific heat fail here because they can only be determined at low temperatures, when, however, the Fermi level lies in the gap. It is precisely these optical measurements which give information about the intermediate valence nature of these materials and yield at room temperature the heavy masses typical for heavy fermions. However, these materials are not heavy fermions because as $T \to 0$ there are no electrons at E_F. In fact, at room temperature there is no fundamental difference between a heavy fermion of the type UPt_3 or UBe_{13} and an intermediate-valent compound of the type SmB_6 or TmSe. But most other standard physical methods, like γ value of the specific heat or de Haas–van Alphen resonances are not capable to give information at high temperatures.

SmB_6 is nevertheless a lucky and thus unique case because of the number of light-weight d electrons, N_d is only 0.6 per formula unit, so the plasma resonance of the heavy-weight f electrons in the far infrared can be discerned even at room temperature. For other typical heavy fermions like UPt_3, $CeAl_3$, etc., the number of electrons in the conduction band are not only those from the lanthanide or actinide element, but also from the alloy partner thus the plasma resonance from these light weight electrons overwhelms the one of the f electrons in the far infrared. A further reason why we spend so much time and space with SmB_6 is experimental in nature. SmB_6 is the only material where large single crystals are available and measurements at about 4 K are sufficient to reveal most of the parameters. For YbB_{12} no single crystals were available, for the Sm chalcogenides one needs high pressure and for the TmSe the antiferromagnetism with a T_N of about 3.5 K interferes. This is a pretty low temperature for far infrared optical measurements.

For the optical measurements on YbB_{12} only a sintered polycrystalline block was available (Wachter and Travaglini 1985, Travaglini and Wachter 1985) which has been polished and measured against a gold reference mirror. After all the measurements were finished the YbB_{12} was covered by a layer of gold and measured again against the gold mirror to calibrate for the diffuse scattering (which for the far infrared is not of great

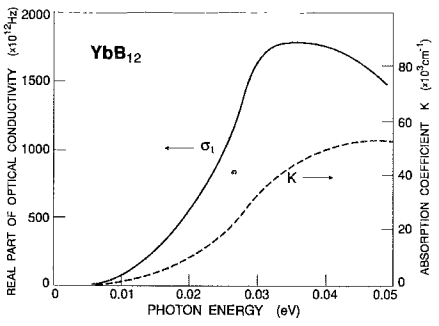

Fig. 16. Real part of the optical conductivity σ_1 and the absorption coefficient K of YbB_{12} at 7 K. (After Wachter and Travaglini 1985.)

importance). In this way fig. 15 has been obtained (where only the dependable spectral range is shown) and the absorption coefficient and the optical conductivity is shown in fig. 16. Again, just as for SmB_6 a far infrared maximum, this time at about 40 meV, with an absorption edge between about 6 meV and 12 meV is observed at low temperatures. The experimental problems with the polycrystalline sample did not allow a detailed analysis of the data, but it is evident that the physics is the same as in SmB_6. For YbB_{12} also the microwave conductivity has been measured by Jackson et al. (1984) and the postulated Wigner crystallization of the electrons as proposed by Kasaya et al. (1985) has been excluded on the basis of these experimental results.

Another interesting spectroscopy related with the hybridization gap is tunneling and point contact spectroscopy. The first and only tunneling spectra on SmB_6, prepared with Pb on an air-oxidized crystal has been performed by Batlogg et al. (1981). The interpretation is compatible with a minimum in the density of states with a 5–8 meV width around the Fermi energy in agreement with the hybridization model. The first point contact spectroscopy on SmB_6 has been performed by Frankowski and Wachter (1982a,b) where a sharply etched Mo wire has been pressed at a single crystal of SmB_6 (the same as used by Travaglini and Wachter 1984a) at 1.8 K and the dynamic resistance has been measured. In this spectroscopy the sign of the signal is the same as in tunneling (Batlogg et al. 1981) although one is not tunneling through an oxide barrier but rather has a metal–metal contact with a current constriction at the contact area acting like a resistivity. The point contact spectra of SmB_6 are compared with a reference material LaB_6 and it is concluded that a gap in the density of states of 4.6 meV is present. Magnetic fields up to 5 T parallel to the contact area did not have any influence on the spectra of SmB_6. Güntherodt et al. (1982) used a Schottky barrier point contact with a degenerately doped GaAs tip. The Schottky barrier created by the contact serves as a tunnel barrier and thus should correspond to the results of Batlogg et al. (1981). Estimates of the energy gap vary between 2.7 and 4.9 meV and independence of magnetic field up to 1.5 T is reported. Similar measurements with a GaAs tip have been described by Kunii and Kagaya (1985). Unfortunately the temperature (4.4 K) was not low enough to obtain a good spectrum but at the lowest temperature a gap of about 3 meV can be estimated. A more recent point contact spectrum on SmB_6 has been obtained by Kunii (1988) which, however, falls with a

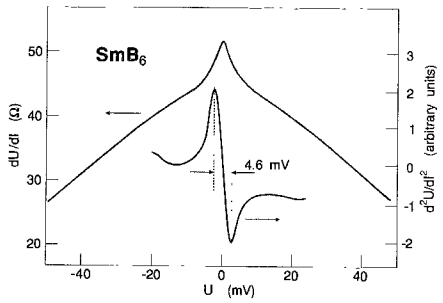

Fig. 17. Dynamic resistance $dU/dI(U)$ and derivative $d^2U/dI^2(U)$ of a SmB_6 single crystal point contact at $T = 1.8$ K. (After Frankowski and Wachter 1982a,b.)

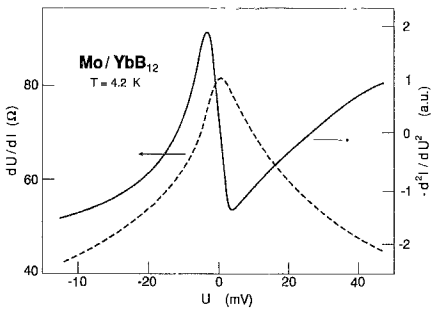

Fig. 18. Dynamic resistance dU/dI and derivative d^2I/dU^2 of a Mo/YbB_{12} point contact at 4.2 K. (After Moser et al. 1985.)

gap value of 16 meV far out of the possible range quoted by all other authors and methods. His so called "clean contacts" do not even show the signature of a gap structure but rather a minimum in the differential resistivity, whereas all other methods have a maximum.

Also for YbB_{12} a point contact spectrum has been obtained using a Mo tip. In figs. 17 and 18 the point contact spectra of SmB_6 by Frankowski and Wachter (1982a,b) and of YbB_{12} by Moser et al. (1985), respectively, are shown, where the gaps are taken to be where the dynamic resistivity shows points of inflection (4.6 and 6.5 meV, respectively), given experimentally by the difference between the peaks of the second derivative. (It should be noted that in fig. 17 d^2U/dI^2 has been used in the ordinate, whereas in fig. 18 $-d^2I/dU^2$ has been used. For nonlinear resistivities the second entity is better and the two quantities are related by $d^2I/dU^2 = -(1/R^3)d^2U/dI^2)$.

Another interesting spectroscopy performed on SmB_6 is nuclear magnetic resonance (NMR) where the temperature dependence of the ^{11}B relaxation rate has been measured by Pena et al. (1981). Above 10 K the temperature dependence is exponential with a gap of 5.6 meV. The authors interpret their results as the consequence of the fluctuations of 4f spins thus relating the measured line width to the contribution of the hyperfine field from these fluctuations. The NMR experiments thus measure directly a gap in the 4f spectrum, where the only other experiment, directly related to a gap in the 4f spectrum, was the IDS obtained by optical reflection by Travaglini and Wachter (1984a). Similar NMR results have been obtained by Takigawa et al. (1983).

Also electron spin resonance (ESR) of rare earth doped SmB_6 is reported by Kojima et al. (1978), Stura et al. (1985) and Kunii et al. (1985). g shifts are observed related

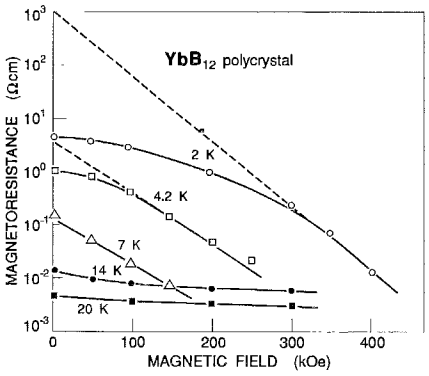

Fig. 19. Magnetoresistance vs. magnetic field of YbB_{12} polycrystals. Dashed lines indicate the intrinsic magnetoresistance. (After Sugiyama et al. 1985.)

to the exchange mechanism between magnetic impurities as well as line broadenings interpreted as being due to d–f hybridization. For non-S-ground state ions such as Er a strong electron–phonon coupling is inferred from a dynamic Jahn–Teller effect by Stura et al. (1985).

4.1.1.3. *Electronic properties under the influence of external parameters.* In this subsection we want to treat the electronic properties under the influence of magnetic field, external pressure and doping.

Magnetic fields up to 5 T have been applied in point contact spectra on SmB_6 by Frankowski and Wachter (1982b) and on YbB_{12} by Moser et al. (1985) with no significant effect on the spectra. However, for polycrystalline YbB_{12} a magnetic field up to 45 T has been applied by Sugiyama et al. (1985) and the magnetoresistance and the magnetization has been measured. The logarithm of the resistivity is decreasing linearly with increasing field at low temperatures. Assume that the gap is reduced linearly by the Zeeman energy $g\mu_B JH$ as $\Delta E(H) = \Delta E(0) - g\mu_B JH$ or $\rho(H) = \rho(0)\exp(-g\mu_B JH)/2k_B T$. Then $\ln[\rho(H)/\rho(0)] = -(\mu_B gJH)/2k_B T$ and one finds that the gap is closed around 40 T, and one can take $gJ \approx 4 \pm 1$ from the slope of the magnetoresistance versus field curve (fig. 19). We can thus calculate $\Delta E(0)$, the gap in the absence of a magnetic field and it amounts to 8–9 meV in agreement with other measurements.

Here we may well ask again the question of the excitation energy in relation to the hybridization energy. With $gJ \approx 4$ and $H = 40$ T and above, the Zeeman energy amounts to over 8 meV which has at least the same order of magnitude as the hybridization energy. The magnetic field thus can break up the hybridization. We think that in fig. 19 the curves below 7 K and for low magnetic fields represent the typical moment quenching well known in intermediate-valent and heavy-fermion systems. For high magnetic fields the gap disappears, the hybridization breaks up and gradually a moment, corresponding to the Yb^{3+} ion with its postulated Γ_7 groundstate of $gJ = 3.4$, appears. This Γ_7 state is now of course below the Fermi level but will be split with increasing field relative to its center of gravity. As a consequence the upper split level will cross the Fermi energy at a

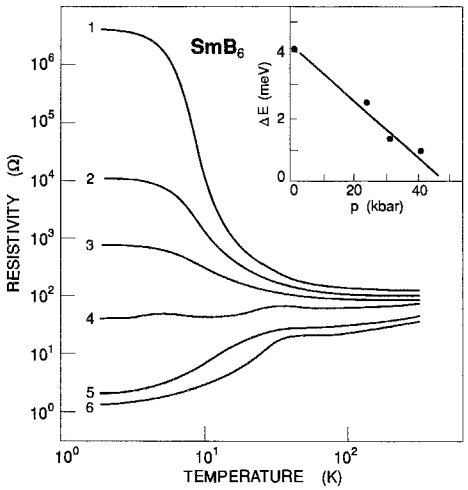

Fig. 20. Temperature dependence of resistivity $R(T)$ in SmB_6 at different pressures in kbar: 1–0, 2–24, 3–40, 4–57, 5–70, 6–108. The inset illustrates the variation of the energy gap with pressure. (After Moshchalkov et al. 1985.)

certain field (estimated to be 83 T) and then the magnetization will increase dramatically. Indications of this can still be seen in the experimental field range up to 50 T in fig. 19.

An excellent external parameter for intermediate-valent materials is pressure because one can change the degree of valence mixing and eventually drive the materials into integer trivalency. Moshchalkov et al. (1985) and Cooley et al. (1994) have measured the temperature dependence of the electrical resistivity of SmB_6 as function of pressure up to 120 kbar (12 GPa) and 80 kbar, respectively, as shown in fig. 20. The gap ΔE is determined from the slopes of the linear parts of $\log R$ versus $1/T$ and it is found that $d\Delta E/dp = -0.08$ meV/kbar. It is shown that ΔE is reduced linearly with pressure (see inset of fig. 20), starting with $\Delta E = 4$ meV at ambient pressure. At 55 kbar the gap is closed and metallic-type conductivity prevails. The negative magnetoresistance observed at ambient pressure changes into a positive magnetoresistance once the gap is closed. The interpretation within the hybridization model is obvious: pressure broadens the quasiparticle bandwidth and closes the hybridization gap, but then the Fermi level should still be in a high density of states region, possibly shown by fig. 1a. At higher pressures all mobile 4f electrons (in total 1 per Sm ion) are emptied into the conduction band and the $4f^5$ state becomes localized and gets situated rather far below E_F ($Sm^{3+}B_6$). At a pressure little above the one necessary to close the gap we should expect a Kondo-like resistivity behavior with a maximum at a low temperature. Unfortunately this pressure range is not well shown in fig. 20 (between curve 3 and 4) but it is very well shown in SmS and SmSe, where similar measurements are reported by Holtzberg and Wittig (1981) and Lapierre et al. (1981a) (to be discussed below). Once the $4f^5$ level falls appreciably below E_F the material is integer trivalent and a metal like LaB_6 or GdB_6 with 1 free electron per metal ion. Moshchalkov et al. (1985) also measured the dc current versus electric field curve of SmB_6 and derived again a gap value of 4 meV.

Doping is another interesting way to change the valency of Sm in SmB_6. Tarascon et al. (1980a,b) have prepared the pseudobinary solid solution system $Sm_{1-x}MB_6$ with $M = Yb^{2+}$, Sr^{2+}, La^{3+}, Y^{3+} and Th^{4+} and measured the L_{III} edge, the magnetic susceptibility and the lattice parameter. Especially the L edge of Sm is an elegant way to determine the valency by integrating the intensity of the Sm^{2+} and the Sm^{3+} peaks separated by 7 eV at 6710 eV. It is found that the substitution of Sm by the divalent Yb and Sr ions decreases the number of conduction electrons and increases the average Sm valence, whereas the opposite is observed for the tri- and tetravalent La, Y and Th ions. The same results can be inferred from susceptibility and lattice constant changes. The question is whether this is a lattice pressure effect or an electronic effect, due to the different charges or radii of the substituted ions relative to the charge and radius of the intermediate-valent Sm ion. The intermediate-valent Sm ion with a valency of 2.6 has a radius of about 1.08 Å. Sr^{2+}, Yb^{2+} and La^{3+} are with radii of about 1.13, 1.12 and 1.15 Å, respectively, larger than the Sm radius, however, Sr and Yb increase the Sm valence, La decreases it. Y^{3+} and Th^{4+}, with radii of about 0.93 and 0.95 Å, respectively, have a smaller radius than intermediate-valent Sm and thus would enhance the lattice pressure on Sm, increasing the valency, however, the contrary is observed. It is thus evident that lattice pressure is not the right answer, but the reason for the change of valency must be the difference in charge between the dopant ions and intermediate-valent Sm. Since Sr and Yb cannot contribute a charge more than 2 to the bonding and the conduction band but there are less Sm ions available per unit cell their charge must increase in agreement with the experiment, and the opposite is the case for doping with ions having more electrons than the valency of the intermediate-valent Sm ion. It is remarkable that for intermediate-valent SmS the argumentation has been used the other way around, namely that, e.g., doping with Y^{3+} will increase the valency due to lattice pressure. As we will see below, Elmiger and Wachter (1987) have shown that also in the Sm chalcogenides the electronic effect is dominant over the lattice effect.

Kasaya et al. (1983b) measured the specific heat of La doped SmB_6. For a composition $Sm_{0.75}La_{0.25}B_6$ where the valence of Sm is about 2.5 the energy gap in the SmB_6 lattice disappears and the γ value of the specific heat amounts to 45 mJ/mol K^2. Whether the Fermi level has moved out of the gap into the density of states peaks on either side of the gap or that the gap has collapsed cannot be decided in this chapter. But the fact that the hybridization gap disappears upon alloying due to a reduction of the coherence in the lattice is well known and reported by Marabelli et al. (1992b).

Kasaya et al. (1983b) also measured the alloy system $La_{1-x}Tm_xB_6$ and $Yb_{1-y}Tm_yB_6$ for $0 \leqslant x, y < 0.5$, but the valency of Tm in TmB_6 has not been determined because the samples were not single phase. It is found that in the given concentration range the apparent valency of Tm is between 2 and 3 as determined by the L_{III} edge, the lattice constant and the susceptibility. However, neither method is capable of deciding whether Tm is in a mixed-valence condition with randomly present Tm^{2+} and Tm^{3+} or in an intermediate-valent state.

4.1.1.4. *Bandstructure.* Generally speaking the bandstructure calculation of lanthanide compounds suffers from the impossibility to treat localized 4f states and itinerant p and d bands simultaneously. For lanthanides and actinides the calculation should also take into account relativistic effects such as spin–orbit coupling and others. The first bandstructure calculation for a lanthanide compound has been performed by Cho (1967), a Slater scholar, treating EuS by an APW calculation. The problem was that he used plane waves for the 4f wave functions which invariably resulted in a 4f band of about 0.5 eV width. The position of this 4f band between the empty d conduction band and the occupied p valence band changed drastically with the reduced Slater parameter α and in the end the 4f states have been adjusted according to the experiment. It appears that there has been little progress since then. Either the 4f states are introduced as atomic levels and they must be arranged within the bands with additional, usually experimental data, or they are treated as 4f bands and this has little resemblance with reality. In an intermediate-valent material, where, experimentally, the width of the hybridized 4f bands is in the meV range one demands in addition a precision of the bandstructure calculation within meV.

It is thus no surprise that bandstructure calculations are mostly done for the non-4f reference materials like LaB_6 and YB_6 by Walch et al. (1977) and Hasegawa and Yanase (1977), for LuB_{12} and YB_{12} by Harima et al. (1985) and for SmB_6 by Faberovich et al. (1982). Even without bandstructure calculations it follows from symmetry arguments that in the CsCl-like structure of the hexaborides the lowest d conduction band is of e_g type and will have its minimum at the X point. Walch et al. (1977) used an APW calculation with $\alpha = 1$, Faberovich et al. (1982) used a local density approximation with α close to 2/3. The two upper subbands of the valence band have a mixed s- and p-type symmetry and are associated genetically with the 2s and 2p states of the boron atoms. This band has a rather flat maximum extending between Γ and X. The conduction band is a hybridized p–d band, where the p character comes from the 2p states of boron, the d character from the d states of Sm. So far the calculations by the two groups of authors agree. However, in LaB_6 the valence and the conduction band touch, in YB_6 there is a gap of about 1 eV between them, the Fermi level lies in both cases far above in the conduction band making them metals. For SmB_6 there is a gap of about 2.5 eV between valence and conduction band. For YB_{12} there is a strong overlap of the valence band with a maximum at Γ and the conduction band minimum at X, E_F lying again high in the conduction band. For LuB_{12}, however, Harima et al. (1985) calculate a nearly zero gap material with the occupied $4f^{14}$ band hybridizing with both the valence and the conduction band, again the Fermi level being high in the conduction band. Faberovich et al. (1982) have included in their calculation the Sm 4f states by using a MOPW method; they even tried to invoke the intermediate valence state. However, the 4f band again has a width of about 0.5 eV, lying at the bottom of the 5d conduction band. Now here it is obvious that these calculations bear no resemblance with reality. Thus we are left with the conclusion that bandstructure calculation can reproduce the valence and conduction bands quite well, but the f states have to be introduced with a more involved quasiparticle theory as, e.g., that proposed by Brandow (1981).

One other remark regarding the electronic structure of intermediate-valent materials having the Fermi level in the hybridization gap is appropriate. We recall that these are the compounds SmB_6, YbB_{12}, the high-pressure phase of SmS, SmSe, SmTe and TmTe and antiferromagnetic TmSe and its alloys with Se and Eu. For all these compounds it is only SmB_6 and YbB_{12} for which the resistivity increase at low temperatures goes over several orders of magnitude. The others have at most one order of magnitude. It thus appears that only in SmB_6 and YbB_{12} the hybridization extends over the whole Brillouin zone and that only these compounds have a true gap. The others seem to have rather a pseudo gap where the density of states does not really become zero. An explanation from the point of view of the quasiparticle bandstructure has been offered by Brandow (1981). The borides have the CsCl-like structure whereas the others have the NaCl structure. The lowest branch of the 5d manifold is nondegenerate for all of these cubic materials. The hybridization matrix element V_k cannot be constant throughout the Brillouin zone and it has been shown by Martin and Allen (1979) that V_k must vanish at the bottom of the 5d band in the NaCl structure, but this is not the case for the borides with the CsCl-like structure. In other words, the borides have the chance that the hybridization goes over the whole Brillouin zone and thus one has a true hybridization gap in contrast to the pseudo gap of the other materials. This could be the explanation for the orders of magnitude larger resistivity increase of the borides compared with the chalcogenides.

Then in conclusion of this section on the electronic properties of the borides it can be said that a vast amount of experimental methods like resistivity, Hall effect, absence of a γ value for the specific heat, Schottky anomaly, optical transmission, optical reflectivity, tunneling, point contact spectroscopy, Schottky barrier tunneling, NMR, magnetoresistance and pressure dependence of the resistivity all point to the existence of a gap in the density of states and this gap can be identified as the hybridization gap. Its magnitude is given by 90% of the measurements as 4 ± 1 meV for SmB_6 and 8 ± 1 meV for YbB_{12}. A gap of about 20 meV, as proposed by Kasuya et al. (1983) appears far from possible. The effective mass of the heavy carriers could be determined as about $1000m$ and at high temperatures, where no gap exists anymore, the materials can be called heavy fermions. The electronic structure at low temperatures can be very well described by fig. 2d where the peak in the density of f-like states amounts to about 10^4 states per Rydberg per cell in SmB_6 with a width of the density of state peaks of about 5 meV. Taking the bandstructure of SmB_6 of Faberovich et al. (1982) for the valence and conduction band seriously, but imposing the f-like structure as of fig. 2d, we calculate from the reflectance peak at about 4 eV of fig. 10 the filling height of the d band of fig. 2d to be about 1 eV.

4.1.2. *Lattice-related properties*

4.1.2.1. *Phonons.* The crystallographic structure of SmB_6 is of the CaB_6 type, where boron octahedra sit on the corners of a simple cubic cell with the metal in the body centered position (fig. 21). The crystal structure of YbB_{12} on the other hand is of the UB_{12} type, which is a face centered cubic cell surrounded by B_{12} icosahedra. The standard

method to obtain phonon dispersion curves, namely inelastic neutron scattering, is extremely difficult for these materials because of the prohibitive absorption cross section of boron for neutrons. Nevertheless, it has been possible to perform inelastic neutron scattering at room temperature by Alekseev et al. (1989) using a double isotope single crystal of $^{154}Sm^{11}B_6$. Phonon properties of intermediate-valent materials are of great interest since a strong electron–phonon interaction may be expected. In early days it has been assumed that the characteristic time of valence fluctuations and lattice vibrations is close enough to enable a strong interaction for breathing type phonon modes (Sherrington and von Molnar 1975, Mook et al. 1978, Bilz et al. 1979, Treindl and Wachter 1980). Now we would say that the effective mass of the electrons is so large ($\approx 1000m$) that it approaches atomic masses and thus a strong coupling can be expected. However, the specific effects discussed below are rather rare within intermediate-valent or heavy-fermion systems, in fact, they are only observed for compounds having the Fermi energy in the hybridization gap like SmB_6, high-pressure SmS, chemically collapsed $Sm_{1-x}Y_xS$ or TmSe. It appears that an additional condition is necessary for observation of special phonon properties, namely a low concentration of conduction electrons, which is present in the above compounds (recall that, e.g., in SmB_6 the carrier concentration in f- and d-bands together is only 1 per formula unit, whereas in $CeAl_3$ it is 4 per formula unit). Thus screening may be reduced in SmB_6.

Raman effect has been a standard procedure to obtain information on phonons. For the SmB_6 structure there are three Raman active modes of A_{1g}, E_g and F_{2g} symmetry. In this first-order Raman effect only zone center modes are involved. The frequencies of these modes plotted against the lattice constant fall on a straight line for both semiconducting $M^{2+}B_6$ and for metallic $M^{3+}B_6$ compounds as Ishii et al. (1976) have shown. For the fully symmetric A_{1g} breathing mode and the E_g mode the lines of semiconducting and metallic hexaborides nearly coincide, but for the F_{2g} (or T_{2g}) mode, the line of the semiconducting hexaborides lies about $90\,cm^{-1}$ above that of the metallic samples, i.e., only the F_{2g} mode depends on valency (Güntherodt et al. 1978). As a consequence the Raman line of the F_{2g} mode in intermediate-valent SmB_6 lies in between the $M^{2+}B_6$ and the $M^{3+}B_6$ frequency and by linear interpolation one obtains again a valency of about 2.6.

In the hexaborides the bottom of the conduction band is formed by the Sm $5de_g$ band plus some p character from the boron atoms (Hasegawa and Yanase 1977). The 5d charge lobes extend from one Sm ion to the 6 next cations and overlap to form a band. As Mörke et al. (1981) have shown the boron atoms move in a Γ-F_{2g} mode in direction of these charge clouds thus directly probing the charge in the 5d band and thus testing the intermediate-valent state. In the A_{1g} or the E_g mode the boron atoms move tangentially to the 5d charge clouds and thus are rather insensitive to the charge in the 5d band in agreement with the experiments.

Besides the three allowed Raman modes which concern only vibrations within the boron cage there exist symmetry-forbidden low-energy modes in which the boron cage vibrates against the Sm ion in an optical mode. In these forbidden modes the selection rules can be relaxed by the presence of defects as is common in lanthanide compounds and

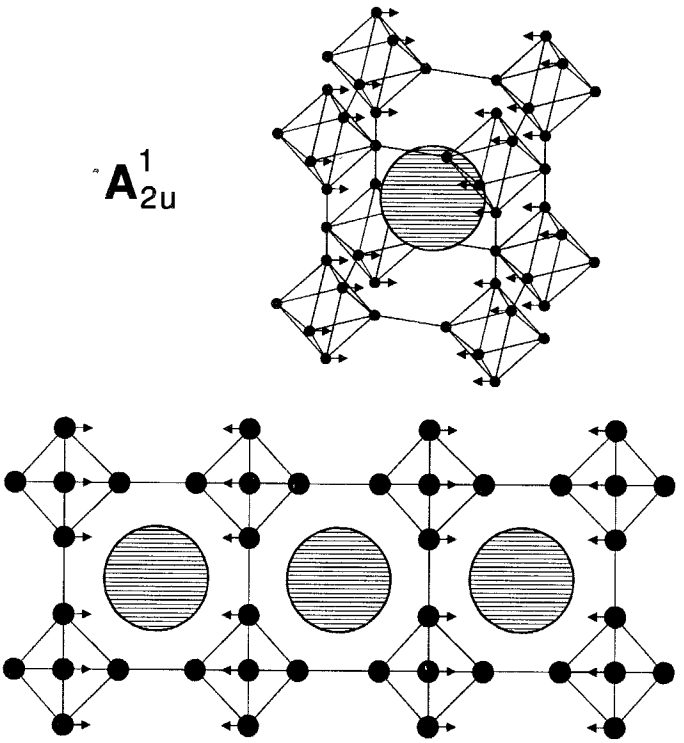

Fig. 21. Normal vibration of the A^1_{2u} mode of SmB_6 at the X point. (After Mörke et al. 1981.)

thus the Raman effect measures a weighted one phonon density of states. This low-energy mode has been found by Mörke et al. (1981) in $La^{3+}B_6$ (214 cm^{-1}), $Eu^{2+}B_6$ (220 cm^{-1}) and in SmB_6 at 172 cm^{-1}, appreciably softer than in the di- or trivalent reference compounds. Such a softening of LO phonons at the L point of the Brillouin zone has been observed before for NaCl type crystals such as chemically collapsed $Sm_{0.75}Y_{0.25}S$ by Güntherodt et al. (1978) and on TmSe by Treindl and Wachter (1980).

Softening of zone boundary LO phonons in the NaCl structure and also of the bulk modulus are the striking effects caused by the electron–phonon interaction due to volume modulations of the lanthanide ion by the phonons as calculated by Bennemann and Avignon (1979), Ghatak and Bennemann (1979) and Cantrell and Stevens (1984). One expects a strong scattering intensity from those deformations which also describe the phonon anomaly.

In SmB_6 the situation is somewhat more complex than in the NaCl structure since each Sm ion has 24 nearest neighbors. The group theoretical analysis of the structure shows that the phonon modes at the Γ point are classified as $A_{1g} + E_g + F_{1g} + F_{2g} + 3F_{1u} + F_{2u}$ with decreasing energy. The situation in both crystal structures may be compared by looking at the intermediate-valent (IV) compounds for phonon modes which are most

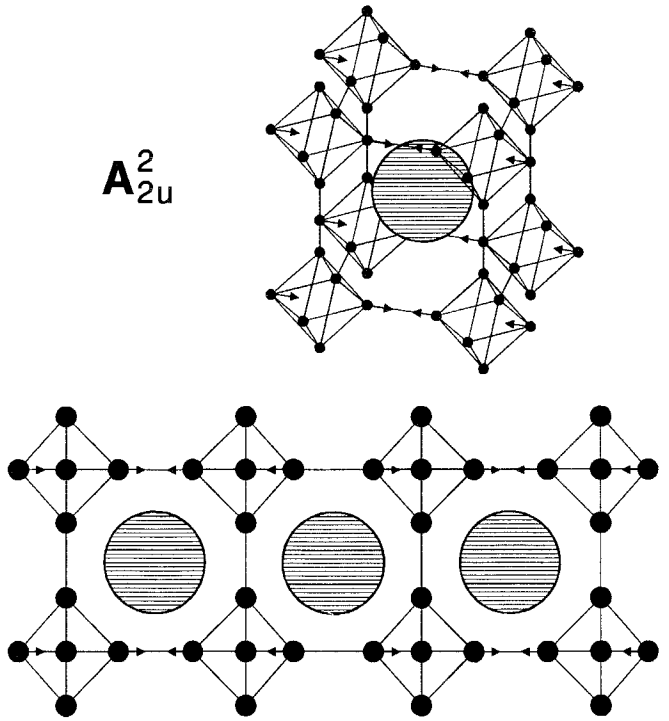

Fig. 22. Normal vibration of the A^2_{2u} mode of SmB_6 at the X point. (After Mörke et al. 1981.)

strongly affected by the electron–phonon coupling. These are modes where planes of anions move against planes containing only the IV ions, i.e., vibrations under which the volume of the IV ion is reduced by a great amount. For the NaCl structure this is at the L point of the Brillouin zone and for the SmB_6 structure this is at the Γ point or the X point. The symmetry of normal modes at the X point (with the origin of the coordinate system in the center of the boron cage) is $3A_{1g} + A_{2g} + B_{1g} + B_{2g} + 3E_g + 2A_{2u} + B_{2u} + 3E_u$. Among these 21 vibrational modes the two of A_{2u} symmetry are those where planes of B ions move in [100] direction against planes of Sm ions as shown in figs. 21 and 22 (Mörke et al. 1981). This vibration will have a low energy because the whole B_6 octahedron with its high mass moves against the Sm ions. A mode of A_{2u} symmetry at the X point may be of A_{1g}, E_g or $F_{1u}(T_{1u})$ symmetry at the Γ point. If one looks at the low-energy F_{1u} (T_{1u}) modes, one of which is the acoustic, one finds two vibrational modes showing exactly the same atomic displacements as for the two A_{2u} modes (see fig. 22). The only difference is that at the Γ point all unit cells move in phase, whereas at the X point neighboring planes of unit cells move in antiphase. Thus at the zone center (F_{1u} or T_{1u}) (Zirngiebl et al. 1986) and in [100] direction at the X point (A_{2u}) the LO phonon branch is expected to soften (Mörke et al. 1981). The lowest energy Raman line in LaB_6

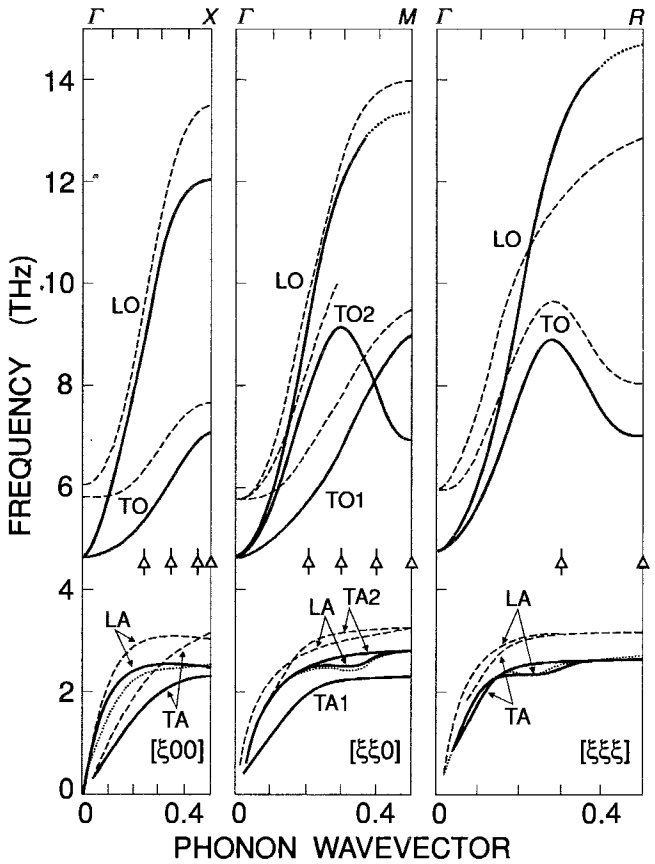

Fig. 23. Phonon dispersion curves for SmB_6. Dashed lines are the phonon branches for LaB_6, dotted lines are the calculated LA branches. (After Alekseev et al. 1989.)

(214 cm^{-1}) and SmB_6 (177 cm^{-1}) should be associated with the lowest energy in the LO branch and this is at the Γ point in the F_{1u} or T_{1u} mode because in this mode more B atoms are involved (Zirngiebl et al. 1986).

The Raman results are beautifully corroborated by the direct inelastic neutron scattering by Alekseev et al. (1989) which are reproduced in fig. 23 together with LaB_6 as reference material. Indeed, the LO branch in the X direction is softened as a whole in SmB_6 compared with LaB_6 the same as the TO branch and the frequency at the Γ point agrees very well with the Raman measurement for both materials. Pronounced anomalies are also observed in SmB_6 contrary to LaB_6 for the LA branches in the [110] and [111] directions. These anomalies resemble the similar softening of LA phonons in the [111] direction in IV SmS and TmSe by Mook et al. (1978) and Mook and Holtzberg (1981).

A new experimental result is the observation of a broad and weak signal in the gap between the acoustic and optic branches and marked in fig. 23 with triangles. Such a mode has been observed before in IV chemically collapsed SmS by Mook et al. (1978). These modes are probably connected with bound heavy-electron plasmon–phonon modes where the f-like quasiparticles in the narrow bands below E_F (described in section 4.1.1.2 and shown in figs. 2d and 14) couple to the phonons and perform collective oscillations. We recall that we have two plasma oscillations, one for normal mass electrons and one for heavy mass electrons in the far infrared. It is the latter plasmon modes which are expected to couple to acoustic phonons in an out of phase motion as first proposed by Varma (1976). This idea has been quantitatively expanded in papers by Entel et al. (1979), Sinha and Varma (1983) and Stüsser et al. (1982). Further investigation of these modes seems necessary, however, they are only rarely observed (see also section 4.3.1.2).

Recently, Alekseev et al. (1992, 1993) investigated also the double isotope crystal $^{154}Sm^{11}B_6$ by means of inelastic neutron scattering at low temperatures. Generally LA frequencies increase near the zone edge at lower temperatures while LO phonons become softer. Of great interest is of course the temperature dependence of the dispersionless gap mode, observed at 300 K at 4.5 THz (18 meV) (see fig. 23). With decreasing temperature it disappears and is not discernable below 100 K. On the other hand, at low temperatures (1.8 K) two dispersionless magnetic excitations at about 36 meV and 14 meV have been found corresponding to spin-flip excitations. The mode at 36 meV, and here we recall that this energy is far above the hybridization energy of about 10 meV, is proposed to be a intermultiplet transition $^7F_0 \rightarrow {}^7F_1$ within the $4f^6$ configuration of Sm^{2+}. The 14 meV peak is only present at the lowest temperatures and its intensity drops rapidly between about 20 and 40 K. Since its energy is appreciably larger than the gap or the width of the IDS (6 meV) it is proposed by Kikoin and Mishchenko (1990) that this wave function can be described as an excitonic bound state combining the 4f hole obital at site i and the 6 5d orbitals of the neighboring Sm sites. On the other hand we think that this still rather high energy excitation can just as well be a crystal-field excitation in the $4f^5\ Sm^{3+}\ {}^6H_{5/2}$ configuration with the same reasoning as the 36 meV mode.

4.1.2.2. *Elastic properties.* The elastic properties of intermediate-valent compounds have been treated generally by Jayaraman (1979), especially concerning valence changes under pressure. For SmB_6, however, the first measurements on elastic properties come from King et al. (1981), where the bulk modulus and its derivative has been measured by observing the lattice constant under pressure at ambient temperature. In a cubic material like SmB_6 the bulk modulus is related to the elastic moduli c_{ij} by $B = (c_{11} + 2c_{12})/3$ and the compressibility $\kappa = 1/B$ is the inverse of the bulk modulus. The bulk modulus, extrapolated to zero pressure, $B_0 = 191$ GPa for $La^{3+}B_6$, 190 GPa for $Gd^{3+}B_6$, 157 GPa for $Eu^{2+}B_6$ and 139 GPa for $Sm^{2.6+}B_6$. The derivative of the bulk modulus, B_0' is largest for SmB_6. A soft bulk modulus or large compressibility is a typical feature of an intermediate-valent compound and the reason for it is that the ionic radius for these materials cannot be considered as a "hard sphere" under pressure as for integral valent materials, but pressure will change the degree of intermediate valence and thus change the f occupation which

in turn is related to the ionic radius. King et al. (1981) could not drive the material with a maximum pressure of 6 GPa to complete trivalency, while Moshchalkov et al. (1985) (fig. 20) showed with resistivity measurements that at least 7 GPa would be necessary.

Table 2
Elastic constants (in GPa) of LaB_6, CeB_6 and SmB_6

Compound	c_{11}	c_{12}	c_{44}	B_0	Reference
LaB_6	450	20	90	160	Tanaka et al. (1977)
CeB_6	410	−90	80	70	Kasuya et al. (1983)
SmB_6	410	−70	80	80	Kasuya et al. (1983)

The measurement of ultrasonic velocities in different crystal directions permits the evaluation of the elastic moduli c_{11}, c_{12} and c_{44}. They are collected in table 2 for LaB_6, CeB_6 and SmB_6 by Kasuya et al. (1983). In fact, the B_0 values in this table have been computed with the above formula from the elastic moduli and they agree poorly (SmB_6 $B_0 = 80$ GPa) even considering the error limits, with the values of King et al. (1981) (SmB_6 $B_0 = 139$ GPa). The negative c_{12} values for CeB_6 and SmB_6 are remarkable. Whereas CeB_6 is considered a metallic Kondo system (Luttinger theorem!) and generally not thought to be intermediate valent, a negative c_{12} is typical for intermediate-valent systems, first observed in TmSe by Boppart et al. (1980a, 1981). It means that when one applies a uniaxial pressure in one direction [100], the crystal contracts in this direction, however, also in the directions perpendicular to this, [010] and [001], trying in first approximation to stay symmetric (cubic) and changing valence under pressure (Boppart et al. 1980a, 1981). The sound velocities measured in the three prominent directions of SmB_6 are all smaller than in the reference compounds and thus exactly predict a lowering of the acoustic phonon branches of SmB_6 compared with LaB_6 as observed later by Alekseev et al. (1989) with inelastic neutron scattering. The temperature dependence of c_{11} of SmB_6 has also been measured by Kasuya et al. (1983) and below 200 K it resembles the thermal expansion curve to be discussed below.

For SmB_6 the temperature dependence of the lattice constant has been measured by X-ray diffraction by Tarascon et al. (1980b) and Alekseev et al. (1988). The lattice constant does not show the usual decrease with decreasing temperature but exhibits a minimum near 150 K. By measuring various mixed borides such as $La_{1-x}Eu_xB_6$ or $Gd_{1-x}Yb_xB_6$ containing di- and trivalent lanthanides a pattern of lattice constant versus valence could be established and be compared with a hypothetical compound of $Sm^{2+}_x Sm^{3+}_{1-x} B_6$, assuming intermediate-valent SmB_6 to be an alloy of di- and trivalent Sm ions. As argued above for temperatures above about 50 K this is not wrong. It has been inferred that between 300 and 4 K the average Sm valence changes from 2.6 to 2.53 or by about 3%, not a very strong contrast to Cohen et al. (1970).

We have measured the thermal contraction of a SmB_6 single crystal as function of temperature by using a capacitance dilatometer, having a sensitivity of 10^{-8} and an accuracy of $\pm 2\%$ (Wachter 1987). The curve is shown in fig. 24. It exhibits a typical

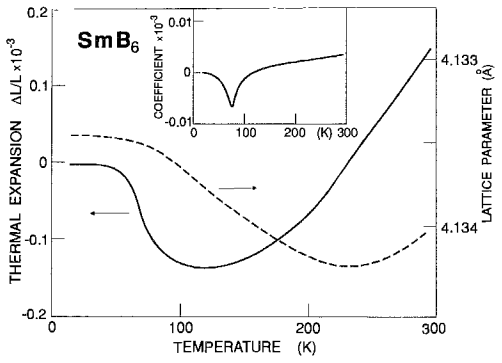

Fig. 24. Thermal expansion of SmB_6. The inset shows the expansion coefficient in units of K^{-1}. (After Wachter 1987.)

linear part above 250 K, a minimum at about 120 K, and, unusually, an increase with further decreasing temperature and a saturation below 50 K. The inset of fig. 24 shows the temperature dependence of the thermal expansion coefficient (differential of the measured curve) in units of K^{-1}. A negative expansion coefficient is not unique for intermediate valence compounds with the Fermi level in the hybridization gap, but it is also reported for YbCuAl, an intermediate-valent and heavy-fermion metal, by Pott et al. (1981). However, our measurements on $CePd_3$ reveal nothing anomalous compared with a normal metal.

In fig. 24 we show also the lattice constant of SmB_6 obtained by integrating the measured thermal expansion (right-hand scale). By its greater precision, a differential measurement is much more powerful than the direct measurement lattice constant versus temperature. We do not obtain quite the same curve as Tarascon et al. (1980b) or Alekseev et al. (1988), especially the total change of lattice parameter is less than reported, so we calculate between 300 and 4 K only a valence change from 2.6 to 2.58 or about 1%.

The precise measurement of the thermal contraction is a necessary condition in order to obtain any theoretical understanding. As mentioned above the degree of valence mixing goes towards more divalency upon cooling. But what is driving the valence change with no change in crystal structure or magnetic ordering. We propose that this valence change is driven electronically and it is inherently connected with the two-peak density of states shown in fig. 2d. Two limiting conditions have to be discussed: at high temperatures the Fermi distribution is much wider than the DOS structure; then many 4f electrons are excited from the narrow 4f peak into the 5d band acquiring a $4f^5 5d$ state with its small $4f^5$ Sm^{3+} core diameter. At low temperatures these 5d electrons are taken back into the 4f band acquiring there a $4f^{5.6}$ valency with a more expanded Sm radius and thus more divalent character.

Negative expansion coefficients are not unique to intermediate-valent compounds. In fact they have also been observed for some heavy-fermion compounds, such as UPt_3 by de Visser et al. (1987a) and $CeAl_3$ by Andres et al. (1975). It is noteworthy that the only theory trying to give an explanation for this effect (Lacroix 1987) shows that a necessary condition for the appearance of a negative expansion coefficient is a two-peak DOS structure. In fact it has been shown experimentally that for heavy fermions

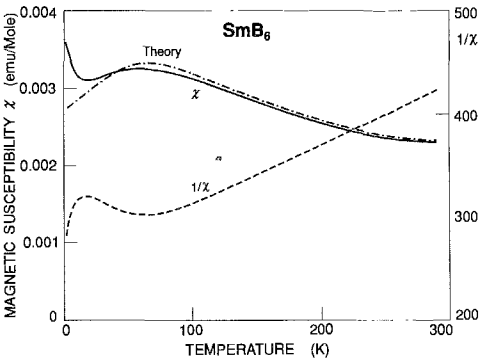

Fig. 25. The magnetic susceptibility and inverse susceptibility of SmB_6 at 10 kOe. The fit is a theory described in the text. (After Wachter 1987.)

also such a two-peak DOS exists, with the Fermi level, however, being located in one of the DOS peaks (Marabelli et al. 1986a, 1987, 1988).

For YbB_{12} the thermal contraction and the variation of lattice constant with temperature has also been measured by Kasaya et al. (1985). Again, a negative expansion coefficient has been found at low temperatures, similar to SmB_6.

4.1.3. *Magnetic measurements*

Magnetic susceptibility measurements were among the first measurements which gave a hint to the fact that intermediate-valent materials are something special inasmuch as, atypical for lanthanide compounds, there is no magnetic order, but for large enough temperatures a Curie–Weiss law is obtained (Menth et al. 1969, Nickerson et al. 1971). All intermediate-valent compounds with the Fermi level in the gap have the same general pattern in their susceptibility (with the exception of TmSe which shows magnetic order), namely a flat maximum between 100 and 10 K.

The interpretation of the susceptibility is the most tricky problem of intermediate valence because now we have to consider the various electronic configurations together with the spin. In the past there have been some ad hoc theories of susceptibility (e.g., Sales and Wohlleben 1975) but until today there is no theory of susceptibility of intermediate valence materials taking into account the experimental fact of a gap in the DOS.

Over the course of time the susceptibility of SmB_6 has been measured by various groups of authors (Nickerson et al. 1971, Tarascon et al. 1980a, Pena et al. 1981) and general agreement is observed, with the exception of the magnitude of a susceptibility increase below about 10 K, which is generally attributed to a contamination with integer valent Sm^{3+} ions. In fig. 25 we show our own susceptibility data on our best SmB_6 samples, measured in a field of 10 kOe. Also shown in fig. 25 is the inverse of the susceptibility, which is indeed a straight line above about 100 K.

A first analysis of the susceptibility has been given on the basis that the susceptibility is the sum of the various Sm^{2+} and Sm^{3+} susceptibilities, given by their relative concentration according to the degree of valence mixing, i.e., the compound is assumed

to be an alloy instead of a hybridized material (Nickerson et al. 1971). The problem that the degree of valence mixing is changing with temperature (see fig. 24) is disregarded.

Following Nickerson et al. (1971) the Sm^{2+} $4f^6$ configuration is given by the ground state $^7F_0$ of $L=S=3$ and the temperature dependence of its susceptibility is given by the standard van Vleck term with the energy difference between the $J=0$ and $J=1$ state of 415 K and the one between the $J=1$ and $J=2$ state of 748 K.

For the Sm^{3+} $4f^5 5d^1$ we have to consider that the 5d electrons are in a wide $5d_{eg}$ band (see fig. 2d) in which, generally, the orbital momentum is quenched, leaving us with s electrons. These will couple to the $4f^5$ core state in a parallel or antiparallel fashion, the ground state, according to Hund's rule will be the parallel configuration with $L=5$, $S=3$ and $J=L-S=2$. This parallel configuration has further J levels, the next $J=3$ being separated from $J=2$ by 1440 K (Nickerson et al. 1971). The first excited level will be the antiparallel alignment with $L=5$, $S=2$ and $J=3$, with the next $J=4$ level too far away to be thermally populated. Again the temperature dependence of the susceptibility is given by the van Vleck term. It follows from our energy level diagram of fig. 2d that the $4f^6$ $^7F_0$ state and the $4f^5 5d^1$ parallel $^7H_2$ state are at the same energy near the top of the bands and that the hybridization gap is separating the antiparallel $^5H_3$ configuration. With increasing temperature, electrons are excited from the ground state configurations of the ions with parallel configurations, into those with antiparallel configurations leaving holes behind, the relative concentrations of which are weighted by Boltzmann factors.

At zero temperature the relative concentration of the $4f^6$ and $4f^5 5d^1$ configurations are given by experiment and we find 0.28 and 0.72, respectively. The best fit to the experimental data (see fig. 25) is obtained with an activation energy of 70 K = 6 meV. This value is not the gap value itself (about 4 meV) but it rather corresponds to the separation of the two DOS peaks, which is 6 meV (Travaglini and Wachter 1984a). The increase of the susceptibility below about 20 K can be accounted for by only 1% of bare Sm^{3+} $4f^5$ state ions.

For YbB_{12} the susceptibility was first measured by Kasaya et al. (1983a). A maximum at about 70 K is observed and a strong increase below about 20 K can be attributed again to bare Yb $4f^{13}$ states as defects. In fig. 26 we show our own measurements where the defect part is much smaller. Also shown is the reciprocal of the susceptibility and a Curie–Weiss law is observed above about 140 K.

One of the important questions arising from fig. 26 is whether the susceptibility extrapolates towards zero for $T \to 0$, i.e., whether the increase of the susceptibility below about 10 K is really only defect dominated. For this purpose the Knight shift of the quadrupole ^{11}B splitting in NMR is observed by Elschner and Weissenberger (1987) which depends on defects only via their relative concentration, i.e., about 1%. The Knight shift on the other hand is proportional to the susceptibility. The measuring frequency was 45.90 MHz and the field strength for resonance at 4 K corresponds exactly to the tabulated values for a ^{11}B resonance without shift.

It is now clear from fig. 26 that the susceptibility is zero for $T \to 0$ in the absence of defects (we disagree here with Kasaya et al. 1985). This can only be caused by a nonmagnetic ground state such as Yb^{2+} $4f^{14}$. This, however, is in contradiction with the

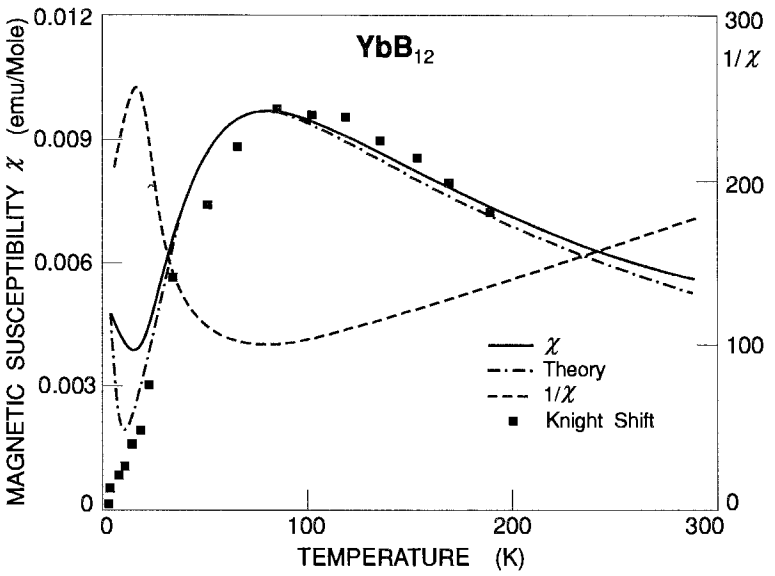

Fig. 26. The magnetic susceptibility, inverse susceptibility and Knight shift of YbB_{12}. The fit is a theory described in the text. (After Wachter 1987.)

valence determination from lattice constant, L edge (Kasaya et al. 1983b) and Mössbauer effect (Bonville et al. 1978) which state nearly trivalency. In the intermediate-valence field the valency and the radius of the ion is determined by the 4f occupation. Thus there is one way out, which is a valence mixing with mostly a configuration $4f^{13}5d^1$ and a few $4f^{14}$ states. The $4f^{13}5d^1$ states must have the same quantum numbers as the $4f^{14}$ states which is possible with parallel alignment of the 5d electron to the core spin and keeping also m_l unchanged. We can thus have $^2S_0$ quantum numbers which we take as the ground state. The excited state is then a $4f^{13}5d^1$ antiparallel alignment which is separated by a gap. The excited 5d band electron in YbB_{12} is in a 5d band, but we can nevertheless assume that here also the orbital momentum is quenched, thus we have $S=1$, $l=0$, $L=3$ (from the core) and $J=4$, or a $^3F_4$ state. When J of ground and excited state is larger than 1 they do not mix and van Vleck terms become unimportant. Now the computation of the susceptibility is straightforward as a Curie term of the excited state where we use Boltzmann factors to determine the relative populations of ground and excited states. The fit with this theory is shown in fig. 26 using a gap of 75 K = 6.5 meV, which is practically the same as those obtained by other methods (see above). The defect part can be completely accounted for by 7.7×10^{-3} of bare $4f^{13}$ states.

In spite of the fact that the fits in figs. 25 and 26 are very good, it leaves one rather unsatisfied because the degree of valence mixing for SmB_6 (0.3 and 0.7) is not what the more recent numbers yield (0.4 and 0.6). However, the model used for the computation of the susceptibility corresponds in a simple way to the alloy analog of the Anderson lattice model, which has been shown to give good results, e.g. by

Martin and Allen (1979). Nevertheless, it is, up to now, the only quantitative model including a gap which starts from atomic numbers (Wachter 1987). Czycholl (1982) has also calculated the dynamic magnetic response of intermediate-valent SmB_6 including a hybridization gap. He obtained pronounced structures in the frequency dependence of the spin–spin correlation function, which can be understood by means of activation over the hybridization gap and should be observable in neutron scattering.

4.2. *The samarium monochalcogenides*

4.2.1. *The semiconducting state*

4.2.1.1. *Electronic properties.* The Sm monochalcogenides have in their semiconducting state a much smaller energy gap $4f^6$–$5dt_{2g}$ than corresponding Eu or Yb chalcogenides. So in order to understand the semiconductor–intermediate-valent metal transition under pressure, it is important to understand the electronic structure of the semiconducting phase. In the following we want to put in direct comparison EuS and SmS, which have practically the same lattice constant in the fcc structure, i.e., 5.96 Å and 5.97 Å, respectively. We assume mainly ionic bonding between cations and anions and ask for transfer energies of an electron from the $3p^6$ level of sulfur into the 5d or 6s level of the cation (charge transfer) or from the 4f into the 5d level of the cation (intra-atomic excitation). The details of the method have been described by Wachter (1979) and references cited therein. For the charge transfer transition we plot the affinity for the second electron of sulfur 6.48 eV (Greenwood 1968) and the second ionization energy of Eu 11.25 eV or Sm 11.07 eV, (Morss 1971) relative to the reference level $3p^5$ or $4f^n$ + a free electron (fig. 27). These energies are relevant for charge transfers into the 6s level, however, the energy difference 5d–6s can also be deduced from spectroscopic tables, and it is about 1 eV. The intra-atomic transition involves the third ionization energies of Eu (25.13 eV) and Sm (23.68 eV), (Morss 1971). These energies are plotted at the left-hand side of fig. 27. Taking into account the Madelung energy (16.8 eV) for both EuS and SmS we have to shift the energy levels by that amount. The polarization energies for holes and electrons have different signs and they are different in size if holes are in a cation or anion level. To estimate the contribution of the polarization energy we assume that charges are trapped in a spherical cavity with the radius of the respective ion (Wachter 1979). The central part of fig. 27 shows the influence of lattice and polarization energies. In the right-hand part of the figure the crystal-field splitting of the 5d states in t_{2g} and e_g levels is indicated. Essentially, the model corresponds to the Γ point of the Brillouin zone, therefore, the dispersion of valence or conduction bands is not shown.

It is obvious from the figure that all band states, 5d, 6s and $3p^6$ practically coincide for both materials. The important difference between EuS and SmS is the value of the intra-atomic transition $4f^n$–5d, 6s which is considerably smaller for SmS. This is due to the 1.45 eV difference in the third ionization energy between EuS and SmS. This ionization energy is exceptionally large for the half filled $4f^7$ configuration of Eu or the $4f^{14}$ configuration of Yb and much less for the $4f^6$ configuration of Sm or $4f^{13}$ of Tm.

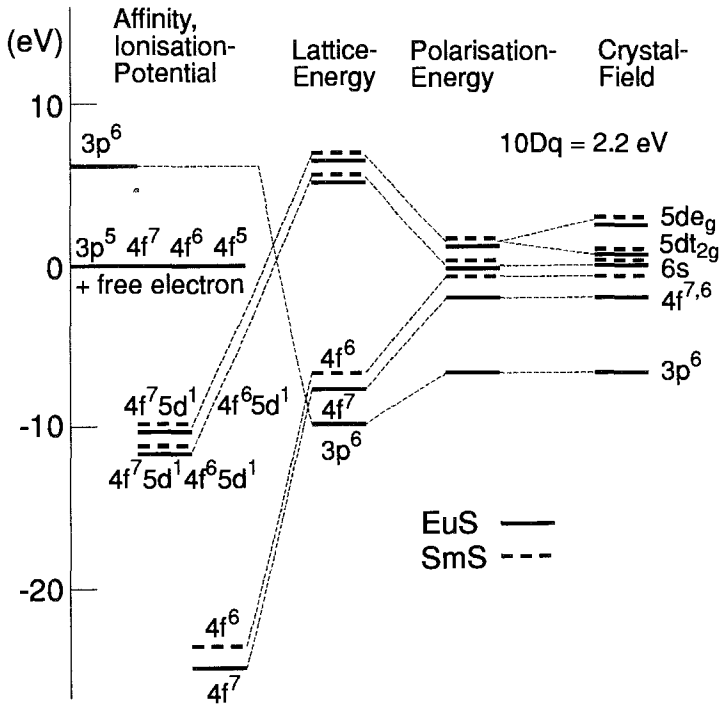

Fig. 27. Energy level diagram of EuS and semiconducting SmS. (After Kaldis and Wachter 1972.)

The Sm monochalcogenides offer the unique feature to follow, as function of pressure, the transition from semiconductor to the intermediate-valent state. Thus it is of great importance to first characterize the semiconducting state. The first measurements to be discussed are resistivity versus temperature data and the first such measurements at temperatures above 400 K have been made by Zhuze et al. (1964) and Golubkov et al. (1966). The activation energy for SmS is about 0.15 eV. Below room temperature the activation energy for various samples and various research groups is always about 60 meV when using an Arrhenius plot with $\exp -\Delta E/2k_BT$ (Jayaraman et al. 1970a,b, Neufeld 1975). It thus appears that the intrinsic gap for SmS is 0.15 eV and an extrinsic gap of 60 meV exists, probably caused by sulfur vacancies. for SmSe the gap determined from the same type of measurement yields 0.45 eV and for SmTe 0.65 eV.

Other means to determine the energy gap of the Sm chalcogenides in the semiconducting state are optical experiments. The first transmission measurements on SmS thin films have been reported by Holtzberg and Torrance (1971) in the photon energy range between 0.6 and 3 eV. The measurements have been supplemented by transmission on thin single crystals of SmS by Kaldis and Wachter (1972) in the spectral range between 30 meV and 0.4 eV. Two aspects must be considered in optical experiments. The ground state of Sm^{2+} is $^7F_0$ and excited states up to $^7F_6$ exist where $^7F_1$ (35 meV) and $^7F_2$ (0.1 eV) fall within the energy gap of 0.15 eV. At room temperature these states are

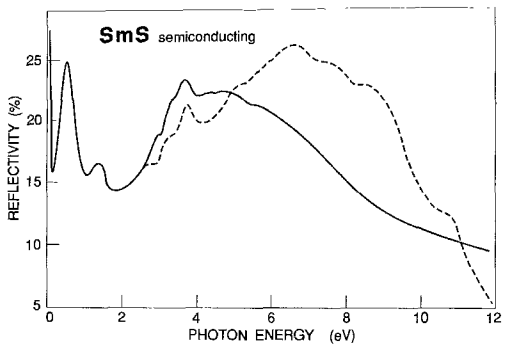

Fig. 28. Reflectivity of semiconducting SmS. The solid curve is after Batlogg et al. (1976b), the dashed curve after Güntherodt et al. (1983).

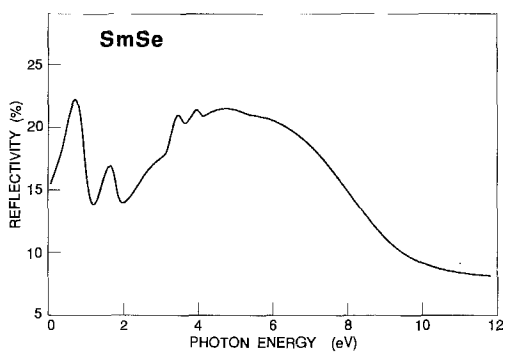

Fig. 29. Reflectivity of SmSe. (After Batlogg et al. 1976b.)

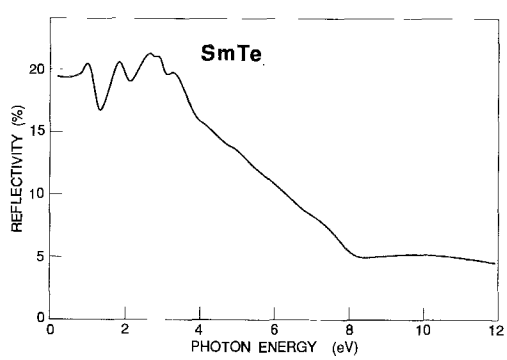

Fig. 30. Reflectivity of SmTe. (After Batlogg et al. 1976b.)

occupied to about 42% and 8%, respectively. Thus optical transitions at room temperature can have as initial state the $^7F_0$, $^7F_1$ and $^7F_2$ states where the latter then has only an energy difference of less than 0.06 eV towards the 5d conduction band. In addition there may be the impurity states at 60 meV below the conduction band mentioned above. It is then no surprise that the optical absorption edge at room temperature is less than the actual gap value (Kaldis and Wachter 1972). When the photon energy is larger than the minimum energy required to transfer an electron into the conduction band, the final state $4f^{n-1}$

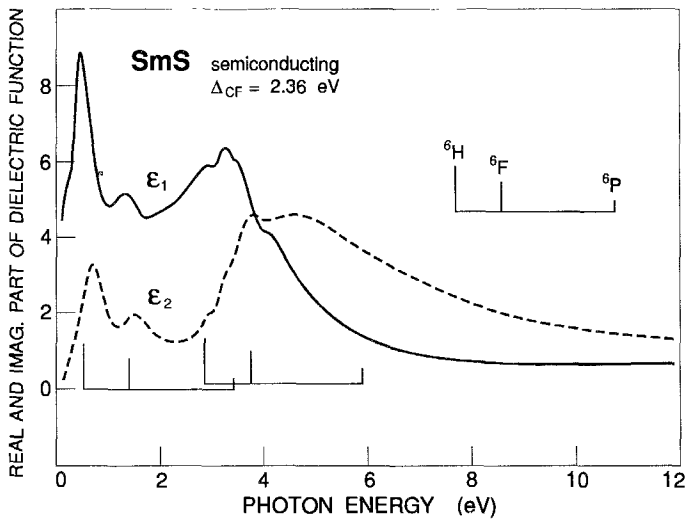

Fig. 31. Real and imaginary parts of the dielectric function of semiconducting SmS. The final state multiplets and the crystal-field splitting Δ_{CF} are indicated. (After Batlogg et al. 1976b.)

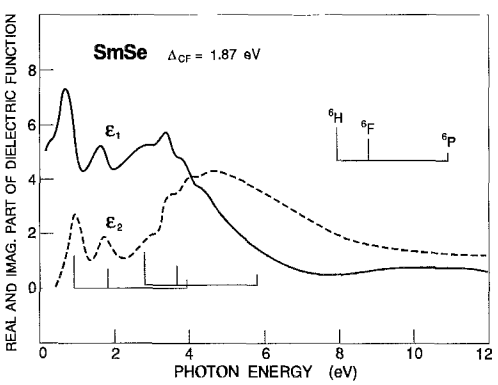

Fig. 32. Real and imaginary parts of the dielectric function of SmSe. The final state multiplets and the crystal-field splitting Δ_{CF} are indicated. (After Batlogg et al. 1976b.)

multiplets ^6H_J, ^6F_J and ^6P_J can be excited also, leading to the characteristic ladder-like structure described in section 3 and observed by Holtzberg and Torrance (1971) and Batlogg et al. (1974) in transmission on thin films of SmS and by Kirk et al. (1972), Batlogg et al. (1976b) and Güntherodt et al. (1983) in reflectivity on single crystals.

In figs. 28–30 we show the reflectivity spectrum of SmS, SmSe and SmTe in the range 30 meV to 12 eV obtained by Batlogg et al. (1976b) which in the case of SmS is completed by measurements of Güntherodt et al. (1983) who used cleaved single crystals instead of the polished ones of Batlogg et al. (1976b). A Kramers–Kronig analysis yields the dielectric constants, and the characteristic ladder-like structure of the final state $4f^5$ multiplets is shown in figs. 31–33. The ladder structure appears twice because through

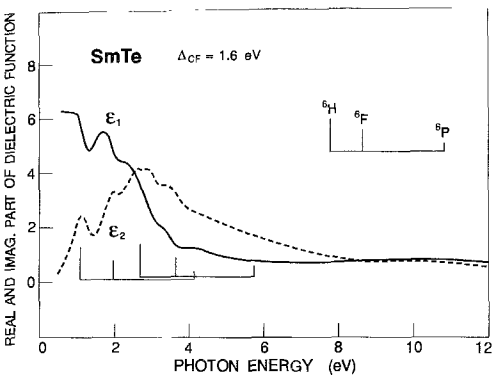

Fig. 33. Real and imaginary parts of the dielectric function of SmTe. The final state multiplets and the crystal-field splitting Δ_{CF} are indicated. (After Batlogg et al. 1976b.)

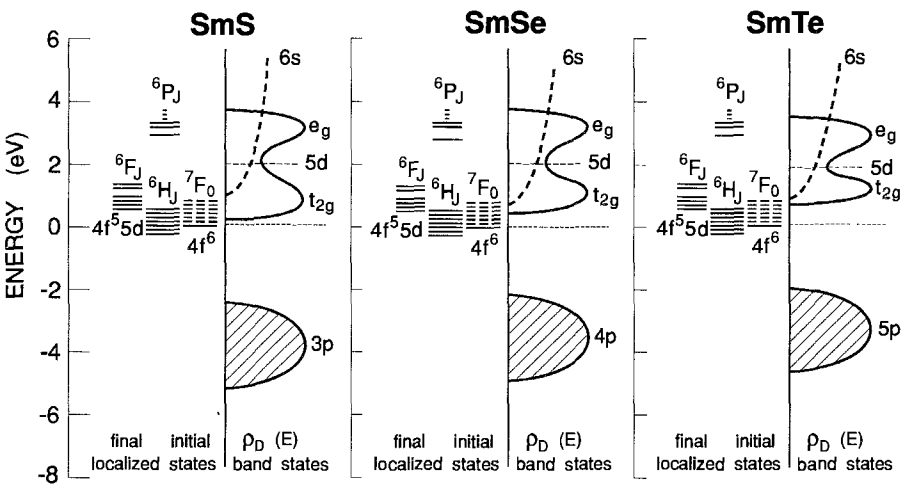

Fig. 34. Energy level diagram of SmS, SmSe and SmTe. Initial and final localized states are shown to the left, and the band density of states to the right. The figures are normalized to the $4f^6$ initial state. (After Batlogg et al. 1976b.)

excitations into the crystal field, split t_{2g} and e_g 5d conduction bands are possible, from where also the value 10 Dq can be obtained. In fig. 34 we show the electronic structure of the Sm chalcogenides plotted relatively to the $4f^6$ level. Localized initial and final states are plotted to the left-hand side, band states to the right-hand side of the figure. Kurita et al. (1984) have further identified the band edge excitons belonging to the p–d transition and typical for the non 4f reference materials.

In addition we have measured the photosensitivity of the Sm chalcogenides using intermittent and monochromatic illumination (Neufeld 1975). In fig. 35 we show as an example for SmSe the photosensitivity at various temperatures and in comparison with the

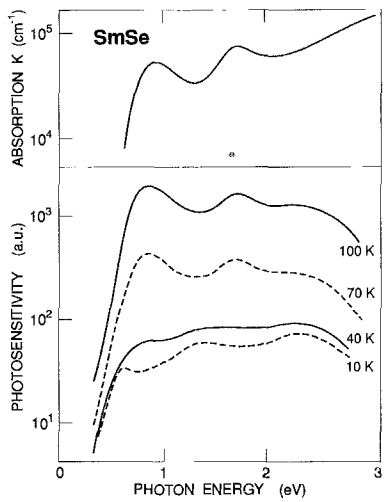

Fig. 35. Absorption coefficient K and photosensitivity of SmSe. (After Neufeld 1975.)

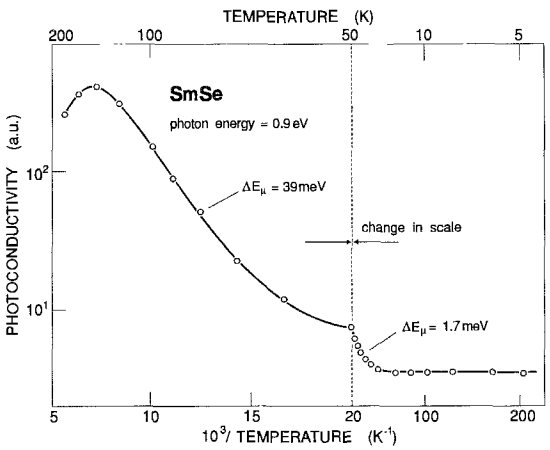

Fig. 36. Photoconductivity of SmSe vs. $1/T$. The mobility gaps ΔE_μ are indicated. (After Neufeld 1975.)

absorption coefficient (measurements on SmTe are completely equivalent). The maximum of the photosensitivity is at about 0.9 eV, close to the lowest energy absorption peak. For lower photon energies and at 20 K the photosensitivity reaches half maximum value at about 0.45 eV, which determines the mobility gap ΔE_μ according to Moss (1952), but agrees precisely with the optical gap. This coincidence is not fortuitous but it is also established for the Eu chalcogenides (Wachter 1979) and it ensures that the optical transition $4f^6 \rightarrow 4f^5(^6H_J)5dt_{2g}$ goes into a conduction band and not into an excitonic state. This especially devaluates the conclusions reached by Mahanti et al. (1976) who assumed that the excited state of the Sm chalcogenides is an excitonic state. In fig. 36 we show the photosensitivity in function of temperature when excited at 0.9 eV. An activated photosensitivity is observed below about 120 K with an activation energy of 39 meV. The

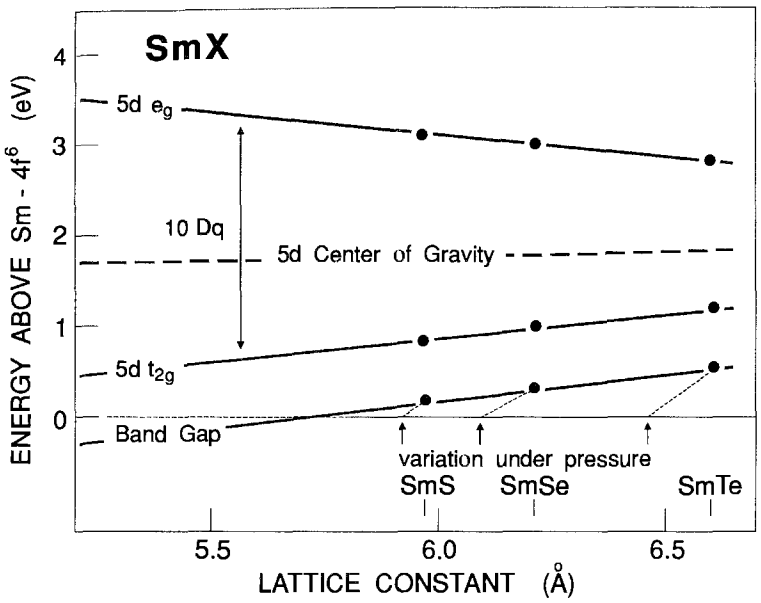

Fig. 37. Comparison of excitation energies between the Sm monochalcogenides, plotted vs. the lattice constant. (After Batlogg et al. 1976b.)

photosensitivity (i.e., photoconductivity per unit light intensity) is proportional to the quantum yield × the mobility × the life time of the carriers. The quantum yield can be taken as constant in this experiment since the 0.9 eV photon energy is always equally absorbed at all temperatures (Wachter 1979). Also the life time of the carriers can be taken as temperature independent below about 150 K in analogy with the Eu chalcogenides (Wachter 1979). The activated photosensitivity then means a hopping type of mobility. The reason is similar as in the Eu chalcogenides: the Sm chalcogenides are strongly ionic compounds, thus the excited electrons polarize the lattice ions and in fact become small polarons.

In fig. 37 we show the energy level scheme of the Sm chalcogenides. Plotted are the experimentally determined optical transition energies $4f^6$–$4f^5(^6H_J)5dt_{2g}$ and $4f^6$–$4f^5(^6H_J)5de_g$ and the band gap, taken either from optical transmission of single crystals or from thermal activation energies of the resistivity, in function of the lattice constant. The zero of the energy scale is the $4f^6$ ground state of Sm^{2+}. It is a remarkable fact that the energy separation $4f^6$–5d center of gravity remains practically constant as is to be expected in an atomic like model (Kaldis and Wachter 1972). This is, however, quite in contrast to band structure calculations of Davis (1971).

Due to the small gap of SmS there is at room temperature and even down to the lowest temperatures, an appreciable free carrier concentration in the conduction band. Thus for optical experiments in the far infrared and for energies less than the phonon frequencies the plasma free carrier absorption dominates the spectrum

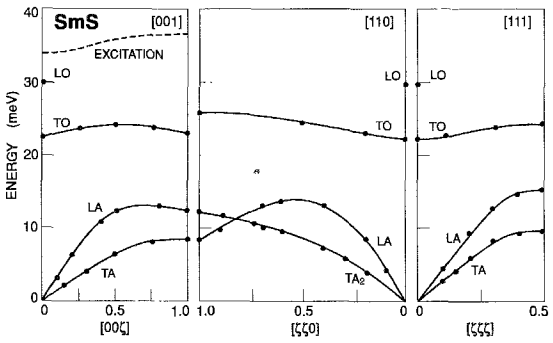

Fig. 38. Phonon dispersion relation of semiconducting SmS at 300 K. The abscissa is in fcc reciprocal lattice units $2\pi/a_0$. (After Birgeneau and Shapiro 1977.)

and a suitable decoupling procedure of interband, phonon and plasmon modes has to be performed. Thus Hillebrands and Güntherodt (1983) find for the static dielectric constant $\varepsilon_{stat} = 30$, whereas Zelezny et al. (1989) compute a value of $\varepsilon_{stat} = 18$. The dielectric constants are larger compared with EuS ($\varepsilon_{stat} = 12$) due to the reduced 4f–5d gap. The latter group observes also a Hall mobility around 50 $cm^2/V s$ above about 150 K with a precipitous drop of the Hall mobility below about 120 K. Their interpretation was that the mobility at this temperature changes over from a $T^{-3/2}$ law to a $T^{+3/2}$ law. Our photoconductivity measurements, however, show that the mobility follows an Arrhenius law below about 120 K which implies polaronic hopping. Zelezny et al. (1989) also compute an effective mass of the carriers and find $m^* = 0.2m$ from which they conclude that the 6s band is lower than the bottom of the $5dt_{2g}$ band. However, this can be ruled out unambiguously. The lowest energy optical absorption from the 4f state goes into a $5dt_{2g}$ band and not a 6s band as demanded by optical selection rules. A thermal excitation from a 4f state will go into the lowest available conduction band, possibly a 6s band since the selection rules do not apply. The shift of the absorption edge under pressure, and this concerns only the 5d band, because of the selection rules, is −10 meV/kbar (Batlogg et al. 1974, 1976b). The shift of the thermally determined energy gap is also −10 meV/kbar (Jayaraman 1979), thus the thermal excitation also ends up in the 5d band, which must then be the lowest band.

4.2.1.2. *Lattice-related properties.* The phononic properties of semiconducting SmS have been investigated by inelastic neutron scattering, Raman effect and far infrared reflectivity. In fig. 38 we show the phonon dispersion as obtained by Birgeneau and Shapiro (1977). The results compare well with those obtained on EuS. The longitudinal optical branch LO could not be measured due to intensity problems. However, a Kramers–Kronig analysis of far infrared data of Hillebrands and Güntherodt (1983) and Zelezny et al. (1989) yield the TO(Γ) energy of 25 meV and 22 meV, respectively, in good agreement with the neutron data at 22.5 meV, but also in addition the LO(Γ) energy of 30 meV. Both values are again in good agreement with similar measurements of Axe (1969) on EuS (TO 22 meV and LO 33 meV) and we have indicated the LO(Γ) in fig. 38. It is remarkable that these measurements do not indicate any precursive effects

of the incipient pressure driven intermediate-valent transition. In fig. 38 there is also indicated the dispersion of the first magnetic exciton $^7F_0 \rightarrow {}^7F_1$, which at the Γ point shows an appreciable softening with decreasing temperature as measured already by Nathan et al. (1975) using the Raman effect. The softening is due to the exchange term $J_{ij}\boldsymbol{S}_i \cdot \boldsymbol{S}_j$ which couples the $^7F_0 \rightarrow {}^7F_1$ ionic excitations on sites i and j. Thus the single ion transition becomes a propagating excitation in the crystal which depends on k and T (Birgeneau and Shapiro 1977).

The bulk modulus of semiconducting SmS has been measured by Penney et al. (1975) and later by Hailing et al. (1984). Using the latter, more recent, data a value of the bulk modulus B_0 of 50 GPa has been found which compares well with the one of EuS (55±5 GPa) by Wachter (1979). The bulk modulus of SmS even increases with an applied pressure of 0.3 GPa (typical for any non IV material). The elastic constants of semiconducting SmS are $c_{11} = 127$ GPa, $c_{12} = 12$ GPa and $c_{44} = 27$ GPa to be compared with those of EuS, $c_{11} = 131$ GPa, $c_{12} = 11$ GPa and $c_{44} = 27$ GPa. Again no precursory softening in SmS compared with EuS at normal pressure, however, such a softening is observed at 0.6 GPa (6.0 kbar) shortly before the first-order valence transition takes place (Hailing et al. 1984). However, even then c_{12} does not become negative as for certain, still semiconducting $TmSe_{1-x}Te_x$ alloys (Boppart et al. 1982).

Bilz et al. (1979) have tried to explain the valence transition, but notably also the semiconducting state of SmS, assuming strong precursory effects. They proposed especially a strong reduction of the energy difference LO(Γ)–TO(Γ) in semiconducting SmS compared with EuS which, however, cannot be substantiated when comparing experimental results. The main reason for this reduction would be an increased dipolar (Γ_{15}) and an increased electronic deformability $(\Gamma_1)^+$ arising from virtual 4f–5d excitations of the Sm ions. The breathing self energy is supposed to reduce the bulk modulus of SmS by about 15% as compared with that of EuS, but as we have seen above, the elastic constants c_{ij}, which are the primary result of ultrasonic measurements, are exactly the same as in EuS. Bulk moduli are then calculated from the elastic constants using $B_0 = (c_{11} + 2c_{12})/3$. However, the proposals of Bilz et al. (1979) are so obviously right that one must search the correct experiments which support this theory. In the case of SmS, they can be found shortly before the valence transition (0.6 GPa or 6 kbar) and in some $TmSe_{1-x}Te_x$ alloys at normal pressure. It must then be concluded that the virtual 4f–5d excitations become significant only when the f–d gap is less than about 0.1 eV or when the f–d hybridization is strong enough (c.g. in TmSe and its alloys).

To complete the section on lattice-related properties we report on measurements of the thermal conductivity of SmS by Benbachir et al. (1985) between 1.5 and 300 K where it is shown that above 150 K, for pure SmS as well as for $SmS_{1-x}Sc_x$ alloys, the thermal conductivity obeys a $T^{-3/2}$ law, typical for phonon point defect scattering.

4.2.1.3. *Magnetic properties.* The magnetic susceptibility of the semiconducting Sm monochalcogenides has been measured by Bucher et al. (1971). Divalent Sm has a nonmagnetic ground state $^7F_0$ and thus will give rise to a van Vleck paramagnetism due to thermal population of the $^7F_1$ state. Since the crystal structure is cubic, crystal-field effects

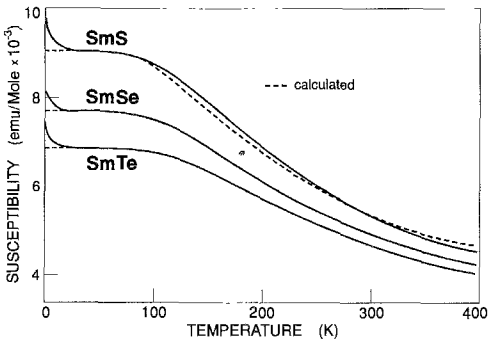

Fig. 39. Magnetic susceptibility of the semiconducting Sm monochalcogenides. Dashed lines represent the calculation according to van Vleck theory. (After Bucher et al. 1971.)

are absent in the $J=0$ and 1 states so the calculation of the susceptibility in function of temperature is quite straightforward. The influence of the exchange in molecular field theory has been assumed small by Bucher et al. (1971) and the measured curve together with a fit with the van Vleck theory is shown in fig. 39. However, we recall that in the previous section we have shown that the $^7F_0 - {}^7F_1 = E_{so}$ energy difference is temperature dependent due to the exchange effects. When one takes this into account then

$$\chi(T=0) = \frac{8N_a\mu_B}{E_{so} - 16J(k=0)}, \tag{5}$$

and the calculated susceptibility is about 7% higher than measured and shown in fig. 39, where the van Vleck susceptibility is assumed without the exchange term. In eq. (5) $J(k=0) = \sum_j J_{ij}$ with J_{ij} being the isotropic exchange coupling between the Sm^{2+} spins i and j. Birgeneau and Shapiro (1977) relate this shift to covalency effects which are not included in eq. (5).

4.2.2. *The valence transition and the IV state*

4.2.2.1. *Electronic properties.* The history of the Sm monochalcogenides as IV materials started when Jayaraman et al. (1970a,b) and Bucher et al. (1971) discovered a pressure-induced semiconductor–metal transition and suggested that the metallic state would be intermediate valent. The surprise was when SmS showed a first-order transition occurring at the incredibly low pressure of 0.65 GPa (6.5 kbar). With decreasing pressure a large hysteresis is observed and the intermediate-valent state snaps back to a semiconductor at 0.15 GPa. For SmSe and SmTe the pressure-induced valence transition is continuous and at higher transition pressures, about 4.5 GPa and 6.0 GPa, respectively. In fig. 40 we show the resistivity change of SmS, SmSe and SmTe in function of pressure after Jayaraman (1979). Figure 41 shows a similar plot for the pseudobinary solution of $SmS_{1-x}Se_x$ (Bucher and Maines 1972) combined with later measurements of Neuenschwander and Wachter (1990b). In fig. 42 we finally plot the valence transition pressure and the semiconductor gap value at zero pressure for various solutions of $SmS_{1-x}Se_x$. It is important to realize that the transition is isostructural, i.e., the NaCl

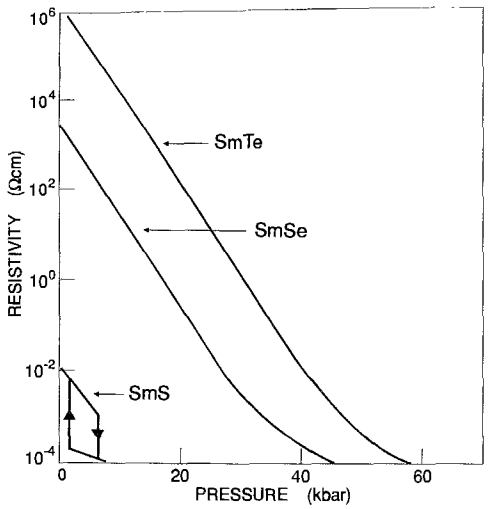

Fig. 40. Resistivity change of SmS, SmSe and SmTe vs. pressure at 300 K. Note the hysteresis of SmS. (After Jayaraman 1979.)

structure persists through the valence transition. The Eu and Yb monochalcogenides can also go through pressure-induced valence transitions, but they occur at much higher pressures and only EuO, YbS, YbSe and YbTe seem to make the valence transition isostructural between 10 and 30 GPa, whereas EuS (21 GPa), EuSe (14 GPa) and EuTe (11 GPa) under pressure, at first make a structural transition to the CsCl structure, before eventually becoming intermediate valent (Jayaraman 1979). The choice whether a material under pressure makes the valence transition or the structural transition first depends on the energy gap in the semiconducting state, i.e., the $4f^n$–5d separation. Including divalent Eu, Yb, and Sm chalcogenides and TmTe it becomes clear that for gap values below about 1.6–1.8 eV the pressure-induced transition is at first to the intermediate-valent state and for higher pressures to the CsCl structure. Only for larger gap values does the structural transition occur first.

In fig. 37 we were able to show the mechanism of the semiconductor–IV metal transition of the Sm chalcogenides. A reduction of the lattice constant results in an increase of the $5dt_{2g}$–$5de_g$ crystal-field splitting 10 Dq until the bottom of the $5dt_{2g}$ band (indicated in fig. 37 with "band gap") coincides with the $4f^6$ level. In fig. 43 we can see this increase in crystal-field splitting directly. Plotted is the optical transmission of a thin film of SmS under hydrostatic pressure. The first two absorption peaks, related to the $4f^6 \rightarrow 4f^5(^6H_J, ^6F_J)5dt_{2g}$ transitions, shift by about 10 meV/kbar towards lower energies, whereas the third absorption peak at about 3 eV, corresponding to the $4f^6 \rightarrow 4f^5(^6H_J)5de_g$ transition, shifts by about 15 meV/kbar towards higher energies. The ratio of the degeneracy of the t_{2g} and e_g states is 3 to 2, respectively, and the experimental numbers 15 to 10 meV/kbar then mean that the center of gravity of the 5d states remains unchanged with pressure (Batlogg et al. 1974).

In actual pressure experiments one does not follow the band gap line in fig. 37 until its intersection with the $4f^6$ state. This variation would only be appropriate in chemical

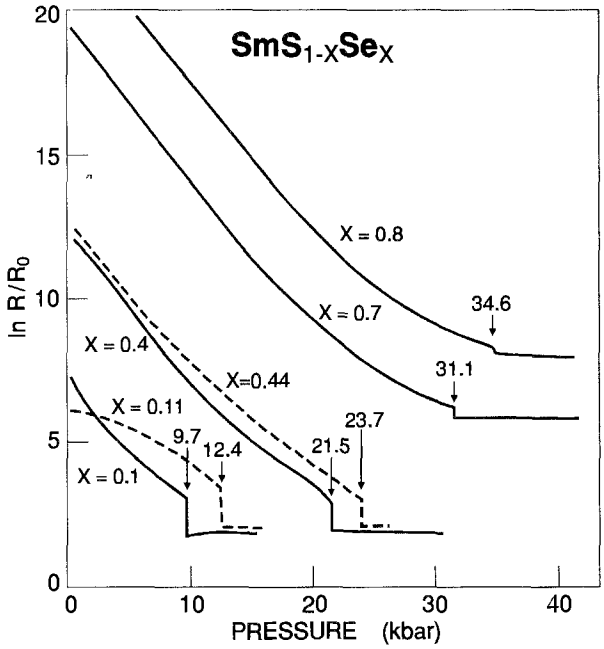

Fig. 41. Resistance ratio of $SmS_{1-x}Se_x$ vs. pressure. The first order transition pressures are noted (after Bucher and Maines 1972 and Neuenschwander and Wachter 1990b).

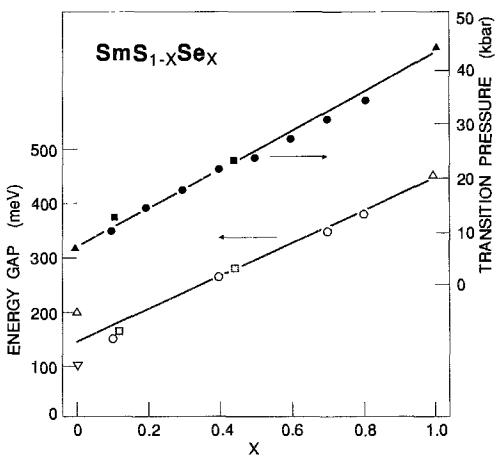

Fig. 42. Transition pressure (right-hand scale) and energy gap (left-hand scale) of $SmS_{1-x}Se_x$ with stoichiometry x: circles after Bucher and Maines (1972), up triangles from Jayaraman et al. (1970b), down triangle after Lapierre et al. (1983), squares after Neuenschwander and Wachter (1990b).

alloying experiments, e.g. $SmS_{1-x}Se_x$ (Bucher and Maines 1972, Neuenschwander and Wachter 1990b), where an exchange of the anion simultaneously changes the covalency of the compound. Instead, one observes experimentally a variation of the band gap with pressure as indicated in fig. 37 by dashed lines. These are derived by computing the

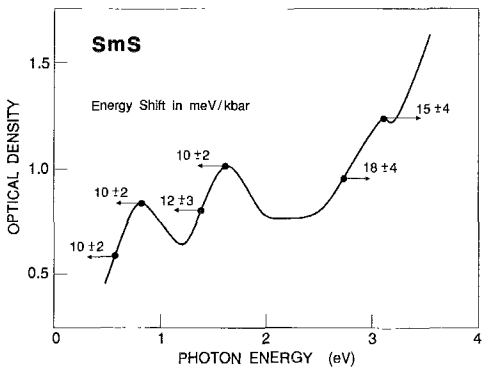

Fig. 43. Optical density from transmission on a thin film of SmS. (After Batlogg et al. 1974.)

changes of the band gap per unit lattice contraction from the pressure shift of the band gap (Batlogg et al. 1974). It is found that the slope of the dashed lines in fig. 37, the deformation potential, is constant for the Sm chalcogenides and it amounts to about 5 eV (Jayaraman 1979).

Now we may speculate on why the semiconductor–IV metal transition in SmS and some $SmS_{1-x}Se_x$ alloys is of first order and in SmSe and SmTe it is continuous. The total reduction in the lattice constant during the transition is experimentally measured (Jayaraman et al. 1970b or Neuenschwander and Wachter 1990b) or can be estimated by the reduction in ionic diameter of Sm^{2+} in going to $Sm[^{2+n}]^{+}$ assuming a hard sphere model. If the reduction of band gap with pressure per concomitant reduction in lattice constant has the same value as the deformation potential (dashed lines in fig. 37) then the transition will be smooth and continuous. This is approximately the case in SmSe and SmTe. If the misfit becomes too large, as in SmS where the closing of the band gap would only correspond to a reduction in lattice constant from 5.97 to 5.90 Å (see fig. 37) instead of the observed one from 5.97 to 5.70 Å, then the lattice adjusts discontinuously in a first-order transition accompanied by a hysteresis as in SmS and some SmS–SmSe alloys. This, of course, is a consequence of the small band gaps of these compounds to start with. Thus, as shown in fig. 41, the transition is of first order in $SmS_{1-x}Se_x$ for x up to 0.8.

In fig. 44 we show the energy level diagram of SmS in the IV state (right-hand side) and in the semiconducting state (left-hand side). The figures are normalized with respect to the 4f state at zero energy or the Fermi energy. We already discussed that the valence transition is driven by the increase in crystal-field splitting of the 5d states and at a given pressure the 5d band overlaps with the $4f^6$ state and the energy gap becomes zero. Since we have seen that there are no precursor effects in the Sm chalcogenides, which will be substantiated below, starting from the overlap of $4f^6$ and 5d states, 4f electrons will spill into the 5d band leaving a $4f^5$ state behind. The ionic radius of such a state is about 15% less than the $4f^6$ state, so that simultaneously with more electrons in the 5d conduction band the lattice will shrink, thus further increasing the crystal-field splitting of the 5d states, resulting in an avalanche effect and a first-order valence transition.

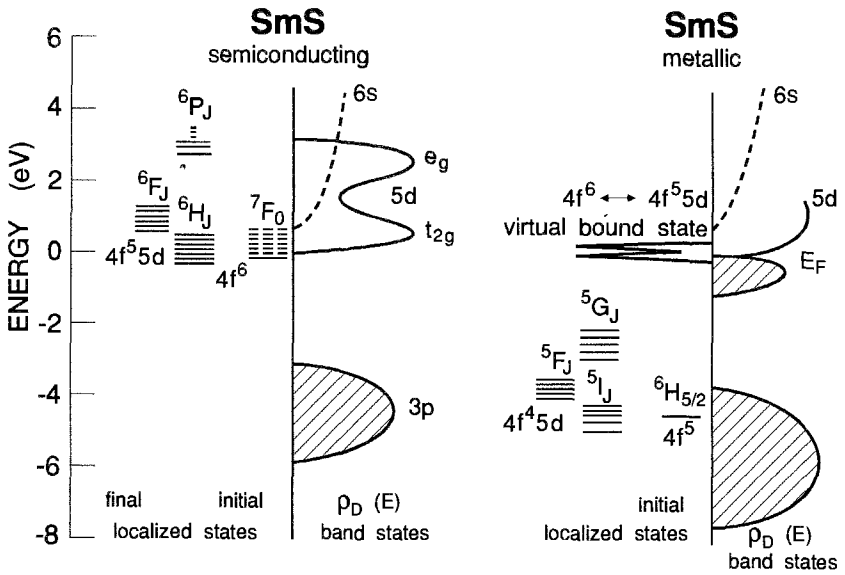

Fig. 44. Energy level scheme of (left) semiconducting and (right) intermediate-valent metallic SmS. Initial and final localized states are at left and band states at right. The figure is normalized with respect to the Fermi energy E_F. (Modified after Batlogg et al. 1976b.)

However, the lattice, now having a smaller lattice constant, becomes more incompressible so the valence transition does not go all the way towards trivalency but stops where the gain in electronic energy (the lowering of the 5d density of states below E_F in fig. 44) is compensated by an increase in lattice energy. The hybridization leads to the well known narrow $4f^6$–$4f^5 5d$ band with a hybridization gap in between and the Fermi level right in the gap as a consequence of the Luttinger theorem. The other bands are drawn to scale from optical and photoemission measurements on GdS (Batlogg et al. 1976b). The above described avalanche effect is caused by the simultaneous lattice collapse with the electronic collapse. This is the case in SmS (Jayaraman 1979) and in all other first-order transitions of $SmS_{1-x}Se_x$ (Neuenschwander and Wachter 1990b). For SmSe and SmTe it has been shown (and will be discussed below) that the electronic gap is closed before the lattice softens, as a consequence there is no avalanche effect and only a second-order transition is observed (Tsiok et al. 1991). It seems that the larger anions Se and Te stabilize the lattice even under pressure, permitting the valence transformation of the Sm ions without concomitant lattice distortion.

For collapsed SmS the determination of the degree of intermediate valence has long been disputed in literature and mostly been taken from the lattice constant of chemically collapsed SmS. However, Batlogg et al. (1976b) have performed a differential Bragg reflex measurement between semiconducting and pressurized SmS and found a lattice constant of 5.68 Å from which a valence mixing of 2.85 can be obtained.

Generally speaking one must be very careful when comparing measurements on chemically collapsed Sm chalcogenides or real pressurized systems. Chemically collapsed systems are obtained by substituting, e.g., Y for Sm where it is thought that the smaller ionic radius of Y compared with Sm creates a lattice pressure on Sm thus inducing the valence transition. For a review of chemically collapsed SmS we refer to Jayaraman (1979). However, Y is always trivalent and in the mixed crystals always donates exactly one electron into the 5d conduction band. It is then the question how much of the lattice collapse is electronic by nature and how much is due to the lattice pressure effect. This can be shown precisely by separating these two effects using a *trivalent* dopant which has the same ionic radius as *divalent* Sm, thus avoiding the lattice pressure effect but keeping the one extra electron in the 5d band. Elmiger and Wachter (1987) have shown that Ce is such an ion and in $Sm_{0.75}Ce_{0.25}Se$ the lattice constant is 6.131 Å at ambient pressure and in SmSe it is 6.1975 Å, only a 1% difference. The exerted lattice pressure is thus extremely small, but there are 25% more electrons in the 5d conduction band than expected by the degree of valence mixing. Elmiger and Wachter (1987) then measured the Raman effect of the Ce-substituted SmSe and found the same softening of the $J = 1$ level as in a Y doped SmSe where it has been assumed by Güntherodt et al. (1981) as a precursor effect to the valence transition at about 4.5 GPa due to chemical pressure. This is then the first hint that the valence transition in the Sm chalcogenides is triggered by a certain concentration of free carriers in the conduction band and not by chemical pressure. This carrier concentration can be obtained by closing the gap with real pressure or by doping with e.g. Y or Ce where the introduction of electrons seems to be the main effect of doping. In a further experiment Elmiger and Wachter (1987) applied pressure to an extremely pure SmSe single crystal and by measuring the Raman effect observed the $^7F_0 \rightarrow {}^7F_1$ transition. There was not the slightest softening of this transition up to 3.2 GPa (fig. 45) where the transition suddenly disappeared because the gap was closed so much already, that the $^7F_1$ level no longer fell into the gap. In fact, one would have to close the gap even further with pressure to create the necessary concentration of carriers in the conduction band to induce softenings as precursor of the valence transition. The absence of any precursor effects up to the valence transition is further substantiated by inelastic neutron scattering under pressure on SmS where the $^7F_0$–$^7F_1$ transition is observed by McWhan et al. (1978) and neither a softening nor an intensity reduction of the transition is observed.

The situation becomes even more obvious by a recent paper by Tsiok et al. (1991) who measured on SmSe and SmTe very precisely (with strain gauges) the volume change and, via conductivity, the energy gap under pressure. It became evident, as shown in fig. 46, that the energy gap was driven to zero before a softening of the lattice occurred. This clearly shows again that it is the concentration of carriers which triggers the lattice-related properties and not vice versa.

To make a final point in this argumentation we prepared large single crystals of $Sm_{0.75}La_{0.25}S$ (Wachter and Jung 1994) and verified the chemical composition by microprobe analysis, measured the phase purity and the lattice constant (5.87 Å), the optical reflectivity also under pressure, the temperature dependence of the resistivity, the pressure dependence of the resistivity, the length change in function of temperature

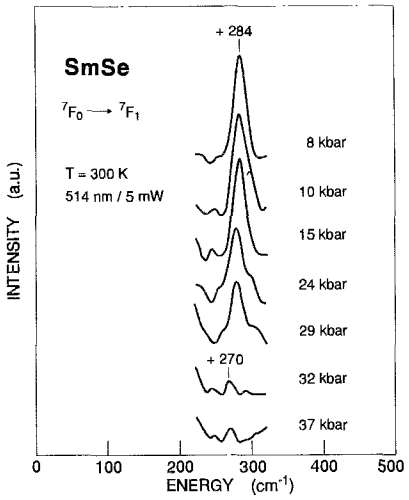

Fig. 45. Raman spectra of the $^7F_0 \rightarrow {}^7F_1$ transition in SmSe at high pressure. The wiggles at both sides of the main peak and the peak at 270 cm^{-1} stem from the pressure-transmitting liquid. (After Elmiger and Wachter 1987.)

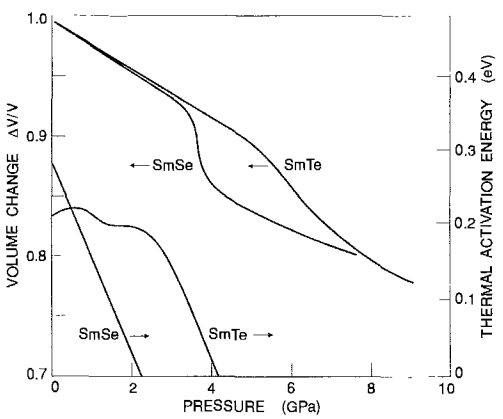

Fig. 46. Volume change (left-hand scale) and thermal activation energy vs. pressure of SmSe and SmTe. (After Tsiok et al. 1991.)

and point contact spectroscopy. Some of these measurements will be discussed in various paragraphs. There exist some prior measurements on the system $Sm_{1-x}La_xS$ by Holtzberg (1974) and Jayaraman et al. (1975) but the physical implications are not discussed. La can only be trivalent and it donates exactly one electron into the 5d conduction band. However, the ionic radius of La^{3+} is with 1.15 Å even larger than the one of Sm^{2+}, thus no lattice pressure is exerted on the Sm, in contrast to Y or Gd doping. Nevertheless the compound is in the intermediate-valent state as verified by the lattice constant, which yields a valency of 2.3. The visible color of the sample is copper-like (like TmSc) and the carrier concentration obtained from the plasma resonance is also 0.3 per formula unit. The length change as function of temperature is below 300 K an expansion and below 200 K a contraction. Jayaraman (1979) has shown that there is, in fact, at 400 K a minimum in the thermal expansion of $Sm_{0.75}Y_{0.25}S$, but the La substitution

yields qualitatively the same, which makes the curve similar to fig. 24 for SmB_6, which is a typical feature of intermediate valence. Last but not least the point contact spectra yield a hybridization gap of about 7 meV, just the same as in high-pressure SmS (see below). Thus there is no doubt that the La doped sample is intermediate valent and in the collapsed phase, but there is no lattice pressure, even to the contrary, since La is larger than divalent Sm it is even much more larger than the radius of $Sm^{2.3+}$, thus it creates negative pressure. With this critical experiment it can be shown that the transition to intermediate valence is mainly caused by the electrons in the 5d band which have to exceed a critical concentration. The explosive first-order transitions of $Sm_{1-x}Gd_xS$ and others (Jayaraman 1979) do not represent the physics correctly. The samples were rapidly quenched from high temperatures and contained a lot of mechanical strain. Thermally annealed samples, in fact, show a continuous expansion when cooled below 300 K.

Thus SmS with its first-order transition was, historically seen, not the best example to study the valence transition in the Sm chalcogenides, but with its low transition pressure and simple alloying it functioned as a pathfinder substance for the others. Only gradually, with more subtle high-pressure techniques, the new picture penetrates the surface. However, there is the old and well known Falicov–Kimball (1969) model which predicted the valence transition in the Sm chalcogenides as due to electronic effects, which seems now to find a late confirmation.

We now have to describe the intermediate-valent state of the Sm chalcogenides itself. In principle this means high-pressure work or, e.g., Y doping. Besides XPS measurements of the type shown in figs. 3a,b, Kaindl et al. (1984) measured the $M_{IV,V}$ spectra of $Sm_{0.30}Y_{0.70}S$. The sample is golden in color and shows features of Sm^{2+} and Sm^{3+} subspectra. A weighted Sm^{3+} spectrum, obtained from Sm_2O_3 was subtracted to obtain the Sm^{2+} difference spectrum. Again a valence mixing of 2.73 was obtained in agreement with the valence determination from the lattice constant (Tao and Holtzberg 1975). By using surface sensitive UPS synchrotron radiation it could be shown by Reihl et al. (1982) that in $Sm_{1-x}Y_xS$ the surface sheet contained basically only Sm^{2+} which can be simply explained with the missing half sphere of atoms at the surface leaving space to expand the Sm ions to the larger Sm^{2+} configuration. However, as mentioned above, these high-energy measurements are unable to give information about the hybridized state itself, especially about the hybridization gap.

For this purpose we need high-pressure–low-temperature measurements, for most meaningful experiments a difficult task. In SmS, however, the high-pressure phase can be stabilized at the surface by polishing (it works even by polishing on your sleeve) with a diamond abrasive. The transformed layer has about the thickness of the diamond grains, i.e., about 10^4 Å and thus is thicker than the penetration depth of light. A microscopic investigation of the surface revealed that it had about 15% of untransformed black SmS, thus it acts like a heterogeneous mixture of two compounds and the reflectivity of both fractions is additive. Thus one can calculate the reflectivity of a 100% golden surface from

$$R(\mathrm{SmS_{gold}}) = 1.18\,[R(\mathrm{SmS_{mix}}) - 0.15R(\mathrm{SmS_{black}})]. \tag{6}$$

The reflectivity obtained in such a way is shown in fig. 47 at ambient temperature and at 9 K. It is remarkable that the reflectivity of golden SmS obtained 20 years earlier by Kaldis and Wachter (1972) and by Batlogg and Wachter (1977) in spite of a more limited spectral range, agrees in details with the 300 K curve in fig. 47. The special and unexpected feature of the low-temperature curve is that, in contrast to fig. 10 for SmB_6, the reflectivity does not tend to a constant value for $\omega \to 0$ but it seems to rise towards 100% as for a metal. The reflectivity spectrum of IV golden SmS has been analyzed in terms of optical constants by means of the Kramers–Kronig relation by Travaglini and Wachter (1984b). For this purpose the reflectivity has been extrapolated towards $\omega \to 0$ (dotted curve in fig. 47) by using the measured dc conductivity and the Hagens–Rubens relation. In fig. 48 we show the real and imaginary part of the dielectric function and in fig. 49 the optical conductivity, both at 9 K. The high-energy region above 3 eV with the peak at 6 eV due to p d (above E_F) transitions results in an ε_{opt} of about 4.9, which on the scale of fig. 48 is barely visible. We then observe a broad peak at 0.2 eV and a very intense and sharp peak with fine structure around 20 meV. ε_2 tends towards infinity for energies less than 7 meV. ε_1 is about 230 between 1 and 5 meV, and it drops to large negative values below 1 meV due to the presence of an appreciable amount of free carriers even at 9 K. However, it is obvious from fig. 48 that we have a gap at 7 meV. This gap can also be seen in fig. 49, where we can also show that the optical conductivity extrapolates fairly well to the measured dc conductivity of 2.3 mΩ cm at 4 K as found by Lapierre et al. (1983). A question can be posed as to how large the pressure is in the mechanically polished golden SmS single crystals. It is evident that the pressure exerted during polishing is larger than 0.65 GPa, but after the polishing the pressure can in principle relax until 0.15 GPa due to the hysteresis shown in fig. 40 and the crystals are still in the IV golden phase. Thus the pressure can be anything between 0.15 and 0.65 GPa which also means that the hybridization gap determined on such samples may be larger than the one obtained by other methods and by applying real pressures greater than 0.65 GPa.

On the same golden SmS crystal as used for optical experiments, point contact spectroscopy has been performed, shown in fig. 50, and a gap of 6.4 meV in good agreement with the optical gap of 7 meV has been found by Frankowski and Wachter (1982c) However, despite the larger gap of SmS compared to SmB_6 (4 meV) the dc conductivity at low temperatures is orders of magnitude larger in SmS than in SmB_6.

In fig. 51 we show the point contact spectrum of intermediate-valent $Sm_{0.75}La_{0.25}S$, which should serve also as proof that the compound is really intermediate valent in spite of the fact that the material has neither chemical pressure nor real pressure (Wachter et al. 1995). The similarity with fig. 50 of SmS under pressure is evident and a hybridization gap of about 7 meV can be extracted, in perfect agreement with other experiments.

In the hybridization model described generally in section 2 and specifically in section 4.1.1 for SmB_6, we will have at least two electronic transitions for SmS, one across the hybridization gap of 7 meV, which has mainly f–f character but with a strong d admixture so that the oscillator strength is about 10^{-2}, and a d–f transition to which

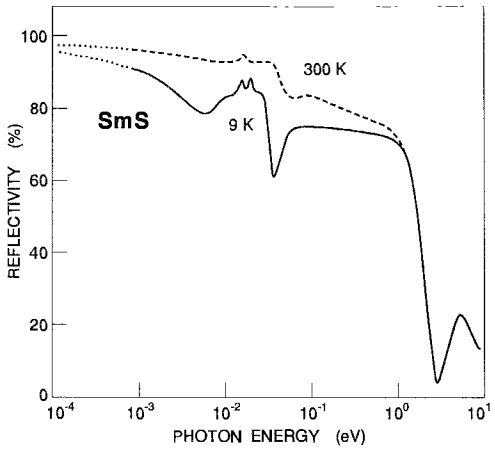

Fig. 47. Reflectivity of mechanically polished (high pressure phase) SmS at 9 and 300 K. The dots indicate the extrapolation towards $\omega \rightarrow 0$. (After Travaglini and Wachter 1984b.)

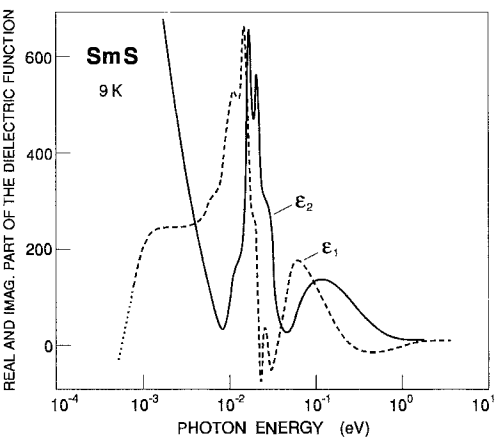

Fig. 48. Real and imaginary parts of the dielectric function of intermediate-valent SmS at 9 K. (After Travaglini and Wachter 1984b.)

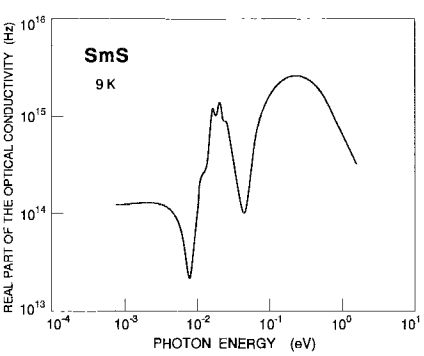

Fig. 49. Real part of the optical conductivity of intermediate-valent SmS at 9 K. (After Travaglini and Wachter 1984b.)

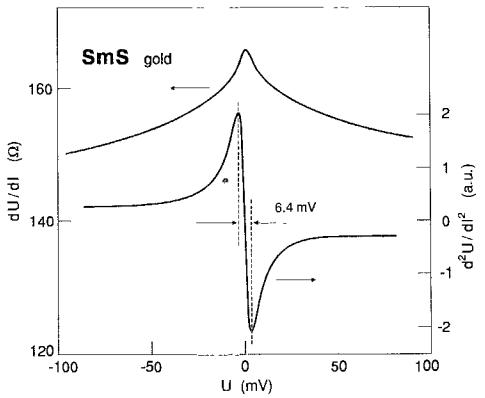

Fig. 50. Point contact spectroscopy of intermediate-valent SmS at 4.2 K. (After Frankowski and Wachter 1982c.)

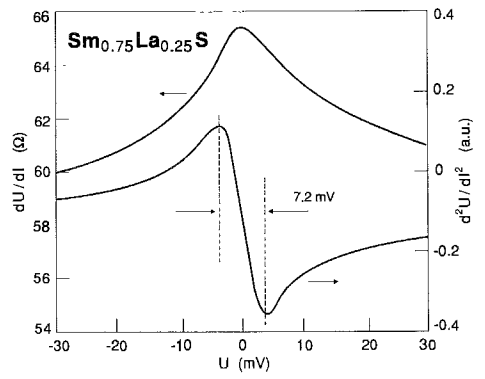

Fig. 51. Point contact spectroscopy of intermediate-valent $Sm_{0.75}La_{0.25}S$ at 4.2 K. (After Wachter et al. 1995.)

we ascribe the peak at 0.2 eV. In fact the oscillator strength for this peak is, with 0.368, typical for such a transition (Travaglini and Wachter 1984b).

In fig. 48 we realize also some collective oscillations. They are defined by $\varepsilon_1 = 0$ and $(d\varepsilon_1/d\omega)_{\varepsilon_1=0} > 0$. The one at highest energy is at 2.45 eV and at room temperature there is only one other zero crossing of ε_1 with positive slope at 25 meV. For lower energy ε_1 remains negative. At room temperature these two resonances correspond to two coupled plasma resonances of light (d) and heavy (f) electrons, where again, because of the large energy difference of the resonances, $\varepsilon_1 = 0$ practically yields the eigenfrequencies of the uncoupled resonators. The frequency of the zero crossings $\omega_p^2 = 4\pi N/m^*\varepsilon_1$ can be used to compute the effective masses m^*. From the degree of valence mixing of about 2.8 we expect $N_f \approx 0.2$ and $N_d \approx 0.8$ per Sm atom and we obtain $m_d^* \approx 1.3m$ and $m_f^* \approx 100 \pm 50m$.

At low temperatures we observe additional zero crossings of ε_1 near 20 meV. The signature is typical for a plasmon–LO phonon coupling, a plasmaron. The lowest zero crossing of ε_1 with a positive slope is at about 5×10^{-4} eV and it yields (even at 9 K) the plasma resonance of excited heavy electrons across the gap. Travaglini and Wachter (1984b) estimate their concentration $N \leqslant 1.5 \times 10^{19}$ cm^{-3} at 9 K by making

use of a Hall effect measurement under pressure by Morillo et al. (1980) and obtain an effective mass of $m^* \leqslant 360m$, again a typical f mass.

A problem rests with the structure around 20 meV for which one can discern at least 3 peaks. Assignments can be phonons, multiplet transitions and f–f transitions. The highest energy peak at 25 meV has a shoulder at 30 meV which coincides with the TO phonon frequency for IV golden SmS (see fig. 54, below). At this energy ε_1 indicates, by its zero crossing with a negative slope, a coupled plasmon–phonon mode. The peak position at 25 meV coincides with the $^7F_0 \rightarrow {}^7F_1$ transition, softened because of a d admixture (Güntherodt et al. 1981) and becoming dipole allowed by the same reasoning. Thus the whole high-energy peak is not considered to be an f–f transition.

We are left with two peaks at 16 and 21 meV which we assume to be due to f–f transitions, exhibiting thus a fine structure. In order to calculate the total oscillator strength and thus derive the joint density of states Travaglini and Wachter (1984 b) construct from these two peaks a single oscillator situated at 18.5 meV. The oscillator strength of this peak can be obtained by using eq. (2), and by means of eqs. (3) and (4) the joint density of states J_{cv} or the interband density of states IDS being $2J_{cv}$ can be computed. The IDS of the total f–f transition assumed at 18.5 meV amounts to 1253 states per Rydberg per cell and for the d–f transition at 0.2 eV to 70 states per Rydberg per cell. We want to remind the reader again that the analysis of J_{cv} implies direct transitions, whereas the hybridization model (section 2) demands an indirect transition for the onset of the f–f transition (Γ–X). The oscillator strength for an indirect transition is less than for a direct one so the quoted values for J_{cv} are lower limits only. It thus becomes clear that IV golden SmS also corroborates the hybridization model with two large density of states peaks with mainly f character separated by 7 meV and having a width of about 6 meV. The states with mainly d character extend over nearly 1 eV.

There remains, however, the problem of the fine structure of the f–f transition, which consists of at least two peaks, which is to be contrasted with SmB_6 where only one f–f peak is observed. This problem must be related with the different crystallographic structure of both compounds, SmB_6 having the bcc CsCl-like structure and IV SmS having the fcc NaCl structure. In SmB_6 the lowest d conduction band has e_g and in SmS t_{2g} character. In both materials the lowest point of the d band is at X in the Brillouin zone, but in SmB_6 the band from Γ to X has Δ_2 symmetry, in SmS Δ_2' symmetry as shown by band structure calculations of Walch et al. (1977), Hasegawa and Yanase (1977) and Davis (1971). As a consequence, in SmB_6 and IV SmS the lowest d bands have different and opposite parity. The f states, however, are the same in both materials, thus it follows that in SmB_6 the f and d bands have the same parity, whereas in IV SmS they have opposite parity. Thus the hybridization gap in SmB_6 can be open over the whole Brillouin zone, whereas in IV SmS one has only a pseudo gap because the bands cannot hybridize at Γ or X (Martin and Allen 1979, Brandow 1988). This effect can result in the fine structure of the f–f transition as observed. Thus we can show in fig. 52 the electronic structure of IV SmS near the Fermi energy where we neglect the fine structure of the f bands.

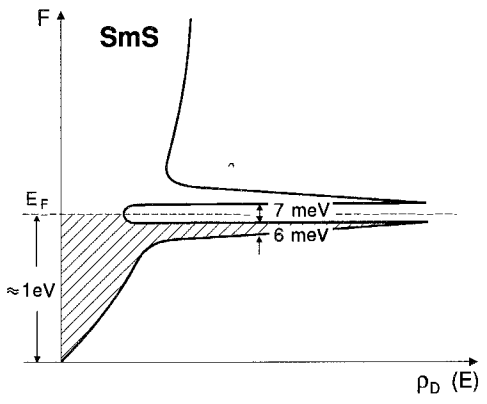

Fig. 52. Energy level scheme and density of states of intermediate-valent SmS. (After Travaglini and Wachter 1984b.)

Martin et al. (1980) measured the L_{III} edge X-ray absorption spectrum on $Sm_{0.75}Y_{0.25}S$ and observed valence mixing, similar as in XPS or M edge experiments (Campagna et al. 1979, Kaindl et al. 1984). More interesting are the extended X-ray absorption fine structure (EXAFS) measurements from which one can show that the S neighbors of each Sm atom adopt an average distance rather than a dynamically distorted environment corresponding to two valence states. The authors conclude that the Sm 4f bandwidth is larger or comparable with the phonon energies. We have discussed above that the highest phonon energy at Γ is 30 meV. When we look at the experimentally determined total 4f bandwidth as shown in fig. 52 we find a total f bandwidth of about 20 meV determined at 9 K, whereas the EXAFS results are room temperature data. Thus we find reasonable agreement under these circumstances. Also Entel et al. (1979) and Entel and Sietz (1981) conclude from the observed phonon anomalies in $Sm_{1-x}Y_xS$ (see below) that the 4f bandwidth has to be comparable with LO phonon energies to cause a phonon renormalization and indeed fig. 52 gives evidence for this.

We already mentioned that the resistivity increase with decreasing temperature in SmB_6 amounts to 5 orders of magnitude, whereas in IV SmS it is only one order of magnitude, which is also true for IV SmSe and IV SmTe as shown by Holtzberg and Wittig (1981) and Lapierre et al. (1983); as an example SmS is shown in fig. 53. The basic reason for this is that in the fcc structures of the Sm chalcogenides one has only a pseudo gap as a hybridization gap, whereas in the SmB_6 structure the hybridization gap goes over the whole Brillouin zone. As a consequence of a finite density of states at E_F the resistivity increase with decreasing temperature due to excitations across the hybridization gap is much smaller in the IV Sm monochalcogenides, but the resistivity should decrease towards zero for $T \to 0$. In fact, we can see this very clearly in the turn-around of the resistivity at pressures of 0.8 and 1 GPa (8 and 10 kbar) in fig. 53 for the lowest temperatures of about 1.5 K. Experimental difficulties prevent high-pressure measurements to still lower temperatures. With further increasing pressures up to 3 GPa (30 kbar) one gradually closes the hybridization gap and at the same time empties the hybridized $4f^6$-5d state more and more into the conduction band, until the 4f state is

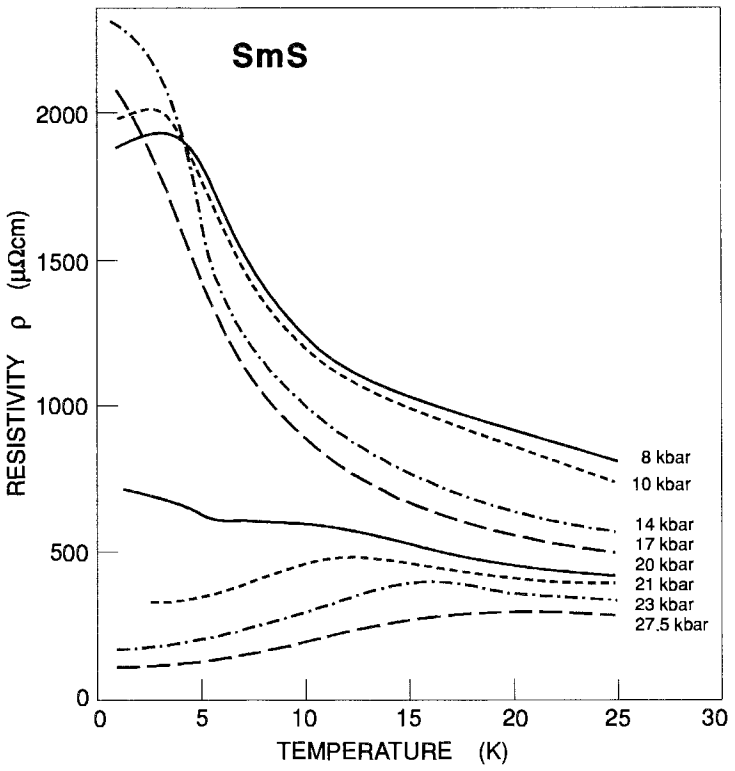

Fig. 53. Resistivity of SmS at high pressures vs. temperature. (After Lapierre et al. 1983.)

completely empty when it appears as probably localized $4f^6$ state above E_F with the occupied $4f^5$ state about 5–6 eV below E_F. Evidently the material is now integer trivalent, having one d electron in the conduction band. That one really has the empty, divalent $4f^n$ state little above E_F can be shown with BIS on trivalent TmS further down (fig. 60, section 4.3.1).

The Hall effect under pressure and at temperatures down to 2.5 K has been measured by Konczykowski et al. (1981) on IV SmS. The Hall effect is positive below 10 K and shows a steep rise with decreasing temperature at pressures above 1 GPa (10 kbar). In a log ρ versus $1/T$ plot one observes at 1 GPa a gap of 2 meV when the formula $\exp \Delta E/2k_B T$ is used, which just means again that the gap at 1 GPA is already partially closed. Since the Hall effect is positive, this must be interpreted in a two band model of the hybridized f bands and it means that the mobility in the lower band with holes is larger than in the upper band with electrons. This, however, has already been concluded from the optical analysis of Travaglini and Wachter (1984b) where for the upper band a larger effective mass has been deduced than for the lower band.

Further evidence that one has a finite density of states at E_F in the IV state of SmS is provided by a measurement of the γ value of the specific heat under pressure where Bader

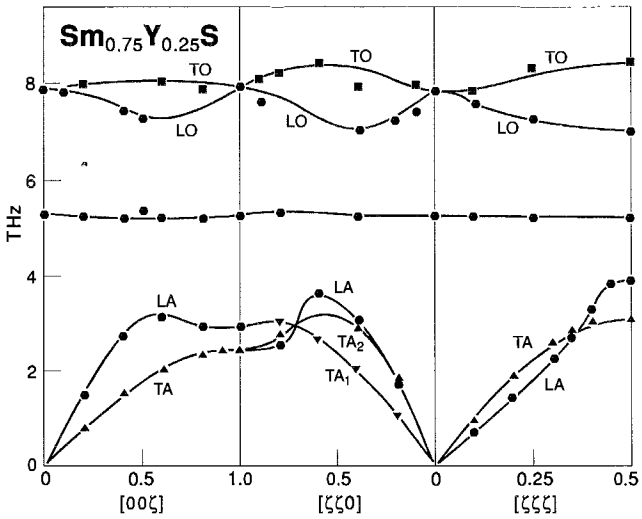

Fig. 54. Phonon dispersion of $Sm_{0.75}Y_{0.25}S$ as obtained by inelastic neutron scattering. (After Mook et al. 1978.)

et al. (1973) found a value of 145 mJ/mol K^2, which appears to be too large and should be remeasured on better defined samples. From this γ value one computes a density of states of 830 per Rydberg per cell which should be compared with the maximum in the density of hybridized f states of 1200 or even 3500 per Rydberg per cell, as computed from the optical data by Travaglini and Wachter (1984b). Qualitatively and even quantitatively the model of the hybridization gap in the IV Sm monochalcogenides seems correct.

4.2.2.2. *Lattice-related properties.* The phonon dispersion of Y-substituted $Sm_{0.75}Y_{0.25}S$ and high-pressure IV SmS has been measured with inelastic neutron scattering by Mook et al. (1978, 1982) and Mook and Holtzberg (1981); it is shown in fig. 54 for the three principal directions. The Sm used was isotopically pure ^{154}Sm. Figure 54 should be compared with fig. 38 where the phonon dispersion of semiconducting SmS is shown and also with fig. 23 which is the phonon dispersion of IV SmB_6.

The most striking aspect of fig. 54 is that the LA branch in the [111] direction lies below the TA branch nearly throughout the Brillouin zone, quite in contrast to the semiconducting phase shown in fig. 38. The LO branches also lie below the TO branches nearly everywhere, coinciding with the TO branches only at Γ and X, whereas in the semiconducting phase the LO branch lies appreciably above the TO at Γ. The sound velocities derived from the slope of the dispersion curves of IV SmS agree well with those obtained directly on the same sample by ultrasonic measurements by Melcher et al. (1975). Similar effects have been observed for SmB_6 (fig. 23), where, however, the LA is below the TA in only a small part of the Brillouin zone in the [110] and the [111] direction, but also in SmB_6 the LO coincides with the TO at Γ. Such a coincidence

in IV SmS as well as in SmB_6 has been explained by Bilz et al. (1979) by an increased dipolar breathing mode Γ_{15} and an increased electronic deformability Γ_1^+ arising from the 4f–5d mixing. It is observed that the TO and TA branches remain nearly the same in their dispersion behavior in semiconducting and IV SmS, apart from a renormalization in energy, but the longitudinal branches change appreciably in the direction of a softening of their energy. At room temperature a hybridization gap in IV SmS is not discernible, thus at E_F the $4f^6$ and $4f^5 5d$ configurations coexist. Thermally induced fluctuations or lattice vibrations can change the local degree of valence mixing and thus lead to a volume fluctuation due to the different radii of the $4f^6$ or $4f^5 5d$ configuration. Consequently, the phonon modes, which change unit cell volume, will be most strongly affected by the configuration change and these are the longitudinal modes.

Figure 54 shows, as a new feature of Y-substituted SmS, a nearly dispersionless mode in the gap between acoustical and optical modes, a gap mode at about 5 THz (21.9 meV). Mook et al. (1978) propose for this mode a localized, mass-defect induced mode due to the Y doping of the SmS. Indeed, in high-pressure SmS and even in IV TmSe the gap mode has not been observed by neutrons (Mook and Holtzberg 1981 and Mook et al. 1982). However, the same gap mode has been found in IV SmB_6 (see fig. 23) by Alekseev et al. (1989) where no doping was necessary to induce the IV state. In spite of the claims of Mook et al. (1978, 1982) and Mook and Holtzberg (1981) this mode rather seems to be inherent to the IV state of the material. It is also surprising that the $^7F_0 \rightarrow {}^7F_1$ excitation is not seen anymore with neutrons (McWhan et al. 1978) in contrast to the semiconducting state, but this is also in agreement with Raman scattering where this excitation can not be seen anymore in the IV state of SmS. However, it is claimed by Alekseev et al. (1993) that the $^7F_0 \rightarrow {}^7F_1$ transition is seen by neutrons in SmB_6.

For the dispersionless gap mode in IV $Sm_{0.75}Y_{0.252}S$ Stüsser et al. (1982) first show with Raman scattering that this mode at about 25 meV is not related to Y or lanthanide doping where the masses are vastly different but the gap mode remains the same. The gap mode is also not related to a two phonon process of some kind as excluded by the temperature dependence of the intensity of this Raman mode. Stüsser et al. (1982) argue that besides the charge deformabilities due to the valence fluctuations induced by phonons, there exist also charge density fluctuations. Whereas this inelastic light scattering mode is expected in the low energy range (Brillouin scattering) a coupling to LO phonons may occur which brings the energy of this coupled mode in the Raman range (plasmaron). Stüsser et al. (1982) further argue that the uncoupled charge density plasmon would be the acoustic plasmon predicted by Varma (1976) where the f and the d plasma vibrates in an out of phase motion. Although this interpretation is possible for the SmS system we will show further down (section 4.3.1.2) that in the TmSe system the situation seems to be different.

To obtain the elastic constants of IV SmS the ultrasound velocities of Y-substituted SmS have been measured in the three principal directions by Melcher et al. (1975) and Penney et al. (1975). Apparently similar measurements under pressure on undoped SmS are not possible because the crystals due to the first-order transition acquire micro-cracks which prevent any further ultrasonic measurements. Melcher et al. (1975) show that c_{44}

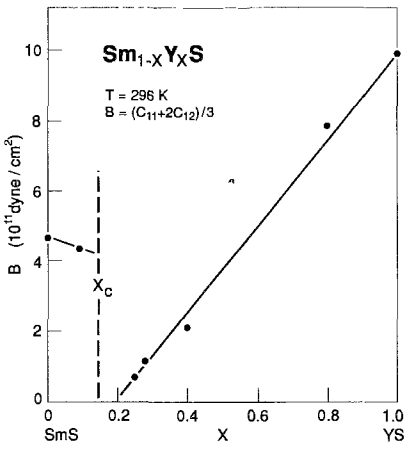

Fig. 55. The bulk modulus of $Sm_{1-x}Y_xS$ vs. composition x. The critical composition for the valence transition is labeled x_c. (After Melcher et al. 1975.)

goes continuously through the valence transition which occurs at a composition of $Sm_{0.85}Y_{0.15}S$ but $(c_{11}-c_{12})/2$ and $(c_{11}+c_{12}+2c_{44})/2$ show discontinuities through the valence transition. Unfortunately these authors did not extract information on c_{12} alone, which would have been possible, so they did not realize that c_{12} became negative in the IV region, an important fact because this means a negative Poisson ratio $c_{12}/(c_{11}+c_{12})$, a feature typical for an IV compound. Although measurements on IV SmS had been done before, it was Boppart et al. (1980a) who first realized the importance and consequences of a negative c_{12} in IV TmSe. In fact we can compute from the data of Melcher et al. (1975) a c_{12} of -51 GPa for IV SmS at the transition. Melcher et al. (1975) could also extract the bulk modulus of IV SmS $B=(c_{11}+2c_{12})/3$ which is displayed in fig. 55. Apparently $B\to 0$ at the valence transition which is a must when the transition is of first order because then the compressibility $\kappa=1/B$ diverges. For SmSe and SmTe the volume change under pressure was displayed in fig. 46. Since $\kappa=-(1/V)(\delta V/\delta p)T$ is the derivative of the volume pressure relation and has its maximum at the point of inflection of the volume–pressure relation of fig. 46 it is evident that in this second-order transition $B=1/\kappa$ has only a minimum.

There is, however, an important difference between high-pressure IV SmS and chemically substituted $Sm_{1-x}Y_xS$, visible again in fig. 55 for $x<0.15$, i.e., in the non IV range. The bulk modulus is decreasing with increasing x indicative for a lattice softening and precursor effects in still semiconducting SmS. However, the opposite occurs in high-pressure experiments. Hailing et al. (1984) have shown that the bulk modulus increases with increasing pressure in the semiconducting range, as typical for any normal material and consequently no precursor effects are observed. Thus, looking back, too many experiments have been performed on chemically collapsed IV SmS and generalized conclusions have been drawn on that basis. However, high-pressure SmS is not the same as chemically collapsed SmS, because, as mentioned above, each Y substitute contributes also one electron in contrast to the pressure experiment, where electrons can only be thermally activated over a semiconductor gap and appear in the order of magnitude of

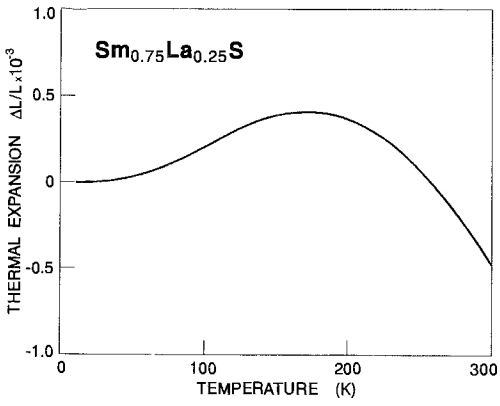

Fig. 56. Thermal expansion of intermediate-valent $Sm_{0.75}La_{0.25}S$. (After Wachter and Jung 1994.)

the atomic concentration only when the semiconductor gap is already closed. Thus again the lattice softening effects observed in Y-substituted SmS are mainly caused by the added electrons and not by the pressure effects and especially precursor effects of the valence transition are absent in real pressure experiments and they can only be observed in alloyed systems like $Sm_{0.85}Y_{0.15}S$ where they are due to the electrons and not due to the chemical pressure.

In a last example we show in fig. 56 the thermal expansion of $Sm_{0.75}La_{0.25}S$ and find below 300 K a lattice expansion with decreasing temperature, as typical for intermediate-valent materials. The minimum in the expansion is a little above 300 K, similar as observed for $Sm_{0.75}Y_{0.25}S$ by Jayaraman et al. (1975). This minimum and the expansion below 300 K in fact serve again as a proof of intermediate valence, however, any lattice pressure effect is absent in doping with La, it just serves to donate electrons. According to the theory of Lacroix (1987) a two-peak density of states with a hybridization gap is necessary to explain such a thermal expansion with decreasing temperature. The thermal energy of this minimum in the expansion coefficient should scale with the hybridization energy and comparing SmB_6 with a hybridization gap of about 4 meV (assumed to be proportional to the hybridization energy) and a minimum at about 150 K (fig. 24) with SmS with a hybridization gap of 7 meV and a minimum near 300 K the proportionality is approximately fulfilled.

4.2.2.3. *Magnetic properties of the IV SmS.* This section is restricted to the susceptibility of IV SmS since the pressure cells for magnetic susceptibility measurements at low temperatures are not capable of producing the necessary pressures to drive SmSe or SmTe into the IV state.

The magnetic susceptibility of polycrystalline SmS under a pressure of 0.75–1.2 GPa has been measured by Maple and Wohlleben (1971) 2 years after that of SmB_6. The general behavior is quite similar as the one of SmB_6 shown in fig. 25, i.e., a saturation below about 50 K and an increase of the susceptibility below about 10 K which can be quantitatively taken care of by assuming a 1% contamination by unhybridized

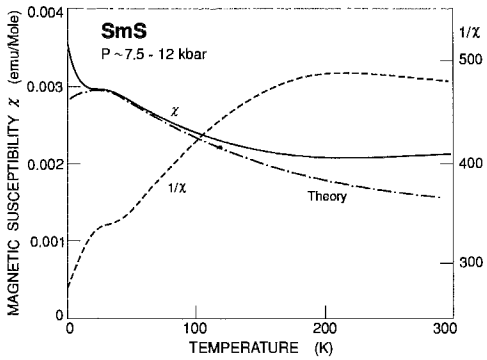

Fig. 57. Magnetic susceptibility of SmS at pressures between 7.5 and 12 kbar (experiment: Maple and Wohlleben 1971, theory: Wachter 1986).

trivalent Sm in the $4f^5$ configuration. After subtracting this paramagnetic term of the Sm^{3+} configuration we are left with a slight maximum in the susceptibility of IV SmS which is shown in fig. 57.

Since the shape of the susceptibility of SmB_6 and IV SmS is nearly the same and the magnetic ion is the same, the equivalent theory as outlined in section 4.1.3 for SmB_6 should also be valid for IV SmS. In short, we again assume an alloy model as outlined before with the Sm^{2+} $4f^6$ configuration $^7F_0$ and for the Sm^{3+} ions we use the $4f^5 5d^1$ configuration, where we again assume a wide 5d band, but this time in a t_{2g} symmetry as demanded by the crystal symmetry. However, since we generally assume that the orbital momentum of the 5d band electrons is quenched, the distinction between a e_g or t_{2g} symmetry is not important, we only use s electrons. The ground state configuration will be again when the s electrons are parallel aligned to the $4f^5$ core. The temperature dependence of the susceptibility will be given by the van Vleck term. An excited term separated by the hybridization gap will be the antiparallel configuration of the $4f^6 5d^1$ state $^5H_3$. With increasing temperature electrons are excited from the ground state of the ions with parallel configurations into those with antiparallel configurations leaving holes behind, where the relative concentration of carriers are weighted by Boltzmann factors.

Adjustable parameters in this model are the valence mixing and the size of the hybridization gap. The best fit of the theory with the experiment is shown in fig. 57 where a good agreement can be stated. The valence mixing is found to be 2.8, i.e., 20% Sm^{2+} and 80% Sm^{3+}, in good agreement with the valence mixing determined from the lattice constant, and the hybridization gap is 6 meV, again in good agreement with determination with optical or point contact means.

4.3. *Thulium monochalcogenides*

4.3.1. *Comparison between TmS, TmSe and TmTe*

The Tm monochalcogenides are special among possible intermediate-valent systems inasmuch as they show long range magnetic order. Their special features are easily accessible without the use of high pressure or chemical alloying, though stoichiometry

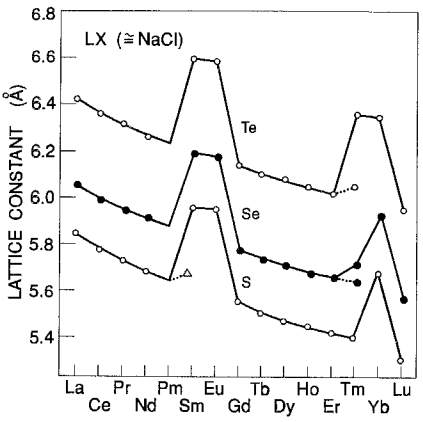

Fig. 58. Lattice constant of the Tm monochalcogenides. (After Bucher et al. 1975.)

variation, chemical alloying and pressure have been used to change the degree of valence mixing. In the series of the Tm monochalcogenides one has the interesting possibility to go from integer trivalent metallic TmS to intermediate-valent TmSe to integer divalent semiconducting TmTe by leaving the important cation unchanged and varying only the anion. The free carrier concentration of the material is thus given by the equilibrium conditions of the material itself and not by additional electrons introduced by a cation dopant as in $Sm_{1-x}Y_xS$.

The simplest argument that TmS is trivalent, TmSe intermediate valent and TmTe divalent under normal conditions comes from comparing the lattice constants of the lanthanide sulfides, selenides and tellurides as shown in fig. 58 (after Bucher et al. 1975). The lanthanide contraction is the cause for the general trend in the curves and the standard divalent Sm, Eu and Yb ions with their larger ionic radius are the obvious deviations. TmTe lies on the divalent curve, TmS on the trivalent one and TmSe is intermediate and by linear interpolation between a hypothetical divalent and trivalent TmSe one obtains a valency of 2.75^+. The figure also shows that SmS, in this case by pressure or trivalent rare earth doping, can be intermediate valent, TmSe, in this case by stoichiometry variation, can become trivalent and TmTe, in this case by pressure, oxidation and stoichiometry variation, can become intermediate valent.

Further evidence that TmS is trivalent comes from XPS measurements by Campagna et al. (1976) or Baer et al. (1994), shown in fig. 59, completed by a BIS spectrum by Baer et al. (1994). The occupied states clearly yield a $4f^{11}$ $4f^{n-1}$ final state spectrum as shown by the ladder-like structure given in the figure, where the initial $4f^n$ $4f^{12}$ state of trivalent Tm is about 6.5 eV below E_F. There is an indication of a divalent spectrum which is attributed to surface states, but part of the 5d band is also occupied. This is corroborated by the metallic character of TmS as judged from resistivity versus temperature curves and from the golden color of the crystals typical for the plasma resonance of trivalent sulfides with one 5d electron.

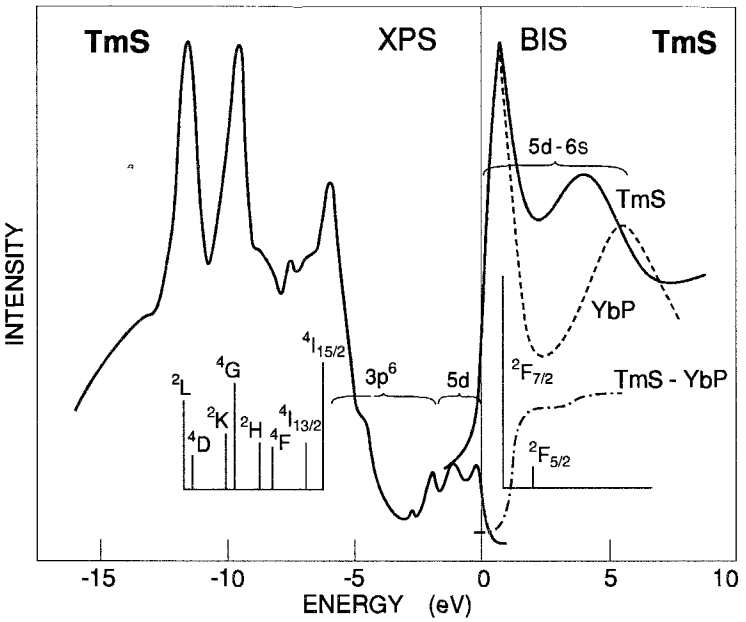

Fig. 59. XPS and BIS spectrum of TmS. The ladder-like final state spectra are shown as vertical bars, the length of which corresponds to the coefficient of fractional parentage. XPS data and BIS data for TmS from Baer et al. (1994), BIS data for YbP from Degiorgi et al. (1990).

The trivalent character of TmS is further confirmed by M edge X-ray absorption (XA) by Kaindl et al. (1983), where one observes a transition $3d^{10}4f^{12} \rightarrow 3d^9 4f^{13}$ which exhibits three dipole allowed lines at the M_V energy as demanded by theory. In addition Kaindl et al. (1982) show also that TmS has a surface sheet of divalent Tm as observed with surface sensitive photoemission. The reason for this is explained below.

TmTe is a material very difficult to be prepared stoichiometrically, which is a fact with all rare earth tellurides. Whenever it is nonstoichiometric it is extremely sensitive to oxidation and trivalent Tm_2O_3 layers form at the surface. They can be observed with surface sensitive methods like photoemission or XA (e.g., Kaindl et al. 1983). The problems connected with the material preparation have been discussed by Kaldis and Fritzler (1982) and Ott and Hulliger (1983).

TmTe is a semiconductor with the divalent Tm ground state $4f^{13}\ ^2F_{7/2}$. This localized 4f state is separated by the energy gap ΔE from the bottom of the $5dt_{2g}$. ΔE for TmTe was first mentioned by Bucher et al. (1971) to be 0.22 eV on the basis of optical measurements and 0.2 eV on the basis of the pressure variation of the resistivity with a closing rate of the gap of -10 meV/kbar (Bucher et al. 1975). Depending on stoichiometry (none of the crystals really were stoichiometric) the semiconductor–intermediate-valent metal transition was completed between 3 and 4 GPa (30–40 kbar). Suryanarayanan et al. (1975) made a complete optical analysis between 0.05 and 20 eV photon energy and determined

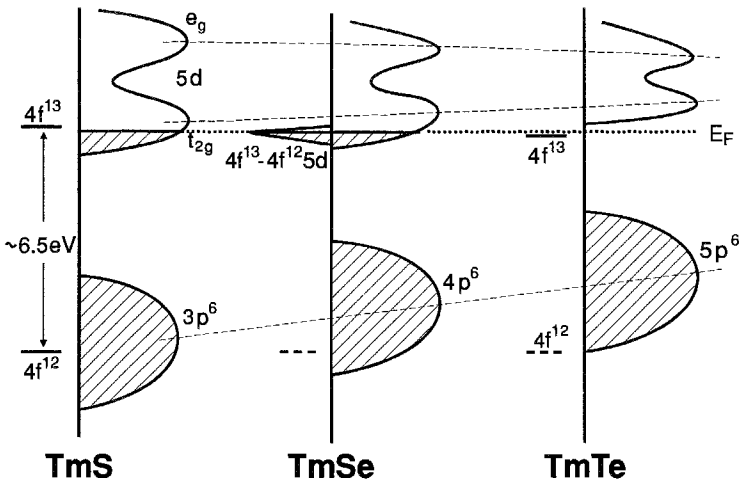

Fig. 60. Electronic structure and density of states of the Tm monochalcogenides normalized to the Fermi level E_F (dotted line). The dashed lines through the density of states peaks serve as guides to the eye.

the energy gap to be 0.35 eV and being due to the transition $4f^{13}$ ($^2F_{7/2}$) → $4f^{12}$ ($^3H_6$)$5dt_{2g}$. The reason why the energy gap is so small in the first place is the same as explained for the Sm monochalcogenides and shown in fig. 27: the third ionization energy is, with 23.89 eV for Tm, nearly the same as for Sm with 23.68 eV (Morss 1971).

The Tm monochalcogenides offer the unique opportunity to follow the evolution of intermediate valence in function of composition. The driving force is the change of lattice constant upon exchanging the anion, since in all compounds the fcc structure persists and the hard sphere model with its close packed structure is valid. The reduction of lattice constant in going from the large Te ion to the smaller S ion manifests itself in an increased crystal-field splitting of the 5d band relative to its center of gravity and the 4f states. This is shown in fig. 60, where we normalized the figures with respect to the Tm $4f^{13}$ level. We start with TmTe on the right-hand side of the figure. We have plotted the empty 5d conduction band with its crystal-field split t_{2g} and e_g sublevels, split by 10 Dq = 1.1 eV (Suryanarayanan et al. 1975). The occupied and localized $4f^{13}$ level is 0.35 eV below the bottom of the conduction band forming the energy gap $4f^{13}$–$5dt_{2g}$. The occupied $5p^6$ valence band of Te has its center about 4 eV below the bottom of the conduction band resulting in a charge transfer gap of about 2 eV and a width of the p band of about 3 eV. By taking one electron out of the $4f^{13}$ state, the localized $4f^{12}$ state would be about 6.5 eV below the $4f^{13}$ state, thus confirming the ladder-like model of Hirst (1971). Evidence for this comes from comparison with TmS, where the $4f^{12}$ level can be observed.

Let us now move to TmSe in the center of fig. 60. Due to the reduced lattice constant the crystal-field splitting 10 Dq of the 5d conduction band increases and – since the separation $4f^{13}$–5d center of gravity remains constant (as shown also for the Sm chalcogenides in fig. 37) – the bottom of the conduction band now overlaps with the $4f^{13}$

level. Now part of the 4f electrons spill into the conduction band, creating $4f^{12}5d$ states with a smaller ionic radius thus further decreasing the lattice constant and increasing the crystal-field splitting until the equilibrium between the gain in electronic energy due to lowering electrons below the Fermi level and the increase in lattice energy is obtained. Due to the hybridization the $4f^{13}$–$4f^{12}5d$ state acquires a width and becomes a narrow 4f band (a possible hybridization gap will be discussed below). The lower conduction band t_{2g} will be filled with quasi-free electrons up to about 1 eV, being able to make a plasma resonance in the visible with a copper-red color. The Se $4p^6$ valence band will exhibit a larger charge transfer gap than TmTe because of decreased covalency and the width of the Se valence band will be larger because the wave functions have a better overlap due to the reduced lattice constant. TmTe under external pressure of about 3–4 GPa will be in exactly the same condition as TmSe at normal conditions, regarding the f and d bands. There exists in fact a band structure calculation by Jansen et al. (1985) who used a local density theory including f–d hybridization and these computations support the electronic structure of TmSe as described above.

Going now to the left-hand side of fig. 60 the lattice constant is further reduced, the 5d crystal-field splitting further enhanced until exactly 1 electron from the $4f^{13}$ state has left and became a 5d electron, the $4f^{13}$ state is now empty and must be above the Fermi level (but close by). The electrons of the conduction band can make a plasma resonance with a golden color, as all metallic rare earth sulfides do. The integral occupied $4f^{12}$ level is about 6.5 eV below E_F as shown in fig. 59 by XPS. Again the separation of the empty $4f^{13}$ and the full $4f^{12}$ state is about 6.5 eV (see below) from where we take the argument that this separation is the same in TmTe. The $3p^6$ valence band of sulfur has again a larger charge transfer gap than the other chalcogenides, its width is again larger because of the better overlap of the p wavefunctions due to the reduced lattice constant.

The beauty of the new BIS measurement of Baer et al. (1994) is that one can directly observe the empty $4f^{13}$ state about 1 eV above E_F and shown in fig. 59 by the narrow peak which can be clearly identified as having f character. In a BIS measurement one observes as final state the $4f^{n+1}$ of the $4f^n 4f^{12}$ state. This $4f^{13}$ state shows a spin–orbit splitting $^2F_{5/2}$–$^2F_{7/2}$ of 1.2 eV, which is well known from XPS measurements on divalent Yb compounds, where one observes as final state the $4f^{n-1}4f^{13}$ state of the initial $4f^{14}$ state. Whereas in the XPS measurement the intensity of the two spin–orbit peaks is about the same (Campagna et al. 1979), in the BIS experiment the matrix element of the $^2F_{5/2}$ is about a factor 10 less than the one of the $^2F_{7/2}$ so that one observes practically only one BIS 4f peak instead of two. However, the BIS spectrum of YbP has been published recently (Degiorgi et al. 1990). There Yb has a $4f^{13}$ configuration and the BIS $4f^{n+1}4f^{14}$ state is a single line. Its half-width is mostly determined by the experimental resolution of the BIS line of about 1 eV and it is observed at exactly the same position, about 1 eV above E_F, as in TmS. In the insert of fig. 59 we show the BIS part of YbP and TmS, matched for the same peak height of the f peak. It is observed that the measured half-width of the 4f peak in TmS is larger than in YbP, thus larger than the instrumental width. There seems to be another peak hidden. The difference spectrum of TmS–YbP is shown in the lower part of the insert and in fact a peak can be

discerned split off by 1.2 eV from the main peak. This then is the second spin–orbit peak in BIS of TmS which has an intensity ten times lower then the primary peak. Thus, for the first time, it has been shown that the empty $4f^{13}$ peak in TmS lies little above E_F. However, a BIS spectrum has only an experimental resolution of about 1 eV, i.e., within this 1 eV width the empty $4f^{13}$ state can be anywhere. Baer et al. (1994) thus performed optical reflectivity spectroscopy, also at He temperatures, on TmS and could clearly find a transition at about 50 meV. This transition then has been identified as from the partially filled 5d conduction band near the Fermi level into the empty $4f^{13}$ state. Optical transitions into empty 4f states have been found for the first time in CeO_2 (Marabelli and Wachter 1987a), CeF_4 (Marabelli et al. 1992a), in YbN (Degiorgi et al. 1990 and in YbP and YbAs (Degiorgi et al. 1993).

This has consequences regarding the surface sheet. At the surface the missing half space can provoke Tm ions to expand, which results at least in a partial occupation of the $4f^{13}$ state immediately above E_F and thus in an intermediate-valent surface sheet of TmS as observed experimentally by surface sensitive techniques such as photoemission (Kaindl et al. 1982, Baer et al. 1994).

It also becomes clear that in TmSe a change of the lattice constant in either direction, which can be achieved by pressure, stoichiometry variation or alloying, will move more or less electrons in or out of the 4f band. One can also say that the 4f band gets moved through the Fermi level. Thus it is no surprise that the Hall effect and the thermopower change sign when the Fermi level crosses the middle of the 4f band. The same effect occurs in SmS, where, however, it has been observed with various amounts of alloying (Jayaraman 1979).

An interesting case is given by $Tm_xY_{1-x}Se$, i.e., the dilution of TmSe with YSe, interesting because there seem to be indications that even with $x = 0.01$ or 0.05 the Tm ions are in the intermediate-valent state (Holtzberg et al. 1979). The best conclusive evidence for this is the observation of the M-edge X-ray absorption technique, which, with its highly selective resonance, is able to detect (as a high-energy technique) Tm in two valence states (Kaindl et al. 1983). The observation is that Tm in these highly diluted compounds is more divalent than in TmSe. As explanation we can offer again fig. 60. YSe has the same electronic structure as TmSe but with no 4f levels. The ionic radius of Y^{3+} corresponds nearly precisely to the one of Tm^{3+}, so as a first idea one would suggest that Tm enters the mixed compound as trivalent ion, having thus an empty $4f^{13}$ level above E_F. However, the Fermi level is in the highly diluted Y compound much higher than in TmSe because each Y donates one electron to the conduction band, not just 0.75 as in TmSe. Thus the Fermi level will reach the $4f^{13}$ level and electrons will partially fill this level. Because there are so many electrons available this level will be filled to a larger extent than in TmSe and the valency will be shifted towards more divalency as observed experimentally. However, no long range antiferromagnetism can exist, no hybridization gap can occur and the question is whether there is at least a hybridized 4f band in the sense of fig. 1a. Holland-Moritz (1983) performed inelastic neutron scattering on TmSe and its diluted alloys with Y. He could show that there may exist a real valence fluctuation in the dilute system i.e., a time coherent fluctuation

process on a single Tm ion. In addition Holland-Moritz (1983) measured the quasi-elastic line width in TmSe and found it to be 7 meV, a value which appeared also in optical experiments and Raman scattering. However, it should be noticed that neutron scattering depends on magnetic dipole transitions, optics on electric dipole transitions, the impurity induced Raman effect could be unaffected by selection rules. A quasi-elastic line width corresponds to a relaxation time of excited magnetic transitions.

It is no surprise that the non-intermediate-valent compounds $Tm^{3+}S$ and $Tm^{2+}Te$ show magnetic order, but it is one of the special features of intermediate-valent TmSe that it also exhibits magnetic order. The magnetic properties of the Tm monochalcogenides have first been described by Bucher et al. (1975) on the basis of classical magnetic measurements. Later neutron scattering experiments by Bjerrum-Møller et al. (1977), Shapiro et al. (1978) and Lassailly et al. (1984) also revealed this type of magnetic ordering. So TmS has a Néel temperature $T_N = 5.2$ K with a modulated incommensurate structure which can be seen in a first approximation as a type II antiferromagnetic ordering. Stoichiometric TmSe orders as a type I antiferromagnet below 3.1 K, while a Tm deficiency leads to a type II antiferromagnet. Above an applied field of about 0.5 T TmSe exhibits ferromagnetic ordering, it should thus be termed a metamagnet. TmTe has been reported to have Néel temperatures of 0.21–0.23 K, depending on unknown stoichiometry, but Lassailly et al. (1984) report on 0.43 K with a type II antiferromagnetic structure.

4.3.1.1. *Electronic properties of TmSe.* In the early days of research on intermediate-valent TmSe a lot of discrepancies occurred between the main research centers of that time, AT&T and IBM, about the physical properties and degree of valence mixing of TmSe (see, e.g., Parks 1976). The reason was that TmSe exists with various stoichiometries and the stoichiometry had not been controlled in the 1970's. However, there was never a question that TmSe can be prepared in an intermediate-valent form and in fig. 61 we show a XPS spectrum of TmSe where the divalent and trivalent final state spectra can be discerned with their typical ladder-like structure.

The first systematic and comprehensive studies of TmSe in its composition range have been performed by Batlogg et al. (1979b). In this work it has been shown that Tm_xSe exists in a homogeneity range of $0.87 < x < 1.05$ where x denotes the ratio mol Tm/mol Se and not the occupation number of either the cation or the anion sublattice. This means that in addition one may have equal vacancies in both sublattices. A critical inspection of all data available in the literature leads to the lattice constant of a $Tm^{3+}Se = 5.63$ Å and the one of a $Tm^{2+}Se = 5.94$ Å. Experimentally it is found that $Tm_{0.87}Se$ has a lattice constant of 5.628 Å (Batlogg et al. 1979b) and we expect the material to contain only trivalent Tm. That a Tm deficiency can lead to an integer trivalent TmSe can be made plausible by inspecting fig. 60. In an integer valent material like GdSe a cation deficiency in the order of 15% does not by itself lead to a drastic reduction in lattice constant, only in the second digit after the decimal point (Hauger et al. 1976). But it leads to a 15% reduction in carrier concentration. Since in TmSe E_F is pinned in the 4f level, the latter is appreciably emptied and the trivalent configuration gets enhanced. This, however, reduces the lattice constant significantly, increasing as a consequence the crystal-field splitting of the 5d states. This

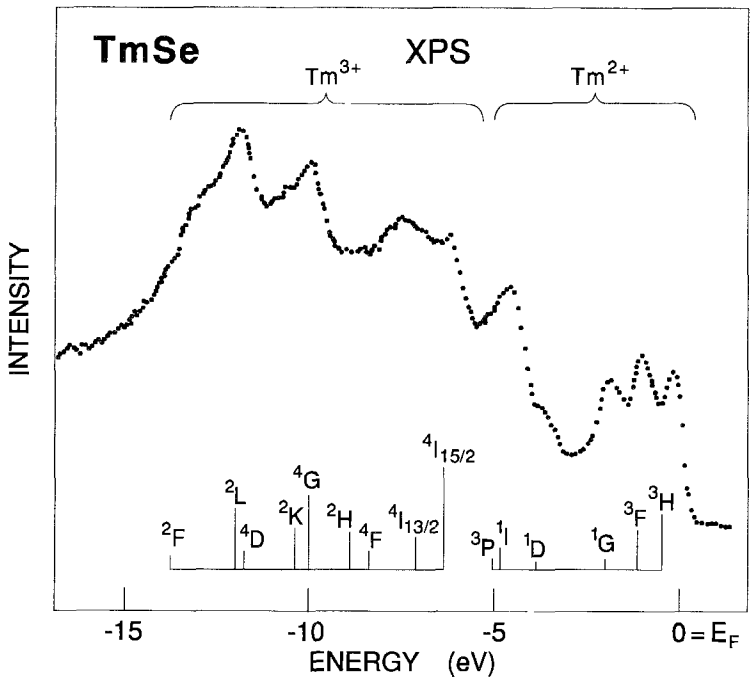

Fig. 61. XPS spectrum of TmSe with ladder-like final state spectrum. (After Campagna et al. 1976.)

turns into an avalanche process until the $4f^{13}$ state is emptied completely and snaps above the Fermi level as in TmS.

The interesting case is that one has within the TmSe system a trivalent reference compound and can investigate the evolution of intermediate valence without using external parameters like pressure or temperature. In the stoichiometry variation of Tm_xSe it is essential that the stoichiometry is chemically controlled, the materials are never handled in air and all physical investigations are made on the same single crystal of the desired composition. Some physical properties of a series of compositions are compiled in table 3.

In fig. 62 we show the temperature dependence of the electrical resistivity for two compositions of Tm_xSe, a nearly stoichiometric one and the trivalent reference compound $Tm_{0.87}Se$. The latter shows a maximum in the resistivity at about 50 K which is probably due to magnetic scattering or thermal excitations into the empty $4f^{13}$ state above E_F. In any case this material behaves metallic. The nearly stoichiometric composition instead, shows an activated behavior of the resistivity. The insets in fig. 62 show the resistivity near the Néel temperature. In fig. 63 we show the temperature behavior of the electrical resistivity for the whole stoichiometry range and it is evident that all compositions of Tm_xSe, with the exception of the trivalent reference compound, show an activated behavior and, in addition, can be judged intermediate valent on the basis of the

Table 3
Physical paramcters of Tm_xSe (after Batlogg ct al. 1979b)

x (= Tm/Se)	0.87	0.97	1.0	1.05
Lattice constant a_0 (Å)	5.628	5.663	5.705	5.715
Valence of Tm from a_0	+3	+2.89	+2.75	+2.72
Compressibility κ at 300 K (10^{-6} bar^{-1})	1.5±0.15	3.8±0.2	4.2±0.2	3.2±0.2
Electrical resistivity at 300 K ($\mu\Omega$cm)	210±10	225±15	235±15	255±20
Paramagnetic Curie temperature θ_p (K)	−19.5	−24	−29	−31.5
Effective magnetic moment p (μ_B/Tm)	7.29	6.77	6.39	6.02
Néel temperaturc T_N (K)	~4.2	~3	2.9	3.5

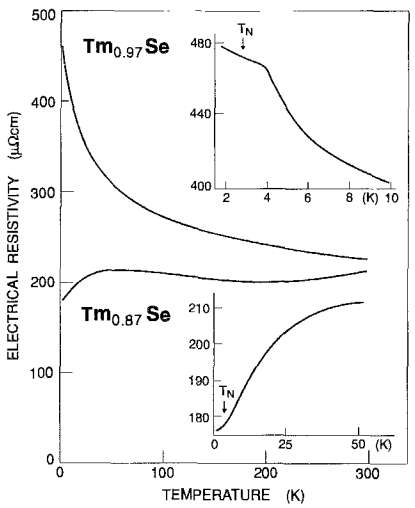

Fig. 62. Temperature dependence of the electrical resistivity of intermediate-valent $Tm_{0.97}Se$ and trivalent $Tm_{0.87}Se$. The inset shows the resistivity near the Néel temperature. (After Batlogg et al. 1979b.)

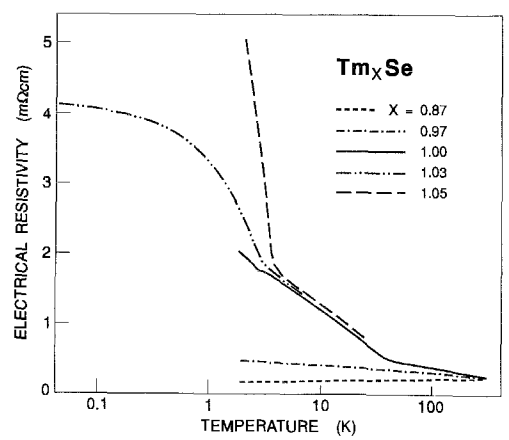

Fig. 63. Electrical resistivity of Tm_xSe of compositions listed in table 3. $Tm_{1.03}Se$ has been measured down to 50 mK. (After Batlogg et al. 1979b.)

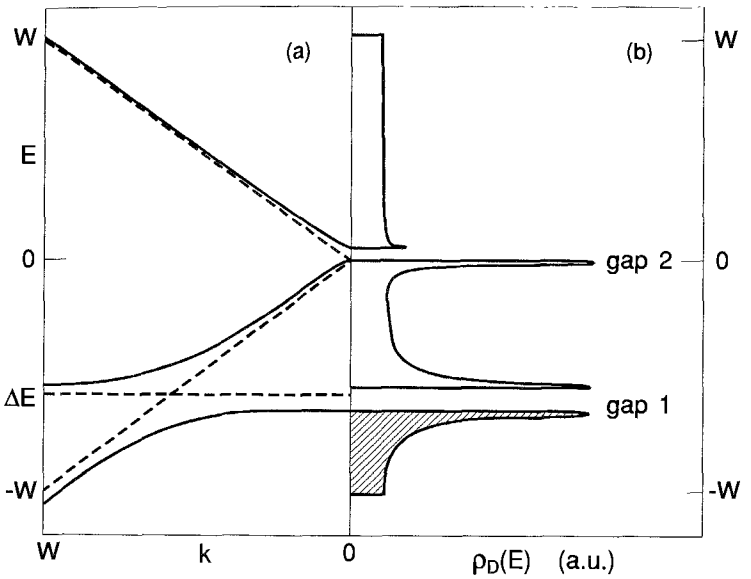

Fig. 64. Sketch of the dispersion and density of states of intermediate-valent, antiferromagnetic TmSe. −W to W represents the bandwidth of the 5d band. (After Alascio et al. 1982.)

lattice constant in table 3. The activation energies ΔE which can be extracted on the basis of an $\exp -\Delta E/2k_B T$ plot (between 5 and 50 K) are about 1 meV. In two cases (Batlogg et al. 1979b and Haen et al. 1979), one of which is shown in fig. 63, the resistivity has been measured down to 50 mK and 8 mK, respectively, but the resistivity still increased. If there is a drop in the resistivity towards zero K then it must be at very low temperatures because the gap is so small. In the light of what has been said for similar measurements in the borides and Sm monochalcogenides it must be concluded that intermediate-valent Tm_xSe also has a hybridization gap.

This is somewhat surprising since, according to the Luttinger theorem, TmSe is an odd electron system, either $4f^{13}$ or $4f^{12}5d$, and it should not have a hybridization gap. However, and this is special, the materials all exhibit antiferromagnetic order. In the antiferromagnetic state the unit cell is twice the chemical cell and the Brillouin zone is half the one for a normal fcc structure. Thus new zone boundaries appear. In the double magnetic unit cell the number of electrons is 26 and thus even, which means that a hybridization gap may exist according to the Luttinger theorem, since in addition all electrons in the 5d band are those originally coming from the 4f state.

It has been argued that the gap which is observed experimentally might be the antiferromagnetic gap in the spin wave spectrum. However, as shown in fig. 64, the magnetic gap would be expected in the middle of the 5d band. The total 5d bandwidth ($-W \div W$) is about 5 eV (see, e.g., the BIS spectrum in fig. 59), so the magnetic gap is about 2.5 eV above the bottom of the band (Alascio et al. 1982, Wachter 1986). However, E_F is only about 1 eV above the bottom of the band (see, e.g., the XPS spectrum in fig. 59).

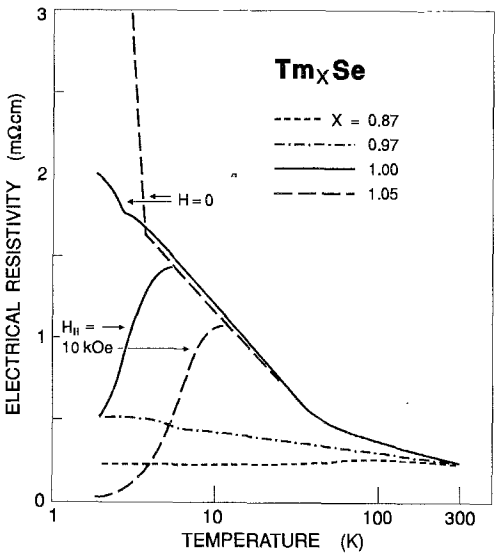

Fig. 65. Temperature and magnetic field dependence of the electrical resistivity of Tm_xSe. (After Batlogg et al. 1977.)

Thus a hybridization gap with the Fermi level in the gap and, in addition, a magnetic gap far above E_F can coexist as shown in fig. 64. Why then does the resistivity in figs. 62 or 63 rise already appreciably above T_N? We propose that the resistivity at first rises with decreasing temperature for the same reason as in non-hybridized trivalent $Tm_{0.87}Se$ due to magnetic scattering, i.e., a mobility effect, above but near T_N it rises due to the freezing out of carriers because of the opening of the hybridization gap in the magnetic short range ordering region.

The resistivity rise is in total only about one order of magnitude. Similarly as for the Sm monochalcogenides the conclusion then is that the gap is only a pseudo gap and that hybridization does not occur over the whole Brillouin zone. As we discussed already in section 4.2.2.1 the fcc structure does not permit complete hybridization and this is in agreement with the observation. In the case of TmSe we do not expect significant help from a specific heat measurement as performed by Bucher et al. (1975) since it is too difficult to subtract a magnetic part from the specific heat to obtain the electronic γ value, since the magnetic moments of an intermediate-valent material are ill defined.

An experimental proof of the idea of the folding of the Brillouin zone in TmSe due to antiferromagnetic order can be given by making resistivity measurements in an applied field of larger than about 0.5 T because then the material becomes ferromagnetic, the folding of the Brillouin zone should disappear and as a consequence the hybridization gap should vanish in agreement with the Luttinger theorem. Indeed this is shown in fig. 65 for Tm_xSe where for some compositions a magnetic field of 1 T (10 kOe) is applied. The resistivity now drops to even below the room temperature values in agreement with the above argumentation. The compounds remain intermediate-valent, ferromagnetic and with no hybridization gap. We consider this as a great success of the ideas developed by means of the Luttinger theorem.

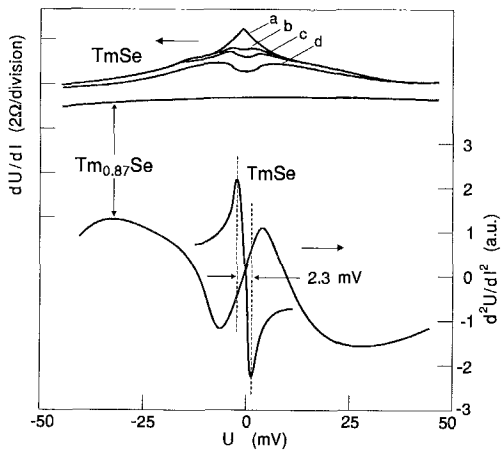

Fig. 66. Dynamic resistance dU/dI and derivative d^2U/dI^2 of a-$Tm_{0.87}Se$ and a-$Tm_{0.98}Se$ at 1.7 K: (a) $H=0$; (b) $H=17$ kOe; (c) $H=26$ kOe; (d) $H=43$ kOe. (After Frankowski and Wachter 1982a.)

Further support of a hybridization gap in the field free antiferromagnetic state can be obtained by point contact spectroscopy. The experiment has been carried out by Frankowski and Wachter (1982a) and is shown in fig. 66. Like in fig. 17 for SmB_6, in fig. 18 for YbB_{12}, or in fig. 50 for IV SmS, we observe for TmSe a peak in the dU/dI spectrum which has a half-width of 2.3 meV (1.2 meV by Güntherodt et al. 1982), as defined by the points of inflection and shown in the second derivative in the lower part of fig. 66. Like in the other materials this number would give the gap value. Proof about this can be obtained by applying a magnetic field larger than necessary to drive the compound into ferromagnetism, i.e., larger than about 0.5 T. It is observed in fig. 66 that the peak gradually transforms into a minimum as we approach ferromagnetic saturation. In the ferromagnetic state TmSe is still intermediate valent but it has no hybridization gap, instead it has a density of states maximum at E_F as in fig. 1a. Pragmatically we may draw the conclusion that a peak in the point contact spectrum represents a gap in the density of states, a minimum represents a density of states maximum. Without driving this point further for the moment we can also look at the integer trivalent $Tm_{0.87}Se$ also shown in fig. 66. The first derivative has no structure anymore and is a flat line, neither is there a minimum nor a maximum in the density of states at E_F. The second derivative of $Tm_{0.87}Se$ shown in the lower part of fig. 66 then, is proportional to inelastic excitations as there are phonon density of states, crystal-field excitations and magnetic excitations. Inelastic neutron scattering also performed on $Tm_{0.87}Se$ by Furrer et al. (1982), revealed a peak at about 4.5 meV which has been ascribed to crystal-field excitations. This energy corroborates our peak at 5 meV in the point contact spectrum.

Further evidence for a hybridization gap in TmSe comes from far infrared spectroscopy at low temperatures. The reflectivity has been measured by Marabelli and Wachter (1987b) between 1 meV and 12 eV using four spectrometers. The samples were mounted in a cryostat in He exchange gas guaranteeing the quoted temperatures. In addition the dc conductivity has been measured on the same crystal at the relevant temperatures.

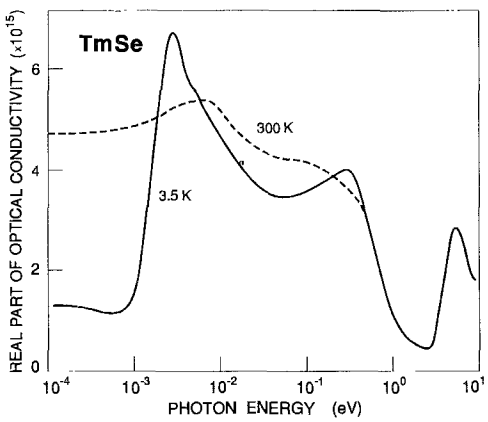

Fig. 67. Real part of the optical conductivity of stoichiometric TmSe at 300 and 3.5 K. (After Marabelli and Wachter 1987b.)

The reflectivity spectrum (relative accuracy 0.1% in the far infrared) has been analyzed in terms of the Kramers–Kronig relation with the usual extrapolations towards $\omega \to \infty$. For the extrapolation towards zero frequency we used the Hagens–Rubens relation and the measured dc conductivity. At room temperature we obtained an excellent fit over a large frequency range. For low temperatures the low-energy structures in the meV range prevented such a simple fit. However, independent of what extrapolation we used, we always found a free carrier behavior for the lowest energies, then a gap or a pseudo gap followed by a first transition at about 3 meV (fig. 67). In the figure the change of the dc conductivity between 300 and 3.5 K, as measured independently by the temperature dependence of the resistivity (fig. 63), is well reproduced. We thus tried to fit the optical conductivity obtained from the Kramers–Kronig relation by subtracting a Drude term (see fig. 68) and tried to perform again a Kramers–Kronig transformation of the dielectric constant ε_{2b} to obtain $\varepsilon_1(\omega) = \varepsilon_{1D} + \varepsilon_{1b}$, where ε_{1b} is the contribution of bound electrons undergoing optical transitions. We thus obtain $\varepsilon_2(\omega)$ and $\varepsilon_1(\omega)$ from which we could calculate the reflectivity again to obtain new starting values for a cyclic fit. In fig. 69 the imaginary part of the dielectric constant of TmSe is depicted with the Drude term separated. It is remarkable that ε_2 at 3.5 K amounts to 2×10^4 in the far infrared, much more than in SmB_6 (fig. 12, 1500) or IV SmS (fig. 48, 600), making the 3 meV transition the dominant one in the spectrum. (On this scale of ε_2 only the far infrared peaks can be discerned.) The reason is of course that the f–f interband transition across the hybridization gap occurs at lower energies than in the other two examples.

The reflectivity of TmSe in the far infrared has been measured before in our laboratory by Batlogg (1981a), but only at 300 K. Our new measurement, represented in fig. 67, is in excellent agreement with this first result with the lowest energy peak at 7 meV. Batlogg (1981b) thought this peak is connected with charge fluctuations, which in our present interpretation, is only true in a very indirect sense. Figures 67 and 68 show that near the Néel temperature of 3.5 K a still lower energy peak at 3 meV appears, which, after subtraction of the Drude term, is shown separately in figs. 68 and 69. In fig. 67

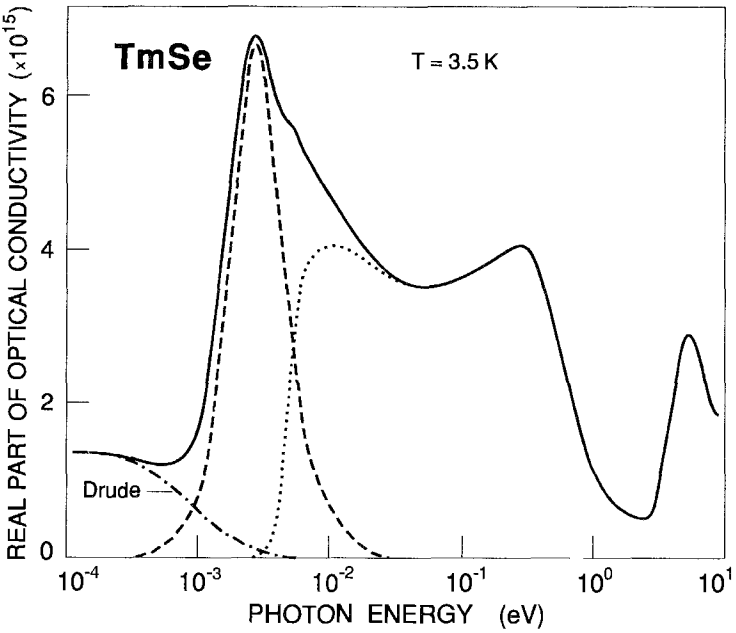

Fig. 68. Real part of the optical conductivity of TmSe at 3.5 K where a Drude term is subtracted. (After Marabelli and Wachter 1987b.)

we can discern a total of four optical transitions besides the Drude term. In analogy with our former far infrared experiments on SmB_6, IV SmS and YbB_{12} we interpret the highest energy transition as p–d interband transition, the peak at 0.3 eV as d–f transition, as exemplified in fig. 2d, and the lowest energy peak at 3 meV as inter 4f transition across a hybridization gap of 1 or 2 meV. (see fig. 2d). The oscillator strength of this lowest energy peak is with 0.01 of a typical magnitude for such an intra 4f transition with a strong 5d admixture due to hybridization effects. The d–f transition at 0.3 eV has an oscillator strength of about 0.3, again typical for such a transition.

So far we have deliberately omitted the discussion on the peak at 7 meV at 300 K which is at about 8 meV at 3.5 K (see fig. 68). This peak must have something to do with phonons, but the question is in what way? Enhanced phonon transitions in intermediate-valent materials have been observed before by Travaglini and Wachter (1984a,b) but there were always optical phonons involved at energies of about 20 meV. In TmSe the optical phonon energy is at 18.6 meV as shown by Treindl and Wachter (1979) and Mook and Holtzberg (1981). However, in the Raman spectrum of TmSe (see below) with stoichiometries exhibiting intermediate valence, a new and additional Raman peak was observed at 300 K, within the acoustic band, at 60 cm^{-1} or conspicuously at 7.4 meV. Similarly the reflectivity peak at 7 meV is only present at intermediate-valent TmSe and not in $Tm_{0.87}Se$ (Marabelli and Wachter 1987b). We think that this peak is the

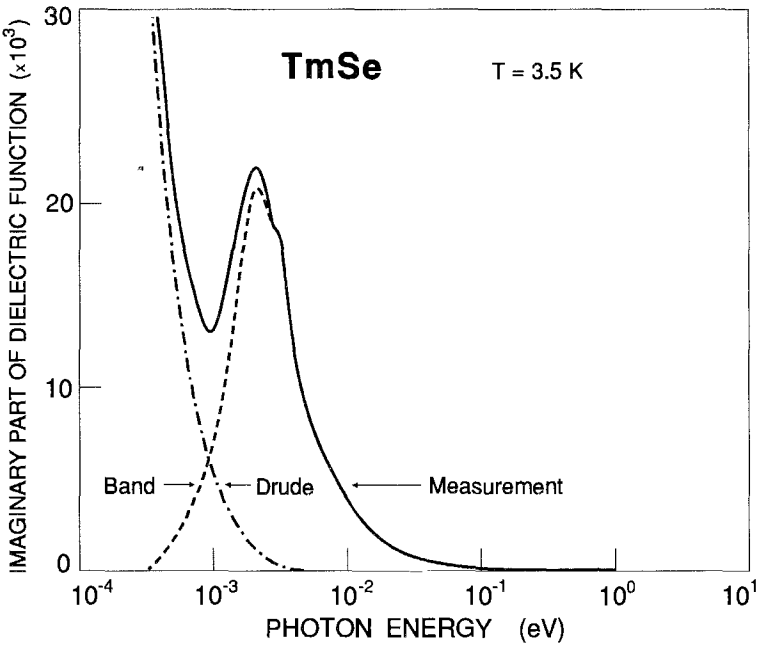

Fig. 69. Imaginary part of the dielectric function of TmSe at 3.5 K. The Drude term (dashed–dotted) and the band contribution (dashed) are shown separately. (After Marabelli and Wachter 1987b.)

long discussed f–d acoustic wave or acoustic plasmon, first mentioned by Varma (1976) and Sinha and Varma (1983). The latter paper also explains a transfer of oscillator strength through the many body correlations, so that this transition can also be observed optically.

For TmSe we refrained from computing the density of states because the optical structures are at such a low energy and consequently at the limits of our spectrometers that the uncertainty becomes too large. However, qualitatively it is evident that the JDS is at least one order of magnitude larger than in SmB_6, where it is already much larger than in IV SmS. Again this is a consequence of the narrow gap to start with.

Just as in the other intermediate-valent compounds with the Fermi level within the hybridization gap, pressure can be used to close the gap. Resistivity experiments up to 3 GPa and low temperatures have been performed by Lapierre et al. (1981b) and simultaneously the lattice constant has been observed with neutron scattering. The trend of pressure increase goes in the direction of a Tm deficiency, i.e., the compound becomes more trivalent, although, quite naturally, a compound under pressure, with the same lattice constant as a Tm deficient compound, does not have the same resistivity. The pressure dependence of the resistivity is complex, because not only does one close the gap, but the magnetic phase also changes from AF I to AF II, which has its influence on the resistivity. It appears that pressure has to be larger than 3 GPa to close the gap completely.

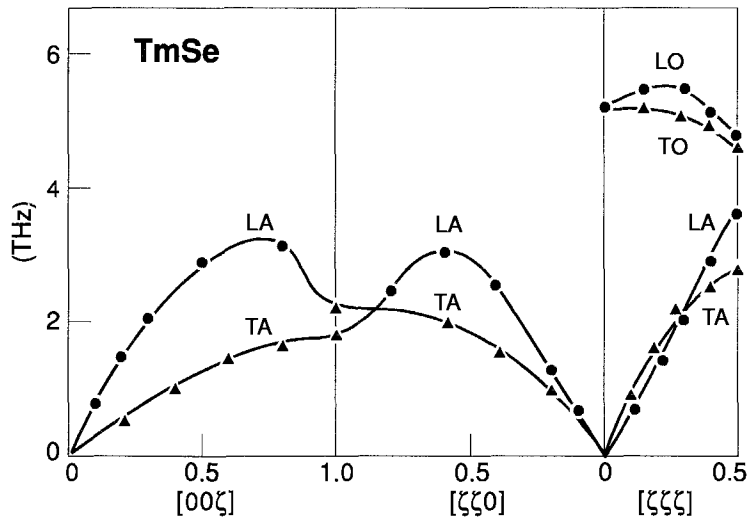

Fig. 70. Phonon dispersion of intermediate-valent TmSe. (After Mook and Holtzberg 1981.)

4.3.1.2. *Lattice-related properties of TmSe.* The phonon dispersion of TmSe has been measured with inelastic neutron scattering by Mook and Holtzberg (1981); it is shown in the main directions in fig. 70. Due to the large absorption cross section for neutrons of Tm, the optical modes could only be obtained in the [111] direction. Bührer et al. (1982) repeated the inelastic neutron scattering on $Tm_{0.99}Se$ and obtained also a few points of the optical branch in the other directions. But more importantly, they measured also the trivalent reference compound $Tm_{0.87}Se$ so that the phonon dispersion is known for both compositions. Just as in SmB_6 or IV SmS the TO and LO modes coincide at Γ, in TmSe also at L and they show softening. For the acoustic modes the LA branch is for the most part of the Brillouin zone below the TA branch and thus reflects the anomalous behavior of an intermediate-valent compound with strong electron–phonon coupling. This behavior is also observed in SmB_6 and IV SmS. The dispersionless gap mode found for the first time in $Sm_{1-x}Y_xS$ by Mook et al. (1978) and attributed to the Y substitution, absent in high-pressure SmS (Mook et al. 1982), but conspicuously present in SmB_6 (Alekseev et al. 1989), is again absent in TmSe. We think that this mode is present in all intermediate-valent compounds discussed so far and in this respect we are in agreement with Stüsser et al. (1982). Crystal-field excitations have not been found in TmSe, just as they are absent (IV SmS) or not clearly defined as in SmB_6 (Alekseev et al. 1993). Again, we want to mention here that when the energy of the crystal-field excitation is much larger than the hybridization energy, we expect to see such transitions with, e.g., inelastic neutrons. Indeed, in trivalent $Tm_{0.87}Se$ a crystal-field excitation has been observed at 5 meV by Furrer et al. (1982) with inelastic neutron scattering.

Raman scattering is also capable of giving information on the phonon properties of TmSe. In fig. 71 we compare the Raman intensity of the trivalent $Tm_{0.87}Se$ (Mörke and

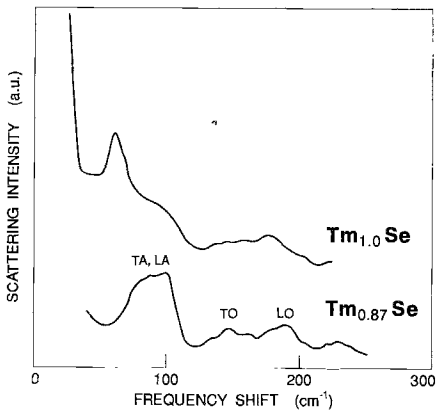

Fig. 71. Raman scattering of cleaved TmSe and trivalent $Tm_{0.87}Se$. (After Treindl and Wachter 1979 and Mörke and Wachter (1983.)

Wachter 1983) with the one of a stoichiometric TmSe (Treindl and Wachter 1979) when excited with Ar^+ 5140 Å. Both crystals are cleaved and at room temperature. Since Raman scattering in rocksalt type structures is symmetry forbidden, one measures, in fact, a defect-induced weighted phonon density of states spectrum. For $Tm_{0.87}Se$ in the lower part of the figure we have indicated an assignment of the peaks to TA, LA, TO and LO modes. For TmSe, however, we find in the optical phonon range only one main peak at 175 cm^{-1} and some smaller structures below 160 cm^{-1} (Treindl and Wachter 1979). This is in complete agreement with Stüsser et al. (1982). However, it is known from the phonon dispersion of Mook and Holtzberg (1981) that the gap between acoustic and optic modes in TmSe is between 3.6 and 4.6 THz (see fig. 70) which corresponds to 121 and 154 cm^{-1}, respectively. Stüsser et al. (1982) now say that a peak at 145 cm^{-1} in the Raman scattering, which can also be discerned in fig. 71, is the gap mode in IV TmSe. This gap mode shows a softening to 123 cm^{-1} in a binary solution of $TmSe_{0.85}Te_{0.15}$ in which the Tm has a valency of 2.6 which at least goes in the right direction. Since Stüsser et al. (1982) have observed these gap modes also in other IV materials of Sm compositions they consider this a general behavior of IV materials, in contrast to the opinion of Mook and Holtzberg (1981) who attributed this gap mode only to local modes due to cation substitutions.

When we look now at the acoustic branch of TmSe we can discern a double peak structure with a strongly enhanced intensity at 60 cm^{-1}, enhanced and shifted with respect to the trivalent $Tm_{0.87}Se$ reference compound. Since the acoustic modes go from zero to 121 cm^{-1} this peak is near the middle of the acoustic spectrum.

Since the Raman effect in these rocksalt structures measures the weighted phonon density of states, it is desirable to compute this entity. Cclio et al. (1981) used an 8 parameter shell model with deformable ions in the spirit of Bilz et al. (1979). They decomposed the density of states into a Γ_1^+ breathing part and a Γ_{25}^+ quadrupolar deformability of the Se ion. The parameters were adjusted using the lattice constant, the

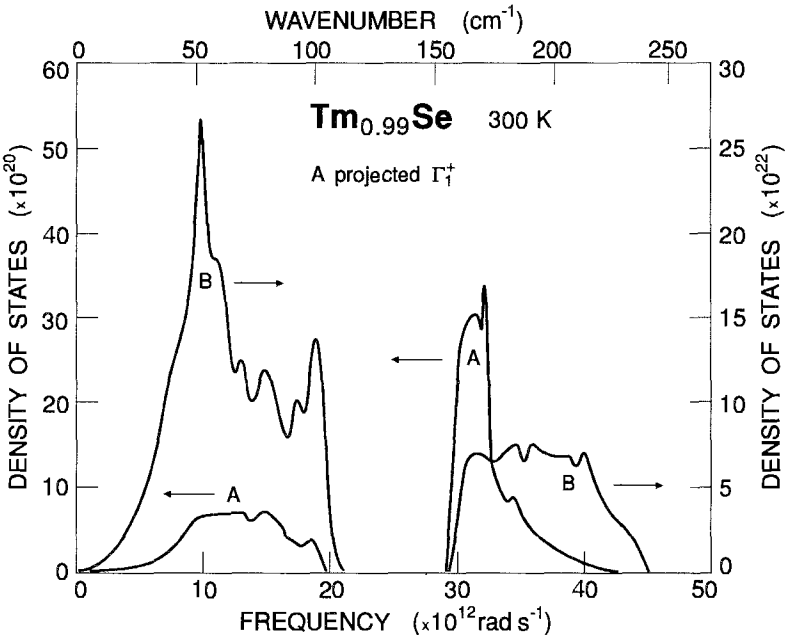

Fig. 72. Calculated phonon density of states of intermediate-valent $Tm_{0.99}Se$ Curve A (left-hand scale): Γ_1^+ projected density of states. Curve B (right-hand scale): total density of states. (After Celio et al. 1981.)

elastic constants from Boppart et al. (1980a) and ωTO and ωLO at the Γ and L points from Mook and Holtzberg (1981). The result is shown in fig. 72, where the one phonon density of states (B) is shown which should be compared with the experimental curve of fig. 71 for TmSe. Very good agreement is obtained indeed. Especially the prominent peak at about 60 cm^{-1} is clearly reproduced by the theory. In the measurement of Stüsser et al. (1982) this 60 cm^{-1} peak is hardly seen, although the measurements on $TmSe_{0.85}Te_{0.15}$ are identical to those of Treindl and Wachter (1980) including the peak now at about 55 cm^{-1}. In fig. 72, represented by curves (A), the Γ_1^+ projected density of states is also shown, which is not very pronounced at the experimentally determined 60 cm^{-1} peak. Thus, the latter is mainly due to density of states effects from flat regions in the phonon dispersion along [100] and [110] near the X point (see fig. 70). A phonon density of states calculation is also reported by Bührer et al. (1982), again for $Tm_{0.99}Se$ and $Tm_{0.87}Se$. It is remarkable that the optic modes in the density of state calculation show 2 peaks for the trivalent reference compound, but only one peak for the IV TmSe, just as is shown experimentally in fig. 71.

To support the quality of the theoretical calculation of the phonon spectra by Celio et al. (1981) we show in fig. 73 the peak position of the LO band from Raman scattering in Tm_xSe, Gd_xSe and LaSe of Treindl and Wachter (1979), which for the trivalent lanthanide selenides represent the effect of the lanthanide contraction, and for the IV Tm_xSe shows the softening of the LO phonons due to IV effects. The asterisks

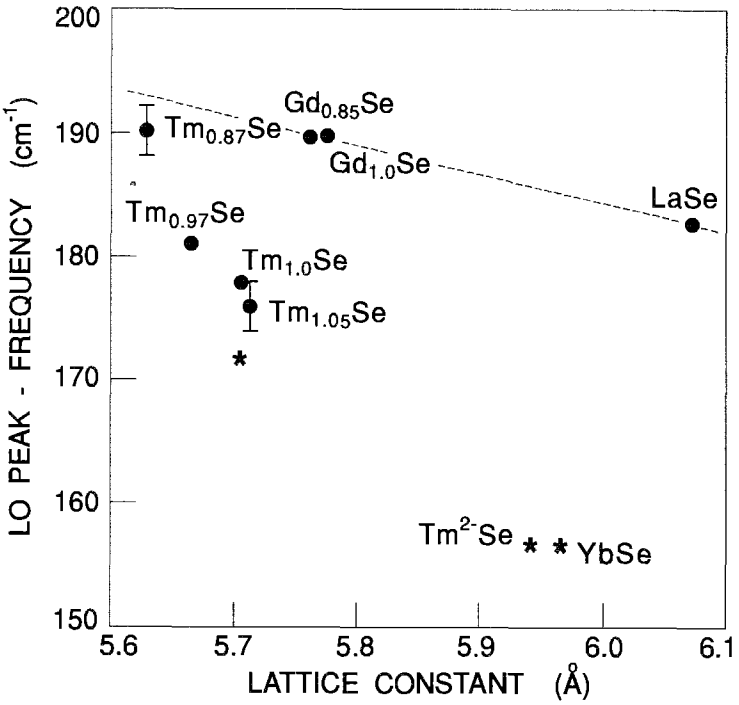

Fig. 73. LO peak Raman frequency of some lanthanide selenides. Experimental points after Treindl and Wachter (1980). The asterisks are the calculated LO peak frequencies according to Celio et al. (1981).

in the figure are the calculations of the LO modes of IV TmSe and divalent reference compounds.

There is, however, another anomaly in the phonon spectrum of TmSe, namely in the [111] direction where the LA branch is for most of the Brillouin zone below the TA branch, a quite general phenomenon for all IV compounds discussed so far. In fig. 74 Treindl and Wachter (1980) have constructed [111] LA dispersion curves for $Tm_{0.87}Se$ and TmSe. For the slope at the zone center they used the measured sound velocities of Boppart et al. (1980a,b) $v_{LA} = 3.48 \times 10^5$ cm s^{-1} for $Tm_{0.87}Se$ and $v_{LA} = 2.56 \times 10^5$ cm s^{-1} for TmSe. For the zone boundary they used the cutoff frequency of the acoustic band at 105 cm^{-1} for both compositions. For the integer trivalent compound a linear chain model with only next neighbor forces is fitted to these values. One obtains the undistorted LA dispersion curve of fig. 74. For the IV TmSe one assumed a renormalization of the phonon frequencies in such a way that it produces the correct slope at $k = 0$ and a flattening of the dispersion curve in the middle of the Brillouin zone as measured by Mook and Holtzberg (1981). The chosen type of renormalization indeed produces an additional peak in the scattering intensity at 60 cm^{-1}. Here we want to remark again that at the same energy of 60 cm$^{-1} \approx 7$ meV we observed in the far infrared, at

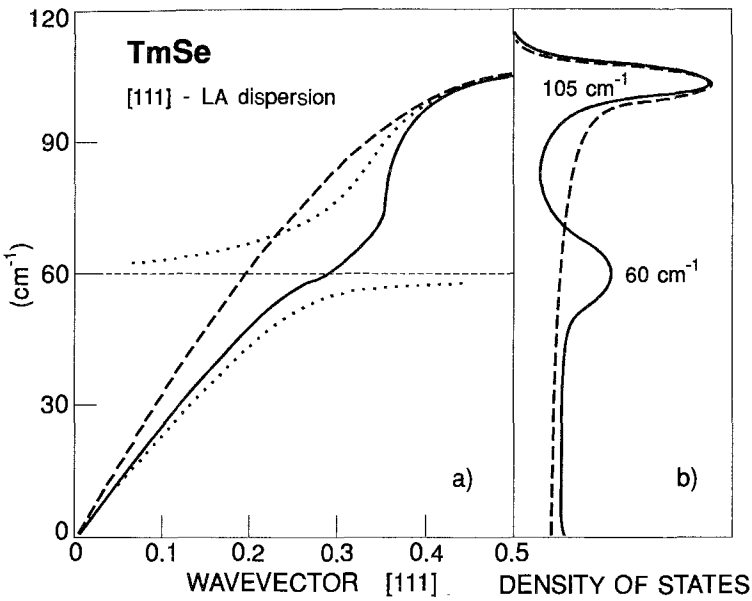

Fig. 74. (a) LA phonon dispersion in the [111] direction for intermediate-valent TmSe. An electronic plasmon mode is shown as the dashed horizontal line. Mixed electronic plasmon–phonon modes are shown with dotted lines. The heavy dashed line is the phonon mode without interaction. (b) Phonon density of states with (solid curve) and without (dashed curve) plasmon interaction. (After Treindl and Wachter 1980.)

room temperature and at 3.5 K, and only in IV TmSe, an absorption mode as shown in fig. 68. We have shown already (as discussed for SmB_6 and IV SmS) that we have a heavy mass plasma resonance and a light weight mass plasma resonance of electrons. The heavy mass plasma resonance in TmSe is near 7 meV (see fig. 68, end of Drude tail). In the acoustic–plasmon mode such a plasmon of heavy mass and a longitudinal vibration mode couples to LA phonons (Varma 1976 and Sinha and Varma 1983). Thus we sketched into fig. 74 the purely electronic plasmon mode at $60\,cm^{-1}$ or 7 meV as the dashed horizontal line. Interaction of this mode with the LA phonons then splits the LA branch and mixes the electronic mode with the phonons as shown by the dotted curves. The excitation remains phonon-like and electron-like in regions of $\omega(k)$ space away from the crossing point. This model also gives a very high density of states at the frequency of the electronic eigenstate and would therefore also explain the anomalous Raman peak. In fact, Ichinose and Tamura (1983) calculated the phonon excitation spectrum of intermediate-valent TmSe starting from the proposal of Treindl and Wachter (1980) and found very good agreement with fig. 74 when the electronic excitation spectrum is near 7 meV.

The $60\,cm^{-1}$ Raman mode becomes much more enhanced when the crystals are not cleaved but polished. Treindl and Wachter (1980) have shown that polishing of an integer-valent crystal (e.g. GdSe) produces no additional peaks in the Raman spectrum. Thus, in fig. 75a we show the Raman scattering of mechanically polished Tm_xSe and clearly

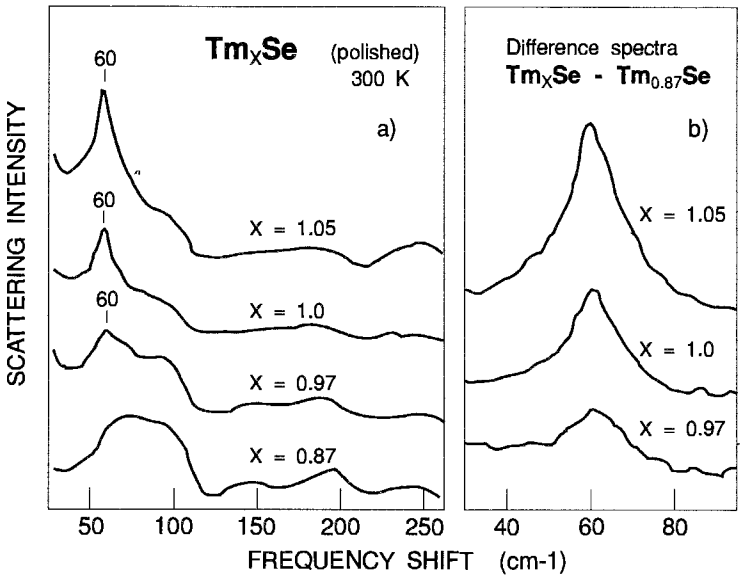

Fig. 75. (a) Raman scattering of polished Tm_xSe single crystals. (b) Difference spectra: intermediate-valent Tm_xSe minus trivalent $Tm_{0.87}Se$. (After Treindl and Wachter 1980.)

observe the evolution of the 60 cm^{-1} peak with increasing valence mixing, in fig. 75b we even show the difference spectrum Tm_xSe–$Tm_{0.87}Se$ from where it also becomes clear that the trivalent referencc compound does not have the 60 cm^{-1} peak.

To obtain the elastic properties of TmSe several attempts to measure the compressibility have been performed. Ott et al. (1977) measured the dynamical compressibility of an unknown quality TmSc and obtained the value $\kappa = 1.9 \times 10^{-6}$ bar^{-1}. Later the static compressibility was remeasured on stoichiometric TmSe using strain gauges and external pressure and the value $\kappa = 4.2 \times 10^{-6}$ bar^{-1} was obtained (Ott et al. 1978, Batlogg et al. 1979b). Boppart ct al. (1980a) measured the ultrasound velocities on $Tm_{0.99}Se$ and the trivalent $Tm_{0.87}Se$ as function of temperature which is shown in fig. 76. From the sound velocities it was possible to compute the elastic constants c_{11}, c_{12} and c_{44} and from these again the compressibility. The data are collcctcd in table 4. For once, the room temperature compressibility of Ott et al. (1978) and Batlogg et al. (1979b) could be confirmcd with $\kappa = 4.61 \times 10^{-6}$ bar^{-1} to be compared with the trivalent reference compound $\kappa = 1.46 \times 10^{-6}$ bar^{-1}. Since $\kappa = 1/B$, the bulk modulus is appreciably softer in IV TmSe than in the reference compound. This remains so even at 4.2 K. Regarding the elastic constants c_{ij} it is remarkable that c_{12} is negative for IV TmSe, but positive for the reference compound. This then was the first time that a negative c_{12} has been reported for any IV substance. Even at 4.2 K c_{12} remained negative for IV TmSe.

In fig. 77 we exploit the possibilities of a negative elastic constant. Boppart et al. (1980a) have glued strain gauges on the faces of a ⟨100⟩ cleaved crystal of IV TmSe

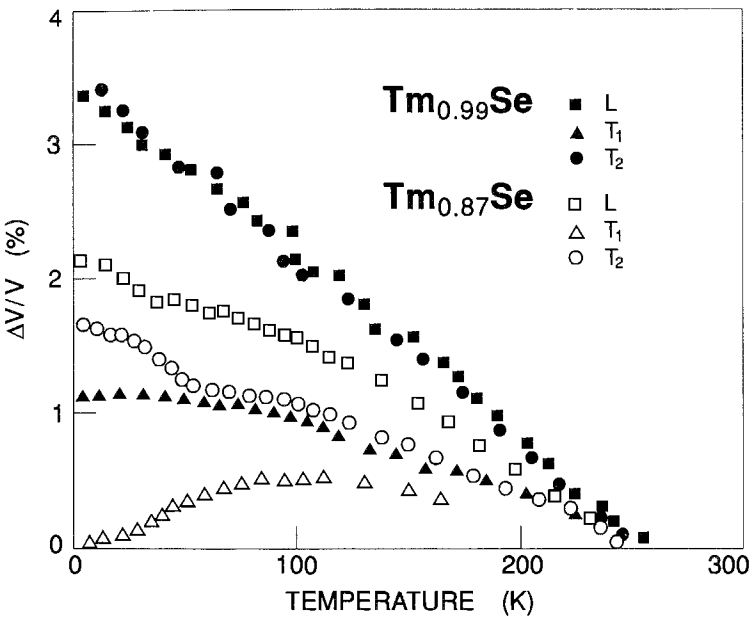

Fig. 76. Relative change in sound velocity of $Tm_{0.99}Se$ and $Tm_{0.87}Se$ with temperature. The symbols refer to v_{T_1} (c_{44} mode), v_{T_2} ($c_{11} - c_{12}$) mode and v_L ($c_{11} + c_{12} + 2c_{44}$). (After Boppart et al. 1980a.)

Table 4
Elastic data for $Tm_{0.87}Se$ and $Tm_{0.99}Se$

Compound	300 K Data		4.2 K Data	
	GPa	10^{-6} bar^{-1}	GPa	10^{-6} bar^{-1}
$Tm_{0.87}$	$c_{11} = 163 \pm 1$,	$\kappa = 1.46 \pm 0.02$[a],	$c_{11} = 172 \pm 1$,	$\kappa = 1.36 \pm 0.02$
	$c_{44} = 29 \pm 1$,	$\kappa = 1.5 \pm 0.15$[b]	$c_{44} = 29 \pm 1$,	
	$c_{12} = 21 \pm 1$		$c_{12} = 24 \pm 1$	
$Tm_{0.99}$	$c_{11} = 179 \pm 1$,	$\kappa = 4.61 \pm 0.1$[a],	$c_{11} = 195 \pm 1$,	$\kappa = 4.0 \pm 0.1$
	$c_{44} = 27 \pm 1$,	$\kappa = 4.2 \pm 0.2$[b]	$c_{44} = 28 \pm 1$,	
	$c_{12} = -57 \pm 1$		$c_{12} = -60 \pm 1$	

[a] Boppart et al. (1980a).
[b] Ott et al. (1978), Batlogg et al. (1979b).

and applied uniaxial pressure along the x direction, looking for length changes in the same direction. This yields the compliance s_{11}, which is positive, i.e., the crystal contracts in the same direction as the pressure is applied. This is normal and selfevident. Now they applied pressure in the x direction and looked in the y direction with strain gauges. A normal material will expand in this direction in order to keep (in first approximation) its volume constant. However, as seen in the lower part of fig. 77, the compliance s_{12} is also positive, meaning that the crystal spontaneously contracts also in this direction, and of course also in the third direction, i.e., its volume shrinks with uniaxial compression. Only

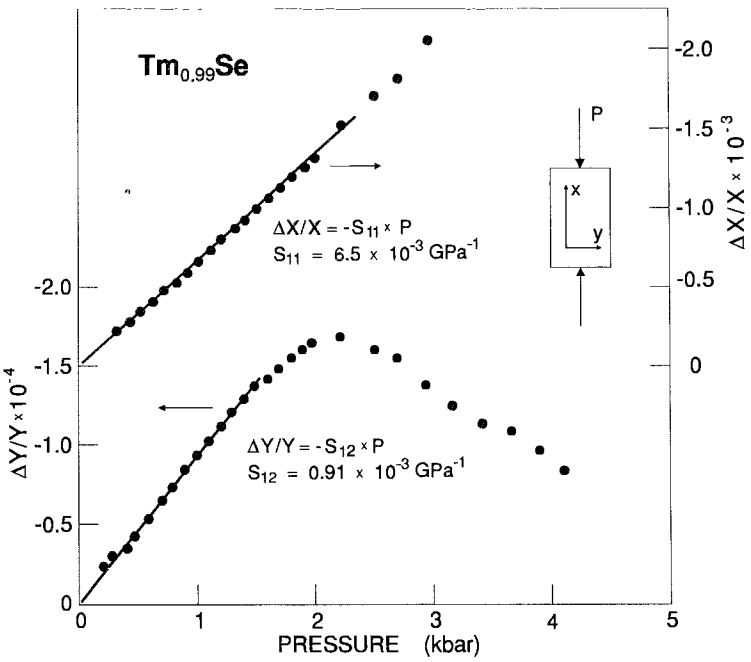

Fig. 77. Elastic compliance s_{ij} of $Tm_{0.99}Se$ under uniaxial pressure p in the x direction. (After Boppart et al. 1980a.)

for pressures more than 2 kbar the material behaves normal. The explanation is of course that pressure changes the relative occupation of f and d bands, and thus the valence, but this effect is isotropic as we have seen already. Thus it is only cubic IV materials which will exhibit this phenomenon. The intriguing effect is that, e.g., the y planes in fig. 77 will be high-pressurized surfaces, but at the same time they are free surfaces on which phenomena like photoemission under pressure can be studied.

Ott et al. (1977) have reported on a positive c_{12} on an undefined TmSe, on the same sample on which also the unexpectedly low compressibility has been observed. It now becomes clear that this sample of TmSe must have had appreciable Tm deficiency because all values are close to the ones of $Tm_{0.87}Se$. In contrast, Barth and Güntherodt (1982) have measured the ultrasound velocities with Brillouin scattering in stoichiometric TmSe and computed the elastic moduli. They obtain with $c_{12} = -68$ GPa nearly the same value as Boppart et al. (1980a) with $c_{12} = -57$ GPa at room temperature. The values for TmSe are of the same size as in IV SmS, where we computed a c_{12} of -51 GPa from the data of Melcher et al. (1975).

A last point shall be made in fig. 76. The temperature dependence of the ultrasound velocity is very different regarding the IV TmSe and the trivalent reference compound $Tm_{0.87}Se$. Characteristic deviations are found near 60 K for the trivalent $Tm_{0.87}Se$ which are typical for crystal-field excitations. In fact 60 K corresponds to about 5 meV,

exactly the value where one observed a peak in the inelastic neutron scattering of Furrer et al. (1982) which has been identified as a crystal-field excitation and where also a peak has been found in the point contact spectroscopy of Frankowski and Wachter (1982a). Thus it is clear that trivalent TmSe compounds show crystal-field effects, whereas IV TmSe compounds do not show crystal-field effects (see fig. 76). Hybridization thus either smears out the crystal-field levels so much that they can no longer be observed or it directly suppresses the crystal-field splitting because J is no longer a good quantum number in IV compounds. It is, however, possible that crystal-field excitations can still be observed when their transition energy is much larger than the hybridization energy.

Lattice anomalies of Tm_xSe as function of temperature, composition and magnetic field have been measured by Ott et al. (1977), Batlogg et al. (1977) and Batlogg et al. (1979b). Unfortunately the temperature range of magnetostriction or lattice contraction was only below about 15 K, i.e., in the range of magnetic ordering. The phenomena are quite complex inasmuch as when one goes from $x=1$ to $x=0.87$ one not only changes the type of magnetic ordering but one also changes the crystal-field effects being absent for $x=1$ but becoming increasingly important for x towards 0.87. As function of a magnetic field one is changing again the magnetic structure, TmSe being metamagnetic and for fields above 0.5 T ferromagnetism sets in. In any case, the lattice anomalies observed below 15 K are mostly related to the various types of magnetic ordering and crystal-field effects. On the other hand the phenomena typical for intermediate valence, namely a lattice expansion below about 50 K, and exemplified for SmB_6 in fig. 24 have not been investigated so far. Thus we performed for the first time a measurement of lattice dilatation on TmSe in the temperature range between 10 K and 300 K with the same equipment used for the thermal expansion of SmB_6. To our disappointment TmSe exhibits only the classical thermal contraction with decreasing temperature expected for any normal solid. No expansion at low temperatures was found as is typical for IV materials. Either the small hybridization gap or the influence of magnetisms may be the cause for this behavior.

4.3.1.3. *Magnetic susceptibility of TmSe.* One of the standard methods to measure the degree of valence mixing in intermediate-valent materials is to investigate the magnetic susceptibility and determine from this the effective magnetic moment. Usually this method yields a different degree of valence mixing than obtained with other standard methods. Here the usual theories tacitly assume an alloy-like mixture of $4f^n$ and $4f^{n-1}$ ions with their standard S, L and J values. For low temperatures the method fails because hybridization, which introduces randomness in the magnitude of the magnetic moments, is not considered. For high temperatures the method may be correct for thermal energies high above the hybridization energy where the system performs real temporal fluctuations of the valence because k_BT is a large energy transfer. Room temperature measurements certainly are not high enough. Most measurements of the Curie constant, however, are performed at temperatures less than room temperature and as a consequence the valence determination is not correct. This can indeed be seen in fig. 25 for SmB_6 and fig. 57 for IV SmS where the fits with the simple theory yield good agreement with the susceptibility

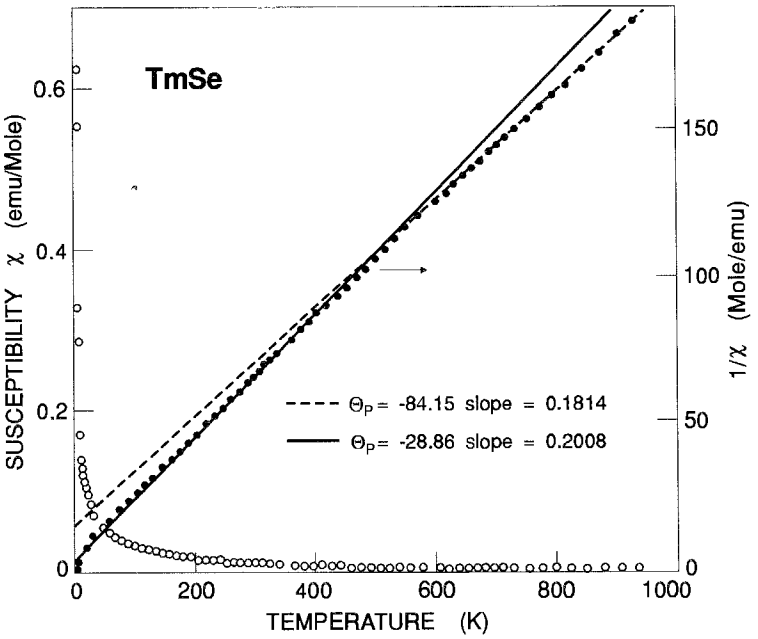

Fig. 78. Magnetic susceptibility and inverse susceptibility of intermediate-valent TmSe. Solid and open circles: experimental points. The dashed and solid lines correspond to $\Theta_p = -84.15$ K and $\Theta_p = -28.86$ K. (After Wachter 1982.)

but the valence mixing is not exactly the same as determined from lattice constant or the Mössbauer effect. In stoichiometric TmSe the valency determined from the Curie constant from temperatures below 300 K is 2.56 (Batlogg et al. 1979b) contrasting with the valency determined from the lattice constant at room temperature 2.75 (Batlogg et al. 1979b).

To clear the situation Wachter (1982) has measured the susceptibility of TmSe up to 950 K. A measurement up to 800 K has been done before by Holtzberg et al. (1979) but the new results are different. The utmost care has been taken to select the sample. It was taken from a batch of stoichiometric TmSe and the lattice constant of the selected crystal was 5.708 Å. The sample was sealed under high vacuum in a quartz ampoule. After two reproducible runs up to the maximum temperature in a carefully calibrated balance checked for its linearity with Gd_2O_3 the sample has been transferred to the low-temperature apparatus. Afterwards the lattice constant has been checked again and found to be the same as before. Subsequently the crystal has been analyzed for its composition by wet chemical analysis and has been found stoichiometric within the error limits of 0.5%.

Figure 78 shows the results obtained. Below 300 K the measurements of Batlogg et al. (1979b) could be reproduced (the numbers in parentheses refer to Batlogg et al. 1979b): $\Theta_p = -28.86$ K (−29), valence mixing obtained from the Curie constant and linear interpolation between $C_M^{3+} = 7.15$ and $C_M^{2+} = 2.56$ yields a valency of 2.53 (2.56).

At temperatures above 650 K one obtains $\Theta_p = -84.1$ K and the valence mixing is 2.64. Thus the valence determined from the lattice constant and from the Curie constant are approaching each other. To be comparable, however, one should also use a valence determined from a high-temperature lattice constant as well. It is thus evident that a valence determined conventionally and a Curie constant below 300 K never agrees. It should also be mentioned that a valence determination from a high-temperature Curie constant is only reasonable for a Tm or Yb compound, because only in these lanthanide ions the next highest spin–orbit split level is about 0.75 and 1.25 eV, respectively, above the ground state and thus separated enough not to be appreciably thermally populated.

It appears that in TmSe we reach the entropy limit at high enough temperatures, i.e., $k_B T \gg \Delta_{CF}$, where all crystal-field levels are equally populated. Then the valence mixing should be given by the degeneracy of the J levels: Tm^{2+} $2J+1 = 8$, Tm^{3+} $2J+1 = 13$. The valence is then $2 + 13/21 = 2.63$, in excellent agreement with the experiment. One can also turn the argument around and say that the spread of energy levels Δ_{CF} should be much less than say 800 K = 66 meV, to be equally populated and then the hybridization energy will be less than about 10 meV in agreement with other estimates. It is also clear that at low temperatures a magnetic saturation cannot be achieved with accessible field strengths, and has never been obtained experimentally for any IV compound, because the magnetic field should have at least the size of the hybridization energy, but fields of 50 T correspond to only 2.9 meV.

4.3.2. *Alloys of TmSe*

4.3.2.1. *$TmSe_{1-x}Te_x$.*

4.3.2.1.1. *Electronic properties.* The alloy system $TmSe_{1-x}Te_x$ is one of the most important alloy systems in the field of intermediate valence since it keeps the important cation untouched and contains intermediate-valent metals, intermediate-valent semiconductors, semiconductor–metal transitions, ferro- and antiferromagnets and a new ground state of condensed matter, the excitonic insulator. The Fermi level generally will be in a hybridization gap, but not in some cases, especially when the material exhibits spontaneous magnetic moments. For the sake of completeness and consistency the entire alloy system will be treated in this section.

The pseudobinary alloy system $TmSe_{1-x}Te_x$ has a miscibility gap for $0.2 < x < 0.4$ (Kaldis et al. 1979, 1982). For $x < 0.2$ the compounds are intermediate-valent metals and for $x > 0.4$ " intermediate-valent semiconductors". Let us first look at the metallic compositions. It has already been mentioned (Batlogg et al. 1979b) that in the stoichiometry variation of Tm_xSe the strongest valence mixing which could be achieved was 2.72^+. However, with the expansion of the Tm lattice by addition of Te, the valence mixing may be enhanced further and more divalent Tm ions may be created. For increased valence mixing above that obtainable in Tm_xSe, Varma has predicted (Varma 1977, 1979) a ferromagnetic exchange interaction on the basis of a double exchange mechanism. The metallic $TmSe_{1-x}Te_x$ compounds with x close to 0.2 offer the highest degree of valence mixing and from the lattice constant a valency of 2.5^+ can be deduced.

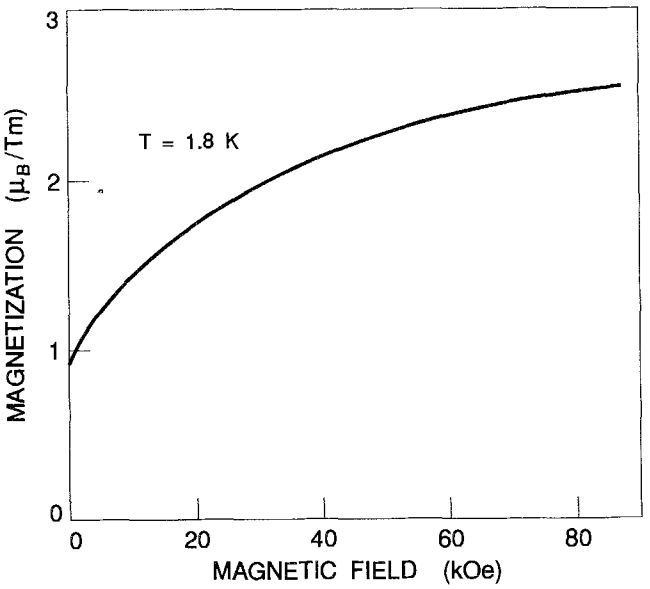

Fig. 79. Magnetization of $TmSe_{0.83}Te_{0.17}$ vs. magnetic field, corrected for demagnetization effects. (After Batlogg et al. 1979c.)

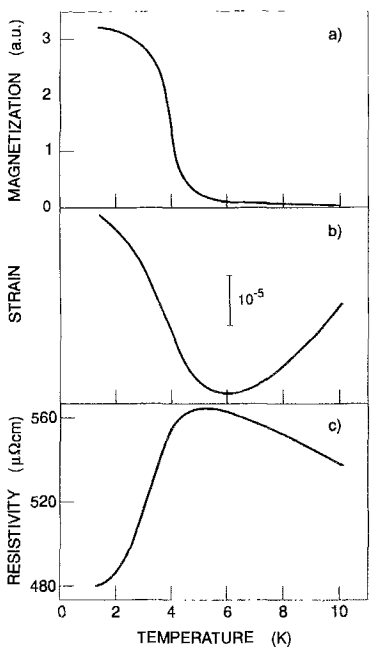

Fig. 80. Temperature dependence of (a) the magnetization in an external field of 100 Oe; (b) the total strain along [100] in zero external field; (c) the zero-field electrical resistivity. (After Batlogg et al. 1979c.)

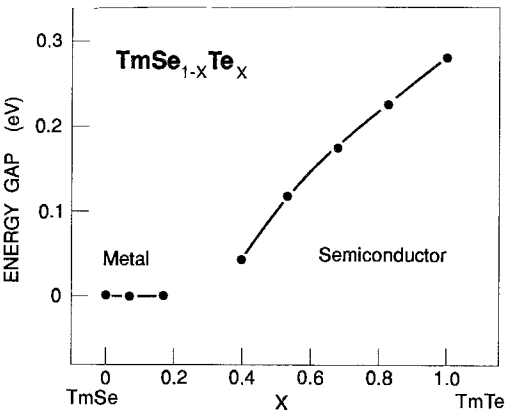

Fig. 81. The energy gap of metallic and semiconducting compositions of $TmSe_{1-x}Te_x$. (After Boppart 1983.)

Indeed, Batlogg et al. (1979c) could show with a composition of $TmSe_{0.83}Te_{0.17}$ a spontaneous magnetization at 1.8 K. The demagnetization correction was carefully taken into account and the magnetization in zero field amounts to $0.8\mu_B$ per Tm ion, reaching $2.5\mu_B$ at 9 T (90 kOe), far below either the divalent or the trivalent saturation moment of Tm (fig. 79). In fig. 80a we show the initial susceptibility in fields of less than 100 Oe and note that here also a signature typical for a spontaneous magnetization is obtained. Similar results are found in another metallic $TmSe_{0.91}Te_{0.09}$ compound where also a spontaneous magnetic moment in zero field of $0.3\mu_B$ exists. In fact, elastic neutron scattering has been performed on these samples by Fischer et al. (1982) and long range ferromagnetism has been found with the absence of any antiferromagnetic Bragg peaks.

We have argued above that in TmSe in an applied magnetic field larger than 0.5 T ferromagnetism sets in which had consequences in the resistivity–temperature curve (fig. 65) and in the point contact spectrum (fig. 66). The evidence seemed to suggest that a hybridization gap disappeared. Qualitatively this can be understood as the appearance of a spontaneous magnetization with a Weiss field of some tens of tesla results in a Zeeman splitting of all levels of several meV, especially in the density of states peaks in fig. 2d, thus closing or smearing out the hybridization gap. Anderson (1981) suspected also that in a ferromagnetic intermediate-valent material no hybridization gap exists and Martin and Allen (1979) even made quantitative estimates.

For $TmSe_{0.83}Te_{0.17}$ we can experimentally show in fig. 80c that the resistivity in zero field, after having a maximum near the magnetic ordering, temperature drops to low values. In fact, this curve looks exactly like the resistivity curve of TmSe in an applied field of 1 T (10 kOe) shown in fig. 65, whereas TmSe in zero field shows a steady increase of the resistivity towards the lowest temperatures. Thus it becomes evident from these experiments that metallic alloys of $TmSe_{1-x}Te_x$ have a larger valence mixing compared with Tm_xSe, even up to 2.5^+, and this, in accordance with the predictions of Varma (1977, 1979), results in the appearance of a spontaneous magnetic moment in zero field which, as a consequence, closes the hybridization gap being present in antiferromagnetic TmSe.

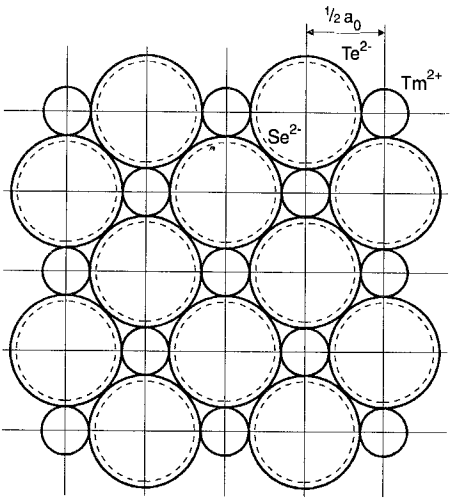

Fig. 82. $TmSe_{1-x}Te_x$ lattice in the rocksalt structure. (After Wachter 1986.)

We now turn to the semiconducting compositions of $TmSe_{1-x}Te_x$ with $0.4 \leqslant x \leqslant 1$. Starting from semiconducting TmTe with an energy gap ΔE of 320 meV between the localized $4f^{13}$ state and the bottom of the empty $5dt_{2g}$ conduction band (Suryanarayanan et al. 1975, Batlogg et al. 1979a), by substituting Te by Se the lattice constant is reduced, which increases the crystal-field splitting of the t_{2g} and e_g states of the 5d conduction band and thus reduces ΔE. In the semiconducting composition range ΔE is reduced from 320 meV for TmTe to 40 meV for $x = 0.4$. These numbers are obtained from Arrhenius plots of the electrical resistivity. In fig. 81 we give the energy gap of $TmSe_{1-x}Te_x$ as a function of x. In fig. 82 we show a quantitative example how such a composite lattice should be visualized. It is obvious that an increase of the lattice constant, concomitant with the Te substitution, exerts a lattice pressure on the Tm ions in addition to the reduction of ΔE. This drives the Tm ions into intermediate valence in spite of the fact that a semiconductor gap still exists. This is proven by plotting the lattice constant in isovalent Vegard lines from which, e.g., a degree of valence mixing of 2.3 for $TmSe_{0.6}Te_{0.4}$ can be derived (Kaldis et al. 1982). Further evidence that semiconducting samples of $TmSe_{1-x}Te_x$ are intermediate valent is given by the negative Poisson ratio which is due to a negative elastic constant c_{12}, which so far has always been found for intermediate-valent materials (see below). For this reason the term "intermediate-valent semiconductor" has been coined by Boppart et al. (1982). We visualize this in the following way. The $4f^{13}$ level, though still genuinely below the bottom of the 5d conduction band is, however, so close by, that virtual transitions between the 4f and 5d state become increasingly possible so the 4f state has a certain 5d admixture and vice versa. The loss of f charge leads to all the lattice-related evidences of intermediate-valent semiconductors. With the narrowing of the gap the effect of local correlations between f holes and d electrons, i.e., excitonic effects, become important. These strongly correlated states retain their quantum numbers L, S and J of the original 4f

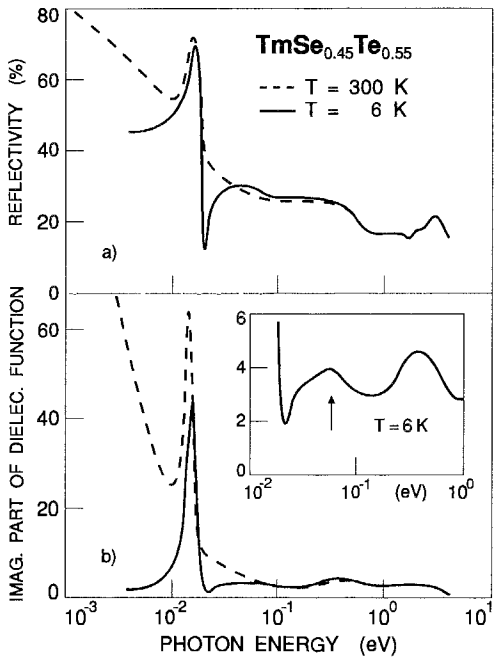

Fig. 83. (a) Optical reflectivity and (b) imaginary part ε_2 of the dielectric function of $TmSe_{0.45}Te_{0.55}$ as function of photon energy. Solid lines at 6 K, dashed lines at 300 K. The structure in ε_2 at 60 meV (arrow in the inset) is suggested to be due to an exciton. (After Neuenschwander and Wachter 1990a,b.)

Table 5
Phonon modes at the Γ point of the Brillouin zone of semiconducting compositions of $TmSe_{1-x}Te_x$ (from Schneider 1983 and Neuenschwander and Wachter 1990a)

Compound	ω_{TO} (meV)	ω_{LO} (meV)
TmTe	13.9	17.2
$TmSe_{0.32}Te_{0.68}$	15.3	19.1
$TmSe_{0.45}Te_{0.55}$	16	20

configuration until the pressure-induced semiconductor–metal transition (SMT), where these states begin to overlap more and more and form an intermediate-valent metal with a hybridization gap at low temperatures, as long as they are antiferromagnetic.

In the semiconducting compositions, especially those with an appreciable f–d hybridization and thus a small energy gap, optical measurements in the far infrared have been performed as exemplified in fig. 83 for $TmSe_{0.45}Te_{0.55}$ (Neuenschwander and Wachter 1990a,b). Here the reflectivity has been measured between 4.3 eV and 1 meV at 300 K and at 6 K (fig. 83a) and a Kramers–Kronig analysis has been performed to obtain the dielectric functions, where the imaginary part ε_2 has been plotted in fig. 83b. At 16 meV which is best observed in ε_2 at low temperature there is a TO (Γ) phonon (the phonons of other $TmSe_{1-x}Te_x$ compositions are compiled in table 5). At room temperature there is in addition a free carrier absorption which is frozen out at low temperature as

Table 6
Physical properties of semiconducting $TmSe_{1-x}Te_x$ (after Boppart and Wachter 1984a)

x	0.40	0.55	0.68	0.83[a]	1.0
Lattice constant (Å)	6.02	6.14	6.21	6.28	6.36
Resistivity at ambient pressure (Ω cm)	1.8×10^{-3}	3.2×10^{-2}	0.28	1.5	18[b]
Resistivity at high pressure (10^{-4} Ω cm)	3.2	4.0	3.6	4.0	
Energy gap ΔE (meV)	40	110	170	210	300
Transition pressure (GPa)	0.3	1.2	1.4	2.0	2.5
$(d\Delta E/dp)$ (meV GPa^{-1}) at lower pressure	−67	−126	−130	−140	−110[c]
$(d\Delta E/dp)$ (meV GPa^{-1}) at higher pressure		−99	−110	−98	
Initial compressibility (10^{-11} Pa^{-1})	5.0	3.3	3.0	2.4	2.2
Maximum compressiblity (10^{-1} Pa^{-1})		35	17	9	
at pressure (GPa)		1.2	1.4	1.9	

[a] Boppart et al. (1980b).
[b] Köbler et al. (1981).
[c] Jayaraman (1979).

expected for a semiconducting composition. The insert of fig. 83b shows besides this phonon two other absorptive peaks at 60 and about 130 meV. The low-energy edge of the latter peak (about 110 meV) coincides with the gap (ΔE) determination from resistivity measurements (table 6). We are left with the 60 meV peak which is suggested to be an exciton peak (see below). On semiconducting $TmSe_{1-x}Te_x$ compositions also the Raman effect has been measured by Mörke and Wachter (1983). In all cases there are weighted phonon density of states peaks near 150 cm^{-1} (about 17 meV) in agreement with the optical spectra, however, in addition there are (at 300 K) the famous 60 cm^{-1} (7 meV) structures, already discussed above for Tm_xSe and related to the acoustic plasmon mode. This is one of the many manifestations that prove that the semiconducting compositions of $TmSe_{1-x}Te_x$ indeed are intermediate valent.

Magneto-optical Kerr effect in the range of several eV has also been measured by Schoenes et al. (1985) on a semiconducting composition of $TmSe_{0.32}Te_{0.68}$ in 4 T and at 10 K. An atomic coupling scheme with JJ coupling of the final state $4f^{12}5d$ of the $4f^{13} \rightarrow 4f^{12}5d$ optical transition could be established which is in agreement with the observed structures. In agreement with earlier statements (see above) these high-energy transitions break up the hybridization so that the atomic values of the mainly divalent ions can be observed. However, this was not the case in IV metallic TmSe which in a field of 4 T is ferromagnetic at 2 K and thus shows a very different magneto-optical structure.

The semiconductor gaps ΔE can be closed by hydrostatic pressure and an intermediate-valent–semiconductor to intermediate-valent–metal transition can take place. Figure 84 shows the behavior of the resistivity under pressure for 4 different $TmSe_{1-x}Te_x$ compositions. The transitions are continuous for the first three compositions with transition pressures of 2.0, 1.4 and 1.2 GPa, respectively. For pure TmTe, which shows quite the same behavior under pressure, the transition occurs at $\approx$2.5 GPa (Jayaraman 1979). For $x \approx 0.4$, however, the transitions are discontinuous with transition

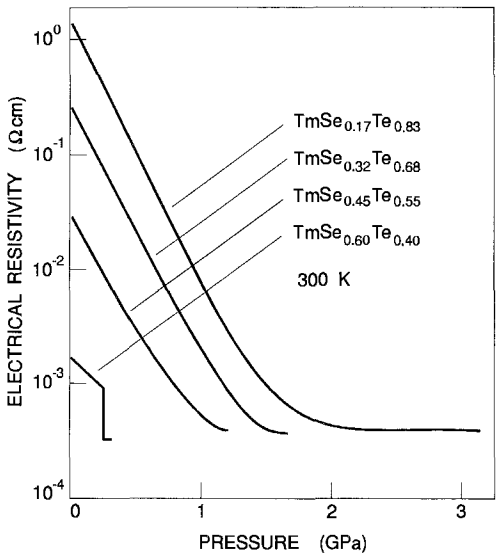

Fig. 84. Electrical resistivity of $TmSe_{1-x}Te_x$ vs. pressure at 300 K. Note the first-order transition for $TmSe_{0.60}Te_{0.40}$. (After Boppart and Wachter 1984a.)

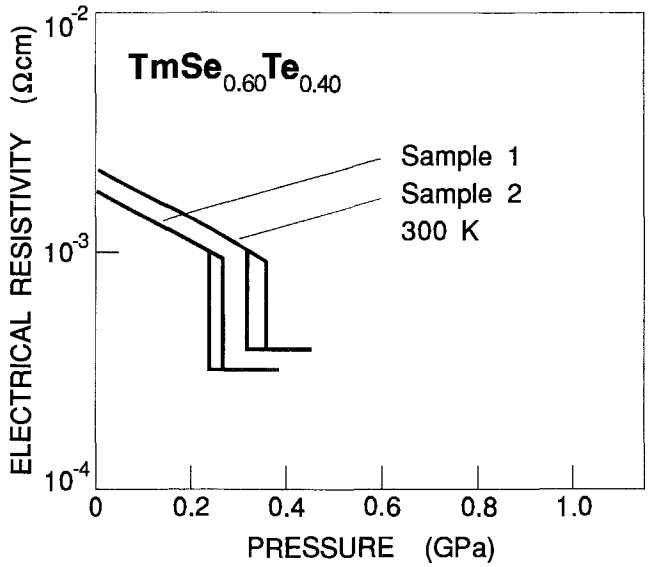

Fig. 85. Electrical resistivity vs. pressure at 300 K of two $TmSe_{0.60}Te_{0.40}$ single-crystal samples from the same batch. (After Boppart 1983.)

pressures varying between 0.3 and 0.5 GPa, as shown by Boppart and Wachter (1984a) and Boppart (1983). The observed first-order transition in $TmSe_{0.6}Te_{0.4}$ is only the second example of a semiconductor–metal transition, SMT, (beside SmS) in the field of intermediate-valent compounds. The proof of a first-order transition is further exemplified by the hysteresis loop shown in fig. 85, as demanded by thermodynamic considerations.

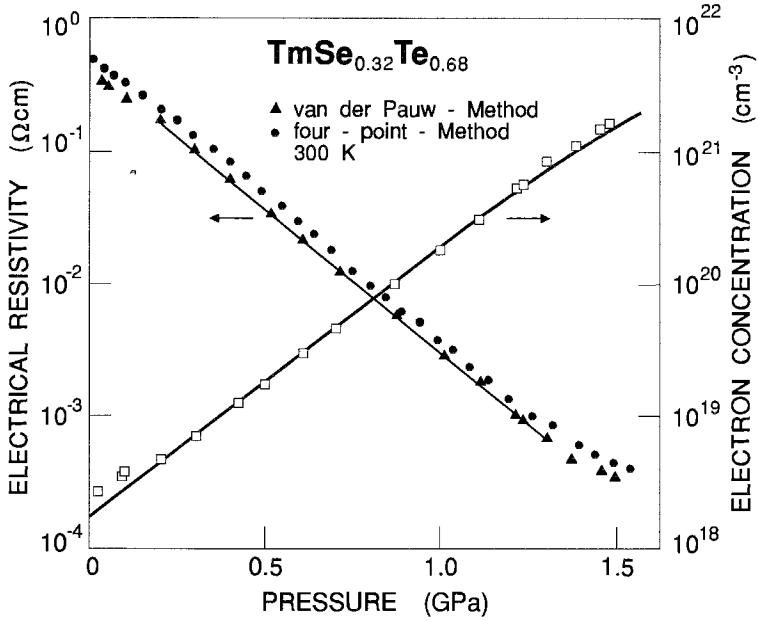

Fig. 86. Electrical resistivity (left-hand scale) and electron concentration (right-hand scale) of $TmSe_{0.32}Te_{0.68}$ vs. pressure at 300 K. (After Boppart and Wachter 1984b.)

From the pressure dependence of the resistivity $\rho(p)$ a value of the energy gap ΔE between the $4f^{13}$–5d states can be obtained. The experimental data suggest the following resistivity–pressure dependence:

$$\log \rho(p) = \log \rho_s + \left[\frac{\mathrm{d} \log \rho}{\mathrm{d}p}\right] \cdot p. \tag{7}$$

Assuming simple carrier statistics for the electron excitation into the conduction band, ρ is given by $\rho(p) = \rho_s \exp[\Delta E(p)/k_B T]$, where ρ_s denotes the experimental value of ρ if the gap ΔE is closed. This formula is valid under the assumption that the Fermi level E_F is pinned at the $4f^{13}$ level (this condition is in general valid for a 4f type semiconductor because of the always present holes in the p bands). The exponential decrease of the resistivity under pressure together with the ansatz for the carrier concentration implies that the gap is closing linearly with pressure, thus

$$\Delta E(p) = \Delta E + \frac{\mathrm{d}\Delta E}{\mathrm{d}p} \cdot p. \tag{8}$$

The numerical values for the closing rate $\mathrm{d}\Delta E/\mathrm{d}p$ and the energy gap ΔE are listed in table 6 together with other experimental data.

We have tacitly assumed above that the mobility of the carriers changes only marginally with pressure and thus that the closing of the gap under pressure mainly enhances the

carrier concentration. This has been verified experimentally by Boppart and Wachter (1984b,d) on a $TmSe_{0.32}Te_{0.68}$ composition by measuring the Hall effect under pressure; the results are shown in fig. 86. With the simple ansatz

$$n(p) \propto \exp\left(\frac{-\Delta E(p)}{k_B T}\right) \tag{9}$$

one finds that the carrier concentration increases with pressure from $2\times10^{18}\,\mathrm{cm}^{-3}$ to about $2\times10^{21}\,\mathrm{cm}^{-3}$ at 1.5 GPa and that the closing rate of the gap $\mathrm{d}\Delta E/\mathrm{d}p$ is equal to -122 meV/GPa which is in excellent agreement with -129 meV/GPa obtained from the resistivity measurement on the same sample. We can thus compute the Hall mobility $\mu_H = R_H/\rho$ which at ambient pressure is about $6\,\mathrm{cm}^2/\mathrm{V\,s}$ and increases to about $10\,\mathrm{cm}^2/\mathrm{V\,s}$ at the semiconductor metal transition. These relatively low mobilities are due to the strong f admixture to the 5d conduction band which is the essence of the intermediate-valent semiconductor or metal.

In fig. 81 the dependence of the energy gap in function of composition reveals a nonlinear relation in the semiconducting range. But if we scale against the lattice constant instead of the composition, the dependence becomes linear (Boppart 1983). This implies that the amount of ligand field splitting (10 Dq) is *linearly* coupled to the lattice constant. On the other hand the energy gap varies linearly under pressure. If both variations, the chemical and the pressure, would be the same then the lattice constant must vary linearly under pressure. This is definitely not the case as all volume–pressure curves reveal. Only in the low-pressure regime (<1 GPa) does the lattice constant vary linearly under pressure (i.e., constant compressibility).

An interesting question arises regarding the high-pressure intermediate-valent metallic state, namely whether a hybridization gap exists? This question has been investigated on $TmSe_{0.45}Te_{0.55}$ by Neuenschwander and Wachter (1990a,b). This compound has a transition pressure into the metallic state of 1.2 GPa (12 kbar) (table 6) at 300 K. At room temperature one had to apply an appreciably higher pressure than necessary, because, when cooling, the pressure relaxes to a certain extent in the Cu–Be pressure cell. We show in fig. 87 the temperature dependence of the resistivity of $TmSe_{0.45}Te_{0.55}$ at various pressures, and for the highest pressure (17 kbar at 300 K, curve f) the sample remains in the metallic state even at the lowest temperature of 3 K. Curve f resembles that for TmSe in a field of 10 kOe (fig. 65) when TmSe is ferromagnetic, or the resistivity curve in fig. 80c of ferromagnetic metallic $TmSe_{0.83}Te_{0.17}$, which is even more corroborated by looking at the inset of fig. 87 where the low-temperature resistivity behavior of high-pressure metallic $TmSe_{0.45}Te_{0.55}$ is shown. The conclusion then would be that the intermediate-valent metallic phase must be ferromagnetic, since there is no evidence of a hybridization gap below about 10 K. However, for larger temperatures an Arrhenius plot reveals, between 50 and 100 K, an activation energy of about 1 meV, typical again for, e.g., TmSe (Neuenschwander and Wachter 1987).

Indeed, neutron scattering performed on $TmSe_{0.45}Te_{0.55}$ at 1.5 K and 15 kbar at this temperature revealed only nuclear Bragg peaks and no AF peaks could be discerned.

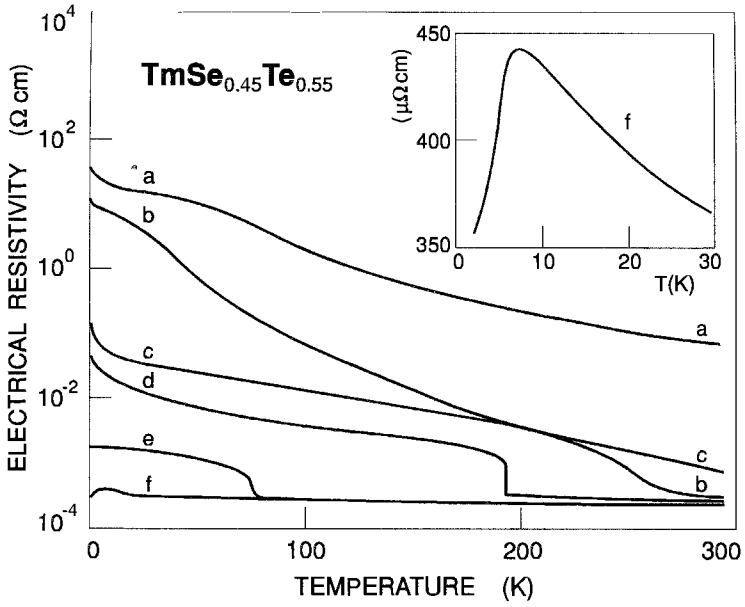

Fig. 87. Temperature dependence of the electrical resistivity of $TmSe_{0.45}Te_{0.55}$. The pressures at room temperature are (a) 0, (b) 9.7 kbar, (c) 11.0 kbar, (d) 12.9 kbar, (e) 15.0 kbar, (f) 17.0 kbar. Note the linear scale of the resistivity in the inset. (After Neuenschwander and Wachter (1990a,b.)

Using the magnetic form factor of the free Tm ion in the dipole approximation, Neuenschwander and Wachter (1990a,b) find that the saturation magnetization μ_B(Tm) at 1.5 K is $1.8 \pm 0.4 \mu_B$, much less than the saturation moment of either Tm^{3+} or Tm^{2+}. The temperature dependence of the magnetization is shown in fig. 88. The data can be fitted surprisingly well with the power law

$$M \propto \left(\frac{T_C - T}{T_C}\right)^{\beta}. \tag{10}$$

From this evaluation we derive the Curie temperature $T_C = 5.07$ K and the critical exponent $\beta = 0.32 \pm 0.03 (T_C - T)/T_C = 0.002 \div 0.3)$. A last important result of the neutron scattering at this pressure is that the lattice constant at 2 K is 5.90 Å which is significantly smaller than at ambient conditions (6.137 Å) indicating that the sample is indeed in the collapsed intermediate-valent phase. The variation of the temperature through T_C has no effect on the position of the nuclear Bragg reflections which again proves the coexistence of ferromagnetism and intermediate valence but with the absence of a hybridization gap.

Batlogg et al. (1982) measured the magnetic susceptibility under pressure and low temperatures of $TmSe_{0.60}Te_{0.40}$, the composition with the first-order SMT (fig. 84), in the metallic state. The conclusion was again that the material is ferromagnetic (thus

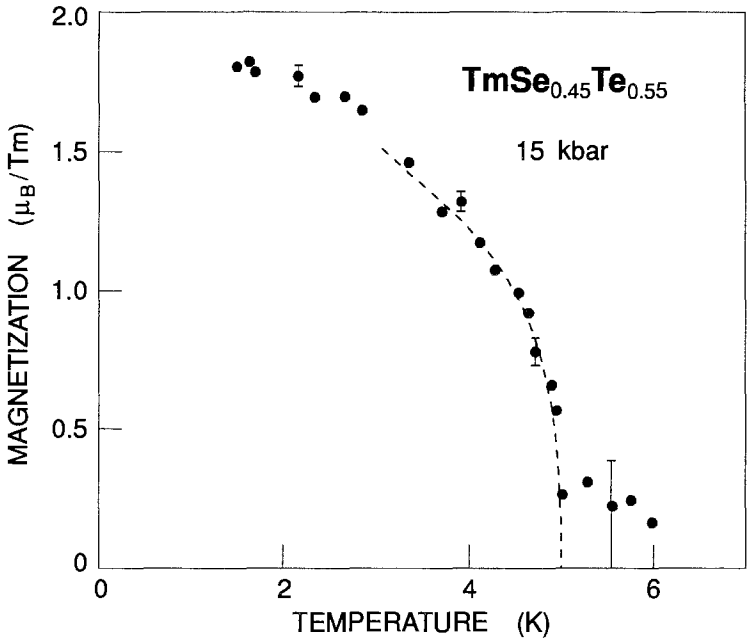

Fig. 88. Temperature dependence of the magnetization of the Tm ions of pressure-driven metallic $TmSe_{0.45}Te_{0.55}$ at 15 kbar. The dashed curve is a power law fit as described in the text. (After Neuenschwander and Wachter 1990b.)

no hybridization gap) with a Curie temperature of 5.6 K, somewhat higher than for $TmSe_{0.45}Te_{0.55}$ (5.07 K). We probably can safely draw the conclusion that the high-pressure metallic phases of $TmSe_{1-x}Te_x$ all order ferromagnetically.

4.3.2.1.2. *The excitonic insulator.* Another extremely important, even fundamental, contribution in the field of intermediate valence is the proposal and experimental verification of a new ground state of condensed matter, the excitonic insulator. Neuenschwander and Wachter (1990a,b) found in the pressure and temperature variation of $TmSe_{0.45}Te_{0.55}$ and $TmSe_{0.32}Te_{0.68}$ an unexpected new feature, displayed in fig. 89 for $TmSe_{0.45}Te_{0.55}$. The pressure dependence of the resistivity at 300 K is the same as in fig. 84. However, at temperatures below about 250 K and most prominent at the lowest temperature of 5 K the resistivity pressure relations show a novel feature. After an initial decrease of resistivity with pressure we observe an increase of resistivity with increasing pressure, followed again by a decrease and a first-order SMT. At 5 K the resistivity goes up by a factor 370 with increasing pressure and such a behavior has never been seen before. In the papers by Neuenschwander and Wachter (1990a,b) it is speculated whether this resistivity increase is caused by a change in mobility due to closing the gap and thus increased f–d mixing, or whether it is caused by a reduction in carrier concentration. Both possibilities are discussed in detail and found equally possible.

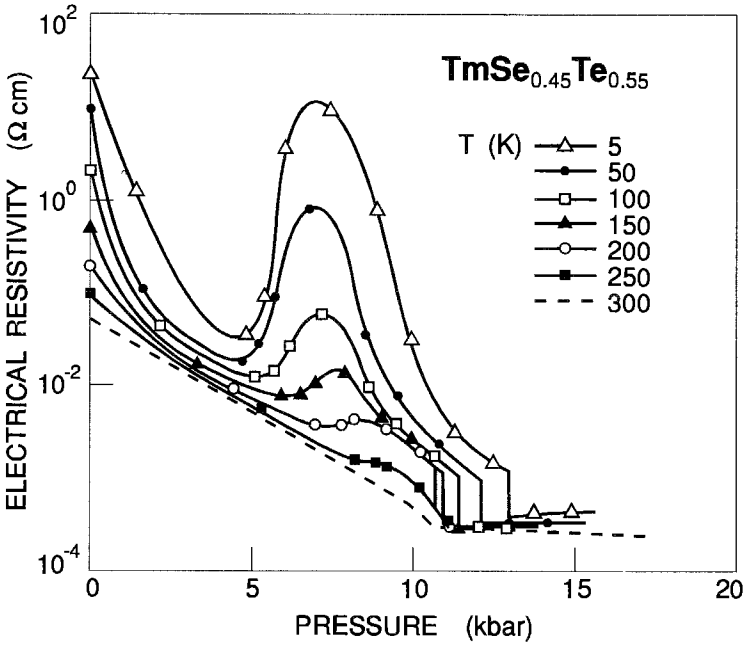

Fig. 89. Pressure dependence of the electrical resistivity of $TmSe_{0.45}Te_{0.55}$ for various temperatures. The thin solid lines are guides to the eye. For temperatures below 200 K a first-order SMT is suggested. (After Neuenschwander and Wachter 1990a,b.)

Thus a critical experiment seemed necessary, and it has been performed by Bucher et al. (1991), where the Hall effect at low temperatures and high pressures has been measured. This experiment combines extremely difficult experimental techniques because, in addition to high pressure and low temperature, a large magnetic field of about 5 T was necessary to separate the normal from the anomalous Hall effect. Figure 90 shows the results at 4.2 K: the resistivity at 300 K and 4.2 K (fig. 90a); the Hall constant R_H at 4.2 K (fig. 90b); and the Hall mobility μ_H (fig. 90c). It is evident that the resistivity increase with increasing pressure is caused by a reduction of carrier concentration and a mobility going towards zero at 9 kbar before increasing again.

To explain these unusual results Neuenschwander and Wachter (1990a,b) and Bucher et al. (1991) have used the concept of an excitonic insulator. The model of an excitonic insulator was proposed for the first time about 30 years ago by Sir Nevil Mott (1961), later it has been used by Knox (1963) and Kohn (1968), however, up until the present day there was no experimental confirmation.

In fig. 91 we show a dispersion of a semiconducting $TmSe_{1-x}Te_x$ with a small energy gap at ambient pressure so that there is already appreciable f–d hybridization. Then the originally dispersion free $4f^{13}$ state acquires a certain width and Jansen et al. (1985) have shown that the narrow 4f band has its maximum at the Γ point. The conduction band has

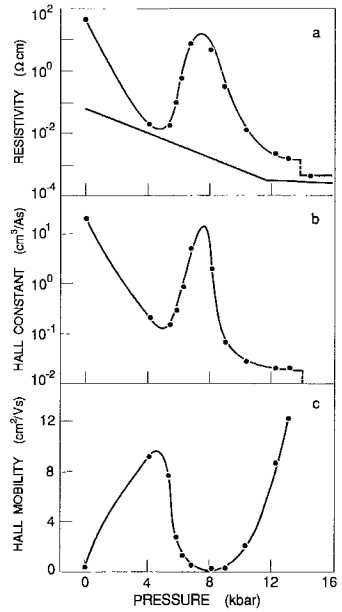

Fig. 90. (a) Pressure dependence of the resistivity of $TmSe_{0.45}Te_{0.55}$ at 300 K (lower curve) and at 4.2 K (upper curve). At 300 K the SMT is at 11.5 kbar, at 4.2 K it is near 14 kbar and it is of first order. (b) R_H at 4.2 K. (c) Hall mobility μ_H as calculated from $\rho=(ne\mu_H)^{-1}$. (After Bucher et al. 1991.)

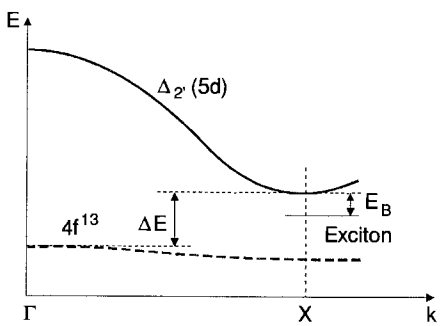

Fig. 91. Schematic $E(k)$ dispersion of semiconducting $TmSe_{1-x}Te_x$. ΔE denotes the energy gap in absence of electron–hole interaction. Below the conduction band minimum at the X point an excitonic level is assumed. (Modified after Neuenschwander and Wachter 1990a,b.)

its minimum at the X point so an optical f–d transition is in principle an indirect transition and we are dealing with an indirect semiconductor. The exciton with its binding energy E_B is shown in the figure.

In fig. 92 the abscissa denotes the band gap ΔE which was calculated from the applied pressure using the linear closing rate of the gap $d\Delta E/dp = -120$ meV/GPa (table 6). The circles indicate the onset of the resistivity anomaly (fig. 89). The squares correspond to the top of the resistivity peak. Hence in region A the resistivity is rising, and in region B it is decreasing with increasing pressure. The triangles represent the first-order transition to the IV metallic phase (SMT). In fig. 93 we have drawn the phase diagram of the excitonic insulator as predicted by Kohn (1968). It is based on the Hartree–Fock approximation neglecting correlations between excitons and it assumes wide bands, $m^*_{hole} = m^*_{electron}$ and

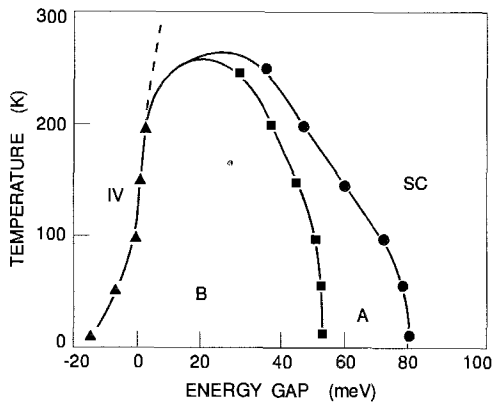

Fig. 92. Phase diagram of $TmSe_{0.45}Tc_{0.55}$ as deduced from resistivity data of fig. 90. The circles represent the onset of the resistivity rise, the squares indicate the summit of the resistivity peak, the triangles are the first-order transition to the metallic state. The different phases are semiconducting (SC), excitonic phases A and B, and intermediate-valent (IV). (After Bucher et al. 1991.)

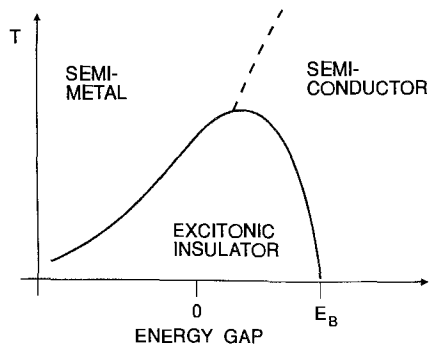

Fig. 93. Phase diagram as proposed by Kohn (1968) for the excitonic ground state of condensed matter. E_B is the binding energy of an exciton. (After Bucher et al. 1991.)

small anisotropy. At $T=0$ the excitonic instability occurs at $\Delta E = E_B$ but for higher temperatures the instability occurs at $\Delta E < E_B$. With respect to our more subtle substance the agreement between experiment and theory is acceptable.

Halperin and Rice (1968) have tried to go beyond the Hartree–Fock theory and treat the more elaborate case of a heavy hole mass as we would expect for our 4f holes. They concluded that for ΔE close to E_B the excitons do not form a Bose fluid of single excitons but build up exciton molecules which condense in a periodic array. This state would be insulating and we associate it with our region A in fig. 92. Then if the density of exciton molecules happens to increase further, the long range Coulomb interaction becomes screened and the excitons begin to delocalize, whereas the heavy holes suffer a Wigner crystallization. In this phase the resistivity decreases and hence, is to be identified with the region B of our experimental phase diagram. As the density is enhanced still further, the Wigner array of holes is expected to melt and the crystal becomes a normal metal in a first-order transition. $TmSe_{0.45}Te_{0.55}$ is intermediate valent in the metallic state because of f–d hybridization.

Our phase diagram reveals a quite small region A, i.e., a high density of excitons is easily reached under pressure. This is understandable with the narrow band dispersion of the f states and the considerable gap closing rate $d\Delta E/dp$. The exciton level effectively crosses the 4f states with applied pressure, whereby the $4f^{13}$ electrons decay to excitons. The localization to excitons should be manifest by a decreasing carrier density as actually seen in fig. 90b between 5 and 7.5 kbar. In our model we assume the lowering of an indirect, deep exciton level below the valence band ($4f^{13}$) maximum at Γ. Thus the delocalization in region B above 7.5 kbar does not end in a metallic state because there is still a narrow gap to the 5d band.

There are other investigations (see above) which support the exciton model. The reflectivity at normal pressure and low temperature (Neuenschwander and Wachter 1990a,b) has shown an optical excitation at $E_{ex} = 60$ meV which they associated with an exciton with binding energy of $E_B = \Delta E - E_{ex}$ in agreement with the phase diagram of fig. 92. Thus the model of the excitonic insulator phase in $TmSe_{0.45}Te_{0.55}$ (and also $TmSe_{0.32}Te_{0.68}$) gains considerable support and we think this experiment has shown the existence of the excitonic insulator phase as a new ground state of matter. (But see also section 4.4.1 for YbO and YbS excitonic insulators).

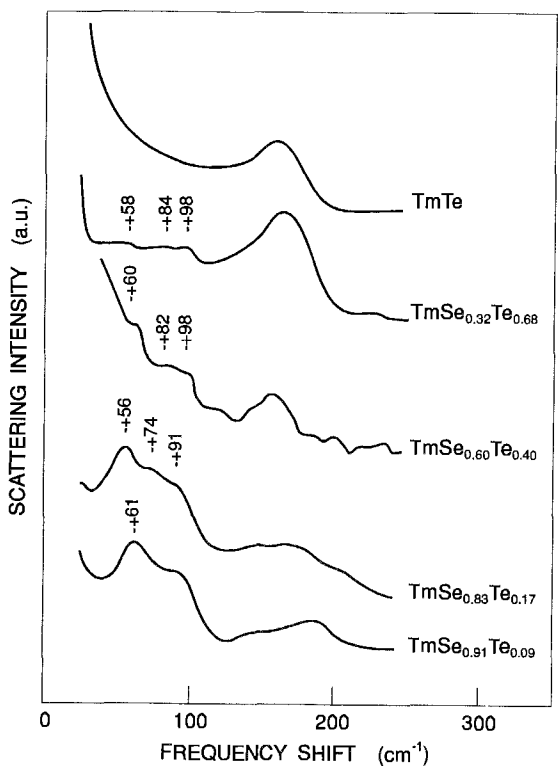

Fig. 94. Raman effect of $TmSe_{1-x}Te_x$ at 300 K. (After Mörke and Wachter 1983.)

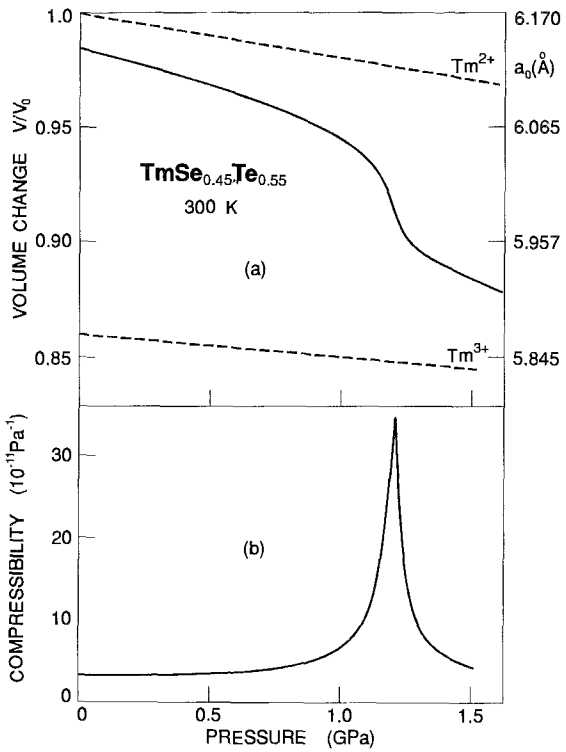

Fig. 95. (a) Volume change and (b) compressibility of $TmSe_{0.45}Te_{0.55}$ vs. pressure. Dashed lines are the expected volume changes for Tm^{2+} and Tm^{3+} ions. (After Boppart 1983.)

4.3.2.1.3. *Lattice-related properties.* At first we want to discuss the phonon-related properties, already mentioned above for $TmSe_{0.45}Te_{0.55}$. Far infrared optical reflectivity has been measured for the semiconducting compositions TmTe, $TmSe_{0.32}Te_{0.68}$ and $TmSe_{0.45}Te_{0.55}$ by Schneider (1983) and Neuenschwander and Wachter (1990a,b). The results are similar to those in fig. 83. The TO(Γ) phonon energies are (maximum of ε_2) 13.9 meV, 15,3 meV and 16 meV, and the LO(Γ) energies (zero crossing of ε_1 with $d\varepsilon_1/d\omega < 0$) 17.2 meV, 19.1 meV and 20 meV, respectively. The substitution of the Te by the lighter weight Se results in an increase of the phonon energy as $\omega^2 \propto 1/M_1 + 1/M_2$. However, the lattice constant is also reduced by substituting Se for Te so by this argument one also expects an increase in phonon energy. Both these effects mask a possible softening of phonon energies by the increased valence mixing, which thus cannot be observed. The phonon energies are collected also in table 5.

In fig. 94 we show the Raman effect of $TmSe_{1-x}Te_x$, metallic as well as semiconducting compositions. Again the Raman effect measures a weighted one phonon density of states (Mörke and Wachter 1983). It is quite interesting to note that in all compositions except the integer trivalent $Tm_{0.87}Se$ (fig. 71) and TmTe, the peak near 60 cm^{-1} (7 meV) is visible which we associate with the acoustic plasmon mode, being typical for intermediate-valent Tm compounds.

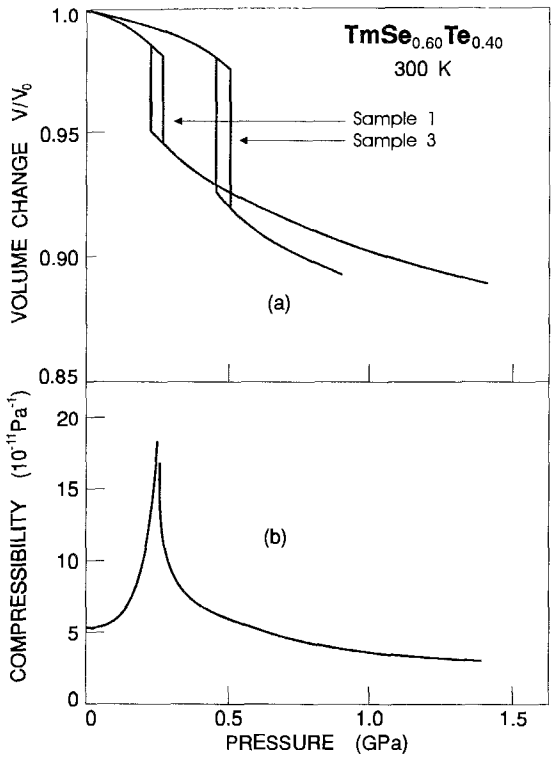

Fig. 96. (a) Volume change and (b) compressibility of $TmSe_{0.60}Te_{0.40}$ vs. pressure. The hysteresis of the first-order transition for two single crystals of the same batch is shown in (a). (After Boppart 1983.)

The volume change under pressure and the compressibility (the reciprocal of the bulk modulus) has been measured for the semiconducting compositions of $TmSe_{1-x}Te_x$ by Boppart et al. (1980b), Boppart et al. (1982) and Boppart and Wachter (1984a,b) using strain gauges glued onto the single crystals. The data are collected in table 6. Figure 95a shows as an example the volume–pressure relation of $TmSe_{0.45}Te_{0.55}$ together with the volume–pressure relation derived by using the Birch–Murnaghan equation for an integer di- or trivalent Tm compound (dashed lines). Even for zero pressure the volume is already partially collapsed as derived from the lattice constant and ionic radii of Tm^{2+}, Se^{2-} and Te^{2-} using the model of fig. 82. Up to pressures of 3.5 GPa (not shown in the figure) trivalency was not yet achieved. The compressibility, $\kappa = -(dV/dp) \times 1/V$, shown in fig. 95b, is the derivative of the volume–pressure relation and thus has its maximum at the point of inflection. Of interest are the curves for $TmSe_{0.60}Te_{0.40}$ with its first-order SMT as shown in fig. 85 for the resistivity. The volume–pressure change is shown in fig. 96 and also a first-order transition with a hysteresis is shown. The compressibility diverges as is demanded by thermodynamics.

Plotting the volume–pressure relation similar to a van-der-Waals diagram for $TmSe_{1-x}Te_x$ we obtain fig. 97 (Boppart and Wachter 1984a). We have been able to produce a $TmSe_{0.50}Te_{0.50}$ sample which has practically the critical composition, and for which

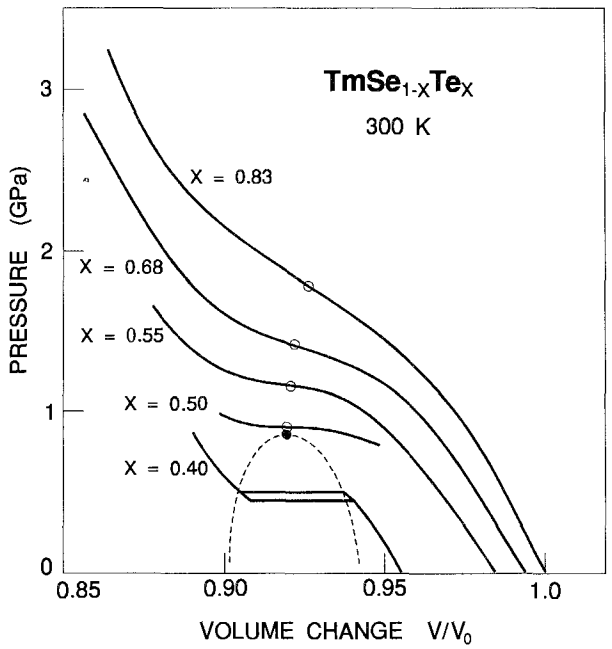

Fig. 97. The pressure versus volume change of $TmSe_{1-x}Te_x$ plotted in the form of a van-der-Waals diagram. The critical point is indicated by the solid circle. (After Boppart and Wachter 1984a.)

the critical pressure of 0.85 GPa and a critical volume ratio of $V/V_0 = 0.92$ could be determined. The volume–pressure curve of $TmSe_{0.50}Te_{0.50}$ shows an almost horizontal slope (infinite compressibility, bulk modulus zero). Figure 97, being identical to the well known liquid–gas pressure–volume behavior suggests a mean field behavior of the valence transition. In order to deduce critical exponents, the pressure–volume curve of $TmSe_{0.50}Tc_{0.50}$ was analyzed by the relation

$$|p - p_c| = |V - V_c|^{\delta}. \tag{11}$$

This relation is shown in fig. 98 and the values of δ are 2.72 for $p < p_c$ and $\delta = 3.1$ for $p > p_c$. These values are very close to $\delta = 3$ predicted by the mean field theory.

At the critical point only the bulk modulus becomes zero whereas the phonons still have a finite energy (no soft phonons). Therefore, no critical fluctuations occur and mean field behavior can be expected very close to T_c. This implies a long range force and suggests that elastic coupling dominates the critical behavior (Cowley 1976).

In summary we can show, in a qualitative way, the transition of valency from divalent over intermediate valent towards trivalency by plotting the bulk modulus as function of pressure as shown in fig. 99. The different regions (semiconductor, intermediate-valent semiconductor, intermediate-valent metal, metal) are clearly indicated (Boppart and Wachter 1984c).

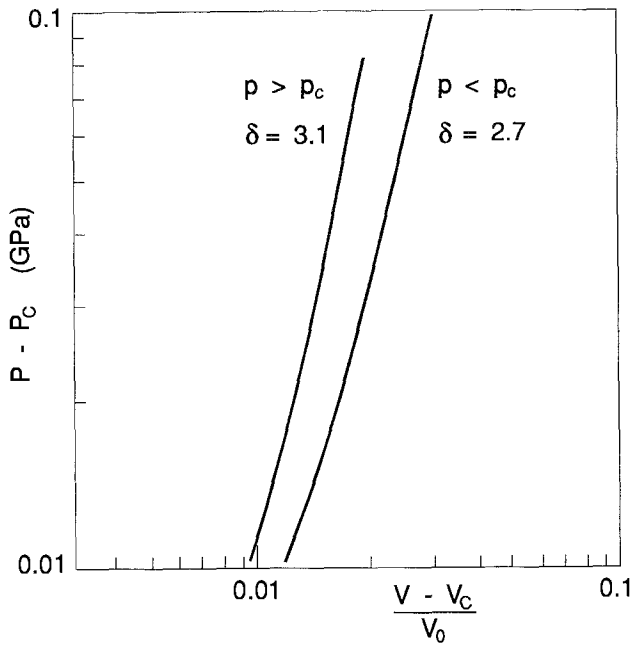

Fig. 98. The critical exponents of the pressure–volume curve of the critical composition $TmSe_{0.50}Te_{0.50}$. (After Boppart 1983.)

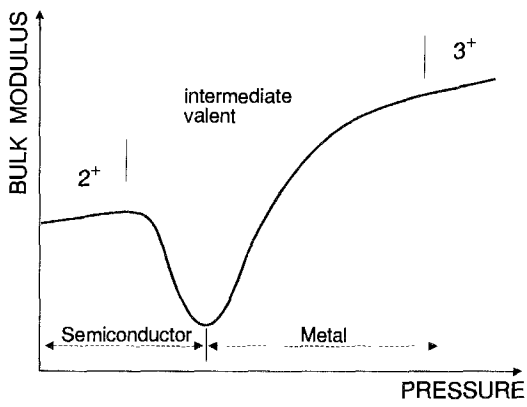

Fig. 99. Behavior of the bulk modulus in a SMT. (After Boppart and Wachter 1984c.)

In a cubic material the elastic behavior can be described by the three second-order elastic constants c_{11}, c_{12} and c_{44}. The longitudinal and the transverse waves propagating along the [100] direction are related to c_{11} and c_{44} by $c_{11} = \rho_d v_L^2$ and $c_{44} = \rho_d v_T^2$, with ρ_d the density and v the sound velocity. In the [110] direction the longitudinal wave is related to $(c_{11} + c_{12} + 2c_{44})/2 = \rho_d v_L^2$ whereas the transverse waves are nondegenerate and related to

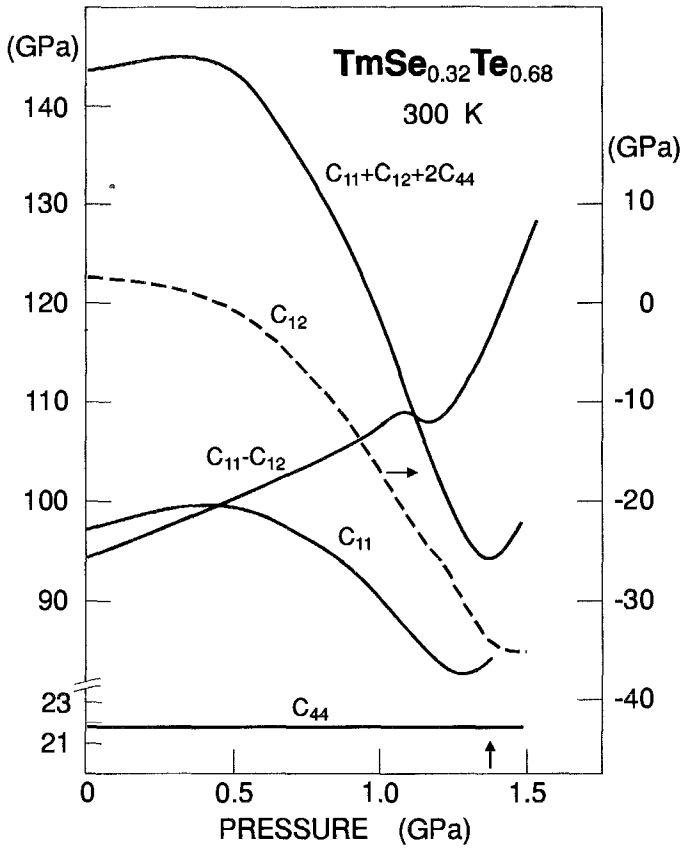

Fig. 100. Elastic moduli and combinations of them vs. pressure for $TmSe_{0.32}Te_{0.68}$ at 300 K. (After Boppart et al. 1982.)

$(c_{11} - c_{12})/2 = \rho_d v_{T1}^2$ with polarization direction $[1\bar{1}0]$ and to $c_{44} = \rho_d v_{T2}^2$ with polarization direction [001]. Boppart et al. (1982) measured both the longitudinal and transverse sound velocity in the [100] direction as well as the longitudinal and one transverse (v_{T1}) sound velocity in the [110] direction. Hydrostatic pressure up to 1.6 GPa could be applied and the compound $TmSe_{0.32}Te_{0.68}$ has been chosen because the largest and most perfect crystals were available for this material.

The experimental results are plotted in fig. 100 and the pressure derivatives of the elastic constants $(\delta c_{ij}/\delta p)_{T,p=0}$ and those for comparable materials are given in table 7. The elastic behavior of $TmSe_{0.32}Te_{0.68}$ under pressure shows a number of interesting and novel features. The shear constant c_{44} remains almost constant over the whole pressure range and shows no influence of the SMT at 1.4 GPa. In contrast, the influence of pressure on c_{11} is unusual. At low pressures it increases in the normal fashion, then it goes through a maximum at 0.4 GPa and then decreases anomalously with pressure: longitudinal mode softening takes place. Of special interest is the elastic constant c_{12}, as calculated from

Table 7
Elastic constants and their pressure derivatives for $TmSe_{0.32}Te_{0.68}$ and $TmSe_{0.60}Te_{0.40}$ in comparison with those of other rocksalt-structure crystals (after Boppart 1983)

Compound	GPa data				Shear anisotropy	Pressure derivatives of elastic constants					Ref.
	c_{11}	c_{12}	c_{44}	$\frac{1}{2}(c_{11}-c_{12})=c'$		$\frac{\partial c_{11}}{\partial p}$	$\frac{\partial c_{12}}{\partial p}$	$\frac{\partial c_{44}}{\partial p}$	$\frac{\partial c'}{\partial p}$	$\frac{\partial B}{\partial p}$	
$TmSe_{0.60}Te_{0.40}$	60	−10	29	35	0.83						1
$TmSe_{0.32}Te_{0.68}$	97.5	2.8	21.8	47.3	0.46	88.4	−38.5	2.8	63.6	4	2
SmSa	127	12	26.9	57.5	0.47	104	−16	−0.8	60	24	3
$Sm_{0.91}Y_{0.09}S$ (semiconducting)	127	5	27	61	0.44						4
$Sm_{0.75}Y_{0.25}S$ (metallic)	113	−41	29	77	0.38						5
$Tm_{0.99}Se$ (metallic)	179	−57	27	118	0.23						6
TmTe (semiconducting)	102	6	18.6	48	0.39						7
PbTe	105	7	13.2	49.1	0.27	134	10	1.9	59.3	51	8
SnTe	104	1.8	11.3	51.3	0.22	140	15	1.4	62.3	57	8
NaCl	49	12.6	12.7	18.2	0.7	117	20.6	3.7	48.3	53	8
KCl	40.5	7	6.3	16.7	0.38	128	16.1	−3.9	55.8	53	8
KBr	34.2	5.2	5.1	14.5	0.35	135	16.1	−3.0	59.3	56	9

References
(1) Mendik and Wachter (1995)
(2) Boppart et al. (1982)
(3) Saunders et al. (1982)
(4) Melcher et al. (1975)
(5) Mook et al. (1978)
(6) Boppart et al. (1980a)
(7) Ott et al. (1977)
(8) Miller et al. (1981)
(9) Anderson and Liebermann (1970)

certain combinations of the other elastic constants, which is shown as a dashed line in fig. 100 (right-hand scale). It decreases rapidly with pressure and goes through zero at about 0.5 GPa, far below the semiconductor–metal transition, when the energy gap is still about 120 mcV. This was the first time that a negative c_{12} has been shown to exist for a semiconducting compound and it is the origin of the term "intermediate-valent semiconductor" by Boppart et al. (1982).

It is, however, a pity that the negative c_{12} is only achieved with a pressure already being applied. If, instead, one would use a stronger hybridized compound than $TmSe_{0.32}Te_{0.68}$, e.g. $TmSe_{0.60}Te_{0.40}$, one could hope that c_{12} might already be negative at ambient conditions and the matcrial being still a semiconductor with $\Delta E = 40$ meV (table 6). As already mentioned above, the single crystals of this composition were not large enough to pcrmit the use of ultrasound transducers. However, Brillouin scattering technique was an alternative. The method of the determination of the elastic constants by means of the angular dcpendence of the Brillouin back scattering on conducting materials has been developed by Elmiger et al. (1989). Mendik and Wachter (1995) have uscd this method for $TmSe_{0.60}Te_{0.40}$. The argument goes as follows: the ve-

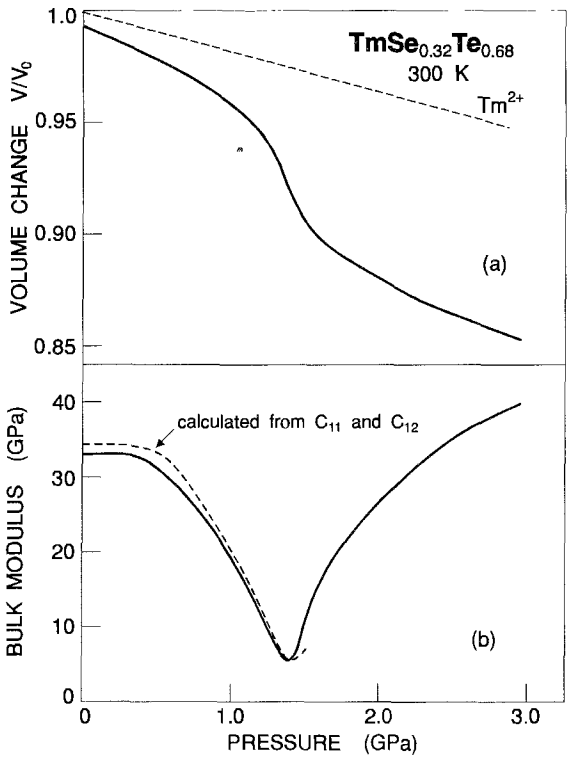

Fig. 101. (a) Volume change and (b) bulk modulus of $TmSe_{0.32}Te_{0.68}$ vs. pressure at 300 K. The dashed curve in (a) is the expected volume change for divalent Tm^{2+} ions. The dashed curve in (b) is the bulk modulus calculated from the independently measured c_{11} and c_{12}. (After Boppart and Wachter 1984b.)

locity of the Raleigh-surface-wave (RSW) for (100) oriented crystals can be directly measured and is in our case $v_{RSW} = 1900$ m/s. Using the lattice constant of 6.02 Å (table 6) the density can be computed and is $\rho_d = 8.132\ \mathrm{gcm}^{-3}$. Thus the shear wave velocity yields $c_{44} = v_{RSW}^2 \rho_d = 29$ GPa. The anisotropy ratio $\eta = 2c_{44}/(c_{11} - c_{12}) < 1$ (obtained from the fact that the angular dispersion is practically flat) and the bulk modulus $B = (1/3)(c_{11} + 2c_{12})$. c_{12} can now be calculated as

$$c_{12} < B - \tfrac{2}{3}c_{44}. \tag{12}$$

Using $B = 20$ GPa (table 6) we obtain $c_{12} < 0.6$ GPa which is, within the error limits, practically zero, in any case much smaller than the value of $c_{12} = 2.8$ GPa of $TmSe_{0.32}Te_{0.68}$. However, by making a fit of the angular dependence of the RSW (Elmiger et al. 1989) we can directly calculate c_{12} and find it to be -10 GPa. The elastic moduli of $TmSe_{0.60}Te_{0.40}$ are included in table 7. Thus it is the first time that one observes a negative c_{12} for a semiconductor with a gap of 40 meV at ambient conditions.

In fig. 101a we show again a volume pressure experiment with strain gauges, this time for $TmSe_{0.32}Te_{0.68}$, similarly as fig. 95 for $TmSe_{0.45}Te_{0.55}$, where the curve expected for a pure divalent Tm is also shown with a dashed line. In fig. 101b, the bulk modulus B,

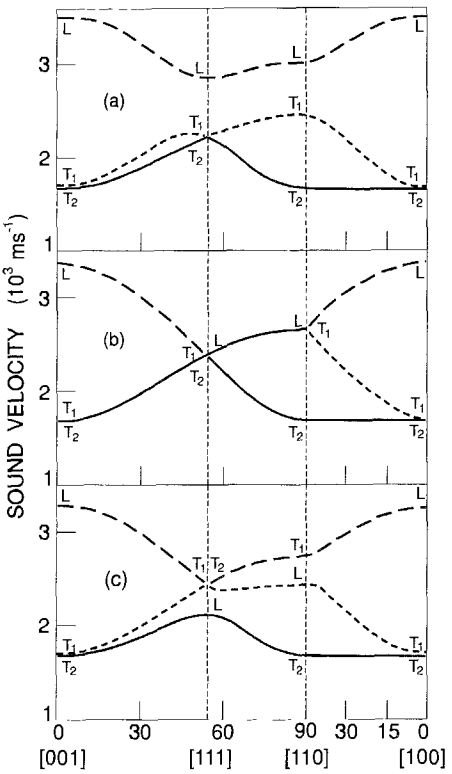

Fig. 102. Dispersion of the acoustic sound velocities of $TmSe_{0.32}Te_{0.68}$: (a) at ambient pressure, (b) at 1.13 GPa and (c) at the transition pressure of 1.4 GPa. (After Boppart 1983.)

being the inverse of the compressibility κ, is also shown, obtained by differentiating the curve in fig. 101a. The initial value of the isothermal bulk modulus B_T is 33±1 GPa. With increasing pressure it softens and reaches a minimum of 6 GPa at 1.4 GPa pressure. Above this pressure the crystal stiffens again. The dashed line in fig. 101b represents the adiabatic bulk modulus $B_S=(c_{11}+2c_{12})/3$ as calculated from the elastic constants c_{11} and c_{12}. The initial value is 34.4 GPa. B_S is related to B_T: $B_S=B_T(1+\alpha_T\gamma_G T)$, where α_T is the thermal coefficient of volume expansion, γ_G is the Grüneisen constant and T the temperature in K. For the alkali halides the initial isothermal bulk modulus is about 4–6% smaller than the adiabatic bulk modulus (Anderson 1966), similar to what we observe for our compound. Of course, the softening of the bulk modulus is due to the breathing deformability of the lanthanide ion (see above).

The ultrasonic waves also detect the dispersion relation in the long wavelength limit ($k=0$) and their velocities represent the initial slope of the different phonon branches. In fig. 102 the sound velocities are plotted in different directions of the wavevector for three different pressures. The three elastic constants serve as input data for the calculation of the sound velocities in the different directions. A normal behavior is found at ambient pressure with velocities higher for the longitudinal modes than for the transverse ones

Table 8
Magnetic properties of semiconducting $TmSe_{1-x}Te_x$ (after Boppart 1983)

x	0.40	0.55	0.68	1.0
Lattice constant (Å)	6.02	6.14	6.20	6.36
Energy gap (meV)	40	120	180	300
p_{eff} (μ_B) [a]	4.56	4.51	4.61	4.73
θ_P (K)	−2	−2	−2	−1.5
T_N (K)			0.20	0.235[a]

[a] From Ott and Hulliger (1983).

(fig. 102a). At a pressure of 1.13 GPa c_{12} becomes equal to $-c_{44}$, the consequences of this are $v_L = v_{T1}$ in [110] and $v_L = v_T$ in [111] directions (fig. 102b). A further consequence of the condition $c_{12} = -c_{44}$ is the degeneracy of two sound velocities in the $[1\bar{1}0]$ plane (denoted 0–90 in fig. 102b). At the semiconductor–metal transition pressure of 1.4 GPa the same anomalous behavior is observed as in the intermediate-valent metallic materials, e.g. TmSe or $Sm_{0.75}Y_{0.25}S$: the longitudinal sound velocity is less than the transverse velocity in [110] and [111] directions (fig. 102c). An interesting point is the change from a pure longitudinal mode in [100] direction to a pure transverse mode in [110] or in [111] directions and vice versa. It has to be considered that only modes propagated in the [100], [110] and [111] directions in a cubic crystal are pure shear or longitudinal; in all other directions the modes are quasi-shear or quasi-longitudinal. The breathing mode exerts its greatest influence on the [110] and [111] directions in which, in fact, we observe the largest decrease of the longitudinal wave velocities. It remains to be noted that the phase transitions are not driven by softening of an acoustic mode, as Boppart (1983) has shown in his thesis by considering also the third-order elastic constants.

4.3.2.1.4. *Magnetic properties.* Since all the above measurements of elastic constants, bulk modulus, lattice constant, anomalous phonon peaks, etc., have shown that the semiconducting compositions of $TmSe_{1-x}Te_x$ are intermediate valent, the magnetic measurements should reveal a similar picture. However, it came as a surprise that the molar Curie constants C_M reveal divalency for all compositions. The C_M values for the free ions $Tm^{2+}(4f^{13})$ and $Tm^{3+}(4f^{12})$ are 2.58 and 7.14μ_B, respectively. The effective magnetic moment p_{eff} is related to the Curie constant by $p_{eff}^2 \approx 8\,C_M$. From magnetic susceptibility measurements and plots of the inverse susceptibility versus temperature for temperatures up to 500 K Boppart (1983) derived the effective moments for the semiconducting compositions of $TmSe_{1-x}Te_x$ which are collected in table 8. The values clearly indicate divalency, where the slightly larger value of TmTe can be explained by a 6% admixture of trivalent Tm in TmTe ($a = 6.36$ Å) yielding a theoretical value of $p_{eff} = 4.72\mu_B$ in excellent agreement with the experimental value of $4.73\mu_B$.

A convincing experiment indeed would be a susceptibility measurement under pressure while driving the $TmSe_{1-x}Te_x$ compound through the SMT. This experiment was performed by Boppart and Wachter (1984c) and it is shown in fig. 103 for $TmSe_{0.32}Te_{0.68}$. The inverse susceptibility is plotted as a function of temperature for a pressure below (0.93 GPa) and above (1.71 GPa) the SMT at 1.4 GPa. Also shown in the figure are the

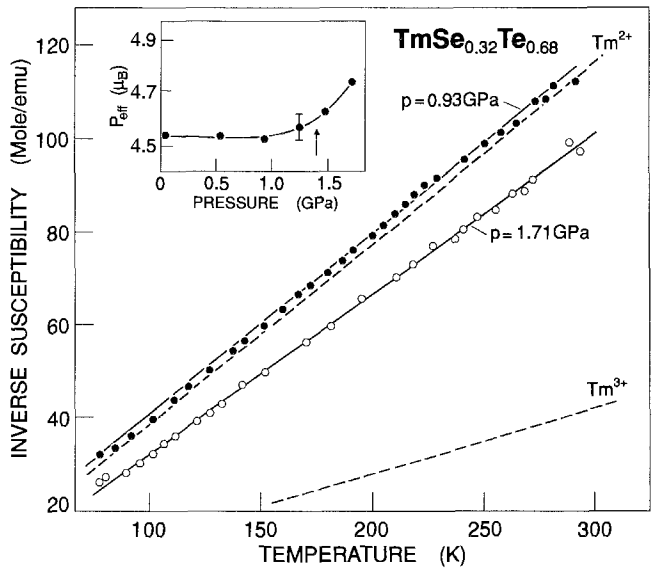

Fig. 103. Inverse magnetic susceptibility vs. temperature of $TmSe_{0.32}Te_{0.68}$ for pressures of 0.93 and 1.71 GPa. In the inset the effective moment p_{eff} is shown vs. pressure. The arrow at 1.4 GPa indicates the SMT. (After Boppart and Wachter 1984c.)

expected inverse susceptibilities for pure di- or trivalent Tm ions (dashed lines). The inset shows the effective moment as function of pressure with the SMT pressure at 1.4 GPa indicated by an arrow. The deviation from the divalent effective moment occurs only in the metallic state. The same behavior has been qualitatively observed in a similar investigation on TmTe under pressure by Wohlleben et al. (1972), but a precise comparison with the lattice constant was not possible at that time.

Thus, again, all lattice-related properties indicate an intermediate-valent Tm state already in the semiconducting state whereas the magnetic susceptibility points to a divalent state of the Tm ions. To elucidate this basic difference, the valence states, as determined either by the lattice constant or by the molar Curie constants, of different compounds from the series $TmSe_{1-x}Te_x$ and Tm_xSe have been compared by Boppart and Wachter (1984d) in fig. 104. The solid line in the figure would correspond to the same valence values for both methods. The dashed line guides the eye. It is now apparent that there is a clear discrepancy in determining the valence from the lattice constant or from the molar Curie constant. This incompatibility does not only exist for the strongly f–d mixed semiconductors but also for the metallic Tm_xSe and $TmSe_{1-x}Te_x$ compositions. For TmSe the lattice constant interpolation yields a Tm valence of 2.75, whereas from the C_M data (for $T < 300$ K) a valence of 2.55 can be deduced. For $T > 650$ K a valence of 2.65 has been obtained from C_M by Wachter (1982).

It is now possible to draw a generalized magnetic phase diagram for intermediate-valent metallic Tm chalcogenides, which is shown in fig. 105 (Boppart 1983). In principle

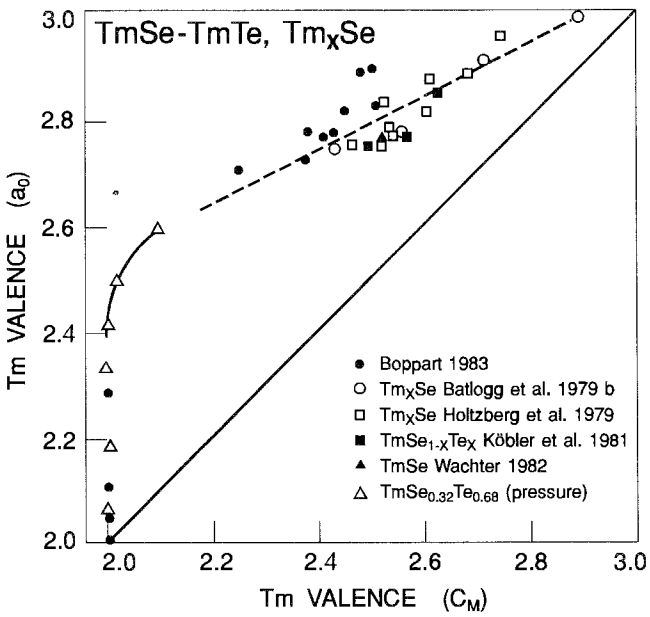

Fig. 104. Comparison between the Tm valences as deduced from the lattice constants (a_0) on the one hand and the molar Curie constants (C_M) on the other. The solid line would correspond to Tm valences being the same for both methods. (After Boppart and Wachter 1984d.)

this phase diagram can be plotted against the valence from the lattice constant (Batlogg et al. 1982) or the valence from the molar Curie constant (Boppart 1983). Since there exist different calibrations of the valence versus the lattice constant we prefer to plot against the valence from the Curie constant.

To start with trivalent TmS we find an ordering temperature of about 7 K where the antiferromagnetic order is mediated by the RKKY interaction (Köbler et al. 1981, Koehler et al. 1979, Bucher et al. 1975). Adding TmSe to TmS causes a valence instability of the Tm ions resulting in a moment quenching and a reduction of the ordering temperature. In the range of Tm_xSe around the minimum of the curve in fig. 105 the ordering temperatures are low, around 3 K, but one comes into the transition region of ferromagnetism; the compounds are in reality metamagnets, where a magnetic field above 0.5 T induces ferromagnetism, but a magnetic saturation cannot be achieved even in the highest magnetic fields. According to Varma (1977, 1979) double exchange now takes over with increasing valence mixing, the ordering temperatures reincrease and ferromagnetism takes over with $TmSe_{1-x}Te_x$ for $0.09 \leqslant x \leqslant 0.2$ (Boppart 1983). The pressure variation of $TmSe_{0.60}Te_{0.40}$ yields ferromagnetic order with ordering temperatures up to 5.5 K (Batlogg et al. 1982). If we also plot the semiconducting compositions in this figure we have to crowd them all at the divalent end with low magnetic ordering temperatures around 0.2 K. The type of magnetic order is unknown. The line separating antiferromagnetism from ferromagnetism near the valence 2.5 is also the separating line between hybridization

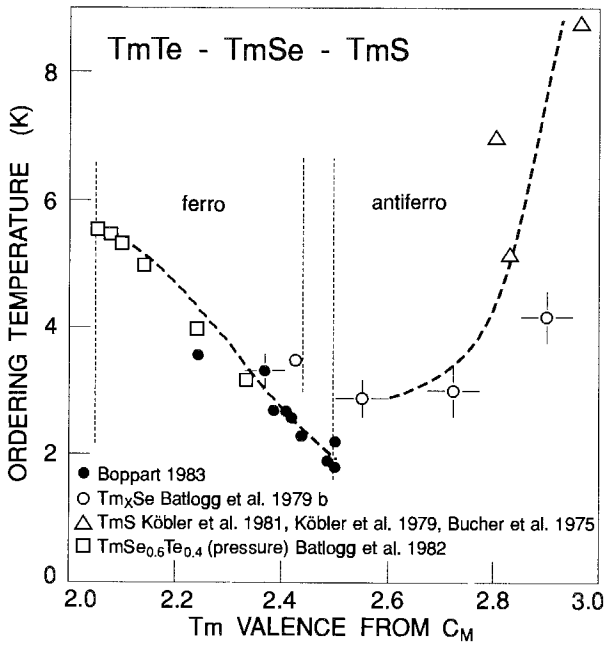

Fig. 105. A generalized magnetic phase diagram for intermediate-valent Tm monochalcogenides. (After Boppart 1983.)

gaps and no gaps. When the hybridization gaps exist, the gap values are around 1 meV and thus the smallest observed so far.

It is quite remarkable that the moment quenching observed in the metallic intermediate-valent compounds is not present in the semiconducting intermediate-valent compositions where the observed effective magnetic moments can be obtained by using the standard L, S and J values. Nevertheless, the latter compounds show dramatic effects and softenings in all lattice-related properties, where however, the phonon energies remain practically unrenormalized. Here we conclude the section on $TmSe_{1-x}Te_x$ which certainly has been one of the richest fields in intermediate valence.

4.3.2.2. *$Tm_{1-x}Eu_xSe$.*

4.3.2.2.1. *Electronic and lattice properties.* In this section the electronic properties of magnetically ordering divalent EuSe are altered by introducing TmSe, provoking possible intermediate valence. In this pseudobinary alloy system the substitution of Eu by Tm decreases the lattice constant, but since divalent Tm has a smaller ionic radius than divalent Eu there is no lattice pressure exerted on Tm as long as the compounds are semiconductors (see fig. 106). Thus Tm as well as Eu remain divalent. Kaldis et al. (1982) have shown that in the pseudobinary alloy system a number of miscibility gaps exist, but at $x=0.2$ a compositionally induced SMT is found, i.e., for $x<0.2$ the compounds

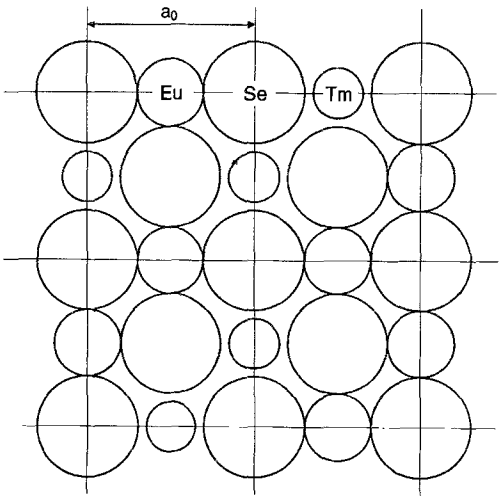

Fig. 106. $Tm_{1-x}Eu_xSe$ ions in the rocksalt structure. (After Wachter 1986.)

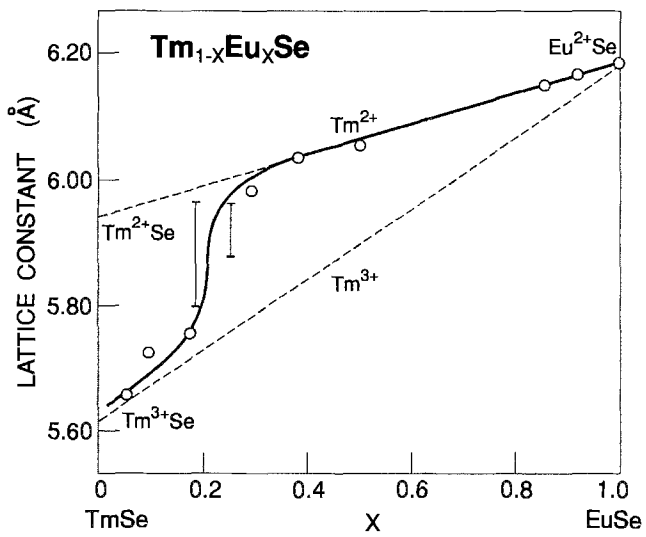

Fig. 107. The lattice constant of $Tm_{1-x}Eu_xSe$ as a function of composition x. Dashed lines are isovalent Vegard lines for Tm^{2+} and Tm^{3+} ions. (After Kaldis et al. 1982.)

are intermediate-valent metals (fig. 107). In this figure also isovalent Vegard lines are drawn and between the two vertical lines a miscibility gap exists. For the semiconducting compositions with $x > 0.2$ there are two localized 4f levels between the $4p^6$ valence band of Se and the 5d–6s conduction bands of the cations. The question is: can Eu become a trivalent donor just as is the case in $Sm_{1-x}Y_xS$, since Eu is known to exist also in two valence states? In EuSe Eu is divalent and the $4f^7$ state is 1.85 eV below

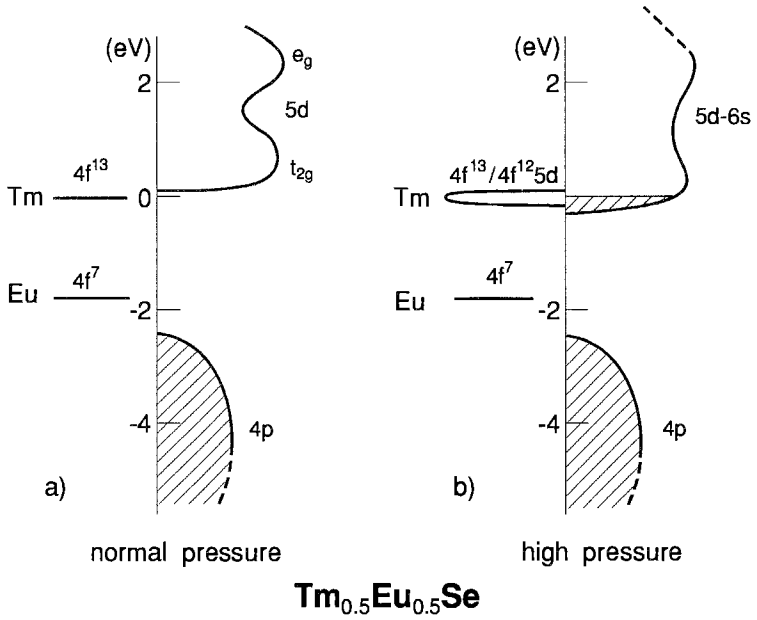

Fig. 108. Energy level scheme of (a) divalent $Tm_{0.50}Eu_{0.50}Se$ and (b) intermediate-valent $Tm_{0.50}Eu_{0.50}Se$ in the high-pressure phase (after Boppart and Wachter 1981a and Batlogg 1981c).

the bottom of the conduction band (Wachter 1979). Thus it can be expected that, in the whole composition range of $Tm_{1-x}Eu_xSe$, Eu remains divalent and its $4f^7$ level retains its position, about 1.85 eV below the bottom of the conduction band. The introduction of divalent Tm $4f^{13}$ will thus create another 4f state, above the one of Eu, but still below the conduction band for semiconducting compositions. Its position can be estimated by the difference in third ionization energy (Morss 1971), $25.13 - 23.89 = 1.24$ eV above the Eu $4f^7$ level which is 1.85 eV below the bottom of the conduction band, which yields the $4f^{13}$ state some tenths eV below the 5d band. An energy level scheme is shown in fig. 108a (Boppart and Wachter 1981a, Batlogg 1981c). The reduction of the lattice constant due to the substitution of Eu ions by smaller Tm ions increases the strength of the ligand field, thus the crystal-field split parts, $5dt_{2g}$ and $5de_g$, of the conduction band move apart in energy, keeping the $4f^{13}$-5d center of gravity essentially the same. At some critical Tm admixture the bottom of the conduction band will overlap the Tm level and the SMT will take place, simultaneously causing an intermediate-valent metal (fig. 108b), or possibly even a trivalent Tm configuration (fig. 107).

In the range of metallic configurations for $x < 0.2$ two compositions with $x = 0.11$ and 0.17 have been prepared. The $x = 0.17$ compound has been investigated more thoroughly (Batlogg 1981c, Boppart and Wachter 1981b). The lattice constant is, with 5.76 Å, near the trivalent Vegard line of fig. 107 and the effective magnetic moment, calculated from the Curie–Weiss law of the temperature dependent susceptibility is $7.07\mu_B$ (table 9). Since the effective moment of Tm^{3+} is $7.56\mu_B$ and the one of divalent Eu $7.94\mu_B$,

Table 9
Magnetic data for $Tm_{1-x}Eu_xSe$ (after Boppart and Wachter 1981c)

x	1.0	0.85	0.50	0.38	0.29	0.17	0
Paramagnetic Curie temperature Θ_p (K)	8.5	17.0	12.8	10.2	7.5	−13.2	−29
Magnetic ordering temperature $T_{C,N}$ (K)	4.6	15	19	17	13	4[a], 7	3.0
Effective magnetic moment per formula unit p_{eff} (μ_B)	7.9	7.53	6.62	5.91	5.16	6.59, 7[a]	6.4
Saturation magnetization M_{sat} [b] per formula unit (μ_B)	7.0	6.0	5.0	4.0	3.2	3.0	2.5

[a] Value from Batlogg (1981c).
[b] Measured in 9 T.

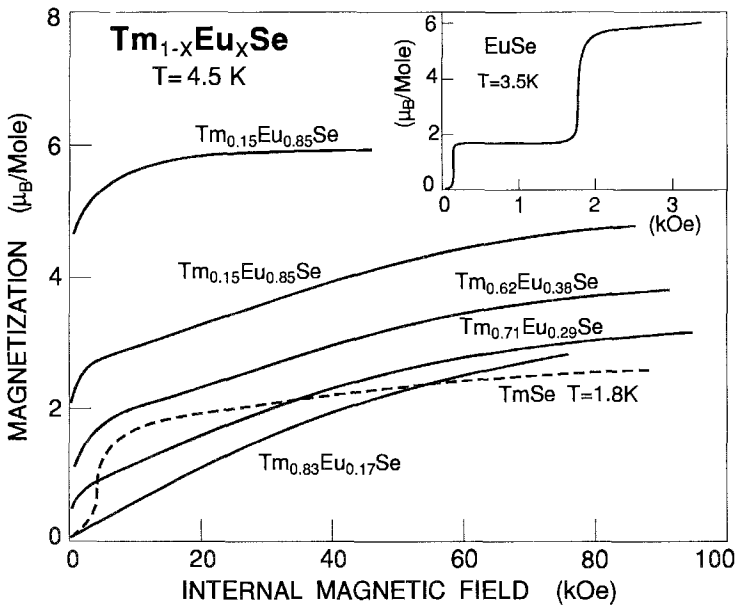

Fig. 109. Magnetization of $Tm_{1-x}Eu_xSe$ vs. magnetic field. The demagnetizing factor is taken into account (after Batlogg 1981c and Boppart and Wachter 1981b).

the composition $Tm^{3+}_{0.83}Eu^{2+}_{0.17}Se$ leads one to expect $7.62\mu_B$, thus Tm would have a valency somewhat less than 3. The magnetic ordering temperature obtained from the kink in the initial susceptibility is 7 K and the magnetization curve does not show a spontaneous moment nor is saturation achieved in fields up to 9 T (fig. 109). The conclusion then is that this composition is antiferromagnetic. Since the saturation moment gJ of Tm^{3+} and Eu^{2+} in both cases is $7\mu_B$, a complete cancellation of magnetic moments can occur in the antiferromagnetic state and thus no net spontaneous magnetization is expected.

The thermal expansion $\Delta L/L$ of metallic $Tm_{0.89}Eu_{0.11}$ has been measured by Reim et al. (1985) together with other $Tm_{1-x}Eu_xSe$ compositions and it is shown in fig. 110. Magnetostrictive effects are small near T_N of 4 K and practically no lattice collapse effects

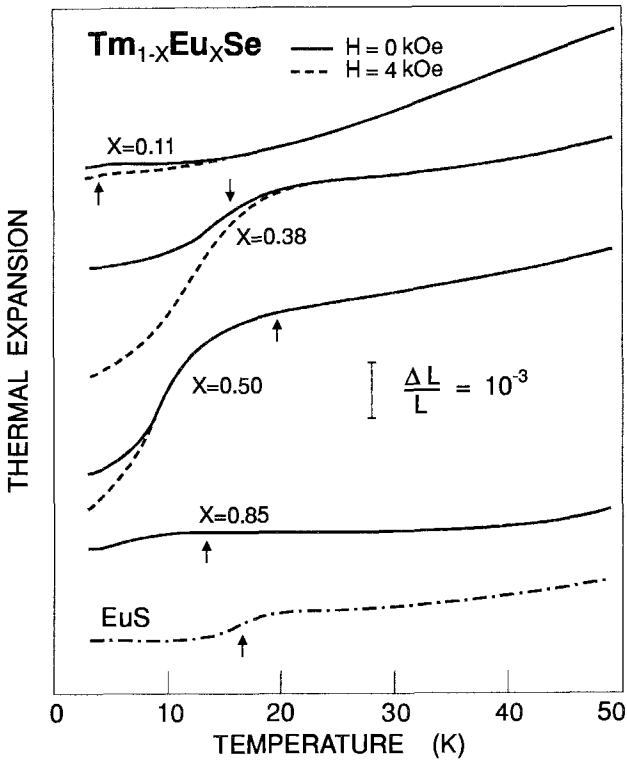

Fig. 110. The relative length change $\Delta L/L$ of $Tm_{1-x}Eu_xSe$ in zero field or with an applied field of 4 kOe. For comparison the magnetostriction of ferromagnetic EuS is also shown. (After Reim et al. 1985.)

are observed. This supports the view that valence mixing in the metallic compounds is small and the Tm is near trivalency.

In fig. 111 we show the resistivity–temperature behavior of $Tm_{0.83}Eu_{0.17}Se$ on a logarithmic temperature scale. Between 220 K and 300 K the resistivity drops with decreasing temperature as is typical for a metal, then it rises again, goes through a maximum and drops again. The Néel temperature is with 7 K on the decreasing branch and for a typical antiferromagnet it should be at the point of inflection. The curve resembles those of $Tm_{0.87}Se$ (Batlogg et al. 1979b) or Tm_5Se_6 (Berger et al. 1977, Andres et al. 1978) in which Tm is taken to be trivalent. Batlogg (1981c) assumes scattering into the empty $4f^{13}$ state, little above E_F, as in TmS (figs. 59 and 60). Only a Hall effect measurement on this sample can show whether the resistivity is caused by scattering or excitation. In fact, Batlogg (1981c) assumed that the Tm ions in this compound are in an inhomogeneously mixed state, i.e., most Tm ions are integer trivalent with a small admixture of integer divalent Tm ions caused by the lattice distortions introduced by the larger Eu^{2+} ions.

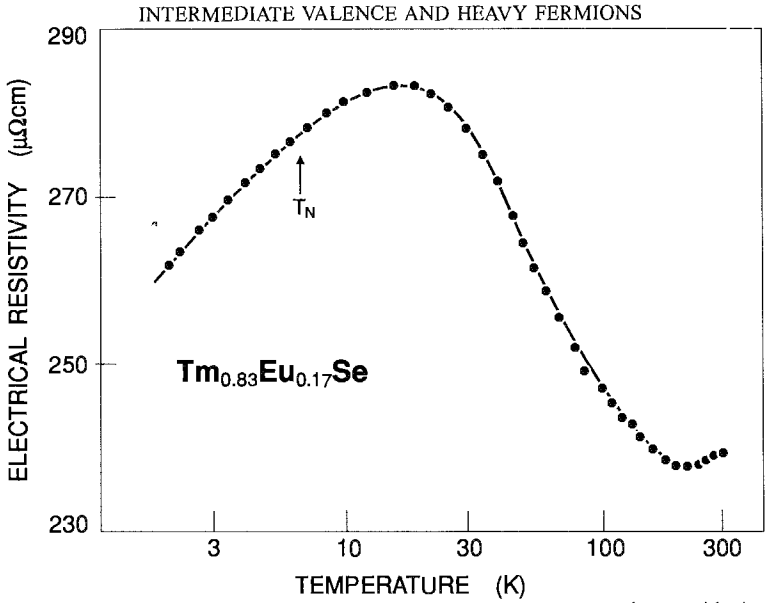

Fig. 111. Electrical resistivity vs. temperature of metallic $Tm_{0.83}Eu_{0.17}Se$. Note the logarithmic temperature scale. The Néel temperature of 7 K is indicated. (After Batlogg 1981c.)

We are now coming to the semiconducting compositions in $Tm_{1-x}Eu_xSe$ with $x > 0.2$. Since the semiconducting part of the series contains more and more Eu^{2+}, the low-temperature properties are dominated by magnetic order induced by the divalent Eu. Especially in the Eu rich compounds one may argue that one has semiconducting EuSe doped with another lanthanide, e.g. Gd where, for Gd concentrations above 5%, one observes an impurity band and metallic behavior. However, in Gd the outer electron is a 5d electron with a larger orbit which easily overlaps with the conduction band and also by inspecting the third ionization energy tables of Morss (1971) it becomes clear that Gd looses its outer electron into the conduction band. On the other hand it is also clear that in EuS doped with Tm, the Tm would also behave like Gd, i.e., act like Tm^{3+}, because the larger crystal-field splitting of the $5dt_{2g}$ and $5de_g$ bands now causes an overlap with the Tm level (see fig. 108b). In the $Tm_{1-x}Eu_xSe$ compositions with $x > 0.2$, Tm is strictly divalent, which can also be seen in fig. 107, it acts like a shallow donor, even with concentrations up to 80%, because the 4f states remain localized.

However, the application of hydrostatic pressure can now close the gap between the $4f^{13}$ and the conduction band and drive the SMT. The results of the resistivity in function of pressure are shown in fig. 112a for three compositions (Boppart and Wachter 1981a). The figures resemble similar measurements on the $TmSe_{1-x}Te_x$ system (e.g., fig. 84). The exponential decrease of the resistivity with pressure then suggests again a linear closing rate of the gap ΔE and with the same analysis as in eq. (8) one obtains the gap values listed in table 10. The closing rate $d\Delta E/dp$ is found to be nearly the same for all investigated compositions and this is in agreement with similar measurements on Eu- and Yb-substituted SmS compounds by Jayaraman and Maines (1979). The gaps ΔE for

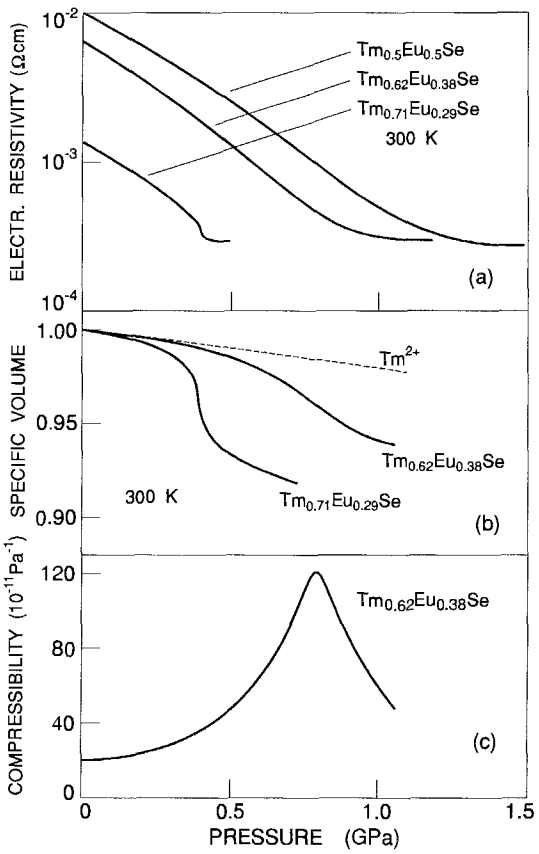

Fig. 112. (a) Electrical resistivity versus pressure of semiconducting $Tm_{1-x}Eu_xSe$; (b) volume change with pressure of $Tm_{0.62}Eu_{0.38}Se$ and $Tm_{0.71}Eu_{0.29}Se$. The dashed line indicates the expected behavior for stable Tm^{2+} valence; (c) compressibility of $Tm_{0.62}Eu_{0.38}Se$, obtained as derivative of the volume change. (After Boppart and Wachter 1981a.)

Table 10
Physical properties of semiconducting $Tm_{1-x}Eu_xSe$ ($x > 0.25$) (after Boppart and Wachter 1981c)

x	0.6	0.38	0.29
Lattice constant (Å)	6.06	6.04	5.99
Resistivity at ambient pressure (Ω cm)	1.1×10^{-2}	6.7×10^{-3}	1.3×10^{-3}
Resistivity at high pressure (Ω cm)	2.5×10^{-4}	2.7×10^{-4}	2.7×10^{-4}
Transition pressure (GPa)	1.3	1.0	0.4
$(d\Delta E/dp)$ for Tm $4f^{13} \rightarrow 5d$ (meV GPa^{-1})	−77	−81	−80
$4f^{13}$–5d energy gap for Tm from pressure data (meV)	100	80	40
Initial compressibility κ (10^{-11} Pa^{-1})		2.3	2.4
Maximum compressibility κ (10^{-11} Pa^{-1})		12	120
at pressure (PGa)		0.8	0.4

the semiconducting $Tm_{1-x}Eu_xSe$ compositions then are between 100 and 40 meV, again the same order of magnitude as in the $TmSe_{1-x}Te_x$ compounds. It is remarkable that the $Tm_{0.71}Eu_{0.29}Se$ compound nearly shows a first-order transition with actually a vertical tangent at the point of inflection, in other words it has the critical composition as in fig. 97 for $TmSe_{0.50}Te_{0.50}$.

In fig. 112b the volume change under pressure has been measured with strain gauges and the expected behavior of a purely divalent Tm compound is calculated with the Birch equation and shown as dashed line. The lattice softening is evident and it can be concluded that the semiconducting divalent $Tm_{1-x}Eu_xSe$ compounds can be driven to intermediate valence of the Tm ions with pressure and eventually into the metallic intermediate-valent state. In fig. 112c the derivative of the volume pressure variation, i.e., the compressibility is shown. Again an interesting behavior is exhibited by $Tm_{0.71}Eu_{0.29}Se$, the compound closest to the compositionally induced SMT. Nearly a first-order transition is observed at 0.4 GPa. Probably only the stabilization of the lattice due to divalent Eu ions prevents the discontinuous valence transition of the Tm ions. It is evident from figs. 112a, b that the materials become intermediate valent before the SMT takes place, i.e., this is another example of "intermediate-valent semiconductors".

4.3.2.2.2. *Optical properties.* A nice proof that under normal conditions Eu as well as Tm ions are divalent can be given by optical reflectivity measurements on $Tm_{0.50}Eu_{0.50}Se$ and $Tm_{0.15}Eu_{0.85}Se$. In figs. 113a and 113b, respectively, we show the reflectivity on cleaved single crystals between 0.03 and 5 eV (Batlogg 1981c, Frey 1981). The peak structure can be identified with the final state spectra $4f^6$ and $4f^{12}$ of divalent Eu ($4f^7$) and divalent Tm($4f^{13}$), similarly as for SmS in fig. 31. Again both ladder-like structures appear twice, corresponding to transitions into the crystal-field split $5dt_{2g}$ and $5de_g$ bands. As a consequence, the crystal-field splitting 10 Dq can be obtained with about 2.0 eV. In fig. 113a a plasma edge due to free carriers at the low-energy end of the spectrum can be discerned which is no longer visible in fig. 113b because the latter compound has with a larger energy gap ΔE less free carriers at 300 K. In addition, it is obvious from fig. 113a, b that in the $Tm_{0.15}Eu_{0.85}Se$ compound the Tm-related peaks are less pronounced than in $Tm_{0.50}Eu_{0.50}Se$, which clearly is related to the Tm concentration.

We have shown in fig. 112a,b,c that $Tm_{0.50}Eu_{0.50}Se$ undergoes a pressure-induced valence transition with hydrostatic pressure. However, one can also, just as in SmS, induce the valence transition by just polishing the surface, and in spite of the fact that under hydrostatic conditions there is no first-order transition with hysteresis, the anisotropic pressure induced by polishing provokes a hysteresis and pressure remains stored in a surface region. The stored pressure can be larger than the SMT, and the crystal be thus in the intermediate-valent state. The reflectivity of this transformed single crystal is shown in fig. 113c (Batlogg and Wachter 1980, Batlogg 1981c, Frey 1981). The Tm^{2+}-related peaks have disappeared, either because the sample is completely transformed to trivalency (the Tm^{3+} final states would be below 6 eV), or because intermediate valency is close to trivalency, thus the concentration of Tm^{2+}-related states (recall this is a high-energy measurement) are relatively small. However, the Eu^{2+}-related peaks are clearly discernible, and their onset remains at about 1.8 eV below E_F, as expected. Also there

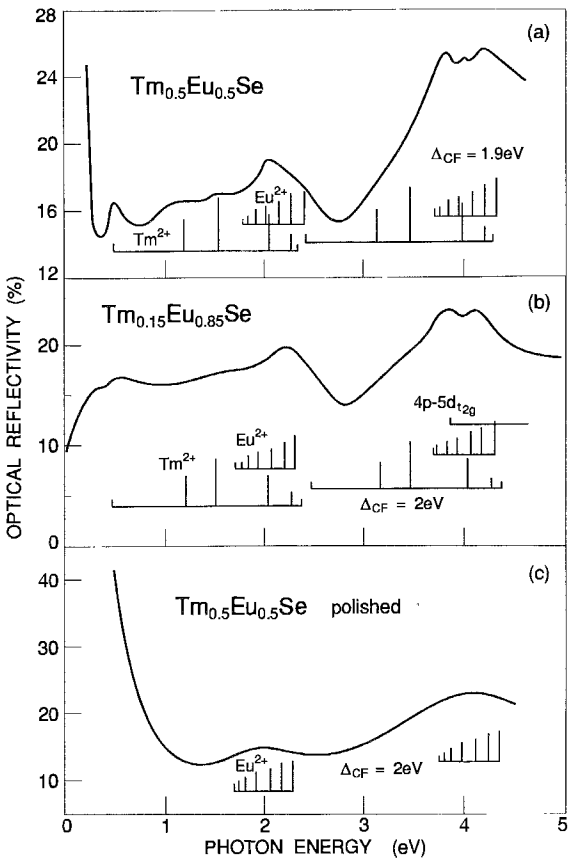

Fig. 113. (a) Optical reflectivity of $Tm_{0.5}Eu_{0.5}Se$ cleaved single crystals. The ladder-like Tm^{2+} and Eu^{2+} final states are indicated in addition the 5d crystal-field splitting Δ_{CF}. (b) Optical reflectivity of cleaved single crystals of $Tm_{0.15}Eu_{0.85}Se$. (c) Optical reflectivity of polished single crystals of $Tm_{0.5}Eu_{0.5}Se$ (high pressure phase); only the Eu^{2+} final states can be discerned. (After Batlogg 1981c and Frey 1981.)

appears a screened plasma edge at about 1.2 eV which is due to the 5d electrons liberated from the $4f^{13}$ state. The energy level scheme now looks like fig. 108b. Since these samples are at the same time ferro- or canted antiferromagnetic (see below), we do not expect a hybridization gap at low temperatures.

4.3.2.2.3. *Magnetic properties.* We have already stated that without external pressure in the semiconducting compositions, Tm as well as Eu are divalent as inferred, e.g., from the lattice constant in fig. 107. This statement is corroborated by measuring the magnetic susceptibility. For $Tm_{0.50}Eu_{0.50}Se$ a Curie–Weiss law is observed by Batlogg (1981c) with an effective moment of $6.53\mu_B$. Comparing this value with the one expected for a 1:1 mixture of divalent Tm and Eu ions one finds that with $6.35\mu_B$ indeed both ions must be divalent. The conclusion is general that in semiconducting $Tm_{1-x}Eu_xSe$, but also in semiconducting $TmSe_{1-x}Te_x$ (see preceding chapters) the L, S and J values of divalent Tm are conserved.

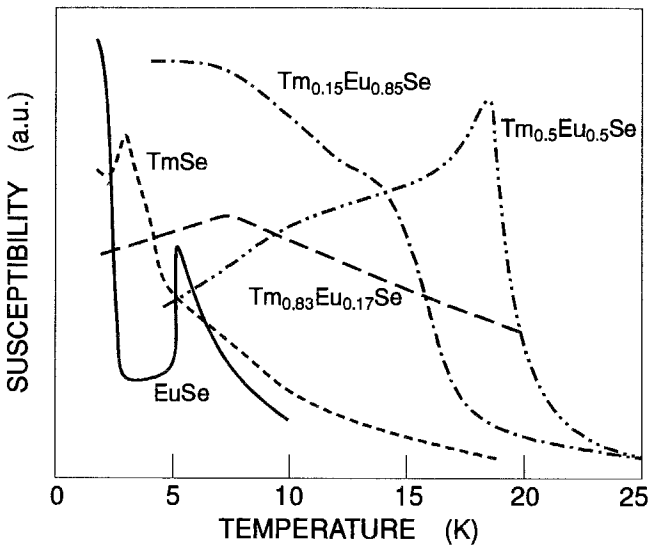

Fig. 114. The initial magnetic susceptibility of semiconducting and metallic $Tm_{1-x}Eu_xSe$ in fields of 10 Oe; TmSe and EuSe are shown for comparison. (After Boppart and Wachter 1981b.)

In fig. 114 the initial susceptibility in fields of 10 Oe are shown for the compositions given in table 9. For EuSe the peak in the susceptibility at about 5 K indicates antiferromagnetism and the sharp rise at 2.8 K is evidence of the transition to ferrimagnetic order (Wachter 1979). A small admixture of 0.15 Tm shifts the ordering temperature to about 15 K. The dip at about 10 K is probably due to the onset of another magnetic phase. In an applied field of 500 Oe the curve is smooth and indicates ferromagnetic order. The 50/50 compound has a sharp peak at about 19 K, indicating some kind of antiferromagnetic order (canted, see below). The Tm rich compound has a peak at about 7 K, suggesting antiferromagnetism and, finally, TmSe is known to be an antiferromagnet with AF I structure, with a Néel point of about 3 K.

The type of magnetic ordering becomes even clearer by looking at the magnetization curves in fig. 109. EuSe and TmSe are both metamagnets with internal critical fields of 0.75 kOe (Wachter 1979) and 4.5 kOe (Batlogg et al. 1979b). EuSe achieves, with an applied field of 15 kOe, the saturation moment of $7\mu_B$ (inset of fig. 109), whereas TmSe, being an intermediate-valent compound, cannot be saturated even with 100 kOe (10 T). $Tm_{0.15}Eu_{0.85}Se$ also exhibits saturation with about $6\mu_B$, less than 10% of the theoretical value $6.55\mu_B$ of both divalent Tm and Eu. The 50/50 composition has a spontaneous moment in zero field of about $2.3\mu_B$ and it seems to be saturated at about $5.5\mu_B$ in a field extrapolated to 120 kOe. This value corresponds to the theoretical value of 0.50 (7+4) of divalent Tm and Eu. The magnetic structure in zero magnetic field seems to be canted antiferromagnetism. Finally, the metallic $Tm_{0.83}Eu_{0.17}Se$ has no spontaneous

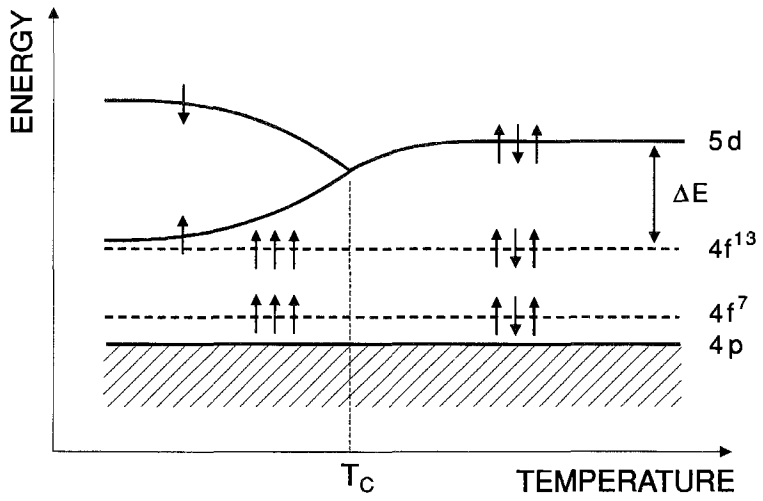

Fig. 115. The bottom of the 5d conduction band and its exchange splitting ("red shift") with temperature. Also shown is the top of the p valence band and the localized levels $4f^7$ and $4f^{13}$. (After Wachter 1986.)

moment at zero field, it achieves $3\mu_B$ at 90 kOe and is far from being saturated, thus it is an antiferromagnet. All other magnetic data are collected in table 9.

4.3.2.2.4. *Exchange-induced valence transition.* It is well known that the ferromagnetic Eu chalcogenides show an exchange splitting of the 5d conduction band upon magnetic order (Wachter 1979). This effect is called "the red shift" since the energy gap ΔE between the localized $4f^7$ and 5d band states is reduced with magnetic order, where the reduction follows the spin correlation function, i.e., it already commences above the ordering temperature. This effect is shown schematically in fig. 115, where the top and the bottom of the respective bands are shown in function of temperature. The splitting is with respect to the $4f^7$ level. When, however, as in the $Tm_{1-x}Eu_xSe$ system, there is a second lanthanide, namely a Tm^{2+} $4f^{13}$ level, only little below the bottom of the 5d conduction band, it can happen that the exchange splitting is so large that at a given temperature the 5d band scans over the $4f^{13}$ level with all the consequences as hybridization and intermediate valence. (The relative positions of the two 4f states remains constant as they are being fixed by the respective third ionization potentials (see above)).

The semiconducting $Tm_{1-x}Eu_xSe$ compounds have energy gaps ΔE (now counted between the upper $4f^{13}$ level and the bottom of the conduction band) between 40 and 160 meV (table 10) for $0.29 < x < 0.85$. The red shift of undoped EuSe amounts to 130 meV in the ferromagnetic state (Wachter 1979). Three competing effects have to be considered. The dilution of the strong magnetic $4f^7$ states by the less magnetic $4f^{13}$ states will reduce the magnetic order and the red shift, the smaller separation of the $4f^{13}$ state and the 5d conduction band will enhance the red shift and the magnetic ordering temperature and thermally excited carriers from the $4f^{13}$ state into the conduction band will give an additional exchange due to the RKKY interaction and thus further enhance

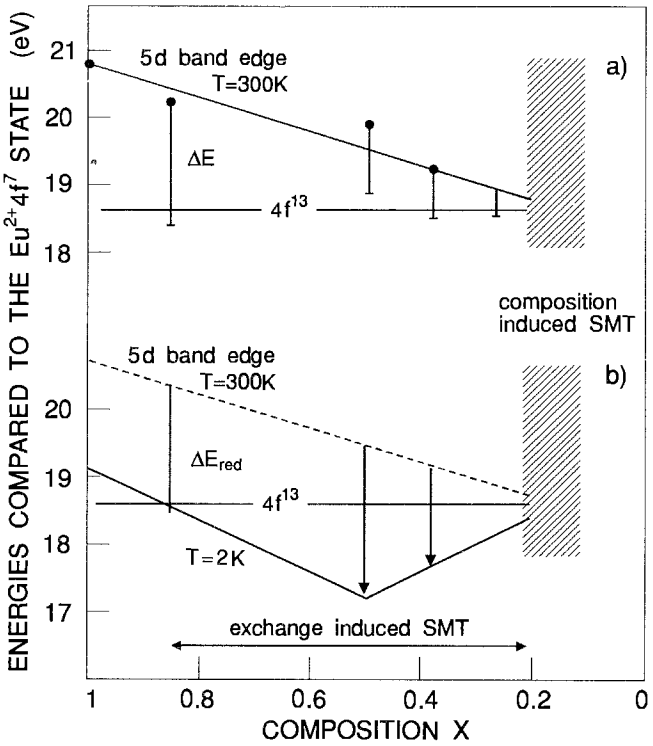

Fig. 116. (a) Onset energy of the Eu^{2+} $4f^7 \rightarrow 4f^6 5dt_{2g}$ transition in $Tm_{1-x}Eu_xSe$ at 300 K as a function of x from the polar Kerr effect. Subtraction of the respective semiconducting gap energy ΔE yields the position of the Tm^{2+} $4f^{13}$ state relative to the Eu^{2+} $4f^7$ level. (b) Onset of the same Eu^{2+} excitation at 2 K. Compared to the value at 300 K this energy is smaller by the size of the magnetic "red shift" ΔE_{red}. The energy separation of the Eu^{2+} and Tm^{2+} 4f states is kept constant. (After Reim et al. 1985.)

the red shift and the ordering temperature. It cannot a priori be said which effect finally wins, but with small and up to moderate substitution we can expect an exchange-induced intermediate valence. In fact fig. 115 is drawn for $x = 0.85$ where the gap is just closed at 2 K. In fig. 116a the 5d band edge and the position of the $4f^{13}$ level of Tm are shown in function of composition with the compositionally induced SMT indicated by the hatched region to the right. The vertical bars indicate the ΔE values from table 10.

It would be advantageous to measure the red shift directly for various x and this is possible by monitoring the Kerr rotation Θ_K of the Eu^{2+} $4f^7$–$5dt_{2g}$ transition as shown by Reim and Wachter (1985) and Reim et al. (1985). At room temperature the onset energy of this transition decreases linearly with x. Subtracting the respective magnitudes of ΔE ($4f^{13}$–$5dt_{2g}$) from these energies (table 10) yields the position of the Tm^{2+} $4f^{13}$ state relative to the $4f^7$ level which comes out to be independent of composition x (fig. 116a). The onset energy at temperatures well below the magnetic ordering temperature, on the

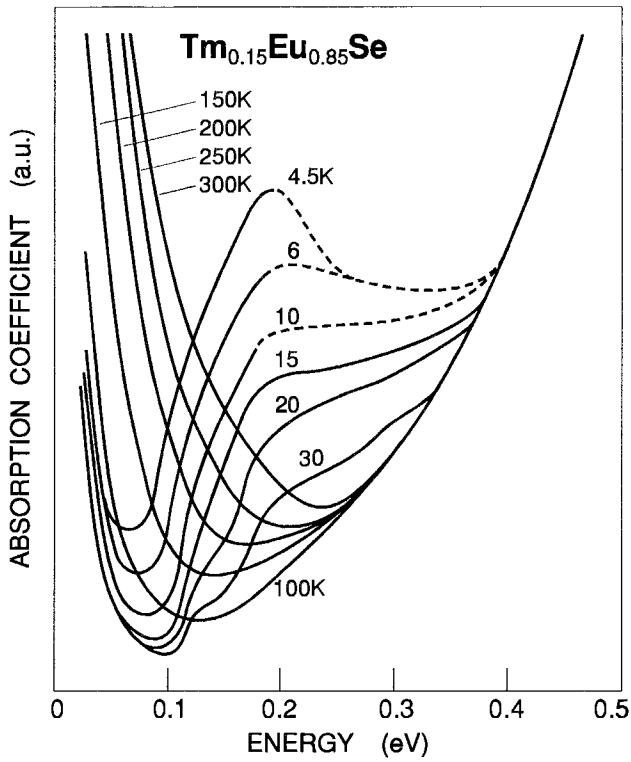

Fig. 117. Absorption coefficient of $Tm_{0.15}Eu_{0.85}Se$ at various temperatures. (After Reim et al. 1985.)

other hand, is reduced by the observed magnetic red shift ΔE_{red} (fig. 116b). It comes as a surprise that ΔE_{red} for $0.25 < x < 0.85$ is larger than in EuSe itself. From the above it becomes clear which one of three possibilities wins, and there is direct evidence in the increase of the magnetic ordering temperatures collected in table 9. Assuming a temperature independent separation in energy of the Tm^{2+} and the Eu^{2+} 4f states, a crossing of the lower 5d band edge with the Tm^{2+} $4f^{13}$ occurs for practically all semiconducting $Tm_{1-x}Eu_xSe$ compositions.

A direct absorption measurement of this transition is difficult because of substantial free carrier absorption in this energy range. Nevertheless, such an experiment was performed by Reim et al. (1985) on $Tm_{0.15}Eu_{0.85}Se$ which has the lowest free carrier concentration. The experiment is shown in fig. 117 where the absorption coefficient is plotted versus the photon energy. At 300 K one observes an absorption edge and a free carrier absorption resulting in a minimum of the absorption coefficient. With lower temperature, but still in the paramagnetic temperature range, this minimum deepens and the free carrier absorption decreases in accordance with the semiconducting behavior of this substance. At temperatures below about 30 K, at the onset of the spin correlation function (about 2–3 times T_N) we discern a red shifting knee in the absorption spectrum

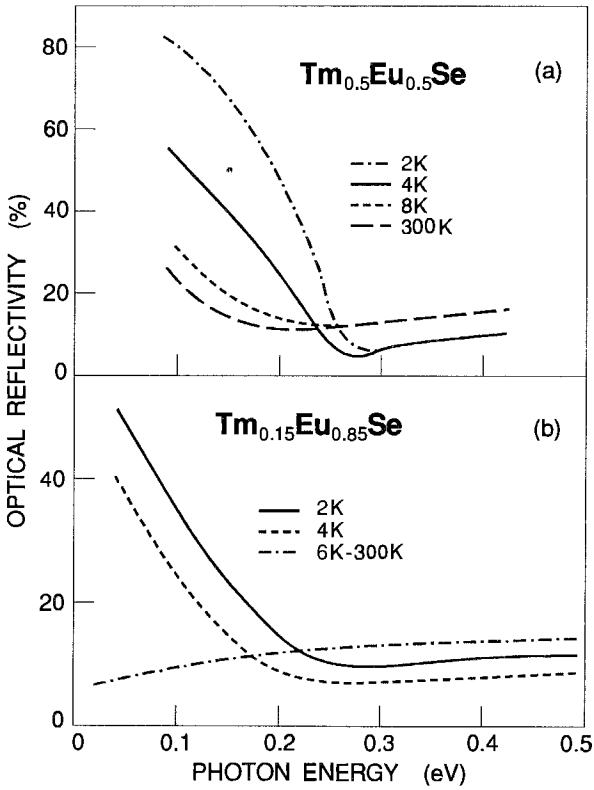

Fig. 118. Optical reflectivity of (a) $Tm_{0.5}Eu_{0.5}Se$ and (b) $Tm_{0.15}Eu_{0.85}Se$ in the far infrared. (After Reim et al. 1985.)

(the Tm concentration is only 15%) and, at the same time, below about 10 K an increase of the free carrier concentration, i.e., the gap closes faster than $k_B T$ with decreasing temperature: $d\Delta E/dT < 0$. At temperatures below 4.5 K the gap is practically closed and transmission is no longer possible.

In addition, the reflectivity which was measured on a cleaved crystal of the same batch, is displayed in fig. 118b. Between 300 and 6 K the reflectivity is unchanged in the given photon energy range, displaying semiconductor behavior with only a few free carriers, the plasma edge being further out in the infrared. Only at 4 and 2 K the reflectivity increases sharply for $\omega \to 0$ because of the plasma edge of the free carriers, indicating metallic behavior. In fig. 118a we also show the reflectivity of a cleaved $Tm_{0.50}Eu_{0.50}Se$ crystal. One already observes at room temperature a plasma edge in the infrared because of the smaller gap. At temperatures below 8 K a large shift of the plasma edge towards higher energies becomes manifest, indicating a significant increase in free carrier concentration.

Now one can understand the transport properties of these compounds. The electrical resistivity of $Tm_{0.50}Eu_{0.50}Se$ is shown in fig. 119 (Batlogg 1981c). Above 300 K the resistivity drops exponentially with temperature, the activation energy being 50 meV when using an Arrhenius plot with $\Delta E/2k_B T$, i.e., taking E_F in the middle between the $4f^{13}$ state

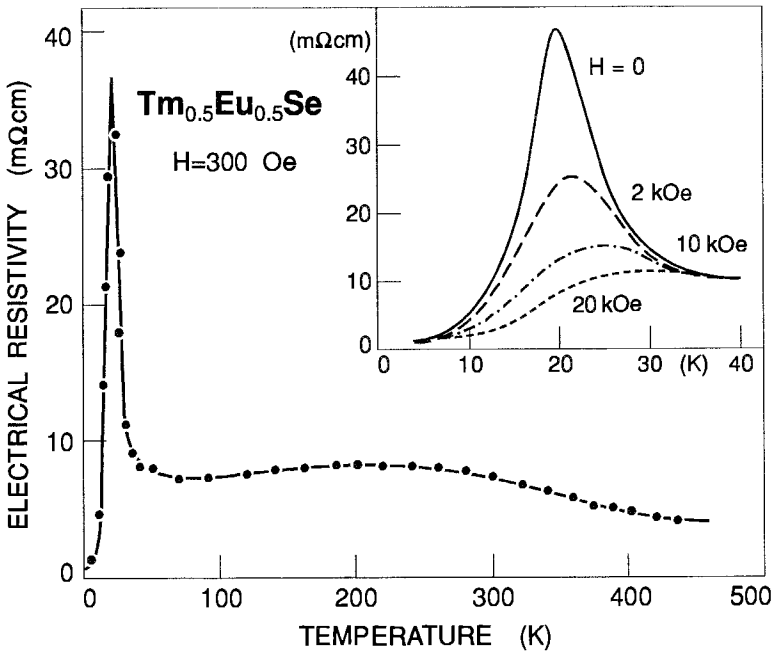

Fig. 119. Resistivity of $Tm_{0.5}Eu_{0.5}Se$ in different magnetic fields. (After Batlogg 1981c.)

and the 5d band edge. At about 300 K E_F is pinned at the $4f^{13}$ level and the activation energy, i.e. ΔE, becomes 100 meV as verified by the pressure dependence of the resistivity and shown in table 10. Near the magnetic ordering temperature of 19 K (table 9) a strong peak is observed in the resistivity which is magnetic in origin as is evident from the inset of fig. 119 where it can be eliminated in large magnetic fields. At a first glance one might ascribe this peak to spin flip scattering but an inspection of fig. 118a reveals that the carrier concentration is changes as well, due to the reduction of the gap caused by the red shift. Thus the phenomenon is very involved.

More insight is gained by investigating the transport phenomena for $Tm_{0.15}Eu_{0.85}Se$ shown in fig. 120. On the left-hand scale the conductivity ($1/\rho$) is shown, which again exhibits a minimum near T_N of about 15 K (table 9). This compound just closes its energy gap at 2 K (fig. 115). To understand the conductivity better ($\sigma = \mu Ne$) also the mobility μ has been measured. This was possible by also investigating the photoconductivity $P = Q\mu\tau$ with Q the quantum efficiency and τ the life time of the carriers (Boppart and Wachter 1981c). The latter quantities can be assumed as being temperature independent (Wachter 1979), and thus the photoconductivity is proportional to the mobility μ. The mobility shows a sharp minimum at T_C due to spin disorder scattering. The deduced carrier concentration (conductivity divided by mobility) in fig. 120 shows near T_C an exchange-induced "evaporation" of electrons where the gap again closes at a faster rate than the thermal energy reduces. The most important effect is seen below 8 K with an extremely sharp increase of the carrier concentration over at

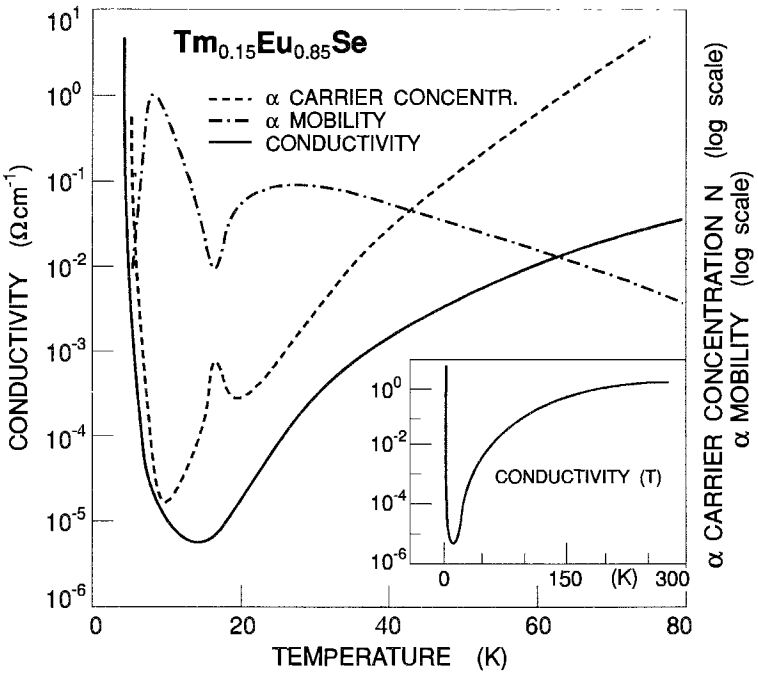

Fig. 120. Electrical transport properties of $Tm_{0.15}Eu_{0.85}Se$ vs. temperature. Left-hand scale: electrical conductivity. Right-hand scale: carrier concentration and mobility. The inset shows the conductivity near the magnetic ordering temperature. (After Boppart and Wachter 1981c.)

least 6 orders of magnitude, indicating a transition to a metallic behavior. We achieve intermediate valence due to the overlap and hybridization of the $4f^{13}$ state with the 5d band edge.

The SMT should be concomitant with a transition to intermediate valence of the Tm ion. Figure 116b postulates the largest valence change for $x = 0.5$ with the bottom of the conduction band 140 meV below E_F at 2 K. It is known from volume versus pressure experiments (Boppart and Wachter 1981a) that the conversion of 15% Tm^{2+} into Tm^{3+} in the average is accompanied by a volume collapse of 1%. This can be seen in the length change measurements performed in fig. 108 where $\Delta L/L$ for $Tm_{1-x}Eu_xSe$ is shown, and, measured in the same apparatus, for comparison also for EuS. The indicated ordering temperatures are given in table 9 and fig. 114 on the identical samples. For the reference material EuS, a classical ferromagnet, an exchange striction $\Delta L/L$ (or a peak in the expansion coefficient $\alpha_T = 1/L(dL/dT)$) at the magnetic ordering temperature and a magnetic contraction $\Delta V/V = 1.2 \times 10^{-3}$ (Levy 1969) is found. The most contrasting behavior is shown by $Tm_{0.50}Eu_{0.50}Se$ with clearly no relation between maximum slope and magnetic ordering temperature (recall that for $0.25 < x < 0.85$ the compounds are canted antiferromagnets with a spontaneous magnetization). In addition this compound shows the largest volume collapse of 1.1%, ten times larger than in EuS. A similar behavior

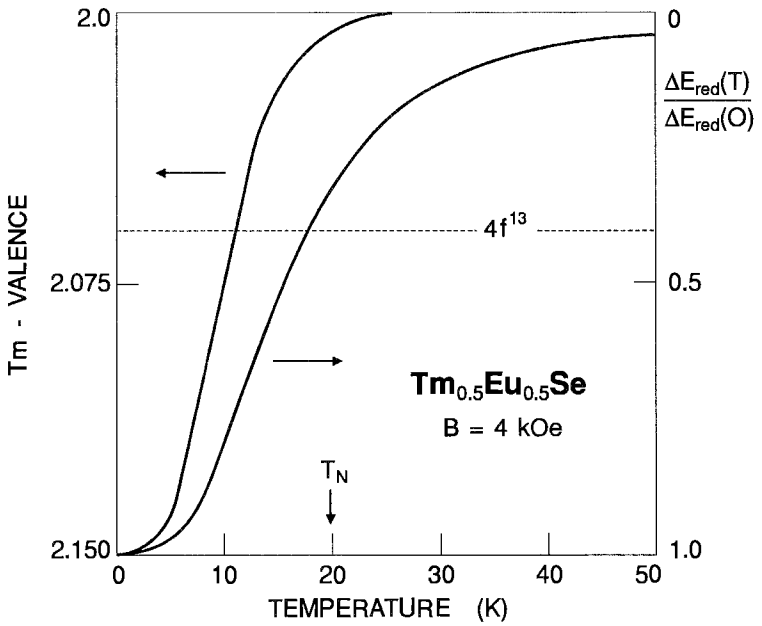

Fig. 121. Temperature dependence of the lower 5d band edge as derived from magneto-optics and magnetization measurements at 4 K for $Tm_{0.5}Eu_{0.5}Se$. The temperature variation of the Tm valence is calculated from the measured volume change by Vegard's law. (After Reim et al. 1985.)

is found for $x=0.38$, whereas the sample with the largest gap, $x=0.85$ displays much smaller contractions. The saturation value. However, as soon as the gap is closed the Tm valence alters rapidly with temperature. It can also be taken from fig. 110 that in the absence of a magnetic field the valence transformation is not complete since the volume change can still be enhanced with a moderate magnetic field.

In summary the alloy systems $TmSe_{1-x}Te_x$ and $Tm_{1-x}Eu_xSe$ have proven to belong to one of the most fruitful areas of research where new phenomena such as exchange-induced valence transitions or the excitonic insulator have been discovered. This only became possible by systematically varying the composition and using only well characterized large single crystals, which were never handled in air.

4.4. *Yb monochalcogenides*

4.4.1. *Electronic properties*

The Yb monochalcogenides belong to the class of materials for which the Luttinger theorem would suggest the Fermi energy to lie within the hybridization gap when they become intermediate valent. However, an inspection of the third ionization energy tables of Morss (1971) shows that the 4f–5d center of gravity separation should be about two tenth of an eV less than in the corresponding Eu monochalcogenides. On the other

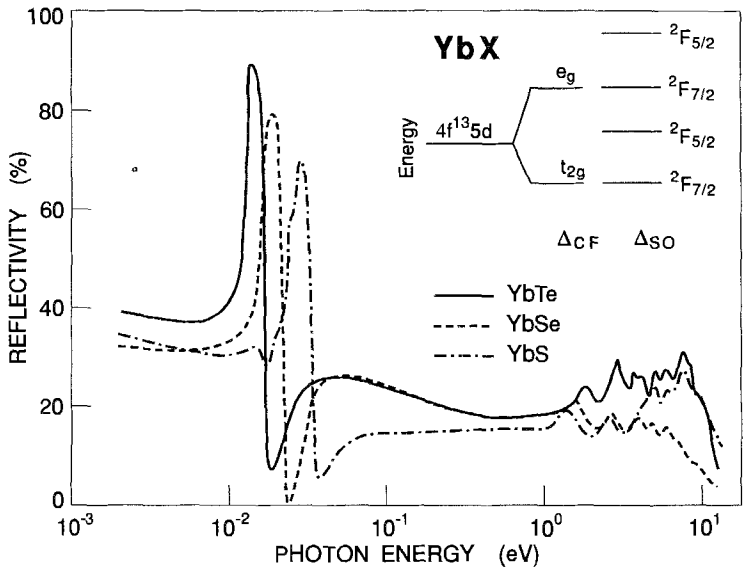

Fig. 122. Optical reflectivity of YbS, YbSe and YbTe single crystals at 300 K. The inset shows the energy level scheme of the $4f^{13}5d$ final state. (After Wachter 1994.)

hand, e.g., with 5.68 Å the lattice constant of YbS is appreciably smaller than that of EuS (5.97 Å), so that the crystal-field splitting of the $5dt_{2g}$ and $5de_g$ bands is larger in YbS than in EuS, which further reduces the $4f–5dt_{2g}$ gap compared to EuS. We can estimate with the help of fig. 37 for the Sm monochalcogenides or from Batlogg et al. (1976b) the energy gap of, e.g., YbS to be about 1.2 eV. For YbSe and YbTe we estimate energy gaps of 1.6 and 1.8 eV which compare favorably with the gap values determined on thin films by Narayanamurti et al. (1974) (1.0 eV, 1.5 eV and 1.8 eV for YbS, YbSe and YbTe, respectively). The complete absorption or reflectivity spectra of the Yb monochalcogenides are made more complex by the final state multiplet spectra of the $4f^{14} \rightarrow 4f^{13}(^2F_{7/2}, ^2F_{5/2})\ 5d(t_{2g}, e_g)$ transition. The final state $4f^{13}5d$ is shown in the inset of fig. 122 together with the reflectivity spectrum of the Yb chalcogenides over 4 decades of photon energy and the latter can be completely identified with the former scheme, but in addition also the phonon residual ray spectrum in the far infrared is shown (Wachter 1994). For YbTe the photoconductivity has been measured in function of photon energy and temperature by Fischer (1973). Photoconductivity sets in below 2 eV and could be measured to above 3 eV, i.e., over the first two reflection (or absorption) peaks of fig. 122 and the existence of photoconductivity at the position of the absorption edge ensures that the lowest energy absorption goes into a conduction band.

We realize of course, that with 4f–5d energy gaps between 1 and 2 eV and with standard deformation potentials of the order of 5 eV (Jayaraman 1979) the pressure-induced valence transition will be between 100 and 200 kbar, and in fact, the pressure-

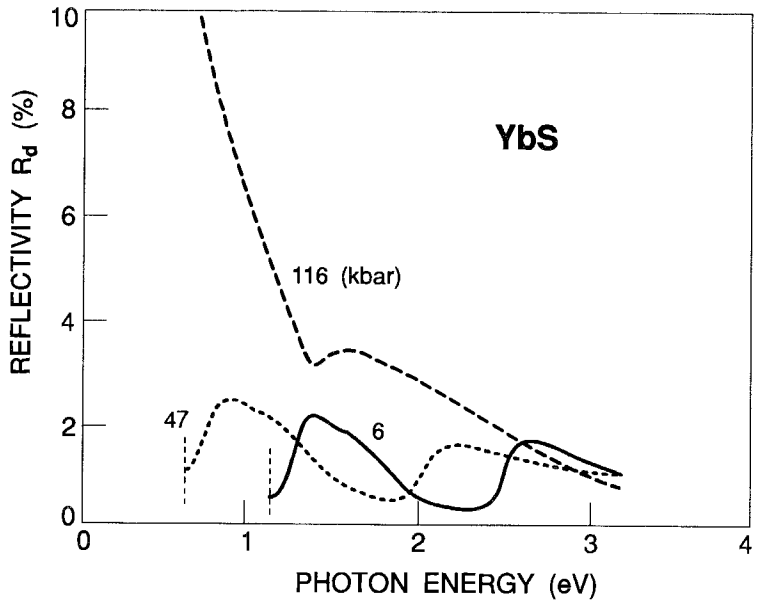

Fig. 123. Optical reflection spectra of YbS at 6, 47 and 116 kbar. The vertical dashed lines indicate the energy below which interference noise is observed. The spectra are not corrected for losses at the diamond face. (After Syassen et al. 1985.)

volume relation shows an anomalous volume change which is attributed to the valence change around these pressures (Jayaraman et al. 1975). Unfortunately, at these pressures it is difficult to perform low-temperature resistivity, Hall effect, point contact spectroscopy or far infrared spectroscopy to determine the hybridization gap or even only an activated resistivity behavior with meV gaps.

However, an interesting measurement of near infrared optical reflectivity under high pressures up to 400 kbar at ambient temperature has been performed by Syassen et al. (1985) on YbS and YbO. The latter compound cannot be prepared at ambient pressure but can be synthesized at high temperature and high pressure. In fig. 123 the optical reflection spectra of YbS at 6, 47 and 116 kbar is shown and in fig. 124 up to 390 kbar. The reflectivity values are not corrected for reflection losses at the diamond faces. At low pressures the two reflectivity peaks corresponding to $4f^{14} \rightarrow 4f^{13}(^2F_{7/2}, {}^2F_{5/2})5dt_{2g}$ transitions shift simultaneously to lower energies with pressure, confirming the above assignment. The gap is closing with pressure due to the increased crystal-field splitting $5dt_{2g}$–$5de_g$. At 116 kbar the gap is nearly closed and a plasma edge due to thermally excited free carriers into the $5dt_{2g}$ band has moved from the far infrared into the observed spectral range. However, at still higher pressures the plasma edge has disappeared again and other reflectivity peaks appear which shift with increasing pressure to higher energy.

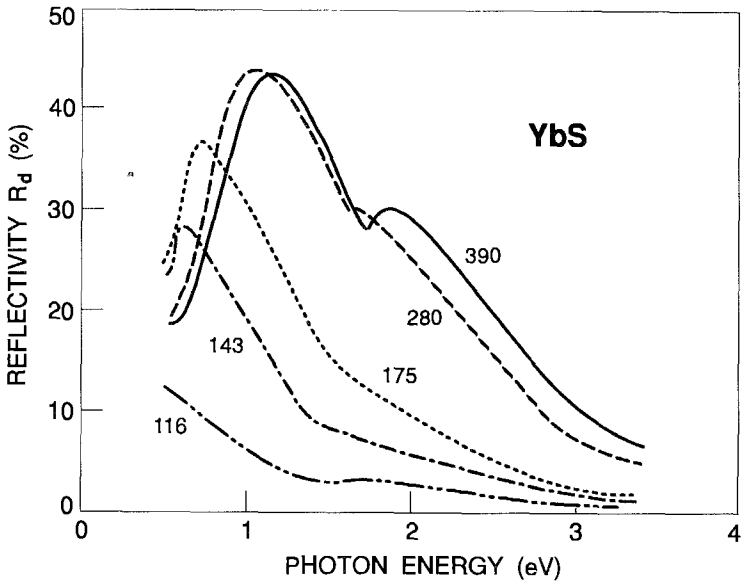

Fig. 124. Optical reflection spectra of YbS above 100 kbar. Numbers correspond to pressure in kbar. The spectra are not corrected for losses at the diamond face. (After Syassen et al. 1985.)

We think we have here a second example of the formation of excitonium or exciton condensation, just as was discovered by Neuenschwander and Wachter (1990a,b) and by Bucher et al. (1991). If we follow the development of the plasma edge with pressure, where the plasma energy ω_p^2 is proportional to N/m^* and thus proportional to σ, we observe that at 300 K at first the resistivity $\rho = 1/\sigma$ decreases with pressure and then suddenly increases with still higher pressure. This phenomenon is experimentally similar to that in figs. 89 or 90 from which the excitonic insulator has been derived. We should not forget that this anomalous resistivity increase with increasing pressure can be observed in $TmSe_{1-x}Te_x$ up to 240 K.

Why then would this phenomenon be observed in YbS and YbO too? In $TmSe_{1-x}Te_x$ we had a small semiconductor gap to close which means the pressure scale is an order of magnitude smaller than in YbS or YbO. With pressure we not only reduce the gap and start valence mixing, but we also increase the electron–hole Coulomb interaction, but only when there are not too many free electrons because they would screen the Coulomb interaction. Thus in $TmSe_{1-x}Te_x$ the alloying of TmSe with TmTe serves to reduce the free carrier concentration in TmSe from about 10^{22} cm^{-3} to about 10^{20} cm^{-3} at 300 K (see fig. 86). So when the gap is reduced to the meV range and the 4f state acquires a dispersion as in fig. 91 the Coulomb electron–hole interaction wins and the excitonic insulator is formed. In YbS and YbO, which have a large gap of about 1 eV to be closed with pressure, we have to consider that at 400 kbar the volume is reduced to about 70% and thus the electron–hole interaction is substantially increased, much more than in $TmSe_{1-x}Te_x$ with

only a volume reduction to 95%. We thus think that in YbS or YbO a few more carriers can be supported than in $TmSe_{1-x}Te_x$ before screening suppresses the whole effect. This is also the reason why in SmS (with only a small gap of 0.2 eV and thus only a low pressure is required to close the gap) the electron–hole interaction is still weak but the number of free electrons and thus screening is already too strong, so up to 250 kbar the plasma edge persists (Syassen et al. 1985).

So a recipe of creating excitonic insulators emerges: take a 4f compound which is insulating at ambient pressure. A 4f compound is favorable because the holes remain localized to start with. When it has a small gap in the order of 0.2 eV reduce the number of electrons which are expected in the trivalent metallic state, usually one per formula unit. Then apply pressure, preferably at low temperature. When the gap is large, about 1 eV, the necessary high pressure to close the gap can support more electrons per formula unit, apparently even at 300 K, but the effect will be much more pronounced at low temperature. The above reasoning is of course only a first guess and many more experiments should be done in this exciting direction. But EuO under high pressure might be a similar candidate although EuO being ferromagnetic cannot have the Fermi energy within a hybridization gap and thus does not belong in this section.

4.5. *Actinides*

The question of actinides and intermediate valence has been pursued for about 20 years and we now think that all the heavy-fermion actinide compounds are also intermediate valent, though the valency may be close to an integer value. However, intermediate valence with the Fermi energy in the hybridization gap has not been suggested until recently by Wachter et al. (1991). We recall that the essence of having the Fermi level in the hybridization gap is determined by the Luttinger theorem, namely that the electrons in the hybridized conduction band are only those which came from the f level and that the number of f and d electrons together is even per formula unit. This theory has been proven to work excellently in the previous sections. Thus, intermetallics are not to be expected to belong to this category (but see section 6). In actinide pnictides in the rocksalt structure, which are the most widely investigated (Vogt and Mattenberger 1993), the p band at Γ and the d band at X overlap, yielding a semimetal due to enhanced covalency in the pnictides compared with the chalcogenides. These effects have been discussed widely in ScN and the Yb pnictides by Travaglini et al. (1986), Degiorgi et al. (1990) and Degiorgi et al. (1993). Thus, the Luttinger theorem is not valid for actinide monopnictides. There remain the chalcogenides. The heavy actinide chalcogenides beyond americium seem to be more and more divalent, and certainly there could be some which become intermediate valent under applied pressure. But the experimental evidence is scarce because the amount of material is so small that only X-ray data exist, sometimes even under pressure. However, there are no electronic data and not even the electronic configuration of the actinides, regarding 5f and 6d occupation, is certain. We thus refrain from discussing the heavy actinide compounds with respect to the Luttinger theorem.

In the lighter actinides, uranium, neptunium and plutonium compounds are more thoroughly investigated. Tetravalent Pa compounds, probably in the form of PaO_2, could become intermediate valent: the electronic configuration would then be the same as in PrO_2, with one or a fraction of one f electron.

4.5.1. *The Pu monochalcogenides*

The Pu monochalcogenides PuS, PuSe and PuTe have the same position in the periodic table as the Sm monochalcogenides from which we know that under pressure they become intermediate valent with the Fermi level in the (pseudo) hybridization gap (section 4.2). However, the physical properties of the Pu chalcogenides at ambient pressure do not compare with insulating or semiconducting divalent- nor with metallic trivalent compounds. Their magnetic susceptibility is to a large extent temperature independent, but rather high when compared with a standard Pauli susceptibility (Vogt and Mattenberger 1987). The temperature dependence of the resistivity for the Pu chalcogenides is semiconductor-like with, apparently, two gaps of the order of 2 meV and 20 meV (Burlet et al. 1988) which seems to oppose a Pauli susceptibility being typical for a metal. The γ value of the specific heat is, with a magnitude of some tens of mJ/mol K^2, rather typical for anomalous metals, although it does not have the size for heavy fermions (Hall and Mortimer 1990). Polarized neutron experiments show that the orbital component of the magnetization density in PuTe is much reduced from that expected in a free Pu^{3+} ion (Lander et al. 1987). This would be compatible with a wide band material. However, the temperature dependence of the resistivity with the indication of an extremely small gap and the Fermi level being in this gap again seem to oppose wide bands. The C_2 coefficient of the magnetic form factor would be 6 for a Pu^{3+} $5f^5$ state, but -1 for a Pu^{2+} $5f^6$ state. Experimentally a C_2 value of $+1$ is observed by Lander et al. (1987) giving a vague clue that PuTe might be intermediate valent. These ideas, however, are always ruled out on the basis of simple lattice constant measurements which show that, e.g., the lattice constant of PuTe with 6.19 Å is less than that of a trivalent or divalent Pu telluride (Mattenberger et al. 1986). There is of course the problem that only the radius of the trivalent Pu ion is known (1.07 Å, e.g. Sargent 1962), whereas no divalent Pu compound seems to exist. By comparison with the corresponding $4f^n$ Sm ionic radius of 1.04 Å for Sm^{3+} and 1.12 Å for Sm^{2+}, we estimate an ionic radius of 1.15 Å for the hypothetical Pu^{2+} ion. With the Te^{2-} radius of 2.21 Å (Sargent 1962) we compute for the rocksalt Pu^{3+}Te 6.56 Å and for the Pu^{2+}Te 6.72 Å. Of course, this simple bookkeeping assumes mainly ionic bonding, which, however, is valid for the corresponding $4f^n$ SmTe, which has nearly the same lattice constants (Batlogg et al. 1976b).

It is then obvious that no consistent description of the anomalous physical properties of the Pu chalcogenides could be given until recently and new aspects must be considered. We will show in the following that the Pu chalcogenides are intermediate valent in spite of what has been argued above. If the Pu chalcogenides were divalent they would be semiconductors with the $5f^6$ state a few tenths of an eV below the 6d band, just as the semiconducting Sm chalcogenides. However, the charge distribution of the 5f orbits

extends more to the outside than the 4f orbitals, nearly making a direct 5f–5f overlap, but not quite. The 5f–6d hybridization between neighboring cations is thus *naturally* much larger than the 4f–5d hybridization. Thus, comparing Sm and Pu chalcogenides, the latter do not need external or chemical pressure to arrive at the same degree of hybridization and intermediate valence as the former.

4.5.1.1. *Electronic properties of the Pu monochalcogenides.* Once we accept that the Pu chalcogenides can be intermediate valent because they resemble the high-pressure form of the corresponding Sm chalcogenides, we proceed by assuming a two-level high density of states with a gap in between, similar to fig. 2d. Because the rocksalt structure does not permit a hybridization across the whole Brillouin zone, a pseudo gap like the one in fig. 2b is more probable. The Luttinger theorem, which would be valid for the Pu chalcogenides, would place the Fermi level into the gap, but the relatively high (though experimentally uncertain) γ value of Hall and Mortimer (1990) of 69 mJ/mol K^2, maybe permits the Fermi level to cut somewhat into the high density of states, making PuTe a "light weight" heavy fermion.

In the following, we present a model calculation which has first been applied to the "heavy weight" or normal heavy fermions of the uranium- or cerium intermetallics by Marabelli et al. (1986b) and Marabelli and Wachter (1987c, 1988, 1989) and adapted for the Pu chalcogenides by Wachter et al. (1991). The model was developed after far-infrared and low-temperature experiments on UPt_3 had been carried out by Marabelli et al. (1986a) and optical transitions across a hybridization gap in the meV range have been found. Although the model is crude and simplified, it permits for the first time a consistent explanation of various heavy-fermion properties with essentially the same set of only two parameters.

We can try to derive the electronic, magnetic and thermodynamic properties of the material by using a renormalized Sommerfeld model of the quasiparticles which acquire heavy masses due to the high density of states (or narrow bands) of the f quasiparticle bands, which are not completely occupied. That the quasiparticles really are in a narrow band and acquire heavy effective masses can be derived from measurements of the de Haas–van Alphen effect, which prove, e.g., the existence in UPt_3 of Fermi surfaces near E_F and effective masses of about $90m$ (Taillefer et al. 1987). This crude model has proven to be successful for practically all existing heavy fermions and some intermediate-valent compounds and has described quantitatively, with only one free adjusting parameter, the temperature dependence of the electrical conductivity, the specific heat, the temperature dependence of the γ value and the temperature- and field dependence of the magnetic susceptibility (Marabelli and Wachter 1987b,c, 1988, 1989, Marabelli et al. 1986b). As experimental entities the measured gap or pseudo gap between the two quasiparticle bands and their bandwidth (when known) have been used in addition to the measured temperature dependence of conductivity, specific heat and magnetic susceptibility. The two band quasiparticle density of states (figs. 2b,d) has been modeled by two Gaussians, although this choice is not too important, but more convenient for the calculations. In the case of the Pu chalcogenides, or more specifically PuTe, measurements

of 2 gaps with 2 and 20 meV come from the temperature dependence of the conductivity by Burlet et al. (1988), the γ value by Hall and Mortimer (1990) and the magnetic susceptibility from Vogt and Mattenberger (1987).

When we adopt, in a first approximation, a temperature independent rigid band model, the main influence of temperature is the change of the Fermi distribution function f_F which at room temperature is much larger than the width of the whole double peak electronic structure near E_F. Regarding the temperature dependence of the resistivity we assume that heavy quasiparticles in the narrow subbands around E_F suffer collisions with other quasiparticles such as phonons or spin fluctuations (however, we think that electron–electron scattering may also be important and even govern some phenomena like point contact spectroscopy, but they are not discussed here). Spin fluctuations will only be relevant at very low temperatures where the experimental conditions due to the self heating of the material are not very precise. So we concentrate on a temperature range above about 4 K. We also take into account thermal excitations of heavy electrons across the pseudo gap, resulting in holes in the lower band and in additional electrons in the upper band. The sum of f and d electrons results in 6, the original occupation of the f state in a hypothetical divalent PuTe before the hybridization.

In principle one would like to use a formula $\rho = 1/\sigma = m^*/(Ne^2\tau)$, where N and τ are temperature dependent. The effective masses of heavy electrons and holes are made equal, $m^* = m_e^* = m_h^*$. For the carrier concentration we have $N = N_{e_c} + N_{c_{exc}} + N_h$, and

$$N_{e_c} + N_{c_{exc}} = \int_{-\Delta E/2}^{\infty} \rho_D(E) \cdot f_F(E - E_F(T),\ T)\, dE, \tag{13}$$

$$N_{c_{exc}} = N_h = \int_{-\infty}^{-\Delta E/2} \rho_D(E)[1 - f_F(E - E_F(T),\ T)]\, dE. \tag{14}$$

N_{e_c} is the carrier concentration at $T = 0$ in the partially filled quasiparticle conduction bands including the d electrons, and ΔE is the gap or pseudo gap. $\rho_D(E)$ is the density of states (DOS) per cell and per eV. In some theories it is assumed that the heavy mass quasiparticles hardly contribute to the conductivity process. However, a simple estimate shows that there are about 10^3 times more heavy-f-like quasiparticles within $k_B T$ of E_F than d electrons, so if their effective mass would be $1000m$ they would contribute about the same to the conductivity than the light weight d electrons. By imposing $N_{c_{exc}} = N_h$, in order to keep the total number of heavy quasiparticles unchanged, we can determine the dependence of E_F on the temperature. With the experimentally determined gaps, $E_F(T)$ changes little with temperature. The important aspect is that one cannot approximate the Fermi function f_F with a Boltzmann distribution as is usually done for semiconductors since the standard condition, that the Fermi energy is far away from the band edges, is violated in this case. Also, one cannot pull the Fermi function or its derivative in front of the integral as is usually done for large bandwidth materials.

For the reciprocal scattering time we use, in a crude and first approximation, for $T > 4\,\mathrm{K}$ a term linear in temperature, typical for electron–phonon scattering (Dallacasa 1981):

$$\frac{m^*}{\tau} = \frac{\hbar k_F k_B \bar{\sigma}_a}{z^2} T \int_{-\infty}^{\infty} -\left(\rho_D(E) \frac{df_F(E)}{dE}\, dE\right), \tag{15}$$

with k_F the Fermi vector, z the valence and $\bar{\sigma}_a$ the average cross section for electron–phonon interaction. Using the latter as an adjustable parameter we obtain, with the measured gap or pseudo gap energies, a relatively good agreement of the temperature dependence of the resistivity with the experiment (see below).

The next step is the computation of the specific heat and the γ value. The essential point being again that with such narrow f-like subbands near and around E_F, the density of states $\rho_D(E)$ cannot be pulled in front of the integral of the total energy, as is done in classical Sommerfeld theory. Thus

$$C_v = \frac{dU_i}{dT} = \int_{+\infty}^{-\infty} E\,\rho_D(E) \frac{df_F(E - E_F(T))}{dT} dE, \tag{16}$$

with $E_F(T)$ the Fermi energy. As experimental entities we used, besides the gap and the double Gaussian form of the density of states, the experimentally determined γ values and their temperature dependence, when experimentally known. It is obvious that, because of the very existence of a finite γ value, there is a certain density of states at the Fermi level, so if the latter falls into a gap it can only be a pseudo gap. Then, in spite of a seemingly semiconductor-like behavior of the electrical resistivity for PuTe, it is clear that the resistivity for $T \to 0$ goes towards zero.

The large and mainly temperature independent magnetic susceptibility of the Pu chalcogenides (Vogt and Mattenberger 1987) prompts one to assume a Pauli susceptibility of heavy quasiparticles in narrow bands. A more or less large temperature region with relatively constant magnetic susceptibility, however, followed at higher temperatures by a Curie-like drop in the susceptibility, is typical for intermediate-valent compounds (Nickerson et al. 1971, Sales and Wohlleben 1975) and heavy fermions (Stewart 1984, Marabelli and Wachter 1987b,c, 1988, Marabelli et al. 1986b). For the Pu chalcogenides we assume as a starting argument that the experimentally observed rather constant susceptibility up to room temperature will be followed by the Curie like drop above room temperature where no measurements exist. The temperature region of the Curie-like behavior commences when $k_B T$ is larger than the Fermi energy. That the latter can become very small for intermediate-valent and heavy-fermion materials can be simply visualized by using an adapted Sommerfeld model for heavy quasiparticles, namely $E_F = (\hbar^2/2m^*) \times (3\pi^2 N)^{2/3}$. With N the carrier concentration being about $10^{22}/\mathrm{cm}^3$ and an effective mass in the order of $1000m$, we obtain E_F in the meV range.

To derive the Pauli magnetic susceptibility we start with the total energy U_{tot} in the following way:

$$U_{tot} = \frac{1}{2}\int_{-\infty}^{+\infty}(E - \mu_0 H)\rho_D(E) f_F(E - \mu_0 H - E_F(T),\ T)\,dE + \frac{1}{2}\int_{-\infty}^{+\infty}(E + \mu_0 H)\rho_D(E) f_F(E + \mu_0 H - E_f(T),\ T)\,dE, \tag{17}$$

with $\mu_0 = gJ\mu_B$ (μ_0 = magnetic moment, g = Landé factor, J = quantum number of the momentum, μ_B = Bohr magneton), H = magnetic field, $\rho_D(E)$ = density of states, $f_F(E,T)$ = Fermi distribution and $E_F(T)$ = Fermi energy which has been obtained from the condition that the total number of carriers is constant. Again it is not permitted to neglect $\mu_0 H$ compared with the Fermi energy, as is done in classical theory. Therefore we obtain for the magnetization M and the susceptibility χ (Marabelli and Wachter 1988)

$$M = \frac{1}{2}\mu_0 \int_{-\infty}^{+\infty} \rho_D(E)\,[f_F(E - \mu_0 H - E_F) - f_F(E + \mu_0 H - E_F)]\,dE, \tag{18}$$

$$\chi = \lim_{H \to 0} M(H)/H, \tag{19}$$

where the integral in eq. (18) is the well-known expression for the Pauli magnetization.

The Pu chalcogenides offer severe experimental problems, mainly because of their high radioactivity (α-emitter) which enforces a strict encapsulation of the crystals or measurements in clumsy glove boxes. Also, the self heating due to the radioactive decay makes measurements below about 4 K extremely difficult and undependable. For example, the specific heat has been measured down to only 10 K by Hall and Mortimer (1990) and was then extrapolated towards zero temperature to obtain the γ value. Another problem is the temperature dependence of the resistivity which yields two activation energies (2 and 20 meV, Burlet et al. 1988). Since these were obtained by an Arrhenius plot, this implies that the Fermi function can be replaced by the Boltzmann factor, an approximation which is valid only when the Fermi energy is far from the band edges which is certainly not the case with such small gaps. The best method to measure the gaps or pseudo gaps directly, would be far infrared optical spectroscopy at very low temperatures, however, it will be a long time before such measurements can be performed on "hot" samples, although visible and near infrared spectroscopy at room temperature have been performed recently for the first time on the Pu chalcogenides (Mendik et al. 1993). In fig. 125 we show the reflectivity of the Pu chalcogenides with the position of the plasma edges indicated. Typical intermediate-valent materials, such as high-pressure SmS or TmSe are also included, and the respective plasma edge is indicated by an arrow. Thus PuS and high-pressure SmS compare quite well, both compounds appear golden to the eye. At room temperature there are, of course, only the light d electrons which take part at the plasma resonance, the heavy f-like quasiparticles have their resonance in the far infrared and can be observed only at low temperatures.

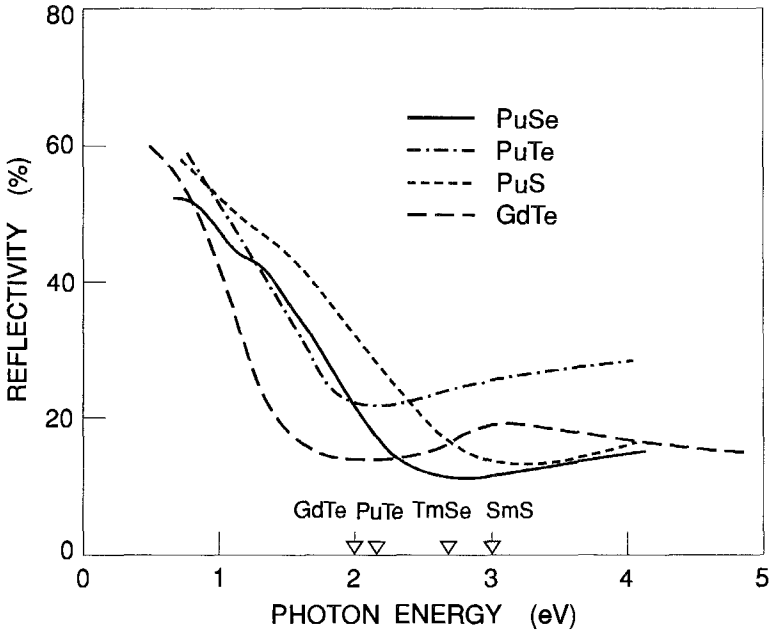

Fig. 125. Optical reflectivity of PuS, PuSe and PuTe at 300 K. The reflectivity is corrected for losses at the quartz cover plate. Also shown for comparison is the reflectivity of GdTe. Triangles represent the plasma energy of the compounds. (After Mendik et al. 1993.)

The experimentally observed two activation energies for PuTe (Burlet et al. 1988) prompted us to assume Gaussian distributions for the density of states of the f-like quasiparticles as shown in fig. 126. A multiple peak density of states structure derived from far infrared spectroscopy is indeed quite common in heavy-fermion compounds such as UPt_3 (Marabelli et al. 1986a) or $CeCu_6$ (Marabelli and Wachter 1989). We then let the computer make an optimal fit for the temperature dependence of the resistivity (Burlet et al. 1988) and the magnetic susceptibility (Vogt and Mattenberger 1987) using eqs. (13)–(15) and (18, 19) above. The fits for each single physical property turned out to be rather good, with optimal adapted gap energies and bandwidths ranging within a factor of two of the values quoted in fig. 126. We preferred, however, to choose gap energy and bandwidth values which remain the same for both physical properties mentioned above, namely those shown in fig. 126, and tolerate a less than optimal fit. Nevertheless, the gap values finally used and shown in fig. 126 are close to those measured experimentally by Burlet et al. (1988). The temperature dependence of the resistivity of PuTe is thus shown with only one fitting parameter, namely the electron–phonon interaction $\bar{\sigma}_a$ (fig. 127). The fit of the magnetic susceptibility is shown in fig. 128. The inset of fig. 128 shows the calculated behavior of the susceptibility in the low temperature range, which is not experimentally accessible at the moment, but can be reached in other, less self heating Pu isotopes. It is remarkable that the theory reproduces the steep increase of the susceptibility

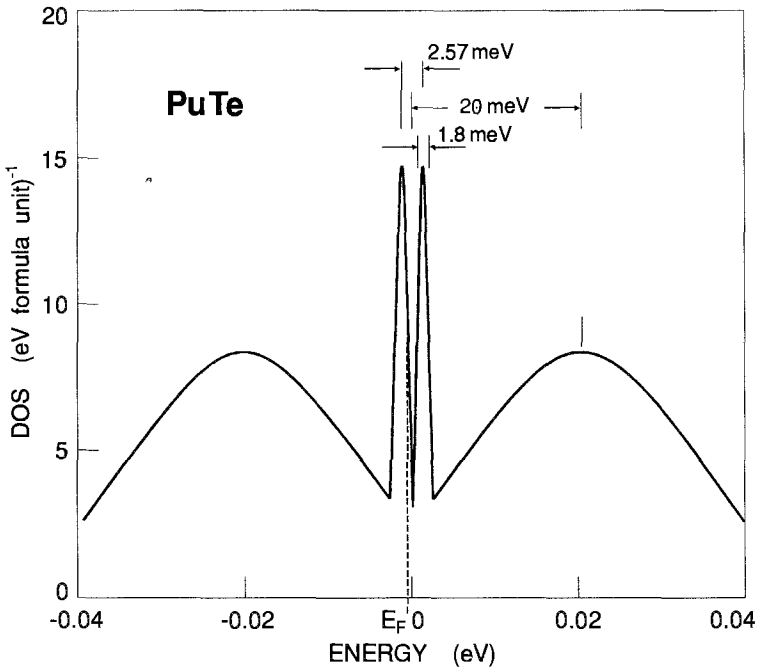

Fig. 126. Density of states per eV and formula unit of PuTe near E_F. (After Wachter et al. 1991.)

below about 30 K, but at the lowest temperatures (which have not been measured) turns into a flat maximum. Finally, in fig. 129, we show how the susceptibility behaves for still higher temperatures than have been measured up to now. We indeed find the $1/T$ (or Curie-like) drop of the susceptibility commencing a little above room temperature. Of course, changes in the energy values of fig. 126 within a factor of two, vary the onset temperatures of this drop also within a factor of about two. The sum rule and the condition for the chemical potential that the total number of the quasiparticles remains constant, served to fix the Fermi energy (fig. 126), which, remarkably enough, nearly falls into the pseudo gap. This is the main reason why one observes an activated resistivity, but the fact that we have only a pseudo gap necessitates the resistivity to drop to very small values for extremely low temperatures. In fact, we believe that the resistivity behavior of PuTe is similar to the one of SmS under a pressure of 8 or 10 kbar (Lapierre et al. 1983), and shown in fig. 53. Because of the higher pressures needed for SmTe, the real 4f counterpart of PuTe, a similar experiment is missing.

In spite of the fact that the Hall effect has been measured on PuTe by Therond et al. (1987) no analysis of the carrier number has been given. However, it has been stated that the Hall resistivity is semiconductor like with two gaps of the already mentioned magnitude. On solid solutions of metallic $PuSb_{0.9}Te_{0.1}$ and $PuSb_{0.8}Te_{0.2}$ an analysis has been made and the carrier concentration was 0.15 and 0.13 per formula unit, respectively (Therond et al. 1987). The trend is going into the direction that for pure PuTe the carrier

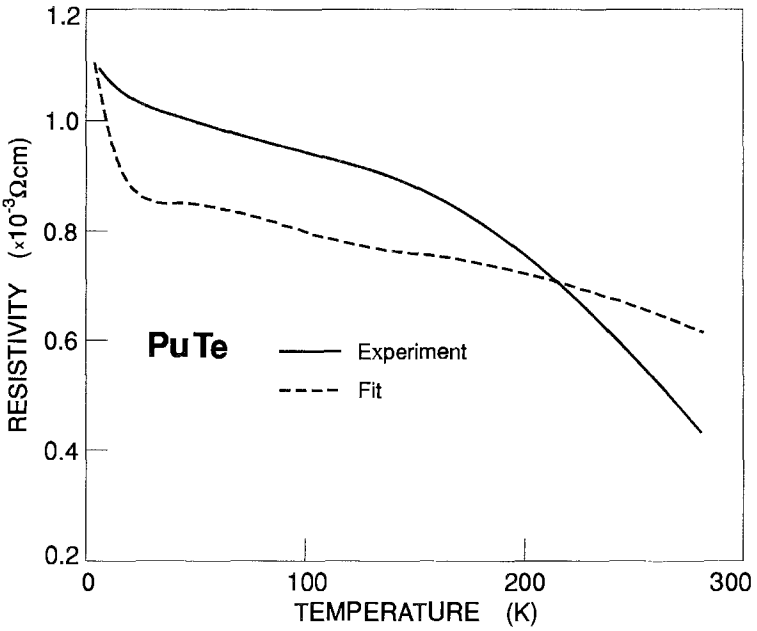

Fig. 127. Temperature dependence of the resistivity of PuTe. Experimental data from Burlet et al. (1988), fit according to eqs. (13–15). (After Wachter et al. 1991.)

concentration will be much less. Our model permits the calculation of the temperature dependence of the carrier concentration $n_{c_{exc}} + n_h$. We find 0.16 carriers per formula unit at ~160 K, 0.024 at 20 K, and 0.005at 1 K. (Recall that the density of states is not zero at E_F). The experimental curve of the Hall resistivity of Therond et al. (1987) permits us to estimate the carrier concentration in a one band model. At 160 K the carrier concentration is 6×10^{20} cm^{-3}, which amounts to 0.04 carriers per formula unit which is a remarkable agreement with the calculated values above.

The specific heat can also be calculated from our model (eq. 16) or from the measured susceptibility. We obtain a γ value between 100 K and 20 K of about 20 mJ/mol K^2, which slightly increases to 25 mJ/mol K^2 towards zero K, similar to the temperature dependence of the magnetic susceptibility (fig. 128). The Wilson ratio is an independent method to calculate the γ value from the susceptibility and it has proven to be valid in other heavy-fermion compounds (Marabelli et al. 1986b, Marabelli and Wachter 1987c, 1988). We obtain 19 mJ/mol K^2 from the Wilson ratio. This good agreement shows the consistency of the models. However, the experimental γ value is with 69 mJ/mol K^2 somewhat larger (Hall and Mortimer 1990), but above we have indicated the experimental problems in obtaining this value. Also, we expect another contribution to the specific heat which has not been taken into account at all, namely a Schottky-type anomaly caused by thermal excitations across the various density of states peaks shown in fig. 126. To give a rough estimate of the temperatures where we expect such anomalies we take the density of states

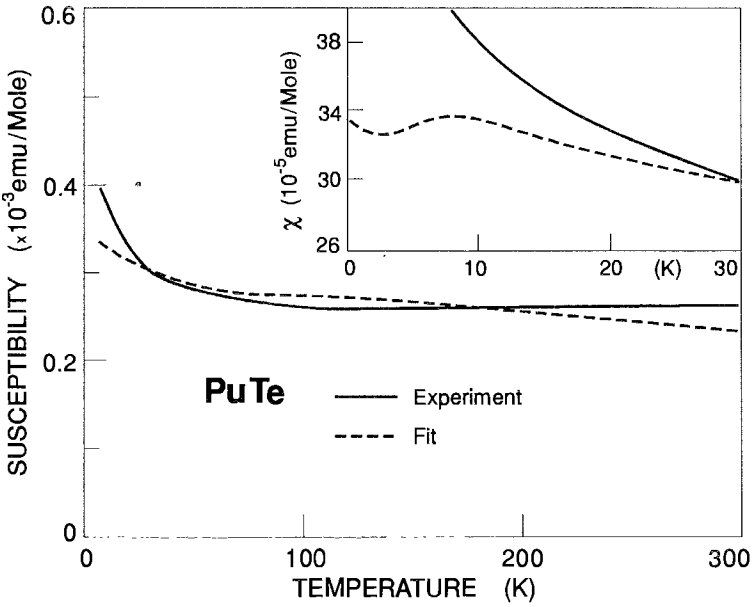

Fig. 128. Temperature dependence of the magnetic susceptibility of PuTe. Experimental data from Vogt and Mattenberger (1987), fit according to eqs. (18, 19). (After Wachter et al. 1991.)

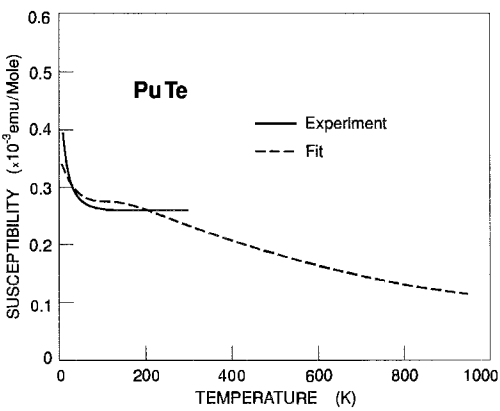

Fig. 129. Temperature dependence of the magnetic susceptibility of PuTe and an extension towards high temperatures. (After Wachter et al. 1991.)

peaks as sharp level systems and calculate with the given energy separations of fig. 126: 11 K, 80 K and 230 K. Because we actually have a distribution of density of states, the peaks will not be as sharp as for classical Schottky anomalies. The one at 11 K certainly would severely affect an estimate of a γ value in lowering it. The one at 230 K can possibly be associated with the observed peak at 260 K for which there is no explanation (Hall and Mortimer 1990). Schottky-type anomalies of the specific heat have been experimentally observed in heavy-fermion systems and we could quantitatively associate them with transitions between the density of states peaks (Marabelli and Wachter 1987c). Only

when the specific heat of PuTe has really been measured down to at least one degree, an experimental confirmation can be obtained.

Our model permits us to calculate from our γ value and the density of states at E_F, the effective mass of the heavy quasiparticles. We obtain $m^* = 65m$ which would fall into the region of a "lightweight" heavy fermion, though with intermediate valence.

4.5.1.2. *Lattice-related properties.* Under the application of external pressure a rocksalt *divalent* 4f compound will have two possibilities: change its electronic structure and become intermediate valent and eventually trivalent, or make a structural change towards a CsCl structure (Jayaraman 1979). For most rocksalt actinides the transition to the CsCl structure is also established (Dabos-Seignon et al. 1990). The transition pressure is usually above 100 kbar, which, for typical deformation potentials, corresponds to about 1 eV. Thus, if the $4f^n$–5d separation, the energy gap of a semiconductor, is larger than about 1 eV one observes at first a transformation to the CsCl structure (Jayaraman 1979); when it is less, the electronic transition towards intermediate valence comes first, followed by the CsCl structural change. For instance, of the Eu chalcogenides only EuO, with a gap of 1.2 eV, makes the electronic transition first; EuS, EuSe and EuTe with their larger gaps make the structural change first. The Sm and Tm chalcogenides with small energy gaps first make the electronic transition. The reason for the small $4f^n$–5d separation lies in the position in the Periodic Table which these lanthanide elements occupy. Divalent $4f^6$ and $4f^{13}$ lanthanides are unstable compared with the half full or completely full neighboring $4f^7$ or $4f^{14}$ elements thus their 4f ionization energy or $4f^n$–5d transition energy is small (Kaldis and Wachter 1972). The divalent Pu chalcogenides would have the same f^6 configuration as the divalent Sm chalcogenides and their gap – obtainable with negative pressure – would be small. In other words they first make the electronic valence transition and at higher pressures the structural transition.

Looking at the experimental volume versus pressure change of PuTe (Dabos-Seignon et al. 1990) we observe the structural transition at 150 kbar. With the above reasoning we would expect that the valence transition has occurred at lower pressures or even at ambient pressure. Comparing the bulk moduli of all measured actinide tellurides it is remarkable that PuTe with 370 kbar, the smallest bulk modulus, is the softest material. It has by an order of magnitude the largest change in the bulk modulus, $B'_0 = 12$. These are indeed indications of intermediate valence. Here we want to remark that the bulk modulus of PuTe is even less than the one of UTe, which has already by itself a soft bulk modulus and a negative Poisson ratio (Neuenschwander et al. 1986). PuSe has the softest bulk modulus of all transuranium selenides, but it is harder than USe (Dabos-Seignon et al. 1990, Neuenschwander et al. 1986), which again has a negative Poisson ratio and is very soft itself. So UTe and USe are not trivalent actinide reference materials.

To make the matter more obvious we replot in fig. 130 the volume–pressure curve of PuTe of Dabos-Seignon et al. (1990). At 150 kbar we can safely assume that the compound is in its stable trivalent configuration, in fact, the bulk modulus is the same as in the trivalent neighbor compound NpTe. Thus, we can fit a Murnaghan equation at 150 kbar and below. However, we observe that the experimental PuTe curve, especially at low

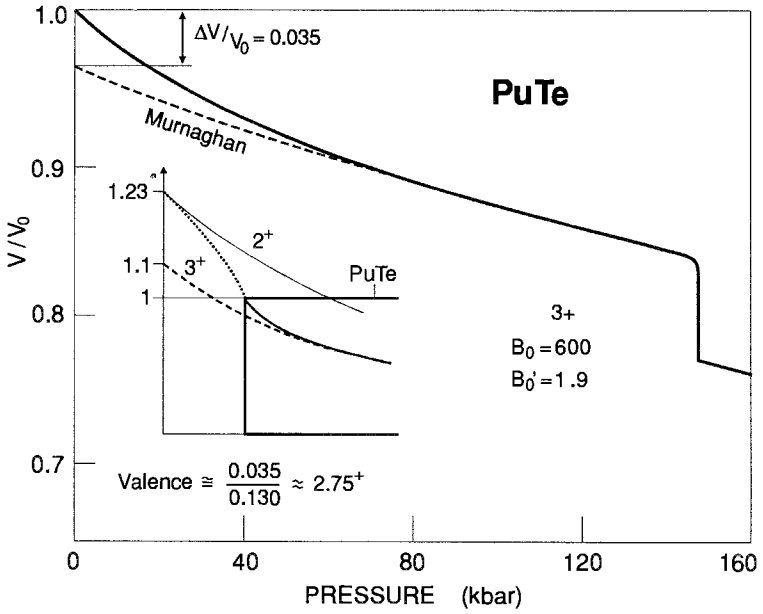

Fig. 130. Relative volume versus pressure of PuTe. Experimental values (solid curve) from Dabos-Seignon et al. (1990). Dashed curve: trivalent Murnaghan equation with a fit at 140 kbar. Inset: relative volume vs. pressure, same as the main figure, but with an extension towards "negative" pressure and inclusion of a divalent Murnaghan equation. (After Wachter et al. 1991.)

pressures, deviates significantly from theory, which has already been noted by Dabos-Seignon et al. (1990). The theory is of course valid only for an integer valent compound, but if we discard physically unrealistic fits (such as: with increasing pressure PuTe transforms from a higher valent to a lower valent i.e., a more voluminous configuration) we are left with the fit, shown in fig. 130, indicating trivalency at high pressure and intermediate valence between 2 and 3 at low pressures. In the inset of fig. 130 we have continued the volume–pressure curves to negative pressures and we show the complete trivalent Murnaghan and a divalent Murnaghan equation and also the expected behavior of PuTe under expansion (dashed). Unusual are the volume ratios larger than one, but this is caused only by the experimental PuTe curve which has a value of one for an applied pressure of zero. We find by linear interpolation between the divalent and the trivalent reference curves that PuTe at ambient pressure has a valency of 2.75^{+}.

We have already mentioned above that PuTe is the actinide counterpart of SmTe. Thus, we can take the experimental volume–pressure relation of SmTe (Jayaraman 1979) and differentiate it to obtain the bulk moduli. This curve is shown in a relative pressure scale (normalized with respect to the fcc–bcc transition pressure) in fig. 131. In the same figure we plot the bulk moduli of PuTe (Dabos-Seignon et al. 1990) also obtained by differentiating the volume–pressure experiment. It is obvious that the PuTe curve now falls exactly on the SmTe curve. The zero pressure bulk modulus of PuTe is now with 370 kbar

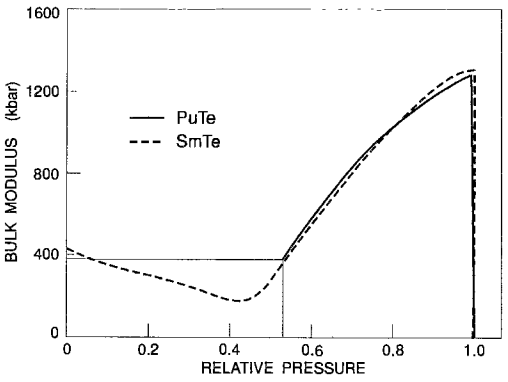

Fig. 131. Bulk moduli vs. relative pressure of PuTe and SmTe obtained by the differentiation of experimental volume vs. pressure curves of Dabos-Seignon et al. (1990) and of Jayaraman (1979). (After Wachter et al. 1991.)

exactly the same as in SmTe under an applied pressure of 58 kbar. It is now indeed less than the one of a divalent (relative pressure 0) or a trivalent (relative pressure ≈ 1) PuTe and thus typical for an intermediate-valent compound. Figure 131 is now identical to fig. 99 which we derived before for the $TmSe_{1-x}Te_x$ system. In addition, the derivative of the bulk moduli, B', is the same for PuTe at zero pressure and SmTe at 58 kbar. Thus it can be safely stated that PuTe at ambient pressure would be in the same condition as SmTe under an applied pressure of 58 kbars. Compared to the hypothetical divalent PuTe the real existing PuTe at ambient pressure has suffered a volume reduction V/V_0 of 0.81 (equal to 1/1.23 shown in the inset of fig. 130). One third of this value yields the change in lattice constant. Starting from a lattice constant of 6.72 Å for the divalent PuTe, we obtain 6.29 Å for the lattice constant of PuTe at ambient pressure. This should be compared with the actually measured one of 6.19 Å, a difference of only 2%. In fact, this lattice constant is now less than the divalent one with 6.72 Å and the trivalent one with 6.56 Å calculated from the ionic radii of Pu and Te. It is exactly this confusing point which has been constantly used as argument against the intermediate-valent nature of PuTe or the other Pu chalcogenides. The resolution of this problem is the convincing evidence that the Pu chalcogenides are the high-pressure collapsed phase of the Sm chalcogenides (Wachter et al. 1991).

As mentioned before, one of the best indications of intermediate valence is the existence of a negative elastic constant c_{12}. Mendik et al. (1993) for the first time attempted to measure the elastic constants on a radioactive "hot" material like PuTe and they used the same encapsulated single crystals as for the reflectivity measurement. The single crystals were cleaved and oriented with a (100) face onto which an Ar^+ 5140 Å laser beam impinged. The crystals could be rotated around a [100] axis and thus an angular dependent Brillouin scattering could be performed. The argumentation is the same as in section 4.3.2.1.3, where Brillouin scattering has been performed on $TmSe_{0.60}Te_{0.40}$. The velocity of the Raleigh Surface Wave, v_{RSW}, has been determined for PuTe and its angular dependence, and it is shown in fig. 132. As usual for metallic samples the angular dependence is small, which implies that the anisotropy ratio $\eta < 1 < c_{44}/(c_{11} - c_{12})$. The RSW velocity for PuTe is 3750 m/s. Using also the measured bulk modulus of

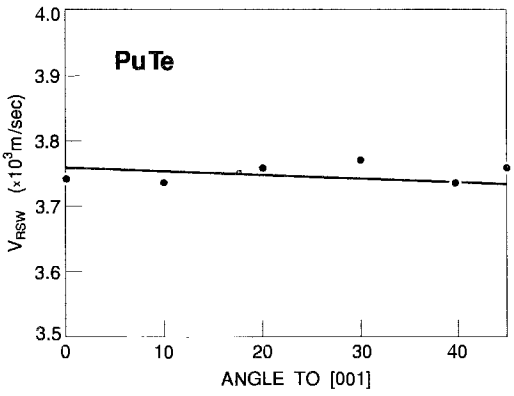

Fig. 132. Velocity of the Raman Surface Wave of PuTe in function of the angle to [001]. (After Mendik et al. 1993.)

PuTe $B = 1/3(c_{11} + 2c_{12})$ (Dabos-Seignon et al. 1990) the three elastic constants could be fitted. A check is the use of only the measured angular dependence and a fit with the theory of Elmiger et al. (1989). Both methods yield the same elastic constants within the error of measurements: $c_{11} = 369 \pm 2$, $c_{44} = 197 \pm 3$, $c_{12} = -39 \pm 17$ GPa and Poisson's ratio is -0.11 0.04.

We think we can show in this section that the surprising and confusing experimental data on the Pu chalcogenides can be consistently explained by the assumption that the Pu chalcogenides represent the high-pressure intermediate-valent form of the isoelectronic Sm chalcogenides. Pressure in the divalent Sm chalcogenides serves only to enhance the f–d hybridization thus to achieve the intermediate-valent state, whereas in the Pu chalcogenides f–d hybridization is achieved without pressure due to the larger orbital extent of the 5f wavefunctions compared with the 4f wavefunctions. By comparing the pressure dependence of the bulk modulus of PuTe with the one of SmTe an estimate of the degree of hybridization of PuTe under normal conditions could be obtained. PuTe at normal condition is in the same state as SmTe under an applied pressure of 58 kbars and its degree of intermediate valence is 2.75^+. Although we have concentrated in this section mostly on PuTe because most experimental data are available for this material, the resulting electronic structure would be typical also for the rest of the Pu chalcogenides.

For the electronic properties we used the model which has proven successful for intermediate-valent and heavy-fermion compounds (Marabelli et al. 1986b, Marabelli and Wachter 1987c, 1988) that the hybridization of f and d wavefunctions leads to (at least) a double peak in the density of states of renormalized heavy quasiparticles which are modeled by a Gaussian distribution. The width of these peaks and their separation in energy is then determined by fits of the temperature dependence of the resistivity, the specific heat and the susceptibility using eqs. (13)–(19). The essential point in using these equations is that in all cases the Fermi function or its derivative cannot be pulled in front of the integrals as is usually done in theory, because the Fermi function is strongly varying over the energy range of the density of states peaks. The position of the Fermi level, the carrier concentration and the effective mass are then consequences of the calculation. It

is remarkable that the Fermi level practically falls into the pseudo gap of PuTe, which is the reason that one observes an activated conductivity and a small γ value of the specific heat.

5. Materials exhibiting intermediate valence having the Fermi energy outside the hybridization gap: Heavy fermions

The title of this section presumes that heavy fermions have hybridization gaps but that the Fermi energy is not in this hybridization gap. The interpretation that heavy fermions have hybridization gaps is inherent in the periodic Anderson model where it is shown that hybridization leads to a gap, which in general cases is only a pseudo gap. In some special cases, namely when the hybridization extends over the whole Brillouin zone, and when the d electrons are only those which originally have come from the f states and the sum of f and d electrons is *odd*, the hybridization gap can be a true gap and the Luttinger theorem predicts the Fermi level *not* to be in the hybridization gap. The Fermi level is most likely in the density of states peaks as shown e.g., in the upper peak in fig. 2b. The consequences of such a situation are that now the γ term of the specific heat can become large up to some J/mol K^2, and since it is a measure of the density of states at E_F, the effective mass can become about $1000m$ because one has only meV wide f bands, the magnetic susceptibility can become Pauli-like at low temperatures and all the intriguing features of heavy fermions (not even considering their superconducting properties) which aroused our interest will become understandable. Depending on how many f quasiparticles can be filled into the high-density bands determines the valence of the material, and it is thus obvious that an integer valence is only accidentally possible. In other words, practically all heavy fermions are intermediate valent, whereas not all intermediate-valent materials are heavy fermions, e.g. SmB_6, since at the Fermi level there are no electrons at $T \to 0$. (The terminology of heavy-fermion insulators by Coleman 1992 appears to be confusing.) In this connection then, the statement of Wohlleben (1981) that all cerium-based alloys are intermediate valent seems to bear some relevance.

In alloys with a lot of electrons from the lanthanide or actinide partner, the existence of a hybridization gap is not at all obvious especially since many measurements below about 4 K can be explained by neglecting a possible hybridization gap, because thermal excitations across a hybridization gap are highly unlikely at these temperatures. However, if one wants to explain physical properties over the whole temperature scale up to about room temperature, it is absolutely necessary to take the hybridization gap into account because the thermal excitations across this gap will fundamentally influence the physical properties. We show in fig. 133 on a quantitative scale the double peak density of state structure, typically for the existence of a hybridization gap with about 4 meV gap width and we plot in the same figure the Fermi distribution for a temperature of 10 K. It is then obvious that one already has at this temperature holes below E_F and additional electrons above E_F which at about 50 K may dominate the physical properties.

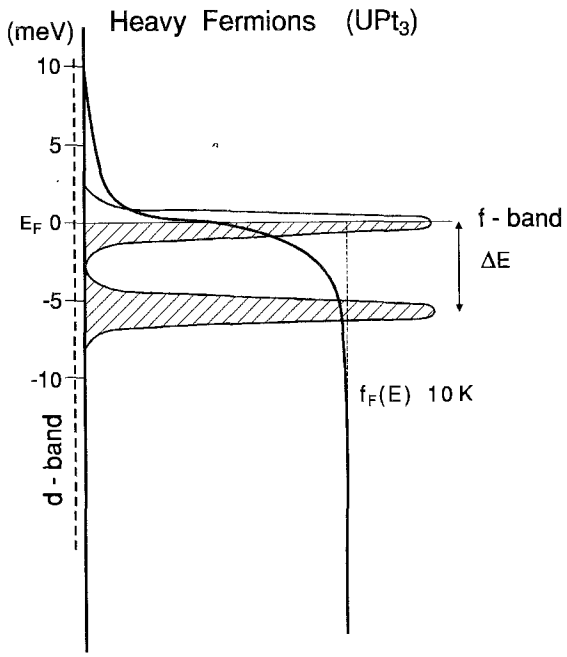

Fig. 133. Density of states for a typical heavy fermion with a hybridization gap of 4 meV and the Fermi level being in the upper density of states peaks. The Fermi distribution function $f_F(E)$ for 10 K is shown on a quantitative scale.

The majority of theoreticians do not take hybridization gaps into account, either because the phenomenon which they want to describe occurs only at the lowest temperatures or because they are not convinced of the existence of the hybridization gap in heavy fermions. However, Czycholl and Schweitzer (1992) in a recent paper take a hybridization gap into account and can thus derive the existing phenomena in a quantitative way. As a general statement we believe that in the year 1992 a breakthrough in the application of the general periodic Anderson Hamiltonian to a hybridization gap has occurred.

As a first step, it is important to prove the existence of hybridization gaps in heavy-fermion systems and then show that thermal excitations across this gap at elevated temperatures influence the physical properties in the observed way. The first experimental evidence of a hybridization gap has been given by Marabelli et al. (1986a) by far infrared optical reflectivity measurements at low temperatures and in more recent years this method has been extended to many other heavy-fermion compounds so that the author now believes that the hybridization (pseudo) gap is a general feature of all heavy fermions.

In this and the following sections we do not review all heavy fermions or intermediate-valent materials having the Fermi energy outside the hybridization gap, since this has been done by articles devoted only to this topic and described in other chapters of the present Handbook series, e.g., chs. 97 (Vol. 14), 98 (15), 105 (16), 111 (17) and chs. 130, 131 and 133 of the present volume. The line of the present chapter is thus clear: we

want to describe the implications of hybridization gaps in classical intermediate-valent compounds and in heavy fermions, both lanthanide and actinide compounds.

5.1. *Experimental determination of hybridization gaps in heavy fermions*

5.1.1. *UPt_3*

UPt_3 is the material best suited for optical investigations in the far infrared because large and perfect single crystals exist (Marabelli et al. 1986a). To perform optical reflectivity measurements on UPt_3 we used the basal plane of the hexagonal crystals as the surface, in order to avoid polarization dependencies. In the infrared and far infrared (FIR) part of the spectrum (0.5 eV–1 meV) we have employed a Fourier spectrometer with 2 tri-glycine-sulfate (TGS) detectors for energies larger than 100 cm^{-1} and with a liquid helium-cooled germanium bolometer from 100 to 8 cm^{-1}. The crystals could be kept in an exchange gas of helium and their temperature could be varied between 5 and 300 K. For photon energies > 30 meV our 300 K data practically agree with the reflectivity measurements in the basal plane of UPt_3 of Schoenes and Franse (1985) and their data have also been used to extend our spectrum beyond 0.5 and up to 12 eV. After various time consuming corrections we claim that our reflectivities have an absolute precision of 0.5% and a relative one of 0.1%. Part of the reflectivity spectrum for 5 K and 300 K is shown in fig. 134.

The reflectivity spectrum at 300 K is typical for a metal with some optical transitions at about 30 meV and 0.3 eV being superimposed on a free carrier behavior with an unscreened plasma resonance at 2.5 eV (Schoenes and Franse 1985). At low temperatures significantly more structure is in the spectrum and especially the minimum in the reflectivity at about 3 meV will lead to important conclusions. Here one should not be disappointed with only small structures in the reflectivity of a metal, when the reflectivity for low energies is practically already 100%, the change in reflectivity cannot be large.

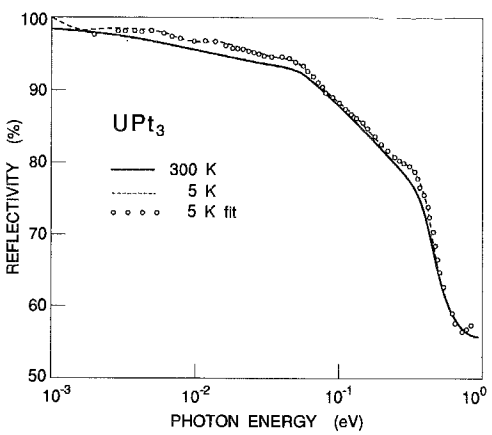

Fig. 134. Near-normal incidence reflectivity of UPt_3 at 5 K and 300 K. The circles correspond to the computed reflectivity from the fit with Lorentz oscillators. (After Marabelli et al. 1986a.)

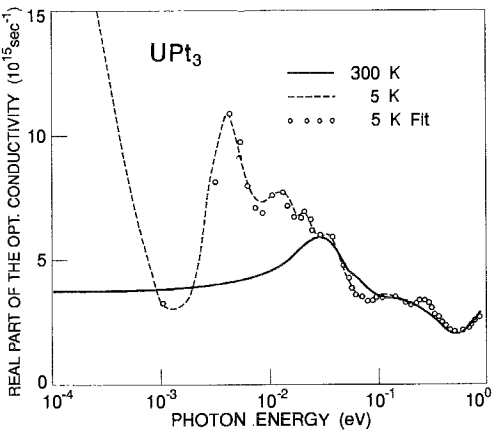

Fig. 135. Real part of the optical conductivity of UPt_3 at 5 K and 300 K. The circles correspond to a fit with Lorentz oscillators. (After Marabelli et al. 1986a.)

For photon energies larger than 12 eV and up to 18 eV the reflectivity has been assumed to drop off as ω^{-2} and for still higher energies as ω^{-4}. Towards zero frequency the spectrum has been extended by means of the Hagens–Rubens relation using the static value of the electrical conductivity at 300 K as measured by de Visser et al. (1984). We obtained an excellent fit over a large frequency range. The complete spectrum was analyzed in terms of optical constants by means of the Kramers–Kronig transformation. In the photon energy range below 0.5 eV we obtain, for the low-temperature conductivity spectrum shown in fig. 135, at the lowest energy, a narrow section with free-carrier behavior and a conductivity minimum. This is a direct consequence of the fact that the reflectivity below the measured range of 1 meV has to be extrapolated towards 100%, and it is unimportant how one does this. In fact Awasthi et al. (1989) have expanded our spectrum even towards 10^{-4} eV using microwaves and find the extension of our free carrier behavior. The spectrum of fig. 135 exhibits, at energies up to 50 meV, a series of 4 pronounced peaks followed by 2 more at higher energies. At room temperature we discern above a basic contribution due to free carriers (the optical conductivity extrapolates towards the dc value measured by de Visser et al. (1984)) only one peak at 30 meV followed by a minimum at 0.5 eV.

The main feature to be observed in fig. 135 is the drastic change in optical structure when cooling below about 50 K. At low temperatures we observe for the lowest energies a free carrier behavior which is to a large extent independent of the extrapolation we use to reach a reflectivity of 100% at zero energy. We observe a screened plasma resonance of heavy quasiparticles near the minimum of the optical conductivity at 1–2 meV. The goal is to find the unscreened plasma resonance and the effective mass of the heavy quasiparticles. For this purpose we subtract a Drude term

$$\sigma_D(\omega) = \frac{\omega\varepsilon_{2D}(\omega)}{4\pi} = \frac{\omega_p^2\Gamma}{4\pi(\omega^2+\Gamma^2)}, \tag{20}$$

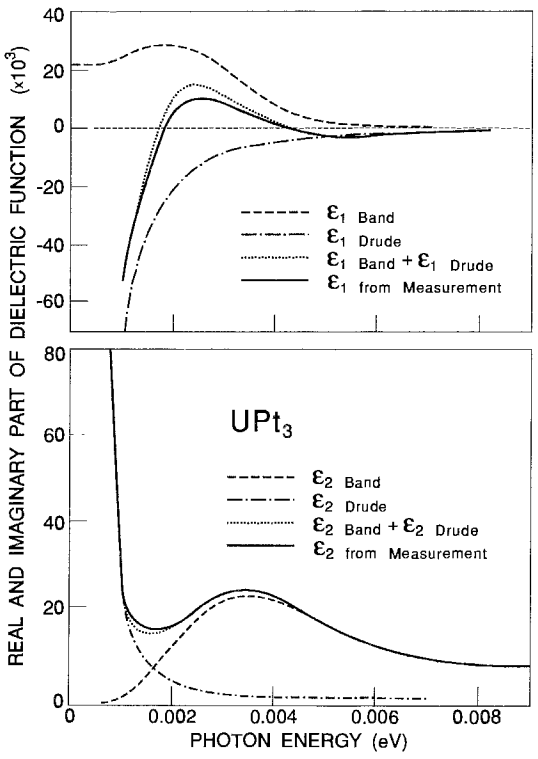

Fig. 136. Real (ε_1) and imaginary (ε_2) parts of the dielectric function of UPt_3 at 5 K. The figure shows the decomposition into a Drude part and an interband transition. (After Marabelli et al. 1986a.)

with $\omega_p^2 = 4\pi\sigma_{dc}\Gamma = 4\pi N e^2/m^*$ from the optical conductivity and perform a Kramers–Kronig transformation of ε_{2b} in order to obtain $\varepsilon_1(\omega) = \varepsilon_{1D}(\omega) + \varepsilon_{1b}(\omega)$, where ε_{1b} is the contribution of bound electrons undergoing optical transitions. $\varepsilon_2(\omega)$ and $\varepsilon_1(\omega)$ obtained in this way are shown in fig. 136 and from these values we calculated the reflectivity in fig. 134, in order to obtain new values for the extrapolation. We pursued this in such a way that, after the cycle, ε_1, ε_2 and reflectivity values all remained as close as possible to their initial values. Thus, we obtained the unscreened plasma resonance $\omega_p = 280$ meV of the heavy quasiparticles (off scale in fig. 136 and where ε_{1D} intersects the zero axis). Since in the formula of the plasma resonance we have two unknown parameters, N and m^*, we use another experimental value on UPt_3, namely the γ value of the specific heat, measured by Stewart (1984) or Quader et al. (1987), and express $\omega_p^2 \propto k_F^3/m^*$ and $\gamma \propto k_F \cdot m^*$. Permitting γ to vary between the experimental values given by the two groups of authors mentioned above and introducing experimental error bars on ω_p our analysis yields values of $k_F = 0.75 \pm 0.025$ Å^{-1} and $m^* = 250m$ (± 10). This value of k_F corresponds to about one f-like heavy quasiparticle per uranium, and not three, as could be expected, making the material nearly integer valent. This one quasiparticle must sit in a narrow (because of the large effective mass) f-like band with high density of states (because of the large γ value)

and the Fermi energy must be near the maximum of the density of states, as indicated in the upper f band in fig. 133. It follows that the f-like quasiparticle band can probably hold only 2 particles per uranium and is thus practically half filled. Uranium, however, has 3 f electrons, and it appears reasonable that the other two f-like quasiparticles fill the lower f-like band as in fig. 133. There may be more and empty f-like quasiparticle bands above those shown in fig. 133, which may account for the narrow peaks in the conductivity spectrum of fig. 135, if every band is still holding only two quasiparticles we may expect a total of seven such narrow bands. In fact, such a band structure has been calculated for UPt_3 by Oguchi and Freeman (1985). However, the calculated width of the subbands is too large to account for the observed γ value of the specific heat.

Above we have described the plasma resonance of the heavy f-like quasiparticles, which have ω_p at 280 meV. However, at the Fermi level there exist also lighter, d type electrons coming mainly from the Pt atoms which hybridize with the f electrons. The d electrons also produce a plasma resonance whose unscreened value has been found by Schoenes and Franse (1985) at 2.5 V. These electrons have an effective mass near the normal value m. In principle these two plasma resonances for light and heavy quasiparticles couple, but since their resonances are so far apart, the eigenmodes of the coupled oscillations are nearly at the same energies as the uncoupled resonances.

Now let us look at the lowest energy interband transition at about 4 meV in the optical conductivity in fig. 135 or in the imaginary part of the dielectric constant ε_{2b} in fig. 136. It is obvious that such a transition goes from a filled state into an empty one and these must be separated by a gap of about 4 meV. It is natural to assume that this gap corresponds to the separation of the two lowest quasiparticle bands shown in fig. 133, although this is only a pseudo gap since also d states exist up to the Fermi level, but with a factor of about 100 lower density of states. The total width of all f-like transitions can be obtained from the plot of N_{eff} and it is about 12 meV, leaving about 4 meV for the bandwidth of each quasiparticle subband, taken to be of equal width and a separation of the density of states peaks of also 4 meV. Inelastic neutron scattering has given a quasielastic line with half-width 4.3 meV (Goldman et al. 1987). Since an interaction of neutrons with heavy electrons is possible only when the latter make a spin flip, we can, by looking at fig. 133, in principle have spin flip excitations within the band around E_F, or across the gap. The problem with UPt_3 is that both energies are near 4 meV so a distinction is difficult. However, it will become clear with the same observation on $CeCu_6$ (see section 5.1.2), where bandwidth and gap are different, that the quasielastic line width corresponds to the width of the band around E_F. Then, with 4 meV the neutron data and our optical determination of the bandwidth nicely agree.

It can be seen from figs. 135 and 136 that the lowest energy transition is the dominant one of the whole spectrum and ε_{1b} and ε_{2b} amount to about 3×10^4, values never heard of before for non-ferroelectrics. The reason is of course, that the optical transition is at such a low energy. Nevertheless, the oscillator strength of the 4 meV transition is only 0.018 (Marabelli et al. 1986a,b) and thus typical for a f–f transition with significant d admixture (an atomic f–f transition would have an oscillator strength of 10^{-6}). Only the two higher energy transitions at 0.114 and 0.27 eV (fig. 135) have an oscillator strength of 0.15

and 0.25, respectively, and are thus typical for f–d or d–f transitions. We note especially that inelastic neutron scattering has not revealed any optical phonons near 4 meV. The lowest energy optical phonon is at about 20 meV (Buyers and Holden 1986).

We want to recollect the main features of these first optical experiments on UPt_3. At low temperatures and low energies we observe a Drude-like free carrier absorption of heavy quasiparticles with an effective mass of about $250m$. The carrier concentration in a 4 meV wide, about half filled quasiparticle band is about one particle per uranium, making it nearly integer valent. These quasiparticles have mainly f character but with a strong d admixture and can be described in a Fermi liquid model. We then observe a gap and an onset of optical transitions of mainly f–f character having a maximum at about 4 meV. More optical transitions exist at higher energy, also of f–f character which can be accounted for by transitions into higher lying empty f-like quasibands, similar as calculated by Oguchi and Freeman (1985). At still higher energy there are d–f and f–d transitions and at 2.5 eV a plasma resonance of light d electrons is observed.

A d–f hybridization model according to Brandow (1986) always yields a hybridization gap in the f quasiparticle density of states. The Fermi level can be in the gap or pseudo gap when the Luttinger theorem permits, as e.g. in SmB_6, high-pressure SmS or YbB_{12}, or it can be in a quasiparticle band as in metallic intermediate-valent systems as YbCuAl, $CePd_3$ or in heavy fermions like UPt_3, $CeAl_3$, $CeCu_6$, etc. Quite recently the same theoretical approach has been taken by Czycholl and Schweitzer (1992) and transport and magnetic properties of heavy fermions with a hybridization gap have been calculated in agreement with experiment.

5.1.2. *$CeCu_6$*

$CeCu_6$ is the next example where gaps in the meV range have been detected, by Marabelli et al. (1988). The experimental method of optical reflectivity measurements over an extremely large photon energy range of more than 4 decades is the same, also at low temperatures, as described in the previous section on UPt_3 and again reasonably large single crystals where available for the measurement. The reflectivity has been measured with unpolarized light at near normal incidence on the a–c plane of the orthorhombic crystal. In fig. 137 we show the reflectivity of $CeCu_6$ at 300 K and 5 K between 1 meV and 12 eV. Generally, metallic behavior is observed with a typical high-energy screened plasma edge near 5 eV. Again, the low-temperature reflectivity exhibits much more structure than at 300 K, especially in the FIR. To perform a Kramers–Kronig analysis of the data, our standard extrapolation, described in the previous section, has been used, employing also the σ_{dc} values of Ott et al. (1985b) and Onuki et al. (1987a). The real part of the optical conductivity is shown in fig. 138 and, again, we observe in the FIR a narrow peak at about 5 meV, practically the same energy where a peak in the reflectivity is observed. Below the minimum of the optical conductivity we assume a Drude term which yields to the experimentally observed σ_{dc}.

In fig. 139 we show the real part of the dielectric constant ε_1, decomposed, as described above, into $\varepsilon_1 = \varepsilon_{1D} + \varepsilon_{1b}$, a Drude- and a band term. The uncoupled Drude term yields the

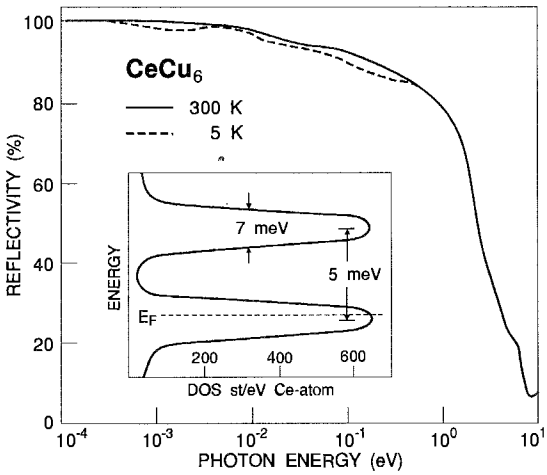

Fig. 137. Near-normal incidence reflectivity of $CeCu_6$ at 5 K and at 300 K. The inset shows the profile of the density of states near the Fermi level as inferred from experimental data. (After Marabelli et al. 1988.)

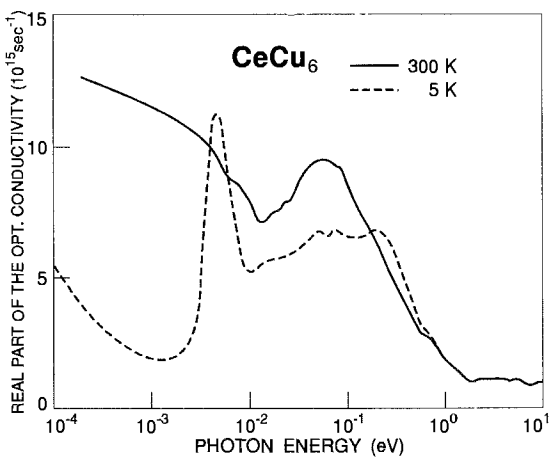

Fig. 138. Real part of the optical conductivity of $CeCu_6$. (After Marabelli et al. 1988.)

plasma resonance (where ε_{1D} intersects the zero axis, off scale in fig. 139) $\omega_p = 150$ meV. Again using the measured γ value of the specific heat of 1.6 J/mol K^2 by Stewart et al. (1984) and Ott et al. (1985b) and using the relations $\omega_p^2 \propto k_F^3/m^*$ and $\gamma \propto k_F \cdot m^*$ we can calculate the effective mass $m^* = 700m$ and the Fermi vector $k_F = 0.7$ Å^{-1}, which corresponds to about 1.2 to 1.4 hybridized quasiparticles per cerium atom. At high temperature the plasma resonance of $LaCu_6$ and $CeCu_6$ are practically the same (see fig. 140) which has as a consequence that at room temperature the f electrons are localized and the conduction bands are about the same in the two compounds. With an unscreened plasma frequency of 1.84 eV at 300 K for both compounds and 1.2 to 1.4 quasiparticles per formula unit, the effective mass of the band electrons becomes $m^* = 4.6m$. The mass enhancement in $CeCu_6$ upon cooling is then about $700/4.6 \approx 150$, which is also

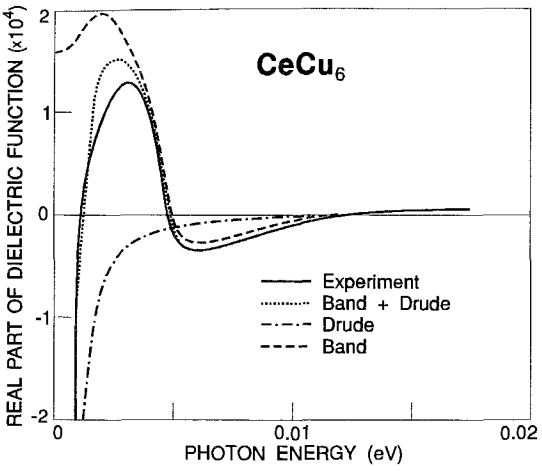

Fig. 139. Real part of the dielectric function of $CeCu_6$ at 5 K. (After Marabelli et al. 1988.)

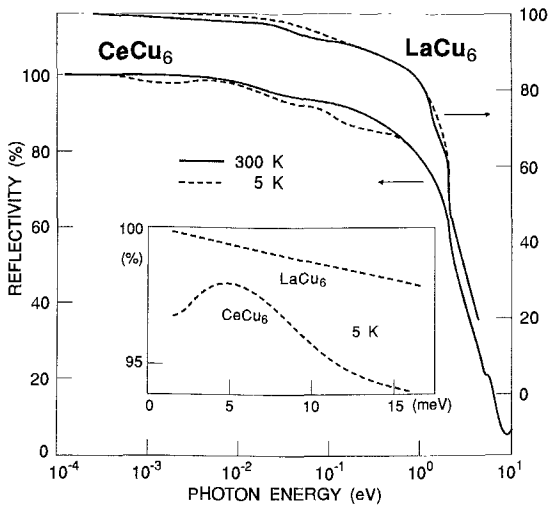

Fig. 140. Near-normal incidence reflectivity of $CeCu_6$ and $LaCu_6$ at 5 K and 300 K. The reflectivities at the lower energies and at low temperature are shown in the inset. (After Marabelli et al. 1988.)

proportional to the change in γ values between $CeCu_6$ and $LaCu_6$. Following the results of Millis et al. (1987) and Becker and Fulde (1987) one can show that the Fermi temperature T^* (related to E_F of the heavy fermion and in the order of some K) is proportional to the screened plasma resonance of the heavy quasiparticles ω_p^* (in the order of meV)

$$\omega_p^* = \sqrt{6(1 + N_f/N_{e_c})}\, T^*, \tag{21}$$

where N_{e_c} and N_f are the concentrations of the conduction electrons and the f electrons, respectively. With $T^* \approx 4.3$ K, $\omega_p^* = 1$ meV for $CeCu_6$ and $N_{e_c} \approx 1.4$ electrons per formula

unit Marabelli and Wachter (1990a) compute for $N_f \approx 0.3$ electrons per formula unit. This then is experimental evidence for the intermediate-valent nature of the heavy fermion $CeCu_6$ with N_f between zero and one.

The effective mass of $700m$ which our experiments yield is several times larger than even the largest masses obtained in the de Haas–van Alphen experiments of Reinders et al. (1986). This is not the only case in which there are discrepancies in the experimental determination of effective masses by different methods and the de Haas–van Alphen masses in heavy fermions, e.g., it also occurs in $CePd_3$ (Webb et al. 1986). The discrepancy can be assigned to at least two reasons: (1) the high magnetic field used in the de Haas–van Alphen measurement can reduce the mass of the carriers, thus the γ value is in $CeCu_6$ in a field of 7.5 T 3 times smaller than in zero field (Reinders et al. 1986, Satoh et al. 1985), so again a smaller γ value in a magnetic field implies a larger bandwidth and thus a smaller effective mass, (2) the high magnetic fields up to 10 T represent an appreciable excitation, and the Fermi surface is composed of different sheets, everyone with different masses. In our derivation we use only one sheet, but also with the de Haas–van Alphen method one does not know whether one has reached the sheet with the highest masses because of limitation in magnetic field.

Let us now turn to the anomalous absorption peak at 5 meV in figs. 138 or 139, which is found only at low temperatures. Again we interpret the corresponding optical transition as being across a hybridization gap of 5 meV. An analysis of the effective number of carriers N_{eff} taking part in this transition yields also the bandwidths of the two high density of states bands so that we obtain a profile of the density of states near E_F as shown in the inset of fig. 137. Compared with UPt_3 the much narrower f quasiparticle bands (1–2 meV) imply a much larger effective mass as is experimentally obtained. In the case of $CeCu_6$ a high-resolution low-temperature photoemission study has been performed by Patthey et al. (1986, 1990). The experiment has been analyzed in the single impurity Anderson Hamiltonian using the Gunnarsson–Schönhammer (1983) approach. In this model there is no hybridization gap and photoemission can only measure the occupied states in the narrow band at E_F. The calculation yields a band filled with f-like quasiparticles to about 1 meV, which is in excellent agreement with our measurements of a total bandwidth of about 2 meV filled to somewhat more than half (inset of fig. 137). A quasi-elastic line width of about 0.5 meV has been obtained by neutron scattering on $CeCu_6$ by Walter et al. (1986). Usually this line width is associated with the Kondo temperature, which, in this case, would correspond to 5.8 K. However, since this neutron scattering corresponds to spin flip excitations, it is also a measure of the half-width of the partially filled quasiparticle band around E_F. (This explanation is given here for the first time.) In this band all states are filled with 2 particles per state with opposite spin up to E_F. Spin flip transitions are thus only possible into the empty states above E_F. The width of the filled part of the quasiparticle band around E_F as measured by photoemission by Patthey et al. (1990) or quasielastic neutron scattering by Walter et al. (1986) is with about 1 meV consistent with our total bandwidth of about 2 meV as measured by FIR spectroscopy.

As in the case of UPt_3 the oscillator strength for the 5 meV transition is only 0.023, typical again for an f–f transition with some d admixture. In fact there are some more

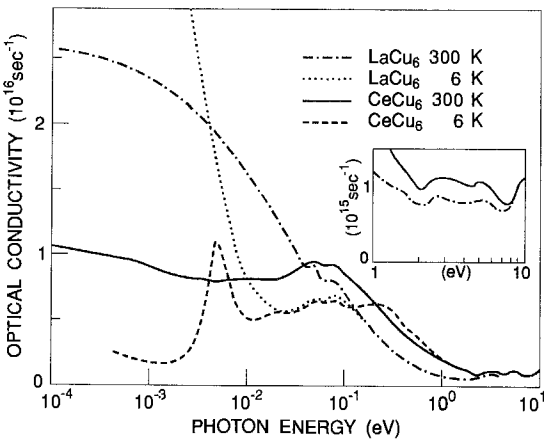

Fig. 141. Optical conductivity of $CeCu_6$ and $LaCu_6$ at 5 K and 300 K. The inset shows a particularity of the conductivity at high energies. (After Marabelli et al. 1989.)

experiments which indicate an excitation at about 5 meV. Inelastic neutron scattering reveals a broad electronic structure at 5.5 meV (Walter et al. 1986). A Schottky-type specific heat has been observed, implying a level 5.6 meV above E_F (Stewart et al. 1984 and Fujita et al. 1985).

For $CeCu_6$ there exists also the reference compound $LaCu_6$ on which comparative studies have been made by Marabelli et al. (1989). While the room temperature reflectivity curves are practically identical, differences occur at low temperatures below about 1 eV. The reflectivity curves of both compounds are shown in fig. 140, where the inset especially compares the FIR range between $LaCu_6$ and $CeCu_6$ at 5 K. It is obvious that only the heavy fermion $CeCu_6$ exhibits the low-energy peak at about 5 meV which we associated with the f–f quasiparticle transition. In fig. 141 we show again for comparison the optical conductivity of $LaCu_6$ and $CeCu_6$ at 6 K and 300 K and it is remarkable that the 5 meV absorptive peak is present in $CeCu_6$, whereas $LaCu_6$ shows only a plasma edge at much higher energies than $CeCu_6$. Thus, also in direct comparison, it is evident that the heavy fermion $CeCu_6$ has a very low energy free carrier part related to the heavy quasiparticles with masses of $700m$ and it has the f–f interband transition typical for two f-like bands separated by a gap, which we take to be the hybridization gap. The structures near 90 meV, common for $LaCu_6$ and $CeCu_6$ at 300 K as well as at 6 K, belong to phonon excitations, whereas at 270 meV in $CeCu_6$ the spin–orbit splitting of the f states can also be observed.

For $CeCu_6$, Marabelli and Wachter (1990a) followed the temperature dependence of the low-energy electronic structure to about 50 K to give experimental evidence of whether this structure disappears above the Kondo temperature as has been suggested by some theories (Grewe 1984). Estimates of the Kondo temperature can be obtained from an analysis of the specific heat by Satoh et al. (1985) or Steglich et al. (1985) or magnetoresistivity by Onuki et al. (1984) or Onuki and Komatsubara (1987) and the measurements yield values ranging between 2 K and 6.2 K, embracing also the determination from the quasielastic line width of neutrons by Walter et al. (1986)

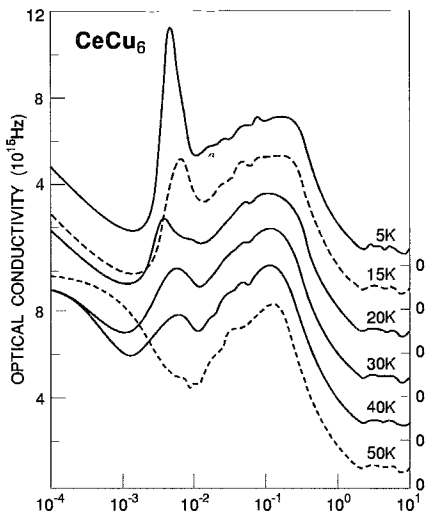

Fig. 142. Optical conductivity of $CeCu_6$ at different temperatures between 5 and 50 K. (After Marabelli and Wachter 1990a.)

with 5.8 K. In other words, the quasiparticle f-like structure in the meV range should disappear above about 6 K according to Grewe (1984).

In fig. 142 we show the temperature dependence of the optical conductivity for $CeCu_6$ up to about 50 K, especially regarding the f–f interband excitation across the hybridization gap at about 5 meV. It is obvious that the f–f transition with its peak at 5 meV can be discerned at least up to 40 K, i.e., far above the Kondo temperature of at most 6 K. This then is in strong contrast to a simple explanation using the dense Kondo effect. On the other hand, using a more or less rigid, i.e., temperature independent f-like quasiparticle density of states, the Fermi energy distribution function $f_F(E)$ at about 50 K will definitely smear out and mix the f-like occupation in the two subbands, as e.g. in fig. 133, so much that a distinct f–f interband transition can no longer be discerned. This is a natural explanation of the disappearance of the 5 meV peak at about 50 K.

Another remarkable feature measured in $CeCu_6$ is the temperature dependence of the plasma resonance ω_p of the heavy quasiparticles, which has been found near 150 meV at 5 K and from which the quasiparticle concentration and the effective mass has been deduced (with the help of the γ value). We show in fig. 143 the plasma frequencies obtained from the optical data at different temperatures. The value at 1.4 K (the asterisk) has been reported from millimeter-wave data from Beyermann et al. (1988) and has a value of about 200 meV, which agrees quite reasonably with our 150 meV. It is remarkable that the plasma frequency preserves practically the same small value up to a temperature of about 20 K. This is in contrast with what one expects from a simple Kondo model where the characteristic temperature for the formation of a resonant state has been estimated to be between 3 and 6 K (Satoh et al. 1985, Steglich et al. 1985, Onuki et al. 1984). Up to room temperature the plasma frequency continuously shifts to 2–3 eV, which means that

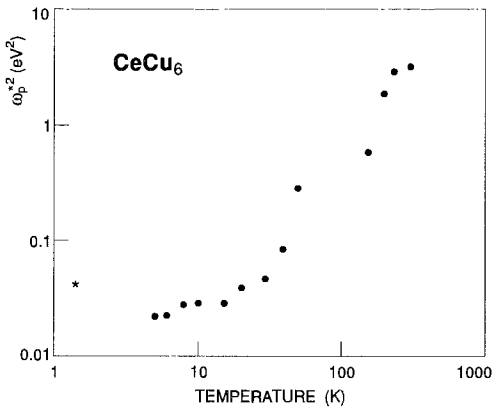

Fig. 143. Values of the plasma frequencies obtained from the optical data at different temperatures. The value at 1.4 K (asterisk) corresponding to 200 meV has been reported from millimeter-wavelength data of Beyermann et al. (1988). (After Marabelli and Wachter 1990a.)

the 4f quasiparticle bands with their low-energy plasma resonance disappear more and more, and only the plasma resonance of the light d electrons prevails. We have to assume that at elevated temperatures the 4f states loose their hybridization with the d band and become localized. We then expect single impurity f electron scattering.

5.1.3. U_2PtC_2

With U_2PtC_2, a "light weight" heavy fermion, we can study the limits of our methods. The material has a relatively small γ value of only 75 mJ/mol U-atom K^2 which leads us to suspect that the effective masses are only in the tens of m. It is also a superconductor with T_c of 1.47 K (Meisner et al. 1984) which puts it between the standard heavy fermions such as UBe_{13} or UPt_3 and the more normal U-based compound U_6Fe (Thompson and Meisner 1985).

Another important prerequisite of our experimental method is the necessity of large enough single crystals with oriented cleaved perfect faces of at least 2×2 mm^2 surface. For U_2PtC_2 we had single crystals, but only 1×2 mm^2, reducing our precision. Nevertheless we could measure our standard spectrum between 1 meV and 12 eV and at 300 K and 6 K (Marabelli and Wachter 1990b). We find above about 100 meV practically the same spectrum at 300 K and at 6 K, so that we show in fig. 144 only the spectral range below 100 meV. The spectrum has been extrapolated in the usual way using also the σ_{dc} values from the literature (Meisner et al. 1984, Thompson and Meisner 1985).

From the Kramers–Kronig transformation we obtain, in the usual way, the dielectric functions and in fig. 145 we show the optical conductivity of U_2PtC_2 at 6 K. At room temperature and at low temperatures we can compute a high-energy plasma resonance at about 2 eV which is due to low-mass, probably d-type, electrons. At low temperatures a second small plasma frequency can be deduced and it is indicated by the minimum in the optical conductivity at about 4 meV which corresponds to the screened plasma frequency, screened by f-like interband transitions at about 9.5 and 30 meV (fig. 145). We realize that these f-like interband transitions occur at appreciably higher energy than in UPt_3

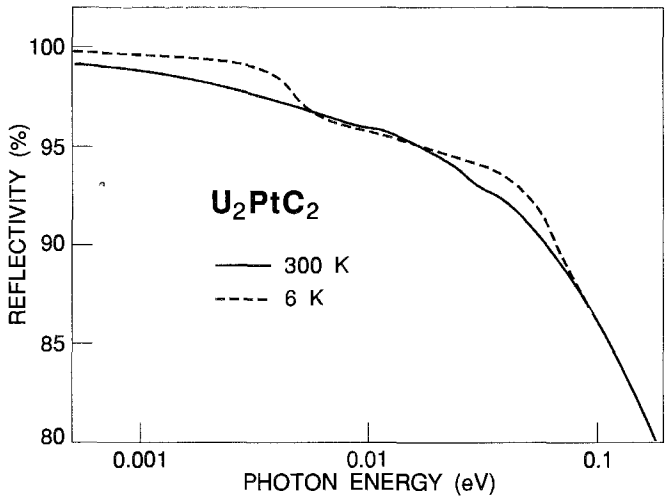

Fig. 144. Optical reflectivity of U_2PtC_2 in the low-energy spectral range at 300 K and at 6 K. (After Marabelli and Wachter 1990b.)

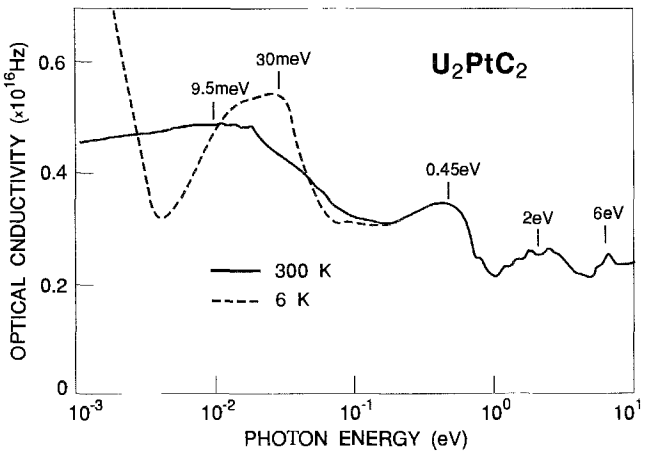

Fig. 145. Optical conductivity of U_2PtC_2 as obtained from Kramers–Kronig transformation of the reflectivity spectra. (After Marabelli and Wachter 1990b.)

and $CeCu_6$ and they have thus a reduced intensity in the optical conductivity. With the help of fig. 146 of the real part of the dielectric function, we can in the described manner decompose ε_1 in contributions from bound (ε_{1b}) and free carriers (ε_{1D}) and with the help of two oscillators at 9.5 and 30 meV (with the one at lowest energy having again a typical f–f oscillator strength of 0.021/U-atom with significant d admixture) and obtain the unscreened plasma resonance at 440 meV. The weaker strength of the interband transitions at 9.5 and 30 meV is reflected by the zero frequency dielectric constant $\varepsilon_{stat} = 6 \times 10^3$,

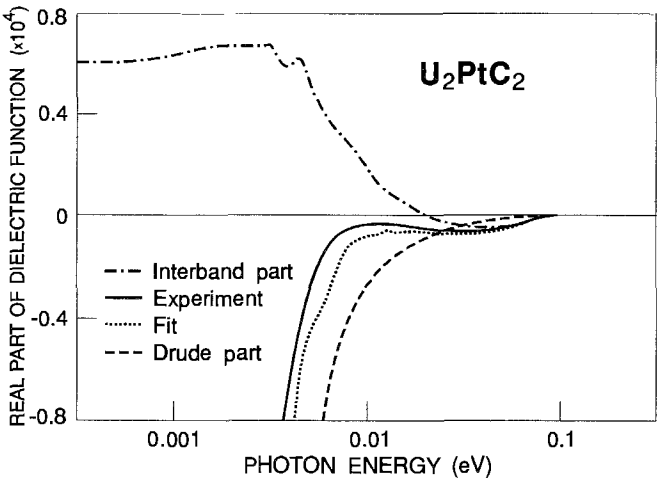

Fig. 146. Real part of the dielectric function of U_2PtC_2 at 6 K and decomposition into a free carrier Drude-like contribution and an interband term. (After Marabelli and Wachter 1990b.)

compared with about 3×10^4 for UPt_3 or $CeCu_6$. By comparing our unscreened plasma resonance of 440 meV with the measured γ value of the specific heat of 75 mJ/mol U-atom K^2, we obtain $m^* = 52\,m$ and the Fermi vector $k_F = 0.6$ Å which corresponds to 0.56 quasiparticles per uranium atom. This, then, is again a typical number for intermediate valence, in contrast to UPt_3 with about 1 quasiparticle per uranium atom we have now a clear cut case, from which we learn that also in heavy-fermion uranium compounds a nearly integer valence is only fortuitous.

The lowest energy f–f interband transition across a gap, the hybridization gap, is 9.5 meV and excitations into higher bands occur at 30 meV, similar to UPt_3. From our optical data we also find a bandwidth of the quasiparticle bands at E_F of about 15 meV so that for this uranium compound, also, we derive a quasiparticle band structure like in fig. 133, with f-like quasiparticles filling the lower band and about 0.5 quasiparticles filling the upper band to less than half, being the reason for the smaller γ value. The larger bandwidth, when compared with UPt_3, accounts for the not so large effective mass of only $52m$ so it is justified to call this material a "light weight" heavy fermion. On the other hand the higher energy quasiparticle plasma resonance and the larger gap make the experimental determination of the typical parameters rather difficult so that we think with U_2PtC_2 we have reached the limit of the experimental determination of the heavy-fermion parameters. Nevertheless also for this material the mechanisms are the same as for the others.

5.1.4. *$CeAl_3$*

$CeAl_3$ is another prototype heavy-fermion material which is worth to be investigated. However, so far no large enough single crystals have been grown to permit high-quality optical spectroscopy as described above. With a γ value of 1.6 J/mol K^2 as measured by

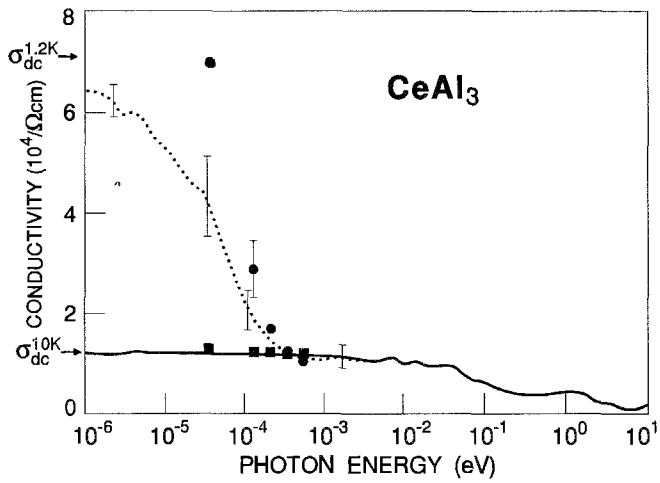

Fig. 147. Frequency-dependent conductivity obtained from the Kramers–Kronig analysis of the absorptivity of $CeAl_3$ at 1.2 K (dotted curve and solid circles) and 10 K (solid line and solid squares). (After Awasthi et al. 1993.)

Andres et al. (1975) it achieves practically the same value as $CeCu_6$. Thus, we should be able to expect more or less the same effective mass and the same bandwidth of the quasiparticle band around E_F as in $CeCu_6$. The width of the hybridization gap may be different between both compounds. In spite of the fact that only polycrystalline material was available Ferreira et al. (1992) made frequency dependent conductivity measurements between dc and 3 eV which later were completed by Awasthi et al. (1993) up to 12 eV, so that the complete optical spectrum as described for other compounds above was available. The frequency dependent conductivity is shown in fig. 147 between 10^{-6} eV and 12 eV employing different experimental methods. A decoupling method similar to the one used by Marabelli et al. (1986a,b) and described in section 5.1.1, yields the unscreened plasma resonance $\omega_p = 190$ meV, similar to $CeCu_6$ with 150 meV. Awasthi et al. (1993) calculate for the effective mass of $CeAl_3$ $m^* = 690m$, again in excellent comparison with $m^* = 700m$ obtained by Marabelli et al. (1988) for $CeCu_6$. By using eq. (21) and the relation $\gamma \propto k_F \cdot m^*$, we compute a $k_F = 0.27$ Å^{-1} for $CeAl_3$ which yields a hybridized carrier concentration of 1.68 carriers per formula unit and a f-like quasiparticle concentration of $N_f \approx 0.44$ per Ce-atom, indicating again intermediate valence. Awasthi et al. (1993) also compute the Kondo temperature from their experimental results and it is found between 6 and 10 K, again similar to that of $CeCu_6$. The Kondo temperature is related to the bandwidth of the quasiparticle band around E_F and, again, there is the bandwidths of $CeCu_6$ and $CeAl_3$ are similar, between 1 and 2 meV. Inelastic neutron scattering has been performed on $CeAl_3$ by Murani (1987) and the quasielastic line width has been determined to be 0.5 meV below 1 K, having reached about 1 meV at 4 K. As has been discussed above, this quasielastic line width corresponds to spin-flip transitions in the band containing E_F, and it is not only a measure of the Kondo temperature but

also of the empty part of the quasiparticle band and it is, with about 1 meV, of the same magnitude as those obtained by other means. Awasthi et al. (1993) also compute the temperature dependence of the effective mass of $CeAl_3$ and find it to decrease sharply with temperature. Again, this is similar to $CeCu_6$, where we have plotted the square of the plasma resonance ω_p^2 in function of temperature in fig. 143. The sharp increase of ω_p^2 with temperature must be due to the strong decrease of the effective mass with increasing temperature.

A low-energy interband transition in $CeAl_3$ is not so clear cut as for the other described heavy fermions. However, Awasthi et al. (1993) can fit their results, shown in fig. 147, only by assuming a relatively broad and badly defined interband transition between 1 and 40 meV. We have to realize that the higher the energy of such an interband transition, the lesser is the intensity displayed, since it is proportional to ε_2/ω. Also, the higher the reflectivity values (the lower the damping) the more difficult it is to discern a reflectivity peak in the spectrum. We will see below that $CeAl_3$ has the largest gap value around 20 meV of all investigated heavy fermions.

5.1.5. $U(Pt_{1-x}Pd_x)_3$

One of the most interesting and effective methods of understanding the heavy-fermion properties, consists of slightly changing the composition and the stoichiometry of the samples in a controlled way and observing the modifications that occur. Examples are UBe_{13} with small amounts of Th, e.g. $Th_{0.033}U_{0.967}Be_{13}$, where the substitution changes the heavy-fermion properties and the superconducting transition temperature appreciably (Smith et al. 1987). Marabelli et al. (1992b) have chosen the system $U(Pt_{1-x}Pd_x)_3$ because the heavy-fermion properties of UPt_3 are well documented but they rapidly disappear when the amount of Pd rises to about 10% (Aeppli et al. 1988, de Visser et al. 1987b). We then expect that one of the typical heavy-fermion properties, namely the quasiparticle bands with a hybridization gap in between, disappear. This, also, is a check that we have measured with our optical properties the fundamental heavy-fermion properties.

Thus, we performed an optical study over our large photon energy range at low temperatures on $U(Pt_{0.95}Pd_{0.05})_3$ and on $U(Pt_{0.9}Pd_{0.1})_3$ single crystals and we compare the results with those previously obtained on UPt_3 (Marabelli et al. 1986a; section 5.1.1). The 5% Pd crystal exhibits antiferromagnetic order at 5.8 K and, thus, we measured especially the reflectivity between 4 and 12 K but no change was observed above and below T_N. The reflectivity at 5 K for UPt_3 and 5% and 10% substitution by Pd is shown in fig. 148 where the inset exhibits the low-frequency behavior. As a result of the Kramers–Kronig analysis we obtain also the optical conductivity which is shown at 5 K for the 3 compositions in fig. 149.

We recall that the main feature of the low-temperature conductivity spectrum of UPt_3 was the existence of a minimum between 1 and 2 meV which separates a low-energy region with free carrier behavior and the first optical structure at 4 meV. The plasma frequency of the free quasiparticles was calculated to be $\omega_p = 280$ meV (Marabelli

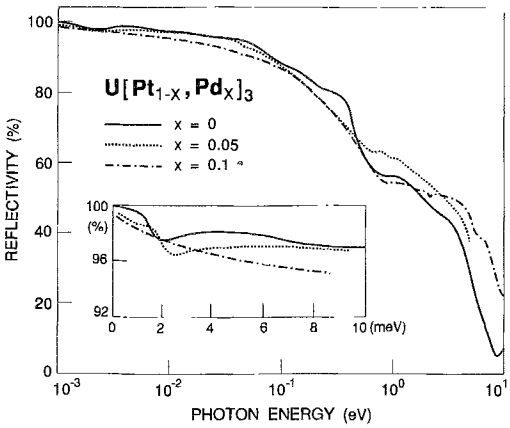

Fig. 148. Optical reflectivity of $U(Pt_{1-x}Pd_x)_3$ at 5 K for three different stoichiometries. In the inset the FIR part of the spectra is shown. (After Marabelli et al. 1992b.)

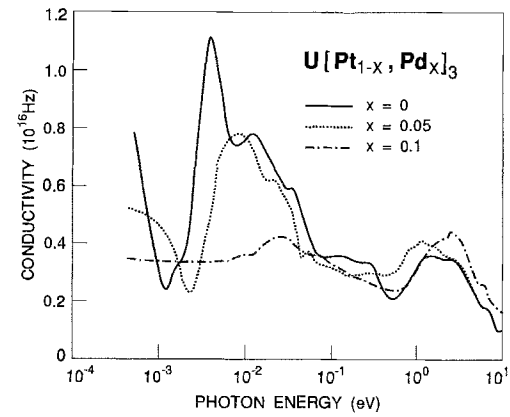

Fig. 149. Optical conductivity of $U(Pt_{1-x}Pd_x)_3$ at 5 K for three different stoichiometries. (After Marabelli et al. 1992b.)

et al. 1986a,b) from which an effective mass $m^* = 250m$ has been derived (section 5.1.1). The lowest-energy interband transition between f-like quasiparticle bands at 4 meV was across a hybridization gap and the oscillator strength of this transition was, with about 0.018, typical for a f–f transition with strong d admixture. The data obtained on the sample with 5% Pd admixture show substantially the same characteristics. The minimum in the conductivity appears slightly shifted towards higher energies, as well as the peak of the structure which is a bit lower and broadened with respect to the pure UPt_3. The σ_{dc} value of the 5% Pd sample is also considerably lower when compared to pure UPt_3. Since the plasma frequency obtained with the usual decoupling procedure is practically the same in UPt_3 and the 5% Pd containing sample, the reduced σ_{dc} values indicate a stronger scattering due to compositional disorder or antiferromagnetic spin fluctuations. The interesting case occurs with the 10% Pd sample where the low-energy features disappear completely (fig. 149). In fact, for this curve there is no significant difference between measurements performed at 5 K or 300 K. The first structure in the

optical spectrum of the 10% sample is centered at about 30 meV and should correspond to a collection of structures at the same energy range in UPt_3. The plasma resonance of the 10% sample has shifted to 1.5–3 eV and is no longer related to a plasma frequency of heavy quasiparticles.

The substitution of Pt with Pd can alter the system in two ways. One is the direct change of the hybridization process due to a volume change. Such an effect has been claimed to be responsible for antiferromagnetism entering in the system $CeCu_{6-x}Au_x$ by von Löhneisen et al. (1990). A second effect is the breaking of the periodicity of the hexagonal cell of UPt_3. The disorder introduced in this way destroys the coherence in the lattice of the interaction between conduction and f-like quasiparticles. In UPd_3 the f electrons of U tend to be localized and no quasiparticle bands are observable (Schoenes and Andres 1982). It is interesting to note, that, when the two quasiparticle bands with their optical transition at 4 meV disappear in the 10% sample, the long range magnetic order is lost too. We then connect these features with the loss of long range periodicity. We suggest that the antiferromagnetic order for Pd concentrations between 0 and 7% (Aeppli et al. 1988, van Sprang 1989) with its low magnetic moment of $0.02\mu_B$ is intrinsically connected with this coherent hybridization of f and d electrons and thus the formation of narrow quasiparticle bands. These bands are an intrinsic feature of the heavy-fermion state and disappear when the heavy-fermion character is lost.

This is not in contrast with the observed increase of the specific heat passing from UPt_3 to $U(Pt_{0.9}Pd_{0.1})_3$ (de Visser et al. 1987b). In the latter compound the periodicity is lost, but we still have a Kondo resonance near the Fermi level, probably of localized f states of uranium just as in UPd_3. However, in this nonperiodic arrangement quasibands do not exist and they do not split, and the γ value can be high (as for other real Kondo systems). But the optical transition giving evidence of split quasibands is absent, just as a plasma resonance of heavy quasiparticles is absent, because for this to occur, a partially filled quasiparticle band must exist. In fact, the resistivity is Kondo-like (steadily increasing for $T \rightarrow 0$) whereas in a heavy fermion the resistivity decreases to 0 for $T \rightarrow 0$.

5.2. *Résumé of quasiparticle bandstructure*

FIR optical experiments have proven to be an extremely valuable tool to obtain the quasiparticle band structure around E_F. For 5 different lanthanide and actinide materials we have measured the plasma resonance of heavy quasiparticles at low temperatures from which we could obtain the effective masses and the concentration of f-like quasiparticles. Effective masses have been found between $50m$ and $700m$ and they are roughly in agreement with de Haas–van Alphen masses, though generally larger (Taillefer et al. 1987). The concentration of carriers per f atom in the quasiparticle bands was always found to be a non-integer number (agreeing with Hall effect measurements (Schoenes and Franse 1986), so that intermediate valence could be established for all compounds. In generalizing, this substantiates the statement that all heavy fermions are intermediate valent, but not all intermediate materials are heavy fermions, inasmuch as some do not have electrons at the Fermi level. Nevertheless, also in the latter materials there exist

heavy electrons in filled quasiparticle bands, as e.g. in SmB_6 with effective masses of about $1000m$. For all five of the investigated materials falling into the class of heavy fermions, we observe gaps in the meV range between 4 and 20 meV which permit optical interband transitions across this gap, having f-like character with a strong admixture of d character. Since this is the essence of f–d hybridization, it is only natural to postulate that the observed gaps are, in fact, hybridization gaps (in general only pseudo gaps), since general theories of periodic arrangement of atoms such as the Anderson lattice or the Kondo lattice model postulate such a hybridization gap (e.g., Brandow 1986, 1988). Our determination of band gaps could be supported in some cases by the measurement of Schottky anomalies implying two-level systems (Stewart et al. 1984, Fujita et al. 1985). Also inelastic neutron scattering reveals electronic transitions implying spin flips (i.e., from the occupied bands into empty states above E_F) with the same magnitude as our optical data (Walter et al. 1986, Murani 1987). It is especially gratifying, and realized in the system $U(Pt_{1-x}Pd_x)_3$, that, when the heavy-fermion properties disappear, the quasiparticle bands also disappear, thus there is no hybridization gap and no plasma resonance of heavy quasiparticles. Localized states never yield a plasma resonance since this is a collective oscillation.

There have been attempts to interpret the inelastic neutron scattering data with crystal-field transitions. However, there has never been proof that one has a clear cut crystal-field transition in any heavy fermion; (1) the crystal-field splitting is not in agreement with the one obtained on non heavy-fermion reference compounds; (2) only one line was observed instead of several according to the crystal-field scheme and the form factor was never in agreement with the one expected. One of the obvious reasons is that the f-like crystal-field levels would contain a large d admixture and form narrow bands.

Purely with optical means also the bandwidth of the quasiparticle bands could be determined and they range for the five investigated materials between 1 meV to 15 meV. These bandwidths are in full agreement with calculated bandwidths from high-resolution photoemission at low temperatures (e.g., Patthey et al. 1990) or with the quasielastic line width of inelastic neutron scattering (e.g., Goldman et al. 1987) and they are also a measure of the Kondo temperature.

We can thus provide a purely experimentally determined quasiparticle band structure, as given in fig. 133 for uranium compounds, and in the inset of fig. 137 for cerium-based heavy fermions. Generally speaking, we have experimentally obtained two parameters, the bandwidth and the gap width, which will be ingredients for any explanation of physical properties such as temperature dependence of electrical resistivity, temperature dependence of the γ value of the specific heat, temperature dependence of the susceptibility and field- and pressure dependence of magnetization etc. Indeed a two parameter fit of physical parameters has been used quite often (e.g., Thompson et al. 1987) taking as the two parameters the Kondo temperature T_K and another temperature somehow correlated with the maximum in the temperature dependence of the electrical resistivity, a "coherence temperature". We think that with the two energy scales, bandwidth ($\propto T_K$) and band gap, we can propose a model which is in good agreement with experiment. We think it is fundamental in any explanation of experimental results to

take thermal excitations across the hybridization gap into account. Indeed, this has been done recently by Czycholl and Schweitzer (1992) with success.

5.3. *Model calculation of physical properties of heavy fermions*

A model to be used as a basis for a quantitative calculation of heavy-fermion properties should be applicable to all "normal" heavy fermions. We understand as normal those heavy fermions which do not show ferromagnetism in addition to relatively large magnetic moments. Also, we will not discuss the heavy fermions in the superconducting state or at temperatures below about 4 K where scattering on spin fluctuations dominates. What we will discuss is the temperature dependence of the electrical resistivity, where we should be able to account for a maximum of the resistivity, as for $CeCu_2Si_2$ (Stewart et al. 1983), or for a smooth curve as in UPt_3 (de Visser et al. 1984) within the same model. This model should, without a change of parameters, yield the temperature dependence of the γ value of the specific heat and the magnetic susceptibility or the magnetization. Only when this is the case can one speak of a new model of general nature.

Several models have been proposed in the past, usually explaining only a specific feature of the heavy fermions, for example the interplay between magnetism and heavy-fermion behavior (de Visser et al. 1991) or the effect of doping and disorder (Rasul 1991) or the transition from impurity to the lattice limit (Schönenberg and Keiter 1992, Wang Xu et al. 1991).

The Kondo effect was often used to explain thermodynamical or magnetic properties of heavy fermions, in particular, the huge enhancement of the γ value of the specific heat at low temperatures. In fact a large γ value is usually taken as evidence of heavy-fermion behavior. As we pointed out in section 5.1.5, $U(Pt_{0.9}Pd_{0.1})_3$ has a large γ value but still is not a heavy fermion, having instead localized f levels and increasing resistivity with decreasing temperature (Kondo metal). It has been pointed out by Lee et al. (1986) that a large γ value is a necessary but not a sufficient condition for heavy fermions (materials with large γ values where already known 20 years ago), it is also necessary to have a decreasing resistivity with decreasing temperature, that is, a metallic character. Several attempts at a periodic Kondo lattice have been made (e.g., Grewe 1984, Lacroix 1987) but the proposal was that the apparent hybridization gap would disappear above the Kondo temperature T_K. We have shown experimentally in section 5.1.2 that quasiparticle bands separated by a gap persist up to temperatures of 50 K, whereas the Kondo temperature of the same material is at most 6 K. Above 50 K transitions across a gap can no longer be discerned because of a smearing due to the temperature dependence of the Fermi distribution function. For the same reason the plasma frequency changes little from 5 up to about 30 K, then tends to increase slowly. In other words, we can assume that the quasiparticle band structure is relatively temperature independent and the persistence of the gap goes far beyond the expected limits. In heavy fermions the Fermi energy must be in one of the narrow sub-bands. Due to the small dispersion, the effective mass of quasiparticles in these bands is much more enhanced with respect to normal metals. Moreover, dielectric functions calculated in such a scheme by using a slave-boson method

to solve the periodic Anderson Hamiltonian (eq. 1) by Millis et al. (1987), confirm the existence of a very low plasma frequency, scaled on the characteristic renormalized Fermi temperature of the system (a few Kelvin) and a strong screening due to a large dielectric constant at the lower energies because of a gap. This is exactly what our experiments have shown.

According to the experimental and theoretical findings discussed above, we now want to evaluate the effects of a two-band structure on the thermodynamic properties. Marabelli et al. (1986a,b) and Marabelli and Wachter (1987c, 1992) have used a crude but successful model: for the two-band density of states they took two Gaussian curves pinned on a wide d-like conduction band, as shown in principle in fig. 2b or for UPt_3 in fig. 133 and for $CeCu_6$ in the inset of fig. 137. It is not very important whether one uses Lorentzians or even rectangularly shaped bands; the Gaussians just make the computation simpler. The Fermi level is placed in one of the bands and the density of states is scaled with the value of γ for $T \to 0$. It is assumed that thermally induced excitations occur across the hybridization gap into empty states above E_F. The statistics which governs this excitation process is not the Boltzmann statistics, because this approximation is valid only when the Fermi energy is separated by more than $k_B T$ from the band edges. Instead, the Fermi–Dirac statistics must be rigorously applied. The bands are assumed "rigid" and the temperature dependence has been obtained through the Fermi function (taking into account the thermally excited f–f interband transitions as well). Then we tried to fit the temperature dependencies of the resistivity, the electronic specific heat and the magnetic susceptibility by varying the bandwidth of the Gaussians and the energy separation of the Gaussians, i.e. the hybridization gap. As mentioned above, this is in principle a two-parameter fit.

5.3.1. *The electrical resistivity*

The resistivity of $CeCu_6$, $CeAl_3$, $CeCu_2Si_2$ or UBe_{13} for example, shows a maximum in the temperature dependence of the resistivity at temperatures ranging between 5 and 30 K (Onuki et al. 1987a, Ott et al. 1984, Stewart et al. 1983). A description in terms of different scattering regimes is generally made (Varma 1985). At the highest temperatures the conduction electrons are incoherently scattered by Ce or U ions. The asymmetry of this scattering is thought to result from Kondo interaction, spin fluctuations or charge fluctuations (Lavagna et al. 1982, de Visser et al. 1984, Capellmann 1988) which make the resistivity increase for decreasing temperatures. At low temperatures coherence effects are thought to prevail, due to the periodic distribution of the ions; the resistivity decreases again and at the lowest temperatures (below 1 K) one observes a temperature-dependent resistivity proportional to T^2 (spin disorder scattering). However, other standard heavy-fermion compounds such as UPt_3, U_2PtC_2 or UPd_2Sn, which also have a T^2 term of the resistivity at the lowest temperatures, do not show any maximum of the resistivity up to room temperature (de Visser et al. 1984, Thompson and Meisner 1985, Rossel et al. 1986).

To start the calculation of the temperature dependence of the resistivity, Marabelli et al. (1986b, 1987) and Marabelli and Wachter (1987b,c, 1988, 1990c, 1992) assume that we have scattering of electrons in the narrow band containing the Fermi level and in addition we have thermal excitations across the gap into empty states above E_F, thus changing the carrier number in the band with E_F and introducing carriers of different sign in the other narrow band. The change of the carrier concentration is derived in eqs. (13, 14). To compute the resistivity $\rho = m^*/(Ne^2\tau) = \hbar k_F/(Ne^2\lambda)$ we assume for the scattering time τ or the mean free path λ an average which depends mainly on the electron–phonon scattering and in heavy fermions also on the electron–electron interaction. By assuming a linear temperature dependence for the electron–phonon scattering rate and introducing the response function $\chi_R(E,T)$, in order to account for the quasiparticle interaction, we use, with the help of Dallacasa (1981) and Overhauser and Appel (1985), the expression

$$\rho = c\frac{T}{N(T)}\int_{-\infty}^{+\infty}\left(-\rho_D(E)\frac{df_F(E)}{dE}dE\right), \tag{22}$$

which is equivalent to eq. (15). Here c is a factor which includes the cross section of electron–phonon scattering, the Fermi vector and the appropriate physical constants, and which is used as a scaling factor in the model. Such a formula is valid for a normal metal, but could be incorrect for strongly energy dependent scattering. However, we assume in our simple model that this dependence is included in the phenomenological $\rho_D(E)$. Below room temperature and when $\rho_D(E)$ is practically constant we obtain

$$\rho = c\,\rho_D(E_F)\frac{T}{N}, \tag{23}$$

the usual linear temperature dependence of a normal metal. If an anomalous structure is placed at the Fermi level a different temperature dependence is introduced by the integral term of eq. (22) when the thermal distribution becomes larger than the width of the structure and by the number of carriers which is increased by interband transitions across the gap.

The best systems where one can study the influence of the narrow energy band structure on the resistivity are those where a non-heavy-fermion reference substance exists. This is the case for $CeCu_6$ ($LaCu_6$) and UPd_2Sn ($ThPd_2Sn$). As can be seen in fig. 150, the resistivity of the heavy-fermion and its reference compound is vastly different. The system $CeCu_6$ and $LaCu_6$ has already been described in section 5.1.2. The density of states at E_F for $LaCu_6$ has been obtained from the specific heat and the concentration of electrons (1.2–1.6 el/f.u.) from the Hall effect by Onuki et al. (1987b) and it is used to fix the Fermi energy. The experimental resistivity values were used to fix the constant c in eq. (23) and we obtain an excellent fit of the linear resistivity for $LaCu_6$ in fig. 150. By keeping the same electron–phonon interaction constant c for $CeCu_6$ also, just introducing the two quasiparticle bands, using the experimentally determined γ value (Stewart et al. 1984) and adjusting only the bandwidth BW and the gap value of the

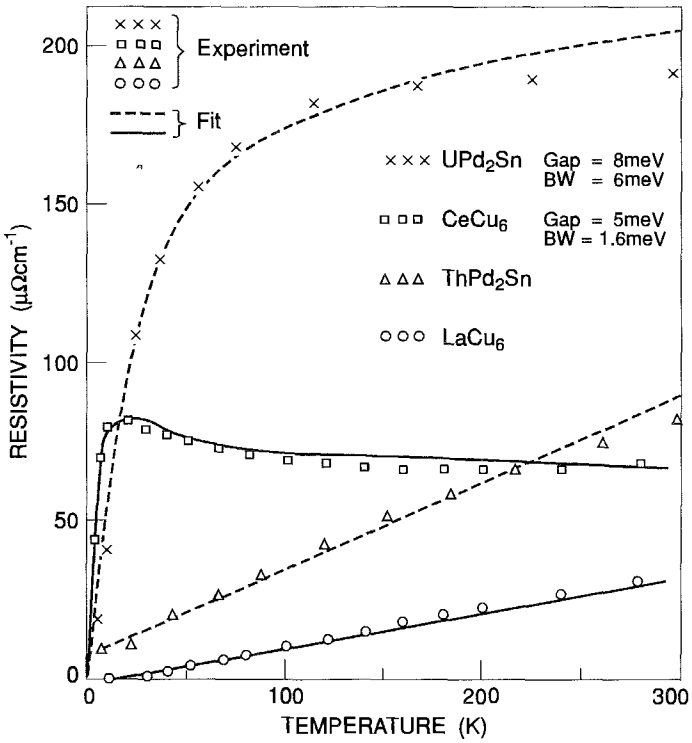

Fig. 150. Temperature dependence of the resistivity of the two heavy-fermion compounds UPd_2Sn and $CeCu_6$ and of the reference compounds $ThPd_2Sn$ and $LaCu_6$. The symbols represent the experimental values, the curves the calculated fit. The parameters used in the fit are shown in the figure. The parameters of $CeCu_6$ agree with those experimentally measured by Marabelli et al. (1989): gap = 5 meV, $B_W = 2$ meV. (After Marabelli and Wachter 1990c.)

two Gaussians introduced in eq. (22), we can fit the experimental resistivity curve of $CeCu_6$ with surprising accuracy (fig. 150). The gap value and the bandwidth, 5 meV and 1.6 meV, respectively, determined from fig. 150 agree excellently with the values determined experimentally from the optical data of $CeCu_6$, described in section 5.1.2, 5 meV and 2 meV, respectively.

For UPd_2Sn and $ThPd_2Sn$ (Rossel et al. 1986) the procedure is the same and again the experimental curves could be fitted excellently (fig. 150). This time the gap and the bandwidth BW of UPd_2Sn are 8 meV and 6 meV, respectively, the same order of magnitude as for the other systems, but there are no other independent optical data available for comparison.

It comes as a surprise that already in this first set of curves for the two heavy fermions $CeCu_6$ and UPd_2Sn, we have two different types of resistivity behavior: a curve with a maximum and a smooth curve. And this within the same model and with

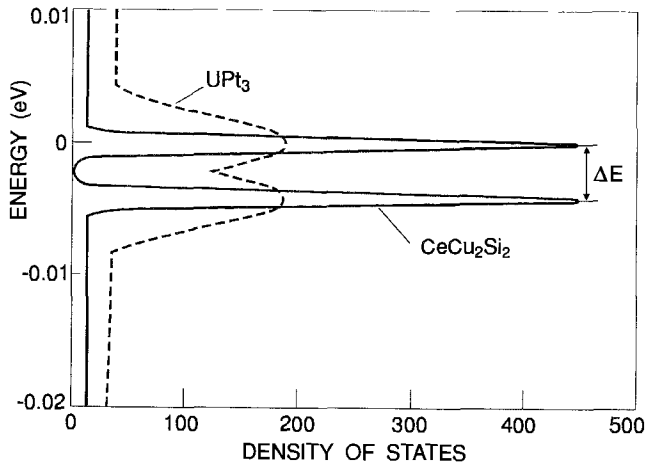

Fig. 151. Quasiparticle band structure of UPt_3 and $CeCu_2Si_2$. Note the d bands at the left-hand side of the figure. (After Marabelli and Wachter 1987c.)

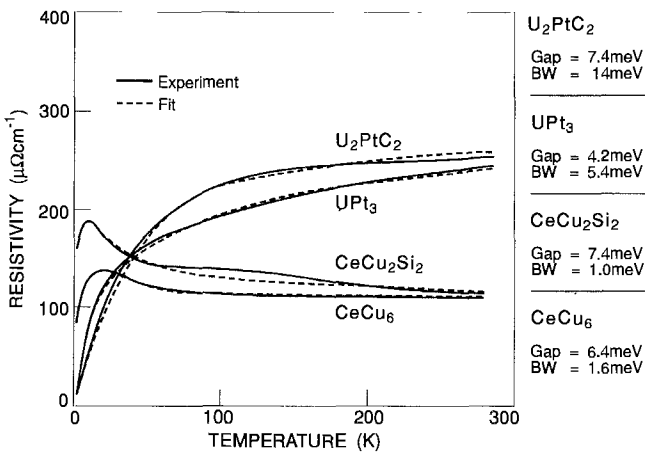

Fig. 152. Fits of the resistivities of U_2PtC_2, UPt_3, $CeCu_2Si_2$ and $CeCu_6$ by using a phenomenological two-band model. (After Marabelli and Wachter 1992.)

only two adjustable parameters, the gap and the bandwidth. We can understand the mechanism behind this difference by looking at fig. 151, which compares the quasiparticle band structure near E_F of UPt_3 and $CeCu_2Si_2$. In UPt_3 the temperature dependence of the resistivity is a smooth curve and for $CeCu_2Si_2$ one observes a maximum, just as in UPd_2Sn and $CeCu_6$, respectively (fig. 152). The model calculations for UPt_3 and $CeCu_2Si_2$ yield practically the same gap value, about 4 meV, and the density of states in fig. 151 is scaled, according to the experimental values of the respective γ values. However, the bandwidth is different for both materials, about 5 meV for UPt_3 and

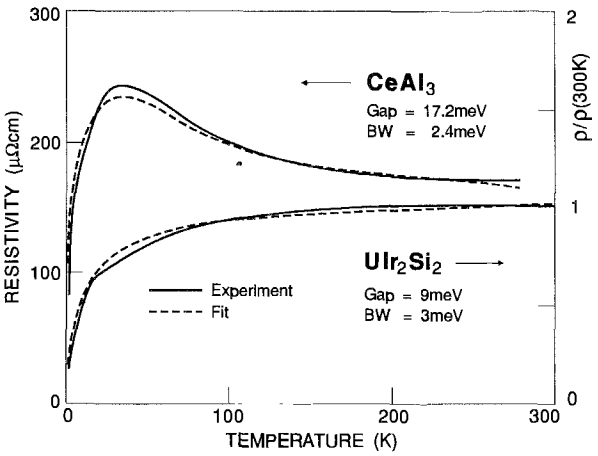

Fig. 153. Temperature dependence of the resistivity of $CeAl_3$ and UIr_2Si_2. Experimental values from Ott et al. (1984) and Chevalier (1988). (After Marabelli and Wachter 1987c.)

about 1 meV for $CeCu_2Si_2$, and this is again shown in fig. 151. Now we find the reason for the different temperature behavior of both compounds: a narrow bandwidth relative to the band gap leads to well separated bands, as in $CeCu_2Si_2$ (and also $CeCu_6$ or $CeAl_3$), so the thermal excitation processes across the gap are well observed and decrease the resistivity with increasing temperature for high enough temperatures. For a larger bandwidth, as in UPt_3 (and also U_2PtC_2 or UPd_2Sn or UIr_2Si_2), the gap is not so pronounced (fig. 151) and neither are the thermal excitation processes across the gap and they result only in a flattening of the resistivity increase with increasing temperature.

Finally, in fig. 153 we show the temperature dependence of the resistivity of $CeAl_3$ and UIr_2Si_2, again with different behavior for the reasons discussed above. One can now also use a more phenomenological approach, materials with a large γ value have narrow bands at E_F, thus large effective masses. Since so far we have not found gaps smaller than about 4 meV, for these materials the gap is well pronounced and thus the resistivity has a maximum in the temperature dependence.

Optical data have not been measured for all of the materials shown in figs. 150–153, but when they are known they agree to within 1 meV with the independent model values which we consider a great success of this simple and rough model. Here we want to mention again that it is not our intention to present a theory which suits or satisfies a theorist, but we want to show, and we think we can show, that intermediate valence is present in heavy fermions and that gaps exist in the density of states, and thermal excitations across these gaps must be taken into account to explain or fit thermodynamical data. A theory, much better based on theoretical grounds but leading to the same results, has been presented by Czycholl and Schweitzer (1992).

5.3.2. *The γ value of the specific heat*

To derive the specific heat and the γ value of the heavy fermions it is essential to point out that with those narrow f-like quasiparticle bands near and around E_F, the density of

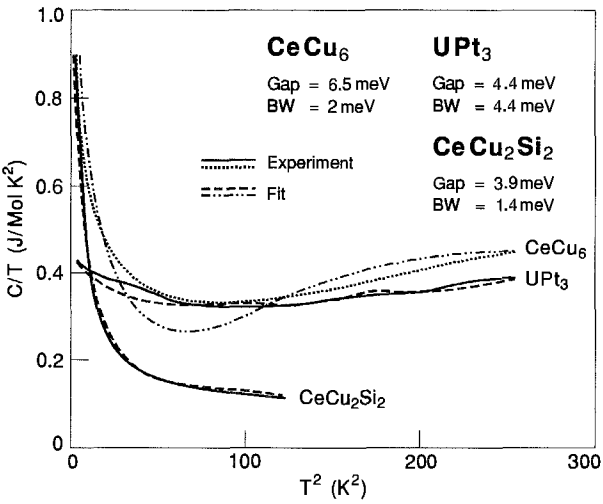

Fig. 154. The $\gamma(c/T)$ values of $CeCu_6$, UPt_3 and $CeCu_2Si_2$. Experimental values from Stewart (1984). (After Marabelli and Wachter 1987b,c.)

states $\rho_D(E)$ cannot be put in front of the integral of the total energy, as is done in the Sommerfeld theory. The equation to be used is eq. (16), which gives the specific heat as function of temperature. In fig. 154 we show a plot of C_v/T versus T^2 of the experimental data of Stewart (1984) for $CeCu_6$, UPt_3 and $CeCu_2Si_2$ and we realize, in agreement with these results and those of other authors, that γ is a function of temperature. Our model calculation again uses the two Gaussians with gap- and bandwidth BW as obtained from the fit of the resistivity data (section 5.3.1). We obtain a good fit with the experimental data. However, we can also make an optimal fit of the model calculation with the specific heat data by using the gap- and the bandwidth BW again as free parameters. This is shown in fig. 154 and indeed we find excellent agreement with the experimental data (Marabelli and Wachter 1987b,c, 1988, Marabelli et al. 1986b). The gap values and the bandwidth BW are very close to the values obtained by the resistivity fit and they are even closer to the experimental optical values, in any case the difference is not larger than 1 meV which we consider as the uncertainty in the fits and the optical derivation of the data.

Our analysis of the specific heat gives, for the first time, an explanation for the strong temperature dependence of the γ values of the heavy fermions. In addition, the specific heat exhibits bumps, which probably correspond to Schottky anomalies (as experimentally observed by Stewart et al. 1984 and Fujita et al. 1985) coming about because of thermal excitations of quasiparticles from the lower into the upper band.

5.3.3. *The magnetic susceptibility*

Most heavy fermions do not show magnetic order, and when they do, the magnctic moments are strongly quenched, compared to the free ion values. We already defined as "normal", heavy fermions which do not exhibit ferromagnetic order and only for these our model calculation can be valid. However, we have conducting heavy quasiparticles and

in our model these should to a great extent explain the observed magnetic susceptibility. The susceptibility of conduction electrons in normal metals has two contributions, the Landau diamagnetism and the Pauli paramagnetism. In our treatment we will completely neglect any diamagnetic contribution. This is justified by looking at the relation $\chi_{\text{Landau}}/\chi_{\text{Pauli}} = m/m^*$ (Ashcroft and Mermin 1981). In heavy fermions the mass ratio is typically in the order of tens or hundreds, so the Landau susceptibility is at least 1000 times smaller than the Pauli contribution.

In normal metals the Pauli susceptibility is constant with temperature, but in normal metals we are dealing with bandwidths in the order of eV and the density of states is practically constant near the Fermi level. In heavy fermions the density of states changes very rapidly with energy which produces drastic effects in the temperature dependence of the susceptibility. The formulae which we adopt for the derivation of the Pauli susceptibility are eqs. (17–19) where the integral in eq. (18) is the well known expression of the Pauli magnetization. When a peak in the density of states occurs at the Fermi level, this term shows a Curie–Weiss dependence with temperature and the susceptibility decreases more rapidly as the peak is enhanced and the bandwidth is reduced. We can also explain the susceptibility of heavy fermions in different, simpler terms. With $E_F = (\hbar^2/2m^*)(3\pi^2 N)^{2/3}$ and the carrier concentration N being about $10^{22}/\text{cm}^3$ and an effective mass in the order of $1000m$, we find E_F in the meV range, i.e., in the magnitude of the quasiparticle bandwidth. With $k_B T$ less than the bandwidth or less than the renormalized Fermi energy, the Pauli susceptibility becomes temperature independent. With $k_B T \gg \text{BW} \gg E_F$, the Pauli paramagnetism approaches the Curie–Weiss behavior (Busch and Schade 1973). In fact, it is the thermal excitations across the gap which produce, for some heavy fermions, a flat maximum in the otherwise temperature independent susceptibility for low temperatures. However, it is exactly such a maximum which is observed experimentally, e.g., for UPt_3 and PuTe, whereas for $CeCu_6$ such a maximum is barely visible, but only a flattening occurs at the lowest temperatures (Stewart 1984).

In fig. 155 we again show a comparison of the magnetic susceptibility obtained experimentally for $CeCu_6$ and UPt_3 (Stewart et al. 1984, Frings et al. 1983) with our model calculation. Again, we have chosen to make an optimal fit and use gap and bandwidth BW as free parameters, and as before they turn out to be within 1 meV of the values obtained by the resistivity- or the specific heat fit and the FIR optical results (Marabelli and Wachter 1987c). An acceptable agreement with the experiments is obtained by assuming the magnetic moment of the quasiparticles to be the same as for free electrons with $J = 1/2$, $g = 2$ and $\mu_0 = \mu_B$.

5.3.4. *The quasiparticle band structure under external parameters*

The external parameters we consider in this section are the effects of a strong magnetic field and high pressure. Concerning an external magnetic field up to 35 T as measured on UPt_3 by Franse et al. (1984), the authors observe a tendency to saturation above about 30 T at 4 K, and by extrapolation that saturation is achieved at about 50 T with a

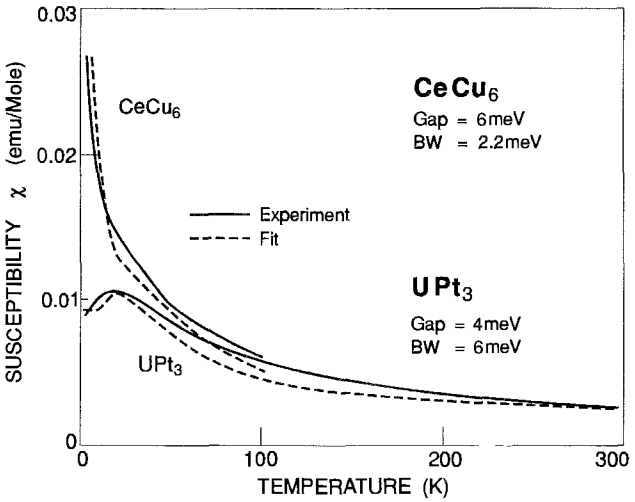

Fig. 155. Magnetic susceptibilities of $CeCu_6$ and UPt_3. Experimental values from Frings et al. (1983) and Stewart et al. (1984).

saturation moment of $1\mu_B$. The energy of a magnetic field of 50 T corresponds to 2.8 meV, i.e., it is comparable with the quasiparticle bandwidth. In the quasiparticle band structure, sketched in fig. 133 for UPt_3, we have shown in section 5.1.1 that the upper subband is practically half filled with about 1 quasiparticle per f.u. and that the total band can host 2 quasiparticles per f.u. This means that in the half filled subband each state (up to half filling) is occupied with two quasiparticles with opposite spin in the absence of a magnetic field. Fields with 50 T, on the other hand, having an energy of 2.8 meV, i.e., practically half the width of the quasiparticle band with 4 meV bandwidth, can spin polarize the whole upper subband, i.e., align all spins parallel to the field and thus necessarily fill the whole bandwidth of 4 meV. The saturation moment then would be $1\mu_B$/uranium, as experimentally observed.

On the other hand, it is also experimentally documented that the γ value of the specific heat already substantially decreases in a magnetic field of 10 T (Reinders et al. 1986 and Satoh et al. 1985). We interpret this result to mean that the magnetic field increases the quasiparticle bandwidth, thus reducing the effective mass. However, an increased quasiparticle bandwidth will, in a rigid band picture, also reduce the gap, and in the extreme case will even create a collapsed band structure of only one band. These things are beyond the power of our simple model (or at least we do not want to overstress our model). So, in spite of the fact that Marabelli and Wachter (1988) could give a reasonable fit of the experimental magnetization curve of Franse et al. (1984) with the quasiparticle model, we believe that the high magnetic field changes the band structure and, thus, the basis of the model.

Under application of external pressure Phillips et al. (1987) could measure the γ value of the specific heat. Pressure has been applied up to 9 kbar at temperatures down

to 0.3 K. The materials investigated were $CeAl_3$, $CeCu_6$, UPt_3 and UBe_{13}. In all cases the γ value substantially decreased under application of pressure. Our model offers a natural explanation. Under pressure we expect that bands broaden due to a better overlap of wavefunctions, the f–d hybridization will also increase and, probably, the gap will be decreased under pressure, as shown in the case of SmB_6 (Moshchalkov et al. 1985). In a measurement of the γ value at temperatures below about 1 K, only the subband around E_F is involved as excitations across a gap can be neglected at these temperatures. A reduction of the γ value upon pressure as found by Phillips et al. (1987) thus indicates that the density of states at E_F is reduced, the subbands have become broader, the effective mass has decreased, all effects which occur naturally in our model. Whether the gap has also decreased does not follow from these measurements.

On the other hand, resistivity measurements under pressure have been performed by Thompson (1987) on, e.g., $CeCu_6$ (see also section 2.3.1 of ch. 133, this volume). We recall that the temperature dependence of the resistivity at ambient pressure exhibits a maximum as shown in fig. 150. Under application of pressure up to 17.5 kbar a tendency is clearly recognizable, namely a change in the direction to decrease the resistivity below the maximum and to increase it above the maximum. It can be expected that at still higher temperatures the curve loses the maximum and will resemble those resistivity curves as e.g., for UPt_3. In fig. 151 we have shown in the same figure an example of a resistivity with a maximum in function of temperature ($CeCu_2Si_2$) and a smooth resistivity curve (UPt_3), having the same gap of about 4 meV, but different bandwidths of 1 and 4 meV. These materials can serve as good examples of what is going on. Pressure will increase the bandwidth of the subbands, and thus fill up the gap and eventually the gap will be reduced. With UBe_{13} the effect is even more pronounced (Thompson 1987, see also section 2.3.1 of ch. 133, this volume). In fact, the author could show that he could fit his results with two parameters using two reduced temperatures. This is equivalent to our two parameters gap and bandwidth BW.

We could of course make a fit with our model on the pressure dependence of the resistivity of $CeCu_6$ or UBe_{13}, and we certainly would get an excellent fit with bandwidth and gap changing in function of pressure. Unfortunately, at present, it is not possible to verify these findings experimentally. We would have to make reflectivity measurements in the FIR at high pressures and low temperatures. Maybe at a later stage we can do this, but then we will soon encounter the problem of the FIR peaks, indicating the gap, moving further into the infrared and, thus, out of the range of measurement as the gaps reduce with pressure. In any case, our model explains in a very satisfactory way the effects of external parameters, such as high magnetic field or pressure on the γ value of the specific heat or the electrical transport properties.

6. Empty f-levels and hybridization

By definition, empty f-levels are above the Fermi level, and, concerning physical properties, they usually are of no importance. Thus, in general, they have been neglected

in the interpretation. The picture changes when the f-levels come so close to the Fermi level that they can be thermally populated and they can even hybridize with the d conduction electrons.

6.1. *CeO_2 and CeF_4*

The first discussion of empty 4f levels concerned the case of CeO_2, where the simple application of the octet-rule leads one to suspect that Ce is tetravalent and CeO_2 would be an insulator. This is supported by the absolute transparency of CeO_2 single crystals (Marabelli and Wachter 1987a). Nevertheless, in the early eighties a big discussion broke out concerning a possible intermediate-valent state of CeO_2, stimulated by the general statement of Wohlleben (1981) that all Ce compounds and alloys would be intermediate valent and by the counter statement of Wachter (1982) that CeO_2 was a tetravalent insulator.

At that time there was also the climax of the discussion about soft and hard spectroscopies and of Ce compounds having their special problems. High-energy spectroscopies (section 3), like XPS or BIS, measure final f-state configurations and identify these configurations by their multiplets. But even in trivalent Ce alloys the final $4f^0$ state of XPS has no multiplet, thus core level spectroscopies are generally used. It is an experimental fact that core level spectroscopy on CeO_2 and CeF_4 (Fujimori 1983a,b, 1984, Wuilloud et al. 1984, Allen 1985, Kaindl et al. 1987) invariably yields a multiple peak structure due to $4f^0$-, $4f^1$- and $4f^2$ derived states from which it has been inferred that the initial state also has an intermediate-valent character. Wuilloud et al. (1984), however, showed in a BIS measurement, i.e., in a non-core level spectroscopy, that the empty $4f^1$ state was about 1.5 eV above E_F. On the other hand it has been shown that the same core level spectra arise, either when a 4f level is mixing with a conduction band in the initial state (intermediate-valent metal) (Gunnarsson and Schönhammer 1983), or when a 4f level is mixing with a filled valence band of an insulator (covalency) (Delley and Beck 1984, Schneider et al. 1986). In addition, Koelling et al. (1983) performed a band structure calculation of CeO_2 and explicitly calculated the degree of covalency for this material and they showed also the strong f mixing into the p valence band. Also, they come to the conclusion that CeO_2 has an empty 4f level above E_F and the material is not intermediate valent.

Marabelli and Wachter (1987a) performed optical spectroscopy on single crystals of CeO_2 and could derive the whole electronic structure with filled and empty electronic states. The empty 4f state could be identified by optical transitions from the filled p-type valence band with significant d and f character into the empty spin–orbit split $4f^1\,{}^2F_{5/2}$ and ${}^2F_{7/2}$ states. A sketch of the electronic density of states of CeO_2 is displayed in fig. 156. The same type of measurement has been performed by Marabelli et al. (1992a) on CeF_4 with a similar electronic structure to CeO_2.

The power of soft spectroscopies can also be demonstrated for CeO_2, where it is capable of clearly distinguishing between a $4f^1$ initial- or final state of an optical transition. When the $4f^1$ state is occupied and thus initial state, one will find, with a photon energy

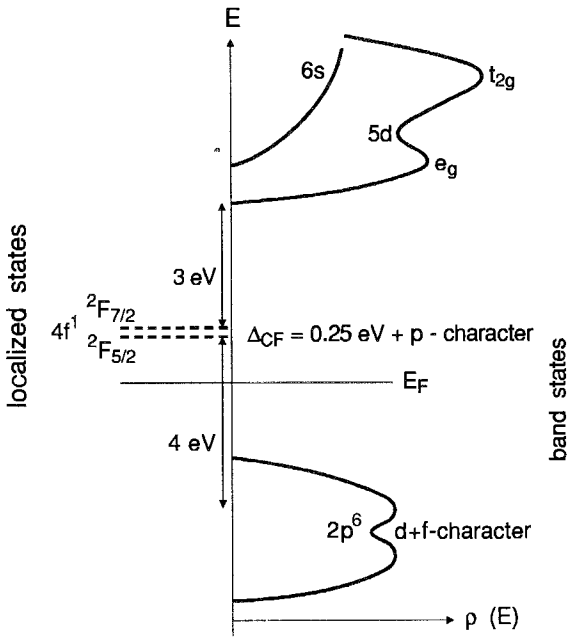

Fig. 156. Sketch of the electronic density of states of CeO_2. (After Marabelli and Wachter 1987a.)

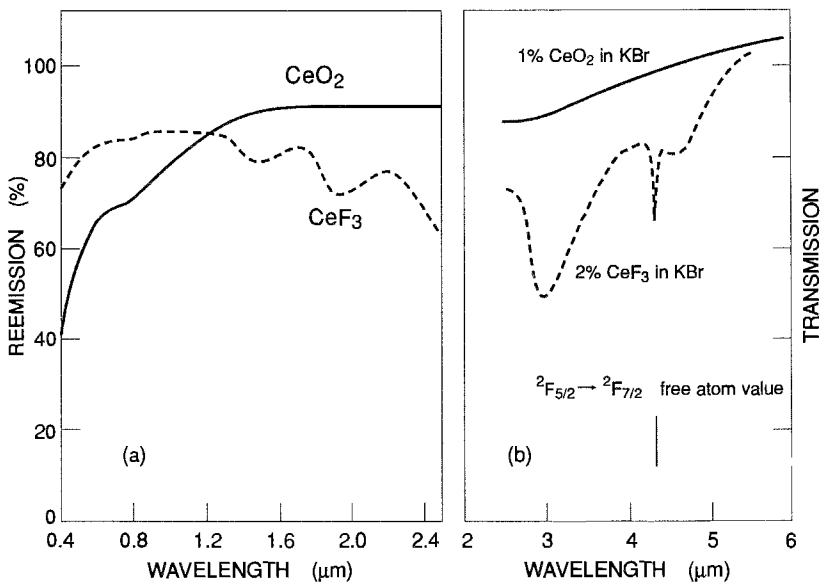

Fig. 157. (a) Re-emission of polycrystalline CeO_2 and CeF_3; (b) optical transmission of pressed KBr pills containing 1% CeO_2 and 2% CeF_3, respectively. (After Marabelli and Wachter 1987a.)

corresponding to the spin–orbit splitting of Ce ≈ 0.28 eV (4.3 μm), an intra 4f excitation. This is shown in fig. 157 (Wachter 1982), where one indeed finds this transition in trivalent CeF_3. In CeO_2 this transition is absent and thus the $4f^1$ state is not occupied and must be the final state in the 4 eV transition of fig. 156, where the spin–orbit splitting of the empty final state is observed. Regarding the possibility of a fractional occupation of the $4f^1$ state in CeO_2 in the spirit of intermediate valence, one can state from the detection limit in fig. 157 that a possible occupation must be less than 5% which is in sharp contrast with the statements from core level spectroscopy which claim an occupation of the $4f^1$ initial state of about 50%.

Thus, it becomes clear that high-energy spectroscopies cannot distinguish between intermediate valence and covalency, especially when the covalency is caused by an f or (less pronounced) d admixture to p derived valence bands, because of the selective sensitivity (matrix elements) of, e.g., XPS to these orbital components.

6.2. *Yb pnictides*

The Yb pnictides YbN, YbP and YbAs have been misinterpreted as heavy fermions on the basis of low-temperature specific heat measurements by Ott et al. (1985b). These materials show antiferromagnetic order between 0.4 K and 0.8 K and it is difficult to decouple the γ part of the specific heat from the magnetic contributions in these materials. The argumentation in favor of a heavy-fermion state by Ott et al. (1985b) was rather an anomalous broad hump in the specific heat of all Yb pnictides around 5 K (Ott et al. 1982) which could not be related to a Schottky anomaly of the crystal-field split ground state of an Yb^{3+} state. However, Monnier et al. (1990) could show that the above feature is a natural consequence of the interplay between crystal field and Kondo effect for an isolated magnetic impurity, and that coherent quasiparticle states need not be invoked. Greber et al. (1987) measured core level XPS on the Yb pnictides and found no evidence of valence mixing. More important, valence band XPS of YbP determined the $4f^{13}$ Yb^{3+} ground state to be about 6 eV below E_F (Degiorgi et al. 1990) and a BIS measurement detected an empty $4f^{14}$ Yb^{2+} state above E_F. No evidence of a 4f state at the Fermi level could be found.

In addition, Dönni et al. (1990a,b) measured elastic and inelastic neutron scattering on the Yb pnictides and found fcc type III antiferromagnetism in stoichiometric single crystals. The crystal-field scheme could also be established with a Γ_6–Γ_8–Γ_7 splitting. The Γ_6–Γ_8 (33 meV) transition in YbN was found to be split in only two lines, probably due to an interaction of crystal field with a phonon (34 meV) in the sense of Thalmeier and Fulde (1982). In any case, no contradiction to a pure $4f^{13}$ ground state typical for a Yb^{3+} configuration could be observed with neutron scattering or the magnetization (Degiorgi et al. 1990).

Degiorgi et al. (1990) also measured the optical properties of YbN over 4 decades of photon energy at 6 K and derived the electronic structure. The material is a self-compensated semimetal just like all other lanthanide pnictides, with a small indirect band overlap of the p-band at Γ and the d-band at X, resulting in an equal electron and hole

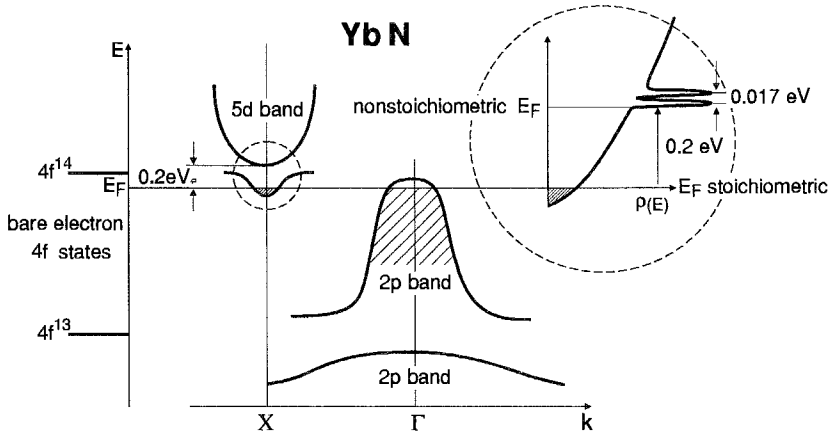

Fig. 158. Sketch of an energy level scheme for YbN. The bare electron 4f states are shown at left; the middle part of the figure presents the hybridized band structure, and at right appears a magnified sketch of the density of states near E_F. (After Degiorgi et al. 1990.)

concentration of $4.8\times10^{20}\,\mathrm{cm}^{-3}$ and an effective mass of $2.2m$. The carrier mass is far from a heavy electron mass typical for heavy fermions. In a last effort to check for intermediate valence or heavy-fermion behavior Mendik and Wachter (1993) measured the elastic constants of the Yb pnictides by Brillouin scattering and found that c_{12} was in no case negative.

Optical spectroscopy (Degiorgi et al. 1990) also permitted a more precise determination of the empty $4f^{14}$ state. It was found to be 0.2 eV above E_F in YbN, which is nearly accessible by thermal energies or doping. In YbP and YbAs the empty $4f^{14}$ state was about 0.3 eV above E_F, in spite of the fact that in these compounds the carrier concentration is nearly an order of magnitude larger (Degiorgi et al. 1993). Thus, YbN lends itself for intentional or unintentional doping in order to lift the Fermi energy by 0.2 eV to coincide with the $4f^{14}$ level and thus create intermediate valency and, because the materials are semimetals, heavy-fermion behavior. Since there was a 20 year development behind the effort to create stoichiometric ($\pm$ 0.5%) large single crystals of YbN (Degiorgi et al. 1990) it was no problem to find a nonstoichiometric single crystal (YbN_x) with about 10 times the carrier concentration of a stoichiometric crystal. In fact we could fill also the $4f^{14}$ state with electrons and obtained a band structure as in fig. 2b with a hybridization gap of 0.017 eV as determined by far infrared spectroscopy at low temperatures. Stoichiometric materials do not show this optical transition. It is thus the first time that one could create a heavy-fermion state by doping. The hybridized and the bare electron states of stoichiometric and nonstoichiometric YbN are shown in fig. 158. This is then the second time an empty 4f level has been determined.

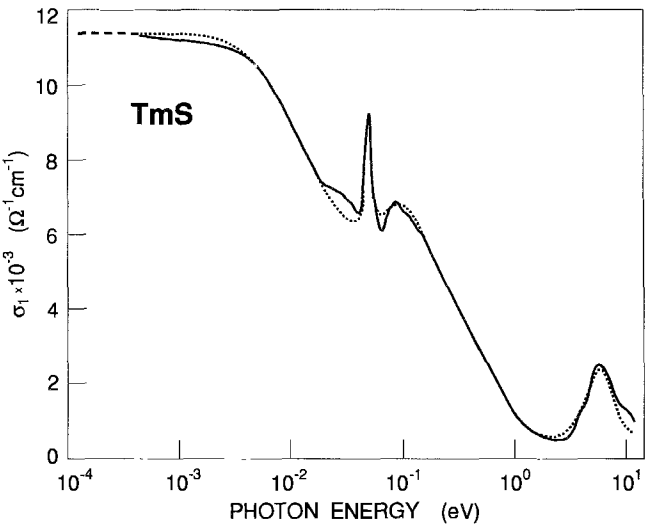

Fig. 159. Optical conductivity of stoichiometric TmS at 300 K. The dashed part is the extrapolation towards σ_{dc}. Dots indicate a fit with Lorentzian oscillators. (After Kamba et al. 1994.)

6.3. *TmS*

In section 4.3.1 we discussed already metallic TmS in connection with intermediate-valent TmSe and semiconducting TmTe. Trivalent TmS has the $4f^{12}$ ground state 6.5 eV below E_F and an empty $4f^{13}$ state could be detected by a BIS measurement about 1 eV above E_F. This BIS structure, displayed in fig. 9, showed spin–orbit splitting $^2F_{5/2}$–$^2F_{7/2}$ of 1.2 eV. However, we have to consider that a BIS measurement has only a resolution of 1 eV. So when we say that the empty $4f^{13}$ state is 1 eV above E_F it can be anywhere between zero and 1 eV above E_F. Examples have been given for YbP (fig. 59) where the BIS peak is also 1 eV above E_F but optical absorption has given instead the value 0.3 eV with no resolution problems (Degiorgi et al. 1990, 1993). Thus, for TmS we have to make a more definite determination of the position of the empty $4f^{13}$ level and we do this again by optical spectroscopy.

Kamba et al. (1994) measured the optical reflectivity of stoichiometric TmS single crystals between 2 meV and 12 eV and determined with a Kramers–Kronig relation the dielectric functions. The general behavior was that of a metal with a plasma edge in the visible yielding the golden color of the crystal, and interband transitions at higher photon energy. The unexpected feature of TmS was a clearly visible peak in the middle infrared part of the spectrum, where the reflectivity was already above 90%. The optical conductivity of TmS in this spectral region is displayed in fig. 159. Dotted is the fit with Lorentzian oscillators. The main line is at 51.5 meV and a second, broader line is at 85 meV.

The first guess is of course in direction phonons. However, in TmTe $\omega_{TO} = 13.9$ meV (table 5) and in LaS $\omega_{TO} = 32.5$ meV (Kress 1987). From both data we compute

under the assumption of constant force strength and different atomic masses the TO phonon frequency of TmS and obtain 23.1 meV and 32.0 meV, respectively. We also performed Raman scattering on TmS. The second-order spectrum showed two main peaks corresponding to acoustical (13 meV) and optical (37 meV) modes which resemble weighted phonon density of states. The maximum of the optical phonon density of states is at the L point, which would roughly correspond to the 37 meV. The dispersion of TO and LO modes is weak. Thus, we conclude that the observed infrared peaks at 51 meV and 80 meV are not related to phonon spectra.

The empty $4f^{13}$ level will be subject to crystal-field splitting. The level scheme will be the same as in YbN, where the $4f^{13}$ state is occupied, namely a Γ_6–Γ_8–Γ_7. The splitting of the Γ_6–Γ_8 in YbN (section 6.2) was 33 meV, conspicuously the same as the splitting of our two infrared lines of TmS. (The Γ_6–Γ_8 transition is optically allowed). Thus, we conclude that the two infrared transitions at 51 meV and 85 meV are due to optical transitions from E_F into the empty, crystal-field split $4f^{13}$ state, which is then only about 50 meV above E_F and can be thermally populated. At room temperature the thermal population is not very large so the optical spectrum is not much different between 6 K and 300 K, but we expect hybridization, intermediate valence and heavy-fermion behavior at elevated temperatures. This is then the third time an empty 4f level has been determined.

6.4. *$Ce_3Bi_4Pt_3$ and $U_3Sb_4Pt_3$*

So far we have found empty 4f levels in CeO_2 1.5 eV above E_F, in YbP and YbAs 0.3 eV above E_F, in YbN 0.2 eV above E_F and in TmS 0.05 eV or 51 meV above E_F. Who says an empty f-level cannot be just some meV above E_F? Here one has to distinguish two cases: either one has a partially full band filled up to E_F and an empty f-level little above E_F and we think CeNiSn (Takabatake et al. 1987) is an example. Or one has a filled band (p band) and an empty f-level little above and the Fermi level right in between and an empty (d band) further above. Hybridization (p–f mixing) is possible. In reality things may turn out to be more complex. Formally, $Ce_3Bi_4Pt_3$ could be a material where Ce is tetravalent, i.e., 3 Ce have each given 4 electrons to 4 Bi^{-3} to fill their p-shell and Pt is in the $5d^{10}$ state. The 5d and 6s bands of Ce would in principle be empty but covalency will push the p-band so high in energy that an indirect overlap with the d-band (e.g. Γ–X) can occur and a self compensated semimetal (with equal number of electrons and holes) will evolve, just as in all other lanthanide pnictides (see, e.g., fig. 158 for YbN). The empty $4f^1$ state will be situated a little above the Fermi level and hybridization will occur. A sketch of the unhybridized electronic structure is shown in fig. 160.

One can make the model even more realistic by considering that the Pt $5d^{10}$ bands also cut the Fermi level somewhat, but, in order not to overload the figure we have ignored this aspect. An important aspect is that the total number of electrons is even and the Luttinger theorem would tell us that the Fermi level lies in a hybridization gap. The material would behave like a semiconductor and the activation energy for the resistivity would be in the order of meV. Indeed this is shown for $Ce_3Bi_4Pt_3$ in fig. 161 (Hundley et al. 1991a,b) from which an activation energy of about 3 meV can be derived. In the model of fig. 160

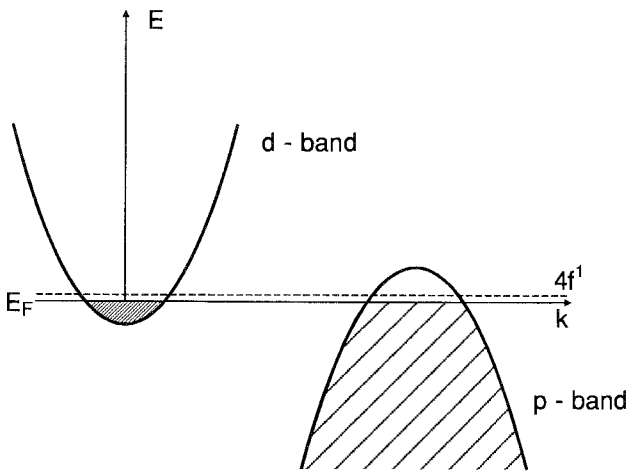

Fig. 160. Sketch of the unhybridized electronic structure of $Ce_3Bi_4Pt_3$ with the empty $4f^1$ state slightly above E_F.

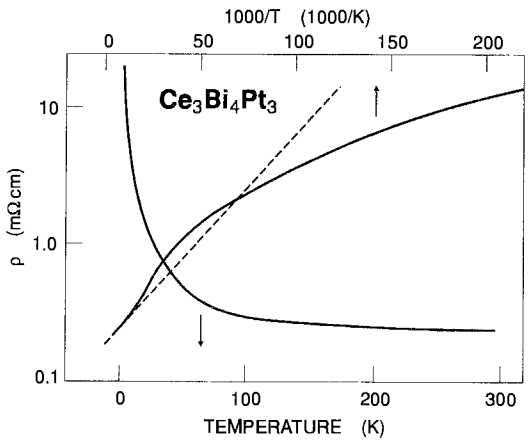

Fig. 161. Temperature dependence of the resistivity of $Ce_3Bi_4Pt_3$; the resistivity is also plotted vs. $1000/T$ (upper scale). The dashed line is a fit with an Arrhenius plot. (After Hundley et al. 1991a.)

this can indicate a hybridization gap but it could also be just a gap between a filled p^6 band of Bi and an empty $4f^1$ state in the sense of a semiconductor. Staying in the model of fig. 160, the Hall effect yields the same activation energy as the resistivity but the sign of the Hall effect can be positive or negative depending on the relative size of the mobility of holes and electrons and it can even change sign with temperature. In fact, the Hall effect is negative and indications for a change in sign are present at low temperatures. The thermopower is positive and since it depends on dE_F/dT it can have a different sign than the Hall effect. In accordance with the assumption that the Fermi level lies in a gap, is the low γ value of the specific heat, so the materials are definitely not heavy fermions, but again (as in YbN or TmS), at finite temperatures a variable degree of

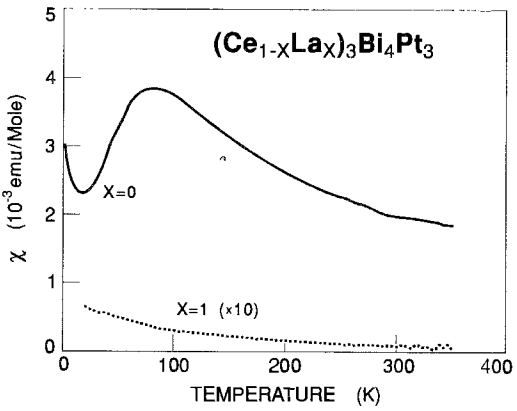

Fig. 162. $(Ce_{1-x}La_x)_3Bi_4Pt_3$: magnetic susceptibility for $x=0$ and $x=1$. (After Hundley et al. 1991b.)

intermediate valence is conceivable. Results of FIR optical reflectivity on $Ce_3Bi_4Pt_3$ by Bucher et al. (1994) indicate a larger energy gap in the order of tens of meV. Here we have to take into consideration that an optical transition has a peak where the joint density of states is maximal and, for a p-d band–$4f^1$ transition this is further down, below E_F. CeN, on the other hand, is the example where, besides the indirect overlap of p and d band with semimetallic behavior, the $4f^1$ state lies at the Fermi level and genuine intermediate valence is achieved. However, the odd number of electrons does not permit the Fermi level to lie in a hybridization gap and, as a consequence, semimetallic behavior prevails (Kamba and Wachter 1994).

Also very significant is the magnetic susceptibility shown in fig. 162 (Hundley et al. 1991a,b). Extrinsic effects at the lowest temperatures mask the fact that the susceptibility for $T \to 0$ goes towards zero, because there is no occupied 4f level and one has only filled bands. Increasing temperature fills the $4f^1$ state more and more, and a normal paramagnetic Curie–Weiss law prevails above about 50 K. In fact, the susceptibility resembles exactly the one of YbB_{12}, shown in fig. 26, but for very different reasons. In YbB_{12}, which is an intermediate-valent material, the occupied $4f^{13}$ state has to be considered also, and valence mixing yields the $4f^{13}5d$–$4f^{14}$ state at E_F. The theory for this type of valence mixing has been proposed in section 4.1.3.

$U_3Sb_4Pt_3$ (Fisk 1992) basically exhibits the same physics as $Ce_3Bi_4Pt_3$, i.e., activated conductivity with a gap of several meV and a susceptibility approaching very small values for $T \to 0$ and for higher temperatures a paramagnetic Curie–Weiss law. Again, we assume an empty 5f level somewhat above E_F. However, tetravalent uranium has a $5f^2$ configuration which must be in a singlet state, thus the empty f state is a $5f^3$ level, which after thermal population would yield the paramagnetic moment.

If our proposal for the electronic structure of these materials is right, the terminology "Kondo insulator" (Fisk 1992) is not correct. The normal Kondo effect in a metal is a scattering of conduction electrons by the occupied 4f states and it manifests itself in

the mobility term of the resistivity. For the above materials, however, we have mainly a thermal excitation into the empty f states and this is a carrier concentration effect.

7. Conclusion

We have shown in this chapter that intermediate valence and heavy fermions can be treated on the same basis. By starting with a periodic solution of the Anderson Hamiltonian (eq. 1) one invariably ends up with a gap. However, starting from a Kondo lattice one also obtains a gap in the density of states of a so-called Kondo resonance. This Kondo resonance, however, has small spectral weight and disappears near or even below the Kondo temperature T_K. However, we have shown experimentally that both ingredients of the Kondo resonance model have been disproved, inasmuch as the spectral weight of the low-energy structures is enormous, with dielectric constants of up to 3×10^4, and that these structures exist at up to 10 times the Kondo temperature. It follows that one has true density of states effects, as also calculated by Brandow (1981, 1986, 1988) with a hybridization gap. As shown in fig. 2b, d, one has at least two narrow f-like subbands with an admixture of d character, which are separated by a hybridization gap. The distinction between semiconducting or insulating or heavy-fermion character comes about only by the position of the Fermi level, being either in the subbands or in the gap. However, both types of materials are intermediate valent, inasmuch as their f occupation is non-integer.

It is so that the hybridization gap, or more generally, at least a gap in the meV range, runs through all sections of this chapter like the thread of Ariadne. The first time such a gap has been measured was with tunneling on SmB_6, by Batlogg et al. (1981), later followed by transport measurements and optical measurements at low temperatures and in the FIR. There was never much opposition to the idea that there was a gap, because, after all, physicists are trained to think of a gap when the resistivity is increasing with decreasing temperature. The unusual feature was the small size of the gap in the meV range. For the heavy fermions with the Fermi level in a subband and a decreasing resistivity with decreasing temperature it is only fair to think of a metal, and some of them even become superconducting. It was then a surprise and it contradicted good physical sense, when for the first time Marabelli et al. (1986a) measured also an optical transition in the meV range on UPt_3, and, as a consequence, postulated that the transition was across a gap between a partially filled narrow band and empty states above E_F. The spectroscopic analysis yielded a gap, narrow bands, high effective masses and intermediate valency. These experimental facts are not known to everyone and they may not even be accepted by some. The experiments of the last seven years have been done on five materials only, and they have been carried out by only one or two groups of researchers in the whole world, because experimental difficulties are enormous. However, when one talks to a theorist and points out that a heavy fermion should have a hybridization gap he usually says: of course. But the consequences regarding the thermodynamic properties are rarely drawn.

The model which we propose for the heavy fermions is simple-minded and rough. The surprise is the excellent fit which can be obtained with the experimental results

regarding the temperature dependence of the resistivity, the specific heat, the magnetic susceptibility and the magnetization. The calculation is a semiclassical one, based on experimental results. Today we make these calculations as exercises in the solid-state physics course at ETH Zürich. The model makes the physics understandable but its basis is not as fundamental as theorists would like it to be. In fact, we do not insist that this model should be generally applicable. There are many variations of this model which result from a more fundamental theoretical calculation, as e.g. by Czycholl and Schweitzer (1992), such as asymmetric subbands which shift with temperature. But the basic idea remains that between two narrow f-like subbands there is a gap which we call a hybridization gap.

It was not the intention of this chapter to review all intermediate-valent materials or all heavy fermions. Rather, we wanted to show that one can treat all these materials on the same basis. We hope we can stimulate further research on this fascinating topic and we hope that in the future theorists take a gap into account, even in heavy fermions.

Acknowledgements

The author would like to thank a number of his graduate students or ex-graduate students for contributing so much to this chapter: Dr. W. Bacsa, Dr. B. Batlogg, Dr. H. Boppart, Dr. B. Bucher, Dr. G. Compagnini, M. Celio, Dr. L. Degiorgi, Dr. M.W. Elmiger, Dr. M. Fischer, Dr. I. Frankowski, Dr. B. Fritzler, L. Frey, Prof. G. Güntherodt, Dr. J. Henz, Dr. O.E. Hüsser, Dr. H. von Känel, Prof. F. Marabelli, Dr. M. Mendik, Dr. I. Mörke, Dr. M. Moser, Dr. J. Neuenschwander, K. Neufeld, Dr. M. Ospelt, Dr. W. Reim, Dr. A. Schlegel, B. Schneider, Prof. J. Schoenes, H. Spychiger, P. Steiner, Dr. G. Travaglini, Dr. A. Treindl, and Dr. Ch. Zürcher.

The single crystals described in this chapter have been grown by Prof. J.M.M. Franse, Dr. F. Hulliger, Prof. E. Kaldis, Dr. G.P. Meisner, Dr. O. Vogt and Dr. E. Walker, to whom the author is very much obliged. For technical assistance the author would like to thank K. Mattenberger, J. Müller and H.P. Staub.

All figures have been redrawn from the originals with a specially developed computer program by H.P. Staub. Without his help this chapter could never have been finished. The editing of this chapter and invaluable help with secretarial work has been performed by Mrs. Doris Gini-Schwarz, who also kept the mood of the whole group at a constant high level.

Last but not least I want to thank my wife Sonja for her everlasting good temper, for keeping my moral up and for accepting that, for more than a year, I spent all the weekends writing this chapter.

References

Aeppli, G., E. Bucher, C. Broholm, J.K. Kjems, J. Baumann and J. Hufnagl, 1988, Phys. Rev. Lett. **60**, 615.

Alascio, B., A.A. Aligia, J. Mazzaferro and C.A. Balseiro, 1982, in: Valence Instabilities, eds P. Wachter and H. Boppart (North-Holland, Amsterdam) p. 493.

Alekseev, P.A., E.S. Konovalenko, V.N. Lazukov, S.I. Lyukshina, Yu.B. Paderno, I.O.P. Sadikov and E.V. Udovenko, 1988, Sov. Phys. Solid State **30**, 1167.

Alekseev, P.A., A.S. Ivanov, B. Dorner, H. Schober, K.A. Kikoin, A.S. Mishchenko, V.N. Lazukov, E.S. Konovalenko, Yu.B. Paderno, A.Yu. Rumyantsev and I.P. Sadikov, 1989, Europhys. Lett. **10**, 457.

Alekseev, P.A., A.S. Ivanov, V.N. Lazukov, I.P. Sadikov and A. Severing, 1992, Physica B **180–181**, 281.

Alekseev, P.A., J.M. Mignot, J. Rossat-Mignod, V.N. Lazukov and I.P. Sadikov, 1993, Physica B **186–188**, 384.

Allen, J.W., 1977, in: Valence Instabilities and Related Narrow Band Phenomena, ed. R.D. Parks (Plenum Press, New York) p. 534.

Allen, J.W., 1985, in: Valence Fluctuations, eds E. Müller-Hartmann, B. Roden and D. Wohlleben, J. Magn. & Magn. Mater. **47–48**, 168.

Allen, J.W., R.M. Martin, B. Batlogg and P. Wachter, 1978, J. Appl. Phys. **49**, 2078.

Allen, J.W., B. Batlogg and P. Wachter, 1979, Phys. Rev. B **20**, 4807.

Anderson, O.L., 1966, J. Phys. & Chem. Solids **27**, 547.

Anderson, O.L., and R.C. Liebermann, 1970, J. Phys. Earth **3**, 61.

Anderson, P.W., 1961, Phys. Rev. **124**, 41.

Anderson, P.W., 1981, in: Valence Fluctuations in Solids, eds L.M. Falicov, W. Hanke and M.B. Maple (North-Holland, Amsterdam) p. 451.

Andres, K., J.E. Graebner and H.R. Ott, 1975, Phys. Rev. Lett. **27**, 1779.

Andres, K., W.M. Walsh Jr, S. Darack, L.W. Rupp Jr and L.D. Longinotti, 1978, Solid State Commun. **27**, 825.

Ashcroft, N.W., and N.D. Mermin, eds, 1981, Solid State Physics (Holt and Saunders, Tokyo) p. 666.

Awasthi, A.M., W.P. Beyermann, J.P. Carini and G. Grüner, 1989, Phys. Rev. B **39**, 2377.

Awasthi, A.M., L. Degiorgi, G. Grüner, Y. Dalichaouch and M.B. Maple, 1993, Phys. Rev. B **48**, 10692.

Axe, J.D., 1969, J. Phys. & Chem. Solids **30**, 1403.

Bader, S.D., N.E. Phillips and D.B. McWhan, 1973, Phys. Rev. B **7**, 4686.

Baer, Y., M. Grioni and P. Wachter, 1994, to be published.

Barth, M., and G. Güntherodt, 1982, in: Valence Instabilities, eds P. Wachter and H. Boppart (North-Holland, Amsterdam) p. 99.

Batlogg, B., 1981a, Phys. Rev. B **23**, 1827.

Batlogg, B., 1981b, in: Valence Fluctuations in Solids, eds L.M. Falicov, W. Hanke and M.B. Maple (North-Holland, Amsterdam) p. 209.

Batlogg, B., 1981c, Phys. Rev. B **23**, 650.

Batlogg, B., and P. Wachter, 1977, in: Valence Instabilities and Related Narrow Band Phenomena, ed. R.D. Parks (Plenum Press, New York) p. 537.

Batlogg, B., and P. Wachter, 1980, J. Phys. (Paris) **41**, C5-59.

Batlogg, B., J. Schoenes and P. Wachter, 1974, Phys. Lett. A **49**, 13.

Batlogg, B., A. Schlegel, E. Kaldis and P. Wachter, 1975, Phys. Rev. B **12**, 3940.

Batlogg, B., E. Kaldis, A. Schlegel, G. von Schulthess and P. Wachter, 1976a, Solid State Commun. **19**, 673.

Batlogg, B., E. Kaldis, A. Schlegel and P. Wachter, 1976b, Phys. Rev. B **14**, 5503.

Batlogg, B., E. Kaldis and H.R. Ott, 1977, Phys. Lett. A **62**, 270.

Batlogg, B., E. Kaldis and P. Wachter, 1979a, J. Phys. (Paris) **40**, C5-370.

Batlogg, B., H.R. Ott, E. Kaldis, W. Thöni and P. Wachter, 1979b, Phys. Rev. B **19**, 247.

Batlogg, B., H.R. Ott and P. Wachter, 1979c, Phys. Rev. Lett. **42**, 278.

Batlogg, B., P.H. Schmidt and J.M. Rowell, 1981, in: Valence Fluctuations in Solids, eds L.M. Falicov, W. Hanke and M.B. Maple (North-Holland, Amsterdam) p. 267.

Batlogg, B., H. Boppart, E. Kaldis, D.B. McWhan and P. Wachter, 1982, in: Valence Instabilities, eds P. Wachter and H. Boppart (North-Holland, Amsterdam) p. 523.

Beaurepaire, E., J.P. Kappler and G. Krill, 1986, Solid State Commun. **57**, 145.

Beckenbaugh, W., J. Evers, G. Güntherodt, E. Kaldis and P. Wachter, 1975, J. Phys. & Chem. Solids **36**, 239.

Becker, K.W., and P. Fulde, 1987, Z. Phys. B **67**, 35.

Benbachir, K., J. Mazuer and J.P. Senateur, 1985, Solid State Commun. **54**, 965.

Bennemann, K.H., and M. Avignon, 1979, Solid State Commun. **31**, 645.

Berger, A., E. Bucher, P. Haen, F. Holtzberg, F. Lapierre, T. Penney and R. Tournier, 1977, in: Valence Instabilities and Related Narrow Band Phenomena, ed. R.D. Parks (Plenum Press, New York) p. 491.

Berkooz, O., M. Malamud and S. Shtrikman, 1968, Solid State Commun. **6**, 185.

Berrada, A., J.P. Mercurio, B. Chevalier, J. Etourneau, P. Hagenmüller, M. Lalanne, J.C. Gianduzzo and R. Georges, 1976, Mater. Res. Bull. **11**, 1519.

Beyermann, W.P., A.M. Awasthi, J.P. Carini and G. Grüner, 1988, J. Magn. & Magn. Mater. **76–77**, 207.

Bilz, H., G. Güntherodt, W. Kleppmann and W. Kress, 1979, Phys. Rev. Lett. **43**, 1998.

Birgeneau, R.J., and S.M. Shapiro, 1977, in: Valence Instabilities and Related Narrow Band Phenomena, ed. R.D. Parks (Plenum Press, New York) p. 49.

Bjerrum-Møller, H., S.M. Shapiro and R.J. Birgeneau, 1977, Phys. Rev. Lett. **39**, 1021.

Bonville, P., P. Imbert, G. Jehanno and F. Gonzalez-Jimenez, 1978, J. Phys. & Chem. Solids **39**, 1273.

Boppart, H., 1983, PhD Thesis No. 7327 (ETH, Zürich).

Boppart, H., and P. Wachter, 1981a, in: Physics of Solids under High Pressure, eds J.S. Schilling and R.N. Shelton (North-Holland, Amsterdam) p. 301.

Boppart, H., and P. Wachter, 1981b, J. Appl. Phys. **52**, 2161.

Boppart, H., and P. Wachter, 1981c, Lecture Notes in Physics, Vol. 152 (Springer Verlag, Berlin) p. 35.

Boppart, H., and P. Wachter, 1984a, Mater. Res. Soc. Symp. Proc. **22**, 341.

Boppart, H., and P. Wachter, 1984b, Mater. Res. Soc. Symp. Proc. **22**, 273.

Boppart, H., and P. Wachter, 1984c, in: Moment Formation in Solids, ed. W.J.L. Buyers (Plenum Press, New York) p. 229.

Boppart, H., and P. Wachter, 1984d, Phys. Rev. Lett. **53**, 1759.

Boppart, H., A. Treindl, P. Wachter and S. Roth, 1980a, Solid State Commun. **35**, 489.

Boppart, H., P. Wachter, B. Batlogg and R.G. Maines, 1980b, Solid State Commun. **38**, 75.

Boppart, H., A. Treindl and P. Wachter, 1981, in: Valence Fluctuations in Solids, eds L.M. Falicov, W. Hanke and M.B. Maple (North-Holland, Amsterdam) p. 103.

Boppart, H., W. Rehwald, E. Kaldis and P. Wachter, 1982, in: Valence Instabilities, eds P. Wachter and H. Boppart (North-Holland, Amsterdam) p. 81.

Brandow, B.H., 1979, Int. J. Quantum Chem. **13**, 423.

Brandow, B.H., 1981, Solid State Commun. **39**, 1233.

Brandow, B.H., 1986, Phys. Rev. B **33**, 215.

Brandow, B.H., 1988, Phys. Rev. B **37**, 250.

Bucher, B., P. Steiner and P. Wachter, 1991, Phys. Rev. Lett. **67**, 2717.

Bucher, B., Z. Schlesinger, P.C. Canfield and Z. Fisk, 1994, Physica B **199–200**, 489.

Bucher, E., and R.G. Maines, 1972, Solid State Commun. **11**, 1441.

Bucher, E., V. Narayanamurti and A. Jayaraman, 1971, J. Appl. Phys. **42**, 1741.

Bucher, E., K. Andres, F.J. di Salvo, J.P. Maita, A.C. Gossard, A.S. Cooper and G.W. Hull, 1975, Phys. Rev. B **11**, 500.

Bührer, W., A. Furrer and P. Wachter, 1982, in: Valence Instabilities, eds P. Wachter and H. Boppart (North-Holland, Amsterdam) p. 103.

Burlet, P., J.M. Fournier, E. Pleska, S. Quezel, J. Rossat-Mignod, J.C. Spirlet, J. Rebizant and O. Vogt, 1988, J. Phys. (Paris) **49**, C8-469.

Busch, G., and H. Schade, 1973, Vorlesungen über Festkörperphysik (Birkhäuser Verlag, Basel) p. 456.

Buyers, W.J.L., and T. Holden, 1986, private communication.

Campagna, M., G.K. Wertheim and E. Bucher, 1975, in: Magnetism and Magnetic Materials, eds C.D. Graham Jr, J.J. Rhyne and G.H. Lander, AIP Conf. Proc. **24**, 22.

Campagna, M., G.K. Wertheim and E. Bucher, 1976, Structure and Bonding, Vol. 30 (Springer, Berlin) p. 99.

Campagna, M., G.K. Wertheim and Y. Baer, 1979, in: Photoemission in Solids II, Case Studies, eds L. Ley and M. Cardona, Vol. 27 of Topics in Applied Physics (Springer, Berlin) p. 217.

Cantrell, D.S., and K.W.H. Stevens, 1984, J. Phys. C **17**, 4575.

Capellmann, H., 1988, Solid State Commun. **65**, 797.

Celio, M., R. Monnier and P. Wachter, 1981, J. Phys. (Paris) Colloq. **42**, C6-11.

Chevalier, B., 1988, private communication.

Cho, J., 1967, Phys. Rev. **157**, 632.

Coey, J.M.D., and O. Massenet, 1977, in: Valence Instabilities and Related Narrow Band Phenomena, ed. R.D. Parks (Plenum Press, New York) p. 211.

Coey, J.M.D., S.K. Ghatak and F. Holtzberg, 1975, AIP Conf Proc. **24**, 38.

Cohen, R.L., M. Eibschütz and K.W. West, 1970, Phys. Rev. Lett. **24**, 383.

Coleman, P., 1992, discussion remark, Int. Conf. on Strongly Correlated Electron Systems, Sendai, Japan.

Cooley, J.C., M.C. Aronson, Z. Fisk and P.C. Canfield, 1994, Physica B **199–200**, 486.

Cooper, J.R., C. Rizzuto and G.L. Olcese, 1971, J. Phys. (Paris) Colloq. **32**, C1-1136.

Coqblin, B., and A. Blandin, 1968, Adv. Phys. **17**, 281.

Coqblin, B., A.K. Bhattacharjee, J.R. Iglesias-Sicardi and R. Jullien, 1977, in: Valence Instabilities and Related Narrow Band Phenomena, ed. R.D. Parks (Plenum Press, New York) p. 365.

Cowley, R.A., 1976, Phys. Rev. B **13**, 4877.

Czycholl, G., 1982, Phys. Rev. B **25**, 3413.

Czycholl, G., and H. Schweitzer, 1992, Phys. Scripta T **45**, 125.

Dabos-Seignon, S., U. Benedict, S. Heathmann, J.C. Spirlet and M. Pages, 1990, J. Less-Common Met. **160**, 35.

Dallacasa, V., 1981, J. Phys. F **11**, 177.

Davis, H.L., 1971, in: Proc IX Rare Earth Conf., Blacksburgh, VA, p. 3.

de Visser, A., J.J.M. Franse and A.A. Menovsky, 1984, J. Magn. & Magn. Mater. **43**, 43.

de Visser, A., A.A. Menovsky and J.J.M. Franse, 1987a, J. Magn. & Magn. Mater. 63 & **64**, 365.

de Visser, A., A.A. Menovsky and J.J.M. Franse, 1987b, Physica B **147**, 81.

de Visser, A., J. Flouquet, J.J.M. Franse, P. Haen, K. Hasselbach, A. Lacerda and L. Taillefer, 1991, Physica B **171**, 190.

Degiorgi, L., W. Bacsa and P. Wachter, 1990, Phys. Rev. B **42**, 530.

Degiorgi, L., S. Teraoka, G. Compagnini and P. Wachter, 1993, Phys Rev. B **47**, 10.

Delley, B., and H. Beck, 1984, J. Phys. C **17**, 4971.

Dönni, A., P. Fischer, A. Furrer, W. Bacsa and P. Wachter, 1990a, Z. Phys. B **80**, 269.

Dönni, A., A. Furrer, P. Fischer, F. Hulliger, P. Wachter and H.R. Ott, 1990b, J. Magn. & Magn. Mater. **90–91**, 143.

Eastman, D.E., and M. Kutznietz, 1971, J. Appl. Phys. **42**, 1396.

Elmiger, M.W., and P. Wachter, 1987, J. Magn. & Magn. Mater. **63–64**, 612.

Elmiger, M.W., J. Henz, H. v. Känel, M. Ospelt and P. Wachter, 1989, Surf. Interf. Anal. **14**, 18.

Elschner, B., and V. Weissenberger, 1987, private communication (Technische Hochschule Darmstadt, Germany).

Entel, P., and M. Sietz, 1981, Solid State Commun. **39**, 249.

Entel, P., N. Grewe, M. Sietz and K. Kowalski, 1979, Phys. Rev. Lett. **43**, 2022.

Faberovich, O.V., S.I. Kurganskii, K.K. Sidorin, M.G. Karin, V.N. Bobrikov, G.P. Nizhnikova, A.I. Shelikh, M.M. Korsukova and V.N. Gurin, 1982, Sov. Phys. Solid State **25**, 404.

Falicov, L.M., and J.C. Kimball, 1969, Phys. Rev. Lett. **22**, 997.

Ferreira, I.B., A.M. Awasthi, L. Degiorgi, G. Grüner, Y. Dalichaouch and M.B. Maple, 1992, Solid State Commun. **83**, 27.

Fischer, M., 1973, Diploma Thesis (ETH, Zürich) unpublished.

Fischer, P., W. Hälg, P. Schobinger-Papamentellos, H. Boppart and P. Wachter, 1982, in: Valence Instabilities, eds P. Wachter and H. Boppart (North-Holland, Amsterdam) p. 551.

Fisk, Z., 1992, Comm. Condens. Matter Phys. **16**, 155.

Frankowski, I., and P. Wachter, 1982a, Solid State Commun. **41**, 577.

Frankowski, I., and P. Wachter, 1982b, in: Valence Instabilities, eds P. Wachter and H. Boppart (North-Holland, Amsterdam) p. 309.

Frankowski, I., and P. Wachter, 1982c, J. Appl. Phys. **53**, 7887.

Franse, J.J.M., P.H. Frings, A. de Visser, A.A. Menovsky, T.T.M. Palstra, P.H. Kes and J.A. Mydosh, 1984, Physica B **126**, 116.

Freeman, A.J., J.O. Dimmock and R.E. Watson, 1966, in: Quantum Theory of Atoms, Molecules and Solid State, ed. O.P. Löwdin (Academic Press, New York).

Frey, L., 1981, Diploma Thesis (ETH, Zürich) unpublished.

Frings, P.H., J.J.M. Franse, F.R. de Boer and A. Menovsky, 1983, J. Magn. & Magn. Mater. **31–34**, 240.

Fujimori, A., 1983a, Phys. Rev. B **27**, 3992.

Fujimori, A., 1983b, Phys. Rev. B **28**, 2281.

Fujimori, A., 1984, Phys. Rev. Lett. **53**, 2581.

Fujita, T., K. Satoh, Y. Onuki and T. Komatsubara, 1985, J. Magn. & Magn. Mater. **47–48**, 66.

Furrer, A., W. Bührer and P. Wachter, 1982, in: Valence Instabilities, eds P. Wachter and H. Boppart (North-Holland, Amsterdam) p. 319.

Gerth, G., P. Kienle and K. Luchner, 1968, Phys. Lett. A **27**, 557.

Ghatak, S.K., and K.H. Bennemann, 1979, J. Phys. F **8**, 571.

Goldman, A.I., G. Shirane, G. Aeppli, E. Bucher and J. Hufnagl, 1987, J. Magn. & Magn. Mater. **63–64**, 380.

Golubkov, A.V., E.V. Goncharova, V.P. Zhuze and I.G. Manoilova, 1966, Sov. Solid State **7**, 1963.

Greber, T., L. Degiorgi, R. Monnier, L. Schlapbach, F. Hulliger and E. Kaldis, 1987, J. Phys (Paris) **48**, C9-943.

Greenwood, N.N., 1968, Ionic Crystals, Lattice Defects and Nonstoichiometry (Butterworths, London).

Grewe, N., 1984, Solid State Commun. **50**, 19.

Gschneidner Jr, K.A., J. Tang, S.K. Dhar and A. Goldman, 1990, Physica B **163**, 507.

Gunnarsson, O., and K. Schönhammer, 1983, Phys. Rev. B **28**, 4315.

Güntherodt, G., R. Merlin, A. Frey and M. Cardona, 1978, Solid State Commun. **27**, 551.

Güntherodt, G., A. Jayaraman, E. Anastassakis, E. Bucher and H. Bach, 1981, Phys. Rev. Lett. **46**, 855.

Güntherodt, G., W.A. Thompson, F. Holtzberg and Z. Fisk, 1982, in: Valence Instabilities, eds P. Wachter and H. Boppart (North-Holland, Amsterdam) p. 313.

Güntherodt, G., J.L. Freeouf and F. Holtzberg, 1983, Solid State Commun. **47**, 677.

Haen, P., F. Lapierre, J.M. Mignot, R. Tournier and F. Holtzberg, 1979, Phys. Rev. Lett. **43**, 304.

Hailing, T., G.A. Saunders and H. Bach, 1984, Phys. Rev. B **29**, 1848.

Hall, R., and M.J. Mortimer, 1990, AERE Report R 13490, unpublished.

Halperin, B.I., and T.M. Rice, 1968, Rev. Mod. Phys. **40**, 755.

Harima, H., A. Yanase and T. Kasuya, 1985, J. Magn. & Magn. Mater. **47–48**, 567.

Hasegawa, A., and A. Yanase, 1977, J. Phys. F **7**, 1245.

Hauger, R., E. Kaldis, G. von Schulthess, P. Wachter and Ch. Zürcher, 1976, J. Magn. & Magn. Mater. **3**, 103.

Hillebrands, B., and G. Güntherodt, 1983, Solid State Commun. **49**, 681.

Hirst, L., 1971, Phys. kondens. Mat. **11**, 255.

Hirst, L., 1974, J. Phys. & Chem. Solids **35**, 1285.

Holland-Moritz, E., 1983, J. Magn. & Magn. Mater. **38**, 253.

Holtzberg, F., 1974, AIP Conf. Proc. **18**, 478.

Holtzberg, F., and J.B. Torrance, 1971, in: Magnetism and Magnetic Materials, AIP Conf. Proc. **5**, 860.

Holtzberg, F., and J. Wittig, 1981, Solid State Commun. **40**, 315.

Holtzberg, H., T. Penney and R. Tournier, 1979, J. Phys (Paris) **40**, C5-314.

Hundley, M.F., P.C. Canfield, J.D. Thompson, Z. Fisk and J.M. Lawrence, 1991a, Phys. Rev. B **42**, 6842.

Hundley, M.F., P.C. Canfield, J.D. Thompson, Z. Fisk and J.M. Lawrence, 1991b, Physica B **171**, 254.

Ichinose, S., and I. Tamura, 1983, J. Magn. & Magn. Mater. **31–34**, 459.

Iglesias, J.R., and P.M. Mors, 1985, Solid State Commun. **56**, 557.

Ishii, M., M. Aano, S. Muranaka and S. Kawai, 1976, Solid State Commun. **20**, 437.

Jackson, C.M., G. Grüner, Z. Fisk and S. von Molnar, 1984, Phys. Rev. B **29**, 4786.

Jansen, H.J.F., A.J. Freeman and R. Monnier, 1985, Phys. Rev. B **31**, 4092.

Jayaraman, A., 1979, in: Handbook on the Physics and Chemistry of Rare Earths, Vol. 2, eds K.A. Gschneidner Jr and L. Eyring (North-Holland, Amsterdam) p. 575.

Jayaraman, A., and R.G. Maines, 1979, Phys. Rev. B **19**, 4154.

Jayaraman, A., V. Narayanamurti, E. Bucher and R.G. Maines, 1970a, Phys. Rev. Lett. **25**, 368.

Jayaraman, A., V. Narayanamurti, E. Bucher and R.G. Maines, 1970b, Phys. Rev. Lett. **25**, 1430.

Jayaraman, A., P.D. Dernier and L.D. Longinotti, 1975, Phys. Rev. B **11**, 2783.

Jullien, R., P. Pfeuty and B. Coqblin, 1981, in: Valence Fluctuations in Solids, eds L.M. Falicov, W. Hanke and M.B. Maple (North-Holland, Amsterdam) p. 169.

Kaindl, G., C. Laubschat, B. Reihl, R.A. Pollak, N. Martenson, F. Holtzberg and D.E. Eastman, 1982, in: Valence Instabilities, eds P. Wachter and H. Boppart (North-Holland, Amsterdam) p. 281.

Kaindl, G., W.D. Brewer, G. Kalkowski and F. Holtzberg, 1983, Phys. Rev. Lett. **51**, 2056.

Kaindl, G., G. Kalkowski, W.D. Brewer, B. Perscheid and F. Holtzberg, 1984, J. Appl. Phys. **55**, 1910.

Kaindl, G., K. Wertheim, G. Schmiester and E.V. Sampathkumaran, 1987, Phys. Rev. Lett. **58**, 606.

Kaldis, E., and B. Fritzler, 1982, Prog. Solid State Chem. **14**, 95.

Kaldis, E., and P. Wachter, 1972, Solid State Commun. **11**, 907.

Kaldis, E., B. Fritzler, E. Jilek and A. Wisard, 1979, J. Phys. (Paris) **40**, C5-366.

Kaldis, E., B. Fritzler, H. Spychiger and E. Jilek, 1982, in: Valence Instabilities, eds P. Wachter and H. Boppart (North-Holland, Amsterdam) p. 131.

Kamba, S., and P. Wachter, 1994, in preparation.
Kamba, S., P. Wachter and Y. Mo, 1994, in preparation.
Kasaya, M., F. Iga, K. Negishi, S. Nakai and T. Kasuya, 1983a, J. Magn. & Magn. Mater. **31–34**, 437.
Kasaya, M., F. Iga, H. Yashima, T. Satoh, M. Ohashi, S. Nakai and T. Kasuya, 1983b, J. Magn. & Magn. Mater. **31–34**, 389.
Kasaya, M., F. Iga, M. Takigawa and T. Kasuya, 1985, J. Magn. & Magn. Mater. **47–48**, 429.
Kasuya, T., 1976, J. Phys. (Paris) **37**, C4-261.
Kasuya, T., K. Takegahara, T. Fujita, T. Tanaka and E. Bannai, 1979, J. Phys. (Paris) **40**, C5-308.
Kasuya, T., M. Kasaya, K. Takegahara, T. Fujita, T. Goto, A. Tamaki, M. Takigawa and H. Yasioka, 1983, J. Magn. & Magn. Mater. **31–34**, 447.
Kikoin, K.A., and A.S. Mishchenko, 1990, J. Phys. C **2**, 6491.
King Jr, H.E., S.J. La Placa, T. Penney and Z. Fisk, 1981, in: Valence Fluctuations in Solids, eds L.M. Falicov, W. Hanke and M.B. Maple (North-Holland, Amsterdam) p. 333.
Kirk, J.L., K. Vedam, V. Narayanamurti, A. Jayaraman and E. Bucher, 1972, Phys. Rev. B **6**, 3023.
Knox, R.S., 1963, Theory of Excitons, Solid State Phys. Suppl. **5**.
Köbler, U., K. Fischer, K. Bickmann and H. Lustfeld, 1981, J. Magn. & Magn. Mater. **24**, 34.
Koehler, W.C., R.M. Moon and F. Holtzberg, 1979, J. Appl. Phys. **50**, 1975.
Koelling, D.D., A.M. Boring and J.H. Wood, 1983, Solid State Commun. **47**, 227.
Kohn, W., 1968, in: Many Body Physics, eds C. de Witt and R. Balian (Gordon & Breach, New York).
Kojima, K., M. Kasaya and Y. Koi, 1978, J. Phys. Soc. Jpn **44**, 1124.
Konczykowski, M., J. Morillo and J.P. Senateur, 1981, in: Valence Fluctuations in Solids, eds L.M. Falicov, W. Hanke and M.B. Maple (North-Holland, Amsterdam) p. 287.
Kress, W., 1987, in: Physics Data, Vol. 26, ISSN 0344-8401, eds H. Berens and P. Luksch (Druckhaus Karlsruhe, Karlsruhe) p. 1.
Kunii, S., 1988, J. Magn. & Magn. Mater. **63–64**, 673.
Kunii, S., and O. Kagaya, 1985, J. Magn. & Magn. Mater. **52**, 165.
Kunii, S., T. Uemura, Y. Chiba, T. Kasuya and M. Date, 1985, J. Magn. & Magn. Mater. **52**, 271.
Kurita, A., Y. Kaneko and T. Koda, 1984, Solid State Commun. **49**, 463.
Lacroix, C., 1987, J. Magn. & Magn. Mater. **63–64**, 239.
Lander, G.H., J. Rebizant, J.C. Spirlet, A. Delapalme, P.J. Brown, O. Vogt and K. Mattenberger, 1987, Physica B **146**, 341.
Lapierre, F., M. Ribault, F. Holtzberg and J. Flouquet, 1981a, Solid State Commun. **40**, 347.
Lapierre, F., M. Mignot, J. Flouquet, P. Haen, M. Ribault and F. Holtzberg, 1981b, in: Valence Fluctuations in Solids, eds L.M. Falicov, W. Hanke and M.B. Maple (North-Holland, Amsterdam) p. 305.
Lapierre, F., M. Ribault, J. Flouquet and F. Holtzberg, 1983, J. Magn. & Magn. Mater. **31–34**, 443.
Lassailly, Y., C. Vettier, F. Holtzberg, A. Benoit and J. Flouquet, 1984, Solid State Commun. **52**, 717.
Lavagna, M., C. Lacroix and M. Cyrot, 1982, J. Phys. F **12**, 745.
Lawrence, J.M., P.S. Riseborough and R.D. Parks, 1981, Rep. Prog. Phys. **44**, 1.
Lee, P.A., T.M. Rice, J.W. Serene, L.J. Sham and J.W. Wilkins, 1986, Comm. Condens. Matter Phys. **12**, 99.
Levy, F., 1969, Phys. kondens. Mater. **10**, 71.
Lustfeld, H., and A. Bringer, 1980, Solid State Commun. **28**, 119.
Luttinger, L.M., 1960, Phys. Rev. **119**, 1153.
Mahanti, S.D., T.A. Kaplan and M. Barma, 1976, Phys. Lett. A **58**, 43.
Maple, M.B., and D. Wohlleben, 1971, Phys. Rev. Lett. **27**, 511.
Marabelli, F., and P. Wachter, 1987a, Phys. Rev. B **36**, 1238.
Marabelli, F., and P. Wachter, 1987b, in: Theoretical and Experimental Aspects of Valence Fluctuations and Heavy Fermions, eds L.C. Gupta and S.K. Malik (Plenum Press, New York) p. 269.
Marabelli, F., and P. Wachter, 1987c, J. Magn. & Magn. Mater. **70**, 364.
Marabelli, F., and P. Wachter, 1988, J. Magn. & Magn. Mater. **73**, 229.
Marabelli, F., and P. Wachter, 1989, Phys. Rev. B **39**, 1407.
Marabelli, F., and P. Wachter, 1990a, Phys. Rev. B **42**, 3307.
Marabelli, F., and P. Wachter, 1990b, Solid State Commun. **74**, 1075.
Marabelli, F., and P. Wachter, 1990c, Physica B **163**, 550.
Marabelli, F., and P. Wachter, 1992, Phys. Scripta T **45**, 120.

Marabelli, F., G. Travaglini, P. Wachter and J.J.M. Franse, 1986a, Solid State Commun. **59**, 381.

Marabelli, F., P. Wachter and J.J.M. Franse, 1986b, J. Magn. & Magn. Mater. **62**, 287.

Marabelli, F., P. Wachter and J.J.M. Franse, 1987, J. Magn. & Magn. Mater. **63–64**, 377.

Marabelli, F., P. Wachter and E. Walker, 1988, Solid State Commun. **67**, 931.

Marabelli, F., P. Wachter and E. Walker, 1989, Phys. Rev. B **39**, 1407.

Marabelli, F., P. Wachter and G. Kaindl, 1992a, Phys. Rev. B **46**, 10012.

Marabelli, F., P. Wachter, A. de Visser and J.J.M. Franse, 1992b, J. Magn. & Magn. Mater. **108**, 79.

Martin, R.M., 1982, Phys. Rev. Lett. **48**, 362.

Martin, R.M., and J.W. Allen, 1979, J. Appl. Phys. **50**, 7561.

Martin, R.M., and J.W. Allen, 1981, in: Valence Fluctuations in Solids, eds L.M. Falicov, W. Hanke and M.B. Maple (North-Holland, Amsterdam) p. 85.

Martin, R.M., J.B. Boyce, J.W. Allen and F. Holtzberg, 1980, Phys. Rev. Lett. **44**, 1275.

Mattenberger, K., O. Vogt, J.C. Spirlet and J. Rebizant, 1986, J. Less-Common Met. **121**, 285.

McWhan, D.B., S.M. Shapiro, J. Eckert, H.A. Mook and R.J. Birgeneau, 1978, Phys. Rev. B **18**, 3623.

Meisner, G.P., A.L. Giorgi, A.C. Lawson, G.R. Stewart, J.O. Willis, M.S. Wire and J.L. Smith, 1984, Phys. Rev. Lett. **53**, 1829.

Melcher, R.L., G. Güntherodt, T. Penney and F. Holtzberg, 1975, in: Ultrasonics Symp. Proc., p. 616. IEE Cat. # 75 CHO 994-4SU.

Mendik, M., and P. Wachter, 1993, Phys. Rev. B **47**, 6110.

Mendik, M., and P. Wachter, 1995, to be published.

Mendik, M., P. Wachter, J.C. Spirlet and J. Rebizant, 1993, Physica B **186–188**, 678.

Menth, A., E. Buehler and T.H. Geballe, 1969, Phys. Rev. Lett. **22**, 295.

Miller, A.J., G.A. Saunders and Y.K. Yogurtcu, 1981, J. Phys. C **14**, 1569.

Millis, A.J., M. Lavagna and P.A. Lee, 1987, Phys. Rev. B **36**, 864.

Mishchenko, A.S., and K.A. Kikoin, 1991, J. Phys.: Condens. Matter **3**, 5937.

Mock, R., E. Zirngiebl, B. Hillebrands, G. Güntherodt and F. Holtzberg, 1986, Phys. Rev. Lett. **57**, 1040.

Monnier, R., L. Degiorgi and B. Delley, 1990, Phys. Rev. B **41**, 573.

Mook, H.A., and F. Holtzberg, 1981, in: Valence Fluctuations in Solids, eds L.M. Falicov, W. Hanke and M.B. Maple (North-Holland, Amsterdam) p. 113.

Mook, H.A., R.M. Nicklow, T. Penney, F. Holtzberg and M.W. Shafer, 1978, Phys. Rev. B **18**, 2925.

Mook, H.A., D.B. McWhan and F. Holtzberg, 1982, Phys. Rev. B **25**, 4321.

Morillo, J., M. Konczykowski and J.P. Senateur, 1980, Solid State Commun. **39**, 931.

Mörke, I., and P. Wachter, 1983, Solid State Commun. **48**, 441.

Mörke, I., V. Dvorak and P. Wachter, 1981, Solid State Commun. **40**, 331.

Morss, L.R., 1971, J. Phys. Chem. **75**, 393.

Moser, M., P. Wachter, F. Hulliger and J.R. Etourneau, 1985, Solid State Commun. **54**, 241.

Moshchalkov, V.V., I.V. Berman, N.B. Brandt, S.N. Pashkevich, E.V. Bogdanov, E.S. Konovalova and M.V. Semenov, 1985, J. Magn. & Magn. Mater. **47–48**, 289.

Moss, T.S., 1952, Photoconductivity in the Elements (Academic Press, New York).

Mott, N.F., 1960, Philos. Mag. **30**, 403.

Mott, N.F., 1961, Philos. Mag. **6**, 287.

Mott, N.F., 1982a, in: Valence Instabilities, eds P. Wachter and H. Boppart (North-Holland, Amsterdam) p. 403.

Mott, N.F., 1982b, in: Valence Instabilities, eds P. Wachter and H. Boppart (North-Holland, Amsterdam) p. 397.

Murani, A.P., 1987, in: Theoretical and Experimental Aspects of Valence Fluctuations and Heavy Fermions, eds L.C. Gupta and S.K. Malik (Plenum Press, New York) p. 287.

Nanba, T., H. Ohta, M. Motokawa, S. Kimura, S. Kunii and T. Kasuya, 1993, Physica B **186–188**, 440.

Narayanamurti, V., A. Jayaraman and E. Bucher, 1974, Phys. Rev. **9**, 2521.

Nathan, M.I., F. Holtzberg, J.E. Smith Jr, J.B. Torrance and J.C. Tsang, 1975, Phys. Rev. Lett. **34**, 467, 1136.

Neuenschwander, J., and P. Wachter, 1987, J. Magn. & Magn. Mater. **63–64**, 606.

Neuenschwander, J., and P. Wachter, 1990a, Phys. Rev. B **41**, 12693.

Neuenschwander, J., and P. Wachter, 1990b, Physica B **160**, 231.

Neuenschwander, J., O. Vogt, E. Voit and P. Wachter, 1986, Physica B **144**, 66.

Neufeld, K., 1975, Masters Thesis (ETH, Zürich) unpublished.
Nickerson, J.C., R.M. White, K.N. Lee, R. Bachmann, T.H. Geballe and G.W. Hull Jr, 1971, Phys. Rev B **3**, 2030.
Nolting, W., 1982, J. Phys. C **15**, 733.
Oguchi, T., and A.J. Freeman, 1985, J. Magn. & Magn. Mater. **52**, 174.
Ohta, H., R. Tanaka, M. Motokawa, S. Kunii and T. Kasuya, 1991, J. Phys. Soc. Jpn. **60**, 1361.
Onuki, Y., and T. Komatsubara, 1987, J. Magn. & Magn. Mater. **63–64**, 281.
Onuki, Y., Y. Shimizu and T. Komatsubara, 1984, J. Phys. Soc. Jpn. **53**, 1210.
Onuki, Y., K. Shibutani, T. Yamazaki, T. Komatsubara, K. Maerawa and S. Wakabayashi, 1987a, J. Magn. & Magn. Mater. **63–64**, 289.
Onuki, Y., M. Nishihara, Y. Fujimura, T. Yamazaki and T. Komatsubara, 1987b, J. Magn. & Magn. Mater. **63–64**, 317.
Ott, H.R., and F. Hulliger, 1983, Z. Phys. B **49**, 323.
Ott, H.R., B. Lüthi and P.S. Wang, 1977, in: Valence Instabilities and Related Narrow Band Phenomena, ed. R.D. Parks (Plenum Press, New York) p. 289.
Ott, H.R., B. Batlogg, E. Kaldis and P. Wachter, 1978, J. Appl. Phys. **49**, 2118.
Ott, H.R., H. Hulliger and H. Rudigier, 1982, in: Valence Instabilities, eds P. Wachter and H. Boppart (North-Holland, Amsterdam) p. 511.
Ott, H.R., H. Rudigier, Z. Fisk and J.L. Smith, 1984, Physica B **127**, 359.
Ott, H.R., H. Rudigier and F. Hulliger, 1985a, Solid State Commun. **55**, 113.
Ott, H.R., H. Rudigier, Z. Fisk, J.O. Willis and G.R. Stewart, 1985b, Solid State Commun. **53**, 235.
Overhauser, A.W., and J. Appel, 1985, Phys. Rev. B **31**, 193.
Parks, R.D., 1976, Valence Instabilities and Related Narrow Band Effects (Plenum Press, New York).
Patthey, F., W.D. Schneider, Y. Baer and B. Delley, 1986, Phys. Rev. B **34**, 2967.
Patthey, F., J.M. Imer, W.D. Schneider, H. Beck, Y. Baer and B. Delley, 1990, Phys. Rev. B **42**, 8864.
Pena, O., M. Lysak and D.E. MacLaughlin, 1981, Solid State Commun. **40**, 539.
Penney, T., R.L. Melcher, F. Holtzberg and G. Güntherodt, 1975, in: Magnetism and Magnetic Materials, eds J.J. Becker, G.H. Lander and J.J. Rhyne, AIP Conf. Proc. **29**, 392.
Phillips, N.E., R.A. Fisher, S.E. Lacy, C. Marcenat, J.A. Olsen, J. Flouquet, A. Amato, D. Jaccard, Z. Fisk, A.L. Giorgi, J.L. Smith and G.R. Stewart, 1987, in: Theoretical and Experimental Aspects of Valence Fluctuations and Heavy Fermions, eds L.C. Gupta and S.K. Malik (Plenum Press, New York) p. 141.
Pott, R., R. Schefzyk, D. Wohlleben and R. Junod, 1981, Z. Phys. **44**, 17.
Quader, K.F., K.S. Bedell and G.E. Brown, 1987, Phys. Rev. B **36**, 156.
Racah, G., 1949, Phys. Rev. **176**, 1352.
Rasul, J.W., 1991, Phys. Rev. B **44**, 11802.
Reihl, B., F. Holtzberg, R.A. Pollak, G. Hollinger, G. Kaindl and N. Martensson, 1982, in: Valence Instabilities, eds P. Wachter and H. Boppart (North-Holland, Amsterdam) p. 287.
Reim, W., and P. Wachter, 1985, Phys. Rev. Lett. **55**, 871.
Reim, W., H. Boppart and P. Wachter, 1985, J. Magn. & Magn. Mater. **52**, 91.
Reinders, P.H.P., M. Springford, P.T. Coleridge, R. Boulet and D. Ravot, 1986, Phys. Rev. Lett. **57**, 1951.
Rossel, C., M.S. Torikachvili, J.W. Chen and M.B. Maple, 1986, Solid State Commun. **60**, 563.
Sales, B.C., and D. Wohlleben, 1975, Phys. Rev. Lett. **35**, 40.
Sargent, E.H., 1962, Periodic Table of the Elements (Chicago).
Satoh, K., T. Fujita, Y. Maeno, Y. Onuki, T. Komatsubara and T. Ohtsuka, 1985, Solid State Commun. **56**, 327.
Saunders, G.A., W.A. Lambson, Tu Hailing, D.W. Bullett, H. Bach and S. Methfessel, 1982, J. Phys. C **15**, L551.
Schneider, B., 1983, Diploma Thesis (ETH, Zürich) unpublished.
Schneider, W.D., B. Delley, E. Wuilloud, J.J.M. Imer and Y. Baer, 1986, Phys. Rev. B **32**, 6819.
Schoenes, J., and K. Andres, 1982, Solid State Commun. **42**, 359.
Schoenes, J., and J.J.M. Franse, 1985, Physica B **130**, 69.
Schoenes, J., and J.J.M. Franse, 1986, Phys. Rev. B **33**, 5138.
Schoenes, J., O.E. Hüsser, W. Reim, E. Kaldis and P. Wachter, 1985, J. Magn. & Magn. Mater. **47–48**, 481.
Schönenberg, P., and H. Keiter, 1992, Europhys. Lett. **17**, 613.

Shapiro, S.M., H. Bjerrum-Møller, J.D. Axe, R.J. Birgeneau and E. Bucher, 1978, J. Appl. Phys. **49**, 2101.

Sherrington, D., and S. von Molnar, 1975, Solid State Commun. **16**, 1347.

Sinha, S.K., and C.M. Varma, 1983, Phys. Rev. B **28**, 1663.

Smith, J.L., Z. Fisk, J.O. Willis, H.R. Ott, S.E. Lambert, Y. Dalichaouch and M.B. Maple, 1987, J. Magn. & Magn. Mater. **63–64**, 464.

Steglich, F., J. Aarts, C.D. Bredl, W. Lieke, D. Meschede, W. Franz and H. Schäfer, 1979, Phys. Rev. Lett. **43**, 1892.

Steglich, F., U. Rauchschwalbe, U. Gottwick, H.M. Mayer, G. Sparn, N. Grewe, U. Poppe and J.J.M. Franse, 1985, J. Appl. Phys. **57**, 3054.

Stewart, G.R., 1984, Rev. Mod. Phys. **56**, 755.

Stewart, G.R., Z. Fisk and J.O. Willis, 1983, Phys. Rev. B **28**, 172.

Stewart, G.R., Z. Fisk and M.S. Wire, 1984, Phys. Rev. B **30**, 482.

Stura, H., B. Elschner and K.H. Höck, 1985, Phys. Rev. Lett. **54**, 1291.

Stüsser, N., G. Güntherodt, A. Jayaraman, K. Fischer and F. Holtzberg, 1982, in: Valence Instabilities, eds P. Wachter and H. Boppart (North-Holland, Amsterdam) p. 69.

Sugiyama, K., A. Ohia, M. Date, F. Iga, M. Kasaya and T. Kasuya, 1985, J. Magn. & Magn. Mater. **52**, 283.

Suryanarayanan, R., G. Güntherodt, J.L. Freeouf and F. Holtzberg, 1975, Phys. Rev. B **12**, 4215.

Syassen, K., H. Winzen, H.G. Zimmer, H. Tups and J.M. Leger, 1985, Phys. Rev. B **32**, 8246.

Taillefer, L., R. Newbury, G.G. Lonzarich, Z. Fisk and J.L. Smith, 1987, J. Magn. & Magn. & Mater. **63–64**, 372.

Takabatake, T., Y. Nakazawa and M. Ishikawa, 1987, Jpn. J. Appl. Phys. Suppl. **26**, 547.

Takabatake, T., F. Teshima, H. Fujii, S. Nishigori, T. Suzuki, T. Fujita, Y. Yamaguchi, J. Sakurai and D. Jaccard, 1990, Phys. Rev. B **41**, 9607.

Takigawa, M., H. Yasioka, T. Tanaka, Y. Ishizawa, M. Kasaya and T. Kasuya, 1983, J. Magn. & Magn. Mater. **31–34**, 391.

Tanaka, T., J. Yoshimoto, M. Ishii, E. Bannai and S. Kawai, 1977, Solid State Commun. **22**, 203.

Tao, L.J., and F. Holtzberg, 1975, Phys. Rev. B **11**, 3842.

Tarascon, J.M., Y. Isikawa, B. Chevalier, J. Etourneau, P. Hagenmüller and M. Kasaya, 1980a, J. Phys (Paris) **41**, 1135.

Tarascon, J.M., Y. Isikawa, B. Chevalier, J. Etourneau, P. Hagenmüller and M. Kasaya, 1980b, J. Phys (Paris) **41**, 1145.

Thalmeier, P., and P. Fulde, 1982, Phys. Rev. Lett. **49**, 1588.

Therond, P.G., A. Blaise, J.M. Fournier, J. Rossat-Mignod, J.C. Spirlet, J. Rebizant and O. Vogt, 1987, J. Magn. & Magn. Mater. **63–64**, 142.

Thompson, J.D., 1987, J. Magn. & Magn. Mater. **63–64**, 358.

Thompson, J.D., and G.P. Meisner, 1985, Physica B **130**, 168.

Thompson, J.D., H.A. Borges, Z. Fisk, S. Horn, R.D. Parks and G.L. Wells, 1987, in: Theoretical and Experimental Aspects of Valence Fluctuations and Heavy Fermions, eds L.C. Gupta and S.K. Malik (Plenum Press, New York) p. 151.

Travaglini, G., and P. Wachter, 1984a, Phys. Rev.B **29**, 893.

Travaglini, G., and P. Wachter, 1984b, Phys. Rev. B **30**, 5877.

Travaglini, G., and P. Wachter, 1985, J. Appl. Phys. **57**, 3176.

Travaglini, G., F. Marabelli, R. Monnier, E. Kaldis and P. Wachter, 1986, Phys. Rev. B **34**, 3876.

Treindl, A., and P. Wachter, 1979, Solid State Commun. **32**, 573.

Treindl, A., and P. Wachter, 1980, Solid State Commun. **36**, 901.

Tsiok, O.B., V.A. Sidorov, V.V. Bredikhin, L.G. Khvostantsev, A.V. Golubkov and I.A. Smirnov, 1991, Solid State Commun. **79**, 227.

van Sprang, M., 1989, Thesis (Natuurkundig Laboratorium der Universiteit van Amsterdam).

Varma, C.M., 1976, Rev. Modern Phys. **48**, 219.

Varma, C.M., 1977, US–Japan Seminar on Physical Properties of Rare Earth Magnetic Semiconductors, Sendai, Japan, unpublished.

Varma, C.M., 1979, Solid State Commun. **30**, 537.

Varma, C.M., 1985, Phys. Rev. Lett. **55**, 2723.

Vogt, O., and K. Mattenberger, 1987, J. Less-Common Met. **133**, 53.

Vogt, O., and K. Mattenberger, 1993, in: Handbook on the Physics and Chemistry of Rare Earths, Vol. 17, Lanthanides/Actinides: Physics – 1, eds K.A. Gschneidner Jr, L. Eyring, G.H. Lander and G.R. Choppin (North-Holland, Amsterdam) ch. 114.

von Löhneisen, H., A. Germann and A. Schröder, 1990, Physica B **163**, 144.

von Molnar, S., T. Theis, A. Benoit, A. Briggs, J. Flouquet and J. Ravex, 1982, in: Valence Instabilities, eds P. Wachter and H. Boppart (North-Holland, Amsterdam) p. 389.

Wachter, P., 1977, in: Valence Instabilities and Related Narrow Band Phenomena, ed. R.D. Parks (Plenum Press, New York) p. 337.

Wachter, P., 1979, in: Handbook on the Physics and Chemistry of Rare Earths, Vol. 2, eds K.A. Gschneidner Jr and L. Eyring (North-Holland, Amsterdam) p. 507.

Wachter, P., 1982, in: Valence Fluctuations, eds P. Wachter and H. Boppart (North-Holland, Amsterdam) p. 145.

Wachter, P., 1986, Lanthanide & Actinide Res. **1**, 265.

Wachter, P., 1987, in: Proc. 9th Int. Symp. on Boron, Borides and Related Compounds, ed. H. Werheit (University of Duisburg, Duisburg) p. 166.

Wachter, P., 1989a, unpublished data.

Wachter, P., 1989b, first proposed at the 19ième Journeé des Actinides, Madonna di Campiglio, Italy.

Wachter, P., 1994, to be publishcd.

Wachter, P., and A. Jung, 1994, IEEE Trans. Mag. **MAG-30**, 954.

Wachter, P., and G. Travaglini, 1985, J. Magn. & Magn. Mater. **47–48**, 423.

Wachter, P., F. Marabelli and B. Bucher, 1991, Phys. Rev. B **43**, 11136.

Wachter, P., A. Jung and P. Steiner, 1995, Phys. Rev. B, in print.

Walch, P.F., D.E. Ellis and F.M. Müller, 1977, Phys. Rev. B **15**, 1859.

Walter, V., D. Wohlleben and Z. Fisk, 1986, Z. Phys. B **62**, 325.

Wang Xu, Chun Chen and Zheng-Zhong Li, 1991, Solid State Commun. **80**, 943.

Webb, B.C., A.J. Sievers and T. Mihalisin, 1986, Phys. Rev. Lett. **57**, 1951.

Weidner, P., K. Keulerz, R. Löhe, B. Roden, J. Röhler, B. Wittershagen and D. Wohlleben, 1985, in: Valence Fluctuations, eds E. Müller-Hartmann, B. Roden and D. Wohlleben, J. Magn. & Magn. Mater. **47–48**, 75.

Wertheim, G.K., A. Rosencwaig, R.L. Cohcn and H.J. Guggenheim, 1971, Phys. Rev. Lett. **27**, 505.

Wickman, H.H., M.P. Klein and D.A. Shirley, 1966, Phys. Rev. **152**, 345.

Wohlleben, D., 1981, in: Valence Fluctuations in Solids, eds L.M. Falicov, W. Hanke and M.B. Maple (North-Holland, Amsterdam) p. 1.

Wohlleben, D., J.G. Huber and M.B. Maple, 1972, in: Magnetism and Magnctic Materials, eds D.C. Graham and J. Rhyne, AIP Conf. Proc. **5**, 1478.

Wuilloud, E., B. Delley, W.D. Schneider and Y. Bacr, 1984, Phys. Rev. Lett. **53**, 202.

Zelezny, V., J. Petzelt, V.V. Kaminski, M.V. Romanova and A.V. Golubkov, 1989, Solid State Commun. **72**, 43.

Zhuze, V.P., A.V. Golubkov, E.V. Goncharova, T.I. Komarova and V.M. Sergeeva, 1964, Sov. Phys. Solid State **6**, 213.

Zirngiebl, E., S. Blumenröder, R. Mock and G. Güntherodt, 1986, J. Magn. & Magn. Mater. **54–57**, 359.

Handbook on the Physics and Chemistry of Rare Earths
Vol. 19 – Lanthanides/Actinides: Physics – II
edited by K.A. Gschneidner, Jr., L. Eyring, G.H. Lander and G.R. Choppin

Chapter 133

HIGH PRESSURE STUDIES – PHYSICAL PROPERTIES OF ANOMALOUS Ce, Yb AND U COMPOUNDS

J.D. THOMPSON
Los Alamos National Laboratory, Los Alamos, NM 87545, USA

J.M. LAWRENCE
Department of Physics, University of California, Irvine, CA, USA

Contents

List of symbols

A	coefficient of the T^2 term in the resistivity
B_0	normal contribution to the bulk modulus
B_c	electronic or anomalous f contribution to the bulk modulus
$\delta B_c(0)$	anomalous f contribution to the bulk modulus at $T=0$
B_s	adiabatic bulk modulus
B_T	isothermal bulk modulus
b	linear coefficient of the low-temperature thermal expansion
BCS	Bardeen–Cooper–Schrieffer theory of superconductivity
BIS	Bremsstrahlung Isochromat Spectroscopy
C	Curie constant; also used for generalized specific heat

C_{ij}	elastic constant tensor
ΔC	specific heat jump at the superconducting transition
C_0	normal contribution to the specific heat
C_{CF}	crystal-field contribution to the specific heat
C_e	electronic or anomalous f contribution to the specific heat
C_{Gr}	specific heat calculated from the thermal expansion using the Grüneisen relation, eq. (1)
C_K	Kondo contribution to the specific heat
C_p	specific heat at constant pressure
C_{ph}	phonon contribution to the specific heat
C_T	total specific heat
C_v	specific heat at constant volume
$\delta C_{l,}$	change in the longitudinal sound velocity
dhcp	double hexagonal close packed crystal structure
E_F	Fermi energy
E_f	energy of the 4f level
E_g	energy of the hybridization gap
E_k	electron energy at wavevector k
F	Helmholtz free energy
F_0	normal contribution to F
F_e	electronic or anomalous f contribution to F
F_K	Kondo contribution to F
f	arbitrary scaling function
fcc	face centered cubic crystal structure
G	Gibbs free energy
g	arbitrary scaling function
H	magnetic field
H_0	characteristic (scaling) field
H_{c2}	upper critical field of a superconductor
H_{c2}'	derivative of H_{c2} with respect to temperature near T_c
H_m	value of magnetic field at which a metamagnetic transition occurs
J	exchange energy that sets the scale for Kondo and RKKY interactions
J	total angular momentum (spin plus orbital)
k_B	Boltzmann constant
L_{III}	$2p_{3/2}$ to 5d (or 6d) transition in X-ray absorption
LDA	band theory in the local density approximation
M	magnetization
m^*	effective mass
N	degeneracy of the ground state
N	number of atoms
n	number of 4f electrons in the configuration $4f^n$
n_f	f occupation number
$N(E_F)$	density of states of the background (non-f) band at the Fermi energy
$N_f(E)$	density of states in the f band or resonant level
P	pressure
Q	wavevector or momentum transfer
R	gas constant
R	Wilson ratio (normalized ratio of $\chi(0)/\gamma$)
R_m	maximum value of the resistance
RKKY	Ruderman–Kittel–Kasuya–Yosida interaction
S	Fermi surface area
S	Stoner enhancement
S	entropy
S_e	electronic or anomalous f contribution to the entropy
S_v	volume magnetostriction as defined by eq. (22)
T	temperature
T_0	characteristic temperature, used in a general sense
$T_{1/2}$	temperature at which the quantity $T\chi/C$ equals 1/2
T_C	Curie temperature for ferromagnetism
T_c	superconducting transition temperature
T_{CF}	crystal-field splitting, expressed in temperature units
T_{coh}	temperature below which the system behaves as a coherent Fermi liquid
T_F	Fermi temperature
T_i	temperature of the inflection in the resistivity
T_K	Kondo temperature (single-ion)
T_m	temperature of the maximum in the resistivity, susceptibility or thermal expansion
T_N	Néel temperature for antiferromagnetism
T_{RKKY}	temperature (energy) scale characterizing RKKY interactions

T_{sf}	spin-fluctuation temperature or characteristic temperature for enhanced itinerant paramagnetism
T_{vf}	valence-fluctuation temperature or characteristic temperature in the limit of strong mixed valence
U_e	electronic or anomalous f contribution to the internal energy
U_K	Kondo contribution to the internal energy
V	volume
V_{kf}	matrix element for hybridization of an f state with the conduction electrons
v_s	velocity of sound
z	valence
α	ratio of the interatomic spacing to the radius of the magnetic orbital
α_c	critical value of α separating magnetic and nonmagnetic ground states
β	volume thermal expansion
β_0	normal contribution to β
β_e	electronic or anomalous f contribution to β
β_{CF}	crystal-field contribution to β
β_j, β_a, β_c	thermal expansion in the j, a or c direction
β_K	Kondo contribution to β
β_{ph}	phonon contribution to β
Γ	linewidth of the inelastic neutron-scattering spectrum
Γ_7	referring to the symmetry of a crystal field ground state doublet
γ	linear coefficient of specific heat per mol
γ_V	linear coefficient of specific heat per unit volume
Δ	width of f level due to hybridization, $\Delta = V_{kf}^2 N(E_F)$
Δ_{CF}	crystal-field splitting energy
Δ_g	gap in the excitation spectrum
ε	strain
ε_{ij}	xx, yy or zz strains
ε_Γ	strain of symmetry Γ
Φ_0	flux quantum
κ	thermal conductivity
μ_B	Bohr magneton
ν	Poisson ratio
ξ	superconducting coherence length
ρ	electrical resistivity
τ_{diff}	thermal diffusion time
χ	magnetic susceptibility
χ_{4f}	4f contribution to χ
χ_c, χ_a	susceptibility for magnetic field in the c or a direction
χ_{imp}	impurity contribution to χ
χ_m	value of χ at T_m, the temperature of the susceptibility maximum
Ω	Grüneisen parameter in the general case; also used for the thermodynamic Grüneisen parameter eq. (14)
Ω_A	estimate of Ω_e from the pressure dependence of the coefficient A of the resistivity
Ω_c	estimate of Ω_e from the pressure dependence of the low-temperature specific heat
Ω_{CF}	Grüneisen parameter for the crystal-field contribution
Ω_e	electronic or anomalous f Grüneisen parameter, equal to $\partial \ln T_0 / \partial \ln V$; also used for the estimate obtained from the ratio of β_e/C_e using eq. (1)
$\Omega_e^{(2)}$	equals $(V^2/T_0)(\partial^2 T_0/\partial V^2)$
Ω_{eff}	proportionality factor between B_c and β_e used in eq. (10) and defined in eq. (12)
Ω_K	Grüneisen parameter for the Kondo contribution
Ω_{ph}	Grüneisen parameter for the phonon contribution
Ω_{T_0}	estimate of Ω_e from the pressure dependence of either T_i or T_m for the resistivity
Ω_{T_m}	estimate of Ω_e from the pressure dependence of T_m for the susceptibility
Ω_Γ	Grüneisen parameter for a strain of symmetry Γ
Ω_χ	estimate of Ω_e from the pressure dependence of the low-temperature susceptibility

1. Introduction

In this review we compare the pressure dependence of electronic and magnetic properties (particularly resistivity ρ, specific heat C_p and magnetic susceptibility χ) of "anomalous" rare-earth and actinide compounds, emphasizing those based on Ce, Yb and U that exhibit heavy-fermion and related behavior. Two themes are stressed: first, the presence (or absence) of "universality" whereby the temperature dependence of various quantities scales with a characteristic temperature (T/T_0) and the effect of pressure P is simply to change T_0; and second, the distinction between the delocalized, itinerant behavior often appropriate for the 5f electrons in light actinides and the more nearly localized behavior of the 4f electrons in rare-earth compounds. As we will see, there are difficulties in establishing the degree both to which universality is valid quantitatively and to which actinides and rare earths differ. There is substantial confusion in the literature about these points. We have attempted to address some of the difficulties and to clarify some of the confusion, but admittedly we have had limited success. Consequently, this review should be considered primarily a progress report, pointing the way to future work to improve our understanding of these issues.

1.1. *Normal lanthanide and actinide behavior versus heavy-electron behavior*

In general, 4f electrons in the lanthanides and 5f electrons in the heavy actinides (Am and beyond) are well-localized and produce magnetic ground states; in the light actinides the 5f electrons are described frequently as itinerant and paramagnetic or even superconducting ground states are favored. However, certain light-actinide compounds are magnetic and certain lanthanide compounds, especially those based on Ce, Sm, Eu, Tm and Yb, are non-magnetic in the ground state. The importance of f-atom spacing for determining which of these states is favored was noted first by Hill (1970) who observed that magnetism appeared predominately at large f–f spacing and superconductivity at the smallest separations. Hill explained these systematics by considering the role of f-wavefunction overlap. For strong overlap, an f-band forms that will not support magnetism, even by Stoner's criterion. As the f-atom separation is increased, the overlap, and hence the f-bandwidth, decreases and magnetism is stabilized. A similar criterion has been proposed by Schilling (1984) who finds there is a critical value, $\alpha_c = 3.2$, of the ratio of half the interatomic spacing to the radius of the magnetic orbital such that for $\alpha > 3.2$, elements are magnetic but for $\alpha < 3.2$, elements are non-magnetic.

From our perspective, what is more interesting are the exceptions to these trends, in particular lanthanide and actinide compounds whose large f–f spacing would by the Hill or Schilling criteria imply that they should be strongly magnetic but instead their ground state is that of a small-moment magnet, a paramagnet or a superconductor. The existence of such "anomalous" materials indicates that interactions other than just f–f overlap must be important. Most obviously, the Hill criterion does not treat the situation where the itineracy of the f electron arises not from direct f–f overlap but from hybridization with s, p, or d states on a neighboring ion. In this situation, the f–f spacing can be large but

the distance to the nearest neighbor is small enough that hybridization delocalizes the f electron. Many non-magnetic uranium compounds fall in this category. A more extreme case occurs in certain compounds of the heavy lanthanides Eu, Sm, Tm, Yb; the 4f orbital is sufficiently small that hybridization is very weak, yet the ground state is non-magnetic. These are the so-called mixed valent compounds, where the ion fluctuates between two local configurations $4f^n$ and $4f^{n-1}$. Cerium is an intermediate case in that the 4f orbital is somewhat larger and the hybridization stronger. Under certain circumstances, e.g. α-Ce or $CeCo_2$, the cerium-4f electrons are probably best treated as itinerant; under others, a mixed-valent or nearly localized description is more relevant. Whether certain uranium compounds are best treated as having localized 5f electrons is more of an open question.

In this class of materials the magnetic/nonmagnetic transition is intimately mixed with the localized/itinerant transition. Whether itinerant with large spin fluctuations, mixed-valent or nearly integral-valent, the appellations "heavy fermion" or "heavy electron" are often used. The study of these materials has become a vital part of materials physics aimed at understanding strong electronic correlations and has been the subject of numerous reviews already. The focus of discussion here will be how aspects of the essential physics are revealed through changes in physical properties of these systems as interactions are modified by applied pressure and the extent to which rare-earths and actinides respond similarly. In the remainder of this Introduction we will address the expected behavior in both the itinerant and localized limits, followed by a discussion of the effect that pressure should have on the electronic and magnetic properties, and finally we will consider the thermodynamics of universality.

1.2. *Itineracy in the light actinides*

The distinction between itinerant and localized behavior can be seen in the crystal structures of actinide and rare-earth elements (McMahan 1989; Schilling 1986). The heavy lanthanides and actinides (beyond Am) have localized f electrons; the characteristic crystal-structure sequence (hcp → samarium type → dhcp → fcc) that occurs with increasing pressure is understood to arise from s - d promotion. The light actinides possess a series of low-symmetry structures (α-U; orthorhombic, monoclinic) that are well-described by treating the 5f electrons as itinerant. Local Density Approximation (LDA) band structures give good agreement with experimental cell volumes and bulk moduli; the parabolic dependence of the cell volume on f-band filling is a natural consequence of 5f banding (McMahan 1989). The low-symmetry structures arise because "when the 5f wave functions overlap to form a band, they impress their low symmetry on the crystal structure" (Schilling 1986). Identical structures are observed in high-pressure phases of the heavy actinides (Am, Cm, Bk, Cf) and the light lanthanides (Ce, Pr, Nd), suggesting that pressure promotes a localized/itinerant transition.

Although an important distinction between delocalized and localized electrons is that LDA gives adequate account of the former but very inadequate account of the latter, it is true that LDA can indicate when a transition from itinerant to localized behavior occurs. An important recent advance (Eriksson et al. 1990) has been the application

of spin *and* orbitally polarized LDA to the γ–α transition in Ce. By including orbital polarization the volume discontinuity at the transition can be accurately reproduced. This strengthens the case that α-Ce and α-like compounds ($CeCo_2$, $CeRu_2$) are best described in the itinerant limit.

The distinction between itineracy and localization also can be seen in photoemission spectra. Typically, U-compounds (even heavy-electron compounds such as UPt_3) exhibit wide (1–2 eV) f bands centered on the Fermi level E_F (Arko et al. 1988). On the other hand, lanthanide compounds and heavy actinides show localized f levels several eV below E_F (Baer and Schneidner 1987). The case of Ce is intermediate, and hotly contested; but for most Ce compounds the spectral weight lies mostly in the localized excitation, with a small amount at E_F. The exceptions are the α-like cerium compounds (e.g. $CeCo_2$) where large weight at E_F (Baer and Schneidner 1987) suggests bandlike behavior.

To examine how the differences between itinerant f electrons (in actinide intermetallics and α-like Ce compounds) and localized f electrons (most Ce and Yb compounds and perhaps some U compounds) are manifest in the pressure dependence of C_p, χ and ρ, we need to distinguish the behavior for the two cases at ambient pressure. For itinerant electrons, LDA treatments show that localization occurs when the Stoner criterion is satisfied. This suggests that paramagnon theory might be applicable (Beal-Monod and Lawrence 1980). In the paramagnetic phase, the susceptibility should be enhanced by a factor S that increases as the system approaches localization. A characteristic "spin fluctuation" energy, which we label T_{sf} for the itinerant case, can be identified as $T_{sf} = T_F/S$, where T_F is the bare Fermi temperature. The low-temperature susceptibility then satisfies $\chi(0) \sim 1/T_{sf}$ and the specific heat is also enhanced, but more weakly (the effective mass is enhanced essentially as $\ln S$). In reality the situation is different for several reasons. First, the discussion above concerning the Ce γ–α transition makes it clear that the Stoner criterion is much more complicated than in the simple spin-1/2 model that is usually considered. Secondly, where paramagnon theory applies to nearly ferromagnetic itinerant systems, the actinide and α-like Cc intermetallics are nearly *anti*ferromagnetic, and close to localization. The large enhancements do not arise from incipient ferromagnetism, but from incipient localization. For this situation, there is less guidance from theory. Experimentally, for the nearly ferromagnetic transition-metal compounds for which paramagnon theory is applicable, enhancement of the specific heat is indeed weaker than that of the susceptibility (as mentioned above), but for the U and α-like Ce heavy fermions the two are equally enhanced (Kaiser and Fulde 1988). This means that $C_p \sim \gamma T$, with $\gamma \sim 1/T_{sf}$, as well as $\chi(0) \sim 1/T_{sf}$. As we will see, this is identical to the phenomenological behavior in the localized case, making it impossible to distinguish between the two cases on such a basis. (It is possible that the resistivity varies differently in the two cases; e.g., as T^2/T_{sf} for the itinerant case and T^2/T_0^2 for the nearly localized case.) In any case it is not clear to us whether the thermodynamic behavior expected from nearly localized band theory is essentially different phenomenologically from that expected on the basis of the Anderson Lattice treatment of localized electrons, to be discussed below.

1.3. *Heavy-fermion behavior of localized electrons*

A characteristic common to many Ce and Yb compounds, where the 4f electrons are described best as localized, as well as a few U-compounds, is a temperature-dependent resistivity with negative slope above ~100 K. Such behavior (Grewe and Steglich 1991) is reminiscent of that found in Kondo-impurity systems in which antiferromagnetic exchange J between conduction electrons and the local moment of the impurity leads to a $-\ln T/T_K$ temperature dependence of the magnetic resistivity for temperatures on the order of the Kondo temperature T_K (Grüner and Zawadowski 1974). Here the Kondo temperature is the characteristic energy scale. For a single spin-1/2 Kondo impurity imbedded in a metallic host,

$$T_K = \frac{E_F}{k_B} \exp(-1/|J|\, N(E_F)),$$

where $N(E_F)$ is the conduction-band density-of-states at the Fermi level. There are two further important consequences of the Kondo effect. (1) For $T \ll T_K$, the local moment is compensated by conduction electrons which are quasi-bound antiferromagnetically to the local moment, leading to a magnetic singlet ground state. (2) A many-body Abrikosov–Suhl resonance of width T_K forms in the density-of-states at an energy near E_F which depends on the angular momentum of scattering channels available to the conduction electrons. As $T \to 0$, these two consequences lead to an enhanced Pauli susceptibility $\chi(0) \propto 1/T_K$ and Sommerfeld coefficient $\gamma \propto 1/T_K$ with strong f-character that are hallmarks of Kondo-like compounds. Thus, T_K can be estimated from measurements of $\chi(0)$ and γ.

In spite of the commonality between predictions of the Kondo-impurity theory and the physical properties of heavy-electron compounds made up of a periodic array of ~10^{23} Kondo impurities, an important distinction exists in the low-temperature transport. Whereas, for a Kondo impurity the $T \to 0$ resistivity $\rho(0)$ is the maximum allowed by unitarity scattering for an f-scattering channel and decreases away from $T = 0$ as $\rho(T) = \rho(0)[1 - (T/T_K)^2]$, the low-temperature resistivity of the lattice increases as $\rho(T) = \rho(0) + AT^2$ from a $T = 0$ value typical of a normal metal but with a T^2-coefficient four-to-six orders of magnitude greater than for electron–electron scattering in a normal metal (Fisk et al. 1988a). Further, in Ce-, Yb- and U-based compounds, the Sommerfeld coefficient γ or equivalently the effective electron mass m^* scales approximately as $A^{-1/2}$ for wide ranges of γ and A (Kadowaki and Woods 1986). This correlation suggests that a single energy scale is responsible for both the large γ and T^2-coefficient of resistivity, which for a single-Kondo impurity is T_K.

One of the outstanding questions raised by the physical properties of these compounds at ambient pressure is how the approximately 10^{23} impurities interact to produce the strongly renormalized, coherent Bloch state at low temperatures. Some insight is provided by inelastic neutron scattering (Aeppli et al. 1991), nuclear magnetic resonance (Asayama et al. 1988) and muon-spin relaxation (Heffner 1992) which show the development of antiferromagnetic correlations at low temperatures, even in those

systems that do not magnetically order. For a periodic lattice of Kondo impurities, the exchange J that determines T_K for an isolated impurity also is responsible for coupling local moments through the Ruderman–Kittel–Kasuya–Yosida (RKKY) interaction to produce antiferromagnetic order at a Néel temperature $T_N \propto J^2[N(E_F)]$. That the same exchange can lead either to long range magnetic order in a lattice of local moments or to a non-magnetic singlet for non-interacting Kondo impurities raises the possibility of a competition between these two effects for the ground state. Thus, the simultaneous consideration of Kondo and RKKY interactions appears to be a minimum requirement for a description of the physical properties. An important distinction, however, is that J can be expanded as a sum of angular momentum components and that for the Kondo interaction in f-electron compounds it is the f-component of J that determines T_K but for the RKKY interaction s, p, d and f-components must be included.

In addition to these, the degeneracy of the f-level is an important consideration relevant both to the development of realistic models and to an interpretation of properties (Schlottmann 1989). The effect of crystalline-electric-field splitting is to lift the degeneracy of the f-level, usually producing a doublet ground state. In this case, the Abrikosov–Suhl resonance is centered at E_F; but for an N-fold degenerate ground state ($N > 2$), the resonance is peaked well away from E_F. In 4f compounds, spin–orbit coupling generally is much greater than crystal-field splitting $\Delta_{CF} \cong k_B T_{CF}$ between the ground and first excited multiplet so that the orbital degeneracy is well-defined. In this case Rajan (1983) has shown that the ground-state degeneracy affects relationships between the Kondo temperature and physical properties like $\chi(0)$ and γ, e.g. $\gamma = (N-1)(\pi R/6\, T_K)$, where R is the gas constant. However, because of the greater spatial extent of 5f wavefunctions, the spin–orbit energy can be comparable to or even smaller than Δ_{CF}, making definition of the ground-state degeneracy less clear.

The discussion thus far has assumed that the f-configuration is well-defined and that only spin hybridization between the f- and conduction electrons occurs through the Kondo effect. However, this is not always the case. Because of hybridization the f-level broadens to a width $\Delta = \pi \langle V_{kf} \rangle^2 N(E_F)$, where V_{kf} is the matrix element that mixes conduction and f-electron wavefunctions and is related to the exchange by $J = -\langle V_{kf} \rangle^2 / E_f$ in the limit of infinite intra-atomic Coulomb repulsion. If the energy of the f-level E_f, relative to E_F, is small, the ratio E_f/Δ approaches zero; it is energetically favorable for the f-electron to spend a fraction of its time in the conduction band so that the f-count is no longer integral. In this mixed-valence limit, the ground state is a quantum mechanical admixture of f^n and f^{n-1} wavefunctions and spin fluctuations are induced primarily by charge fluctuations (Schlottmann 1989). The characteristic energy scale (often called the valence-fluctuation temperature T_{vf}) is typically greater than T_{CF} and the concept of crystal-field splitting, in the classical sense, breaks down. Mixed-valence behavior is well-documented in a number of Ce-, Sm-, Yb- and Eu-compounds but is not so clear in U-compounds because the $5f^2$ and $5f^3$ configurations have similar energies and comparable effective magnetic moments. As a working definition, we consider those materials that have a temperature region of negative $\partial\rho/\partial T$, show evidence for crystal-field splitting and

have nearly integral f-occupancy as being in the Kondo limit; whereas, those in which clearly defined crystal-field excitations are absent and the f-occupancy is strongly non-integral are termed mixed valence. Although we will attempt to distinguish the itinerant behavior appropriate for most U-compounds from the mixed-valence behavior appropriate for Sm, Eu, Tm and Yb compounds, we note that Ce is a borderline case. When the characteristic energy becomes very large, we expect the band-like and the mixed-valent descriptions to be more or less equivalent.

1.4. *Pressure dependence of interactions*

For the essentially localized heavy fermions, by far the most pressure sensitive interaction is that due to the single-ion Kondo effect. In reviewing the effect of pressure on the Kondo temperature of dilute Ce impurities in La, Y, $La_{1-x}Y_xAl_2$ and $La_{1-x}Th_x$ hosts, Schilling (1979) found a volume dependence $\partial \ln T_K/\partial \ln V$ that ranged from -29 to as large as -134! In these systems the ambient-pressure Kondo temperature $T_K(0)$ varied from approximately 1 mK to 40 K, with the magnitude of $\partial \ln T_K/\partial \ln V$ being approximately inversely proportional to $T_K(0)$, i.e. the smaller $T_K(0)$ the greater its increase with pressure. Assuming a free-electron value for the volume dependence of the conduction band density-of-states, $\partial \ln N(E_F)/\partial \ln V = +0.67$, these huge changes in T_K imply $\partial \ln|J|/\partial \ln V = -4.5$ to -9.9. Unfortunately, a similar analysis has not been made for Kondo-impurity systems based on Sm, Eu and Yb (Maple et al. 1978), but there is no reason to believe that the results would be substantially different from Ce, except that the sign of $\partial \ln T_K/\partial \ln V$ should be positive for Yb since to first order it is the 4f hole-analog to Ce. By this we mean that for Yb the two relevant configurations are $4f^{14}$ and $4f^{13}$ which have a filled f-shell and one hole in the f-shell, respectively, but for Ce the relevant configurations are $4f^0$ and $4f^1$ which have no 4f electrons and one 4f electron, respectively.

Uranium and Pu, when dissolved in dilute amounts into a non-magnetic host such as Th or Zr, also display classic Kondo-impurity behavior (Maple et al. 1978). Again, direct measurements of the pressure dependence of T_K are few, but de Novion et al. (1982) have found that the Kondo temperature of U in ThS increases as $\partial \ln T_K/\partial P = 0.004$/kbar from its value of 141 K at ambient pressure. Taking a reasonable bulk modulus of 600 kbar for this system, implies $\partial \ln T_K/\partial \ln V = -2.4$, a value smaller but of the same sign as found in Ce systems. Because $T_K(0)$ is much larger than in the Ce systems considered by Schilling (1979), we would expect a relatively smaller $\partial \ln T_K/\partial \ln V$. The larger $T_K(0)$ for U is also consistent with the expectation that hybridization is generally stronger in 5f systems because of the greater spatial extent of 5f wavefunctions.

For a lattice of nearly localized Ce or U impurities in which $|J|$ is small, the application of pressure should enhance RKKY interactions and consequently T_N. However, for sufficiently high pressure, or equivalently large $|J|$, Kondo compensation of the local moments should dominate RKKY interactions and suppress the development of long-range magnetic order. This intuitive conclusion, which follows simply from considering that T_N depends geometrically on $|J|$ whereas T_K varies exponentially, is supported

theoretically by the work of Doniach (1977) who considered the competition between RKKY and Kondo interactions in a one-dimensional Kondo lattice. A schematic representation of these effects is shown in fig. 1, which is referred to as a Doniach phase diagram. Experimental verification of the qualitative behavior predicted by Doniach has come from pressure measurements on CeAg (Eiling and Schilling 1981) in which the magnetic transition increased initially with pressure, passed through a maximum and finally decreased at pressures above ~70 kbar. The competition between Kondo and RKKY interactions revealed in the pressure dependence of CeAg is in marked contrast to the pressure dependence of the ordering temperature in heavy lanthanide elements in which T_N or the Curie temperature T_C monotonically decreases with pressures up to 85 kbar, with essentially no change in the magnitude of the ordered moment (Rhyne 1972).

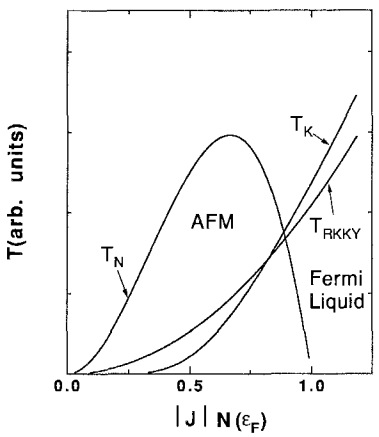

Fig. 1. Schematic phase diagram for a one-dimensional lattice of Kondo sites showing the Néel temperature, T_N, for antiferromagnetic order, the Kondo temperature, T_K, and the RKKY energy, T_{RKKY}, as a function of the product $|J|N(E_F)$, after Doniach (1977).

The extent to which pressure can promote a local/itinerant transition depends on the applied pressure and nearness of the material to Hill's criterion for magnetic instability. As a crude estimate, consider a hypothetical Ce- or U-compound with nearest f–f spacing of 4.5 Å, which is about 1 Å larger than Hill's criterion separating magnetic versus non-magnetic behavior. Taking a typical bulk modulus of 1 Mbar implies that a pressure of ~0.7 Mbar is required to reduce the f–f spacing by 1 Å. Thus, interactions, such as f-overlap, that depend linearly on f-atom spacing in general require substantial applied pressure for their change to be an important consideration. On the contrary, a comparable 25% decrease in lattice parameter would increase the Kondo temperature of a Ce impurity by a factor of roughly 20–90. In this case the Kondo temperature easily can exceed crystal-field splitting of the ground and first excited states and thereby change the effective degeneracy of the f-level. Hence, a much smaller pressure may be required for demagnetization in the Kondo regime than in the case of direct overlap.

For the itinerant systems (light actinides and α-like cerium compounds) there is less guidance from theory. As discussed above, the relationship between susceptibility $\chi(0)$ and specific heat coefficient γ is believed to be the same as for nearly localized heavy fermions, i.e., $\chi(0) \propto \gamma \propto 1/T_{sf}$. Hence, differences between the two cases may not be

distinguished by studies of the pressure dependence of these quantities. On the other hand it is possible that the resistivity varies differently with characteristic temperature $T_0(P)$ in the two cases; e.g., as T^2/T_0^n with $n=2$ for the localized case and $n \neq 2$ for the delocalized case.

1.5. *Thermodynamics of universality*

A number of important relationships between experimental quantities follow from combining thermodynamics (Maxwell relations) with the assumption that the free energy F obeys a scaling law: $F=F_0(T,V)+F_e(T,V)$ where the electronic contribution $F_e(T,V)=Nk_BTf(T/T_0(V))$ and where N is the number of atoms and T_0 is the characteristic energy. This may be T_K, T_{sf} or T_{vf}, depending on context. (Throughout this review we will often be non-specific but will simply use the symbol T_0 for the relevant characteristic energy scale.) As will be discussed in sect. 3, this form, valid for the Kondo problem, yields the relationship

$$\beta_e = \frac{\Omega_e C_e}{V B_T}, \tag{1}$$

where β_e and C_e are electronic contributions to the volume-thermal expansion coefficient and specific heat, B_T is the isothermal bulk modulus, V is the volume and Ω_e is an electronic Grüneisen parameter

$$\Omega_e = \frac{-\partial \ln T_0}{\partial \ln V}. \tag{2}$$

More generally the electronic Grüneisen parameter, which can also be written

$$\Omega_e = B_T \frac{1}{T_0}\frac{\partial T_0}{\partial P} \tag{3}$$

is a key parameter in determining the pressure dependence of essential thermodynamic quantities insofar as they obey a scaling law. For example, as $T \to 0$

$$\chi(0) \sim \frac{1}{T_0} \Rightarrow \frac{\partial \ln \chi}{\partial \ln V} \equiv \Omega_\chi = \Omega_e, \tag{4}$$

$$\rho(T) - \rho(0) \sim AT^2 \sim \left(\frac{T}{T_0}\right)^2 \Rightarrow \frac{\partial \ln \rho}{\partial \ln V} \equiv 2\Omega_A = 2\Omega_e, \tag{5}$$

$$C_p(T) = \gamma T \sim \frac{T}{T_0} \Rightarrow \frac{\partial \ln \gamma}{\partial \ln V} \equiv \Omega_c = \Omega_e. \tag{6}$$

(We distinguish here, for future convenience, Grüneisen parameters based on experimental measurements of χ, ρ and C_p.) A Grüneisen analysis can correlate measurements of the

pressure dependence of a large number of quantities to the ambient pressure specific heat and thermal expansion, given that single-energy scaling holds. Further, it can serve to determine the extent to which (i.e. the temperature intervals over which) universality is valid.

One of the consequences of universality, well known from the study of phase transitions, is that systems with different microscopic Hamiltonians can have similar behaviors. This may be an important contributing factor to the observation that despite the basic difference between lanthanides and actinides (localized vs. delocalized electrons) the heavy-fermion behavior is similar. To the extent that this is so, pressure studies will not distinguish the two cases. Conversely, it is only to the extent that universality is violated, or is not expected, that we can expect to observe differences between itinerant and localized systems. Apart from deviations from scaling in measurements where universal behavior is expected, we will show from measurements of magnetic phase boundaries and of X-ray absorption spectra that differences between lanthanide and actinide behaviors are observable.

1.6. *Scope of the review*

In addition to chapters in volumes 17–19 of this "Handbook" series, there have been a number of excellent reviews on anomalous 4f and 5f compounds as well as conferences dedicated to the physical properties of these systems. Some experimental reviews focus on single-ion Kondo properties of lanthanides and actinides at ambient (Maple et al. 1978) and high pressure (Schilling 1979), on the mixed-valence nature of lanthanide compounds at ambient (Lawrence, Riseborough and Parks 1981) and high pressure (Jayaraman 1978; Jayaraman 1979), on the effect of pressure on magnetic properties of actinide (Fournier 1985) and lanthanide intermetallics (Schilling 1981; Schilling 1986), and on the nature of physical properties and phase transitions in heavy-electron systems (Ott and Fisk 1987; Stewart 1984; Brandt and Moshchalkov 1984; Fisk et al. 1988a; Grewe and Steglich 1991). Particularly informative theoretical reviews include Schlottmann's (1989) on dilute mixed-valent and heavy-fermion systems, theories of heavy-electron systems (Lee et al. 1986) and pressure effects on the electronic structure of 4f and 5f materials (McMahan 1989). Recent conference proceedings on mixed-valence and heavy-electron behavior of rare earths and actinides at ambient and high pressure include the Fifth International Conference on Valence Fluctuations (Gupta and Malik 1987), Sixth International Conference on Crystal-Field Effects and Heavy-Fermion Physics (Assmus et al. 1988), International Conference on the Physics of Highly Correlated Electron Systems (Willis et al. 1990), Sixth International Conference on Valence Fluctuations (Barberis et al. 1991), and the International Conference on Strongly Correlated Electron Systems (Yanase 1993).

The intent here is to develop a perspective on the physics of lanthanide and actinide compounds, principally intermetallics, that exhibit Kondo-lattice/heavy-electron behavior and how that perspective derives from pressure-induced changes in physical properties. To keep the scope within a reasonable bound, the discussion will be limited primarily

to results obtained since the mid-1980's on Ce, Yb and U materials, although, for a proper perspective these bounds will be exceeded occasionally. In sect. 2 we review pressure effects on physical properties that are measured through specific heat, magnetic susceptibility and electrical transport. Thermodynamics of scaling behavior and Grüneisen relationships from ambient pressure measurements are presented in sect. 3. A critical discussion of results presented in sects. 2 and 3 will be given in sect. 4. Section 5 contains an overview of the pressure dependence of magnetic and superconducting phase transitions in principally heavy-electron compounds. We review studies of the pressure dependence of X-ray absorption spectra in sect. 6. Finally, in sect. 7 we will discuss basic conclusions drawn from this review concerning universality and differences between lanthanide and actinide compounds and suggest directions for future investigation.

2. Physical properties

In this section we describe how the specific heat, magnetic susceptibility and electrical resistivity of anomalous lanthanide and actinide intermetallics respond to applied pressure. Generally each subsection is organized by material type: first Ce-based compounds, then those based on Yb and finally U-based systems. Only in the last subsection on semiconductors are these systematics broken. Although on occasions we digress into a brief discussion of the experimental observations, the bulk of critical discussion related to data presented here and in sect. 3 is reserved for sect. 4.

2.1. *Specific heat*

Relatively few studies have been made of the effect of pressure on the specific heat of anomalous lanthanide and actinide compounds and, in these cases, to pressures less than 9 kbar. However, what data do exist provide a significant basis for interpreting other pressure-dependent quantities. The dramatic effect of pressure on the low-temperature specific heat of Ce-based heavy-electron compounds is typified by the response of $CeCu_6$ shown in fig. 2. In this case the Sommerfeld coefficient γ is depressed from 1.67 J/mol K^2 at ambient pressure to half this value at 8.8 kbar (Fisher et al. 1987a). This huge pressure dependence leads to a variation of the electronic Grüneisen parameter $\Omega_e = \Omega_c(T=0)$ from $\Omega_c = 115$ at low pressure to $\Omega_c = 65$–70 for $P > 3$ kbar. By assuming that $C_p(T,P)/T = \gamma(T)$ Phillips et al. (1987) have calculated the temperature dependence of $\Omega_c(T,P)$ at the different pressures (fig. 3). At low pressures Ω_c is positive at $T = 10$ K, negative at intermediate temperatures, and positive below 1.5 K. This temperature dependence, however, should not be confused with a temperature dependence of the electronic Grüneisen parameter $\Omega_e = -\partial \ln T_0 / \partial \ln V$ (Thompson et al. 1994). This can be seen most easily by noting that the curves for $\gamma(T)$ at different pressures are similar to those expected for the single-impurity Kondo problem, namely s-shaped with $\gamma(0) \propto 1/T_K$ and having an inflection point at $T_i \propto T_K$. Assuming that T_K increases with pressure, then $\gamma(0)$ decreases and T_i increases in such a way that the curves cross at some finite

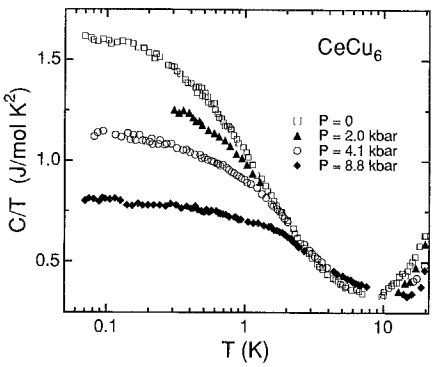

Fig. 2. Specific heat divided by temperature for $CeCu_6$ at various pressures as a function of $\log T$. Data from Phillips et al. (1987).

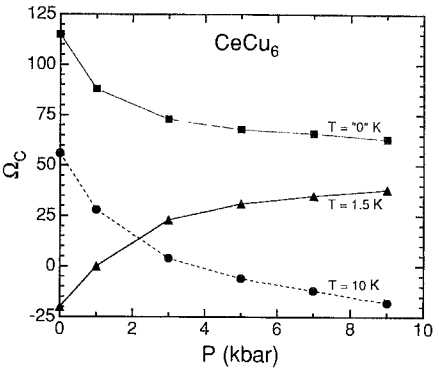

Fig. 3. Ω_c isotherms versus pressure for $CeCu_6$. Lines are guides only. Data from Phillips et al. (1987).

temperature. This leads to a region of negative $\Omega_c(T)$ even when Ω_e is constant with temperature.

If C_p obeys a scaling assumption $C_p(T,V)=C_p(T/T_0(V))=(T/T_0)\,g(T/T_0(V))$ where g is a universal function of T/T_0 and where the effect of P is to increase T_0 uniformly at all T, then the appropriate way to determine Ω_e is to find the temperatures $T_0(P)$ such that the scaled quantities $T_0(P)\gamma(T/T_0(P))$ all collapse on to a single universal curve, and then set $\Omega_e=(B/T_0(0))\partial T_0/\partial P$. Alternatively, under the scaling assumption, it is straightforward to show that $\Omega_c(T)$ only approaches the electronic Grüneisen parameter Ω_e at temperatures well below T_0. One way to estimate T_0 is to associate it with the Kondo temperature. Because the ground state of $CeCu_6$ is a doublet, the appropriate formula (Andrei et al. 1983) is $T_K=0.68R/\gamma$; this gives $T_K=3.5$ K for $\gamma=1.6$ J/mol K^2. The data of fig. 2 at fixed P are only constant for $T<0.1\,T_K$; and, hence, it is only in this region that Ω_c can be meaningfully associated with Ω_e. As we will see in sect. 3, Ω_e can be estimated from volume-thermal expansion measurements (de Visser et al. 1989b); for that measurement (fig. 28) values of Ω observed below 0.3 K are in good agreement with Phillip's result. For comparison between different experiments in different materials, it is thus important either that a scaling approach (collapse onto a single universal curve) be used or that only the lowest temperature data should be used. This statement applies to most of the other measurements discussed in this review. Low T values of Ω_c are compiled in table 1 for various Ce-based compounds. To date it has not been establishcd whether specific heat exhibits scaling over a broader temperature interval.

A similar behavior is found in $CeAl_3$ at pressures above 0.4 kbar (Brodale et al. 1986a). In this case, though, the $T\to 0$ value of Ω_c varies more rapidly with pressure (52 at 1 kbar to 15 at 8 kbar (Phillips et al. 1987)) even though values of C_p/T are comparable in $CeAl_3$ and $CeCu_6$. A notable difference between the two is that C_p/T for $CeAl_3$ passes over a maximum at 0.3 K that is suppressed rapidly with pressure, giving an estimated $\Omega_c(0.4\,\text{K})$ of 132 (Brodale et al. 1986a). This maximum in C_p/T was originally

Table 1
Summary of Grüneisen parameters Ω_c determined from pressure-dependent specific heat

Compound	Sommerfeld coefficient		Bulk modulus		Electronic Grüneisen parameter	
	γ (J/mol K^2)	Ref.	B (Mbar)	Ref.	Ω_c	Ref.
$CeAl_3$	1.2	1	0.46	2	160[a]	3
$CeCu_6$	1.67	3	0.91	4	115	3
$CeCu_2Si_2$	0.97[b]	5	1.25	6	80[b]	5
UBe_{13}	0.93[c]	3	1.03	7	63[c]	3
UPt_3	0.45	3	2.08	8	59	3
URu_2Si_2	0.064[d]	9	1.0[e]	–	36[d]	9
$YbCu_{4.5}$	0.70	10	1.0[e]	–	−23[f]	11
YbBiPt	⩾8.0[g]	10	1.0[e]	–	20[h]	13
YbCuAl	0.24	14	1.0[e]	–	−50	14

[a] At $T=0$ and $P=0.2$ kbar; this valuc is extremely pressure and temperature dependent.
[b] Value at 0.65 K, just above the superconducting transition temperature T_c and for $P>0.5$ kbar.
[c] At 1 K, just above T_c.
[d] At 1.5 K, just above T_c.
[e] Assumed value.
[f] Value at 0.5 K.
[g] Single-crystal result; part of this value may be due to a low-energy crystal-field Schottky anomaly (Thompson et al. 1993).
[h] Value at 0.4 K on crushed single crystals; this value decreases rapidly with increasing temperature.

References
(1) Brodale et al. (1986a)
(2) Niksch et al. (1980)
(3) Phillips et al. (1987)
(4) Shibata et al. (1986)
(5) Bleckwedel and Eichler (1985)
(6) Mock et al. (1985)
(7) Robinson et al. (1986)
(8) de Visser et al. (1987)
(9) Fisher et al. (1990)
(10) Fisk et al. (1988a)
(11) Amato et al. (1990)
(12) Fisk et al. (1991)
(13) Lacerda et al. (1992)
(14) Bleckwedel and Eichler (1981)

attributed to the manifestation of a second, strongly pressure dependent energy scale T_{coh} at which interactions between strongly renormalized quasiparticles become important. However, more recent muon-spin rotation experiments (Barth et al. 1987) find short range magnetic correlations developing on a temperature scale of 0.4 K. Though intersite magnetic correlations are generally believed to be important for the development of the low-temperature Fermi liquid (Bloch) state in heavy-electron systems, it is clear that $CeAl_3$ at ambient pressure is close to a magnetic instability. That the peak in C_p/T at ambient pressure is suppressed so rapidly, with no evidence for it above 0.3 K at 0.4 kbar, is not surprising because a large positive $\partial T_K/\partial P$ would lead to more nearly complete compensation of the interacting local moments.

The temperature derivative of the thermal expansion β is related thermodynamically to the pressure derivative of γ; $\partial\beta/\partial T|_P = -1/V\ \partial\gamma/\partial P$. Near and above 1 K, agreement between $\partial\gamma/\partial P$ (Brodale et al. 1986a) and thermal expansion measurements (Andres et al. 1975; Ribault et al. 1979) is reasonable for $CeAl_3$; both measurements give a Grüneisen parameter of about 50. At lower temperatures, though, there is both a sign and magnitude disagreement between these two measurements. Invariance of thermodynamics requires this disagreement to be resolved at lower temperatures and pressures (<0.4 kbar)

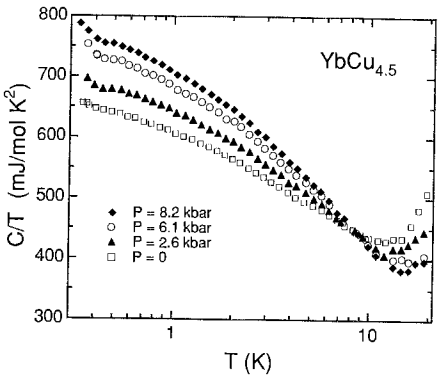

Fig. 4. Specific heat divided by temperature for $YbCu_{4.5}$ at various pressures versus $\log T$. Data from Amato et al. (1990).

than covered by the specific heat measurements. Most likely, the discrepancy arises from the extreme sensitivity to pressure of short-range magnetic correlations, which will be discussed further in sect. 3.2.2.

In contrast to the large, negative pressure derivative of γ in Ce-compounds, the Sommerfeld coefficient of YbCuAl increases with pressure at a relative rate of 0.05/kbar from its ambient pressure value of 240 mJ/mol K^2 (Bleckwedel and Eichler 1981). Although the bulk modulus is not known, if we assume a typical value (1 Mbar), then the Grüneisen parameter is $\Omega_c = -50$. By eq. (1), a negative Ω_c implies a negative thermal expansion. Indeed, the data of Pott (1982) to be discussed in sect. 3.2.1. show $\beta < 0$ and give an estimate $\Omega_e = -35$, in fair agreement with Ω_c. The negative Ω_c also implies that $\partial T_0/\partial P < 0$, or from a Kondo interpretation, that the exchange parameter J decreases with pressure. Intuitively this is reasonable because the trivalent state of Yb should be stabilized relative to the larger divalent state with increasing pressure and because the Kondo temperature goes to zero as trivalence is approached. The behavior described for YbCuAl is found as well in $YbCu_{4.5}$ and is shown in fig. 4 (Amato et al. 1990; Spendeler 1992a). At the lowest temperatures of these measurements, there is a weak upturn in C_p/T that becomes more pronounced with increasing pressure and that may reflect the onset of a phase transition to a magnetically ordered or superconducting state.

The only other example of an Yb-compound for which pressure-dependent specific heat measurements have been made is YbBiPt. This system is particularly interesting because it has a carrier density (about 5×10^{20} cm^3) typical of semimetals and an extremely large, low-temperature Sommerfeld coefficient $\gamma \geqslant 8$ J/mol K^2 that is essentially unaffected by an unconventional magnetic transition at 0.4 K (Fisk et al. 1991). In this case, the specific heat feature at 0.4 K associated with magnetism moves to higher temperatures, becomes broadened to look much like C_p/T versus T in $CeAl_3$ at ambient pressure, and decreases in magnitude with increasing pressure (Lacerda et al. 1992). This behavior is not expected in the light of results on YbCuAl and $YbCu_{4.5}$. However, at this time very little is known in detail about YbBiPt at ambient pressure, making interpretation of the pressure measurements difficult. It is in the regime of low carrier concentration where

Kondo and RKKY interactions may become poorly defined and strongly stress dependent. Thus, plausibly the pressure-dependent behavior described above reflects contributions not found in metallic heavy-electron systems.

The specific heat has been measured as a function of pressure for only three anomalous actinide compounds UPt_3 (Brodale et al. 1986b), UBe_{13} (Phillips et al. 1987) and URu_2Si_2 (Fisher et al. 1990); all are superconductors, with transition temperatures of 0.5, 0.9, and 1.5 K respectively, which makes an accurate estimate of the $T \to 0$ specific heat more difficult. Nevertheless, it is clear that in these cases the electronic specific heat is depressed strongly by pressure, as in the case of Ce compounds. Inspection of table 1 shows that the Grüneisen parameter is comparably large and positive for U and Ce materials. The specific heat of UPt_3 has the form $C_p/T = \gamma + dT^2 \ln T + eT^2$ at ambient pressure (Phillips et al. 1987). This existence of the $T^2 \ln T$ term was taken originally (Stewart et al. 1984) to imply the presence of paramagnetic spin fluctuations; although, it is now believed to arise more generally within Fermi-liquid theory (Pethick et al. 1986). In any event this contribution to C_p/T is suppressed extremely rapidly with pressure. Interestingly, the zero-temperature Grüneisen parameter for UPt_3 is nearly constant (Phillips et al. 1987) as a function of pressure, as it is for YbCuAl (Bleckwedel and Eichler 1981), but not in $CeCu_6$, $CeAl_3$ or UBe_{13} (Phillips et al. 1987).

2.2. *Susceptibility*

An additional benefit of susceptibility relative to specific heat measurements is that in non-cubic compounds information about anisotropic interactions may be obtained provided studies are made on single crystals. We consider first, however, a cubic compound $CeSn_3$ that is considered to be weakly mixed valent (Lawrence et al. 1981). Below room temperature its magnetic susceptibility increases with decreasing temperature, reaches a maximum χ_m near $T_m = 140$ K and then decreases to a modestly large $T = 0$ value, 1.9×10^{-3} emu/mol (provided a small, low-temperature "Curie tail" consistent with less than 1% Ce^{3+} impurities is subtracted) (Shaheen et al. 1983). This general temperature dependence is well-described by a Bethe Ansatz solution of the Coqblin–Schrieffer model of Kondo impurities of arbitrary total angular momentum J (Rajan 1983; Schlottmann 1989). For Ce^{3+} in the absence of crystal-field effects $J = 5/2$ and this theory predicts a single-impurity Kondo temperature $T_K \cong 3\,T_m$, which for $CeSn_3$ corresponds to about 420 K, a value larger than typical crystal-field splittings in Ce compounds.

Results of pressure measurements (Shaheen et al. 1983) on single crystal $CeSn_3$ are shown in fig. 5. In this figure, a low-temperature "Curie-tail" and non-4f contribution, given by the susceptibility of $LaSn_3$, have been subtracted from the raw data to give the temperature-dependent 4f contribution from $CeSn_3$. With increasing pressure T_m increases at a rate of about 3.4 K/kbar and the magnitude of χ decreases at all temperatures. From $\Omega = (B/T_m)\partial T_m/\partial P$ we obtain $\Omega = 13$ but from pressure-induced changes in $\chi(0)$, we estimate a magnetic Grüneisen parameter $\Omega_\chi \equiv \partial \ln \chi(0)/\partial \ln V = 9 \pm 1$, where the variation arises from the pressure interval over which Ω_χ is determined. In this calculation, a bulk modulus of 543 kbar (Takke et al. 1980) has been used. This relatively

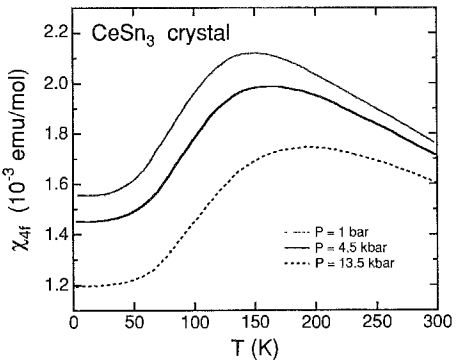

Fig. 5. Cerium 4f contribution to the susceptibility of single-crystal $CeSn_3$ at various pressures versus temperature. χ_{4f} was obtained by subtracting an "impurity trail" given by $\chi_{imp} = 0.0026/(T+3.2)$ and $\chi(T)$ of $LaSn_3$ at ambient pressure. The corrections to $\chi(T)$ for $CeSn_3$ are assumed to be pressure independent. Data are from Shaheen et al. (1983).

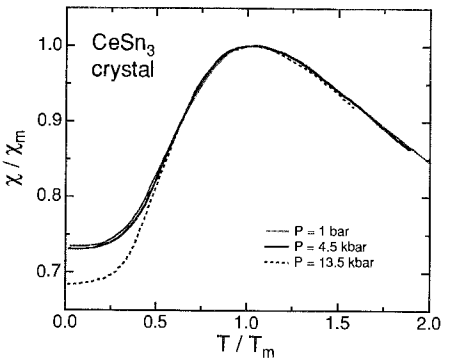

Fig. 6. Data of fig. 5 normalized by the maximum susceptibility $\chi_m \equiv \chi(T = T_m)$ which occurs at a temperature T_m versus reduced temperature.

small Grüneisen parameter, compared to those of Ce compounds in table 1, may reflect the much larger characteristic energy scale in $CeSn_3$, which has an ambient pressure $\gamma \approx 53\ \mathrm{mJ/mol\,K^2}$ (Lawrence et al. 1981). As discussed above in the Introduction and elaborated on in sect. 4 below, there appears to be an inverse relationship between Ω and T_0.

Shaheen et al. (1983), following an analysis applied to the series $CeIn_{3-x}Sn_x$ by Lawrence (1979), showed that the pressure-dependent susceptibility of $CeSn_3$ could be scaled onto a universal curve of the form $\chi T/C$ vs $T/T_{1/2}(P)$, where C is the Curie constant and $T_{1/2}(P)$ is defined as the temperature where $\chi T/C = 0.5$. The pressure-induced increase in $T_{1/2}$, within the framework of a Kondo-impurity model, is consistent with an increase in width Δ of the hybridized 4f level and not a shift of E_f toward the Fermi energy. Figure 6 shows that scaling also results if the data are plotted as $\chi(T)/\chi_m$ vs T/T_m. The maximum deviation from scaling, ~5%, occurs at the lowest temperatures and highest pressure where corrections to the data given in fig. 5 are the largest and most uncertain. Figure 6 appears to have two scaling parameters, χ_m and T_m; however, because scaling holds to $T = 0$, where $\chi(0)$ is inversely proportional to some characteristic energy T_0, and $T_m \propto T_0$, there is only single-parameter scaling. A point to emphasize is that, when data scale, any arbitrary energy works equally well and a unique identification of the essential energy scale should come from firm theoretical underpinning.

The pressure-dependent anisotropic susceptibility has been studied (for $T \leqslant 40\ \mathrm{K}$) in the tetragonal heavy-electron material $CeRu_2Si_2$ (Voiron et al. 1988). For a magnetic field applied along the c-axis, χ_c exhibits a weak maximum near $T_m = 10\ \mathrm{K}$ at $P = 0$ that becomes less pronounced and moves to approximately 30 K at $P = 5.7$ kbar. On the other hand, H perpendicular to the c-axis gives a weakly temperature-dependent susceptibility

that, from a crystal-field analysis, is shown to be dominantly a Van Vleck susceptibility and is only about 7% of χ_c at 4.2 K. With increasing pressure the anisotropy in χ decreases by 50% at 5.7 kbar and 4.2 K, principally because the Van Vleck contribution is only weakly pressure dependent. The magnetic Grüneisen parameters for H parallel and perpendicular to the c-axis are 171 and 70, respectively, assuming a bulk modulus of 1 Mbar. Such a large Grüneisen parameter for χ_c implies the dominance of a small energy scale, e.g., T_m or $T_K(P=0) \approx 24$ K extracted from specific heat measurements (Besnus et al. 1985). In either case, even at 6 kbar these characteristic scales remain less than the crystal-field splitting, derived from inelastic neutron scattering (Dakin et al. 1992) to be on the order of 400 K.

As was found for $CeSn_3$, a plot of $\chi_c T/C$ versus $T/T_{1/2}(P)$ scales all the $CeRu_2Si_2$ data onto a universal curve, with only slight deviations for T greater than two-to-three times $T_{1/2}$ (Voiron et al. 1988). Comparably good scaling was found if $T_m(P)$ was used to scale the curves instead of $T_{1/2}(P)$. This observation of scaling is particularly important in two respects. The first is that scaling of the form $\chi T/C$ versus $T/T_{1/2}(P)$ or $T/T_m(P)$ is equally valid independent of the ground-state degeneracy of the Ce ion: both $CeSn_3$ (degeneracy 6) and $CeRu_2Si_2$ (degeneracy 2) show such scaling but with different curves in each case. The second is that scaling holds in $CeRu_2Si_2$ at low temperatures where inelastic neutron scattering shows (Rossat-Mignod et al. 1988) the coexistence of strong intersite magnetic correlations that are incommensurate with the crystallographic lattice and of Kondo-like scattering with an energy scale of 23 K. The application of a sufficiently large magnetic field causes the incommensurate correlations to collapse, resulting in a metamagnetic transition at $H_m = 8.3$ T which is seen as a peak in isothermal $\partial\chi_c/\partial H$ and $\rho(H)$ plots. Mignot et al. (1988) have shown that the energy scales $1/\chi(0)$, T_m and H_m, normalized to their ambient-pressure values, have a common pressure dependence (fig. 7) with Grüneisen constant equal to 171. As will be discussed in sect. 2.2, the energy scale that characterizes the T^2-coefficient of resistivity ($1/\sqrt{A}$) also has the pressure dependence given in fig. 7. The comparison between $CeSn_3$ and $CeRu_2Si_2$ is significant in that scaling is valid in these two cases even though the microscopic physics (mixed valence vs. coexistence of heavy-fermion behavior and magnetic correlations) is quite different.

Less thorough studies have been made of the pressure-dependent susceptibility of a number of other Ce-based intermetallics, most of which have a characteristic temperature scale that is comparable to or greater than crystal-field splitting. As with $CeSn_3$, their magnetic Grüneisen parameters are correspondingly small. Table 2 shows that in all cases Ω_χ is positive, indicating that the characteristic scale on which the correlated electron state develops increases with pressure. In table 2 we have indicated the relative magnitudes of the characteristic temperature for these materials. Generally, a large energy scale implies that the characteristic correlated-electron energy scale is larger than Δ_{CF}. It should be pointed out that values of Ω_χ deduced from room-temperature values of $\partial\chi/\partial P$ for $CeSn_3$, $CeBe_{13}$ and $CePd_3$ are consistently smaller than the values of Ω_e deduced from thermal expansion (sect. 3). As was also noted in the discussion of specific heat, Ω_c is obtained most reliably by overall scaling of $\chi(T)/\chi_m$ versus T/T_m with $\Omega_e = -\partial \ln T_m/\partial \ln V$ or from a determination of Ω_χ at very low temperatures ($T \ll T_m$).

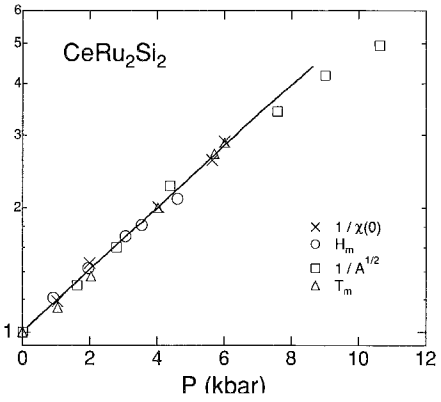

Fig. 7. Pressure dependence of the inverse susceptibility $1/\chi(0)$, metamagnetic field H_m, temperature T_m of the maximum in χ_c and inverse square root of the T^2 coefficient of resistivity $1/\sqrt{A}$ of $CeRu_2Si_2$ normalized to their respective values at ambient pressure. The solid line represents a Grüneisen parameter of 171. Data are from Mignot et al. (1988).

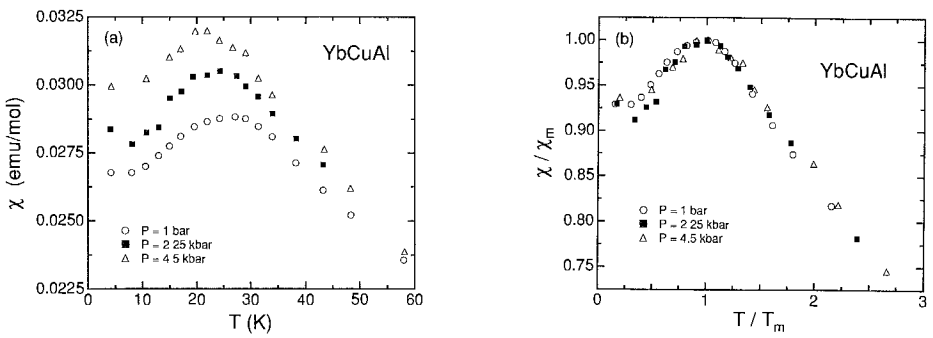

Fig. 8. (a) Pressure dependence of the magnetic susceptibility of polycrystalline YbCuAl at temperatures below 60 K, after Mattens et al. (1980). (b) Temperature-dependent susceptibility of YbCuAl, normalized to its value at T_m, as a function of reduced temperature. Note that no background subtraction has been performed.

Contrary to Ce-based compounds, the magnetic Grüneisen parameters of Yb-based materials are negative, as found in specific-heat measurements. Ambient-pressure properties of Yb-compounds listed in table 2 have been reviewed by Fisk and Maple (1992). Although by the designation used in table 2 all of these compounds have a large energy scale, in some cases, e.g., $YbCu_2Si_2$ and YbCuAl, the low-temperature Sommerfeld coefficients are substantial, $\geqslant 200\,\mathrm{mJ/mol\,K^2}$. Zell et al. (1981) have found that the maximum value of $\partial \ln\chi/\partial P$ occurs for the Yb valence at 2.5. This interesting observation contradicts the systematics of Ce compounds, in which $\partial \ln\chi/\mathrm{d}P$ is largest for systems with smaller characteristic energy scales, ie., more nearly integrally valent. However, the conclusion is based primarily on room-temperature data for $\partial\chi/\partial P$ (see also table 2) and hence subject to the same uncertainty as for Ce compounds mentioned above. For resolution of this apparent difference between Ce and Yb compounds and for understanding the extent to which Yb compounds are 4f-hole analogues of their Ce counterparts, systematic investigation of overall scaling in Yb intermetallics is necessary. In this regard we have plotted the pressure-dependent susceptibility data of

Table 2
Comparison of magnetic Grüncisen parameters Ω_χ determined from pressure-dependent susceptibility measurement

Compound[a]	$-\partial\ln\chi/\partial P$		Bulk modulus		Ω_χ	Energy scale[b]
	Mbar^{-1}	Ref.	Mbar	Ref.		
p-$CeBe_{13}$	9.7[c]	1	0.88	1	8.6	ls
p-$CePd_3$	4.3[c]	1	1.02	2	4.4	ls
p-$CeRh_2$	5.0[c]	1	0.70	1	3.5	ls
p-$CeSn_3$	4.7[c]	1	0.54	2	2.6	ls
s-$CeSn_3$	16.6	3	0.54	2	9.0	ls
p-$CeNi_2Ge_2$	37	I	0.42	1	15.5	ss
p-$CePt_2Si_2$	26	4	1.0[d]	–	26	ss
p-CeRhPt	21	1	1.0[d]	–	21	ss
s-$CeRu_2Si_2$	171[e]	5	1.05	6	171	ss
s-$CeRu_2Si_2$	70[e]	5	1.05	6	70	ss
p-YbCuAl	−26	7	1.0[d]	–	−26	ls
p-$YbCu_2Si_2$	−3.6[c]	8	0.92	9	−3.3	ls
p-YbInAu	−11[c]	8	1.0[d]	–	−11	ls
p-YbInPd	−64[c]	8	1.0[d]	–	−64	ls
p-$YbNi_2Ge_2$	−3.1[c]	8	1.0[d]	–	−3.1	ls
p-$UA1_2$	25	10	0.74	11	18	nd
p-UBe_{13}	9	12	1.03	13	9	nd
s-UCd_{11}	15[f]	14	1.0[d]	–	15	nd
p-UPt_3	24	15	2.08	11	50	nd
s-UPt_3	28[g]	16	2.08	11	58	nd
s-UPt_3	5[h]	16	2.08	11	10	nd
s-URu_2Si_2	29[i]	16	1.0[d]	–	29	nd

[a,b] Abbreviations: p, polycrystal; s, single crystal; ls, large energy scale; ss, small energy scale; nd, not determined.
[c] Room temperature valuc.
[d] Assumed value.
[e] Larger value is for $\boldsymbol{H} \parallel$ tetragonal c-axis, smaller value for $\boldsymbol{H} \perp c$.
[f] Value at 10 K.
[g] For H in the hexagonal basal plane.
[h] for H parallel to the c-axis.
[i] for H parallel to the tetragonal c-axis.

References

(1) Zell et al. (1982)
(2) Takke et al. (1980)
(3) Shahcen et al. (1983)
(4) Ayache et al. (1987)
(5) Voiron et al. (1988)
(6) Lacerda et al. (1989a)
(7) Mattens et al. (1980)
(8) Zell et al. (1981)
(9) Mock et al. (1985)
(10) Fournier and Beille (1979)
(11) de Visser et al. (1987)
(12) McElfresh et al. (1993)
(13) Robinson et al. (1986)
(14) Thompson et al. (1989a)
(15) Willis et al. (1985)
(16) Louis et al. (1986)

Mattens et al. (1980) for YbCuAl (fig. 8a) as $\chi(T)/\chi_m$ versus T/T_m, shown in fig. 8b, and find reasonably good scaling over the temperature range covered by these measuremcnts. In the case of YbCuAl, T_m decreases linearly from an ambient-pressure value of 26.9 K to 21.8 K at 4.5 kbar, which gives $\partial \ln T_m/\partial P = -0.04\,\text{kbar}^{-1}$ and hence $\Omega_e = -40$, in

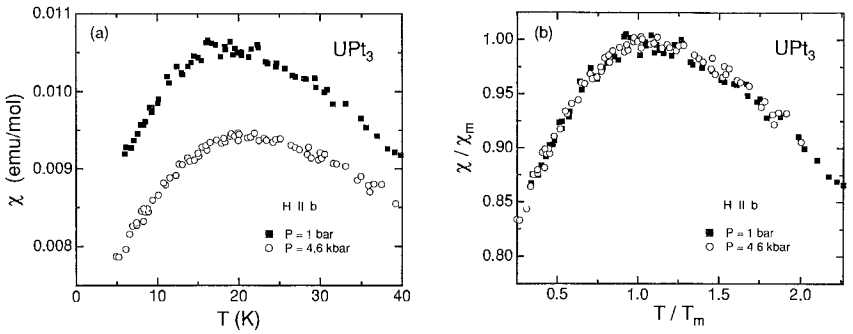

Fig. 9. (a) Susceptibility of single-crystal UPt_3 at ambient and 4.6 kbar pressures as a function of temperature. Measurements were performed with a field of 5 T applied parallel to the b-axis. (After de Visser et al. 1987.) (b) Data of part (a) normalized to isobaric values of T_m versus reduced temperature T/T_m.

reasonable agreement with Ω_c. Alternatively, we can attempt to estimate this from low-temperature values of $\partial\chi/\partial P$, but because of the relatively large scatter in the low-temperature data of fig. 8a and of the absence of pressure-dependent data on a non-magnetic analogue, e.g., LuCuAl, it is not possible to extract a meaningful value of Ω_χ at low temperatures for this compound. A crude estimate, though, gives $\Omega_\chi(T \to 0) = -26$ which is about one order-of-magnitude more negative than the value reported by Zell et al. (1981) at room temperature, and comparable to Ω_c (table 1).

The anomalous U-intermetallics UAl_2, UPt_3, URu_2Si_2 and UBe_{13} all display a negative pressure derivative of their susceptibility (see table 2). Of these, only UAl_2 does not undergo a phase transition. The overall shape of $\chi(T)$ for UAl_2 remains unchanged at pressures to 6.65 kbar (Fournier and Beille 1979), suggesting that the isobaric curves should scale. Unfortunately, the pressure dependence of a non-magnetic reference compound was not measured so that scaling cannot be tested quantitatively.

UPt_3 is a particularly interesting compound for comparison to $CeRu_2Si_2$ because, like $CeRu_2Si_2$, UPt_3 has a metamagnetic transition, albeit at a higher field $H_m = 21$ T (Frings et al. 1983), and both have similar Sommerfeld coefficients (de Visser et al. 1987). Notable differences, however, are that metamagnetism appears in the hexagonal basal plane of UPt_3 but along the tetragonal c-axis of $CeRu_2Si_2$ and that UPt_3 superconducts below 0.5 K whereas $CeRu_2Si_2$ remains paramagnetic to 30 mK.

Shown in fig. 9a is $\chi(T)$ for H parallel to the b-axis of UPt_3 at ambient pressure and 4.6 kbar. The maximum in χ at $T_m = 17.6$ K for $P = 1$ bar increases to 19.6 K with applied pressure giving $\Omega = (B/T_m)\partial T_m/\partial P = 51$ and the overall magnitude of $\chi(T)$ decreases at a rate of -28 ± 3 Mbar^{-1} (de Visser et al. 1987) giving $\Omega_\chi = 58$. Both values of the Grüneisen parameters agree well with estimates of Ω_e from thermal expansion (sect. 3). For H along the c-axis (not shown), χ is only weakly temperature and pressure dependent, $\partial \ln \chi_c/\partial P = -5 \pm 3$ Mbar^{-1} (de Visser et al. 1987). Both values agree well with those obtained (de Visser et al. 1986) from forced magnetostriction but are nearly an order-of-magnitude smaller than in $CeRu_2Si_2$. However, the dependence of H_m, determined

resistively in UPt_3 (Bakker et al. 1992a), is the same as χ for H along the b-axis. In fig. 9b we plot χ/χ_m versus T/T_m for UPt_3 and see that this normalization produces scaling between the two data sets given in fig. 9a. Therefore, as with $CeSn_3$ and YbCuAl, scaling of the form given in fig. 6 suggests that the physics responsible for the maximum in χ at low temperature determines the magnitude of χ as $T \to 0$ and the response of $\chi(T)$ to pressure. Again, though, we emphasize that as with $CeRu_2Si_2$ the physics producing χ_m in UPt_3 is different than in $CeSn_3$ or YbCuAl.

URu_2Si_2 is a very complicated system in that below 17.5 K antiferromagnetic order develops with an ordered moment of only $0.03\pm0.01\,\mu_B$ (Broholm et al. 1987a) in which spins point along the tetragonal c-axis. This transition is followed at 1.5 K by superconductivity (Maple et al. 1986, Palstra et al. 1985). An analysis of thermal-expansion and specific-heat measurements is consistent with a magnetic crystal-field singlet ground state, with crystal-field effects dominating even in the temperature range 20–40 K (Franse et al. 1987). Louis et al. (1986) have measured the magnetization of URu_2Si_2 at 4.2 K, for H along the c-axis, and at pressures of 0.001 and 4.6 kbar. From these measurements, they find that χ_c decreases at a rate of $-29\pm5\,\text{Mbar}^{-1}$, a value comparable to that of UPt_3 for H perpendicular to its c-axis. The authors also comment that for temperatures between 20 and 30 K the relative rate of χ suppression with pressure is reduced to a value of $-21\pm5\,\text{Mbar}^{-1}$. Whether this change in $\partial \ln\chi/\partial P$ is due to weak antiferromagnetism or crystal-field effects remains to be determined. Certainly, it would be extremely useful to obtain a more comprehensive set of data on URu_2Si_2 for comparison to isostructural $CeRu_2Si_2$.

The susceptibility decrease with pressure in UBe_{13} is anomalously small, never exceeding a relative rate of $-10\,\text{Mbar}^{-1}$ for the temperature and pressure range of the measurements, $1.5 < T < 300$ K and $0 \leqslant P < 8$ kbar, respectively (McElfresh et al. 1993). In cases where comparison of Ω_c and Ω_χ values can be made in tables 1 and 2, we see that with the exception of UBe_{13} these values agree reasonably well. Given the relatively large Sommerfeld coefficient of UBe_{13}, we would expect a correspondingly large Grüneisen parameter, which is not the case for Ω_χ. Therefore, among lanthanide and actinide heavy-electron materials, the susceptibility response to pressure for UBe_{13} seems quite anomalous. At ambient pressure, the ratio $\chi(0)/\gamma(0)$ (also called the Wilson ratio) is close to unity, as is the case for UPt_3 (Ott and Fisk 1987). The observation that Ω_c is much larger than Ω_χ implies that with applied pressure the Wilson ratio exceeds unity and UBe_{13} tends to become "more magnetic" (Thompson et al. 1987a). We will further discuss this point in sect. 4.

2.3. *Resistivity*

Electrical resistivity has been a popular means of studying the pressure response of anomalous lanthanide and actinide compounds, both because of the relative simplicity of the measurement and because techniques are readily available for extending the measurements to pressures substantially higher than achievable with specific heat or susceptibility. Consequently, there is a rather large body of $\rho(T,P)$ data that can be chosen

to illustrate trends among various systems. In this selection process we will focus on materials that do not order magnetically, principally because the pressure-induced change in $\rho(T)$ tends to be more pronounced than in those that do order. The reason for this will be discussed in sect. 5.1., where some resistivity data also will be given for magnetically ordered compounds.

2.3.1. *Electronically correlated metals*

As mentioned in the Introduction, the application of only tens of kilobars pressure may be expected to modify the ground-state degeneracy in those materials having a characteristic electronic energy scale that is smaller than Δ_{CF}. Therefore, it is instructive first to consider materials in which this condition is established already at ambient pressure, ie., Ce-based mixed-valence compounds. A classic example is α-Ce, which exhibits many of the characteristics common to mixed-valence Ce intermetallics. At the lowest pressure of their measurements on α-Ce (3.2 kbar, which was required to suppress the existence of some β-Ce), Katzman and Mydosh (1972) found the low-temperature resistivity to increase as AT^2, with the T^2-coefficient taking a value $A \approx 4.5 \times 10^{-3}$ μΩ cm/K^2. This T^2-dependence held in the temperature range 1 to about 7 K. With increasing pressure, A decreased markedly and the temperature interval over which $\rho \propto AT^2$ increased. Accompanying these changes was an overall decrease in the magnitude of $\rho(T)$ below 80 K, including $\rho(0)$. A plot of $1/\sqrt{A}$ versus pressure gives an approximately linear relationship with a slope of about 5 K/kbar (μΩ cm)$^{1/2}$. Because A should be inversely proportional to the square of a characteristic energy scale, the linear increase in $1/\sqrt{A}$ implies a linear increase in this scale with applied pressure. Voronov et al. (1979) have reported a bulk modulus for α-Ce in the range 150–300 kbar; hence the Grüneisen parameter $\Omega_A \equiv B\,\partial \ln(1/\sqrt{A})/\partial P = 50$–$100$.

A similar behavior has been found in $CeSn_3$ (Thompson et al. 1994). In this case, though $\rho \propto T^3$ at the lowest temperatures, we found that $\rho \propto T^2$ over an extended temperature range and the T^2-coefficient decreased from its 1-bar value of $\sim 1.1 \times 10^{-3}$ μΩ cm/K^2 at a rate $\mathrm{d}(1/\sqrt{A})/\mathrm{d}P \approx 0.4$ K/kbar (μΩ cm)$^{1/2}$. Taking the bulk modulus of $CeSn_3$ to be 0.54 Mbar (Takke et al. 1980) gives a Grüneisen parameter for $1/\sqrt{A}$ of 7, a value that agrees well with Ω_χ at low temperatures (table 2). Figure 10a shows the response of polycrystalline $CeSn_3$ to pressure where we see behavior similar to that just described for α-Ce. Given scaling found for $\chi(T,P)$, we have normalized the temperature axis by $T_0(P) \propto 1/\sqrt{A}(P)$ and plotted $\rho(T,P)$ versus $T/T_0(P)$ in fig. 10b. As can be seen, this normalization collapses the data onto a common curve at low ($T \leqslant 50$ K) and possibly high temperature; however, scaling does not work well at intermediate temperatures. There could be several reasons for this: (1) A single-energy scale determined at low temperatures may not reflect the physics at higher temperatures, e.g., phonons may be important. In fact, the phonon contribution to $\rho(T)$ has not been subtracted from these data. This observation applies as well to estimates of Ω from inflection temperatures $T_i(P)$ or temperatures of resistivity maxima $T_m(P)$ when phonon scattering is appreciable at those temperatures. For example, the value of Ω obtained from $\partial T_i/\partial P$ for $CeSn_3$ is 18

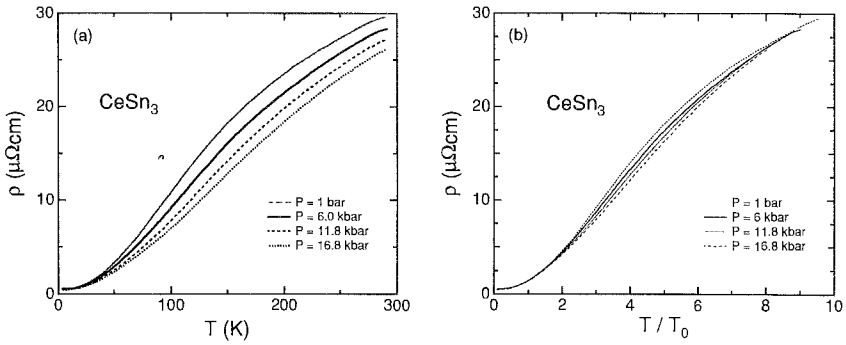

Fig. 10. (a) Temperature-dependent resistivity of $CeSn_3$ at various pressures. (b) Data of part (a) in which the temperature scale has been normalized by a factor $T_0(P)$ which is the inverse square root of the low-temperature T^2-coefficient of resistivity. Actual units on the horizontal axis are then $(\mu\Omega\,\mathrm{cm})^{1/2}$.

(tables 3 and 6), a value two times larger than most other estimates of Ω. (2) Thermal contraction of the sample upon cooling causes the curves to be substantially non-isobaric. (3) It is known that pressures generated in self-clamping cells, such as the one used in these experiments, are a function of temperature (Thompson 1984). Given these caveats, it is indeed surprising to find scaling of any physical quantity over an appreciable high temperature range.

$CePd_3$ is in many respects similar to $CeSn_3$ (Lawrence et al. 1981). However, $\rho(T)$ for $CePd_3$ is substantially different, exhibiting a maximum near $T_m = 125$ K and an overall magnitude roughly a factor of five larger than in $CeSn_3$. These differences may arise from details of the ligand 5s,p and Ce-5d band structures (Lawrence et al. 1985a). The application of pressures less than 16 kbar causes T_m to increase at a rate of between 0.67 (Oomi et al. 1990) and ~1 K/kbar (Lawrence et al. 1985a) and the room-temperature resistivity to increase at a relative rate of about 0.005 kbar. The latter observation is contrary to that in $CeSn_3$, which does not exhibit a maximum in $\rho(T)$. Lawrence et al. (1985a) showed that, if the resistivity, normalized to its maximum value at T_m, is plotted as a function of T/T_m, the $\rho(T,P)$ data scale reasonably well onto a universal curve for the entire range of temperatures ($1.5 < T < 300$ K) and pressure ($P \leqslant 15.5$ kbar) investigated. Given $\partial T_m/\partial P = 1$ K/kbar, we calculate a Grüneisen parameter of 8, which agrees fairly well with the value of 10 obtained from thermal expansion (sect. 3.2.1). Scaling, however, was not quite as good at temperatures below about 40 K, where Lawrence et al. (1985a) found a small pressure dependence of $\rho(T)$, even though a well-defined T^2-resistivity behavior was observed ($A = 72 \times 10^{-3}$ μΩ cm/K^2 at ambient pressure) for $T < 10$ K. From these observations and those made on the pressure-dependent resistivity of $Ce_{0.97}La_{.03}Pd_3$, the argument was made that 40 K represented a second energy scale T_{coh}, related to the single-ion Kondo or spin-fluctuation scale by a factor of $1/(2J+1)$ where $J = 5/2$ for Ce^{3+}, over which coherence developed among spin and valence fluctuations on different Ce sites. That the coherence temperature should be related to the single-site scale through the orbital degeneracy, $N = 2J+1$, was suggested originally by Anderson

Table 3
Pressure dependence of resistivity features

Compound	Bulk modulus		$T_0(P=0)$[a]		$\partial T_0/\partial P$		$A(P=0)$[b]		$\partial(1/\sqrt{A})/\partial P$		E.S.[c]
	Mbar	Ref.	K	Ref.	K/kbar	Ref	μΩ cm/K²	Ref.	$\left(\frac{(\mu\Omega\,\mathrm{cm/K^2})^{-1/2}}{\mathrm{kbar}}\right)$	Ref.	
$CeAl_3$	0.46	1	31	2m	2.5[d]	2	35	3	0.14[e]	2	ss
$CeCu_6$	0.91	4	15[f]	5m	2.1[f]	5	14.40[g]	6	0.32	7[h]	ss
$CePd_3$	1.02	8	124	9m	1.0	9	0.072	9	0.006	9	ls
	–	–	–	–	0.7	10	0.073	10	0.05	10	–
$CeSn_3$	0.54	8	88	11i	2.9	11	0.011	11	0.4	11	ls
Ce_3Al	nd	–	15[i]	12i	3.6[i]	–	nd	–	nd	–	ss
Ce_3In	nd	–	2.2	12i	1.5	12	nd	–	nd	–	ss
Ce_3Sn	nd	–	6.2	12i	1.8	12	~0.5	13	nd	–	ss
$Ce(In_{0.8}Sn_{0.2})_3$	nd	–	21	14m	~2.5[j]	14	nd	–	nd	–	ss
$CeCu_2Si_2$	1.25	15	23	16m	0.4[k]	17	10[l]	18	nd	–	ss
$CeInCu_2$	0.91	19	27	19m	1.9	19	0.5	19	0.05	17	ss
CePtSi	1.08	20	23	20m	1.1	20	nd	–	nd	–	ss
$CePt_2Si_2$	nd	–	66	21m	1.8	21	0.11	21	0.18	21	ss
	nd	–	77	22m	2.1	22	nd	–	nd	–	ss
$CeRu_2Si_2$	1.05	23	nd	–	nd	–	0.40	24	0.28	24	ss
$CeAgCu_4$	nd	–	60	25m	3.0	25	nd	–	nd	–	ss
$YbCu_{4.5}$	nd	–	19	26m	−0.21	26	0.1	26	<0	26	ss
$YbAgCu_4$	nd	–	23	25i	−0.4	25	0.66	25	−0.11[m]	25	ls
YbCuAl	nd	–	28	27[n]	−0.9	27	nd	–	nd	–	ls
$YbCu_2Si_2$	0.92	15	195	25m	−6.5	25	0.04	25	−0.26[o]	25	nd
$YbRh_2Si_2$	nd	–	111	25m	−1.9	25	nd	–	nd	–	nd
UAl_2	0.74	28	26	29[p]	0.77	29	0.04	29	0.13	29	nd
UBe_{13}	1.03	30	2.3	31m	0.23[q]	31	23[r]	31	0.0034[s]	31	nd
UPt_3	2.08	32	6.5[t]	32i	0.24[t]	32	1.6–0.7[u]	32	0.035[v]	–	nd
URu_2Si_2	nd	–	73	33m	1.4	33	0.18	34	>0	33	nd

[a] T_m or T_i, indicated by the letter following the reference number.
[b] A, coefficient of the T^2 term in the resistivity.
[c] Energy scale: ss, small electronic energy scale; ls, large electronic energy scale; nd, not determined.
[d] Value for $8.2 < P < 16.8$ kbar; for $P < 3$ kbar, $\partial T_0/\partial P \approx 0.9$ K/kbar.
[e] Approximate value for $P > 5$ kbar; at lower pressures the value is slightly negative.
[f] Values for $P < 18$ kbar.
[g] Value depends on crystallographic direction.
[h] For $P > 25$ kbar.
[i] At ambient pressure Ce_3Al undergoes a first-order phase transition near 115 K that resembles the γ–α transition in elemental Ce and that is suppressed for $P > 8$ kbar. The value given is for $P = 8.5$ kbar.
[j] Value for $P > 7$ kbar.
[k] For $P < 20$ kbar; above 30 kbar the value increases to 1.1 K/kbar.
[l] The pressure dependence of A has been studied only for $P > 80$ kbar (Bellarbi et al. 1984).
[m] Value for $P < 5$ kbar; above 5 kbar the value is −0.05.
[n] T_0 is somewhat arbitrarily defined here.
[o] Value for $P < 5$ kbar; at higher P the value is −0.1.
[p] See text for the definition of T_0 in this case.
[q] Above about 30 kbar the value becomes 0.65 (McElfresh et al. 1990).
[r] Extrapolated to $P = 0$ from above 4 kbar.
[s] Above about 50 kbar the value becomes 0.026 (McElfresh et al. 1990).
[t] In the basal plane.
[u] Depending on crystallographic direction, see text.
[v] Along the c-axis (Willis et al. 1985).

continued on next page

Table 3, *continued*

References

(1) Niksch et al. (1980)
(2) Fierz et al. (1988)
(3) Andres et al. (1975)
(4) Shibata et al. (1986)
(5) Thompson and Fisk (1985)
(6) Sumiyama et al. (1985)
(7) Kagayama and Oomi (1993)
(8) Takke et al. (1980)
(9) Lawrence et al. (1985a)
(10) Oomi et al. (1990)
(11) Lawrence and Thompson (1994)
(12) Chen et al. (1989)
(13) Thompson et al. (1987c)
(14) Oomi et al. (1988b)
(15) Mock et al. (1985)
(16) Bellarbi et al. (1984)
(17) Horn et al. (1985)
(18) Lieke et al. (1982)
(19) Kagayama et al. (1992)
(20) Yang and Lee (1991)
(21) Borges et al. (1985)
(22) Ayache et al. (1987)
(23) Lacerda et al. (1989a)
(24) Mignot et al. (1989)
(25) Thompson et al. (1987b)
(26) Spendeler et al. (1992b)
(27) Mignot and Wittig (1981)
(28) de Visser et al. (1987)
(29) Wire et al. (1984)
(30) Robinson et al. (1986)
(31) Thompson et al. (1987a)
(32) de Visser et al. (1984)
(33) McElfresh et al. (1987)

(1981) and subsequently received further theoretical support (Coleman 1983). Although the interpretation of Lawrence et al. (1985a) has some theoretical justification, we should note that Oomi et al. (1990) did observe a negative pressure derivative of A in $CePd_3$, about ten times larger than found by Lawrence et al. (1985a) (see table 3). Also, the use of their value for $\partial A/\partial P$ leads to a Grüneisen parameter of 13.6, which agrees well with $\Omega_e = 10$ quoted above. In defense of the older work and interpretation, it should be noted that the sample studied by Oomi et al. (1990) had a residual resistivity (150 $\mu\Omega$ cm) five times greater than that in the sample of Lawrence et al. (1985a). Hence, it is possible that the pressure dependence of A measured by Oomi et al. (1990) is an impurity effect. If so, the low-temperature Grüneisen parameter Ω_A would have, from the results of Lawrence et al., the value 1.7, which is much smaller than the high-temperature value.

$CeRu_3Si_2$ is another compound that appears to be mixed valent and becomes superconducting at ambient pressure below $T_c \approx 1$ K (Rauchschwalbe et al. 1984). Its pressure-dependent resistivity is similar to that of $CeSn_3$, with decreasing T^2-coefficient of resistivity and $\rho(300\,\text{K})$ (Meng et al. 1985; Yomo et al. 1986). However, a quantitative interpretation of its pressure response is complicated by possible sample inhomogeneity and/or pressure-induced structural change and will not be discussed further.

Having described the response of Ce compounds with an electronic energy scale greater than Δ_{CF}, we now turn to those in the opposite limit, namely Ce compounds in which the single-ion Kondo or spin-fluctuation temperature has been determined (from inelastic neutron scattering, an interpretation of their large Sommerfeld coefficient of specific heat or from an analysis of high-temperature specific-heat data) to be smaller than the lowest crystal-field splitting. In some of these systems, e.g., $CeCu_6$, a region of T^2 variation in the resistivity occurs at very low temperatures, typically less than 0.1 K. Consequently, there are, unfortunately, few reports of pressure studies on the T^2-coefficient of resistivity for these very strongly correlated Ce-systems. In spite of this limitation, substantial information has been learned from higher temperature measurements.

Consider first $CeCu_6$ which has an ambient-pressure resistivity maximum at $T_m = 15$ K that increases approximately linearly with pressure at a rate of 2.1 K/kbar to 30 kbar (Thompson and Fisk 1985; Shibata et al. 1986). In the temperature interval slightly below T_m to room temperature, its pressure response is similar to that of $CePd_3$. A notable

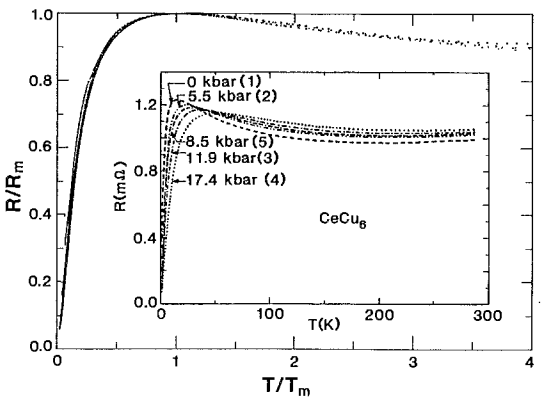

Fig. 11. Normalized resistance of $CeCu_6$ plotted versus $T/T_m(P)$. The inset shows raw data used to construct the normalized curves. Numbers in parenthesis reflect the order in which the data were obtained. (From Thompson and Fisk 1985.)

difference between these two compounds, however, is that at the lowest temperature of these measurements, 1 K, the resistivity $\rho(1\,\mathrm{K})$ decreases strongly with increasing pressure. Even with this, data to 17.4 kbar scale very well as $\rho(T,P)/\rho(T_m(P))$ versus $T/T_m(P)$ from 1 K to about 4 $T_m(P)$, as shown in fig. 11 (Thompson and Fisk 1985). Above 30 kbar, $\rho(T)$ begins to assume a new temperature dependence (fig. 12). Near 30 kbar, two things happen: T_m becomes comparable to or greater than the crystal-field splitting of 65 K (Onuki et al. 1985) between the ground and first excited states and the orthorhombic-to-monoclinic transition, which occurs at 186 K at $P=0$, is shifted to ~100 K (Oomi et al. 1988a). Yomo et al. (1988) report the appearance of a T^2 dependence of $\rho(T)$ for $T < 1.4$ K near 20 kbar that extends to 26 K at 120 kbar, with the value of A decreasing from about 2 $\mu\Omega\,\mathrm{cm/K^2}$ to 10^{-3} $\mu\Omega\,\mathrm{cm/K^2}$ in this pressure range. At the highest pressure $\rho(T)$ for $CeCu_6$ resembles that of $CeSn_3$ at ambient pressure and the T^2-coefficients of resistivity are quite comparable, suggesting that $CeCu_6$ has been driven by pressure into the strongly mixed-valence regime. Interestingly, they also find that the data, scaled as $\rho(T,P)/\rho(T_m(P))$ versus $T/T_m(P)$, fall on two universal curves, one for pressures less than 60 kbar and one for higher pressures. A possible interpretation is that this behavior reflects a change in the degeneracy of the ground state that develops as T_m is increased to well-above Δ_{CF} (Yomo et al. 1988). (The systematics shown in fig. 12 also are found in measurements to 80 kbar for $CeInCu_2$ (Kagayama et al. 1992).)

At ambient pressure, $CeCu_2Si_2$ has a temperature-dependent resistivity similar to that of $CeCu_6$ at 41 kbar. The origin of a low-temperature maximum in $CeCu_2Si_2$ at 23 K is believed to represent the cross-over from single-ion Kondo scattering above the maximum to increasingly coherent-type scattering among the "impurities" at lower temperatures (Grewe and Steglich 1991), an interpretation applied generally to Kondo-lattice systems. However, in $CeCu_2Si_2$ there is a second broad maximum centered around 70 K that is attributed (Horn et al. 1981) to Kondo-like scattering on a thermally populated crystal-field level (Cornut and Coqblin 1972). Measurements of $\rho(T,P)$ to 197 kbar (Bellarbi et al. 1984) find that modest (~30 kbar) pressures are sufficient to increase the temperature of

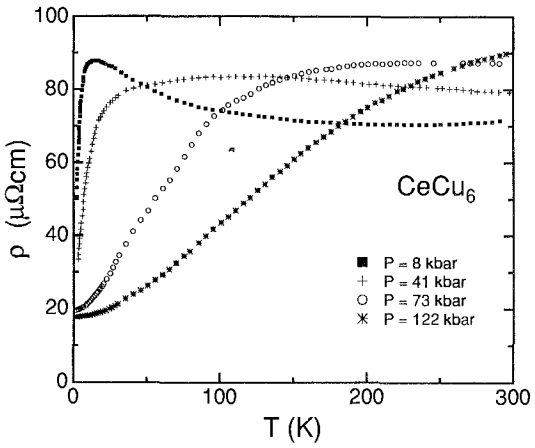

Fig. 12. Resistivity of polycrystalline $CeCu_6$ at various pressures plotted as a function of temperature. Note the temperature dependence at 41 kbar where a weak maximum appears near 100 K which is followed at lower temperatures by a shoulder and then a rapid decrease below about 20 K. Not shown is the fact that the residual resistivity increases between 20 and 41 kbar pressure. Data have been selected from Yomo et al. (1988).

the lower maximum so that it merges with the upper one. With further increase in pressure, the response is similar to that of $CeCu_6$ at comparable pressures. A comparison, then, between the pressure-dependent resistivities of $CeCu_2Si_2$ and $CeCu_6$ lends credibility to the interpretation of high-pressure $CeCu_6$ results, namely, that the qualitative change in $\rho(T)$ is dominated by a change in the degeneracy of the ground state and not the orthorhombic-to-tetragonal transition. In $CeCu_2Si_2$ this change appears to happen at pressures $\geqslant 32$ kbar (Horn et al. 1985; Bellarbi et al. 1984; Jaccard et al. 1985). However, unlike $CeCu_6$, the normalized resistivity of $CeCu_2Si_2$ scales as a function of $T/T_m(P)$ at $P=0$ and for pressures above 32 kbar. At intermediate pressures scaling does not hold if the *observed* value of T_m is used, presumably because T_m in this pressure range reflects a mixture of single-ion Kondo and crystal-field effects (Horn et al. 1985). If $\rho(T,P)$ is modeled as a sum of Kondo and crystal-field contributions, the energy scale T_0 representing the interaction between conduction electrons and 4f moments is found to increase linearly with pressure ($P<20$ kbar) from a $P=0$ value of 18.5 K at a rate 0.4 K/kbar; whereas, above 30 kbar, T_0 increases from 77.9 K at a rate of 1.1 K/kbar (Horn et al. 1985). However, the value of $\Omega=22$ deduced from this analysis at low pressure is substantially smaller than inferred from pressure-dependent specific heat or from thermal expansion measurements. Either this means the low-temperature coherent regime scales differently ($\Omega=50$–100) than the high-temperature regime ($\Omega \sim 20$) or it is an artifact of the analysis.

At ambient pressure, the resistivity of $CeCu_2Si_2$ decreases linearly with temperature from approximately 2 K to the superconducting transition temperature $T_c=0.67$ K. A T^2-variation in $\rho(T)$ is found only well below 1 K when a magnetic field is applied that is sufficiently large to suppress superconductivity. Under these conditions the value of A is about 10 μΩ cm/K^2 (Lieke et al. 1982). Its variation with pressure has not been studied for $P<80$ kbar. However, with increasing pressure the T-linear contribution decreases monotonically and eventually gives way to a T^2 term above T_c that is 0.072 μΩ cm/K^2

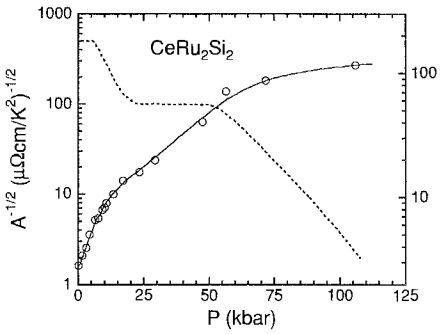

Fig. 13. Inverse square root of the T^2-coefficient of resistivity for $CeRu_2Si_2$ at various pressures (open circles) and corresponding Grüneisen parameter $\Omega = \partial \ln A^{-1/2}/\partial \ln V$ (dashed line) versus pressure. (After Payer et al. 1993.) A bulk modulus of 1 Mbar has been assumed in calculating Ω. However, recent measurements by Haen et al. (1993) give $B = 1.22 \pm 0.1$ Mbar.

at 80 kbar and decreases to ~0.001 μΩ cm/K^2 at 160 kbar. These values of A are typical of Ce mixed-valence compounds (table 3) and are consistent with the broadly-peaked or S-shaped $\rho(T)$ curves at these pressures.

$CeRu_2Si_2$ is the only Ce-based heavy-electron system in which the T^2-coefficient of resistivity has been studied from low (Thompson et al. 1985; Mignot et al. 1989) to very high pressures (Payer et al. 1993). As discussed in sect. 2.2, normalized values of $1/\sqrt{A}$, $1/\chi(0)$ and H_m all have a common Grüneisen parameter of 171 at low pressures. Figure 13 shows the variation of $1/\sqrt{A}$ and Ω for single-crystal $CeRu_2Si_2$ at pressures to 105 kbar (Payer et al. 1993). An interpretation of $\Omega(P)$ is not clear. However, we suggest that correlations responsible for the anomalously large value of Ω (given a $P = 0$ Sommerfeld coefficient about one-fourth that of $CeCu_6$) are suppressed over the pressure range 10 to ~25 kbar. The plateau value of $\Omega \approx 60$ for $P > 25$ kbar is close to Ω_χ for a field perpendicular to the c-axis. These strongly pressure-dependent correlations must be of intersite origin because the neutron quasi-elastic linewidth $\Gamma/2 \approx 25$ K (Grier et al. 1988; Severing et al. 1989), which gives a direct measure of the Kondo spin-fluctuation temperature, agrees well with T_K inferred from a single-ion Kondo interpretation of the $P = 0$ Sommerfeld coefficient. The monotonic decrease in Ω above 50 kbar is consistent with T_K becoming comparable to the crystal-field splitting estimated to be 250±30 K from specific heat (Besnus et al. 1985) or thermal expansion (Lacerda et al. 1989a) and 385 K from inelastic neutron scattering (Dakin et al. 1992). In this view, $CeRu_2Si_2$ enters the mixed-valence regime only above ~50 kbar.

The systematics described for the pressure dependence of resistivity features, e.g., A and T_m, are consistent with a pressure-induced increase in the characteristic electronic energy scale in Ce-based intermetallics, a result that can be understood if the hybridization between conduction and 4f electrons increases with pressure. As noted by Kadowaki and Woods (1986), there appears to be a universal relationship between Sommerfeld coefficient and A values among anomalous lanthanide and actinide compounds. We will show later that this "universality" continues to hold at modest pressures as well. Presumably this relationship is valid because it is a ground-state property of the underlying electronic correlations responsible for both γ and A. However, it must be remembered that γ is a thermodynamically-defined quantity; whereas A depends on (anisotropic) electronic

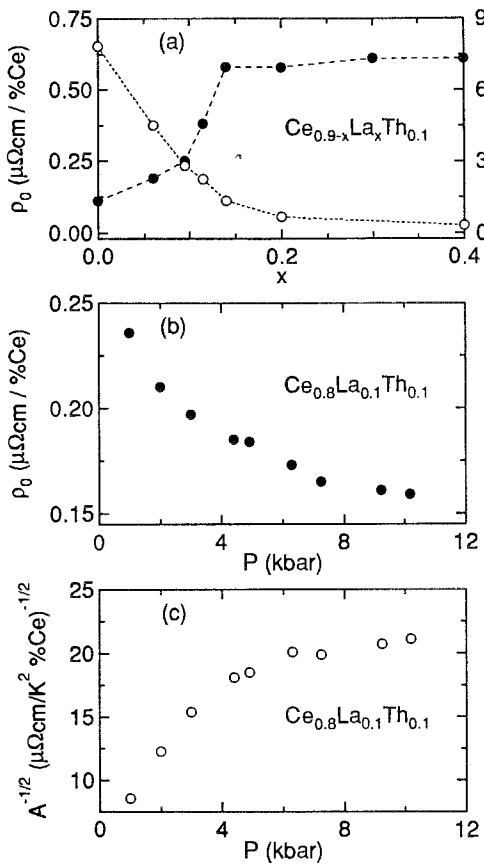

Fig. 14. (a) Residual resistivity per atomic percent Ce (solid circles) in $Ce_{0.9-x}La_xTh_{0.1}$ (Grier and Parks 1981) and characteristic temperature T_0 (open circles) versus x (Grier et al. 1981). (b) Residual resistivity as a function of pressure in $Ce_{0.8}La_{0.1}Th_{0.1}$. (c) $1/\sqrt{A}$ versus pressure in $Ce_{0.8}La_{0.1}Th_{0.1}$. The $P=0$ data have been normalized to the value in (a). (After Lawrence et al. 1985b.)

scattering processes. There are clear examples at ambient pressure of a breakdown in the relationship $\gamma \propto \sqrt{A}$ when the periodicity of the Ce-sublattice is broken. For example, when half of the Ce-atoms are replaced by non-magnetic La in $Ce_{1-x}La_xCu_6$, γ is enhanced slightly over that of $CeCu_6$ (Satoh et al. 1988) but there is no positive T^2-coefficient of resistivity (Sumiyama et al. 1985): $\rho(T)$ is that of a Kondo-impurity with $\rho(T=0)$ large and $\partial\rho/\partial T$ negative. Even in undoped $CeCu_6$ there is anisotropy in A by a factor of three, depending on crystallographic direction, and in the magnitude of $\rho(0)$ (Sumiyama et al. 1985). In this case, anisotropy introduced by crystal-field effects (Evans et al. 1992) and/or an exchange that depends on momentum transfer $\boldsymbol{Q}$ (Thompson et al. 1987a) may be responsible for the anisotropy in A. Therefore, considerable care must be taken in attempts to make quantitative comparisons between thermodynamic and transport characteristics at ambient as well as high pressure.

Another point is that the residual $T=0$ resistivity $\rho(0)$ varies strongly with pressure in certain compounds. As an example of this we show in fig. 14b the pressure dependence

of $\rho(0)$ for $Ce_{0.8}La_{0.1}Th_{0.1}$ (Lawrence et al. 1985b). It can be seen that $\rho(0)$ varies by a factor of 1.5 over the pressure interval 1–10 kbar. The quantity $(1/A)^{1/2}$ varies by an even larger factor of 2.5 (fig. 14c), which implies that $\rho(0)$ varies more slowly than the characteristic energy $k_B T_0$. The large magnitude of the effect suggests that the residual scattering is not simply due to potential scattering from the nonmagnetic solute atoms, but involves the Ce-4f electrons in an essential way. An idea which has gained popularity to explain such scattering is that of the "Kondo Hole" (e.g., Lawrence et al. 1985a) whereby the presence of a non-magnetic ion, or even a magnetic ion other than Ce, creates a hole in the otherwise periodic Ce sublattice that scatters resonantly. Lawrence et al. (1985a) argued for $Ce_{1-x}La_xPd_3$ that the resulting resistivity would have the temperature dependence of a Kondo impurity, as discussed above for $Ce_{0.5}La_{0.5}Cu_6$. In a perfectly periodic lattice, the Ce-4f phase shift is uniform from site to site so that the resistivity vanishes at $T=0$. However, disruption of periodicity through the introduction of alloy disorder causes fluctuations in the phase shift which give rise to residual scattering at $T=0$. As a measure of the magnitude of the effect, we note that in a Local Fermi Liquid Theory (Newns and Hewson 1981) the residual resistivity should obey the proportionality $\rho(0) \propto \sin^2(\pi n_f/2J+1)$, where n_f is the 4f-occupation number and $2J+1$ is the ground-state degeneracy. Hence, the effect of pressure would be to a decrease $\rho(0)$, due to a decrease in n_f with increasing pressure and crossover from crystal-field doublet ground state to full $J=5/2$ degeneracy as $T_K(P)$ becomes larger than the crystal-field splitting. The $Ce_{0.9-x}La_xTh_{0.1}$ alloy data can be understood in this way: the residual resistivity at ambient pressure (Grier and Parks 1981) (fig. 14a) varies by about a factor of six as x varies and at the same time T_K (as measured by neutron linewidths and dc susceptibility (Grier et al. 1981)) decreases from values much larger than the crystal-field splitting (which is of order 200 K in these materials) to smaller values. Because the f occupation should be of order 0.8 for the large-T_K compounds and of order 1 for the small-T_K compounds and the degeneracy varies simultaneously from six to two, a change in $\rho(0)$ of six is precisely as expected. For fixed $x=0.1$ the change with pressure is smaller because the material is closer to the large-T_K limit at ambient pressure. A similar, large variation of the low-temperature resistivity $\rho(1\,K)$ has been reported (Thompson and Fisk 1985) in $CeCu_6$, but the resistivity varies rapidly with temperature near 1 K making it difficult to establish $\rho(0)$. On the other hand, the residual resistivity of $CeAl_3$ decreases by nearly a factor of two between $P=0$ and $P=10$ kbar (Flouquet et al. 1988); whereas, the low-temperature specific heat results mentioned above (Phillips et al. 1987) indicate that T_K varies from 3.5 K to about 10 K in the same pressure interval. This latter variation is not sufficient to cause changes in either n_f or $2J+1$. Consequently, the explanation given above simply does not work for this compound. An alternative suggestion is that $\rho(0)$ varies inversely with T_K (Flouquet et al. 1988; Barbara et al. 1989). As will be seen in the ensuing discussion of Yb compounds, pressure decreases T_0 but increases $\rho(0)$, which lends support to the notion that $\rho(0) \propto 1/T_0$.

The negative Grüneisen parameters found from specific heat and susceptibility measurements on anomalous Yb intermetallics are consistent with the pressure-induced resistive response of these materials as well. For pressures less than 16 kbar, the

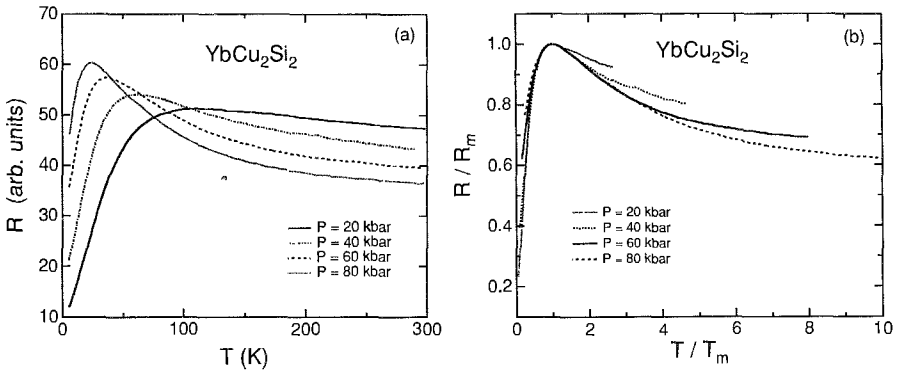

Fig. 15. (a) Resistance versus temperature for a $YbCu_2Si_2$ single crystal at pressures of 20 kbar and greater. (After Uwatoko et al. 1992.) (b) Data of part (a) plotted on normalized scales as $R/R_m(P)$ vs $T/T_m(P)$.

resistive maximum at T_m in $YbCu_2Si_2$ moves to lower temperatures at a rate of $\partial T_m/\partial P = -6.5$ K/kbar and the T^2-coefficient A increases (Thompson et al. 1987b). Accompanying these changes are a decrease in $\rho(300\,\mathrm{K})$ and an increase in $\rho(0)$. Figure 15a shows the evolution of $\rho(T)$ for $YbCu_2Si_2$ at pressures above 20 kbar (Uwatoko et al. 1992). At the lowest temperature (5 K) of these measurements, $\rho(5\,\mathrm{K})$ increases by over a factor of four as pressure is raised to 80 kbar. This huge increase clearly is not due to the development of microcracks in the sample, because $\rho(300\,\mathrm{K})$ decreases monotonically with P, but roughly tracks the decrease in T_m (112 K at 20 kbar and 24 K at 80 kbar). Similar trends are found in $\rho(T,P)$ for $YbAgCu_4$, $YbRh_2Si_2$ (Thompson et al. 1987b) and $YbCu_{4.5}$ (Spendeler 1992a; Spendeler et al. 1992b) and suggest that the data might scale. In fig. 15b we have plotted the high-pressure data for $YbCu_2Si_2$ as $\rho(T)/\rho(T = T_m(P))$ versus $T/T_m(P)$ where reasonable scaling appears for $5 < T \leqslant 156$ K. At the lowest temperatures the scaled data do not lie on a universal curve, indicating that electronic scattering is stronger there than expected on the basis of the maximum observed at T_m, a point discussed further in sect. 4. These trends can be understood if the (negative) pressure dependence of Kondo-like scattering is stronger than that of inter-site (RKKY) correlations responsible for producing coherence. In this regard, good scaling has been found in $YbRh_2Si_2$ (Thompson et al. 1987b) if the "residual" resistivity $\rho(T \to 0,P)$ is subtracted in the normalization process, ie., if R^*/R^* $(T = T_m(P))$ is plotted versus $T/T_m(P)$, where $R^* = R(T,P) - R(T \to 0,P)$.

The decrease in T_m and increase in A in $YbCu_2Si_2$ are consistent with $\partial T_K/\partial P < 0$, which would arise if $\partial|J|/\partial P$ were negative. As P increases, T_m should approach zero, so that at experimentally accessible temperatures the resistivity would be that of an array of resonantly scattering, incoherent impurities. However as $|J|$ and hence T_K become sufficiently small, there should be a qualitative change in $\rho(T)$ at low temperatures as intersite correlations lead to long-range antiferromagnetic order among only partially Kondo-compensated Yb moments, as suggested by the Doniach diagram in fig. 1. Evidence for this sort of behavior has been found in YbCuAl (Mignot and Wittig 1981)

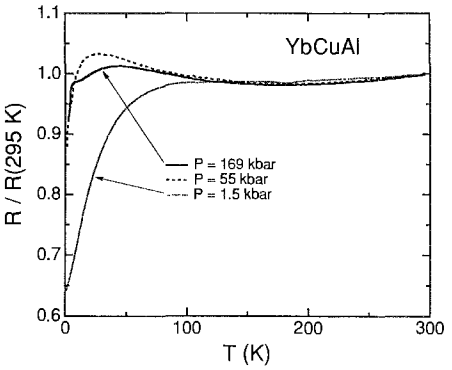

Fig. 16. Normalized resistance versus temperature curves for YbCuAl at selected pressures. (After Mignot and Wittig 1981).

and is shown in fig. 16. With increasing pressure there is a systematic shift of T_m to lower temperatures until $P = 108$ kbar, where $\rho(T)$ has the general shape shown for $P = 55$ kbar. At $P = 135$ kbar, $\rho(T)$ qualitatively changes to that shown for $P = 169$ kbar. The sharp drop in $\rho(T)$ near 5 K is believed to represent a loss in spin-disorder scattering due to antiferromagnetic order. For $P > 135$ kbar, the high-temperature maximum moves to higher temperatures with increasing P as a result of crystal-field effects and the maximum that was present below 135 kbar manifests itself only as a plateau between 10 and 5 K. It is interesting that, as the critical pressure for this qualitative change is approached, T_m is virtually unaffected by P, ie., $\partial T_m/\partial P \approx 0$, but at lower pressures T_m decreases several Kelvin per kilobar. This same tendency appears in $YbCu_2Si_2$ data as well, where at low pressure $\partial T_m/\partial P \gtrsim -6$ K/kbar but between 60 and 80 kbar $\partial T_m/\partial P$ has decreased by one order-of-magnitude. Extending measurements on $YbCu_2Si_2$ to pressures greater than 80 kbar would be worthwhile to determine if it also would undergo a pressure-induced magnetic order.

The temperature-dependent resistivity of UAl_2 is S-shaped (Buschow and van Daal 1972) and believed to be dominated at low temperatures by spin fluctuations that produce a $T^3 \ln T$ contribution to its specific heat (Trainor et al. 1975). With applied pressure the resistivity is reduced at all temperatures below 300 K, with the exception of $\rho(0)$ which is weakly, if at all, affected (Wire et al. 1984). When these data were analyzed using a parallel resistor model to account for the saturation of $\rho(T)$ above about 150 K, the low-T resistance was found to follow a T^2-dependence in which A decreased monotonically with increasing P and the region over which $\rho \propto AT^2$ increased. Wire et al. (1984) showed that, if the temperature scale was normalized by $1/\sqrt{A}$, all $\rho(T,P)$ data scaled onto a universal curve. Normalizing $1/\sqrt{A}$ at ambient pressure to the spin-fluctuation temperature T_{sf} inferred from specific heat and susceptibility measurements ($T_{sf}(P=0)=26$ K), Wire et al. (1984) found that T_{sf} increased linearly with pressure at a rate $\partial T_{sf}/\partial P = 0.77$ K/kbar which implies a resistive Grüneisen parameter of 18, a value that agrees well with Ω_χ (table 2) and with estimates to be discussed below in sect. 3.

The resistivity of UPt_3 is similar to that of UAl_2 but is highly anisotropic, having $\rho(300\,\text{K})$ equal to 130 and 240 μΩ cm and A equal to 0.7 and 1.6 μΩ cm/K^2 along the

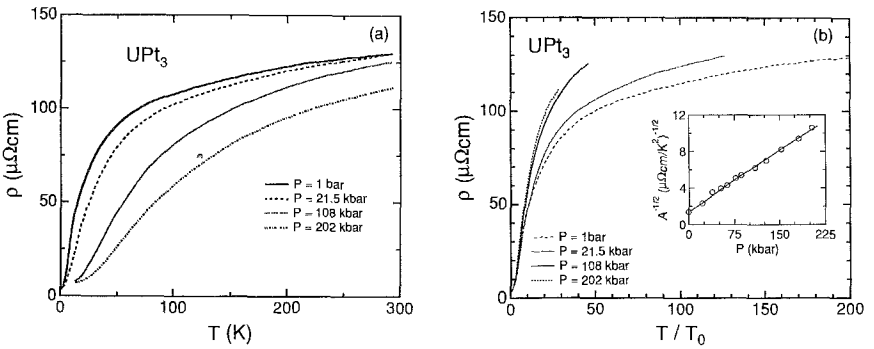

Fig. 17. (a) c-axis resistivity as a function of temperature for UPt_3 at various pressures. (After Ponchet et al. 1986). (b) Data of part (a) in which the temperature axis has been normalized by $T_0(P)$ where $T_0 \equiv 1/\sqrt{A}$. Units for the horizontal axis are $(\mu\Omega\,\mathrm{cm})^{1/2}$. The inset gives the pressure variation of $1/\sqrt{A}$ after Ponchet et al. (1986).

c-axis and in the basal plane, respectively (de Visser et al. 1984). Pressure studies of single crystal UPt_3 show $\partial\rho(T)/\partial P < 0$ and relative rates of increase in $1/\sqrt{A}$ that are comparable along the different crystallographic directions (Wire et al. 1984; Franse et al. 1986), a result in contrast to the notably different values of Ω_χ. In the basal plane, the rate of increase is $36\,\mathrm{Mbar}^{-1}$ which is close to the rate of increase in the inflection temperature T_i, found by a peak in $\partial\rho/\partial T$ (de Visser et al. 1984). Together, these suggest that the pressure-dependent resistivity of UPt_3 might scale as in UAl_2. However, Wire et al. (1984) report that scaling of this form holds to only 50 K for resistance measured along the c-axis and to 70 K for the a–b plane resistance.

Ponchet et al. (1986) have extended the range of pressure to over 200 kbar in their study of c-axis resistivity of UPt_3 (fig. 17a). At low pressures, where their measurements overlap those reported earlier to 19 kbar (Willis et al. 1985), good agreement is found in the overall response of $\rho(T)$ and $1/\sqrt{A}$ to pressure. The inset of fig. 17b shows a smooth, monotonic increase in $1/\sqrt{A}$ out to the highest pressures, corresponding to a decrease in A from 0.52 $\mu\Omega\,\mathrm{cm/K^2}$ at ambient pressure to slightly less than 0.01 $\mu\Omega\,\mathrm{cm/K^2}$ at 202 kbar. The inflection temperature T_i has a similar pressure dependence but more pronounced downward curvature above ~100 kbar that may be due partly to the lack of subtracting a phonon contribution to $\rho(T)$. In fig. 17b we plot $\rho(T,P)$ as a function of $T/T_0(P)$ where T_0 is defined as $1/\sqrt{A}(P)$. As found by Wire et al. (1984), reasonably good scaling holds at low temperatures but not at higher temperatures. Whether this lack of scaling is intrinsic or also results from a substantial phonon correction that has not been made remains an open question. Normalizing the resistivity axis, as done for $CeCu_6$ in fig. 11, might improve the scaling; however, this was not necessary for UAl_2 and there is no clearly identified feature in $\rho(T)$ to choose for this purpose.

In the cases of UBe_{13} and URu_2Si_2 there is a resistivity maximum and for these compounds plots of $\rho/\rho(T_m)$ versus $T/T_m(P)$ produce scaling. In UBe_{13} scaling is valid only at temperatures from 1 to about 5 K ($T_m(P=0)=2.3$ K) (Thompson et al. 1987a) for

pressures less than 15 kbar, but in URu_2Si_2 $\rho(T,P)$ data fall on a universal curve over a much wider temperature interval $1\,K < T < 1.2\,T_m(P)$ where $T_m(0) = 73$ K (McElfresh et al. 1987). It should be noted, however, that $\rho(T_m) \approx 700\,\mu\Omega$ cm in URu_2Si_2 and any phonon contribution should be negligible. As with strongly correlated Ce compounds, increasing pressure moves T_m to higher temperatures, decreases A and increases the temperature range over which $\rho \propto T^2$ in both UBe_{13} and URu_2Si_2.

The resistivity maximum in UBe_{13} is unusual for correlated-electron compounds in that it is very sharp and develops at a temperature roughly one order-of-magnitude lower than in other Ce-, Yb- or U-based compounds (see table 3). Indeed, the overall temperature dependence of ρ for UBe_{13} at ambient pressure is unique among U-based compounds, increasing monotonically with decreasing T below 300 K and reaching a plateau around 10 K before increasing to a maximum at T_m. This $\rho(T)$ is somewhat reminiscent of that in $CeCu_2Si_2$ in which a broad high-temperature (relative to T_m) maximum is attributed to crystal-field effects. Although there is no evidence for crystal fields in UBe_{13} from inelastic neutron scattering (Lander et al. 1992; Goldman et al. 1986), an interpretation of high-temperature specific heat measurements (Felten et al. 1986) suggests a Γ_6 (magnetic) crystal-field doublet ground state.

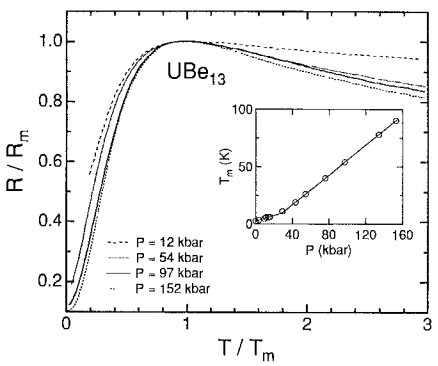

Fig. 18. Resistance of UBe_{13} normalized to its maximum value $R_m(P)$ as a function of reduced temperature $T/T_m(P)$. (After McElfresh et al. 1990). The inset gives the pressure variation of T_m.

With applied pressure the resistivity maximum in UBe_{13} increases linearly to a value of about 10 K at 30 kbar (McElfresh et al. 1990) and there is a concomitant increase in $\rho(T_m(P))$. Above 30 kbar, $\partial T_m/\partial P$ increases by a factor of 2.6, $\partial(1/\sqrt{A})/\partial P$ increases by one order-of-magnitude, $\rho(0)$ decreases sharply and $\rho(T_m(P))$ begins to decrease. Further, scaling observed at low pressures does not continue smoothly at these higher pressures; instead, they collapse onto another nearly "universal" curve as shown in fig. 18. (The curve at 54 kbar is intermediate to the low and high pressure scaling regimes). At 152 kbar, the resistivity of UBe_{13} is quite similar to that of $CePd_3$ at ambient pressure. Together these results suggest an analogy to behavior found in $CeCu_6$ and $CeCu_2Si_2$ as a function of pressure, namely a change in ground-state degeneracy induced by sufficiently high pressure. In UBe_{13}, such a change appears to take place in the pressure range 30–50 kbar. On the basis of high pressure magnetoresistance measurements, Aronson et al. (1989) have argued that a fully coherent state only develops in UBe_{13} at pressures greater than

60 kbar above which there is also a low-temperature sign change in the thermoelectric power (Mao et al. 1988). However, the criterion used to define coherence, namely that the elastic scattering rate becomes equal to the inelastic scattering rate characteristic of incoherent Kondo impurities, is not used widely and is more restrictive than the more common criterion of the existence of a Fermi-liquid like T^2-variation in $\rho(T)$ at low temperatures (Grewe and Steglich 1991). Although the interpretations by Aronson et al. (1989) and McElfresh et al. (1990) differ, they are not necessarily incompatible and emphasize the need for additional high pressure/high magnetic field experiments on strongly correlated electron compounds as well as for a theoretical understanding of interacting Kondo ions.

Finally, we comment on $\rho(T,P)$ for the heavy-electron antiferromagnet ($T_N(P=0)=5$ K) UCd_{11} which has a $T_m(P=0)$ of 84 K that decreases with increasing pressure at a rate of -1.6 K/kbar (Thompson et al. 1989a). This negative pressure derivative of T_m is opposite to that found in all non-magnetic Ce and U intermetallics but like that in Yb compounds. Because the system orders magnetically, the condition $T_K < T_{RKKY}$ should be satisfied and it is unlikely that the resistivity maximum at 84 K arises from a transition from impurity-like Kondo scattering to more nearly coherent scattering in the ground state. Although there is no evidence for crystal-field splitting from temperature-dependent magnetic susceptibility, we believe that the behavior in UCd_{11} is similar to that in antiferromagnets $CeAl_2$ (Nicolas-Francillon et al. 1972) and CePt (Itoh et al. 1987). In these cases, when the phonon contribution to $\rho(T)$ is subtracted, there is a well-defined high-temperature resistivity maximum that moves to lower temperatures with applied pressure, an effect that may be attributed clearly to an apparent reduction in splitting between the crystal-field ground and first excited states.

We have mentioned already the linear relationship between γ and $\sqrt{A}$ found by Kadowaki and Woods (1986) for a wide range of anomalous lanthanide and actinide compounds at ambient pressure. Figure 19 suggests that this continues to hold as a function of pressure for UPt_3 and UBe_{13}. (Slopes of the solid lines in fig. 19 are comparable but do differ by about 25%.) For UBe_{13} (Thompson et al. 1987a), as well as for $CeInCu_2$ (Kagayama et al. 1992), $CeCu_6$ at pressures greater than 20 kbar (Kagayama and Oomi 1993) and $YbCu_2Si_2$ (Thompson et al. 1987b), $1/\sqrt{A}(P)$ is linear in $T_m(P)$, so that in UBe_{13} $\gamma(P)$ also would be linear in $1/T_m(P)$. This behavior is not unique to U compounds but has been reported for $CeCu_6$ (Thompson et al. 1989b) at pressures to 8.8 kbar and follows for a similar pressure range in $YbCu_{4.5}$, as shown in fig. 20. However, for an impurity of arbitrary angular momentum, $\partial \ln \gamma(P)/\partial \ln(1/T_0(P))$ should be identically equal to unity (Rajan 1983), provided the degeneracy of the ground state is not changed with pressure. Taking $\sqrt{A} \propto 1/T_0$, we find from fig. 19 that $\partial \ln \gamma/\partial \ln \sqrt{A}$ is equal to 1.2 and 2.7 for UPt_3 and UBe_{13}, respectively. Although this derivative is close to the impurity value for UPt_3, this is not the case for UBe_{13}. To clarify this point we note that (under the basic assumption that $\gamma \propto 1/T_0$) if A is proportional to $1/T_0^2$ then at $T_0=0$ the value of $1/A$ should also vanish, i.e., $(1/A)^{1/2}$ vs. $1/\gamma$ should extrapolate to the origin. This is approximately the case for UPt_3 but is not at all true for UBe_{13}, where there is a large positive intercept. There are two ways the data for UBe_{13} can be analyzed: (a) under

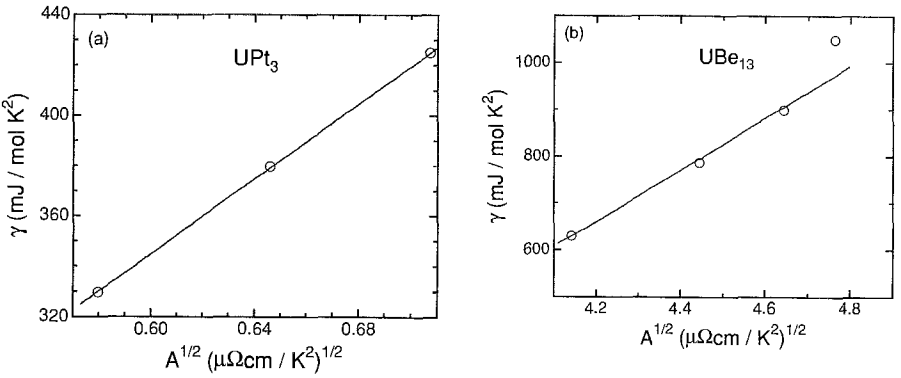

Fig. 19. (a) Sommerfeld coefficient γ as a function of the square root of the T^2-coefficient of resistivity for UPt_3 with pressure as the implicit variable. Value of $\gamma(P)$ from Phillips et al. (1987) and $A(P)$ from Willis et al. (1985). (b) γ versus $\sqrt{A}$ for UBe_{13} with pressure as the implicit parameter. Value of $\gamma(P)$ after Phillips et al. (1987) and $A(P)$ after Thompson et al. (1987a). Lines in both (a) and (b) are guides only.

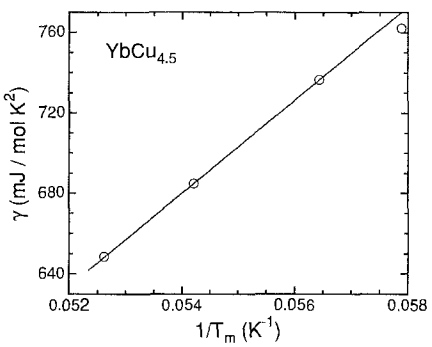

Fig. 20. Sommerfeld coefficient γ at 0.4 K versus $1/T_m$ for $YbCu_{4.5}$ where pressure is the implicit variable. Values of $\gamma(P)$ from Amato et al. (1990) and $T_m(P)$ from Spendeler et al. (1992b). The solid line is a guide only.

the assumption that $(1/A)^{1/2} = a + bT_0$, which means that A never gets larger than $1/a^2$ as $T_0 \to 0$ ($\gamma \to \infty$); and (b) under the assumption that $A \propto T_0^{-n}$ with $n = 1/2$. In either case the simple assumption that $A \propto 1/T_0^2$, which appears to be valid for UPt_3, does not hold for UBe_{13}.

Another common assumption is that T_m, the temperature of the resistivity maximum, should be proportional to T_K or T_0. Again assuming that T_0 is best measured as $1/\gamma$, we find that the logarithmic derivatives $\partial \ln \gamma / \partial \ln(1/T_m)$ are 0.73 and 0.99 for UBe_{13} and $CeCu_6$ respectively (Thompson et al. 1989b) and from fig. 20 we find a value of 1.9 for $YbCu_{4.5}$. Thus the assumption works well for $CeCu_6$, but not so well for UBe_{13}, and rather badly for $YbCu_{4.5}$. In the latter case the data can be fitted by the assumption $T_0 = T_0^0 + (a/\gamma)$; i.e., the plot has a finite intercept. The significance of this is not clear. Clearly caution must be taken in casually applying impurity concepts to compounds, whether they be lanthanide or actinide-based. In this regard, though, we believe it is significant that these logarithmic derivatives for U-, Ce- and Yb-based compounds are, within roughly a factor of two, equal to each other and to the impurity-limit expectation.

2.3.2. *Electronically correlated semiconductors*

Thus far we have focused on anomalous lanthanide and U-compounds that are metallic in the sense that their resistivity at low temperatures approaches that of normal metals and $\partial\rho/\partial T$ is positive for $T > 0$. There is another interesting class of anomalous 4f and 5f compounds that display a small, typically 10–100 K, semiconducting gap E_g in their low-temperature electronic excitation spectrum. Classic examples of this behavior are SmB_6 (Allen et al. 1979) and YbB_{12} (Kasaya et al. 1985). Recently, several new Ce and U compounds have been discovered that appear to belong to this class and that have revitalized interest in these types of materials. (See Aeppli and Fisk (1992) for a brief review and discussion of these systems at ambient pressure.) A central question raised here is to what extent the physics of these semiconductors is related to that in anomalous metallic compounds, particularly as revealed from high pressure measurements.

Pressure-dependent resistivity studies of SmB_6 show its $P = 0$ energy gap decreases linearly with pressure at rates dE_g/dP that vary from -0.5 to -0.9 K/kbar and closes completely at critical pressures of 67 and 50 kbar, respectively, (Beille et al. 1983; Moshchalkov et al. 1985). The results appear to be somewhat sample dependent. For pressures greater than critical, $\rho(T)$ exhibits a maximum near 40 K that becomes less prominent with further increase in pressure (Beille et al. 1983). Thus, once the electronic system is metallized, $\rho(T)$ resembles that of some anomalous Ce-metallic compounds, suggesting that the small gap at low pressure arises from the same sort of interactions responsible for $\rho(T)$ in metallic compounds. X-ray diffraction at room temperature (King et al. 1981) is consistent with the valence of Sm in SmB_6 increasing from 2.8 at $P = 0$ to 2.9 at 60 kbar. Thus, at ambient pressure SmB_6 is weakly mixed valent, containing an admixture of $4f^6$ ($J = 0$) and $4f^5$ ($J = 5/2$) wavefunctions, and with increasing pressure the magnetic $4f^5$ configuration is favored. Assuming that Yb in YbB_{12} also is weakly mixed valent at ambient pressure, under applied pressure the smaller volume $4f^{13}$ (magnetic) configuration would be favored and we might expect that the gap ($E_g(P = 0) = 78$ K) in YbB_{12} also would close with pressure. Indeed, this recently has been shown to be the case (Iga et al. 1993): E_g extrapolates to zero for $P \approx 1100$ kbar but the bulk modulus of YbB_{12} is also one order-of-magnitude larger ($B = 13\,100$ kbar) than that of SmB_6 ($B = 1390$ kbar).

On the other hand, for a Ce-based compound we would expect increased 4f-ligand hybridization with applied pressure and the gap to increase. $Ce_3Bi_4Pt_3$ has a gap at ambient pressure similar to that in YbB_{12} (Hundley et al. 1990) and appears from thermal expansion (Kwei et al. 1992) and L_{III}-edge experiments (Kwei et al. 1994) to be weakly mixed valent. Figure 21 shows the pressure response of $Ce_3Bi_4Pt_3$, where we see a clear trend for $\rho(T)$ to increase at all temperatures with increasing pressure suggesting that $dE_g/dP > 0$. Similar, though less distinct, trends have been reported for the small-gap semiconductor $U_3Sb_4Pt_3$ (Canfield et al. 1992). The opposite behaviors of $E_g(P)$ between SmB_6 and YbB_{12} on the one hand and $Ce_3Bi_4Pt_3$ and possibly $U_3Sb_4Pt_3$ on the other indicate that the pressure dependence of E_g is not governed solely by band filling because in all cases the f^{n-1} configuration is favored over the f^n with applied pressure. Instead,

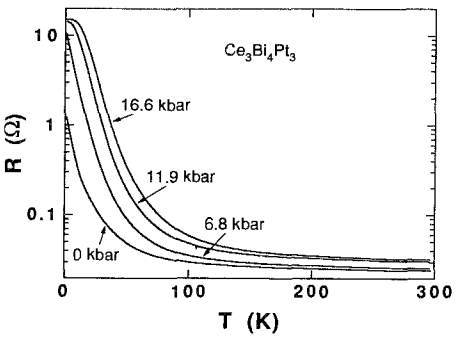

Fig. 21. Temperature-dependent resistance of $Ce_3Bi_4Pt_3$ at various pressures. At $P=0$, $T=300$ K, the resistivity is approximately 200 μΩ cm. Saturation of the low-temperature resistance at the highest pressures most likely reflects the presence of parallel conduction due to impurity states in the gap.

the pressure dependence of E_g appears to follow the change in hybridization expected on the basis of the pressure response of anomalous metals.

A compound where this does not appear to be true is CeNiSn. At ambient pressure E_g is about 6 K and the sharp increase in $\rho(T)$ signaling the gap appears at low temperatures only after $\rho(T)$ has passed over maxima near 12 and 65 K (Takabatake et al. 1993). This temperature dependence is strongly anisotropic, with the 12 K maximum barely discernible for current along the orthorhombic c-axis, and in sharp contrast to $\rho(T)$ for the cubic semiconductors discussed above in which $\partial\rho/\partial T$ is negative at all temperatures below 300 K and $\rho(T)$ is at least one order-of-magnitude larger. The gap in CeNiSn is depressed rapidly with pressure, approaching zero at pressures between 12 (Kurisu et al. 1993) and 30 kbar (Kurisu et al. 1988). At 20 kbar, the 12 K maximum has shifted to about 30 K and the 65 K maximum to near 180 K, strongly suggesting increased 4f-ligand hybridization. Considering these observations one must question either the interpretation given for $E_g(P)$ in SmB_6, YbB_{12} and $Ce_3Bi_4Pt_3$ or whether the pressure dependence of the gap in CeNiSn is governed by changes in addition to hybridization.

Generally it is believed that the gap derives from hybridization between a renormalized f-level and the conduction band, which also is responsible for anomalous behavior in metals (Riseborough 1992). However, if there is only a single conduction band crossing E_F and the electron count, which includes the strongly interacting f-electrons, is exactly two, the lower hybridized band will be filled and the upper hybridized band empty, leading to a gap in the electronic spectrum at E_F. This picture implies that at temperatures greater than E_g/k_B the physics of small gap semiconductors and metals is identical (Aeppli and Fisk 1992). Given the strong anisotropy in $\rho(T)$ and $\chi(T)$ in CeNiSn (Takabatake et al. 1993), we must wonder if the condition of a simple band structure is realized. If not, then the rapid depression of E_g may arise from pressure-induced band crossing that produces a finite density-of-states at E_F.

3. Scaling behavior and Grüneisen relations

3.1. *Thermodynamics of scaling*

As discussed briefly in the Introduction, important relationships existing between the pressure derivatives of susceptibility, specific heat and resistivity follow from a scaling assumption whereby the predominant volume dependence is that of a characteristic temperature $T_0(V)$. This can be quantified in terms of the electronic Grüneisen parameter $\Omega_e = -\partial \ln T_0 / \partial \ln V$. From the assumed scaling with $T_0(V)$, the logarithmic volume derivatives of the low-temperature susceptibility, resistivity and specific heat are interrelated through Ω_e, as given by eqs. (4)–(6). A more detailed analysis (Takke et al. 1981) is based on the assumption that the free energy obeys a scaling law, $F = F_0(T, V) + F_e(T, V)$, where the electronic contribution is

$$F_e(T, V) = -Nk_B T_0 - Nk_B T f(T/T_0(V)). \tag{7}$$

This form, often believed to be valid for the Kondo problem, yields the relationship $\beta_e = \Omega_e C_e / V B_T$, given as eq. (1), where $\beta = \beta_0 + \beta_e$ and $C_v = C_0 + C_e$ are the thermal expansion and specific heat, $B_T = B_0 + B_e$ is the isothermal bulk modulus, and the subscripts 0 and e refer to the background and electronic (e.g. Kondo) contributions, respectively. The magnitude of β_e can be anomalously large in the materials of interest and often β_e exhibits a maximum as a function of temperature. We will discuss the nature of the lattice coupling that causes these lattice anomalies in some detail in sect. 4. For now, it will suffice to say that the 4f-ionic size is sensitive to changes in valence and/or hybridization. The isothermal bulk modulus is then (Yoshizawa et al. 1986)

$$B_T = B_0 + \frac{U_e}{V}\Omega_e^{(2)} - \frac{T}{V}C_e\Omega_e^2, \tag{8}$$

where $U_e = F_e + TS_e$ and $\Omega_e^{(2)} = (V^2/T_0)\,\partial^2 T_0/\partial V^2$. At low temperatures, where $C_e \approx \gamma T$ and $U_e \approx -Nk_B T_0 + \frac{1}{2}\gamma T^2$, the bulk modulus then satisfies

$$B_T \approx B_0 - \frac{Nk_B T_0}{V}\Omega_e^{(2)} - \frac{TC_e}{V}\left[\Omega_e^{(2)} - \tfrac{1}{2}\Omega_e^{(2)}\right]. \tag{9}$$

Using eq. (1) this can be written as

$$B_T \approx B_0 - \delta B_e(0) - B_T T \beta_e \Omega_{eff}, \tag{10}$$

where

$$\delta B_e(0) = \frac{-Nk_B T_0 \Omega_e^{(2)}}{V} \qquad \Omega_{eff} = \frac{\Omega_e^2 - \frac{1}{2}\Omega_e^{(2)}}{\Omega_e}. \tag{11,12}$$

For higher temperatures, there are correction terms to eqs. (9) and (10). The second-derivative term $\Omega_e^{(2)}$ is often set to zero (Takke et al. 1981, Yoshizawa et al. 1986). This is not necessarily justified. For the situation that Ω_e is independent of V, it follows that $T_0 \propto V^{-\Omega_e}$ which implies $\Omega_e^{(2)} = \Omega_e^2$. This appears to be the case for UPt_3 and YbCuAl, as discussed in sect. 2.1. Hence, Ω_{eff} can vary from the value Ω_e (when $\Omega_e^{(2)} = 0$) to the value $\Omega_e/2$ (when $T_0 \propto V^{-\Omega_e}$). The magnitude of $\Omega_e^{(2)}$ can be determined using eq. (11) from the shift $\delta B_e(0)$ of the bulk modulus at $T = 0$. For example, $\delta B_e(0)$ can be estimated from a non-magnetic counterpart compound.

As discussed below, sound propagation in heavy-fermion materials is believed to be adiabatic. When the bulk modulus is measured via ultrasonics, the appropriate parameter is the adiabatic bulk modulus B_s, which is related to the isothermal bulk modulus by a thermodynamic relation (Yoshizawa et al. 1986, Thalmeier 1988):

$$B_s = B_T + \frac{T}{V} C_v \Omega^2, \tag{13}$$

where C_v is the total specific heat and Ω is the thermodynamic Grüneisen parameter,

$$\Omega = -\frac{V}{T} \left.\frac{\partial T}{\partial V}\right|_s = \frac{V B_T \beta}{C_v}. \tag{14}$$

For heavy fermions at low temperatures, $\Omega_e \gtrsim 50$ dominates Ω and $C_e/T \approx 1\,\mathrm{J/mol\,K^2}$ dominates C_v so this correction can be quite large. For example, for UPt_3 at 10 K, where $\Omega = 40$, $V = 42.4\,\mathrm{cm^3/mol}$ and $C = 3.25\,\mathrm{J/mol\,K}$ the correction is of order 12 kbar, which is a large fraction of the total anomaly in the bulk modulus. (For mixed-valent compounds with $T_0 \gtrsim 100\,\mathrm{K}$ this is less of a problem because the thermodynamic Grüneisen parameter is dominated by the phonon term, which is small.) Note that for heavy fermions, when $\Omega \approx \Omega_e$ and $C \approx C_e$, we have, by eqs. (8) and (13),

$$B_s \approx B_0 + \frac{U_e}{V} \Omega_e^{(2)}. \tag{15}$$

For a Kondo-like free energy (eq. 7), U_e increases monotonically with temperature, so B_s also will increase with T unless $\Omega_e^{(2)}$ happens to be negative (Yoshizawa et al. 1986, Thalmeier 1988).

The specific heat at constant volume C_v is related to the measured isobaric specific heat C_p by the thermodynamic relation

$$C_p - C_v = T V \beta^2 B_T. \tag{16}$$

For a mixed-valent compound with a maximum thermal expansion anomaly of order 10^{-4}/K at $T_m = 100\,\mathrm{K}$ and $V = 50\,\mathrm{cm^3/mol}$, $B_T = 10^3$ kbar, this difference is as large as $5\,\mathrm{J/mol\,K^2}$, which is an appreciable fraction of the expected anomaly in C_v. (On the other

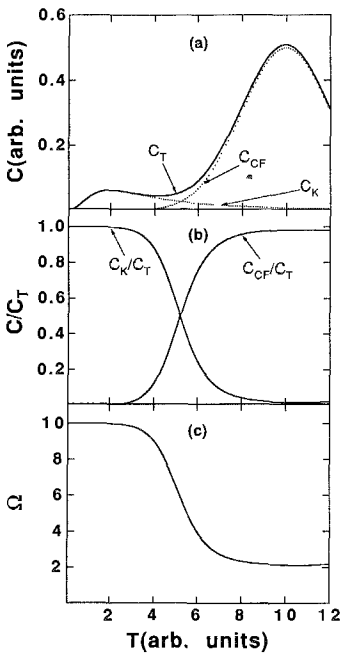

Fig. 22. (a) Hypothetical plot of the specific heat $C_T = C_{CF} + C_K$ with two contributions, a Kondo contribution C_K with $T_K = 2$ and a crystal-field contribution C_{CF} centered at $T_{CF} = 10$. (b) Temperature variation of the ratios C_K/C_T and C_{CF}/C_T. (c) Temperature-dependent Grüneisen parameter for the case $\Omega_K = 10$ and $\Omega_{CF} = 2$ obtained from eq. (17).

hand, if β_e is a small fraction of β, the correction term will be similar in the non-magnetic counterpart and can be subtracted out.)

The Grüneisen "constant", defined in terms of experimental parameters $\Omega(T) = VB_T\beta/C_p$, can exhibit significant variation with temperature (de Visser et al. 1989a, Franse et al. 1989). This arises because for heavy-fermion and mixed-valent compounds there can be several relevant temperature scales and concomitant contributions to the free energy: phonon, crystal field, single-ion Kondo, RKKY, etc. For each mechanism, there will be a different Grüneisen constant. To see the effect of this, suppose there are two contributions, e.g. a Kondo and a crystal-field contribution, with separate Grüneisen constants Ω_K and Ω_{CF}. Then

$$\Omega_T = VB\frac{\beta_K + \beta_{CF}}{C_K + C_{CF}} = \Omega_K\frac{C_K}{C_T} + \Omega_{CF}\frac{C_{CF}}{C_T}, \tag{17}$$

where the subscripts K, CF and T refer to the Kondo, crystal field and total contributions, respectively. In fig. 22 we show the effect of adding these contributions for a case where $\Omega_K = 5\Omega_{CF}$, and for a situation where $\Delta_{CF} > k_B T_K$. The total Grüneisen constant crosses over from its high-temperature value to its low-temperature value in a manner that clearly depends on the details (T_{CF}/T_K and Ω_K/Ω_{CF}). Alternatively, if $\Omega_T(T)$ is known from β, C and B and if the high- and low-temperature values are used to determine Ω_K and Ω_{CF}, then eq. (17) can be solved for $C_K(T)$ and $C_{CF}(T)$ separately, e.g.

$$C_K(T) = \frac{\Omega_T - \Omega_{CF}}{\Omega_K - \Omega_{CF}} C_T(T). \tag{18}$$

Hence, knowledge of β, C_p and B_T allows for separation of the ground-state doublet specific heat from the crystal field contribution – a very useful result.

3.2. *Grüneisen analysis for Ce-, Yb- and U-compounds*

3.2.1. *Ce and Yb mixed-valent compounds*

$CeSn_3$ is one of the few cases where C, β and B have all been measured over an appreciable temperature range; hence it is an important test case for the Grüneisen analysis. In fig. 23a we test eq. (1). This is done by comparing the 4f contribution β_e to the thermal expansion (obtained by Umlauf et al. 1980 using X-ray diffraction data) to the 4f contribution to the specific heat (Costa et al. 1982) by multiplying the former by VB_T/Ω_e; a value $\Omega_e = 11.4$ was utilized to make the maximum values of $C(T)$ and $C_{Gr}(T) = VB\beta_e/\Omega_e$ coincide. (Application of eq. 16 shows that C_p differs from C_v by only a few percent in $CeSn_3$). At the lowest temperatures, the thermal-expansion coefficient determined from the data of Umlauf et al. (1980) is linear, varying approximately as $\beta_e = bT$ where $b = 0.22 \times 10^{-6}/K^2$. Values of b are given in table 4 for a number of compounds. Comparing this to the 4f contribution to the specific heat ($C_e = \gamma T$ with $\gamma = 0.042$ J/mol K^2) gives $\Omega_e = 18$. Takke et al. (1981), using data for b obtained via capacitive dilatometry, obtain a value $\Omega = 10$. The Grüneisen parameters compare reasonably well to that discussed in sect. 2.2 and shown in table 6.

In order to perform this analysis, the background contributions C_0 and β_0 to C_p and β must be determined. Typically these are estimated from a non-magnetic counterpart, e.g. $\beta_e(CeSn_3) = \beta(CeSn_3) - \beta(LaSn_3)$. Because phonon contributions to β and C_p become important above 30–50 K, this kind of subtraction can contribute error to the determination of β_e and C_e. A difference of 10 K or more in the Debye temperatures of a cerium compound and its lanthanum counterpart can lead to comparable error in the temperature of the specific-heat maximum (Pott et al. 1981a). This is especially problematic for mixed-valent compounds in which the peak in C_e occurs at temperatures greater than 30 K. Indeed, C_e can be difficult to determine in this situation as it involves a small difference between two large quantities (Costa et al. 1982). Furthermore, the low-temperature thermal expansion is quite small and difficult to determine. Given these uncertainties, the comparison between β_e and C_e is quite respectable; it suggests that the scaling assumption is valid to 10–20% over the whole temperature range.

We next test the relationship between β_e and the bulk modulus B_e. This is done in fig. 23b for $CeSn_3$ and in fig. 24 for the mixed-valent compounds $CeBe_{13}$, $CePd_3$ and $Ce_3Bi_4Pt_3$. In using eq. (10) we choose a value of Ω_{eff} that gives a reasonable fit to the data at low temperatures and we ignore the distinction between B_T and B_S. (As discussed above, although eq. (1) is expected to be valid at all temperatures, eq. (10) is only valid for small T/T_0; hence, deviations are expected at high temperatures). For $CePd_3$ and $CeBe_{13}$, Ω_{eff} is comparable to Ω (table 5), suggesting that $\partial^2 T_0/\partial V^2$ is negligible. For $CeSn_3$ and $Ce_3Bi_4Pt_3$, the value $\Omega_{eff} = \Omega/2$ gives a good fit to the low-temperature bulk modulus (suggesting $\partial^2 T_0/\partial V^2$ is not negligible). The difference between the two cases can be understood by examining the values of $\Omega_e^{(2)}$ (table 5) which are derived from eq. (11) by

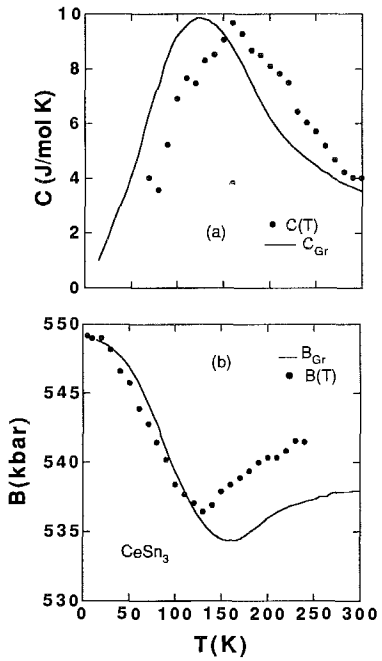

Fig. 23. Grüneisen analysis for the mixed-valent compound $CeSn_3$. Part (a) compares the 4f contribution to the specific heat C (closed circles) to the thermal expansion β_e (solid line) where the latter has been multiplied by VB/Ω_e, after eq. (1). A value of $\Omega_e = 11.4$ is utilized. Part (b) compares the measured bulk modulus B to the prediction of eq. (10), $B_{Gr} = B_0 - TB_0\,\Omega_{eff}\,\beta$; a value $\Omega_{eff} = \Omega_e/2 = 5.7$ is used for the comparison. Data for C from Costa et al. (1982); for β_e from Umlauf et al. (1980); and for B from Takke et al. (1981).

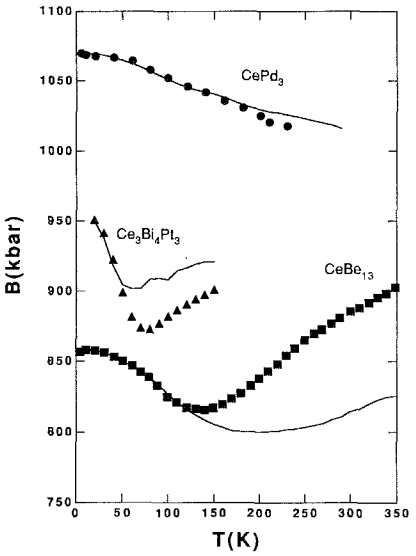

Fig. 24. The measured bulk moduli of $CePd_3$, $Ce_3Bi_4Pt_3$ and $CeBe_{13}$ compared to the thermal expansion using eq. (10). Values for Ω_{eff} are listed in table 5. Data for $CePd_3$ from Takke et al. (1981); for $CeBe_{13}$ from Lenz et al. (1984); for $Ce_3Bi_4Pt_3$ from Kwei et al. (1992).

determining the difference $\delta B_e(0) = B_{Ce}(0) - B_{La}(0)$ between the low-temperature bulk moduli of the Ce compound and its La counterpart. By eq. (12), if $\delta\Omega = \Omega_e^{(2)}/2\Omega_e$ is much less than Ω_e, then we expect $\Omega_{eff} = \Omega_e$. For $CePd_3$, in which $\delta B_e(0) = -6$ kbar is small so that $\delta\Omega = 0.3$–0.4, then $\Omega_{eff} = \Omega_e$. However, for $Ce_3Bi_4Pt_3$, $\delta B_e(0) = -260$ kbar is substantial and $\delta\Omega = 10$ is large, so that $\Omega_{eff} < \Omega_e$. From the observation that Ω_e is independent of pressure in UPt_3 and YbCuAl, as discussed earlier, we expect a large value of $\delta\Omega$ and hence a large value of $B_e(0)$. Overall, the Grüneisen prediction is consistent with the observed bulk moduli, lending further credibility to the scaling assumption. It is to be noted further that $Ce_3Bi_4Pt_3$ is a small-gap semiconductor (Hundley et al. 1990); the Grüneisen analysis gives an excellent estimate of the low-temperature bulk modulus even in this situation.

Table 4
Experimental quantities necessary for estimating the Grüneisen parameters Ω_T and Ω_H [a]

Compound	V ($\frac{cm^3}{mol}$)	$\chi(0)$ $\frac{10^{-3}emu}{mol}$	Ref.	γ $\frac{J}{mol\,K^2}$	Ref.	b $10^{-6}/K$	Ref.	S_V $\frac{10^{-15}}{Oe^2}$	Ref.	B Mbar	Ref.	T_K (K)	$3T_m$ K	Ref
$CeAl_3$	51.5	36	1	1.4–1.6	1,2	−126	3	14.0	3,4	0.46	5	2.9	– –	
$CeBe_{13}$	84.2	2.1	6	0.155	7	0.27	8	0.41	9	0.86	10	189	420	6
$CeCu_6$	63.3	27	11	1.6	2	26	12	18.0	4	0.91	13	2.7	– –	
$CePd_3$	41.8	1.4(2.0)	14	0.035	7	0.08	15	–	–	1.02	15	621	375	14
$CeSn_3$	62.1	2.0	16	0.042	7	0.12	15[b]	0.75	9	0.54	15	518	420	16
$Ce_3Bi_4Pt_3$	50.2	2.2	17	–	–	–	–	–	–	0.96	18	–	240	17
$CeCu_2Si_2$	50.4	8	11	1.0	11	8.6	19	6.1[c]	4	1.25	20	4.3	– –	
$CeRu_2Si_2$	51.7	16	21	0.385	21	12.9	22	50[d]	22	1.05	22	11.3	– –	
YbCuAl	33.2	26	23	0.255	24	−2.6	23	−22	9	1.0[e]	–	120	78	23
$YbCu_2Si_2$	46.4	27	25	0.135	26	–	–	−18	4	0.92	20	226	– –	
UAl_2	35.9	3–4	27	0.133	28	0.99	28	–	–	0.74	28	–	– –	
UBe_{13}	81.2	15	11	1.0	2	–	–	0.6	29	1.03	20	–	– –	
UPt_3	42.4	8.2	11	0.450	11	4.5	30	2.3	31	2.08	32	–	– –	

[a] Abbreviations: V, molar volume; $\chi(0)$, $T \to 0$ limit of the magnetic susceptibility; γ, Sommerfeld coefficient; b, linear coefficient of thermal expansion; S_V, volume magnetostriction at 4.2 K; B, bulk modulus; T_K, Kondo temperature derived from the relation $T_K = (N-1)\pi R/6\gamma$, where N is the ground-state degeneracy; $3T_m$, three times the temperature at which $\chi(T)$ is a maximum and an alternative estimate of T_K for systems in which $N = 6$ or 8.

[b] A value of $b = 0.22 \times 10^{-6}/K^2$ for $CeSn_3$ was reported originally by Umlauf et al. (1980).

[c] Value for a non-superconducting sample.

[d] Value at 1.3 K.

[e] Estimate used in this article.

References

(1) Andres et al. (1975)
(2) Phillips et al. (1987)
(3) Ribault et al. (1979)
(4) Zieglowski et al. (1986)
(5) Niksch et al. (1980)
(6) Kappler and Meyer (1979)
(7) Cooper et al. (1971)
(8) Pott et al. (1981b)
(9) Häfner (1985)
(10) Lenz et al. (1984)
(11) Stewart (1984)
(12) de Visser et al. (1990a)
(13) Shibata et al. (1986)
(14) Lawrence et al. (1987)
(15) Takke et al. (1981)
(16) Shaheen et al. (1983)
(17) Hundley et al. (1990)
(18) Kwei et al. (1992)
(19) Lang (1991)
(20) Robinson et al. (1986)
(21) Thompson et al. (1985)
(22) Lacerda et al. (1989a)
(23) Mattens et al. (1980)
(24) Pott et al. (1981a)
(25) Shimizu et al. (1987)
(26) Sales and Viswanathan (1976)
(27) Wire (1985)
(28) de Visser et al. (1987)
(29) de Visser et al. (1989a)
(30) de Visser et al. (1990b)
(31) de Visser et al. (1986)
(32) Benedict et al. (1987)

We next demonstrate these relations for the mixed-valent compound YbCuAl. As seen in fig. 8, this material has a susceptibility maximum near 25 K, with a linear coefficient of specific heat $\gamma = 0.26$ J/mol K^2 (Mattens et al. 1980, Pott et al. 1981a). These numbers imply (Rajan 1983) a Kondo temperature in the range 60–100 K. The thermal-expansion anomaly is negative in Yb compounds because the trivalent state has a smaller volume than the divalent state that is increasingly favored at low temperature due to the hybridization. In the inset of fig. 25 we show the volume expansion

Table 5
Grüneisen parameters[a] for some mixed-valence and heavy-fermion compounds

Compound	Ω_e	Ω_{eff}	$\Omega_e^{(2)}$	$2\Omega_H - \Omega_c$	Ω_H
$CeAl_3$	−210[b]	−400	–	18[c]	–
$CeBe_{13}$	17	13.5	–	28	22
$CeCu_6$	110	–	–	102	113
$CePd_3$	10	10	5–8[d]	–	–
$CeSn_3$	11[e],10	5.7	–	26	18
$Ce_3Bi_4Pt_3$	36[f]	18	654[g]	–	–
$CeCu_2Si_2$	54	–	–	96	75
$CeRu_2Si_2$	175	–	–	339	270
YbCuAl	−34[e]	–	–	−56	−45
$YbCu_2Si_2$	–	–	–	−57	–
UAl_2	20	–	–	–	–
UBe_{13}	>35[e]	–	–	8	34[h]
UPt_3	70	–	–	50	69

[a] Ω_e, determined from eq. (1) and entries in table 4; Ω_{eff}, determined from eq. (10) and data in figs. 23, 24 and 30; $2\Omega_H - \Omega_c$, determined from values of S_V given in table 4 and eq. (24); $\Omega_e^{(2)}$, determined from eq. (11) with $\delta B = B_{Ce} - B_{La}$.

[b] At 0.1 K.

[c] At 4.2 K.

[d] Bulk modulus for $LaPd_3$ from Takke et al. (1980).

[e] Determined from overall comparison of C and β in figs. 23, 25 and 28.

[f] Derived from the pressure dependence of the temperature at which the thermal expansion is a maximum (Kwei et al. 1992).

[g] Bulk modulus for $La_3Bi_4Pt_3$ from Kwei et al. (1992).

[h] Derived using $\Omega_c = 60$ from table 6.

$\Delta V/V$, which clearly varies as T^2. The resulting low-temperature thermal expansion coefficient $b = -2.6 \times 10^{-6}/K^2$, when compared to γ gives $\Omega/B = Vb/\gamma = -0.034$/kbar. This compares quite favorably to the shift in the susceptibility maximum with pressure ($\partial T_m/\partial P = -1$ K/kbar (Mattens et al. 1980) so that $\partial \ln T_m/\partial P = -0.04$/kbar). Although the bulk modulus has not been measured, if we assume a typical value $B = 1$ Mbar, then $\Omega = -34$. In fig. 25a we compare the measured 4f specific heat C_e to the prediction C_{Gr} where this value $\Omega = -34$ is utilized in eq. (1). Although the fit is good at low temperatures, there is substantial deviation above 30 K. To emphasize this point we plot in fig. 25b the ratio $\beta_e/C_e = \Omega_e/B$ as a function of temperature. Under the assumption $B = 1$ Mbar, it is seen that Ω_e varies from −34 at $T = 0$ to about −6 at 250 K. Except for the change in sign (expected for an Yb compound), the temperature dependence of the data in fig. 25b is similar to that shown in fig. 22c; this suggests that the temperature variation arises from excitation of higher-lying crystal-field levels (with $\Omega_{CF} = -6$, which implies that $\partial T_{CF}/\partial P < 0$). As we will see, crystal fields play a clear role in heavy-fermion compounds in which $T_K \ll T_{CF}$; whereas they are unimportant in mixed-valent compounds where $T_K \gg T_{CF}$. YbCuAl clearly forms an intermediate case ($T_K \approx T_{CF}$) so the Grüneisen analysis is affected by the crystal fields.

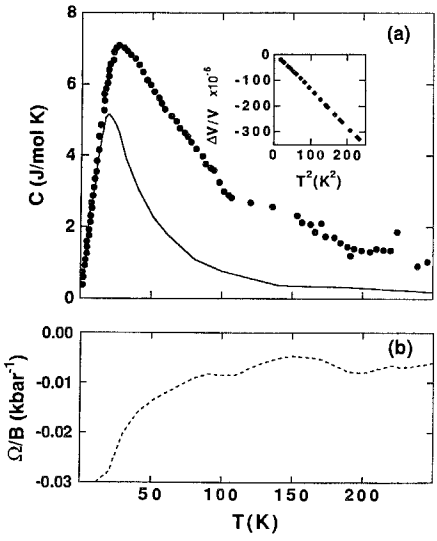

Fig. 25. Grüneisen analysis for the mixed-valent compound YbCuAl. The inset shows that the low-temperature volume expansion is negative and quadratic in temperature. (a) Comparison of the measured specific heat (solid circles) to the thermal expansion (solid line) where the latter has been multiplied by $V(B/\Omega_e)$ after eq. (1). A value $\Omega_e/B = -0.034$ kbar is utilized. (b) Variation of Ω_e/B as a function of temperature ($\Omega_e/B = V\beta_e/C_e$). If the bulk modulus is assumed to have a value 1 Mbar, the Grüneisen parameter then varies from a value -35 at low temperature to -6 at 250 K. (After Pott et al. 1981a and Mattens et al. 1980.)

3.2.2. *Ce and U heavy-fermion compounds*

For heavy-fermion compounds the specific heat is large at low temperatures and the phonon terms are more readily separated than for mixed-valent compounds. For U-based heavy fermions, where it is not necessarily clear which non-magnetic counterpart compound to use to estimate the phonons, the Grüneisen analysis can be used to separate the phonon contribution (Franse et al. 1989). In fig. 26 we show Ω_T for UPt_3 at $T < 35$ K. At low temperatures Ω_T approaches the value 70 but at 35 K it is less than 5. At room temperature $\Omega_T = 2.35$. An analysis similar to that of eq. (18) and fig. 22 can be performed, assuming two contributions, a heavy-fermion contribution with $\Omega_K = 73$ and a phonon contribution with $\Omega_{ph} = 2.35$. The results are shown in fig. 26. The resulting peak for $C_K(T)$ resembles the predicted anomaly for a spin 1/2 Kondo-ion with $T_K = 16$ K. The curve for $C_{ph}(T)$ is compared to the lattice-specific heat which is deduced from phonon-dispersion curves. Although the Grüneisen prediction for C_{ph} has the correct overall temperature dependence, it is larger than the expected phonon contribution below 10 K, which may imply that an additional electronic contribution exists. These comparisons suggest that the Grüneisen analysis is reasonable. Two key points are that the Grüneisen constant is very large at low temperature and that it does not appear to approach a constant value as expected on the basis of fig. 22.

For Ce-based heavy fermions, lanthanum-based counterparts can be used to estimate the lattice contributions. In general the heavy-fermion characteristic temperature is much smaller than the crystal-field splitting so the Grüneisen analysis allows ready separation into crystal-field and heavy-fermion contributions. This is shown for $CeRu_2Si_2$ (Lacerda et al. 1989a) in fig. 27. The Grüneisen constant approaches an extremely large value $\Omega = 190$ as $T \to 0$ but is negative above 60 K. The thermal expansion is compared

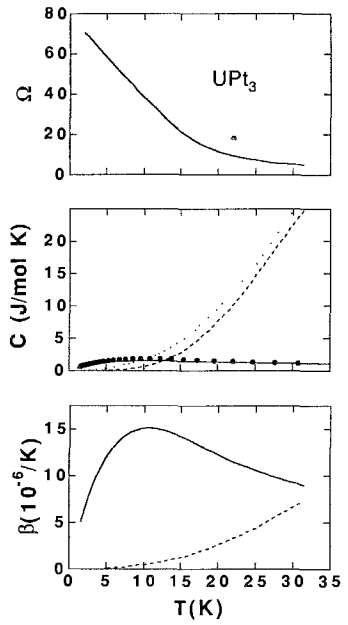

Fig. 26. Grüneisen analysis for UPt_3. The upper plot shows the temperature-dependent Grüneisen parameter $\Omega(T)$ determined from $C(T)$ and $\beta(T)$ using eq. (1). The equation $\Omega(T) = \Omega_K(C_K/C_T) + \Omega_{ph}(C_{ph}/C_T)$ is then solved for $C_K(T)$ and $C_{ph}(T)$ under the assumption $\Omega_K = 73$ and $\Omega_{ph} = 2.35$. These are shown in the middle plot (C_K: solid circles; C_{ph}: dotted curve) and compared to the theoretical prediction for a Kondo doublet with $T_K = 16\,K$ (solid lines) and to the lattice-specific heat deduced from phonon dispersion curves (dashed line). The bottom plot shows the Kondo and phonon contributions to the thermal expansion deduced from the same analysis. Data are from Franse et al. (1989).

favorably to that predicted for a Schottky anomaly with $\Delta_{CF} = 288\,K$ (a value 220 K is inferred from a similar analysis of the specific heat) and a negative parameter $\Omega_{CF} = -5.3$. At low temperatures the thermal expansion compares favorably to the prediction of a resonance-level approximation to a Kondo doublet ($\Omega = 190$ and $T_K = 19\,K$). As for UPt_3, the Grüneisen constant is enormous at low temperatures but does not appear to saturate to a constant low-temperature value.

Figure 28 shows the temperature-dependent Grüneisen parameter for three heavy-fermion compounds: UBe_{13}, $CeRu_2Si_2$ and $CeCu_6$. (For the cerium compounds the phonon contribution has been subtracted.) In each case the low-temperature value of Ω appears to be larger than 50. Furthermore, as can be seen from tables 5 and 6, the Grüneisen parameters are in good agreement with those deduced from the pressure dependence of thermodynamic quantities.

For $CeCu_6$ and UBe_{13} no saturation of $\Omega(T)$ is observed below 1 K. This lack of saturation is disturbing because it suggests the basic scaling assumption may not be valid in the heavy-fermion ground state. For $CeRu_2Si_2$ no saturation of $\Omega(T)$ is observed in fig. 27; however, when Ω is recomputed (Lacerda 1990) using more recent specific-heat data, saturation (to a value 170) occurs below 5 K, as shown in fig. 28. This suggests that part of the difficulty is simply that more accurate low-temperature measurements of β and C_p (preferably on identical samples) may be required. Another possible explanation of the lack of observed saturation is that the Grüneisen parameter reaches its saturation value only below the temperature T_{coh} where coherence sets in. Assuming that T_{coh} is a small

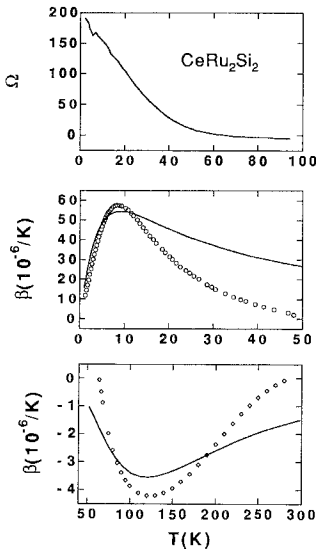

Fig. 27. The temperature-dependent Grüneisen parameter for $CeRu_2Si_2$ deduced from data for $C(T)$ and $\beta(T)$ and using eq. (1). Use of eq. (8) with $\Omega_K = 190$ and $\Omega_{CF} = -5.3$ allows separation of the thermal expansion into Kondo and crystal-field contributions (open symbols in the middle and bottom plots). These are compared to the predictions of a resonance-level approximation for a Kondo doublet with $T_K = 19$ K (solid line, middle plot) and a Schottky anomaly with $\Delta_{CF} = 288$ K (solid line, bottom plot). Data from Lacerda et al. (1989a).

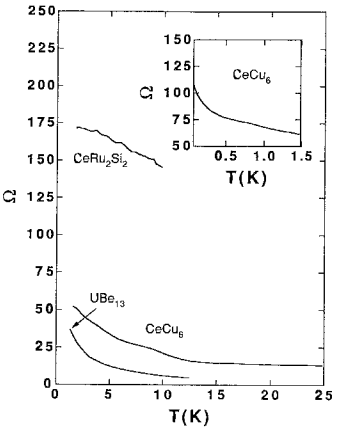

Fig. 28. Temperature-dependent Grüneisen parameters for $CeCu_6$, $CeRu_2Si_2$ and UBe_{13}. Data for $CeCu_6$ from de Visser et al. (1989b) and de Visser et al. (1990a); for $CeRu_2Si_2$ from Lacerda (1990); for UBe_{13} from de Visser et al. (1989b).

fraction of the single-ion Kondo temperature (e.g. $T_{coh} = 0.1\,T_K$), we expect saturation below 0.3 K, 0.5 K, 1.3 K and 1.7 K for $CeCu_6$, UBe_{13}, UPt_3 and $CeRu_2Si_2$, respectively (de Visser et al. 1990a). The measurements shown for $T > 1.5$ K may thus need to be extended to a lower temperature. This has been done for $CeCu_6$ (inset of fig. 28). The value of Ω at $T = 0$ agrees well with Ω_c (table 1), but it is surprising that $\Omega(T)$ is not constant over any temperature range.

A few comments are in order:

(a) The crystal-field Grüneisen parameters are negative for $CeRu_2Si_2$ and YbCuAl but positive for $CeCu_6$. For the former cases we expect $\partial\Delta_{CF}/\partial P$ to be negative. As discussed in sect. 2.3.1 this is also believed to be true for CePt, $CeAl_2$ and UCd_{11}. On the basis of a point-charge model, $\Delta_{CF} \propto 1/r$, where r is the interatomic distance, and we would expect $\partial\Delta_{CF}/\partial P$ always to be positive. In a metal, though, screening can alter the situation fundamentally and can lead to a pressure-induced decrease in the crystal-field splitting.

(b) Lacerda et al. (1989a) have suggested that the interplay between Kondo and crystal-field effects may to some extent invalidate the assumption of single-energy

Table 6
Comparison of low-temperature Grüneisen parameters derived from various sources[a]

Compound	Ω_C	Ω_χ	Ω_{T_m}	Ω_A	Ω_{T_0}
$CeAl_3$	160[b]	nd[c]	nd	383[b]	37
$CeCu_6$	115	nd	nd	nd	127
$CeSn_3$	nd	9	13[d]	7	18
$CeCu_2Si_2$	80	nd	nd	nd	22
$CePt_2Si_2$	nd	26	nd	60	28
$CeRu_2Si_2$	nd	171	nd	177	nd
$YbCu_{4.5}$	−23	nd	nd	<0	−11
YbCuAl	−50	−26	−40[e]	nd	−32
UAl_2	nd	18	nd	19	22
UBe_{13}	63	9	nd	17	103
UPt_3	59	58	51[f]	61	76
URu_2Si_2	36	29	nd	>0	19

[a] Ω values derived as follows: Ω_C from low-pressure specific heat; Ω_χ from magnetic susceptibility; Ω_{T_m} from pressure dependence of the temperature T_m where the susceptibility is a maximum; Ω_A from T^2-coefficient of resistivity; Ω_{T_0} from T_0 which is derived from resistivity as either T_m or T_i.

[b] At very low temperatures $\Omega_c = -200$ and Ω_A is slightly negative.

[c] nd, not determined.

[d] Shaheen et al. (1983).

[e] Mattens et al. (1980).

[f] de Visser et al. (1987).

scaling for the crystal-field contribution. This is corroborated by calculations using the $1/N$ approximation (Gunnarsson and Schönhammer 1985) which show that $\Delta_{CF} = \Delta^0_{CF} + k_B T_K$, where Δ^0_{CF} is the crystal-field splitting in the absence of a Kondo effect. Because for Ce compounds T_K is expected to increase with pressure, the negative Δ_{CF} mentioned above must come from the volume dependence of Δ^0_{CF}.

(c) When the Grüneisen parameter is very large, the heavy-fermion contribution dominates the thermal expansion, as can be seen in fig. 26 for UPt_3. This makes it substantially easier to deduce the heavy-fermion specific heat.

(d) For all the compounds discussed here, measurements have been performed on single crystals. The thermal expansion is in general highly anisotropic. Data in figs. 26–28 for the volume-expansion coefficient are given for the appropriate directional average. There is considerable further information about strain dependence to be deduced from the single-crystal studies. For example, in $CeCu_6$ (de Visser et al. 1989a) the crystal field has the biggest effect on the b-axis expansion but at low temperatures in the heavy-fermion regime the c-axis shows the biggest expansion, consistent with the c-axis being the magnetic easy axis. Similarly, in $CeRu_2Si_2$ (Lacerda et al. 1989a) the c-axis expansion is four times larger than the a-axis expansion and the c-axis is the magnetic easy axis. It is believed that the low-temperature anisotropy in thermal expansion reflects the antiferromagnetic correlations that are known to exist in these compounds.

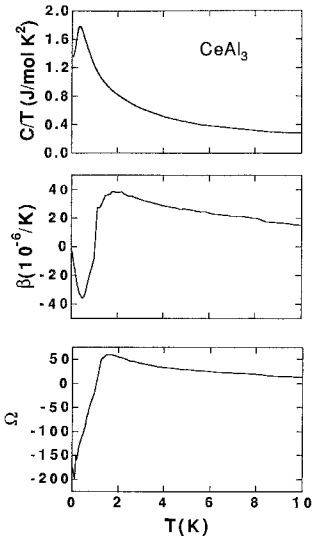

Fig. 29. Grüneisen analysis for $CeAl_3$ showing the measured coefficients of specific heat (upper plot), thermal expansion (middle plot) and the Grüneisen parameter deduced from their ratio (lower plot). As the temperature is lowered Ω approaches saturation to a value ~50. Below 1 K it crosses over to a large negative value (−200) appropriate to the ground state. Data for $C(T)$ from Phillips et al. (1987); for β from Andres et al. (1975) and from Ribault et al. (1979).

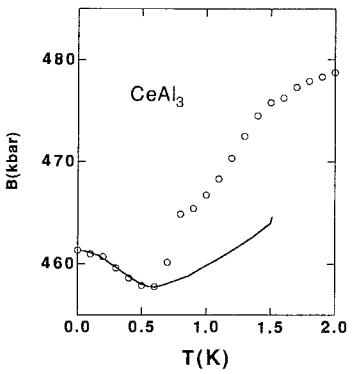

Fig. 30. The measured bulk modulus of $CeAl_3$ (open circles) compared to the thermal expansion using a value $\Omega_{eff} = -400$ in eq. (10). Data for B from Niksch et al. (1980); for β from fig. 29.

Finally we consider the case of $CeAl_3$, data for which are shown in fig. 29. It can be seen that the Grüneisen parameter rises between 1 and 2 K to a value $\Omega_K \approx 50$, which agrees well with the low-temperature Ω_c deduced by Phillips et al. (1987) for $P > 0.4$ kbar. However, below 0.5 K it crosses to an extremely large negative value of order −200. As mentioned in sect. 2.1, the initial belief (Flouquet et al. 1982, Bredl et al. 1984) was that this unusual change reflects single-ion behavior above 0.5 K and then the onset of coherence below 0.5 K, thus validating the notion that the value of Ω in the coherent regime can be very different from the value in the single-ion Kondo regime. More recently (Barth et al. 1987) NMR and muon-resonance data have been interpreted in terms of the onset of small-moment antiferromagnetic order below 0.5 K. (Because there is a measurable amount of entropy ~$0.1R \ln 2$ developed below 0.5 K, the lack of a sharp peak in C_p due to the phase transition would imply substantial sample or spin inhomogeneity.)

Negative Ω implies that the specific heat should increase with pressure at the lowest temperature. As discussed in sect. 2.1, experiments on $CeAl_3$ (Phillips et al. 1987) show that an increase of P from 0 to 0.4 kbar causes the specific heat to decrease for all temperatures above 0.2 K. This appears to be a major violation of the Grüneisen analysis. A possible explanation is as follows: The thermal-expansion data of fig. 29 can be interpreted as having two contributions: a Kondo-like contribution

with $\Omega_K = 50$, dominating above 1 K, and an anomalous contribution with large negative Ω that peaks at $T_m = 0.4$ K. The former contribution has negative $\partial\gamma/\partial P$; the latter, positive. If, however, T_m decreases sufficiently rapidly with pressure that $T_m(P)$ becomes less than the lower limit of the measurement (0.2 K), then its positive contribution to $\partial\gamma/\partial P$ would go unobserved. Because a Grüneisen analysis suggests $\Omega = (B/T_m)\,\partial T_m/\partial P$, from $B = 460$ kbar (fig. 30) and $T_m = 0.4$ K, the requirement that $|\partial T_m/\partial P| > 0.2\,\text{K}/0.4\,\text{kbar}$ implies that $-\Omega = \partial \ln T_m/\partial \ln V$ must be greater than 575. Although the data for β and C_p do not support such a large negative value of Ω, it should be pointed out that the measurements shown in fig. 29 were performed on different samples and that $CeAl_3$ is notoriously difficult to prepare as a single-phase material. An analysis of the bulk modulus (fig. 30) requires a value of $\Omega_{eff} = -400$ to give a good fit to the low-temperature data, suggesting than an even larger value of Ω and hence $|\partial T_m/\partial P|$ may not be implausible.

3.2.3. *Moderately heavy-fermion uranium compounds*

Several uranium compounds with Sommerfeld coefficients in the range $\gamma = 90$–150 mJ/mol K^2 have had both thermal expansion and specific heat measured. Results for UAl_2 are shown in fig. 31. The Grüneisen parameter increases with temperature in a similar way as in UPt_3, except that the limiting value at $T = 0$ ($\Omega = 18$) is smaller. Indeed, this value is comparable to the value of Ω in mixed-valent compounds with similar values of γ. At higher temperatures Ω approaches values characteristic of phonons.

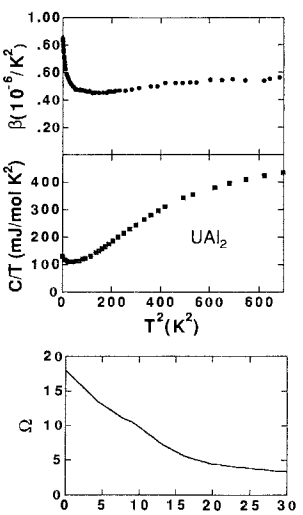

Fig. 31. Grüneisen analysis for the spin-fluctuation compound UAl_2. The upper plots show the measured coefficients of thermal expansion β and specific heat C_p/T. The lower plot shows the temperature-dependent Grüneisen parameter deduced using eq. (1). Data for C_p from Frings (1984); for β from de Visser (1986).

3.3. *Magnetostriction*

The Grüneisen analysis can be extended (Thalmeier 1988) to include the presence of a magnetic field. Starting from a Gibbs energy $dG = dU - SdT + VdP - MdH$ and the concomitant relation

$$\frac{\partial M}{\partial P} = -\frac{\partial V}{\partial H}, \tag{19}$$

it then follows in the low-field limit when $M = \chi H$ that the volume magnetostriction satisfies

$$\frac{V(H) - V(0)}{V} = \frac{H^2}{2BV}\chi\Omega_\chi, \tag{20}$$

where Ω_χ is given by eq. (5). To proceed further requires an assumption on how the free energy scales. The most general assumption (Thalmeier 1988, Kaiser and Fulde 1988) is that

$$F_e = -Nk_B T f\left(\frac{T}{T_0}, \frac{H}{H_0}\right), \tag{21}$$

i.e., H and T scale independently and H_0 is a field-scaling parameter. Defining

$$S_v = \frac{1}{V}\frac{\partial V}{\partial (H^2)}, \tag{22}$$

then under the scaling assumption it can be shown that

$$S_v = \frac{1}{2B_T V}\left[\left(\frac{M}{H} + \frac{\partial M}{\partial H}\right)\Omega_H + \left(\frac{T\,\partial M}{H\,\partial T} - \frac{M}{H}\right)\Omega_e\right], \tag{23}$$

where $\Omega_e = -\partial \ln T_0/\partial \ln V$ and $\Omega_H = -\partial \ln H_0/\partial \ln V$. In the low-field limit this becomes (Kaiser and Fulde 1988)

$$S_v = \frac{1}{2BV}\left[\chi(2\Omega_H - \Omega_e) + T\frac{\partial \chi}{\partial T}\Omega_e\right]. \tag{24}$$

In general at low temperatures $T \ll T_0$, where $\chi = \chi(0)[1 \pm b(T/T_0)^2]$ and b is a constant of order unity, the second term can be ignored. Measurement of the forced magnetostriction then allows extraction of the quantity $(2\Omega_H - \Omega_e)$. If Ω_e is known, Ω_H can be determined.

In fig. 32 we show the magnetostriction for UPt_3, $CeBe_{13}$ and YbCuAl. The values of S_v at 4.2 K for a number of compounds are given in table 4. Although different groups report values of S_v differing by factors of two, it is clear that most of the values of $2B_T V S_v/\chi$ are

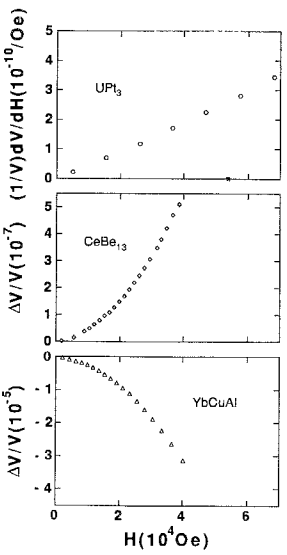

Fig. 32. Forced magnetostriction for $CeBe_{13}$ and YbCuAl and coefficient of magnetostriction for UPt_3 versus magnetic field at $T = 4.2$ K. Data for UPt_3 are from de Visser et al. (1986); for YbCuAl and $CeBe_{13}$ from Häfner (1985).

comparable to the values of Ω_e reported in table 5. (An exception is $CeAl_3$. However, the value reported at 4.2 K is comparable to $\Omega(4.2)$ for that compound, as seen from fig. 29.) This implies that $\Omega_H \approx \Omega_e$. For example, for $CeBe_{13}$ using $\Omega_e = 17$ and $2\Omega_H - \Omega_e = 30$ implies $\Omega_H = 23.5$. If we assume strict equality of Ω_H and Ω_e, then μH_0 and $k_B T_0$ are essentially identical. In this case the magnetostriction $2BVS_v/\chi$ will essentially equal Ω_e.

Other phenomenological versions of the scaling assumption have appeared in the literature. For example, Takke et al. (1981) assume

$$F = -Nk_B T f\left(\frac{(k_B T)^2 + (\mu H)^2}{T_0}\right). \tag{25}$$

This form clearly equates μH_0 and $k_B T_0$, hence $\Omega_H = \Omega_e$. Zieglowski et al. (1986) show that the relation $\Delta V/V = AH^2/(T + T_0)^2$ fits the data for a number of Ce and Yb compounds. For this formula $\mu H_0 = k_B T_0$, so again we expect $\Omega_H = \Omega_e$. Because $\chi \approx C/(T + T_0)$ for most heavy fermions, this form for $\Delta V/V$ follows from $\Delta V/VH^2 = (1/2B)\,\partial\chi/\partial V$, i.e., $A = -(C/2B)\,\partial T_0/\partial V$.

The scaling assumption need not be restricted to the low-field limit. Assuming that $\Omega_H = \Omega_e$ and that $\partial M/\partial T$ can be ignored, eq. (19) becomes (Thalmeier 1988)

$$\frac{1}{V}\frac{\partial V}{\partial H} = \frac{\Omega_e}{BV} H \frac{\partial M}{\partial H} \tag{26}$$

or

$$\frac{V(H) - V_0}{V_0} = \frac{\Omega_e}{2V} \int \frac{\partial M}{\partial H}\, \mathrm{d}(H^2) = \frac{\Omega_e}{BV_0} \int_0^H H\, \mathrm{d}M. \tag{27}$$

This form for the magnetostriction can be derived (Puech et al. 1988) from a simpler assumption, namely $M = m(H/H_0(P))$. Puech et al. (1988) noted, using this assumption, that the value of Ω so derived agreed with Ω_e for $CeRu_2Si_2$. This is seen in the present analysis to be a consequence of the equality of H_0 and T_0. That is, only a single-energy scale matters. In fig. 33 the magnetostriction coefficient of $CeRu_2Si_2$ is shown at 1.3 and 4.2 K and compared to the derivative of the magnetization as a test of eq. (26). The extracted value of Ω is 198 at 4.2 K and 176 at 1.3 K.

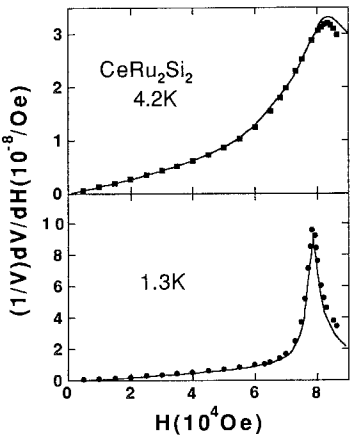

Fig. 33. Coefficient of magnetostriction for $CeRu_2Si_2$ at $T = 4.2$ and $T = 1.3$ K. Solid symbols are data from Lacerda et al. (1989a). Note that the anomaly at 8 T becomes narrower and more pronounced as the temperature is lowered. Similar data (Lacerda et al. 1991) for $0.12\,K < 1.3\,K$ suggest that at $T = 0$ the coefficient diverges at 8 T, so that a second order phase transition to the polarized state at $T = 0$ may occur in a magnetic field. The solid lines utilize the measured field-dependent susceptibility $\partial M/\partial H$ to predict the magnetostriction coefficient using eq. (26). Values of Ω equal 198 at 4.2 K and 176 at 1.3 K are utilized.

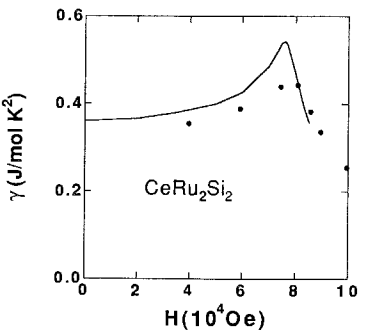

Fig. 34. The low-temperature Sommerfeld coefficient of $CeRu_2Si_2$ $\gamma(B) = C_p/T$ measured in fixed magnetic field (solid circles) compared to the field-dependent coefficient of thermal expansion using eq. (29). A value $\Omega = 158$ was utilized. Data for $\beta(B)$ are from Lacerda et al. (1989b); for $\gamma(B)$ from van der Meulen et al. (1991).

The scaling assumption, eq. (21), further implies that

$$\beta(H, T) = \frac{\Omega_e}{B_T V} C + \frac{\Omega_H}{B_T V} H \frac{\partial S}{\partial H}. \tag{28}$$

In the low-field limit, where $\beta = b(H)\,T$, $S = \gamma(H)\,T$ and $C_p = \gamma(H)\,T$, it follows that for $\Omega_H = \Omega_e$

$$b = \frac{\Omega_e}{BV}\left(\gamma + H\frac{\partial \gamma}{\partial H}\right). \tag{29}$$

This differential equation for $\gamma(H)$ can be integrated to determine $\gamma(H)$ in terms of $b(H)$ (Lacerda et al. 1989b). Data for C_p/T at 1.5 K are shown for $CeRu_2Si_2$ in fig. 34 and

are compared to the prediction for $\gamma(H)$ determined by using low-temperature thermal-expansion data $\beta(H, T)$ in the solution of eq. (29). The fit is quite reasonable if a value $\Omega_e = 158$ is used.

The peak in $\gamma(H)$ and $\partial V/\partial H$ at $H_m = 8\,\mathrm{T}$ in $CeRu_2Si_2$ arises from a continuous transition to a polarized state in magnetic field, as indicated in sect. 2.2; this will be discussed further below. Similar maxima occur (de Visser et al. 1989a) in UPt_3 near 21 T. Use of eq. (26) gives a Grüneisen parameter $\Omega_H \approx 50$ at 4.2 K which agrees with Ω_e (fig. 26).

3.4. *Sound velocities and anisotropic effects*

The Grüneisen analysis can be extended to include anisotropic thermal expansion and/or sound velocities (Lüthi 1985, Yoshizawa et al. 1986, Thalmeier 1988). To accomplish this it is assumed that a strain ε_Γ of symmetry Γ creates a deformation potential

$$E_k \rightarrow E_k + \frac{\partial E_k}{\partial \varepsilon_\Gamma}\varepsilon_\Gamma. \tag{30}$$

The Grüneisen assumption is that

$$\frac{\partial E_k}{\partial \varepsilon_\Gamma} = -\Omega_\Gamma E_k. \tag{31}$$

Different strains can have different Grüneisen parameters. The general belief is that only those deformations ε_{ij} with $i=j$ that are connected to volume change will have large Grüneisen parameters. Under these circumstances, as pointed out by Yoshizawa et al. (1986), the directional thermal expansion β_j is related to the specific heat via a generalization of eq. (1):

$$C(T;\, \varepsilon_{ii})\Omega_i = \sum C_{ij}\beta_j. \tag{32}$$

Here the C_{ij} are the full elastic constants for which the small heavy-fermion contribution can be ignored; on the contrary, $C(T;\varepsilon_{ii})$ [the specific heat at constant strain], β_j and Ω_i are dominated by heavy-fermion contributions. From eq. (32) β_j can be calculated, given knowledge of C_{ij} from experiment, and given a model density-of-states and assumed values of Ω_i so that $C(T;\varepsilon_{ii})$ can be calculated. (The model density-of-states is constrained by the low-temperature specific heat at constant volume.) Yoshizawa et al. (1986) have done this for hexagonal UPt_3 and have reproduced β_a and β_c (which is negative) very well. The negative β_c arises from different signs in the inverse elastic-constant matrix. Presumably a similar set of considerations can explain the anisotropic thermal expansions, mentioned above for $CeCu_6$, in the crystal-field regime.

Yoshizawa et al. (1986) argue that sound propagation in heavy-fermion systems is adiabatic. Assuming that ultrasound is damped by thermal conduction, the thermal diffusion time satisfies

$$\tau_{\text{diff}} = \frac{C_v}{Q^2\kappa} = v_s^2 \frac{C_v}{\omega^2\kappa}, \tag{33}$$

where Q is a wavevector and v_s is the sound velocity. For UPt_3 where the specific heat C_v is large and the thermal conductivity κ is small, this gives $\omega\tau_{\text{diff}} \approx 10^4$ at 10 MHz and 1 K, compared to $\sim 10^{-2}$ for normal metals. This implies adiabatic propagation. The adiabatic and isothermal elastic constants are related by a thermodynamic relation similar to eq. (13), namely

$$C_s - C_T = \Omega^2 T C_v. \tag{34}$$

Because Ω and C_v are large, this difference can be large. For example, for UPt_3 at 10 K where $\Omega = 70$, $C = 3$ J/mol K and $V = 42.4$ cm^3/mol, the result is $C_s - C_T = 34$ kbar, which is a large fraction of the anomaly in C_T. For this reason, the adiabatic elastic constants must be calculated for comparison to data.

Use of a model density-of-states with anisotropic Grüneisen coupling allows for calculation of the sound-velocity anomalies. In the heavy-fermion regime the adiabatic sound velocity computed for a single band under a scaling assumption analogous to eq. (7) has the same form as the adiabatic bulk modulus, eq. (15) (Thalmeier 1988). This implies that $C_s(T)$ must be monotonically increasing with temperature. This is the case for $CeCu_6$, and Thalmeier (1988) has demonstrated that the longitudinal sound velocity is indeed proportional to the internal energy computed for an Anderson lattice. For UPt_3, however, both C_{11} and C_{33} initially decrease with temperature. To fit the data, Yoshizawa et al. (1986) had to assume the existence of two heavy-fermion bands with slightly different state densities and Grüneisen couplings (see also Lüthi and Yoshizawa 1987). The model gives good simultaneous fits to C_{11}, C_{33}, β_a and β_c. The procedure, however, seems ad hoc.

The basic assumption that breathing-mode coupling (i.e. coupling to ε_{ii}) dominates the elastic response is probably valid for both mixed-valent and heavy-fermion compounds. An important difference is that several mixed-valent compounds ($Ce_{1-x}Th_x$, SmB_6, $Sm_{1-x}Y_xS$) have negative Poisson ratios $\nu = -\varepsilon_\perp/\varepsilon_\parallel$ (the ratio of the strains perpendicular and parallel the applied stress). Lüthi (1985) interprets this to mean that in these compounds, uniaxial stress can still lead to a change in valence or occupation number n_f which leads to a (symmetric) volume change. If so, this makes an important distinction between heavy-fermion and strongly mixed-valent compounds.

A scaling law also relates the softening of the longitudinal modes in the presence of a magnetic field to the differential susceptibility (Kouroudis et al. 1987, Thalmeier 1988):

$$\delta C_L(H, T) = -\Omega_H^2 H^2 \chi(H, T). \tag{35}$$

A maximum in $\chi(H, T)$ is observed at 8 T in $CeRu_2Si_2$ and at 21 T in UPt_3, with a corresponding minimum in the longitudinal sound modes at the same fields. The values of Ω_H extracted from the ratio $\delta C_L/H^2\chi$ (60 for UPt_3; 129 for $CeRu_2Si_2$) agree with those deduced for Ω_e.

4. Discussion of scaling behavior

The preceding description of pressure-dependent physical quantities raises several important questions: To what extent do Grüneisen parameters derived from different measurements reflect the same underlying physics, i.e., is the assumption of universality that led to eqs. (4)–(6) valid? Do scaling relationships found for $\chi(T,P)$ and $\rho(T,P)$ have a physical basis, and, if so, is it the same in anomalous lanthanide and actinide intermetallics? The response to these questions is quite simple: we do not have an answer. In some cases, perhaps there are partial answers which we will address in the following. Although substantial progress has been made in achieving a qualitative understanding (see, for example, Fisk et al. 1988a and Grewe and Steglich 1991), it is the lack of answers to these questions that makes the study of anomalous lanthanide and actinides such a challenging and exciting area.

If the assumption of universality is correct, Grüneisen parameters for various physical quantities should be identical (eqs. 4–6). We have calculated Grüneisen parameters from the entries in table 3 for the T^2-coefficient of resistivity, $\Omega_A \equiv B\sqrt{A}\,\partial(1/\sqrt{A})/\partial P$ and for T_0, $\Omega_{T0} \equiv (B/T_0)\,\partial T_0/\partial P$, and compare these in table 6 to values of Ω_c and Ω_χ given in tables 1 and 2, respectively. Comparison of results in tables 5 and 6 suggests that agreement among the various Grüneisen parameters is at best qualitative. Before discussing this further, we would first like to mention several sources for disagreements. We remind the reader that there are two methods that should give accurate values of Ω. One is to examine such quantities as $\partial \ln \gamma/\partial P$ in the limit $T \to 0$; the other is to demonstrate that the data exhibit a scaling law (such as $\chi(T)/\chi(T_m)$ versus T/T_m) and then calculate the pressure dependence of the scaling temperature (for the given case, this would be $\partial \ln T_m/\partial P$). Both methods suffer characteristic problems. For the first method, it may be difficult to make measurements at sufficiently low temperatures. For example, from fig. 28 it can be seen that for $CeCu_6$ measurement below 100 mK is required to get a good estimate of Ω. Both methods require estimation of background effects, e.g., non-f contributions to $\chi(0)$ or phonon contributions to $C_p(T)$ or $\rho(T)$. Background effects can be particularly significant when a broad temperature range is examined. Next we mention that the resistivity, which is the most widely studied pressure-dependent quantity, is the most poorly understood theoretically: the extent to which scaling of ρ is expected in periodic heavy-fermion compounds is not well established. This, together with the difficulties of estimating phonon contributions, can cause error in estimation of Ω, except for low-temperature measurements of the coefficient A. Furthermore, for some measurements, anisotropy may be important and could be responsible for discrepancies between estimates of Ω via uniaxial measurements (of χ or ρ) and isotropic measurements (of C_p or β).

Finally, much of the analysis is based on measurements performed on different samples. Because there is considerable sample dependence, this can lead to erroneous values of $\Omega(T)$. Ideally, measurements of ρ, χ, C_p, β, B, M and S_V would be performed on one high quality sample over a broad enough temperature range to encompass all the relevant scales (phonon, crystal-field, single-ion Kondo and coherent Fermi liquid). Such sample dependence should be most pronounced at low temperatures where impurity effects are most severe.

Given this, we note that in at least a few cases the agreement is surprisingly good: e.g., $CeCu_6$, $CeRu_2Si_2$, UAl_2 and UPt_3. For $CeSn_3$ the estimate Ω_{T0} from table 6 is based on the pressure dependence of the inflection point in the resistivity; this estimate suffers from the difficulties mentioned above. Otherwise, the agreement is rather good for $CeSn_3$. Indeed, for such compounds, the overall agreement suggests scaling is valid at the 15% level. The origin of the larger (~30%) disagreement for YbCuAl and $CeCu_2Si_2$ is not clear. We will discuss other anomalous cases below. Our conclusion is that scaling is only established for a few cases to the 15% level and that further work is in order.

The microscopic origin of scaling is best understood in the context of the Anderson Model. It is well-established that specific heat, susceptibility and resistivity for a spin-1/2 Kondo impurity are each universal functions of T/T_K (Andrei et al. 1983), provided k_BT is low compared to the bandwidth of the system. Rajan (1983) has used the Coqblin–Schrieffer model (Coqblin and Schrieffer 1969), appropriate for an impurity of arbitrary degeneracy $N=2J+1$, where J is the total angular momentum, to show that the susceptibility and specific heat assume universal functions of T/T_K that depend on N. Therefore, if N changes with pressure, scaling, e.g. of the form $\chi(T)/\chi(T_m)$ versus $T/T_m(P)$, should *not* hold over the entire pressure range but for fixed N scaling is expected. (In general, for modest pressures of the order ten kilobars, N should remain unchanged for the anomalous compounds we have discussed.) Further, Bickers et al. (1985) have established that for fixed N scaling of $\chi(T)$ and $\rho(T)$ with T/T_K is independent of the f-level occupancy for n_f in the range $0.86 < n_f < 1$, provided k_BT_K remains less than the f-level hybridization width, the bandwidth or spin-orbit splitting. We note that in this impurity limit, it is $\chi(T)$ and $\rho(T)$ normalized to their $T=0$ values that are universal functions of T/T_K. Because $\chi(T)$ exhibits a maximum at $T_m>0$ if $N>2$, scaling by $T/T_m(P)$ would be valid as well. Likewise, $\rho(T=0)$ is maximum for an impurity so scaling of ρ is of the form $\rho(T)/\rho(T_m)$ versus T/T_K. The extent to which these calculations for impurities are relevant to anomalous compounds is less clear but the similarity in scaling forms found experimentally for compounds and theoretically for impurities is suggestive. Indeed, for compounds such as $CeRu_2Si_2$ and UPt_3, where the low-temperature behavior is strongly affected by proximity to a metamagnetic transition, the fact that scaling works so well (e.g. figs. 7 and 9b) over a temperature range where magnetic correlations are obviously important clearly implies that the scaling is not a simple single-ion effect.

Although the scaling assumption that underlies the Grüneisen analysis – that $F(T,V) = -Nk_BTf(T/T_0(V))$ – appears to be a natural consequence of the scaling property of Kondo/Anderson models, the Anderson model does not in and of itself include coupling to

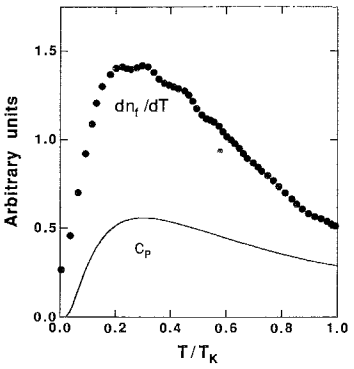

Fig. 35. Predictions of a slave-boson treatment of a Kondo insulator for the specific heat C_p (solid line) and temperature derivative of the f-occupation number dn_f/dT (solid circles). As opposed to the Anderson impurity model, where dn_f/dT peaks at a temperature which is 2–3 times larger than the temperature where C_p is maximum, for this Anderson Lattice calculation both quantities peak at roughly the same temperature. From Riseborough (1992).

the cell volume. Historically there have been two approaches to including this coupling. The first is to assume that the cell volume increases as the valence decreases. i.e., as n_f increases. This approach is clearest in Eu compounds in which large changes in lattice constants are accompanied by large changes in valence, as measured by L_{III} X-ray absorption or Mössbauer-isomer shift. However, when this form of coupling, for which ΔV varies proportionally to Δn_f at fixed T_K, is included in the Anderson impurity model, the Grüneisen relations do not follow. This can be seen for the case $n_f \approx 0.8$–0.9 where the Bethe-Ansatz (Schlottmann 1989) or $1/N$ expansion methods (Bickers et al. 1987) predict that the peak in $\partial n_f/\partial T$ occurs at a temperature 2–3 times greater than temperatures where the specific heat and susceptibility peak. Because the assumption $\Delta V \propto \Delta n_f$ implies that the temperature of the thermal expansion maximum coincides with the maximum in $\partial n_f/\partial T$, the Grüneisen proportionality between β and C_p cannot hold under these circumstances.

Although there are few treatments of the Anderson Lattice that simultaneously compute C_p, χ and n_f over a broad temperature range, two recent examples suggest that for the lattice case temperatures where C_p and $\partial n_f/\partial T$ peak are nearly equal. Brandow (1988) shows this for the metallic case and Riseborough (1992) shows it for the small-gap semiconducting case (fig. 35). Though these approaches do not include a coupling of T_K to V that underlies the scaling assumption, they do prevent the gross discrepancy between peak temperatures for β and C_p discussed above for the impurity case.

The second approach (Allen and Martin 1982) to include coupling to the lattice is to assume that the hybridization matrix element V_{kf} between the conduction electrons and the 4f electrons varies as the volume varies. This form of coupling receives justification (Freeman et al. 1988) from band theoretic treatments of cerium and its compounds that show that the cell volume can decrease when the 4f/conduction-band hybridization increases, without significant associated change in f-count. One way to include this in the Anderson model is to assume that the volume dependence of V_{kf} is reflected in a dependence of the characteristic (Kondo) temperature T_K on V. In the Kondo limit, where the occupation number $n_f \approx 1$ does not vary with temperature,

the assumption that $T_K = T_K\ [V_{kf}(V)]$ leads directly to the Grüneisen assumption $F_K(T,V) = -Nk_BTf[T/T_K(V)]$.

Thalmeier (1988) has calculated the adiabatic bulk modulus of the Anderson Lattice by including a strain dependence of V_{kf}: $V_{kf} \rightarrow V_{kf} + (\partial V_{kf}(V)/\partial\varepsilon)\varepsilon$. Using a slave-boson method for $\varepsilon = 0$ and second order perturbation theory with respect to $\partial V_{kf}(V)/\partial\varepsilon$, he finds

$$\delta B_s(T) = -\Omega^2\,[1 - n_f(T)]\ U_K(T), \tag{36}$$

where $U_K(T)$ is the Kondo-internal energy calculated in the slave-boson approximation. This expression yields a good fit to the longitudinal elastic constant anomaly of $CeCu_6$.

In reality both forms of coupling to the lattice are doubtless present. Under these circumstances nonlinear effects can occur. As the temperature increases, the concomitant increase in n_f will cause ΔV to increase which will decrease V_{kf} and hencc decrease T_K. This will lead to a further increase of $n_f = n_f(T/T_K(V))$ and will cause the thermal expansion to be more rapid than for fixed T_K. It is the basis of the "Kondo volume collapse" treatment of the γ–α phase transition in cerium (Allen and Martin 1982).

The dependence of T_K on V, which arises from this variation of V_{kf} with V, has a nonlinear property: the slope ($\Omega = -\partial \ln T_K/\partial \ln V$) is larger for small T_K than for large T_K. This trend has been noted already in sect. 1.4. from values of Ω and T_K tabulated for Kondo-impurity systems by Schilling (1979). In fig. 36 we have plotted the $T = 0$ Grüneisen constants versus the Sommerfeld coefficient, which is assumed to leading order to be proportional to $1/T_K$ for a lattice of Kondo ions. Although there is substantial scatter in this plot, the basic point is that large Ω corresponds to small T_K and vice versa. Recently Hong (1992) argued that for a Kondo temperature satisfying $T_K = E_F \exp(-\pi E_f/N_f N(E_F) V_{kf}^2)$, where only the hybridization depends significantly on volume V, then it follows that $\Omega = 2\lambda \ln(1/N(E_F)T_K)$ where $\lambda = \partial \ln V_{kf}/\partial \ln V$. According to this the Grüneisen parameter varies logarithmically, not linearly, with $1/T_K$; the volume dependence of the hybridization is equally important in enhancing Ω. Hence, a universal curve for $\Omega(T_K)$ is not expected, but Ω should increase with γ as observed. It should bc pointed out that, if T_K is a strictly linear function of P, then $\Omega = (B/T_K)\partial T_K/\partial P$ will vary as $1/T_K$ provided B is pressure independent.

As mentioned in the Introduction, the Grüneisen analysis implies *universality* that can be expected to obscure the microscopic differences between itinerant-f actinides and localized-f lanthanides. However, the analysis does permit distinctions to be made. For example, the equality of Ω_H, determined from magnetostriction, and Ω_e, determined from comparing β and C_p, has been discussed by Kaiser and Fulde (1988) and contrasted to the case of nearly ferromagnetic transition-metal paramagnets such as $Ni_{1-x}Pt_x$, where $\Omega_H \gg \Omega_e$. Assuming $C_p \propto N_f(E_F)T$ and $\chi \propto RN_f(E_F)$ where $N_f(E_F)$ is the heavy-electron density-of-states and R the susceptibility enhancement, or Wilson ratio, then $\Omega_H = \partial \ln \chi/\partial \ln V = \Omega_e + \partial \ln R/\partial \ln V$ (Thalmeier 1988). For the nearly ferromagnetic transition metals the susceptibility is more strongly enhanced than the specific heat, as can be seen from the large (5–100) Wilson ratio. This provides a sharp contrast to the

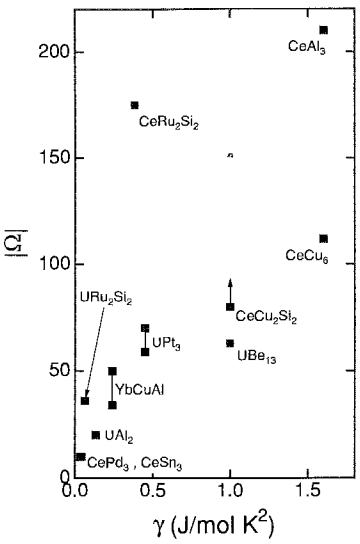

Fig. 36. Low-temperature Grüneisen parameter versus low-temperature coefficient of specific heat for several Ce, U and Yb compounds.

heavy-fermion compounds in which χ and C_p are enhanced approximately the same, with the result that $R \sim 1$–3 and $\Omega_H \approx \Omega_e$. This difference has its origin in the long wavelength character of spin fluctuations in the nearly ferromagnetic compounds, as opposed to the highly localized spin fluctuations in the nearly antiferromagnctic heavy fermions.

A potentially important use of the Grüneisen analysis is the exploration of anomalous cases. For example, while there is considerable scatter in fig. 36, the Grüneisen constant for $CeRu_2Si_2$ is exceptionally large for such a small value of γ. For this compound the scaling assumption, with $\Omega_e = \Omega_H$, correctly describes the relationships between M, V and C_p for $T < 10\,K$ (fig. 28) and $H < 10\,T$ (figs. 33 and 34). The peaks in $\partial V/\partial H$ and $\partial M/\partial H$ are due to a continuous transition from thc ground state, where heavy-fermion demagnetization and antiferromagnetic correlations coexist, to a polarized state for $H > H_m = 8\,T$ (Lacerda et al. 1989a). It is quite surprising that single-energy scaling is valid in this situation over such a broad range of temperature and magnetic field. In our opinion this may result from proximity to a fixed point at $T = 0$ and $H = H_m$. From fig. 33 it can be seen that the peak in the coefficient of volume magnetostriction becomes larger and sharper as the temperature decreases. Recent data (Lacerda et al. 1991) show that this trend continues as T is lowered to 0.12 K; the transition width approaches zero and the height of the maximum increases in such a way as to suggest that at $T = 0$ the magnetostriction diverges. This would imply a $T = 0$ phase transition as a function of field (de Visser et al. 1991). Proximity to such a fixed point could result in single-energy scaling in the H–T plane and may explain why Ω has such a large value relative to other compounds in which no such fixed point exists (Continentino 1994).

UBe_{13} also may be anomalous. First wc note that there is a large scatter in the estimate of Ω in tables 5 and 6. In particular values of Ω_χ and Ω_H (deduced from magnetostriction)

are smaller than estimates from C_p and β. This does not mean that $\chi(0)$ is less enhanced than γ because the ratio $\chi(0)/\gamma$ is very similar in UBe_{13} to the ratio observed in UPt_3. It does suggest that H_0 and T_0 in eq. (21) scale differently with volume such that the Wilson ratio increases with pressure. Two other facts appear anomalous: the value of Ω deduced from the ratio β/C_p is small for such a large value of γ (fig. 36) although this may be an artifact of not being sufficiently close to the $T \to 0$ limit; and, as mentioned in sect. 2, the relationship $A \sim \gamma^{-2}$ is not simply valid. (The value of Ω_A also appears small relative to Ω_c or Ω_e.) The origin of these anomalies is unclear to us.

Another potential use of the Grüneisen analysis is to distinguish the coherent heavy-fermion regime from the incoherent (single-ion) regime. This was initially the explanation for the large *negative* value of Ω in $CeAl_3$, however, as discussed above, it seems more likely at present that the observed negative value arises from a low-temperature phase transition. Negative thermal expansion is observed below the antiferromagnetic transition in $Ce_{0.8}La_{0.2}Ru_2Si_2$ (Lacerda 1990), an observation consistent with the explanation that some form of small moment antiferromagnetism occurs in $CeAl_3$ below 0.4 K. Similarly, an initial explanation for the low-temperature upturn below 0.3 K in Ω_e for $CeCu_6$ (fig. 28 inset) might be the onset of coherence. As temperature is lowered Ω begins to saturate to a value of order 75, (perhaps characteristic of the single-ion regime) but begins to increase further below 0.3 K as the system becomes truly coherent. The resistivity, for example, only follows a T^2 law below this temperature, suggesting $T_{coh} \approx 0.3$ K (Flouquet et al. 1985). However, the $T \to 0$ limit of Ω_e is close to the value Ω_c deduced from the low-temperature limit of the specific heat; and furthermore, it equals the value deduced from the pressure dependence of the resistivity maximum. Since the latter occurs at $T_m = 15$ K, this suggests that one value of Ω is appropriate over the broader range (0–20 K) and that the T dependence of Ω_e at low temperature may be an artifact of the analysis. If so, *single* energy scaling describes both the coherent and the single-ion regimes. As discussed in sect. 2.3.1, Anderson (1981) and Coleman (1983) have proposed that $T_{coh} = T_K/N$, where N is the ground-state degeneracy, so that single energy scaling should be valid over any region where N is constant.

On the other hand the Grüneisen parameter $\Omega = 22$ deduced from the pressure dependence of the resistivity maximum in $CeCu_2Si_2$ is substantially smaller than the values 50–80 deduced from low-temperature measurements. It is not clear whether this is an experimental artifact or whether it means that single-energy scaling is not valid.

Similar anomalies may occur in the large-T_K mixed-valent compounds. For example, the bulk modulus of $CeBe_{13}$ shows a downturn below 25 K (fig. 24) that represents a deviation from the Grüneisen prediction and may result from a coherence effect. As mentioned in sect. 2, the resistivity of $CePd_3$ may be far less pressure dependent below 40 K than above; this has been taken as evidence that the coherent Fermi liquid scales differently than the single-ion regime. At present these effects are best taken as tantalizing suggestions, rather than well established effects.

Given the potential of achieving an integrated view of scaling behavior in heavy fermions by combining studies of the pressure dependence of C_p, χ and ρ with ambient pressure Grüneisen analysis, given the overall importance of determining the extent that

the free energy exhibits scaling behavior, and given the ability to make distinctions and discern anomalous cases, it is important that such studies be refined in the future. We have attempted throughout this review to delineate the difficulties involved, as a contribution to such an effort.

5. Cooperative phase transitions

Superconductivity in anomalous lanthanide and actinide intermetallics has been a focus of research because of possible unconventional Cooper pairing leading to a non-BCS ground state. There is mounting evidence that pairing in these compounds is mediated at least in part by spin fluctuations, instead of only phonons as in BCS superconductors, and that the superconducting energy-gap structure consists of lines and/or point nodes on the Fermi surface and has symmetry other than imposed by the underlying crystal structure. That the superconducting order parameter may have odd-parity is very exciting and has motivated substantial theoretical and experimental study. We refer the reader to the reviews by Ott and Fisk (1987) and Grewe and Steglich (1991) for a more detailed discussion of the experimental and theoretical basis for odd-parity superconductivity. There are, however, several points that will be helpful in understanding the pressure dependence of superconductivity in these systems: (1) The specific heat jump ΔC at the superconducting transition temperature T_c is consistent with the transition taking place within a narrow band of heavy-mass quasiparticles. (2) In most, if not all cases, superconductivity co-exists with long-range magnetic order, often of the small-moment type. (3) Disruption of f-site periodicity invariably induces antiferromagnetism, often at the expense of superconductivity.

Fisk et al. (1985) observed a regular progression in the ground state of anomalous U-compounds if the Sommerfeld coefficient was normalized per unit volume γ_v. Although the basis for this observation was limited to only seven compounds, they noted that superconductors UPt_3 and UBe_{13} had a γ_v nearly two times larger than heavy-electron antiferromagnets UCu_5, $UAgCu_4$, U_2Zn_{17} and UCd_{11}. Interestingly, γ_v for superconducting $CeCu_2Si_2$ is about $19.8\,mJ\,cm^3\,K^2$, which is comparable to γ_v of UBe_{13} ($\gamma_v = 13.6\,mJ\,cm^3\,K^2$). If one were to take seriously the observation by Fisk et al. (1985), then the large Grüneisen parameters given in table 1 would imply that magnetic ground states would be favored with applied pressure in many Ce- and U-based heavy-electron compounds; whereas, superconducting ground states would be favored ultimately in Yb-compounds. At least for Ce-intermetallics, this conclusion is counter-intuitive and certainly must be incorrect because with increasing pressure the non-magnetic $4f^0$ configuration becomes energetically more stable. However, we note that U is unique in this comparison with Ce and Yb because pressures of order 10–100 kbar will stabilize one magnetic f configuration relative to another, with an admixture of configurations at intermediate pressures. In this regard, one might speculate that in Yb-compounds the sequence non-magnetic, magnetic, superconducting ground states could be realized with sufficient pressure. This raises the question, then, of what is the pressure response

of magnetism in anomalous lanthanide and actinides, and, therefore we begin with a discussion of this question.

5.1. *Magnetism*

In addressing magnetism, we will not discuss several studies on cubic Ce binaries because in many cases, e.g. CeSb (Chattopadhyay et al. 1987), CeTl (Kurisu et al. 1985), CeZn (Kadomatsu et al. 1986), $CeAl_2$ (Schefzyk et al. 1985; Morin et al. 1988) and $CePb_3$ (Morin et al. 1988), these compounds undergo a series of crystallographic- and magnetic-structure changes at pressures less than 20 kbar. These changes, which are effected by pressure-induced modification of the crystal-field configuration and anisotropic exchange, make it difficult to interpret generic systematics, the intent of this section. Though for the most part these effects will not be discussed, it is important to remember that they should be present to some degree in the materials that will be considered in more detail.

In the Introduction we cited the pressure dependence of the ordering temperature in CeAg as an example of the behavior that might be expected on the basis of Doniach's model (Doniach 1977) for competing Kondo and RKKY interactions. Although this interpretation may be true, there is evidence (Kurisu 1987) that the depression of the transition temperature to zero at $P \approx 35$ kbar (Eiling and Schilling 1981) may bc an artifact of non-hydrostatic pressure conditions. In spite of this controversy, pressure-dependent magnetization (Kurisu et al. 1981) and inelastic-neutron scattering (Frick et al. 1983) studies are consistent with an increase of the Kondo temperature and decrease of the ordered moment in CeAg at modest pressures, results anticipated from the Doniach model.

Similar trends have been reported (Shaheen and Schilling 1987) in the alloys $CeSi_x$ ($1.67 < \times < 2.0$) in which the Curie temperature T_C increases initially with x from $T_C \approx 10$ K, passes over a broad maximum and then decreases to zero for $x \approx 1.85$. In the region where T_C is a maximum and only weakly dependent on x, logarithmic pressure derivatives of T_C and the saturated moment M_s are near zero; but as $x = 1.85$ is approached, both derivatives become strongly negative, as expected for Kondo compensation of the Ce moment. An interesting aspect of $CeSi_x$, however, is that x and pressure have similar effects on T_C and M_s but increasing values of x correspond to *increasing* unit cell volumes. The authors interpret this x-dependence as arising from an increase in the valence-electron count, leading to increased hybridization that dominates the reduced hybridization due to unit-cell expansion. Irrespective of whether this interpretation is correct or not, it does make a valid point, namely that caution is needed when comparing the volume response of even isostructural compounds in which cell-volume and bandstructure changes may be induced by non-f substitutions.

Germann and v. Löhneysen (1989) arrived at the same conclusion from ambient-pressure specific-heat studies on the series $CeCu_{6-x}Au_x$ and $C_p(P)$ on antiferromagnetic $CeCu_{5.5}Au_{0.5}$, which at ambient pressure has an ordered moment of $\sim 0.5 \mu_B$/Ce (Chattopadhyay et al. 1990). A comparison of the derivatives $\partial T_N(P)/\partial \ln V = 0.57$ K obtained for $x = 0.5$ with increasing pressure and $\partial T_N(x)/\partial \ln V = 1.3$ K found for $P = 0$

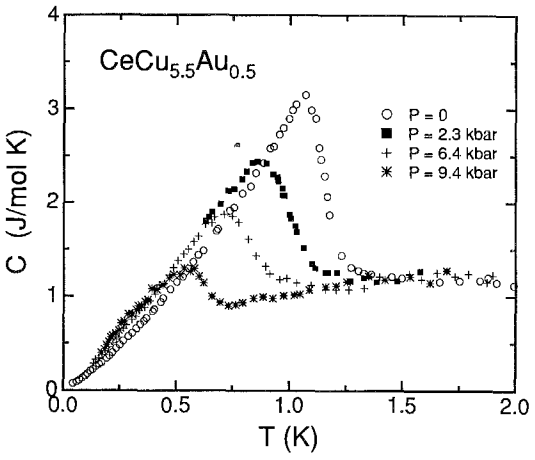

Fig. 37. Specific heat versus temperature for $CeCu_{5.5}Au_{0.5}$ at various pressures. Data after Germann and v. Löhneysen (1989). The anomaly in C_p vs T signals antiferromagnetic order.

by varying x in the range $0.2 \leqslant x \leqslant 0.8$ suggests that gold substitution both increases the cell-volume and decreases the ligand-derived density-of-states. Results of their pressure-dependent specific heat measurements are shown in fig. 37. There are three points to notice. With increasing pressure the Néel temperature decreases linearly at a rate -52 mK/kbar, the anomaly at T_N becomes smaller and, at temperatures well below T_N, the specific heat is larger. Referring to the Doniach diagram (fig. 1), these observations are consistent with the following picture: (1) Au substitution for Cu increases the cell-volume and reduces the sd–density-of-states, both of which reduce $|J|N(E_F)$ and move $CeCu_6$ from just above the AFM/Fermi-liquid boundary to below it. Now long range order is permitted among partially Kondo-compensated local moments. (We infer partial compensation from the fact that $T_K \approx 4\,K > T_N = 1\,K$, where we have used the relationship $T_K = \pi R/6\,\gamma$ and evaluated γ at temperatures just above T_N.) (2) With pressure, $|J|N(E_F)$ increases, producing further Kondo compensation and leading to a reduced T_N with smaller ordered moments (since T_K/T_N increases substantially with pressure). Entropy then is transferred from the system of local moments to Kondo-like spin fluctuations (Fisk et al. 1988b) which produces a larger C_p below T_N. From this picture we would expect that still higher pressures would drive $CeCu_{5.5}Au_{0.5}$ to a non-magnetic ground state. Indeed, such pressure-induced transitions from antiferromagnetic to non-magnetic states have been reported for several Ce-based intermetallics, e.g. $CeIn_3$ (Mignot and Wittig 1981; Morin et al. 1988), $CeRh_2Si_2$ (Thompson et al. 1986a), $CeRu_2Si_{1.5}Ge_{0.5}$ (Borges et al. 1987) and $CeCu_2Ge_2$ (Jaccard et al. 1992).

This last compound is especially interesting because, not only does pressure suppress the Néel state ($T_N(P=0) = 4.1$ K), but it also induces superconductivity with $T_c \approx 0.64$ K. The T–P phase diagram for $CeCu_2Ge_2$ is shown in fig. 38. Because this phase diagram was determined through transport measurements, there remains the possibility that superconductivity and weak antiferromagnetism co-exist above 80 kbar. At ambient pressure, the ordered moment is $0.74\,\mu_B$/Ce (Knopp et al. 1989), a value close to

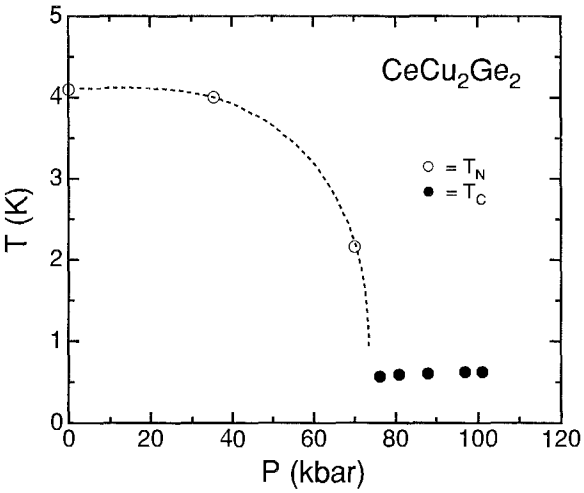

Fig. 38. Values of the Néel temperature T_N and superconducting transition temperature T_c determined from electrical resistivity measurements on $CeCu_2Ge_2$ as a function of pressure. The dashed line is a guide to the eye. Data are from Jaccard et al. (1992). Below 6 kbar, $\partial T_N/\partial P > 0$ (Sparn et al. 1993).

that expected for a Γ_7 crystal-field-doublet ground state and suggesting that Kondo-compensation of the 4f moment is negligible, ie., $T_K < T_{RKKY}$. A positive thermal expansion anomaly at $T_N(0)$ (Steglich 1991) implies by Ehrenfest's relation that at low pressures $\partial T_N/\partial P$ is positive, which experimentally has been verified for $P < 6$ kbar (Sparn et al. 1993). Together these results place $CeCu_2Ge_2$ to the weak-coupling side of the maximum in T_N versus $|J|N(E_F)$ in the Doniach diagram. With applied pressures, we expect $|J|N(E_F)$ to increase in a Ce-compound so that $T_N(P)$ for $CeCu_2Ge_2$ should increase initially, reach a broad maximum and then decrease rapidly at still higher pressures, precisely the sequence shown in fig. 38. Therefore, $CeCu_2Ge_2$ appears to follow the response expected for competing Kondo and RKKY interactions.

Temperature variations in the electrical resistivity of $CeCu_2Ge_2$ as a function of pressure also follow the expected behavior (see fig. 39). For $P = 1$ bar and 35 kbar, the low-temperature increase in $\rho(T)$ is interrupted abruptly by the onset of magnetic order, characteristic of a system in which $T_{RKKY} > T_K$. In this case RKKY interactions are sufficiently strong that they preempt the development of a "coherence" peak in $\rho(T)$. The internal magnetic field established by the ordered moments at $T < T_N$ further suppresses the Kondo interaction (Fisk et al. 1988b) so that relatively high pressures are required to produce a qualitative change in the shape of $\rho(T)$. This is found as well in other Ce-based systems in which $\partial T_N/\partial P$ is positive at low pressures, e.g. $CeAg_2Si_2$ (Thompson et al. 1986a), $CeRu_2Si_{2-x}Ge_x$ for $x = 1.5$ and 1.0 (Borges et al. 1987), CePtGe (Rebelsky et al. 1990) and $CePt_2$ (Rebelsky et al. 1990), or in which T_N decreases only weakly with pressure, e.g. $CeAu_2Si_2$ (Thompson et al. 1986a) and $CeIr_2Sn_2$ (Beyermann et al. 1991). Inspection of fig. 39 shows that $CeCu_2Ge_2$ at an applied pressure of 70 kbar (close to the antiferromagnetic/superconducting boundary) has a temperature-dependent resistivity similar to that of superconducting $CeCu_2Si_2$ at ambient pressure, ie., a well-defined "coherence peak" exists at low temperatures along with a higher temperature

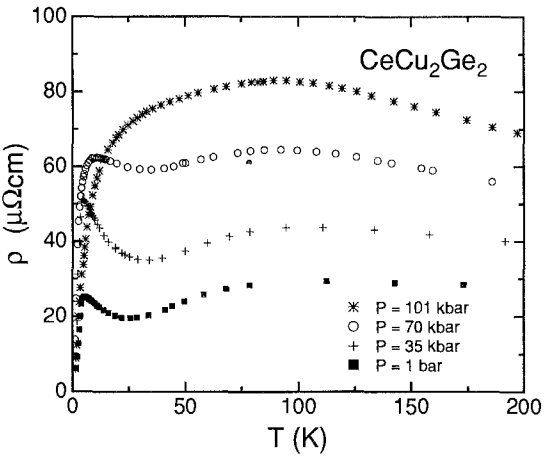

Fig. 39. Temperature-dependent resistivity of $CeCu_2Ge_2$ at various pressures. (After Jaccard et al. 1992.) At the two lowest pressures, the sharp drop in $\rho(T)$ signals the onset of antiferromagnetic order.

maximum due to crystal-field effects. This is also the case for antiferromagnetic $CePd_2Si_2$ (Thompson et al. 1986a). At higher pressures, the low-temperature peak moves to higher temperatures and nearly merges with the crystal-field peak, also true for $CePd_2Si_2$, suggesting the approach to a mixed-valence state in $CeCu_2Ge_2$ at 101 kbar.

The body of evidence for Ce-based antiferromagnets is qualitatively consistent with the idea of competing Kondo and RKKY interactions, first discussed by Doniach, whereby pressure favors an approach to the strong-coupling regime, ie., the diagram in fig. 1 is traversed from left-to-right with applied pressure. On the other hand, for Yb compounds pressure variations in the specific heat, susceptibility and resistivity suggest that Yb becomes more trivalent with increasing pressure. Unlike the case of Ce-based materials, where it is believed that the f-level position E_f remains constant but the hybridization increases with pressure, pressure-induced changes in physical properties of Yb compounds probably reflect motion of the f^{14} level away from the Fermi level with increasing pressure. Concomitant to this, the Kondo temperature becomes vanishingly small. In this case the Doniach phase diagram would be traversed from right-to-left. Such an interpretation has been applied to the pressure dependence of the Curie temperature of YbNiSn (Sparn et al. 1992), which has an ambient-pressure Sommerfeld coefficient of about 300 mJ/mol K^2 (Kasaya et al. 1991). (As an aside, we note that the existence of a ferromagnetic ground state does not exclude the concept of competing Kondo and RKKY interactions because the sign of the RKKY interaction oscillates with increasing inter-ionic separation (Freeman 1972) which can account for many different kinds of magnetic order. In YbNiSn weak ferromagnetism arises from canting of the antiferromagnetic sublattice within the orthorhombic a–c plane (Kasaya et al. 1992)). Results of measurements on YbNiSn are given in fig. 40 where we see that with increasing pressure changes in $\rho(T)$ become less pronounced as $\partial T_C/\partial P$ approaches zero. These trends with pressure are just the opposite shown by $CeCu_2Ge_2$ and are consistent with

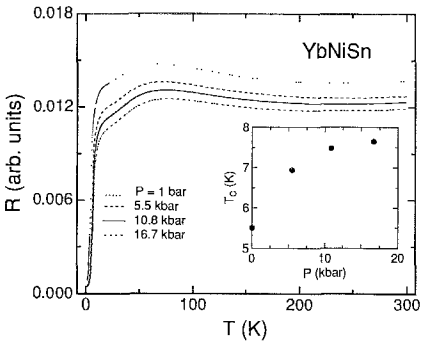

Fig. 40. Electrical resistance versus temperature for YbNiSn at various pressures. The inset shows the pressure dependence of the Curie temperature T_C. (After Sparn et al. 1992.)

$\partial|J|/\partial P < 0$ in YbNiSn. One might expect that at still higher pressures, T_C would begin to decrease as T_{RKKY} increasingly dominates T_K.

To our knowledge the only other Yb compound in which the pressure dependence of magnetic order has been studied is $YbBe_{13}$. This compound, which is isostructural to UBe_{13}, orders antiferromagnetically at 1.28 K (Heinrich et al. 1979). With pressures to 16 kbar there is essentially no change in T_N (Thompson et al. 1984) suggesting that this compound is already in the weak coupling regime at ambient pressure. There is no evidence for superconductivity in $YbBe_{13}$ above 80 mK.

We turn now to U-based systems, focusing on those compounds that exhibit heavy-electron behavior co-existing with antiferromagnetic order. We refer the reader to the review by Fournier (1985) for a discussion of pressure-induced variations in U-based antiferromagnets that are not considered to belong to the class of heavy-electron compounds. A key issue in this older work is that localized-moment magnets can be distinguished from itinerant magnets by the fact that for the former the ordered moment does not vary substantially with pressure as T_N decreases but for the latter both the moment and T_N change with pressure. Ott and Fisk (1987) have reviewed the ambient-pressure properties of the heavy-electron antiferromagnets UCu_5, $UAgCu_4$, U_2Zn_{17} and UCd_{11}. An interesting feature of these systems is that the large value of C_p/T just above their Néel temperature is reduced to about 30% of this value as $T \to 0$. That is, a substantial T-linear contribution to C_p remains well below T_N, suggesting either that a portion of the heavy-mass state is unaffected by the magnetic transition or that the internal field created by the ordered moments is not sufficient to quench the continued development of C_p/T with decreasing temperature below T_N. In this regard, U-based magnets appear to be different than those based on Ce in which usually only a small T-linear specific heat is found much lower than T_N. Fisk et al. (1988b) have argued that this difference arises because the Kondo temperature of U-based magnets is typically an order-of-magnitude larger than in Ce magnets. This argument is consistent with results of neutron diffraction experiments that find substantially reduced ordered moments, e.g. 0.9 μ_B/U (Murasik et al. 1974) to 1.3 μ_B/U (Chakravarthy et al. 1985) in UCu_5, 0.8 μ_B/U in U_2Zn_{17} (Cox et al. 1986) and an upper limit of 1.5 μ_B/U in UCd_{11} (Thompson et al. 1988).

Table 7
Pressure dependence of the Néel temperature in U-based heavy-electron antiferromagnets[a]

Compound	γ (J/mol K^2)	γ_V (mJ/cm^3 K^2)	T_N (K)	$\partial T_N/\partial P$ (K/kbar)	Reference
UCd_{11}	0.84	5.21	5.21	0.070	1
UCu_5	>0.25	>4.80	15.0	0.034	2
U_2Zn_{17}	0.50	5.08	9.6	0.017	1
$UAgCu_4$	0.31	5.95	18.2	0.032	1

[a] Values of the ambient-pressure Sommerfeld coefficient normalized per mol U (γ) and normalized per unit volume (γ_V) as well as values of the ambient-pressure Néel temperature T_N are from Fisk et al. (1985). $\partial T_N/\partial P$-values for small applied pressure.

References
(1) Thompson et al. (1986b) (2) Thompson (1987)

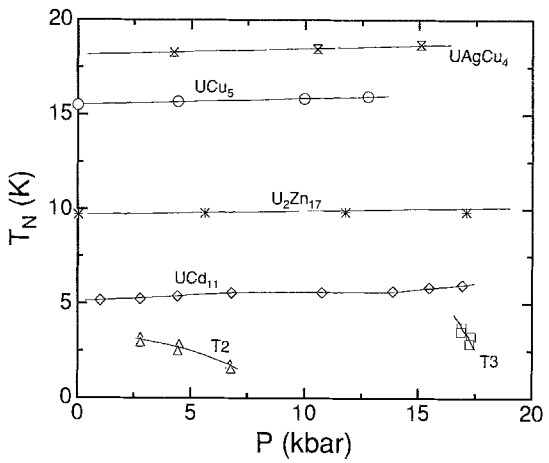

Fig. 41. Pressure dependence of the Néel temperature in $UAgCu_4$, UCd_{11} and U_2Zn_{17} (after Thompson et al. 1986b) and UCu_5 (after Thompson 1987). Transitions labeled T_2 and T_3 appear in UCd_{11} as a function of pressure and their origin is unknown.

Actually, little is known in detail about the pressure dependence of magnetism in these compounds. There have been no specific heat or magnetic susceptibility studies as a function of pressure so that there is no information regarding the pressure dependence of the ordered moment. This makes it particularly speculative to say whether these compounds follow the behavior expected for competing Kondo and RKKY interactions. Resistivity measurements as a function of pressure to less than 20 kbar on U_2Zn_{17} (Thompson et al. 1986b), $UAgCu_4$ (Thompson et al. 1986b) UCd_{11} (Thompson et al. 1989a) and UCu_5 (Thompson 1987) show only modest, if any, changes in the qualitative shape of $\rho(T)$, but in all cases $\partial T_N/\partial P$ is positive (table 7 and fig. 41). There are several general comments that should be made about these results. (1) If we assume that $\gamma \propto 1/T_K$, there is no apparent correlation between T_K and $\partial T_N/\partial P$. This contrasts to observations on Ce-based antiferromagnets, in particular the series CeM_2Si_2 (where M

= Au, Pd, Rh or Ru) in which $\partial T_N/\partial P$ correlates reasonably well with the quasi-elastic neutron-scattering linewidth (Grier et al. 1988; Severing et al. 1989) and with the unit cell volume. The same is true for the quasi-elastic linewidth (Rainford et al. 1992) and $\partial T_N/\partial P$ (Borges et al. 1987) in the $CeRu_2Si_{2-x}Ge_x$ series. (2) From the pressure response of χ, C_p and ρ of anomalous U compounds, we have argued that the characteristic energy scale increases with pressure. Taking this to imply that $\partial|J|/\partial P$ is positive leads to the conclusion that pressure would move T_N in U-magnets from left-to-right in a Doniach picture. The positive $\partial T_N/\partial P$ for these compounds then places them at ambient pressure to the weak-coupling side of the maximum in T_N versus $|J|N(E_F)$ and with sufficiently high pressure a non-magnetic ground state should be favored ultimately, contrary to the suggestion by Fisk et al. (1985) that a magnetic ground state should be favored at high pressure. However, this conclusion assumes that γ will decrease with applied pressure and, in the absence of any such information, remains an open question. (3) Of the four heavy-electron magnets, U_2Zn_{17} shows most clearly a dependence $T_N(P)$ consistent with the Doniach picture. Above about 5 kbar, $T_N(P)$ begins to saturate as if it were to start decreasing at higher pressure. Inelastic neutron scattering from single crystal U_2Zn_{17} may be analyzed (Broholm et al. 1987b) in terms of a Kondo-like single-ion response modified by RKKY interactions between ions, suggesting that a Doniach model might be applicable.

UCu_5, at ambient-pressure, and UCd_{11}, at pressures greater than 2.5 kbar, provide examples that the antiferromagnetic state is unstable with respect to further phase transitions. Below ~1.2 K, UCu_5 undergoes a transition to an insulating state (Ott et al. 1985) due possibly to charge-or spin-density wave formation (Bruls et al. 1987; Nakamura et al. 1991). The application of pressure causes this low-temperature transition to move to lower temperatures at the same rate as T_N increases (Thompson 1987), suggesting that these two phases compete for the Fermi surface. This conclusion is supported by bandstructure calculations (Norman et al. 1988) showing that only 70% of the density-of-states at E_F is removed by the magnetic transition at ~15 K, a result qualitatively consistent with the reduction in C_p/T below T_N. Further, these calculations that treat both spin-and orbital-moment effects give a total moment of 1 μ_B/U, which is close to that found by neutron diffraction and which arises from the partial cancellation of spin and orbital contributions. Therefore, the magnetism in UCu_5 at ambient pressure appears to be explained qualitatively without involving competing Kondo and RKKY interactions. Whether these same arguments apply to other U-antiferromagnets, and especially UCd_{11}, remain open questions, but it should be noted that neither U_2Zn_{17} nor UCd_{11} exhibit Cr-like anomalies in $\rho(T)$ at T_N, but UCu_5 and $UAgCu_4$ do.

To summarize briefly, it appears that the pressure response of anomalous Ce- and Yb-based magnets can be interpreted qualitatively in terms of competing Kondo and RKKY interactions, even though, we reiterate, this problem is far from being understood at a microscopic level. Whereas, one might try to argue that U compounds could be discussed in the same language, this is much less clear and underscores our profound lack of understanding these compounds.

5.2. *Superconductivity*

Until recently, four anomalous compounds were known with superconducting ground states: $CeCu_2Si_2$, UBe_{13}, UPt_3 and URu_2Si_2. In 1991, two new compounds, UNi_2Al_3 (Geibel et al. 1991a) and UPd_2Al_3 (Geibel et al. 1991b) with T_c's of 1 and 2 K, respectively, were added to this list. Both compounds have large U–U spacing, which by our definition, includes them in the class of anomalous compounds. Superconductivity coexists with antiferromagnetism ($T_N \approx 14$ K with ordered moment of $0.85\,\mu_B$/U in UPd_2Al_3 (Krimmel et al. 1992) and $T_N = 4.6$ K with ordered moment of $0.1\,\mu_B$/U in UNi_2Al_3 (Amato et al. 1992)), which also is the case with UPt_3 (Aeppli et al. 1988), URu_2Si_2 (Broholm et al. 1987a) and possibly UBe_{13} (Kleiman et al. 1990; de Visser et al. 1992) and $CeCu_2Si_2$ (Nakamura et al. 1988). In these latter materials, the ordered moment is quite small, $\sim 10^{-2}\,\mu_B$/U. Values of γ_V for URu_2Si_2, UNi_2Al_3 and UPd_2Al_3 are 1.63, 2.11 and 2.39 mJ/cm^3 K^2, respectively, making them appear from this perspective to be more nearly similar to the non-superconducting spin-fluctuator USn_3 with $\gamma_V = 2.84$ mJ/cm^3 K^2 (Fisk et al. 1985) than to the heavy-electron superconductors $CeCu_2Si_2$, UBe_{13} and UPt_3 in which γ_V exceeds 10 mJ/cm^3 K^2. It would be interesting to compare the pressure dependence of γ_V among these systems, but no pressure measurements on UNi_2Al_3 or UPd_2Al_3 have been reported.

In their careful study of superconductivity in single crystals of $CeCu_2Si_2$, Assmus et al. (1984) noted a strong functional dependence of normal and superconducting properties on copper stoichiometry. Compared to superconductive crystals grown from a Cu-rich melt, crystals grown from a stoichiometric melt were not superconductive and had a large residual resistivity that was accompanied by a much reduced value of T_m in $\rho(T)$. Interestingly, there was also a difference in unit cell volume of about 0.3%, corresponding to "chemical" pressure of a few kilobars, with the superconducting crystals having the smaller volume. This observation correlated with the observation (Aliev et al. 1983) that a few kilobars applied pressure was sufficient to induce superconductivity in otherwise non-superconducting polycrystalline samples. Together these results suggested that superconductivity in $CeCu_2Si_2$ might depend strongly on pressure and on sample composition.

Contrary to this first suggestion, Chen et al. (1984) found for a nominally stoichiometric, well-annealed sample of $CeCu_2Si_2$ that, after a small initial increase in T_c for $P < 2$ kbar, the inductively-measured T_c was essentially pressure independent to 10 kbar. Bleckwedel and Eichler (1985) came to the same conclusion from specific heat measurements to 5.9 kbar on a nominally Cu-rich sample. In addition they reported that the specific heat jump at T_c, ΔC, increased nearly 70% in going from 1 bar to 3 kbar and then decreased at higher pressures. Variations in $\Delta C(P)$ were attributed to pressure-induced changes in structure of the density-of-state near E_F. However, given the observations of Assmus et al. (1984), a pressure-induced rise in the superconducting volume fraction can not be ruled out as an explanation for the initial increase in ΔC.

Resistive measurements on nominally Cu-rich, polycrystalline samples (Bellarbi et al. 1984) at pressures to 90 kbar showed the weak, if any, pressure dependence of T_c remained

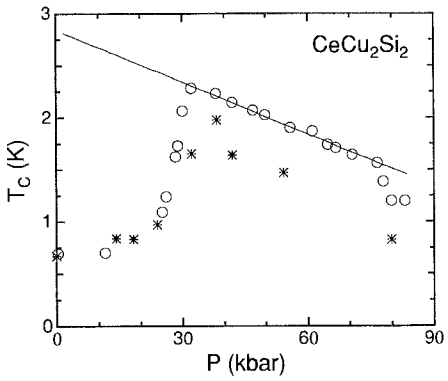

Fig. 42. Superconducting transition temperature T_c, defined by an extrapolation of the resistive transition to $\rho(T)=0$ (asterisks), as a function of pressure for $CeCu_2Si_2$. The apparent discontinuity at 40 kbar is due to a mismatch in T_c in two different samples, after Bellarbi et al. (1984). Inductively measured T_c versus pressure for $CeCu_2Si_2$ is shown by open circles. The line is a guide to the eye, after Thomas et al. (1993).

to ~20 kbar above which T_c increased by over a factor of two at 38 kbar and then decreased gradually (fig. 42). In the pressure range where T_c changes rapidly, there is pronounced broadening of the transition. The authors proposed that qualitative differences in behavior for $P \geqslant 25$ kbar are associated with a valence transition of the Ce-ion from trivalent to intermediate valence, as suggested from high-temperature resistance measurements (sect. 2.3.1).

A rather different view has emerged from recent reinvestigations of $T_c(P)$ in $CeCu_2Si_2$ (Thomas et al. 1993). Results of inductive measurements of T_c under more nearly hydrostatic pressure conditions are shown also in fig. 42. The overall shape of $T_c(P)$ is like that found by Bellarbi et al. (1984); however, for $31 \leqslant P \leqslant 77$ kbar, T_c decreases linearly at a rate of -16.6 mK/kbar and there is a marked drop in T_c above 77 kbar. Notably, the inductive-transition width never exceeded ± 20 mK at any pressure in these measurements. On the basis of these results Thomas et al. (1993) argue that there are three different superconducting states in $CeCu_2Si_2$: one for $P < 30$ kbar, a second for $30 \leqslant P \leqslant 77$ kbar and a third for $P > 77$ kbar. Further, they suggest that T_c of the lowest pressure state is not intrinsic; rather T_c is depressed from a $P=0$ intrinsic value of 2.8 K (obtained by a linear extrapolation of $T_c(P)$ in the second pressure region to $P=0$) by some unknown "destructive mechanism", perhaps whatever is responsible for the still unexplained phase transitions found in the magnetic field-temperature phase diagram of $CeCu_2Si_2$ at ambient pressure (Wolf et al. 1993). Clearly, additional measurements will be required to resolve the issues raised by pressure studies of $CeCu_2Si_2$.

There are no known Yb-based heavy-electron superconductors.

The Cr-like anomaly in $\rho(T)$ at $T_N \approx 17.5$ K in URu_2Si_2 has been analyzed as arising from a spin-density wave that produces a gap in the magnetic excitation spectrum of $\Delta_g/k_B = 71$ to 90 K (McElfresh et al. 1987; Palstra et al. 1986); whereas, specific-heat measurements give $\Delta_g/k_B = 129$ K and are consistent with about 40% of the Fermi surface being removed by the density-wave transition (Maple et al. 1986). (Non-linear susceptibility suggests (Ramirez et al. 1992) that this transition is driven by the development of staggered quadrupole order.) Co-existing with the density-wave is

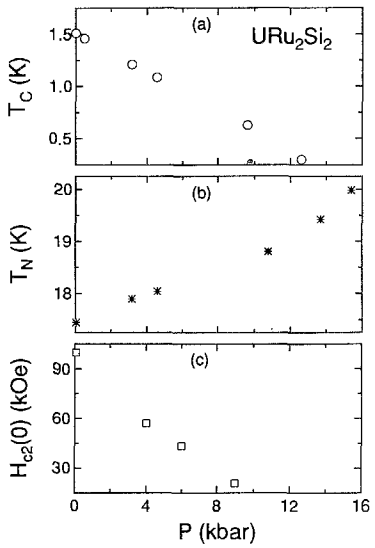

Fig. 43. (a) Superconducting transition temperature T_c (resistive mid-point) of URu_2Si_2 versus pressure, after McElfresh et al. (1987). (b) Néel temperature T_N of URu_2Si_2 as a function of pressure. (c) $T=0$ superconducting upper critical field versus pressure, after Onuki et al. (1987).

bulk superconductivity that appears below ~1.5 K (Broholm et al. 1987a). As shown in figs. 43a+b, pressure causes T_N and T_c to move at nearly equal but opposite rates, $\partial T_c/\partial P = -95$ mK/kbar and $\partial T_N/\partial P = 113$ mK/kbar (McElfresh et al. 1987; de Boer et al. 1986). An extrapolation of $T_c(P)$ suggests that superconductivity would be suppressed completely at an applied pressure of about 16 kbar. Specific heat measurements (Fisher et al. 1990) show that the superconducting anomaly $\Delta C(T_c)$ already becomes so broadened at 5.8 kbar that it is not clear whether bulk superconductivity exists above this pressure. However, the specific-heat anomaly associated with T_N remains well-defined. Together these observations are consistent with the argument (Maple et al. 1986) that superconductivity and antiferromagnetism compete for parts of the Fermi surface. Recent uniaxial-stress studies (Bakker et al. 1992b) support this conclusion. In addition, though, these authors find that the stress response of URu_2Si_2 is highly anisotropic. For stress applied along the tetragonal c-axis, T_c increases at a rate of 25 mK/kbar whereas T_N decreases at a rate of −41 mK/kbar; but for stress along the a-axis, T_c decreases −35 mK/kbar and T_N increases 126 mK/kbar. Given variations in sample quality, a polycrystalline average of these agrees reasonably well with hydrostatic pressure results.

Onuki et al. (1987) have reported that the superconducting upper-critical field $H_{c2}(0)$ of polycrystalline URu_2Si_2 decreases at a rate of −8.4 kOe/kbar (fig. 43c). For BCS superconductors, $H_{c2}(0)$ is related to the superconducting coherence length ξ by $H_{c2}(0) = \Phi_0/2\pi\xi^2$, where Φ_0 is the flux quantum (Tinkham 1975). Because it is not clear whether URu_2Si_2 is in the clean or dirty limit (Schlabitz et al. 1986), we consider two approaches to analyzing this pressure result. If the electronic mean-free path is less than the coherence length (dirty limit), ξ is proportional to $(\gamma\rho T_c)^{-1/2}$ (Orlando

et al. 1979). From the pressure dependence of γ (table 1) and T_c (the pressure dependence of ρ just above T_c is very weak (McElfresh et al. 1987)), we calculate $(1/H_{c2}(0))\ \partial H_{c2}(0)/\partial P = -0.099$/kbar, which is close to that found by Onuki et al. (1987), -0.084/kbar. On the other hand, if URu_2Si_2 is in the clean limit, which appears more likely (Schlabitz et al. 1986), then ξ is proportional to $S/\gamma T_c$, where S is the Fermi-surface area that participates in superconductivity (Orlando et al. 1979). From these relationships, the Fermi-surface area must decrease at a relative rate $\partial \ln S/\partial P = -0.058$/kbar to explain the results of Onuki et al. (1987). That is, at 10 kbar, about 60% of the Fermi surface would be removed, a value close to the estimate by Maple et al. (1986) for the fraction of the Fermi surface that participates in superconductivity at ambient pressure. This provides a natural explanation of why superconductivity disappears at pressures on this order, but how it relates to the uniaxial stress results remain unclear. Additionally, though, if this interpretation is correct, it would imply that at least part of the large specific-heat Grüneisen parameter is due to a loss of Fermi-surface taken by the density-wave transition and not solely due to an increase in the characteristic energy scale, which may account partially for differences among Grüneisen parameters noted in table 6. We emphasize that these conclusions have been reached assuming BCS-type relationships.

Almost without doubt, UPt_3 is not a BCS-superconductor. Taillefer et al. (1991) and Aeppli et al. (1991) have reviewed the compelling evidence for coupling between superconducting and antiferromagnetic order parameters. That the anomalous normal- and superconducting-state properties are related was noted in the original work of Willis et al. (1985) in which they pointed out that the logarithmic derivatives $\partial \ln \chi/\partial P \approx \partial \ln T_c/\partial P \approx \partial \ln H_{c2}'/\partial P \approx -0.025$/kbar, where H_{c2}' is the temperature derivative of H_{c2} near T_c. From table 6, we see that the logarithmic derivatives of γ and T^2-coefficient of resistivity also are nearly equal to those for χ, T_c and H_{c2}'. On the basis of data to 19 kbar (fig. 44), both T_c and H_{c2}' extrapolate to zero at 37 ± 1 kbar, which, of course, is also where γ would go to zero because the logarithmic derivatives are the same.

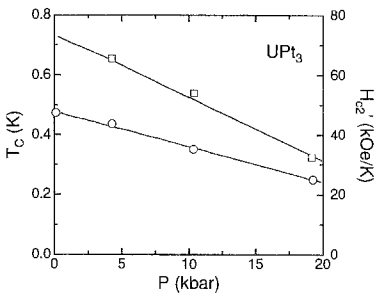

Fig. 44. Resistively measured T_c (circles) and H_{c2}' (squares) for UPt_3 as a function of pressure. Lines are guides to the eye. Slopes of these lines are -12.6 mK/kbar and -2.05 kOe/K kbar, respectively, after Willis et al. (1985).

Thermodynamic measurements, such as specific heat (Fisher et al. 1989) and thermal expansion (Hasselbach et al. 1990), clearly establish the existence of two superconducting phases in UPt_3 for zero-applied magnetic field, an effect which has been interpreted (Hess et al. 1989) as due to a two-component-vector order parameter that is coupled to a

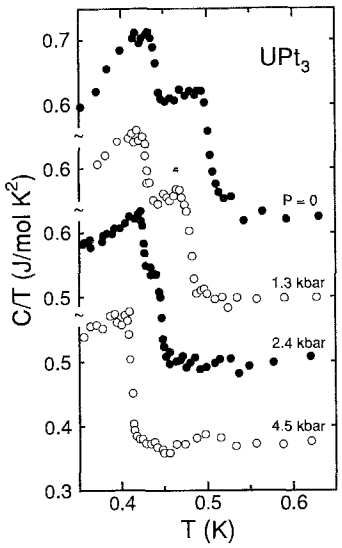

Fig. 45. Specific heat divided by temperature versus temperature for a polycrystalline sample of UPt_3 at various pressures. Two transitions are seen clearly for $P \leq 2.4$ kbar but only one transition at the highest pressure, after Trappmann et al. (1991).

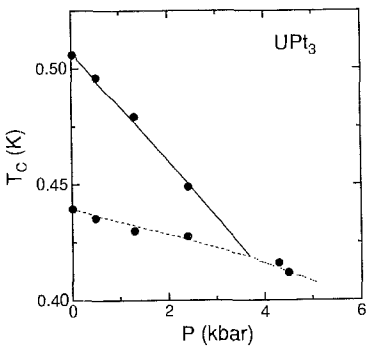

Fig. 46. Zero-field temperature versus pressure phase diagram for UPt_3 based on the data shown in fig. 45, after Trappmann et al. (1991).

symmetry-breaking field. In this model, the symmetry-breaking field, which quite possibly is the weak ($\approx 0.02\,\mu_B$/U moment) antiferromagnetic order that sets in below $T_N \approx 5$ K (Aeppli et al. 1988), lifts the two-fold degeneracy of the superconducting transition. High resolution specific-heat measurements (fig. 45) show that with pressure the upper transition decreases more rapidly (-24 ± 5 mK/kbar) than the lower one (-5 ± 1 mK/kbar) so that it merges with the lower transition at an applied pressure of $P = 3.7$ kbar (Trappmann et al. 1991). The resulting zero-field phase diagram is shown in fig. 46. As seen in this figure, a pressure of 3.7 kbar appears to restore the degeneracy that exists in the absence of the symmetry-breaking field.

Evidence supporting the interpretation of two transitions comes from neutron-diffraction measurements on single crystal UPt_3 as a function of pressure. Hayden et al. (1992) have shown that the antiferromagnetic peak at the $(\frac{1}{2}, 1, 0)$ position is suppressed to zero at a critical pressure of 5.4 ± 2.9 kbar, a value in close agreement with that required to collapse the splitting of two anomalies in specific heat. Their data show that the moment is suppressed with essentially no change in the Néel temperature, a quite unexpected result which they attribute to a strongly pressure-dependent effective coupling between magnetic moments. Whether this is "normal" for magnetism in anomalous actinides, especially the antiferromagnets, remains an open question.

There is another superconducting system $U_{1-x}Th_xBe_{13}$ in which two specific heat anomalies appear, one at T_c and one below T_c, and in which superconductivity

and magnetism are intimately coupled. Figure 47 gives the ambient-pressure phase diagram that has been established by specific heat (Ott 1989), ac susceptibility and dc magnetization (Heffner et al. 1991). For $0.019 \leqslant x \leqslant 0.043$ and temperatures below the lower phase boundary, muon-spin resonance experiments find a magnetic moment of $(10^{-3}$–$10^{-2})\,\mu_B$/U. (Heffner et al. 1991) It is not known whether this tiny moment is due to coexistence of antiferromagnetism and superconductivity or to a magnetic superconducting phase. For undoped UBe_{13} ($x=0$) there is only a single transition at $T_c = 0.9$ K. Pressure moves T_c to lower temperatures at a rate of about -16 mK/kbar (Lambert et al. 1986). Unlike UPt_3, the logarithmic derivatives $\partial \ln T_c/\partial P \approx -0.018$/kbar, $\partial \ln \gamma/\partial P \approx -0.061$/kbar (table 1) and $\partial \ln \chi/\partial P \approx -0.009$/kbar (table 2) differ substantially. The pressure dependence of T_c found for $x=0$ persists for $0 \leqslant x \leqslant 0.0172$, but for $0.019 \leqslant x \leqslant 0.0603$ $T_c(P)$ decreases more strongly and, for $x=0.0603$, non-monotonically (Lambert et al. 1986). From their ac susceptibility measurements, which are sensitive only to the highest temperature transitions shown in fig. 47, Lambert et al. (1986) have constructed the phase diagram given in fig. 48. This plot shows that two different behaviors are present for each pressure, separated by a minimum in $T_c(x)$ at a Th concentration x_{min}, which Lambert et al. (1986) argue separates two superconducting states. With increasing pressure the value of x_{min} moves to higher Th concentrations, indicating that the effects of pressure and Th content (which expands the unit-cell volume) are coupled.

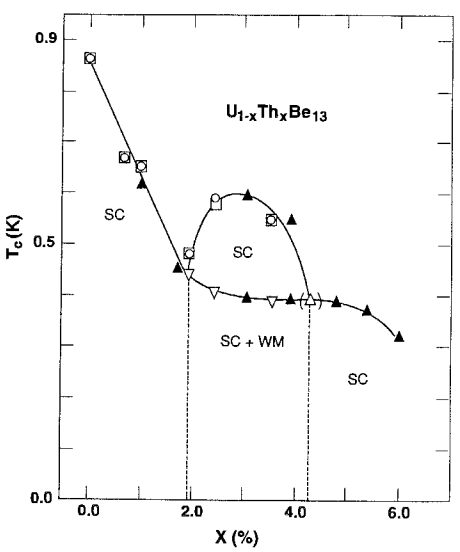

Fig. 47. Temperature versus Th concentration x in $U_{1-x}Th_xBe_{13}$. Solid upright triangles are from specific heat measurements (Ott, 1989). Open squares are T_c values determined by ac susceptibility; open circles and inverted triangles from dc magnetization. The symbol in parentheses denotes merging of the two transitions. Phases labeled SC are superconducting, without evidence for magnetism; whereas the phase labeled SC + WM exhibits coexisting superconductivity and weak magnetism, after Heffner et al. (1991).

On the basis of resistivity measurements on a series of $U_{1-x}Th_xBe_{13}$ compounds as a function of pressure, such as shown in fig. 49, Borges et al. (1988a,b) have suggested a correspondence between normal-state properties and the appearance of a minimum in $T_c(x,P)$, i.e., the onset of a second phase transition. With increasing Th content the low-

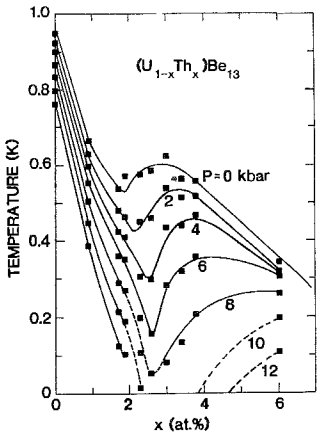

Fig. 48. Phase diagram of the highest superconducting transition temperature T_c versus Th concentration in $U_{1-x}Th_xBe_{13}$ at various pressures. Solid lines are guides to the eye and dashed lines represent extrapolations, after Lambert et al. (1986).

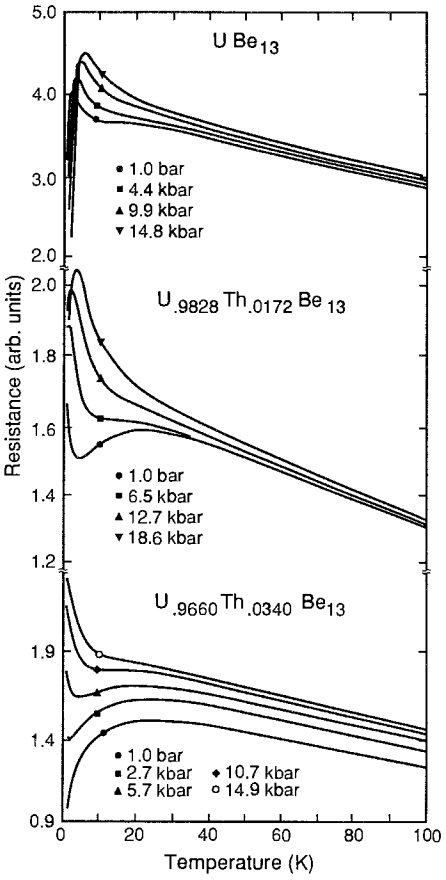

Fig. 49. Resistance as a function of temperature for selected $U_{1-x}Th_xBe_{13}$ compounds at various pressures, after Borges et al. (1988b). Results for $x=0.0093$ and 0.0536 are not shown for clarity.

temperature maximum T_m in $\rho(T)$ shifts to lower temperatures at ambient pressure and with applied pressure T_m moves back up in temperature for fixed x. For $x \leqslant 0.0172$, in which T_m was clearly defined, they could scale the normalized resistance as $T/T_m(P)$, as shown in fig. 11 for $CeCu_6$. Further, although no maximum in $\rho(T)$ was found above 1.2 K for $x=0.034$ and 0.0536 even at their highest pressure, qualitatively they could scale all $\rho(T, P)$ data for $0 \leqslant x \leqslant 0.0536$ onto a single curve by assuming that 1% Th produces a negative chemical pressure of about −7 kbar. Though this result confirmed the suggestion by Lambert et al. (1986) that pressure and Th content were coupled, they noted that the correspondence between x and chemical pressure was much greater than expected (~0.45 kbar/x) on the basis of lattice-parameter changes alone. Perhaps more significantly, from an analysis of $T_m(x, P)$ they noted that within experimental uncertainty $T_m(x, P)$ was coincident with $T_c(x, P)$ at the minimum value of T_c, i.e., at $x_{min}(P)$ shown in fig. 48, suggesting that T_m being below T_c is a necessary condition for the development of a second phase transition. This suggestion has received corroborating

support from specific heat (Fisher et al. 1987b) and from an extensive set of electrical resistance measurements as functions of temperature and magnetic field in samples with $0 \leqslant x \leqslant 0.06$ (Knetsch et al. 1993). Therefore, understanding the origin of the maximum in $\rho(T)$ for pure UBe_{13} appears essential to an interpretation of the nature of the lower transition in $U_{1-x}Th_xBe_{13}$ for $0.019 \leqslant x \leqslant 0.043$. Knetsch et al. (1993) speculate that this behavior is related to rapidly fluctuating, short-range magnetic correlations in UBe_{13} that are suppressed with the addition of Th and that become frozen as they are shifted below T_c. In this picture, the lower transition for $0.019 \leqslant x \leqslant 0.043$ is one to a state with static (on the time scale of the muon-decay time constant 2 μs) magnetic moments and is not to a magnetic superconducting state. That the physics of two transitions in $U_{1-x}Th_xBe_{13}$ might differ from that in UPt_3 also is supported by specific heat studies (Fisher et al. 1987b) of $U_{0.97}Th_{.03}Be_{13}$ which show both transitions have identical pressure dependencies, ie. they do not merge under pressure contrary to what is found in UPt_3.

There is as yet no unifying picture of superconductivity in heavy-electron materials but magnetism clearly plays a role. Understanding magnetism and its connection to superconductivity remains an outstanding challenge to both experimentalists and theorists. Pressure has been and will continue to be a significant variable in achieving this goal.

6. L_{III} spectra

In rare-earth mixed-valence and heavy-fermion compounds, the L_{III} X-ray absorption edge has been used widely to assess the valence or f count n_f. In actinides, on the other hand, L_{III} spectra are believed to reflect the degree of delocalization due to changing hybridization at more-or-less fixed f count. Hence, the pressure dependence of L_{III} spectra in principle allows determination of the degree to which pressure causes a change in hybridization as opposed to a change in f count. This is a fundamental issue concerning the pressure dependence of heavy-fermion compounds and is intimately related to the issue of whether the f electrons are better described in the localized or delocalized limit.

As an example of the dependence of the L_{III} spectra of mixed-valent compounds on f count, suppose the ground-state samarium wavefunction can be symbolically expressed as

$$a_6 \left|2p^6 \ldots 4f^6 5d^0 6s^2\right\rangle + a_5 \left|2p^6 \ldots 4f^5 5d^1 6s^2\right\rangle .$$

The L_{III} transition, which favors a $2p \rightarrow 5d$ transition by a $\Delta l = \pm 1$ selection rule, leads to two possible final states,

$$\left|2p^5 \ldots 4f^6 5d^1 6s^2\right\rangle , \qquad \left|2p^5 \ldots 4f^5 5d^2 6s^2\right\rangle .$$

These are separated in energy by about 9 eV because the core hole attracts the $4f^n$ configuration more than the $4f^{n-1}$ (Herbst and Wilkins 1982). In the absence of other effects there will be two absorption peaks ("white lines") in the L_{III} spectra, the

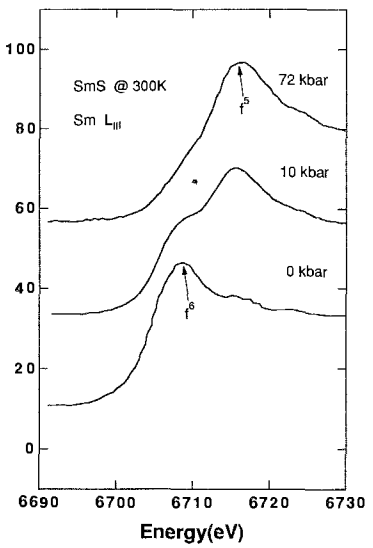

Fig. 50. L_{III} absorption edge of Sm in SmS at 0, 10 and 72 kbar at 300 K. At $P=0$, Sm is in the divalent state (f^6); at 72 kbar, it is essentially trivalent (f^5); at 10 kbar, it is in a mixed-valent state, after Röhler (1987).

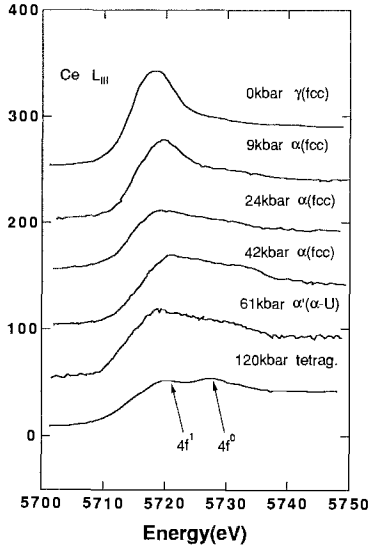

Fig. 51. L_{III} absorption of elemental cerium at six pressures. The crystal structure of each pressure is noted in the plot, after Röhler (1987).

relative intensities of which are proportional to the ground-state occupations a_5^2 and a_6^2 and hence give a determination of the valence. Figure 50 shows spectra for SmS; at $P=0$ the peak at 6706 eV represents the divalent $4f^6$ configuration and the peak at 6715 eV for $P=72$ kbar represents the trivalent $4f^5$ configuration. At 10 kbar both peaks are clearly visible; the valence deduced from the area ratio is 2.6.

Important valence changes occur for many lanthanide compounds in the range 0–200 kbar, either continuously or via phase transitions. High-pressure L_{III} spectroscopy can elucidate these changes. Röhler and coworkers (Röhler 1987; Röhler 1989) have measured the L_{III} spectra in this pressure range for a number of lanthanide elements and compounds, e.g. Ce, $CeCu_2Si_2$, Eu, $EuPd_2Si_2$, SmS, Yb and $YbAl_2$. They find, for example, that divalent Eu and Yb transform to a mixed-valent state at pressures of order 40 kbar and approach trivalence at the highest pressures. These valence changes are accompanied by a series of crystal-structure changes. $EuPd_2Si_2$ undergoes a continuous valence change from $z=2.2$–2.6 in the range 0–30 kbar. The valence of SmS is observed (fig. 50) to change discontinuously at the transition pressure (6.5 kbar) for the isomorphic transition, as expected. A study of a stoichiometric, non-superconducting sample of the heavy-fermion compound $CeCu_2Si_2$ exhibits a first-order transition at 38 kbar to a weakly mixed-valence phase ($z=3.1$). The valence of the nonstoichiometric ($CeCu_{2.2}Si_2$) superconducting sample at ambient pressure is already 3.1, suggesting that excess copper causes the equivalent of an internal pressure of at least 38 kbar. The valence changes of

cerium metal at the γ–α transition and the α–α' transitions also have been determined. According to the interpretation given above for the L_{III} spectra, the valence changes from 3.03 to 3.15 at 8 kbar and then changes continuously to a value 3.25 as the pressure increases through the α, α' and tetragonal phases (fig. 51).

This interpretation of the L_{III} spectra as measuring the valence in a straightforward way depends on several assumptions that can be incorrect for certain compounds (Krill et al. 1987). First, the spectra for the integer-valence case are assumed to have a particularly simple form (Lorentzian white line plus arctangent continuous absorption). This can ignore one-electron effects arising from structure in the empty 5d states. Results (Lawrence et al. 1994) for $YbXCu_4$ (X = Au, Ag) show a pronounced two-peak structure for the trivalent compounds. The high energy peak correlates with a high density of d-states several volts above the Fermi energy, which can be seen clearly in BIS results (Kang et al. 1990). The standard interpretation also ignores possible multiple scattering of the outgoing electron. As an example of this latter effect, Röhler's analysis gives a valence of 2.1 for SmS and SmSe at ambient pressure, even though both materials are believed, on the basis of a wide variety of thermodynamic and spectroscopic evidence, to be divalent (Lawrence et al. 1981). Krill and coworkers (Krill et al. 1987; Beaurepaire et al. 1990) have shown that the so-called trivalent L_{III} component (visible in fig. 50 at ambient pressure as a small maximum near 6715 eV) arises from multiple scattering and is already present in GdS.

Secondly, this approach ignores "final state" effects; in particular, integral-valent components of the ground state can couple to more than one final-state configuration. Such "configuration interaction" effects are very important in 3d photoemission (Fuggle et al. 1983; Campagna and Hillebrecht 1987) and are expected to be present for L_{III} spectra as well (Hüfner 1987). Consider the case of cerium: in addition to $4f^0 5d^3$ and $4f^1 5d^2$ final states, a $4f^2 5d^1$ final state is possible. In the presence of the core hole the excitation energy of this state is 2–3 eV smaller than that of the $4f^1 5d^2$ configuration (Herbst and Wilkins 1982) and would thus appear as a low energy shoulder on the white line. In principle, either integral-valent component of the ground state can couple to all three of these final states. Viewed as a two-step process

$$h\nu + \left|2p^6 \ldots 4f^n 5d^{2-m}\right\rangle \rightarrow \left|2p^5 \ldots 4f^n 5d^{3-m}\right\rangle \rightarrow \left|2p^5 \ldots 4f^{n\pm1} 5d^{3-m\mp1}\right\rangle,$$

the final-state transfer can be seen by simple perturbation theory to depend on the square of the ratio of the final-state mixing energy to the energy separation between the final states. Calculations using an orbitally degenerate Anderson-impurity approach (Gunnarsson and Schönhammer 1987) treat the mixing in the final state as equal to that of the initial state; this mixing energy is 1–2 eV for cerium, compared to $4f^1 \rightarrow 4f^2$ and $4f^1 \rightarrow 4f^0$ energy separations of 2–3 eV and 10 eV, respectively. Hence, $4f^1 \rightarrow 4f^2$ transfer is probable, but $4f^1 \rightarrow 4f^0$ is not. Under these circumstances the intensity of the $4f^0$ white line in the final state should accurately reflect the ground state $4f^0$ occupation. It is for this reason that L_{III} determination of valences are trusted (Fuggle et al. 1983).

However, this approach makes a strong assumption about the strength of the hybridization in the final state and ignores other relevant interactions, particularly screening interactions that promote local charge neutrality in the final states. Extensions of the model that treat such interactions yield L_{III} spectra which have important final-state effects (Kotani et al. 1988; Malterre 1991). For example, Brito and Frota (1990) have shown that the Coulomb interaction of the core hole with the conduction electrons favors final states f^n with smaller n (e.g. f^0 for cerium) but interaction of the core hole with the f shell favors final states with larger n (e.g. f^1 and f^2 for cerium). These final state effects complicate the relation between the white-line intensities and the valence; the actual ground state valence can be greater or smaller than implied by the standard interpretation of the spectra.

Although there are indications that such final-state effects are important in intermetallics (see, for example, Wortmann et al. (1991) who report two peaks in the L_{III} spectra of *integral* valent europium compounds), they are believed to be particularly important in insulators such as CeO_2 and CeF_4 (Kaindl et al. 1987; Kaindl et al. 1988). These are tetravalent compounds that show no 4f peak in valence-band photoemission, suggesting that the 4f-occupation number n_f is zero in the ground state. The L_{III} spectra of both compounds show, however, a two-peaked structure that was interpreted originally (Röhler 1987) as proof that the ground state is mixed valent ($z = 3.3$). Kaindl et al. (1987) suggest that the resolution of this apparent contradiction lies in realizing the importance of covalent bonding in these materials. Band-structure calculations (Koelling et al. 1983) for CeO_2 show significant 4f admixture into the oxygen 2p bands. The 4f partial charge within the cerium muffin tin is approximately 0.5 and there is substantial (0.3 electrons) f-symmetry charge in the interstitial region. The 4f-spectral density is spread over the 2p valence band and does not appear as a separate peak in photoemission. Model calculations (Kotani et al. 1988) show that the strong oxygen 2p-cerium 4f hybridization leads to an enhancement of the $4f^1$ component in the L_{III} final state.

The pressure dependence of the L_{III} spectra of CeF_4, CeO_2 (Kaindl et al. 1987; Kaindl et al. 1988) and UO_3 (Bertram et al. 1989) is shown in fig. 52. The high binding energy component (presumably the $4f^0$ final state) decreases with increasing pressure; whereas, for mixed-valent compounds the $4f^0$ weight should *increase* with pressure. The explanation is that the oxygen 2p-cerium 4f hybridization increases with pressure, which shifts more weight into the $4f^1$ final state. This is a particularly nice application of high pressure techniques. It demonstrates that in the limit of strong covalent bonding, both Ce and U behave similarly. (It should be mentioned that Röhler (1987) disagrees with this interpretation.)

In actinide insulators the L_{III} binding energy decreases with f count: the binding energy for UCl_3 is 4 eV smaller than that of UO_2 but that of UO_3 is 2 eV greater (Kalkowski et al. 1987a,b). Unlike the lanthanides, actinide intermetallics do not show two peaks in L_{III} spectra and the *position* of the white line varies substantially among compounds (Lawrence et al. 1984; Kalkowski et al. 1987a). It is believed (Kalkowski et al. 1987b) that the position reflects both the f count (where this is treated as a band-theoretic concept rather than a mixed-valence concept) and the degree of 5f localization. The L_{III} edge of

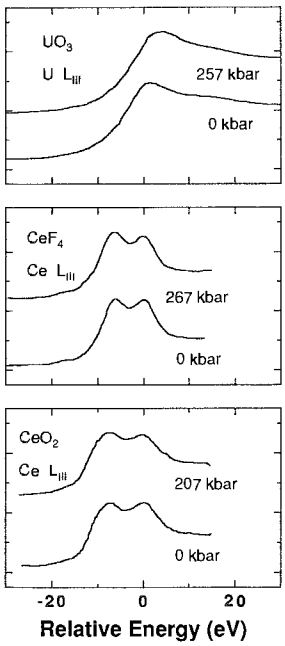

Fig. 52. L_{III} absorption of Ce in CeO_2 and CeF_4 and of U in UO_3 at ambient and high pressure. In each case the low binding energy component is enhanced at high pressure. CeO_2 and CeF_4 after Kaindl et al. (1988); UO_3 after Bertram et al. (1989).

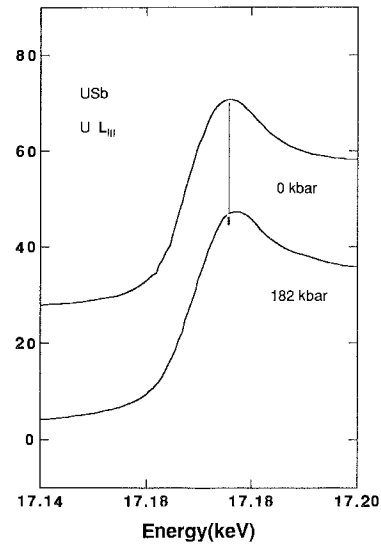

Fig. 53. L_{III} absorption of U in USb at ambient and high pressure. The peak shifts to higher binding energy at high pressure, after Schmeister et al. (1987).

USb shifts up by about 2 eV between 0 and 180 kbar (fig. 53). Pressure increases the 5f-ligand p overlap, and this reduces the degree of localized f character which decreases the screening of the 2p core hole (Schmeister et al. 1987).

Summarizing, in the heavy lanthanide mixed-valence compounds, where the concept of a fluctuation between two localized states makes sense, the L_{III} spectra appear to determine adequately the valence as long as single-electron, multiple scattering and mild final-state effects are taken into account. The pressure depcndcnce then reflects valence changes. In the opposite extreme are actinides, which have delocalized electrons and where the concept of a local f count and its relation to valence (number of bonding electrons) and ionicity (degree of charge transfer) is less obvious. Here therc is only one L_{III} component, whose position reflects both f count and degree of localization. In covalent insulators, configuration mixing in the final state is very important. The pressure dependence of the double-peaked spectrum may reflect increasing hybridization rather than changing f count. The L_{III} results for α-Ce and related large T_K compounds, such as $CeCo_2$, should be reexamined in the light of these results for actinides and covalent cerium compounds. Because band theory appears to describe the α-Ce ground state, with f count

fairly close to unity, the 4f electron is a delocalized bonding electron. It is reasonable to suppose that the double-peaked L_{III} spectra and its change with pressure (fig. 51) reflects increasing hybridization and delocalization rather than changing f count. For such cerium compounds, greater attention in the future needs to be given to assess the effects of final-state screening interactions on the spectra.

7. Epilogue

We have focused on two issues: (1) the degree to which the pressure response of the electrical resistivity, magnetic susceptibility and specific heat is similar in a given material or class of materials and how this pressure dependence is related to the Grüneisen parameter obtained from ambient pressure measurements; and (2) the extent to which this comparison holds in both anomalous lanthanide and actinide compounds.

For several systems – $CeSn_3$, $CeRu_2Si_2$, $CeCu_6$, YbCuAl, UPt_3 and UAl_2 – there is consistency among various measurements of Ω_e to the level of ± 10–20%, suggesting that scaling is valid to that degree. An excellent demonstration of this is given in fig. 7 for $CeRu_2Si_2$, where different measures of the characteristic energy T_0 are shown to have the same pressure dependence. For some of the systems, e.g. $CeCu_6$, estimates of Ω_e obtained at high temperatures agree with those found at very low temperature, suggesting that single energy scaling is valid over a broad temperature range. On the other hand, differences between high- and low-temperature estimates of the Grüneisen parameters for $CeCu_2Si_2$ or $CePd_3$, if intrinsic, may mean that scaling works differently in the single-ion Kondo regime and in the coherent Fermi-liquid regime. We also have seen that examination of anomalous cases may point to different microscopic origins for the scaling. For example, the large value of Ω_e in $CeRu_2Si_2$ relative to its modest value of γ may indicate that the underlying physics is dominated by a $T=0$, finite $H=H_m$ fixed point for transition to metamagnetism. The large negative Ω_e seen below 0.5 K in $CeAl_3$ also may arise from a phase transition to small moment antiferromagnetism. Aside from these last two compounds, there appears to be a correlation between the magnitudes of Grüneisen parameters and Sommerfeld coefficients for many different anomalous lanthanide and actinide compounds (fig. 36). Experimentally determining the precise functional dependence of Ω on γ would be helpful in guiding theory. Another key point is that (with the noted exception of UBe_{13}) the magnetic Grüneisen parameter deduced from magnetostriction and magnetization appears to coincide with the electronic Grüneisen parameter. The equality $\Omega_e=\Omega_H$ means that the scaling field H_0 equals k_BT_0/μ_B and can arise because heavy fermions have a Wilson ratio close to unity, i.e. C_p and χ are equally enhanced.

Pressure studies also can contribute to understanding the transport behavior of anomalous compounds, for which theory is not so well-established, and for which scaling behavior cannot be directly deduced by applying thermodynamic relations to a free energy that is assumed to scale with T/T_0. A common assumption is that at low temperatures ρ varies as AT^2, with $A \propto 1/T_0^2$, so that the relation $A/\gamma^2=$constant should hold. For

UPt_3 high pressure studies support this assumption, but we have shown that it is not simply valid for UBe_{13}. A second assumption is that the temperatures T_m or T_i should be proportional to T_0 and hence to $1/\gamma$; this appears to be true for $CeCu_6$ and UPt_3 and approximately for UBe_{13}, but not for $CeCu_2Si_2$ or strictly for $YbCu_{4.5}$. It is possible that the temperature of the resistivity maximum does not have a simple relationship to T_0. Third, the "residual" resistivity for some systems ($Ce_{0.9-x}La_xTh_{0.1}$ and $CeAl_3$) varies dramatically with pressure; but, while in the first case the magnitude of the variation is consistent with a Kondo-hole mechanism, the magnitude is too large for this in the second case.

Concerning itinerant versus localized electron behavior, we first note that the Grüneisen analysis works equally well for both actinide and lanthanide systems, so that it is difficult to utilize high pressure studies to make such distinctions. One exceptional case is UBe_{13}, where the Ω_χ appears to be anomalously small given its large Sommerfeld coefficient. On the other hand, studies of magnetic ordering show distinctive differences between lanthanides and actinides. The linear coefficient of specific heat remains large in the antiferromagnetic state of U-based magnets, which is not the case for the lanthanide Kondo-lattice magnets. The transition temperatures of the U-magnets consistently *increase* with pressure, but the opposite is the case for the vast majority of Ce-based antiferromagnets. In one case, UCu_5, band theory gives adequate description of the ordered phase. The concept of competing Kondo and RKKY interactions appears to provide an adequate account of the pressure dependence of magnetic ordering in Ce- and possibly Yb-based magnets but this is not so clearly the case for those based on U.

The nature of superconductivity in anomalous lanthanide and actinide intermetallics remains a fascinating topic. Pressure measurements, in part, have been responsible for implicating spin fluctuations as a possible pairing mechanism. Additional examples of superconductivity in strongly correlated Ce-compounds are needed to say with certainty that the mechanism is similar in both actinide and lanthanide systems. It is possible that both just sample different parts of the same phase space. Pressure studies using microscopic probes, e.g. nuclear magnetic resonance, would be helpful in this regard. The absence of superconductivity in any correlated Yb compound also raises the question of the extent to which pressure measurements indicate these to represent hole analogues of Ce compounds.

The L_{III} absorption spectra of actinides and lanthanides also are clearly different, as is their response to pressure. For lanthanides, changes with pressure mostly represent changes in the f count n_f, but in the actinides, the effect of pressure is to change the 5f/conduction hybridization, without necessarily affecting the f count. Whether this is also true for α-like cerium compounds (i.e. those that appear to be described well by LDA band theory) remains an open question.

Overall, none of the issues raised in this review – degree of validity of scaling, single-ion versus coherence-regime scaling, equality of electronic and magnetic Grüneisen parameters, different microscopic origins of scaling (magnetic correlations versus Kondo-like behavior), the nature of the transport behavior – is well established, and because these

are significant issues for our understanding of anomalous lanthanides and actinides, this leaves substantial work for the future. Attention needs to be paid to the following:

(1) The various measurements (ρ, χ, C_p, β, S_v) wherever possible should be carried out on a single sample, preferably a high quality single crystal. This would eliminate variations due to differing levels of sample quality in the measurements.

(2) For determination of Ω_e from the ratio of β/γ or from Ω_c, Ω_χ or Ω_A, experiments must be performed at temperatures well below T_0. This holds as well for estimates of Ω_H from measurements of S_V. Many of the existing discrepancies in values of Ω_e arise from not measuring at sufficiently low temperatures.

(3) Establishment of scaling over a broad temperature range in properties such as C_p, χ, ρ or β is very important. While scaling appears valid for χ in $CeSn_3$, UPt_3 and YbCuAl and for resistivity in a number of systems, it has not been established for other materials or for other physical properties such as C_p or β. This requires very careful determination of background contributions, such as phonon contributions to C_p, ρ and β or non-f contributions to χ. Furthermore, data for C_p need to be converted to C_v, which is the quantity involved in Grüneisen relations.

(4) Studies of the bulk modulus are few and those that exist suffer from lack of distinction between isothermal and adiabatic moduli. In cases where the adiabatic modulus has been measured, it does not increase monotonically with temperature as predicted for single-energy scaling. Furthermore, studies of the nonmagnetic counterparts are needed to determine $\delta B_e(0)$ and hence d^2T_0/dV^2, which is valuable for evaluating the variation of Ω_e with pressure.

(5) These issues need to be explored to gain a better understanding of how scaling works in the various ground states – mixed-valent, heavy-fermion paramagnet, superconductor, or antiferromagnet, systems with strong magnetic correlations, and small gap semiconductors. Furthermore, more extensive measurements are needed so that a complete scaling analysis relating $V(T, P, H)$, $S(T, P, H)$ and $M(T, P, H)$ or alternatively $\beta(T, P, H)$, $C_v(T, P, H)$ and $\chi(T, P, H)$ can be made. For distinguishing itineracy from localized electron behavior, the presumed equality of Ω_e and Ω_H needs to be carefully examined, as the two are known to differ in itinerant transition-metal paramagnets and in UBe_{13} as well.

(6) Theoretical guidance is needed for several issues. The nature of coupling to cell volume in the heavy fermions, i.e. the volume dependence of n_f and V_{kf}, is essential for understanding the pressure dependence of physical quantities but little progress has been made in this regard. The broad spectrum of temperature-dependent resistivities, determined by the interplay among strong spin scattering, phonon and crystal-field contributions as well as between single-ion and periodic lattice effects, is poorly understood at ambient pressure let alone as a function of pressure. The extent to which scaling of the resistivity is expected under these conditions is not clear.

Finally, throughout, we have assumed that $\gamma(P)$ is inversely proportional to a single characteristic temperature $T_0(P)$. Though this may be true, identity of the physics responsible for T_0 and hence its pressure dependence remains unexplained.

Acknowledgments

We thank Zachary Fisk and Alex Lacerda for insightful discussions, Thomas Graf for preparing some of the figures, and especially Julie Gallegos for her skill and patience in typing the manuscript. Portions of this review were written while JML was a guest scientist at the Los Alamos Center for Materials Science, under the auspices of the University of California Personnel Assignment Program, and while JDT was a guest at Kumamoto University as Senior Fellow of the Japan Society for the Promotion of Science. It is a pleasure to acknowledge, respectively, Mike Boring and Gendo Oomi for their support and hospitality during these visits. Work at Los Alamos was performed under the auspices of the US Department of Energy.

References

Aeppli, G., and Z. Fisk, 1992, Comm. Condens. Matter Phys. **16**, 155.

Aeppli, G., E. Bucher, C. Broholm, J.K. Kjems, J. Baumann and J. Hufnagl, 1988, Phys. Rev. Lett. **60**, 615.

Aeppli, G., C. Broholm, E. Bucher and D.J. Bishop, 1991, Physica B **171**, 278.

Aliev, F.G., N.B. Brandt, V.V. Moshchalkov and S.M. Chudinov, 1983, Solid State Commun. **45**, 215.

Allen, J.W., and R.M. Martin, 1982, Phys. Rev. Lett. **49**, 1106.

Allen, J.W., B. Batlogg and P. Wachter, 1979, Phys. Rev. B **20**, 4807.

Amato, A., R.A. Fisher, N.E. Phillips, D. Jaccard and E. Walker, 1990, Physica B **165–166**, 389.

Amato, A., C. Geibel, F.N. Gygax, R.H. Heffner, E. Knetsch, D.E. MacLaughlin, C. Schank, A. Schenck, F. Steglich and M. Weber, 1992, Z. Phys. B **86**, 159.

Anderson, P.W., 1981, in: Valence Fluctuations in Solids, eds L.M. Falicov, W. Hanke and M.B. Maple (North-Holland, Amsterdam) p. 53.

Andrei, N., K. Fuyura and J.H. Lowenstein, 1983, Rev. Mod. Phys. **55**, 331.

Andres, K., J.E. Graebner and H.R. Ott, 1975, Phys. Rev. Lett. **35**, 1779.

Arko, A.J., D.D. Koelling, B.D. Dunlap, A.W. Mitchell, C. Capasso and M. delGiudice, 1988, J. Appl. Phys. **63**, 3680.

Aronson, M.C., J.D. Thompson, J.L. Smith, Z. Fisk and M.W. McElfresh, 1989, Phys. Rev. Lett. **63**, 2311.

Asayama, K., Y. Kitaoka and Y. Kohori, 1988, J. Magn. & Magn. Mater. **76–77**, 449.

Assmus, W., M. Herrmann, U. Rauchschwalbe, S. Riegel, W. Lieke, H. Spille, S. Horn, G. Weber, F. Steglich and G. Cordier, 1984, Phys. Rev. Lett. **52**, 469.

Assmus, W., P. Fulde, B. Lüthi and F. Steglich, 1988, in: Proc. 6th Int. Conf. on Crystal-Field Effects and Heavy-Fermion Physics, J. Magn. & Magn. Mater. **76–77**.

Ayache, C., J. Beille, E. Bonjour, R. Calemczuk, G. Creuzet, D. Gignoux, A. Najib, D. Schmitt, J. Voiron and M. Zerguine, 1987, J. Magn. & Magn. Mater. **63–64**, 329.

Baer, Y., and W.-D. Schneidner, 1987, in: Handbook on the Physics and Chemistry of Rare Earths, Vol. 10, eds K.A. Gschneidner Jr, L. Eyring and S. Hüfner (North-Holland, Amsterdam) p. 1.

Bakker, K., A. de Visser, A.A. Menovsky and J.J.M. Franse, 1992a, Phys. Rev. B **46**, 544.

Bakker, K., A. de Visser, E. Bruck, A.A. Menovsky and J.J.M. Franse, 1992b, J. Magn. & Magn. Mater. **108**, 63.

Barbara, B., J. Beille, B. Cheiato, A. Najib and S. Zemirli, 1989, Phys. Lett. A **138**, 509.

Barberis, G.E., M.E. Foglio, J.E. Crow and P. Schlottmann, 1991, Proc. 6th Int. Conf. on Valence Fluctuations, Physica B **171**.

Barth, S., H.R. Ott, F.N. Gygax, B. Hitti, E. Lippelt, A. Schenck, C. Baines, B. van den Brandt, T. Konter and S. Mango, 1987, Phys. Rev. Lett. **59**, 2991.

Beal-Monod, M.T., and J.M. Lawrence, 1980, Phys. Rev. B **21**, 5400.

Beaurepaire, E., J.P. Kappler and G. Krill, 1990, Phys. Rev. B **41**, 6768.

Beille, J., M.B. Maple, J. Wittig, Z. Fisk and L. DeLong, 1983, Phys. Rev. B **28**, 7397.

Bellarbi, B., A. Benoit, D. Jaccard, J.M. Mignot and H.F. Broun, 1984, Phys. Rev. B **30**, 1182.

Benedict, U., S. Dabos, L. Gerward, J. Staun Olsen, J. Beuers, J.C. Spirlet and C. Dufour, 1987, J. Magn. & Magn. Mater. **63–64**, 403.

Bertram, S., G. Kaindl, J. Jove, M. Pages and J. Gal, 1989, Phys. Rev. Lett. **63**, 2680.

Besnus, M.J., J.P. Kappler, P. Lehmann and A. Meyer, 1985, Solid State Commun. **55**, 779.

Beyermann, W.P., M.F. Hundley, P.C. Canfield, J.D. Thompson, M. Latroche, C. Godart, M. Selsane, Z. Fisk and J.L. Smith, 1991, Phys. Rev. B **43**, 13130.

Bickers, N.E., D.L. Cox and J.W. Wilkins, 1985, Phys. Rev. Lett. **54**, 230.

Bickers, N.E., D.L. Cox and J.W. Wilkins, 1987, Phys. Rev. B **36**, 2036.

Bleckwedel, A., and A. Eichler, 1981, in: Physics of Solids under High Pressure, eds J.S. Schilling and R.N. Shelton (North-Holland, Amsterdam) p. 323.

Bleckwedel, A., and A. Eichler, 1985, Solid State Commun. **56**, 693.

Borges, H.A., J.D. Thompson, R.D. Parks and S. Horn, 1985, unpublished.

Borges, H.A., J.D. Thompson, C. Godart and L.C. Gupta, 1987, in: Theoretical and Experimental Aspects of Valence Fluctuations and Heavy Fermions, eds L.C. Gupta and S.K. Malik (Plenum Press, New York) p. 413.

Borges, H.A., J.D. Thompson, M.C. Aronson, J.L. Smith and Z. Fisk, 1988a, J. Magn. & Magn. Mater. **76–77**, 235.

Borges, H.A., J.D. Thompson, J.L. Smith and Z. Fisk, 1988b, unpublished.

Brandow, B.H., 1988, Phys. Rev. B **37**, 250.

Brandt, N.B., and V.V. Moshchalkov, 1984, Adv. Phys. **33**, 373.

Bredl, C.D., S. Horn, F. Steglich, B. Luthi and R.M. Martin, 1984, Phys. Rev. Lett. **52**, 1982.

Brito, J.J.S., and H.O. Frota, 1990, Phys. Rev. B **42**, 6378.

Brodale, G.E., R.A. Fisher, N.E. Phillips and J. Flouquet, 1986a, Phys. Rev. Lett. **56**, 390.

Brodale, G.E., R.A. Fisher, N.E. Phillips, G.R. Stewart and A.L. Giorgi, 1986b, Phys. Rev. Lett. **57**, 234.

Broholm, C., J.K. Kjems, W.J.L. Buyers, P. Matthews, T.T.M. Palstra, A.A. Menovsky and J.A. Mydosh, 1987a, Phys. Rev. Lett. **58**, 1467.

Broholm, C., J.K. Kjems, G. Aeppli, Z. Fisk, J.L. Smith, S.M. Shapiro, G. Shirane and H.R. Ott, 1987b, Phys. Rev. Lett. **58**, 917.

Bruls, G., W. Joss, U. Welp, H.R. Ott, Z. Fisk, G. Cors and M. Karnut, 1987, J. Magn. & Magn. Mater. **63–64**, 181.

Buschow, K.H.J., and H.J. van Daal, 1972, in: Magnetism and Magnetic Materials, eds C.D. Graham and J.J. Rhyne, AIP Conf. Proc. **5**, 1464.

Campagna, M., and F.U. Hillebrecht, 1987, in: Handbook on the Physics and Chemistry of Rare Earths, Vol. 10, eds K.A. Gschneidner Jr, L. Eyring and S. Hüfner (North-Holland, Amsterdam) p. 75.

Canfield, P.C., A. Lacerda, J.D. Thompson, G. Sparn, W.P. Beyermann, M.F. Hundley and Z. Fisk, 1992, J. Alloys & Compounds **181**, 77.

Chakravarthy, R., S.K. Paranjpe, M.R.L.N. Murthy, L.M. Rao and N.S.S. Murthy, 1985, Phys. Status Solidi a 88, K155.

Chattopadhyay, T., P. Burlet, J. Rossat-Mignod, H. Bartholin, C. Vettier and O. Vogt, 1987, J. Magn. & Magn. Mater. **63–64**, 52.

Chattopadhyay, T., H. v. Löhneysen, T. Trappmann and M. Loewenhaupt, 1990, Z. Phys. B **80**, 159.

Chen, J.W., S.E. Lambert, M.B. Maple, Z. Fisk, J.L. Smith and H.R. Ott, 1984, in: Proc. 17th Int. Conf. on Low Temperature Physics (LT17), eds U. Eckern, A. Schmid, W. Weber and H. Wuhl (North-Holland, Amsterdam) p. 325.

Chen, Y.-Y., J.M. Lawrence, J.D. Thompson and J.O. Willis, 1989, Phys. Rev. B **40**, 10766.

Coleman, P., 1983, Phys. Rev. B **28**, 5255.

Continentino, M.A., 1994, Phys. Rep. **239**, 179.

Cooper, J.R., C. Rizzuto and G.L. Olcese, 1971, J. Phys. (Paris) Colloq. **32**, C1-1136.

Coqblin, B., and J.R. Schrieffer, 1969, Phys. Rev. **185**, 847.

Cornut, B., and B. Coqblin, 1972, Phys. Rev. B **5**, 4541.

Costa, G.A., F. Canepa and G.L. Olcese, 1982, Solid State Commun. **44**, 67.

Cox, D.E., G. Shirane, S.M. Shapiro, G. Aeppli, Z. Fisk, J.L. Smith, J. Kjems and H.R. Ott, 1986, Phys. Rev. B **33**, 3614.

Dakin, S., G. Rapson and B.D. Rainford, 1992, J. Magn. & Magn. Mater. **108**, 117.

de Boer, F.R., J.J.M. Franse, E. Louis, A.A. Menovsky, J.A. Mydosh, T.T.M. Palstra, U. Rauchschwalbe, W. Schlabitz, F. Steglich and A. de Visser, 1986, Physica B **138**, 1.

de Novion, C.H., M. Konczykowski and M. Haessler, 1982, J. Phys. C **15**, 1251.

de Visser, A., 1986, Ph.D. Thesis (University of Amsterdam).

de Visser, A., J.J.M. Franse and A. Menovsky, 1984, J. Magn. & Magn. Mater. **43**, 43.

de Visser, A., J.J.M. Franse and A. Menovsky, 1985, J. Phys. F 15, L53.

de Visser, A., E. Louis, J.J.M. Franse and A. Menovsky, 1986, J. Magn. & Magn. Mater. **54–57**, 387.

de Visser, A., A. Menovsky and J.J.M. Franse, 1987, Physica B **147**, 81.

de Visser, A., J.J.M. Franse and J. Flouquet, 1989a, Physica B **161**, 324.

de Visser, A., A. Lacerda, P. Haen, J. Flouquet, F.E. Kayzel and J.J.M. Franse, 1989b, Phys. Rev. B **39**, 11301.

de Visser, A., J.J.M. Franse, A. Lacerda, P. Haen and J. Flouquet, 1990a, Physica B **163**, 49.

de Visser, A., A.A. Menovsky, J.J.M. Franse, K. Hasselbach, A. Lacerda, L. Taillefer, P. Haen and J. Flouquet, 1990b, Phys. Rev. B **41**, 7304.

de Visser, A., J. Flouquet, J.J.M. Franse, P. Haen, K. Hasselbach, A. Lacerda and D.L. Taillefer, 1991, Physica B **171**, 190.

de Visser, A., N.H. van Dijk, J.J.M. Franse, A. Lacerda, J. Flouquet, Z. Fisk and J.L. Smith, 1992, J. Magn. & Magn. Mater. **108**, 56.

Doniach, S., 1977, in: Valence Instabilities and Related Narrow Band Phenomena, ed. R.D. Parks (Plenum Press, New York) p. 169.

Eiling, A., and J.S. Schilling, 1981, Phys. Rev. Lett. **46**, 364.

Eriksson, O., M.S.S. Brooks and B. Johansson, 1990, Phys. Rev. B **41**, 7311.

Evans, S.M.M., A.K. Bhattacharjee and B. Coqblin, 1992, Phys. Rev. B **45**, 7244.

Felten, R., F. Steglich, G. Weber, H. Rietschel, F. Gompf, B. Renker and J. Beuers, 1986, Europhys. Lett. **2**, 323.

Fierz, Ch., D. Jaccard, J. Sierro and J. Flouquet, 1988, J. Appl. Phys. **63**, 3898.

Fisher, R.A., S.E. Lacy, C. Marcenat, J.A. Olsen, N.E. Phillips, J. Flouquet, A. Amato and D. Jaccard, 1987a, Jpn. J. Appl. Phys. **26**, 1257.

Fisher, R.A., S.E. Lacy, C. Marcenat, J.A. Olsen, N.E. Phillips, Z. Fisk and J.L. Smith, 1987b, Jpn. J. Appl. Phys. **26**, 1219.

Fisher, R.A., S. Kim, B.F. Woodfield, N.E. Phillips, L. Taillefer, K. Hasselbach, J. Flouquet, A.L. Giorgi and J.L. Smith, 1989, Phys. Rev. Lett. **62**, 1411.

Fisher, R.A., S. Kim, Y. Wu, N.E. Phillips, M.W. McElfresh, M.S. Torikachvili and M.B. Maple, 1990, Physica B **163**, 419.

Fisk, Z., and M.B. Maple, 1992, J. Alloys & Compounds **183**, 303.

Fisk, Z., J.L. Smith, H.R. Ott and B. Batlogg, 1985, J. Magn. & Magn. Mater. **52**, 79.

Fisk, Z., D.W. Hess, C.J. Pethick, D. Pines, J.L. Smith, J.D. Thompson and J.O. Willis, 1988a, Science **239**, 33.

Fisk, Z., J.D. Thompson and H.R. Ott, 1988b, J. Magn. & Magn. Mater. **76–77**, 637.

Fisk, Z., P.C. Canfield, W.P. Beyermann, J.D. Thompson, M.F. Hundley, H.R. Ott, E. Felder, M.B. Maple, M.A. de le Torre, P. Visani and C.L. Seaman, 1991, Phys. Rev. Lett. **67**, 3310.

Flouquet, J., J.C. Lasjaunias, J. Peyrard and M. Ribault, 1982, J. Appl. Phys. **53**, 2127.

Flouquet, J., P. Haen, C. Marcenat, P. Lejay, A. Amato, D. Jaccard and E. Walker, 1985, J. Magn. & Magn. Mater. **52**, 85.

Flouquet, J., P. Haen, L. Lapierre, Ch. Fierz, A. Amato and D. Jaccard, 1988, J. Magn. & Magn. Mater. **76–77**, 285.

Fournier, J.M., 1985, Physica B **130**, 268.

Fournier, J.M., and J. Beille, 1979, J. Phys. (Paris) Colloq. **4**, C4-145.

Franse, J.J.M., A. de Visser and A. Menovsky, 1986, Physica B **139–140**, 445.

Franse, J.J.M., A.A. Menovsky, A. de Visser, J. van den Berg and G.J. Nieuwenhuys, 1987, J. Appl. Phys. **61**, 3383.

Franse, J.J.M., M. van Sprang, A. de Visser and P.E. Brommer, 1989, Physica B **154**, 379.

Freeman, A.J., 1972, in: Magnetic Properties of Rare Earth Metals, ed. R.J. Elliot (Plenum Press, New York) p. 245.

Freeman, A.J., B.I. Min and M.R. Norman, 1988, in: Handbook on the Physics and Chemistry of Rare Earths, Vol. 10, eds K.A. Gschneidner Jr, L. Eyring and S. Hüfner (North-Holland, Amsterdam) p. 165.

Frick, B., M. Loewenhaupt, D. Debray and W. Just, 1983, Z. Phys. B **52**, 223.

Frings, P.H., 1984, Ph.D. Thesis (University of Amsterdam).

Frings, P.H., J.J.M. Franse, F.R. de Boer and A. Menovsky, 1983, J. Magn. & Magn. Mater. **31–34**, 240.

Fuggle, J.C., F.U. Hillebrecht, J.-M. Esteva, R.C. Karnatak, O. Gunnarsson and K. Schönhammer, 1983, Phys. Rev. B **27**, 4637.

Geibel, C., C. Schank, S. Thies, H. Kitazawa, C.D. Bredl, A. Bohm, M. Rau, A. Grauel, R. Caspary,

R. Helfrich, U. Ahlheim, G. Weber and F. Steglich, 1991b, Z. Phys. **84**, 1.

Geibel, L., S. Thies, D. Kaczorowski, A. Mehner, A. Grauel, B. Seidel, U. Ahlheim, R. Helfrich, K. Peterson, C.D. Bredl and F. Steglich, 1991a, Z. Phys. B **83**, 305.

Germann, A., and H. v. Löhneysen, 1989, Europhys. Lett. **9**, 367.

Goldman, A.I., S.M. Shapiro, G. Shirane, J.L. Smith and Z. Fisk, 1986, Phys. Rev. B **33**, 1627.

Grewe, N., and F. Steglich, 1991, in: Handbook on the Physics and Chemistry of Rare Earths, Vol. 14, eds K.A. Gschneidner Jr and L. Eyring (North-Holland, Amsterdam) p. 343.

Grier, B.H., and R.D. Parks, 1981, in: Valence Fluctuations in Solids, eds L.M. Falicov, W. Hanke and M.B. Maple (North-Holland, Amsterdam) p. 263.

Grier, B.H., R.D. Parks, S.M. Shapiro and C.F. Majkrzak, 1981, Phys. Rev. B **24**, 6242.

Grier, B.H., J.M. Lawrence, S. Horn and J.D. Thompson, 1988, J. Phys. C **21**, 1099.

Grüner, G., and A. Zawadowski, 1974, Rep. Prog. Phys. **37**, 1497.

Gunnarsson, O., and K. Schönhammer, 1985, in: Theory of Heavy Fermion and Valence Fluctuations, eds T. Kasuya and T. Saso (Springer, Berlin) p. 100.

Gunnarsson, O., and K. Schönhammer, 1987, in: Handbook on the Physics and Chemistry of Rare Earths, Vol. 10, eds K.A. Gschneidner Jr, L. Eyring and S. Hüfner (North-Holland, Amsterdam) p. 103.

Gupta, L.C., and S.K. Malik, 1987, Theoretical and Experimental Aspects of Valence Fluctuations and Heavy Fermions (Plenum Press, New York).

Haen, P., J.-M. Laurant, K. Payer and J.-M. Mignot, 1993, in: Transport and Thermal Properties of f-Electron Systems, eds G. Oomi, H. Fujii and T. Takabatake (Plenum Press, New York) p. 145.

Häfner, H.U., 1985, J. Magn. & Magn. Mater. **47–48**, 299.

Hasselbach, K., A. Lacerda, A. de Visser, K. Behnia, L. Taillefer and J. Flouquet, 1990, J. Low Temp. Phys. **81**, 299.

Hayden, S.M., L. Taillefer, C. Vettier and J. Flouquet, 1992, Phys. Rev. B **46**, 8675.

Heffner, R.H., 1992, J. Magn. & Magn. Mater. **108**, 23.

Heffner, R.H., H.R. Ott, A. Schenck, J.A. Mydosh and D.E. MacLaughlin, 1991, J. Appl. Phys. **70**, 5782.

Heinrich, G., J.P. Kappler and A. Meyer, 1979, Phys. Lett. A **74**, 121.

Herbst, J.F., and J.W. Wilkins, 1982, Phys. Rev. B **26**, 1689.

Hess, D.W., T.A. Tokuyasu and J.A. Sauls, 1989, J. Phys.: Condens. Matter **1**, 8135.

Hill, H.H., 1970, in: Plutonium 1970 and Other Actinides, ed. W.N. Miner (Metallurgical Society of the American Institute of Mining, Metallurgical and Petroleum Engineers, New York) p. 2.

Hong, T.M., 1992, Phys. Rev. B **46**, 13862.

Horn, S., E. Holland-Moritz, M. Loewenhaupt, F. Steglich, A. Benoit and J. Flouquet, 1981, Phys. Rev. B **23**, 3171.

Horn, S., M.A. Edwards, J.D. Thompson and R.D. Parks, 1985, J. Magn. & Magn. Mater. **52**, 385.

Hüfner, S., 1987, in: Handbook on the Physics and Chemistry of Rare Earths, Vol. 10, eds K.A. Gschneidner Jr, L. Eyring and S. Hüfner (North-Holland, Amsterdam) p. 301.

Hundley, M.F., P.C. Canfield, J.D. Thompson, Z. Fisk and J.M. Lawrence, 1990, Phys. Rev. B **42**, 6842.

Iga, F., M. Kasaya, H. Suzuki, Y. Okayama, H. Takahashi and N. Mori, 1993, Physica B **186–188**, 419.

Itoh, Y., H. Kadomatsu, M. Kurisu and H. Fujiwara, 1987, J. Phys. Soc. Jpn. **56**, 1159.

Jaccard, D., J.M. Mignot, B. Bellarbi, A. Benoit, H.F. Braun and J. Sierro, 1985, J. Magn. & Magn. Mater. **47–48**, 23.

Jaccard, D., K. Behnia and J. Sierro, 1992, Phys. Lett. A **163**, 475.

Jayaraman, A., 1978, in: Handbook on the Physics and Chemistry of Rare Earths, Vol. 1, eds K.A. Gschneidner Jr and L. Eyring (North-Holland, Amsterdam) p. 707.

Jayaraman, A., 1979, in: Handbook on the Physics and Chemistry of Rare Earths, Vol. 2, eds K.A. Gschneidner Jr and L. Eyring (North-Holland, Amsterdam) p. 575.

Kadomatsu, H., H. Tanaka, M. Kurisu and H. Fujiwara, 1986, Phys. Rev. B **33**, 4799.

Kadowaki, K., and S.B. Woods, 1986, Solid State Commun. **58**, 307.

Kagayama, T., and G. Oomi, 1993, in: Transport and Thermal Properties of f-Electron Systems, eds G. Oomi, H. Fujii and T. Fujita (Plenum Press, New York) p. 155.

Kagayama, T., G. Oomi, H. Takahashi, N. Mori, Y. Onuki and T. Komatsubara, 1992, J. Magn. & Magn. Mater. **108**, 103.

Kaindl, G., G.K. Wertheim, G. Schmeister and E.V. Sampathkumaran, 1987, Phys. Rev. Lett. **58**, 606.

Kaindl, G., G. Schmeister, E.V. Sampathkumaran and P. Wachter, 1988, Phys. Rev B **38**, 10174.

Kaiser, A.B., and P. Fulde, 1988, Phys. Rev. B **37**, 5357.

Kalkowski, G., G. Kaindl, W.D. Brewer and W. Krone, 1987a, Phys. Rev. B **35**, 2667.

Kalkowski, G., G. Kaindl, S. Bertram, G. Schmeister, J. Rebizant, J.C. Spirlet and O. Vogt, 1987b, Solid State Commun. **64**, 193.

Kang, J.-S., J.W. Allen, C. Rossel, C.L. Seaman and M.B. Maple, 1990, Phys. Rev. B **41**, 4078.

Kappler, J.P., and A. Meyer, 1979, J. Phys. F **9**, 143.

Kasaya, M., F. Iga, M. Takigawa and T. Kasuya, 1985, J. Magn. & Magn. Mater. **47–48**, 429.

Kasaya, M., T. Tani, K. Kawate, T. Mizushima, Y. Isikawa and K. Sato, 1991, J. Phys. Soc. Jpn. **60**, 3145.

Kasaya, M., T. Tani, K. Ohoyama, M. Kohgi and Y. Isikawa, 1992, J. Magn. & Magn. Mater. **104–107**, 665.

Katzman, H., and J.A. Mydosh, 1972, Phys. Rev. Lett. **29**, 998.

King Jr, H.E., S.J. La Placa, T. Penney and Z. Fisk, 1981, in: Valence Fluctuations in Solids, eds L.M. Falicov, W. Hanke and M.B. Maple (North-Holland, Amsterdam) p. 333.

Kleiman, R.N., D.J. Bishop, H.R. Ott, Z. Fisk and J.L. Smith, 1990, Phys. Rev. Lett. **64**, 1975.

Knetsch, E.A., J.A. Mydosh, R.H. Heffner and J.L. Smith, 1993, Physica B **186–188**, 251.

Knopp, G., A. Loidl, K. Knorr, L. Pawlak, M. Duczmal, R. Caspary, U. Gottwick, H. Spille, F. Steglich and A.P. Murani, 1989, Z. Phys. B **77**, 95.

Koelling, D.D., A.M. Boring and J.H. Wood, 1983, Solid State Commun. **47**, 227.

Kotani, A., T. Jo and J.C. Parlebas, 1988, Adv. Phys. **37**, 37.

Kouroudis, I., D. Weber, M. Yoshizawa, B. Luthi, L. Puech, P. Haen, J. Flouquet, G. Bruls, U. Welp, J.J.M. Franse, A. Menovsky, E. Bucher and J. Hufnagl, 1987, Phys. Rev. Lett. **58**, 820.

Krill, G., J.P. Kappler, E. Beaurepaire, N. Wetta, D. Malterre and C. Godart, 1987, in: Theoretical and Experimental Aspects of Valence Fluctuations and Heavy Fermions, eds L.C. Gupta and S.K. Malik (Plenum Press, New York) p. 205.

Krimmel, A., P. Fischer, B. Roessli, H. Maletta, C. Geibel, C. Schank, A. Grauel, A. Loidl and F. Steglich, 1992, Z. Phys. B **86**, 161.

Kurisu, M., 1987, J. Phys. Soc. Jpn. **56**, 4064.

Kurisu, M., H. Kadomatsu and H. Fujiwara, 1981, Phys. Lett. A **84**, 496.

Kurisu, M., H. Tanaka, H. Kadomatsu, K. Sekizawa and H. Fujiwara, 1985, J. Phys. Soc. Jpn. **54**, 3548.

Kurisu, M., T. Takabatake and H. Fujiwara, 1988, Solid State Commun. **68**, 595.

Kurisu, M., T. Takabatake and H. Fujiwara, 1993, in: Transport and Thermal Properties of f-Electron Systems, eds G. Oomi, H. Fujii and T. Fujita (Plenum Press, New York) p. 265.

Kwei, G.H., J.M. Lawrence, P.C. Canfield, W.P. Beyermann, J.D. Thompson, Z. Fisk, A.C. Lawson and J.A. Goldstone, 1992, Phys. Rev. B **46**, 8067.

Kwei, G.H., J.M. Lawrence and P.C. Canfield, 1994, Phys. Rev. B **49**, 14708.

Lacerda, A., 1990, Ph.D. Thesis (University Joseph Fourier).

Lacerda, A., A. de Visser, P. Haen, P. Lejay and J. Flouquet, 1989a, Phys. Rev. B **40**, 8759.

Lacerda, A., A. de Visser, L. Puech, P. Lejay, P. Haen, J. Flouquet, J. Voiron and F.J. Okhawa, 1989b, Phys. Rev. B **40**, 11429.

Lacerda, A., A. de Visser, L. Puech, C. Paulsen, P. Haen, P. Lejay and J. Flouquet, 1991, Physica B **171**, 312.

Lacerda, A., M.F. Hundley, P.C. Canfield, G. Sparn, J.D. Thompson and Z. Fisk, 1992, Bull. Amer. Phys. Soc. **37**, 637.

Lambert, S.E., Y. Dalichaouch, M.B. Maple, J.L. Smith and Z. Fisk, 1986, Phys. Rev. Lett. **57**, 1619.

Lander, G.H., S.M. Shapiro, C. Vettier and A.J. Dianoux, 1992, Phys. Rev. B **46**, 5387.

Lang, M., 1991, Ph.D. Thesis (University Darmstadt).

Lawrence, J.M., 1979, Phys. Rev. B **20**, 3770.

Lawrence, J.M., and J.D. Thompson, 1994, to appear.

Lawrence, J.M., P.S. Riseborough and R.D. Parks, 1981, Rep. Prog. Phys. **44**, 1.

Lawrence, J.M., M.L. den Boer, R.D. Parks and J.L. Smith, 1984, Phys. Rev. B **29**, 568.

Lawrence, J.M., J.D. Thompson and Y.Y. Chen, 1985a, Phys. Rev. Lett. **54**, 2537.

Lawrence, J.M., J.D. Thompson, Z. Fisk and B. Batlogg, 1985b, J. Appl. Phys. **57**, 3131.

Lawrence, J.M., Y.Y. Chen and J.D. Thompson, 1987, in: Theoretical and Experimental Aspects of Valence Fluctuations and Heavy Fermions, eds

L.C. Gupta and S.K. Malik (Plenum Press, New York) p. 169.

Lawrence, J.M., G.H. Kwei, P.C. Canfield, J.G. DeWitt and A.C. Lawson, 1994, Phys. Rev. B **49**, 1627.

Lee, P.A., T.M. Rice, J.W. Serene, L.J. Sham and J.W. Wilkins, 1986, Comm. Condens. Matter Phys. **12**, 99.

Lenz, D., H. Schmidt, S. Ewert, W. Boksch, R. Pott and D. Wohlleben, 1984, Solid State Commun. **52**, 759.

Lieke, W., U. Rauchschwalbe, C.D. Bredl, F. Steglich, J. Aarts and F.R. de Boer, 1982, J. Appl. Phys. **53**, 2111.

Louis, E., A. de Visser, A. Menovsky and J.J.M. Franse, 1986, Physica B **144**, 48.

Lüthi, B., 1985, J. Magn. & Magn. Mater. **52**, 70.

Lüthi, B., and M. Yoshizawa, 1987, J. Magn. & Magn. Mater. **63–64**, 274.

Malterre, D., 1991, Phys. Rev. B **43**, 1391.

Mao, S.Y., D. Jaccard, J. Sierro, Z. Fisk and J.L. Smith, 1988, J. Magn. & Magn. Mater. **76–77**, 241.

Maple, M.B., L.E. DeLong and B.C. Sales, 1978, in: Handbook on the Physics and Chemistry of Rare Earths, Vol. 1, eds K.A. Gschneidner Jr and L. Eyring (North-Holland, Amsterdam) p. 797.

Maple, M.B., J.W. Chen, Y. Dalichaouch, T. Kohara, C. Rossel, M.S. Torikachvili, M.W. McElfresh and J.D. Thompson, 1986, Phys. Rev. Lett. **56**, 185.

Mattens, W.C.M., H. Holscher, G.J.M. Tuin, A.C. Moleman and F.R. de Boer, 1980, J. Magn. & Magn. Mater. **15–18**, 982.

McElfresh, M.W., J.D. Thompson, J.O. Willis, M.B. Maple, T. Kohara and M.S. Torikachvili, 1987, Phys. Rev. B **35**, 43.

McElfresh, M.W., M.B. Maple, J.O. Willis, Z. Fisk, J.L. Smith and J.D. Thompson, 1990, Phys. Rev. B **42**, 6062.

McElfresh, M.W., M.B. Maple, J.O. Willis, D. Schiferl, J.L. Smith, Z. Fisk and D.L. Cox, 1993, Phys. Rev. B **48**, 10395.

McMahan, A.K., 1989, J. Less-Common Met. **149**, 1.

Meng, R.L., P.H. Hor, S. Yomo and C.W. Chu, 1985, Physica B **135**, 394.

Mignot, J.-M., J. Flouquet, P. Haen, F. Lapierre, L. Peuch and J. Voiron, 1988, J. Magn. & Magn. Mater. **76–77**, 97.

Mignot, J.-M., A. Ponchet, P. Haen, F. Lapierre and J. Flouquet, 1989, Phys. Rev. B **40**, 10917.

Mignot, J.M., and J. Wittig, 1981, in: Physics of Solids under High Pressure, eds J.S. Schilling and R.N. Shelton (North-Holland, Amsterdam) p. 311.

Mock, R., B. Hillebrands, H. Schmidt, G. Güntherodt, Z. Fisk and A. Meyer, 1985, J. Magn. & Magn. Mater. **47–48**, 312.

Morin, P., C. Vettier, J. Flouquet, M. Konczykowski, Y. Lassailly, J.-M. Mignot and U. Welp, 1988, J. Low Temp. Phys. **70**, 377.

Moshchalkov, V.V., I.V. Berman, N.B. Brandt, S.N. Pashkevich, E.V. Bogdanov, E.S. Konovalova and M.V. Semenov, 1985, J. Magn. & Magn. Mater. **47–48**, 289.

Murasik, A., S. Ligenza and A. Zygmunt, 1974, Phys. Status Solidi a 23, K163.

Nakamura, H., Y. Kitaoka, H. Yamada and K. Asayama, 1988, J. Magn. & Magn. Mater. **76–77**, 517.

Nakamura, H., Y. Kitaoka, K. Asayama and Y. Onuki, 1991, Physica B **171**, 329.

Newns, D.M., and A.C. Hewson, 1981, in: Valence Fluctuations in Solids, eds L.M. Falicov, W. Hanke and M.B. Maple (North-Holland, Amsterdam) p. 27.

Nicolas-Francillon, M., A. Percheron, J.C. Achard, O. Gorochov, B. Cornut, D. Jerome and B. Coqblin, 1972, Solid State Commun. **11**, 845.

Niksch, M., B. Lüthi and K. Andres, 1980, Phys. Rev. B **22**, 5774.

Norman, M., B.I. Min, T. Oguchi and A.J. Freeman, 1988, Phys. Rev. B **38**, 6818.

Onuki, Y., Y. Shimizu, T. Komatsubara, A. Sumiyama, Y. Oda, N. Nagona, T. Fujita, Y. Maeno, K. Satoh and T. Ohtsuka, 1985, J. Magn. & Magn. Mater. **52**, 344.

Onuki, Y., T. Yamazaki, I. Ukon, T. Omi, K. Shibutani, T. Komatsubara, I. Sakamoto, Y. Sugiyama, R. Onodera, K. Yonemitsu, A. Umezawa, W.K. Kwok, G.W. Crabtree and D.G. Hinks, 1987, Physica B **148**, 29.

Oomi, G., A. Shibata, Y. Onuki and T. Komatsubara, 1988a, J. Phys. Soc. Jpn. **57**, 152.

Oomi, G., T. Numata and J. Sakurai, 1988b, Physica B **149**, 73.

Oomi, G., Y. Onuki and T. Komatsubara, 1990, Physica B **163**, 405.

Orlando, T.P., E.J. McNiff, S. Foner and M.R. Beasley, 1979, Phys. Rev. B **19**, 4545.

Ott, H.R., 1989, Physica C **162–164**, 1669.

Ott, H.R., and Z. Fisk, 1987, in: Handbook on the Physics and Chemistry of the Actinides, Vol. 5,

eds A.J. Freeman and G.H. Lander (North-Holland, Amsterdam) p. 85.
Ott, H.R., H. Rudiger, E. Felder, Z. Fisk and B. Batlogg, 1985, Phys. Rev. Lett. **55**, 1595.
Palstra, T.T.M., A.A. Menovsky, J. van den Berg, A.J. Dirkmaat, P.H. Kes, G.J. Nieuwenhuys and J.A. Mydosh, 1985, Phys. Rev. Lett. **55**, 2727.
Palstra, T.T.M., A.A. Menovsky and J.A. Mydosh, 1986, Phys. Rev. B **33**, 6527.
Payer, K., P. Haen, J.-M. Laurant, J.-M. Mignot and J. Flouquet, 1993, Physica B **186–188**, 503.
Pethick, C.J., D. Pines, K.F. Quader, K.S. Bedell and G.E. Brown, 1986, Phys. Rev. Lett. **57**, 1985.
Phillips, N.E., R.A. Fisher, S.E. Lacy, C. Marcenat, J.A. Olson, J. Flouquet, A. Amato, D. Jaccard, Z. Fisk, A.L. Giorgi, J.L. Smith and G.R. Stewart, 1987, in: Theoretical and Experimental Aspects of Valence Fluctuations and Heavy Fermions, eds L.C. Gupta and S.K. Malik (Plenum Press, New York) p. 141.
Ponchet, A., J.M. Mignot, A. de Visser, J.J.M. Franse and A. Menovsky, 1986, J. Magn. & Magn. Mater. **54–57**, 399.
Pott, R., 1982, Ph.D. Thesis (Universität Köln, Germany).
Pott, R., R. Schefzyk, D. Wohlleben and A. Junod, 1981a, Z. Phys. B **44**, 17.
Pott, R., R. Schefzyk, W. Boksch and D. Wohlleben, 1981b, in: Valence Fluctuations in Solids, eds L.M. Falicov, W. Hanke and M.B. Maple (North-Holland, Amsterdam) p. 337.
Puech, L., J.-M. Mignot, P. Lejay, P. Haen, J. Flouquet and J. Voiron, 1988, J. Low Temp. Phys. **70**, 237.
Rainford, B.D., S. Dakin and A. Severing, 1992, J. Magn. & Magn. Mater. **108**, 119.
Rajan, V.T., 1983, Phys. Rev. Lett. **51**, 308.
Ramirez, A.P., P. Coleman, P. Chandra, E. Bruck, A.A. Menovsky, Z. Fisk and E. Bucher, 1992, Phys. Rev. Lett. **68**, 2680.
Rauchschwalbe, U., W. Lieke, F. Steglich, C. Godart, L.C. Gupta and R.D. Parks, 1984, Phys. Rev. B **30**, 444.
Rebelsky, L., K. Reilly, S. Horn, H. Borges, J.D. Thompson and R. Caspary, 1990, J. Appl. Phys. **67**, 5206.
Rhyne, J.J., 1972, in: Magnetic Properties of Rare Earth Metals, ed. R.J. Elliot (Plenum Press, New York) p. 129.
Ribault, M., A. Benoit, J. Flouquet and J. Palleau, 1979, J. Phys. (Paris) Lett. 40, L-413.
Riseborough, P.S., 1992, Phys. Rev. B **45**, 13934.
Robinson, R.A., J.D. Axe, A.I. Goldman, Z. Fisk, J.L. Smith and H.R. Ott, 1986, Phys. Rev. B **33**, 6488.
Röhler, J., 1987, in: Handbook on the Physics and Chemistry of Rare Earths, Vol. 10, eds K.A. Gschneidner Jr, L. Eyring and S. Hüfner (North-Holland, Amsterdam) p. 453.
Röhler, J., 1989, J. Less-Common Met. **149**, 37.
Rossat-Mignod, J., L.P. Regnault, J.L. Jacoud, C. Vettier, P. Lejay, J. Flouquet, E. Walker, D. Jaccard and A. Amato, 1988, J. Magn. & Magn. Mater. **76–77**, 376.
Sales, B.C., and R. Viswanathan, 1976, J. Low Temp. Phys. **23**, 449.
Satoh, K., T. Fujita, Y. Maeno, Y. Onuki and T. Komatsubara, 1988, J. Magn. & Magn. Mater. **76–77**, 128.
Schefzyk, R., W. Lieke and F. Steglich, 1985, Solid State Commun. **54**, 525.
Schilling, J.S., 1979, Adv. Phys. **28**, 657.
Schilling, J.S., 1981, in: Physics of Solids Under High Pressure, eds J.S. Schilling and R.N. Shelton (North-Holland, Amsterdam) p. 345.
Schilling, J.S., 1984, Mater. Res. Soc. Symp. Proc. **22**, 79.
Schilling, J.S., 1986, Physica B **139–140**, 369.
Schlabitz, W., J. Baumann, B. Pollit, U. Rauchschwalbe, H.M. Mayer, U. Ahlheim and C.D. Bredl, 1986, Z. Phys. B **62**, 171.
Schlottmann, P., 1989, Phys. Rep. **181**, 1.
Schmeister, G., S. Bertram, G. Kaindl and O. Vogt, 1987, in: Theoretical and Experimental Aspects of Valence Fluctuations and Heavy Fermions, eds L.C. Gupta and S.K. Malik (Plenum Press, New York) p. 397.
Severing, A., E. Holland-Moritz and S. Frick, 1989, Phys. Rev. B **39**, 4164.
Shaheen, S.A., and J.S. Schilling, 1987, Phys. Rev. B **35**, 6880.
Shaheen, S.A., J.S. Schilling, S.H. Liu and O.D. McMasters, 1983, Phys. Rev. B **27**, 4325.
Shibata, A., G. Oomi, Y. Onuki and T. Komatsubara, 1986, J. Phys. Soc. Jpn. **55**, 2086.
Shimizu, T., H. Yasuoka, Z. Fisk and J.L. Smith, 1987, J. Phys. Soc. Jpn. **56**, 411.
Sparn, G., J.D. Thompson and A. Hamzic, 1992, J. Alloys & Compounds **181**, 197.
Sparn, G., W.P. Beyermann, P.C. Canfield, J.D. Thompson, Z. Fisk and F. Steglich, 1993, in: Proc. Int. Conf. on the Physics of Transition Metals, Vol. 1, eds P.M. Oppeneer and J. Kübler (World Scientific, Singapore) p. 54.

Spendeler, L., 1992a, Ph.D. Thesis (University Joseph Fourier, France).

Spendeler, L., D. Jaccard and J. Sierro, 1992b, J. Magn. & Magn. Mater. **114**, 237.

Steglich, F., 1991, J. Magn. & Magn. Mater. **100**, 186.

Stewart, G.R., 1984, Rev. Mod. Phys. **56**, 755.

Stewart, G.R., Z. Fisk, J.O. Willis and J.L. Smith, 1984, Phys. Rev. Lett. **52**, 679.

Sumiyama, A., Y. Oda, H. Nagona, Y. Onuki and T. Komatsubara, 1985, J. Phys. Soc. Jpn. **54**, 877.

Taillefer, L., J. Flouquet and G.G. Lonzarich, 1991, Physica B **169**, 257.

Takabatake, T., G. Nakamoto, H. Tanaka, H. Fujii, S. Nishigori, T. Suzuki, T. Fujita, M. Ishikawa, I. Oguro, M. Kurisu and A.A. Menovsky, 1993, in: Transport and Thermal Properties of f-Electron Systems, eds G. Oomi, H. Fujii and T. Fujita (Plenum Press, New York) p. 1.

Takke, R., W. Assmus, B. Luthi, T. Goto and K. Andres, 1980, in: Crystalline Electric Field and Structural Effects in f-Electron Systems, eds J.E. Crow, R.P. Guertin and T.W. Mihalisin (Plenum Press, New York) p. 321.

Takke, R., M. Niksch, W. Assmus, B. Luthi, R. Pott, R. Schefzyk and D.K. Wohlleben, 1981, Z. Phys. B **44**, 33.

Thalmeier, P., 1988, J. Magn. & Magn. Mater. **76–77**, 299.

Thomas, F., J. Thomasson, C. Ayache, C. Geibel and F. Steglich, 1993, Physica B **186–188**, 303.

Thompson, J.D., 1984, Rev. Sci. Instrum. **55**, 231.

Thompson, J.D., 1987, J. Magn. & Magn. Mater. **63–64**, 358.

Thompson, J.D., and Z. Fisk, 1985, Phys. Rev. B **31**, 389.

Thompson, J.D., Z. Fisk and J.O. Willis, 1984, in: Proc. 17th Int. Conf. on Low Temperature Physics (LT17), eds U. Eckern, A. Schmid, W. Weber and H. Wuhl (North-Holland, Amsterdam) p. 323.

Thompson, J.D., J.O. Willis, C. Godart, D.E. MacLaughlin and L.C. Gupta, 1985, J. Magn. & Magn. Mater. **47–48**, 281.

Thompson, J.D., R.D. Parks and H. Borges, 1986a, J. Magn. & Magn. Mater. **54–57**, 377.

Thompson, J.D., Z. Fisk and H.R. Ott, 1986b, J. Magn. & Magn. Mater. **54–57**, 393.

Thompson, J.D., M.W. McElfresh, J.O. Willis, Z. Fisk, J.L. Smith and M.B. Maple, 1987a, Phys. Rev. B **35**, 48.

Thompson, J.D., H.A. Borges, Z. Fisk, S. Horn, R.D. Parks and G.L. Wells, 1987b, in: Theoretical and Experimental Aspects of Valence Fluctuations and Heavy Fermions, eds L.C. Gupta and S.K. Malik, (Plenum Press, New York) p. 151.

Thompson, J.D., Z. Fisk, Y.-Y. Chen and J.M. Lawrence, 1987c, J. Less-Common Met. **127**, 385.

Thompson, J.D., A.C. Lawson, M.W. McElfresh, A.P. Sattelberger and Z. Fisk, 1988, J. Magn. & Magn. Mater. **76–77**, 437.

Thompson, J.D., Z. Fisk, M.W. McElfresh, H.R. Ott and M.B. Maple, 1989a, Phys. Rev. B **39**, 2578.

Thompson, J.D., Z. Fisk and G.G. Lonzarich, 1989b, Physica B **161**, 317.

Thompson, J.D., P.C. Canfield, A. Lacerda, M.F. Hundley, Z. Fisk, H.R. Ott, E. Felder, M. Chernikov, M.B. Maple, P. Visani, C.L. Seaman and G. Aeppli, 1993, Physica B **186–188**, 355.

Thompson, J.D., J.M. Lawrence and Z. Fisk, 1994, J. Low Temp. Phys. **95**, 59.

Tinkham, M., 1975, Introduction to Superconductivity (McGraw-Hill, New York).

Trainor, R.J., M.B. Brodsky and H.V. Culbert, 1975, Phys. Rev. Lett. **34**, 1019.

Trappmann, T., H. v. Löhneysen and L. Taillefer, 1991, Phys. Rev. B **43**, 13714.

Umlauf, E., P. Sutsch and E. Hess, 1980, in: Crystalline Electric Field and Structural Effects in f-Electron Systems, eds J.E. Crow, R.P. Guertin and T.W. Mihalisin (Plenum Press, New York) p. 341.

Uwatoko, Y., G. Oomi, J.D. Thompson, P.C. Canfield and Z. Fisk, 1992, unpublished.

van der Meulen, H.P., A. de Visser, J.J.M. Franse, T.T.J.M. Berendschot, J.A.A.J. Perenboom, H. van Kempen, A. Lacerda, P. Lejay and J. Flouquet, 1991, Phys. Rev. B **44**, 814.

Voiron, J., J.-M. Mignot, P. Lejay, P. Haen and J. Flouquet, 1988, J. Phys. (Paris) **49**, 1555.

Voronov, F.F., V.A. Goncharova and O.V. Stal'gorova, 1979, Sov. Phys.-JETP **49**, 687.

Willis, J.O., J.D. Thompson, Z. Fisk, A. de Visser, J.J.M. Franse and A. Menovsky, 1985, Phys. Rev. B **31**, 1654.

Willis, J.O., J.D. Thompson, R.P. Guertin and J.E. Crow, 1990, Physics of Highly Correlated Electron Systems, Physica B **163**.

Wire, M.S., 1985, Ph.D. Thesis (University of California, San Diego).

Wire, M.S., J.D. Thompson and Z. Fisk, 1984, Phys. Rev. B **30**, 5591.

Wolf, B., G. Bruls, S. Sun, W. Assmus, B. Lüthi, H. Schimanski, K. Gloos and F. Steglich, 1993, Physica B **186–188**, 279.

Wortmann, G., I. Nowik, B. Perscheid, G. Kaindl and I. Felner, 1991, Phys. Rev. B **43**, 5261.

Yanase, A., 1993, unpublished.

Yang, H.D., and W.H. Lee, 1991, Phys. Rev. B **43**, 3664.

Yomo, S., P.H. Hor, R.L. Meng and C.W. Chu, 1986, J. Magn. & Magn. Mater. **54–57**, 477.

Yomo, S., L. Gao, R.L. Meng, P.H. Hor, C.W. Chu and J. Susaki, 1988, J. Magn. & Magn. Mater. **76–77**, 257.

Yoshizawa, M., B. Luthi and K.D. Schotte, 1986, Z. Phys. B **64**, 169.

Zell, W., R. Pott, B. Roden and D. Wohlleben, 1981, Solid State Commun. **40**, 751.

Zell, W., K. Keulerz, P. Weidner, B. Roden and D. Wohlleben, 1982, in: Valence Instabilities, eds P. Wachter and H. Boppart (North-Holland, Amsterdam) p. 527.

Zieglowski, J., H.U. Häfner and D. Wohlleben, 1986, Phys. Rev. Lett. **56**, 193.

Handbook on the Physics and Chemistry of Rare Earths
Vol. 19 – Lanthanides/Actinides: Physics – II
edited by K.A. Gschneidner, Jr., L. Eyring, G.H. Lander and G.R. Choppin

Chapter 134

THERMODYNAMIC PROPERTIES OF METALLIC SYSTEMS

C. COLINET and A. PASTUREL
Laboratoire de Thermodynamique et Physico-Chimie Métallurgiques, U.R.A. CNRS no. 29, Institut National Polytechnique de Grenoble, ENSEEG, BP 75, 38402 Saint Martin d'Hères, France

Contents

1. Introduction

The phase diagrams, the structure of possible intermetallic compounds and the thermodynamic data, enthalpies and entropies of formation or of mixing, of alloys based on rare earths and actinides have been compiled for the purpose of comparing the behavior of rare earths and actinides on alloying. Concerning the rare earths, information has often been obtained for all the elements of the series except of course promethium. Concerning the actinides, the behavior of only three elements of the series, thorium, uranium and plutonium, has been studied because of the lack of data for all the other elements.

1.1. *Literature search*

The information reported for the phase diagrams has been obtained from the second edition of *Binary alloy phase diagrams* by Massalski (1990). Only references to more recent work (1990–1991) will be given.

The structures of the intermetallic compounds have been taken from *Binary alloy phase diagrams* by Massalski (1990) but also from the last edition of *Pearson's Handbook of crystallographic data for intermetallic phases* by Villars and Calvert (1991) when more information was needed. Let us mention that Iandelli and Palenzona (1979) have performed a systematic study on the crystal chemistry of intermetallic compounds of rare earth elements and that Dwight (1969) has analyzed the alloy chemistry of thorium, uranium and plutonium compounds.

The thermodynamic data, Gibbs energies, enthalpies and entropies of formation of intermetallic compounds have been obtained from a literature search. We have also consulted the handbook *Selected values of thermodynamic properties of binary alloys* by Hultgren et al. (1973a) and a compilation of thermodynamic data on transition metal based alloys done by de Boer et al. in 1988. For the actinide-based alloys a literature search and a critical analysis of the data was done by Rand and Kubaschewski (1963) for uranium compounds, by Rand et al. (1966) for plutonium alloys, by Rand et al. (1975) for thorium alloys, and more recently by Chiotti et al. (1981) for binary actinide alloys. We have included in our review the data obtained from the original publications and also the assessed data of Chiotti et al. (1981) when they were different.

Several compilations concerning particular systems or series of systems have also been published by Gschneidner (1961) for rare earth alloys, by Bayanov (1971, 1975) for alloys of rare earths with low-melting elements, by Colinet et al. (1984a,b) for alloys of rare earths with Sn, Pb, Sb and Bi, by Delfino et al. (1984) and Saccone et al. (1988) for alloys of indium and thallium with rare earths, by Mogutnov and Shvartsman (1980) and Colinet and Pasturel (1987) for transition-metal–rare-earth alloys, by Gibson and Wengert (1984) for intermetallic compounds involving lanthanides and actinides, by Johnson (1964), Kubaschewski (1968), Smith (1974), Smith et al. (1975), Peterson (1985a) and Alcock (1989) for actinide-based alloys. Gschneidner and Calderwood (1986a) studied the intra-rare-earth binary alloys. More recently Gschneidner (1990a) analyzed the thermodynamic behavior of rare earths with most of the elements in the Periodic Table.

Many systematic studies of series of alloys have been published in *Bulletin of Alloy Phase Diagrams* (now *Journal of Phase Equilibria*); these papers each contain a complete description of a system or series of systems including phase diagram, crystallographic data and thermodynamic data. Many of these papers concern rare-earth- or actinide-based alloys and will be quoted in the following.

1.2. *The current state of experimental studies*

Concerning the rare-earth-based alloys there is a continuous increase in the volume of experimental work: determination of phase diagrams, characterization of intermetallic compounds, and thermodynamic measurements. In some cases a good agreement between recent values obtained by different authors has finally allowed a decision to be made between several data with a large scatter.

A large proportion of the experimental work concerning the alloys of thorium, uranium and plutonium was performed between 1960 and 1980. Since this time little experimental work has been done. This was noted by Alcock (1989). We will quote some interesting new investigations in the 1990–1991 period concerning uranium–transition-metal alloys. Unfortunately large discrepancies between values obtained by several authors have been observed and are not actually resolved. Moreover Rand and coworkers (Rand and Kubaschewski 1963, Rand et al. 1966, 1975) and Chiotti et al. (1981) have often found incompatibilities of data with the phase diagram and these points have not yet been solved either.

We may also remark that very few experiments have been performed at high temperature in the liquid state especially for the actinide-based alloys.

Our literature search includes all work published before the end of 1991. We apologize for any inadvertent omissions. We must remark that it was impossible for us to obtain some papers found in the literature search because of their unavailability in the European libraries. This point concerns especially Russian articles but also, to a lesser extent, some papers of researchers from South East Asia.

The experimental method which has most often been used is measurement of the electromotive force (emf) with liquid or solid electrolyte. This method leads to the values of the partial Gibbs energy of one of the constituents. Under certain conditions, the Gibbs energies of formation of compounds present in the system under study are obtained. However, the enthalpies and entropies of formation of these compounds are obtained indirectly from the variation of the Gibbs energy of formation with temperature. This requires measurements in a large temperature range, but unfortunately the experiments do not always fulfil this condition and very unlikely values of enthalpies and entropies of formation are sometimes obtained. The difficulties in obtaining reliable values of enthalpies and entropies of formation from emf measurements have been discussed by Kubaschewski (1981), Hertz (1989), Castanet (1989) and Notin et al. (1992).

While calorimetric methods, direct reaction calorimetry or solution calorimetry using tin or aluminum as solvent have been performed in rare earth based alloys, this has not been the case in actinide-based alloys, where acid solution calorimetry has sometimes

been used. This method, even when performed at room temperature, requires several precautions to ensure good dissolution of the compounds.

To a lesser extent, vapor pressure measurements have been performed on rare-earth- and actinide-based alloys. These measurements present the same disadvantage as the emf method because the enthalpies and entropies of formation are obtained indirectly.

In our presentation of the thermodynamic data, we have preferred to quote the values of the enthalpies of formation instead of the values of the Gibbs energies of formation because the latter data vary with temperature. The variation of the enthalpy of formation with temperature is relatively small and thus values of enthalpies of formation are more easily compared from one system to another.

1.3. *Presentation of the information*

1.3.1. *Phase diagrams*

The information concerning the phase diagrams has been presented for each element studied in the form of a figure consisting of squares, each of which contains data for a rare-earth or an actinide element. The square contains the principal features of the phase diagram using the following abbreviations:

?: phase diagram is unknown
no C: no intermetallic compound in the phase diagram
xC, C: number of congruent melting intermetallic compounds
xC, P: number of intermetallic compounds with peritectic decomposition
?C: number of intermetallic compounds unknown
C?: no information concerning the fusion of the intermetallic compounds
liq.m.g.: miscibility gap in the liquid alloy
sol.m.g.: miscibility gap in the solid alloy
sol sol'n: complete solid solution
ex sol sol'n: extended solid solution
E: eutectic
P: peritectic

The stoichiometry and the melting temperature of the compound possessing the highest congruent melting temperature are also indicated.

1.3.2. *Structures of the intermetallic compounds*

The information concerning the structures of the compounds are displayed in figures, where one finds on the left the stoichiometry of the compound and on the right the prototype of the structure. When no prototype is defined in the *Pearson Handbook of Crystallographic data for intermetallic phases*, an example of the structure is given in parenthesis. In a separate table the crystallographic characteristics of the prototype or of the 'example' are given (Pearson symbol, space group, Strukturbericht designation). When allotropic forms exist, they are indicated using the abbreviations: RT (room temperature), LT (low temperature), HT (high temperature), HP (high pressure).

1.3.3. *Thermodynamic data*

The thermodynamic data of the compounds are presented in tables, the first column indicating the considered system, the second one the stoichiometry of the compounds. In the third and the fourth columns the values of the enthalpies and entropies of formation are reported

The fifth column reports the reference state of the values reported in columns 3 and 4, as well as the temperature, when known; the aggregation state of the pure components is indicated as follows:

X_l, element X is liquid; X_s, element X is solid; α-X: element X is solid in structure α.

The last column lists the reference and the method used to obtain the values of the enthalpies and entropies of formation are given. The method is indicated by an abbreviation as follows:

emf: electromotive force measurement. The aggregation state of the electrolyte is specified as either liquid (liq.) or solid (sol.) electrolyte; the temperature investigated is given when possible.

react.calorim.: reaction calorimetry

sol'n calorim: solution calorimetry; the nature of the solvent is specified: liquid aluminum (Al), liquid tin (Sn), or acid; the temperature of the solvent is given.

solute+solvent drop calorim: solute+solvent drop calorimetry

mixing and drop calorim.: mixing and drop calorimetry

vap.press.: vapor pressure measurement; different methods may be used (Knudsen effusion, with eventually mass spectrometry, dew-point)

diff.therm.anal.: differential thermal analysis

dyn.diff.calorim: dynamic differential calorimetry

phase diag.optimization: phase diagram optimization

We have reported in all cases the values as published, and where necessary we list on the second line the values taking as reference state the pure solid elements. When an element possesses allotropic forms we have referred the enthalpy of the formation to the aggregation state at room temperature.

In some cases only the values of the Gibbs energies of formation have been reported because the experiments have been performed at a single temperature.

The change of the reference state has been made assuming that the enthalpies and entropies of fusion or of allotropic transformation do not vary with temperature. These values have been taken from Hultgren et al. (1973b) for the rare earths and from Oetting et al. (1976) for the actinides. This choice was motivated by the fact that many authors have used these values to calculate the changes of the reference state (see for example Chiotti et al. 1981).

We must remark that the reference state of some experimental data was not explicitly stated by the authors; in these cases we have assumed that the reference state was the pure elements in the considered temperature range. However, it was sometimes impossible to

define it clearly when a transition (fusion or allotropic transformation) of one component occurred in temperature range considered.

The thermodynamic data of the liquid alloys are also presented in tables. When gathering the information for this review, we had first compiled all the data obtained in the liquid phase. Considering the results of this compilation, i.e. large differences between values, we have decided to keep only the results obtained by mixing or solution calorimetry. The second column of the table gives the partial enthalpy of mixing of the rare earth or of the actinide at infinite dilution in the considered metal; the third column gives the enthalpy of mixing at 0.5 composition or for a composition as indicated, the fourth column gives the partial enthalpy at infinite dilution of the considered element in the rare earth or actinide.

The reference state of the values is the pure element in the liquid state. In most cases recalculation of the as-published data appeared necessary; however, this requires knowledge of the enthalpy of fusion and eventually the enthalpy of allotropic transformation of the element. In recalculation we assumed that these values do not vary with temperature.

1.4. *A first look at the alloying behavior of rare earths and actinides*

In figs. 1–7 we report the principal features of the La, Gd, Y, Sc, Th, U and Pu phase diagrams with metallic elements. The elements La and Gd have been chosen because they represent the first elements of the heavy and the light lanthanide series, respectively. We must state that europium and ytterbium are excluded from the present analysis because they are divalent. When these are alloyed the valence may change when the content of the other component increases. This behavior will be analyzed below.

A first look at figs. 1–7 indicates that rare earths and actinides behave like early transition metals. When alloyed with elements of columns IB to VB the phase diagrams exhibit many intermetallic compounds. The exceptions are of interest: uranium possesses a miscibility gap in the liquid state when alloyed with Cu, Ag, Au, Zn, Cd, Pb and Bi even if intermetallic compounds are found in the solid state (except in the Ag–U system); plutonium also has a miscibility gap in the liquid state when alloyed with Ag and Cd.

When alloyed with late transition metals the rare earths and actinides have a similar behavior. With Mn, Re and Fe, lanthanum behaves differently: no intermetallic compound is formed with these elements, and a miscibility gap in the liquid state is observed with Mn and Re. Rare earths and actinides behave differently when alloyed with early transition metals. Miscibility gaps are observed with rare earths while the actinides and these elements are totally miscible in the liquid state.

The intra-rare-earth phase diagrams often exhibit total miscibility in the liquid state and in the solid state (except for Eu and Yb). A miscibility gap in the liquid state is present when uranium is alloyed with thorium. The analysis of the phase diagrams of actinides with rare earths shows a particular behavior of uranium and, to a lesser extent, of plutonium. All phase diagrams of uranium alloyed with rare earths have a miscibility gap in the liquid state. This is also observed with plutonium; however, with the elements

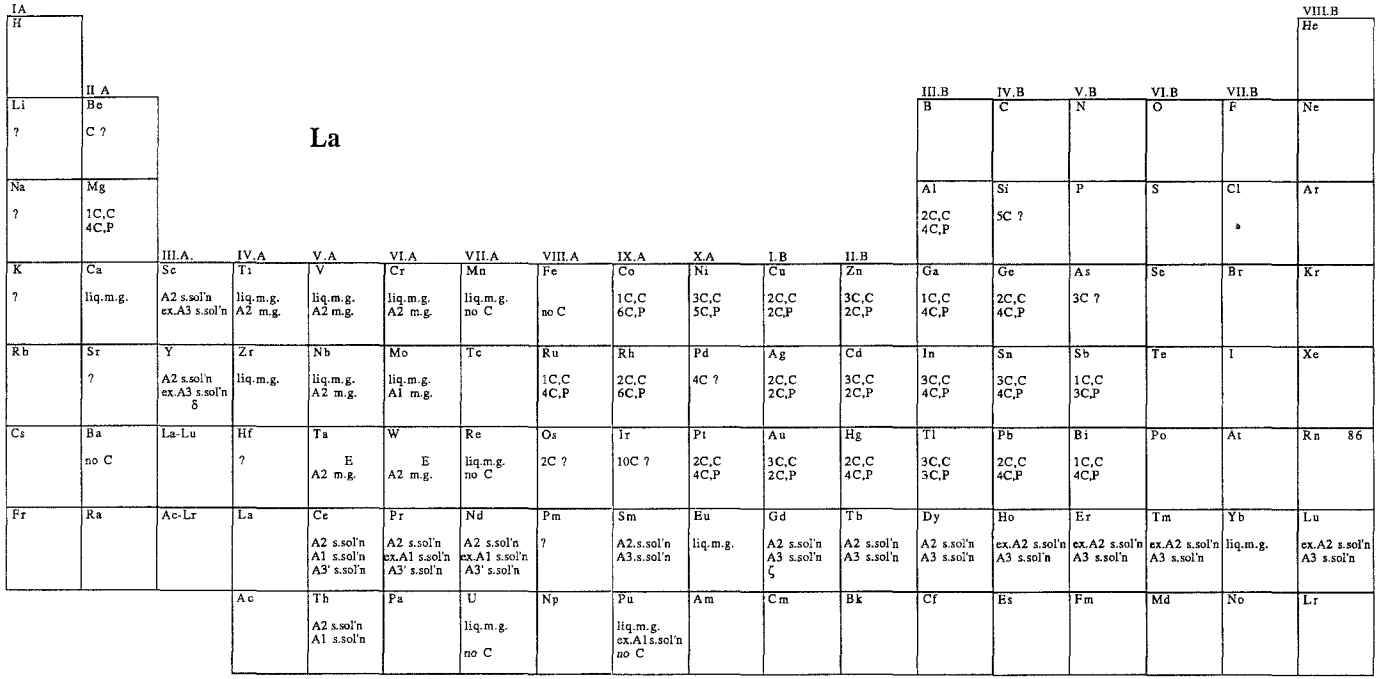

Fig. 1. Main features of the phase diagrams of lanthanum with metallic elements.

IA	II A	III.A.	IV.A	V.A	VI.A	VII.A	VIII.A	IX.A	XA	I.B	II.B	III.B	IV.B	V.B	VI.B	VII.B	VIII.B
H																	He
Li ?	Be ? C		**Gd**									B	C	N	O	F	Ne
Na ?	Mg 4C,P											Al 1C,C 4C,P	Si 4C,C 1C,P ?	P	S	Cl	Ar
K ?	Ca liq.m.g.	Sc A2 s.sol'n A3 s.sol'n	Ti liq.m.g. A2 m.g. A3 m.g.	V liq.m.g. A2 m.g.	Cr liq.m.g.	Mn 3C,P	Fe 4C,P	Co 1C,C 7C,P	Ni 2C,C 7C,P	Cu 3C,C 4C,P	Zn 8C ?	Ga 1C,C 4C,P	Ge 1C,C 4C,P	As 1C ?	Se	Br	Kr
Rb	Sr ?	Y A2 s.sol'n A3 s.sol'n	Zr E A2 m.g. A3 m.g.	Nb liq.m.g.	Mo liq.m.g. A2 m.g.	Tc	Ru 2C,C 2C,P	Rh 3C,C 6C,P	Pd 3C,C 4C,P	Ag 2C,C 1C,P	Cd 1C,C 5C,P	In 4C,C 1C,P	Sn 2C,C 8C,P	Sb 1C,C 3C,P	Te	I	Xe
Cs	Ba no C	La-Lu	Hf ?	Ta E A2 m.g.	W E A2 m.g.	Re 1C,P	Os 2C ?	Ir 1C,C ? 5C,P	Pt 2C,C ? 6C,P	Au 3C,C 3C,P	Hg 2C,C 2C,P	Tl 3C,C 3C,P	Pb 1C,C 5C,P	Bi 1C,C 2C,P	Po	At	Rn 86
Fr	Ra	Ac-Lr	La A2 s.sol'n A3' s.sol'n ζ	Ce A2 s.sol'n A3 s.sol'n ζ	Pr ?	Nd A2 s.sol'n A3 s.sol'n	Pm	Sm A2 s.sol'n A3 s.sol'n	Eu ?	Gd	Tb A2 s.sol'n A3 s.sol'n	Dy A2 s.sol'n A3 s.sol'n	Ho ex.A2 s.sol'n A3 s.sol'n	Er ex.A2 s.sol'n A3 s.sol'n	Tm ?	Yb liq.m.g.	Lu ?
			Ac	Th A2 s.sol'n	Pa	U liq.m.g.	Np	Pu liq.m.g.	Am	Cm	Bk	Cf	Es	Fm	Md	No	Lr

Fig. 2. Main features of the phase diagrams of gadolinium with metallic elements.

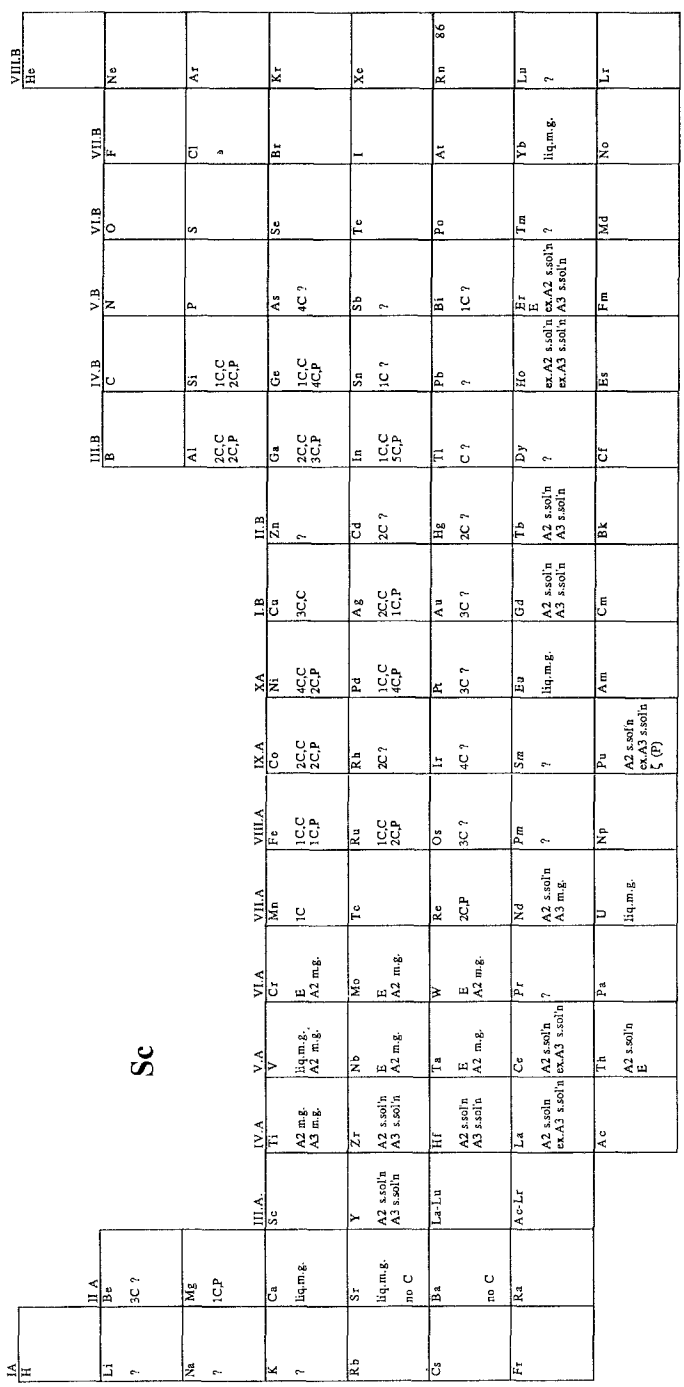

Fig. 3. Main features of the phase diagrams of scandium with metallic elements.

IA	II A	III.A.	IV.A	V.A	VI.A	VII.A	VIII.A	IX.A	XA	I.B	II.B	III.B	IV.B	V.B	VI.B	VII.B	VIII.B
H																	He
Li ?	Be 1C,C					**Y**						B	C	N	O	F	Ne
Na ?	Mg 3C,P											Al 2C,C 3C,P	Si 2C,C 3C,P	P	S	Cl	Ar
K ?	Ca liq.m.g.	Sc A2 s.sol'n A3 s.sol'n	Ti liq.m.g. A2 m.g. A3 m.g.	V liq.m.g. A2 m.g.	Cr E	Mn 2C,C 1C,P	Fe 3C,C 1C,P	Co 2C,C 9C,P	Ni 2C,C 7C,P	Cu 3C,C 2C,P	Zn 3C,C 5C,P	Ga 2C,C 2C,P	Ge 1C,C 7C,P	As 1C ?	Se	Br	Kr
Rb	Sr liq.m.g. no C	Y	Zr E A2 m.g. A3 m.g.	Nb liq.m.g.	Mo E	Tc	Ru 2C,C 3C,P	Rh 3C,C 5C,P	Pd 3C,C 6C,P	Ag 3C,C	Cd 1C,C 5C,P	In 3C,C 2C,P	Sn 1C,C 4C,P	Sb 1C,C 2C,P	Te	I	Xe
Cs	Ba liq.m.g. no C	La-Lu	Hf E A3 m.g.	Ta liq.m.g. A2 m.g.	W E A2 m.g.	Re 1C,P	Os 1C,C 1C,P	Ir 2C,C 5C,P	Pt 2C,C ? 8C,P	Au 3C ?	Hg 2C,C 2C,P	Tl 4C ?	Pb 1C,C 3C,P	Bi 1C,C 1C,P	Po	At	Rn 86
Fr	Ra	Ac-Lr	La A2 s.sol'n A3 s.sol'n δ	Ce A2 s.sol'n A3 s.sol'n δ	Pr A2 s.sol'n A3 s.sol'n δ	Nd A2 s.sol'n A3 s.sol'n	Pm	Sm A2 s.sol'n A3 s.sol'n	Eu liq.m.g.	Gd A2 s.sol'n A3 s.sol'n	Tb A2 s.sol'n A3 s.sol'n	Dy A2 s.sol'n A3 s.sol'n	Ho ex.A2 s.sol'n A3 s.sol'n	Er ex.A2 s.sol'n A3 s.sol'n	Tm A3 s.sol'n	Yb liq.m.g.	Lu A3 s.sol'n
			Ac	Th A2 s.sol'n	Pa	U liq.m.g.	Np	Pu ex.A3 s.sol'n	Am	Cm	Bk	Cf	Es	Fm	Md	No	Lr

Fig. 4. Main features of the phase diagrams of yttrium with metallic elements.

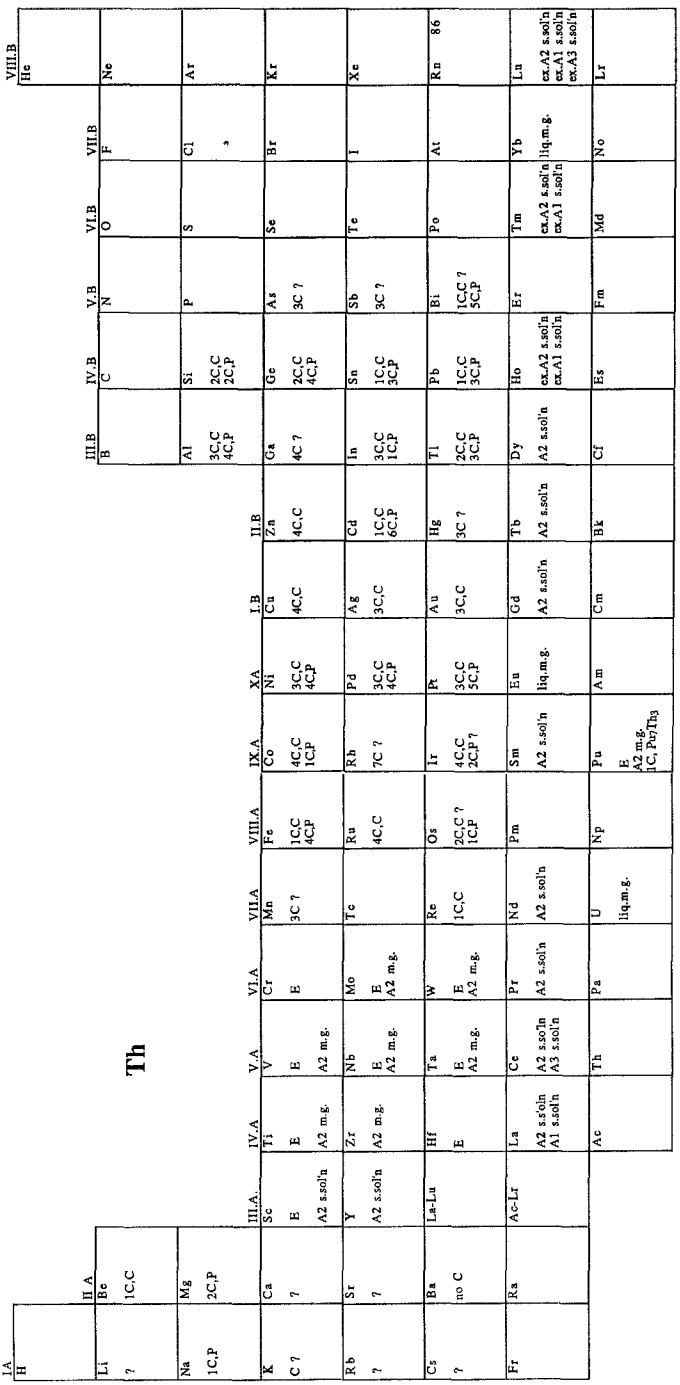

Fig. 5. Main features of the phase diagrams of thorium with metallic elements.

1A	II A	III.A.	IV.A	V.A	VI.A	VII.A	VIII.A	IX.A	X.A	I.B	II.B	III.B	IV.B	V.B	VI.B	VII.B	VIII.B
H																	He
Li liq.m.g.	Be liq.m.g. 1C,C											B	C	N	O	F	Ne
Na liq.m.g.	Mg liq.m.g. no C											Al 1C,C 2C,P	Si 2C,C 4C,P	P	S	Cl	Ar
K C ? ?	Ca ? no C	Sc liq.m.g. no C	Ti A2 s.sol'n 1C	V E A2 m.g.	Cr E A2 m.g.	Mn 1C,C 1C,P	Fe 1C,C 1C,P	Co 3C,C 3C,P	Ni 1C,C 6C,P	Cu liq.m.g. 1C,P	Zn liq.m.g. 1C,C 1C,P	Ga 1C,C 2C,P	Ge 3C,C 4C,P	As 3C ?	Se	Br	Kr
Rb	Sr ? no C	Y liq.m.g. no C	Zr A2 s.sol'n A2 m.g.	Nb A2 s.sol'n A2 m.g.	Mo P Al m.g. 1C,MoU_2	Tc	Ru 1C,C 4C,P	Rh 1C,C 3C,P	Pd 1C,C 6C,P	Ag liq.m.g. no C	Cd liq.m.g. 1C,P	In 1C ?	Sn 1C,C 2C,P	Sb 2C,C 2C,P	Te	I	Xe
Cs ?	Ba ?	La-Lu	Hf m.g.A2	Ta E A2 m.g.	W E A2 m.g.	Re 1C,C 1C,P	Os 2C,C 2C,P	Ir 2C,C 3C,P	Pt 1C,C 3C,P	Au liq.m.g. 2C,C	Hg 4C ?	Tl 1C ?	Pb liq.m.g. 1C,C 1C,P	Bi liq.m.g. 3C,P	Po	At	Rn 86
Fr	Ra	Ac-Lr	La liq.m.g. no C	Ce liq.m.g. no C	Pr liq.m.g. no C	Nd liq.m.g. no C	Pm	Sm liq.m.g. no C	Eu liq.m.g. no C	Gd liq.m.g. no C	Tb liq.m.g. no C	Dy liq.m.g. no C	Ho liq.m.g. no C	Er ?	Tm liq.m.g. no C	Yb liq.m.g. no C	Lu liq.m.g. no C
			Ac	Th liq.m.g. no C	Pa	U	Np	Pu A2 s.sol'n	Am	Cm	Bk	Cf	Es	Fm	Md	No	Lr

U

Fig. 6. Main features of the phase diagrams of uranium with metallic elements.

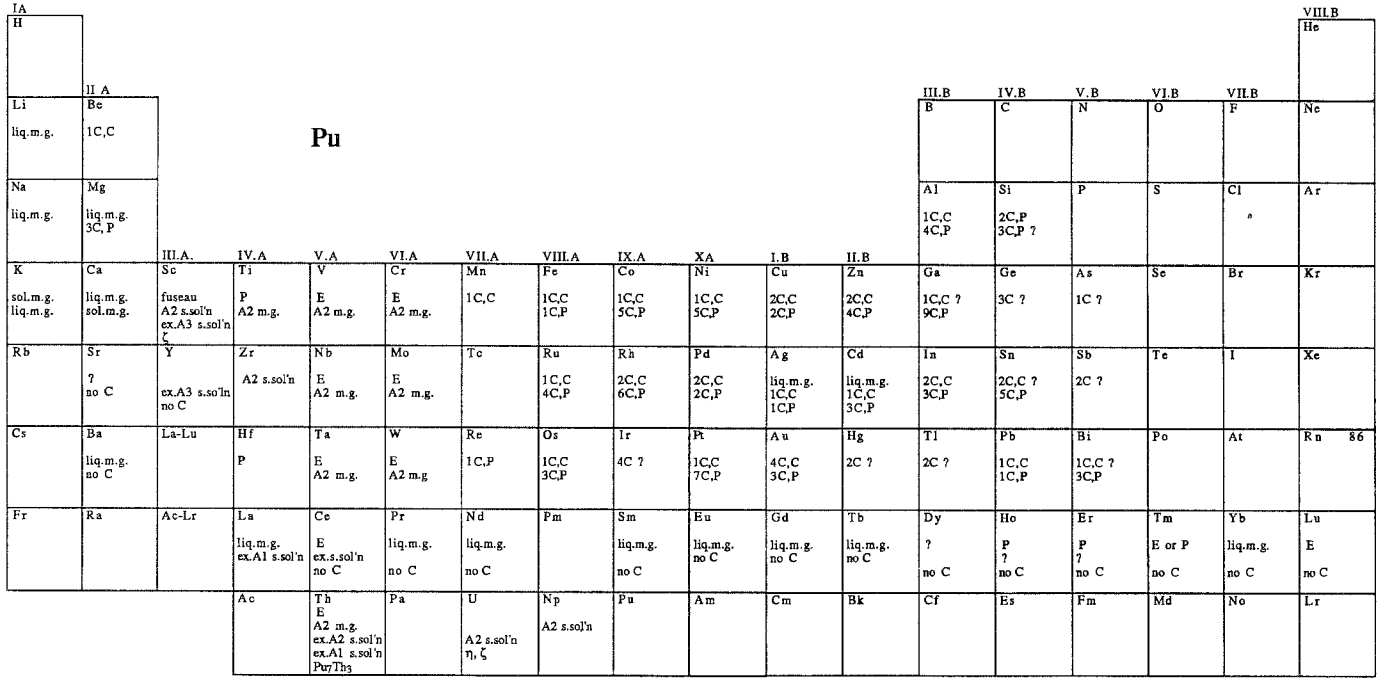

Fig. 7. Main features of the phase diagrams of plutonium with metallic elements.

at the end of the lanthanide series, Ho to Lu (except Yb) and with Sc and Y, plutonium exhibits complete solubility in the liquid state.

Many phase diagrams of elements of columns IA and IIA are unknown and it is difficult to draw similarities and differences. It seems, however, that uranium and plutonium have a different behavior from that of thorium.

To conclude this preliminary look we may state that the behavior of cerium is very similar to that of lanthanum and no possible particular behavior may be discerned using the shapes of the phase diagrams as a guide.

Considering the relative similarities between the behavior of lanthanides and actinides and that of elements from the same column of the Periodic Table we organize our study accordingly.

2. Rare earths and actinides with elements of columns IA and IIA

2.1. *Rare earths and actinides with elements of column IA*

Very little is known about the phase diagrams of rare earths and actinides with elements of column IA. It seems that these binary systems do not form any intermetallic compounds except for the Th–Na, Th–K and U–K systems where the existence of one compound is noted. A miscibility gap in the liquid phase is reported in the U–Li, Pu–Li, U–Na, Pu–Na, Pu–K and Pr–Cs phase diagrams.

No information is currently available concerning thermodynamic data in these binary alloys.

2.2. *Rare earths and actinides with elements of column IIA*

2.2.1. *Phase diagrams and intermetallic compounds*

The main features of the binary phase diagrams of elements of column IIA and rare earths or actinides are reported in figs. 8–12. The formation of intermetallic compounds is observed with beryllium and magnesium. The stoichiometry and the structures of the compounds are reported in figs. 13 and 14 for Be and Mg respectively. Table 1 lists the characteristics of the observed structures.

In the case of beryllium, the phase diagrams contain at least one intermetallic compound which has the same stoichiometry (RBe_{13} and $AnBe_{13}$) and the same structure (prototype $NaZn_{13}$). In the Sc–Be system other intermetallic compounds have been detected.

In the case of magnesium, many intermetallic compounds are observed with rare earths, thorium and plutonium; they are all at the Mg-rich side of the phase diagram. The intermetallic compounds possessing the highest melting temperature have the stoichiometry RMg_3 for the first four elements of the lanthanide series, and the stoichiometry RMg for MgSm and GdMg compounds. The intermetallic compound $ThMg_2$ has the same structure (Cu_2Mg) at high temperature as the compounds RMg_2

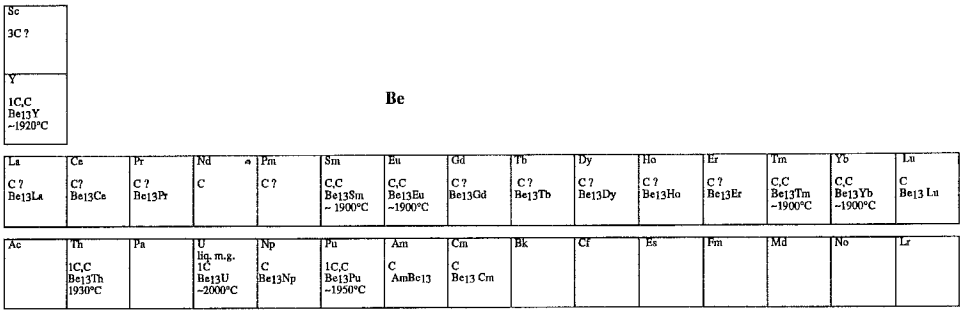

Fig. 8. Main features of the phase diagrams of beryllium with rare earths and actinides.

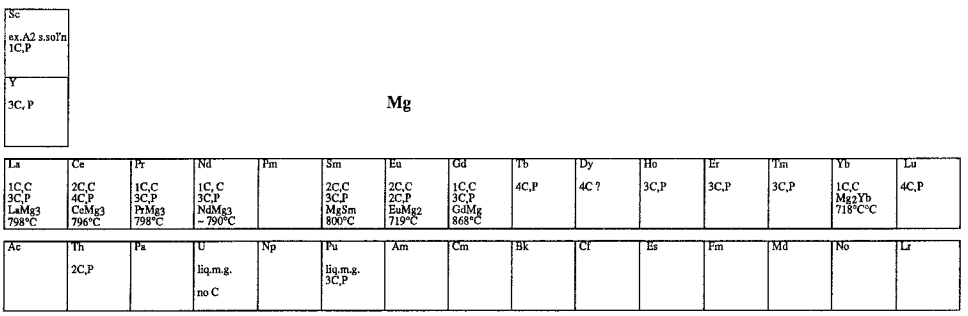

Fig. 9. Main features of the phase diagrams of magnesium with rare earths and actinides.

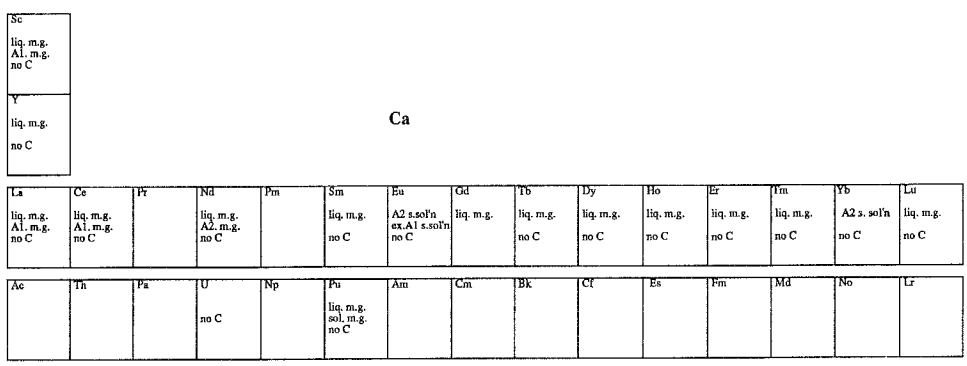

Fig. 10. Main features of the phase diagrams of calcium with rare earths and actinides.

with R = La–Sm. With uranium and plutonium the phase diagrams exhibit a miscibility gap in the liquid phase.

Recently, investigations in Mg–Sm, Mg–Dy and Mg–Er systems have been performed by Saccone et al. (1989a, 1991, 1992). We may also indicate the assessments of some

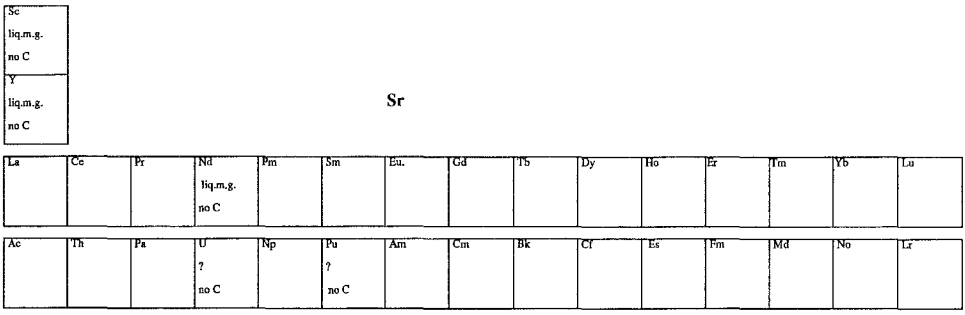

Fig. 11. Main features of the phase diagrams of strontium with rare earths and actinides.

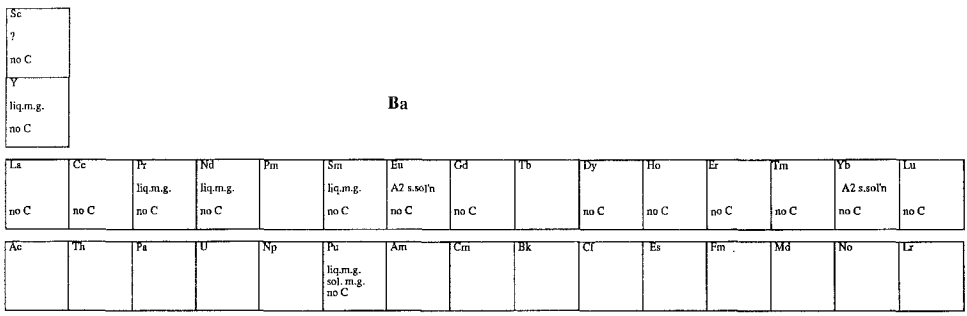

Fig. 12. Main features of the phase diagrams of barium with rare earths and actinides.

Phase	Sc	Y	La	Ce	Pr	Nd	Pm	Sm	Eu	Gd	Tb	Dy	Ho	Er	Tm	Yb	Lu	Ac	Th	Pa	U	Np	Pu	Prototype or
MBe_5 83.3%	x																							$CaCu_5$
M_2Be_{17} 89.5%	x •?																							$Ni_{17}Th_2$ x Th_2Zn_{17} •
MBe_{13} 92.9%	x	x	x	x	x	x?		x	x	x	x	x	x	x	x	x	x		x		x	x	x	$NaZn_{13}$ x
Be composition	Sc	Y	La	Ce	Pr	Nd	Pm	Sm	Eu	Gd	Tb	Dy	Ho	Er	Tm	Yb	Lu	Ac	Th	Pa	U	Np	Pu	example ()

Fig. 13. Stoichiometry and structure prototype (or example) of the intermetallic compounds of Be with rare earths and actinides (M = R or An).

phase diagrams presented by Nayeb-Hashemi and Clark (1984, 1986, 1988a–c, 1989): Mg–Th (1984), Mg–Sc (1986), Ce–Mg (1988a), La–Mg (1988b), Mg–Nd (1988c), Mg–Pr (1989) and by Axler et al. (1989) for the Mg–Pu system. Updated Mg–Nd, Eu–Mg and Mg–Y phase diagrams have been published by Okamoto (1991a, 1992a,b).

The phase diagrams of calcium, strontium and barium with rare earths and actinides generally exhibit miscibility gaps in the liquid phase. It is important to point out the exceptions to this common behavior: the phase diagrams of Eu and Yb, respectively,

Phase	Sc	Y	La	Ce	Pr	Nd	Pm	Sm	Eu	Gd	Tb	Dy	Ho	Er	Tm	Yb	Lu	Ac	Th	Pa	U	Np	Pu	Prototype or
MMg 50%	x	x	x	x	x	x		x	x			x	x	x	x		x							ClCs x
MMg_2 33.3%			x	x	x	x		x	•			•	•	•	•	•	•		xHT +HT			?		Cu_2Mg x $MgZn_2$ • $MgNi_2$ +
MMg_3 25%			x	x	x	x		x				x												BiF_3
M_6Mg_{23} 20.7%																			x					$Mn_{23}Th_6$ x
MMg_4 20%																						x		(Mg_4Pu) x
M_5Mg_{24} 17.2%		x										x	x	x	x		x							αMn x
MMg_5 16.7%								x	•															(Mg_5Sm) x $ErZn_5$ •
MMg_6 14.3%																						x		(Mg_6Pu)
M_5Mg_{41} 10.9%				x	x	x		x																$Mg_{41}Ce_5$ x
M_2Mg_{17} 10.5%			x						x															$Ni_{17}Th_2$ x
$MMg_{10.3}$ 8.85%				x																				$Ni_{17}Th_2$ x
MMg_{12} 7.7%			x	x •	•	•																		$Mg_{12}Ce$ x $Mn_{12}Th$ •
Mg composition	Sc	Y	La	Ce	Pr	Nd	Pm	Sm	Eu	Gd	Tb	Dy	Ho	Er	Tm	Yb	Lu	Ac	Th	Pa	U	Np	Pu	example ( )

Fig. 14. Stoichiometry and structure prototype (or example) of the intermetallic compounds of Mg with rare earths and actinides (M = R or An).

Table 1
Structure characteristics of X = Mg or Be and rare earth or actinide (M = R, An) intermetallic compounds

Phase	Pearson symbol	Space group	Strukturbericht designation	Prototype or (example)
MX_{13}	cF112	$Fm\bar{3}c$	$D2_3$	$NaZn_{13}$
MX_{12}	tI26	I4/mmm	$D2_b$	$Mn_{12}Th$
	oI338	Immm		$(CeMg_{12}$-II)
$MX_{10.3}$	hP38	$P6_3/mmc$		$Ni_{17}Th_2$
M_2X_{17}	hP38	$P6_3/mmc$		$Ni_{17}Th_2$
	hR19	R3m		Th_2Zn_{17}
M_5X_{41}	tI92	I4/m		Ce_5Mg_{41}
MX_6	cF*			(Mg_6Pu)
MX_5	cF440–448	$F\bar{4}3m$		(Mg_5Sm)
	hP36	$P6_3/mmc$		$ErZn_5$
	hP6	P6/mmm	$D2_d$	$CaCu_5$
M_5X_{24}	cI58	$I\bar{4}3m$	A12	αMn
MX_4	hP*			(Mg_4Pu)
M_6X_{23}	cF116	$Fm\bar{3}m$	$D8_a$	$Mn_{23}Th_6$
MX_3	cF16	$Fm\bar{3}m$	DO_3	BiF_3
MX_2	cF24	$Fd\bar{3}m$	C15	Cu_2Mg
	hP12	$P6_3/mmc$	C14	$MgZn_2$
	hP24	$P6_3/mmc$	C36	$MgNi_2$
MX	cP2	$Pm\bar{3}m$	B2	ClCs

with Ca and Ba exhibit complete solubility in the solid and liquid states. This behavior is explained by the fact that pure Eu and Yb are divalent and behave similarly to Ca and Ba when they maintain their divalency in the alloy for all compositions. Assessments of the binary calcium– and barium–rare-earth systems have been performed by Gschneidner and Calderwood (1987, 1988a). Updated Ba–Eu and Ba–Yb phase diagrams have been published by Okamoto (1991b,c). An attempt to evaluate the thermodynamic data of the Ba–Y system has been done by Mey et al. (1990).

2.2.2. *Thermodynamic data of the binary alloys*

The thermodynamic data of the RBe_{13} and $AnBe_{13}$ compounds are reported in table 2. The enthalpies of formation of these compounds are presented in fig. 15 as a function of the atomic number of the rare-earth element or of the actinide. The values obtained by Ivanov and Tumbakov (1959) and Pyatkov et al. (1971) for the enthalpy of formation of UBe_{13} intermetallic compound are rather different. The values given for $LaBe_{13}$ and $CeBe_{13}$ are partial Gibbs energy of Be in the compound. The only conclusion which can be drawn is that the enthalpies of formation of UBe_{13} and $PuBe_{13}$ are less exothermic than that of YBe_{13}.

The thermodynamic data of the compounds formed by magnesium alloyed with rare earths and thorium are reported in table 3. There appear to be serious discrepancies between the values of the Gibbs energies of formation of the RMg compounds obtained by Ogren et al. (1967) and later by Pahlman and Smith (1972) (fig. 16).

Table 2
Enthalpies and entropies of formation of intermetallic compounds of Be with rare earths and actinides ($\Delta_f H°$: kJ/mol of atoms, $\Delta_f S°$: $J\,K^{-1}$/mol of atoms)

System	Compound	$\Delta_f H°$	$\Delta_f S°$	Reference state	Authors and method
Y–Be	YBe_{13}	−16.2	(a)	α-Y, Be_s	Amonenko et al. 1964 vap. press. 1313–1563 K see Hultgren et al. 1973a
	YBe_{13}	−20.3		α-Y, Be_s; 298 K	Ivanov et al. 1980 acid sol'n calorim.
La–Be	$LaBe_{13}$	−12.8	(b)	Be_s	Amonenko et al. 1964 vap. press. 1355–1540 K; see Hultgren et al. 1973a
Ce–Be	$CeBe_{13}$	−8.0	(b)	Be_s	Amonenko et al. 1964 vap. press. 1193–1523 K see Hultgren et al. 1973a
U–Be	UBe_{13}	−11.7		α-U, Be_s; 298 K	Ivanov and Tumbakov 1959 acid sol'n calorim.
	UBe_{13}	−2.7	−1.1	α-U, Be_s; 973–1123 K	Pyatkov et al. 1971 emf liq. electrolyte 973–1123 K
Pu–Be	$PuBe_{13}$	−10.7		α-Pu, Be_s; 298 K	Akhachinskij and Kopytin 1960 acid sol'n calorim.

[a] $\Delta_f G°$, 1330 K. [b] $\overline{\Delta G}_{Be}$, 1400 K.

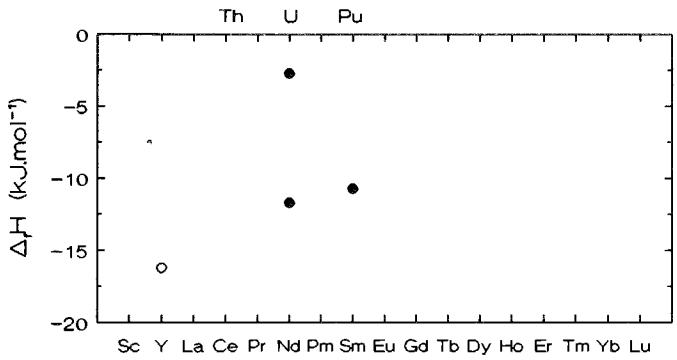

Fig. 15. Enthalpies of formation RBe_{13} and $AnBe_{13}$ intermetallic compounds as a function of atomic number (solid circles, actinides; open circle, rare earths). The references of the data are quoted in table 2.

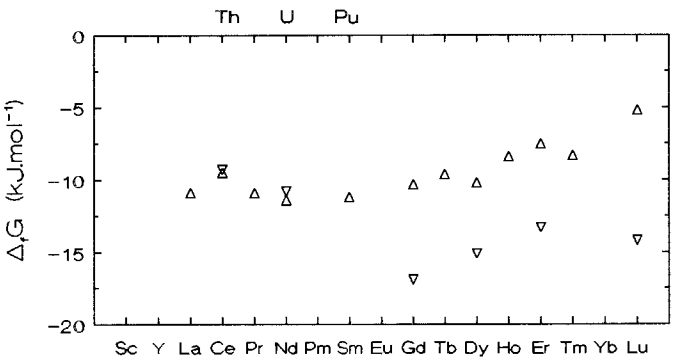

Fig. 16. Gibbs energies of formation of RMg intermetallic compounds as a function of atomic number. The data (open triangles, inverted open triangles) are from Ogren et al. (1967) and Pahlman and Smith (1972), respectively.

The enthalpies of formation of RMg_2 and $AnMg_2$ compounds are reported in fig. 17 as a function of the atomic number. It appears that the enthalpy of formation decreases from Ce to Lu. However when the Gibbs energies of formation of these compounds are analyzed, one observes a decrease from Ce to Gd and a slight increase from Gd to Lu. It seems that the values of the enthalpy and entropy of formation obtained by Pahlman and Smith (1972) in the Lu–Mg system are both too negative. For thorium two values of the enthalpy of formation are reported; the more-negative one is the value as published by Novotny and Smith (1963), the less-negative one was derived by Chiotti et al. (1981) after analysis of the compatibility of the data of Novotny and Smith (1963) and the shape of the phase diagram. The difference is of importance although the values of the Gibbs energy of

Table 3
Enthalpies and entropies of formation of intermetallic compounds of Mg with rare earths and actinides ($\Delta_f H°$: kJ/mol of atoms, $\Delta_f S°$: $J K^{-1}$/mol of atoms)

System	Compound	$\Delta_f H°$	$\Delta_f S°$	Reference state	Authors and method
Y–Mg	Y_5Mg_{24}	−7.4		α-Y, Mg_s; 298 K	Smith et al. 1965
	YMg_2	−14.2		(same)	acid sol'n calorim.
	YMg	−12.6		(same)	
	Y_5Mg_{24}	−8.5	−1.3	α-Y, Mg_s; 688–922 K	Smith et al. 1965
	YMg_2	−12.4	−1.3	(same)	vap. press. 688–922 K
	YMg	−11.6	+0.4	(same)	
	Y_4Mg_{24}	−7.9	−2.6	α-Y, Mg_s	Ran et al. 1988
	YMg_2	−18.2	−8.0	(same)	phase diag. optimization $\Delta_f H$ and
	YMg	−15.9	−5.3	(same)	$\Delta_f S$ supposed temperature independent
La–Mg	LaMg	−3.7	+9.2	β-La, Mg_s; 773 K	Ogren et al. 1967
		−3.5	9.5	α-La, Mg_s	vap. press. 675–910 K
	$LaMg_3$	−3.2		α-La, Mg_s; 298 K	Canneri and Rossi 1932
	LaMg	−2.4		(same)	acid sol'n calorim.
Ce–Mg	$CeMg_3$	−18.8		γ-Ce, Mg_s; 298 K	Biltz and Pieper 1924
	CeMg	−27.2		(same)	acid sol'n calorim.
	CeMg	−8.0	+1.9	γ-Ce, Mg_s; 773 K	Ogren et al. 1967
					vap. press. 675–910 K
	$CeMg_{12}$	−14.1	−7.5	γ-Ce, Mg_s; 773 K	Pahlman and Smith 1972
	Ce_5Mg_{41}	−18.1	−9.3	(same)	vap. press. 625–934 K
	$CeMg_3$	−18.9	−9.1	(same)	
	$CeMg_2$	−11.4	−1.4	(same)	
	CeMg	−13.1	−4.9	(same)	
	$CeMg_3$	−14.9		γ-Ce, Mg_s; 298 K	Nagarajan and Sommer 1988
					Mg sol'n calorim. 945 K
Pr–Mg	$PrMg_3$	−11.4		α-Pr, Mg_s; 298 K	Canneri and Rossi 1933
	PrMg	−17.2		(same)	acid sol'n calorim.
	PrMg	−12.7	−2.4	α-Pr, Mg_s; 773 K	Ogren et al. 1967
					vap. press. 675–910 K
	PrMg	−9.7		α-Pr, Mg_s; 773 K	Pahlman and Smith 1972
					revision of the results obtained by Ogren et al. 1967
Nd–Mg	NdMg	−9.9	+1.9	α-Nd, Mg_s; 773 K	Ogren et al. 1967
					vap. press. 675–910 K
	$NdMg_{12}$	−13.9	−4.8	α-Nd, Mg_s; 773 K	Pahlman and Smith 1972
	Nd_5Mg_{24}	−18.0	−5.9	(same)	vap. press. 636–934 K
	$NdMg_3$	−18.7	−5.1	(same)	
	$NdMg_2$	−18.7	−6.3	(same)	
	NdMg	−13.9	−4.0	(same)	
Sm–Mg	SmMg	−3.9	+9.4	α-Sm, Mg_s; 773 K	Ogren et al. 1967
					vap. press. 675–910 K
Eu–Mg	$EuMg_2$	−16.7	−4.0	Eu_s, Mg_s; 953–1003 K	Bayanov et al. 1975a
					vap. press. 953–1003 K

continued on next page

Table 3, *continued*

System	Compound	$\Delta_f H^o$	$\Delta_f S^o$	Reference state	Authors and method
Gd–Mg	GdMg	−7.3	−3.8	α-Gd, Mg_s; 773 K	Ogren et al. 1967 vap. press. 675–910 K
	$GdMg_{4.5}$	−17.0	−3.6	α-Gd, Mg_s; 773 K	Pahlman and Smith 1972
	$GdMg_3$	−19.2	−2.4	(same)	vap. press. 650–930 K
	$GdMg_2$	−19.7	−2.5	(same)	
	GdMg	−17.4	−0.6	(same)	
Tb–Mg	TbMg	−3.6	+7.7	α-Tb, Mg_s; 773 K	Ogren et al. 1967 vap. press. 695–910 K
Dy–Mg	Dy_5Mg_{24}	−13.7	−4.1	α-Dy, Mg_s; 773 K	Pahlman and Smith 1972
	$DyMg_3$	−16.1	−0.3	(same)	vap. press. 650–930 K
	$DyMg_2$	−16.3	−1.9	(same)	
	DyMg	−12.0	−2.3	(same)	
Ho–Mg	HoMg	−1.0	+9.6	α-Ho, Mg_s; 773 K	Ogren et al. 1967 vap. press. 695–910 K
Er–Mg	ErMg	−6.7	−1.0	Er_s, Mg_s; 773 K	Ogren et al. 1967 vap. press. 695–910 K
	Er_5Mg_{24}	−16.1	−9.5	Er_s, Mg_s; 773 K	Pahlman and Smith 1972
	$ErMg_2$	−22.0	−12.1	(same)	vap. press. 650–930 K
	ErMg	−21.3	−10.5	(same)	
Tm–Mg	TmMg	−4.2	−0.6	Tm_s, Mg_s; 773 K	Ogren et al. 1967 vap. press. 695–910 K
Lu–Mg	LuMg	−1.9	+4.6	Lu_s, Mg_s; 773 K	Ogren et al. 1967 vap. press. 695–910 K
	Lu_5Mg_{24}	−25.2	−22.6	Lu_s, Mg_s; 773 K	Pahlman and Smith 1972
	$LuMg_2$	−35.7	−30.8	(same)	vap. press. 650–930 K
	LuMg	−35.7	−27.8	(same)	
Th–Mg	$ThMg_2$	−19.9	−21.2	α-Th, Mg_s; 692–812 K α-Th, Mg_s	Novotny and Smith 1963 vap. press 692–812 K
	$ThMg_2$	−9.7	−7.6	α-Th, Mg_s	Chiotti et al. 1981 assessment

formation are quite similar. In fig. 18 the Gibbs energies of formation of the compounds obtained by Pahlman and Smith (1972) in the Ce–Mg, Gd–Mg and Lu–Mg systems are plotted as a function of composition at 773 K. The values become less asymmetrical with respect to equiatomic composition going from Ce to Lu. The Gibbs energy of formation of the $ThMg_2$ compound obtained by Novotny and Smith (1963) is less negative than the values obtained at the same composition of the rare earth elements.

To our best knowledge no thermodynamic data have been published for the systems formed with elements Ca, Sr and Ba. Except when Eu and Yb are involved, the presence of miscibility gap in the liquid phase indicates large positive deviations from ideality.

The only thermodynamic data obtained using a calorimetric method in liquid alloys have been proposed by Nagarajan and Sommer (1988) and concern the Ce–Mg system.

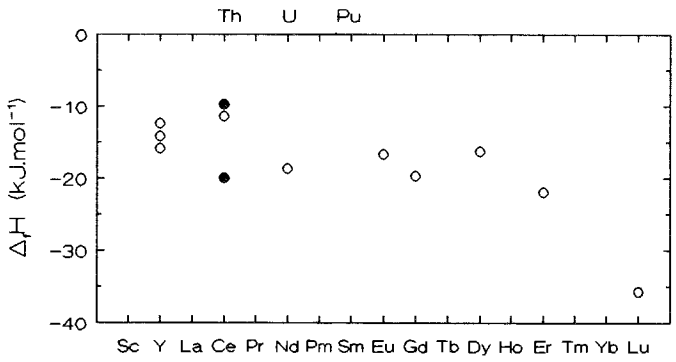

Fig. 17. Enthalpies of formation of RMg_2 and $ThMg_2$ intermetallic compounds as a function of atomic number (solid circle, actinides; open circle, rare earths). The references of the data are quoted in table 3.

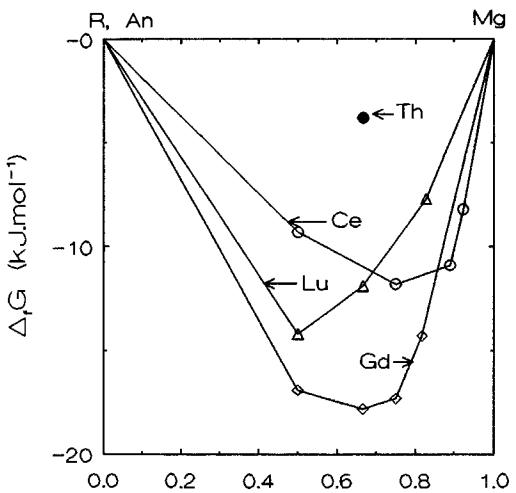

Fig. 18. Gibbs energies of formation of $R_{1-x}Mg_x$ intermetallic compounds: the data for M = Ce (open circles), Gd (slashed circles), Lu (triangles) are from Pahlman and Smith (1972). The data for the $MgTh_2$ (solid circles) intermetallic compound is from Novotny and Smith (1963).

3. Rare earths and actinides with transition metals

3.1. *Phase diagrams and intermetallic compounds*

The main features of the phase diagrams of transition metals with rare earths and actinides are presented in figs. 19–38.

One first notices the distinct behaviors of rare earths and actinides with early transition metals (columns of Ti, V and Cr) and with late transition metals (columns of Mn, Fe, Co and Ni):

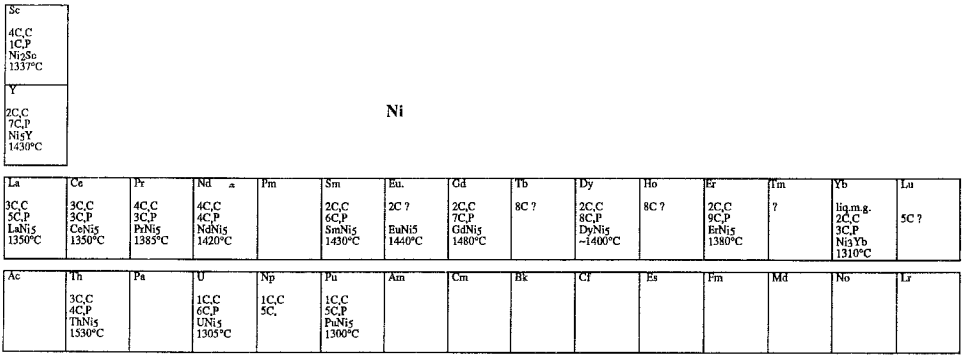

Fig. 19. Main features of the phase diagrams of nickel with rare earths and actinides.

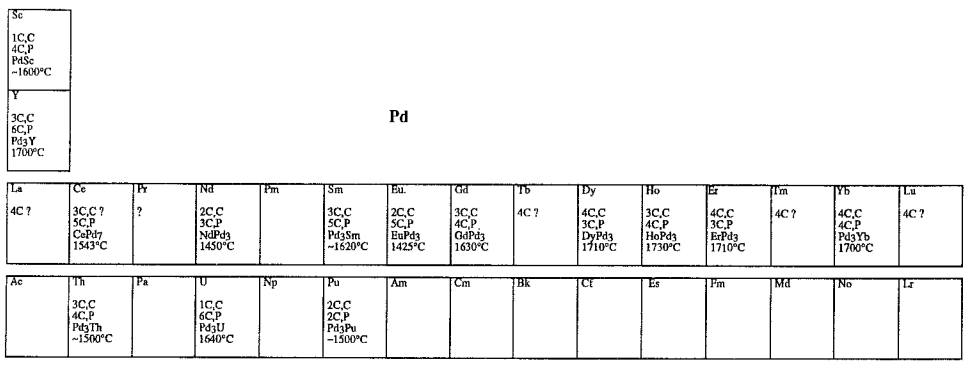

Fig. 20. Main features of the phase diagrams of palladium with rare earths and actinides.

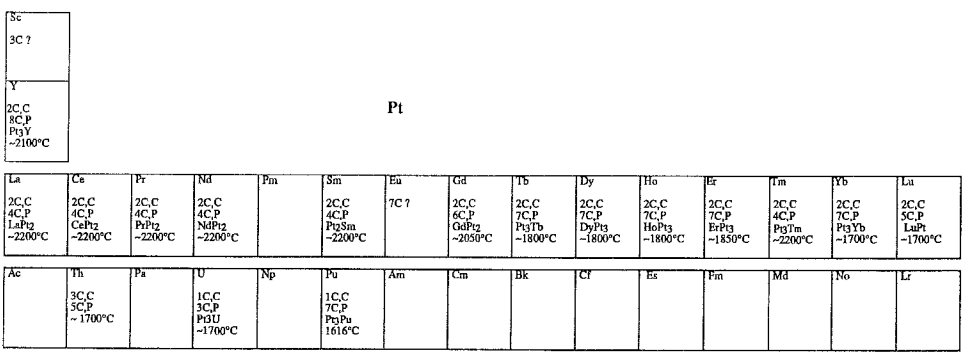

Fig. 21. Main features of the phase diagrams of platinum with rare earths and actinides.

(i) Many intermetallic compounds are observed between late transition metals and rare earths or actinides. However the number of compounds decreases in the same row, from Ni to Mn, from Pd to Tc, from Pt to Re.

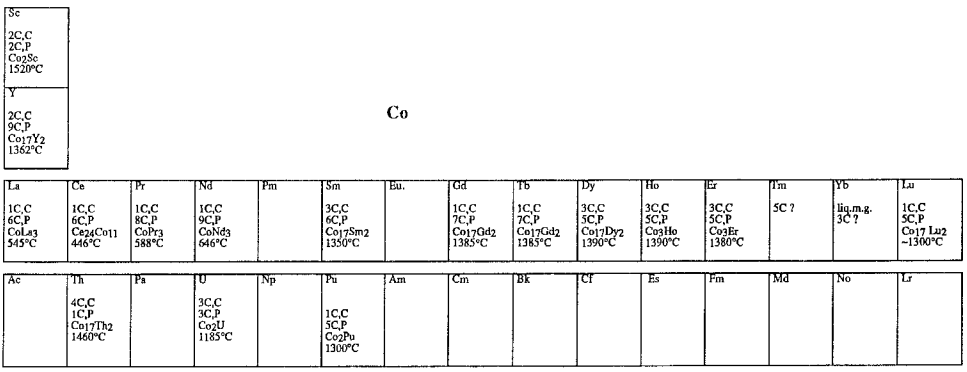

Fig. 22. Main features of the phase diagrams of cobalt with rare earths and actinides.

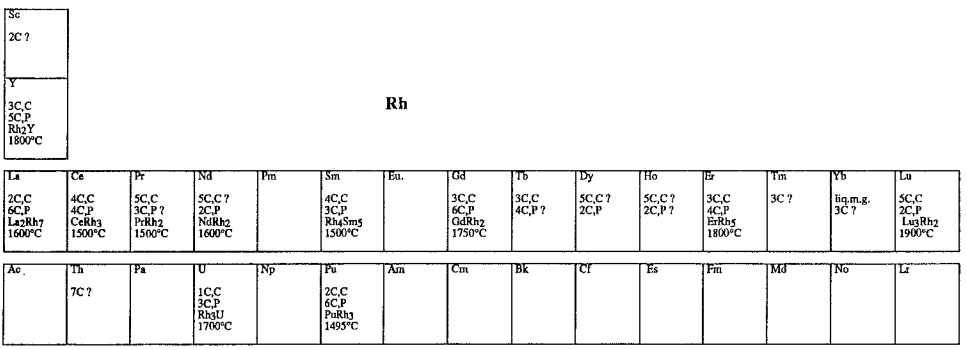

Fig. 23. Main features of the phase diagrams of rhodium with rare earths and actinides.

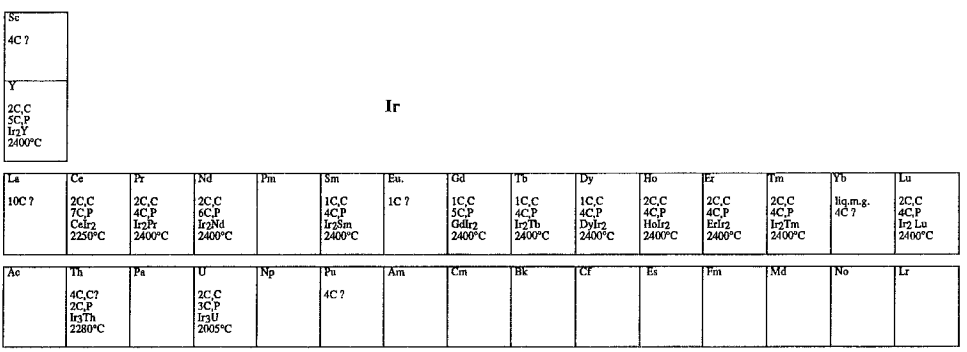

Fig. 24. Main features of the phase diagrams of iridium with rare earths and actinides.

(ii) On the contrary, no intermetallic compounds are observed in the binary phase diagrams of early transition metals with rare earths and actinides (exceptions: in the U–Mo and U–Zr binary phase diagrams). It is important, however, to notice the differences in behavior of rare earths and actinides. Most of the binary phase

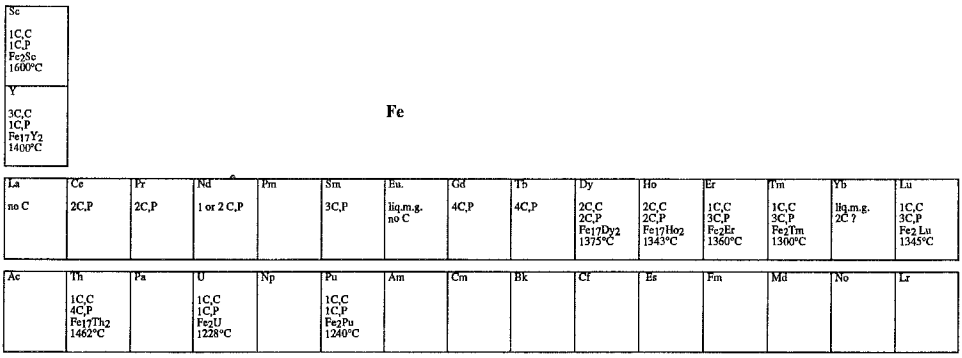

Fig. 25. Main features of the phase diagrams of iron with rare earths and actinides.

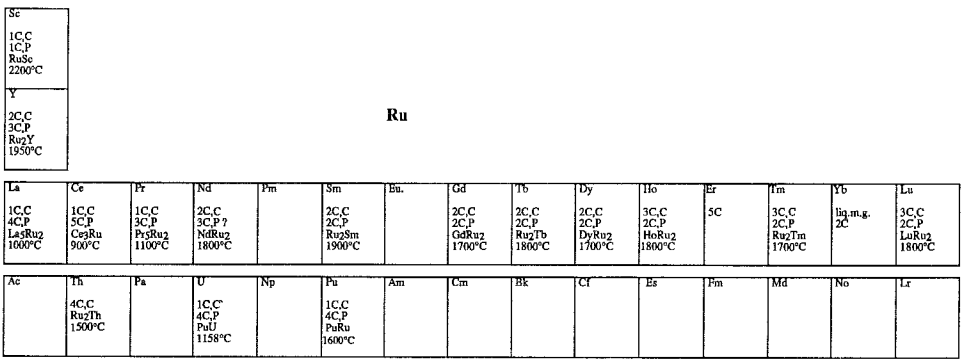

Fig. 26. Main features of the phase diagrams of ruthenium with rare earths and actinides.

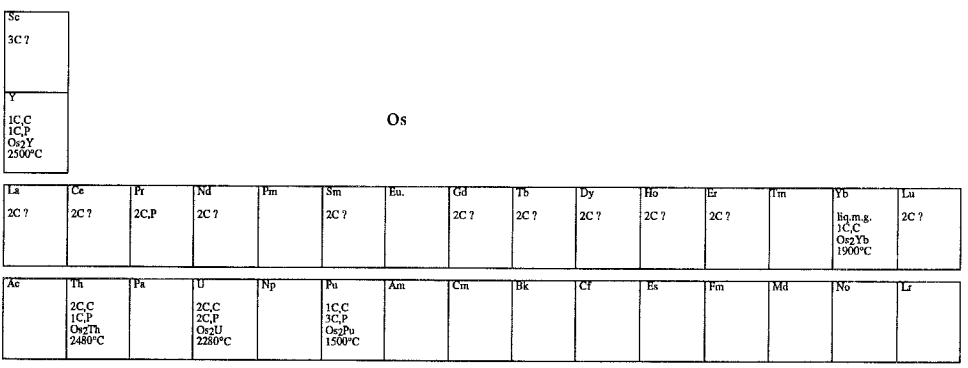

Fig. 27. Main features of the phase diagrams of osmium with rare earths and actinides.

diagrams of early transition metals and rare earths exhibit a miscibility gap in the liquid phase while early transition metals and actinides are completely miscible in the liquid state. The phase diagrams, when this occurs, often exhibit a simple

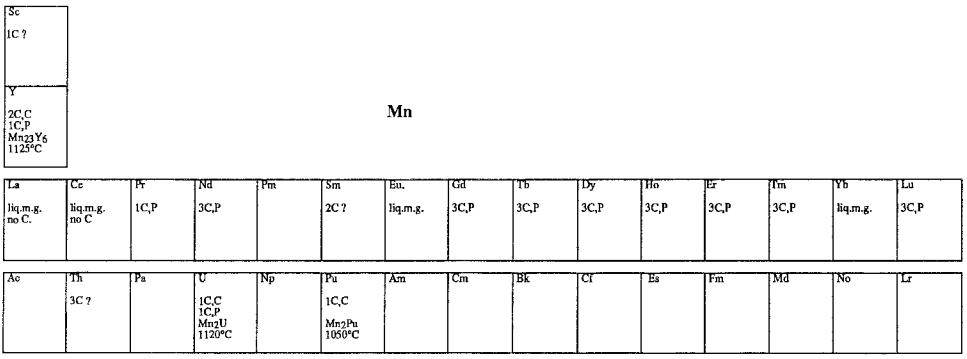

Fig. 28. Main features of the phase diagrams of manganese with rare earths and actinides.

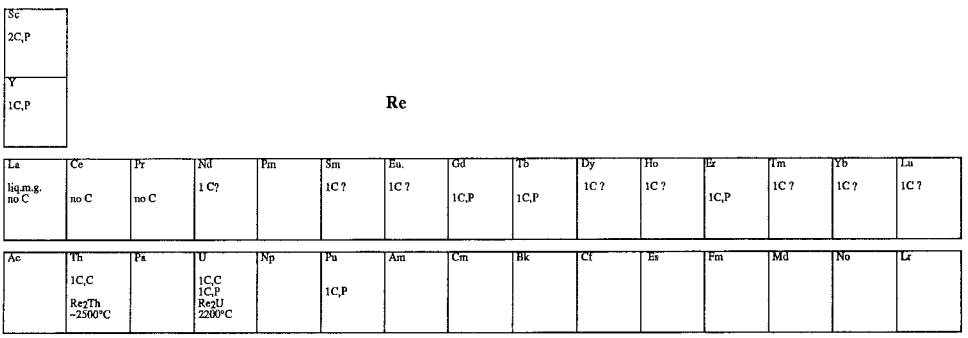

Fig. 29. Main features of the phase diagrams of rhenium with rare earths and actinides.

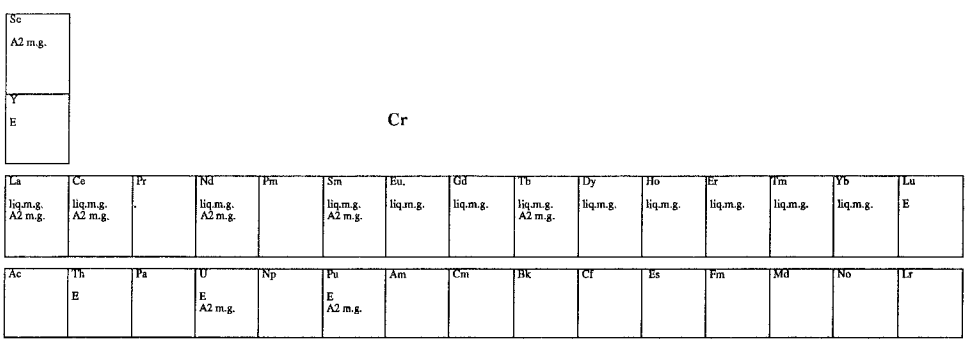

Fig. 30. Main features of the phase diagrams of chromium with rare earths and actinides.

eutectic between the liquid phase and the two solid solutions based on the pure components.

For elements of the columns headed by Fe and Mn different behaviors in the lanthanide series are clearly apparent. No intermetallic compounds are observed in the La–Fe phase diagram, while compounds are present with the other elements of the column, Ru and Os. With manganese no compounds and a miscibility gap in the liquid state are

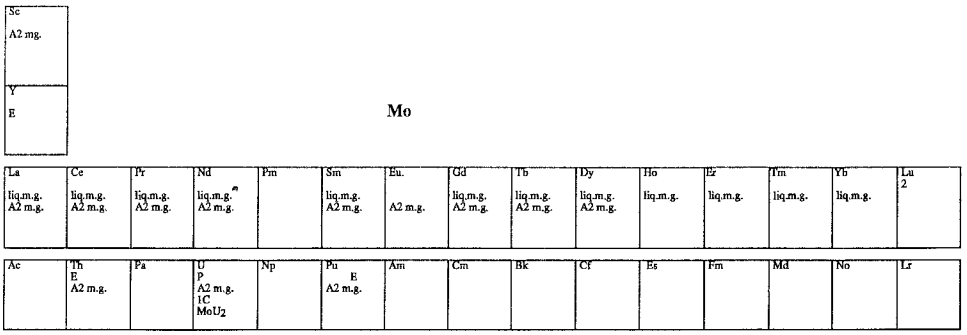

Fig. 31. Main features of the phase diagrams of molybdenum with rare earths and actinides.

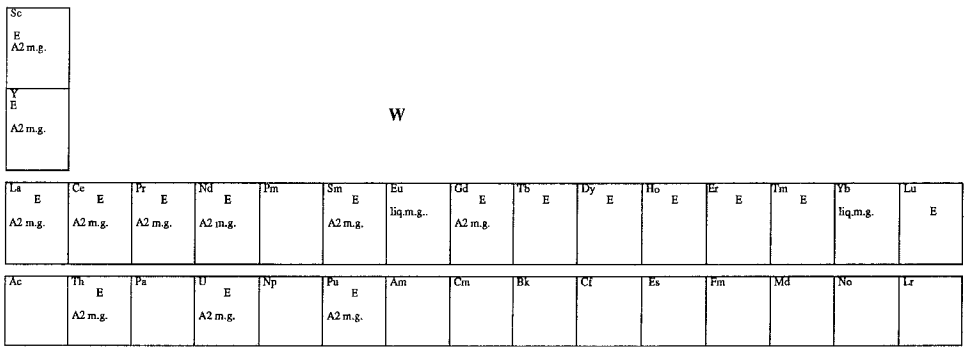

Fig. 32. Main features of the phase diagrams of tungsten with rare earths and actinides.

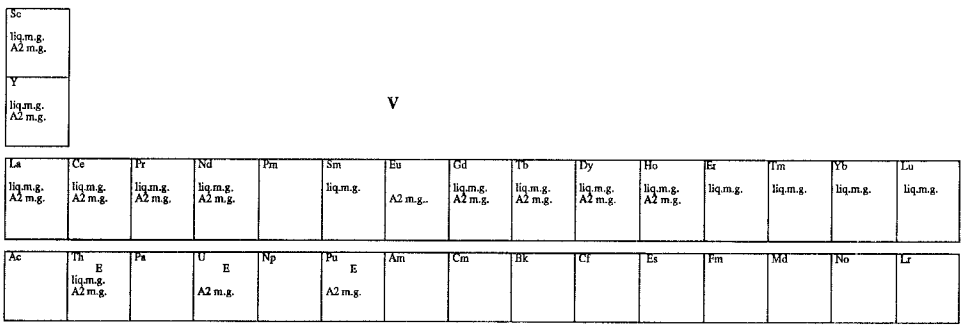

Fig. 33. Main features of the phase diagrams of vanadium with rare earths and actinides.

observed in the La–Mn and Ce–Mn phase diagrams. For all other rare earth elements one or more intermetallic compounds are found. With Re no compound forms with La, Ce and Pr, and the La–Re phase diagram exhibits a miscibility gap in the liquid phase.

It is important to remark on the behavior of europium and ytterbium. When alloyed with late transition metals, Eu and Yb form compounds on the transition-metal-rich side of the phase diagram but they are immiscible in the liquid phase in the Eu- or Yb-rich side

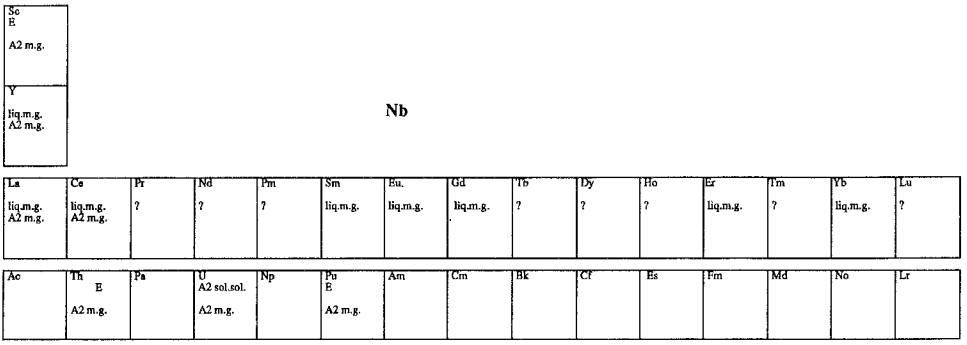

Fig. 34. Main features of the phase diagrams of niobium with rare earths and actinides.

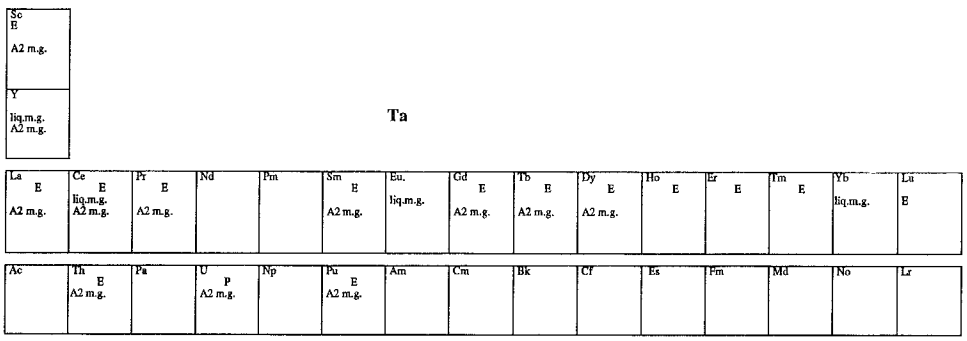

Fig. 35. Main features of the phase diagrams of tantalum with rare earths and actinides.

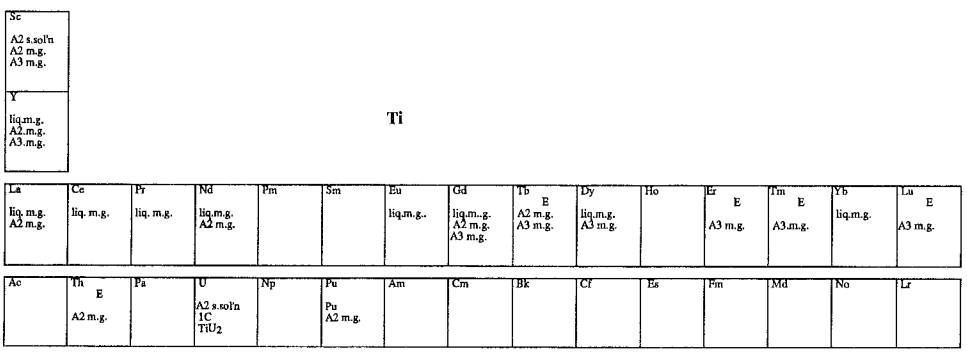

Fig. 36. Main features of the phase diagrams of titanium with rare earths and actinides.

of the phase diagram. Presumably in the transition-metal-rich side Eu and Yb become trivalent like the other lanthanides. When Eu and Yb are alloyed with early transition metals their binary phase diagrams exhibit miscibility gaps. Moreover if one remembers the low vaporization temperature of Eu and Yb at normal pressure, and the very high melting temperatures of elements of columns headed by Ti, V and Cr one often observes

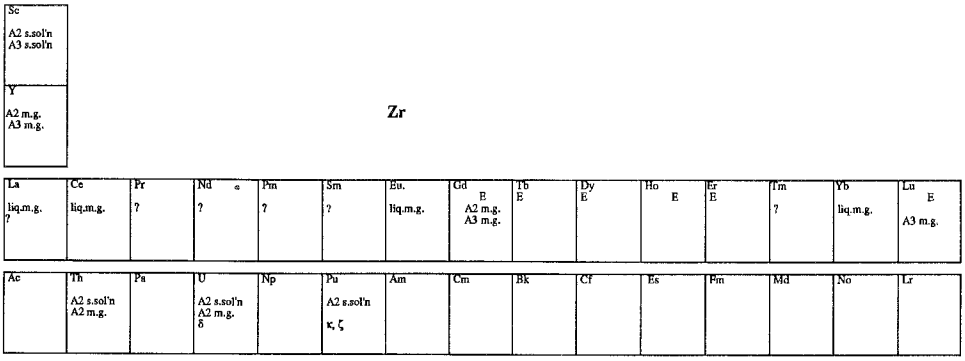

Fig. 37. Main features of the phase diagrams of zirconium with rare earths and actinides.

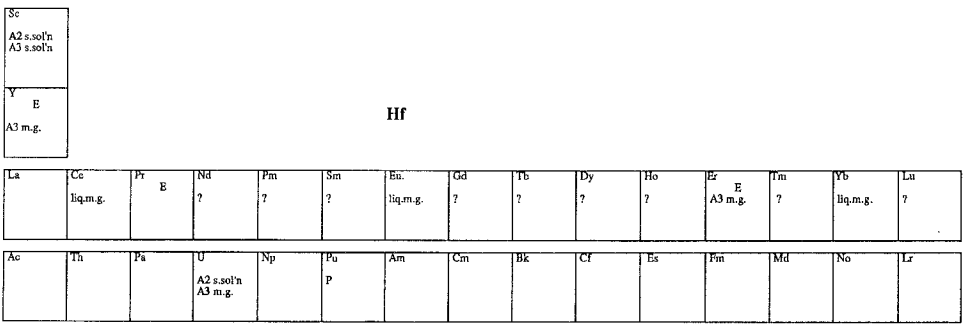

Fig. 38. Main features of the phase diagrams of hafnium with rare earths and actinides.

equilibrium between a gaseous phase rich in Eu or Yb and a liquid phase rich in the transition metal element.

Considering the structures of the various intermetallic compounds in the transition metal–rare earth or actinide binary alloys (figs. 39–49, table 4), it is difficult to see similarities because many compounds do not appear at the same composition. Let us just point out that the Cu_2Mg structure is often found for the RT_2 and AnT_2 compounds (T = transition metal), the $Ni_{17}Th_2$ structure for the R_2T_{17} and An_2T_{17} compounds, and the $CaCu_5$ structure for the majority of the RT_5 and AnT_5 compounds.

With Ni the intermetallic compound with the highest melting point has the stoichiometry RNi_5 or $AnNi_5$; with Pd the composition of this compound is often RPd_3 or $AnPd_3$; and with Pt the composition of this compound is RPt_2 for the elements of the beginning of the lanthanide series and RPt_3 or $AnPt_3$ for the other rare earths (except Lu), uranium and plutonium.

With Co the compound which exhibits the highest melting temperature has a variable stoichiometry. However it is surprising that in the Co–La, Co–Ce, Co–Pr and Co–Nd phase diagrams the compounds at the Co-rich side undergo a peritectic decomposition at high temperature while the only congruent melting compound is on the lanthanide-rich side of the phase diagram and possesses a low melting temperature. For Rh the

Phase	Sc	Y	La	Ce	Pr	Nd	Pm	Sm	Eu	Gd	Tb	Dy	Ho	Er	Tm	Yb	Lu	Ac	Th	Pa	U	Np	Pu	Prototype or
M_6Ni 14.3%																					x			MnU_6
M_3Ni 25%		x	x		x	x		x		x	x	x	x	x										CFe_3 x
M_7Ni_3 30%			x	x	x	x													x					Fe_3Th_7 x
M_2Ni 33.3%	x																							$NiTi_2$ x
M_3Ni_2 40%		+								+	x	x	x o											Dy_3Ni_2 x Er_3Ni_2 o Ni_2Y_3 +
MNi 50%	x	⊛	•	•	•	•		•		•	+ o •	⊛	⊛	⊛		⊛	⊛ ⊛		x				•	ClCs x BCr • NiTb + NiTb o BFe ⊛ AgSr ⊛
M_7Ni_9 56.2%																						?		
M_5Ni_7 58.3%																						?		
M_2Ni_3 60%			x																					La_2Ni_3 x
MNi_2 66.7%	x	x	x	x	x	x		x		x	x	x	x	x		x	x		•		+	x	x	Cu_2Mg x AlB_2 • $MgZn_2$ +
M_7Ni_{16} 69.6%			x																					
MNi_3 75%		x •?	x	•	x	x		x		x	x	x	x	x		x	x						x	Be_3Nb x $CeNi_3$ •
M_2Ni_7 77.8%	x	•	x	x	x •?	x		x •?		x •?	x •?	x •?		•							?			Ce_2Ni_7 x Co_7Er_2 •
MNi_4 80%		?						?		•		?							?		?		x	Ni_4Pu x ($GdNi_4$) •
MNi_5 83.3%	xHT ?LT	x	x	x	x	x		x	x	x	x	x	x	x		x	x		x		•		x	$CaCu_5$ x $AuBe_5$ •
M_2Ni_{17} 89.5%		x				x		x	x	x	x	x	x	x		x	x		x				x	$Ni_{17}Th_2$ x
M_2Ni_{19} 90.5%																			x					$Ni_{19}Th_2$ x
Ni composition	Sc	Y	La	Ce	Pr	Nd	Pm	Sm	Eu	Gd	Tb	Dy	Ho	Er	Tm	Yb	Lu	Ac	Th	Pa	U	Np	Pu	example

Fig. 39. Stoichiometry and structure prototype (or example) of the intermetallic compounds of Ni with rare earths and actinides (M = R or An).

stoichiometry of the compound exhibiting the highest melting temperature also has various compositions. With Ir it is RIr_2 for all rare-earth elements and $AnIr_3$ for the actinides.

With the other late transition metals, Fe, Ru, Os, Mn and Re, the intermetallic compound with the highest melting point or the highest peritectic decomposition temperature generally has the formula RT_2 or AnT_2.

Recent phase-diagram investigations have been performed in several transition metal based alloys. Concerning the alloys of transition metals with rare earths we may quote the studies performed by Bretschneider and Schaller (1990a) in the Ce–Pd alloy, by Sakamoto et al. (1990, 1991) in the Pd–(Ce, Ho, Er) systems, by Palenzona and Canepa (1989, 1990a,b) and Palenzona (1991) in the rare-earth–ruthenium systems, by Zhou et al. (1991)

Phase	Sc	Y	La	Ce	Pr	Nd	Pm	Sm	Eu	Gd	Tb	Dy	Ho	Er	Tm	Yb	Lu	Ac	Th	Pa	U	Np	Pu	Prototype or
M_4Pd 20%	?																							
M_3Pd 25%		x														?								CFe_3 x
M_5Pd_2 28.5%		x							o		• x?	• x?	•	• +?	x	?								Pd_2Dy_5 x (Pd_2Dy_5) • $NiTi_2$ + B_2Pd_5 o
M_7Pd_3 30%			x	x		x		x		x														Fe_3Th_7 x
M_2Pd 33%	x																		•					$NiTi_2$ x Al_2Cu •
M_3Pd_2 40%		x		?				?	x	•		•	•	•										Er_3Ni_2 x Si_2U_3 •
M_5Pd_4 44.4%																							?	
MPd 50%	x	?	•	• ?		•		• ?	•	• ?	• +	+LT xHT	+LT xHT	?LT xHT	x	x ?	x		+		?		+	ClCs x BCr • BFe +
M_5Pd_6 54.5%																					?			
M_4Pd_5 55.5%																							?	
M_3Pd_4 57.1%		x	x	x		x		x		x	x	x	x	x	x	x	x		x					Pd_4Pu_3 x
M_2Pd_3 60%		?								?		?	?	?										
M_3Pd_5 62.5%				x												?			•					Ce_3Pd_5 x Pd_5Th_3 •
MPd_2 66.7%	?	?							?			?		?		?								
$M_{10}Pd_{21}$ 67.7%								x								?								$Pd_{21}Sm_{10}$ x
MPd_3 75%	x	x	x	x		x		x	x	x	x	x	x	x	x	x	x		•		•	x •	x	AuCu$_3$ x Ni_3Ti •
MPd_4 80%																			x		x			AuCu$_3$
M_3Pd_{13} 81.2%																			x					$Pd_{13}Th_3$
MPd_5 83.3%				x •?		•		+	+												?			$CaCu_5$ x $(NdPd_5)$ • (Pd_5Sm) +
M_2Pd_{11} 84.5%																					?			
MPd_7 87.5%		x		x				x	x	x		x												Ca_7Ge x
M_2Pd_{17} 89.5%																					?			
Pd composition	Sc	Y	La	Ce	Pr	Nd	Pm	Sm	Eu	Gd	Tb	Dy	Ho	Er	Tm	Yb	Lu	Ac	Th	Pa	U	Np	Pu	example

Fig. 40. Stoichiometry and structure prototype (or example) of the intermetallic compounds of Pd with rare earths and actinides (M = R or An).

in the Ho–Ni system, by Qi et al. (1989c) in the Ni–(La, Ce, Pr, Nd) systems, by Ning et al. (1989) in several transition-metal–rare-earth systems, by Paul-Boncour et al. (1987) for the RNi_2 compounds, and by Zhang et al. (1991) and Klimyenko et al. (1988) in the La–Ni system. Several studies of the Fe–Nd system have recently been published

Phase	Sc	Y	La	Ce	Pr	Nd	Pm	Sm	Eu	Gd	Tb	Dy	Ho	Er	Tm	Yb	Lu	Ac	Th	Pa	U	Np	Pu	Prototype or
M_9Pt 10%									x															(Eu_9Pt) x
M_3Pt 25%		x								x	x	x	x	x	x		x							CFe_3 x
M_5Pt_2 28.5%									x							x								Be_2Pd_5 x
M_7Pt_3 30%		x	x	x	x	x		x		x									x					Fe_3Th_7 x
M_2Pt 33.3%	x	•?								x	x	x	x	x	x	x	x						x	Co_2Si x Ni_2Si •
M_5Pt_3 37.5%		x								x	x	x	x	x	x	x	x						x	Mn_5Si_3 x
$M_{31}Pt_{20}$ 39.1%																							x	$Pu_{31}Rh_{20}$ x
M_3Pt_2 40%			x	x	x	x		?	x															Er_3Ni_2 x
M_5Pt_4 44.4%		x							x		x	x	x	x	x	x	x							Ge_4Sm_5 x
MPt 50%	x	•	x	x	• +	• +				•	•	•	•	•	•	•	•		+ ?		+	+	+	ClCs x BFe • BCr + Pd_4Pu_3 x
M_3Pt_4 57.1%		x	x	x	x	x		x		x	x	x	x	x	x	x	x							
M_3Pt_5 63%																x			•					Pt_5Yb_3 x Pd_5Th_3 •
MPt2 66.7%		x	x	x	x	x		x	x	x	x	x	x	x	x	x			?		•		x	Cu_2Mg x $InNi_2$ •
MPt_3 75%	x	x									x	x	x	x	x	x	x		?	•	•	+	x o	AuCu3 x Ni_3Sn • Ni_3Ti + Ni_3P o
M_2Pt_7 77.8%									x															Ce_2Ni_7 x
MPt_4 80%																			?					
MPt_5 83.3%		x	•	•	•	•		+	x	x	+	+	+	+	+				+	o	o	+	• +?	YPt_5 x $CaCu_5$ • Pt_5Sm + $AuBe_5$ o
Pt composition	Sc	Y	La	Ce	Pr	Nd	Pm	Sm	Eu	Gd	Tb	Dy	Ho	Er	Tm	Yb	Lu	Ac	Th	Pa	U	Np	Pu	example ( )

Fig. 41. Stoichiometry and structure prototype (or example) of the intermetallic compounds of Pt with rare earths and actinides (M = R or An).

(Faudot et al. 1989a,b, Cabral and Gama 1989, 1990, Schneider et al. 1989, Landgraf et al. 1990, Moreau et al. 1990). Concerning the alloys of transition metals with actinides we report on work performed by Palenzona and Cirafici (1988a, 1989a) and by Cirafici and Palenzona (1990) in the Th–(Fe, Co, Ni) systems, by Chandrasekharaiah et al. (1986) for the U–(Re, Ta, W) systems, by Radchenko et al. (1989, 1990) in the Bk–(Rh, Ir) and Pt–(Am, Cm, Bk, Cf) systems, and by Kleykamp and Kang (1991) in the U–Pd and U–Rh systems.

Many assessments of binary transition-metal–rare-earth or actinide phase diagrams are found in the literature. Let us quote the articles by Leibowitz et al. (1989) and Leibowitz and Blomquist (1991) on the U–Zr system, by Chiotti et al. (1982a–d) on (Ir, Mo, Os, W)–Th systems, by Garg et al. (1990) on the Pu–Ta system, by Baxi et al. (1991) and Baxi

Phase	Sc	Y	La	Ce	Pr	Nd	Pm	Sm	Eu	Gd	Tb	Dy	Ho	Er	Tm	Yb	Lu	Ac	Th	Pa	U	Np	Pu	Prototype or
M_6Co 14.3%																					x		x	MnU_6 x
M_3Co 25%	•	x	+		+	+		+		+	+	+	+	+			+						o	Al_3Ni x $CoSc_3$ • CFe_3 + BRe_3 o
M_5Co_2 28.6%					x			x																B_2Pd_5 x
M_7Co_3 30%						x				?									x					Fe_3Th_7 x
M_9Co_4 30.8%								x																(Co_4Sm_9) x
$M_{24}Co_{11}$ 31.4%				x		x?																		$Ce_{24}Co_{11}$ x
M_2Co 33.3%	x																						•	Al_2Cu x Fe_2P •
$M_{17}Co_7$ 36.8%										x	x	x	x	x										Co_7Ho_{12} x
M_8Co_5 38.5%		?																						
M_3Co_2 40%		xM																						Dy_3Ni_2 x
M_4Co_3 42.9%										x	x	x	x	x	x		x							Co_3Ho_4
M_9Co_7 43.7%		?																						
$M_{20}Co_{17}$ 45.9%			?		x	x																		$(Co_{17}Pr_{20})x$
MCo 50%	x	?								•?									+		o			ClCs x BFe • BCr + CoU o
M_2Co_3 60%		?	x			x																		La_2Ni_3 x
MCo_2 66.7%	x	x		x	x	x		x •		x	x	x	x	x	x	x	x				x	x	x	Cu_2Mg x Co_2Sm •
MCo_3 75%		x		•	•	•		•		•	•	•	•	•	•	•	•				•		•	CeNi$_3$ x Be_3Nb •
M_2Co_7 77.8%		x	•LT xHT		•LT xHT	•LT xHT		x •		x •	x	x	x	x	x		x		•LT xHT					Co_7Er_2 x Ce_2Ni_7 •
MCo_4 80%																					?			
M_5Co_{19} 79.2%			?	x	x	x		x																Ce_5Co_{19} x
MCo_5 83.3%		x	x	x	x	x		x ?		x	x	x	x	x					x					$CaCu_5$ x
M_2Co_{17} 89.5%		x •		xLT •HT	x	x		xLT •HT		x •	xLT •HT	xLT •HT	x • +	•	•	•	•		x				•	Th_2Zn_{17} x $Ni_{17}Th_2$ • $Co_{17}Ho_2$ +
MCo_{13} 92.9%			x																					$NaZn_{13}$ x
Co Composition	Sc	Y	La	Ce	Pr	Nd	Pm	Sm	Eu	Gd	Tb	Dy	Ho	Er	Tm	Yb	Lu	Ac	Th	Pa	U	Np	Pu	example ()

Fig. 42. Stoichiometry and structure prototype (or example) of the intermetallic compounds of Co with rare earths and actinides (M = R or An).

and Massalski (1991) on the Pu–(Ta, V) systems, by Wu and Chuang (1991) on the Co–Y system, by Wu et al. (1991a,b, 1992) on the Ce–Co system, by Pan and Nash (1989a,b)

Phase	Sc	Y	La	Ce	Pr	Nd	Pm	Sm	Eu	Gd	Tb	Dy	Ho	Er	Tm	Yb	Lu	Ac	Th	Pa	U	Np	Pu	Prototype or
M_4Rh 20%						x		x																CFe_3 x
M_3Rh 25%		x	•		x					x	x	x	x	x			x							CFe_3 x (La_3Rh) •
M_7Rh_3 30%		x	x	x	x	x		x		x	x	x	x	x			x		x					Fe_3Th_7 x
M_2Rh 33.3%																							?	
M_5Rh_3 37.5%		?	?	?LT ? xHT				?		? ? • •		xLT ? •HT •	•	•	•		•						+	(Dy_5Rh_3) x Mn_5Si_3 • Pu_5Rh_3 +
$M_{31}Rh_{20}$ 39.2%																							x	$Pu_{31}Rh_{20}$ x
M_3Rh_2 40%		x		•	•	• ?		•		x	x	x	•	x			?							Rh_2Y_3 x Er_3Ni_2 •
M_4Rh_3 42.9%			x	?																	?			P_3Th_4 x
M_5Rh_4 44.4%			x			x		x		x													x	Ge_4Sm_5 x
MRh 50%	x	x	•	•	•	•		x		x	x	x	x	x	x	x	x		•				?	ClCs x BCr •
M_3Rh_4 57.1%																			x		?		?	(Rh_4Th_3) x
M_3Rh_5 62.5%																			?		?			
MRh_2 66.7%		x	xLT ?HT	x	x	x		x		x	x	x	x	x	x	x	x		• ?				?	Cu_2Mg x $InNi_2$ •
MRh_3 75%	x	•	• +	x	•	•		•		•									x	x	x	x	?	AuCu$_3$ x $CeNi_3$ • Be_3Nb +
M_2Rh_7 77.8%			xLT •HT																					Co_7Er_2 x Ce_2Ni_7 •
MRh_5 83.3%		x								x	x	x	x	x		?	x		?					$CaCu_5$ x
Rh Composition	Sc	Y	La	Ce	Pr	Nd	Pm	Sm	Eu	Gd	Tb	Dy	Ho	Er	Tm	Yb	Lu	Ac	Th	Pa	U	Np	Pu	example ( )

Fig. 43. Stoichiometry and structure prototype (or example) of the intermetallic compounds of Rh with rare earths and actinides (M = R or An).

on the Ni–(Pr, Tm) systems, by Pandian et al. (1987, 1988a–c) on systems with W and rare-earths, Th, U and Pu, by Peterson (1988a,b, 1989a–f) on the Ni–(Pu, U) (1988) and Pt–actinides (1989) systems, by Santandrea and Peterson (1988) on the Ni–Th system, by Smith and Lee (1987a,b) and Smith et al. (1985) on the (Ce, Eu, Yb, Th)–V systems, by Venkatraman and Neumann (1985) and Venkatraman et al. (1985a–g) on the Cr–(Y, Sc, actinides) systems, and by Palenzona and Cirafici (1991a–e) on the Zr–(Ce, Sc) and Y–(Mn, Nb, Zr) systems. Okamoto (1991d–n) has presented updated phase diagrams of the Ir–(La, Ce, Th), Ni–(La, Th), Pd–(Ce, Ho, Tb) and Ru–(La, Nd, Sm) systems.

Phase	Sc	Y	La	Ce	Pr	Nd	Pm	Sm	Eu	Gd	Tb	Dy	Ho	Er	Tm	Yb	Lu	Ac	Th	Pa	U	Np	Pu	Prototype or
$M_{44}Ir_7$ 13.7%	x																							$Mg_{44}Rh_7$ x
M_4Ir 20%			?	?		?																		
M_3Ir 25%		x	x	?	x	x		x		x	x	x	x	x	x		x						?	CFe_3 x
$M_{11}Ir_4$ 26.7%	x																							Ir_4Sc_{11} x
M_5Ir_2 28.6%		x			x	x				x	x	x	x	x	x		x							B_2Pd_5 x
M_7Ir_3 30%			x	x	x														x					Fe_3Th_7 x
M_5Ir_3 37.5%		?	x	x	x	?		x		x	x •	xHT •LT	x •?	?	x •?	x •?	x •?						+	Pu_5Rh_3 x Mn_5Si_3 • Si_3W_5 +
M_3Ir_2 40%		x								x	x	x	x	x	?	?	x		?		?			Rh_2Y_3 x
M_5Ir_4 44.4%				x																			x	Ge_4Sm_5 x
MIr 50%	x	x	?										x	x	x	x	x		•		?			ClCs x BCr •
MIr_2 66.7%	x	x	x	x	x	x		x	x	x	x	x	x	x	x	x	x		x		?	x	x	Cu_2Mg x
MIr_3 75%		x	x	x	x	x				x									?		o			Be_3Nb x $AuCu_3$ o
M_2Ir_7 77.8%			x	•	•	•																		Ce_2Ni_7 x Co_7Er_2 •
MIr_5 83.3%			•	x	•	•													•					$AuBe_5$ x $CaCu_5$ •
Ir Composition	Sc	Y	La	Ce	Pr	Nd	Pm	Sm	Eu	Gd	Tb	Dy	Ho	Er	Tm	Yb	Lu	Ac	Th	Pa	U	Np	Pu	example ( )

Fig. 44. Stoichiometry and structure prototype (or example) of the intermetallic compounds of Ir with rare earths and actinides (M = R or An).

Phase	Sc	Y	La	Ce	Pr	Nd	Pm	Sm	Eu	Gd	Tb	Dy	Ho	Er	Tm	Yb	Lu	Ac	Th	Pa	U	Np	Pu	Prototype or
M_6Fe 14.3%																					x		x	MnU_6
M_3Fe 25%	?																							
M_7Fe_3 30%																			x					Fe_3Th_7 x
MFe_2 66.7%	• x +	x		x	x			x		x	x	x	x	x	x		x				x	x	x ?	Cu_2Mg x $MgZn_2$ • $MgNi_2$ +
MFe_3 75%		x						x		x	x	x	x	x	x		x		x					Be_3Nb x
M_2Fe_7 77.8%																			xLT •HT					Ce_2Ni_7 x Co_7Er_2 •
M_6Fe_{23} 79.3%		x								x	x	x	x	x	x	x	x							$Mn_{23}Th_6$ x
MFe_5 83.3%						x?													x					$CaCu_5$ x
M_2Fe_{17} 89.5%		x •		• x	x	x		x		• x?	x •	•	•	•	•	•	•		x					Th_2Zn_{17} x $Ni_{17}Th_2$ •
Fe Composition	Sc	Y	La	Ce	Pr	Nd	Pm	Sm	Eu	Gd	Tb	Dy	Ho	Er	Tm	Yb	Lu	Ac	Th	Pa	U	Np	Pu	example ( )

Fig. 45. Stoichiometry and structure prototype (or example) of the intermetallic compounds of Fe with rare earths and actinides (M = R or An).

Phase	Sc	Y	La	Ce	Pr	Nd	Pm	Sm	Eu	Gd	Tb	Dy	Ho	Er	Tm	Yb	Lu	Ac	Th	Pa	U	Np	Pu	Prototype or
$M_{19}Ru$ 5%																							?	
M_4Ru 20%				?																				
M_3Ru 25%		x	x	?	x	x		x	x	x	x	x	x	x			x						+	CFe_3 x (Pu_3Ru) +
$M_{11}Ru_4$ 26.7%	x																							Ir_4Sc_{11} x
M_5Ru_2 28.6%		x	x		x	x	x	x		x	x	x	x	x			x							B_2Pd_5 x
M_7Ru_3 30%			?	x															x					Fe_3Th_7 x
M_2Ru 33.3%				?																	?			
$M_{44}Ru_{25}$ 36.2%		x									x			x										$Ru_{25}Y_{44}$ x
M_5Ru_3 37.5%			?	?	?	?	?	?		?		?	?				x						•	Mn_5Si_3 x Si_3W_5 •
M_3Ru_2 40%		?											?	x •?			?		?					(Er_3Ru_2) x C_3Pu_2 •
MRu 50%	x					?										x	x		+		?		x	ClCs x BCr +
M_3Ru_4 57.1%																					?			
MRu_2 66.6%	x	x	•	•	•	•	•	•		x •?	x	x	x	x		x	x		•			x	•	$MgZn_2$ x Cu_2Mg •
M_3Ru_5 62.5%																					?			
MRu_3 75%																					x			$AuCu_3$ x
Ru Composition	Sc	Y	La	Ce	Pr	Nd	Pm	Sm	Eu	Gd	Tb	Dy	Ho	Er	Tm	Yb	Lu	Ac	Th	Pa	U	Np	Pu	example ( )

Fig. 46. Stoichiometry and structure prototype (or example) of the intermetallic compounds of Ru with rare earths and actinides (M = R or An).

Phase	Sc	Y	La	Ce	Pr	Nd	Pm	Sm	Eu	Gd	Tb	Dy	Ho	Er	Tm	Yb	Lu	Ac	Th	Pa	U	Np	Pu	Prototype or
$M_{19}Os$ 5%																							xLT •HT	α-$OsPu_{19}$ x β-$OsPu_{19}$ •
$M_{44}Os_7$ 13.7%	x																							$Mg_{44}Rh_7$ x
M_3Os 25%	x	x	x	x	x			x		x	x	x	x		x		x				?		?	CFe_3 x
$M_{11}Os_4$ 26.7%	x																							Ir_4Sc_{11} x
M_7Os_3 30%																			x					Fe_3Th_7 x
M_2Os 33.3%																					x			(OsU_2) x
M_5Os_3 37.5%																							x	Si_3W_5 x
MOs_x																			?					
M_5Os_4 44.4%																					?			
MOs_2 66.7%	x	•	x	•	xHP •	x		x		x	x	x	x		x	x	x		•		•	x	x	$MgZn_2$ x Cu_2Mg •
Os Composition	Sc	Y	La	Ce	Pr	Nd	Pm	Sm	Eu	Gd	Tb	Dy	Ho	Er	Tm	Yb	Lu	Ac	Th	Pa	U	Np	Pu	example ( )

Fig. 47. Stoichiometry and structure prototype (or example) of the intermetallic compounds of Os with rare earths and actinides (M = R or An).

Phase	Sc	Y	La	Ce	Pr	Nd	Pm	Sm	Eu	Gd	Tb	Dy	Ho	Er	Tm	Yb	Lu	Ac	Th	Pa	U	Np	Pu	Prototype or
M_6Mn 14.3%																					x			MnU_6 x
MMn_2 66.7%	x	• xHT HP				x		x •		•	•	•	•	x •?	x		x		x		+RT •LT		•	$MgZn_2$ x Cu_2Mg • Mn_2U +
M_6Mn_{23} 79.3%		x			x	x		x		x	x	x	x	x	x		x		x					$Mn_{23}Th_6$ x
MMn_5 83.3%																	x							$LuMn_5$ x
MMn_{12} 92.3%		x				x				x	x	x	x	x	x				x					$Mn_{12}Th$ x
Mn Composition	Sc	Y	La	Ce	Pr	Nd	Pm	Sm	Eu	Gd	Tb	Dy	Ho	Er	Tm	Yb	Lu	Ac	Th	Pa	U	Np	Pu	example ()

Fig. 48. Stoichiometry and structure prototype (or example) of the intermetallic compounds of Mn with rare earths and actinides (M = R or An).

Phase	Sc	Y	La	Ce	Pr	Nd	Pm	Sm	Eu	Gd	Th	Dy	Ho	Er	Tm	Yb	Lu	Ac	Th	Pa	U	Np	Pu	Prototype or
M_2Re 33.3%																					?			
MRe_2 66.7%	x	x				x		x	x	x	x	x	x	x	x	x	x		x		x •?	x	x	$MgZn_2$ x Re_2U •
M_5Re_{24} 82.8%	x																							α-Mn x
Re Composition	Sc	Y	La	Ce	Pr	Nd	Pm	Sm	Eu	Gd	Tb	Dy	Ho	Er	Tm	Yb	Lu	Ac	Th	Pa	U	Np	Pu	example ()

Fig. 49. Stoichiometry and structure prototype (or example) of the intermetallic compounds of Re with rare earths and actinides (M = R or An).

3.2. *Thermodynamic data of the binary alloys*

The enthalpies and entropies of formation of intermetallic compounds between transition metals and rare earth or actinide elements are reported in tables 5–15. As can be seen, data are available for late transition metals. For early transition metals some data concerning the U–Zr, U–Nb, U–Mo solid solutions have been found and are reported in table 16. When calorimetric experiments have been performed in the liquid state, the values of the partial or integral enthalpies of mixing are reported in tables 17–20. These data concern only rare-earth-based alloys with Ni, Co, Fe and Mn.

Despite the large amount of experimental data for late transition metals, appreciable differences between values obtained in the same system are observed. It is also important to note that with Rh, Ir, Ru, Os, Mn and Re only a few experiments have been performed with rare-earth elements. Moreover we remark that very few experiments have been performed with plutonium. Thus, it is difficult to define the alloying behavior in the lanthanide series as well as in the actinide series and finally to compare the two series.

A large number of experimental results have been obtained using emf measurements using either a liquid or a solid electrolyte. While the Gibbs energies of formation of

Table 4
Structure characteristics of transition-metal (X) and rare-earth or actinide (M = R, An) intermetallic compounds

Phase	Pearson symbol	Space group	Strukturbericht designation	Prototype or (example)
MX_{13}	cF112	$Fm\bar{3}c$	$D2_3$	$NaZn_{13}$
MX_{12}	tI26	I4/mmm	$D2_b$	$Mn_{12}Th$
M_2X_{19}	hP80	$P6_3/mmc$		$Ni_{19}Th_2$
M_2X_{17}	hP38	$P6_3/mmc$		$Ni_{17}Th_2$
	hR19	$R\bar{3}m$		Th_2Zn_{17}
	hP52	$P6_3/mmc$		$Co_{17}Ho_2$
MX_7	cF32	$Fm\bar{3}m$		Ca_7Ge
MX_5	hP6	P6/mmm	$D2_d$	$CaCu_5$
	cF24	$F\bar{4}3m$	$C15_b$	$AuBe_5$
	hP12	$P6_3mc$		$LuMn_5$
	cF*			$(NdPd_5)$, $(CePd_5)$
	o*72, o**			$(SmPd_5)$, $(SmPt_5)$, (YPt_5)
M_5X_{24}	cI58	$I\bar{4}3m$	A12	α-Mn
M_3X_{13}	tI*			$(Pd_{13}Th_3)$
MX_4	cP4	$Pm\bar{3}m$	$L1_2$	$AuCu_3$
	h*10			$(GdNi_4)$
	hP36	$P6_3/mmc$		Ce_2Ni_7
	mc30	C2/m		Ni_4Pu
M_6X_{23}	cF116	$Fm\bar{3}m$	$D8_a$	$Mn_{23}Th_6$
M_5X_{19}	hR24	$R\bar{3}m$		Ce_5Co_{19}
M_2X_7	hP36	$P6_3/mmc$		Ce_2Ni_7
	hR18	$R\bar{3}m$		Co_7Er_2
MX_3	hP24	$P6_3/mmc$		$CeNi_3$
	hR12	$R\bar{3}m$		Be_3Nb
	cP4	$Pm\bar{3}m$	$L1_2$	$AuCu_3$
	oP16	Pnma	DO_{11}	CFe_3
	hP8	$P6_3/mmc$	DO_{19}	Ni_3Sn
	hP16	$P6_3/mmc$	DO_{24}	Ni_3Ti
	tI32	$I\bar{4}$	DO_c	Ni_3P
M_7X_{16}	tI46	$I\bar{4}2m$		La_7Ni_{16}
$M_{10}X_{21}$	mC124	C2/m		$Pd_{21}Sm_{10}$
MX_2	cF24	$Fd\bar{3}m$	C15	Cu_2Mg
	hP3	P6/mmm	C32	AlB_2
	hP12	$P6_3/mmc$	C14	$MgZn_2$
	hR4	$R\bar{3}m$		(Co_2Sm)
	hP24	$P6_3/mmc$	C36	$MgNi_2$
	hP6	$P6_3/mmc$	$B8_2$	$InNi_2$
	oC12	Ama2		Pt_2U
	oI12	Imma		γ-Mn_2U
	oC24	Cmcm		Re_2U
M_3X_5	mC32	c2m		Pt_5Yb_3
	hP8	$P\bar{6}2m$		Pd_5Th_3
	hP8	P62		(Ce_3Pd_5)

continued on next page

Table 4, *continued*

Phase	Pearson symbol	Space group	Strukturbericht designation	Prototype or (example)
M_2X_3	oC20	Cmca		La_2Ni_3
M_3X_4	cF*	$R\bar{3}$		(Rh_4Th_3)
	hR14			Pd_4Pu_3
MX	cP2	$Pm\bar{3}m$	B2	ClCs
	oC8	Cmcm	Bf	BCr
	oP8	Pnma	B27	BFe
	cI16	$I2_13$	Ba	CoU
	oP16	Pnma		AgSr
	oP24	Pnma		NiTb
	mP24	$P2_1/m$		NiTb
$M_{20}X_{17}$	hP*			$(Co_{17}Pr_{20})$
M_5X_4	oP36	Pnma		Ge_4Sm_5
M_4X_3	cI28	$I\bar{4}3d$	$D7_3$	P_4Th_3
	hP22	$P6_3/m$		Co_3Ho_4
M_3X_2	hR15	$R\bar{3}$		Er_3Ni_2
	tI140	I4/mcm		Rh_2Y_3
	tP10	P4/mbm	$D5_a$	Si_2U_3
	mC20	C2/m		Dy_3Ni_2
	tP80	$P4_12_12$		Ni_2Y_3
	hP10	$P6_3/m$		(Er_3Ru_2)
	cI40	$I\bar{4}3d$		C_3Pu_2
$M_{31}X_{20}$	tI204	I4/mcm		$Pu_{31}Rh_{20}$
M_5X_3	hP16	$P6_3/mcm$	$D8_8$	Mn_5Si_3
	tP32	P4/ncc		Pu_5Rh_3
	c**			$(\alpha\text{-}Dy_5Rh_3)$
	tI32	I4/mcm	$D8_m$	Si_3W_5
$M_{12}X_7$	mP38	$P2_1/c$		Co_7Ho_{12}
$M_{44}X_{25}$	oP276	Pnna		$Ru_{25}Y_{44}$
M_2X	m*12			(OsU_2)
	tI12	I4/mcm	C16	Al_2Cu
	hP9	$P6_2m$	C22	Fe_2P
	oP12	Pnma	C23	Co_2Si
	hP6	$P6_322$		Ni_2Si
	cF96	$Fd\bar{3}m$		$NiTi_2$
$M_{24}X_{11}$	hP70	$P6_3mc$		$Ce_{24}Co_{11}$
M_9X_4	o52			(Co_4Sm_9)
M_7X_3	hP20	$P6_3mc$	$D10_2$	Fe_3Th_7
M_5X_2	mc28	C2/c		B_2Pd_5
	cF144	Fd3m		Dy_5Pd_2
	tI49	I41/a		(Dy_5Pd_2)
	cF96	$Fd\bar{3}m$		$NiTi_2$
$M_{11}X_4$	cF120	$Fm\bar{3}m$		Ir_4Sc_{11}
M_3X	oP16	Pnma	DO_{11}	CFe_3
	oP16	Pmmm		(Pu_3Ru)
	o**			(La_3Rh)
	oP16	Pnma	DO_{20}	Al_3Ni
	oP32	Pnma		$CoSc_3$
	oC16	Cmcm	$E1_a$	BRe3

continued on next page

Table 4, *continued*

Phase	Pearson symbol	Space group	Strukturbericht designation	Prototype or (example)
M_4X	oP16	Pnma	DO_{11}	CFe_3
M_6X	tI28	I4/mcm	$D2_c$	MnU_6
$M_{44}X_7$	cF408	$F\bar{4}3m$		$Mg_{44}Rh_7$
M_9X	cF*			(Eu_9Pt)
$M_{19}X$	oC40	Cmca		α-$OsPu_{19}$
	oP52	Pnna		β-$OsPu_{19}$

the compounds obtained by this method seem to be correct, this is often not the case for the enthalpies and entropies of formation derived from the variation of the emf with temperature. We remark that generally too negative enthalpies and entropies of formation are found. Moreover, when this experimental method is used the thermodynamic data are obtained by successive studies of equilibrium between two compounds, with the first experiment concerning the equilibrium between the pure transition metal and the first compound found in the phase diagram in the transition-metal-rich side. This results in an accumulation of errors for the last equilibria studied. If the solubility of the rare-earth element in the transition metal is not negligible corrections must be made. If one or more compounds are not detected the values obtained for the compounds determined subsequently can be incorrect. This can be also the case when one or more compounds present a large range of nonstoichiometry.

We also recall here that the reference state of the Gibbs energies of formation was not always stated by the authors in their experimental results. It was thus impossible for the reviewers to define the reference state when a phase transition (allotropic transformation or melting) of one component occurred in the investigated temperature range.

Numerous systems exhibit anomalies in the enthalpies and entropies of formation. In the Y–Ni system the values of the entropies of formation proposed by Subramanian and Smith (1985b) become more and more negative with increasing Y content, which seems unreliable. It is however surprising or perhaps fortuitous that the value of the enthalpy of formation of the Y–Ni intermetallic compound found by these authors is in good agreement with the values obtained by Colinet et al. (1987b) and by Sidorov et al. (1989) using calorimetric methods. In the Th–Ni and Th–Co systems emf experiments have been performed by Skelton et al. (1970, 1971). Rand et al. (1975) pointed out that the values of the enthalpies and entropies of formation derived from these experiments cannot be reliable because of inconsistencies with the respective phase diagrams. The values of the enthalpies and entropies of formation obtained by Lebedev et al. (1973a–c, 1974a,b) in the U–(Ni, Co, Fe, Mn) clearly seem too negative. This is also the case for the values obtained by Kazanskii and Ilyushchenko (1987) in the La–Co system. Kemmler (1977) performed a systematic study of the lanthanide–platinum systems using emf measurements. The values obtained for the Gibbs energies of formation are in good agreement with the values obtained recently by Jacob and Waseda (1990a–d) but the enthalpies and entropies of

Table 5
Enthalpies and entropies of formation of intermetallic compounds of Ni with rare earths and actinides ($\Delta_f H°$: kJ/mol of atoms, $\Delta_f S°$: $J K^{-1}$/mol of atoms)

System	Compound	$\Delta_f H°$	$\Delta_f S°$	Reference state	Authors and method
Sc–Ni	$ScNi_2$	−43.0		α-Sc; Ni_s; 298 K	Selhaoui and Kleppa 1993a
	ScNi	−44.7			react. and drop calorim. 1473 K
Y–Ni	Y_2Ni_{17}	−18.7		α-Y, Ni_s; 298 K	Colinet et al. 1987b
	YNi_5	−30.8		(same)	Al sol'n calorim. 990 K
	Y_2Ni_7	−35.4		(same)	
	YNi_3	−37.2		(same)	
	YNi_2	−38.7		(same)	
	YNi	−36.6		(same)	
	Y_3Ni_2	−29.9		(same)	
	Y_3Ni	−19.3		(same)	
	Y_2Ni_{17}	−13.1	−0.9	α-Y, Ni_s; 973 K	Subramanian and Smith 1985b
	YNi_5	−21.3	−1.5	(same)	emf sol. electrolyte 900–1225 K
	YNi_4	−25.0	−1.6	(same)	
	Y_2Ni_7	−27.8	−1.6	(same)	
	YNi_3	−29.1	−1.7	(same)	
	YNi_2	−31.3	−2.5	(same)	
	YNi	−35.4	−5.1	(same)	
	Y_3Ni_2	−35.3	−6.8	(same)	
	Y_3Ni	−33.3	−8.6	(same)	
	YNi	−37		α-Y, Ni_s; 298 K	Sidorov et al. 1989
					solute + solvent drop calorim. 1873 K
	YNi_5	−34.1		α-Y, Ni_s; 298 K	Colinet and Pasturel 1983
					Al sol'n calorim. 995 K
La–Ni	$LaNi_5$	−25.2	−2.0	β-La, Ni_s; 900 K	Rezukhina and Kutsev 1982a
		−23.6	0.7	α-La,Ni_s; 298 K	emf sol. electrolyte 800–1100 K
	La_2Ni_7	−28.1	−2.6	β-La, Ni_s; 900 K	
		−26.5	0.0	α-La,Ni_s; 298 K	
	$LaNi_3$	−29.6	−3.3	β-La, Ni_s; 900 K	
		−28.0	−0.6	α-La,Ni_s; 298 K	
	$LaNi_2$	−31.3	−3.6	β-La, Ni_s; 900 K	
		−29.6	−0.8	α-La,Ni_s; 298 K	
	$LaNi_{1.4}$	−30.1	−2.2	β-La, Ni_s; 900 K	
		−28.6	−0.3	α-La,Ni_s; 298 K	
	$LaNi_5$	−21.1		α-La, Ni_s; 298 K	Semenenko et al. 1979
	$LaNi_3$	−20.6		(same)	acid sol'n calorim.
	$LaNi_{1.1}$	−14.7		(same)	
	$LaNi_2$	−20.4		α-La, Ni_s; 298 K	Semenenko et al. 1982
					acid sol'n calorim.
	$LaNi_5$	−26.3		α-La, Ni_s; 298 K	Watanabe and Kleppa 1983
					sol'n calorim. 1376 K
	LaNi	−24.8		α-La, Ni_s; 298 K	Watanabe and Kleppa 1983
	La_3Ni	−13.1		(same)	mixing and drop calorim. 1376 K
	$LaNi_5$	−22.0		α-La, Ni_s; 298 K	Chatillon-Colinet et al. 1979
					Al sol'n calorim. 987 K

continued on next page

Table 5, *continued*

System	Compound	$\Delta_f H^\circ$	$\Delta_f S^\circ$	Reference state	Authors and method
	$LaNi_5$	−26.8		α-La, Ni_s; 298 K	Pasturel et al. 1984a,b Al sol'n calorim. 987 K
	$LaNi_5$	−27.4		α-La, Ni_s; 298 K	Colinet et al. 1987a Al sol'n calorim. 987 K
	$LaNi_5$	−26.5		α-La, Ni_s; 298 K	Hubbard et al. 1983 acid sol'n calorim.
	La_2Ni_7	−27.9		unknown	Shilov 1987
	$LaNi_3$	−29.3		(same)	indirect determination
	$LaNi_2$	−33.8		(same)	
Ce–Ni	$CeNi_5$	−33.2		γ-Ce, Ni_s; 298 K	Colinet and Pasturel 1983 Al sol'n calorim. 990 K
Pr–Ni	$PrNi_2$	−8.4		α-Pr, Ni_s; 820 K	Deodhar and Ficalora 1975 diff. therm. anal. 820 K
	$PrNi_5$	−26.8		α-Pr, Ni_s; 298 K	Pasturel et al. 1984b Al sol'n calorim. 970 K
Sm–Ni	$SmNi_5$	−30.3		α-Sm, Ni_s; 298 K	Pasturel et al. 1984b Al sol'n calorim. 987 K
	Sm_2Ni_7	−34.3		unknown	Shilov 1987
	$SmNi_3$	−35.7		(same)	indirect determination
	$SmNi_2$	−37.7		(same)	
	$SmNi_2$	−34.5		unknown	Sirotina 1985 quoted by Shilov 1987
Gd–Ni	Gd_2Ni_{17}	−20.0		α-Gd, Ni_s; 298 K	Colinet et al. 1986
	$GdNi_5$	−31.3		(same)	Al sol'n calorim. 995 K
	Gd_2Ni_7	−35.4		(same)	
	$GdNi_3$	−37.6		(same)	
	$GdNi_2$	−38.5		(same)	
	GdNi	−36.3		(same)	
	Gd_3Ni	−18.2		(same)	
	$GdNi_5$	−23.1		α-Gd, Ni_s; 298 K	Schott and Sommer 1986
	$GdNi_2$	−32.0		(same)	Sn sol'n calorim. 1095 K
	GdNi	−25.8		(same)	
	Gd_3Ni	−13.9		(same)	
	$GdNi_2$	−25.1		α-Gd, Ni_s; 931 K	Deodhar and Ficalora 1975 diff. therm. anal. 931 K
Dy–Ni	$DyNi_5$	−25.1		α-Dy, Ni_s; 298 K	Schott and Sommer 1986
	$DyNi_2$	−32.6		(same)	Sn sol'n calorim. 1098 K
	DyNi	−33.4		(same)	
	Dy_3Ni	−22.2		(same)	
	$DyNi_2$	−38.5		α-Dy, Ni_s; 960 K	Deodhar and Ficalora 1975 diff. therm. anal. 960 K
Er–Ni	Er_2Ni_{17}	−12.9		Er_s, Ni_s; 298 K	Schott and Sommer 1986
	$ErNi_5$	−20.2		(same)	Sn sol'n calorim. 1098 K
	$ErNi_2$	−31.3		(same)	
	ErNi	−30.6		(same)	
	Er_3Ni	−17.1		(same)	

continued on next page

Table 5, *continued*

System	Compound	$\Delta_f H°$	$\Delta_f S°$	Reference state	Authors and method
	$ErNi_2$	−49.2		Er_s, Ni_s; 1027 K	Deodhar and Ficalora 1975 diff. therm. anal. 1027 K
Th–Ni	Th_2Ni_{17}	−24.8	−1.8	α-Th, Ni_s; 973 K	Skelton et al. 1970
	$ThNi_5$	−43.3	−7.1	(same)	emf sol. electrolyte 841–1141 K;
	$ThNi_2$	−44.7	−3.2	(same)	see Rand et al. 1975 and Chiotti et
	ThNi	−45.3	−2.4	(same)	al. 1981 for discussion of these
	Th_7Ni_3	−29.0	−1.4	(same)	results
U–Ni	UNi_5	−44.4	−15.9	γ-U, Ni_s; 1000 K	Lebedev et al. 1974a
		−43.1	−14.6	α-U, Ni_s	emf 1073–1173 K
	η(0.178)	−46.4	−16.3	γ-U, Ni_s; 1000 K	reviewed by Chiotti et al. 1981; see
		−45.1	−15.0	α-U, Ni_s	also Peterson 1988b
	ε(0.222)	−53.1	−19.2	γ-U, Ni_s; 1000 K	
		−51.4	−17.5	α-U, Ni_s	
	δ(0.231)	−53.6	−18.8	γ-U, Ni_s; 1000 K	
		−51.9	−17.1	α-U, Ni_s	
	UNi_2	−54.0	−19.2	γ-U, Ni_s; 1000 K	
		−51.5	−16.7	α-U, Ni_s	
	U_5Ni_7	−54.8	−23.0	γ-U, Ni_s; 1000 K	
		−51.7	−19.9	α-U, Ni_s	
	U_7Ni_9	−53.1	−22.2	γ-U, Ni_s; 1000 K	
		−49.8	−18.9	α-U, Ni_s	
	U_6Ni	−21.3	−10.0	γ-U, Ni_s; 1000 K	
		−14.8	−3.5	α-U, Ni_s	
	UNi_5	−30.1		γ-U, Ni_s; 1023 K	Dannöhl and Lukas 1974
		−28.8		α-U, Ni_s	Al sol'n calorim. 1023 K
	UNi_2	−32.2		γ-U, Ni_s; 1023 K	
		−29.6		α-U, Ni_s	
Pu–Ni	Pu_2Ni_{17}	−9.0	−1.5	Pu_l, Ni_s; 950–1080 K	Campbell 1974
		−8.1	+0.2	α-Pu, Ni_s	emf liq. electrolyte 950–1080 K
	Pu_2Ni_{17}	−8.8	−1.3	Pu_l, Ni_s; 913–1125 K	Chiotti et al. 1981
		−7.8	0.4	α-Pu, Ni_s	assessment 913–1125 K; see also Peterson 1988a

formation are much more negative (see fig. 50 for a comparison of the values of the enthalpies of formation obtained by different authors in the Gd–Pt system). The values of the entropies of formation obtained in the U–Rh system by Naraine and Bell (1974) and by Schmidt (1974) also appear too negative.

Some experimental results have been obtained using calorimetric methods. Unfortunately there are also discrepancies in the enthalpies of formation obtained by different authors in the Gd–Ni and Gd–Co systems where the enthalpies of formation have been obtained by Schott and Sommer (1986) using tin solution calorimetry and by Colinet et al. (1986, 1987c) using aluminum solution calorimetry. In both cases the values obtained by Schott and Sommer (1986) are less negative than the values obtained by Colinet et al. (1986, 1987c).

Table 6
Enthalpies and entropies of formation of intermetallic compounds of Pd with rare earths and actinides ($\Delta_f H°$: kJ/mol of atoms, $\Delta_f S°$: JK^{-1}/mol of atoms)

System	Compound	$\Delta_f H°$	$\Delta_f S°$	Reference state	Authors and method
Sc–Pd	ScPd	−106		β-Sc, Pd_s; 1681 K	Gachon et al. 1985
		−104		α-Sc, Pd_s	direct react. calorim. 1681 K
	ScPd	−89.3	5	α-Sc, Pd_s; 298 K	Selhaoui and Kleppa 1993a
					react. and drop calorim. 1473 K
	$ScPd_3$	−81.7	(a)	α-Sc, Pd_s	Möbius 1978
					emf coupled reduction 1573 K
Y–Pd	YPd_3	−93.8	−8.1	α-Y, Pd_s; 1023 K	Paasch and Schaller 1983
					emf solid electrolyte 973–1073 K
	YPd_3	−79.0		α-Y, Pd_s; 298 K	Selhaoui and Kleppa 1993b
	Y_3Pd_4	−92.8		(same)	react. and drop calorim. 1473 K
	YPd	−94.9		(same)	
La–Pd	LaPd	−56.5		β-La, Pd_s; 883 K	Palenzona and Cirafici 1975a
				α-La, Pd_s	dyn. diff. calorim. 883 K
	$LaPd_3$	−77.1		α-La, Pd_s; 298 K	Selhaoui and Kleppa 1993c
	LaPd	−76.2		(same)	react. and drop calorim. 1473 K
Ce–Pd	CePd	−63.6		γ-Ce, Pd_s; 828 K	Palenzona and Cirafici 1975a
					dyn. diff. calorim. 828 K
	CePd	−110		δ-Ce, Pd_s; 1000–1100 K	Bretschneider and Schaller 1990b
					emf sol. electrolyte 1000–1100 K
	$CePd_3$	−73.0		γ-Ce, Pd_s; 298 K	Selhaoui and Kleppa 1993d
	CePd	−78.3		(same)	react. and drop calorim. 1473 K
Pr–Pd	PrPd	−63.2		α-Pr, Pd_s; 873 K	Palenzona and Cirafici 1975a
					dyn. diff. calorim. 873 K
Nd–Pd	NdPd	−67.4		α-Nd, Pd_s; 913 K	Palenzona and Cirafici 1975a
					dyn. diff. calorim. 913 K
Sm–Pd	SmPd	−63.2		α-Sm, Pd_s; 958 K	Palenzona and Cirafici 1975a
					dyn. diff. calorim. 958 K
Gd–Pd	$GdPd_3$	−89.2		α-Gd, Pd_s; 298K	Colinet et al. 1987c
	$GdPd_2$	−89.2		(same)	Al sol'n calorim. 986 K
	Gd_3Pd_4	−88.3		(same)	
	GdPd	−85.7		(same)	
	Gd_7Pd_3	−52.8		(same)	
	GdPd	−62.8		α-Gd, Pd_s; 1038 K	Palenzona and Cirafici 1975a
					dyn. diff. calorim. 1038 K
	$GdPd_3$	−86.1	−2.7	α-Gd, Pd_s; 1023 K	Paasch and Schaller 1983
					emf sol. electrolyte ~973–1073 K
Tb–Pd	TbPd	−61.1		α-Tb, Pd_s; 1073 K	Palenzona and Cirafici 1975a
					dyn. diff. calorim. 1073 K
	$TbPd_3$	−58.8	−2.1	α-Tb, Pd_s; 1475 K	Zaitsev et al. 1986b
	$TbPd_2$	−63.2	−2.5	(same)	vap. press. Knudsen 1370–1619 K
	Tb_2Pd_3	−64.0	−2.5	(same)	
	Tb_4Pd_5	−63.8	−2.3	(same)	
	TbPd	−62.1	−2.1	(same)	
	$Tb_{0.68}Pd_{0.28}$	−35.6		α-Tb, Pd_s; 1083 K	Palenzona and Cirafici 1974a
					dyn. diff. calorim. 1083 K

continued on next page

Table 6, *continued*

System	Compound	$\Delta_f H^\circ$	$\Delta_f S^\circ$	Reference state	Authors and method
Dy–Pd	DyPd	−61.1		α-Dy, Pd_s; 1108 K	Palenzona and Cirafici 1975a dyn. diff. calorim. 1108 K
	$Dy_{0.68}Pd_{0.28}$	−33.9		α-Dy, Pd_s; 1128 K	Palenzona and Cirafici 1974a dyn. diff. calorim. 1128 K
	$Dy_{0.12}Pd_{0.88}$	−43.6	+0.8	α-Dy, Pd_s; 1430 K	Zaitsev et al. 1982, 1986a
	$Dy_{0.22}Pd_{0.78}$	−52.3	0.0	(same)	vap. press. Knudsen 1248–1569 K
	$DyPd_3$	−55.0	−0.2	(same)	
		−56.0	−1.4	(same)	
	$DyPd_2$	−61.0	−2.0	(same)	
	Dy_2Pd_3	−62.1	−2.2	(same)	
	Dy_4Pd_5	−62.0	−2.0	(same)	
	DyPd	−60.5	−1.8	(same)	
Ho–Pd	HoPd	−60.2		α-Ho, Pd_s; 1158 K	Palenzona and Cirafici 1975a dyn. diff. calorim. 1158 K
	$Ho_{0.68}Pd_{0.28}$	−33.1		α-Ho_s, Pd_s; 1173 K	Palenzona and Cirafici 1974a dyn. diff. calorim. 1173 K
Er–Pd	ErPd	−59.8		Er_s, Pd_s; 1183 K	Palenzona and Cirafici 1975ε dyn. diff. calorim. 1183 K
	$Er_{0.68}Pd_{0.28}$	−41.0		Er_s, Pd_s; 1198 K	Palenzona and Cirafici 1974a dyn. diff. calorim. 1198 K
Tm–Pd	TmPd	−59.4		Tm_s, Pd_s; 1203 K	Palenzona and Cirafici 1975a dyn. diff. calorim. 1203 K
	$Tm_{0.68}Pd_{0.28}$	−37.7		Tm_s, Pd_s; 1213 K	Palenzona and Cirafici 1974a dyn. diff. calorim. 1213 K
Lu–Pd	LuPd	−58.6		Lu_s, Pd_s; 1243 K	Palenzona and Cirafici 1975a dyn. diff. calorim. 1243 K
	$Lu_{0.68}Pd_{0.28}$	−39.8		Lu_s, Pd_s ; 1253 K	Palenzona and Cirafici 1974a dyn. diff. calorim. 1253 K
	$LuPd_3$	−88.7		Lu_s, Pd_s ; 298 K	Selhaoui and Kleppa 1993d
	LuPd	−91.1		(same)	react. and drop calorim. 1473 K
Th–Pd	$Th_{0.16}Pd_{0.84}$	−67.2	−1.6	α-Th, Pd_s; 1073 K	Schaller 1979 emf sol. electrolyte 973–1073 K
	$ThPd_4$	−90.0	(b)	α-Th, Pd_s	Möbius 1978 emf coupled reduction 1423 K
U–Pd	U_2Pd_{11}	−60.8	(c)	γ-U, Pd_s	Schmidt 1974 or Möbius et al. 1986
	UPd_5	−61.7	(d)	U_l, Pd_s	emf coupled reduction 1073–1673 K
	UPd_4	−69.9	(d)	U_l, Pd_s	
	UPd_3	−131		α-U, Pd_s; 298 K	Wijbenga 1982 fluorine bomb calorim.
	UPd_3	−62	(e)	U_l, Pd_s; 1673 K	Lorenzelli and Marcon 1972 vap. press. 1673 K
	UPd_3	−71.5		α-U, Pd_s; 298 K	Jung and Kleppa 1991a solute+solvent drop calorim. 1473 K
	UPd_3	−73.7		α-U, Pd_s; 298 K	Jung and Kleppa 1991a mixing and drop calorim. 1473 K

continued on next page

Table 6, *continued*

System	Compound	$\Delta_f H°$	$\Delta_f S°$	Reference state	Authors and method
Am–Pd	$AmPd_4$	−83.1	−7.4	unknown	Möbius 1978 emf coupled reduction

[a] $\Delta_f G°$, 1573 K.
[b] $\Delta_f G°$, 1423 K.
[c] $\Delta_f G°$, 1073 K.
[d] $\Delta_f G°$, 1473 K.
[e] $\Delta_f G°$.

In several systems disagreement between values obtained by different authors using various methods has been noticed but it is impossible to determine the reason for this disagreement. In the Ce–Pd system the value of the enthalpy of formation at equiatomic composition obtained by Palenzona and Cirafici (1975a,b) differs considerably from the value obtained by Bretschneider and Schaller (1990b). This is also the case in the Gd–Pd system where the values of the enthalpy of formation of Gd–Pd intermetallic compounds obtained by Colinet et al. (1987c) differ considerably from the value obtained by Palenzona and Cirafici (1975a). However, for the $GdPd_3$ compound Colinet et al. (1987c) found a value for the enthalpy of formation which is in good agreement with that obtained by Paasch and Schaller (1983). This discrepancy has been studied recently by Borzone et al. (1990). These authors have remarked that the values obtained by Palenzona and Cirafici (1975a) and by Zaitsev et al. (1986b) for the compound TbPd are in good agreement. They have also pointed out that it is impossible to have a large difference in the enthalpies of formation of TbPd and GdPd compounds. Unfortunately the study performed by Borzone et al. (1990) on phase diagram optimization did not allow them to make a choice.

There is some disagreement between the values of the enthalpies of formation of GdPt compounds obtained by Colinet et al. (1987c) using aluminum solution calorimetry and those derived from emf measurements by Jacob and Waseda (1990c). However the value proposed by Palenzona and Cirafici (1978) for the equiatomic composition is in good agreement with the value obtained by interpolation between Gd_3Pt_4 and Gd_2Pt by Colinet et al. (1987c) (fig. 50).

The values of the Gibbs energies of formation obtained by Möbius et al. (1986) and Peterson (1985b) for the compounds $PuPt_5$ and $PuPt_3$ differ considerably.

Considering the values obtained by Campbell (1976) for alloys of Pu with Ru and Os one observes a rather large disagreement with the values obtained by Peterson (1980, 1985b). Moreover it seems unlikely that the enthalpies of formation of $PuRu_2$ and $PuOs_2$ compounds should be less exothermic than the enthalpy of formation of the $PuFe_2$ compound (Campbell 1976).

In the U–Fe system a large scatter exists in thc values obtained for the UFe_2 compound (see table 11).

In some systems, only one determination has been made, using an experimental method which cannot be considered as very reliable. This is the case for the values published by Deodhar and Ficalora (1975) who obtained widely divergent values for the enthalpies of

Table 7
Enthalpies and entropies of formation of intermetallic compounds of Pt with rare earths and actinides ($\Delta_f H^\circ$: kJ/mol of atoms, $\Delta_f S^\circ$: $J\,K^{-1}$/mol of atoms)

System	Compound	$\Delta_f H^\circ$	$\Delta_f S^\circ$	Reference state	Authors and method
Sc–Pt	$ScPt_3$	−103.4	−5.9	α-Sc, Pts; 1273–1673 K	Möbius 1978 emf coupled reduction 1273–1673 K
	ScPt	−104.8		α-Sc, Pts; 298 K	Selhaoui and Kleppa 1993a react. and drop calorim. 1473 K
Y–Pt	YPt_5	−64.3	−0.9	α-Y, Pt_s; 1100–1700 K	Hellwig 1978
	YPt_3	−96.7	−4.9	(same)	emf coupled reduction 1100–1700 K
	YPt_3	−86.9		α-Y, Pt_s; 298 K	Selhaoui and Kleppa 1993b
	YPt	−104.0			react. and drop calorim. 1473 K
La–Pt	$LaPt_5$	−62.2	−1.1	β-La, Pt_s; 870–1100 K	Jacob and Waseda 1990a emf sol. electrolyte 870–1100 K
	$LaPt_5$	−72.8	−8.0	La,[a] Pt_s; 1073–1373 K	Kemmler 1977
	$LaPt_2$	−128.0	−17.0	La_l, Pt_s; 1373–1673 K	emf sol. electrolyte 1073–1673 K
	LaPt	−87.0		β-La, Pt_s; 903 K	Palenzona and Cirafici 1978
		−86.8		α-La, Pt_s	diff. dyn. calorim. 903 K
	$LaPt_2$	−90.0		α-La, Pt_s; 298 K	Selhaoui and Kleppa 1993c
	LaPt	−92.1			react. and drop calorim. 1473 K
Ce–Pt	$CePt_5$	−61.2	−1.0	γ-Ce, Pt_s; 870–999 K	Jacob and Waseda 1990a
	$CePt_5$	−61.7	−1.5	δ-Ce, Pt_s; 999–1070 K	emf sol. electrolyte 870–1070 K
		−61.2	−1.0	γ-Ce, Pt_s	
	$CePt_5$	−71.0	−8.0	Ce_l, Pt_s; 1073–1373 K	Kemmler 1977
		−69.6	−6.7	γ-Ce, Pt_s	emf coupled reduction 1073–1673 K
	$CePt_2$	−131.3	−20.7	Ce_l, Pt_s; 1373–1673 K	
		−128.5	−18.0	γ-Ce, Pt_s	
	CePt	−102.9		γ-Ce, Pt_s; 883 K	Palenzona and Cirafici 1978 dyn. diff. calorim. 883 K
	$CePt_2$	−90.6		γ-Ce, Pt_s; 298 K	Selhaoui and Kleppa 1993d
	CePt	−103.8			react. and drop calorim. 1473 K
Pr–Pt	$PrPt_5$	−61.8	−0.8	α-Pr, Pt_s; 870–1100 K	Jacob and Waseda 1990a emf sol. electrolyte 870–1100 K
	$PrPt_5$	−74.0	−8.7	Pr,[a] Pt_s; 1073–1373 K	Kemmler 1977
	$PrPt_2$	−132.0	−18.3	Pr_l, Pt_s; 1373–1673 K	emf coupled reduction 1073–1673 K
		−128.6	−15.4	α-Pr, Pt_s;	
	PrPt	−101.7		α-Pr, Pt_s; 923 K	Palenzona and Cirafici 1978 dyn. diff. calorim. 923 K
Nd–Pt	$NdPt_5$	−61.9	−0.92	α-Nd, Pt_s; 900–1100 K	Jacob and Waseda 1990d emf sol. electrolyte 900–1100 K
	$NdPt_5$	−72.5	−8.3	Nd,[a] Pt_s; 1073–1373 K	Kemmler 1977
	Nd_2Pt_7	−92.4	−11.8	Nd,[b] Pt_s; 1273–1673 K	emf coupled reduction 1073–1673 K
	$NdPt_2$	−138.7	−24.0	Nd_l, Pt_s; 1373–1673 K	
		−135.3	−21.3	α-Nd, Pt_s	
	NdPt	−99.2		α-Nd, Pt_s; 973 K	Palenzona and Cirafici 1978 dyn. diff. calorim. 973 K
Sm–Pt	$SmPt_5$	−62.6	−0.8	α-Sm, Pt_s; 900–1100 K	Jacob and Waseda 1990d emf sol. electrolyte 900–1100 K

continued on next page

Table 7, *continued*

System	Compound	$\Delta_f H^\circ$	$\Delta_r S^\circ$	Reference state	Authors and method
	$SmPt_5$	−69.0	−5.2	Sm,[a] Pt_s; 1073–1373 K	Kemmler 1977
	Sm_2Pt_7	−90.4	−9.3	Sm,[b] Pt_s; 1273–1673 K	emf coupled reduction 1073–1673 K
	$SmPt_2$	−133.0	−18.7	Sm_l, Pt_s; 1373–1673 K	
		−129.1	−15.7	α-Sm, Pt_s	
	SmPt	−93.3		α-Sm, Pt_s; 993 K	Palenzona and Cirafici 1978 dyn. diff. calorim. 993 K
Eu–Pt	$EuPt_5$	−44.0	+0.42	Eu_s, Pt_s; 900–1100 K	Jacob and Waseda 1990d emf sol. electrolyte 900–1100 K
	$EuPt_5$	−55.5	−8.3	Eu,[a] Pt_s; 1073–1373 K	Kemmler 1977
	Eu_2Pt_7	−70.2	−11.6	Eu_l, Pt_s; 1273–1673 K	emf coupled reduction 1073–1673 K
		−68.2	−9.7	Eu_s, Pt_s	
	$EuPt_2$	−98.7	−17.7	Eu_l, Pt_s; 1373–1673 K	
		−95.6	−14.9	Eu_s, Pt_s	
Gd–Pt	$Gd_{0.28}Pt_{0.72}$	−74.1		α-Gd, Pt_s; 298 K	Colinet et al. 1987c
	$GdPt_2$	−94.2		(same)	Al sol'n calorim. 1091 K
	Gd_3Pt_4	−96.1		(same)	
	Gd_2Pt	−71.5		(same)	
	Gd_7Pt_3	−72.6		(same)	
	Gd_3Pt	−59.4		(same)	
	$GdPt_5$	−60.7	−1.3	α-Gd, Pt_s; 925–1125 K	Jacob and Waseda 1990c
	$Gd_{0.23}Pt_{0.77}$	−78.2	−1.8	(same)	emf sol. electrolyte 925–1125 K
	$Gd_{0.25}Pt_{0.75}$	−83.3	−1.9	(same)	
	$Gd_{0.28}Pt_{0.72}$	−91.7	−2.1	(same)	
	$Gd_{0.32}Pt_{0.68}$	−94.8	+2.5	(same)	
	$Gd_{0.33}Pt_{0.67}$	−96.1	+2.1	(same)	
	$Gd_{0.43}Pt_{0.57}$	−103.6	+1.31	(same)	
	GdPt	−104.0	−0.8	(same)	
	$GdPt_5$	−73.0	−8.5	α-Gd, Pt_s; 925–1125 K	Kemmler 1977
	Gd_2Pt_7	−91.8	−10.0	Gd,[a] Pt_s; 1273–1673 K	emf coupled reduction 1073–1673 K
	$GdPt_2$	−137.3	−20.0	Gd,[a] Pt_s; 1373–1673 K	
	GdPt	−89.5		α-Gd, Pt_s; 1153 K	Palenzona and Cirafici 1978 dyn. diff. calorim. 1153 K
Tb–Pt	$TbPt_5$	−62.7	−0.7	α-Tb, Pt_s; 970–1100 K	Jacob and Waseda 1990a emf sol. electrolyte 870–1100 K
	$TbPt_5$	−73.7	−7.3	α-Tb, Pt_s; 1073–1373 K	Kemmler 1977
	$TbPt_3$	−106.3	−11.5	Tb_s,[a] Pt_s; 1273–1573 K	emf coupled reduction 1073–1673 K
	TbPt	−87.0		α-Tb, Pt_s; 1153 K	Palenzona and Cirafici 1978 dyn. diff. calorim. 1153 K
Dy–Pt	$DyPt_5$	−63.6	−1.2	α-Tb, Pt_s; 900–1100 K	Jacob and Waseda 1990d emf liq. electrolyte 900–1100 K
	$DyPt_5$	−73.0	−8.0	α-Dy, Pt_s; 1073–1373 K	Kemmler 1977
	$DyPt_3$	−106.0	−12.8	α-Dy, Pt_s; 1273–1573 K	emf coupled reduction 1073–1673 K
	DyPt	−85.4		α-Dy, Pt_s; 1153 K	Palenzona and Cirafici 1978 dyn. diff. calorim. 1153 K
Ho–Pt	$HoPt_5$	−62.8	−0.72	α-Ho, Pt_s; 900–1100 K	Jacob and Waseda 1990d emf sol. electrolyte 900–1100 K

continued on next page

Table 7, *continued*

System	Compound	$\Delta_f H°$	$\Delta_f S°$	Reference state	Authors and method
	$HoPt_5$	−74.2	−7.8	α-Ho, Pt_s; 1073–1373 K	Kemmler 1977
	$HoPt_3$	−110.5	−14.0	α-Ho, Pt_s; 1273–1573 K	emf coupled reduction 1073–1673 K
	HoPt	−83.7		α-Ho, Pt_s; 1183 K	Palenzona and Cirafici 1978 dyn. diff. calorim. 1183 K
Er–Pt	$ErPt_5$	−63.5	−0.77	Er_s, Pt_s; 900–1100 K	Jacob and Waseda 1990d emf sol. electrolyte 900–1100 K
	$ErPt_5$	−74.0	−7.5	Er_s, Pt_s; 1073–1373 K	Kemmler 1977
	$ErPt_3$	−110.5	−12.5	Er_s, Pt_s; 1273–1573 K	emf coupled reduction 1073–1573 K
	ErPt	−81.2		Er_s, Pt_s; 1293 K	Palenzona and Cirafici 1978 dyn. diff. calorim. 1293 K
Tm–Pt	$TmPt_5$	−61.4	−0.81	Tm_s, Pt_s; 870–1100 K	Jacob and Waseda 1990a emf sol. electrolyte 870–1100 K
	$TmPt_5$	−72.2	−7.7	Tm_s, Pt_s; 1073–1373 K	Kemmler 1977
	$TmPt_3$	−110.8	−14.0	Tm_s, Pt_s; 1273–1573 K	emf sol. electrolyte 1073–1573 K
Yb–Pt	$YbPt_3$	−80.5	−0.1	α-Yb, Pt_s; 1000 K	Jacob and Waseda 1990b emf sol. electrolyte 880–1100 K
	$YbPt_3$	−103.5	−14.3	Yb,[a] Pt_s; 1073–1373 K	Kemmler 1977 emf coupled reduction 1073–1673 K
Lu–Pt	$LuPt_3$	−91.7	−1.0	Lu_s, Pt_s; 1000 K	Jacob and Waseda 1990b emf sol. electrolyte 880–1100 K
	$LuPt_3$	−111.0	−14.0	Lu_s, Pt_s; 1273–1573 K	Kemmler 1977 emf coupled reduction 1273–1573 K
	$LuPt_3$	−89.2		Lu_s, Pt_s; 298 K	Selhaoui and Kleppa 1993d
	LuPt	−90.6			react. and drop calorim. 1473 K
Th–Pt	$ThPt_5$	−93.4	−11	Th_s,[a] Pt_s; 1323–1673 K	Möbius 1978 or Möbius et al. 1986 emf coupled reduction 1323–1673 K
U–Pt	UPt_5	−81.7	−9.2	U,[a] Pt_s; 873–1673 K	Schmidt 1974 or Möbius et al. 1986
	UPt_3	−111.1	−12.7	(same)	emf coupled reduction 873–1673 K
	UPt_2	−127.5	−15.2	(same)	
Np–Pt	$NpPt_5$	−51.7	−3.0	Np_l, Pt_s; 1100–1600 K	Hellwig 1978 or Möbius et al. 1986
	$NpPt_3$	−80.3	−9.0	(same)	emf coupled reduction 1100–1600 K
Pu–Pt	$PuPt_5$	−49.9	−14.3	Pu_l, Pt_s; 1614 K	Peterson 1985b
		−44.1[b]		α-Pu, Pt_s; 298 K	vap. press. Knudsen with mass.
	$PuPt_4$	−54.6	−14.2	Pu_l, Pt_s; 1596 K	spect.
		−49.0[b]		α-Pu, Pt_s; 298 K	
	$PuPt_3$	−61.7	−15.2	Pu_l, Pt_s; 1579 K	
		−54.8[b]		α-Pu, Pt_s; 298 K	
	$PuPt_2$	−70.5	−15.3	Pu_l, Pt_s; 1629 K	
		−63.3[b]		α-Pu, Pt_s; 298 K	
Am–Pt	$AmPt_5$	−73.2	−8	Am,[a] Pt_s; 1073–1673 K	Möbius 1978 or Möbius et al. 1986
	$AmPt_2$	−137.7	−19	(same)	emf coupled reduction 1073–1673 K

[a] Aggregation state not specified.

[b] Using the Third Law.

Table 8
Enthalpies and entropies of formation of intermetallic compounds of Co with rare earths and actinides ($\Delta_f H°$: kJ/mol of atoms, $\Delta_f S°$: J K^{-1}/mol of atoms)

System	Compound	$\Delta_f H°$	$\Delta_f S°$	Reference state	Authors and method
Sc–Co	$ScCo_2$	−32.5		α-Sc, α-Co; 298 K	Selhaoui and Kleppa 1993a
	Sc_2Co	−26.7		(same)	react. and drop calorim. 1473 K
Y–Co	Y_2Co_{17}	−7.6	0.2	α-Y, β-Co; 973 K	Subramanian and Smith 1985a
		−7.2	0.8	α-Y, α-Co	emf sol. electrolyte 850–1200 K
	YCo_5	−12.2	−0.2	α-Y, β-Co; 973 K	
		−11.8	0.3	α-Y, α-Co	
	Y_2Co_7	−17.3	−1.4	α-Y, β-Co; 973 K	
		−16.9	−0.9	α-Y, α-Co	
	YCo_3	−19.4	−1.6	α-Y, β-Co; 973 K	
		−19.1	−1.1	α-Y, α-Co	
	YCo_2	−22.8	−2.4	α-Y, β-Co; 973 K	
		−22.5	−2.0	α-Y, α-Co	
	Y_2Co_3	−27.1	−6.5	α-Y, β-Co; 973 K	
		−26.8	−6.1	α-Y, α-Co	
	Y_9Co_7	−26.0	−7.2	α-Y, β-Co; 973 K	
		−25.8	−6.9	α-Y, α-Co	
	Y_8Co_5	−21.8	−3.3	α-Y, β-Co; 973 K	
		−21.6	−3.1	α-Y, α-Co	
	Y_3Co	−15.8	−0.7	α-Y, β-Co; 973 K	
		−15.7	−0.5	α-Y, α-Co	
	YCo_5	−5.9		α-Y, α-Co; 298 K	Meyer-Liautaud et al. 1987b
					Sn sol'n calorim. 1173 K
	YCo_5	−13.8		α-Y, α-Co; 298 K	Colinet and Pasturel 1987
					Al sol'n calorim. 989 K
	YCo_3	−20.0		α-Y, α-Co; 298 K	Sidorov et al. 1989
					solute + solvent drop calorim. 1873 K
La–Co	$LaCo_{13}$	−4.1	−0.1	β-La, β-Co; 1134–1193 K	Rezukhina and Kutsev 1982b
		−3.7	0.5	α-La, α-Co	emf liq. electrolyte 940–1193 K,
	$LaCo_5$	−3.9	2.3	β-La, β-Co; 1134–1193 K	depending of the domain
		−3.5	2.9	α-La, α-Co	
	La_2Co_7	−5.2	2.0	β-La, β-Co; 1050–1078 K	
		−4.8	2.6	α-La, α-Co	
	La_2Co_3	−7.6	0.9	β-La, β-Co; 940–970 K	
		−7.2	1.5	α-La, α-Co	
	$LaCo_{13}$	−3, −4		Unknown	Shilov et al. 1983
	$LaCo_5$	−6.8		(same)	indirect determination
	$LaCo_5$	−2.9		α-La, α-Co; 298 K	Colinet et al. 1987a
					Al sol'n calorim. 990 K
	$LaCo_{13}$	−11.6	−11.4	β-La, β-Co; 713 K	Kazanskii and Ilyushchenko 1987
		−11.2	−10.8	α-La, α-Co	emf liq. electrolyte T ≈ 713 K[a]
	$LaCo_5$	−16.8	−15.3	β-La, β-Co; 713 K	
		−16.4	−14.7	α-La, α-Co	
	La_2Co_7	−16.5	−14.5	β-La, β-Co; 713 K	
		−16.1	−13.9	α-La, α-Co	
	La_2Co_3	−14.8	−12.2	β-La, β-Co; 713 K	
		−14.4	−11.6	α-La, α-Co	
	$La_2Co_{1.7}$	−12.1	−9.6	β-La, β-Co; 713 K	
		−12.7	−8.9	α-La, α-Co	

continued on next page

Table 8, *continued*

System	Compound	$\Delta_f H^\circ$	$\Delta_f S^\circ$	Reference state	Authors and method
La–Co	La_3Co	−7.7	−5.6	β-La, β-Co; 713 K	Kazanskii and Ilyushchenko 1987
(*cont'd*)		−7.3	−4.9	α-La, α-Co	emf liq. electrolyte $T \approx 713$ K[a]
Ce–Co	$CeCo_5$	−20.1		γ-Ce, α-Co; 298 K	Semenenko et al. 1982
	$CeCo_3$	−19.3		(same)	acid sol'n calorim.
	$CeCo_2$	−18.6		(same)	
	$CeCo_5$	−13.2		γ-Ce, α-Co; 298 K	Meyer-Liautaud et al. 1987b
					Sn sol. calorim. 1173 K
Pr–Co	$PrCo_2$	−4.3		α-Pr, β-Co; 778 K	Deodhar and Ficalora 1975
		−4.0		α-Pr, α-Co	diff. therm. anal. 778 K
Sm–Co	Sm_2Co_{17}	−8.2		Unknown	Shilov 1987
	$SmCo_5$	−11.7		(same)	indirect determination
	Sm_2Co_7	−14.4		(same)	
	$SmCo_3$	−15.6		(same)	
	$SmCo_2$	−17.8		(same)	
	Sm_2Co_{17}	−8		α-Sm, α-Co; 298 K	Meyer-Liautaud et al. 1987a
	$SmCo_5$	−6.8		(same)	Sn sol'n calorim. 1173 K
	Sm_2Co_7	−11		(same)	
Gd–Co	Gd_2Co_{17}	−8.1		α-Gd, α-Co; 298 K	Colinet et al. 1987c
	$GdCo_5$	−13.8		(same)	Al sol'n calorim. at 1000 K
	$GdCo_3$	−18.3		(same)	
	$GdCo_2$	−17.4		(same)	
	Gd_4Co_3	−12.3		(same)	
	$Gd_{12}Co_7$	−10.5		(same)	
	Gd_3Co	−8.8		(same)	
	Gd_2Co_{17}	−4.5		α-Gd, α-Co; 298 K	Schott and Sommer 1986
	$GdCo_5$	−8.3		(same)	Sn sol. calorim 1095 K
	$GdCo_2$	−11.7		(same)	
	$Gd_{12}Co_7$	−6.3		(same)	
	$GdCo_2$	−10.7		α-Gd, β-Co; 1000 K	Deodhar and Ficalora 1975
		−10.4		α-Gd, α-Co	diff. therm. anal. 1000 K
Dy–Co	Dy_2Co_{17}	−8.7		α-Gd, α-Co; 298 K	Schott and Sommer 1986
	$DyCo_3$	−18.3		(same)	Sn sol'n calorim. 1098 K
	$DyCo_2$	−17.4		(same)	
	$DyCo_2$	−9.1		α-Gd, β-Co; 964 K	Deodhar and Ficalora 1975
		−8.8		α-Gd, α-Co	diff. therm. anal. 964 K
Er–Co	$ErCo_3$	−15.1		Er_s, α-Co; 298 K	Schott and Sommer 1986
	$ErCo_2$	−18.8		(same)	Sn sol'n calorim. 1098 K
	Er_3Co	−7.0		(same)	
	$ErCo_2$	−11.5		Er_s, β-Co; 1023 K	Deodhar and Ficalora 1975
		−11.2		Er_s, α-Co	diff. therm. anal. 1023 K
Th–Co	Th_2Co_{17}	−16.5	−3.3	α-Th, β-Co; 973 K	Skelton et al. 1971
		−16.1	−2.7	α-Th, α-Co	emf sol. electrolyte 917–1233 K
	$ThCo_5$	−29.9	−8.9	α-Th, β-Co; 973 K	
		−29.5	−8.4	α-Th, α-Co	
	Th_2Co_7	−41.8	−14.3	α-Th, β-Co; 973 K	
		−41.4	−13.8	α-Th, α-Co	
	ThCo	−46.8	−14.3	α-Th, β-Co; 973 K	
		−46.6	−14.0	α-Th, α-Co	
	Th_7Co_3	−28.1	−3.3	α-Th, β-Co; 973 K	
		−28.0	−3.1	α-Th, α-Co	

continued on next page

Table 8, *continued*

System	Compound	$\Delta_f H°$	$\Delta_f S°$	Reference state	Authors and method
U–Co	U_2Co_{11}	−23.8	−6.3	γ-U, β-Co; 1000 K	Lebedev et al. 1973c
		−22.3	−4.6	α-U, α-Co	emf liq. electrolyte 873–1123 K;
	UCo_4	−32.2	−10.6	γ-U, β-Co; 1000 K	reviewed by Chiotti et al. 1981 [b]
		−30.3	−8.6	α-U, α-Co	
	UCo_3	−48.5	−22.6	γ-U, β-Co; 1000 K	
		−46.3	−20.2	α-U, α-Co	
	UCo_2	−68.6	−36.7	γ-U, β-Co; 1000 K	
		−65.8	−33.8	α-U, α-Co	
	U_5Co_7	−68.6	−38.3	γ-U, β-Co; 1000 K	
		−65.2	−34.8	α-U, α-Co	
	U_7Co_9	−67.3	−37.9	γ-U, β-Co; 1000 K	
		−63.7	−34.3	α-U, α-Co	
	UCo	−64.9	−37.7	γ-U, β-Co; 1000 K	
		−60.9	−33.6	α-U, α-Co	
	U_6Co	−46.9	−36.6	γ-U, β-Co; 1000 K	
		−40.4	−30.1	α-U, α-Co	
	U_2Co_{11}	−15.9	1.1	β-U, β-Co T<1053 K	Yoshihara and Kanno 1974a, Kanno
		−15.1	2.1	α-U, α-Co	1974
		−16.7	−0.4	γ-U, β-Co T>1053 K	emf liq. electrolyte 993–1153 K
		−15.2	1.3	α-U, α-Co	

[a] The values given by Kazanskii and Ilyushchenko (1987) were the Gibbs energy of formation of the compounds at 713 K, $\Delta_f G$ ($LaCo_{13}$, −3.5; $LaCo_5$: −5.9; La_2Co_7, −6.1; La_2Co_3, −6.0; $La_2Co_{1.7}$, −5.3; La_3Co, −3.7 kJ/mol of atoms). We have calculated the values of $\Delta_f H°$ and $\Delta_f S°$ from the expressions of the emf in each domain.

[b] The compound UCo was not detected by Lebedev et al. (1973c); Chiotti et al. (1981) estimated the values of $\Delta_f H$ and $\Delta_f S$ for this compound.

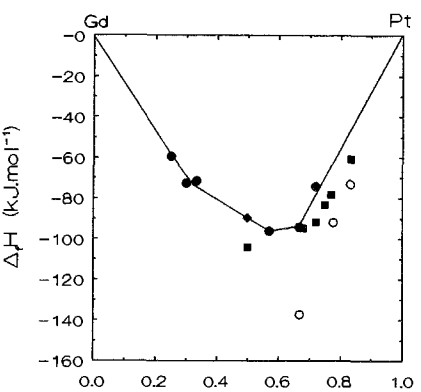

Fig. 50. Enthalpies of formation of the intermetallic compounds in the Gd–Pt system. The data are from Colinet et al. (1987c) (solid circles), Jacob and Waseda (1990c) (solid squares), Palenzona and Cirafici (1978) (solid diamonds) and Kemmler (1977) (open circles).

Table 9
Enthalpies and entropies of formation of intermetallic compounds of Rh with rare earths and actinides ($\Delta_f H°$: kJ/mol of atoms, $\Delta_f S°$: JK^{-1}/mol of atoms)

System	Compound	$\Delta_f H°$	$\Delta_f S°$	Reference state	Authors and method
ScRh	$ScRh_3$	−51.7		α-Sc, Rh_s; 298 K	Selhaoui and Kleppa 1993a
	ScRh	−94.5		(same)	react. and drop calorim. 1473 K
Y–Rh	YRh_2	−65.4		α-Y, Rh_s; 298 K	Selhaoui and Kleppa 1993b
	YRh	−76.1		(same)	react. and drop calorim. 1473 K
La–Rh	$LaRh_2$	−57.5		α-La, Rh_s; 298 K	Selhaoui and Kleppa 1993c
	LaRh	−56.3		(same)	react. and drop calorim. 1473 K
Ce–Rh	$CeRh_3$	−55.2		γ-Ce, Rh_s; 298 K	Selhaoui and Kleppa 1993d
	$CeRh_2$	−66.5		(same)	react. and drop calorim. 1473 K
	Ce_5Rh_4	−70.5		(same)	
Lu–Rh	$LuRh_2$	−68.1		Lu_s, Rh_s; 298 K	Selhaoui and Kleppa 1993d
	Lu_3Rh_2	−58.7		(same)	react. and drop calorim. 1473 K
Th–Rh	$ThRh_5$	−56.1	−8.4	α-Th, Rh_s; 990–1170 K	Murabayashi and Kleykamp 1975
	$ThRh_3$	−83.7	−12.1	(same)	emf sol. electrolyte 990–1170 K
	$ThRh_2$	−98.3	−12.6	(same)	
	Th_3Rh_5	−105.4	−13.0	(same)	
	Th_3Rh_4	−111.3	−10.0	(same)	
	ThRh	−119.7	−15.5	(same)	
	Th_7Rh_3	−79.1	−13.4	(same)	
	$ThRh_5$	−55.9	−7.9	α-Th, Rh_s; 1100 K	Assessment of Chiotti et al. 1981
	$ThRh_3$	−83.7	−11.9	(same)	
	$ThRh_2$	−98.3	−12.4	(same)	
	Th_3Rh_5	−105.6	−12.7	(same)	
	Th_3Rh_4	−114.5	−13.0	(same)	
	ThRh	−116.7	−12.7	(same)	
	Th_7Rh_3	−77.5	−11.8	(same)	
U–Rh	URh_3	−70.6	−27	U_s[a], Rh_s; 1000–1200 K	Naraine and Bell 1974
	U_3Rh_5	−77.9	−32	(same)	emf sol. electrolyte 1000–1200 K;
	U_3Rh_4	−78.2	−32	(same)	893–978 K for U_2Rh
	URh	−76.4	−34	(same)	
	U_2Rh	−60.7	−28	U_s[a], Rh_s; 893–978 K	
	URh_3	−79.1	−2.3	U_s[a], Rh_s; 950–1115 K	Wijbenga and Cordfunke 1982
		−75.3[b]		α-U, Rh_s; 298 K	emf sol. electrolyte 950–1115 K
	URh_3	−64.0	+1.1	U_s[a], Rh_s; 1100 K	Holleck and Kleykamp 1972/73
					emf sol. electrolyte 1000–1150 K
	URh_3	−106.2	−20	U[a], Rh_s; 1073–1773 K	Schmidt 1974
					emf sol. electrolyte 1073–1773 K
	URh_3	−79.1	−3.3	U_s[a], Rh_s; 980–1320 K	Jacob and Chandrasekharaiah 1990
		−73.3[b]		α-U, Rh_s; 298 K	emf sol. electrolyte 980–1320 K
	URh_3	−69.7		α-U, Rh_s; 298 K	Jung and Kleppa 1991a
					mixing and drop calorim. 1473 K
	URh_3	−78.4	−5.2	U_s,[a] Rh_s; 900–1100 K	Kleykamp 1991b
		−74.2[b]		α-U, Rh_s; 298 K	emf sol. electrolyte 900–1100 K

continued on next page

Table 9, *continued*

System	Compound	$\Delta_f H^\circ$	$\Delta_f S^\circ$	Reference state	Authors and method
Pu–Rh	$PuRh_3$	−62.7	−18.7	Pu_l,Rh_s; 1725 K	Peterson 1985b
		−49.5[b]		α-Pu, Rh_s; 298 K	vap. press. Knudsen.
	$PuRh_2$	−75.0	−20.0	Pu_l, Rh_s; 1519 K	
		−59.8[b]		α-Pu, Rh_s; 298 K	

[a] Aggregation state of U not specified. [b] Using the Third Law.

Table 10

Enthalpies and entropies of formation of intermetallic compounds of Ir with rare earths and actinides ($\Delta_f H^\circ$: kJ/mol of atoms, $\Delta_f S^\circ$: $J\,K^{-1}$/mol of atoms)

System	Compound	$\Delta_f H^\circ$	$\Delta_f S^\circ$	Reference state	Authors and method
Sc–Ir	$ScIr_2$	−66.3		α-Sc, Ir_s; 298 K	Selhaoui and Kleppa 1993a
	ScIr	−89.7		(same)	react. and drop calorim. 1473 K
	$Sc_{0.52}Ir_{0.48}$	−90.1		(same)	
	$Sc_{0.6}Ir_{0.4}$	−82.0		(same)	
Y–Ir	YIr_2	−59.4		α-Y, Ir_s; 298 K	Selhaoui and Kleppa 1993b
	YIr	−65.9		(same)	react. and drop calorim. 1473 K
	Y_3Ir_2	−62.5		(same)	
La–Ir	$LaIr_2$	−61.4	−1.6	β-La, Ir_s; 950–1200 K	Rezukhina et al. 1973
					emf sol. electrolyte 950–1200 K
	$LaIr_3$	−49.7		α-La, Ir_s; 298 K	Selhaoui and Kleppa 1993c
	$LaIr_2$	−62.9		(same)	react. and drop calorim. 1473 K
Ce–Ir	$CeIr_5$	−44.4	1.1	Ce[a], Ir_s; 1000–1200 K	Dmitrieva et al. 1973
	Ce_2Ir_7	−58.9	1.1	(same)	emf sol. electrolyte 1000–1200 K
	$CeIr_3$	−65.7	1.3	(same)	
	$CeIr_2$	−87.2	−0.1	(same)	
	$CeIr_2$	−73.8		γ-Ce, Ir_s; 298 K	Selhaoui and Kleppa 1993d
					react. and drop calorim. 1473 K
Lu–Ir	$LuIr_2$	−71.0		Lu_s, Ir_s; 298 K	Selhaoui and Kleppa 1993d
	LuIr	−85.5		(same)	react. and drop calorim. 1473 K
Th–Ir	$ThIr_5$	−59.2	−7.5	α-Th, Ir_s; 1200–1250 K	Kleykamp 1979
	$ThIr_3$	−73.8	(b)	α-Th, Ir_s	emf sol. electrolyte 1200–1250 K
U–Ir	UIr_3	−108.8	−22.0	U[a], Ir_s; 1073–1773 K	Schmidt 1974
					emf sol. electrolyte 1073–1773 K
	UIr_3	−60.9	+2.4	U_s[a], Ir_s; 1040–1130 K	Holleck et al. 1990
	UIr_2	−71.3	1.1	U_s[a], Ir_s; 940–1090 K	emf sol. electrolyte 940–1130 K;
					a revision of the results obtained by Holleck et al. 1975
Pu–Ir	$PuIr_2$	−69.2	−2.2	Pu_l, Ir_s; 1929 K	Peterson and Starzynski 1985
		−65.1[c]		α-Pu, Ir_s; 298 K	vap. press. Knudsen 1600–2100 K
Am–Ir	$AmIr_2$	−85.4			Peterson and Starzynski 1985
					estimation 1929 K

[a] Aggregation state not specified. [b] $\Delta_f G^\circ$,1200 K [c] Using the Third Law.

Table 11
Enthalpies and entropies of formation of intermetallic compounds of Fe with rare earths and actinides ($\Delta_f H°$: kJ/mol of atoms, $\Delta_f S°$: $J K^{-1}$/mol of atoms)

System	Compound	$\Delta_f H°$	$\Delta_f S°$	Reference state	Authors and method
Sc–Fe	$ScFe_2$	≈ -11.2		α-Sc, α-Fe; 298 K	Selhaoui and Kleppa 1993a react. and drop calorim. 1473 K
Y–Fe	Y_2Fe_{17}	−6.4	−1.9	α-Y, α-Fe; 973 K	Subramanian and Smith 1984
	Y_6Fe_{23}	−8.1	−2.2	(same)	emf sol. electrolyte 893–1121 K
	YFe_3	−9.0	−3.0	(same)	
	YFe_2	−7.1	−1.0	(same)	
	YFe_3	−9.0		α-Y, α-Fe; 298 K	Sidorov et al. 1989 solute + solvent drop calorim. 1873 K
GdFe	Gd_2Fe_{17}	−2.3		α-Gd, α-Fe; 298 K	Colinet et al. 1987c
	$GdFe_3$	−9.3		(same)	Al sol. calorim. 1000 K
	$GdFe_2$	−11.6		(same)	
	$GdFe_2$	−3.5		α-Gd, α-Fe; 1078 K	Deodhar and Ficalora 1975 diff. therm. anal. 1078 K
Dy–Fe	$DyFe_2$	−29.3		α-Dy, α-Fe; 1091 K	Deodhar and Ficalora 1975 diff. therm. anal. 1091 K
Er–Fe	$ErFe_2$	−48.8		Er_s, α-Fe; 1138 K	Deodhar and Ficalora 1975 diff. therm. anal. 1138 K
	Er_6Fe_{23}	−39.1		unknown	Shilov et al. 1983
	$ErFe_3$	−47.8		(same)	indirect determination
Th–Fe	Th_2Fe_{17}	−12.5	−5.0	α-Th, α-Fe; 973 K	Skelton et al. 1973
	$ThFe_5$	−19.2	−8.5	(same)	emf sol. electrolyte 928–1164 K
	Th_2Fe_7	−22.8	−11.2	(same)	
	$ThFe_3$	−24.8	−12.6	(same)	
	Th_7Fe_3	−5.0	+1.7	(same)	
U–Fe	UFe_2	−11.0		α-U, α-Fe; 298 K	Ivanov and Podol'skaya 1962 or
	U_6Fe	−2.3		(same)	Akhachinskij et al. 1962 acid sol'n calorim.
	UFe_2	−72.4	−47.3	γ-U, α-Fe; 900 K α-U, α-Fe	Lebedev et al. 1973b emf liq. electrolyte 833–1148 K
	U_6Fe	−23.4	−15.1	γ-U, α-Fe; 900 K α-U, α-Fe	
	UFe_2	−23.5	−3.5	β-U, α-Fe; T<1043 K	Yoshihara and Kanno 1974b
		−24.5	−4.5	γ-U, α-Fe; T>1043 K	emf liq. electrolyte 993–1153 K; see
		−20.6	−0.03	α-U, α-Fe; 298 K	also Campbell 1977
	UFe_2	−11.3	1.8	α-U, α-Fe	Chiotti et al. 1981
	U_6Fe	−2.3	2.3	(same)	calculated from phase diag.; $\Delta_f H$ and $\Delta_f S$ assumed temperature independent
	UFe_2	−17.9	(a)	β-U, α-Fe; 998 K	Gardie et al. 1991
		−18.5	(a)	β-U, α-Fe; 1500 K	vap. press. mass spectro. over liquid
	U_6Fe	−4.4	(a)	γ-U, α-Fe; 998 K	phase and phase diagram
Pu–Fe	$PuFe_2$	−9.1		α-Pu, α-Fe; 298 K	Akhachinskij et al. 1962 acid sol'n calorim.

continued on next page

Table 11, *continued*

System	Compound	$\Delta_f H°$	$\Delta_f S°$	Reference state	Authors and method
	Pu_6Fe	−2.0		α-Pu, α-Fe; 298 K	Akhachinskij et al. 1962 estimation
	$PuFe_2$	−18.6	−4.4	Pu_l, α-Fe; 1000 K	Campbell 1976
		−16.6	−2.0	α-Pu, α-Fe; 298 K	emf liq. electrolyte 793–1099 K
	$PuFe_2$	−15.3	−1.0	ε-Pu, α-Fe; 739–913 K	Chiotti et al. 1981
		−13.1	3.5	α-Pu, α-Fe	assessment 739–913 K

[a] $\Delta_f G°$.

formation of various lanthanides with the same transition metal, so this seems unrealistic. This is also the case for the values presented by Shilov et al. (1983) and Shilov (1987) because the method which was used is quite indirect.

Finally, let us indicate the systems for which recent measurements, which can be considered as being reliable, may help resolve some of the discrepancies previously noted. Several measurements have been performed in the La–Ni system at the 1:5 composition. From the more recent results (Watanabe and Kleppa 1983, Pasturel et al. 1984b, Hubbard et al. 1983, Colinet et al. 1987a) it appears that the enthalpy of formation stands between −26 and −28 kJ/mol of atoms which is a very satisfying result. For the UPd_3, URh_3 and URu_3 compounds, Jung and Kleppa (1991a) performed calorimetric measurements either by solute + solvent drop calorimetry or by mixing and drop calorimetry. The results obtained by Kleppa and coworkers are often used as a reference and may be considered to be very reliable. The results they obtained for the URh_3 compound may be compared with results published simultaneously by Jacob and Chandrasekharaiah (1990) and Kleykamp (1991b) using emf measurements and the Third Law to derive the enthalpy of formation at 298 K. Considering the differences between the methods used the agreement is satisfying.

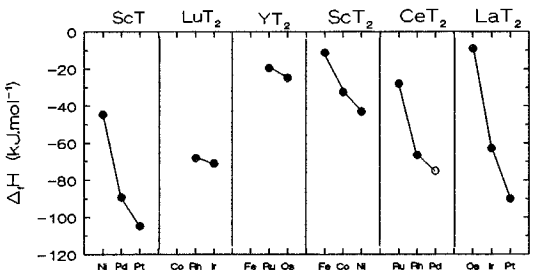

Fig. 51. Enthalpies of formation of the intermetallic compounds of rare earths with transition metals. The data are from Selhaoui and Kleppa (1993a–d).

To conclude the above discussion we see that only a few of the values presented in tables 5–16 can be considered to be trustworthy. Thus, it appears that considerable experimental work is needed for the rare earth or actinide transition metal alloys. However we must point out the results obtained recently by Selhaoui and Kleppa (1993a–d) using reaction and drop calorimetry in rare-earth–transition-metal systems for which no

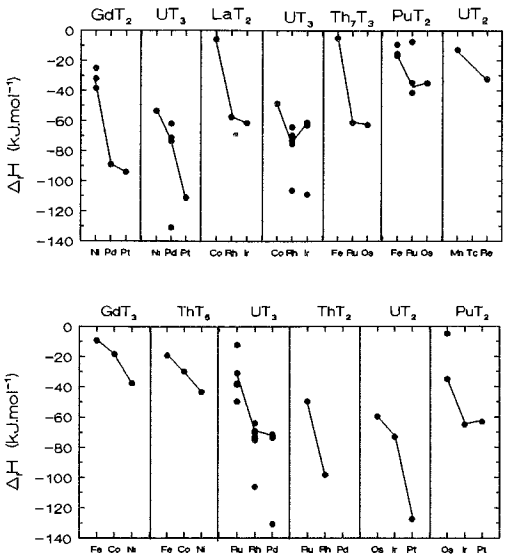

Fig. 52. (top) Enthalpies of formation of intermetallic compounds of lanthanides and actinides (Th, U, Pu) with transition elements of the columns headed by Ni, Co and Fe. (bottom) Enthalpies of formation of intermetallic compounds of gadolinium and actinides (Th, U, Pu) with transition elements of the thirst row (Mn → Ni), second row (Ru → Pd) and third row (Re → Pt). The references of the data are quoted in tables 5 to 20. The data which appear the more reliable have been joined by lines (see the text for discussion).

thermodynamic experiment had been performed up to now. Some of these results are presented in fig. 51.

In the following, we will attempt to derive some trends in the behavior of rare earths and actinides alloyed with transition metals:

(i) When alloyed with the same rare-earth or actinide element the enthalpies of formation become more negative from Ni to Pd and Pt, from Co to Rh and Ir, from Fe to Ru and Os, from Mn to Re. The enthalpies of formation are of the same order of magnitude when elements of the second and third rows of the transition metal series are concerned (figs. 51, 52).

(ii) The enthalpies of formation become less negative from Ni to Mn, Pd to Ru, Pt to Re (figs. 51, 52).

(iii) The alloying behavior of rare earths with the same transition metal is more difficult to discuss because of a lack of data or because of the large discrepancies noted previously. However it seems that in the lanthanide series the enthalpies of formation become slightly more negative from La to Gd and are quite similar for the light lanthanides (see figs. 53 and 54, respectively, for the enthalpies of formation of (R, An)Ni_5 and (R, An)Pt_5 compounds). It seems also that the enthalpies of formation are more negative from La to Y.

(iv) In the actinide series the Gibbs energies and the enthalpies of formation become less negative from thorium to uranium and to plutonium (see figs. 53 and 54 and also figs. 55–58 where the Gibbs energies of formation of Ni, Co, Fe and Rh based alloys, respectively, have been plotted as a function of the composition).

Table 12
Enthalpies and entropies of formation of intermetallic compounds of Ru with rare earths and actinides ($\Delta_f H°$: kJ/mol of atoms, $\Delta_f S°$: J K^{-1}/mol of atoms)

System	Compound	$\Delta_f H°$	$\Delta_f S°$	Reference state	Authors and method
Sc–Ru	ScRu	−44.5		α-Sc, Ru_s; 298 K	Selhaoui and Kleppa 1993a react. and drop calorim. 1473 K
Y–Ru	YRu_2	−19.5		α-Y, Ru_s; 298 K	Selhaoui and Kleppa 1993b
	Y_5Ru_2	−27.3			react. and drop calorim. 1473 K
La–Ru	$LaRu_2$	−11.3		unknown	Shilov et al. 1983 indirect determ.
	$LaRu_2$	−10.3		α-La, Ru_s; 298 K	Selhaoui and Kleppa 1993c react. and drop calorim. 1473 K
Ce–Ru	$CeRu_2$	−27.9		γ-Ce, Ru_s; 298 K	Selhaoui and Kleppa 1993d react. and drop calorim. 1473 K
Nd–Ru	$NdRu_2$	−19.0		unknown	Shilov et al. 1983 ind. determ.
Th–Ru	$ThRu_2$	−49.7	−13.6	α-Th, Ru_s; 1020–1170 K	Kleykamp and Murabayashi 1974
	ThRu	−64.0	−15.3	(same)	emf sol. electrolyte 1020–1170 K
	Th_3Ru_2	−56.3	−10.3	(same)	
	Th_7Ru_3	−54.7	−13.5	(same)	
	$ThRu_2$	−49.7	−13.5	α-Th, Ru_s	Chiotti et al. 1981
	ThRu	−65.1	−16.2	(same)	assessment.
	Th_3Ru_2	−64.6	−17.7	(same)	
	Th_7Ru_3	−61.0	−6.5	(same)	
U–Ru	URu_3	−49.8	−9.0	U_s[a],Ru_s; 950–1130 K	Holleck et al. 1975 and Kleykamp 1991a
		−38.5[b]		α-U,Ru_s; 298 K	emf sol. electrolyte 950–1130 K[c]
	U_3Ru_5	−49.8	−5.5	U_s[a],Ru_s; 960–1130 K	Kleykamp 1991a emf sol. electrolyte 960–1130 K
	URu_3	−44.6	−4.1	γ-U, Ru_s; 1090–1180 K	Wijbenga and Cordfunke 1982
		−37.7[b]		α-U, Ru_s; 298 K	emf sol. electrolyte 1090–1180 K
	URu_3	−19.9	−8.8	U_l, Ru_s; 1896 K	Edwards et al. 1980
		−12.3[b]		α-U, Ru_s; 298 K	vap. press. Knudsen 1690–2100 K
	URu_3	−62.5	(d)	1500 K	Möbius et al. 1986
	URu_3	−31.0		α-U, Ru_s; 298 K	Jung and Kleppa 1991a mixing drop calorimetry 1473 K
Pu–Ru	$PuRu_2$	−37.4	−9.6	Pu_l, Ru_s; 935–1069 K	Campbell et al. 1967
		−34.3	−4.1	α-Pu, Ru_s	emf liq. electrolyte 935–1069 K
	$PuRu_2$	−11.3	−1.8	Pu_l, Ru_s; 1000 K	Campbell 1976
		−7.4		α-Pu, Ru_s; 298 K	emf liq. electrolyte 882–1078 K
	$PuRu_2$	−49.0	−11.3	Pu_l, Ru_s; 1640 K	Peterson 1980
		−41.3[b]		α-Pu, Ru_s; 298 K	vap. press. Knudsen 1503–1778 K

[a] Aggregation state not specified.
[b] Using the Third Law.
[c] Update of previous result of Holleck and Kleykamp (1970).
[d] $\Delta_f G°$.

Table 13
Enthalpies and entropies of formation of intermetallic compounds of Os with rare earths and actinides ($\Delta_f H°$: kJ/mol of atoms, $\Delta_f S°$: J K^{-1}/mol of atoms)

System	Compound	$\Delta_f H°$	$\Delta_f S°$	Reference state	Authors and method
Y–Os	YOs_2	−24.8		α-Y, Os_s; 298 K	Selhaoui and Kleppa 1993b react. and drop calorim. 1473 K
La–Os	$LaOs_2$	−9.0		α-La, Os_s; 298 K	Selhaoui and Kleppa 1993c react. and drop calorim. 1473 K
Th–Os	$ThOs_2$	−53.5	−16.6	α-Th, Os_s; 1020–1220 K	Kleykamp 1979
	Th_3Os_2	−67.0	−28.0	α-Th, Os_s; 1070–1230 K	emf sol. electrolyte 1020–1230 K
	Th_7Os_3	−62.5	−26.7	α-Th, Os_s; 1030–1230 K	
U–Os	UOs_2	−59.7	−13.5	β-U, Os_s; 1000 K	Holleck et al. 1975
		−58.8	−12.5	α-U, Os_s	emf sol. electrolyte 950–1140 K
Pu–Os	$PuOs_2$	−42	−9.8	Pu_l, Os_s; 1573 K	Peterson 1985a
		−35[a]		α-Pu, Os_s; 298 K	vap. press. ~1573 K
	$PuOs_2$	−8.6	−4.4	Pu_l, Os_s; 1000 K	Campbell 1976
		−4.9		α-Pu, Os_s; 298 K	emf liq. electrolyte 883–1093 K

[a] Using the Third Law.

Table 14
Enthalpies and entropies of formation of intermetallic compounds of Mn with rare earths and actinides ($\Delta_f H°$: kJ/mol of atoms, $\Delta_f S°$: J K^{-1}/mol of atoms)

System	Compound	$\Delta_f H°$	$\Delta_f S°$	Reference state	Authors and method
Sc–Mn	$ScMn_2$	−17,		unknown	Shilov et al. 1983 ind. determ. 1100 K
Sm–Mn	Sm_6Mn_{23}	−3.2		unknown	Shilov et al. 1983 ind. determ. 1320 K
U–Mn	UMn_2	−12.7	−4.1	γ-U, β-Mn; 933–1133 K	Lebedev et al. 1973a
		−8.7	−2.6	α-U, α-Mn	emf liq. electrolyte 933–1133 K
	U_6Mn	−12.6	−10.0	γ-U, β-Mn; 933–1133 K	
		−5.8	−3.2	α-U, α-Mn	

Table 15
Enthalpies and entropies of formation of intermetallic compounds of Re with rare earths and actinides ($\Delta_f H°$: kJ/mol of atoms, $\Delta_f S°$: J K^{-1}/mol of atoms)

System	Compound	$\Delta_f H°$	$\Delta_f S°$	Reference state	Authors and method
Y–Re	YRe_2	−45.3	−2.5	α-Y, Re_s; 1010–1080 K	Rezukhina and Pokarev 1971 emf sol. electrolyte 1010–1080 K
Th–Re	$ThRe_2$	−58.0	−0.9	α-Th, Re_s; 880–1020 K	Rezukhina and Pokarev 1971 emf sol. electrolyte 880–1020K
U–Re	URe_2	−37.9	−0.8	U_l, Re_s; 1700–1900 K	Storms and Czechowicz 1989
		−32.3	+3.7	α-U, Re_s	equilibrium 1700–1900 K

Table 16
Enthalpies and entropies of formation of intermetallic phases of uranium with Zr, Nb and Mo ($\Delta_f H^o$: kJ/mol of atoms, $\Delta_f S^o$: J K^{-1}/mol of atoms)

System	Compound	$\Delta_f H^o$	$\Delta_f S^o$	Reference state	Authors and method
U–Zr	$U_{0.25}Zr_{0.75}$	−8.2	1.7	γ-U,β-Zr; 1100 K	Fedorov and Smirnov 1966
		−4.9	6.2	α-U,α-Zr	emf 1033–1183 K; reviewed by
	$U_{0.5}Zr_{0.5}$	−8.2	2.5	γ-U,β-Zr; 1100 K	Chiotti et al. 1981
		−3.5	8.0	α-U,α-Zr	
	$U_{0.75}Zr_{0.25}$	−3.9	3.7	γ-U,β-Zr; 1100 K	
		2.2	11.9	α-U,α-Zr	
U–Zr	$U_{0.098}Zr_{0.902}$	−7.1	(a)	U_l, β-Zr; 1773 K	Kanno et al. 1988
	$U_{0.285}Zr_{0.715}$	−12.2	(a)	(same)	vap. press. Knudsen mass spectro.
	$U_{0.478}Zr_{0.522}$	−14.8	(a)	(same)	1723–1823 K
	$U_{0.654}Zr_{0.346}$	−16.5	(a)	(same)	
	$U_{0.860}Zr_{0.140}$	−10.1	(a)	(same)	
U–Zr	$U_{0.756}Zr_{0.244}$	−5.7	(b)	U_l, 1773 K	Maeda et al. 1992
					vap. press. Knudsen mass spectro.
					1673–1873 K
U–Nb	$U_{0.7}Nb_{0.3}$	9.8	15.8	γ-U, Nb_s; 1048–1173 K	Vamberskii et al. 1975a,b
		15.1	21.1	α-U, Nb_s	emf liq. electrolyte 1048–1173 K;
	$U_{0.5}Nb_{0.5}$	4.7	14.2	γ-U, Nb_s; 1048–1173 K	reviewed by Chiotti et al. 1981
		8.5	18.0	α-U, Nb_s	
	$U_{0.3}Nb_{0.7}$	−8.9	1.8	γ-U, Nb_s; 1048–1173 K	
		−6.6	4.1	α-U, Nb_s	
U–Mo	$U_{0.2}Mo_{0.8}$	1.4	2.4	γ-U, Mo_s; 1048–1173 K	Vamberskii et al. 1973, 1975b
		2.9	3.9	α-U, Mo_s	emf liq. electrolyte 1048–1173 K;
	$U_{0.4}Mo_{0.6}$	3.0	4.9	γ-U, Mo_s; 1048–1173 K	reviewed by Chiotti et al. 1981
		6.0	7.9	α-U, Mo_s	
	$U_{0.6}Mo_{0.4}$	5.1	7.7	γ-U, Mo_s; 1048–1173 K	
		9.6	12.2	α-U, Mo_s	
	$U_{0.8}Mo_{0.2}$	2.0	5.8	γ-U, Mo_s; 1048–1173 K	
		8.0	11.8	α-U, Mo_s	

[a] $\Delta_f G$. [b] $\overline{\Delta G}_U$.

(v) The Gibbs energies and enthalpies of formation of thorium-based alloys are much more negative than those of rare-earth-based alloys. With uranium they are more often than not more negative than those with rare-earth elements. With plutonium they are usually of the same order of magnitude or less negative than those observed with rare-earth elements (figs. 53–58).

Let us now consider the data obtained in the liquid alloys using calorimetric methods. These data concern only rare-earth-based alloys. The values of the partial enthalpies at infinite dilution of rare earths in liquid Ni, Co, Fe and Mn (tables 17–20) have been plotted as a function of atomic number in figs. 59–62. Even though large discrepancies between values obtained in a same system exist, one may discern a decrease of the partial enthalpy from La to Lu (except with Fe) and from La to Y to Sc.

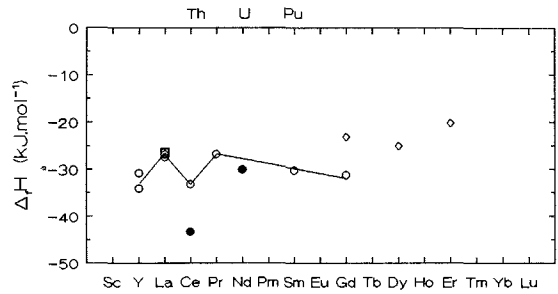

Fig. 53. Enthalpies of formation of RNi_5, $ThNi_5$ and UNi_5 intermetallic compounds. The data are from Schott and Sommer (1986) (open diamonds), Pasturel et al. (1984b) (open circles), Watanabe and Kleppa (1983) (solid squares), Hubbard et al. (1983) (triangle), and Colinet and Pasturel (1983), and Colinet et al. (1987b) (open circles) and from Skelton et al. (1970) and Dannöhl and Lukas (1974), respectively, for the $ThNi_5$ and UNi_5 compounds (solid circles).

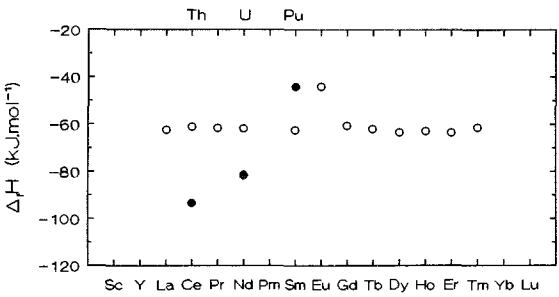

Fig. 54. Enthalpies of formation of RPt_5 and $AnPt_5$ intermetallic compounds. The data are from Jacob and Waseda (1990a, 1990c, 1990d) for the lanthanides (open circles) and from Möbius (1978), Schmidt (1974) and Peterson (1985a), respectively, for the $ThPt_5$, UPt_5 and $PuPt_5$ compounds (solid circles).

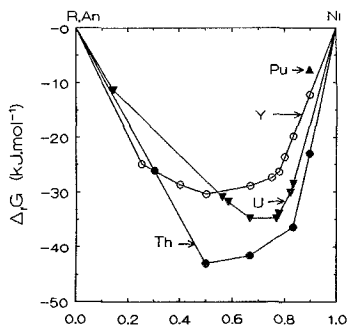

Fig. 55. Gibbs energies of formation at 973 K of $R_{1-x}Ni_x$ and $An_{1-x}Ni_x$ intermetallic compounds. The data for Th (solid circles) are from Skelton et al. (1970), for U (solid inverted triangles) from Lebedev et al. (1974a,b), for Y (open circles) from Subramanian and Smith (1985b). The data reported for the Pu_2Ni_{17} (solid triangles) compound is from Campbell (1974).

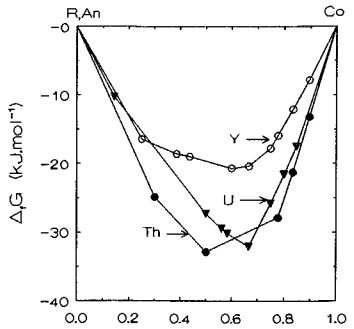

Fig. 56. Gibbs energies of formation at 973 K of $R_{1-x}Co_x$ and $An_{1-x}Co_x$ intermetallic compounds. The data for Th (solid circles) are from Skelton et al. (1971), for U (solid inverted triangles) from Lebedev et al. (1973a–c), for Y (open circles) from Subramanian and Smith (1985a).

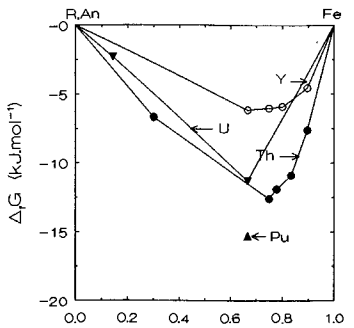

Fig. 57. Gibbs energies of formation at 973 K of $R_{1-x}Fe_x$ and $An_{1-x}Fe_x$ intermetallic compounds. The data for Th (solid circles) are from Skelton et al. (1973), for U (solid inverted triangles) and Pu (solid triangles) from assessments of Chiotti et al. (1981) and for Y (open circles) from Subramanian and Smith (1984).

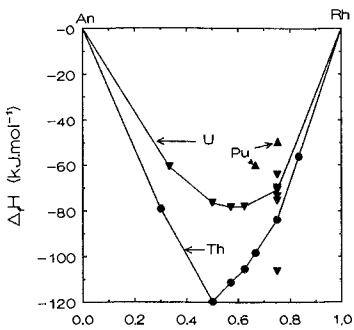

Fig. 58. Enthalpies of formation of $An_{1-x}Rh_x$ intermetallic compounds. The references of the data are quoted in table 9.

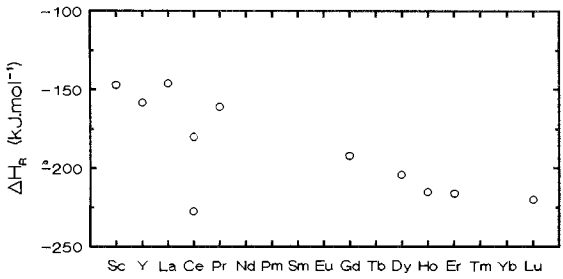

Fig. 59. Partial enthalpy at infinite dilution in liquid nickel of rare earth elements. The references of the data are quoted in table 17.

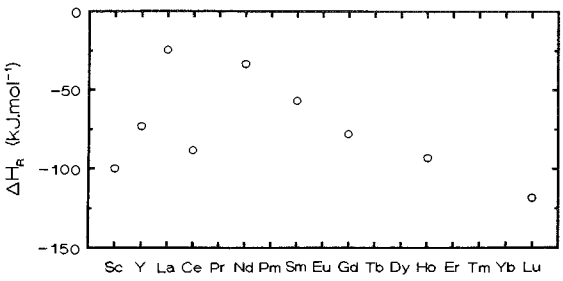

Fig. 60. Partial enthalpy at infinite dilution in liquid cobalt of rare earth elements. The references of the data are quoted in table 18.

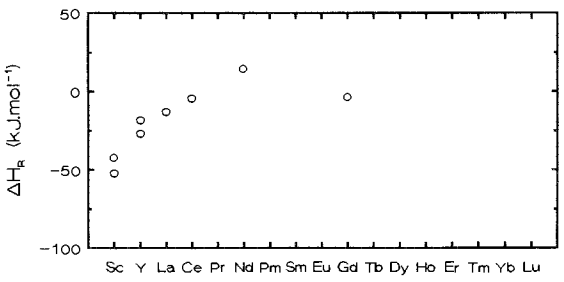

Fig. 61. Partial enthalpy at infinite dilution in liquid iron of rare earth elements. The references of the data are quoted in table 19.

Table 17
Values for the enthalpy of alloying of liquid nickel with rare earths[a]

System	$\Delta_m\bar{H}^{\infty}_{(R)}$ (kJ mol^{-1})	$\Delta_m H$ (kJ mol^{-1})	$\Delta_m\bar{H}^{\infty}_{(Ni)}$ (kJ mol^{-1})	T (K)	Refcrence
Ni–Sc	−147	−24.3(0.20)		1873	Esin et al. 1985a
Ni–Y		−10.9(0.5)		1923	Batalin et al. 1977
	−158	−23.7(0.5)		1963	Sidorov et al. 1988
Ni–La		−26.6(0.17)		1376	Watanabe and Kleppa 1983
		−28.0(0.5)			
		−15.9(0.75)			
Ni–La	−146	−28.3(0.40)	−75	1750	Nikolaenko 1992
Ni–Ce	−180	−20.0(0.20)		1870	Sudavtsova et al. 1988
Ni–Ce	−227	−33.0(0.39)	−80	1750	Nikolaenko 1992
Ni–Pr	−161	−30.7(0.42)	−83	1750	Nikolaenko 1992
Ni–Gd	−192	−35.9(0.38)	−89	1750	Nikolaenko 1990
Ni–Dy	−204	−36.7(0.5)	−98	1760	Nikolaenko and Beloborodova 1991
		−38.1(0.4)			
Ni–Ho	−215	−30.8(0.2)		1760	Nikolaenko and Beloborodova 1991
Ni–Er	−216	−43.1(0.38)	−117	1750	Nikolaenko 1992
Ni–Lu	−220	−41.7(0.3)		1760	Nikolaenko and Beloborodova 1991

[a] Quantities: $\Delta_m\bar{H}^{\infty}_{(R)}$: limiting partial enthalpy of R.
$\Delta_m\bar{H}^{\infty}_{(Ni)}$: limiting partial enthalpy of Ni.
$\Delta_m H$: heat of mixing for a given composition of the rare earth.
The reference state is the liquid elements. All enthalpy values are in kJ mol^{-1}.

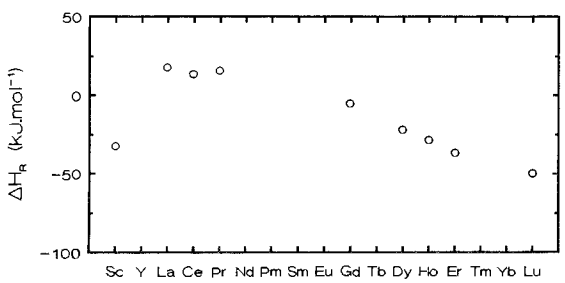

Fig. 62. Partial enthalpy at infinite dilution in liquid manganese of rare earth elements. The references of the data are quoted in table 20.

Table 18
Values for the enthalpy of alloying of liquid cobalt with rare earths

System	$\Delta_m\bar{H}^{\infty}_{(R)}$ (kJ mol^{-1})	$\Delta_m\bar{H}$ (kJ mol^{-1})	$\Delta_m\bar{H}^{\infty}_{(Co)}$ (kJ mol^{-1})	T (K)	Reference
Sc–Co	−100	−13.2(0.15)		1873	Esin et al. 1985a
Y–Co	−73	−13.1(0.5)		1963	Sidorov et al. 1988
La–Co	−24	−8.1(0.5)	−35	1823	Nikolaenko et al. 1990
Ce–Co	−88			1823	Nikolaenko 1992
Lu–Co	−118			1823	Nikolaenko 1992
Nd–Co	−33	−10.5(0.49)	−48	1823	Nikolaenko and Turchanin 1989
Sm–Co	−57	−14.5(0.5)	−63	1823	Nikolaenko and Turchanin 1989
Gd–Co	−78	−17.8(0.46)	−78	1823	Nikolaenko and Turchanin 1989
Ho–Co	−93	−21.4(0.46)	−88	1823	Nikolaenko et al. 1990

[a] Quantities: $\Delta_m\bar{H}^{\infty}_{(R)}$: limiting partial enthalpy of R.
$\Delta_m\bar{H}^{\infty}_{(Co)}$: limiting partial enthalpy of Co.
$\Delta_m H$: heat of mixing for a given composition of the rare earth.
The reference state is the liquid elements. All enthalpy values are in kJ mol^{-1}.

Table 19
Values for the enthalpy of alloying of liquid iron with rare earths and uranium

System	$\Delta_m\bar{H}^{\infty}_{(M)}$ (kJ mol^{-1})	$\Delta_m H$	$\Delta_m\bar{H}^{\infty}_{(M)}$ (kJ mol^{-1})	T (K)	Authors
Sc–Fe	−52			1870	Sudavtsova et al. 1984a
	−42			1873	Esin et al. 1984
Y–Fe	−27	−8.4(0.5)	−23	1873	Ryss et al. 1976a
	−18.0	−5.5(0.3)		1870	Sudavtsova et al. 1987
La–Fe	−13	−1.4(0.20)		1923	Esin et al. 1981a
		+0.1(0.5)		1923	
Ce–Fe	−4	−0.7(0.20)		1900	Esin et al. 1981a
		+0.7(0.40)			
Nd–Fe	+15			1850	Nikolaenko 1992
Gd–Fe	−3	−7.2(0.5)	−48	1850	Nikolaenko and Nosova 1989
U–Fe			−26	1423	Vieth and Pool 1972

[a] Quantities: $\Delta_m\bar{H}^{\infty}_{(M)}$ (kJ mol^{-1}): limiting partial enthalpy of R or An.
$\Delta_m\bar{H}^{\infty}_{(Fe)}$ (kJ mol^{-1}): limiting partial enthalpy of Fe.
$\Delta_m H$: heat of mixing for a given composition of the rare earth.
The reference state is the liquid elements. All enthalpy values are in kJ mol^{-1}.

Table 20
Values for the enthalpy of alloying of liquid manganese with rare earths

System	$\Delta_m\bar{H}^{\infty}_{(M)}$ (kJ mol^{-1})	$\Delta_m H$	$\Delta_m\bar{H}^{\infty}_{(Mn)}$ (kJ mol^{-1})	T (K)	Authors
Sc–Mn	−32	−3.8(0.15)			Esin et al. 1985a
La–Mn	18	8(0.42)	13	1600	Nikolaenko 1992
Ce–Mn	14	3(0.37)	7	1600	Nikolaenko 1992
Pr–Mn	16	2.6(0.39)	9	1600	Nikolaenko 1992
Gd–Mn	−5	−2.3(0.52)	−2	1600	Nikolaenko and Nosova 1989
Dy–Mn	−21.7	0.5(0.05)		1600	Nikolaenko 1992
Ho–Mn	−28.3			1600	Nikolaenko 1992
Er–Mn	−36.4			1600	Nikolaenko 1992
Lu–Mn	−49.5			1600	Nikolaenko 1992

[a] Quantities: $\Delta_m\bar{H}^{\infty}_{(M)}$ (kJ mol^{-1}): limiting partial enthalpy of R.
$\Delta_m\bar{H}^{\infty}_{(Mn)}$ (kJ mol^{-1}): limiting partial enthalpy of Mn.
$\Delta_m\bar{H}$ (kJ mol^{-1}): heat of mixing for a given composition of the rare earth.
The reference state is the liquid elements. All enthalpy values are in kJ mol^{-1}.

4. Intra-rare-earth, actinide–rare-earth and intra-actinide binary alloys

As pointed out in the introduction, the majority of the intra-rare-earth, actinide–rare earth and intra-actinide binary alloys do not possess any intermetallic compounds in the solid state (the exceptions will be pointed out later). The phase diagrams generally exhibit complete or extended solid solutions depending of course on the respective crystalline structures of the components. The allotropic forms of rare earths and actinides (Gschneidner 1990b) are presented in fig. 63 with the purpose of making the following more understandable.

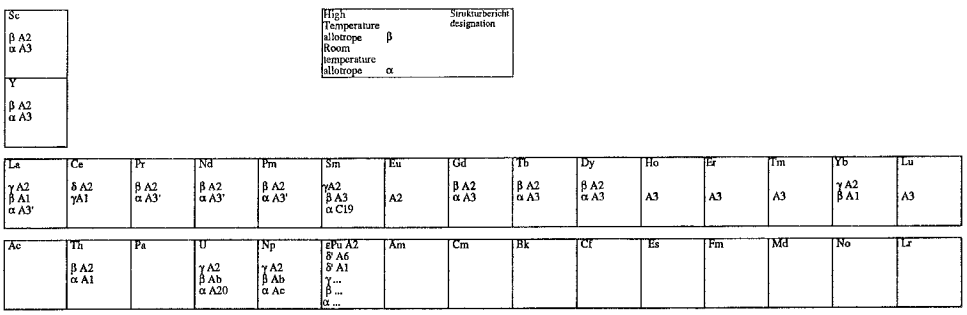

Fig. 63. Allotropic transformations of rare earth elements and actinides from room temperature to high temperature. For simplicity, the Strukturbericht designation, when available, has been given (A1, Cu;cF4; A2, W;cI2; A3, Mg;hP2; A3′, α-La;hP4; A6, In,tI2; A20, α-U, oC4; Ab, β-U, tP30; Ac, αNp, oP8; Ad, βNp, tP4; α-Pu, P21/m; β-Pu, C2/m; γPu, Fddd, C19, α-Sm, hR3).

4.1. *Intra-rare-earth binary alloys*

A large number of intra-rare-earth binary alloys have been evaluated by Gschneidner and Calderwood (1982a–c, 1983a–c) in a series of papers published in *Bulletin of Alloy Phase Diagrams.* These studies have been collected in a chapter of this handbook series (Gschneidner and Calderwood 1986a). A classification of the intra-rare-earth binary alloys was proposed by Gschneidner (1985) who considered the structures of the lanthanides and the lattice spacing in the alloys. Harris and Speight (1985) have also studied the variation of the lattice spacing in some binary intra-rare-earth alloys.

There is little information concerning the thermodynamic data of binary intra-rare-earth alloys. However the interactions between the rare-earth elements are small, and when thermodynamic data have been obtained they show either slight positive or negative deviations from ideality.

We remark that europium and ytterbium are divalent: both have molar volumes, melting and boiling temperatures which are different from the other lanthanides. Consequently they exhibit a completely different behavior when alloyed with rare earths. The binary phase diagrams based on europium and ytterbium exhibit a large miscibility gap in the liquid state. The boiling temperature under the normal pressure of europium and ytterbium is lower than the melting temperature of some other rare earth elements; this is the case in the binary alloys Eu–Lu, Yb–Gd to Lu, Yb–Sc and Yb–Y.

4.2. *Actinide–rare-earth binary alloys*

The main features of the phase diagrams of thorium, uranium and plutonium with rare-earth elements are presented in figs. 64–66. The Th–Sc phase diagram has recently been investigated by Terekhov and Sinyakova (1990) and assessed by Okamoto (1991o).

In the liquid state thorium is totally miscible in the rare-earth elements (except in europium and ytterbium). In the solid state thorium–rare-earth phase diagrams exhibit total or extended solid solutions depending on the structures of the elements considered and their respective temperatures of allotropic transformation.

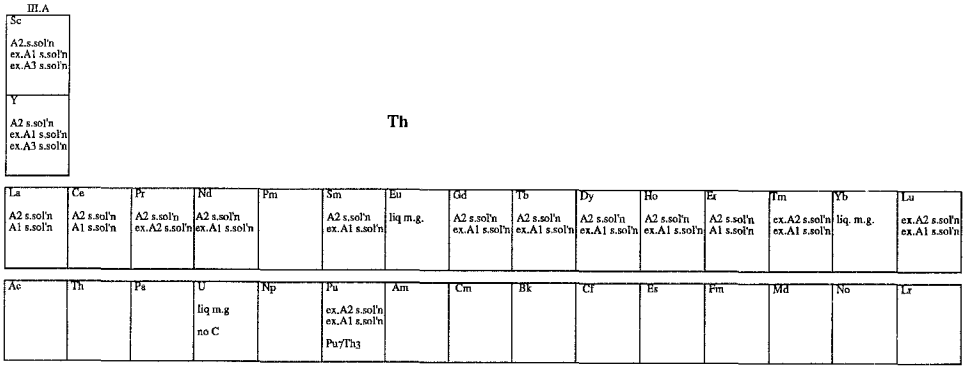

Fig. 64. Main features of the phase diagrams of thorium with rare earths and actinides.

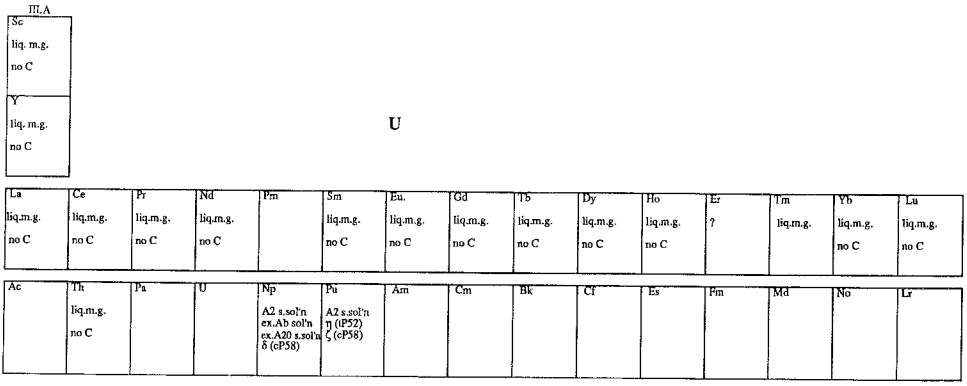

Fig. 65. Main features of the phase diagrams of uranium with rare earths and actinides.

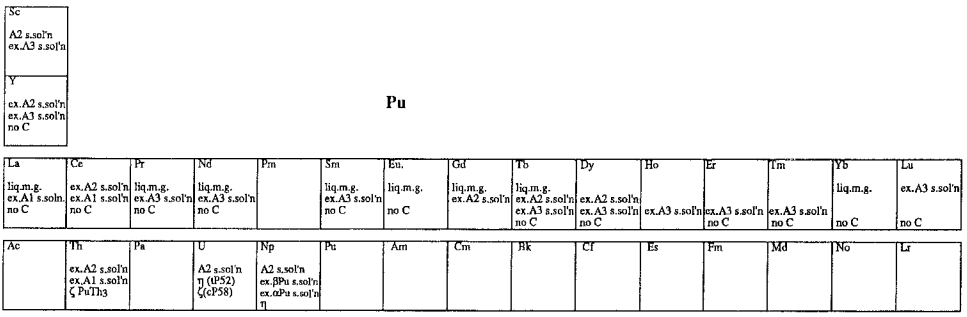

Fig. 66. Main features of the phase diagrams of plutonium with rare earths and actinides.

The uranium–rare earth binary phase diagrams each present a miscibility gap in the liquid state and no extended solubility in the solid state.

The behavior of plutonium with rare-earth elements is more complex. A miscibility gap in the liquid state is observed with the first elements of the lanthanide series from La to Tb. Complete liquid miscibility is observed with the heavy lanthanides Ho to Lu (except Yb) and also with scandium and yttrium.

4.3. *Intra-actinide binary alloys*

The main features of the phase diagrams of intra-thorium, -uranium and -plutonium phase diagrams have also been presented in figs. 64–66. The uranium–thorium phase diagram exhibits a miscibility gap in the liquid state. The plutonium–thorium phase diagram is more complex, with the two elements miscible in the liquid state; in the A2-solid solution a small miscibility gap is observed, however a compound at composition Pu_7Th_3 appears at low temperature.

The uranium–neptunium and uranium–plutonium alloys show a total miscibility in the liquid phase and in the A2-solid solution, moreover they exhibit phases with structures different from those of the pure components in a rather large range of composition in the middle of the phase diagram.

The binary phase diagrams Np–Pu, Np–U, Pu–Th, Th–U and Pu–U have been assessed, respectively, by Sheldon and Peterson (1985a,b), Peterson (1985c,d) and Peterson and Foltyn (1989a). Thermodynamic modeling of the Pu–U phase diagram has been performed by Leibowitz et al. (1991); more recently Okamoto (1992c) presented an updated Pu–U phase diagram. Chan et al. 1980 performed calculations of intra-actinide alloys using the Kaufman approach. Chart and Pugh (1990) proposed phase diagram and thermodynamic data for the Am–Pu system.

5. Rare earths and actinides with elements of column IB

5.1. *Phase diagrams and intermetallic compounds*

The main features of the phase diagrams of the elements of column IB (Cu, Ag and Au) with rare earths and actinides are presented in figs. 67–69. All the phase diagrams exhibit intermetallic compounds except U–Ag where a miscibility gap in the liquid phase is observed. A unique behavior of uranium with Cu and Au is also observed, that is the presence of one or more intermetallic compounds in the solid state and a miscibility gap in the liquid phase. In the Pu–Ag system a similar behavior is observed.

With Cu, the compound which exhibits the highest melting temperature is RCu_6 or $AnCu_6$ for the first six elements of the lanthanide series, La → Sm, and also for Th. In the middle of the lanthanide series (Gd → Dy) the compound is R_2Cu_9, and at the end of the series and also with Sc, it is RCu. The temperature and the enthalpy of fusion, and the heat content of some R–Cu compounds have recently been obtained by Qi et al. (1989a,b).

With Ag, the compound which possesses the highest melting temperature has the formula $R_{14}Ag_{51}$ for the early elements of the lanthanide series (La → Nd), it has the formula RAg for the other lanthanide elements (except Eu and Yb) and also for Y and Sc. The stoichiometry of this compound is Ag_3Th and $Ag_{3.6}Pu$ for the actinides.

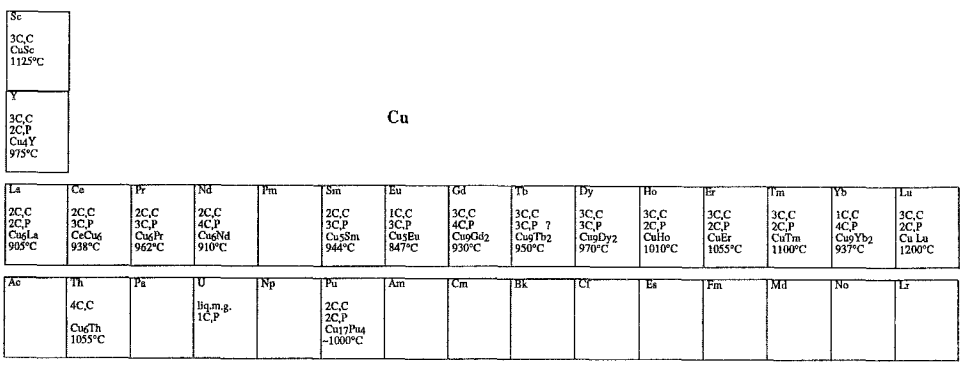

Fig. 67. Main features of the phase diagrams of copper with rare earths and actinides.

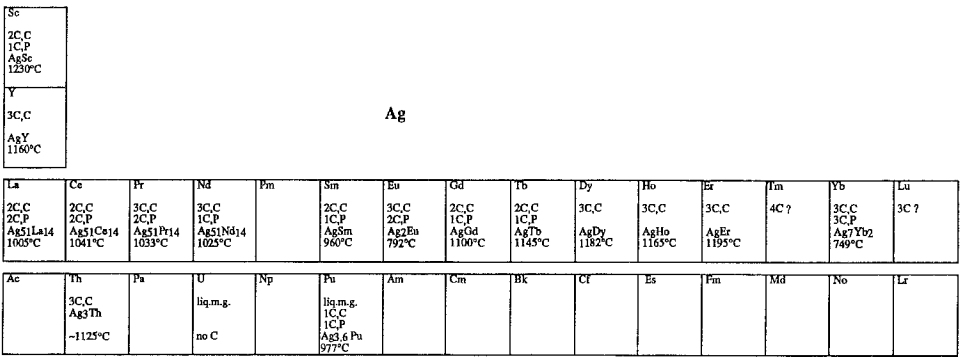

Fig. 68. Main features of the phase diagrams of silver with rare earths and actinides.

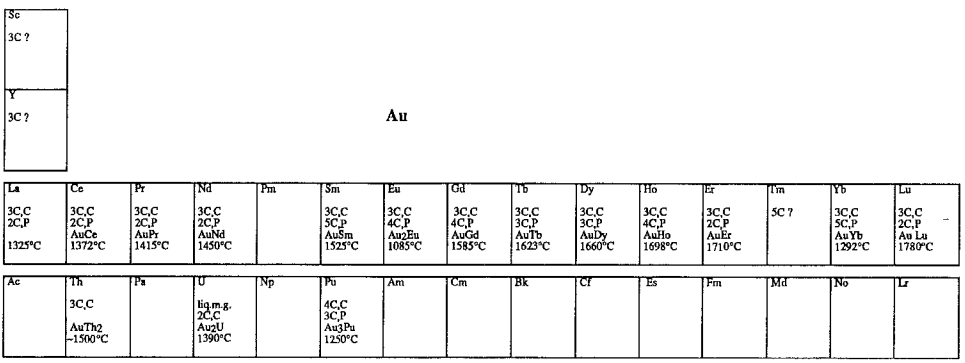

Fig. 69. Main features of the phase diagrams of gold with rare earths and actinides.

With Au, the stoichiometry of the compound which exhibits the highest melting point is RAu for the majority of the rare earth elements, and it is $AuTh_2$, Au_2U and Au_3Pu for the actinides.

Figures 70–72 display the structures of the intermetallic compounds encountered respectively with Cu, Ag and Au. Table 21 displays the characteristics of these structures. The compounds RCu_6 (R = La → Gd) and $ThCu_6$ crystallize with the same structure, $CeCu_6$ prototype. $ThCu_2$, $PuCu_2$ and $LaCu_2$ have the same structure (AlB_2 prototype); UCu_5 crystallize with the same structure as the heavy lanthanides (prototype $AuBe_5$).

With gold one similarity in the crystalline structure is found, that is, many $R_{14}Au_{51}$ as well as $U_{14}Au_{51}$ compounds crystallize with the $Ag_{51}Gd_{14}$ prototype structure. The $R_{14}Ag_{51}$ compounds also crystallize in this structure, but the same behavior is not found in the actinides.

It is also interesting to note that when alloyed with copper and silver, rare earths (except Eu and Yb) do not exhibit any compounds at the rare-earth-rich side of the phase diagram, but in the Th–Cu and Th–Ag phase diagrams one finds the compounds Th_2Cu and Th_2Ag. All the gold–rare-earth binary phase diagrams exhibit a compound R_2Au, as does the Au–Th system. The behaviors of europium and ytterbium also are interesting: one or more

Phase	Sc	Y	La	Ce	Pr	Nd	Pm	Sm	Eu	Gd	Tb	Dy	Ho	Er	Tm	Yb	Lu	Ac	Th	Pa	U	Np	Pu	Prototype or
M_2Cu 33.3%																			x					Al_2Cu x $(CuEu_2)$ •
MCu 50%	x	x	•	•	•	•		x	•	x	x	x	x	x	x	•	x							ClCs x BFe •
MCu_2 66.7%	•	+	x	+	+[a]	+		+	+	+	+	+	+	+	+	+	+		x				x	AlB_2 x $MoSi_2$ • $CeCu_2$ +
M_2Cu_7 77.8%		?								?	?	?	?	?	?	?	?							
$M_{14}Cu_{51}$ 78.5%																			x					$Ag_{51}Gd_{14}$ x
MCu_4 80%		?		x	x	x		x														?		$(CeCu_4)$ x
M_2Cu_9 81.8%										?	?	?	?	?	?	?	?						?	
MCu_5 83.3%			•	•	•	•		•	•	xLT •HT	xLT •HT	xLT •HT	xLT •HT	x	x	•	x				x			AuBe5 x $CaCu_5$ •
MCu_6 85.7%		?	x	x	x	x		x		x									x				?	$CeCu_6$ x
Cu composition	Sc	Y	La	Ce	Pr	Nd	Pm	Sm	Eu	Gd	Tb	Dy	Ho	Er	Tm	Yb	Lu	Ac	Th	Pa	U	Np	Pu	example ( )

Fig. 70. Stoichiometry and structure prototype (or example) of the compounds of Cu with rare earths and actinides.

Phase	Sc	Y	La	Ce	Pr	Nd	Pm	Sm	Eu	Gd	Tb	Dy	Ho	Er	Tm	Yb	Lu	Ac	Th	Pa	U	Np	Pu	Prototype or
M_2Ag 33.3%																			x					Al_2Cu x
M_5Ag_3 37.5%																x								B_3Cr_5 x
M_3Ag_2 40%									x							x								Si_2U_3 x
MAg 50%	x	x	x	x	x	x		x	•	x	x	x	x	x	x	•LT xHT	x							ClCs x BFe •
MAg_2 66.7%	x	x	•	•	•LT +HT	•LT +HT		?	•	x	x	x	x	x	x	•	x		+				?	$MoSi_2$ x $CeCu_2$ • AlB_2 +
MAg_3 75%															xHT •LT				?					$AuCu_3$ x Cu_3Ti •
M_2Ag_7 77.8%																x								Ag_7Yb_2 x
$M_{14}Ag_{51}$ 78.5%		x	x	x	x	x		x		x	x	x	x	x	x								?	$Ag_{51}Gd_{14}$ x
MAg_4 80%	x								x								x							MoNi4 x
MAg_5 83.3%			?						x															$CaCu_5$ x
Ag composition	Sc	Y	La	Ce	Pr	Nd	Pm	Sm	Eu	Gd	Tb	Dy	Ho	Er	Tm	Yb	Lu	Ac	Th	Pa	U	Np	Pu	example ( )

Fig. 71. Stoichiometry and structure prototype (or example) of the compounds of Ag with rare earths and actinides.

intermetallic compounds with Cu, Ag and Au are observed in the lanthanide-rich side of the phase diagram.

Phase	Sc	Y	La	Ce	Pr	Nd	Pm	Sm	Eu	Gd	Tb	Dy	Ho	Er	Tm	Yb	Lu	Ac	Th	Pa	U	Np	Pu	Prototype or
M_3Au 25%									x															CFe_3 x
M_7Au_3 30%									x							x								Fe_3Th_7
M_2Au 33.3%			x	x	x	x		x		x	x	x	x	x	x	x	x		•					Co_2Si x Al_2Cu •
M_5Au_3 37.5%																x								B_3Cr_5 x
M_3Au_2 40%									x															Er_3Ni_2 x
M_5Au_4 44.4%																x								Ge_4Sm_5
MAu 50%	x	x	•LT +HT	•LT +HT	•LT + xHT	•LT + xHT		+LT xHT	•LT ?	+LT xHT	+LT xHT	+LT xHT	+LT xHT	+LT xHT	+LT xHT	•LT xHT	x						?	ClCs x BFe • BCr +
M_6Au_7 53.8%								x																(Au_7Sm_6)
M_7Au_{10} 58.8%								x																$(Au_{10}Sm_7)$
MAu_2 66.7%	x	x	•	•	•LT +HT	+		+	•	x	x	x	x	x	x	x	x		o		Δ		?	$MoSi_2$ x $CeCu_2$ • (Au_2Nd) + AlB_2 o Cd_2Ce Δ
MAu_3 75%		x						x		x	x	x	x	x	x	x	x		?					Cu_3Ti x
$M_{14}Au_{51}$ 78.5%			x	x	x	x		x		x	x	x	x								x			$Ag_{51}Gd_{14}$ x
MAu_4 80%	x								?				x	x	x	x	x						?	$MoNi_4$ x
MAu_5 83.3%									x														?	$CaCu_5$ x
MAu_6 85.7%			x	x	x	x		•		•	•	•	•											Au_6Pr x Au_6Sm •
Au composition	Sc	Y	La	Ce	Pr	Nd	Pm	Sm	Eu	Gd	Tb	Dy	Ho	Er	Tm	Yb	Lu	Ac	Th	Pa	U	Np	Pu	example ( )

Fig. 72. Stoichiometry and structure prototype (or example) of the compounds of Au with rare earths and actinides.

Assessments of copper–rare-earth phase diagrams have been published by Subramanian and Laughlin (1988). Recently Okamoto (1992d) presented an updated Cu–Y phase diagram. Gschneidner and Calderwood (1983d, 1985a–c) made a systematic study of the silver–rare-earth systems. Okamoto and Massalski (1986) have presented analyses of gold-based binary alloy phase diagrams. Okamoto et al. (1986) have also published a review of gold–actinide binary phase diagrams. We also refer to the recent assessments of the La–Cu system by Okamoto (1991p), and of the Ag–U and Ag–Th systems by Baren (1989, 1991). New investigations have been performed by Bolmgren and Lundstrom (1990) in the La–Cu system.

5.2. *Thermodynamic data of binary alloys*

The thermodynamic data of the intermetallic compounds of Cu, Ag and Au with rare earths and actinides are reported in tables 22–24. The values of the integral and partial enthalpies of mixing in the liquid state are shown in tables 25–27.

Table 21
Structure characteristics of X = Cu, Ag, Au and rare-earth or actinide (M = R, An) intermetallic compounds

Phase	Pearson symbol	Space group	Strukturbericht designation	Prototype or (example)
MX_6	oP28	Pnma		$CeCu_6$
	mC28	C2/c		Au_6Pr
	tP56	$P4_2/ncm$		Au_6Sm
MX_5	hP6	P6/mmm	$D2_d$	$CaCu_5$
	cF24	$F\bar{4}3m$	$C15_b$	$AuBe_5$
MX_4	oP20	Pnnm		$(CeCu_4)$
	tI10	I4/m	$D1_a$	$MoNi_4$
$M_{14}X_{51}$	hP68	P6/m		$Ag_{51}Gd_{14}$
M_2X_7	hP18			(Ag_7Yb_2)
MX_3	cP4	$Pm\bar{3}m$	$L1_2$	$AuCu_3$
	oP8	Pmmn	$D0_a$	Cu_3Ti
MX_2	hP3	P6/mmm	C32	AlB_2
	tI6	I4/mmm	$C11_b$	$MoSi_2$
	oI12	Imma		$CeCu_2$
	tP108	P4/nmm		(Au_2Nd)
	hP3	P3m1		Cd_2Ce
M_7X_{10}	tI136	$I4_1/acd$		$(Au_{10}Sm_7)$
M_6X_7	hR13	$R\bar{3}m$		(Au_7Sm_6)
MX	cP2	$Pm\bar{3}m$	B2	ClCs
	oC8	Cmcm	Bf	BCr
	oP8	Pnma	B27	BFe
M_5X_4	oP36	Pnma		Ge_4Sm_5
M_3X_2	tP10	P4/mbm	$D5_a$	Si_2U_3
	hR15	$R\bar{3}$		Er_3Ni_2
M_5X_3	tI32	I4/mcm	$D8_l$	B_3Cr_5
M_2X	tI12	I4/mcm	C16	Al_2Cu
	oP12	Pnam		$CuEu_2$
	oP12	Pnma	C23	Co_2Si
M_7X_3	hP20	$P6_3mc$	$D10_2$	Fe_3Th_7
M_3X	oP16	Pnma	DO_{11}	CFe_3

The enthalpies of formation of the intermetallic compounds of the La–Cu system have been determined by Watanabe and Kleppa (1984), Meyer-Liautaud et al. (1985a) and Sommer et al. (1986) using various calorimetric methods. We note that there is good agreement between these sets of measurements. The results reported by Yang et al. (1989) for the Y–Cu system and by Dubinin et al. (1984) for the La–Cu system, using emf measurements with a liquid electrolyte, give values much too negative for the enthalpies and entropies of formation of the intermetallic compounds. We have also reported in table 22 some of the values obtained by phase diagram optimization (Subramanian and Laughlin 1988). If the order of magnitude of the values obtained by optimization, using no experimental data, for the enthalpies of formation of the

Table 22
Enthalpies and entropies of formation of intermetallic compounds of Cu with rare earths and actinides ($\Delta_f H°$: kJ/mol of atoms, $\Delta_f S°$: $J K^{-1}$/mol of atoms)

System	Compound	$\Delta_f H°$	$\Delta_f S°$	Reference state	Authors and method
Sc–Cu	$ScCu_4$	−14.0		α-Sc,Cu_s; 298 K	Watanabe and Kleppa 1984
	$ScCu_2$	−17.4		(same)	mixing and drop calorim. 1373 K
	ScCu	−20.9		α-Sc,Cu_s; 298 K	Watanabe and Kleppa 1984
					Cu sol'n calorim. 1373 K
Y–Cu	YCu_4	−16.0		α-Y, Cu_s; 298 K	Watanabe and Kleppa 1984
	YCu_2	−19.5		(same)	mixing and drop calorim. 1373 K
	YCu	−19.3		(same)	
	YCu_5	−14.5		α-Y, Cu_s; 298 K	Meyer 1985
					Al sol'n calorim. 1000 K
	YCu	−24		α-Y, Cu_s; 298 K	Sidorov et al. 1989
					solute solvent drop calorim. 1873 K
	YCu_6	−9.6	−1.2	α-Y, Cu_s; 298 K	Itagaki et al. 1990
	YCu_4	−14.1	−2.5	(same)	phase diag. and thermodynamic data
	Y_2Cu_7	−14.8	−2.7	(same)	optimization
	YCu_2	−17.4	−3.2	(same)	
	YCu	−18.2	−3.6	(same)	
	YCu_6	−15.3	−0.5	α-Y, Cu_s; 973 K	Yang et al. 1989
	YCu_4	−20.5	−0.8	(same)	emf liq. electrolyte 973–1103 K
	YCu_2	−29.6	−2.4	(same)	
	YCu	−37.7	−6.3	(same)	
La–Cu	$LaCu_6$	−9.9		α-La, Cu_s; 298 K	Watanabe and Kleppa 1984
	$LaCu_2$	−16.2		(same)	mixing and drop calorim. 1373 K
	$LaCu_6$	−11.3		α-La, Cu_s; 298 K	Meyer-Liautaud et al. 1985a
	$LaCu_5$	−12.4		(same)	Al sol'n calorim. 990 K
	$LaCu_4$	−13.2		(same)	
	$LaCu_2$	−17.7		(same)	
	LaCu	−15.8		(same)	
	$La_{0.7}Cu_{0.3}$	−10.7		(same)	
	$LaCu_6$	−12.9		α-La, Cu_s; 298 K	Sommer et al. 1986
	$LaCu_2$	−15.1		(same)	Sn sol'n calorim. 1098 K
	$LaCu_6$	−33.5	−8.8	β-La, Cu_s; 800 K	Dubinin et al. 1984, Kober 1991
		−33.5	−8.7	α-La,Cu_s	emf liq. electrolyte 630–850 K
	$LaCu_4$	−47.2	−19.3	β-La, Cu_s; 800 K	
		−47.1	−19.2	α-La,Cu_s	
	$LaCu_2$	−70.9	−47.4	β-La, Cu_s; 800 K	
		−70.8	−47.2	α-La,Cu_s	
	LaCu	−61.4	−32.1	β-La, Cu_s; 800 K	
		−61.2	−31.8	α-La,Cu_s	
	$LaCu_6$	−11.7		α-La, Cu_s; 298 K	Qi et al. 1989c
	$LaCu_5$	−14.3		(same)	phase diag. optimization
	$LaCu_2$	−15.0		(same)	
	LaCu	−12.7		(same)	
Ce–Cu	$CeCu_2$	−18.7		γ-Ce, Cu_s; 298 K	Nagarajan and Sommer 1989
					Ce sol'n calorim. 1123 K

continued on next page

Table 22, *continued*

System	Compound	$\Delta_f H°$	$\Delta_f S°$	Reference state	Authors and method
Ce–Cu (*cont'd*)	$CeCu_5$	−13		γ-Ce, Cu_s; 298 K	Meyer-Liautaud et al. 1985b extrapolation of the results obtained for $Ce(Ni_{1-x}Cu_x)_5$ compounds by Al sol'n calorim.
	$CeCu_6$	−7.9		γ-Ce, Cu_s	Subramanian and Laughlin 1988
	$CeCu_5$	−8.2		(same)	phase diag. optimization
	$CeCu_4$	−4.3		(same)	$\Delta_f H$ assumed temperature
	$CeCu_2$	−24.4		(same)	independent
	CeCu	−21.8		(same)	
Sm–Cu	$SmCu_6$	−11.2		α-Sm, Cu_s; 298 K	Meyer 1985
	$SmCu_5$	−13.5		(same)	Al sol'n calorim. 990 K
Gd–Cu	Gd_2Cu_9	−12.7		α-Gd, Cu_s; 298 K	Sommer et al. 1986
	$GdCu_2$	−13.5		(same)	Sn sol'n calorim. 1095 K
	GdCu	−10.6		(same)	
	$GdCu_6$	−17.0		α-Gd, Cu_s	Subramanian and Laughlin 1988
	$GdCu_5$	−14.4		(same)	phase diag. optimization
	Gd_2Cu_9	−16.0		(same)	$\Delta_f H$ assumed temperature
	$GdCu_2$	−12.2		(same)	independent
	GdCu	−25.4		(same)	
Dy–Cu	Dy_2Cu_9	−12.7		α-Dy, Cu_s; 298 K	Sommer et al. 1986
	$DyCu_2$	−16.4		(same)	Sn sol'n calorim. 1098 K
	DyCu	−12.5		(same)	
	$DyCu_7$	0.6		α-Dy, Cu_s	Subramanian and Laughlin 1988
	$DyCu_5$	−5.6		(same)	phase diag. optimization
	Dy_2Cu_9	−12.7		(same)	$\Delta_f H$ assumed temperature
	$DyCu_2$	−8.0		(same)	independent
	DyCu	−22.5		(same)	
Er–Cu	$ErCu_5$	−10.7		Er_s, Cu_s; 298 K	Sommer et al. 1986
	$ErCu_2$	−17.2		(same)	Sn sol'n calorim. 1092 K
	ErCu	−14.6		(same)	
Th–Cu	$ThCu_6$	−8.7	+4.4	α-Th, Cu_s; 850–949 K	Magnani et al. 1969 emf sol. electrolyte 850–949 K; reviewed by Skelton et al. 1971
	$ThCu_6$	−10.5	+3.3	α-Th, Cu_s; 973 K	Bailey and Smith 1975
	$ThCu_{3.6}$	−17.2	3.7	(same)	emf sol. electrolyte 729–1219 K
	$ThCu_2$	−26.0	0.3	(same)	
	Th_2Cu	−27.2	−0.5	(same)	
	$ThCu_6$	−11.7	2.2	α-Th, Cu_s; 1000 K	Chiotti et al. 1981
	$ThCu_{3.6}$	−18.4	2.6	(same)	review of the results of Bailey and
	$ThCu_2$	−27.1	−7.4	(same)	Smith 1975
	Th_2Cu	−27.8	−10.3	(same)	
	$ThCu_6$	−8.4		α-Th, Cu_s; 973 K	Chakrabarti et al. 1986
	$ThCu_{3.6}$	−4.6		(same)	phase diag. optimization
	$ThCu_2$	−25.6		(same)	
	Th_2Cu	−23.5		(same)	

continued on next page

Table 22, *continued*

System	Compound	$\Delta_f H°$	$\Delta_f S°$	Reference state	Authors and method
U–Cu	UCu_5	−1.7	1.7	β-U, Cu_s; 993–1053 K	Yoshihara and Kanno 1974b or Kanno 1974
		−1.2	2.2	α-Cu,Cu_s	
		−3.0	0.5	γ-U, Cu_s; 1053–1153 K	emf sol. electrolyte 993–1153 K
		−1.7	1.8	α-Cu,Cu_s	

Table 23

Enthalpies and entropies of formation of intermetallic compounds of Ag with rare earths and actinides ($\Delta_f H°$: kJ/mol of atoms, $\Delta_f S°$: $J K^{-1}$/mol of atoms)

System	Compound	$\Delta_f H°$	$\Delta_f S°$	Reference state	Authors and method
Y–Ag	YAg	−23.9	(a)	α-Y, Ag_l; 1346 K	Ivanov and Lukashenko 1983, 1987 vap. press 1346 K
Sc–Ag	$ScAg_2$	−27.1		α-Sc, Ag_s; 298 K	Fitzner et al. 1991
	ScAg	−26.2		(same)	mixing and drop calorim. 1473 K
Y–Ag	$Y_{14}Ag_{51}$	−22.2		α-Y, Ag_s; 298 K	Fitzner et al. 1991
	YAg	−26.8		(same)	mixing and drop calorim. 1473 K
La–Ag	$La_{14}Ag_{51}$	−21.4		α-La, Ag_s; 298 K	Fitzner et al. 1991
	LaAg	−16.9		(same)	mixing and drop calorim. 1473 K
Tb–Ag	TbAg	−23.6	(a)	α-Tb, Ag_l; 1363 K	Ivanov and Lukashenko 1987 vap. press. 1363 K

[a] $\Delta_f G°$.

Table 24

Enthalpies and entropies of formation of intermetallic compounds of Au with rare earths and actinides ($\Delta_f H°$: kJ/mol of atoms, $\Delta_f S°$: $J K^{-1}$/mol of atoms)

System	Compound	$\Delta_f H°$	$\Delta_f S°$	Reference state	Authors and method
Sc–Au	ScAu	−76.1		α-Sc, Au_s; 298 K	Fitzner et al. 1991 mixing and drop calorim. 1473 K
Y–Au	YAu	−78.7		α-Y, Au_s; 298 K	Fitzner et al. 1991 mixing and drop calorim. 1473 K
La–Au	LaAu	−69.9		α-La, Au_s; 298 K	Fitzner et al. 1991 mixing and drop calorim. 1473 K
Th–Au	$ThAu_3$	−17.9		α-Th, Au_s	Okamoto et al. 1986
	$ThAu_2$	−16.7		(same)	phase diag. optimization
	Th_3Au	−13.7		(same)	$\Delta_f H$ assumed temperature independent
U–Au	UAu_3	−2.4		α-U, Au_s	Okamoto et al. 1986 phase diag. and thermo. data optimization $\Delta_f H$ assumed temperature independent

Table 25
Values for the enthalpy of alloying of liquid copper with rare earths[a]

System	$\Delta_m\bar{H}^{\infty}_{(R)}$	$\Delta_m H$	$\Delta_m\bar{H}^{\infty}_{(Cu)}$	T (K)	Reference
Sc–Cu	−102	−24.5(0.5)		1373	Watanabe and Kleppa 1984
	−88	−12.0(0.15)		1873	Esin et al. 1985a
	−102				Sudavtsova et al. 1985
Y–Cu	−105	−22.8(0.5)		1373	Watanabe and Kleppa 1984
	−114	−13.7(0.14)		1410	Sudavtsova et al. 1983
	−89	−21.5(0.4)		1963	Sidorov et al. 1990
	−200				Sudavtsova et al. 1985
La–Cu	−103	−12.0(0.5)	−35	1373	Watanabe and Kleppa 1984
		−13.0(0.33)			
		−10.0(0.14)			
		−13.2(0.15)			Sommer et al. 1986, Sommer
		−13.2(0.34)			et al. 1989
	−89	−11.5(0.38)	−30		Turchanin et al. 1988c
		−10.9(0.5)			
	−79				Sudavtsova et al. 1985
Ce–Cu		−12.1(0.2)		1473	Nagarajan and Sommer 1989
		−14.9(0.5)		1130	
		−15.7(0.5)		1095	
	−97	−11.2(0.5)	−29	1523	Turchanin et al. 1988c
	−61				Batalin et al. 1985a
	−59	−6.0(0.08)		1555	Sudavtsova et al. 1988
Pr–Cu	−80	−12.6(0.5)	−36	1523	Turchanin et al. 1988b
Nd–Cu	−90	−12.8(0.5)	−37	1523	Turchanin et al. 1988b
Sm–Cu	−106	−14.8(0.5)	−38	1390	Turchanin et al. 1988a
Gd–Cu	−103	−18.0(0.4)		1523	Turchanin et al. 1988d
		−12.4(0.18)			Sommer et al. 1986
		−11.2(0.33)			
		−7.6(0.5)			
		−17.0(0.5)			Vitusevich and Ivanov 1987
	−103	−18.7(0.33)		1523	Nikolaenko 1990
Dy–Cu		−13.9(0.18)			Sommer et al. 1986
		−14.8(0.33)			
Ho–Cu	−111	−18.6(0.35)		1523	Turchanin et al. 1988d
Er–Cu	−127	−21.5(0.5)		1523	Turchanin et al. 1987
	−112			1453	Nikolaenko et al. 1983
		−10.8(0.17)			Sommer et al. 1986
		−19.5(0.33)			
		−19.4(0.5)			
Tm–Cu	−120	−22.1(0.35)		1523	Turchanin et al. 1988d
Lu–Cu	−124	−19.2(0.2)		1523	Turchanin et al. 1988d
	−120	−11.0(0.1)		1373	Watanabe and Kleppa 1984

[a] Quantities: $\Delta_m\bar{H}^{\infty}_{(R)}$: limiting partial enthalpy of R; $\Delta_m\bar{H}^{\infty}_{(Cu)}$: limiting partial enthalpy of Cu; $\Delta_m H$: heat of mixing for a given composition of the rare earth; reference state is the liquid elements; all enthalpy values in kJ mol^{-1}.

Table 26
Values for the enthalpy of alloying of liquid silver with rare earths[a]

System	$\Delta_m\bar{H}^{\infty}_{(R)}$ (kJ mol^{-1})	$\Delta_m H$ (kJ mol^{-1})	$\Delta_m\bar{H}^{\infty}_{(Ag)}$ (kJ mol^{-1}) T (K)	Reference	
Sc–Ag		−22.0(0.33)		1473	Fitzner et al. 1991
		−24.0(0.5)			
Y–Ag		−21.3(0.215)		1473	Fitzner et al. 1991
		−27.7(0.5)			
La–Ag		−17.5(0.215)		1473	Fitzner et al. 1991
		−20.3(0.5)			
Gd–Ag	−77	−20.3(0.4)		1600	Batalin et al. 1985a
Eu–Ag	−74	−143.0(0.4)		1487	Ivanov and Vitusevich 1990

[a] Quantities: $\Delta_m\bar{H}^{\infty}_{(R)}$ (kJ mol^{-1}): limiting partial enthalpy of R.
$\Delta_m\bar{H}^{\infty}_{(Ag)}$ (kJ mol^{-1}): limiting partial enthalpy of Ag.
$\Delta_m H$: heat of mixing for a given composition of the rare earth.
The reference state is the liquid elements. All enthalpy values are in kJ mol^{-1}.

Table 27
Values for the enthalpy of alloying of liquid gold with rare earths[a]

System	$\Delta_m\bar{H}^{\infty}_{(R)}$ (kJ mol^{-1})	$\Delta_m H$ (kJ mol^{-1})	$\Delta_m\bar{H}^{\infty}_{(Au)}$ (kJ mol^{-1}) T (K)	Reference	
Sc–Au	−230			1379	Kleppa and Topor 1985
Y–Au		−75.0(0.5)			Fitzner et al. 1991
La–Au		−65.0(0.5)			Fitzner et al. 1991

[a] Quantities: $\Delta_m\bar{H}^{\infty}_{(R)}$ (kJ mol^{-1}): limiting partial enthalpy of R.
$\Delta_m\bar{H}^{\infty}_{(Au)}$ (kJ mol^{-1}): limiting partial enthalpy of Au.
$\Delta_m H$: heat of mixing for a given composition of the rare earth.
The reference state is the liquid elements. All enthalpy values are in kJ mol^{-1}.

intermetallic compounds is correct then discrepancies with the experimental values may still exist. For comparison, the values proposed by Subramanian and Laughlin (1988) and the experimental values obtained in the Gd–Cu and Dy–Cu systems by Sommer et al. (1986) using tin solution calorimetry are different. When experimental thermodynamic data are used in the optimization process the agreement is much better; see Qi et al. (1989c) for the La–Cu system or Itagaki et al. (1990) for the Y–Cu system.

The composition MCu_2 has been chosen for comparing the behavior of the rare earths and actinides when alloyed with copper. It appears that the enthalpies of formation of the MCu_2 intermetallic compounds are quite similar for all the elements of the rare-earth series, with the enthalpy of formation of the $ThCu_2$ compound being more negative (fig. 73). To compare the enthalpies of formation with composition, we have plotted in fig. 74 the enthalpies of formation of the intermetallic compounds of La–Cu obtained by

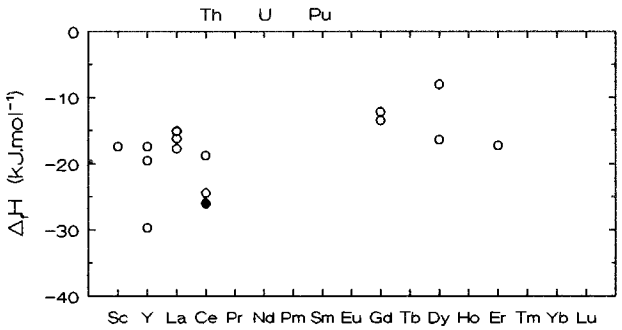

Fig. 73. Enthalpies of formation of RCu_2 and $AnCu_2$ intermetallic compounds as a function of the atomic number (open circle, rare earths; solid circle, actinides). The references of the data are quoted in table 22.

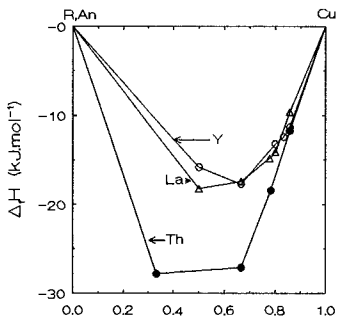

Fig. 74. Enthalpies of formation of La–Cu (open triangles), YCu (open circles) and Th–Cu (solid circles) intermetallic compounds, the data are from Meyer-Liautaud et al. (1985a), Itagaki et al. (1990) and Chiotti et al. (1981), respectively.

Meyer-Liautaud et al. (1985a), of Y–Cu obtained by Itagaki et al. (1990) and of Th–Cu obtained by Chiotti et al. (1981). We point out that the enthalpies of formation of the Th–Cu compounds are less asymmetric with respect to 0.5 composition than those of the rare earth–copper compounds.

Values of partial and integral enthalpies of mixing have been obtained by calorimetric methods in liquid-phase Cu–R (table 25). The variation of the partial enthalpy at infinite dilution of rare earth elements in liquid copper is displayed in fig. 75 as a function of atomic number. Even though large discrepancies exist between the reported values, one observes a slight decrease of these values from La to Lu.

Thermodynamic data on the Ag- and Au-based alloys are scarce. We have not found any thermodynamic data for alloys of silver with actinides. The data reported in table 24 for Au with actinides have never been obtained directly. It is important to note the recent values obtained by Fitzner et al. (1991) in the (Ag, Au)–(Sc, Y, La) binary systems using calorimetric methods.

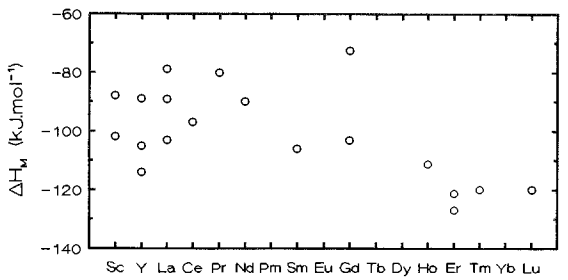

Fig. 75. Partial enthalpy at infinite dilution of rare earth elements in liquid copper. The references of the data are quoted in table 25.

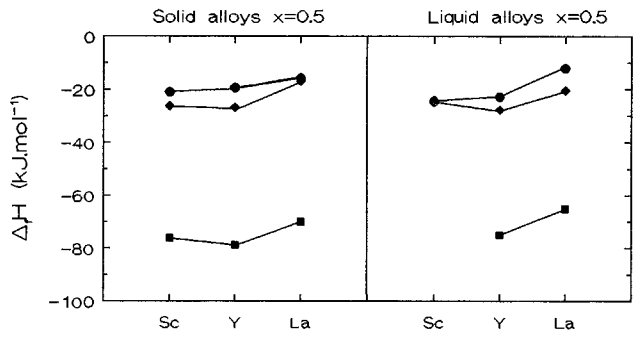

Fig. 76. Left-hand side: enthalpies of formation of R (Cu, Ag, Au) equiatomic compounds (R = Sc, Y, La). Right-hand side: enthalpies of mixing in liquid alloys (Sc, Y, La)–(Cu, Ag, Au) for equiatomic composition. Symbols: solid circle, solid diamond, solid square, correspond to Cu, Ag and Au based alloys, respectively.

In fig. 76 the values of the enthalpies of formation of equiatomic R(Cu, Ag, Au) compounds (R = Sc, Y, La) as well as the enthalpies of mixing at equiatomic composition for these systems in the liquid state are shown. The enthalpies of formation or of mixing become more negative from Cu to Ag and to Au. In the rare-earth series it appears that the values obtained with Sc and Y are of the same order of magnitude while the values obtained with La are less negative. The behavior of actinides with elements of column IB is difficult to describe because of a serious lack of data; however, considering the shape of the phase diagrams and the available thermodynamic data, it appears that: the enthalpies of formation in the Th–Au system are less negative than those obtained in the Th–Cu system; the enthalpies of formation in the U–Cu system are less negative than in the U–Au system; while in the U–Ag system the enthalpies of mixing are presumably positive because of the presence of a miscibility gap in the liquid phase and the absence of compound in the solid state.

When alloyed with elements of column IB, elements of the rare-earth series behave completely different than those of the actinide series.

6. Rare earths and actinides with elements of column IIB

6.1. *Phase diagrams and intermetallic compounds*

The main features of the phase diagrams of Zn, Cd and Hg with rare earths and actinides are presented in figs. 77–79. Several intermetallic compounds are observed in each of these phase diagrams, but the presence of a miscibility gap in the liquid phase on the uranium-rich side must be pointed out in the U–Zn and U–Cd phase diagrams.

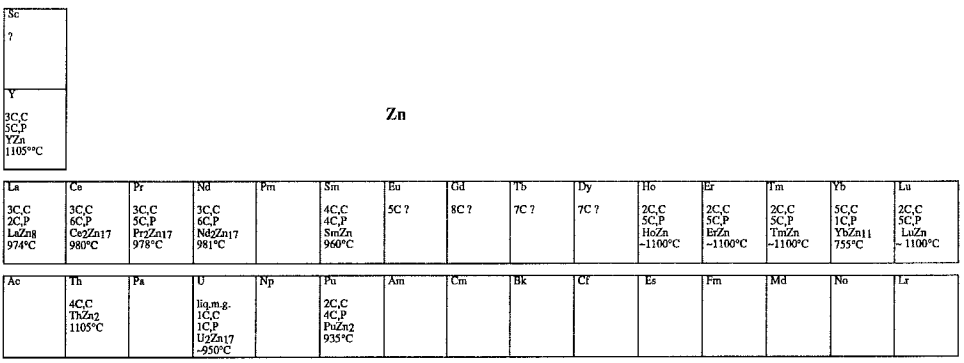

Fig. 77. Main features of the phase diagrams of zinc with rare earths and actinides.

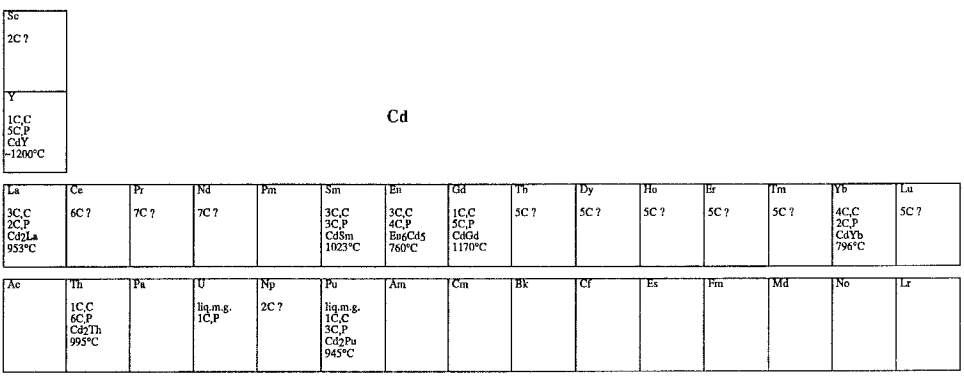

Fig. 78. Main features of the phase diagrams of cadmium with rare earths and actinides.

The compound R_2Zn_{17} or An_2Zn_{17} is observed and moreover has the same structure in the rare-earth and in the actinide series (fig. 80). Cd-based compounds, of compositions $RCd_6/AnCd_6$ and $RCd_{11}/AnCd_{11}$, respectively, possess the same structure (fig. 81). With Hg some similarities are found with rare earths and uranium for the compositions 11:45 and 1:2 (fig. 82). The characteristics of the structures are reported in table 28. It is also important to note that the compounds are all at the Zn- or Cd- or Hg-rich side of the phase diagram, except for Th_2Zn and Ho_2Hg.

The compounds with the highest melting temperatures are $LaZn_8$, Ln_2Zn_{17} for Ln = Ce, Nd and lastly LnZn for Ln = Sm → Lu for the lanthanide elements; $ThZn_2$, U_2Zn_{17}

Sc																			
2C ?																			
Y																			
2C,C 2C,P HgY ~1200°C																			
La	Ce	Pr	Nd	Pm	Sm	Eu	Gd	Tb	Dy	Ho	Er	Tm	Yb	Lu					
2C,C 4C,P HgLa ~1100°C	5C ?	2C,C 3C,P HgPr ~1100°C	2C,C 3C,P HgNd ~1200°C		2C,C 3C,P HgSm ~1200°C	4C ?	2C,C 2C,P GdHg ~1200°C	2C,C 2C,P HgTb ~1200°C	2C,C 2C,P DyHg ~1200°C	2C,C 2C,P HgHo ~1200°C	4C ?	2C ?	1C,C 4C,P HgYb ~1100°C	2C ?					
Ac	Th	Pa	U	Np	Pu	Am	Cm	Bk	Cf	Es	Fm	Md	No	Lr					
	3C ?		4C ?		2C ?														

Hg

Fig. 79. Main features of the phase diagrams of mercury with rare earths and actinides.

Phase	Sc	Y	La	Ce	Pr	Nd	Pm	Sm	Eu	Gd	Tb	Dy	Ho	Er	Tm	Yb	Lu	Ac	Th	Pa	U	Np	Pu	Prototype or
M_2Zn 33.3%																			x					Al_2Cu x
MZn 50%	x	x	x	x	x	x		x	x	x	x	x	x	x	x	x	x							ClCs x
MZn_2 66.7%		x ?	x	x	xLT ?HT	x		x	x	x	x	x	x	x	x	x ?	x		•				+	$CeCu_2$ x AlB_2 • Cu_2Mg +
MZn_3 75%		x		•	x	x		x		x	x	x	x	x	x		x							YZn_3 + ($CeZn_3$) •
M_3Zn_{11} 78.6%		x		x	x	x		x		x	x	x		x		x								$Al_{11}La_3$ x
M_6Zn_{23} 79.3%										x	x	x	x	x	x		x							$Mn_{23}Th_6$ x
MZn_4 80%			x																•					($LaZn_4$) x Al_4Ba •
$M_{13}Zn_{58}$ 81.7%		x		x	x	x		x		x	x		x	x	x	x	x						x	$Gd_{13}Zn_{58}$ x
MZn_5 83.3%		x	•	•		•			•	•		•	•	•	•		•							$ErZn_5$ x $CaCu_5$ •
M_3Zn_{17} 85%																x?								$Be_{17}Ru_3$ x
M_3Zn_{22} 88%			x		x	x		x		x													x	Pu_3Zn_{22} x
M_2Zn_{17} 89.5%		x	•	•	xLT •HT	x •?		x •?		xLT •HT	xLT •HT	xLT •HT	xLT •HT	xLT •HT	xLT •HT	x •?	xLT •HT		xLT •HT		xLT •HT? o ?		x +? o	$Ni_{17}Th_2$ x Th_2Zn_{17} • •Pu_2Zn_{17} + U_2Zn_{17} o
MZn_{11} 91.7%			x	x	x	x			x							x								BaCd$_{11}$
MZn_{12} 92.3%		x				?		x		x	x	x	x	x	x		x				•			$Mn_{12}Th$ x UZn_{12} •
MZn_{13} 92.9%			x						x															$NaZn_{13}$
Zn composition	Sc	Y	La	Ce	Pr	Nd	Pm	Sm	Eu	Gd	Tb	Dy	Ho	Er	Tm	Yb	Lu	Ac	Th	Pa	U	Np	Pu	example ( )

Fig. 80. Stoichiometry and structure prototype (or example) of the compounds of Zn with rare earths and actinides.

and $PuZn_2$ for the actinide elements. A large number of liquid–solid phase equilibria in cadmium-based alloys are not known. However we may remark that the compound with the highest melting point is RCd_2 or $AnCd_2$ for R = La/An = Th, Pu, and RCd for Sm,

Phase	Sc	Y	La	Ce	Pr	Nd	Pm	Sm	Eu	Gd	Tb	Dy	Ho	Er	Tm	Yb	Lu	Ac	Th	Pa	U	Np	Pu	Prototype or
MCd 50%	x	x	x	x	x	x		x	x	x	x	x	x	x	x	x	x		•					$ClCs$ Cd_7Th_6 •
MCd_2 66.7%			x	x	x	x		x	o	x	x	x	x	x	x	+	x		•				?	CdI_2 x AlB_2 • $MgZn_2$ + $CeCu_2$ o
M_3Cd_8 72.7%									?							?								
MCd_3 75%	•	+		x	x	x				•	•HT +LT	+	+	+	+		+		•					BiF_3 x Ni_3Sn • Cd_3Er +
M_4Cd_{51} 78.5%									x							x								$Ag_{51}Gd_{14}$ x
M_6Cd_{23} 79.3%																			x					$Mn_{23}Th_6$ x
MCd_4 80%																							?	
$M_{11}Cd_{45}$ 80.4%					x	x		x		x	x	x	x	x	x		x							$Cd_{45}Sm_{11}$ x
$M_{13}Cd_{58}$ 81.7%		x	x	x	x	x		x	x	x														$Gd_{13}Zn_{58}$ x
MCd_5 83.3%																			x					$ErZn_5$ x
$MCd_{5.7}$ 85.1%																?								
MCd_6 85.7%		x		x	x	x		x	x	x	x	x	x	x	x	x	x					x	x	Cd_6Y x
M_2Cd_{17} 89.5%			x																					$Ni_{17}Th_2$ x
MCd_{11} 91.7%			x	x	x	x		x	•										x		x	x	x	$BaHg_{11}$ x $BaCd_{11}$ •
Cd composition	Sc	Y	La	Ce	Pr	Nd	Pm	Sm	Eu	Gd	Tb	Dy	Ho	Er	Tm	Yb	Lu	Ac	Th	Pa	U	Np	Pu	example ( )

Fig. 81. Stoichiometry and structure prototype (or example) of the compounds of Cd with rare earths and actinides.

Phase	Sc	Y	La	Ce	Pr	Nd	Pm	Sm	Eu	Gd	Tb	Dy	Ho	Er	Tm	Yb	Lu	Ac	Th	Pa	U	Np	Pu	Prototype or
M_2Hg 33.3%													x											Co_2Si x
MHg 50%	x	x	x	x		x		x	x	x	x		x			x	x		?		?			$ClCs$ x
MHg_2 66.7%		x	x	•		•		x	•	•	x		x			x					x			AlB_2 x $CeCd_2$ •
MHg_3 75%	x	x	x	x		x		x	x	x	x		x			x	x		?		?		?	Ni_3Sn x
$M_{14}Hg_{51}$ 78.4%									x							x								$Ag_{51}Gd_{14}$ x
MHg_4 80%																							?	
$M_{11}Hg_{45}$ 80.4%		x	x	x		x		x		?	?										x			$Cd_{45}Sm_{11}$ x
$M_{13}Hg_{58}$ 81.7%			x																					$Gd_{13}Zn_{58}$ x
$MHg_{6.5}$ 88.0%			x	x		x		x																$Hg_{6.5}La$ x
Hg composition	Sc	Y	La	Ce	Pr	Nd	Pm	Sm	Eu	Gd	Tb	Dy	Ho	Er	Tm	Yb	Lu	Ac	Th	Pa	U	Np	Pu	example ( )

Fig. 82. Stoichiometry and structure prototype (or example) of the compounds of Hg with rare earths and actinides.

Table 28
Structure characteristics of X = Zn, Cd, Hg and rare-earth or actinide (M = R, An) intermetallic compounds

Phase	Pearson symbol	Space group	Strukturbericht designation	Prototype or (example)
MX_{13}				
	cF112	$Fm\bar{3}c$	$D2_3$	$NaZn_{13}$
MX_{12}	tI26	I4/mmm	$D2_b$	$Mn_{12}Th$
	hP45	P6/mmm		UZn_{12}
MX_{11}	tI48	$I4_1/amd$		$BaCd_{11}$
	cP36	$Pm\bar{3}m$	$D2_c$	$BaHg_{11}$
M_2X_{17}	hP38	$P6_3/mmc$		$Ni_{17}Th_2$
	hR19	$R\bar{3}m$		Th_2Zn_{17}
	hP76	P6/mmm		(Pu_2Zn_{17})
	hP114	P6m2		U_2Zn_{17}
M_3X_{22}	tI100	$I4_1/amd$		Pu_3Zn_{22}
$MX_{6.5}$	oC*	Cmcm		$(Hg_{6.5}La)$
MX_6	cI184	$Im\bar{3}$		Cd_6Y
M_3X_{17}	cI160	$Im\bar{3}$		$Be_{17}Ru_3$
MX_5	hP36	$P6_3/mmc$		$ErZn_5$
	hP6	P6/mmm	$D2_d$	$CaCu_5$
$M_{13}X_{58}$	hP142	$P6_3mc$		$Gd_{13}Zn_{58}$
$M_{11}X_{45}$	cF448	$F\bar{4}3m$		$Cd_{45}Sm_{11}$
MX_4	oC20	Cmcm		$(LaZn_4)$
	tI10	I4/mmm	$D1_3$	Al_4Ba
M_6X_{23}	cF116	$Fm\bar{3}m$	$D8_a$	$Mn_{23}Th_6$
M_3X_{11}	oI28	Immm		α-$Al_{11}La_3$
$M_{14}X_{51}$	hP68	P6/m		$Ag_{51}Gd_{14}$
MX_3	oP16	Pnma		YZn_3
	oC16	Cmcm		$(CeZn_3)$, (Cd_3Er)
	cF16	$Fm\bar{3}m$	DO_3	BiF_3
	hP8	$P6_3/mmc$	DO_{19}	Ni_3Sn
MX_2	cF24	$Fd\bar{3}m$	C15	Cu_2Mg
	oI12	Imma		$CeCu_2$
	hP3	P6/mmm	C32	AlB_2
	hP3	$P\bar{3}m1$	C6	CdI_2
	hP12	$P6_3/mmc$	C14	$MgZn_2$
	hP3	$P\bar{3}m1$	C32	Cd_2Ce
MX	cP2	$Pm\bar{3}m$	B2	ClCs
	oP26	Pbam	C46	(CdTh) or Cd_7Th_6
M_2X	tI12	I4/mcm	C16	Al_2Cu
	oP12	Pnma	C23	Co_2Si

Gd and Y. With Hg the equiatomic compound RHg or AnHg appears to be congruent melting with a high melting temperature (1200°C).

An extensive study of the Cd–rare-earth binary alloys has been performed by Gschneidner and Calderwood (1988b,c).

6.2. *Thermodynamic data of the alloys*

The enthalpies of formation of the intermetallic compounds of Zn, Cd and Hg with rare earths and actinides are reported in tables 29–31.

The enthalpies of formation of the MZn_{12} and MZn_2 as well as those of the M_2Z_{17} compounds are plotted as a function of the atomic number in figs. 83 and 84. The enthalpies of formation of the intermetallic compounds reported by Chiotti and Mason (1965) for the Ce–Zn system, by Chiotti and Mason (1967) for the Sm–Zn system and by Chiotti and Gill (1961) for the Th–Zn system have been plotted as a function of Zn content in fig. 85. All these figures show that the enthalpies of formation of the compounds of Zn with lanthanides become less negative from La to Lu but the variation is small. The values obtained for the Th–Zn system are of the same order of magnitude as those obtained with samarium at the Zn-rich side of the phase diagram but are clearly less negative when the Zn content decreases. The values obtained for the compounds formed with uranium are less negative than those obtained with rare-earth elements. With plutonium the value proposed by Chiotti et al. (1981) for the compound Pu_2Zn_{17} is comparable to the value proposed by these authors for the Th_2Zn_{17} compound.

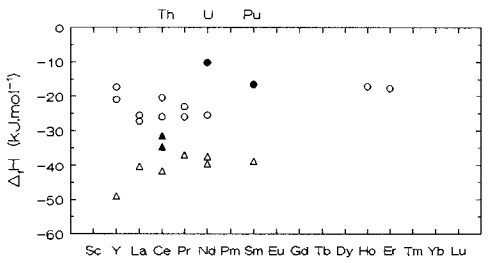

Fig. 83. Enthalpies of formation of rare earth (open symbols) and actinides (solid symbols) RZn_{12} or $AnZn_{12}$ compounds (open circle; solid circles) and RZn_2 or $AnZn_2$ compounds (open triangle; solid triangles) as a function of atomic number. The references of the data are quoted in table 29.

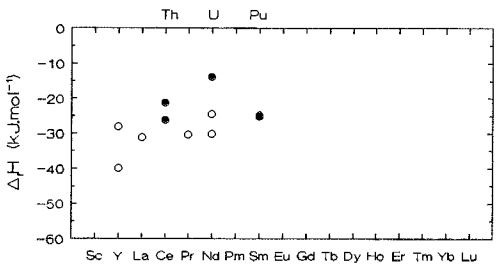

Fig. 84. Enthalpies of formation of rare earth (open circles) and actinide (solid circles). R_2Zn_{17} or An_2Zn_{17} compounds as a function of atomic number. The references of the data are quoted in table 29.

Thermodynamic data on Cd-based alloys are scarce. They concern only alloys very rich in Cd, and there are no data for the Cd–Th system. All the values of the enthalpies of formation have been reported in fig. 86. The evolution in the rare-earth series cannot be discussed because there is a lack of data for the end of the lanthanide series. The enthalpies of formation of UCd_{11} and $PuCd_{11}$ are less negative than the enthalpies of

Table 29
Enthalpies and entropies of formation of intermetallic compounds of Zn with rare earths and actinides ($\Delta_f H^\circ$: kJ/mol of atoms, $\Delta_f S^\circ$: $J\,K^{-1}$/mol of atoms)

System	Compound	$\Delta_f H^\circ$	$\Delta_f S^\circ$	Reference state	Authors and method
Y–Zn	YZn_{12}	−24.1	−11.7	α-Y, Zn_l; 773 K	Hoshino and Plambeck 1970
		−17.3	−1.9	α-Y, Zn_s	emf liq. electrolyte 723–843 K
	YZn_{12}	−24.1	−11.9	α-Y, Zn_l; 723 K	Yamshchikov et al. 1979a
		−17.3	−2.1	α-Y, Zn_s	emf liq. electrolyte 690–1040 K
	Y_2Zn_{17}	−34.7	−18.4	α-Y, Zn_l; 973 K	
		−28.1	−9.0	α-Y, Zn_s	
	Y_2Zn_{17}	−46.5	−29.3	α-Y, Zn_l; 973 K	Butorov et al. 1973
		−39.9	−19.8	α-Y, Zn_s	emf liq. electrolyte 948–1173 K
	YZn_{12}	−27.7	−15.6	α-Y, Zn_l; 725–915 K	Chiotti et al. 1963, Mason and
		−20.9	−5.9	α-Y, Zn_s	Chiotti 1976
	Y_2Zn_{17}	−34.5	−17.9	α-Y, Zn_l;750–1100 K	vap. press. dewpoint 725–1290 K
		−27.9	−8.4	α-Y, Zn_s	
	YZn_6	−37.7	−17.5	α-Y, Zn_l; 775–1125K	
		−31.4	−8.5	α-Y, Zn_s	
	$Y_{13}Zn_{58}$	−41.5	−17.7	α-Y, Zn_l; 800–1140 K	
		−35.6	−9.0	α-Y, Zn_s	
	Y_3Zn_{11}	−44.2	−18.1	α-Y, Zn_l; 815–1150 K	
		−38.4	−9.8	α-Y, Zn_s	
	YZn_3	−47.0	−18.7	α-Y, Zn_l; 785–1185 K	
		−41.5	−10.8	α-Y, Zn_s	
	β-YZn_2	−51.1	−18.4	α-Y, Zn_l; 1035–1290 K	
		−46.2	−11.3	α-Y, Zn_s	
	α-YZn_2	−53.9	−21.1	α-Y, Zn_l; 800–1015 K	
		−49.0	−14.0	α-Y, Zn_s	
	YZn	−50.3	−18.3	α-Y, Zn_l; 900–1145 K	
		−46.6	−13.0	α-Y, Zn_s	
La–Zn	$LaZn_{11}$	−34.0	−18.6	β-La, Zn_l; 723 K	Lesourd and Plambeck 1969
		−27.2	−8.9	α-La, Zn_s	emf liq. electrolyte 703–873 K
	$LaZn_{11}$	−32.6	−17.1	β-La, Zn_l; 1000 K	Mullayanov et al. 1969
		−25.9	−7.4	α-La, Zn_s	emf liq. electrolyte 715–1022 K
	$LaZn_{11}$	−32.3	−16.7	β-La, Zn_l; 723 K	Johnson and Yonco 1970
		−25.6	−7.0	α-La, Zn_s	emf liq. electrolyte 705–793 K
	$LaZn_{11}$	−32.2	−17.2	β-La, Zn_l; 1000 K	Kovalevskiy et al. 1972
		−25.5	−7.5	α-La, Zn_s	emf liq. electrolyte 720–1120 K
	$LaZn_9$	−36.0	−18.4	β-La, Zn_l; 1000 K	
		−29.4	−8.9	α-La, Zn_s	
	$LaZn_8$	−37.7	−18.8	β-La, Zn_l; 1000 K	
		−31.2	−9.4	α-La, Zn_s	
	$LaZn_7$	−38.9	−18.8	β-La, Zn_l; 1000 K	
		−32.5	−9.5	α-La, Zn_s	
	$LaZn_6$	−40.2	−18.4	β-La, Zn_l; 1000 K	
		−33.9	−9.3	α-La, Zn_s	
	$LaZn_4$	−42.3	−16.7	β-La, Zn_l; 1000 K	
		−36.3	−8.2	α-La, Zn_s	
	$LaZn_2$	−45.2	−14.2	β-La, Zn_l; 1000 K	
		−40.2	−7.1	α-La, Zn_s	
	LaZn	−35.6	−9.2	β-La, Zn_l; 1000 K	
		−31.7	−3.9	α-La, Zn_s	

continued on next page

Table 29, *continued*

System	Compound	$\Delta_f H°$	$\Delta_f S°$	Reference state	Authors and method
Ce–Zn	$CeZn_{11}$	−27.1	−15.0	γ-Ce, Zn_l; 773–973 K	Bayanov and Serebrennikov 1965
		−20.4	−5.3	γ-Ce, Zn_s	emf liq. electrolyte 773–973 K
	$CeZn_{11}$	−30.7	−15.7	γ-Ce, Zn_l; 723 K	Johnson and Yonco 1970
		−24.0	−6.0	γ-Ce, Zn_s	emf liq. electrolyte 710–1018 K
	$CeZn_{11}$	−32.6	−16.9	γ-Ce, Zn_l; 773 K	Chiotti and Mason 1965
		−25.9	−7.2	γ-Ce, Zn_s	vap. press. dewpoint 410–895 K
	Ce_2Zn_{17}	−36.9	−17.3	γ-Ce, Zn_l; 773 K	
		−30.4	−7.9	γ-Ce, Zn_s	
	$CeZn_7$	−38.9	−17.7	γ-Ce, Zn_l; 773 K	
		−32.5	−8.4	γ-Ce, Zn_s	
	$CeZn_{5.25}$	−41.3	−17.8	γ-Ce, Zn_l; 773 K	
		−35.2	−8.9	γ-Ce, Zn_s	
	$Ce_{13}Zn_{58}$	−42.3	−17.6	γ-Ce, Zn_l; 773 K	
		−36.3	−9.0	γ-Ce, Zn_s	
	Ce_3Zn_{11}	−43.4	−17.4	γ-Ce, Zn_l; 773 K	
		−37.6	−9.1	γ-Ce, Zn_s	
	$CeZn_3$	−44.4	−17.3	γ-Ce, Zn_l; 773 K	
		−38.9	−9.3	γ-Ce, Zn_s	
	$CeZn_2$	−46.5	−17.4	γ-Ce, Zn_l; 773 K	
		−41.6	−10.3	γ-Ce, Zn_s	
	CeZn	−41.0	−14.6	γ-Ce, Zn_l; 773 K	
		−37.3	−9.4	γ-Ce, Zn_s	
	$CeZn_{11}$	−30.1	−15.0	γ-Ce, Zn_l; 715–1022 K	Lebedev et al. 1971a
		−23.4	−5.3	γ-Ce, Zn_s	emf liq. electrolyte 715–1022 K
Pr–Zn	$PrZn_{11}$	−29.7	−14.9	α-Pr, Zn_l; 723 K	Johnson and Yonco 1970
		−23.0	−5.2	α-Pr, Zn_s	emf liq. electrolyte 710–1018 K
	$PrZn_{11}$	−31.2	−15.9	α-Pr, Zn_l; 773 K	Chiotti and Mason 1971, Chiotti
		−26.0	−9.9	α-Pr, Zn_s ; 298 K	1972, 1974
	Pr_2Zn_{17}	−35.4	−16.2	α-Pr, Zn_l; 773 K	vap. press. dewpoint 430–930 K
		−30.3	−10.3	α-Pr, Zn_s ; 298 K	
	Pr_3Zn_{22}	−36.6	−15.9	α-Pr, Zn_l; 773 K	
		−31.6	−10.2	α-Pr, Zn_s ; 298 K	
	$Pr_{13}Zn_{58}$	−39.2	−14.4	α-Pr, Zn_l; 773 K	
		−34.6	−9.0	α-Pr, Zn_s ; 298 K	
	Pr_3Zn_{11}	−40.0	−13.8	α-Pr, Zn_l; 773 K	
		−35.5	−8.7	α-Pr, Zn_s ; 298 K	
	$PrZn_3$	−40.4	−12.9	α-Pr, Zn_l; 773 K	
		−36.1	−8.1	α-Pr, Zn_s ; 298 K	
	$PrZn_2$	−40.7	−10.6	α-Pr, Zn_l; 773 K	
		−37.0	−6.3	α-Pr, Zn_s ; 298 K	
	PrZn	−36.0	−8.0	α-Pr, Zn_l; 773 K	
		−33.3	−4.6	α-Pr, Zn_s ; 298 K	
Nd–Zn	Nd_2Zn_{17}	−24.5		α-Nd, Zn_s; 300 K	Borzone et al. 1987
	Nd_3Zn_{22}	−25.2		(same)	react. calorim. and acid sol'n
	$Nd_{13}Zn_{58}$	−29.0		(same)	calorim.
	Nd_3Zn_{11}	−31.7		(same)	
	$NdZn_3$	−32.7		(same)	
	$NdZn_2$	−37.5		(same)	
	NdZn	−32.2		(same)	

continued on next page

Table 29, *continued*

System	Compound	$\Delta_f H^o$	$\Delta_f S^o$	Reference state	Authors and method
	$NdZn_{11}$	−32.1	−17.6	α-Nd, Zn_l; 773 K	Chiotti and Mason 1973
		−25.4	−7.9	α-Nd, Zn_s; 298 K	vap. press. dewpoint 695–1215 K
	Nd_2Zn_{17}	−36.7	−18.1	α-Nd, Zn_l; 773 K	
		−30.1	−8.6	α-Nd, Zn_s; 298 K	
	Nd_3Zn_{22}	−39.0	−18.9	α-Nd, Zn_l; 773 K	
		−32.5	−9.5	α-Nd, Zn_s; 298 K	
	$Nd_{13}Zn_{58}$	−41.8	−17.3	α-Nd, Zn_l; 773 K	
		−35.8	−8.7	α-Nd, Zn_s; 298 K	
	Nd_3Zn_{11}	−43.4	−17.3	α-Nd, Zn_l; 773 K	
		−37.6	−9.0	α-Nd, Zn_s; 298 K	
	$NdZn_3$	−43.8	−16.5	α-Nd, Zn_l; 773 K	
		−38.3	−8.6	α-Nd, Zn_s; 298 K	
	$NdZn_2$	−44.5	−14.5	α-Nd, Zn_l; 773 K	
		−39.6	−7.5	α-Nd, Zn_s; 298 K	
	NdZn	−39.1	−10.6	α-Nd, Zn_l; 773 K	
		−35.5	−5.4	α-Nd, Zn_s; 298 K	
	Nd_2Zn_{17}	−27.7	−5.4	α-Nd, Zn_s; 300 K	Borzone et al. 1987
	Nd_3Zn_{22}	−28.7	−5.6	(same)	phase diag. and thermodynamic data
	Nd_3Zn_{58}	−32.0	−5.3	(same)	optimization
	Nd_3Zn_{11}	−33.5	−5.5	(same)	
	$NdZn_2$	−38.0	−5.8	(same)	
	NdZn	−32.0	−2.5	(same)	
Sm–Zn	Sm_2Zn_{17}	−34.5	−15.5	α-Sm, Zn_l; 773 K	Chiotti and Mason 1967
		−24.8	−0.21	α-Sm, Zn_s; 298 K	vap. press. dewpoint 405–890 K
	Sm_3Zn_{22}	−35.6	−15.1	α-Sm, Zn_l; 773 K	
		−26.1	0.0	α-Sm, Zn_s; 298 K	
	$Sm_{13}Zn_{58}$	−40.3	−14.8	α-Sm, Zn_l; 773 K	
		−31.5	−0.8	α-Sm, Zn_s; 298 K	
	Sm_3Zn_{11}	−41.9	−14.6	α-Sm, Zn_l; 773 K	
	$SmZn_3$	−33.5	−1.2	α-Sm, Zn_s; 298 K	
		−43.3	−14.5	α-Sm, Zn_l; 773 K	
	$SmZn_2$	−35.3	−1.7	α-Sm, Zn_s; 298 K	
		−46.0	−13.7	α-Sm, Zn_l; 773 K	
	SmZn	−38.8	−2.3	α-Sm, Zn_s; 298 K	
		−40.2	−9.1	α-Sm, Zn_l; 773 K	
		−34.7	−0.5	α-Sm, Zn_s; 298 K	
Ho–Zn	$HoZn_{12}$	−23.9	−13.0	α-Ho, Zn_l; 823 K	Yamshchikov et al. 1985a
		−17.1	−3.2	α-Ho, Zn_s	emf liq. electrolyte 690–1020 K
Er–Zn	$ErZn_{12}$	−17.7	−4.2	α-Er, Zn_s; 683 K	Yamshchikov et al. 1985b
					emf liq. electrolyte 664–1070 K
	$ErZn_{12}$	−24.4	−13.6	α-Er, Zn_l; 883 K	
		−17.6	−3.8	α-Er, Zn_s	
	Er_2Zn_{17}	−19.1	−4.4	α-Er, Zn_l; 1023 K	
				α-Er, Zn_s	
	$ErZn_{12}$	−24.3	−15.8	Er_s, Zn_l; 773–973 K	Bayanov and Serebrennikov 1965
		−17.5	−6.0	Er_s, Zn_s	emf liq. electrolyte 773–973 K
Th–Zn	Th_2Zn_{17}	−30.9	−14.8	α-Th, Zn_l; 773 K	Chiotti and Gill 1961
		−21.2	−0.8	α-Th, Zn_s; 298 K	vap. press. dewpoint 655–1220 K
	$ThZn_4$	−36.9	−13.3	α-Th, Zn_l; 773 K	
		−28.2	0.4	α-Th, Zn_s; 298 K	

continued on next page

Table 29, *continued*

System	Compound	$\Delta_f H^\circ$	$\Delta_f S^\circ$	Reference state	Authors and method
Th–Zn	$ThZn_2$	−38.6	−13.3	α-Th, Zn_l; 773 K	Chiotti and Gill 1961
(*cont'd*)		−31.4	−2.4	α-Th, Zn_s; 298 K	vap. press. dewpoint 655–1220 K
	Th_2Zn	−22.3	−7.0	α-Th, Zn_l; 773 K	
		−18.7	−1.3	α-Th, Zn_s; 298 K	
	Th_2Zn_{17}	−32.6	−18.1	α-Th, Zn_l; 1000 K	Kanashin et al. 1972
		−26.1	−8.6	α-Th, Zn_s	emf liq. electrolyte 973–1123K
	Th_2Zn_{17}	−31.0	−15.5	α-Th, Zn_l; 723–973 K	Chiotti and Koizumi 1960
		−24.4	−6.0	α-Th, Zn_s	emf. liq. electrolyte 723–973 K
	Th_2Zn_{17}	−32.4	−16.4	α-Th, Zn_l; 723–923 K	Chiotti and Dock 1975
		−25.9	−6.9	α-Th, Zn_s	emf liq. electrolyte 723–923 K
	Th_2Zn_{17}	−25.9	−6.9	α-Th, Zn_s; 298 K	Chiotti et al. 1981
	$ThZn_4$	−32.1	−6.9		assessment 298–692.6 K
	$ThZn_2$	−34.6	−7.4		
	Th_2Zn	−20.3	−4.0		
U–Zn	UZn_{12}	−17.0	−11.8	α-U, Zn_l; 693–942 K	Chiotti and Mason 1975 or Chiotti
		−10.2	−2.0	α-U, Zn_s	et al. 1981
	U_2Zn_{17}	−20.5	−13.6	α-U, Zn_l; 693–942 K	assessment[a]
		−13.9	−4.1	α-U, Zn_s	
Pu–Zn	$PuZn_{12}$	−16.5	−3.4	α-Pu, Zn_s; 298–392 K	Johnson and Chasanov 1964
	Pu_2Zn_{17}	−25.3	−8.6	α-Pu, Zn_s; 298–698 K	emf liq. electrolyte 695–913 K; reviewed by Chiotti et al. 1981

[a] Assessment based on a large number of experimental determinations performed by Johnson and Feder (1962b), Chiotti et al. (1966), Volkovich et al. (1968, 1971), Hoshino and Plambeck (1969), Chiotti and Koizumi (1960) and Chiotti and Kateley (1967) using emf measurements, and by Chiotti and Kilp (1960) and Chiotti and Mason (1975) using vapour pressure measurements.

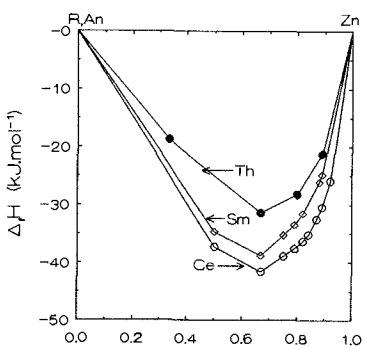

Fig. 85. Enthalpies of formation $R_{1-x}Zn_x$ or $An_{1-x}Zn_x$ compounds. The data for M=–Ce (open circles), Sm (open diamonds) and Th (solid circles) are from Chiotti and Mason (1965), Chiotti and Mason (1967), and Chiotti and Gill (1961), respectively.

formation of (La, Ce, Pr)Cd_{11}, and the enthalpies of formation of $NpCd_6$ and $PuCd_6$ are less negative than the enthalpy of formation of $GdCd_6$.

Regarding the thermodynamic data concerning Hg based alloys, one notices that the data obtained by Jangg and Steppan (1965) in the Th–Hg system seem very negative,

Table 30
Enthalpies and entropies of formation of intermetallic compounds of Cd with rare earths and actinides ($\Delta_f H°$: kJ/mol of atoms, $\Delta_f S°$: $J K^{-1}$/mol of atoms)

System	Compound	$\Delta_f H°$	$\Delta_f S°$	Reference state	Authors and method
La–Cd	$LaCd_{11}$	−25.2	−15.2	β-La, Cd_l; 723 K	Johnson and Yonco 1970
		−19.2	−5.1	α-La, Cd_s	emf liq. electrolyte 670–804 K
Ce–Cd	$CeCd_{11}$	−22.7	−16.2	γ-Ce, Cd_l; 673–823 K	Bayanov and Serebrennikov 1965
		−17.0	−6.6	γ-Ce, Cd_s	emf liq. electrolyte 673–823 K
	$CeCd_{11}$	−24.6	−15.6	γ-Ce, Cd_l; 723 K	Johnson and Yonco 1970
		−18.9	−6.0	γ-Ce, Cd_s	emf liq. electrolyte 638–884 K
Pr–Cd	$PrCd_{11}$	−24.1	−15.6	α-Pr, Cd_l; 723 K	Johnson and Yonco 1970
		−18.4	−6.1	α-Pr, Cd_s	emf liq. electrolyte 635–825 K
Gd–Cd	$GdCd_6$	−28.2	−15.7	α-Gd, Cd_l; 728 K	Roshchina and Bayanov 1981
		−22.9	−7.1	α-Gd, Cd_s	emf liq. ectrolyte 663–801 K
U–Cd	UCd_{11}	−9.5	−12.6	α-U, Cd_l; 700 K	Johnson and Feder 1962a,b
		−3.8	−3.1	α-U, Cd_s	emf liq. electrolyte 671–746 K
	UCd_{11}	−12.0	−15.7	α-U, Cd_l; 673 K	Veleckis 1961
		−6.3	−6.2	α-U, Cd_s	vap. press. 578–651 K
Np–Cd	$NpCd_{11}$	−14.7	−13.5	β-Np, Cd_l; 700 K	Krumpelt et al. 1974
		−8.5	−3.1	α-Np, Cd_s	emf liq. electrolyte 650–850 K
	$NpCd_6$	−16.4	−11.8	β-Np, Cd_l; 800 K	
		−10.3	−1.4	α-Np, Cd_s	
Pu–Cd	$PuCd_{11}$	−16.0	−12.4	δ-Pu, Cd_l; 672 K	Johnson et al. 1965
		−9.9	−1.9	Pu_s, Cd_s	emf liq. electrolyte 625–900 K
	$PuCd_6$	−23.5	−15.5	ε-Pu, Cd_l; 800 K	
		−17.2	−4.7	Pu_s, Cd_s	

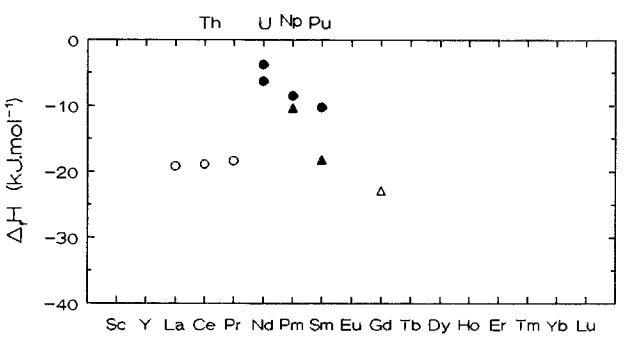

Fig. 86. Enthalpies of formation of rare earth (open symbols) and actinide (solid symbols) $(R, An)Cd_{11}$ compounds (open circle; solid circles) and $(R, An)Cd_6$ compounds (open triangle; solid triangles) as a function of atomic number. The references of the data are quoted in table 30.

Table 31
Enthalpies and entropies of formation of intermetallic compounds of Hg with rare earths and actinides ($\Delta_f H°$: kJ/mol of atoms, $\Delta_f S°$: $J K^{-1}$/mol of atoms)

System	Compound	$\Delta_f H°$	$\Delta_f S°$	Reference state	Authors and method
Y–Hg	YHg_3	−19	−8	α-Y, Hg_l; 700 K	Kirchmayr and Jangg 1965
	YHg_2	−27	−17	(same)	vap. press. 557–778 K
	YHg	−27	−21	(same)	
Ce–Hg	$CeHg_4$	−9.5	(a)	γ-Ce, Hg_s	Biltz and Meyer 1928
					vap. press. 538–646 K; see Hultgren et al. 1973a
Th–Hg	$ThHg_3$	−123	−12.2	α-Th, Hg_l; 623–743 K	Jangg and Steppan 1965
	$ThHg_2$	−137	−13.4	α-Th, Hg_l; 713–773 K	vap. press. 623–893 K
	ThHg	−132	−12.8	α-Th, Hg_l; 813–893 K	
U–Hg	UHg_4	−15.6	−13.3	α-U, Hg_l; 388–683 K	Chiotti et al. 1979
	UHg_3	−15.9	−11.7	α-U, Hg_l; 433–684 K	assessment[b]
	UHg_2	−17.6	−12.5	α-U, Hg_l; 548–853 K	
	UHg	−13.8	−10.0	α-U, Hg_l; $T < 942$ K	

[a] $\Delta_f G$, 613 K.
[b] This assessment has been done using the data of Forsberg (1960) and Jangg and Steppan (1965) and those of Chiotti et al. (1979) obtained by vapour pressure and emf measurements.

and consequently unrealistic. The only conclusion that may safely be drawn is that the enthalpies of formation of the compounds of the U–Hg system are less negative than those obtained for the corresponding composition in the Y–Hg system.

7. Rare earths and actinides with elements of column IIIB

7.1. *Phase diagrams and intermetallic compounds*

The main features of the binary phase diagrams of rare earths and actinides with elements Al, Ga, In and Tl are presented in figs. 87–90. All these binary systems exhibit intermetallic compounds.

With Al the intermetallic compound RAl_2 or $AnAl_2$ appears in all phase diagrams. These compounds, in each diagram, always have the highest melting point, and the structure is always the same (prototype Cu_2Mg) except for Th (AlB_2 prototype). The $LaAl_2$ compound exhibits two allotropic forms; one has the structure of Cu_2Mg, the other the structure of AlB_2. One may also notice that a compound with stoichiometry RAl_3 or $AnAl_3$ is present in all phase diagrams: $ThAl_3$ has the same structure (Ni_3Sn) as the heavy-lanthanide-based compounds, UAl_3, $NpAl_3$ and $PuAl_3$ have the same structure ($AuCu_3$) as the light-lanthanide-based compounds (fig. 91). Investigations in rare-earth–aluminum phase diagrams have recently been performed by Kononenko and Golubev (1990).

With Ga, the stoichiometry of the compound with the highest melting temperature is RGa_2 or $AnGa_2$ for the first elements of the lanthanide series (La → Ho) and for

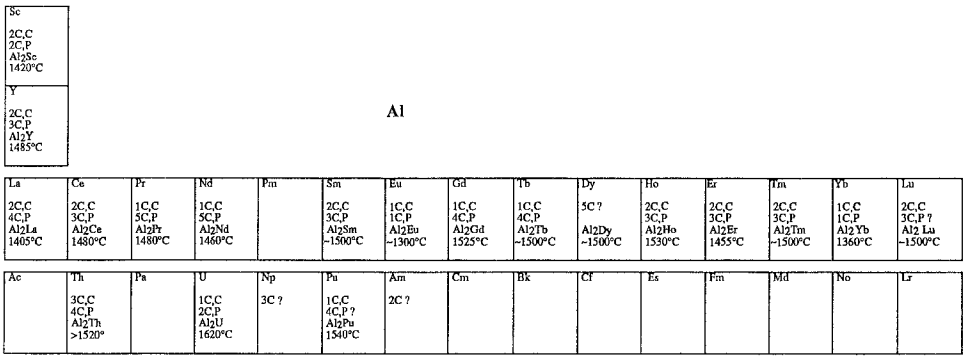

Fig. 87. Main features of the phase diagrams of aluminum with rare earths and actinides.

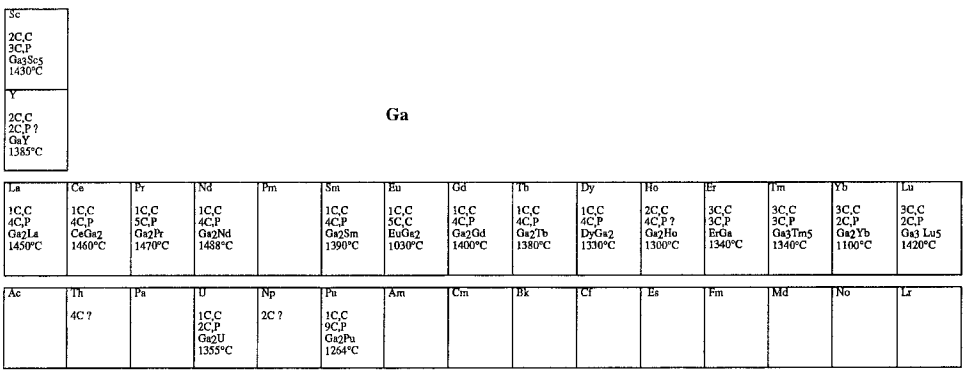

Fig. 88. Main features of the phase diagrams of gallium with rare earths and actinides.

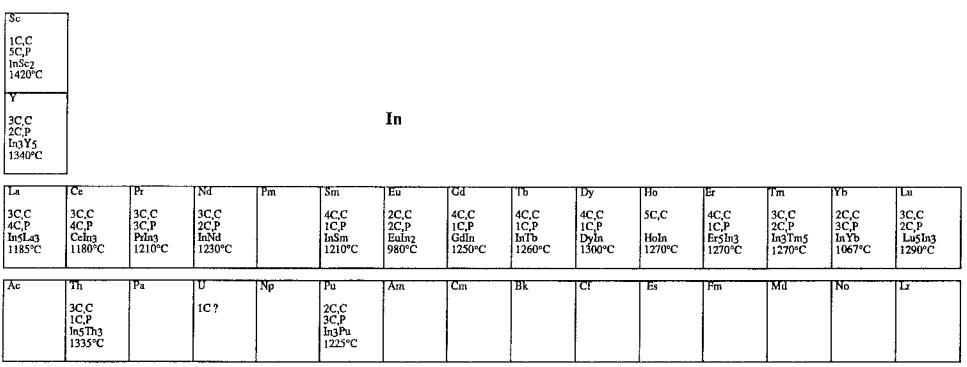

Fig. 89. Main features of the phase diagrams of indium with rare earths and actinides.

uranium and plutonium. No information is available concerning the compounds present in the Th–Ga phase diagram. For the elements at the end of the lanthanide series the stoichiometry of the compound with the highest melting temperature corresponds to a

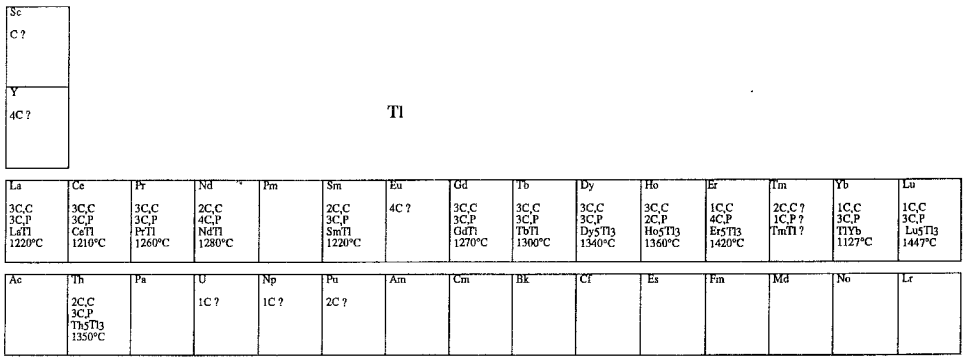

Fig. 90. Main features of the phase diagrams of thallium with rare earths and actinides.

Phase	Sc	Y	La	Ce	Pr	Nd	Pm	Sm	Eu	Gd	Tb	Dy	Ho	Er	Tm	Yb	Lu	Ac	Th	Pa	U	Np	Pu	Prototype or
M_3Al 25%		x	•	•LT xHT	•LT xHT	•																+ ?		$AuCu_3$ x Ni_3Sn • $(AlPu_3)$ +
M_2Al 33.3%	x	•			•	•		•		•	•	•	•	•					+					$InNi_2$ x Co_2Si • Al_2Cu +
MAl_x 36.4 → 38.7%																			?					
M_3Al_2 40%		x								x	x	x	x	x					•					Al_2Zr_3 x Si_2U_3 •
MAl 50%	x	•	+	+	oLT +HT	o		o		o	o	o	o	o	o				•				Δ	ClCs x BCr • AlCe + AlDy o AlPu Δ
M_2Al_3 60%																			?					
M_4Al_7 63.6%																			?					
MAl_2 66.7%	x	x	x •	x	x	x		x	x	x	x	x	x	x	x	x	x		•		x ?	x	x	Cu_2Mg x AlB_2 •
MAl_3 75%	x	•LT +HT	•	•	•	•		•		•	+	oLT ΔHT	Δ	x	x	x	x		•		x ?	x	x ❑	$AuCu_3$ x Ni_3Sn • $BaPb_3$ + Ni_3Ti o Al_3Ho Δ Al_3Pu ❑
M_2Al_7 77.8%																			x					Al_7Th_2 x
M_3Al_{11} 78.6%			xLT •HT	xLT •HT	xLT •HT	xLT •HT		•																α-$Al_{11}La_3$ x Al_4Ba •
MAl_4 80%									x												•	•	•	Al_4Ba x Al_4U •
Al composition	Sc	Y	La	Ce	Pr	Nd	Pm	Sm	Eu	Gd	Tb	Dy	Ho	Er	Tm	Yb	Lu	Ac	Th	Pa	U	Np	Pu	example ( )

Fig. 91. Stoichiometry and structure prototype (or example) of the compounds of Al with rare earths and actinides.

Phase	Sc	Y	La	Ce	Pr	Nd	Pm	Sm	Eu	Gd	Tb	Dy	Ho	Er	Tm	Yb	Lu	Ac	Th	Pa	U	Np	Pu	Prototype or
M_3Ga 25%			x	x		x		x															•	$AuCu_3$ x $(AlPu_3)$ •
M_2Ga 33.3%					x														+					Co_2Si x Al_2Cu +
M_5Ga_3 37.5%	x	x	•	+	Δ	•		•	?	•	•	•	x	x		+	x						+	Mn_5Si_3 x B_3Cr_5 • Si_3W_5 + Ba_5Si_3 Δ
M_3Ga_2 40%				x						•									+					Al_2Zr_3 x Si_2U_3 + Ga_2Gd_3 •
M_5Ga_4 44.4%	x																							$Ge_{10}Ho_{11}$
MGa 50%	x	x	x	x	x	x		x	?	x	x	x	x	x	x	•	x		+				o	BCr x AuCu • AgSr + GaPu o
M_2Ga_3 60%									?												x		?	(Ga_3U_2) x
M_3Ga_5 62.5%		x											x	x	x	x								Ga_5Tm_3 x
MGa_2 66.7%	x	?	•	•	•	•		•	+LT •HT	•	•	•	•	•	x	+	x		o		ΔLT •RT		•	$CeCu_2$ x AlB_2 • $CaIn_2$ + Si_2Th o (Ga_2U) Δ
M_2Ga_5 71.4%									?															
MGa_3 75%	x										xHT •LT	xHT +LT	x	x	x		x				x		• +	$AuCu_3$ x Ni_3Sn • Ga_3Pu +
M_2Ga_7 77.8%																							?	
$MGa_{3.7}$ 78.7%																							?	
MGa_4 80%			x		?				•							•							+	(Ga_4La) x Al_4Ba • Al_4U +
MGa_6 85.7%			x	?	x	x		? x		x	x	x	x	x	x	x							x	Ga_6Pu x
M_2Ga_{15} 88.2%																							?	
Ga composition	Sc	Y	La	Ce	Pr	Nd	Pm	Sm	Eu	Gd	Tb	Dy	Ho	Er	Tm	Yb	Lu	Ac	Th	Pa	U	Np	Pu	example ( )

Fig. 92. Stoichiometry and structure prototype (or example) of the compounds of Ga with rare earths and actinides.

higher lanthanide content. Various structures are observed for compounds of the same stoichiometry (fig. 92); one may only notice that many RGa_2 and $AnGa_2$ compounds crystallize in the $CeCu_2$ structure. Recently investigations have been performed by Cirafici and Fornasini (1990) in the Ga–Yb system.

Regarding indium-based alloys the stoichiometry of the compound with the highest melting temperature varies in the lanthanide series; the lanthanide content of this compound increases with atomic number. From this point of view thorium has a similar behavior to the light lanthanides. A more remarkable similarity between the lanthanide and

Phase	Sc	Y	La	Ce	Pr	Nd	Pm	Sm	Eu	Gd	Tb	Dy	Ho	Er	Tm	Yb	Lu	Ac	Th	Pa	U	Np	Pu	Prototype or
M_3In 25%	•		x	xLT +HT	x	x		x															x	$AuCu_3$ x Ni_3Sn • Cu +
M_2In 33.3%	•	•	•	•	•	•				•	•	•	•	•	•		•		x				?	Al_2Cu x $InNi_2$ •
M_5In_3 37.5%	?	x								•	•	•	•LT xHT	x	x		x							Mn_5Si_3 x Si_3W_5 •
MIn 50%	?	+	+	?	+			+		+		+	+	+	+	+			x				•	ThTl x AuCu • ClCs +
M_3In_5 62.5%	?	x	x	x		x		x		x	x	x	x	x	x				x					Pd_5Pu_3 x
MIn_2 66.7%			x	x					•							•								$CeCu_2$ x $CaIn_2$ •
MIn_3 75%	x	x	x	x	x	x		x		x	x	x	x	x	x	x	x		x		x		x	$AuCu_3$ x
MIn_4 80%									?															
In composition	Sc	Y	La	Ce	Pr	Nd	Pm	Sm	Eu	Gd	Tb	Dy	Ho	Er	Tm	Yb	Lu	Ac	Th	Pa	U	Np	Pu	example ( )

Fig. 93. Stoichiometry and structure prototype (or example) of the compounds of In with rare earths and actinides.

Phase	Sc	Y	La	Ce	Pr	Nd	Pm	Sm	Eu	Gd	Tb	Dy	Ho	Er	Tm	Yb	Lu	Ac	Th	Pa	U	Np	Pu	Prototype or
M_3Tl 25%			xLT •HT	xLT •HT	xLT •HT	xLT •HT																	x	$AuCu_3$ x Cu •
M_8Tl_3 27.3%																x								Tl_3Yb_8 x
M_2Tl 33.3%					•	•		•			•	•				+			x					Al_2Cu x $InNi_2$ • Co_2Si +
M_5Tl_3 37.5%		x	•	•	•	•		•			• x	x	x	x	x		x		x					Mn_5Si_3 x Si_3W_5 •
M_5Tl_{3+x}											x	x	x	x										B_3Cr_5 x
MTl 50%		•	•RT +HT oLT	•RT +HT oLT	•RT +HT oLT	•RT +HT oLT		•RT +HT oLT	•		•RT +HT oLT	•RT +HT oLT	•RT +HT oLT	•RT +HT oLT	•	•RT +HT	?		x					ThTl x ClCs • W + AuCu o
M_3Tl_5 62.5%		x	x	x	x	x		x			x	x	x	x			x		x					Pd_5Pu_3 x
MTl_2 66.7%									x															$CaIn_2$ x
MTl_3 75%		x	x	x	x	x		x	+? x		x	x	x	x	x	x	x		x		x	x	•	$AuCu_3$ x Mg • Ni_3Sn +
Tl composition	Sc	Y	La	Ce	Pr	Nd	Pm	Sm	Eu	Gd	Tb	Dy	Ho	Er	Tm	Yb	Lu	Ac	Th	Pa	U	Np	Pu	example ( )

Fig. 94. Stoichiometry and structure prototype (or example) of the compounds of Tl with rare earths and actinides.

actinide series is that the compounds RIn_3 and $AnIn_3$ always exhibit the $AuCu_3$ structure (fig. 93). The same observation is made considering the compounds RTl_3 and $AnTl_3$ (fig. 94). With thallium the compound with the highest melting point is RTl for the first

Table 32
Structure characteristics of X = Al, Ga, In, Tl and rare-earth or actinide (M = R, An) intermetallic compounds

Phase	Pearson symbol	Space group	Strukturbericht designation	Prototype or (example)
MX_6	tP14	P4/nbm		Ga_6Pu
MX_4	o*			(Ga_4La)
	tI10	I4/mmm	$D1_3$	Al_4Ba
	oI20	Imma	$D1_b$	Al_4U
M_3X_{11}	oI28	Immm		α-$Al_{11}La_3$
	tI10	I4/mmm	$D1_3$	Al_4Ba(Al deficient)
M_2X_7	oP18	Pbam		Al_7Th_2
MX_3	cP4	$Pm\bar{3}m$	$L1_2$	$AuCu_3$
	hP8	$P6_3/mmc$	DO_{19}	Ni_3Sn
	hR12	$R\bar{3}m$		$BaPb_3$
	hP16	$P6_3/mmc$	DO_{24}	Ni_3Ti
	hR20	$R\bar{3}m$		Al_3Ho
	hR16	$R\bar{3}m$		Ga_3Pu
	hP2	$P6_3/mmc$	A_3	Mg
	hP24	$P6_3/mmc$		Al_3Pu
MX_2	cF24	$Fd\bar{3}m$	C15	Cu_2Mg
	hP3	P6/mmm	C32	AlB_2
	oI12	Imma		$CeCu_2$
	hP6	$P6_3/mmc$		$CaIn_2$
	tI12	$I4_1/amd$	C_c	Si_2Th
	oC*	Cmmm		$(\alpha$-$Ga_2U)$
M_3X_5	oP32	Pnma		Ga_5Tm_3
	oC32	Cmcm		Pd_5Pu_3
M_2X_3	oC32	Cmcm		(Ga_3U_2)
MX	cP2	$Pm\bar{3}m$	B2	ClCs
	oC8	Cmcm	Bf	BCr
	oC16	Cmcm		AlCe
	oP16	Pbcm		AlDy
	cI58	$I\bar{4}3m$		$(\eta$-AlPu)Cu_5Zn_8
	tP4	P4/mmm	$L1_0$	AuCu
	oP16	Pnma		AgSr
	tI16	I4mm		GaPu
	oP24	Pbcm		ThTl
	cI2	$Im\bar{3}m$	A2	W
M_5X_4	tI84	I4/mmm		$Ge_{10}Ho_{11}$
M_3X_2	tP20	$P4_2/mnm$		Al_2Zr_3
	tP10	P4/mbm	$D5_a$	Si_2U_3
	tI80	I4/mcm	$D8_l$	Ga_2Gd_3
M_5X_3	hP16	$P6_3/mcm$	$D8_8$	Mn_5Si_3
	tI32	I4/mcm	$D8_l$	B_3Cr_5
	tI32	I4/mcm	$D8_m$	Si_3W_5
	tP32	P4/ncc		Ba_5Si_3
M_2X	tI12	I4/mcm	C16	Al_2Cu
	hP6	$P6_3/mmc$	$B8_2$	$InNi_2$
	oP12	Pnma	C23	Co_2Si

continued on next page

Table 32, *continued*

Phase	Pearson symbol	Space group	Strukturbericht designation	Prototype or (example)
M_8X_3	aP22	P1		(Tl_3Yb_8)
M_3X	cP4	$Pm\bar{3}m$	$L1_2$	$AuCu_3$
	hP8	$P6_3/mmc$	DO_{19}	Ni_3Sn
	tP4	P4/mmm	$L6_0$	$(AlPu_3)$
	cF4	$Fm\bar{3}m$	A1	Cu

elements of the lanthanide series and R_5Tl_3 or An_5Tl_3 for the last elements of the series and also with thorium. The characteristics of the structures of the intermetallic compounds of Al, Ga, In and Tl and rare earths or actinides are reported in table 32.

Assessments or systematic studies of rare-earth or actinide binary alloys with elements of column IIIB have been performed by Gschneidner and Calderwood (1988d, 1989a) for all aluminum–rare-earth systems, and by Kassner and Peterson (1989a–d) and Kassner et al. (1990) for Al–actinides systems. Updated Al–Sc, Al–Eu and Al–Nd phase diagrams have been presented by Okamoto (1991r–t). Palenzona and Cirafici (1990a,b) and Peterson and Kassner (1988) studied the Ga–Gd, Ga–La and Ga–Pu systems. A systematic study of the behavior of rare earths with indium has been performed by Delfino et al. (1984). More recently Palenzona and Cirafici (1989b–d) and Okamoto (1990) presented assessments of In–(Yb, La, Gd, Eu) systems. Delfino et al. (1983, 1987) and Saccone et al. (1988, 1989b) studied the behavior of rare earths with thallium. An updated Tl–Y phase diagram has been presented by Okamoto (1991q).

7.2. *Thermodynamic data*

The enthalpies and entropies of formation of intermetallic compounds of Al, Ga, In and Tl with rare earths and actinides are reported in tables 33–36. Values of partial and integral enthalpies of mixing in Al, Ga and In based alloys have been obtained using calorimetric methods, and are reported in tables 37–39.

There is a large amount of data concerning the R–Al alloys, but unfortunately there is also a rather large discrepancy between some of the reported values. The enthalpies of formation of the RAl_2 compounds have been plotted as a function of atomic number in fig. 95. The disagreement between some values, though certainly discernable, is much less perceptible than that for other compositions, especially for those with a higher lanthanide content. We observe there is good agreement between the values obtained by Colinet et al. (1985), Sommer and Keita (1987), and recent results reported by Borzone et al. (1991) and Jung et al. (1991) using various calorimetric methods (Al solution calorimetry, direct reaction calorimetry, mixing and drop calorimetry). Therefore it appears that a large number of the values reported in table 33 must be rejected. In fig. 95 we have indicated by an arrow the values which seem more reliable to us. A slight decrease of the enthalpy of formation of the RAl_2 compounds from Sc to Y to La, and a slight increase from

Table 33
Enthalpies and entropies of formation of intermetallic compounds of Al with rare earths and actinides ($\Delta_f H°$: kJ/mol of atoms, $\Delta_f S°$: $J K^{-1}$/mol of atoms)

System	Compound	$\Delta_f H°$	$\Delta_f S°$	Reference state	Authors and method
Sc–Al	$ScAl_3$	−59.8		α-Sc, Al_s; 298 K	Pyagai and Vakhodov 1990
	$ScAl_2$	−94.1		(same)	acid sol'n calorim.
	ScAl	−62.0		(same)	
	Sc_2Al	−28.2		(same)	
	$Sc_{0.36}Al_{0.64}$	−47.7		α-Sc, Al_s; 298 K	Jung et al. 1991
					mixing and drop calorim. 1473 K
Y–Al	YAl_3	−47		α-Y, Al_s; 298 K	Snyder 1960
	YAl_2	−81		(same)	combustion calorim.
	YAl	−88		(same)	
	YAl_3	−47.5	−9.1	α-Y, Al_s; 620–906 K	Yamshchikov et al. 1975
		−57.0	−19.4	α-Y, Al_l; 906–1073 K	emf liq. electrolyte 620–1073 K
		−48.9	−10.7	α-Y, Al_s	
	YAl_3	−45.2	−6.7	α-Y, Al_s; 800 K	Kober et al. 1979a
	YAl_2	−57.7	−9.6	(same)	emf liq. electrolyte 673–873 K
	YAl	−76.6	−10.0	(same)	
	Y_3Al_2	−87.9	−13.4	(same)	
	Y_2Al	−79.9	−12.1	(same)	
	YAl_3	−69.7	−13.4	α-Y, Al_s; 298 K	Ran et al. 1989a
	YAl_2	−83.6	−12.8	(same)	optimization using data of phase
	YAl	−84.8	−18.3	(same)	diagram and thermodynamic
	Y_3Al_2	−72.4	−13.9	(same)	experiments
	Y_2Al	−61.1	−12.1	(same)	
	YAl_2	−50.4		α-Y, Al_s; 298 K	Jung et al. 1991
					mixing and drop calorim. 1473 K
La–Al	La_3Al_{11}	−65.8	−22.4	β-La, Al_l; 1000 K	Lebedev et al. 1972a
		−57.2	−13.2	α-La, Al_s	emf liq. electrolyte 953–1123 K
	$LaAl_4$	−35.3		α-La, Al_s; 292 K	Canneri and Rossi 1932
	$LaAl_2$	−50		(same)	acid sol'n calorim.
	La_3Al_{11}	−42.7	−7.9	β-La, Al_s; 800 K	Kober et al. 1977, Kober 1991
		−42.6	−7.8	α-La, Al_s	emf liq. electrolyte 683–873 K
	$LaAl_3$	−52.3	−8.8	β-La, Al_s; 800 K	
		−52.2	−8.6	α-La, Al_s	
	$LaAl_2$	−67.0	−10.0	β-La, Al_s; 800 K	
		−66.9	−9.8	α-La, Al_s	
	LaAl	−83.3	−14.2	β-La, Al_s; 800 K	
		−83.1	−13.9	α-La, Al_s	
	La_3Al	−49.4	−17.6	β-La, Al_s; 800 K	
		−49.1	−17.1	α-La, Al_s	
	$LaAl_2$	−54.2		α-La, Al_s; 298 K	Colinet et al. 1985
					Al sol'n calorim. 990 K
	La_3Al_{11}	−41		α-La, Al_s; 298 K	Sommer et al. 1988a
	$LaAl_2$	−47.1		(same)	Al sol'n calorim. 1120 K
	La_3Al	−25.0		(same)	
	$LaAl_2$	−50.0		α-La, Al_s; 298 K	Jung et al. 1991
					mixing and drop calorim. 1473 K

continued on next page

Table 33, *continued*

System	Compound	$\Delta_f H^o$	$\Delta_f S^o$	Reference state	Authors and method
Ce–Al	$CeAl_4$	−39		γ-Ce, Al_s; 292 K	Biltz and Pieper 1924
	Ce_3Al	−22		(same)	acid sol'n calorim.
	$CeAl_4$	−43.5	−10.2	γ-Ce, Al_s; 700–907 K	Kober et al. 1973a
		−52.7	−20.2	γ-Ce, Al_s; 907–1004K	emf liq. electrolyte 700–1004 K
		−44.1	−11.0	γ-Ce, Al_s	
	$CeAl_4$	−40.0	−6.1	γ-Ce, Al_s; 800 K	Kober et al. 1982a
	$CeAl_3$	−48.2	−5.8	(same)	emf liq. electrolyte 673–873 K
	$CeAl_2$	−50.0	−1.4	(same)	
	CeAl	−77.6	−8.2	(same)	
	Ce_3Al	−76.6	−41.8	(same)	
	$CeAl_2$	−52.2		γ-Ce, Al_s; 298 K	Colinet et al. 1985
					Al sol'n calorim. 998 K
	Ce_3Al_{11}	−39.5		γ-Ce, Al_s; 298 K	Sommer and Keita 1987
	$CeAl_2$	−48.9		(same)	Al sol'n calorim. 1125 K
	Ce_3Al	−16.4		(same)	
	Ce_3Al_{11}	−41		γ-Ce, Al_s; 300 K	Borzone et al. 1991
	$CeAl_2$	−50		(same)	direct react. calorim.
	CeAl	−46		(same)	
	Ce_3Al	−27		(same)	
	$CeAl_4$	−52.2	−19.8	γ-Ce, Al_l; 940–1100 K	Yamshchikov et al. 1977a
		−43.6	−10.6	γ-Ce, Al_s	emf liq. electrolyte 940–1100 K
Pr–Al	Pr_3Al_{11}	−46.2	−13.8	α-Pr, Al_s; 800 K	Kober et al. 1983a
	$PrAl_3$	−53.8	−21.4	(same)	emf liq. electrolyte
	$PrAl_2$	−71.0	−21.2	(same)	
	PrAl	−99.2	−40.4	(same)	
	Pr_2Al	−110.8	−57.3	(same)	
	Pr_3Al	−99.4	−67.1	(same)	
	Pr_3Al_{11}	−43.6		α-Pr, Al_s; 298 K	Canneri and Rossi 1933
					acid sol'n calorim.
	Pr_3Al_{11}	−44.3	−8.4	α-Pr, Al_s; 676–914 K	Efremov et al. 1975
		−54.8	−19.8	α-Pr, Al_l; 914–1023 K	emf liq. electrolyte 676–1023 K
		−46.3	−10.7	α-Pr, Al_s	
	$PrAl_2$	−54.2		α-Pr, Al_s; 298 K	Colinet et al. 1985
					Al sol'n calorim. at 998 K
Nd–Al	Nd_3Al_{11}	−47.8	−14.2	α-Nd, Al_s; 800 K	Kober et al. 1984
	$NdAl_3$	−55.4	−16.5	(same)	emf liq. electrolyte 673–873 K
	$NdAl_2$	−71.3	−21.9	(same)	
	NdAl	−95.8	−34.9	(same)	
	Nd_2Al	−107.8	−49.8	(same)	
	Nd_3Al	−88.2	−52.5	(same)	
	$NdAl_2$	−53.6		α-Nd, Al_s; 298 K	Colinet et al. 1985
					Al sol'n calorim. at 1000 K
	Nd_3Al_{11}	−41.0		α-Nd, Al_s; 300 K	Borzone et al. 1993a
	$NdAl_3$	−45.0		(same)	react. calorim.
	$NdAl_2$	−53.0		(same)	
	NdAl	−50.0		(same)	
	Nd_2Al	−36.5		(same)	
	Nd_3Al	−27.5		(same)	

continued on next page

Table 33, *continued*

System	Compound	$\Delta_f H^\circ$	$\Delta_f S^\circ$	Reference state	Authors and method
Sm–Al	$SmAl_2$	−54.3		α-Sm, Al_s; 298 K	Colinet et al. 1985 Al sol'n calorim. 1000 K
Eu–Al	$EuAl_2$	−36.0		Eu_s, Al_s; 298 K	Colinet et al. 1985 Al sol'n calorim. 1000 K
	$EuAl_4$	−40.2	−26.7	Eu_s, Al_s; 673–923 K	Dubinin et al. 1985b emf liq. electrolyte 673–1000 K
	$EuAl_4$	−50.6	−37.9	Eu_s, Al_l; 953–1073 K	Kober et al. 1986a
		−41.9	−28.7	Eu_s, Al_s	emf liq. electrolyte 953–1073 K
Gd–Al	$GdAl_3$	−46.4	−7.9	α-Gd, Al_s; 800 K	Kober et al. 1979b
	$GdAl_2$	−63.6	−15.1	(same)	emf liq. electrolyte 673–873 K
	GdAl	−86.6	−22.2	(same)	
	Gd_3Al_2	−98.3	−27.6	(same)	
	Gd_2Al	−89.5	−27.2	(same)	
	$GdAl_2$	−51.4		α-Gd, Al_s; 298 K	Sommer and Keita 1987
	GdAl	−39.4		(same)	Al sol'n calorim. 1125 K
	Gd_2Al	−34.7		(same)	
	$GdAl_3$	−43.4		α-Gd, Al_s; 298 K	Colinet et al. 1985, 1988a
	$GdAl_2$	−53.2		(same)	Al sol'n calorim. 1000 K
	GdAl	−42.9		(same)	
	Gd_3Al_2	−33.3		(same)	
	Gd_2Al	−29.0		(same)	
Tb–Al	$TbAl_2$	−52.4		α-Tb, Al_s; 298 K	Colinet et al. 1985 Al sol'n calorim. 1000 K
Dy–Al	$DyAl_2$	−52.7		α-Dy, Al_s; 298 K	Colinet et al. 1985 Al sol'n calorim. 1000 K
Ho–Al	$HoAl_2$	−52.5		α-Ho, Al_s; 298 K	Colinet et al. 1985 Al sol'n calorim. 1000 K
Er–Al	$ErAl_2$	−50.5		Er_s, Al_s; 298 K	Colinet et al. 1985 Al sol'n calorim. 1000 K
	$ErAl_2$	−49.1		Er_s, Al_s; 298 K	Sommer and Keita 1987 Al sol'n calorim. 1125 K
Tm–Al	$TmAl_2$	−51.0		Tm_s, Al_s; 298 K	Colinet et al. 1985 Al sol'n calorim. 1000 K
Yb–Al	$YbAl_2$	−33.5		α-Yb, Al_l; 933 K	Palenzona et al. 1978
		−25.4		α-Yb, Al_s; 298 K	dyn. diff. calorim. 933 K
	$YbAl_2$	−37.3	−4.6	Yb_l, Al_l; 1208 K	Palenzona et al. 1978
		−25.8		α-Yb, Al_s; 298 K	vap. press. 1120–1296 K
	$YbAl_2$	−24.4		α-Yb, Al_s 773–873 K	Kulifeev et al. 1971 vap. press. 773–873 K
	$YbAl_3$	−32.5		α-Yb, Al_s; 298 K	Pasturel et al. 1983
	$YbAl_2$	−36.4		(same)	Al sol'n calorim. 960 K
	$YbAl_2$	−38.2		α-Yb, Al_s; 298 K	Colinet et al. 1985 Al sol'n calorim. 1000 K
Th–Al	Th_2Al_7	−47.9	−18.0	α-Th, Al_l; 946–1080 K	Poyarkov et al. 1973
		−39.5	−9.0	α-Th, Al_s	emf liq. electrolyte 946–1080 K
U–Al	UAl_4	−24.9		α-U, Al_s; 298 K	Chiotti and Kateley 1969
	UAl_3	−27.1		(same)	adiabatic calorim.
	UAl_2	−30.8		(same)	

continued on next page

Table 33, *continued*

System	Compound	$\Delta_f H^\circ$	$\Delta_f S^\circ$	Reference state	Authors and method
	UAl_4	−21.8	−0.9	α-U, Al_s; 674–912 K	Chiotti and Kateley 1969
	UAl_3	−26.4	−0.5	α-U, Al_s; 672–979 K	cmf liq. electrolyte 673–1113 K
	UAl_2	−28.9	−0.3	α-U, Al_s; 715–1113 K	
	UAl_4	−26.1		α-U, Al_s; 298 K	Ivanov et al. 1958
	UAl_3	−26.3		(same)	acid sol'n calorim.
	UAl_2	−31.1		(same)	
	UAl_2	−33.2		β-U, Al_l; 1023 K	Dannöhl and Lukas 1974
		−24.9		α-U, Al_s	Al sol'n calorim. 1023 K
	UAl_4	−24.9	−3.6	α-U, Al_s; 900 K	Lebedev et al. 1972b
	UAl_3	−30.9	−4.4	(same)	emf liq. electrolyte 913–1143 K
	UAl_2	−33.1	−3.1	(same)	
	UAl_4	−23.8	−4.5	α-U, Al_s	Kassner et al. 1988, 1990
	UAl_3	−29.4	−5.6	(same)	assessment
	UAl_2	−37.7	−8.6	(same)	$\Delta_f H$ and $\Delta_f S$ assumed temperature independent
Pu–Al	$PuAl_4$	−36.2		α-Pu, Al_s; 298 K	Akhachinskij et al. 1962
	$PuAl_3$	−45.2		(same)	acid sol'n calorim.
	$PuAl_2$	−47.3		(same)	
	$Pu_{0.91}Al_{0.09}$	−1.63		α-Pu, Al_s; 298 K	Akhachinskij and Timofeeva 1980
	$Pu_{0.94}Al_{0.06}$	−0.67		(same)	acid sol'n calorim.
	$PuAl_4$	−37.6	−9.4	ε-Pu, Al_s; 843 K	Lebedev et al. 1976
		−36.3	−8.8	α-Pu, Al_s	emf liq. electrolyte 803–913 K
	$PuAl_3$	−47.0	−13.3	ε-Pu, Al_s; 843 K	
		−45.4	−10.0	α-Pu, Al_s	
	$PuAl_2$	−49.8	−11.3	ε-Pu, Al_s; 843 K	
		−47.6	−6.8	α-Pu, Al_s	

La to Lu, is apparent. We note here that the values obtained for the $EuAl_2$ and $YbAl_2$ compounds are less exothermic than the values obtained for the other elements of the lanthanide series.

The values obtained by Kober et al. (1973a,b, 1977, 1979a,b, 1982a,b, 1983a, 1984, 1986a) in various R–Al systems have been previously considered as reliable by Gschneidner and Calderwood (1988d, 1989a) and used for Y–Al phase-diagram optimization by Ran et al. (1989a). The values obtained by Kober et al. lead to too negative values of the enthalpies of formation and to a shape of the enthalpy of formation versus composition curve which is not in agreement with that obtained by Sommer and Keita (1987) and Borzone et al. (1991) in the Ce–Al system and by Sommer and Keita (1987) and Colinet et al. (1988a) in the Gd–Al system, thus we suggest that all values obtained by emf measurements in the Al-based systems should be rejected.

The values obtained by Borzone et al. (1991) and Sommer and Keita (1987) for the Ce–Al system, by Colinet et al. (1988a) and Sommer and Keita (1987) for the Gd–Al system and by Kassner et al. (1988, 1990) for the U–Al system have been plotted as a function of composition in fig. 96. The single value obtained in the Th–Al system by Poyarkov et al.

Table 34
Enthalpies and entropies of formation of intermetallic compounds of Ga with rare earths and actinides ($\Delta_f H°$: kJ/mol of atoms, $\Delta_f S°$: $J K^{-1}$/mol of atoms)

System	Compound	$\Delta_f H°$	$\Delta_f S°$	Reference state	Authors and method
Sc–Ga	$ScGa_3$	−51.3	−16.3	α-Sc, Ga_l; 873 K	Yamshchikov et al. 1985c
		−47.1	−2.5	α-Sc, Ga_s; 298 K	emf liq. electrolyte 623–1113 K
Y–Ga	YGa_2	−69		α-Y, Ga_s;298K	Merker 1991
	YGa	−71		(same)	Ga sol'n calorim. 1176 K
	$Y_{0.62}Ga_{0.38}$	−57		(same)	
	α-YGa_2	−72.1	−15.9	α-Y,Ga_l; 854–1150 K	Yamshchikov et al. 1979b
		−63.4	−3.6	α-Y, Ga_s	emf liq. electrolyte 650–1150 K
	β-YGa_2	−74.6	−18.8	α-Y, Ga_l; 650–854 K	
		−70.8	−6.5	α-Y, Ga_s	
La–Ga	$LaGa_2$	−95.7	−21.6	β-La, Ga_l; 675–975 K	Vnuchkova et al. 1971a
		−92.0	−9.1	α-La, Ga_s	emf liq. electrolyte 675–975 K [a]
Ce–Ga	$CeGa_2$	−106.3	−49.5	γ-Ce, Ga_l; 675–975 K	Vnuchkova et al. 1971b
		−102.6	−37.2	γ-Ce, Ga_s	emf liq. electrolyte 675–975 K [a]
	$CeGa_2$	−92.6	−29.3	γ-Ce, Ga_l; 660–1090 K	Yamshchikov et al. 1977a
		−88.8	−17.0	γ-Ce, Ga_s	emf liq. electrolyte 660–1090 K [a]
Pr–Ga	$PrGa_6$	−96.7	−26.0	α-Pr, Ga_l; 675–975 K	Vnuchkova et al. 1972a
		−93.0	−13.7		emf liq. electrolyte 675–975 K [a]
Nd–Ga	$NdGa_2$	−83.3		α-Nd, Ga_s; 298 K	Serebrennikov et al. 1977
	NdGa	−73.2		(same)	acid sol'n calorim.
	Nd_5Ga_3	−55.2		(same)	
	Nd_3Ga	−41.0		(same)	
	$NdGa_2$	−97.4	−27.3	α-Nd, Ga_l; 675–975 K	Vnuchkova et al. 1972b
		−93.7	−15.0	α-Nd, Ga_s	emf liq. electrolyte 675–975 K [a]
Eu–Ga	$EuGa_4$	−57.4	−44.8	Eu_s, Ga_l; 743–1023 K	Dubinin et al. 1985c
		−52.9	−30.0	Eu_s, Ga_s	emf liq. electrolyte 743–1023 K
Gd–Ga	$GdGa_2$	−110.6	−40.7	α-Gd, Ga_l; 673–973 K	Shkol'nikova et al. 1972a
		−106.9	−28.4	α-Gd, Ga_s	emf liq. electrolyte 673–973 K
	$GdGa_2$	−87.2	−21.4	α-Gd, Ga_l; 723–923 K	Bayanov and Ganchenko 1975
		−83.5	−9.1	α-Gd, Ga_s	emf liq. electrolyte 723–923 K
Dy–Ga	$DyGa_3$	−83.3	−44.1	α-Dy, Ga_l; 673–1073 K	Serebrennikov et al. 1971
		−79.1	−30.3	α-Dy, Ga_s	emf liq. electrolyte 673–1073 K
	$DyGa_3$	−56.9	−15.7	α-Dy, Ga_l; 632–1125 K	Yamshchikov et al. 1988
		−52.7	−1.9	α-Dy, Ga_s	emf liq. electrolyte 632–1125 K
Ho–Ga	$HoGa_6$	−33.1	−12.2	α-Ho, Ga_l; 660–887 K	Yamshchikov et al. 1986
		−28.3	+5.4	α-Ho, Ga_s	emf liq. electrolyte 660–1065 K
	$HoGa_3$	−62.0	−22.8	α-Ho, Ga_l; 887–1065 K	
		−57.8	−8.9	α-Ho, Ga_s	
Er–Ga	$ErGa_3$	−71.1	−37.7	Er_s, Ga_l; 723–923 K	Shkol'nikova et al. 1972b
		−66.9	−23.9	Er_s, Ga_s	emf liq. electrolyte 723–923 K
	$ErGa_3$	−53.4	−11.2	Er_s, Ga_l; 773 K	Bayanov et al. 1975c
		−49.2	2.6	Er_s, Ga_s	emf liq. electrolyte 673–875 K
Tm–Ga	$TmGa_3$	−52.3	−24.8	Tm, Ga_l; 723–923 K	Shkol'nikova et al. 1973
		−48	−11	Tm, Ga_s	emf liq. electrolyte 723–923 K
Lu–Ga	$LuGa_3$	−45.2	−6.9	Lu_s, Ga_l; 773 K	Bayanov et al. 1975c
		−41.0	+6.9	Lu_s, Ga_s	emf liq. electrolyte 673–875 K

continued on next page

Table 34, *continued*

System	Compound	$\Delta_f H^\circ$	$\Delta_f S^\circ$	Reference state	Authors and method
Th–Ga	$ThGa_2$	−76.0	−21.6	α-Th, Ga_l; 1000 K	Poyarkov et al. 1975a
		−72.3	−9.3	α-Th, Ga_s	emf liq. electrolyte 648–1056 K [b]
U–Ga	UGa_3	−25.5		α-U, Ga_s; 298 K	Palenzona and Cirafici 1975b
					react. calorim. at 433 K
	UGa_3	−42.7	−14.3	α-U, Ga_l; 643–1013 K	Johnson and Feder 1962b
		−38.5	−0.5	α-U, Ga_s	emf liq. electrolyte 643–1013 K
	UGa_3	−42.1	−14.1	α-U, Ga_l; 696–1084 K	Lebedev et al. 1973d
		−37.9	−0.3	α-U, Ga_s	emf liq. electrolyte 696–1084 K
	UGa_3	−28.2	−11.0	α-U, Ga_l; 1250 K	Alcock et al. 1966
		−24.0	2.8	α-U, Ga_s	vap. press. corrected for change of
	UGa_2	−28.0	−8.1	α-U, Ga_l; 1250 K	stoichiometry of one compound
		−24.3	4.2	α-U, Ga_s	
	U_2Ga_3	−24.6	−5.1	α-U, Ga_l; 1250 K	
		−21.2	6.0	α-U, Ga_s	
	UGa_3	−42.4	−14.2	α-U, Ga_l; $T < 942$ K	Chiotti et al. 1981
		−39.3	−0.4	α-U, Ga_s	assessment 298–942 K
	UGa_2	−46.9	−12.4	α-U, Ga_l; $T < 942$ K	
		−43.2	−0.1	α-U, Ga_s	
	U_2Ga_3	−47.3	−10.4	α-U, Ga_l; $T < 942$ K	
		−43.9	+0.7	α-U, Ga_s	
	U_2Ga_3	−38.4	−12.8	γ-U, Ga_l; 1100–1293 K	Gardie et al. 1991
		−32.0	+1.3	α-U, Ga_s	vap. press. mass. spectro.
					1100–1293K
Pu–Ga	$\beta PuGa_6$	−34		α-Pu, Ga_s; 298 K	Akhachinskij and Kopytin 1968
	$PuGa_2$	−63.3		(same)	acid sol'n calorim.
	βPu_3Ga	−39.5		(same)	
	$PuGa_4$	−46		α-Pu, Ga_s; 298 K	Akhachinskij and Kopytin 1968
	$\alpha PuGa_3$	−57.5		(same)	estimation
	αPuGa	−60		(same)	
	Pu_5Ga_3	−52.5		(same)	

[a] Values as reported in the publication but subject to caution because the saturated solution is in equilibrium with RGa_6 at low temperature.

[b] We have supposed that the saturated solution is in equilibrium with $ThGa_2$ compound.

(1973) has also been presented in this figure. For the Pu–Al system there are two sets of data, obtained respectively by Akhachinskij et al. (1962) and Lebedev et al. (1976), which are in good agreement. The values obtained for the U–Al system by different authors exhibit some scatter, and we present in fig. 96 the values assessed by Kassner et al. (1988, 1990), although they appear more negative than the experimental values. The behavior of Th and Pu with aluminum appears similar to that of the lanthanides; the values obtained with uranium are clearly less negative than those obtained with the rare earths, thorium and plutonium.

Some data for the liquid phase obtained by calorimetric measurements exists. The partial enthalpies of the rare earths and uranium at infinite dilution in liquid aluminum

Table 35
Enthalpies and entropies of formation of intermetallic compounds of In with rare earths and actinides ($\Delta_f H^\circ$: kJ/mol of atoms, $\Delta_f S^\circ$: $J K^{-1}$/mol of atoms)

System	Compound	$\Delta_f H^\circ$	$\Delta_f S^\circ$	Reference state	Authors and method
Sc–In	$ScIn_3$	−33.7	−12.0	α-Sc In_l ; 873 K	Yamshchikov et al. 1985c
		−31.3	−6.2	α-Sc, In_s; 298 K	emf liq. electrolyte
Y–In	YIn_3	−41.8		α-Y, In_s; 298 K	Palenzona and Cirafici 1975b diff. dyn. calorim.
	YIn_3	−49.3	−13.9	α-Y In_l; 650–1110 K	Yamshchikov et al. 1979b
		−46.9	−8.2	α-Y, In_s	emf liq. electrolyte 650–1110 K
	YIn_3	−50.5	−16.9	α-Y In_l; 723–923 K	Vdovkina et al. 1973
		−48.1	−11.2	α-Y, In_s	emf liq. electrolyte 723–923 K
La–In	$LaIn_3$	−58.6		α-La, In_s; 298 K	Borsese et al. 1977a
	LaIn	−65		(same)	react. calorim.
	$LaIn_3$	−52.3		α-La, In_s; 298 K	Palenzona and Cirafici 1974b diff. dyn. calorim.
	$LaIn_3$	−70		α-La, In_s; 298 K	Novozhenov et al. 1975
	La_2In_3	−61		(same)	acid sol'n calorim.
	$LaIn_3$	−56.7	−17.5	β-La, In_l; 725–975 K	Degtyar et al. 1971b
		−54.2	−11.8	α-La, In_s	emf liq. electrolyte 725–975 K
	$LaIn_3$	−56.4	−16.1	β-La, In_l; 953–1083 K	Kober et al. 1983b, Kober 1991
		−53.9	−10.2	α-La, In_s	emf liq. electrolyte 953–1083 K
	$LaIn_2$	−76.7	−23.3	β-La, In_l; 953–1083 K	
		−74.4	−18.0	α-La, In_s	
	LaIn	−94.8	−23.9	β-La, In_l; 953–1083 K	
		−93.0	−19.8	α-La, In_s	
	La_2In	−124.4	−42.9	β-La, In_l; 953–1083 K	
		−123.1	−39.9	α-La, In_s	
	La_3In	−97.1	−15.8	β-La, In_l; 953–1083 K	
		−96.0	−13.4	α-La, In_s	
Ce–In	$CeIn_3$	−58.6	−19.0	γ-Ce, In_l; 660–1030 K	Yamshchikov et al. 1977a
		−56.2	−13.3	γ-Ce, In_s	emf liq. electrolyte 660–1030 K
	$CeIn_3$	−60.3	−22	γ-Ce, In_l; 725–975 K	Degtyar et al. 1971c
		−57.9	−16.3	γ-Ce, In_s	emf liq. electrolyte 725–975 K
	$CeIn_3$	−50.2		γ-Ce, In_s; 298 K	Palenzona and Cirafici 1974b dyn. diff. calorim.
Pr–In	$PrIn_3$	−55.6		α-Pr, In_s; 298 K	Palenzona and Cirafici 1974b dyn. diff. calorim.
	$PrIn_3$	−65.3		α-Pr, In_s; 298 K	Serebrennikov et al. 1976
	Pr_2In_3	−63.6		(same)	acid sol'n calorim.
	PrIn	−56.5		(same)	
	Pr_2In	−33		(same)	
	Pr_3In	−25		(same)	
	$PrIn_3$	−61.0	−22.8	α-Pr, In_l; 725–975 K	Degtyar et al. 1971a
		−57.9	−16.3	α-Pr, In_s	emf liq. electrolyte 725–975 K
	$PrIn_3$	−58.2		α-Pr, In_s; 648–973 K	Kober et al. 1979c emf liq. electrolyte 648–973 K
Nd–In	$NdIn_3$	−58.5	−17.8	α-Nd, In_s; 725–975 K	Degtyar et al. 1971a emf liq. electrolyte 725–975 K

continued on next page

Table 35, *continued*

System	Compound	$\Delta_f H^\circ$	$\Delta_f S^\circ$	Reference state	Authors and method
	$NdIn_3$	−54.4		α-Nd, In_s; 298 K	Palenzona and Cirafici 1974b dyn. diff. calorim.
	$NdIn_3$	−61.5		α-Nd, In_s; 298 K	Novozhenov et al. 1979
	Nd_2In_3	−63.2		(same)	acid sol'n calorim.
	NdIn	−57.3		(same)	
	$NdIn_3$	−55.9		α-Nd, In_s; 678–973 K	Kober et al. 1979d emf liq. electrolyte 678–973 K
Sm–In	$SmIn_3$	−49.8		α-Sm, In_s; 298 K	Palenzona and Cirafici 1974b dyn. diff. calorim.
Eu–In	$EuIn_2$	−58.3	−35.4	Eu_s, In_l; 743–1023 K	Dubinin et al. 1985a
		−56.1	−30.4	Eu_s, In_s	emf liq. electrolyte 743–1023 K [a]
Gd–In	$GdIn_3$	−45.6		α-Gd, In_s; 298 K	Palenzona and Cirafici 1974b dyn. diff. calorim.
	$GdIn_3$	−49.4	−12.9	α-Gd, In_l; 673–875 K	Bayanov et al. 1973
		−47.0	−7.2	α-Gd, In_s	emf liq. electrolyte 673–875 K
	$GdIn_3$	−59.5	−22.3	α-Gd, In_l; 723–923 K	Vdovkina et al. 1973
		−57.1	−16.6	α-Gd, In_s	emf liq. electrolyte 723–923 K
	$GdIn_3$	−55.6	−21.5	α-Gd, In_l; 638–1011 K	Kober et al. 1983c
		−53.1	−15.8	α-Gd, In_s	emf liq. electrolyte 638–1011 K
	$GdIn_3$	−53.1	−17.5	α-Gd, In_l; 641–823 K	Vasilev and Vu 1985
		−50.7	−11.8	α-Gd, In_s	emf liq. electrolyte 641–823 K
	Gd_3In_5	−72.3	−33.1	α-Gd, In_l; 641–823 K	
		−70.3	−28.4	α-Gd, In_s	
	GdIn	−73.9	−29.0	α-Gd, In_l; 641–823 K	
		−72.3	−25.2	α-Gd, In_s	
Tb–In	$TbIn_3$	−51.1	−15.1	α-Tb, In_l; 673–873 K	Bayanov et al. 1977a
		−48.6	−9.4	α-Tb, In_s	emf liq. electrolyte 673–873 K
	$TbIn_3$	−44.8		α-Tb, In_s; 298 K	Palenzona and Cirafici 1974b dyn. diff. calorim.
	$TbIn_3$	−49.3		Tb_s, In_s; 643–793 K	Vasilev et al. 1986
	TbIn	−69.8			emf liq. electrolyte 643–793 K
Dy–In	$DyIn_3$	−44.8		α-Dy, In_s; 298 K	Palenzona and Cirafici 1974b dyn. diff. calorim.
	$DyIn_3$	−46.7	−12.8	α-Dy, In_l; 632–950 K	Yamshchikov et al. 1988
		−44.2	−7.1	α-Dy, In_s	emf liq. electrolyte 632–950 K
Ho–In	$HoIn_3$	−48.4	−16.8	α-Ho, In_l; 680–950 K	Yamshchikov et al. 1984a
		−45.9	−11.1	α-Ho, In_s	emf liq. electrolyte 680–950 K
	$HoIn_3$	−40.1		α-Ho,In_s; 298 K	Palenzona and Cirafici 1974b dyn. diff. calorim.
Er–In	$ErIn_3$	−38.9		Er_s, In_s; 298 K	Palenzona and Cirafici 1974b dyn. diff. calorim.
	$ErIn_3$	−42.3	−10.1	Er_s, In_l; 673–873 K	Bayanov et al. 1973
		−39.9	−4.4	Er_s, In_s	emf liq. electrolyte 673–873 K
	$ErIn_3$	−41.2		Er_s, In_s; 644–804 K	Vasilev et al. 1982 emf liq. electrolyte 644–804 K

continued on next page

Table 35, *continued*

System	Compound	$\Delta_f H^o$	$\Delta_f S^o$	Reference state	Authors and method
	$ErIn_3$	−36.3		Er_s, In_s; 673–755 K	Yamshchikov et al. 1979c emf liq. electrolyte 673–755 K
	$ErIn_3$	−39.0		Er_s, In_s; 675–925 K	Vdovkina 1977 emf liq. electrolyte 675–925 K
	$ErIn_{2.5}$	−47.5	−8.4	Er_s, In_s; 644–804 K	Vasilev et al. 1982 emf liq. electrolyte 644–804 K
	Er_2In_5	−51.4	−3.8	Er_s, In_s; 723 K	Vasilev 1989
	ErIn	−60.3	−6.2	Er_s, In_s; 723 K	emf liq. electrolyte 654–814 K
Tm–In	$TmIn_3$	−36.4		Tm_s, In_s; 298 K	Palenzona and Cirafici 1974b dyn. diff. calorim.
Yb–In	$YbIn_3$	−39.7		α-Yb, In_s; 298 K	Palenzona and Cirafici 1974b dyn. diff. calorim.
Lu–In	$LuIn_3$	−34.7		Lu_s, In_s; 298 K	Palenzona and Cirafici 1974b dyn. diff. calorim.
	$LuIn_3$	−33.5	−9.0	Lu_s, In_l; 674–873 K	Bayanov et al. 1975b
		−31.0	−3.3	Lu_s, In_s	emf liq. electrolyte 674–873 K
	$LuIn_{2.5}$	−42.0	−9.0	Lu_s, In_s; 723 K	Vasilev et al. 1985 emf liq. electrolyte 643–810 K
	LuIn	−50.3	−4.5	Lu_s, In_s; 723 K	Vu and Vasilev 1982
	Lu_3In_2	−55.6	−8.1	(same)	emf liq. electrolyte 643–810 K
	Lu_2In	−52.3	−5.1	(same)	
	Lu_3In	−42.8	−5.5	(same)[b]	
	$LuIn_3$	−36.4	−6.9	(same)[c]	
	$LuIn_3$	−35.3		Lu_s, In_s; 674–925 K	Vdovkina 1977 emf liq. electrolyte 674–925 K
Th–In	$ThIn_3$	−44.0	−15.9	α-Th, In_l; 954–1310 K	Poyarkov et al. 1975b
		−41.6	−10.2	α-Th, In_s	emf liq. electrolyte 954–1310 K
	$ThIn_3$	−37.7		α-Th, In_s; 298 K	Palenzona and Cirafici 1975b diff. dyn. calorim.
U–In	UIn_3	−27.5	−13.6	α-U, In_l; 626–949 K	Johnson and Feder 1962a,b
		−25.0	−7.9	α-U, In_s	emf liq. electrolyte 626–949 K
	UIn_3	−30.8	−18.1	γ-U, In_l; 723–1123 K	Lebedev et al. 1974b
		−26.4	−10.5	α-U, In_s	emf liq. electrolyte 723–1123 K
	UIn_3	−24.1	−11.8	α-U, In_l; 1093–1314 K	Alcock et al. 1966
		−21.7	−6.1	α-U, In_s	vap. press. 1093–1314 K
	UIn_3	−15.9		α-U, In_s; 298 K	Palenzona and Cirafici 1975b diff. dyn. calorim.
Pu–In	$PuIn_3$	−49.7	−21.3	ε-Pu, In_l; 660–979 K	Lebedev et al. 1977
		−45.6	−12.3	α-Pu, In_s	emf liq. electrolyte 660–979 K

[a] Approximate result because the solubility of Eu in liquid In is not negligible.
[b] Phase diagram determined by Vasilev et al. 1985.
[c] Values considering the composition $LuIn_3$ and not $LuIn_{2.5}$.

have been plotted in fig. 97 as a function of atomic number. As for the enthalpies of formation of the RAl_2 compounds, one observes a decrease of the partial enthalpy at

Table 36
Enthalpies and entropies of formation of intermetallic compounds of Tl with rare earths and actinides ($\Delta_f H°$: kJ/mol of atoms, $\Delta_f S°$: $J K^{-1}$/mol of atoms)

System	Compound	$\Delta_f H°$	$\Delta_f S°$	Reference state	Authors and method
Y–Tl	YTl_3	−35.3	−6.9	α-Y, Tl_s; 800 K	Demykina et al. 1980 emf liq. electrolyte 673–723 K
LaTl	$LaTl_3$	−45.3		α-La, Tl_s; 298 K	Palenzona and Cirafici 1974b dyn. diff. calorim.
	$LaTl_3$	−46.4	−11.7	β-La, Tl_l; 800 K	Demykina et al. 1980, Fryanova et al. 1978 emf liq. electrolyte 725–973 K
		−43.4	−6.7	α-La, Tl_s	
	$LaTl_3$	−47.4	−11.5	β-La, Tl_s; 725–975 K	Degtyar et al. 1971b emf liq. electrolyte 725–975 K
		−47.3	−11.3	α-La, Tl_s	
Ce–Tl	$CeTl_3$	−50.0	−16.3	γ-Ce, Tl_l; 800 K	Demykina et al. 1980, Fryanova et al. 1978 emf liq. electrolyte 723–923 K
		−46.7	−10.6	γ-Ce, Tl_s	
	$CeTl_3$	−45		γ-Ce, Tl_s; 298 K	Palenzona and Cirafici 1974b dyn. diff. calorim.
Pr–Tl	$PrTl_3$	−48.4	−14.7	α-Pr, Tl_l; 800 K	Fryanova et al. 1978, Demykina et al. 1980 emf liq. electrolyte 723–923 K
		−45.5	−9.6	α-Pr, Tl_s	
	$PrTl_3$	−45.8		α-Pr, Tl_s; 298 K	Palenzona and Cirafici 1974b dyn. diff. calorim.
Nd–Tl	$NdTl_3$	−46.5	−12.1	α-Nd, Tl_l; 800 K	Fryanova et al. 1978, Demykina et al. 1980 emf liq. electrolyte 723–873 K
		−43.6	−6.9	α-Nd, Tl_s	
	$NdTl_3$	−41.7		α-Nd, Tl_s; 298 K	Palenzona and Cirafici 1974b dyn. diff. calorim.
SmTl	$SmTl_3$	−39.7		α-Sm, Tl_s; 298 K	Palenzona and Cirafici 1974b react. calorim.
Gd–Tl	$GdTl_3$	−36.8		α-Gd, Tl_s; 298 K	Palenzona and Cirafici 1974b dyn. diff. calorim.
	$GdTl_3$	−36.5	−6.9	α-Gd, Tl_s; 800 K	Demykina et al. 1980 emf liq. electrolyte 673–973 K
Tb–Tl	$TbTl_3$	−35.7		α-Tb, Tl_s; 298 K	Palenzona and Cirafici 1974b dyn. diff. calorim.
Dy–Tl	$DyTl_3$	−34.1		α-Dy, Tl_s; 298 K	Palenzona and Cirafici 1974b dyn. diff. calorim.
Yb–Tl	$YbTl_3$	−37.0		α-Yb, Tl_s; 298 K	Palenzona and Cirafici 1974b dyn. diff. calorim.
U–Tl	UTl_3	−27.5	−13.6	α-U, Tl_l; 723 K	Johnson and Feder 1962b emf liq. electrolyte 658–946 K
		−24.4	−8.2	α-U, Tl_s	
	UTl_3	−15.1		α-U, Tl_s; 298 K	Palenzona and Cirafici 1975b estimation

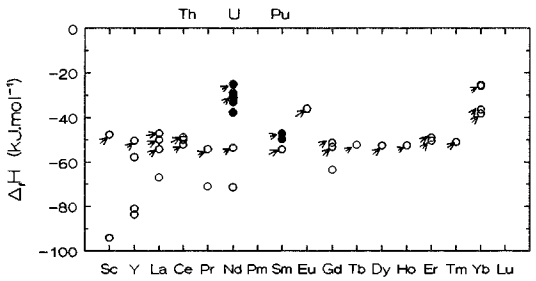

Fig. 95. Enthalpies of formation of rare earths (open circles) and actinides (solid circles) RAl_2 and $AnAl_2$ compounds as a function of atomic number. The references of the data are quoted in table 33. The values obtained recently by calorimetric measurements have been indicated by an arrow.

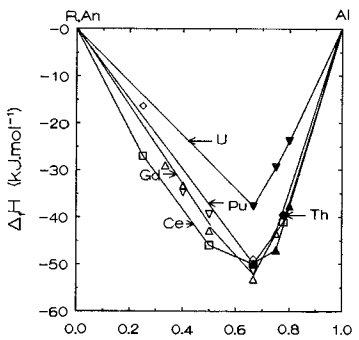

Fig. 96. Enthalpies of formation of $R_{1-x}Al_x$ and $An_{1-x}Al_x$ compounds. The data for R = Ce (open diamond, open squares), Gd (open inverted triangle, open triangles) and An = Th (solid circles), U (solid inverted triangles), Pu (solid triangles) are from Sommer and Keita (1987) and Borzone et al. (1991), Sommer and Keita (1987) and Colinet et al. (1988a), Poyarkov et al. (1973), Kassner et al. (1988, 1990), and Akhachinskij et al. (1962) and Lebedev et al. (1976), respectively.

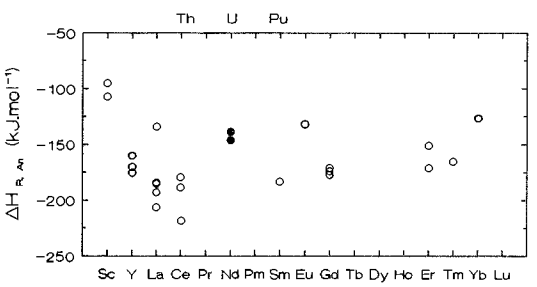

Fig. 97. Limiting partial enthalpies of rare earths (open circles) and actinides (solid circles) in liquid aluminium. The references of the data are quoted in table 37.

infinite dilution from Sc to Y and subsequently to La, and an increase from La to Lu. Experiments have been performed by Sommer et al. (1988a,b) showing that the partial enthalpy at infinite dilution decreases in absolute value with temperature. In other respects

Table 37
Values for the enthalpy of alloying of liquid aluminium with rare earths and uranium[a]

System	$\Delta_m\bar{H}^{\infty}_{(M)}$ (kJ mol^{-1})	$\Delta_m H$ (kJ mol^{-1})	$\Delta_m\bar{H}^{\infty}_{(Al)}$ (kJ mol^{-1})	T (K)	Reference
Al–Sc	−107.1	−31.2(0.38)		1873	Litovskii et al. 1986
	−95.1			1700	Batalin et al. 1985b
Y–Al	−170.1			1213	Lee and Sommer 1985
	−175.2			1000	Colinet and Pasturel 1983
	−160.2	−49.6(0.5)		1873	Ryss et al. 1976b
La–Al	−193			951	Chatillon-Colinet et al. 1979
	−184.8			1201	Lee and Sommer 1985
	−135	−44.9(0.45)		1920	Esin et al. 1981b
	−185.2			1200	Sommer et al. 1988a
	−184.1			1120	
	−206.5			983	
		−36.6(0.53)		1200	
			−90	1230	
Ce–Al	−188.7			966	Pasturel et al. 1983
	−218.6			1013	Yamshchikov et al. 1983
	−179.7			1125	Sommer and Keita 1987
	−218.5	−39.6(0.35)	−2.8	1870	Esin et al. 1979
Sm–Al	−183.3			966	Pasturel et al. 1983
Eu–Al	−131.4			992	Colinet et al. 1985
Gd–Al	−177.4			966	Pasturel et al. 1983
	−173.1			1198	Lee and Sommer 1985
	−174.1			1125	Sommer and Keita 1987
Er–Al	−170.7			966	Pasturel et al. 1983
	−150.8			1125	Sommer and Keita 1987
Tm–Al	−165.3			966 K	Pasturel et al. 1983
Yb–Al	−126.6			956	Pasturel et al. 1983
U–Al	−138.6			986	Colinet et al. 1988b
	−146.3			1023	Dannöhl and Lukas 1974

[a] Quantities: $\Delta_m\bar{H}^{\infty}_{(M)}$: limiting partial enthalpy of R or U.
$\Delta_m\bar{H}^{\infty}_{(Al)}$: limiting partial enthalpy of Al.
$\Delta_m H$: heat of mixing for a given composition of the rare earth.
The reference state is the liquid elements. All enthalpy values are in kJ mol^{-1}.

Table 38
Values for the enthalpy of alloying of liquid gallium with rare earths[a]

System	$\Delta_m\bar{H}^{\infty}_{(R)}$ (kJ mol^{-1})	T (K)	Reference
Y–Ga	−174	1176	Merker 1991
Ce–Ga	−233	1213	Yamshchikov et al. 1983

[a] $\Delta_m\bar{H}^{\infty}_{(R)}$: limiting partial enthalpy of R. Reference state: the liquid elements.

Table 39
Values for the enthalpy of alloying of liquid indium with rare earths[a]

System	$\Delta_m\bar{H}^{\infty}_{(R)}$ (kJ mol^{-1})	$\Delta_m H$ (kJ mol^{-1})	T (K)	Reference
Ce–In	−136		1170	Yamshchikov et al. 1983
Eu–In	−157	−41.2(0.5)	1300	Bushmanov et al. 1987

[a] $\Delta_m\bar{H}^{\infty}_{(R)}$: limiting partial enthalpy of R.
$\Delta_m H$: heat of mixing for a given composition of the rare earth.
The reference state is the liquid elements. All enthalpy values are in kJ mol^{-1}.

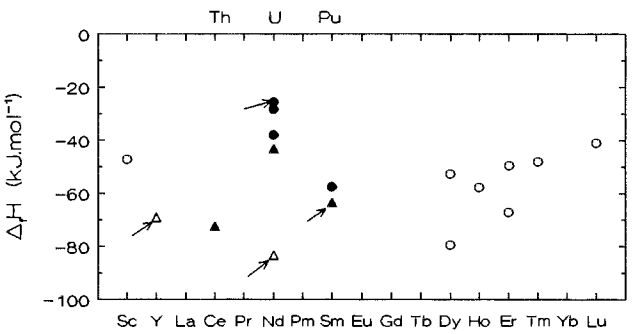

Fig. 98. Enthalpies of formation of rare earth (open symbols) and actinides (solid symbols) of (R,An)Ga_2 compounds (open triangle, solid triangles) and (R,An)Ga_3 compounds (open circle, solid circles) as a function of atomic number. The references of the data are quoted in table 34. The values obtained by a calorimetric method have been indicated by an arrow.

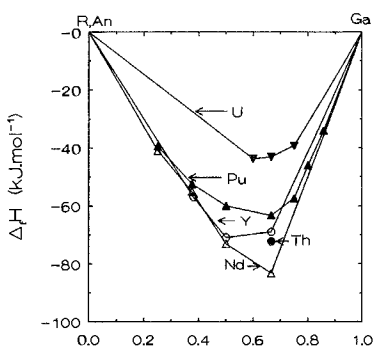

Fig. 99. Enthalpies of formation of $R_{1-x}Ga_x$ and $An_{1-x}Ga_x$ compounds. The data for R = Y (open circles), Nd (open triangles) and An = Th (solid circles), U (solid inverted triangles) and Pu (solid triangles) are from Merker (1991), Serebrennikov et al. (1977), Poyarkov et al. (1975a), Chiotti et al. (1981) and Akhachinskij and Kopytin (1968), respectively.

the partial enthalpies at infinite dilution of Eu and Yb in liquid aluminum are less negative than the values obtained in the lanthanide series.

In fig. 98 we plot the values of the enthalpies of formation of the RGa_3 or $AnGa_3$ and RGa_2 or $AnGa_2$ compounds as a function of atomic number. For the 1:3 stoichiometry,

data have been obtained only for the late lanthanide elements; for the 1:2 stoichiometry data have been obtained only for the early lanthanide elements. Few of the data have been obtained by calorimetric methods; these are indicated by arrows in fig. 98. The enthalpies of formation of the $ThGa_2$ and $PuGa_2$ compounds are of the same order of magnitude as the enthalpies of formation of the rare-earth-based compounds for the same stoichiometry; this is also true for the value of the enthalpy of formation of the $PuGa_3$ compound. The enthalpies of formation of the UGa_2 and UGa_3 compounds are less negative than those of rare-earth-based compounds. Figure 99 shows plots of the enthalpies of formation obtained in the Th–Ga, U–Ga, Pu–Ga, Nd–Ga and Y–Ga systems (by Poyarkov et al. 1975a, Chiotti et al. 1981, Akhachinskij and Kopytin 1968, Serebrennikov et al. 1977, and Merker 1991, respectively) versus Ga content. The same conclusions as above are deduced. In liquid alloys there are only two sets of data obtained using calorimetric methods: the partial enthalpy at infinite dilution of cerium in liquid gallium is more negative than that of yttrium in liquid gallium.

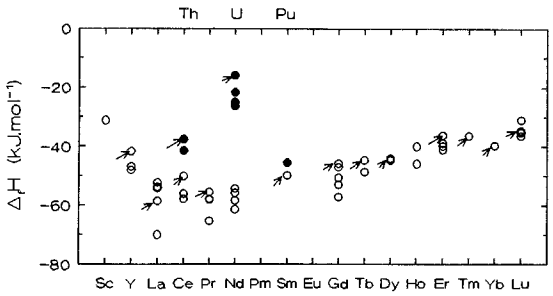

Fig. 100. Enthalpies of formation of rare earth (open circles) and actinides (solid circles) RIn_3 and $AnIn_3$ compounds as a function of atomic number. The references of the data are quoted in table 35. The values obtained by a calorimetric method have been indicated by an arrow.

In fig. 100 we plot the enthalpies of formation of the RIn_3 and $AnIn_3$ compounds as a function of atomic number. Even though large discrepancies exist between the values obtained by different authors for the same element, one observes clearly that the enthalpy of formation becomes less negative from La to Lu in the lanthanide series and more negative from Sc to Y to La. The enthalpies of formation of the $ThIn_3$ and $PuIn_3$ compounds are of the same order of magnitude as those obtained for light-lanthanide or yttrium-based compounds. The enthalpy of formation of UIn_3 is less negative than the enthalpies of formation of $ThIn_3$ and $PuIn_3$.

There are also only few data obtained by calorimetric methods for the liquid indium alloys. Considering the two values reported in table 39 it seems unlikely that the partial enthalpy at infinite dilution of Eu in indium will be more negative than the value obtained for Ce in liquid indium (see the results obtained in liquid aluminum).

In fig. 101 the enthalpies of formation of the RTl_3 and $AnTl_3$ compounds have been plotted as a function of atomic number. As for the RIn_3 compounds, one observes a decrease of the enthalpies of formation from Y to La and an increase from La to Lu.

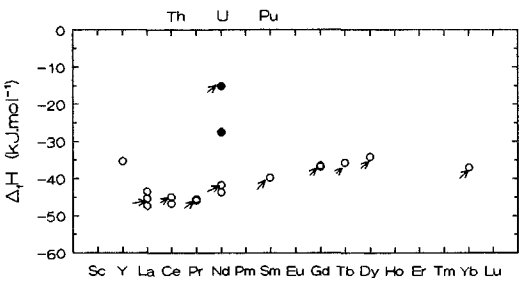

Fig. 101. Enthalpies of formation of rare earth (open circles) and actinides (solid circles). RTl_3 and $AnTl_3$ compounds as a function of atomic number. The references of the data are quoted in table 36. The values obtained by a calorimetric method have been indicated by an arrow.

Concerning actinide based alloys there are only two data points for the UTl_3 compound, with the value proposed by Palenzona and Cirafici (1975b) being an estimation, and the value proposed by Johnson and Feder (1962a,b) resulting from emf measurements. There is a large difference between the two values, nevertheless we see that the enthalpy of formation of UTl_3 is less negative than the enthalpies of formation of the RTl_3 compounds.

8. Rare earths and actinides with elements of column IVB

8.1. *Phase diagrams and intermetallic compounds*

Figures 102 to 105 portray the main features of the binary phase diagrams of rare earths and actinides with Si, Ge, Sn and Pb. All these phase diagrams contain many intermetallic compounds. The U-Pb phase diagram exhibits a miscibility gap in the uranium rich side while intermetallic compounds are found on the lead rich side. The structures of the compounds found in the considered phase diagrams are presented in figures 106 to 109. In table 40 the crystallographic characteristics of these compounds are described.

Many silicon–rare-earth or -actinide phase diagrams are not completely known, and in particular the liquidus is unknown for all the light lanthanides (Tb–Lu). In the phase diagrams known, the compound with the highest melting point has the stoichiometry RSi_2 or $AnSi_2$ for the first elements of the series Ce → Gd and also for Pu; the stoichiometry of the compound is R_5Si_3 for Y and Sc; and it is Th_3Si_2 and Si_5U_3 for Th and U. The RSi_2 and $AnSi_2$ compounds have either the AlB_2 or the Si_2Th structure. For the stoichiometry R_3Si_5 or An_3Si_5, the same structure is observed with Th, U, Pu and Sm to Tm. For the equiatomic composition the structure is BFe for the actinide elements as well as for the light lanthanides.

With germanium the compound with the highest melting temperature has the composition RGe_2 for La, Ce and Pr, and the composition R_5Ge_3 or An_5Ge_3 for all the other rare-earth elements, as well as for uranium. There is a large number of intermetallic

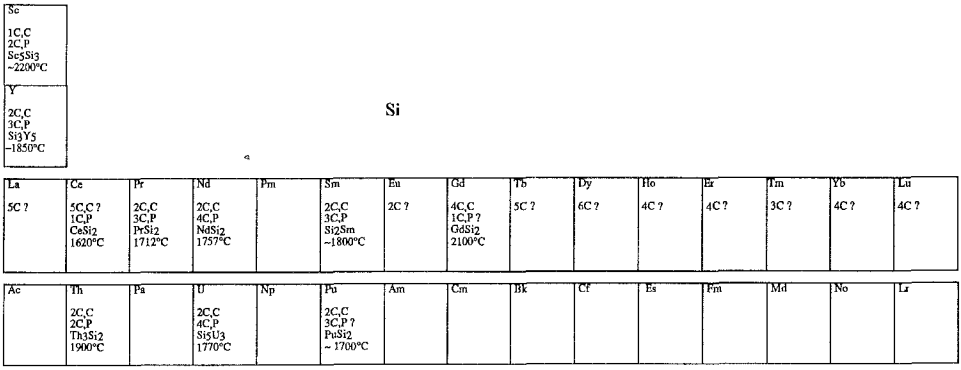

Fig. 102. Main features of the phase diagrams of silicon with rare earths and actinides.

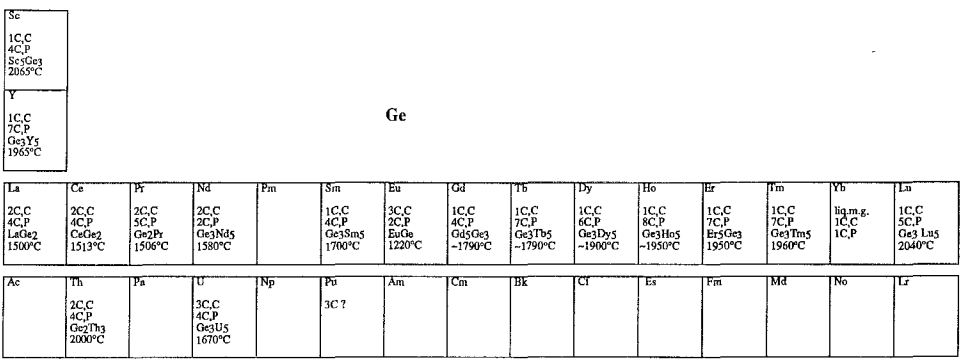

Fig. 103. Main features of the phase diagrams of germanium with rare earths and actinides.

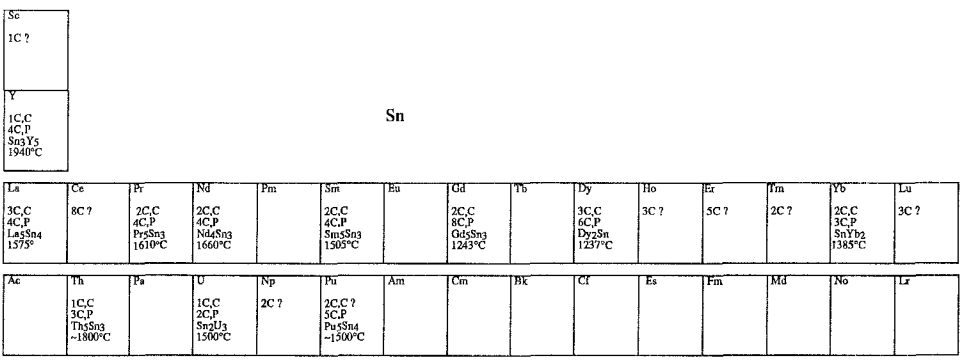

Fig. 104. Main features of the phase diagrams of tin with rare earths and actinides.

Sc														
Y 1C,C 3C,P Pb_3Y_5 1760°C														
La	Ce	Pr	Nd	Pm	Sm	Eu	Gd	Tb	Dy	Ho	Er	Tm	Yb	Lu
2C,C 4C,P La_5Pb_3 1450°C	2C,C 4C,P Ce_2Pb 1380°C	3C,C 4C,P Pb_3Pr_5 1495°C	5C ?		3C,C 3C,P Pb_3Sm_5 1580°C	3C,C 1C,P Eu_2Pb 1250°C	1C,C 5C,P Gd_5Pb_3 1670°C	3C ?	1C,C 4C,P Dy_5Pb_3 1695°C	3C ?		3C ?	3C,C 1C,P $PbYb_2$ 1246°C	1C,C 3C,P Lu_5Pb_3 1695°C
Ac	Th	Pa	U	Np	Pu	Am	Cm	Bk	Cf	Es	Fm	Md	No	Lr
	1C,C 3C,P Pb_3Th_5 ~1900°C		liq.m.g. 1C,C 1C,P Pb_3U 1220°C		1C,C 1C,P Pb_3Pu ~900°C									

Fig. 105. Main features of the phase diagrams of lead with rare earths and actinides.

Phase	Sc	Y	La	Ce	Pr	Nd	Pm	Sm	Eu	Gd	Tb	Dy	Ho	Er	Tm	Yb	Lu	Ac	Th	Pa	U	Np	Pu	Prototype or
M_3Si 25%																					x			$AuCu_3$ x
M_5Si_3 37.5%	x	x	•	+	•LT ?HT	•		x		x	x	x	x	x	x	x	x						+	Mn_5Si_3 x B_3Cr_5 • Si_3W_5 +
M_3Si_2 40%			x	x															x		x	x	x	Si_2U_3 x
M_5Si_4 44.4%		x	•	•	•	•		x		x	x	x	x	x			x							Ge_4Sm_5 x Si_4Zr_5 •
MSi 50%	x	x	•	•	•	•		•	x	•	•	xLT •HT	xLT •HT	xLT •HT	x	x	x		•		•		•	BCr x BFe •
M_3Si_4 57.1%					?																			
M_2Si_3 60%						x				+		•												AlB_2 x Si_2Th • Gd_2Si_3 +
M_3Si_5 62.5%	x	•LT ?HT		+		+LT		x		xLT	x	x		x	x	x	Δ	o		x		x		AlB_2 x Mn_5Si_3 o Si_2Th • Gd_2Si_3 + Pd_5Th_3 Δ
MSi_2 66.7%		xLT •HT	?LT •HT	•	?LT •HT	•HT		+LT •HT	?LT •HT	+ • x	?	?	xLT ?HT			x			•		x	•	•	AlB_2 x Si_2Th • Gd_2Si_3 +
MSi_3 75%																					x			$AuCu_3$
Si composition	Sc	Y	La	Ce	Pr	Nd	Pm	Sm	Eu	Gd	Tb	Dy	Ho	Er	Tm	Yb	Lu	Ac	Th	Pa	U	Np	Pu	example ( )

Fig. 106. Stoichiometry and structure prototype (or example) of the compounds of Si with rare earths and actinides.

compounds with various stoichiometry in the Ge based phase diagrams; the situation is difficult to clarify on the germanium-rich side. No clear similarities of the observed structures with rare earths and actinides appear in fig. 107.

With tin the compound which possesses the highest melting temperature has either the stoichiometry $(R, An)_5Sn_3$ or $(R, An)_5Sn_4$. Considering the structures of the intermetallic compounds of tin with rare earths and actinides a clear similarity appears for the composition $(R, An)Sn_3$; all the compounds have the $AuCu_3$ structure type.

Phase	Sc	Y	La	Ce	Pr	Nd	Pm	Sm	Eu	Gd	Tb	Dy	Ho	Er	Tm	Yb	Lu	Ac	Th	Pa	U	Np	Pu	Prototype or
M_7Ge 12.5%																					?			
M_3Ge 25%			x	?	x																			PTi_3 x
M_2Ge 33.3%																			x					Al_2Cu x
M_5Ge_3 37.5%	x	x	x	x	x[e]	x		x		x	x	x	x	x	x		x				x			Mn_5Si_3 x
M_3Ge_2 40%																			x					Si_2U_3 x
M_4Ge_3 42.9%			x	x	x																			P_4Th_3 x
M_5Ge_4 44.5%	x	x	x	x	x	x		x		x	x	x	x	x	x		x							Ge_4Sm_5 x
$M_{11}Ge_{10}$ 47.6%	x	x									x		x	x	x	x	x							$Ge_{10}Ho_{11}$ x
MGe 50%	x	x	•	•	x •	x		x	x	x	x	x	x	x	x				+		?			BCr x BFe • ClNa +
M_4Ge_5 55.6%														?	?		?							
M_3Ge_4 57.1%																					x			(Ge_4U_3) x
M_2Ge_3 60%		x						xLT ?HT		x •	?LT xHT	xLT ?HT	xLT ?HT	?LT xHT	x	?LT xHT	xLT						x	AlB_2 x Si_2Th •
MGe_{2-x} ~62%			xLT •HT	xLT •HT	xLT •HT	xLT •HT		•		•	?LT •HT	?	• ?				+							α-$GdSi_2$ x Si_2Th • Si_2Zr +
M_3Ge_5 62.5%		xLT •HT								xLT +HT									o		?			Si_2Th x GeS_2 • $GdSi_2$ + AlB_2 o
M_5Ge_9 64.3%															?									
MGe_2 66.7%	x	x			•				+		?	•		?					xLT •HT		x o		•	Si_2Zr x Si_2Th • CdI_2 + AlB_2 o
$M_{0.9}Ge_2$ 69%															x				•					Si_2Zr x Ge_2Th •
M_2Ge_5 71.4%										xHT														(Gd_2Ge_5) x
MGe_{3-x} ~72%										x?	x	?	•	x										$(ErGe_3)$ x (Ge_3Ho) •
MGe_3 75%																					x		x	$AuCu_3$ x
M_2Ge_7 77.8%		x?																						(Ge_7Y_2) x
Ge composition	Sc	Y	La	Ce	Pr	Nd	Pm	Sm	Eu	Gd	Tb	Dy	Ho	Er	Tm	Yb	Lu	Ac	Th	Pa	U	Np	Pu	example ( )

Fig. 107. Stoichiometry and structure prototype (or example) of the compounds of Ge with rare earths and actinides.

With lead the intermetallic compound possessing the highest melting point has the stoichiometry R_5Pb_3 (La → Lu, except Ce, Eu, Yb, and Y and Th) or less often, MPb_3 (UPb_3, $PuPb_3$). As with the tin-based compounds, all the (R, An)Pb_3 compounds have the same structure (prototype $AuCu_3$).

Many assessments of binary phase diagrams have been performed: Si–(Sc, Y, Sm, Gd) by Gokhale and Abbaschian (1986a,b, 1988c,b), Si–Ce by Munitz et al. (1989), Si–Nd

Phase	Sc	Y	La	Ce	Pr	Nd	Pm	Sm	Eu	Gd	Tb	Dy	Ho	Er	Tm	Yb	Lu	Ac	Th	Pa	U	Np	Pu	Prototype or
M_3Sn 25%			x	x	x																	x	x	$AuCu_3$ x
M_2Sn 33.3%												?		?		x								$InNi_2$ x
M_5Sn_3 37.5%	x	x	•LT xHT	•LT xHT	•LT xHT	x		x		x		x	x	x	x	x +	x		x				?	Mn_5Si_3 x Si_3W_5 • B_3Cr_5 +
M_3Sn_2 40%																					?			
M_4Sn_3 42.9%								x																P_4Th_3 x
M_5Sn_4 44.4%		x	x	x	x	x		x		x		x				x			•				?	Ge_4Sm_5 x Ga_4Ti_5 •
M_8Sn_7 46.7%																							?	
$M_{11}Sn_{10}$ 47.6%		x	?	x		x		x		x		x	x	x										$Ge_{10}Ho_{11}$ x
MSn 50%			x		?	?			x			?				•								BCr x AuCu •
M_8Sn_9 52.9%												?												
M_7Sn_8 53.3%																							?	
M_2Sn_3 60%			?					x																(Sm_2Sn_3) x
M_3Sn_5 62.5%			x	x	?	?															?			Pd_5Pu_3 x
M_4Sn_7 63.6%												?												
MSn_2 66.7%		x								x		x	x	x	x		?		x				•	Si_2Zr x Ga_2Hf •
M_3Sn_7 70%				x						x														(Gd_3Sn_7) x
M_2Sn_5 71.4%				x																				(Ce_2Sn_5) x
M_4Sn_{11} 73.3%										x														Gd_4Sn_{11} x
MSn_3 75%		x	x	x	x	x		x		x				?		x	?		x		x	x	x	$AuCu_3$ x
MSn_4 80%												?												
Sn composition	Sc	Y	La	Ce	Pr	Nd	Pm	Sm	Eu	Gd	Tb	Dy	Ho	Er	Tm	Yb	Lu	Ac	Th	Pa	U	Np	Pu	example ( )

Fig. 108. Stoichiometry and structure prototype (or example) of the compounds of Sn with rare earths and actinides.

by Gokhale et al. (1989a), Ge–(Sc, Y, La, Ce, Nd, Gd, Eu) by Gokhale and Abbaschian (1986c, 1988a, 1989a–d, 1991), Ge–Pr by Gokhale et al. (1989b), La–(Sn, Pb), Gd–(Sn, Pb) and Yb–(Sn, Pb) by Palenzona and Cirafici (1992a,b, 1991g,d, 1991h,i), U–(Sn, Pb) by Sheldon et al. (1987a,b), Sn–Th by Peterson and Foltyn (1989b) and Pb–Pu by Foltyn and Peterson (1988).

New determinations in the rare-earth–tin binary phase diagrams have been performed by Eremenko et al. (1990).

Table 40
Structure characteristics of X = Si, Ge, Sn, Pb and rare-earth or actinide (M = R, An) intermetallic compounds

Phase	Pearson symbol	Space group	Strukturbericht designation	Prototype or (example)
M_2X_7	oC18	$C222_1$		(Ge_7Y_2)
MX_3, MX_{3-x}	cP4	$Pm\bar{3}m$	$L1_2$	$AuCu_3$
	oC16	$C222_1$		$(ErGe_3)$
	o**			(Ge_3Ho)
M_4X_{11}	oC16	Amm2		Gd_4Sn_{11}
M_2X_5	o**			(Ce_2Sn_5)
	oC*			(Gd_2Ge_5)
M_3X_7	oC20	Cmmm		Gd_3S_7
$M_{0.9}X_2$	oC12	Cmcm	C49	Si_2Zr
MX_2	oC12	Cmmm		Ge_2Th
MX_{2-x}	hP3	P6/mmm	C32	AlB_2
M_3X_5	tI12	$I4_1/amd$	C_c	Si_2Th
M_2X_3	oI12	Imma		Gd_2Si_3
	hP3	$P\bar{3}m1$	C6	CdI_2
	tI24	$I4_1/amd$		Ga_2Hf
	tI6	I4/mmm	$C11_b$	$MoSi_2$
	o**			(Pb_2Th)
	hP16	$P6_3/mcm$	$D8_8$	Mn_5Si_3
	hP8	$P\bar{6}2m$		Pd_5Th_3
	oF72	Fdd2	C44	GeS_2
	oC32	Cmcm		Pd_5Pu_3
	t**			(Sm_2Sn_3)
M_3X_4	o**			(Ge_4U_3)
M_4X_5	hP*	$P6_322$		Pb_5Pu_4
MX	cF8	$Fm\bar{3}m$	B1	ClNa
	oP8	Pnma	B27	FeB
	oC8	Cmcm	Bf	CrB
	tP4	P4/mmm	$L1_0$	AuCu
$M_{11}X_{10}$	tI84	I4/mmm		$Ge_{10}Ho_{11}$
M_5X_4	oP36	Pnma		Ge_4Sm_5
	tP36	$P4_12_12$		Si_4Zr_5
	hP18	$P6_3/mcm$		Ga_4Ti_5
M_4X_3	cI28	$I\bar{4}3d$	$D7_3$	P_4Th_3
M_3X_2	tP10	P4/mbm	$D5_a$	Si_2U_3
M_5X_3	hP16	$P6_3/mcm$	$D8_8$	Mn_5Si_3
	tI32	I4/mcm	$D8_l$	B_3Cr_5
	tI32	I4/mcm	$D8_m$	Si_3W_5
M_2X	tI12	I4/mcm	C16	Al_2Cu
	oP12	Pnma	C23	Co_2Si
	hP6	$P6_3/mmc$	$B8_2$	$InNi_2$
M_3X	cP4	$Pm\bar{3}m$	$L1_2$	$AuCu_3$
	tP32	$P4_2/n$		PTi_3

Phase	Sc	Y	La	Ce	Pr	Nd	Pm	Sm	Eu	Gd	Tb	Dy	Ho	Er	Tm	Yb	Lu	Ac	Th	Pa	U	Np	Pu	Prototype or
M_3Pb 25%				x	x			?															x	$AuCu_3$
M_2Pb 33.3%				?		?			x							x								Co_2Si x
M_5Pb_3 37.5%		x	x	x	x	x		x	•	x	x	x	x		x	x	x		x				x	Mn_5Si_3 x Si_3W_5 •
M_4Pb_3 42.9%			x																					P_4Th_3 x
M_5Pb_4 44.4%		x	x	x	x	x		x		x	x	x	x		x		x? ?		•				•	Ge_4Sm_5 x Ga_4Ti_5 •
$M_{11}Pb_{10}$ 47.6%					x		?																	
MPb 50%				?		?			xLT ?HT			?				x	?				x			AuCu x
M_4Pb_5 55.6%																							x	Pb_5Pu_4 x
M_3Pb_4 57.1%			?		?																			
MPb_2 66.7%		x	?		•			?				?					+		o				•	Si_2Zr x Ga_2Hf • $MoSi_2$ + (Pb_2Th) o
MPb_3 75%		x	x	x	x	x		x	x	x	x	x	x		x	x			x		x		x	$AuCu_3$ x
Pb composition	Sc	Y	La	Ce	Pr	Nd	Pm	Sm	Eu	Gd	Tb	Dy	Ho	Er	Tm	Yb	Lu	Ac	Th	Pa	U	Np	Pu	example ( )

Fig. 109. Stoichiometry and structure prototype (or example) of the compounds of Pb with rare earths and actinides.

8.2. *Thermodynamic data of the binary alloys*

The enthalpies and entropies of formation of the intermetallic compounds formed between elements of column IVB and rare earths and actinides are reported in tables 41–44. Data concerning liquid alloys, obtained using calorimetric methods, have also been found in the literature, and are reported in tables 45–48.

There are rather few data concerning the intermetallic compounds of Si with rare earths, and there are no data with plutonium. We report in fig. 110 the enthalpies of formation of the (R, An)Si_2 compounds as a function of atomic number. In fig. 111 we plot the enthalpies of formation of R_5Si_3 and An_3Si_2 compounds. Figure 112 shows plots of the enthalpies of formation of $An_{1-x}Si_x$ and $Gd_{1-x}Si_x$ compounds as a function of Si content. The data are from Alcock et al. (1966) for the thorium-based alloys, have been assessed by Chiotti et al. (1981) for the uranium-based alloys, and are from Lukashenko et al. (1992) for the Gd-based alloys. The only trend which can be seen from these three figures is that the enthalpies of formation of the actinide compounds are less negative than those of the rare earth compounds.

In the liquid state some values of partial enthalpies at infinite dilution of rare earths in silicon and enthalpies of mixing have been obtained by calorimetric measurements; they concern only rare earth elements. Nothing can be deduced from these values.

Table 41
Enthalpies and entropies of formation of intermetallic compounds of Si with rare earths and actinides ($\Delta_f H°$: kJ/mol of atoms, $\Delta_f S°$: JK^{-1}/mol of atoms)

System	Compound	$\Delta_f H°$	$\Delta_f S°$	Reference state	Authors and method
Sc–Si	Sc_3Si_5	−71		α-Sc, Si_s; 298 K	Golutvin et al. 1984
	ScSi	−117		(same)	combustion calorim.
	Sc_5Si_3	−161		(same)	
	Sc_5Si_3	−89.9		α-Sc, Si_s; 298 K	Topor and Kleppa 1989
					solute + solvent drop calorim.
					1473 K
	ScSi	−87.1	−14.5	α-Sc, Si_s; 825–1045 K	Lukashenko et al. 1990b,1992
	Sc_5Si_3	−102.8	−14.5	α-Sc, Si_s; 835–985 K	emf liq. electrolyte 825–1045 K
Y–Si	Y_5Si_3	−71.7		α-Y, Si_s; 298 K	Topor and Kleppa 1990
					solute + solvent drop calorim.
					1473 K
	YSi_2	−38.9	−2.5	α-Y, Si_s; 298 K	Ran et al. 1989b
	h-Y_3Si_5	−44.4	−4.0	(same)	phase diag. optimisation
	r-Y_3Si_5	−45.2	−5.0	(same)	
	YSi	−61.9	−10.7	(same)	
	Y_5Si_4	−65.1	−12.6	(same)	
	Y_5Si_3	−60.0	−11.2	(same)	
La–Si	$La_{0.37}Si_{0.63}$	−99.1	−28.4	β-La, Si_s; 960–1050 K	Polotskaya 1988, Lukashenko et al.
		−99.0	−28.2	α-La, Si_s	1992
					emf liq. electrolyte 960–1050 K
	$LaSi_{1.69}$	−61.9		unknown	Samsonov et al. 1963 quoted by
					Lukashenko et al. 1992
Nd–Si	$Nd_{0.36}Si_{0.64}$	−89.0	−20.1	α-Nd, Si_s; 930–1050 K	Polotskaya and Buyanov 1986
					emf liq. electrolyte 930–1050 K
Gd–Si	$GdSi_2$	−79.3	−22.2	α-Gd, Si_s; 830–960 K	Lukashenko and Polotskaya 1986
					emf liq. electrolyte 830–960 K
	$GdSi_{1.89}$	−82.3	−23	Gd, Si_s; 600–960 K	Lukashenko et al. 1992
	Gd_2Si_3	−94.3	−25.9	(same)	emf liq. electrolyte 600–960 K
	GdSi	−109.8	−32.1	(same)	
	Gd_5Si_4	−115.6	−38.2	Gd, Si_s; 600–910 K	
	Gd_5Si_3	−118.6	−39.4	(same)	
Th–Si	$ThSi_2$	−58.2		α-Th, Si_s; 298 K	Robins and Jenkins 1955
					direct react. calorim.
	$ThSi_2$	−55.1	−0.81	α-Th, Si_s[a]	Alcock et al. 1966
	Th_3Si_5	−57.9	−1.51	(same)	vap. press. of Si 1700–1960 K
	ThSi	−61.1	−2.53	(same)	
	Th_3Si_2	−54.1	−3.26	(same)	
U–Si	USi_3	−33.9	−1.1	α-U, Si_s[a]	Alcock and Grieveson 1961/62
	USi_2	−41.4	−1.2	(same)	vap. press. of Si 1675–1840 K;
	$USi_{1.88}$	−43.9	−2.0	(same)	reviewed by Rand and
	U_3Si_5	−42.0	−1.1	(same)	Kubaschewski 1963 and Chiotti et
	USi	−41.8	−0.9	(same)	al. 1981
	U_3Si_2	−36.0	−0.9	(same)	
	USi_3	−32.6		α-U, Si_s; 298 K	Gross et al. 1962
	$USi_{1.88}$	−43.9		(same)	direct react. calorim.; see also
	U_3Si_5	−45.6		(same)	Chiotti et al. 1981

continued on next page

Table 41, *continued*

System	Compound	$\Delta_f H^\circ$	$\Delta_f S^\circ$	Reference state	Authors and method
U–Si	USi	−41.8		α-U, Si_s; 298 K	Gross et al. 1962
(*cont'd*)	U_3Si_2	−33.9		(same)	direct react. calorim.; see also
	U_3Si	−21.3		(same)	Chiotti et al. 1981
	U_3Si	−26.0		α-U, Si_s; 298 K	O'Hare et al. 1974
					fluorine bomb calorim.

[a] Values calculated by the authors assuming that the enthalpies and entropies of formation and of transition are temperature independent.

The enthalpies of formation of the (R, An)Ge_2 and (R, An)$_5Ge_3$ (except for Th with the enthalpy of formation of Th_3Ge_2) have been plotted as a function of the atomic number in figs. 113 and 114 respectively. The enthalpies of formation of $R_{1-x}Ge_x$ and $An_{1-x}Ge_x$ compounds have been plotted as a function of Ge content in fig. 115. The enthalpies of formation of the actinide-based compounds are less exothermic than the enthalpies of formation of rare-earth-based compounds.

In the liquid state a systematic study of the partial enthalpy at infinite dilution of rare earths in liquid germanium has been performed by Nikolaenko et al. (1979a,b, 1980a,b, 1987, 1988). A decrease of the partial enthalpy at infinite dilution from Sc to Y to La and an increase of these values from La to Lu is seen (fig. 116). Figure 117 shows the values of the enthalpy of mixing at equiatomic composition obtained by the same authors, plotted as a function of the atomic number. The same trend as mentioned above is observed. The values of the enthalpies of formation at equiatomic composition (table 46) have also been reported in figure 117. The same trends of the enthalpies of mixing and of the enthalpies of formation at equiatomic composition are observed.

The enthalpies of formation of the RSn_3 and $AnSn_3$ compounds have been plotted as a function of the atomic number in fig. 118. A rather large scatter is observed for the enthalpy of formation of the USn_3 compound. If one considers the evolution of the enthalpies of formation in the actinide series, for example comparison between the behavior of Th and U with other metallic elements, it seems that the values obtained by Johnson and Feder (1962a,b) and more recently by Colinet et al. (1988a,b) lead to too negative values of the enthalpies of formation. However, it must be pointed out that the values reported by Colinet et al. (1988) have been obtained using various calorimetric methods: aluminum and tin solution calorimetry of the USn_3 compound, and calorimetry of USn_3 compound precipitation in liquid tin. The value obtained by Akhachinskij and Kopytin (1968) for $PuSn_3$ compound leads to a more negative value of the enthalpy of formation of the $PuSn_3$ compound than for the $ThSn_3$ compound.

Considering the rare-earth elements one observes for the composition RSn_3 less negative values of the enthalpies of formation from La to Lu and more negative values from Sc to Y to La. In fig. 119, the values proposed by Sheldon et al. (1987a) in the U–Sn system, by Borzone et al. (1983) in the La–Sn system and by Percheron et al. (1968) in the Sm–Sn system have been plotted as a function of Sn content. The decrease of

Table 42
Enthalpies and entropies of formation of intermetallic compounds of Ge with rare earths and actinides ($\Delta_f H°$: kJ/mol of atoms, $\Delta_f S°$: JK^{-1}/mol of atoms)

System	Compound	$\Delta_f H°$	$\Delta_f S°$	Reference state	Authors and method
Sc–Ge	$ScGe_2$	−71.5	−17.9	α-Sc, Ge_s; 900 K	Lukashenko et al. 1990a
	ScGe	−95.7	−18.5	(same)	emf liq. electrolyte 825–1000 K
	Sc_5Ge_3	−93.4		α-Sc, Ge_s; 298 K	Jung and Kleppa 1991b solute + solvent drop calorim. 1473 K
	$Sc_{11}Ge_{10}$	−99.6	−19.1	α-Sc, Ge_s; 825–990 K	Lukashenko et al. 1991a,b, 1992
	Sc_5Ge_4	−104.1	−19.3	α-Sc, Ge_s; 825–1040 K	emf liq. electrolyte 825–1040 K
	Sc_5Ge_3	−105.2	−12.6	α-Sc, Ge_s; 830–1040 K	
Y–Ge	Y_5Ge_3	−89.8		α-Y, Ge_s; 298 K	Jung and Kleppa 1991b solute + solvent drop calorim. 1473 K
La–Ge	$LaGe_{1.70}$	−82.4	−1.1	β-La, Ge_s; 960–1060 K	Buyanov et al. 1981
		−82.3	−0.9	α-La, Ge_s	emf liq. electrolyte 960–1060 K
	LaGe	−116.4	−17.6	β-La, Ge_s; 960–1060 K	Buyanov et al. 1988
	La_5Ge_4	−116.2	−17.3	α-La, Ge_s	emf liq. electrolyte 960–1060 K
		−117.4	−15.3	β-La, Ge_s; 960–1060 K	
		−117.2	−14.9	α-La, Ge_s	
	La_5Ge_3	−68.0		α-La, Ge_s; 298 K	Jung and Kleppa 1991b mixing and drop calorim. 1473 K
Nd–Ge	$NdGe_{1.63}$	−103.6	−13.3	α-Nd, Ge_s; 930–1020 K	Polotskaya and Buyanov 1986 emf liq electrolyte 930–1020 K
Gd–Ge	$GdGe_{1.63}$	−80.2	−5.22	α-Gd, Ge_s; 930–1030 K	Batalin et al. 1983 emf liq electrolyte 930–1030 K
	$GdGe_{1.63}$	−82.9	−9.3	α-Gd, Ge_s; 760–960 K	Polotskaya 1991, Lukashenko et al. 1991b, 1992 emf liq. electrolyte 760–960 K
	$GdGe_{1.5}$	−87.4	−10.5	(same)	
	GdGe	−105.4	−17.2	(same)	
	Gd_5Ge_4	−115.3	−22.1	(same)	
	Gd_5Ge_4	−112.8	−19.0	(same)	
Th–Ge	$ThGe_2$	−40.2	−1.1	α-Th, Ge_s[a]	Alcock et al. 1966
	Th_3Ge_5	−41.2	−1.3	(same)	vap. press. Knudsen 1330–1490 K;
	ThGe	−42.4	−1.7	(same)	reviewed by Chiotti et al. 1981
	Th_3Ge_2	−42.0	−1.4	(same)	
	Th_2Ge	−36.4	−1.3	(same)	
U–Ge	UGe_3	−26.8	−1.4	α-U, Ge_s[a]	Alcock and Grieveson 1961/62
	UGe_2	−29.3	−1.3	(same)	vap. press. Knudsen meth.
	U_3Ge_5	−30.1	−1.2	(same)	1300–1450 K; see also Rand and
	UGe	−30.8	−1.1	(same)	Kubaschewski 1963
	U_5Ge_3	−29.4	−0.3	(same)	

[a] Values calculated by the authors assuming that the enthalpies and entropies of formation and of transition are temperature independent.

Table 43
Enthalpies and entropies of formation of intermetallic compounds of Sn with rare earths and actinides ($\Delta_f H°$: kJ/mol of atoms, $\Delta_f S°$: $J K^{-1}$/mol of atoms)

System	Compound	$\Delta_f H°$	$\Delta_f S°$	Reference state	Authors and method
Sc–Sn	$ScSn_3$	−40.3	−9.5	α-Sc, Sn_l; 610–1140 K	Yamshchikov et al. 1985d
		−34.9	+0.9	α- Sc, Sn_s	emf liq electrolyte 610–1140 K [a]
Y–Sn	YSn_3	−52.3		α-Y, Sn_s; 300 K	Borzone et al. 1983
	YSn_2	−64.8		(same)	react. calorim.
	Y_5Sn_3	−87.9	−14.4	α-Y, Sn_s; 300 K	Borsese et al. 1980
					react. calorim.
	YSn_2	−71.8	−14.4	α-Y, Sn_l; 680–1150 K	Yamshchikov et al. 1979b
		−67.1	−5.1	α-Y, Sn_s	emf liq. electrolyte 680–1150 K [b]
La–Sn	$LaSn_3$	−60.7		α-La, Sn_s; 300 K	Borzone et al. 1983
	La_3Sn_5	−78.2		(same)	react. calorim.
	La_5Sn_4	−87.4		(same)	
	La_5Sn_3	−77.4		(same)	
	La_3Sn	−51.5		(same)	
	La_5Sn_3	−73.2		α-La, Sn_s; 300 K	Borsese et al. 1980
					react. calorim.
	$LaSn_3$	−65.2		α-La,Sn_l; 510 K	Palenzona 1973
		−60.2		α-La, Sn_s; 298 K	dyn. diff. calorim.
	$LaSn_3$	−65.6	−8.6	β-La, Sn_s; 773–973 K	Matigorova and Bayanov 1971
		−65.5	−8.4	α-La, Sn_s	emf liq. electrolyte 773–973 K
	$LaSn_3$	−67.6	−15.3	β-La, Sn_l; 650–875 K	Lukashenko and Polotskaya 1982
		−63.4	−6.3	α-La, Sn_s	emf liq. electrolyte 650–875 K
	$LaSn_3$	−59.1		α-La, Sn_s; 298 K	Colinet et al. 1988b
					Sn sol'n calorim. 1147 K
	$LaSn_3$	−69.0	−18.0	β-La, Sn_l; 1000 K	Kober et al. 1982b
		−63.6	−7.4	α-La, Sn_s	emf liq. electrolyte ~1000 K
	La_2Sn_3	−99.6	−29.0	β-La, Sn_l; 1000 K	
		−95.2	−20.4	α-La, Sn_s	
	La_2Sn	−133.2	−81.9	β-La, Sn_l; 1000 K	
		−130.6	−76.8	α-La, Sn_s	
Ce–Sn	$CeSn_3$	−58.6		γ-Ce, Sn_s; 300 K	Borzone et al. 1982a
	Ce_3Sn_5	−75.3		(same)	react. calorim.
	Ce_5Sn_4	−83.7		(same)	
	Ce_5Sn_3	−73.2		(same)	
	Ce_3Sn	−49.4		(same)	
	$CeSn_3$	−51.3		γ-Ce, Sn_l; 510 K	Palenzona 1973
		−49.1		γ-Ce, Sn_s; 298 K	dyn. diff. calorim.
	$CeSn_3$	−62.0		γ-Ce, Sn_s; 298 K	Colinet et al. 1988b
					Sn sol'n calorim. 1130 K
	$CeSn_3$	−62.0		γ-Ce, Sn_l; 930 K	Colinet et al. 1988b
		−56.8		γ-Ce, Sn_s	Sn precipitation calorim. 930 K
	Ce_5Sn_3	−75.3		γ-Ce, Sn_s; 300 K	Borsese et al. 1980
					react. calorim.
	$CeSn_3$	−68.9	−17.6	γ-Ce, Sn_l; 660–1100 K	Yamshchikov et al. 1977a
		−63.6	−7.2	γ-Ce, Sn_s	emf liq electrolyte 660–1100 K

continued on next page

Table 43, *continued*

System	Compound	$\Delta_f H^\circ$	$\Delta_f S^\circ$	Reference state	Authors and method
Pr–Sn	$PrSn_3$	−60.9		α-Pr, Sn_l; 520 K	Palenzona 1973
		−55.9		α-Pr, Sn_s; 298 K	dyn. diff. calorim.
Nd–Sn	$NdSn_3$	−70.9		α-Nd, Sn_l; 620 K	Palenzona 1973
		−66.0		α-Nd, Sn_s; 298 K	dyn. diff. calorim.
	$NdSn_3$	−65.0	−13.5	α-Nd, Sn_l; 773–973 K	Kulagina and Bayanov 1974b
		−59.7	−3.1	α-Nd, Sn_s	emf liq. electrolyte 773–973 K
	$NdSn_3$	−69.6	−19.6	α-Nd, Sn_l; 843 K	Kober et al. 1979d
		−64.4	−9.2	α-Nd, Sn_s	emf liq. electrolyte 843 K
Sm–Sn	$SmSn_3$	−58.5		α-Sm, Sn_l; 570 K	Palenzona 1973
		−53.6		α-Sm, Sn_s; 298 K	dyn. diff. calorim.
	$SmSn_3$	−56.3		α-Sm, Sn_s; 298 K	Percheron et al. 1968
	Sm_2Sn_3	−72.7		(same)	Sn sol'n calorim. 967 K
	Sm_5Sn_3	−63.6		(same)	
Eu–Sn	$EuSn_3$	−52.8		Eu_s, Sn_s; 298 K	Bacha et al. 1973
					Sn sol'n calorim. 957 K
	$EuSn_3$	−55.2	−26.0	Eu_s, Sn_l; 743–1023 K	Kober et al. 1985
		−49.9	−15.6	Eu_s, Sn_s	emf liq. electrolyte 743–1023 K[c]
$EuSn_3$	−56.3	−51.0	−28.9	Eu_s, Sn_l; 743–1023 K	Kober et al. 1985
			−18.5	Eu_s, Sn_s	emf liq. electrolyte 743–1023 K[d]
Gd–Sn	$GdSn_3$	−53.7		α-Gd, Sn_l; 600 K	Palenzona 1973
		−48.8		α-Gd, Sn_s; 298 K	dyn. diff. calorim.
	$GdSn_3$	−51.9		α-Gd, Sn_s; 298 K	Bacha et al. 1972a
					Sn sol'n calorim. 969 K
	$GdSn_3$	−55.7	−10.8	α-Gd, Sn_l; 773–973 K	Kulagina and Bayanov 1974a
		−50.4	−0.4	α-Gd, Sn_s	emf liq. electrolyte 773–973 K
	$GdSn_3$	−60.1	−18.3	α-Gd, Sn_l; 680–790 K	Batalin et al. 1983
		−54.8	−7.8	α-Gd, Sn_s	emf liq. electrolyte 680–790 K
Dy–Sn	$DySn_2$	−69.1	−13.6	α-Dy, Sn_l; 632–1125 K	Yamshchikov et al. 1990
		−64.3	−4.1	α-Dy, Sn_s	emf liq. electrolyte 632–1125 K
Ho–Sn	$HoSn_3$	−53.6	−14.2	Ho_s, Sn_l; 670–945 K	Yamshchikov et al. 1984b
		−48.3	−3.8	Ho_s, Sn_s	emf liq. electrolyte 670–945 K
Yb–Sn	$YbSn_3$	−50.8		α-Yb, Sn_l; 540 K	Palenzona 1973
		−45.9		α-Yb, Sn_s; 298 K	dyn. diff. calorim.
Yb–Sn	$YbSn_3$	−44.0		α-Yb, Sn_s; 298 K	Chatillon-Colinet et al. 1970
					Sn sol'n calorim. 857 K
Lu–Sn	$LuSn_3$	−39.1	−4.4	Lu_s, Sn_l; 733–873 K	Bayanov et al. 1974
		−33.8	+6.0	Lu_s, Sn_s	emf liq. electrolyte 733–873 K
Th–Sn	$ThSn_3$	−37.9	−9.1	α-Th, Sn_l; 950–1130 K	Kadochnikov et al. 1977
		−32.6	1.3	α-Th, Sn_s	cmf liq. electrolyte 950–1130 K
	$ThSn_3$	−40.6		α-Th, Sn_s; 298 K	Palenzona and Cirafici 1975b
					dyn. diff. calorim. 793 K
U–Sn	USn_3	−24.0	−0.6	α-U, Sn_s[e]	Alcock and Grieveson 1961/62
	U_3Sn_5	−27.2	−1.2	α-U, Sn_s[e]	vap. press. Knudsen 1150–1300 K
	U_3Sn_2	−26.8	1.0	α-U, Sn_s[e]	
	USn_3	−42.7	−14.5	α-U, Sn_l; 636–950 K	Johnson and Feder 1962b
		−37.4	−4.1	α-U, Sn_s	emf liq. electrolyte 636–950 K

continued on next page

Table 43, *continued*

System	Compound	$\Delta_f H^\circ$	$\Delta_f S^\circ$	Reference state	Authors and method
	USn_3	−22.5		α-U, Sn_s; 298 K	Alcock and Grieveson 1961/62 acid sol'n calorim.
	USn_3	−24.2		α-U, Sn_s; 298 K	Rand and Kubaschewski 1963
	U_3Sn_5	−27.3		(same)	assessment
	U_3Sn_2	−27.3		(same)	
	USn_3	−26.0	−2.5	γ-U, Sn_s	Sheldon et al. 1987a
		−24.1	−0.6	α-U, Sn_s	phase diag. optimization
	U_3Sn_5	−29.2	−4.0	γ-U, Sn_s	$\Delta_f H$ and $\Delta_f S$ supposed temperature
		−26.3	−1.2	α-U, Sn_s	independent.
	U_3Sn_2	−31.3	−5.5	γ-U, Sn_s	
		−26.8	−1.0	α-U, Sn_s	
	USn_3	−48.2	−20.8	γ-U, Sn_l; 813–1117 K	Kadochnikov et al. 1976
		−42.9	−10.4	α-U, Sn_s	emf liq. electrolyte 813–1117 K
	USn_3	−35.3		α-U, Sn_s; 298 K	Colinet et al. 1988a,b Al sol'n calorim. at 986 K
	USn_3	−35.0		α-U, Sn_s; 298 K	Colinet et al. 1988a,b Sn sol'n calorim. at 1145 K
	USn_3	−43.5		β-U, Sn_l; 1145 K	Colinet et al. 1988a,b
		−36.3		α-U, Sn_s	Sn precipitation calorim. at 1145 K
Pu–Sn	$PuSn_3$	−54.9		α-Pu, Sn_s; 298 K	Akhachinskij and Kopytin 1968
	Pu_3Sn	−55.2			acid. sol'n calorim.

[a] We assume that the intermetallic compound present in the saturated liquid is $ScSn_3$.
[b] These data are subject to caution because of the peritectic reaction $YSn_3 + L \rightarrow YSn_2$ at 788 K.
[c] Reference of the cell Eu–Bi (sat. sol.).
[d] Reference of the cell Eu_s.
[e] Values calculated by the authors assuming that the enthalpies and entropies of formation and of transition are temperature independent.

the absolute value of the enthalpies of formation from La to Sm is confirmed, with the enthalpies of formation of the compounds of the U–Sn system being less negative than those of the rare earths.

Values of the partial enthalpies of rare earths at infinite dilution in liquid tin have been obtained by several authors. These values have been plotted as a function of the atomic number in fig. 120. The variation with temperature of the partial enthalpy of lanthanum in liquid tin has been studied by Sommer et al. (1988a,b), with less negative values being obtained by increasing the temperature. In the lanthanide series the partial enthalpy at infinite dilution of Ln in liquid tin becomes less negative from La to Lu. The partial enthalpy of uranium at infinite dilution in liquid tin is less negative than the values obtained with the rare earth elements. Let us point out that some data obtained by calorimetric measurements at low temperature have not been included in our compilation because it appeared that the measurements had been performed in the two-phase region, i.e., equilibrium between the saturated liquid and the compound RSn_3 (see Colinet et al. 1988a,b).

Table 44
Enthalpies and entropies of formation of intermetallic compounds of Pb with rare earths and actinides ($\Delta_f H^\circ$: kJ/mol of atoms, $\Delta_f S^\circ$: $J K^{-1}$/mol of atoms)

System	Compound	$\Delta_f H^\circ$	$\Delta_f S^\circ$	Reference state	Authors and method
Sc–Pb	$ScPb_3$	−22.6	−1.6	α-Sc, Pb_l; 610–1140 K,	Yamshchikov et al. 1985d
		−19.0	+4.5	α-Sc, Pb_s	emf liq electrolyte 610–1140 K
Y–Pb	YPb_3	−37.7		α-Y, Pb_s; 298 K	Palenzona and Cirafici 1975b dyn. diff. calorim. 613 K
	YPb_3	−28.0		α-Y, Pb_s; 300 K	Borsese et al. 1975a
	YPb_2	−37.2		(same)	react. calorim.
	Y_5Pb_4	−60.2		(same)	
	Y_5Pb_3	−66.9		(same)	
	YPb_3	−39.8	−8.3	α-Y, Pb_l; 650–1080 K	Yamshchikov et al. 1979b
		−36.2	−2.3	α-Y, Pb_s	emf liq electrolyte 650–1080 K
La–Pb	$LaPb_3$	−51.5		α-La, Pb_s; 298 K	Palenzona and Cirafici 1973 dyn. diff. calorim. 590 K
	$LaPb_3$	−57.3		α-La, Pb_s; 300 K	Ferro et al. 1975
	$LaPb_2$	−60.2		(same)	react. calorim.
	La_3Pb_4	−64.0		(same)	
	La_5Pb_4	−69.0		(same)	
	La_4Pb_3	−69.9		(same)	
	La_5Pb_3	−72.0		(same)	
	$LaPb_3$	−58.0	−14.9	β-La, Pb_l; 1000 K	Lebedev et al. 1972a,b
		−54.3	−8.7	α-La, Pb_s	emf liq electrolyte 953–1123 K
	$LaPb_3$	−59.1	−13.2	β-La, Pb_s; 828–1003 K	Morisson et al. 1986
		−59.0	−13.0	α-La, Pb_s	emf sol. electrolyte 828–1003 K
Ce–Pb	$CePb_3$	−49.0		γ-Ce, Pb_s; 298 K	Palenzona and Cirafici 1973 dyn. diff. calorim. 585 K
	$CePb_3$	−58.7	−17.9	γ-Ce, Pb_l; 940–1100 K	Yamshchikov et al. 1977a
		−55.1	−11.9	γ-Ce, Pb_s	emf liq. electrolyte 940–1100 K
	$CePb_3$	−58.6	−28.9	γ-Ce, Pb_l; 673–823 K	Bayanov and Serebrennikov 1965
		−55.0	−22.9	γ-Ce, Pb_s	emf liq. electrolyte 673–823 K
	$CePb_3$	−59.3	−18.2	Ce[a], Pb_l; 703–1033 K	Kober et al. 1973b
		−55.7	−12.2	Ce_s, Pb_s	emf liq. electrolyte 703–1033 K
	$CePb_3$	−43.5	−28.0	δ-Ce, Pb_l; 1000 K	Otopkov et al. 1961
		−39.9	−22.0	γ-Ce, Pb_s	vap. press. 993–1073 K
	CePb	−61.1	−34.3	δ-Ce, Pb_l; 1000 K	
		−58.7	−30.3	γ-Ce, Pb_s	
	Ce_2Pb	−56.9	−34.7	δ-Ce, Pb_l; 1000 K	
		−55.3	−32.0	γ-Ce, Pb_s	
	$CePb_3$	−58.6	−12.6	Ce_s[a], Pb_s; 828–1028 K	Morisson and Petot 1987a emf sol. electrolyte 828–1028 K
Pr–Pb	$PrPb_3$	−52.6		α-Pr, Pb_s; 298 K	Palenzona and Cirafici 1973 dyn. diff. calorim. 585 K
	$PrPb_3$	−36.4	−15.9	α-Pr, Pb_l; 1000 K	Otopkov et al. 1961
		−32.8	−9.9	α-Pr, Pb_s	vap. press. 993–1073 K
	PrPb	−51.9	−22.6	α-Pr, Pb_l; 1000 K	
		−49.5	−18.6	α-Pr, Pb_s	
	Pr_2Pb	−50.3	−23.9	α-Pr, Pb_l; 1000 K	
		−48.7	−21.2	α-Pr, Pb_s	

continued on next page

Table 44, *continued*

System	Compound	$\Delta_f H°$	$\Delta_f S°$	Reference state	Authors and method
Nd–Pb	$NdPb_3$	−52.1		α-Nd, Pb_s; 298 K	Palenzona and Cirafici 1973 dyn. diff. calorim. 595 K
	$NdPb_3$	−52.9	−11.6	α-Nd, Pb_l; 796–873 K	Roshchina and Bayanov 1974b
		−49.3	−5.4	α-Nd, Pb_s	emf liq. electrolyte 796–873 K
	$NdPb_3$	−41.0	−25.1	α-Nd, Pb_l; 1000 K	Otopkov et al. 1961 vap. press.
		−37.4	−19.1	α-Nd, Pb_s	993–1073 K
	NdPb	−54.4	−31.8	α-Nd, Pb_l; 1000 K	
		−52.0	−27.8	α-Nd, Pb_s	
	Nd_2Pb	−55.7	−36.0	α-Nd, Pb_l; 1000 K	
		−54.1	−33.3	α-Nd, Pb_s	
Sm–Pb	$SmPb_3$	−49.5		α-Sm, Pb_s; 298 K	Palenzona and Cirafici 1973 dyn. diff. calorim. 600 K
Eu–Pb	$EuPb_3$	−43.9		Eu_s, Pb_s; 298 K	Palenzona and Cirafici 1973 dyn. diff. calorim. 595 K
	$EuPb_3$	−46.0	−19.5	Eu_s, Pb_l; 666–1023 K	Kober et al. 1985
		−42.4	−13.5	Eu_s, Pb_s	emf liq. electrolyte 666–1023 K
Gd–Pb	$GdPb_3$	−44.9		α-Gd, Pb_s; 298 K	Palenzona and Cirafici 1973 dyn. diff. calorim. 600 K
	$GdPb_3$	−38.2	−8.3	α-Gd, Pb_l; 773–879 K	Roshchina and Bayanov 1974c
		−34.5	−2.0	α-Gd, Pb_s	emf liq. electrolyte 773–879 K
Tb–Pb	$TbPb_3$	−39.3	−6.2	α-Tb, Pb_l; 673–873 K	Bayanov et al. 1977a
		−35.7	−0.2	α-Tb, Pb_s	emf liq. electrolyte 673–873 K
	$TbPb_3$	−43.8		α-Tb, Pb_s; 298 K	Palenzona and Cirafici 1973 dyn. diff. calorim. 595 K
Dy–Pb	$DyPb_3$	−42.8		α-Dy, Pb_s; 298 K	Palenzona and Cirafici 1973 dyn. diff. calorim. 610 K
	$DyPb_3$	−46.8	−15.4	α-Dy, Pb_l; 695–873 K	Bayanov et al. 1977b
		−42.1	−9.4	α-Dy, Pb_s	emf liq. electrolyte 695–873 K
	$DyPb_3$	−38.6	−8.3	α-Dy, Pb_l; 642–915 K	Yamshchikov et al. 1989
		−35.0	−2.3	α-Dy, Pb_s	emf liq. electrolyte 642–915 K
Ho–Pb	$HoPb_3$	−40.9		Ho_s, Pb_s; 298 K	Palenzona and Cirafici 1973 dyn. diff. calorim. 600 K
	$HoPb_3$	−36.3	−7.7	Ho_s, Pb_l; 680–950 K	Yamshchikov et al. 1986
		−32.7	−1.7	Ho_s, Pb_s	emf liq. electrolyte 680–950 K
Er–Pb	$ErPb_3$	−37.4		Er_s, Pb_s; 298 K	Palenzona and Cirafici 1973 dyn. diff. calorim. 610 K
	$ErPb_3$	−36.9	−9.9	Er_s, Pb_l; 773–873 K	Roshchina and Bayanov 1974a
		−33.3	−3.9	Er_s, Pb_s	emf liq. electrolyte 773–873 K
TmPb	$TmPb_3$	−35.4		Tm_s, Pb_s; 298 K	Palenzona and Cirafici 1973 dyn. diff. calorim. 600 K
Yb–Pb	$YbPb_3$	−37.0		Yb_s, Pb_s; 298 K	Palenzona and Cirafici 1973 dyn. diff. calorim. 590 K
	$YbPb_3$	−38.1		Yb_s, Pb_s; 298 K	Schiffman 1982
	$YbPb_{1.04}$	−57.3		(same)	vap. press. mass. spect. 750–1381 K
	Yb_5Pb_3	−57.7		(same)	
	Yb_2Pb	−58.2		(same)	

continued on next page

Table 44, *continued*

System	Compound	$\Delta_f H^\circ$	$\Delta_f S^\circ$	Reference state	Authors and method
Th–Pb	$ThPb_4$	−39.4	−22.5	α-Th, Pb_l; 873–1273 K	Gans et al. 1966 vap. press.
		−35.6	−16.1		Knudsen eff. 873–1273 K reviewed
	$ThPb_3$	−41.8	−21.4	α-Th, Pb_s	by Chiotti et al. 1981, 1982e
		−38.2	−15.4	α-Th, Pb_s	
	$ThPb_2$	−38.7	−14.0	α-Th, Pb_l; 873–1273 K	
		−35.5	−8.7	α-Th, Pb_s	
	ThPb	−32.0	−5.8	α-Th, Pb_l; 873–1273 K	
		−29.6	−1.8	α-Th, Pb_s	
	$ThPb_4$	−30.4	−8.7	α-Th, Pb_l; 949–1043 K	Poyarkov et al. 1976 emf liq.
		−26.5	−2.3	α-Th, Pb_s	electrolyte 949–1043 K
U–Pb	UPb_3	−18.4		α-U, Pb_s; 298 K	Alcock and Grieveson 1961/62
					acid sol'n calorim.
	UPb_3	−15.4	−0.4	α-U, Pb_s [b]	Alcock and Grieveson 1961/62
	UPb	−21.2	−5.3	(same)	vap. press. Knudsen eff. 945–1000 K
	UPb_3	−29.2	−18.2	γ-U, Pb_l; 933–1143 K	Lebedev et al. 1971b
		−23.7	−10.3	α-U, Pb_s	emf liq. electrolyte 933–1143 K
	UPb_3	−21.9	−9.8	α-U, Pb_l; 648–1227 K	Johnson and Feder 1962b
		−18.3	−3.8	α-U, Pb_s	emf liq. electrolyte 648–1227 K
	UPb_3	−18.2	−3.8	α-U, Pb_s; 298 K	Chiotti et al. 1981
	UPb	−29.3	−13.7	(same)	assessment
Pu–Pb	$PuPb_3$	−23.5	$(\Delta_f G^\circ)$	Pu_l, Pb_l; 1000 K	Chiotti et al. 1981
					estimation

[a] Aggregation state not specified.

[b] Values calculated by the authors assuming that the enthalpies and entropies of formation or of transition are temperature independent.

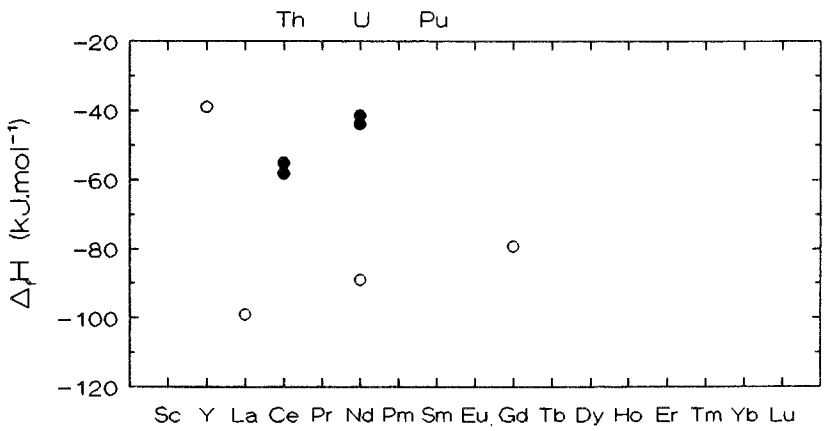

Fig. 110. Enthalpies of formation of rare earth (open circles) and actinide (solid circles) $(R, An)Si_2$ compounds as a function of atomic number. The references of the data are quoted in table 41.

Table 45
Values for the enthalpy of alloying of liquid silicon with rare earths[a]

System	$\Delta_m\bar{H}^{\infty}_{(R)}$ (kJ mol^{-1})	$\Delta_m H$ (kJ mol^{-1})	$\Delta_m\bar{H}^{\infty}_{(Si)}$ (kJ mol^{-1})	T (K)	Reference
Sc–Si	−100	−20.0(0.1)		1820	Sudavtsova et al. 1984b
Y–Si	−205	−69.0(0.475)	−162	1870	Ryss et al. 1979a
	−210	−70.0(0.4)		1880	Esin et al. 1976
		−57.0(0.45)		2053	Stukalo et al. 1980
		−54.0(0.72)			
La–Si	−162	−44.0(0.5)		1920	Esin et al. 1980
	−117			1821	Batalin et al. 1985c
Ce–Si	−237	−74.0(0.5)	−208	1923	Ryss et al. 1977, 1979b
	−245	−45.0(0.2)		1890	Sudavtsova et al. 1988

[a] Quantities: $\Delta_m\bar{H}^{\infty}_{(R)}$: limiting partial enthalpy of R.
$\Delta_m\bar{H}^{\infty}_{(Si)}$: limiting partial enthalpy of Ni.
$\Delta_m H$: heat of mixing for a given composition of the rare earth.
The reference state is the liquid elements. All enthalpy values are in kJ mol^{-1}.

Table 46
Values for the enthalpy of alloying of liquid germanium with rare earths[a]

System	$\Delta_m\bar{H}^{\infty}_{(R)}$ (kJ mol^{-1})	$\Delta_m H$ (kJ mol^{-1})	$\Delta_m\bar{H}^{\infty}_{(Ge)}$ (kJ mol^{-1})	T (K)	Reference
Sc–Ge	−140			1973	Nikolaenko et al. 1980b
Y–Ge	−258		−255	1900	Nikolaenko et al. 1979b
	−250	−60.0(0.25)		1523	Nikolaenko et al. 1987
	−176	−64.0(0.45)	−200	1920	Esin et al. 1985b
La–Ge	−293	−81.0(0.4)		1900	Nikolaenko et al. 1980a
	−214	−48.0(0.45)		1923	Esin et al. 1980
Ce–Ge	−295			2000	Nikolaenko et al. 1979a
Nd–Ge	−252			1925	Nikolaenko and Beloborodova 1980
Gd–Ge	−241			1973	Nikolaenko et al. 1988
Tb–Ge	−232			1973	Nikolaenko et al. 1980b
Dy–Ge	−214			1973	Nikolaenko et al. 1980b
Ho–Ge	−196			1973	Nikolaenko et al. 1988
Er–Ge	−213			1973	Nikolaenko et al. 1980b
Yb–Ge	−197	−31.0(0.16)		1223	Nikolaenko et al. 1988
Lu–Ge	−190	−29.0(0.16)		1275	Nikolaenko et al. 1988

[a] Quantities: $\Delta_m\bar{H}^{\infty}_{(R)}$: limiting partial enthalpy of R.
$\Delta_m\bar{H}^{\infty}_{(Ge)}$: limiting partial enthalpy of Ni.
$\Delta_m H$: heat of mixing for a given composition of the rare earth.
The reference state is the liquid elements. All enthalpy values are in kJ mol^{-1}.

Table 47
Values for the enthalpy of alloying of liquid tin with rare earths and uranium[a]

System	$\Delta_m\bar{H}^{\infty}_{(M)}$ (kJ mol^{-1})	$\Delta_m H$ (kJ mol^{-1})	$\Delta_m\bar{H}^{\infty}_{(Sn)}$ (kJ mol^{-1})	T (K)	Reference
Sc–Sn	−58	−18.6(0.25)		1890	Sudavtsova and Batalin 1990
Y–Sn	−165			999	Colinet et al. 1984a
	−154	−52.8(0.45)	−181	1920	Esin et al. 1985b
	−143			1173	Meyer-Liautaud et al. 1987b
	−195	−49.4(0.25)		1523	Nikolaenko et al. 1987
La–Sn	−198			1174	Castanet 1984
	−205			1000	Colinet et al. 1984a
	−140	−42.1(0.35)		1890	Esin et al. 1981b
	−216			930	Colinet et al. 1988b
	−203			1129	Sommer et al. 1988b
	−211			1098	
	−174			1227	
	−159			1274	
	−167			1357	
	−171			1421	
	−157			1472	
Ce–Sn	−209			1221	Yamshchikov et al. 1983
	−213			1178	Castanet 1984
	−202			999	Colinet et al. 1984a
	−209			930	Colinet et al. 1988b
	−196			1129	
	−200			1133	
	−212			1870	Sudavtsova and Batalin 1990
Sm–Sn	−202			967	Percheron et al. 1968
	−173			1173	Meyer-Liautaud et al. 1987a
Eu–Sn	−178.3			957	Bacha et al. 1973
Gd–Sn	−177			969	Bacha et al. 1972a
	−166			1095	Sommer et al. 1988b
	−161			1274	
	−154			1468	
Dy–Sn	−160.4			957	Bacha et al. 1972b
	−162			1098	Sommer et al. 1988b
	−154			1273	
	−155			1379	
	−152			1478	
Er–Sn	−124			963	Bacha et al. 1972b
	−130			1096	Sommer et al. 1988b
	−128			1183	
	−121			1271	
	−126			1371	
	−127			1470	

continued on next page

Table 47, *continued*

System	$\Delta_m\bar{H}^{\infty}_{(M)}$ (kJ mol^{-1})	$\Delta_m H$ (kJ mol^{-1})	$\Delta_m\bar{H}^{\infty}_{(Sn)}$ (kJ mol^{-1})	T (K)	Reference
Tm–Sn	−151			995	Colinet et al. 1984a
Yb–Sn	−149			957	Chatillon-Colinet et al. 1970
Lu–Sn	−139			998	Colinet et al. 1984a
	−143			1133	Colinet et al. 1988b
U–Sn	−111			1145	Colinet et al. 1988b

[a] Quantities: $\Delta_m\bar{H}^{\infty}_{(M)}$: limiting partial enthalpy of R.
$\Delta_m\bar{H}^{\infty}_{(Sn)}$: limiting partial enthalpy of Ni.
$\Delta_m H$: heat of mixing for a given composition of the rare earth.
The reference state is the liquid elements. All enthalpy values are in kJ mol^{-1}.

Table 48
Values for the enthalpy of alloying of liquid lead with rare earths[a]

System	$\Delta_m\bar{H}^{\infty}_{(R)}$ (kJ mol^{-1})	$\Delta_m H$ (kJ mol^{-1})	$\Delta_m\bar{H}^{\infty}_{(Pb)}$ (kJ mol^{-1})	T (K)	Reference
Y–Pb	−143	−35.0(0.25)		1307	Nikolaenko et al. 1987
Ce–Pb	−146			1157	Yamshchikov et al. 1983

[a] Quantities: $\Delta_m\bar{H}^{\infty}_{(R)}$: limiting partial enthalpy of R.
$\Delta_m\bar{H}^{\infty}_{(Pb)}$: limiting partial enthalpy of Ni.
$\Delta_m H$: heat of mixing for a given composition of the rare earth.
The reference state is the liquid elements. All enthalpy values are in kJ mol^{-1}.

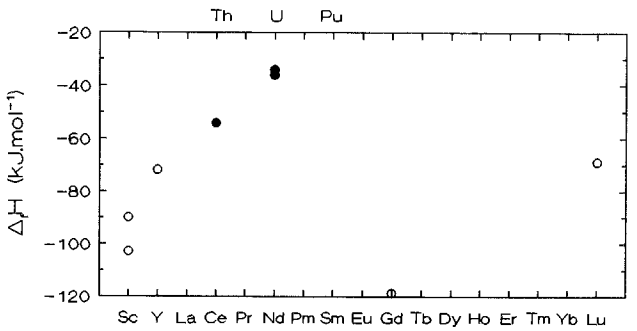

Fig. 111. Enthalpies of formation of rare earth (open circles) and actinide (solid circles). R_5Si_3 and An_3Si_2 compounds as a function of atomic number. The references of the data are quoted in table 41.

The enthalpies of formation of the RPb_3 and $AnPb_3$compounds have been plotted in fig. 121 as a function of the atomic number. Even with discrepancies between the values, one observes a decrease of the absolute value of the enthalpies of formation from La to Lu and an increase from Sc to Y to La, similar to the RSn_3 compounds. The enthalpy of

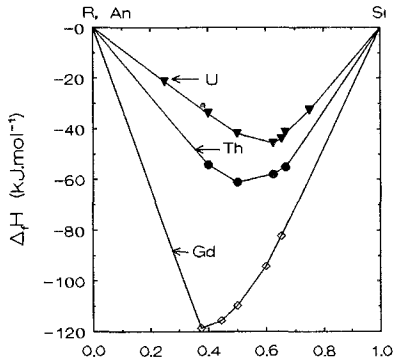

Fig. 112. Enthalpies of formation of $R_{1-x}Si_x$ and $An_{1-x}Si_x$ compounds. The data for An = Th (solid circles) and U (solid inverted triangles) are from Alcock et al. (1966) and Chiotti et al. (1981), respectively. The data for R = Gd (open diamonds) are from Lukashenko and Polotskaya (1986) and Lukashenko et al. (1992).

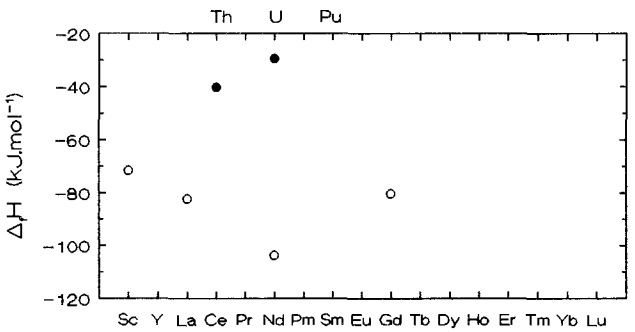

Fig. 113. Enthalpies of formation of rare earth (open circles) and actinide (solid circles). (R, An)Ge_2 compounds as a function of atomic number. The references of the data are quoted in table 42.

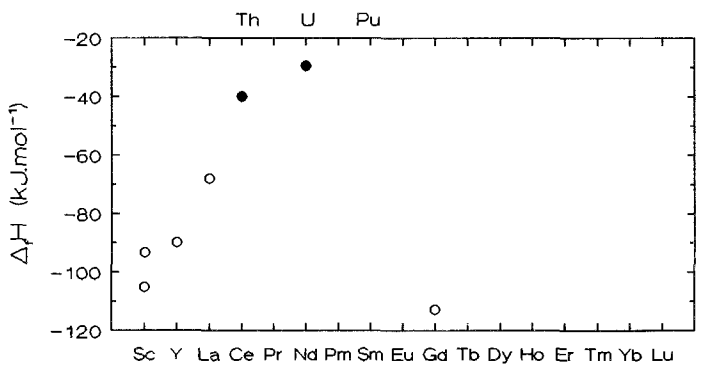

Fig. 114. Enthalpies of formation of rare earth (open circles) and actinide (solid circles) (R_5Ge_3), U_5Ge_3 and Th_3Ge_2 compounds as a function of atomic number. The references of the data are quoted in table 42.

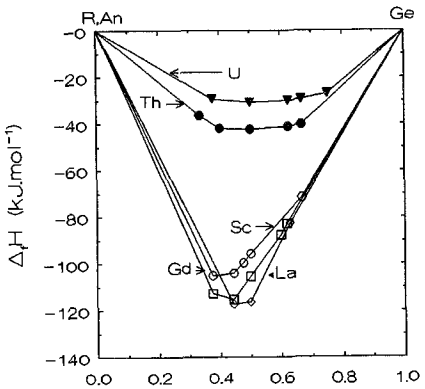

Fig. 115. Enthalpies of formation of $R_{1-x}Ge_x$ and $An_{1-x}Ge_x$ compounds. The data for An = Th (solid circles) and U (inverted solid triangles) are from Alcock et al. (1966) and Alcock and Grieveson (1961/62), respectively. The data for R = Sc (open circles), La (open diamonds) and Gd (open squares) have been summarized by Lukashenko et al. (1992).

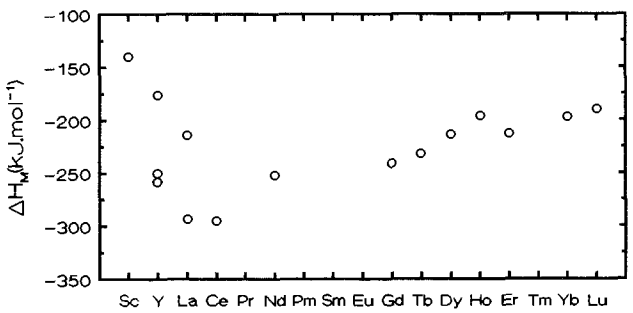

Fig. 116. Limiting partial enthalpies of rare earths (open circles) and actinides (solid circles) in liquid germanium as function of atomic number. The references of the data are quoted in table 46.

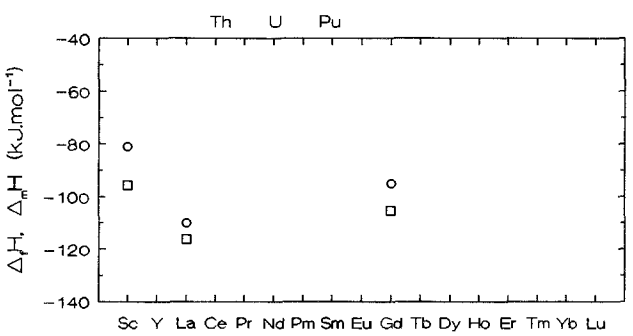

Fig. 117. Enthalpy of mixing (open circles) and enthalpies of formation (open squares) at equiatomic composition in the R–Ge alloys. The references of the data are quoted in tables 42 and 46.

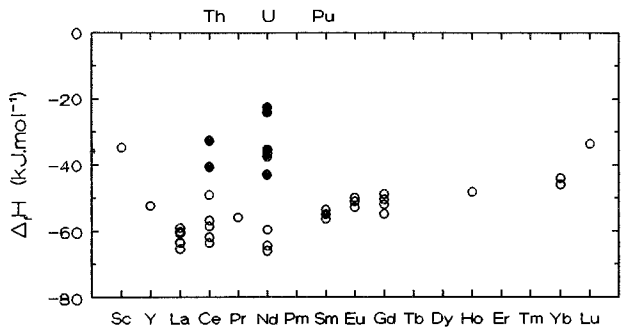

Fig. 118. Enthalpies of formation of rare earth (open circles) and actinide (solid circles). (R, An)Sn_3 compounds as a function of atomic number. The references of the data are quoted in table 43. The values obtained by a calorimetric method have been indicated by an arrow.

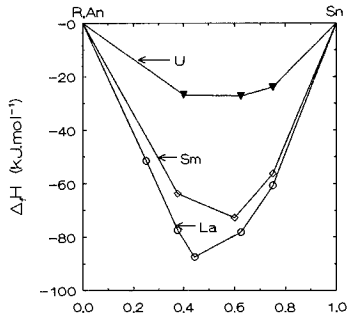

Fig. 119. Enthalpies of formation of $R_{1-x}Sn_x$ and $An_{1-x}Sn_x$ compounds. The data for R = La (open circles), Sm (open diamonds) and An = U (solid inverted triangles) are from Borzone et al. (1983), Percheron et al. (1968), and Rand and Kubaschewski (1963), respectively.

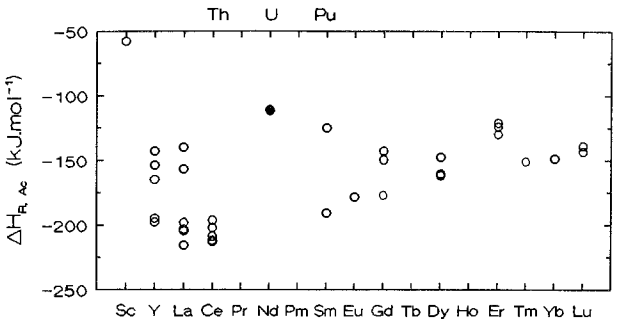

Fig. 120. Limiting partial enthalpies of rare earths (open circles) and actinides (solid circles) in liquid tin as a function of atomic number. The references of the data are quoted in table 47.

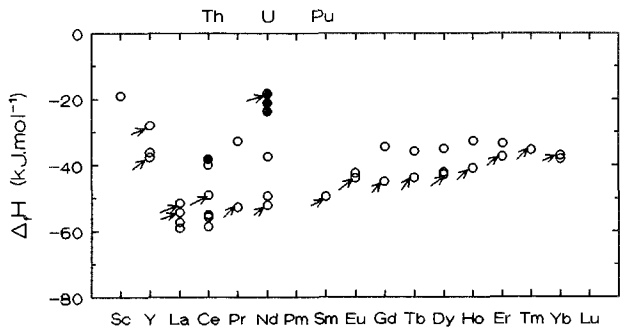

Fig. 121. Enthalpies of formation of rare earth (open circles) and actinides (solid circles) (R, An)Pb_3 compounds as a function of atomic number. The references of the data are quoted in table 44. The values obtained by a calorimetric method are indicated by an arrow.

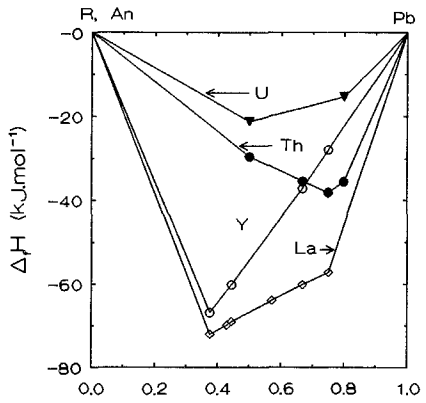

Fig. 122. Enthalpies of formation of $R_{1-x}Pb_x$ and $An_{1-x}Pb_x$ compounds. The data for R = La, Y and An = Th, U are from Ferro et al. (1975), Borsese et al. (1975a) and Chiotti et al. (1981), respectively.

formation of the $ThPb_3$ compound is of the same order of magnitude as the enthalpy of formation of the compounds based on light lanthanides.

The enthalpies of formation obtained by Ferro et al. (1975) in the La–Pb system and by Borsese et al. (1975a) in the Y–Pb system using calorimetric methods as well as the enthalpies of formation proposed by Chiotti et al. (1981) in the Th–Pb and U–Pb systems have been plotted in fig. 122 as a function of Pb content. The asymmetric shape of the enthalpy of formation with respect to 0.5 composition appears to be different for rare earths and actinides.

Only two sets of data have been obtained by a calorimetric method in the liquid lead alloys; they are presented in table 48.

9. Rare earths and actinides with elements of column VB

9.1. *Phase diagrams and intermetallic compounds*

The main features of the binary phase diagrams of rare earths and actinides with Sb, Bi and As are presented in figs. 123–125. All the known phase diagrams contain several intermetallic compounds. The stoichiometries and the respective structures of these compounds are reported in figs. 126–128. Table 49 gives the characteristics of the structures encountered. All of the considered phase diagrams display an intermetallic compound at the equiatomic composition. This compound always has the same structure (prototype NaCl). It is often the compound which has the highest congruent melting temperature. Few exceptions to this behavior may be detected in figs. 123–125. One exception may be pointed out: the UBi compound undergoes a peritectic decomposition and the U–Bi phase diagram exhibits a miscibility gap in the liquid phase for uranium-rich alloys.

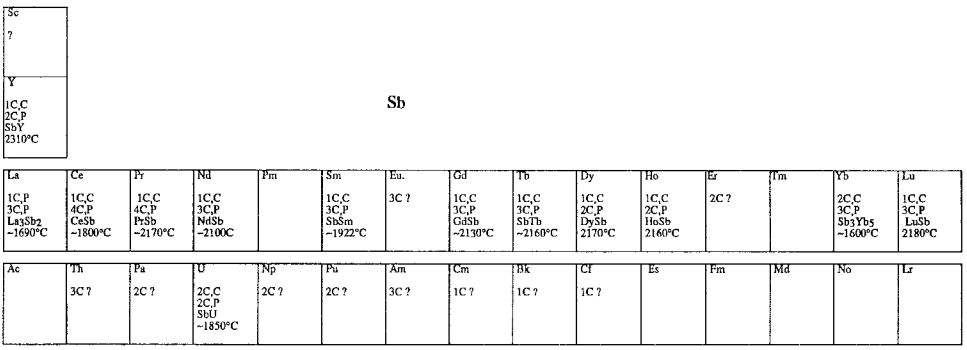

Fig. 123. Main features of the phase diagrams of antimony with rare earths and actinides.

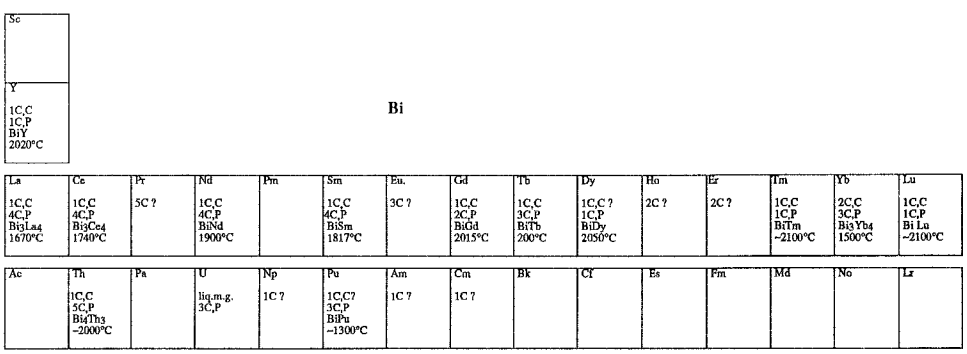

Fig. 124. Main features of the phase diagrams of bismuth with rare earths and actinides.

Recent investigations of rare-earth–antimony binary phase diagrams have been performed by Abdusalyamova et al. (1990a,b). All the R–As and R–Bi binary systems have been evaluated by Gschneidner and Calderwood (1986b, 1989b). Ferro et al. (1988) have

Sc 4C ?															
Y 1C ?						As									
La 3C ?	Ce 3C ?	Pr 3C ?	Nd 1C,C 2C,P 2220°C	Pm	Sm 1C,C ? AsSm ~2200°C	Eu 12C ?	Gd 1C ?	Tb 1C,C AsTb > 2500°C	Dy 1C,C AsDy > 2500°C	Ho 1C,C AsHo > 2500°C	Er 1C,C AsEr > 2500°C	Tm 1C,C AsTm > 2500°C	Yb 2C,C 1C,P AsYb > 2500°C	Lu 1C,C As Lu ~ 2400°C
Ac	Th 3C ? AsTh 2780°C	Pa	U 3C ? AsU 2705°C	Np 3C ?	Pu 1C ?	Am	Cm	Bk	Cf	Es	Fm	Md	No	Lr	

Fig. 125. Main features of the phase diagrams of arsenic with rare earths and actinides.

Phase	Sc	Y	La	Ce	Pr	Nd	Pm	Sm	Eu	Gd	Tb	Dy	Ho	Er	Tm	Yb	Lu	Ac	Th	Pa	U	Np	Pu	Prototype or
M_3Sb 25%		x																						PTi_3 x
M_2Sb 33.3%	•		x	x	x	x		x																La_2Sb x Cu_2Sb •
M_5Sb_3 37.5%	•	x	x	x	x	x		x	•	x	x	x	x			xHT •LT								Mn_5Si_3 x Sb_3Yb_5 •
M_4Sb_3 42.9%		x	x	x	x	x		x		x	x	x	x			x					?			P_4Th_3 x
M_5Sb_4 44.4%																x								(Sb_4Yb_5) x
$M_{11}Sb_{10}$ 47.6%		,							x							x								$Ge_{10}Ho_{11}$ x
MSb 50%	x	x	x	x	x	x		x		x	x	x	x	x	x	x	x		x		x	x	x	ClNa x
M_3Sb_4 57.1%																			x	x	x			P_4Th_3 x
M_2Sb_3 60%									x															(As_3Eu_2) x
MSb_2 66.7%		oHP	x	x	x	x		x	•	x oHP	x oHP	oHP ?	oHP ?	oHP ?	oHP ?	+	o		Δ	Δ	Δ	x	x	Sb_2Sm x $CaSb_2$ • Si_2Zr + $HoSb_2$ o Cu_2Sb Δ
Sb composition	Sc	Y	La	Ce	Pr	Nd	Pm	Sm	Eu	Gd	Tb	Dy	Ho	Er	Tm	Yb	Lu	Ac	Th	Pa	U	Np	Pu	example ()

Fig. 126. Stoichiometry and structure prototype (or example) of the compounds of Sb with rare earths and actinides.

performed a comparative analysis of R–Sb binary systems. Assessment of the binary Bi–Th and Bi–Pa phase diagrams has been performed by Chiotti et al. (1982g,f). An updated Lu–Sb phase diagram was presented by Okamoto (1991u).

9.2. *Thermodynamic data of the binary alloys*

The enthalpies and entropies of formation of the intermetallic compounds of rare earths and actinides with Sb, Bi and As are reported in tables 50–52.

Phase	Sc	Y	La	Ce	Pr	Nd	Pm	Sm	Eu	Gd	Tb	Dy	Ho	Er	Tm	Yb	Lu	Ac	Th	Pa	U	Np	Pu	Prototype or
M_5Bi_2 28.6%																x								(Bi_3Yb_5) x
M_2Bi 33.3%			x	x	x	x		•															?	La_2Sb x Cu_2Sb •
M_5Bi_3 37.5%		•	x	x	x	x		x	•	x	x •?	•	•	•	•	•			x					Mn_5Si_3 x Sb_3Yb_5 •
M_4Bi_3 42.9%			x	x	x	x		x	x	x	x					x								P_4Th_3 x
$M_{11}Bi_{10}$ 47.6%									x							xHT ?LT								$Ge_{10}Ho_{11}$ x
MBi 50%	x	x	x	x	x	x		x		x	x	x	x	x	x		x		x		x	x	x	ClNa x
M_3Bi_4 57.1%																			x		x			P_4Th_3 x
MBi_2 66.7%			x +? •	x •?	x •?	x •?		•								+			o		o		?	La_2Sb x Bi_2La • Si_2Zr + Cu_2Sb o
Bi composition	Sc	Y	La	Ce	Pr	Nd	Pm	Sm	Eu	Gd	Tb	Dy	Ho	Er	Tm	Yb	Lu	Ac	Th	Pa	U	Np	Pu	example ()

Fig. 127. Stoichiometry and structure prototype (or example) of the compounds of Bi with rare earths and actinides.

The enthalpies of formation of three series of compounds have been plotted as a function of atomic number: those of (R, An)Sb_2 and (R, An)$_5Sb_3$ compounds in fig. 129, and those of the (R, An)Sb compounds in fig. 130. The following trends may be pointed out:

– The enthalpies of formation become less negative from La to Lu in the lanthanide series and become more negative from Sc to Y to La.

– The enthalpies of formation of $ThSb_2$ and $PuSb_2$ are similar to those of $CeSb_2$ and $SmSb_2$ respectively.

– The enthalpy of formation of USb_2 is less negative than the enthalpies of formation of $LnSb_2$ compounds and also than those of $ThSb_2$ and $PbSb_2$. Thc enthalpy of formation of USb is of the same order of magnitude as the enthalpy of formation of ScSb.

The enthalpies of formation in the U–Sb, La–Sb, Dy–Sb systems (obtained, respectively, by Baskin and Smith 1970, Borzone et al. 1979 and Ferro et al. 1988) have been plotted as a function of composition in fig. 131. The values of the enthalpies of formation obtained at equiatomic composition are more negative for lanthanide based systems.

The enthalpies of formation of three series of Bi intermetallic compounds have been plotted as a function of the atomic number: for the (R, An)Bi_2 and (R, An)$_5Bi_3$ compounds in fig. 132, and for the (R, An)Bi compounds in fig. 133. The following trends may be pointed out:

– The enthalpies of formation have quite the same values for the first elements of the lanthanide series (La–Nd) and become less negative from Nd to Lu for the 1:1 stoichiometry.

– The enthalpies of formation of $ThBi_2$ and $PuBi_2$ are less negative than the enthalpies of formation of the RBi_2 compounds. However the enthalpy of formation of ThBi is of the same order of magnitude as the enthalpies of formation of ScBi and ErBi compounds.

Phase	Sc	Y	La	Ce	Pr	Nd	Pm	Sm	Eu	Gd	Tb	Dy	Ho	Er	Tm	Yb	Lu	Ac	Th	Pa	U	Np	Pu	Prototype or
M_3As 25%					?																			
M_7As_3 30%	x																							As_3Sc_7 x
M_5As_3 37.5%	•								x +							x								Sb_3Yb_5 • Mn_5Si_2 x Ca_5Pb_3 +
$M_{3+x}As_2$ <40%									?															
M_3As_2 40%	x +								•															C_2Cr_3 x P_4Th_3 • S_3Sb_2 +
M_4As_3 42.8%			x	x	x				x •							x •								P_4Th_3 x (As_3Eu_4) •
M_5As_4 44.4%									x															As_4Eu_5 x
$M_{11}As_{10}$ 47.6%									x															$Ge_{10}Ho_{11}$ x
MAs 50%	x	x	x	x	x	x		x	•	x	x	x	x	x	x	x	x		x	x	?	x ?	x	NaCl x Na_2O_2 •
M_3As_4 57.1%									•										x	x	?	x		P_4Th_3 x As_4Eu_3 •
M_2As_3 60%									x															(As_3Eu_2) x
M_2As_{3+x} >60%									?															
MAs_2 66.7%			xLT •HT	x	x	x			Δ										+ o	o	?	o		As_2Nd x β-As_2La • Co_2Si + Cu_2Sb o (As_2Eu) Δ
MAs_3 75%									x •															$(\alpha$-$As_3Eu)$ x BaP_3 •
As composition	Sc	Y	La	Ce	Pr	Nd	Pm	Sm	Eu	Gd	Tb	Dy	Ho	Er	Tm	Yb	Lu	Ac	Th	Pa	U	Np	Pu	example ( )

Fig. 128. Stoichiometry and structure prototype (or example) of the compounds of As with rare earths and actinides.

The enthalpies of formation of the various intermetallic compounds of the Th–Bi, U–Bi, Ce–Bi and Gd–Bi systems have been represented as a function of Bi content in fig. 134. One observes that the enthalpies of formation of the compounds of the U–Bi system always have less negative values than for the other lanthanide and actinide elements. For thorium the enthalpies of formation are of the same order of magnitude as in the Gd–Bi system. For compounds on the Bi-rich side, they are clearly less negative than on the Th rich side.

Table 52 reports the enthalpies and entropies of formation of As-based alloys. With rare-earth elements the enthalpies of formation are known for the 1:1 composition. For the actinides thermodynamic data are known only for the U–As system. The enthalpies of formation of all Ln–As compounds are nearly the same, the enthalpy of formation of U–As being clearly less negative (fig. 135).

Table 49
Structure characteristics of X = Sb, Bi, As and rare earth or actinide (M = R, An) intermetallic compounds

Phase	Pearson symbol	Space group	Strukturbericht designation	Prototype or (example)
MX_3	mC16	C2/m		BaP_3
	aP8			(α-As_3Eu)
MX_2	oP12	Pnma	C23	Co_2Si
	oP12	Pnma, Pna21		(As_2Eu)
	aP*, o*12	Pmmm		(Bi_2La)
	mP12	$P2_1/C$		As_2Nd
	mC48	c2/c		(β-As_2La)
	mP6	$P2_1/m$		$CaSb_2$
	oC6	C222		$HoSb_2$
	oC12	Cmcm	C49	Si_2Zr
	oC24	Cmca		Sb_2Sm
	tP6	P4/nmm	C38	Cu_2Sb
	aP27	P1 or P$\bar{1}$		distorted anti La_2Sb
M_2X_3	mP40	P2/C		(As_3Eu_2)
M_3X_4	cI28	I$\bar{4}$3d	$D7_3$	P_4Th_3
	oF56	Fdd2		As_4Eu_3
MX	cF8	Fm$\bar{3}$m	B1	ClNa
	hP12	P$\bar{6}$2m		Na_2O_2
$M_{11}X_{10}$	tI84	I4/mmm		$Ge_{10}Ho_{11}$
M_5X_4	oP108	Pnma		(Yb_5Sb_4)
	oC36	Cmca		As_4Eu_5
M_4X_3	cI28	I$\bar{4}$3d	$D7_3$	P_4Th_3
	hR28			(As_3Eu_4)
M_3X_2	oP20	Pnma		S_3Sb_2
	oP20	Pnma	$D5_{10}$	C_2Cr_3
	cI28	I$\bar{4}$3d		P_4Th_3
M_5X_3	hP16	$P6_3$/mcm	$D8_8$	Mn_5Si_3
	oP32	Pnma		Sb_3Yb_5
	hP48	$P6_3$mc		Ca_5Pb_3
M_2X	tI12	I4/mmm		La_2Sb
	tP6	P4/nmm		Cu_2Sb
M_7X_3	tI84	I4/mcm		As_3Sc_7
M_5X_2	oP*	$Pn2_1a$		(Bi_2Yb_5)
M_3X	tP32	$P4_2/n$		PTi_3

In liquid alloys of rare earths or actinides with elements of column VB, we may just quote the value of the partial enthalpy at infinite dilution of cerium in liquid bismuth obtained by Yamshchikov et al. (1983) using a calorimetric method.

Table 50
Enthalpies and entropies of formation of intermetallic compounds of Sb with rare earths and actinides ($\Delta_f H°$: kJ/mol of atoms, $\Delta_f S°$: $J K^{-1}$/mol of atoms)

System	Compound	$\Delta_f H°$	$\Delta_f S°$	Reference state	Authors and method
Sc–Sb	ScSb	−65.7		α-Sc, Sb_s; 753 K	Chua and Pratt 1974 react. calorim. 753 K
	ScSb	−99.7	0.03	α-Sc, Sb_s; 613–873 K	Yamshchikov et al. 1985c
		−108.8	−10.4	α-Sc, Sb_l; 873–1113 K	emf liq. electrolyte 613–1113 K
		−98.3	0.60	α-Sc, Sb_s	
Y–Sb	YSb	−111.1		α-Y, Sb_s; 767 K	Chua and Pratt 1974 react. calorim. 767 K
	YSb	−104.6		α-Y, Sb_s; 300 K	Borsese et al. 1977c
	Y_5Sb_3	−96.2		(same)	react. calorim.
	Y_5Sb	−64.0		(same)	
	YSb	−123.0	−4.0	α-Y, Sb_s; 650–886 K	Yamshchikov et al. 1979b
		−136.4	−11.1	α-Y, Sb_l; 886–1110 K	emf liq electrolyte 650–1110 K
		−126.5	−0.09	α-Y, Sb_s	
La–Sb	$LaSb_2$		−92.0	α-La, Sb_s; 300 K	Borzone et al. 1979
	LaSb		−130.5	(same)	react. calorim.
	La_4Sb_3		−118.8	(same)	
	La_5Sb_3		−106.7	(same)	
	La_2Sb		−97.9	(same)	
	$LaSb_2$	−97.3	−5.4	β-La, Sb_s; 653–803 K	Goryacheva et al. 1971b
		−97.2	−5.2	α-La, Sb_s	emf liq. electrolyte 653–803 K
	$La_{0.53}Sb_{0.47}$	−148.2	−12.3	β-La, Sb_s; 653–803 K	
		−148	−12.0	α-La, Sb_s	
	La_4Sb_3	−148.9	−11.8	β-La, Sb_s; 730	Goryacheva et al. 1971c
		−148.7	−11.4	Kα-La, Sb_s	emf liq. electrolyte 653–798 K
	La_5Sb_3	−147.9	−12.8	β-La, Sb_s; 730 K	
		−147.7	−12.4	α-La, Sb_s	
	La_2Sb	−142.1	−14.8	β-La, Sb_s; 730 K	
		−140.9	−14.4	α-La, Sb_s	
	LaSb	−109		unknown	Chua and Pratt 1974 vap. press. T unknown
	LaSb	−147.5		α-La, Sb_s; 298 K	Viksman et al. 1980 vap. press. 2083–2356 K
		−134.3		α-La, Sb_s; 298 K	Viksman and Gordienko 1984 vap. press. 2160–2280 K
Ce–Sb	$CeSb_2$	−90.0		γ-Ce, Sb_s; 300 K	Borsese et al. 1981
	CeSb	−126.4		(same)	react. calorim.
	Ce_4Sb_3	−116.7		(same)	
	Ce_5Sb_3	−108.8		(same)	
	Ce_2Sb	−102.9		(same)	
	CeSb	−128.9		γ-Ce, Sb_s; 298 K[a]	Schiffman and Franzen 1982 vap. press. 1958–2179 K
	$CeSb_2$	−95.7	−4.6	γ-Ce, Sb_s; 650–957 K	Yamshchikov et al. 1977a,b
		−108.8	−19.8	γ-Ce, Sb_l; 857–1100 K	emf liq. electrolyte 650–1100 K
		−95.5	−5.1	γ-Ce, Sb_s	

continued on next page

Table 50, *continued*

System	Compound	$\Delta_f H^o$	$\Delta_f S^o$	Reference state	Authors and method
Pr–Sb	$PrSb_2$	−97		α-Pr, Sb_s; 300 K	Borzone et al. 1982c
	PrSb	−126		(same)	react. calorim.
	Pr_4Sb_3	−120		(same)	
	Pr_5Sb_3	−99		(same)	
	Pr_2Sb	−112		(same)	
	PrSb	−149.1		α-Pr, Sb_s; 298 K[a]	Viksman et al. 1980 vap. press. 1938–2293 K
	PrSb	−132.8		α-Pr, Sb_s; 298 K[a]	Viksman and Gordienko 1984 vap. press. 2095–2216 K
	$PrSb_2$	−111.6	−25.7	α-Pr, Sb_l; 953–1008 K	Kober et al. 1986c
		−98.3	−11.0	α-Pr, Sb_s	emf liq electrolyte 953–1108 K
Nd–Sb	$NdSb_2$	−90.8		α-Nd, Sb_s; 300 K	Borsese et al. 1977d
	NdSb	−123.0		(same)	react. calorim.
	Nd_4Sb_3	−113.8		(same)	
	Nd_5Sb_3	−107.5		(same)	
	NdSb	−146.5		α-Nd, Sb_s; 298 K[a]	Viksman et al. 1980 vap. press. 1725–2230 K
	NdSb	−129.6		α-Nd, Sb_s; 298 K[a]	Viksman and Gordienko 1984 vap. press. 1990–2087 K
Sm–Sb	$SmSb_2$	−89.5		α-Sm, Sb_s; 300 K	Borzone et al. 1985
	SmSb	−122.0		(same)	react. calorim.
	Sm_4Sb_3	−118.0		(same)	
	Sm_5Sb_3	−112.0		(same)	
	Sm_2Sb	−102.0		(same)	
	SmSb	−135.8		α-Sm, Sb_s; 298 K[a]	Viksman et al. 1980 vap. press. 1663–1961 K
	SmSb	−133.5		α-Sm, Sb_s; 298 K[a]	Viksman and Gordienko 1984 vap. press. 1752–1918 K
Gd–Sb	$Gd_{0.52}Sb_{0.48}$	−137.1	−7.5	α-Gd, Sb_s; 668–833 K	Goryacheva et al. 1971a, 1977 emf liq electrolyte 668–833 K
	GdSb	−103		α-Gd, Sb_s; 695 K	Pratt and Chua 1970 react. calorim. 695 K
	GdSb	−131.0		α-Gd, Sb_s; 298 K[a]	Viksman and Gordienko 1984 vap. press. 2122–2209 K
Tb–Sb	TbSb	−117		α-Tb, Sb_s; 726 K	Pratt and Chua 1970 react. calorim. 726 K
Dy–Sb	$DySb_2$	−76		α-Dy, Sb_s; 300 K	Ferro et al. 1988
	DySb	−114		(same)	react. calorim.
	Dy_4Sb_3	−111.5		(same)	
	Dy_5Sb_3	−105.5		(same)	
	$DySb_2$	−83.4	−2.5	α-Dy, Sb_s; 661–904 K	Yamshchikov et al. 1990
		−86.3	−6.2	α-Dy, Sb_l; 913–1077	emf liq. electrolyte 661–1077 K
		−73.0	+8.5	Kα-Dy, Sb_s	
	DySb	−181		α-Dy, Sb_s; 681 K	Pratt and Chua 1970 react. calorim. 681 K
Ho–Sb	HoSb	−126.5	−6.9	α-Ho, Sb_s[b]; 647–783 K	Goryacheva et al. 1981
	$HoSb_2$	−84.4	−4.6	(same)	emf liq electrolyte 647–783 K

continued on next page

Table 50, *continued*

System	Compound	$\Delta_f H^o$	$\Delta_f S^o$	Reference state	Authors and method
	HoSb	−64		α-Ho, Sb_s; 733 K	Pratt and Chua 1970 react. calorim. 733 K
Er–Sb	ErSb	−113.4	−7.6	Er_s, Sb_s [b]; 588–833 K	Goryacheva et al. 1981
	$ErSb_2$	−75.6	−5.0	(same)	emf liq electrolyte 588–833 K
	ErSb	−109		Er_s, Sb_s; 743 K	Pratt and Chua 1970 react. calorim.743 K
Yb–Sb	YbSb	−62		Yb_s, Sb_s; 683 K	Pratt and Chua 1970 react. calorim. 683 K
Tm–Sb	TmSb	−157		Tm_s, Sb_s; 755 K	Pratt and Chua 1970 react. calorim. 755 K
Lu–Sb	LuSb	−94		Lu_s, Sb_s [b]; 751 K	Chua and Pratt 1974 react. calorim. 751 K
	LuSb	−119	−9.6	Lu_s, Sb_s; 588–833 K	Gerasimov et al. 1979
	$LuSb_2$	−79.3	−6.4	(same)	emf liq. electrolyte 588–833 K
Th–Sb	$ThSb_2$	−106.4	−25.8	α-Th, Sb_l; 939–1093 K	Kadochnikov et al. 1974
		−93.1	−11.1	α-Th, Sb_s	emf liq electrolyte 939–1093 K
U–Sb	USb_2	−79.1	−21.8	γ-U, Sb_l; 900–1123 K	Seregin et al. 1972
		−63.3	−4.6	α-U, Sb_s	emf liq electrolyte 900–1123 K
	USb_2	−57.9		α-U, Sb_s; 298 K	Baskin and Smith 1970
	U_3Sb_4	−64.6		(same)	react. calorim.
	USb	−69.2		(same)	
	USb_2	−57.8		α-U, Sb_s; 750–900 K	Lebedev et al. 1982
	U_3Sb_4	−68.0		(same)	emf liq electrolyte 750–900 K
	USb	−62.5		(same)	
Pu–Sb	$PuSb_2$	−93.1	−24.3	ε-Pu, Sb_s; 808–950 K	Lebedev et al. 1984
		−90.9	−19.8	α-Pu, Sb_s	emf liq electrolyte 808–950 K

[a] Using the Third Law.

[b] Values calculated considering that the compound in equilibrium with solid Sb is $LnSb_2$ instead of LnSb as suggested by recent phase diagrams.

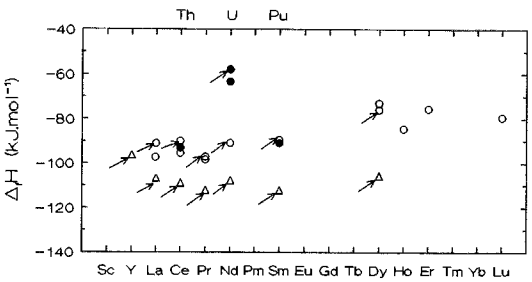

Fig. 129. Enthalpies of formation of rare earth (open symbols) and actinide (solid symbols) $(R, An)Sb_2$ compounds (open circle; solid circles) and $(R, An)_5Sb_3$ compounds (open triangle; solid triangles) as a function of the atomic number. The references of the data are quoted in table 50. The data obtained by a calorimetric method are indicated by an arrow.

Table 51
Enthalpies and entropies of formation of intermetallic compounds of Bi with rare earths and actinides ($\Delta_f H^\circ$: kJ/mol of atoms, $\Delta_f S^\circ$: $J\,K^{-1}$/mol of atoms)

System	Compound	$\Delta_f H^\circ$	$\Delta_f S^\circ$	Reference state	Authors and method
Sc–Bi	ScBi	−78.1	−8.1	α-Sc, Bi_l; 725–975 K	Petrashkevich et al.1977
		≙72.5	2.3	α-Sc,Bi_s	emf liq electrolyte 725–975 K
	ScBi	−79.9	−11.4	α-Sc, Bi_l; 712–970 K	Yamshchikov et al. 1985e
		−74.3	−1.0	α-Sc,Bi_s	emf liq electrolyte 712–970 K
Y–Bi	YBi	−92.0		α-Y, Bi_s; 300 K	Ferro et al. 1974
	Y_5Bi_3	−81.6			react. calorim.
	YBi	−106.9	−10.6	α-Y, Bi_l; 660–950 K	Kober et al. 1971b
		−101.3	−0.2	α-Y, Bi_s	emf liq electrolyte 660–950 K
La–Bi	LaBi	−110.9		α-La, Bi_s; 300 K	Borsese et al. 1974b
	La_4Bi_3	−103.3		(same)	react. calorim.
	$LaBi_2$	−92.2	−21.1	β-La, Bi_l; 743–963 K	Kober et al. 1968
		−84.8	−7.0	α-La, Bi_s	emf liq electrolyte 743–963 K
	LaBi	−116.4		α-La, Bi_s; 298 K	Viksman and Gordienko 1987 vap. press. 1340–1500 K
	$LaBi_2$	−82.8	−4.9	β-La, Bi_s; 823–1023 K	Morisson and Petot 1987b
		−82.7	−4.7	α-La, Bi_s	emf sol electrolyte 823–1023 K
Ce–Bi	$CeBi_2$	−77.4		γ-Ce, Bi_s; 300 K	Borzone et al. 1978
	CeBi	−114.6		(same)	react. calorim.
	Ce_4Bi_3	−101.3		(same)	
	Ce_5Bi_3	−91.6		(same)	
	Ce_2Bi	−81.6		(same)	
	$CeBi_2$	−90.5	−21.2	γ-Ce, Bi_l; 773–923 K	Kober et al. 1971a
		−83.0	−7.4	γ-Ce, Bi_s	emf liq electrolyte 773–923 K
	$CeBi_2$	−92.2	−35.3	γ-Ce, Bi_l; 698–823 K	Bayanov and Serebrennikov 1965
		−84.7	−21.5	γ-Ce, Bi_s	emf liq electrolyte 698–823 K
	$CeBi_2$	−83.3	−6.4	γ-Ce, Bi_s; 823–1023 K	Morisson and Petot 1987b emf sol electrolyte 823–1023 K
Pr–Bi	PrBi	−100.0		α-Pr, Bi_s; 300 K	Borsese et al. 1975b
	Pr_4Bi_3	−93.7		(same)	react. calorim.
	PrBi	−115.7		α-Pr, Bi_s; 298 K[b]	Viksman and Gordienko 1987 vap. press. 1340–1500 K
Nd–Bi	$NdBi_2$	−87.9		α-Nd, Bi_s; 300 K	Borsese et al. 1974a
	NdBi	−111.3		(same)	react. calorim.
	Nd_4Bi_3	−104.6		(same)	
	Nd_5Bi_3	−92.0		(same)	
	Nd_3Bi	−62.8		(same)	
	NdBi	−117.8		α-Nd, Bi_s; 298 K[b]	Viksman and Gordienko 1987 vap. press. 1340–1500 K
	$NdBi_2$	−87.7	−21.8	α-Nd, Bi_l; 810–1019 K	Kober et al. 1986b
		−80.2	−8.0	α-Nd, Bi_s	emf liq electrolyte 810–1019 K
Sm–Bi	$SmBi_2$	−76		α-Sm, Bi_s; 300 K	Borzone et al. 1993b
	SmBi	−108		(same)	react. calorim.
	Sm_4Bi_3	−104		(same)	
	Sm_5Bi_3	−94		(same)	
	Sm_2Bi	−88		(same)	

continued on next page

Table 51, *continued*

System	Compound	$\Delta_f H^\circ$	$\Delta_f S^\circ$	Reference state	Authors and method
Eu–Bi	$EuBi_2$	−74.8	−27.0	Eu_s, Bi_l; 760–998 K	Kober et al. 1985
		−67.3	−13.2	Eu_s, Bi_g	emf liq electrolyte 760–998 K
Gd–Bi	GdBi	−96.7		α-Gd, Bi_s; 300 K	Borzone et al. 1980
	Gd_4Bi_3	−92.0		(same)	react. calorim.
	Gd_5Bi_3	−87.5		(same)	
	$Gd_{5+x}Bi_3$	−83.7		(same)	
	GdBi	−110.9		α-Gd, Bi_s; 298 K[b]	Viksman and Gordienko 1987 vap. press. 1340–1500 K
Dy–Bi	DyBi	−96.2		α-Dy, Bi_s; 300 K	Borsese et al. 1977b
	Dy_5Bi_3	−81.6		(same)	react. calorim.
	DyBi	−100.8	−9.0	Dy_s, Bi_l; 670–1018 K	Yamshchikov et al. 1989
		−95.1	+1.4	Dy_s, Bi_s	emf liq electrolyte 670–1018 K
Er–Bi	ErBi	−85.6		Er_s, Bi_l; 773–973 K	Bayanov and Serebrennikov 1965
		−80.0		Er_s, Bi_s	emf liq. electrolyte 773–973 K
	ErBi	−90		Er_s, Bi_s; 300 K	Borzone et al. 1993b react. calorim.
Th–Bi	$ThBi_2$	−74.7	−22.6	α-Th, Bi_l; 953–1093 K	Poyarkov et al. 1974
		−67.2	−8.8	α-Th, Bi_s	emf liq electrolyte 953–1093 K
	Th_3Bi_4	−95.3	−33.7	α-Th, Bi_l	Chiotti et al. 1981
		−88.8	−21.8	α-Th, Bi_s	using the data of Poyarkov et al. 1974 and Dahlke et al. 1969
	$ThBi_2$	−69.0		α-Th, Bi_s; 300 K	Borzone et al. 1982b
	Th_3Bi_4	−85.4		(same)	react. calorim.
	ThBi	−81.2		(same)	
	Th_5Bi_3	−66.5		(same)	
U–Bi	UBi_2	−23.4	($\Delta_f G$)	β-U, Bi_l	Gross et al. 1958
	U_3Bi_5	−25.8		(same)	vap. press. 1015 K
	U_3Bi_4	−28.0		(same)	
	UBi	−29.7		(same)	
	UBi_2	−47.7	−32.6	U_s[a], Bi_l; 1018–1115 K	Cosgarea et al. 1961
		−40.2	−18.8	U_s[a], Bi_s	vap. press. 1018–1115 K
	U_3Bi_4	−55.8	−33.6	U_s[a], Bi_l; 1018–1115 K	
		−50.9	−24.7	U_s[a], Bi_s	
	UBi	−50.6	−29.9	U_s[a], Bi_l; 1018–1115 K	
		−44.9	−19.5	U_s[a], Bi_s	
	UBi_2	−36.7	−13.9	α-U, Bi_s; 298 K	Rand and Kubaschewski 1963
	U_3Bi_4	−54.9	−13.0	(same)	assessment
	UBi	−59.2	−21.8	(same)	
	UBi_2	−47.9	−20.5	γ-U, Bi_l;1018–1115 K	Rice et al. 1962
		−37.9	−4.2	α-U, Bi_s	vap. press. optical absorption
	U_3Bi_4	−54.3	−21.3	γ-U, Bi_l;1018–1115 K	1018–1115 K
		−44.6	−6.2	α-U, Bi_s	
	UBi	−51.6	−18.4	γ-U, Bi_l;1018–1115 K	
		−42.2	−4.3	α-U, Bi_s	
	UBi_2	−45.8	−15.1	γ-U, Bi_l; 773–1023 K	Lebedev et al. 1968a,b
		−35.7	1.2	α-U, Bi_s	emf liq electrolyte 773–1103 K
	U_3Bi_4	−52.4	−15.5	γ-U, Bi_l; 973–1093 K	
		−42.7	−0.4	α-U, Bi_s	
	UBi	−50.6	−14.3	γ-U, Bi_l; 973–1103 K	
		−41.2	−0.2	α-U, Bi_s	

continued on next page

Table 51, *continued*

System	Compound	$\Delta_f H^\circ$	$\Delta_f S^\circ$	Reference state	Authors and method
U–Bi	UBi_2	−41.0	−10.6	γ-U, Bi_l	Tien et al. 1962
(*cont'd*)		−33.5	3.2	γ-U, Bi_s	emf liq electrolyte in dilute solution, solubility data 673–873 K
	UBi_2	−36.8	−1.51	α-U, Bi_s; 298 K	Chiotti et al. 1981
	U_3Bi_4	−43.6	−3.3	(same)	assessment using values of Rice et al. (1962) and Lebedev et al. (1968a,b)
	UBi	−41.6	−2.2	(same)	
Pu–Bi	$PuBi_2$	−69.6	−17.7	δ-Pu, Bi_l; $T < 507$ K	Lebedev et al. 1969
		−74.6	−24.3	ε-Pu, Bi_l; $T > 507$ K	emf liq electrolyte 693–833 K (mean value)
		−62.5	−3.2	α-Pu, Bi_s	
	$PuBi_2$	−72.2	−21.5	ε-Pu, Bi_l	Chiotti et al. 1981
		−60.2	−0.4	α-Pu, Bi_s	from sol. data and values in dilute solutions

[a] Aggregation state not specified. [b] Using the Third Law.

Table 52

Enthalpies and entropies of formation of intermetallic compounds of As with rare earths and actinides ($\Delta_f H^\circ$: kJ/mol of atoms, $\Delta_f S^\circ$: $J K^{-1}$/mol of atoms)

System	Compound	$\Delta_f H^\circ$	$\Delta_f S^\circ$	Reference state	Authors and method
R–As	ScAs	−136		Sc_s, As_s; 698–728 K	Hanks and Faktor 1967
	YAs	−162		Y_s, As_s; 648–678 K	dyn. diff. calorim. 573–850 K
	LaAs	−153		La_s, As_s; 583–638 K	
	CeAs	−144		Ce_s, As_s; 603–608 K	
	PrAs	−154		Pr_s, As_s; 603–623 K	
	NdAs	−152		Nd_s, As_s; 618–658 K	
	SmAs	−151		Sm_s, As_s; 608–648 K	
	GdAs	−156		Gd_s, As_s; 638–728 K	
	TbAs	−157		Tb_s, As_s; 653–743 K	
	DyAs	−163		Dy_s, As_s; 668–848 K	
	HoAs	−151		Ho_s, As_s; 578–688 K	
	ErAs	−158		Er_s, As_s; 678–718 K	
	TmAs	−152		Tm_s, As; 628–703 K	
	YbAs	−129		Yb_s, As; 568–578 K	
	LuAs	−158		Lu_s, As; 693–723 K	
	SmAs	−156		unknown	Hayman, quoted by Hanks and Faktor 1967
U–As	UAs_2	−84		α-U, As_s; 298 K	Baskin and Smith 1970
	U_3As_4	−103		(same)	react. calorim.
	UAs	−117		(same)	

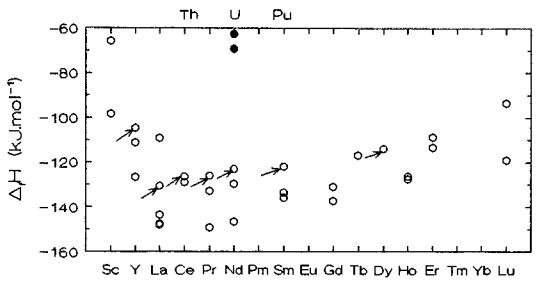

Fig. 130. Enthalpies of formation of rare earth and actinide (R, An)Sb compounds as a function of the atomic number. The references of the data are quoted in table 50. The data obtained by a calorimetric method are indicated by an arrow.

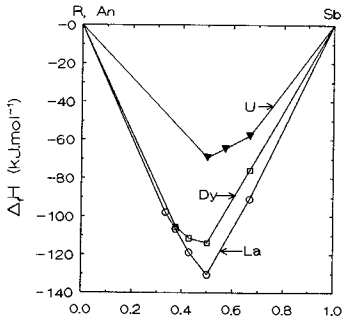

Fig. 131. Enthalpies of formation of $R_{1-x}Sb_x$ and $An_{1-x}Sb_x$ compounds. The data for R:La (open circles), Dy (open squares) and An = U (solid inverted triangles) are taken from Borzone et al. (1979), Borzone et al. (1985), Ferro et al. (1988), and Baskin and Smith (1970), respectively.

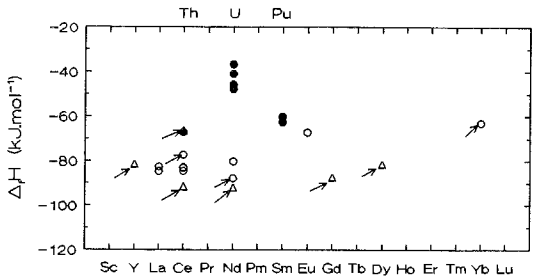

Fig. 132. Enthalpies of formation of rare earth (open symbols) and actinide (solid symbols) (R, An)Bi_2 (open circle; solid circles) compounds and $(R, An)_5Bi_3$ (open triangle; solid triangles) compounds as a function of atomic number. The references of the data are quoted in table 51. The values obtained by a calorimetric method are indicated by an arrow.

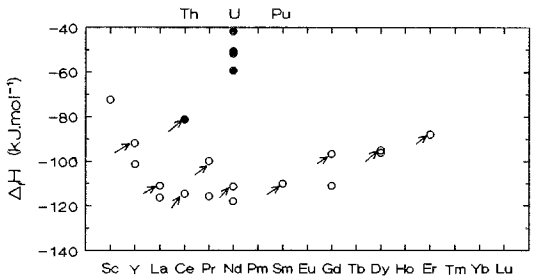

Fig. 133. Enthalpies of formation of rare earth (open circles) and actinide (solid circles) (R, An)Bi compounds as a function of atomic number. The references of the data are quoted in table 52. The values obtained by a calorimetric method are indicated by an arrow.

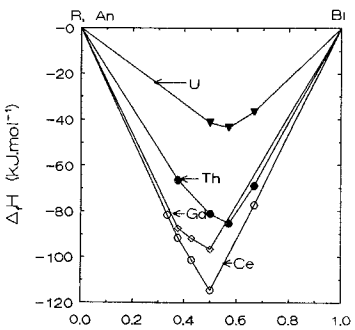

Fig. 134. Enthalpies of formation of $R_{1-x}Bi_x$ and $An_{1-x}Bi_x$ compounds. The data R:Ce (open circles), Gd (open diamonds) and An=Th (solid circles), U (solid inverted triangles) are taken from Borzone et al. (1978), Borzone et al. (1980), Borzone et al. (1982a) and Chiotti et al. (1981), respectively.

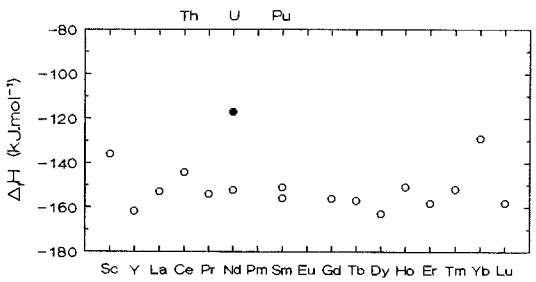

Fig. 135. Enthalpies of formation of rare earths and actinide RAs (open circles) and AnAs (solid circles) compounds as a function of atomic number. The references of data are quoted in table 52.

10. Special topics

Rare-earth-based alloys display interesting properties which have been presented in some review papers, for example Gschneidner (1984) and Buschow (1984). The magnetic properties of many rare-earth-based alloys have been extensively studied, such as in the reports published by Buschow (1977, 1979, 1991) concerning the intermetallic compounds of rare-earth and 3d-transition metals, the intermetallic compounds of rare-earth and nonmagnetic metals and the new developments in hard magnetic materials. Recent reviews on the magnetic properties of rare-earth-based alloys may also be mentioned, for example those of Givord and Nozières (1990), Allibert (1990) and Kirchmayr (1992). Other properties of rare-earth-based alloys are worth noting:

(i) The glass-forming ability when rare-earth elements are alloyed with transition metals and also with non-transition elements such as aluminum.

(ii) the ability of rare earth–3d-metal compounds to absorb large amounts of hydrogen gas (Buschow et al. 1982).

The major interest of the actinide-based alloys is due to applications in the nuclear industry; for example, the interest in metallic fuels for liquid-metal fast breeder reactors and the interest in high-temperature techniques for the reprocessing of irradiated nuclear fuel have always persisted.

These applications of rare-earth- or actinide-based alloys have evidently led to an increase in the volume of information available concerning the thermodynamic properties: phase diagrams and thermodynamic data. Many of the publications containing this information have been reviewed in the preceding paragraphs. We will here give some information which has not been previously quoted.

Concerning amorphous alloys thermodynamic measurements have been performed on binary rare-earth-based alloys. The enthalpies of formation of Gd–Ni and Y–Ni amorphous alloys have been determined by Colinet et al. (1986, 1987b) using aluminum solution calorimetry. Using the same method Maret and Pasturel (1987) obtained the enthalpies of formation of amorphous $Ni_{0.33}Y_{0.67}$ and $Cu_{0.33}Y_{0.67}$ alloys. Moreover temperature of crystallization and enthalpies of crystallization of many rare-earth-based amorphous phases have been obtained using differential scanning calorimetry. To the best of our knowledge, few investigations have been performed in amorphous alloys containing actinide elements. Let us just mention the existence of metallic glass in the Pd–U–Si system and point out that a metastable quasicrystalline phase may be obtained by devitrification of the metallic glass in a narrow composition range near $Pd_{0.60}U_{0.20}Si_{0.20}$ (Poon et al. 1985, Shen et al. 1986, Antonione et al. 1989).

Concerning the ability of intermetallic compounds to absorb large amounts of hydrogen, many studies have been performed on the compound $LaNi_5$ (structure prototype: $CaCu_5$) but also for ternary compounds possessing the same structure. These ternary compounds are obtained by substitution of nickel atoms by another metallic element with the purpose to determine the hydrogen content and the H_2 equilibrium pressure of the hydride. For this purpose measurements of the enthalpies of formation of $LaNi_5$ and substituted ternary compounds as well as experimental

determinations of enthalpies of hydrogenation have been performed; this includes the work of Pasturel et al. (1982) concerning the $LaNi_4M$ compounds with M = Mn, Cu, Fe, of Diaz et al. (1979) concerning the $LaNi_4Al$ compound, of Hubbard et al. (1983) concerning the $La(Ni_{1-x}Al_x)_5$ compounds, of Pasturel et al. (1984a) concerning the $La(Ni_{1-x}Cu_x)_5$ compounds, and of Colinet et al. (1987a) concerning the $La(Ni_{1-x}Co_x)_5$ compounds.

All of these studies provided an opportunity for obtaining enthalpies of formation of ternary alloys. We mention here other determinations of enthalpies of formation in ternary systems where one constituent is a rare-earth element: Meyer-Liautaud et al. (1985b, 1987b) determined the enthalpies of formation of $Ce(Ni_{1-x}Cu_x)_5$ and of $R(Co_{1-x}Cu_x)_5$ with R = Ce, Y and Sm alloys as a function of x using either aluminum solution calorimetry or tin solution calorimetry. Nagarajan and Sommer (1989) measured the integral enthalpies of mixing of some Ce–Mg–Cu ternary liquid alloys by mixing calorimetry.

Some binary alloys based on actinides also have the ability to absorb hydrogen (see table A4 of Buschow et al. 1982). For example, ternary alloys such as $Th(Ni_{1-x}Al_x)$ with $x \geqslant 1$ have this ability. However no thermodynamic study, such as a measurement of the enthalpy of formation, has been performed on this ternary alloy.

Many ternary phase diagrams based on rare earths or actinides have been partly or completely determined. It would be impossible to cite here all of these systems. Let us just point out the multicomponent systems which are currently studied because they display interesting properties:

– The $Nd_2Fe_{14}B$ system and those obtained by substitution of Nd by another rare-earth element display interesting magnetic properties (Sinnema et al. 1984, Sagawa et al. 1984). This is the reason why several studies of the Fe–Nd binary phase diagram have been performed in the last five years.

– The Y–Ba–Cu–O system is extensively studied because the $YBa_2Cu_3O_7$ phase displays superconducting properties. The complete study of the quaternary system requires knowledge of the limiting binary systems, in particular of the Y–Ba and Y–Cu alloys. Studies are now being performed to obtain thermodynamic data for these alloys.

11. Conclusion

The rare earths (except Eu and Yb) and actinides exhibit strong interactions with many metallic elements, Be and Mg, the late transition elements (columns headed by Mn, Fe, Co and Ni), and with the elements of columns IB to VB. The corresponding phase diagrams exhibit intermetallic compounds. With elements of column IA and column IIA from calcium to barium, comparison of rare earth and actinide thermodynamic behavior is difficult because many phase diagrams are unknown or subject to caution. With early transition metals, rare earths exhibit positive deviations from ideality, characterized in the phase diagram by a miscibility gap in the liquid phase, while actinides are completely miscible in these elements in the liquid state.

Table 53
Evolution of the enthalpies of formation of intermetallic compounds based on rare earth elements

Compound	$\Delta_f H$(Sc → Y → La)[a,d]		$\Delta_f H$(La → Lu)[b,d]			Figure[c]
RMg_2	↑	Y → La				17
RMg[e]		unknown	≈	La → Sm	↑ Gd → Lu	16
RNi_5	↑	Y → La	↓	La → Gd	≈ Gd → Er	53
RPt_5		unknown	≈	La → Tm		54
RCu_2	≈	Sc → La	≈			73
MZn_{12}	↓	Y → La	↑	La → Er		83
M_2Zn_{17}	≈	Y → La	≈	La → Nd		84
MZn_2	↑	Y → La	≈	La → Sm		83
MCd_6		unknown	≈	La → Pr		86
MAl_2	↓	Sc → La	↑	La → Tm		95
MGa_3		unknown	↑	Dy → Lu		98
MIn_3	↓	Sc → La	↑	La → Lu		100
MTl_3	↓	Y → La	↑	La → Lu		101
MSi_2	↓	Y → La	↑	La → Gd		110
M_5Si_3	↑	Sc → Y		unknown		111
MGe_2	↓		↑	Nd → Gd		113
M_5Ge_3	↑		↓	La → Gd		114
MGe	↓		↑	La → Gd		117
MSn_3	↓		↑			118
MPb_3	↓		↑	La → Tm		121
MSb_2		unknown	≈	La → Sm	↑ Sm → Lu	129
M_5Sb_3	↓	Y → La	≈	La → Sm		129
MSb	↓		↑			130
MBi_2		unknown	≈	La → Nd	↑	132
MBi	↓		↑	La → Er		133
M_5Bi_3		unknown	≈	La → Nd	↑ Nd → Dy	132
MAs	↓	Sc → Y,	≈			135
MAs	↑	Y → La				135

[a] Evolution in the column headed by Sc.
[b] Evolution in the lanthanide series.
[c] Number of the corresponding figure.
[d] Symbols: ↑ (↓), $\Delta_f H$ becomes less (more) negative; ≈, no appreciable change.
[e] $\Delta_f G$.

In tables 53 and 54 the evolutions detected in the rare-earth series for the enthalpy of formation (or for the Gibbs energy of formation) and for the partial enthalpy of mixing at infinite dilution have been summarized. As noted previously, we have distinguished the evolution of the thermodynamic data in column IIIA, Sc to La, from the evolution in the lanthanide series La → Lu. Let us point out that the evolution of the enthalpy of formation with atomic number in the lanthanide series is in good agreement with the predictions of Gschneidner (1990a).

Among the rare-earth elements, Eu and Yb exhibit a particular behavior which has been noted considering the phase diagrams, that is, the presence of a miscibility gap

Table 54
Evolution of the partial enthalpy at infinite dilution of rare earths in liquid metallic solvent

Liquid solvent	$\Delta_m \bar{H}^{\infty}_{(R)}$(Sc → La)[a,d]	$\Delta_m \bar{H}^{\infty}_{(R)}$(La → Lu)[b,d]	Figure[c]
Mn	↑	↓	62
Fe	↑	↓	61
Co	↑	↓	60
Ni	↑	↓	59
Cu	≈	↓	75
Al	↓	↑	97
Ge	↓	↑	116
Sn	≈ Y → La	↑	120

[a] Evolution in the column headed by Sc.
[b] Evolution in the lanthanide series.
[d] Number of the corresponding figure.
[d]Symbols: ↑ (↓), $\Delta_f H$ becomes less (more) negative; ≈, no appreciable change.

at the europium- or ytterbium-rich side of the phase diagram when alloyed with some metallic elements, the presence of a miscibility gap in the liquid phase when alloyed with other rare earths and actinides, and, on the contrary, miscibility in the solid and liquid state when alloyed with Ba and Ca. Considering the values of the enthalpies of formation of europium- and ytterbium-based compounds, less negative values are obtained when alloyed with aluminum and platinum than when other rare earths are alloyed with these elements. However, in other cases, where thermodynamic data are available for Eu and Yb based alloys, no difference with the other elements of the rare earth series is observed (Sn, In, Tl, ...).

Eu and Yb at the standard states (298 K, 1 atm) arc divalent. In 1969, Gschneidner (1969) pointed out that in a compound in which these elements are trivalent a promotion energy is needed to change the valence state of Eu and Yb from 2 to 3. Thus the formation energies of the compounds where Eu or Yb take the valence 3 will be less by this amount when compared to those of their neighboring trivalent lanthanides (see also Gschneidner 1984 and Gschneidner 1990b).

Cerium is often considered as a peculiar rare earth element because it may take the valence 4 in some alloys. More often, cerium has behaved similarly to its two neighbors in the lanthanide series La and Pr. Let us just point out the more negative values of the enthalpies of formation of $CeNi_5$ and $CeCo_5$ than respectively for $LaNi_5$ and $PrNi_5$ and for $LaCo_5$ and $PrCo_5$. This behavior is not observed in the $LnPt_5$ series of alloys.

From a thermodynamic point of view the behavior of the thorium-, uranium- and plutonium-based alloys invite us to distinguish two categories of alloys: the alloys with non-transition elements and the alloys with transition elements. The enthalpies of formation of compounds with the same stoichiometry of thorium, uranium and plutonium with a non-transition element are schematically presented in fig. 136: the more negative values are obtained with thorium, the less negative values with uranium (we often observed a miscibility gap in the liquid phase in the uranium rich side of the phase

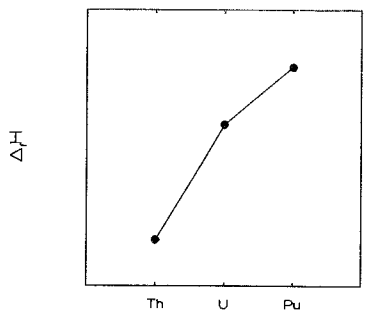

Fig. 136. Schematical trend of the enthalpies of formation of thorium, uranium and plutonium intermetallic compounds with non-transition metals.

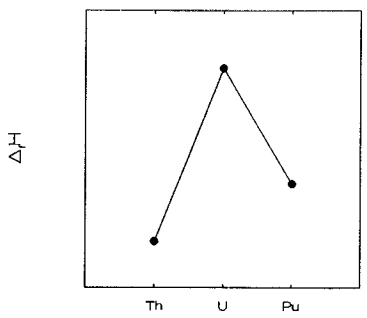

Fig. 137. Schematical trend of the enthalpies of formation of thorium, uranium and plutonium intermetallic compounds with transition metals.

diagram). With plutonium generally slightly less negative values than with thorium are observed. The enthalpies of formation of compounds with the same stoichiometry of thorium, uranium and plutonium with a transition metal are schematically presented in fig. 137. The more negative values are obtained with thorium, the less negative with plutonium. With uranium the values are slightly more negative than with plutonium.

With the purpose of comparing the thermodynamic behavior of rare earths and actinides when alloyed with metallic elements we will again use the same classification as above: alloys with non-transition metals and alloys with transition metals. When alloyed with non-transition metals, the enthalpies of formation of uranium-based alloys are less negative than the enthalpies of formation of rare-earth based alloys. With thorium and plutonium, the order of magnitude is the same as obtained with the rare-earth elements which give the less negative values. When alloyed with transition metals the enthalpies of formation of thorium- and uranium-based alloys are more negative than the enthalpies of formation obtained with rare-earth elements. For plutonium-based alloys the enthalpies of formation are of the same order of magnitude.

Possible valence changes might be found for U and Pu in their compounds since both of these elements exhibit variable valences, but the lack of data prevents one from verifying this. In addition there are other difficulties, such as determining the valence states in the various compounds, although the valence in the pure metallic states seems to be well

established. A third problem exists with Pu, since even in the pure metallic state its various polymorphic forms have different valences.

However, these conclusions derived from values of enthalpies of formation near equiatomic composition may be questionable either at the rare-earth or actinide-rich side or at the side rich in the other component, because the asymmetric shape of the enthalpy of formation versus composition curve may differ considerably within the rare-earth series and from rare earths to actinides.

Updated thermodynamic data

In 1993 and 1994 several experimental determinations of enthalpies of formation of rare-earth based intermetallic compounds have been published. These determinations have been performed using calorimetric methods and they concern systems where the data are very scarce. We briefly outline this information here.

Standard enthalpies of formation of the congruently melting intermetallic compounds have been obtained in the following systems: Pr–(Ni, Pd, Pt, Rh, Ir, Ru) by Qiti Guo and Kleppa (1994); (Pr, Nd)–(Cu, Ag, Au) by Fitzner and Kleppa (1994); Sc–Al by Meschel and Kleppa (1994a); Y–Al by Meschel and Kleppa (1993a); La–Al by Meschel and Kleppa (1993b); (La, Ce, Pr)–Si and (Ce, Pr)–Ge by Meschel and Kleppa (1994b).

Enthalpies of mixing in the liquid alloys (Cu, Ag, Au)–Ce were obtained by Fitzner and Kleppa (1993). Borzone et al. (1994a,b) have studied the Sm–Al and Lu–Pb systems.

Acknowledgment

The authors wish to acknowledge I. Ansara for access to Thermet, D. Albert for reading the manuscript, and J. Cuoq and Y. Potier for preparing the manuscript. The authors are grateful to Professor O.J. Kleppa and Dr. N. Selhaoui, and Professor G. Borzone and Professor R. Ferro for providing us with preprints of their publications and to Dr. I.V. Nikolaenko for giving us results prior to publication.

References

Abdusalyamova, M.N., N.D. Faslyeva, A.A. Eliseev, E.A. Shishkin, O.I. Rakhmatov, A.G. Chuiko and T.P. Shumakova, 1990a, J. Less-Common Met. **166**, 229.

Abdusalyamova, M.N., H.S. Shokirov and O.I. Rakhmatov, 1990b, J. Less-Common Met. **166**, 221.

Akhachinskij, V.V., and L.M. Kopytin, 1960, At. Energ. **9**, 504 [Sov. At. Energy **9**, 1051].

Akhachinskij, V.V., and L.M. Kopytin, 1968, in: Thermodynamics of Nuclear Materials, Proc. Symp., Vienna (IAEA, Vienna) p. 789.

Akhachinskij, V.V., and L.F. Timofeeva, 1980, in: Thermodynamics of Nuclear Materials, Vol. 2 (IAEA, Vienna) p. 161.

Akhachinskij, V.V., L.M. Kopytin, M.I. Ivanov and N.S. Podol'skaya, 1962, in: Thermodynamics of Nuclear Materials, Proc. Symp., Vienna (IAEA, Vienna) p.309.

Alcock, C.B., 1989, J. Nucl. Mater. **167**, 7.

Alcock, C.B., and P. Grieveson, 1961/62, J. Inst. Met. **90**, 304.

Alcock, C.B., J.B. Cornish and P. Grieveson, 1966, in: Thermodynamics, Proc. Symp., Vienna, Vol. 1 (IAEA, Vienna) p. 211.

Allibert, C., 1990, in: Semiconductors and Rare Earth Based Materials, Int. Workshop on Materials Science, Hanoi, Vietnam, October 15–26, eds C.A.J. Ammerlaan, F.F. Bekker, J.J.M. Franse, Nguyen Van Hieu and Than Duc Hien, p. 147.

Amonenko, V.M., A.A. Kruglykl, V.S. Pavlov and G.P. Tikhinskii, 1964, Izv. Akad. Nauk SSSR, Met. **3**, 158 [Russ. Metall. **3**, 97].

Antonione, C., L. Battezzati, F. Marino, R. Marazza and D. Mazzone, 1989, J. Less-Common Met. **154**, 169.

Axler, K.M., and D.E. Peterson, 1989, Bull. Alloy Phase Diagrams **10**, 472.

Axler, K.M., E.M. Foltyn, D.E. Peterson, R.I. Sheldon and W.B. Hutchinson, 1989, J. Nucl. Mater. **161**, 132.

Bacha, A., C. Chatillon-Colinet, A. Percheron and J.C. Mathieu, 1972a, C.R. Acad. Sci., Paris **274C**, 680.

Bacha, A., C. Chatillon-Colinet, A. Percheron and J.C. Mathieu, 1972b, C.R. Acad. Sci., Paris **275C**, 921.

Bacha, A., C. Chatillon-Colinet, A. Percheron and J.C. Mathieu, 1973, C.R. Acad. Sci., Paris **276C**, 995.

Bailey, D.M., and J.F. Smith, 1975, in: Thermodynamics of Nuclear Matererials, Proc. Symp., Vienna, Vol. 2 (IAEA, Vienna) p. 355.

Baren, M.R., 1989, Bull. Alloys Phase Diagrams **10**, 644.

Baren, M.R., 1991, J. Phase Equilibria **12**, 321.

Baskin, Y., and S.D. Smith, 1970, J. Nucl. Mater. **37**, 209.

Batalin, G.I., V.A. Stukalo, N.Ya. Neshchimenko, V.A. Gladkikh and O.I. Lyuborets, 1977, Izv. Akad. Nauk SSSR, Met. **6**, 44 [Russ. Metall. **6**, 35].

Batalin, G.I., V.S. Sudavtsova and M.V. Mikhailovskaya, 1985a, in: Ninth All-Union Conference on Thermodynamic Analysis Abstracts of Reports (Academy of Sciences, Ukrainian SSR, Kiev) p. 137.

Batalin, G.I., V.S. Sudavtsova and N.N. Maryanchik, 1985b, Ukr. Khim. Zh. **51**, 817 [Sov. Prog. Chem. **51**, 35].

Batalin, G.I., V.S. Sudavtsova and N.V. Stroganova, 1985c, Ukr. Khim. Zh. **51**, 775 [Sov. Prog. Chem. **51**].

Batalin, V.G., G.M. Lukashenko and R.I. Polotskaya, 1983, Poroshk. Metall. **11**, 61 [Sov. Powder Metall. Met. Ceram. **22**, 922].

Baxi, H.C., and T.B. Massalski, 1991, J. Phase Equilibria **12**, 598.

Baxi, H.C., T.B. Massalski and H.F. Rizzo, 1991, J. Phase Equilibria **12**, 593.

Bayanov, A.P., 1971, Zh. Fiz. Khim. **45**, 1889 [Russ. J. Phys. Chem. **45**, 1077].

Bayanov, A.P., 1975, Usp. Khim. **44**, 236 [Russ. Chem. Rev. **44**, 122].

Bayanov, A.P., and E.N. Ganchenko, 1975, Zh. Fiz. Khim. **49**, 1355 [Russ. J. Phys. Chem. **49**, 801].

Bayanov, A.P., and V.V. Serebrennikov, 1965, Zh. Fiz. Khim. **39**, 717 [Russ. J. Phys. Chem. **39**, 375].

Bayanov, A.P., Yu.A. Afanasev and N.M. Pogorelaya, 1973, Zh. Fiz. Khim. **47**, 2105 [Russ. J. Phys. Chem. **47**, 1186].

Bayanov, A.P., E.N. Ganchenko and N.G. Kulagina, 1974, Zh. Fiz. Khim. **48**, 2120 [Russ. J. Phys. Chem. **48**, 1258].

Bayanov, A.P., Yu.A. Frolov and Yu.A. Afanasev, 1975a, Zh. Fiz. Khim. **49**, 2605 [Russ. J. Phys. Chem. **49**, 1527].

Bayanov, A.P., E.N. Ganchenko, Yu.A. Afanasaev, T.A. Parkhomenko and N.A. Soboleva, 1975b, Zh. Fiz. Khim. **49**, 202 [Russ. J. Phys. Chem. **49**, 112].

Bayanov, A.P., N.A. Soboleva and E.N. Ganchenko, 1975c, Izv. Akad. Nauk SSSR, Met. **1**, 198 [Russ. Metall. **1**, 167].

Bayanov, A.P., E.N. Ganchenko and Yu.A. Afanasev, 1977a, Zh. Fiz. Khim. **51**, 2381 [Russ. J. Phys. Chem. **51**, 1397].

Bayanov, A.P., E.N. Ganchenko and Yu.A. Afanasev, 1977b, Zh. Fiz. Khim. **51**, 216 [Russ. J. Phys. Chem. **51**, 122].

Biltz, W., and F. Meyer, 1928, Z. Anorg. Allg. Chem. **261**, 23.

Biltz, W., and H. Pieper, 1924, Z. Anorg. Chem. **134**, 13.

Bolmgren, H., and T. Lundstrom, 1990, J. Less-Common Met. **163**, 79.

Borsese, A., R. Capelli, S. Delfino and R. Ferro, 1974a, Thermochim. Acta **8**, 393.

Borsese, A., R. Capelli, S. Delfino and R. Ferro, 1974b, Thermochim. Acta **9**, 313.

Borsese, A., R. Ferro, R. Capelli and S. Delfino, 1975a, J. Less-Common Met. **42**, 179.

Borsese, A., R. Ferro, R. Capelli and S. Delfino, 1975b, Thermochim. Acta **11**, 205.

Borsese, A., A. Calabretta, S. Delfino and R. Ferro, 1977a, J. Less-Common Met. **51**, 45.

Borsese, A., G. Borzone, R. Ferro and S. Delfino, 1977b, J. Less-Common Met. **55**, 115.

Borsese, A., G. Borzone, A. Saccone and R. Ferro, 1977c, J. Less-Common Met. **52**, 123.
Borsese, A., R. Ferro, R. Capelli and S. Delfino, 1977d, J. Less-Common Met. **55**, 77.
Borsese, A., G. Borzone and R. Ferro, 1980, J. Less-Common Met. **70**, 213.
Borsese, A., G. Borzone, D. Mazzone and R. Ferro, 1981, J. Less-Common Met. **79**, 57.
Borzone, G., A. Borsese, A. Calabretta and R. Ferro, 1978, J. Less-Common Met. **58**, 31.
Borzone, G., A. Borsese, A. Saccone and R. Ferro, 1979, J. Less-Common Met. **65**, 253.
Borzone, G., A. Borsese and R. Ferro, 1980, Thermochim. Acta **41**, 175.
Borzone, G., A. Borsese and R. Ferro, 1982a, J. Less-Common Met. **85**, 195.
Borzone, G., A. Borsese and R. Ferro, 1982b, J. Less-Common Met. **84**, 165.
Borzone, G., A. Borsese, G. Zanicchi and R. Ferro, 1982c, J. Therm. Anal. **25**, 433.
Borzone, G., A. Borsese and R. Ferro, 1983, Z. Anorg. Allg. Chem. **501**, 109.
Borzone, G., A. Borsese, S. Delfino and R. Ferro, 1985, Z. Metallk. **76**, 208.
Borzone, G., G. Cacciamani, R. Ferro, J. Charles and J. Hertz, 1987, J. Less-Common Met. **128**, 297.
Borzone, G., G. Cacciamani and R. Ferro, 1990, CALPHAD **14**, 139.
Borzone, G., G. Cacciamani and R. Ferro, 1991, Metall. Trans. **22A**, 2119.
Borzone, G., A.M. Cardinale, G. Cacciamani and R. Ferro, 1993a, Z. Metallk. **84**, 635.
Borzone, G., N. Parodi and R. Ferro, 1993b, J. Phase Equilibria **14**, 485.
Borzone, G., A.M. Cardinale, A. Saccone and R. Ferro, 1994a, J. Alloys & Compounds, in press.
Borzone, G., N. Parodi, N. Ferro, M. Gambino, V. Vassiliev and J.P. Bros, 1994b, J. Alloys & Compounds, in press.
Bretschneider, T., and H.J. Schaller, 1990a, Z. Metallk. **81**, 84.
Bretschneider, T., and H.J. Schaller, 1990b, Ber. Bunsenges. Phys. Chem. **94**, 185.
Buschow, K.H.J., 1977, Rep. Prog. Phys. **40**, 1179.
Buschow, K.H.J., 1979, Rep. Prog. Phys. **42**, 1477.
Buschow, K.H.J., 1984, J. Less-Common Met. **100**, 29.
Buschow, K.H.J., 1991, Rep. Prog. Phys. **54**, 1123.
Buschow, K.H.J., P.C.P. Bouten and A.R. Miedema, 1982, Rep. Prog. Phys. **45**, 937.
Bushmanov, V.D., E.G. Fedorova and S.P. Yatsenko, 1987, Zh. Fiz. Khim. **61**, 1797 [Russ. J. Phys. Chem. **61**, 936].
Butorov, V.P., I.F. Nichkov, E.A. Novikov and S.P. Raspopin, 1973, Izv. Vyssh. Uchebn. Zaved. Tsvetn. Metall. **3**, 96 [Sov. Non-Ferrous Met. Res. **1**, 145].
Buyanov, Yu.I., G.M. Lukashenko and R.I. Polotskaya, 1981, Dokl. Akad. Nauk. Ukr. SSR **11**, 84.
Buyanov, Yu.I., G.M. Lukashenko and R.I. Polotskaya, 1988, Poroshk. Met. **9**, 76 [Sov. Powder Metall. Met. Ceram. **27**, 744].
Cabral, F.A.O., and S. Gama, 1989, J. Mater. Eng. **11**, 83.
Cabral, F.A.O., and S. Gama, 1990, J. Less-Common Met. **167**, 31.
Campbell, G.M., 1974, J. Chem. Thermodyn. **6**, 1110.
Campbell, G.M., 1976, in: Plutonium and Other Actinides, eds H. Blanck and R. Lindner (North-Holland, Amsterdam) p. 95.
Campbell, G.M., 1977, Metall. Trans. **8A**, 1493.
Campbell, G.M., L.J. Mullins and J.A. Leary, 1967, in: Thermodynamics of Nuclear Materials, Proc. Symp., Vienna (IAEA, Vienna) p. 75.
Canneri, G., and A. Rossi, 1932, Gazz. Chim. Ital. **62**, 202.
Canneri, G., and A. Rossi, 1933, Gazz. Chim. Ital. **63**, 182.
Castanet, R., 1984, C.R. Acad. Sci. Ser. B **298**, 5.
Castanet, R., 1989, in: Thermochemistry of Alloys. Recent Developments in Experimental Methods, Nato ASI series C, eds H. Brodowsky and H.J. Schaller (Kluwer Academic Publishers, Dordrecht) p. 145.
Chakrabarti, D.J., D.E. Laughlin and D.E. Peterson, 1986, Bull. Alloy Phase Diagrams **7**, 36.
Chan, K.S., J.K. Lee and H.I. Aaronson, 1980, J. Nucl. Mater. **92**, 237.
Chandrasekharaiah, M.S., S.R. Dharwadkar and D. Darsarathi, 1986, Z. Metallk. **77**, 509.
Chart, T.G., and N.J. Pugh, 1990, Report DMM(A), UK 16 (National Physics Laboratory).
Chatillon-Colinet, C., A. Perchcron, J.C. Mathieu and J.C. Achard, 1970, C. R. Acad. Sci. ser. C **270**, 473.
Chatillon-Colinet, C., H. Diaz, J.C. Mathieu, A. Percheron-Guegan and J.C. Achard, 1979, Ann. Chim. (Paris) **4**, 657.
Chiotti, P., 1972, Metall. Trans. **3**, 2911.
Chiotti, P., 1974, J. Nucl. Mater. **51**, 178.

Chiotti, P., and C.H. Dock, 1975, J. Less-Common Metals **41**, 225.
Chiotti, P., and K.J. Gill, 1961, Trans. Metall. Soc. AIME **221**, 573.
Chiotti, P., and J.A. Kateley, 1967, Q. Res. Rep. Ames Lab, Ames, IA.
Chiotti, P., and J.A. Kateley, 1969, J. Nucl. Mater. **32**, 135.
Chiotti, P., and G.R. Kilp, 1960, Trans. Metall. Soc. AIME **218**, 41.
Chiotti, P., and M. Koizumi, 1960, Report IS-193 (Ames Laboratory, Ames, IA) p. 32.
Chiotti, P., and J.T. Mason, 1965, Trans. Metall. Soc. AIME **233**, 786.
Chiotti, P., and J.T. Mason, 1967, Trans. Metall. Soc. AIME **239**, 547.
Chiotti, P., and J.T. Mason, 1971, Metall. Trans. **2**, 967.
Chiotti, P., and J.T. Mason, 1973, Metall. Trans. **4**, 1527.
Chiotti, P., and J.T. Mason, 1975, J. Less-Common Met. **40**, 39.
Chiotti, P., J.T. Mason and K.J. Gill, 1963, Trans. Metall. Soc. AIME **227**, 910.
Chiotti, P., W.C. Robinson and M. Kanno, 1966, J. Less-Common Met. **10**, 273.
Chiotti, P., J.T. Mason and T.S. Lee, 1979, J. Less-Common Met. **66**, 41.
Chiotti, P., V.V. Akhachinskij, I. Ansara and M.H. Rand, 1981, in: The Chemical Thermodynamics of Actinide Elements and Compounds, Part 5: The Actinide Binary Alloys (IAEA, Vienna).
Chiotti, P., V.V. Akhachinskij, I. Ansara and M.H. Rand, 1982a, Bull. Alloy Phase Diagrams **3**, 98.
Chiotti, P., V.V. Akhachinskij, I. Ansara and M.H. Rand, 1982b, Bull. Alloy Phase Diagrams **3**, 100.
Chiotti, P., V.V. Akhachinskij, I. Ansara and M.H. Rand, 1982c, Bull. Alloy Phase Diagrams **3**, 101.
Chiotti, P., V.V. Akhachinskij, I. Ansara and M.H. Rand, 1982d, Bull. Alloy Phase Diagrams **3**, 104.
Chiotti, P., V.V. Akhachinskij, I. Ansara and M.H. Rand, 1982e, Bull. Alloy Phase Diagrams **3**, 102.
Chiotti, P., V.V. Akhachinskij, I. Ansara and M.H. Rand, 1982f, Bull. Alloy Phase Diagrams, **2**, 484.
Chiotti, P., V.V. Akhachinskij, I. Ansara and M.H. Rand, 1982g, Bull. Alloy Phase Diagrams **3**, 96.
Chua, K.S., and J.N. Pratt, 1974, Thermochim. Acta **8**, 409.
Cirafici, S., and M.L. Fornasini, 1990, J. Less-Common Met. **163**, 331.
Cirafici, S., and A. Palenzona, 1987, J. Less-Common Met. **135**, 1.
Cirafici, S., and A. Palenzona, 1990, Thermochim. Acta **162**, 117.
Colinet, C., and A. Pasturel, 1983, Phys. Status Solidi a **80**, K75.
Colinet, C., and A. Pasturel, 1987, CALPHAD **11**, 323.
Colinet, C., A. Pasturel, A. Percheron-Guégan and J.C. Achard, 1984a, J. Less-Common Met. **102**, 167.
Colinet, C., A. Pasturel, A. Percheron-Guégan and J.C. Achard, 1984b, J. Less-Common Met. **102**, 239.
Colinet, C., A. Pasturel and K.H.J. Buschow, 1985, J. Chem. Thermodyn. **17**, 1133.
Colinet, C., A. Pasturel and K.H.J. Buschow, 1986, Metall. Trans. **17A**, 777.
Colinet, C., A. Pasturel, A. Percheron-Guegan and J.C. Achard, 1987a, J. Less-Common Met. **134**, 109.
Colinet, C., A. Pasturel and K.H.J. Buschow, 1987b, J. Appl. Phys. **62**, 3712.
Colinet, C., A. Pasturel and K.H.J. Buschow, 1987c, Metall. Trans. **18A**, 903.
Colinet, C., A. Pasturel and K.H.J. Buschow, 1988a, Physica B **150**, 397.
Colinet, C., A. Bessoud, A. Pasturel and W. Muller, 1988b, J. Less-Common Met. **143**, 265.
Cosgarea, A., E.E. Hucke and D.V. Ragone, 1961, Acta Metall. **9**, 225.
Dahlke, O., W. Gans, O. Knacke and F. Müller, 1969, Z. Metallk. **60**, 465.
Dannöhl, H.D., and H.L. Lukas, 1974, Z. Metallk. **65**, 642.
de Boer, F.R., R. Boom, W.C.M. Mattens, A.R. Miedema and A.K. Niessen, 1988, in: Cohesion in Metals, Vol. 1, Transition Metal Alloys, eds F.R. de Boer and D.G. Pettifor (North-Holland, Amsterdam) p. 103.
Degtyar, V.A., A.P. Bayanov, L.A. Vnuchkova and V.V. Serebrennikov, 1971a, Zh. Fiz. Khim. **45**, 1816 [Russ. J. Phys. Chem. **45**, 1032].
Degtyar, V.A., A.P. Bayanov, L.A. Vnuchkova and V.V. Serebrennikov, 1971b, Izv. Akad. Nauk SSSR, Met. **4**, 149 [Russ. Metall. **4**, 103].
Degtyar, V.A., L.A. Vnuchkova, A.P. Bayanov and V.V. Serebrennikov, 1971c, Zh. Fiz. Khim. **45**, 1594 [Russ. J. Phys. Chem. **45**, 906].
Delfino, S., A. Saccone, G. Borzone and R. Ferro, 1983, Z. Anorg. Allg. Chem. **503**, 184.
Delfino, S., A. Saccone and R. Ferro, 1984, J. Less-Common Met. **102**, 289.

Delfino, S., A. Saccone, G. Cacciamani and R. Ferro, 1987, Z. Metallk. **78**, 344.

Demykina, T.K., V.T. Fryanova, V.A. Degtyar and V.V. Serebrennikov, 1980, Izv. Akad. Nauk SSSR, Met. **4**, 58 [Russ. Metall. **4**, 52].

Deodhar, S.S., and P.J. Ficalora, 1975, Metall. Trans. **6A**, 1909.

Diaz, H., A. Percheron-Guégan, J.C. Achard, C. Chatillon-Colinet and J.C. Mathieu, 1979, Int. J. Hydrogen Energy **4**, 445.

Dmitrieva, V.N., T.N. Rezukhina, L.M. Varekha, V.D. Vorob'ev, V.F. Domashev, B.A. Gusynin, L.I. Kravchenko and V.A. Mel'nikova, 1973, Metallofizika **49**, 109.

Dubinin, V.A., V.I. Kober and A.R. Pechnikov, 1984, Izv. Vyssh. Uchebn. Zaved. Tsvetn. Metall. **4**, 123 [Sov. Non-Ferrous Met. Res. **12**, 331].

Dubinin, V.A., V.I. Kober, V.I. Kochkin and I.F. Nichkov, 1985a, Zh. Fiz. Khim **59**, 1258 [Russ. J. Phys. Chem. **59**, 735].

Dubinin, V.A., V.I. Kober, V.I. Kochkin and I.F. Nichkov, 1985b, Zh. Fiz. Khim. **49**, 1041 [Russ. J. Phys. Chem. **49**, 610].

Dubinin, V.A., V.I. Kober, V.I. Kochkin and S.P. Raspopin, 1985c, Zh. Fiz. Khim. **59**, 1260 [Russ. J. Phys. Chem. **59**, 735].

Dwight, A.E., 1969, in: Developments in the Structural Chemistry of Alloy Phases, ed. B.G. Giessen (Plenum Press, New York) p. 181.

Dzkuraev, T.D., 1989, Dokl. Akad. Nauk Tadzh. SSR **32**, 754.

Edwards, J.G., J.S. Starynski and J.E. Peterson, 1980, J. Chem. Phys. **73**, 908.

Efremov, V.V., V.I. Kober, V.A. Lebedev, I.F. Nichkov, S.P. Raspopin and L.F. Yamshchikov, 1975, Izv. Vyssh. Uchebn. Zaved. Tsvetn. Metall. **3**, 142 [Sov. Non-Ferrous Met. Res. **3**, 124].

Eremenko, V.N., M.V. Bulanova and P.S. Martsenyuk, 1990, in: Fazovye Ravnovesiyia, Strukt, Svoistva Splavov, p. 70.

Esin, Yu.O., M.G. Valishev, P.V. Geld and L.M. Tushkova, 1976, Izv. Akad. Nauk SSSR, Met. **1**, 19 [Russ. Metall. **1**, 19].

Esin, Yu.O., G.M. Ryss and P.V. Geld, 1979, Zh. Fiz. Khim. **53**, 2380 [Russ. J. Phys. Chem. **53**, 1360].

Esin, Yu.O., S.P. Kolesnikov, V.M. Baev, M.S. Petrushevskii and P.V. Geld, 1980, Zh. Fiz. Khim. **54**, 485 [Russ. J. Phys. Chem. **54**, 279].

Esin, Yu.O., A.F. Ermakov, M.G. Valishev, G.M. Ryss, P.V. Geld and E.S. Levin, 1981a, Zh. Fiz. Khim. **55**, 2168 [Russ. J. Phys. Chem. **55**, 1234].

Esin, Yu.O., S.P. Kolesnikov, V.M. Baev, M.S. Petrushevskii and P.V. Geld, 1981b, Zh. Fiz. Khim. **55**, 1587 [Russ. J. Phys. Chem. **55**, 893].

Esin, Yu.O., M.G. Valishev, A.F. Ermakov, S.E. Demin and P.V. Geld, 1984, Teplofiz. Vys. Temp. **22**, 1214 [High Temp. **22**].

Esin, Yu.O., S.E. Demin and V.V. Litovskii, 1985a, Zh. Fiz. Khim. **59**, 223 [Russ. J. Phys. Chem. **59**, 131].

Esin, Yu.O., A.F. Ermakov, S.P. Kolesnikov and P.V. Geld, 1985b, Zh. Fiz. Khim. **59**, 481 [Russ. J. Phys. Chem. **59**, 277].

Faudot, F., M. Harmelin and J. Bigot, 1989a, Scripta Metall. **23**, 795.

Faudot, F., M. Harmelin, J. Bigot, S. Argouin and P. Gouerou, 1989b, Thermochim. Acta **147**, 205.

Fedorov, G.B., and E.A. Smirnov, 1966, At. Energ. **21**, 189 [Sov. At. Energy **21**, 837].

Ferro, R., A. Borsese, R. Capelli and S. Delfino, 1974, Thermochim. Acta **8**, 387.

Ferro, R., A. Borsese, R. Capelli and S. Delfino, 1975, Z. Anorg. Allg. Chem. **413**, 279.

Ferro, R., G. Borzone and G. Cacciamani, 1988, Thermochim. Acta, **129**, 99.

Fitzner, K., and O.J. Kleppa, 1993, Metall. Trans. A **24**, 1827.

Fitzner, K., and O.J. Kleppa, 1994, Metall. Trans. A **25**, 1495.

Fitzner, K., W.G. Jung and O.J. Kleppa, 1991, Metall. Trans. **22A**, 1103.

Foltyn, E.M., and D.E. Peterson, 1988, Bull. Alloy Phase Diagrams **9**, 267.

Forsberg, H.C., 1960, Thermodynamic Properties of Uranium Mercurides, Rep. ORNL-2885 (Oak Ridge National Laboratory, Oak Ridge, TN).

Fryanova, T.V., T.K. Demykina, V.A. Degtyar, S.P. Vdovkina and V.V. Serebrennikov, 1978, Zh. Fiz. Khim. **52**, 504 [Russ. J. Phys. Chem. **52**, 291].

Gachon, J.C., J. Charles and J.H. Hertz, 1985, CALPHAD **9**, 29.

Gama, S., and F.A.O. Cabral, 1988, J. Mater. Sci. Lett. **7**, 405.

Gans, W., F. Muller, O. Knacke and H. Witte, 1966, Z. Metallk. **57**, 46.

Gardie, P., J.J. Poupeau, G. Bordier and J. Le Ny, 1991, JCAT **22**, 69.

Garg, S.P., M. Venkatraman and N. Krishnamurthy, 1990, J. Alloy Phase Diagrams **6**, 111.

Gerasimov, Ya.I., V.I. Goryacheva and V.P. Vasilev, 1979, Dokl. Akad. Nauk SSSR **247**, 135.

Gibson, J.K., and P. Wengert, 1984, High Temp. Sci. **17**, 371.

Givord, D., and J.P. Nozières, 1990, in: Semiconductors and Rare Earth Based Materials, Int. Workshop on Materials Science, Hanoi, Vietnam, October 12–26, eds C.A.J. Ammerlaan, F.F. Bekker, J.J.M. Franse, Nguyen Van Hieu and Than Duc Hien, p. 147.

Gokhale, A.B., and G.J. Abbaschian, 1986a, Bull. Alloy Phase Diagrams **7**, 333.

Gokhale, A.B., and G.J. Abbaschian, 1986b, Bull. Alloy Phase Diagrams **7**, 485.

Gokhale, A.B., and G.J. Abbaschian, 1986c, Bull. Alloy Phase Diagrams **7**, 540.

Gokhale, A.B., and G.J. Abbaschian, 1988a, Bull. Alloy Phase Diagrams **9**, 64.

Gokhale, A.B., and G.J. Abbaschian, 1988b, Bull. Alloy Phase Diagrams **9**, 574.

Gokhale, A.B., and G.J. Abbaschian, 1988c, Bull. Alloy Phase Diagrams **9**, 582.

Gokhale, A.B., and G.J. Abbaschian, 1989a, Bull. Alloy Phase Diagrams **10**, 385.

Gokhale, A.B., and G.J. Abbaschian, 1989b, Bull. Alloy Phase Diagrams **10**, 142.

Gokhale, A.B., and G.J. Abbaschian, 1989c, Bull. Alloy Phase Diagrams **10**, 153.

Gokhale, A.B., and G.J. Abbaschian, 1989d, Bull. Alloy Phase Diagrams **10**, 147.

Gokhale, A.B., and G.J. Abbaschian, 1991, J. Phase Equilibria **12**, 490.

Gokhale, A.B., A. Munitz and G.J. Abbaschian, 1989a, Bull. Alloy Phase Diagrams **10**, 246.

Gokhale, A.B., A. Munitz and G.J. Abbaschian, 1989b, Bull. Alloy Phase Diagrams **10**, 241.

Golutvin, Yu.M., E.G. Maslennikova and L.G. Titov, 1984, Izv. Akad. Nauk SSSR, Met. **6**, 47 [Russ. Metall. **6**, 45].

Goryacheva, V.I., Ya.I. Gerasimov and A.V. Nikol'skaya, 1971a, Dokl. Akad. Nauk SSSR **197**, 389.

Goryacheva, V.I., A.V. Nikol'skaya and Ya.I. Gerasimov, 1971b, Dokl. Akad. Nauk SSSR **199**, 380.

Goryacheva, V.I., A.V. Nikol'skaya and Ya.I. Gerasimov, 1971c, Dokl. Akad. Nauk SSSR **199**, 632.

Goryacheva, V.I., N. Messauden, A.V. Nikolskaya and Ya.I. Gerasimova, 1977, Vestn. Mosk. Univ. Khim. **18**, 749.

Goryacheva, V.I., Ya.I. Gerasimov and V.P. Vasilev, 1981, Zh. Fiz. Khim **55**, 1080 [Russ. J. Phys. Chem. **55**, 610].

Gross, P., D.L. Levi and R.H. Lewin, 1958, Angew. Chem. **70**, 473.

Gross, P., C. Hayman and H. Clayton, 1962, in: Thermodynamics of Nuclear Materials, Proc. Symp., Vienna (IAEA, Vienna) p. 653.

Gschneidner Jr, K.A., 1961, Rare Earth Alloys (Van Nostrand, Princeton, NJ).

Gschneidner Jr, K.A., 1969, J. Less-Common Met. **17**, 13.

Gschneidner Jr, K.A., 1984, J. Less-Common Met. **100**, 1.

Gschneidner Jr, K.A., 1985, J. Less-Common Met. **114**, 29.

Gschneidner Jr, K.A., 1990a, Met. Mater. & Processes **1**, 241.

Gschneidner Jr, K.A., 1990b, Bull. Alloy Phase Diagrams **11**, 216.

Gschneidner Jr, K.A., and F.W. Calderwood, 1982a, Bull. Alloy Phase Diagrams **3**, 85.

Gschneidner Jr, K.A., and F.W. Calderwood, 1982b, Bull. Alloy Phase Diagrams **3**, 183.

Gschneidner Jr, K.A., and F.W. Calderwood, 1982c, Bull. Alloy Phase Diagrams **3**, 348–358.

Gschneidner Jr, K.A., and F.W. Calderwood, 1983a, Bull. Alloy Phase Diagrams **4**, 74–81.

Gschneidner Jr, K.A., and F.W. Calderwood, 1983b, Bull. Alloy Phase Diagrams **4**, 160–178.

Gschneidner Jr, K.A., and F.W. Calderwood, 1983c, Bull. Alloy Phase Diagrams **4**, 290–306.

Gschneidner Jr, K.A., and F.W. Calderwood, 1983d, Bull. Alloy Phase Diagrams **4**, 370–379.

Gschneidner Jr, K.A., and F.W. Calderwood, 1985a, Bull. Alloy Phase Diagrams **6**, 12–26.

Gschneidner Jr, K.A., and F.W. Calderwood, 1985b, Bull. Alloy Phase Diagrams **6**, 131–148.

Gschneidner Jr, K.A., and F.W. Calderwood, 1985c, Bull. Alloy Phase Diagrams, **6**, 434–443.

Gschneidner Jr, K.A., and F.W. Calderwood, 1986a, in: Handbook on the Physics and Chemistry of Rare Earths, Vol. 8, eds K.A. Gschneidner Jr and L. Eyring (North-Holland, Amsterdam) p. 1.

Gschneidner Jr, K.A., and F.W. Calderwood, 1986b, Bull. Alloy Phase Diagrams **7**, 274–354.

Gschneidner Jr, K.A., and F.W. Calderwood, 1987, Bull. Alloy Phase Diagrams **8**, 510–522.

Gschneidner Jr, K.A., and F.W. Calderwood, 1988a, Bull. Alloy Phase Diagrams **9**, 218–225.

Gschneidner Jr, K.A., and F.W. Calderwood, 1988b, Bull. Alloy Phase Diagrams **9**, 16–35.

Gschneidner Jr, K.A., and F.W. Calderwood, 1988c, Bull. Alloy Phase Diagrams **9**, 128–143.

Gschneidner Jr, K.A., and F.W. Calderwood, 1988d, Bull. Alloy Phase Diagrams **9**, 658–691.

Gschneidner Jr, K.A., and F.W. Calderwood, 1989a, Bull. Alloy Phase Diagrams **10**, 28–49.

Gschneidner Jr, K.A., and F.W. Calderwood, 1989b, Bull. Alloy Phase Diagrams **10**, 419–459.

Gschneidner Jr, K.A., and A.H. Daane, 1988, in: Handbook on the Physics and Chemistry of Rare Earths, Vol. 11, eds K.A. Gschneidner Jr and L. Eyring (North-Holland, Amsterdam).

Hanks, R., and M.M. Faktor, 1967, Trans. Faraday Soc. **63**, 1130.

Harris, I.R., and J.D. Speight, 1985, J. Less-Common Met. **114**, 183.

Hellwig, L., 1978, Report KFK 2687 (Kernforschungszentrum Karlsruhe).

Herbst, J., J. Croat, F.E. Pinkerton and W. Yellon, 1984, Phys. Rev. **B29**, 4176.

Hertz, J., 1989, in: Thermochemistry of Alloys. Recent Developments in Experimental Methods, Nato ASI series C, eds H. Brodowsky and H.J. Schaller (Kluwer Academic Publishers, Dordrecht) p. 307.

Holleck, H., and H. Kleykamp, 1970, J. Nucl. Mater. **35**, 158.

Holleck, H., and H. Kleykamp, 1972/73, J. Nucl. Mater. **45**, 47.

Holleck, H., H. Kleykamp and J.I. Franco, 1975, Z. Metallk. **66**, 298.

Holleck, H., H. Kleykamp and J.I. Franco, 1990, J. Nucl. Mater. **175**, 55.

Hoshino, Y., and J.A. Plambeck, 1969, Can. J. Chem. **47**, 965.

Hoshino, Y., and J.A. Plambeck, 1970, Can. J. Chem. **48**, 685.

Hubbard, W.N., P.L. Rawlins, P.A. Connick, R.E. Stedwell and P.A.G. O'Hare, 1983, J. Chem. Thermodyn. **15**, 785.

Hultgren, R., P.D. Desai, D.T. Hawkins, M. Gleiser and K.K. Kelley, 1973a, in: Selected Valucs of the Thermodynamic Properties of Binary Alloys (American Society for Metals, Metals Park, OH).

Hultgren, R., P.D. Desai, D.T. Hawkins, M. Gleiser, K.K. Kelley and D.D. Wagman, 1973b, in: Selected Values of the Thermodynamic Properties of the Elements (American Society for Metals, Metals Park, OH).

Iandelli, A., and A. Palenzona, 1979, in: Handbook on the Physics and Chemistry of Rare Earths, Vol. 2, Alloys and Intermetallics, eds K.A. Gschneidner Jr and L. Eyring (North-Holland, Amsterdam) p. 1.

Itagaki, K., G. Qi, S. Mey and P.J. Spencer, 1990, CALPHAD **14**, 377.

Ivanov, M.I., and G.M. Lukashenko, 1983, Ukr. Khim. Zh. **49**, 1034 [Sov. Prog. Chem. **49**, 28].

Ivanov, M.I., and G.M. Lukashenko, 1987, J. Less-Common Met. **133**, 181.

Ivanov, M.I., and N.S. Podol'skaya, 1962, At. Energ. **13**, 572 [Sov. At. Energy **13**, 37].

Ivanov, M.I., and V.A. Tumbakov, 1959, At. Energ. **7**, 33 [Sov. At. Energ. **7**, 559].

Ivanov, M.I., and V.T. Vitusevich, 1990, Ukr. Khim. Zh. **56**, 549 [Sov. Prog. Chem. **56**].

Ivanov, M.I., V.A. Tumbakov and N.S. Podol'skaia, 1958, At. Energ. **5**, 166 [Sov. At. Energy **5**, 1007].

Ivanov, M.I., T.F. Karpova and N.Yu. Dalago, 1980, Izv. Akad. Nauk SSSR, Neorg. Mater. **16**, 830 [Inorg. Mater. **16**, 573].

Jacob, K.T., and M.S. Chandrasekharaiah, 1990, Z. Metallkd. **81**, 509.

Jacob, K.T., and Y. Waseda, 1990a, Bull. Mater. Sci. **13**, 235.

Jacob, K.T., and Y. Waseda, 1990b, J. Chem. Thermodyn. **22**, 929.

Jacob, K.T., and Y. Waseda, 1990c, Mater. Trans. JIM **31**, 135.

Jacob, K.T., and Y. Waseda, 1990d, Thermochim. Acta **165**, 223.

Jangg, G., and F. Steppan, 1965, Z. Metallk. **56**, 172.

Johnson, I., 1964, in: Nuclear Metallurgy, Vol. 10, Compounds of Interest in Nuclear Reactor Technology (Am. Inst. Mining, Metallurgical and Petroleum Engineers, New York) p. 171.

Johnson, I., and M.G. Chasanov, 1964, J. Inorg. Nucl. Chem. **26**, 2059.

Johnson, I., and H.M. Feder, 1962a, Trans. Metall. Soc. AIME **224**, 468.

Johnson, I., and H.M. Feder, 1962b, in: Thermodynamics of Nuclear Materials, Proc. Symp., Vienna (IAEA, Vienna) p. 319.

Johnson, I., and R.M. Yonco, 1970, Metall. Trans. **1**, 905.

Johnson, I., M.G. Chasanov and R.M. Yonco, 1965, Trans. Metall. Soc. AIME **233**, 1408.

Jung, W.G., and O.J. Kleppa, 1991a, J. Chem. Thermodyn. **23**, 147.

Jung, W.G., and O.J. Kleppa, 1991b, J. Less-Common Met. **169**, 85.

Jung, W.G., O.J. Kleppa and L. Topor, 1991, J. Alloys & Compounds 176, 309.

Kadochnikov, V.A., A.M. Poyarkov, V.A. Lebedev, I.F. Nichkov and S.P. Raspopin, 1974, At. Energ. **37**, 418 [Sov. At. Energy **37**, 1174].

Kadochnikov, V.A., V.A. Lebedev, I.F. Nichkov and S.P. Raspopin, 1976, Izv. Akad. Nauk SSSR, Met. **4**, 67 [Russ. Metall. **4**, 61].

Kadochnikov, V.A., V.A. Lebedev, I.F. Nichkov, A.M. Poryakov and S.P. Raspopin, 1977, Izv. Vyssh. Uchebn. Zaved. Tsvetn. Metall. **20**, [2], 146 [Sov. Non-Ferrous Met. Res. **5**, 80].

Kanashin, Yu.P., V.A. Lebedev, I.F. Nichkov and S.P. Raspopin, 1972, Izv. Akad. Nauk. SSSR, Met. **3**, 46 [Russ. Metall. **3**, 38].

Kanno, M., 1974, J. Nucl. Mater. **51**, 24.

Kanno, M., M. Yamawaki, T. Koyama and N. Morioka, 1988, J. Nucl. Mater. **154**, 154.

Kassner, M.E., and D.E. Peterson, 1989a, Bull. Alloy Phase Diagrams **10**, 111.

Kassner, M.E., and D.E. Peterson, 1989b, Bull. Alloy Phase Diagrams **10**, 277.

Kassner, M.E., and D.E. Peterson, 1989c, Bull. Alloy Phase Diagrams **10**, 459.

Kassner, M.E., and D.E. Peterson, 1989d, Bull. Alloy Phase Diagrams **10**, 466.

Kassner, M.E., P.H. Adler, M.G. Adamson and D.E. Peterson, 1988, J. Nucl. Mater. **167**, 160.

Kassner, M.E., M.G. Adamson, P.H. Adler and D.E. Peterson, 1990, Bull. Alloy Phase Diagrams **11**, 82.

Kazanskii, E.G., and N.G. Ilyushchenko, 1987, Rasplavy **1**, 114.

Kemmler, G., 1977, Report KFK 2452 (Gesellschaft für Kernforschung, Karlsruhe).

Kirchmayr, H., 1992, CEAM Meeting, Schellerhau IV.

Kirchmayr, H.R., and G. Jangg, 1965, Monatsch. Chem. **96**, 1147.

Kleppa, O.J., and L. Topor, 1985, Metall. Trans. **16A**, 93.

Kleykamp, H., 1979, J. Less-Common Met. **63**, 25.

Kleykamp, H., 1991a, J. Less-Common Met. **167**, 373.

Kleykamp, H., 1991b, Pure Appl. Chem. **63**, 1401.

Kleykamp, H., and S.G. Kang, 1991, Z. Metallk. **82**, 544.

Kleykamp, H., and M. Murabayashi, 1974, J. Less-Common Met. **35**, 227.

Klimyenko, A.V., J. Seuntjens, L.L. Miller, B.J. Beaudry, R.A. Jacobson and K.A. Gschneidner Jr, 1988, J. Less-Common Met. **144**, 133.

Kober, V.I., 1991, Chem. Ztg. **115**, 155.

Kober, V.I., V.A. Lebedev, I.F. Nichkov and S.P. Raspopin, 1968, Zh. Fiz. Khim. **42**, 686 [Russ. J. Phys. Chem. **42**, 360].

Kober, V.I., V.A. Lebedev, I.F. Nichkov and S.P. Raspopin, 1971a, Zh. Fiz. Khim. **45**, 569 [Russ. J. Phys. Chem. **45**, 313].

Kober, V.I., V.A. Lebedev, I.F. Nichkov, S.P. Raspopin and A.I. Belousov, 1971b, Zh. Fiz. Khim. **45**, 1986 [Russ. J. Phys. Chem. **45**, 1127].

Kober, V.I., V.A. Lebedev, I.F. Nichkov, S.P. Raspopin and L.F. Yamshchikov, 1973a, Izv. Akad. Nauk SSSR, Met. **2**, 217 [Russ. Metall. **2**, 163].

Kober, V.I., V.A. Lebedev, I.F. Nichkov, S.P. Raspopin and L.F. Yamshchikov, 1973b, Izv. Akad. Nauk SSSR, Metall. **3**, 90 [Russ. Metall. **3**, 79].

Kober, V.I., I.F. Nichkov, S.P. Raspopin and V.A. Nauman, 1977, Izv. Vyssh. Uchebn. Zaved. Tsvetn. Metall. **20**(5), 83 [Sov. Non-Ferrous Met. Res. **5**, 184].

Kober, V.I., I.F. Nichkov, S.P. Raspopin and V.A. Nauman, 1979a, Izv. Vyssh. Uchebn. Zaved. Tsvetn. Metall. **22**(5), 40 [Sov. Non-Ferrous Met. Res. **7**, 520].

Kober, V.I., I.F. Nichkov, S.P. Raspopin and V.A. Nauman, 1979b, Izv. Vyssh. Uchebn. Zaved. Tsvetn. Metall. **22**(1), 144 [Sov. Non-Ferrous Met. Res. **7**, 116].

Kober, V.I., I.F. Nichkov, S.P. Raspopin and V.M. Kuz'minykh, 1979c, in: Thermodynamics of Metallic Systems, Vol. 2 (Alma-Ata) p. 67. In Russian.

Kober, V.I., I.F. Nichkov, S.P. Raspopin and V.M. Kuz'minykh, 1979d, in: Thermodynamics of Metallic Systems, Vol. 2 (Alma-Ata) p. 72. In Russian.

Kober, V.I., I.F. Nichkov, S.P. Raspopin and A.S. Kondratov, 1982a, Izv. Vyssh. Uchebn. Zaved. Tsvetn. Metall. **24**(5), 101 [Sov. Non-Ferrous Met. Res. **10**, 406].

Kober, V.I., I.F. Nichkov, S.P. Raspopin and P.S. Ignatchenko, 1982b, Izv. Vyssh. Uchebn. Zaved. Tsvetn. Metall. **25**(3), 107 [Sov. Non-Ferrous Met. Res. **10**, 248].

Kober, V.I., I.F. Nichkov, S.P. Raspopin and A.A. Bogdanov, 1983a, Izv. Vyssh. Uchebn. Zaved. Tsvetn. Metall. **25**(3), 58 [Sov. Non-Ferrous Met. Res. **11**, 218].

Kober, V.I., V.A. Dubinin, A.I. Kochkin, I.F. Nichkov and S.P. Raspopin, 1983b, Izv. Vyssh. Uchebn. Zaved. Tsvetn. Metall. **25**(6), 113 [Sov. Non-Ferrous Met. Res. **11**, 499].

Kober, V.I., I.F. Nichkov, S.P. Raspopin and V.M. Kuz'minykh, 1983c, in: Splary Redk Met. Osobymi

Fiz, Svoistvami: Redkozem. Blagorodn. Met., ed E.M. Savitskii (Nauka, Moskow) p. 132.

Kober, V.I., I.F. Nichkov, S.P. Raspopin and A.G. Osvald, 1984, Izv. Vyssh. Uchebn. Zaved. Tsvetn. Metall. **5**, 125 [Sov. Non-Ferrous Met. Res. **12**, 422].

Kober, V.I., V.A. Dubinin, V.I. Kochkin and S.P. Raspopin, 1985, Zh. Fiz. Khim. **59**, 2124 [Russ. J. Phys. Chem. **59**, 1264].

Kober, V.I., I.F. Nichkov, S.P. Raspopin and Yu.Yu. Kanaev, 1986a, Izv. Vyssh. Uchebn. Zaved. Tsvetn. Metall. **3**, 123 [Sov. Non-Ferrous Met. Res. **14**, 258].

Kober, V.I., V.A. Dubinin, I.F. Nichkov and S.R. Kanevskii, 1986b, Zh. Fiz. Khim. **60**, 197 [Russ. J. Phys. Chem. **60**, 111].

Kober, V.I., I.F. Nichkov, S.P. Raspopin and V.V. Shvydenko, 1986c, Zh. Fiz. Khim. **60**, 1785 [Russ. J. Phys. Chem. **60**, 1070].

Kononenko, V.I., and S.V. Golubev, 1990, Izv. Akad. Nauk SSSR, Met. **2**, 197 [Russ. Metall. **2**, 193].

Kovalevskiy, A.V., V.A. Lebedev, I.I. Nichkov and S.P. Raspopin, 1972, Izv. Akad. Nauk SSSR, Met. **1**, 183 [Russ. Metall. **1**, 131].

Krishnan, R., S.P. Garg and N. Krishnamurthy, 1988, J. Alloy Phase Diagrams **4**, 204.

Krishnan, R., S.P. Garg and N. Krishnamurthy, 1989, J. Alloy Phase Diagrams **5**, 27.

Krumpelt, M., I. Johnson and J.J. Heiberger, 1974, Metall. Trans. **5**, 65.

Kubaschewski, O., 1968, in: Thermodynamics of Nuclear Materials, Proc. Symp., Vienna (IAEA, Vienna) p. 685.

Kubaschewski, O., 1981, Physica B **103**, 101.

Kulagina, N.G., and A.P. Bayanov, 1974a, Zh. Fiz. Khim. **48**, 233 [Russ. J. Phys. Chem. **48**, 143].

Kulagina, N.G., and A.P. Bayanov, 1974b, Zh. Fiz. Khim. **48**, 466 [Russ. J. Phys. Chem. **48**, 273].

Kulifeev, V.K., G.P. Stanolevich and V.G. Kozlov, 1971, Izv. Vyssh. Uchebn. Zaved. Tsvet. Met. **14**, 146.

Laabs, F.C., M.A. Noack and J.F. Smith, 1991, J. Phase Equilibria **12**, 23.

Landgraf, F.J.G., G.S. Schneider, V. Villas-Boas and F.P. Missell, 1990, J. Less-Common Met. **163**, 209.

Lebedev, V.A., I.F. Nichkov and S.P. Raspopin, 1968a, Zh. Fiz. Khim. **42**, 690 [Russ. J. Phys. Chem. **42**, 363].

Lebedev, V.A., I.F. Nichkov, S.P. Raspopin and V.I. Kapitonov, 1968b, Zh. Fiz. Khim. **42**, 694 [Russ. J. Phys. Chem. **42**, 365].

Lebedev, V.A., L.G. Babikov, S.K. Vavilov, I.F. Nichkov, S.P. Raspopin and O.V. Skiba, 1969, At. Energ. **27**, 59 [Sov. At. Energy **27**, 748].

Lebedev, V.A., I.F. Nichkov, S.P. Raspopin, R.Kh. Mullayanov and B.G. Semenov, 1971a, Zh. Fiz. Khim. **45**, 1983 [Russ. J. Phys. Chem. **45**, 1126].

Lebedev, V.A., A.M. Poyarkov, I.F. Nichkov and S.P. Raspopin, 1971b, At. Energ. **31**, 621 [Sov. At. Energy, **31**, 1408].

Lebedev, V.A., V.I. Kober, I.F. Nichkov, S.P. Raspopin and A.A. Kalinovskii, 1972a, Izv. Akad. Nauk SSSR, Met. **2**, 91 [Russ. Metall. **2**, 69].

Lebedev, V.A., V.I. Sal'nikov, I.F. Nichkov and S.P. Raspopin, 1972b, At. Energ. **32**, 115 [Sov. J. Atom. Energy **32**, 129].

Lebedev, V.A., V.I. Lyazgin, A.V. Ishutin, I.F. Nichkov and S.P. Raspopin, 1973a, Izv. Akad. Nauk SSSR, Met. **6**, 179 [Russ. Metall. **6**, 107].

Lebedev, V.A., N.V. Nazarov, V.I. Pyatkov, I.F. Nichkov and S.P. Raspopin, 1973b, Izv. Akad. Nauk SSSR, Met. **2**, 212 [Russ. Metall. **2**, 160].

Lebedev, V.A., N.V. Nazarov, V.I. Pyatkov, I.F. Nichkov and S.P. Raspopin, 1973c, Elektrokhimiya **9**, 920 [Sov. Electrochem. **9**, 878].

Lebedev, V.A., V.M. Seregin, A.M. Poyarkov, I.F. Nichkov and S.P. Raspopin, 1973d, Zh. Fiz. Khim. **47**, 712 [Russ. J. Phys. Chem. **47**, 402].

Lebedev, V.A., V.I. Pyatkov, R.R. Abdrakhmanov, I.F. Nichkov, S.P. Raspopin and N.V. Nazarov, 1974a, Zh. Fiz. Khim. **48**, 2521 [Russ. J. Phys. Chem. 48, 1489].

Lebedev, V.A., V.M. Seregin, A.M. Poyarkov, I.F. Nichkov and S.P. Raspopin, 1974b, Zh. Fiz. Khim. **48**, 542 [Russ. J. Phys. Chem. **48**, 317].

Lebedev, V.A., V.I. Kober, V.I. Salnikov, G.N. Kazantsev, I.F. Nichkov, S.P. Raspopin, O.V. Skiba and V.V. Efremov, 1976, Radiokhimiya **18**, 123 [Sov. Radiochem. **18**, 113].

Lebedev, V.A., V.I. Kober, V.G. Serebryakov, G.N. Kazantsev, I.F. Nichkov, S.P. Raspopin and O.V. Skiba, 1977, At. Energ. **42**, 496 [Sov. At. Energy **42**, 568].

Lebedev, V.A., V.I. Pyatkov and L.V. Khalturin, 1982, Izv. Akad. Nauk SSSR, Met. **2**, 210 [Russ. Metall. **2**, 192].

Lebedev, V.A., V.I. Kober, G.N. Kazantsev, I.F. Nichkov, S.P. Raspopin and O.V. Skiba, 1984, Radiokhim. **26**, 259 [Sov. Radiochem. **26**].

Lee, J.J., and F. Sommer, 1985, Z. Metallk. **76**, 750.

Leibowitz, L., and R.A. Blomquist, 1991, J. Nucl. Mater. **184**, 47.

Leibowitz, L., R.A. Blomquist and A.D. Pelton, 1989, J. Nucl. Mater. **167**, 76.

Leibowitz, L., R.A. Blomquist and A.D. Pelton, 1991, J. Nucl. Mater. **184**, 59.

Lesourd, J.P.F., and J.A. Plambeck, 1969, Can. J. Chem. **47**, 3387.

Litovskii, V.V., M.G. Valishev, Yu.O. Esin, P.V. Geld and M.S. Petrushevskii, 1986, Zh. Fiz. Khim. **60**, 2310 [Russ. J. Phys. Chem. **60**, 1385].

Lorenzelli, N., and J.P. Marcon, 1972, J. Nucl. Mater. **44**, 57.

Lukashenko, G.M., and R.I. Polotskaya, 1982, Ukr. Khim. Zh. **48**, 357 [Sov. Prog. Chem. **48**].

Lukashenko, G.M., and R.I. Polotskaya, 1986, Poroshk. Metall. **6**, 70 [Sov. Powder Metall. Met. Ceram. **25**, 504].

Lukashenko, G.M., V.R. Sidorko and Yu.I. Buyanov, 1990a, Poroshk. Metall. **7**, 66 [Sov. Powder Metall. Met. Ceram. **29**, 568].

Lukashenko, G.M., V.P. Sidorko and K.A. Meleshevich, 1990b, Dopov. Akad. Nauk Ukr. RSR, Ser. A **5**, 83.

Lukashenko, G.M., V.R. Sidorko and Yu.I. Buyanov, 1991a, Dokl. Akad. Nauk Ukr. SSR **4**, 73.

Lukashenko, G.M., R.I. Polotskaya and V.R. Sidorko, 1991b, Ukr. Khim. Zh. **57**, 1056 [Sov. Prog. Chem. **57**].

Lukashenko, G.M., R.I. Polotskaya and V.R. Sidorko, 1992, J. Alloys & Compounds, **179**, 299.

Maeda, A., Y. Suzuki and T. Ohmichi, 1992, J. Alloys & Compounds **179**, L21.

Magnani, N.J., W.H. Skelton and J.F. Smith, 1969, Nucl. Metall. **15**, 727.

Maret, M., and A. Pasturel, 1987, J. Phys. (Paris) **48**, 1541.

Mason, J.T., and P. Chiotti, 1976, Metall. Trans. **7A**, 287.

Massalski, T.B., 1990, in: Binary Alloy Phase Diagrams, 2nd Ed., eds T.B. Massalski, H. Okamoto, P.R. Subramanian and L. Kacprzak (ASM International, Metals Park, OH) 3 volumes.

Matigorova, N.G., and A.P. Bayanov, 1971, Zh. Fiz. Khim. **45**, 2440 [Russ. J. Phys. Chem. **45**, 1384].

Merker, P., 1991, J. Less-Common Met. **169**, L23.

Meschel, S.V., and O.J. Kleppa, 1993a, J. Alloys & Compounds **191**, 111.

Meschel, S.V., and O.J. Kleppa, 1993b, J. Alloys & Compounds **197**, 75.

Meschel, S.V., and O.J. Kleppa, 1994a, J. Alloys & Compounds, in press.

Meschel, S.V., and O.J. Kleppa, 1994b, in: Metallic Alloys: Experimental and Theoretical Perspectives, eds J.S. Faulkner and R.G. Jordan (Kluwer Academic Publishers, Dordrecht).

Mey, S., K. Hack, K. Itagaki, P.J. Spencer and D. Neuschutz, 1990, CALPHAD **14**, 175.

Meyer, F., 1985, Thesis (University of Grenoble, France).

Meyer-Liautaud, F., A. Pasturel, C. Allibert and C. Colinet, 1985a, J. Less-Common Met. **110**, 75.

Meyer-Liautaud, F., A. Pasturel, C.H. Allibert and C. Colinet, 1985b, J. Less-Common Met. **110**, 119.

Meyer-Liautaud, F., C.H. Allibert and R. Castanet, 1987a, J. Less-Common Met. **127**, 243.

Meyer-Liautaud, F., S. Derkaoui, C.H. Allibert and R. Castanet, 1987b, J. Less-Common Met. **127**, 231.

Möbius, S., 1978, Report KFK 2634 (Kernforschungszentrum Karlsruhe).

Möbius, S., L. Hellwig and C. Keller, 1986, J. Less-Common Met. **121**, 43.

Mogutnov, B.M., and L.A. Shvartsman, 1980, Zh. Fiz. Khim. **54**, 568 [Russ. J. Phys. Chem. **54**, 328].

Moreau, J.M., L. Paccard, J.P. Nozières, F.P. Missell, G. Schneider and V. Villas-Boas, 1990, J. Less-Common Met. **163**, 245.

Morisson, A., and C. Petot, 1987a, Thermochim. Acta **112**, 307.

Morisson, A., and C. Petot, 1987b, Thermochim. Acta **115**, 167.

Morisson, A., C. Petot and A. Percheron-Guegan, 1986, Thermochim. Acta **101**, 177.

Mullayanov, R.Kh., V.A. Lebedev, Yu.P. Kanashin, I.F. Nichkov and S.P. Raspopin, 1969, Zh. Fiz. Khim. **43**, 2776 [Russ. J. Phys. Chem. **43**, 1559].

Munitz, A., A.B. Gokhale and G.J. Abbaschian, 1989, Bull. Alloy Phase Diagrams **10**, 73.

Murabayashi, M., and H. Kleykamp, 1975, J. Less-Common Met. **39**, 235.

Nagarajan, K., and F. Sommer, 1988, J. Less-Common Met. **142**, 319.

Nagarajan, K., and F. Sommer, 1989, J. Less-Common Met. **146**, 89.

Naraine, N.G., and H.B. Bell, 1974, J. Nucl. Mat. **50**, 83.

Nash, P., 1989, Bull. Alloy Phase Diagrams **10**, 129.

Nayeb-Hashemi, A.A., and J.B. Clark, 1984, Bull. Alloy Phase Diagrams **5**, 43.

Nayeb-Hashemi, A.A., and J.B. Clark, 1986, Bull. Alloy Phase Diagrams **7**, 574.

Nayeb-Hashemi, A.A., and J.B. Clark, 1988a, Bull. Alloy Phase Diagrams **9**, 162.

Nayeb-Hashemi, A.A., and J.B. Clark, 1988b, Bull. Alloy Phase Diagrams **9**, 172.

Nayeb-Hashemi, A.A., and J.B. Clark, 1988c, Bull. Alloy Phase Diagrams **9**, 618.

Nayeb-Hashemi, A.A., and J.B. Clark, 1989, Bull. Alloy Phase Diagrams **10**, 23.

Nikolaenko, I.V., 1990, Izv. Akad. Nauk SSSR, Met. **4**, 191 [Russ. Metall **4**, 195].

Nikolaenko, I.V., 1992, private communication; J. Alloys & Compounds, in press.

Nikolaenko, I.V., and E.A. Beloborodova, 1980, Ukr. Khim. Zh. **46**, 868 [Sov. Prog. Chem. **46**].

Nikolaenko, I.V., and N.I. Beloborodova, 1991, Izv. Akad. Nauk SSSR, Met. **1**, 57 [Russ. Metall. **1**, 55].

Nikolaenko, I.V., and V.V. Nosova, 1989, Ukr. Khim. Zh. **55**, 1260 [Sov. Prog. Chem. 55].

Nikolaenko, I.V., and M.A. Turchanin, 1989, Rasplavy **5**, 77.

Nikolaenko, I.V., E.A. Beloborodova and G.I. Batalin, 1979a, Izv. Akad. Nauk SSSR, Met. **6**, 71 [Russ. Metall. **6**, 59].

Nikolaenko, I.V., E.A. Beloborodova and G.I. Batalin, 1979b, Zh. Fiz. Khim., **53**, 1873 [Russ. J. Phys. Chem. **53**, 1070].

Nikolaenko, I.V., E.A. Beloborodova and G.I. Batalin, 1980a, Izv. Akad. Nauk SSSR, Neorg. Mater. **16**, 155 [Inorg. Mater. (USSR) **16**, 155].

Nikolaenko, I.V., G.I. Batalin and E.A. Beloborodova, 1980b, Dopov. Akad. Nauk Ukr. RSR, Ser. B **12**, 50.

Nikolaenko, I.V., E.A. Beloborodova, G.I. Batalin, N.I. Frumina and V.S. Zhuravlev, 1983, Zh. Fiz. Khim. **57**, 1897 [Russ. J. Phys. Chem. **57**, 1154].

Nikolaenko, I.V., M.A. Turchanin and G.I. Batalin, 1987, Izv. Akad. Nauk SSSR, Met. **3**, 67 [Russ. Metall. **3**, 66].

Nikolaenko, I.V., M.A. Turchanin and G.I. Batalin, 1988, Izv. Akad. Nauk SSSR, Neorg. Mater. **24**, 680 [Inorg. Mater. (USSR) **24**, 566].

Nikolaenko, I.V., M.A. Turchanin and N.I. Beloborodova, 1990, Izv. Akad. Nauk SSSR, Neorg. Mater. **26**, 2309 [Inorg. Mater. (USSR) **26**, 2309].

Ning, Y., X. Zhou, Y. Zhen, N. Chen, H. Xu and J. Zhu, 1989, J. Less-Common Met. **14**, 167.

Notin, M., J.C. Gachon and J. Hertz, 1992, Thermochim. Acta **204**, 55.

Novotny, D.B., and J.F. Smith, 1963, J. Inst. Met. **92**, 122.

Novozhenov, V.A., T.M. Shkolnikova and V.V. Serebrennikov, 1975, Zh. Fiz. Khim. **49**, 3012 [Russ. J. Phys. Chem. **49**, 1789].

Novozhenov, V.A., T.M. Shkolnikova and V.V. Serebrennikov, 1979, Zh. Fiz. Khim. **53**, 2117 [Russ. J. Phys. Chem. **53**, 1210].

Oetting, F.L., M.H. Rand and R.J. Ackermann, 1976, in: The Chemical Thermodynamics of Actinide Elements and Compounds, Part 1, the Actinide Elements (IAEA, Vienna).

Ogren, J.R., N.J. Magnani and J.F. Smith, 1967, Trans. Met. Soc. AIME **239**, 766.

O'Hare, P.A.G., M. Ader, W.N. Hubbard, G.K. Johnson and J.L. Settle, 1974, in: Thermodynamics of Nuclear Materials, Proc. Symp., Vienna, Vol. 2 (IAEA, Vienna) p. 452.

Okamoto, H., 1990, Bull. Alloy Phase Diagrams, **11**, 140.

Okamoto, H., 1991a, J. Phase Equilibria **12**, 249.

Okamoto, H., 1991b, J. Phase Equilibria **12**, 698.

Okamoto, H., 1991c, J. Phase Equilibria **12**, 502.

Okamoto, H., 1991d, J. Phase Equilibria **12**, 565.

Okamoto, H., 1991e, J. Phase Equilibria **12**, 563.

Okamoto, H., 1991f, J. Phase Equilibria **12**, 568.

Okamoto, H., 1991g, J. Phase Equilibria **12**, 615.

Okamoto, H., 1991h, J. Phase Equilibria **12**, 704.

Okamoto, H., 1991i, J. Phase Equilibria **12**, 700.

Okamoto, H., 1991j, J. Phase Equilibria **12**, 246.

Okamoto, H., 1991k, J. Phase Equilibria **12**, 252.

Okamoto, H., 1991l, J. Phase Equilibria **12**, 247.

Okamoto, H., 1991m, J. Phase Equilibria **12**, 250.

Okamoto, H., 1991n, J. Phase Equilibria **12**, 253.

Okamoto, H., 1991o, J. Phase Equilibria **12**, 123.

Okamoto, H., 1991p, J. Phase Equilibria **12**, 504.

Okamoto, H., 1991q, J. Phase Equilibria **12**, 255.

Okamoto, H., 1991r, J. Phase Equilibria **12**, 612.

Okamoto, H., 1991s, J. Phase Equilibria **12**, 499.

Okamoto, H., 1991t, J. Phase Equilibria **12**, 500.

Okamoto, H., 1991u, J. Phase Equilibria **12**, 393.

Okamoto, H., 1992a, J. Phase Equilibria **13**, 103.

Okamoto, H., 1992b, J. Phase Equilibria **13**, 105

Okamoto, H., 1992c, J. Phase Equilibria **13**, 107.

Okamoto, H., 1992d, J. Phase Equilibria **13**, 102.

Okamoto, H., and T.B. Massalski, 1986, Gold-based Binary Alloy Phase Diagrams (ASM International, Metals Park, OH).

Okamoto, H., T.B. Massalski and D.E. Peterson, 1986, Bull. Alloy Phase Diagrams **7**, 525–535.

Otopkov, P.P., Y.A. Gerasimov and A.M. Evseev, 1961, Dokl. Akad. Nauk. SSSR **139**, 616.

Paasch, S., and H.J. Schaller, 1983, Ber. Bunsenges. Phys. Chem. **87**, 812.
Pahlman, J.E., and J.F. Smith, 1972, Metall. Trans. **3**, 2423.
Palenzona, A., 1973, Thermochim. Acta **5**, 473.
Palenzona, A., 1991, J. Alloys & Compounds **176**, 241.
Palenzona, A., and F. Canepa, 1989, J. Less-Common Met. **155**, L31.
Palenzona, A., and F. Canepa, 1990a, J. Less-Common Met. **157**, 307.
Palenzona, A., and F. Canepa, 1990b, J. Less-Common Met. **162**, 267.
Palenzona, A., and S. Cirafici, 1973, Thermochim. Acta **6**, 455.
Palenzona, A., and S. Cirafici, 1974a, Thermochim. Acta **10**, 313.
Palenzona, A., and S. Cirafici, 1974b, Thermochim. Acta **9**, 419.
Palenzona, A., and S. Cirafici, 1975a, Thermochim. Acta **12**, 267.
Palenzona, A., and S. Cirafici, 1975b, Thermochim. Acta **13**, 357.
Palenzona, A., and S. Cirafici, 1978, Thermochim. Acta **25**, 252.
Palenzona, A., and S. Cirafici, 1986, J. Less-Common Met. **124**, 245.
Palenzona, A., and S. Cirafici, 1988a, J. Less-Common Met. **142**, 311.
Palenzona, A., and S. Cirafici, 1988b, J. Less-Common Met. **143**, 167.
Palenzona, A., and S. Cirafici, 1989a, J. Less-Common Met. **154**, 61.
Palenzona, A., and S. Cirafici, 1989b, Bull. Alloy Phase Diagrams **5**, 580.
Palenzona, A., and S. Cirafici, 1989c, Bull. Alloy Phase Diagrams **5**, 588.
Palenzona, A., and S. Cirafici, 1989d, Bull. Alloy Phase Diagrams **10**, 234.
Palenzona, A., and S. Cirafici, 1990a, Bull. Alloy Phase Diagrams **11**, 67.
Palenzona, A., and S. Cirafici, 1990b, Bull. Alloy Phase Diagrams **11**, 72.
Palenzona, A., and S. Cirafici, 1991a, J. Phase Equilibria **12**, 49.
Palenzona, A., and S. Cirafici, 1991b, J. Phase Equilibria **12**, 53.
Palenzona, A., and S. Cirafici, 1991c, J. Phase Equilibria **12**, 204.
Palenzona, A., and S. Cirafici, 1991d, J. Phase Equilibria **12**, 474.
Palenzona, A., and S. Cirafici, 1991e, J. Phase Equilibria **12**, 485.
Palenzona, A., and S. Cirafici, 1991f, J. Phase Equilibria **12**, 686.
Palenzona, A., and S. Cirafici, 1991g, J. Phase Equilibria **12**, 690.
Palenzona, A., and S. Cirafici, 1991h, J. Phase Equilibria **12**, 482.
Palenzona, A., and S. Cirafici, 1991i, J. Phase Equilibria **12**, 479.
Palenzona, A., and S. Cirafici, 1992a, J. Phase Equilibria **13**, 42.
Palenzona, A., and S. Cirafici, 1992b, J. Phase Equilibria **13**, 36.
Palenzona, A., S. Cirafici, G. Balducci and G. Bardi, 1978, Thermochim. Acta **23**, 393.
Pan, Y.Y., and P. Nash, 1989a, Bull. Alloy Phase Diagrams **10**, 253.
Pan, Y.Y., and P. Nash, 1989b, Bull. Alloy Phase Diagrams **10**, 602.
Pandian, S., S.V. Nagender Naidu and P. Rama Rao, 1987, J. Alloy Phase Diagrams **3**, 152.
Pandian, S., S.V. Nagender Naidu and P. Rama Rao, 1988a, J. Alloy Phase Diagrams **4**, 73.
Pandian, S., S.V. Nagender Naidu and P. Rama Rao, 1988b, J. Alloy Phase Diagrams **4**, 148.
Pandian, S., S.V. Nagender Naidu and P. Rama Rao, 1988c, J. Alloy Phase Diagrams **4**, 154.
Pasturel, A., C. Chatillon-Colinet, A. Percheron-Guégan and J.C. Achard, 1982, J. Less-Common Met. **84**, 73.
Pasturel, A., C. Chatillon-Colinet, A. Percheron-Guegan and J.C. Achard, 1983, J. Less-Common Met. **90**, 21.
Pasturel, A., F. Liautaud, C. Colinet, C. Allibert, A. Percheron-Guégan and J.C. Achard, 1984a, J. Less-Common Met. **96**, 93.
Pasturel, A., C. Colinet, C. Allibert, P. Hicter, A. Percheron-Guegan and J.C. Achard, 1984b, Phys. Status Solidi B **125**, 101.
Paul-Boncour, V., A. Percheron-Guegan, M. Diaf and J.C. Achard, 1987, J. Less-Common Met. **131**, 201.
Percheron, A., J.C. Mathieu and F. Trombe, 1968, C. R. Acad. Sci. Paris, Ser. C **266**, 848.
Peterson, D.E., 1980, J. Nucl. Mater. **91**, 306.
Peterson, D.E., 1985a, High Temp. Sci. **19**, 151.
Peterson, D.E., 1985b, J. Nucl. Mater. **131**, 44.
Peterson, D.E., 1985c, Bull. Alloy Phase Diagrams **6**, 342.
Peterson, D.E., 1985d, Bull. Alloy Phase Diagrams 6, 443.

Peterson, D.E., 1988a, Bull. Alloy Phase Diagrams **9**, 483.

Peterson, D.E., 1988b, Bull. Alloy Phase Diagrams **9**, 490.

Peterson, D.E., 1989a, Bull. Alloy Phase Diagrams **10**, 471.

Peterson, D.E., 1989b, Bull. Alloy Phase Diagrams **10**, 115.

Peterson, D.E., 1989c, Bull. Alloy Phase Diagrams **10**, 119.

Peterson, D.E., 1989d, Bull. Alloy Phase Diagrams **10**, 120.

Peterson, D.E., 1989e, Bull. Alloy Phase Diagrams **10**, 117.

Peterson, D.E., 1989f, Bull. Alloy Phase Diagrams **10**, 474.

Peterson, D.E., and E.M. Foltyn, 1989a, Bull. Alloy Phase Diagrams **10**, 160.

Peterson, D.E., and E.M. Foltyn, 1989b, Bull. Alloy Phase Diagrams **10**, 478.

Peterson, D.E., and M.E. Kassner, 1988, Bull. Alloy Phase Diagrams **9**, 261.

Peterson, D.E., and J.S. Starzynski, 1985, J. Less-Common Met. **105**, 273.

Petrashkevich, S.E., V.A. Degtyar, L.A. Vnuchkova and V.V. Serebrennikov, 1977, Zh. Metall. Abstr. N. **1A**, 72.

Polotskaya, R.I., 1988, Poroshk. Metall. **2**, 73 [Sov. Powder Metall. Met. Ceram. **27**, 154].

Polotskaya, R.I., 1991, Poroshk. Metall. **1**, 64 [Sov. Powder Metall. Met. Ceram. **30**, 57].

Polotskaya, R.I., and Yu.I. Buyanov, 1986, Poroshk. Metall. **12**, 31 [Sov. Powder Metall. Met. Ceram. **25**, 969].

Poon, S.J., A.J. Drehman and K.R. Lawless, 1985, Phys. Rev. Lett. **55**, 2324.

Poyarkov, A.M., V.A. Lebedev, I.F. Nichkov and S.P. Raspopin, 1973, At. Energ. **35**, 434 [Sov. At. Energy **35**, 1138].

Poyarkov, A.M., V.A. Lebedev, I.F. Nichkov and S.P. Raspopin, 1974, Izv. Akad. Nauk SSSR, Met. **5**, 118 [Russ. Metall. **5**, 96].

Poyarkov, A.M., V.A. Lebedev, I.F. Nichkov and S.P. Raspopin, 1975a, Izv. Akad. Nauk SSSR, Met. **3**, 87 [Russ. Metall. **3**, 70].

Poyarkov, A.M., V.A. Lebedev, I.F. Nichkov and S.P. Raspopin, 1975b, Zh. Fiz. Khim. **49**, 2615 [Russ. J. Phys. Chem. **49**, 1533].

Poyarkov, A.M., V.A. Lebedev, I.F. Nichkov and S.P. Raspopin, 1976, Izv. Akad. Nauk SSSR, Met. **6**, 64 [Russ. Metall. **6**, 64].

Pratt, J.N., and K.S. Chua, 1970, Final report 2027/048/RL (Department of Physical Metallurgy and Science of Materials, University of Birmingham, UK).

Pyagai, I.N., and A.V. Vakhodov, 1990, Izv. Akad. Nauk SSSR, Met. **5**, 55 [Russ. Metall. **5**, 50].

Pyatkov, V.I., V.A. Lebedev, I.F. Nichkov, S.P. Raspopin, A.V. Kuznetsov and A.K. Shtolts, 1971, Zh. Fiz. Khim. **45**, 2088 [Russ. J. Phys. Chem. **45**, 1184].

Qi, G., Z. Li, K. Itagaki and A. Yazawa, 1989a, Mater. Trans. JIM **30**, 583.

Qi, G., K. Itagaki and A. Yazawa, 1989b, Mater. Trans. JIM **30**, 273.

Qi, G., K. Itagaki, S. Mey and P.J. Spencer, 1989c, Z. Metallkd. **80**, 883.

Qiti Guo, and O.J. Kleppa, 1994, Metall. Trans. B **25**, 73.

Radchenko, V.M., V.D. Shushakov, L.S. Lebedeva, M.A. Ryabinin, R.R. Droznik, E.N. Shiryaev and V.L. Vasilev, 1989, Radiokhim. **31**, 20 [Sov. Radiochem. **31**].

Radchenko, V.M., V.D. Shushakov, A.G. Seleznev, M.A. Ryabinin, L.S. Lebedeva, V.Ya. Vasiliev and V.M. Nikolayev, 1990, J. Less-Common Met. **157**, 147.

Ran, Q., H.L. Lukas, G. Effenberg and G.E.G. Petzow, 1988, CALPHAD **12**, 375.

Ran, Q., H.L. Lukas, G. Effenberg and G. Petzow, 1989a, J. Less-Common Met. **146**, 213.

Ran, Q., H.L. Lukas, G. Effenberg and G. Petzow, 1989b, Z. Metallkd. **80**, 402.

Rand, M.H., and O. Kubaschewski, 1963, in: The Thermochemical Properties of Uranium Compounds (Interscience Publishers, New York).

Rand, M.H., D.T. Livey, P. Feschotte, H. Nowotny, K. Seifert and R. Ferro, 1966, in: Plutonium: Physico-Chemical Properties of its Compounds and Alloys, ed. O. Kubaschewski (IAEA, Vienna).

Rand, M.H., O. Von Goldbeck, R. Ferro, K. Girgis and A.L. Dragoo, 1975, in: Thorium: Physico-Chemical Properties of its Compounds and Alloys, ed. O. Kubaschewski (IAEA, Vienna).

Rezukhina, T.N., and S.V. Kutsev, 1982a, Zh. Fiz. Khim. **56**, 1 [Russ. J. Phys. Chem. **56**, 1].

Rezukhina, T.N., and S.V. Kutsev, 1982b, Zh. Fiz. Khim. **56**, 278 [Russ. J. Phys. Chem. **56**, 173].

Rezukhina, T.N., and B.S. Pokarev, 1971, J. Chem. Thermodyn. **3**, 369.

Rezukhina, T.N., L.I. Kravchenko and B.S. Pokarev, 1973, Metallofizika **6**, 21.

Rice, P.A., R.E. Balzhiser and D.V. Ragone, 1962, in: Thermodynamics of Nuclear Materials, Proc. Symp., Vienna (IAEA, Vienna) p. 331.

Robins, D.A., and I. Jenkins, 1955, Acta Metall. **3**, 598.

Roshchina, V.R., and A.P. Bayanov, 1974a, Zh. Fiz. Khim **48**, 421 [Russ. J. Phys. Chem. **48**, 242].

Roshchina, V.R., and A.P. Bayanov, 1974b, Zh. Fiz. Khim. **48**, 424 [Russ. J. Phys. Chem. **48**, 244].

Roshchina, V.R., and A.P. Bayanov, 1974c, Izv. Akad. Nauk SSSR, Met. **4**, 183 [Russ. Metall. **4**, 131].

Roshchina, V.R., and A.P. Bayanov, 1975, Zh. Fiz. Khim. **49**, 271 [Russ. J. Phys. Chem. **49**, 62].

Roshchina, V.R., and A.P. Bayanov, 1981, Zh. Fiz. Khim. **55**, 3017 [Russ. J. Phys. Chem. **55**, 1721].

Ross, B.A.S., and D.E. Peterson, 1990, Bull. Alloy Phase Diagrams **11**, 240.

Ryss, G.M., A.I. Stroganov, Yu.O. Esin and P.V. Geld, 1976a, Zh. Fiz. Khim. **50**, 771 [Russ. J. Phys. Chem. **50**, 454].

Ryss, G.M., Yu.O. Esin, A.I. Stroganov and P.V. Geld, 1976b, Zh. Fiz. Khim. **50**, 985 [Russ. J. Phys. Chem. **50**, 587].

Ryss, G.M., Yu.O. Esin, A.I. Stroganov and P.V. Geld, 1977, Zh. Fiz. Khim. **51**, 232 [Russ. J. Phys. Chem. **51**, 134].

Ryss, G.M., Yu.O. Esin, M.S. Petrushevskii, A.I. Stroganov and P.V. Geld, 1979a, Izv. Akad. Nauk SSSR, Met. **6**, 67 [Russ. Metall. **6**, 57].

Ryss, G.M., Yu.O. Esin, M.S. Petrushevskii, A.I. Stroganov and P.V. Geld, 1979b, Zh. Fiz. Khim. **53**, 1352 [Russ. J. Phys. Chem. **53**, 767].

Saccone, A., S. Delfino and R. Ferro, 1988, J. Less-Common Met. **143**, 1.

Saccone, A., S. Delfino, G. Borzone and R. Ferro, 1989a, J. Less-Common Met. **154**, 47.

Saccone, A., S. Delfino, G. Cacciamani and R. Ferro, 1989b, J. Less-Common Met. **154**, 99.

Saccone, A., S. Delfino, D. Maccio and R. Ferro, 1991, Z. Metallkd. **82**, 568.

Saccone, A., S. Delfino, D. Maccio and R. Ferro, 1992, Metall. Trans. **23A**, 1005.

Sagawa, M., S. Fujimura, M. Togawa, H. Yamamoto and Y. Matsuura, 1984, J. Appl. Phys. **55**, 2083.

Sakamoto, Y., K. Takao and M. Ohmaki, 1990, J. Less-Common Met. **162**, 343.

Sakamoto, Y., K. Takao and Y. Nagaoka, 1991, J. Mater. Sci. Lett. **10**, 341.

Samsonov, G.V., V.S. Neshpor and Yu.B. Paderno, 1963, in: Redkozemelnie Elementi (Nauka, Moscow) p. 22.

Santandrea, C.J., and D.E. Peterson, 1988, Bull. Alloy Phase Diagrams **9**, 487.

Schaller, H.J., 1979, Z. Naturforsch. **34A**, 464.

Schiffman, R.A., 1982, J. Phys. Chem. **86**, 3855.

Schiffman, R.A., and H.F. Franzen, 1982, High Temp. Sci. **15**, 179.

Schmidt, N., 1974, Report KFK 1987 (Gesellschaft für Kernforschung, Karlsruhe).

Schneider, G., F.J.G. Landgraf, V. Villas-Boas, G.H. Bezerra, F.P. Missell and A.E. Ray, 1989, Mater. Lett. **8**, 472.

Schott, J., and F. Sommer, 1986, J. Less-Common Met. **119**, 307.

Selhaoui, N., and O.J. Kleppa, 1993a, J. Alloys & Compounds **191**, 145.

Selhaoui, N., and O.J. Kleppa, 1993b, J. Chim. Phys. **90**, 435.

Selhaoui, N., and O.J. Kleppa, 1993c, J. Alloys & Compounds **191**, 155.

Selhaoui, N., and O.J. Kleppa, 1993d, Z. Metallkd. **84**, 11.

Semenenko, K.N., R.A. Sirotina and A.P. Savchenkova, 1979, Zh. Fiz. Khim. **53**, 2373 [Russ. J. Phys. Chem. **53**, 1356].

Semenenko, K.N., R.A. Sirotina, A.P. Savchenkova and T.S. Ilina, 1982, Zh. Fiz. Khim. **56**, 2555 [Russ. J. Phys. Chem. **56**, 1564].

Serebrennikov, V.V., E.I. Perov, T.M. Shkolnikova and V.A. Novozhenov, 1971, Zh. Fiz. Khim. **45**, 1395 [Russ. J. Phys. Chem. **45**, 790].

Serebrennikov, V.V., V.A. Novozhenov and T.M. Shkol'nikova, 1976, Zh. Fiz. Khim. **50**, 2401 [Russ. J. Phys. Chem. **50**, 1437].

Serebrennikov, V.V., V.A. Novozhenov and T.M. Shkolnikova, 1977, Izv. Akad. Nauk SSSR, Met. **6**, 42 [Russ. Metall. **6**, 33].

Seregin, V.M., A.M. Poyarkov, V.A. Lebedev, I.F. Nichkov and S.P. Raspopin, 1972, At. Energ. **32**, 419 [Sov. At. Energy **32**, 490].

Shamrai, V.F., Yu.V. Efimov, O.G. Karpinskii, A.A. Babareko, G.M. Leitus, T.M. Frolova, E.A. Myasnikova, A.M. Postnikov, M.E. Savel'yeva and Yu.L. Lipikhin, 1990, J. Less-Common Met. **162**, 181.

Sheldon, R.I., and D.E. Peterson, 1985a, Bull. Alloy Phase Diagrams **6**, 215.

Sheldon, R.I., and D.E. Peterson, 1985b, Bull. Alloy Phase Diagrams **6**, 217.

Sheldon, R.I., and D.E. Peterson, 1989, Bull. Alloy Phase Diagrams **10**, 165.

Sheldon, R.I., E.M. Foltyn and D.E. Peterson, 1987a, Bull. Alloy Phase Diagrams, **8**, 347.

Sheldon, R.I., E.M. Foltyn and D.E. Peterson, 1987b, Bull. Alloy Phase Diagrams, **8**, 536.

Shen, Y., S.J. Poon and G.J. Shiflet, 1986, Phys. Rev. B **34**, 3516.

Shilov, A.L., 1987, Zh. Fiz. Khim. **61**, 1384 [Russ. J. Phys. Chem. **61**, 719].

Shilov, A.L., L.N. Padurets and M.E. Kost, 1983, Zh. Fiz. Khim. **57**, 555 [Russ. J. Phys. Chem. **57**, 338].

Shkol'nikova, T.M., A.P. Bayanov and V.V. Serebrennikov, 1972a, Zh. Fiz. Khim. **46**, 602 [Russ. J. Phys. Chem. **46**, 346].

Shkol'nikova, T.M., A.P. Basin and V.V. Serebrennikov, 1972b, Zh. Fiz. Khim. **46**, 804 [Russ. J. Phys. Chem. **46**, 467].

Shkol'nikova, T.M., A.P. Bayanov and V.V. Serebrennikov, 1973, Tr. Tomsk. Gos. Univ. **237**, 192.

Sidorov, O.Yu., Yu.O. Esin, P.V. Geld and S.M. Kirova, 1988, Rasplavy **2**, 101.

Sidorov, O.Yu., M.G. Valishev, A.F. Ermakov, Yu.O. Esin and P.V. Geld, 1989, Zh. Fiz. Khim. **63**, 1123 [Russ. J. Phys. Chem. **63**, 627].

Sidorov, O.Yu., M.G. Valishev, Yu.O. Esin, P.V. Geld, V.M. Zamyatin and A.Ya. Dubrovskii, 1990, Izv. Akad. Nauk SSSR, Met. **4**, 188 [Russ. Metall. **4**, 192].

Sinnema, S., R.J. Radwanski, J.J.M. Franse, D.B. de Mooij and K.H.J. Buschow, 1984, J. Magn. & Magn. Mater. **45**, 1.

Sirotina, R.A., 1985, Abstract, Candidate's Thesis in Chemical Sciences (Moscow State University).

Skelton, W.H., N.J. Magnani and J.F. Smith, 1970, Metall. Trans. **1**, 1833.

Skelton, W.H., N.J. Magnani and J.F. Smith, 1971, Metall. Trans. **2**, 473.

Skelton, W.H., N.J. Magnani and J.F. Smith, 1973, Metall. Trans. **4**, 917.

Smith, J.F., 1974, J. Nucl. Mater. **51**, 136.

Smith, J.F., and K.J. Lee, 1987a, Bull. Alloy Phase Diagrams **8**, 523.

Smith, J.F., and K.J. Lee, 1987b, Bull. Alloy Phase Diagrams **8**, 221.

Smith, J.F., D.M. Bailey, D.B. Novotny and J.E. Davison, 1965, Acta Metall. **13**, 889.

Smith, J.F., O.N. Carlson, D.T. Peterson and T.E. Scott, 1975, in: Thorium: Preparation and Properties (Iowa State University Press, Ames, IA).

Smith, J.F., K.J. Lee and D.E. Peterson, 1985, Bull. Alloy Phase Diagrams **6**, 369.

Snyder, R.L., 1960, Diss. Abstr. **21**, 581.

Sommer, F., and M. Keita, 1987, J. Less-Common Met. **136**, 95.

Sommer, F., J. Schott and B. Predel, 1986, J. Less-Common Met. **125**, 175.

Sommer, F., M. Keita, H.G. Krull, B. Predel and J.J. Lee, 1988a, J. Less-Common Met. **137**, 267.

Sommer, F., J. Schott and H.G. Krull, 1988b, J. Less-Common Met. **144**, 53.

Sommer, F., D.K. Choi and H.G. Krull, 1989, J. Less-Common Met. **146**, 319.

Storms, E.K., and D.G. Czechowicz, 1989, J. Nucl. Mater. **167**, 169.

Stukalo, V.A., G.I. Batalin, N.Ya. Neshchimenko and V.P. Kurach, 1980, Ukr. Khim. Zh. **46**, 98 [Sov. Prog. Chem. 46].

Subramanian, P.R., and D.E. Laughlin, 1988, Bull. Alloy Phase Diagrams **9**, 322.

Subramanian, P.R., and J.F. Smith, 1984, CALPHAD **8**, 295.

Subramanian, P.R., and J.F. Smith, 1985a, Metall. Trans. **16A**, 1195.

Subramanian, P.R., and J.F. Smith, 1985b, Metall. Trans. **16B**, 577.

Sudavtsova, V.S., and G.I. Batalin, 1990, Rasplavy **2**, 106.

Sudavtsova, V.S., G.I. Batalin, A.V. Kalmykov and F.F. Kuznetsov, 1983, Izv. Vyssh. Uchebn. Zaved. Tsvetn. Metall. **6**, 107 [Sov. Non-Ferrous Met. Res. **11**, 492].

Sudavtsova, V.S., G.I. Batalin and V.P. Kurach, 1984a, Izv. Akad. Nauk SSSR, Neorg. Mater. **20**, 1925 [Inorg. Mater. **20**, 1672].

Sudavtsova, V.S., G.I. Batalin and V.P. Kurach, 1984b, Ukr. Khim. Zh. **50**, 339 [Sov. Prog. Chem. **50**, 339].

Sudavtsova, V.S., G.I. Batalin, A.V. Kalmykov and I.G. Starchevskaya, 1985, Izv. Vyssh. Uchebn. Zaved. Tsvetn. Metall. **6**, 98 [Sov. Non-Ferrous Met. Res. **13**, 501].

Sudavtsova, V.S., V.D. Kurach and G.I. Batalin, 1987, Izv. Akad. Nauk SSSR, Met. **3**, 60 [Russ. Metall. **3**, 59].

Sudavtsova, V.S., Yu.G. Gorobets and G.I. Batalin, 1988, Rasplavy **2**, 79.

Terekhov, G.I., and L.N. Aleksandrova, 1988, Izv. Akad. Nauk SSSR, Met. **5**, 197 [Russ. Metall. **5**, 197].

Terekhov, G.I., and S.I. Sinyakova, 1990, Izvest. Akad. Nauk, Met. **3**, 215 [Russ. Metall. **3**, 211].

Terekhov, S.V., and E.L. Korzun, 1990, Zh. Fiz. Khim. **64**, 1203 [Russ. J. Phys. Chem. **64**, 643].

Tien, L.C., K.J. Guion and R.D. Pehlke, 1962, in: Thermodynamics of Nuclear Materials, Proc. Symp., Vienna (IAEA, Vienna).

Topor, L., and O.J. Kleppa, 1989, Metall. Trans. **20B**, 879.

Topor, L., and O.J. Kleppa, 1990, J. Less-Common Met. **167**, 91.

Tung, C.H., and P. Nash, 1989, Bull. Alloy Phase Diagrams **10**, 127.

Turchanin, M.A., I.V. Nikolaenko and G.I. Batalin, 1987, Rasplavy **1**, 124.

Turchanin, M.A., I.V. Nikolaenko and G.I. Batalin, 1988a, Ukr. Khim. Zh. **54**, 773 [Sov. Prog. Chem. **54**, 773].

Turchanin, M.A., I.V. Nikolaenko and G.I. Batalin, 1988b, Rasplavy **2**, 118.

Turchanin, M.A., I.V. Nikolaenko and G.I. Batalin, 1988c, Rasplavy **2**, 25 [Melts **2**, 20].

Turchanin, M.A., I.V. Nikolaenko and G.I. Batalin, 1988d, Rasplavy **2**, 127.

Vamberskii, Yu.V., A.L. Udovskii and O.S. Ivanov, 1973, J. Nucl. Mater. **46**, 192.

Vamberskii, Yu.V., A.L. Udovskii and O.S. Ivanov, 1975a, J. Nucl. Mater. **55**, 96.

Vamberskii, Yu.V., A.L. Udovskii and O.S. Ivanov, 1975b, in: Thermodynamics of Nuclear Materials, Proc. 4th Symp., Vol. 2 (IAEA, Vienna) p. 321.

Vasilev, V.P., 1989, Vestn. Mosk. Univ. Khim. **44**, 115 [Moscow Univ. Chem. Bull. **44**, 1].

Vasilev, V.P., and D.H. Vu, 1985, Izv. Akad. Nauk SSSR, Neorg. Mater. **21**, 1144 [Inorg. Mater. **21**, 997].

Vasilev, V.P., D.H. Vu, Ya.I. Gerasimov, M.D. Bespalova and V.I. Goryacheva, 1982, Vestn. Mosk. Univ. Khim. **23**, 17.

Vasilev, V.P., D.H. Vu and Ya.I. Gerasimov, 1985, **59**, 2694 [Russ. J. Phys. Chem. **59**, 1613].

Vasilev, V.P., L.A. Khramtsova and V.V. Morozova, 1986, Vestn. Mosk. Univ. Khim **27**, 38.

Vdovkina, S.P., 1977, in: Papers from the Regional Scientific-Practical Conference, Young Scientists and Specialists for the National Economy (Tomsk) p. 4.

Vdovkina, S.P., V.A. Degtyar, L.A. Vnuchkova and V.V. Serebrennikov, 1973, Tr. Tomsk. Gos. Univ. **249**, 143.

Veleckis, E., 1961, J. Phys. Chem. **66**, 362.

Venkatraman, M., and J.P. Neumann, 1985, Bull. Alloy Phase Diagrams **6**, 429.

Venkatraman, M., J.P. Neumann and D.E. Peterson, 1985a, Bull. Alloy Phase Diagrams **6**, 418.

Venkatraman, M., J.P. Neumann and D.E. Peterson, 1985b, Bull. Alloy Phase Diagrams **6**, 415.

Venkatraman, M., J.P. Neumann and D.E. Peterson, 1985c, Bull. Alloy Phase Diagrams **6**, 413.

Venkatraman, M., J.P. Neumann and D.E. Peterson, 1985d, Bull. Alloy Phase Diagrams **6**, 425.

Venkatraman, M., J.P. Neumann and D.E. Peterson, 1985e, Bull. Alloy Phase Diagrams **6**, 422.

Venkatraman, M., J.P. Neumann and D.E. Peterson, 1985f, Bull. Alloy Phase Diagrams **6**, 423.

Venkatraman, M., J.P. Neumann and D.E. Peterson, 1985g, Bull. Alloy Phase Diagrams **6**, 419.

Vieth, D.L., and M.J. Pool, 1972, Rep. N073–30, Project Themis.

Viksman, G.Sh., and S.P. Gordienko, 1984, Izv. Akad. Nauk. SSSR Neorg. Mater. **20** 1441 [Inorg. Mater. **20**, 1239].

Viksman, G.Sh., and S.P. Gordienko, 1987, Poroshk. Metall. **7**, 63 [Sov. Powder Metall. Met. Ceram. **26**, 570].

Viksman, G.Sh., S.P. Gordienko and M.N. Abdusalyamova, 1980, Poroshk. Metall. **12**, 56 [Sov. Powder Metall. Met. Ceram. **19**, 851].

Villars, P., and L.D. Calvert, eds, 1991, Pearson's Handbook of Crystallographic Data for Intermetallic Phases, Vols. 1–4 (ASM International, Metals Park, OH).

Vitusevich, V.T., and M.I. Ivanov, 1987, Dopov. Akad. Nauk Ukr. RSR Ser B **11**, 30.

Vnuchkova, L.A., A.P. Bayanov and V.V. Serebrennikov, 1971a, Zh. Fiz. Khim. **45**, 177 [Russ. J. Phys. Chem. **45**, 99].

Vnuchkova, L.A., A.P. Bayanov and V.V. Serebrennikov, 1971b, Zh. Fiz. Khim. **45**, 2010 [Russ. J. Phys. Chem. **45**, 1140].

Vnuchkova, L.A., A.P. Bayanov and V.V. Serebrennikov, 1972a, Zh. Fiz. Khim. **46**, 1051 [Russ. J. Phys. Chem. **46**, 617].

Vnuchkova, L.A., A.P. Bayanov and V.V. Serebrennikov, 1972b, Zh. Fiz. Khim. **46**, 1053 [Russ. J. Phys. Chem. **46**, 618].

Volkovich, A.V., I.F. Nichkov, S.P. Raspopin, V.I. Tutarenko and V.A. Lebedev, 1968, Zh. Fiz. Khim. **42**, 682 [Russ. J. Phys. Chem. **42**, 358].

Volkovich, A.V., Yu.P. Kanashin, V.A. Lebedev, I.F. Nichkov, S.P. Raspopin and V.I. Titarenko, 1971, Zh. Fiz. Khim. **45**, 1979 [Russ. J. Phys. Chem. **45**, 1123].

Vu, D.H., and V.P. Vasilev, 1982, Dokl. Akad. Nauk SSSR **262**, 123.

Watanabe, S., and O.J. Kleppa, 1983, J. Chem. Thermodyn. **15**, 633.

Watanabe, S., and O.J. Kleppa, 1984, Metall. Trans. **15B**, 357.

Wijbenga, G., 1982, J. Chem. Thermodyn. **14**, 483.

Wijbenga, G., and E.H.P. Cordfunke, 1982, J. Chem. Thermodyn. **14**, 409.

Wu, C.H., and Y.C. Chuang, 1991, J. Phase Equilibria **12**, 587.

Wu, C.H., Y.C. Chuang, X.M. Jin and X.H. Guan, 1991a, Z. Metallkd. **82**, 621.

Wu, C.H., Y.C. Chuang and X.P. Su, 1991b, Z. Metallkd. **82**, 73.

Wu, C.H., Y.C. Chuang and X.M. Jin, 1992, J. Alloys & Compounds **179**, 27.

Yamshchikov, L.F., V.I. Kober, V.A. Lebedev, I.F. Nichkov and S.P. Raspopin, 1975, Zh. Fiz. Khim. **49**, 2933 [Russ. J. Phys. Chem. **49**, 1730].

Yamshchikov, L.F., V.A. Lebedev, V.I. Kober, I.F. Nichkov and S.P. Raspopin, 1977a, Izv. Akad. Nauk SSSR, Met. **5**, 90 [Russ. Metall. **5**, 60].

Yamshchikov, L.F., V.A. Lebedev, I.F. Nichkov, V.I. Kober and G.D. Korchinskii, 1977b, Izv. Vyssh. Uchebn. Zaved. Tsvetn. Metall. **20**, no 1, 85 [Sov. Non-Ferrous Met. Res. **5**, 26].

Yamshchikov, L.F., V.A. Lebedev and I.F. Nichkov, 1979a, Izv. Akad. Nauk SSSR, Met. **1**, 83 [Russ. Metall. **1**, 69].

Yamshchikov, L.F., V.A. Lebedev, I.F. Nichkov, S.P. Raspopin and O.K. Kakoulin, 1979b, Zh. Fiz. Khim **53**, 1163 [Russ. J. Phys. Chem. **53**, 657].

Yamshchikov, L.F., V.A. Lebedev, I.F. Nichkov, S.P. Raspopin and B.A. Karmanov, 1979c, in: Thermodynamics of Metallic Systems (Alma-Ata) p. 181. In Russian.

Yamshchikov, L.F., V.A. Lebedev, I.F. Nichkov, S.P. Raspopin and V.G. Shein, 1983, Izv. Vyssh. Uchebn. Zaved. Tsvetn. Metall. **25**, no 2, 64 [Sov. Non-Ferous Met. Res. **11**, 128].

Yamshchikov, L.F., V.A. Lebedev, S.P. Raspopin and P.A. Arkhipov, 1984a, Izv. Vyssh. Uchebn. Zaved. Tsvetn. Metall. **26**, no 5, 122 [Sov. Non-Ferrous Met. Res. **12**, 419].

Yamshchikov, L.F., V.A. Lebedev, S.P. Raspopin and P.A. Arkhipov, 1984b, Izv. Vyssh. Uchebn. Zaved. Tsvetn. Metall. **4**, 83 [Sov. Non-Ferrous Met. Res. **12**, 304].

Yamshchikov, L.F., V.A. Lebedev and F.N. Sattarov, 1985a, Izv. Akad. Nauk SSSR, Met. **3**, 219 [Russ. Metall. **3**, 222].

Yamshchikov, L.F., V.A. Lebedev, I.F. Nichkov and S.P. Raspopin, 1985b, Izv. Akad. Nauk SSSR, Met. **1**, 213 [Russ. Metall. **1**, 218].

Yamshchikov, L.F., V.A. Lebedev, I.F. Nichkov, S.P. Raspopin and S.E. Puchinskis, 1985c, Izv. Akad. Nauk SSSR, Met. **5**, 188 [Russ. Metall. **5**, 186].

Yamshchikov, L.F., V.A. Lebedev, S.P. Raspopin and S.E. Puchinskis, 1985d, Zh. Fiz. Khim. **59**, 2930 [Russ. J. Phys. Chem. **59**, 1756].

Yamshchikov, L.F., V.A. Lebedev and A.N. Klenikov, 1985e, Izv. Akad. Nauk SSSR, Met. **4**, 202 [Russ. Metall. **4**, 197].

Yamshchikov, L.F., V.A. Lebedev, S.P. Raspopin and P.A. Arkhipov, 1986, Zh. Fiz. Khim. **60**, 289 [Russ. J. Phys. Chem. **60**, 174].

Yamshchikov, L.F., S.P. Raspopin, F.N. Sattarov and N.I. Moskalenko, 1988, Rasplavy, **2**, 119 [Melts **2**].

Yamshchikov, L.F., A.V. Volynchuk, S.V. Kurochkin, F.N. Sattarov and S.P. Raspopin, 1989, Izv. Akad. Nauk SSSR, Met. **3**, 204 [Russ. Metall. **3**, 195].

Yamshchikov, L.F., F.N. Sattarov, I.V. Brettser-Portnov and S.P. Raspopin, 1990, Izv. Akad. Nauk SSSR, Met. **4**, 209 [Russ. Metall. **4**, 214].

Yang, Q., G. Liu and Z. Liu, 1989, Jinshu Xuebao **25**, B250.

Yoshihara, K., and M. Kanno, 1974a, J. Inorg. Nucl. Chem. **36**, 226.

Yoshihara, K., and M. Kanno, 1974b, J. Inorg. Nucl. Chem. **36**, 309.

Zaitsev, A.I., Yu.A. Priselkov and A.N. Nesmeyanov, 1982, Teplofiz. Vys. Temp. **20**, 866 [High Temp. (USSR) **20**, 701].

Zaitsev, A.I., Yu.A. Priselkov and A.N. Nesmeyanov, 1986a, Zh. Fiz. Khim. **60**, 2150 [Russ. J. Phys. Chem. **60**, 1290].

Zaitsev, A.I., A.V. Pronin, Yu.A. Priselkov and A.N. Nesmeyanov, 1986b, Teplofiz. Vys. Temp. **24**, 271 [High Temp. (USSR) **24**, 204].

Zandbergen, H.W., G. Van Tendeloo, D.B. de Mooij and K.H.J. Buschow, 1989, J. Less Common Met. **154**, 375.

Zhang, D., J. Tang and K.A. Gschneidner Jr, 1991, J. Less-Common Met. **169**, 45.

Zhou, H., X. Ou and X. Zhong, 1991, J. Alloys & Compounds **177**, 101.

SUBJECT INDEX